DE GRUYTER

STEM

THE CHEMISTRY OF OIL AND PETROLEUM PRODUCTS

Edited by Merv Fingas

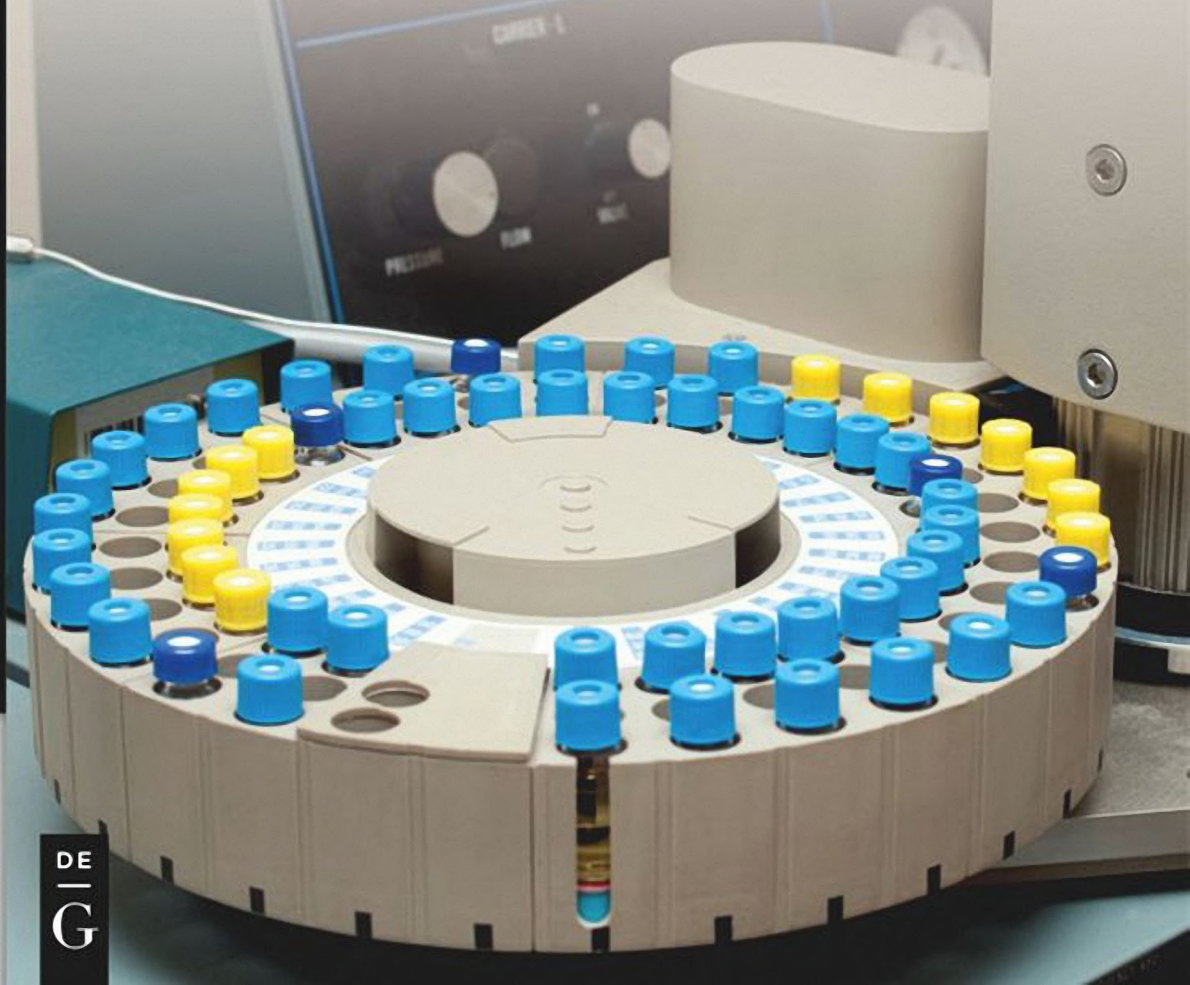

DE G

Merv Fingas (Ed.)
The Chemistry of Oil and Petroleum Products

Also of Interest

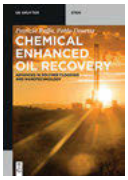

Chemical Enhanced Oil Recovery.
Advances in Polymer Flooding and Nanotechnology
Raffa, Druetta, 2019
ISBN 978-3-11-064024-3, e-ISBN (PDF) 978-3-11-064025-0

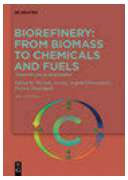

Biorefinery: From Biomass to Chemicals and Fuels.
Towards Circular EconomyTowards Circular Economy
Aresta, Dibenedetto, Dumeignil, 2021
ISBN 978-3-11-070536-2, e-ISBN (PDF) 978-3-11-070538-6

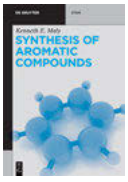

Synthesis of Aromatic Compounds
Maly, 2022
ISBN 978-3-11-056267-5, e-ISBN (PDF) 978-3-11-056268-2

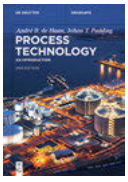

Process Technology.
An Introduction
De Haan, Padding, 2022
ISBN 978-3-11-071243-8, e-ISBN (PDF) 978-3-11-071244-5

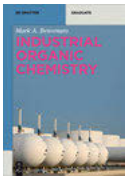

Industrial Organic Chemistry
Benvenuto, 2017
ISBN 978-3-11-049446-4, e-ISBN (PDF) 978-3-11-049447-1

The Chemistry of Oil and Petroleum Products

Edited by
Merv Fingas

DE GRUYTER

Editor
Dr. Merv Fingas
Spill Science
Edmonton, Alberta, Canada

ISBN 978-3-11-069436-9
e-ISBN (PDF) 978-3-11-069452-9
e-ISBN (EPUB) 978-3-11-069461-1

Library of Congress Control Number: 2022931644

Bibliographic information published by the Deutsche Nationalbibliothek
The Deutsche Nationalbibliothek lists this publication in the Deutsche Nationalbibliografie; detailed bibliographic data are available on the Internet at http://dnb.dnb.de.

Cover image: Gannet77/E+/Getty Images
Typesetting: Integra Software Services Pvt. Ltd.
Printing and binding: CPI books GmbH, Leck

www.degruyter.com

About the Editor

Merv Fingas is a scientist working on oil and chemical spills. He was Chief of the Emergencies Science Division of Environment Canada for over 30 years and is currently working on research in Western Canada. Dr. Fingas has a PhD in environmental physics from McGill University, three master degrees; chemistry, business and business mathematics, all from University of Ottawa. He also has a bachelor of science in Chemistry from Alberta and a bachelor of arts from Indiana. He has published more than 1000 papers and publications in the field. Merv has prepared 10 books on spill topics, this book will be his eleventh.He has served on two committees on the U.S. National Academy of Sciences of the United States on oil spills including the 'Oil in the Sea'. He is chairman of several ASTM committees on spill matters.

Dr. Fingas' specialities include; oil chemistry, spill dynamics and behaviour, spill treating agents, remote sensing and detection, and in-situ burning.

https://doi.org/10.1515/9783110694529-202

Preface

This book focuses on the chemistry of oil. All material in this book has been peer reviewed by at least two persons. The following peer reviewers are acknowledged (in alphabetical order): Han Bin, Paolo Bomben, Roman Borisov, Efim Brodsky, Pamela Brunswick, Aleksey Buryak, Silvio Canonica, Camilo Gelvez, Camilo Gonzalez, Murray Gray, Lindsay Hounjet, Abdul Gani Abdul Jameel, Lian Jiang, Hilkka Kenttamaa, Sudipa Mitra Kirtley, Anzor Mikaia, Oliver Mullins, Ed Overton, Todd Pugsley, Kuangnan Qian, Jagos Radovic, Yosadara Ruiz-Morales, Dayue Shang, Quan Shi, Greg Slater, Matt Tarr, Colin Ward, and Zeyu Yang. A special thanks goes out to the authors, many of whom put in their own time to complete their chapters. This is especially true because many of the authors were working on many other tasks during the preparation of this book. This "double duty" was greatly appreciated. The authors names appear throughout the text. I also like to thank the many people who provided support and encouragement throughout this project, including my colleagues and the staff of De Gruyter.

Merv Fingas,
January 2022

https://doi.org/10.1515/9783110694529-203

Contents

Merv Fingas

1 Introduction to oil chemistry

Abstract: This chapter is a review of petroleum chemistry, particularly as it relates to environmental issues. The traditional separation of saturates, aromatics, resins, and asphaltene (SARA) oil components is summarized. Further explanation of these groupings is given. A more detailed look at compounds found in oil and the amount of these common compounds is summarized. The compounds described are related to the overall composition and the SARA composition. Details of more than 500 compounds will be given in this introduction. The introduction provides a link to the various chapters in this book.

1.1 Introduction

Oil is a general term that describes a wide variety of natural substances of plant, animal, or mineral origin, and a range of synthetic compounds. This chapter covers crude oil and petroleum products derived from such oils. Crude oils are made up of hundreds of major constituents and thousands of minor ones.

The identification of compounds in an oil is known as "petroleomics." This field has expanded very rapidly in the past few years. Recently, it was possible to provide the elemental composition of 30,000 compounds of 1 crude oil [1]. Only a few years ago, it was considered advanced to have a few thousand compounds approximately identified [2]. There may be as many as 1 million compounds in that same oil if one were able to determine minor components. There is no doubt that in the future, there will be still more significant advances. An important point is that determining the elemental composition of compounds is not important in identifying the actual structure of those same compounds. Structure identification remains the challenge of the future.

1.2 The general composition of oil

Crude oils are complex mixtures of hydrocarbons and hydrocarbons, sometimes combined with other elements (such as N, S, and O), and ranging in size from smaller, volatile compounds to very large, nonvolatile compounds [3]. The mixture of compounds varies with the geological formation of the area in which the crude oil is found. Crude oil's compositions are often similar in a given region and when drawn from a similar reservoir. Petroleum products, such as gasoline and diesel

Merv Fingas, Spill Science, Edmonton, Alberta, Canada

https://doi.org/10.1515/9783110694529-001

fuel, are still very complex mixtures but have fewer compounds and are refined to specific operational standards in terms of their vapor pressures and viscosities. Thus, their properties are more specific and less variable. Crude oil contains many compounds of different sizes and different classes. In fact, there are so many that as time goes by, more and more compounds are identified in oil.

Hydrocarbon compounds are composed of hydrogen and carbon, which are the main elements in oils. Oils also contain varying amounts of sulfur, nitrogen, oxygen, and trace metals such as nickel, vanadium, and chromium. This section will detail some of these compounds. In general, the hydrocarbons found in oils are characterized by their structures.

Saturates are those hydrocarbons saturated with hydrogen. The saturate group includes straight-chain alkanes and branched-chain alkanes and also includes cycloalkanes, which are compounds made up of the same carbon and hydrogen constituents, but with the carbon atoms bonded to each other in rings or circular structures. Straight-chain saturate compounds from C18 and up are often referred to as waxes.

The elemental composition of oil is sometimes of interest. Crude oils have a typical composition as shown in Table 1.1 [4].

Table 1.1: Elemental composition of oil.

Element	Contents (%)
Carbon	83–87
Hydrogen	10–14
Nitrogen	0.05–6
Sulfur	0.1–2
Oxygen	0.05–1.5

1.2.1 Assessment of whole oil

Total petroleum hydrocarbons or TPH is one way to assess the overall composition of oils. TPH means different things for different situations [5]. For example, TPH of heavy oils may be carried out by solvent extraction and then measured gravimetrically. TPH in oil labs is often synonymous with gas chromatographic (GC)-resolvable hydrocarbons. TPH carried out by flame ionization detectors on a chromatograph responds only to simple hydrocarbon compounds and not to most polar compounds. It is often viewed as giving the GC-resolvable fraction of oil. GC-resolvable refers to single-column GC resolution and not more advanced techniques as described later in this book.

Yang et al. [6] carried out TPH measurements of several oils and petroleum products as shown in Table 1.2.

Table 1.2: Examples of TPH measurement data from [6].

	Crude oils			**(mg/g)**		
	Bakken Crude	Prudhoe Bay	Troll	Platform Elly	Oil sands bitumen	
Class	Light	Medium	Light	Heavy	Heavy	
TPH (mg/g)	691	549	723	436	302	
	Refined products					
	Jet A	Diesel fuel	IFO 180	Fuel oil #5	Bunker C	Lube oil (10 W-30)
Class				Heavy	Heavy	
TPH (mg/g)	914	957	463	476	370	808

Table 1.2 shows that heavy oils have few GC-resolvable compounds. For example, only about 30% of bitumen is readily resolvable by GC. On the other hand, diesel fuel can have about 95.7% readily resolvable compounds.

Worton et al. [7] studied Macondo oil that was spilled in the Gulf of Mexico incident and found that about 22% was not GC amendable. A summary of the findings is listed in Table 1.3.

Table 1.3: The eluting mass fractions of Macondo oil compared to simulated distillation (after Worton et al. [7]).

Mass fraction eluting	**Percent GC amendable**
(C9–C11)	13
(C12–C18)	27
(C19–C30)	24
(>C30)	4
Total	68

Table 1.3 shows that approximately 32% of the Macondo oil was not readily resolvable by GC. This 32% probably consists of polar compounds and high-molecular-weight compounds.

On a similar note, there have been efforts to study the molecular weight of various boiling point fractions of oil. Azinfar et al. [8] studied a bitumen and measured the molecular weight of the various boiling point fractions. The summary data as shown in Table 1.4 shows that the molecular weight of the bitumen fractions is high. The average molecular weight of this sample is 641 dalton.

These findings are interesting in that the Azinfar findings show that the molecular weight of oils may be higher than often thought and the Worton findings show

Table 1.4: Molecular weight of bitumen fractions (after Azinfar [8]).

Percent boiled off	Corrected molecular weight (dalton)
1	335.6
5	435.5
10	480.9
15	510.1
20	533
25	553
30	569.5
35	584.3
40	599.5
45	612.9
50	626.5
55	640.5
60	654.7
65	669.3
70	686.8
75	702.1
80	720.3
85	744.5
90	772.4
95	816.1
100	1222.4
Average	641

that there is a relatively large amount of material in even a light oil such as the Macondo oil that is not GC amendable.

1.2.2 SARA

A common and older method of classification is by SARA – saturates, aromatics, resins, and asphaltenes [3]. SARA's composition of oil is a more general analytical method which defines oils by precipitation and then by weight. Newer methods now employ thin-layer chromatography with flame ionization detection, and the values from both methods vary somewhat. This method is still useful, however, and it provides useful data both to the refiner and to the environmentalist. The saturate group of components in oils consists primarily of alkanes. The term, saturate, is used because the carbons are saturated with hydrogen. The saturate group includes straight-chain alkanes and branched-chain alkanes and also includes cycloalkanes, which are compounds made up of the same carbon and hydrogen constituents, but

with the carbon atoms bonded to each other in rings. Straight-chain saturate compounds from C18 and up are often referred to as waxes.

Table 1.5 shows the gross composition of some typical oils and petroleum products [3]. It is noted that the ranges of these compositions vary widely. Aromatics are hydrocarbon compounds with at least one benzene ring. Resins and asphaltenes are larger compounds containing mostly carbon and hydrogen but also containing other elements such as oxygen, sulfur, nitrogen, and metals.

Table 1.5: Typical composition of some oils and petroleum products.

Group	(% – except for metals)			Light crude	Heavy crude	IFO*	Bunker C
	Compound class	Gasoline	Diesel				
Saturates		50–60	65–95	55–90	25–80	25–35	20–30
	Alkanes	45–55	35–45	40–85	20–60	10–25	10–20
	Cycloalkanes	5	25–50	5–35	0–10	0–5	0–5
Olefins		5–10	0–10	nd	nd	nd	nd
Aromatics		25–40	5–25	10–35	15–40	40–60	30–50
	BTEX	15–25	0.5–2.0	0.1–2.5	0.01–2.0	0.05–1.0	0.00–1.0
	PAHs	nd	0–5	10–35	15–40	30–50	30–50
Polar compounds		nd	0–2	1–15	5–40	15–25	10–30
	Resins	nd	0–2	0–10	2–25	10–15	10–20
	Asphaltenes	nd	nd	0–10	0–20	5–10	5–20
Sulfur		0.02	0.1–0.5	0–2	0–5	0.5–2.0	2–4
Metals (in parts per million)			nd	30–250	100–500	100–1,000	100–2,000

*IFO is intermediate fuel oil which is residual fraction diluted by diesel fractions.
nd is not determined because quantities are very low.

1.2.3 Saturates

As noted in the general discussion on SARA, saturates are important economical constituents of oils. Saturates are largely used to produce gasoline and diesel fuel, the most sold products of crude oil. Saturates are often the most abundant compounds in any oil or petroleum product.

1.2.4 Alkanes

Alkanes, an important part of saturate composition, are hydrocarbons with a chain-like structure and without double bonds or other elements such as sulfur, nitrogen, or oxygen attached [9]. Alkanes, sometimes called paraffins, are typically the most abundant compounds in crude oils as well as in most fuels such as diesel fuel and

gasoline. Most crude oils have anywhere between a few percent up to 30% alkanes. Alkanes are typically the target compounds sought by petroleum producers. It should be noted, however, that larger alkanes are also called waxes, and these are less desirable from a petroleum producer's point of view.

Normal alkanes are those which are unbranched. All normal and branched alkanes have the generalized molecular formula of C_nH_{n+2} where n is the number of carbons present. All alkanes are saturated that is they contain the most hydrogen that the configuration can have. The branching potential for alkanes increases as the size of the alkane increases. Table 1.6 shows the typical alkanes contained in crude oils and some fuels [10–16]. Some properties and content of *n*-alkanes in some crude oils are also shown in this table. The column in Table 1.6 indicating the number of isomers shows the possible number of branched compounds. As can be seen in this table, the number of possible branched compounds rises to over 1 million by the time that carbon number 22 is reached. In fact, it is impossible to separate most branched compounds during chemical analysis. Thus, the specific nature of branched compounds in crude oils may be unknown for some time to come. The molecular weight of the compounds is given next and then the Chemical Abstracts number (CAS) and the solubility of the compound in water. The solubility of alkanes is low and beyond C20 is not measurable. The selective ion GCMS monitoring ion(s) (SIM) are given next.

Table 1.7 shows the amounts of alkanes in some typical oils. This table shows that the lowest molecular weight alkanes are most abundant in these oils.

1.2.5 Cycloalkanes

Cycloalkanes, compounds containing rings or cyclic structures, are also saturated alkanes. These are sometimes called naphthenes and have the general formula C_nH_{2n}. Figure 1.1 illustrates the three common baseline structures: cyclopentane, cyclohexane, and decahydronaphthalene. These base structures contribute to the majority of the cycloalkanes found in oil. The smaller cycloalkanes such as cyclopropane and cyclobutane are not common because they are not as stable since the smaller ring carbon bonds have considerable ring strain, being stretched above the normal carbon–carbon tetrahedral angle of 109°. Because of the carbon-to-carbon bond stress, there is no free rotation and thus there are stereoisomers (e.g., *cis*- and *trans*-isomers) for molecules above carbon number 6 (C6). Some cycloalkanes found in oils are shown in Table 1.8. Because cycloalkanes are low in abundance and may be difficult to separate in chromatographic analysis, there is not much data on their abundance in oils.

Table 1.6: Typical alkane compounds in oil.

Carbon number	Number of isomers	Formula	IUPAC name	Molecular weight	CAS number	Ref.	Solubility in water*(g/L)	Ref.	SIMS
5	3	C_5H_{12}	Pentane	72.149	109-66-0	[12]	$3.9\ E^{-2}$	[13]	57,71
6	5	C_6H_{14}	Hexane	86.175	110-54-3	[12]	~ 0.01	[15]	57,71,85
7	9	C_7H_{16}	Heptane	100.202	142-82-5	[12]	~ 0.003	[15]	57,71,85
8	18	C_8H_{18}	Octane	114.229	111-65-9	[12]	$0.7\ E^{-3}$	[15]	57,71,85
9	35	C_9H_{20}	Nonane	128.255	111-84.2	[12]	$1.2\ E^{-4}$	[13]	57,71,85
10	75	$C_{10}H_{22}$	Decane	142.282	124-18-5	[12]	~ $5\ E^{-5}$	[13]	57,71,85
11	159	$C_{11}H_{24}$	Undecane	156.309	1120-21-4	[12]	~ $6\ E^{-6}$	[13]	57,71,85
12	355	$C_{12}H_{26}$	Dodecane	170.334	112-40-3	[12]	~ $2\ E^{-6}$	[13]	57,71,85
13	802	$C_{13}H_{28}$	Tridecane	184.361	629-50-5	[12]	~ $4\ E^{-7}$	[13]	57,71,85
14	1858	$C_{14}H_{30}$	Tetradecane	198.388	629-59-4	[12]	~ $3\ E^{-7}$	[13]	57,71,85
15	4347	$C_{15}H_{32}$	Pentadecane	212.415	629-62-9	[12]	~ $4\ E^{-8}$	[13]	57,71,85
16	1.04E + 04	$C_{16}H_{34}$	Hexadecane	226.441	544-76-3	[12]	<$6\ E^{-6}$	[13]	57,71,85
17	2.49E + 04	$C_{17}H_{36}$	Heptadecane	240.468	629-78-7	[12]			57,71,85
18	6.05E + 04	$C_{18}H_{38}$	Octadecane	254.495	593-45-3	[12]	$5.8\ E^{-6}$	[13]	57,71,85
19	1.48E + 05	$C_{19}H_{40}$	Nonadecane	268.521	629-92-5	[12]			57,71,85
20	3.66E + 05	$C_{20}H_{42}$	Icosane	282.547	112-95-8	[12]			57,71,85
21	9.11E + 05	$C_{21}H_{44}$	Henicosane	296.574	629-94-7	[12]			57,71,85
22	2.28E + 06	$C_{22}H_{46}$	Docosane	310.6	629-97-0	[12]			57,71,85
23	5.73E + 06	$C_{23}H_{48}$	Tricosane	324.627	638-67-5	[12]			57,71,85
24	1.45E + 07	$C_{24}H_{50}$	Tetracosane	338.654	646-31-1	[12]			57,71,85
25	3.68E + 07	$C_{25}H_{52}$	Pentacosane	352.681	629-99-2	[12]			57,71,85
26	9.38E + 07	$C_{26}H_{54}$	Hexacosane	366.707	630-01-3	[12]			57,71,85
27	2.40E + 08	$C_{27}H_{56}$	Heptacosane	380.734	593-49-7	[12]			57,71,85
28	6.17E + 08	$C_{28}H_{58}$	Octacosane	394.761	630-02-4	[12]			57,71,85
29	1.59E + 09	$C_{29}H_{60}$	Nonacosane	408.786	630-03-5	[12]			57,71,85
30	4.11E + 09	$C_{30}H_{62}$	Triacontane	422.813	638-68-6	[12]			57,71,85

*Approximate sign ~ indicates that solubility values are variable.

Table 1.7: Typical alkane compound quantity in oils.

Carbon number	Formula	IUPAC name	Levels in ASMB* (mg/g oil)	Ref.	Levels in ANS* (mg/g oil)	Levels in diesel fuel (mg/g oil)	Levels in heavy fuel oil (mg/g oil)	Ref.
5	C_5H_{12}	Pentane						
6	C_6H_{14}	Hexane						
7	C_7H_{16}	Heptane						
8	C_8H_{18}	Octane	5	[10]		1	–	[11]
9	C_9H_{20}	Nonane	4	[10]	4	4	–	[11]
10	$C_{10}H_{22}$	Decane	4	[10]	4	11	–	[11]
11	$C_{11}H_{24}$	Undecane	4	[10]	4	13	0.5	[11]
12	$C_{12}H_{26}$	Dodecane	4	[10]	4	13	1	[11]
13	$C_{13}H_{28}$	Tridecane	4	[10]	4	13	1	[11]
14	$C_{14}H_{30}$	Tetradecane	4	[10]	3	12	1	[11]
15	$C_{15}H_{32}$	Pentadecane	3	[10]	3	12	1	[11]
16	$C_{16}H_{34}$	Hexadecane	3	[10]	3	11	2	[11]
17	$C_{17}H_{36}$	Heptadecane	3	[10]	3	9	2	[11]
18	$C_{18}H_{38}$	Octadecane	3	[10]	3	7	2	[11]
19	$C_{19}H_{40}$	Nonadecane	2	[10]	2	5	2	[11]
20	$C_{20}H_{42}$	Icosane	2	[10]	2	3	2	[11]
21	$C_{21}H_{44}$	Henicosane	2	[10]	2	2	2	[11]
22	$C_{22}H_{46}$	Docosane	2	[10]	2	1	2	[11]
23	$C_{23}H_{48}$	Tricosane	2	[10]	2	0.5	1	[11]
24	$C_{24}H_{50}$	Tetracosane	2	[10]	2	0.2	1	[11]
25	$C_{25}H_{52}$	Pentacosane	1	[10]	1	–	1	[11]
26	$C_{26}H_{54}$	Hexacosane	1	[10]	1	–	1	[11]
27	$C_{27}H_{56}$	Heptacosane	1	[10]	1	–	0.5	[11]
28	$C_{28}H_{58}$	Octacosane	1	[10]	1	–	0.5	[11]
29	$C_{29}H_{60}$	Nonacosane	1	[10]	1	–	–	[11]
30	$C_{30}H_{62}$	Triacontane	1	[10]	1	–	–	[11]

*ASMB is Alberta Sweet Mixed Blend crude oil.
**ANS is Alaska North Slope crude oil.

1.2.6 Alkenes or olefins

The olefins, or unsaturated compounds, are another group of compounds that contain less hydrogen atoms than the maximum possible. Olefins have at least one double carbon-to-carbon bond which displaces two hydrogen atoms. Significant amounts of olefins are found only in refined products; however, some cyclic alkenes have been observed in crude oils [2]. It should be noted that SARA analysis does not include alkenes, and there is no simple method to separate to them from many other hydrocarbons.

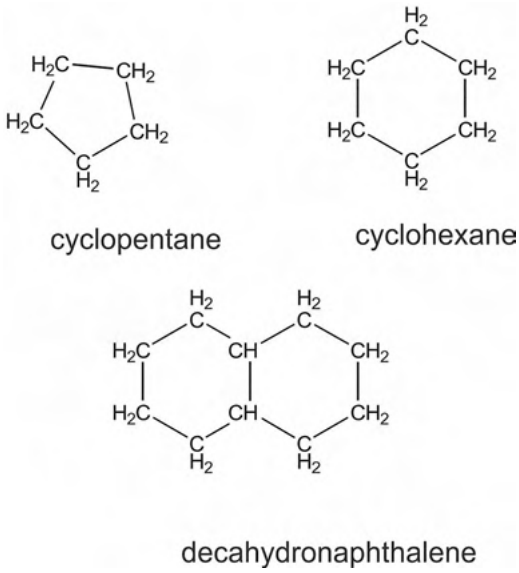

Figure 1.1: Structures of common cycloalkanes in oils.

1.2.7 Aromatic compounds

The aromatic compounds include at least one benzene ring of six carbons. Three carbon-to-carbon double bonds float around the ring and all six carbons are equivalent and thus providing high stability to the ring. Because of this stability, benzene rings are very persistent and can have toxic effects on the environment. The most common smaller aromatic compounds found in oil are often referred to as BTEX (benzene, toluene, ethyl-benzene, and xylenes). BTEX compounds and data on them are shown in Table 1.9. The quantity of BTEX compounds in typical oils is shown in Table 1.10.

Polycyclic hydrocarbons or PAHs are compounds consisting of at least two benzene rings. PAHs make up between 0% and 60% of the composition of crude oil. Common PAHs and their substituted counterparts are shown in Table 1.11. As these are easily separated, there are plenteous data on their presence in oils. These compounds have also been used somewhat as indicators of presence of certain types of oils. Table 1.12 shows the typical amounts of PAHs in some oils and oil products. Table 1.12 shows that naphthalenes have the highest concentrations in these oils.

Table 1.8: Cycloalkanes found in oil and petroleum.

Carbon number	Formula	IUPAC name	Molecular weight	CAS number	Reference	Solubility in water* (g/L)	Reference
5	C_5H_{10}	Cyclopentane	70.133	287-92-3	[12]	0.16	[13]
6	C_6H_{12}	Methylcylopentane	84.159	96-37-7	[12]	4.1 E^{-2}	[13]
7	C_7H_{14}	Dimethylcyclopentane	98.186	1	[12]		
8	C_8H_{16}	Trimethylcyclopentane	112.21	2	[12]	~ 3.7 E^{-3}	[13]
6	C_6H_{12}	Cyclohexane	84.159	110-82-7	[12]	5.5 E^{-2}	[13]
7	C_7H_{14}	Methylcyclohexane	98.186	108-87-2	[12]	~ 1.6 E^{-2}	[13]
8	C_8H_{16}	Dimethylcyclohexane	112.213	*3*	[12]	6 E^{-3}	[13]
8	C_8H_{16}	Ethylcyclohexane	112.213	1678-91-7	[12]	<6 E^{-3}	[13]
9	C_9H_{18}	Trimethylcyclohexane	126.239	4	[12]	1.7 E^{-3}	[13]
10	$C_{10}H_{18}$	*cis*-Decahydronaphthalene	138.25	493-01-6	[12]	~ 8.5 E^{-4}	[13]
10	$C_{10}H_{18}$	*trans*-Decahydronaphthalene	138.25	493-02-7	[12]	~ 8.5 E^{-4}	[13]

*Approximate sign ~ indicates that solubility values are variable.

1 CAS numbers for dimethylcyclopentanes: 1,1 – 1638-26-2; *cis*-1,2 – 1192-18-3; *trans*-1,2 – 822-50-4; *cis*-1,3 – 2532-58-3; *trans*-1,3 – 1759-58-6.

2 CAS numbers for trimethylcyclopentanes: 1,1,2 – 4259-00-1; 1,1,3 – 4516-69-2; 1α,2α,4β-1,2,4 – 4850-28-6; 1α,2β,4α,-1,2,4 – 16883-48-0.

3 CAS numbers for dimethylcyclohexanes: 1,1 – 590-66-9; *cis*-1,2 – 2207-01-4; *trans*-1,2 – 6876-23-9; *cis*-1,3 – 638-04-0; *trans*-1,3 – 2207-03-6; *cis*-1,4 – 624-29-3; *trans*-1,4 – 2207-04-7.

4 CAS numbers for trimethylcyclohexanes: 1,1,2 – 7094-26-0; 1,1,3 – 3073-66-3; 1α,2β,4β,-1,2,4 – 7667-60-9; 1α,3α,5β-1,3,5 – 1795-26-2.

Table 1.9: BTEX compounds found in oils and petroleum.

Carbon number	Name	Formula	Molecular weight	CAS number*	Ref.	Solubility in water** (g/L)	Ref.	SIMS
6	Benzene	C_6H_6	78.112	71-43-2	[12]	~1.8	[13]	78
7	Toluene	C_7H_8	92.139	108-88-3	[12]	0.5 to 0.6	[13]	92
8	Ethyl-benzene	C_8H_{10}	106.165	100-41-4	[12]	0.15 to 0.2	[13]	106
8	*m*-Xylene	C_8H_{10}	106.165	108-38-3	[12]	0.14 to 0.16	[13]	106
8	*o*-Xylene	C_8H_{10}	106.165	95-47-6	[12]	0.17 to 0.2	[13]	106
8	*p*-Xylene	C_8H_{10}	106.165	106-42-3	[12]	~ 0.16	[13]	106
9	1,2,3-Trimethyl-benzene	C_9H_{12}	120.191	526-73-8	[12]	~ 7 E^{-2}	[13]	120
9	1,2,4-Trimethyl-benzene	C_9H_{12}	120.191	95-63-6	[12]	5.9 E^{-2}	[13]	120
9	1,3,5-Trimethyl-benzene	C_9H_{12}	120.191	108-67-8	[12]	~ 5 E^{-2}	[13]	120
9	1-Ethyl-2-methyl-benzene	C_9H_{12}	120.191	611-14-3	[12]	~ 7.5 E^{-2}	[13]	120
9	1-Ethyl-3-methyl-benzene	C_9H_{12}	120.191		[12]			120
9	1-Ethyl-4-methyl-benzene	C_9H_{12}	120.191	622-96-8	[12]			120
9	*iso*-Propyl-benzene	C_9H_{12}	120.191	98-82-8	[12]	5 to 6 E^{-2}	[13]	120
9	Propyl-benzene	C_9H_{12}	120.191	103-65-1	[12]	~ 5 E^{-2}	[13]	120
10	1,2,3,4-Tetramethyl-benzene	$C_{10}H_{14}$	134.218	488-23-3	[12]			134
10	1,2,3,5-Tetramethyl-benzene	$C_{10}H_{14}$	134.218	537-53-7	[12]			134
10	1,2,4,5-Tetramethyl-benzene	$C_{10}H_{14}$	134.218	95-93-2	[12]	3.5 E^{-3}	[13]	134
10	1,2-Diethyl-benzene	$C_{10}H_{14}$	134.218	135-01-3	[12]	~ 7 E^{-2}	[13]	134
10	1,3-Diethyl-benzene	$C_{10}H_{14}$	134.218	141-93-5	[12]			134
10	1,4-Diethyl-benzene	$C_{10}H_{14}$	134.218	105-5-5	[12]	~ 2.5 E^{-2}	[13]	134
10	1-Ethyl-2,4-dimethyl-benzene	$C_{10}H_{14}$	134.218	874-41-9	[12]			134
10	1-Ethyl-3,5-dimethyl-benzene	$C_{10}H_{14}$	134.218	934-74-7	[12]			134
10	1-Methyl-2-propyl-benzene	$C_{10}H_{14}$	134.218	1074-17-5	[12]	~ 1 E^{-2}	[13]	134
10	1-Methyl-3-propyl-benzene	$C_{10}H_{14}$	134.218	1074-43-7	[12]	~ 1 E^{-2}	[13]	134

Table 1.9 (continued)

Carbon number	Name	Formula	Molecular weight	CAS number*	Ref.	Solubility in water** (g/L)	Ref.	SIMS
10	1-Methyl-4-propyl -benzene	$C_{10}H_{14}$	134.218	1074-55-1	[12]	~ 1 E^{-2}	[13]	134
10	2-Ethyl-1,3-dimethyl-benzene	$C_{10}H_{14}$	134.218	2870-04-4	[12]			134
10	2-Ethyl-1,4-dimethyl-benzene	$C_{10}H_{14}$	134.218	1758-88-9	[12]			134
10	3-Ethyl-1,2-dimethyl-benzene	$C_{10}H_{14}$	134.218	933-98-2	[12]			134
10	4-Ethyl-1,2-dimethyl-benzene	$C_{10}H_{14}$	134.218	934-80-5	[12]			134
10	Butyl-benzene	$C_{10}H_{14}$	134.218	104-51-8	[12]	1.2 to 1.4 E^{-2}	[13]	134
10	*sec*-Butyl benzene	$C_{10}H_{14}$	134.218	135-98-8	[12]	1.1 to 1.8 E^{-2}	[13]	134
10	*iso*-Butyl benzene	$C_{10}H_{14}$	134.218	538-93-2	[12]			134
10	*m*-Cymene	$C_{10}H_{14}$	134.218	535-77-3	[12]			134
10	*p*-Cymene	$C_{10}H_{14}$	134.218	99-87-6	[12]	~ 3 E^{-2}	[13]	134
10	*tert*-Butyl-benzene	$C_{10}H_{14}$	134.218	98-06-6	[12]	1.8 to 3 E^{-2}	[13]	134
11	Pentyl-benzene	$C_{11}H_{16}$	148.245	538-68-1	[12]			148
	iso-Pentyl-benzene	$C_{11}H_{16}$	148.245	2049-94-7	[12]	~ 3.5 E^{-3}	[13]	148
11	Diethyl-trimethyl-benzene	$C_{11}H_{16}$	148.245		[12]		[13]	148
11	Ethyl-tetramethyl-benzene	$C_{11}H_{16}$	148.245		[12]		[13]	148
11	Methyl-diethyl-benzene	$C_{11}H_{16}$	148.245		[12]		[13]	148
11	Methyl-butyl-benzene	$C_{11}H_{16}$	148.245		[12]		[13]	148
11	Pentamethyl-benzene	$C_{11}H_{16}$	148.245	700-12-9	[12]	~ 1.5 E^{-2}	[13]	148
12	C6-Benzenes	$C_{12}H_{18}$	162.271	1077-16-3*	[12]		[13]	162
13	C7-Benzenes	$C_{14}H_{20}$	176.298	1078-71-3*	[12]		[13]	176
14	C8-Benzenes	$C_{16}H_{22}$	190.325	2189-60-8*	[12]		[13]	190

*CAS number is applicable to simplest aliphatic compound only.

**Approximate sign ~ indicates that solubility values are variable; a range indicates the range of values.

There exists a set of compounds designated by the U.S. EPA as priority PAHs [10]. The priority is based on the toxicity to humans and the environment. The list of 16 EPA priority chemicals is shown in Table 1.13 and the typical quantities of these in some oils in Table 1.14. Table 1.14 shows that even moderate molecular weight compounds are found in oils such as heavy fuel oil.

Table 1.10: Quantity of BTEX compounds found in oils and petroleum.

Carbon number	Name	Formula	Levels in ASMB (µg/g oil)	Ref.	Levels in ANS (µg/g oil)	Levels in diesel fuel (µg/g oil)	Levels in heavy fuel oil (µg/g oil)	Ref.
6	Benzene	C_6H_6	2,300	[11]	2,900	140	40	[11]
7	Toluene	C_7H_8	5,300	[11]	5,900	1,000	140	[11]
8	Ethyl-Benzene	C_8H_{10}	1,600	[11]	1,300	620	60	[11]
8	*m*-Xylene	C_8H_{10}	8,900**	[11]	6,200**	3,800**	400**	[11]
8	*o*-Xylene	C_8H_{10}	–		–	–	–	
8	*p*-Xylene	C_8H_{10}	–		–	–	–	
9	1,2,3-Trimethyl-benzene	C_9H_{12}	1,200**	[11]	5,600**	14,800**	940**	[11]
9	1,2,4-Trimethyl-benzene	C_9H_{12}	–		–	–	–	
9	1,3,5-Trimethyl-benzene	C_9H_{12}	–		–	–	–	
9	1-Ethyl-2-methyl-benzene	C_9H_{12}	–		–	–	–	
9	1-Ethyl-3-methyl-benzene	C_9H_{12}	–		–	–	–	
9	1-Ethyl-4-methyl-benzene	C_9H_{12}	–		–	–	–	
9	*iso*-Propyl-benzene	C_9H_{12}	–		–	–	–	
9	Propyl-benzene	C_9H_{12}	–		–	–	–	

**Quantitation for all isomers of these compounds.

Andersson and Achten [17] reviewed the toxicity of the 16 priority PAHs and concluded that many NSO compounds are more toxic than these 16 priority compounds. They advocate for a review of priority toxic compounds and made several suggestions for toxic compounds as shown in Table1.15.

EPA also developed a list of 34 priority PAHs in addition to those found on their initial list of 16 priority pollutants. The list of 34 EPA priority chemicals is shown in Table 1.16. The quantities of these 34 compounds typically found in typical oils is shown in Table 1.17. The concern with these compounds is that many of them are known to be relatively toxic.

Aromatic compounds have the general formula C_nH_{2n-6r}, where r is the number of rings. The amount of aromatics in a typical crude oil varies, but ranges from near 0% to 15%. Larger aromatics are frequently concentrated by distillation in the refining processes into the heavier or residual fractions. Diesel fuel typically contains 5–25% aromatics while gasoline contains 25–40% aromatics, mostly BTEX compounds, but little or no benzene. In crude oils, the alkylated compounds occur more frequently than the parent unalkylated rings. This can be of use in identifying

Table 1.11: PAHs and alkylated PAHS found in oils and petroleum.

Carbon number	Number of rings	Name	Formula	Abbreviation	Molecular weight	CAS number	Ref.	Solubility in Water* g/L	Ref.	SIMS
10	2	Naphthalene	$C_{10}H_8$	C_0N	128.717	91-20-3	[12]	30 to 30 E^{-3}	[15]	128
11	2	Methyl-naphthalene	$C_{11}H_{10}$	C_1N	142.197	*1*	[12]	26 to 28 E^{-3}	[15]	142
12	2	Di-methyl-naphthalene	$C_{12}H_{12}$	C_2N	156.233	*2*	[12]	~ 2.4 E^{-3}	[15]	156
12	2	Ethyl-naphthalene	$C_{12}H_{12}$	C_2N	156.233	*3*	[12]	~ 1 E^{-2}	[13]	156
13	2	C3-Naphthalenes	$C_{13}H_{14}$	C_3N	170.25	*4*	[12]	~ 1.6 E^{-3}	[15]	170
14	2	C4-Naphthalenes	$C_{14}H_{16}$	C_4N						184
14	3	Phenanthrene	$C_{14}H_{10}$	C_0P	178.229	85-01-8	[12]	~ 1 E^{-3}	[13]	178
15	3	C1-Phenanthrenes	$C_{15}H_{12}$	C_1P	192.256	5	[12]	~ 7 E^{-5}	[13]	192
16	3	C2-Phenanthrenes	$C_{16}H_{14}$	C_2P						206
17	3	C3-Phenanthrenes	$C_{17}H_{16}$	C_1P						220
18	3	C4-Phenanthrenes	$C_{18}H_{16}$	C_1P						234
12	3	Dibenzothiophene	$C_{12}H_8S$	C_0D	184.257	132-65-0	[12]	5 E^{-4}	[13]	184
13	3	C1-Dibenzothiophenes	$C_{13}H_{10}S$	C_1D						198
14	3	C2-Dibenzothiophenes	$C_{14}H_{12}S$	C_2D						212
15	3	C3-Dibenzothiophenes	$C_{15}H_{14}S$	C_3D						226
13	3	Fluorene	$C_{13}H_{10}$	C_0F	166.218	86-73-7	[12]	~ 8 E^{-5}	[15]	166
14	3	C1-Fluorenes	$C_{14}H_{12}$	C_0F	180.245	6	[12]			180
15	3	C2-Fluorenes	$C_{15}H_{14}$	C_0F						194
16	3	C3-Fluorenes	$C_{16}H_{16}$	C_0F						208
18	4	Chrysene	$C_{18}H_{12}$	C_0C	228.288	218-01-9	[12]	~ 1.5 E^{-6}	[15]	228
19	4	C1-Chrysenes	$C_{19}H_{14}$	C_0C	242.314	7	[12]			242

20	4	C2-Chrysenes	$C_{20}H_{16}$	C_0C						256
21	4	C3-Chrysenes	$C_{21}H_{18}$	C_0C						270
20	5	Perylene	$C_{20}H_{12}$		252.309	198-55-0	[12]	~ 4 E^{-7}	[15]	252

*Approximate sign ~ indicates that solubility values are variable; a range indicates the range of values.

1 CAS numbers for methyl naphthalenes – ***1*** – 90-12-0; ***2*** – 91-57-6

2 CAS numbers for di-methyl naphthalenes – **1,2** – 573-98-8; ***1,3*** – 575-41-7; ***1,4*** – 571-58-4; ***1,5*** – 571-61-9; **1,6** – 575-43-9; **1,7** – 575-37-1; **1,8** – 569-41-5 ***2,3*** – 581-40-8; ***2,6*** – 581-42-0; ***2,7*** – 582-16-1.

3 CAS numbers for ethyl naphthalenes – ***1*** – 1127-76-0; ***2*** – 939-27-5.

4 CAS numbers for 1,4,5-trimethyl naphthalene – 2131-41-1

5 CAS numbers for methyl phenanthrenes – ***1*** – 832-69-9; ***3*** – 832-71-3; ***4*** – 832-64-4.

6 CAS numbers for methyl fluorenes – ***1*** – 1730-37-6; ***9*** – 2523-37-7.

7 CAS numbers for methyl chrysenes – ***3*** – 3351-31-3; ***5*** – 3697-24-3; ***6*** – 1705-85-7.

Table 1.12: Quantity of PAHs and alkylated PAHS found in oils and petroleum.

Carbon number	Number of rings	Name	Formula	Abbreviation	Levels in ASMB (µg/g oil)	Ref.	Levels in ANS (µg/g oil)	Levels in diesel fuel (µg/g oil)	Levels in heavy fuel oil (µg/g oil)	Ref.
10	2	Naphthalene	$C_{10}H_8$	C_0N	680	[10]	260	820	140	[11]
11	2	Methyl-naphthalene	$C_{11}H_{10}$	C_1N	1,180	[10]	1,000	3,700	1,300	[11]
12	2	Di-methyl-naphthalene	$C_{12}H_{12}$	C_2N	1,600	[10]	1,800	7,000	2,900	[11]
12	2	Ethyl-naphthalene	$C_{12}H_{12}$	C_2N	"		"	"	"	
13	2	C3-Naphthalenes	$C_{13}H_{14}$	C_3N	1,560	[10]	1,700	6,600	2,900	[11]
14	2	C4-Naphthalenes	$C_{14}H_{16}$	C_4N	450	[10]	820	2,800	1,400	[11]
14	3	Phenanthrene	$C_{14}H_{10}$	C_0P	170	[10]	210	440	420	[11]
15	3	C1-Phenanthrenes	$C_{15}H_{12}$	C_1P	400	[10]	670	1,000	1,900	[11]
16	3	C2-Phenanthrenes	$C_{16}H_{14}$	C_2P	400	[10]	710	620	2,900	[11]
17	3	C3-Phenanthrenes	$C_{17}H_{16}$	C_1P	160	[10]	490	190	3,100	[11]
18	3	C4-Phenanthrenes	$C_{18}H_{16}$	C_1P	60	[10]	300	50	2,200	[11]
12	3	Dibenzothiophene	$C_{12}H_8S$	C_0D	200	[10]	120	70	100	[11]
13	3	C1-Dibenzothiophenes	$C_{13}H_{10}S$	C_1D	370	[10]	230	110	320	[11]
14	3	C2-Dibenzothiophenes	$C_{14}H_{12}S$	C_2D	450	[10]	320	100	620	[11]
15	3	C3-Dibenzothiophenes	$C_{15}H_{14}S$	C_3D	220	[10]	270	40	700	[11]
13	3	Fluorene	$C_{13}H_{10}$	C_0F	50	[10]	140	570	220	[11]
14	3	C1-Fluorenes	$C_{14}H_{12}$	C_0F	110	[10]	330	800	570	[11]
15	3	C2-Fluorenes	$C_{15}H_{14}$	C_0F	150	[10]	450	760	1,000	[11]
16	3	C3-Fluorenes	$C_{16}H_{16}$	C_0F	85	[10]	380	360	940	[11]
18	4	Chrysene	$C_{18}H_{12}$	C_0C	25	[10]	50	<1	380	[11]
19	4	C1-Chrysenes	$C_{19}H_{14}$	C_0C			70	<1	1,200	[11]
20	4	C2-Chrysenes	$C_{20}H_{16}$	C_0C			100	<1	1,800	[11]
21	4	C3-Chrysenes	$C_{21}H_{18}$	C_0C			80		1,400	[11]
20	5	Perylene	$C_{20}H_{12}$							

Table 1.13: EPA top 16 priority PAHs.

Compound	Molecular formula	Structure	CAS no.	MW	Ref.	Human* carcinogenicity	Solubility in water** (µg/L)	Ref.	SIMS
Naphthalene	$C_{10}H_8$		91-20-3	128.171	[12]		~ 3.5 E^{-2}	[13]	128
Acenaphthene	$C_{12}H_{10}$		83-32-9	154.207	[12]		3.4 E^{-3}	[13]	153
Acenaphthylene	$C_{12}H_8$		208-96-8	152.192	[12]		~ 4 E^{-3}	[13]	152
Fluorene	$C_{13}H_{10}$		86-73-7	166.218	[12]		~ 2 E^{-3}	[13]	166
Phenanthrene	$C_{14}H_{10}$		85-01-8	178.229	[12]		~ 1 E^{-3}	[13]	178
Anthracene	$C_{14}H_{10}$		120-12-7	178.229	[12]		4 to 7 E^{-5}	[13]	178
Fluoranthene	$C_{16}H_{10}$		206-44-0	202.25	[12]		2.7 E^{-4}	[13]	202
Pyrene	$C_{16}H_{10}$		129-00-0	202.25	[12]		0.9 to 1.4 E^{-4}	[13]	202
Benz(a)anthracene	$C_{18}H_{12}$		56-55-3	228.288	[12]	2	0.9 to 1.3 E^{-5}	[13]	228
Chrysene	$C_{18}H_{12}$		218-01-9	228.288	[12]	1	2 to 1.6 E^{-6}	[13]	228

(continued)

Table 1.13 (continued)

Compound	Molecular formula	Structure	CAS no.	MW	Ref.	Human* carcinogenicity	Solubility in water** (µg/L)	Ref.	SIMS
Benzo(b)fluoranthene	$C_{20}H_{12}$		205-99-2	252.309	[12]	3	~ 1.5 E^{-6}	[13]	252
Benzo(k)fluoranthene	$C_{20}H_{12}$	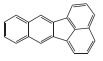	207-08-9	252.309	[12]		~ 1 E^{-6}	[13]	252
Benzo(a)pyrene	$C_{20}H_{12}$		50-32-8	252.309	[12]	4	1.4–3.8 E^{-6}	[13]	252
Dibenz(a,h)anthracene	$C_{22}H_{14}$	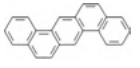	53-70-3	278.346	[12]	4	~ 1 E^{-6}	[13]	278
Benzo(g,h,i)perylene	$C_{22}H_{12}$		191-24-2	276.33	[12]		1.8–2.6 E^{-7}	[13]	276
Indeno(1,2,3-cd) pyrene	$C_{22}H_{12}$	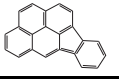	193-39-5	276.33	[12]	2	~ 2 E^{-7}	[13]	276

*Carcinogenic potency, 1 is a suspected carcinogen, and 4 is a known potent carcinogen.
**Approximate sign ~ indicates that solubility values are variable; a range indicates the range of values.

Table 1.14: Quantities of EPA top 16 priority PAHs in some oils.

Compound	Molecular formula	Structure	CAS no.	Levels in ASMB (µg/g oil)	Ref.	Levels in ANS (µg/g oil)	Levels in diesel fuel (µg/g oil)	Levels in heavy fuel oil (µg/g oil)	Ref.
Naphthalene	$C_{10}H_8$		91-20-3	250	[11]	260	820	140	[11]
Acenaphthene	$C_{12}H_{10}$	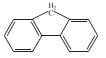	83-32-9	16	[11]	13	150	90	[11]
Acenaphthylene	$C_{12}H_8$		208-96-8	8	[11]	12	35	20	[11]
Fluorene	$C_{13}H_{10}$	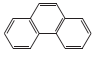	86-73-7	80	[11]	140	560	220	[11]
Phenanthrene	$C_{14}H_{10}$	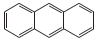	85-01-8	140	[11]	210	440	420	[11]
Anthracene	$C_{14}H_{10}$		120-12-7	2	[11]	3	13	95	[11]
Fluoranthene	$C_{16}H_{10}$		206-44-0	2	[11]	3	7	40	[11]
Pyrene	$C_{16}H_{10}$		129-00-0	18	[11]	8	31	230	[11]
Benz(a)anthracene	$C_{18}H_{12}$		56-55-3	3	[11]	5	0.3	200	[11]

(continued)

Table 1.14 (continued)

Compound	Molecular formula	Structure	CAS no.	Levels in ASMB (µg/g oil)	Ref.	Levels in ANS (µg/g oil)	Levels in diesel fuel (µg/g oil)	Levels in heavy fuel oil (µg/g oil)	Ref.
Chrysene	$C_{18}H_{12}$		218-01-9	30	[11]	50	<1	380	[11]
Benzo(b)fluoranthene	$C_{20}H_{12}$	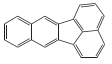	205-99-2	3	[11]	5	0	50	[11]
Benzo(k)fluoranthene	$C_{20}H_{12}$	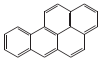	207-08-9	3	[11]	1	0	10	[11]
Benzo(a)pyrene	$C_{20}H_{12}$	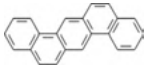	50-32-8	1	[11]	2	0	150	[11]
Dibenz(a,h)anthracene	$C_{22}H_{14}$		53-70-3	1	[11]	1	0	20	[11]
Benzo(g,h,i)perylene	$C_{22}H_{12}$	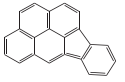	191-24-2	3	[11]	3	0	30	[11]
Indeno(1,2,3-cd) pyrene	$C_{22}H_{12}$	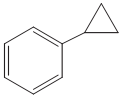	193-39-5	1	[11]	0.1	0	10	[11]

Table 1.15: Suggested alternative priority candidates (after Andersson and Achten [17]).

Class	Compounds	Class	Compounds
PAOH		**Metabolites**	
1	Benzofuran	**NSO heterocycles**	
2	Methylbenzofurans	1	Quinolinone
3	Dimethylbenzofurans	2	Isoquinolinone
4	Dibenzofuran	3	Methylquinolinones
5	Methyldibenzofuran	4	Acridone
6	Xanthene	5	Phenanthridone
PANH		6	Xanthenone
7	Indole	**Oxy-PAHs**	
8	Quinoline	1	1-Indanone
9	Methylquinolines	2	Fluoren-9-one
10	Dimethylquinolines	3	Phenanthrene-9,10-dione
11	Isoquinoline	4	2-Methylanthracenedione
12	Methylisochinolines	5	Cyclopenta[def]phenanthrenone
13	Carbazole	6	Benzo[a]fluorenone
14	Phenanthridine	7	Benzo[de]anthracene-7-one
15	Acridine	8	Benzo[a]anthracene-7,12-dione
16	Benzo[h]quinoline	9	Naphthacene-5,12-dione
17	Dibenzo[c,g]carbazole	10	Benzo[cd]pyren-6-one
18	Dibenzo[a,h]acridine	**Nitro-PAHs**	
19	Dibenzo[a,j]acridine	1	2-Nitronaphthalene
PASH		2	3,7-Dinitrofluoranthene
20	Benzothiophene	3	3,9-Dinitrofluoranthene
21	Methylbenzothiophene	4	1-Nitropyrene
22	Dibenzothiophene	5	4-Nitropyrene
23	Methyldibenzothiophene	6	1,6-Dinitropyrene
		7	1,8-Dinitropyrene
		8	6-Nitrochrysene
		9	7-Nitrobenzo[a]anthracene
		10	6-Nitrobenzo[a]pyrene
		Amino-PAHs	
		1	1-Aminonaphthalene
		2	2-Aminonaphthalene
		3	Aminophenanthrenes
		4	2-Aminoanthracene
		5	Aminofluoranthenes
		6	Aminopyrenes

the source of contamination as many PAH pollution sources have more abundant parent compounds than alkylated ones. Most alkylated PAHs are often less toxic and soluble than their unalkylated counterparts [18].

Table 1.16: EPA 34 priority PAHs.

Carbon number	Number of rings	Name	Formula	Abbreviation	Molecular weight	CAS number	Ref.	Solubility in water* (g/L)	Ref.	U.S. EPA toxicity value **	SIMS
10	2	Naphthalene	$C_{10}H_8$	NAP	128.717	91-20-3	[12]	~ 3.5 E^{-2}	[13]	193.47	128
11	2	1-Methyl-naphthalene	$C_{11}H_{10}$	1MN	142.197	90-12-0	[12]	~ 2.8 E^{-2}	[13]	72.16	142
11	2	2-Methyl-naphthalene	$C_{11}H_{10}$	2MN	142.197	91-57-6	[12]	~ 1.8 E^{-2}	[13]	75.37	142
12	2	C2-Naphthalenes	$C_{12}H_{12}$	C_2N	156.233	1	[12]	1 to 8 E^{-3}	[13]	30.24	156
13	2	C3-Naphthalenes	$C_{13}H_{14}$	C_3N	170.25	2	[12]	~ 2 E^{-3}	[13]	11.1	170
14	2	C4-Naphthalenes	$C_{14}H_{16}$	C_4N						4.05	184
12	2	Acenaphthene	$C_{12}H_{10}$	ACE	154.207	83-32-9	[12]	3.4 E^{-3}	[13]	306.85	
12	2	Acenaphthylene	$C_{12}H_8$	ACEY	152.192	208-96-8	[12]	~ 4 E^{-3}	[13]	55.85	
13	3	Fluorene	$C_{13}H_{10}$	FLU	166.218	86-73-7	[12]	~ 2 E^{-3}	[13]	39.3	166
14	3	C1-Fluorenes	$C_{14}H_{12}$	C1F	180.245	*3*	[12]	~ 1 E^{-3}	[13]	13.99	180
15	3	C2-Fluorenes	$C_{15}H_{14}$	C2F						5.3	194
16	3	C3-Fluorenes	$C_{16}H_{16}$	C3F						1.92	208
14	3	Anthracene	$C_{14}H_{10}$	ANT	178.229	120-12-7	[12]	~ 1 E^{-3}	[13]	19.13	178
14	3	Phenanthrene	$C_{14}H_{10}$	PHE	178.229	85-01-8	[12]	2.7 E^{-4}	[13]	20.72	178
15	3	C1-Phenanthrenes	$C_{15}H_{12}$	C1P	192.256	*4*	[12]	~ 2.7 E^{-4}	[13]	7.44	192
16	3	C2-Phenanthrenes	$C_{16}H_{14}$	C2P						3.2	206
17	3	C3-Phenanthrenes	$C_{17}H_{16}$	C3P						1.26	220
18	3	C4-Phenanthrenes	$C_{18}H_{16}$	C4P						0.56	234
16	4	Fluoranthene	$C_{16}H_{10}$	FLUOA	202.25	206-44-0	[12]	2.7 E^{-4}	[13]	7.11	202
16	4	Pyrene	$C_{16}H_{10}$	PYR	202.25	129-00-0	[12]	0.9 to 1.4 E^{-4}	[13]	10.11	202
17	4	C1-Fluoranthenes/pyrene	$C_{17}H_{12}$	C1FP	216.277	*5*	[12]		[13]	4.89	
18	4	Chrysene	$C_{18}H_{12}$	CHR	228.288	218-01-9	[12]	2 to 1.6 E^{-6}	[13]	2.04	228
19	4	C1-Chrysenes	$C_{19}H_{14}$	C1C	242.314		[12]	~ 6 E^{-5}	[13]	0.86	242
20	4	C2-Chrysenes	$C_{20}H_{16}$	C2C				~ 3 E^{-5}	[13]	0.48	256

21	4	C3-Chrysenes	$C_{21}H_{18}$	C3C						0.17	270
18	4	Benz(a)anthracene	$C_{18}H_{12}$	BAA	228.288	56-55-3	[12]	0.9 to 1.3 E^{-5}	[13]	2.23	228
20	5	Perylene	$C_{20}H_{12}$	PER	252.309	198-55-0	[12]	4 E^{-7}	[13]	0.9	252
20	5	Benzo(a)pyrene	$C_{20}H_{12}$	BAP	252.309	50-32-8	[12]	1.4 to 3.8 E^{-6}	[13]	0.65	252
20	5	Benzo(e)pyrene	$C_{20}H_{12}$	BEP	252.309	192-97-2	[12]			0.9	252
20	5	Benzo(b)fluoranthene ***	$C_{20}H_{12}$	BBF	252.309	205-99-2	[12]	~ 1.5 E^{-6}	[13]	0.96	252
20	5	Benzo(k)fluoranthene ***	$C_{20}H_{12}$	BKF	252.309	207-08-9	[12]	~ 1 E^{-6}	[13]	0.96	252
22	5	Dibenz(a,h)anthracene	$C_{22}H_{14}$	DAH	278.346	53-70-3	[12]	~ 1 E^{-6}	[13]	0.27	278
22	6	Indeno(1,2,3-cd)pyrene	$C_{22}H_{12}$	IND	276.33	193-39-5	[12]	~ 2 E^{-7}	[13]	0.28	276
22	6	Benzo(g,h,i)perylene	$C_{22}H_{12}$	BGP	276.33	191-24-2	[12]	1.8 to 2.6 E^{-7}	[13]	0.44	276

*Approximate sign ~ indicates that solubility values are variable; a range indicates the range of values.

**U.S. EPA Chronic Toxicity Value taken from EPA. 2003 – smaller numbers indicate higher toxicity.

***These two compounds are combined for EPA-34 considerations.

1 CAS numbers for di-methyl naphthalenes – **1,2** – 573-98-8; ***1,3*** – 575-41-7; ***1,4*** – 571-58-4; ***1,5*** – 571-61-9; ***1,6*** – 575-43-9; ***1,7*** – 575-37-1; **1,8** – 569-41-5; ***2,3*** – 581-40-8; ***2,6*** – 581-42-0; ***2,7*** – 582-16-1. CAS numbers for ethyl naphthalenes – 1 – 1127-76-0; 2- 939-27-5.

2 CAS numbers for 1,4,5-trimethyl naphthalene – 2131-41-1.

3 CAS numbers for methyl fluorenes – ***1*** – 1730-37-6; ***9*** – 2523-37-7.

4 CAS numbers for methyl phenanthrenes – ***1*** – 832-69-9; ***3*** – 832-71-3; ***4*** – 832-64-4.

5 CAS numbers for methyl pyrenes – ***1*** – 2381-21-7; ***2*** – 3442-78-2.

6 CAS numbers for methyl chrysenes – ***3*** – 3351-31-3; ***5*** – 3697-24-3; ***6*** – 1705-85-7.

Table 1.17: EPA 34 priority PAHs found in typical oils.

Carbon number	Number of rings	Name	Formula	Abbreviation	Levels in ASMB (µg/g oil)	Ref.	Levels in ANS (µg/g oil)	Levels in diesel fuel (µg/g oil)	Levels in heavy fuel oil (µg/g oil)	Ref.
10	2	Naphthalene	$C_{10}H_8$	NAP	680	[11]	260	820	140	[11]
11	2	1-Methyl-naphthalene	$C_{11}H_{10}$	1MN						
11	2	2-Methyl-naphthalene	$C_{11}H_{10}$	2MN						
12	2	C2-Naphthalenes	$C_{12}H_{12}$	C_2N	1,600	[11]	1,800	7,000	2,900	[11]
13	2	C3-Naphthalenes	$C_{13}H_{14}$	C_3N	1,560	[11]	1,700	6,600	2,900	[11]
14	2	C4-Naphthalenes	$C_{14}H_{16}$	C_4N	450	[11]	820	2,800	1,400	[11]
12	2	Acenaphthene	$C_{12}H_{10}$	ACE						
12	2	Acenaphthylene	$C_{12}H_8$	ACEY						
13	3	Fluorene	$C_{13}H_{10}$	FLU	50	[11]	140	570	220	[11]
14	3	C1-Fluorenes	$C_{14}H_{12}$	C1F	110	[11]	330	800	570	[11]
15	3	C2-Fluorenes	$C_{15}H_{14}$	C2F	150	[11]	450	760	1000	[11]
16	3	C3-Fluorenes	$C_{16}H_{16}$	C3F	85	[11]	380	360	940	[11]
14	3	Anthracene	$C_{14}H_{10}$	ANT	2	[10]	3	13	95	[11]
14	3	Phenanthrene	$C_{14}H_{10}$	PHE	170	[11]	210	440	420	[11]
15	3	C1-Phenanthrenes	$C_{15}H_{12}$	C1P	400	[11]	670	1000	1900	[11]
16	3	C2-Phenanthrenes	$C_{16}H_{14}$	C2P	400	[11]	710	620	2900	[11]
17	3	C3-Phenanthrenes	$C_{17}H_{16}$	C3P	160	[11]	490	190	3100	[11]
18	3	C4-Phenanthrenes	$C_{18}H_{16}$	C4P	60	[11]	300	50	2200	[11]
16	4	Fluoranthene	$C_{16}H_{10}$	FLUOA	2	[10]	3	7	40	[11]
16	4	Pyrene	$C_{16}H_{10}$	PYR	18	[10]	8	31	230	[11]
17	4	C1-Fluoranthenes/pyrene	$C_{17}H_{12}$	C1FP						
18	4	Chrysene	$C_{18}H_{12}$	CHR	25	[11]	50	<1	380	[11]
19	4	C1-Chrysenes	$C_{19}H_{14}$	C1C			70	<1	1200	[11]
20	4	C2-Chrysenes	$C_{20}H_{16}$	C2C			100	<1	1800	[11]

21	4	C3-Chrysenes	$C_{21}H_{18}$	C3C			80		1400	[11]
18	4	Benz(a)anthracene	$C_{18}H_{12}$	BAA	3	[10]	5	0.3	200	[11]
20	5	Perylene	$C_{20}H_{12}$	PER						
20	5	Benzo(a)pyrene	$C_{20}H_{12}$	BAP	1	[10]	2	0	150	[11]
20	5	Benzo(e)pyrene	$C_{20}H_{12}$	BEP						
20	5	Benzo(b)fluoranthene	$C_{20}H_{12}$	BBF	3	[10]	5	0	50	[11]
20	5	Benzo(k)fluoranthene	$C_{20}H_{12}$	BKF	3	[10]	1	0	10	[11]
22	5	Dibenz(a,h)anthracene	$C_{22}H_{14}$	DAH	1	[10]	1	0	20	[11]
22	6	Indeno(1,2,3-cd)pyrene	$C_{22}H_{12}$	IND	1	[10]	0.1	0	10	[11]
22	6	Benzo(g,h,i)perylene	$C_{22}H_{12}$	BGP	3	[10]	3	0	30	[11]

1.2.8 Naphthenoaromatic compounds

There exists a series of compounds that contain both aromatic and cyclic alkane rings. These are not typically analyzed for either petroleum or environmental purposes and thus there is not a large amount of data on their contents in crude oils or in petroleum products. Table 1.18 shows some of the naphthenoaromatic compounds found in crude oils and petroleum products.

1.2.9 Sulfur compounds

Sulfur compounds constitute a significant percentage of some crude oils and are also found in petroleum products as an unwanted contaminant [9]. The sulfur compounds found in oils and petroleum are generally found as one of four groups:

1. mercaptans or thiols with general structure of H-S-R, where R is another hydrocarbon group,
2. Sulfides with the general structure of R-S-R,
3. thiophenes with a general structure of a five-membered rings with sulfur as one leg and with two double bonds, or
4. as part of an asphaltene structure, and these structures are largely unknown.

Dibenzothiophenes are often used as forensic markers to track oil spills [11]. Sulfur containing compounds found in typical oil and fuels are shown in Table 1.19.

Gascon et al. [19] analyzed a series of heavy Venezuelan oils and their residues for a number of elements including sulfur. The first horizontal line in Table 1.20 shows the percentage of the oil constituted by the particular SARA fraction. The second line in the table shows the sulfur content in mg/kg (~ppm). The results of this analysis are shown in Table 1.20. The results show that aromatic, resin, and asphaltene fractions account for most of the sulfur in these samples.

Guadalupe analyzed oils for total sulfur and for sulfides [20]. Table 1.21 shows a summary of the results. This table shows that the sulfides and asphaltenes correlate with the total sulfur found in the oil. Nishioka and Tomich developed a method for analyzing oils for thiols noting that many thiols had not yet been identified [21].

Most sulfur compounds in oil are foul-smelling and corrosive. The presence of these compounds lowers the price of the crude oils, as sulfur compounds have to be removed before or during refining. In recent years, the standards for the sulfur content of fuels have been lowered, increasing the expense of refining.

Table 1.18: Naphthenoaromatic compounds found in oils.

Compound	Molecular formula	Structure	CAS no.	MW	Ref.	Solubility in water (g/L) *	Ref.	SIMS
Cyclopropylbenzene	C_9H_{10}	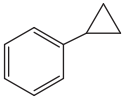	873-49-4	118.175	[12]			118
Cyclopentylbenzene	$C_{11}H_{14}$	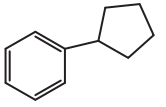	700-88-9	146.229	[12]			146
1,2,3,4-Tetrahydronaphthalene (tetralin)	$C_{10}H_{12}$	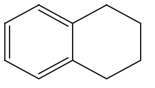	119-64-2	132.202	[12]	~0.045	[13]	132
Methyl-1,2,3,4-tetrahydronaphthalene	$C_{11}H_{14}$	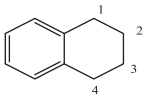	1	146.229	[12]			146
Dimethyl-1,2,3,4-tetrahydronaphthalene	$C_{11}H_{14}$	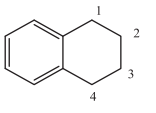	2	160.255	[12]			160
Trimethyl-1,2,3,4-tetrahydronaphthalene	$C_{11}H_{14}$	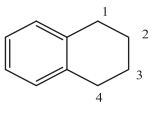	3	174.282	[12]			174

(continued)

Table 1.18 (continued)

Compound	Molecular formula	Structure	CAS no.	MW	Ref.	Solubility in water (g/L) *	Ref.	SIMS
1,2,3,4-Tetrahydrophenanthrene	$C_{14}H_{14}$	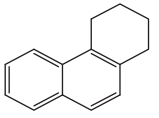	1013-08-7	182.261	[12]			182
Cyclopentanephenanthrene	$C_{17}H_{14}$	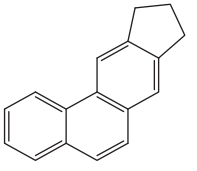						

*Solubility values are given as about or ~ if there is variance in the quoted values.

1 CAS number for 1-methyl-1,2,3,4-tetrahydronaphthalene – 1559-81-5; 5-methyl – 2809-64-5; 6-methyl – 1680-561-9.

2 CAS number for 1,5-methyl-1,2,3,4-tetrahydronaphthalene – 21564-91-0.

3 CAS number for 1,1,6-methyl-1,2,3,4-tetrahydronaphthalene – 475-03-6.

Table 1.19: Sulfur compounds found in oils.

Carbon number	Number of rings	Name	Formula	Molecular weight	CAS number	Ref.	Solubility in water (g/L)	Ref.
		Sulfides						
2		Dimethyl sulfide	C_2H_6S	62.134	75-18-3	[12]	$6.3\ E^{-3}$	[15]
4		Diethyl sulfide	$C_4H_{10}S$	90.187	352-93-2	[12]	$3.1\ E^{-3}$	[15]
4		Diethyl disulfide	$C_4H_{10}S_2$	122.252	110-81-6	[12]		
6		Dipropyl sulfide	$C_6H_{14}S$	118.24	111-47-7	[12]		
8		Dibutyl sulfide	$C_8H_{18}S$	146.294	544-40-1	[12]	$3.4\ E^{-2}$	[15]
8		Di-*sec*-butyl sulfide	$C_8H_{18}S$	146.294	626-26-6	[12]		
8		Di-*tert*-butyl sulfide	$C_8H_{18}S$	146.294	107-47-1	[12]		
8		Dibutyl disulfide	$C_8H_{18}S_2$	178.359	629-45-8	[12]		
8		Di-*tert*-butyl disulfide	$C_8H_{18}S_2$	178.359	110-06-5	[12]	$2\ E^{-3}$	[15]
12		Dihexyl sulfide	$C_{12}H_{26}S$	202.399	6294-31-1	[12]		
14		Diheptyl sulfide	$C_{14}H_{30}S$	230.453	629-65-2	[12]		
16		Dioctyl sulfide	$C_{16}H_{34}S$	258.506	2690-08-6	[12]		
		Thiols (mercaptans)						
2		Ethanethiol	C_2H_6S	62.134	75-08-1	[12]	15	[15]
2		1,2-Ethanedithiol	$C_2H_6S_2$	94.199	540-63-6	[12]		
3		1-Propanethiol	C_3H_8S	76.161	107-03-9	[12]		
3		2-Propanethiol	C_3H_8S	76.161	75-33-2	[12]		
3		1,2-Propanedithiol	$C_3H_8S_2$	108.226	814-67-5	[12]		
3		1,3-Propanedithiol	$C_3H_8S_2$	108.226	109-80-8	[12]		
4		1-Butanethiol	$C_4H_{10}S$	90.187	109-79-5	[12]	0.59	[15]
4		2-Butanethiol	$C_4H_{10}S$	90.187	91840-99-2	[12]		
4		1,4-Butanedithiol	$C_4H_{10}S_2$	122.252	1191-08-8	[12]		
5		1-Pentanethiol	$C_5H_{12}S$	104.214	110-66-7	[12]		
5		2-Pentanethiol	$C_5H_{12}S$	104.214	2084-19-7	[12]		
5		3-Pentanethiol	$C_5H_{12}S$	104.214	616-31-9	[12]		

(continued)

Table 1.19 (continued)

Carbon number	Number of rings	Name	Formula	Molecular weight	CAS number	Ref.	Solubility in water (g/L)	Ref.
		Sulfides						
6		1-Hexanethiol	$C_6H_{14}S$	118.24	111-31-9	[12]		
6		2-Hexanethiol	$C_6H_{14}S$	118.24	1679-06-7	[12]		
6		1,6-Hexanedithiol	$C_6H_{14}S_2$	150.305	1191-43-1	[12]		
6	1	1,2-Benzenedithiol	$C_6H_6S_2$	142.242	17534-15-5	[12]		
6	1	1,3-Benzenedithiol	$C_6H_6S_2$	142.242	626-04-0	[12]		
7	1	Benzenemethanethiol	C_7H_8S	124.204	100-53-8	[12]		
7		1-Heptanethiol	$C_7H_{16}S$	132.267	1639-09-4	[12]		
		Dibenzothiophenes	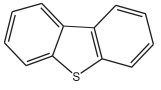					
12	3	Dibenzothiophene	$C_{12}H_8S$	184.257	132-65-0	[12]	$1.4\ E^{-3}$	[13]
13	3	C1-Dibenzothiophenes	$C_{13}H_{10}S$			[12]		
14	3	C2-Dibenzothiophenes	$C_{14}H_{12}S$			[12]		
15	3	C3-Dibenzothiophenes	$C_{14}H_{12}S$			[12]		

Table 1.20: Distributions of sulfur in crude oils and residues.

Sample		Total (mg/kg)	Saturates	Aromatics	Resins	Asphaltenes
Crude 1	% SARA	Total	19	23	39	17
	S	34,500	2,772	40,018	42,374	33,866
Crude 2	% SARA		22	30	34	12
	S	35,000	2,603	42,093	449,67	38,351
Crude 3	% SARA		31	34	29	7
	S	26,260	2,595	33,808	36,478	36,156
Crude 4	% SARA		35	25	25	6
	S	23,250	2,821	44,962	32,254	45,991
Vacuum residue	% SARA		16	33	36	15
	S	49,470	1,726	46,735	43,381	61,672
Atmospheric Residue	% SARA		17	35	34	14
	S	41,300	3,851	48,178	35,819	51,101

Table 1.21: Guadalupe results on sulfur in oil analysis.

Oil	Total sulfur %	Asphaltenes (%)	Sulfides (% of total sulfur)
A	3.3	6.3	0.2
B	2.7	21.9	1.5
C	0.9	0.3	0.4

1.2.10 Oxygen compounds

Oxygen compounds are found in oils and petroleum. Measurement of these compounds is not frequent because they do not have known forensic potential, and because they are generally soluble in water. They are more difficult to measure than many hydrocarbons. The common groups of oxygen compounds found in oils are:

1. naphthenic acids or their salts,
2. phenols and phenolic compounds,
3. fatty acids, and
4. inclusions in asphaltenes.

Some of the compounds that have been found in oils are shown in Table 1.22. Analysis has shown that some of the acid species include complex compounds with 2 to 6 aromatic rings and often including sulfur and nitrogen compounds [22]. Porter et al. analyzed several resins and determined the presence of carbazole and similar compounds in these oils [23]. Fingas and Banta [24] prepared a literature review of polar compounds and found the presence of dozens of oxygenated compounds in oils.

Table 1.22: Oxygenated compounds sometimes found in oils and petroleum.

Compound	Molecular formula	Structure	CAS no.	MW	Reference	Solubility in water* (g/L)	Reference
Naphthenic acids							
Cyclopentanecarboxylic acid	$C_6H_{10}O_2$	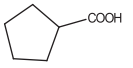	3400-45-1	114.142	1		
Cyclohexanecarboxylic acid	$C_7H_{12}O_2$	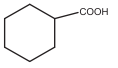	98-89-5	128.169	1	2	2
Cyclohexaneacetic acid	$C_8H_{14}O_2$	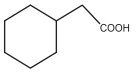	5292–21-7	142.196	1		
Phenols							
Phenol	C_6H_6O	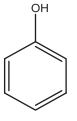	108-95-2	94.111	1	80	2
Resorcinol	$C_6H_6O_2$	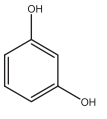	108-46-3	110.111	1	700	2
o-Cresol	C_7H_8O	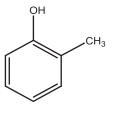	95-48-7	108.138	1	25	2

m-Cresol	C_7H_8O	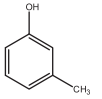	108-39-4	108.138	1	20	2
p-Cresol	C_7H_8O	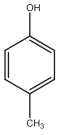	106-44-5	108.138	1	20	2
(Dimethyl) xylenol	$C_8H_{10}O$	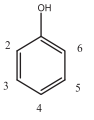	1	122.164	1	4 to 8	2
1-Naphthol	$C_{10}H_8O$	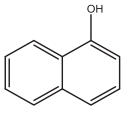	90-15-3	144.17	1	0.9	2
2-Naphthol	$C_{10}H_8O$	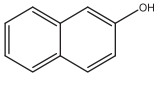	135-19-3	144.17	1	0.7	2
Fatty acids							
Fatty acids	CH_3-$(Ch_2)_n$-COOH	CH_3-$(Ch_2)_n$-COOH	Many	Many			

*Approximate sign ~ indicates that solubility values are variable; a range indicates the range of values; of these values are the average of several determinations/

1 CAS numbers for dimethylxylenols: 2,3- 526-75-0; 2,4- 105-67-9; 2,5- 95-87-4; 2,6- 576-26-1; 3,4- 95-65-8; 108-69-9.

References 1 CRC Handbook, 2020 2 Yalkowsky, 2010.

1.2.11 Nitrogen compounds

Nitrogen compounds are abundant in most crude oils and constitute about 0.1–2 wt % of the total. Several workers have carried out qualitative and quantitative analyses on nitrogen compounds in oils [25–28]. Nitrogen compounds in oils are often divided into two groups of basic or nonbasic compounds. This division is also useful for separation schemes. Most compounds are present as cyclic compounds as shown in Table 1.23. Furthermore, there is significant nitrogen content in the asphaltenes and in metal-binding compounds such as porphyrins.

1.3 Metals

Crude oils and their heavy refined petroleum products often contain significant amounts of metals. Metals are found in oils as follows:

1. inorganic salts,
2. metal soaps,
3. organic metal complex compounds, and
4. attached to asphaltenes.

Table 1.24 shows the metal content in several oils. The metals shown here are the most common metals identified in oils. In the past, some metals, notably chromium, vanadium, and nickel, were used for crude oil identification. The ratios of these metals have a tendency to remain constant. Further, the ratios of these metals can be used to identify tanks from which the oils may have come, as there is exchange of metals with the tank bodies. At the present time, there is little use of this type of identification as the use of biomarkers is easier and better understood.

Gascon et al. [19] analyzed a series of heavy Venezuelan oils and their residues for vanadium and nickel. The results of this analysis are shown in Table 1.25. The first horizontal line in the table shows the percentage of SARA constituted by the SARA fraction. The second line in the table shows the vanadium content in mg/kg (~ppm). The third line in the table shows the nickel content in mg/kg (~ppm). The results show that resins and asphaltenes account for most of the vanadium and nickel in these samples.

Quadros et al. studied the simultaneous measurement of nickel and vanadium in Brazilian and Venezuelan crude oils [29]. They found that the total nickel in three Brazilian crudes ranged from 9 to 25 μg/g and from 29 to 69 μg/g in three Venezuelan crudes. The total vanadium in the same Brazilian crudes ranged from 13 to 32.7 μg/g and in the Venezuelan crudes ranged from 224.7 to 277.0 μg/g.

The bonding of metals, particularly nickel, vanadium, iron, and cobalt into porphyrins, is a known source of metal stability in oils. Figure 1.2 shows the porphyrin

Table 1.23: Table of nitrogen compounds sometimes found in oils and petroleum.

Compound	Molecular formula	Structure	CAS no.	MW	Ref.	Solubility in water* (g/L)	Ref.	Levels in LGO oil (ppm N)	Ref.
Pyrrole	C_4H_5N		109-97-7	67.09	[12]	48	[13]		
Pyridine	C_5H_5N		110-86-1	79.101	[12]				
Indole (1-H-indole)	C_8H_7N	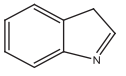	120-72-9	117.149	[12]	3.6–10	[13]		
Methyl indole	C_9H_9N	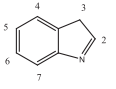	1	131.174	[12]	~ 0.5	[13]		
Quinoline	C_9H_7N	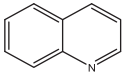	91-22-5	129.159	[12]	~ 6	[13]		
Isoquinoline	C_9H_7N	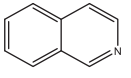	119-65-3	129.159	[12]				
Methyl quinoline	$C_{10}H_9N$	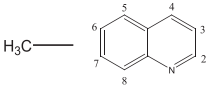	2	143.185	[12]				

(continued)

Table 1.23 (continued)

Compound	Molecular formula	Structure	CAS no.	MW	Ref.	Solubility in water* (g/L)	Ref.	Levels in LGO oil (ppm N)	Ref.
Methyl isoquinoline	$C_{10}H_9N$	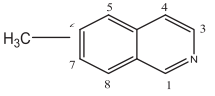	3	143.185	[12]	~ 1	[13]		
Dimethyl quinoline	$C_{11}H_{11}N$		4	157.212	[12]	1.8	[13]		
Carbazole	$C_{12}H_9N$	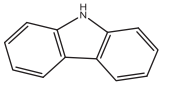	86-74-8	167.206	[12]	1.2 E^{-3}	[13]	38	[26]
Methyl carbazole	$C_{12}H_9N$	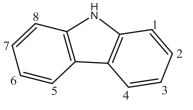	5	181.233	[12]			∑ 190	[26]
Dimethyl carbazole	$C_{13}H_{11}N$							∑ 196	[26]
Trimethyl carbazole	$C_{14}H_{13}N$							∑ 74	[26]
Tetrahydro carbazole	$C_9H_{11}N$		6	171.238					

*Approximate sign ~ indicates that solubility values are variable; a range indicates the range of values; many of these values are the average of several determinations.

1 CAS numbers for methyl indoles: 1-methyl – 603-76-9; 2-methyl – 95-20-5; 3-methyl – 83-34-1; 5-methyl – 614-96-0; 7-methyl – 933-67-5.

2 CAS numbers for methyl quinolines: 2-methyl – 91-63-4; 3-methyl – 612-58-8; 4-methyl – 491-35-0; 5-methyl – 7661-55-4; 6-methyl – 91-62-3; 7-methyl – 612-60-2; 8-methyl – 611-32-5.

3 CAS numbers for methyl isoquinolines: 1-methyl – 1721-93-3; 3-methyl – 1125-80-0.

4 CAS numbers for dimethyl quinolines: 2,4-dimethyl – 1198-37-4; 2,6-dimethyl – 877-43-0; 2,7-dimethyl – 93-37-8.

5 CAS numbers for methyl carbazoles: 3-methyl – 4630-20-0; 9-methyl – 1484-12-4.

6 CAS numbers for tetrahydro carbazoles: 2,3,4,9 – 942-01-8; 1,2,3,4 – 635-46-1; 5,6,7,8 – 10500-57-9.

Table 1.24: Metal content in various oils.

	(All content is in ppm)								
	Light fuels					Heavy fuel oils		Refinery intermediates	
Metal	**Aviation gas 80**	**Aviation gas 100**	**Jet A**	**Jet B**	**Diesel**	**Bunker C**	**IFO – marine**	**FCC – heavy cycle**	**Heavy reformate**
Chromium	<	1.4	<	<	<	<	<	<	<
Copper	1.1	<	<	<	<	<	<	<	<
Iron	<	<	39	13	4.6	3.5	29.5	<	<
Lead	175	795	<	<	<	<	<	<	<
Magnesium	8.2	7.5	9.8	3.6	12.3	23.9	10.2	3.8	10.6
Molybdenum	0.6	<	1.9	<	<	<	<	<	<
Nickel	<	<	<	<	<	8.6	29.5	<	<
Titanium	<	<	2.7	<	<	<	0.6	<	1.2
Vanadium	<	<	<	<	<	42	76.4	<	<
Zinc	<	<	2.4	0.6	1.2	1.6	1.1	0.4	<
	Light crude oils							**Heavy crudes**	
Metal	**Brent**	**Panuke**	**Norman Wells**	**Pitas Point**	**Oseberg**	**Ninian**	**Empire**	**Iranian Heavy**	**Maya**
Country of origin	UK	Canada	Canada	USA – Cal	Norway	UK	USA – Cal	Iran	Mexico
Chromium		<	<	<	<	<	<	<	<

(continued)

Table 1.24 (continued)

	Light crude oils							Heavy crudes	
Metal	**Brent**	**Panuke**	**Norman Wells**	**Pitas Point**	**Oseberg**	**Ninian**	**Empire**	**Iranian Heavy**	**Maya**
Copper		<	<	<	<	<	<	0.6	<
Iron		<	<	10.3	4.2	4.2	39.5	6	<
Lead		<	<	<	<	<	<	<	<
Magnesium		<	<	<	1	<	17.4	8.8	16.7
Molybdenum		<	<	<	<	<	<	<	1.2
Nickel	1	<	3.3	<	3.8	<	<	22.6	46.5
Titanium		<	<	0.6	<	<	105	<	<
Vanadium	6	<	8.7	<	2.7	4	<	81	257
Zinc		<	<	3.3	<	<	<	<	<

	Heavy crudes								Bitumen
Metal	**Lago Medio**	**Platform Irene**	**Port Hueneme**	**Hondo**	**Dos Cuadras**	**Carpenteria**	**California 11**	**California 15**	**Cold Lake Bitumen**
Country of Origin	Venezuela	USA – Cal	USA – Cal	USA – Cal	USA – Cal	USA – Cal	USA – Cal	USA – Cal	Canada
Chromium	<	2.3	<	<	<	>	1.5	1.7	<
Copper	<	0.8	<	<	<	<	<	<	<

Iron	<	44	16	30.5	42.1	29.5	21.5	9.1	15.2
Lead	<	<	<	<	<	<	3	3	<
Magnesium	3.8	237	3.1	5.4	16	<	237	8	9
Molybdenum	<	<	0.6	2.3	<	<	4	5.1	3.7
Nickel	5.6	60.5	68	75	62	48.9	106	111	69
Titanium	<	1.1	0.6	1.6	<	<	2.2	2	<
Vanadium	163	238	253	196	70.5	112	245	266	190
Zinc	<	5.1	0.6	0.5	<	4.3	<	<	4.3

Table 1.25: Distributions of vanadium and nickel in crude oils and residues.

Sample	In ppm		Saturates	Aromatics	Resins	Asphaltenes
Crude 1	% SARA	Total (mg/kg)	19	23	39	17
	V	416.7	1.4	2.5	553	1306
	Ni	102.2	0.6	2.9	141	319
Crude 2	% SARA		22	30	34	12
	V	472.8	2.3	0.3	802	1967
	Ni	100.8	0.6	2.5	185	408
Crude 3	% SARA		31	34	29	7
	V	432.4	2.2	1.7	980	2,561
	Ni	57.4	0.6	1.3	127	341
Crude 4	% SARA		35	25	25	6
	V	459.5	0.6	23.1	1019	3,884
	Ni	51.3	0.2	4.8	112	404
Vacuum residue	% SARA		16	33	36	15
	V	141.4	0.8	2.1	167	554
	Ni	44.6	0.5	1.5	51.1	172.6
Atmospheric residue	% SARA		17	35	34	14
	V	576.2	0.5	5.2	762	2,596
	Ni	125.2	0.2	4.5	183	534

skeleton. These compounds are residuals of chlorophyll from the original plant material forming the oil.

Metals are concentrated into petroleum residuals and often in the asphalt fractions of the oil. Metals are very low in the diesel fraction and absent in gasoline.

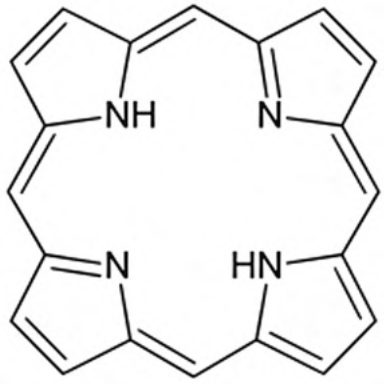

Figure 1.2: A typical porphyrin structure. This compound is called porphin.

1.4 Resins

Resins are polar compounds that are defined by precipitation or by open-column liquid chromatography fractionation. The composition of resins is largely unknown. The nitrogen compounds noted above may be present in resins, largely as alkylated variants of the basic compounds.

Porter et al. [23] analyzed several resins and determined the presence of carbazole and similar compounds in these oils. They also looked at the average molecular weight of resins using electrospray tandem mass spectrometry. Table 1.26 shows the maximum and minimum of these molecular weights. It can be seen from this table that the residual resins in diesel are of smaller molecular weight than in crude oils.

Table 1.26: Average molecular weights of resins in various crude oils and petroleum products (from [23]).

	Crude oils						
	Alberta	**Maui**	**Tchat**	**Alaskan**	**Arabian Heavy**	**Hibernia**	**Mars**
Maximum	395	370	382	394	417	423	415
Minimum		361	376	393	408	410	411
	Petroleum products						
	Fuel oil #5	**Heating fuel oil**	**Diesel**				
Maximum	409	405	212				
Minimum	404	378	209				

1.5 Asphaltenes

The important fact concerning asphaltenes is that currently the structures and compositions of this broad class of compounds are not fully elucidated [30, 31, 32]. See the chapter in this book by Mullins and colleagues (Chapter 5). Currently, asphaltenes are defined by their precipitation from oil in pentane, hexane, or heptane. The mass of asphaltenes, typically defined as percentage by weight, increases as one uses smaller compounds as solvents. As Mullins points out in his chapter that until a number of structures of asphaltenes have been identified, asphaltenes will remain a mystery such as the whole field of genetics before Watson and Crick identified the structure of DNA [31, 32]. Despite recent progress in the field, only a few compounds have been positively characterized in the asphaltene mix.

Some basic facts about asphaltenes will be summarized below, but includes the fact that the molecular weight has been found to be about 760, ranging from 500 to

1,000 [33]. The aromatic ring system is felt to contain about seven fused rings, a range of four to ten rings, and that these rings are fused and thus the asphaltene is felt to have a "hand-shape" with the alkenic chains (fingers) radiating outward from the central fused ring (palm). Further, analysis has been problematic because asphaltene molecules aggregate at low concentrations, typically about 150 mg/L in toluene. These nanoaggregates can range up to 10 or more individual compounds and do not easily lend themselves to analysis or separation.

Yen proposed that asphaltene molecule aggregates are like micelles and will behave like stacks of fused aromatic ring systems [33]. This is now known as the "Yen" model. The micelles will grow to a limiting size and reaggregate into "aggregates" until there is again a limiting size. So, there is a double mode of aggregation.

Mass spectrometry can yield more information that just a series of peaks for such complicated mixtures. There are two plotting techniques that can yield further information about petroleum mixtures [33]. The Kendrick plot shows the IUPAC 14.0156 mass spacing associated with carbon (CH_2 methylene groups) to show compounds of the same class. The Kendrick mass is defined as

$$\text{Kendrick mass} = \text{IUPAC mass spectrometry mass} \times (14/14.01565) \tag{1.1}$$

Using the Kendrick mass thus changes the mass of CH_2, the basic hydrocarbon building block, to become exactly 14. A further unit is defined as the Kendrick mass defect (KMD):

$$\text{Kendrick mass defect (KMD)} = (\text{nominal mass} - \text{Kendrick mass}) \times 1,000 \tag{1.2}$$

Each family of compounds shares the same mass defect, and thus a plot of KMD versus nominal Kendrick mass yields a graph of the different families of compounds, separated by the number of methylene groups. If one can identify the smaller compounds of a particular family, then the larger members can be identified by summing the methylene groups. Rodgers and Marshall show how this technique can be used to yield three levels of compositional detail, starting from accurate masses of complex mixtures obtained from FT-ICR MS [33]. First, a plot of class by relative abundance is created. The classes include functional groups such as N, O_2, NO, and O_3. These functional groups are noted by the unique masses of heteroatoms. Then for a heteroatom, the relative abundance is plotted for the double-bond equivalents (DBE). Then for each DBE grouping, the relative abundance of each carbon atom can be plotted.

The DBE is calculated as

$$\text{DBE (double bond equivalent)} = \text{C} - \text{H}/2 + \text{N}/2 + 1 \tag{1.3}$$

where C, H, and N are the number of carbons, hydrogens, and nitrogens, respectively.

Another value that can be used to provide discrimination in the mass spectrum of numbers is the *Z* number or the total number of heteroatoms:

$$Z\,\text{number} = -2(\text{DBE}) + n + 2 \tag{1.4}$$

A simple plot of the KMD versus the nominal Kendrick mass can yield the points of different compound families separated by methylene groups.

Another graphing technique which assists in the identification of various compounds is the van Krevelen diagram [32]. A van Krevelen diagram employs the ratio of noncarbon atoms and the H/C ratio to provide discrimination between various compounds.

References

[1] McKenna AM, Nelson RK, Reddy CM, Savory JJ, Kaiser NK, Fitzsimmons JE, Marshall AG, Rodgers RP. Expansion of the analytical window for oil spill characterization by ultrahigh resolution mass spectrometry: Beyond gas chromatography. Environ Sci Technol, 2013, 47, 7530–7539.

[2] Kinghorn RRF. An introduction to the physics and chemistry of petroleum. John Wiley & Sons, New York, 1983.

[3] Fingas M. Introduction to oil chemistry and properties. In: Fingas M, ed. Oil spill science and technology. Elsevier Publishers, NY, 2011, 51–70.

[4] Speight JG. The chemistry and technology of petroleum. Fifth Edition. CRC Press, Boca Raton, FL, 2015.

[5] Kuppusamy S, Maddela N, Megharaj M, Venkateswarlu K. Total petroleum hydrocarbons, environmental fate, toxicity and remediation. Springer Nature, Switzerland, 2020.

[6] Yang C, Brown CE, Hollebone B, Yang Z, Lambert P, Fieldhouse B, Landriault M, Wang Z. Chemical fingerprints of crude oils and petroleum products, Chapter 4. In: Oil Spill Science and Technology. Fingas M, Ed, 2nd. Gulf Publishing Company, Cambridge, MA, 2016, 210–299.

[7] Worton DR, Zhang H, Isaacman-Vanwertz G, Chan AWH, Wilson KR, Goldstein AH. Comprehensive chemical characterization of hydrocarbons in NIST standard reference material 2779 Gulf of Mexico crude oil. Environ Sci Tech, 2015, 49, 13130–13138.

[8] Azinfar B, Zirrahi M, Hassanzadeh H, Abedi J. Characterization of heavy crude oils and residues using combined Gel Permeation Chromatography and simulated distillation. Fuel, 2018, 233, 885–893.

[9] Neumann H-J, Paczynska-Lahme B, Severin D. Composition and properties of petroleum. Halsted Press, NY, 1981.

[10] Wang Z, Fingas M, Li K. Fractionation of ASMB oil and identification and quantitation of aliphatic, aromatic and biomarker compounds by GC/FID and GC/MS. In: Proceedings AMOP. Environment Canada, Ottawa, Ontario, 1993, 11–30.

[11] Wang Z, Hollebone BP, Fingas M, Fieldhouse B, Sigouin L, Landriault M, Smith P, Noonan J, Thouin G. Characteristics of spilled oils, fuels and petroleum products: 1. Composition and properties of selected oils. Environment Canada, Ottawa, Ontario, Canada, 2003.

[12] CRC. Handbook of chemistry and physics. CRC Press, Boca Raton, FL, 2020.

[13] Yalkowsky SH, He Y, Jain P. Handbook of aqueous solubility data. CRC Press, Boca Raton, FL, 2010.

[14] Mackay D, Shiu WY, Ma KC. Illustrated handbook of physical-chemical properties and environmental fate for organic chemicals. Lewis Publishers, Boca Raton, FL, Vol. 1 to 5m, 1992.
[15] Verchueren K. Handbook of environmental data on organic chemicals. John Wiley and Sons, New York, NY, 2001.
[16] Wang Z, Brown C. Chapter 3: Chemical fingerprinting of petroleum hydrocarbons, in Environmental Forensic Investigation. CRC Press, NY, 2006, 43–115.
[17] Andersson JT, Achten C. Time to say goodbye to the 16 EPA PAHs? Toward an up-to-date use of PACs for environmental purposes. Polycyclic Aromat Compd, 2015, 35, 330–354.
[18] Kang H-J, Lee S-Y, Kwon J-H. Physico-chemical properties and toxicity of alkylated polycyclic aromatic hydrocarbons. J Haz Mat, 2016, 312, 200–207.
[19] Gascon G, Vargas V, Feo L, Castellano O, Castillo J, Giusti P, Acavedo S, Lienemann C-P, Bouyssiere B. Size distributions of sulfur, vanadium, and nickel compounds in crude oils, residues, and their saturate, aromatic, resin, and asphaltene fractions determined by gel permeation chromatography inductively coupled plasma high-resolution mass spectrometry. Energy Fuels, 2017, 31, 7783–7788.
[20] Gaudalupe MFM, Castello Branco VA, Schmid JC. Isolation of sulfides in sils. Org Geochem, 1991, 17, 355.
[21] Nishioka M, Tomisch RS. Isolation of aliphatic sulfur compounds in a crude oil by a non-reactive Procedure. Fuel, 1993, 72, 1007–1016.
[22] Tomczyk NA, Winans RE, Shinn JH, Robinson RC. On the nature and origin of acidic species in petroleum. 1. Detailed acid type distribution in a California crude oil. Energy Fuels, vol. 15, 2001, 1498–1506.
[23] Porter DJ, Mayer PM, Fingas MF. Analysis of petroleum resins using electrospray ionization tandem mass spectrometry. Energy Fuels, vol. 18, 2004, 987–996.
[24] Fingas M, Banta J. Polar compounds in oils and their aquatic toxicity. AMOP, 2016, 197–259.
[25] Oliveira EC, Vaz de Campos MC, Rorigues MR, Perez VF, Melecchi MIS, MGR Vale, Zini CA, Caramao EB. Identification of alkyl carbazoles and alkyl benzocarbazoles in Brazilian petroleum derivatives. J Chrom, 1105(1-2 SPEC. ISS.), 2006, 186.
[26] Li N, Ma X, Zha Q, Song C. Analysis and comparison of nitrogen compounds in different liquid hydrocarbon streams derived from petroleum and coal. Energy Fuels, 24(10), 2010, 5539.
[27] Von Muehlen C, de Oliveria EC, Zini CE, Caramao EB, Mariott PJ. 2010, Characterization of nitrogen-containing compounds in heavy gas oil petroleum fractions using comprehensive two-dimensional gas chromatography coupled to time-of-flight mass spectrometry. Energy Fuels, 2010, 3572.
[28] Zhang Y, Xu C, Shi Q, Zhao S, Chung KH, Hou D. Tracking neutral nitrogen compounds in subfractions of crude oil obtained by liquid chromatography separation using negative-ion electrospray ionization Fourier transform ion cyclotron resonance mass spectrometry. Energy Fuels, 24(12), 2010, 6321–6330.
[29] Quadros DPC, Chaves ES, Lepri FG, Borges DLG, Welz B, Becker-Ross H, Curtius AJ. Evaluation of Brazilian and Venezuelan Crude oil samples by means of the simultaneous determination of Ni and V as their total and non-volatile fractions using high-resolution continuum source graphite furnace atomic absorption spectrometry. Energy Fuels, 24(11), 2010, 5907–5916.
[30] Mullins OC, Sheu EY, Hammami A, Marshall AG. Editors, Asphaltenes, heavy oils and petroleomics. Springer Publications, NY, 2007.

[31] Chacón-Patiño ML, Rowland SM, Rodgers RP. Advances in asphaltene petroleomics. Part 2: Selective separation method that reveals fractions enriched in island and archipelago structural motifs by mass spectrometry. Energy Fuels, 2018, 32, 314–328.
[32] Groenzin H, Mullins OC. Asphaltene molecular size and weight by time-resolved fluorescence depolarization. Chapter 2 in Asphaltenes, Heavy oils and petroleomics. Springer Publications, NY, NY, 2007, 17–40.
[33] Rodgers RP, Marshall AG. Petroleomics: Advanced characterization of petroleum-derived materials by Fourier transform ion cyclotron resonance mass spectrometry (FT-ICR MS) Chapter 3 in Asphaltenes, Heavy Oils and Petroleomics. Springer Publications, NY, 2007, 63–78.

Chun Yang, Zhendi Wang, Zeyu Yang, Bruce Hollebone,
Ben Fieldhouse, Patrick Lambert, Merv Fingas

2 Chemical fingerprints and chromatographic analysis of crude oils and petroleum products

Abstract: Crude oil is an extremely complex combination of a wide range of constituents. Petroleum products are derived from crude oil by a variety of refining processes. The chemical compositions of oil released into the environment are affected by weathering and mixing with background substances. Variation among crude oils provides a basis for differentiation and identification of oils and the sources of spilled oils. Refined oil petroleum partially inherits fingerprints from the parent crude oil, and weathered oil could retain the unique characteristics of the source oil, which enables a potential to trace its origin. The most important criteria for a forensic oil analysis are the concentration, distribution profiles, and diagnostic ratios of source-specific petroleum compounds. In recent decades, the technologies of oil analysis have continually progressed due to advanced and automated instrumental techniques. This chapter overviews oil chemistry and analytical methodologies for separation, identification, and quantitative analysis of selected petroleum hydrocarbons in crude oils and various refined petroleum products. We also discuss the effect on oil chemical composition of weathering processes such as evaporation, photodegradation, and biodegradation.

2.1 Introduction

Crude oil is a fossil fuel. It is widely accepted that crude oil originates mainly from the remains of prehistoric natural organic substances such as microscopic, photosynthetic organisms as phytoplankton, buried in the primeval mud of swamps, lakes, and oceans. The original chemistry of the organic matter, the environment of deposition, and the time and heat imposed on the organic matter dictate the type of crude oil formed [1]. Every crude oil exhibits a unique chemical fingerprint due to the variety of original organic matter, geological conditions, and ages under which it was formed. Oil composition may be altered to various extents by post-generation processes such

Chun Yang, Zhendi Wang, Zeyu Yang, Bruce Hollebone, Ben Fieldhouse, Patrick Lambert, Merv Fingas Emergencies Science and Technology Section (ESTS), Environment and Climate Change Canada, Ottawa, ON, Canada, e-mail: chun.yang@ec.gc.ca

https://doi.org/10.1515/9783110694529-002

as thermal alteration, migration, or biodegradation, consequently generating light, medium, or heavy crude oils.

To classify petroleum, properties such as viscosity, sulfur content, and American Petroleum Institute (API) gravity are usually used. The higher the API gravity, the lighter (less viscous) the oil, and vice versa. API values of crude oil with commercial value mostly fall within the range of 10° to 40°. Based on density, crude oils can be roughly classified into light, medium, heavy, and extra heavy oil. Light oils have an API > 31.1°. The medium oils are defined as having an API gravity between 22.3° and 31.1°. Heavy oils have a <22.3° API, and the extra heavy oils or bitumen have a gravity below 10.0° API and tend to sink if spilled on water.

Although crude oil may be used directly as an energy source, the full benefit of the different properties of the constituents may be realized only when they are separated. Distillation is the principal method for separating crude oil into valuable products. Based on the distillation pointing, petroleum products can be generally classified into light distillates, medium fuels, and heavy residuals with boiling points generally <200 °C, 200–350 °C, and >350 °C, respectively. Specific products are also generated from crude oil through a variety of refining and blending processes according to the requirement for desired end uses. Each product is comprised of different constituents. The chemical fingerprints of crudes are altered during the manufacture of refined petroleum products in the refining processes. However, the refined oil partially inherits its unique fingerprint from the parent crude oil, which enables the potential to track back its origin.

The lightest distillate of crude oil, gasoline, is the combination of a mainly lower boiling point C_4 to C_{12} hydrocarbons, including alkanes, alkenes, benzene, and alkylbenzenes, and a small portion of performance additives such as metal deactivators, corrosion inhibitors, oxygenates, and antioxidants. Now it has become universal to blend a portion of alcohols in gasoline, for example, E10 is a blend of 10% ethanol with petroleum-based gasoline.

Middle distillates generally include mineral spirits, kerosene, most jet fuels, automotive and marine diesel, and light fuel oils. These products are characterized by a predominance of C_{10} to C_{24} alkanes and polycyclic aromatics with no or little olefins. Diesel is one of the most important fuels used by automobiles due to its high efficiency. Marine diesel oil (MDO) is purposely produced for light marine and freshwater vessel fuel. MDO is formulated from mid-range distillates, typically containing a more extended carbon range than on-road diesel.

Blends of biodiesel and petroleum-derived diesel are now commonly distributed for use in the retail diesel fuel marketplace. Typically, biodiesel consists of fatty acid methyl esters (FAME) produced by transesterification of plant or animal-derived triacylglycerols. The fatty acid chains can be saturated, monounsaturated, or polyunsaturated. The distribution profiles of free fatty acids, glycerol, and monoacylglyceride congeners as well as the byproducts of biofuel could be applied for the differentiation and identification of biodiesels.

Heavy fuel oils (HFOs) are used for off-road diesel engines, boilers, furnaces, and other combustion equipment. They are the heavy residual part of the vacuum distillation and cracking processes. These oils are often blended with lighter oils such as gas oil and kerosene streams to meet the desired product specification for the convenience of transportation and operation. These heavy fuels are considered to be less acutely toxic relative to other lighter oil types. Heavy fuels have variable acute toxicity, depending on the amount of the light fraction. Their composition is complex and varies with the feedstock of crude oil. In general, these oils contain a mixture of saturated, aromatic, and olefinic hydrocarbons with carbon numbers predominantly in the C_9 to C_{50} range. As residual distillates, these oils often contain relatively high concentrations of sulfur, oxygen, nitrogen compounds, and heavy metals (e.g., vanadium and nickel). Relative to other types of refined oil products, spills of HFOs potentially cause the most significant environmental impact with respect to their vast usage as well as their physical and chemical properties.

Lubricating oil (or simply lube oil) consists largely of base oil and a small portion of chemical additives. Mineral base oil typically originates from petroleum products; however, the use of high-performance synthetic lubricants that no longer containing petroleum base oils has become widespread. Lube oil is usually distinguished from other fractions of crude oil by its high boiling point and viscosity. Hydrogenation and hydrocracking significantly influence the chemical structures of mineral oil molecules. Unstable molecules are chemically stabilized by the removal of heteroatoms (sulfur, oxygen, and nitrogen). Severe hydrogenation can convert aromatics into saturated naphthenic and paraffinic compounds. In addition to hydrogenation, hydrocracking can break large molecules down into smaller ones.

Small and large crude oil spills occur frequently during their exploration, production, and transportation. Inland oil spills may come from pipeline ruptures, tank spills, and road transportation accidents. Most massive oil spills are usually related to accidental crude oil releases on the oceans from drilling rigs, offshore platforms, and super-tankers. The particular operating conditions and severe weather often make it more difficult to control an ocean oil spillage than an on-land incident.

Spillages of refined oils frequently occur around oil development and production facilities. Massive spills of refined petroleum products rarely occur like crude oil spills. Small and chronic spillages of refined oils also pose a great environmental problem. Unsurprisingly, fuel oils are among the mostly spilled petroleum products in waters, both by volume and by occurrences [2]. Spillages of petroleum products on open waters sometimes involve mystery illegal discharges of marine vessels and their ship bilges. The waste from the cleaning engine chambers is sometimes accidentally or deliberately released from vessels. Biomarker compounds of lubricating oil in bilges can provide a valuable clue to trace the spill source. Accurate analysis and unambiguous results are critical to identify the spill source and allocate the legal liability.

Although oil spills in the open area are unlikely to cause an immediate health threat to humans, they often have widespread damage to the ecosystem and influence

the local economy; the long-term adverse effect could last decades. The analysis of spilled oil is essential for monitoring the contamination and evaluating the recovery of the environment.

2.2 General chemical components of petroleum

The composition of crude oil is extremely complex and is highly variable from field to field, and even within a given field, it is possible to exhibit differences. Despite wide variations in the chemical composition of crudes, their elemental compositions generally fall within the following narrow ranges: carbon (84–87%) and hydrogen (10–14%), nitrogen (0.1–2.0%), oxygen (0.05–1.5%), sulfur (0.05–6.0%), and a small portion of minerals and salts [3]. Crude oil contains proportions of hydrocarbons and nonhydrocarbons including heterocyclic compounds of nitrogen, oxygen, and sulfur, organometallic compounds, inorganic sediments, and water. Although the total number of compounds in crude oil is still unknown, it is recognized that crude oil is likely comprised of thousands of compounds [4]. These petroleum hydrocarbons naturally exist in gas, liquid, or solid state. The distribution pattern and profiles of components are, in general, different from oil to oil and from oil to refined products.

Petroleum compounds are generally classified into saturates, olefins, aromatics, as well as polar resin and asphaltene fractions [3].

***Saturates*:** Saturates are hydrocarbons that only contain single bonds between carbon atoms. They are generally the predominant class of hydrocarbons in crude oil. Overall, there are two major types of saturated compounds: paraffins and naphthenes. Paraffins, also called alkanes, are saturated hydrocarbons with straight or branched chains but without any ring structure. They are one of the major constituents of crude oil and are found in refined petroleum products such as gasoline, kerosene, diesel fuel, and heating oil. The *n*-alkanes (linear alkanes) have carbon atoms arranged in a line and there are only two ends to these molecules. Branched alkanes have carbon atoms arranged similar to the *n*-alkanes; however, some of the carbon atoms are branched, thus creating many different configurations. Paraffins (mainly *n*-alkanes) ranging from C_{18} to C_{40}, which occur in solid state at room temperature, are often referred to as crude wax. Naphthenes, also known as cycloalkanes, are saturated hydrocarbons containing one or more rings, each of which may have attached paraffin side-chains. Naphthenes are also relatively stable compounds in petroleum.

A variety of petroleum saturates are composed of isoprenoid units (isoprene, C_5H_8-). The following types are the most distinguished in crude oil: (1) monoterpanes (C_{10}), both aliphatic and monocyclic; (2) sesquiterpanes (C_{15}), aliphatic, mono- and bicyclic; (3) diterpanes (C_{20}), aliphatic, bi-, tri-, and possibly tetracyclic; (4) triterpanes (C_{30}), aliphatic as well as tri-, tetra-, and pentacyclic. Among these terpenoids,

tetra- and pentacyclic terpanes and steranes are the most important compounds for petroleum chemistry and forensic oil analysis.

***Olefins*:** Olefins are also called alkenes.These unsaturated hydrocarbons have one or more pairs of carbon atoms attached by a double bond. Various types of olefins have been identified in the oils and condensates worldwide [5]. Olefins are not present in large amounts in crude oils or straight-run distillates such as kerosene, gas oil, or fuels [6]. These compounds are found in large quantities only in some refined products, produced primarily from larger molecules in cracking processes.

***Aromatics*:** Aromatics contain one or more benzene rings as structural components. A monoaromatic compound has one benzene ring with either six hydrogen groups or a combination of alkyl and hydrogen groups, attached to that six-carbon aromatic ring. Polycyclic aromatic compounds (PACs) have multiple aromatic rings such as naphthalene, phenanthrene, and pyrene.

***Resin*:** Resin includes a large group of polar compounds in crude oil. These include hetero-substituted aromatics (such as nitrogen, oxygen, and sulfur-containing polycyclic aromatic hydrocarbons (PAHs)), phenols, acids, ketones, alcohols, and monoaromatic steranes (MASs). Resins are assumed insoluble in liquid propane but soluble in *n*-pentane. Because of their polarity, these compounds are more soluble in polar solvents, including water, than the nonpolar compounds, such as waxes and aromatics, of similar molecular weight. They are largely responsible for oil adhesion. Sulfur compounds are among the most important heteroatomic constituents of petroleum and may be present in several forms, including elemental sulfur, hydrogen sulfide, mercaptans, thiophenes (thiophene, benzothiophenes, dibenzothiophenes, and naphthobenzothiophenes), and their alkylated homologues.

***Asphaltenes*:** Asphaltene is defined as the part of petroleum, coal, or oil shale, which is precipitated by the addition of a low-boiling paraffin solvent such as *n*-pentane but soluble in benzene. Asphaltene constituents are the heaviest and polar constituents in crude oil, together with other high molecular weight (HMW) content resulting in the colloidal nature of crude oil. During petroleum refining, the asphaltene constituents are nondistillable and remain in the residual fuels as the distillable fractions are removed [7]. The black color of crude oils and residues is due to the combined effect of neutral resins and asphaltenes. On heating above 300–400 °C, asphaltenes are not melted, but decompose, forming carbon and volatile products. Asphaltenes make up the largest percentage of the asphalt used to pave roads. As asphaltenes are determined as a whole, this information provides little information to distinguish an oil, and asphaltenes are not often listed as target analytes for forensic oil analysis. However, its content can reflect the oil type.

***Other components*:** Other than the main fraction of hydrocarbons, crude oil also contains compounds consisting of oxygen, sulfur, nitrogen, and trace amounts of phosphorus, and a trace amount of water. Crude oil also contains a small quantity of heavy metals such as vanadium (V) and nickel (Ni). Metals are encountered in petroleum in the form of salts of carboxylic acids or as porphyrin chelates. V and Ni predominantly occur at the highest concentration in crude oil and residual fuel oils. Refined petroleum products contain variable content of these components due to their removal or enrichment during refining processes.

In this chapter, we will mainly discuss the fingerprinting analysis of selected gas chromatography (GC)-detectable aliphatic and aromatic compounds in petroleum. Later sections will further detail the chemical fingerprints of these petroleum compounds.

2.3 Fingerprinting analysis of petroleum compounds

Database on the oil physical and chemical properties plays an important role in preparedness and response to oil spill events. In the case of an oil spill, fingerprinting analysis is essential to monitor the contamination, evaluate the damage, and overlook the environmental recovery of an oil spill. Accurate analysis and unambiguous results are critical to identify the spill source and allocate the legal liability.

The fingerprinting of oil spills can be a considerable challenge to analytical chemists due to the complexity of petroleum oil and the low concentrations of many constituents of interest. In addition, once released into the environment, oil is immediately subjected to a series of weathering processes that alter its compositional distribution, and environmental samples are often a mixture of more than one oil and background matrix, and subsequently becomes difficult to recognize its spill source. These combined factors pose significant challenges in unequivocal spill source identification [8, 9].

The most commonly used methods for oil fingerprinting include those developed by Environment and Climate Change Canada (ECCC) [10–15] and European institutes [16–20]. These analytical methods, based on GC, have been demonstrated to be efficient and suitable for the identification and quantitative characterization of petroleum hydrocarbons in both crude oils and refined products.

Figure 2.1 depicts the procedure of an oil fingerprinting analysis used in the ECCC. Forensic oil fingerprinting analysis usually involves three major approaches [11, 13, 20]:

– Characterization of hydrocarbon groups by GC-flame ionization detection (GC-FID). Information obtained from GC-FID analysis is used: to identify the oil type; to determine total saturated hydrocarbons (TSHs), total aromatic hydrocarbons (TAHs), total petroleum hydrocarbons (TPHs), and unresolved complex materials

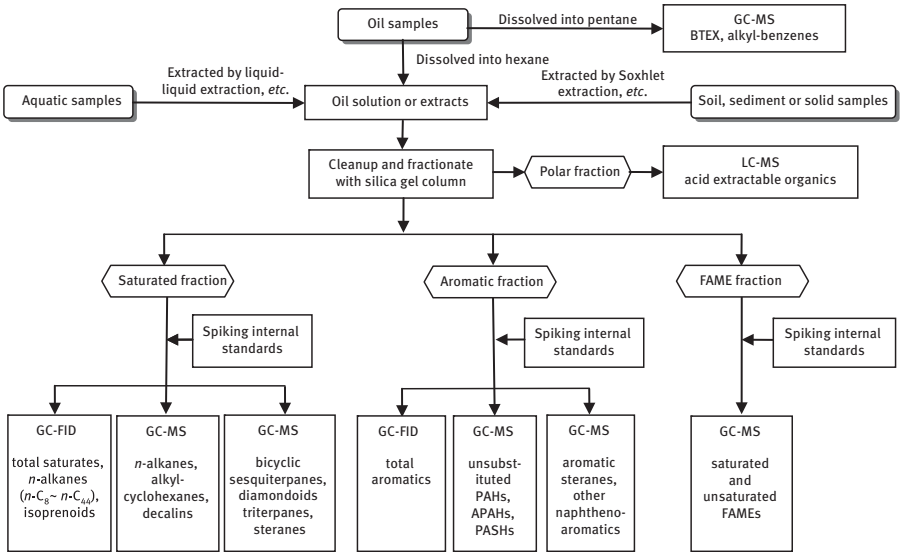

Figure 2.1: Schematic of oil analysis procedure.

(UCM); to acquire the diagnostic ratios such as UCM/TPH, Norpri/Pri, n-C_{17}/Pri; n-C_{18}/Phy, and Pri/Phy; to assess the weathering degree; and to visual preliminary examine the correlation of oils.

- Fingerprinting analysis of selected target analytes by GC-mass spectrometry (GC-MS) (selective ion monitoring, SIM). Information obtained from GC-MS analysis is used: to determine target analytes of interest including PAHs and biomarker compounds; to investigate chromatographic characteristics of source-specific compounds; and to acquire the diagnostic ratios of relevant analytes.
- Overview information from both GC-FID and GC-MS analyses; identification and characterization of major unknown peaks (e.g., additives); determination of weathering effect to the oil; and identifying the correlation of analyzed oils.

2.3.1 Sample preparation and separation

The collection of representative oil or environmental samples is not discussed in this chapter, but it is a crucial step for a successful forensic approach. Valid oil analysis must be obtained from the analysis of an aliquot representing the whole sample, which is particularly important to heavy oils and solid environmental samples. It is cautious that chemical fingerprints can be distorted or altered due to sample inhomogeneity and sample treatment prior to analysis [20].

Pure oil samples could be directly weighed and dissolved into suitable solvents for analysis. The analysis of oil-contaminated environmental samples first involves

the recovery of target compounds from their matrices such as water and soil. To select the proper extraction technique, one should consider the complex nature of petroleum. Traditional liquid–solid and liquid–liquid extractions are still used as the first choice in many laboratories due to their simplicity, relatively low cost, and proven high extraction efficiency, despite being very time-consuming. Some other techniques are used nowadays, but they may be unable to process highly oil-contaminated samples. Hexane and dichloromethane (DCM) are often used to extract oil for analysis. DCM needs to be replaced by hexane if a silica gel column is used for cleanup and fractionation. For environmental samples, if the extract appears very concentrated, it is necessary to determine the total solvent extractable materials (TSEMs) to calculate the proper aliquot of the extract to load on the chromatographic column for further sample processing and analysis and to facilitate a comparison of abundance of target compounds in samples. To determine TSEM, a 1.0 mL aliquot of extract is placed in a preweighed vial and blown to dryness under nitrogen. Alternatively, the concentration sample can be firstly evaluated by a preliminary GC-FID analysis [20].

It is not a rare practice to directly inject diluted oil solutions or extracts into an instrument, particularly for fast screening oil types. Fingerprinting analysis simply accomplished without chromatographic column fractionation could provide efficient qualitative information for oil identification but can prevent accurate quantitation of certain analytes. Typical oil concentration for direct GC injection varied from 1.5 to 10 mg/mL depending on oil types [20]. However, considering the complex nature of petroleum, proper sample cleanup, and further fractionation are essential prior to instrumental analysis in order to achieve accurate quantification of individual components and unbiased identification of the spill source, while protecting the instrument from contamination. It is strongly recommended to clean the "black oils," such as HFOs, slops, and bilges, in order to remove the high amount of asphaltenes and/or soot particles that are typically detrimental to instrumentation [20].

The most widely applied analysis scheme is to separate the petroleum compounds into aliphatic (mostly saturated hydrocarbons), aromatic, and other component groups. Silica gel and Florisil® column are often used to remove the alien objects and to separate saturated and aromatic compounds for accurate quantitative analysis without interference to each other. The chromatographic columns can be either lab-packed or commercially available SPE cartridges such as the silica gel Resprep™ Massachusetts EPH and the silica gel/cyanopropyl varieties [14, 15, 21–23].

According to ECCC's methods, an aliquot of oil solution or extract with equivalent TSEM of environmental sample is transferred to the top of a chromatographic column for sample cleanup and fractionation, with the column preconditioned using hexane. Saturated and aromatic hydrocarbons are effectively eluted with hexane and a mixture of hexane–DCM (1:1, v/v), respectively. The column can be further eluted for the analyses of other components such as FAME, nitrogen-containing polycyclic aromatic heterocycles (PANHs), and acid-extractable organics including naphthenic acids [24–26]. If these components are to be determined in the environmental samples, it is essential

to effectively recover them in the sample extraction step, which is not discussed herein. FAMEs as the primary component of biofuel are investigated where relevant. Ion of m/z 74 is used to determine saturated FAMEs, and m/z 55, 67, and 79 for monounsaturated, diunsaturated, and polyunsaturated FAMEs in biodiesel, respectively.

Saturated and aromatic fractions are carefully concentrated under a stream of nitrogen to appropriate volumes and spiked with internal standards. These fractions are finally adjusted to an accurate preinjection volume for analyses. The saturated hydrocarbon fraction (F_{sat}) is used for the analysis of TSHs, *n*-alkanes, acyclic isoprenoids, diamondoids, bicyclic sesquiterpanes, and biomarker terpanes and steranes. The aromatic hydrocarbon fraction (F_{arom}) is used for the analysis of TAHs, unsubstituted PAHs, and alkylated PAHs (APAHs), aromatic steranes, and polycyclic aromatic sulfur heterocycles (PASHs).

2.3.2 GC analysis of petroleum compounds

Petroleum contains a large number of different types of compounds. Analysis of the whole composition of petroleum can be endless and impractical; therefore, the information to be collected should be limited to those critical data. The technologies of oil analysis have been continually progressed due to advanced and automated instrumental techniques in recent decades. The methods most commonly used are to approach the major petroleum components using GC and other techniques [12, 14, 15, 17, 18, 20, 27, 28]. This chapter does not intend to provide an exhaustive list of analytical methods rather it discusses the well-established chromatographic methods. Capillary GC has been routinely used in environmental laboratories to provide a detailed analysis of most of the individual organic compounds. The characterization of individual saturated and aromatic compounds in petroleum is mainly based on GC-FID and GC-MS analyses. GC-FID is a robust, reliable, and universal technique for the detection of all species of hydrocarbons. However, this technique only produces two-dimensional data (i.e., retention time and abundance). GC-FID analysis aims to determine the oil type and to investigate if the oil is weathered through the overall distribution of hydrocarbons. These methods do not give access to detailed information of individual target compounds, and only the TPH concentration or carbon number fractions can be obtained. GC-MS instrument can provide accurate quantitation for volatile and semivolatile organic compounds in petroleum, particularly those petroleum biomarkers, which are at relatively low concentrations but of interest to forensic oil analysis.

By choosing a proper GC column based on its length, internal diameter, stationary phase, and film thickness, a wide range of petroleum hydrocarbons can be separated under optimal instrumental parameters. The most commonly used columns for petroleum hydrocarbon separation include nonpolar inert capillary columns such as DB-1 and DB-5, filmed inside with 100% methylpolysiloxane and 5% phenyl–95%

methylpolysiloxane, respectively. A conventional fused silica capillary column (30 m, 0.25 mm ID, and 0.25 μm film thickness) is used for most oil analyses. To reduce column bleeding under high temperature, some specific capillary column is used for GC-FID analysis, such as DB-5HT fused silica column (30 m, 0.25 mm ID, and 0.10 μm film thickness). Resolution of a capillary GC column is limited; it is impractical to resolve all individual oil components of interest with the chromatographic separation.

For GC-MS analysis of petroleum, electron impact ionization (EI) is most commonly used. To obtain the best sensitivity for quantitative measurement, the mass spectrometer is usually operated in SIM mode that only acquires positive ions of interest. A full scan MS is a useful mode of operation that acquires all ions formed in the ion source. This is helpful information for developing SIM acquisitions and alerts analysts to untargeted compounds other than compounds of interest. At present, the identification and characterizations of these petroleum compounds mainly rely on GC coupled to single quadrupole mass spectrometers. Low-resolution and low-mass accuracy mass spectrometers (LRMS) are sufficient for general oil analysis. LRMS analyses can face interference by other co-eluted petroleum components and external matrix material even with chromatographic separation. This is especially true to analyze target compounds in refined petroleum products and environmental samples, where their chemical fingerprints that are usually relied upon for the identification of target compounds have been significantly altered. Inaccurate and inconclusive oil analysis potentially results in misidentification and overestimation of target analytes [29].

Recently, high-resolution and high-mass accuracy mass spectrometry (HRAM-MS) such as quadrupole time-of-flight mass spectrometer (QTOF-MS) and quadrupole Orbitrap mass spectrometer has become more accessible for routine analysis with improvements in instrumentation [31]. HRAM-MS provides the simultaneous universal screening of targeted and untargeted analytes, increases detection selectivity with less sample preparation and compound optimization, and allows for retrospective analyses, which are crucial factors contributing to the increasing interest in HRAM-MS. An HRAM-MS coupled to capillary GC inherits both the advantages of both the powerful separation of GC and the rapid and accurate detection of HRAM-MS. GC-HRAM-MS can deliver higher resolution, a more accurate mass measurement, and faster full spectrum acquisition than a single quadrupole MS. Thus, it simultaneously provides good tools for solving complex analytical problems, resolving structural elucidation of unknowns, and confirming untargeted compounds. To date, there are only a few reports related to GC-HRAM-MS for oil analysis. Yang et al. have applied GC-QTOF-MS in the quantitative analysis of PAHs and biomarkers in petroleum oils and environmental samples from petroleum-impacted areas [29, 32]. The results demonstrated that accurate mass measurement by GC-QTOF-MS effectively improved characterization and differentiation of PASHs and PAHs, achieving significantly better results compared to those from the single quadrupole GC-MS method.

The improvement in quantitative analysis of one specific target compound is generally decided by many factors, such as the instrumental resolution and mass

accuracy, uniqueness of quantitation fragment, difference of monoisotopic mass between target and interfering compounds, abundance of analytes, natural complexity of samples, and so on. Practically, high-resolution and accurate MS alone cannot solve all analytical issues, particularly when the interference to a target compound is from its isomers. Therefore, according to a specific case demand, proper sample preparation, chromatographic separation, application of HRMS, and meticulous data analysis still play a critical role in reliable oil analysis.

2.3.3 Identification and quantitation of target petroleum hydrocarbons

The analysis of petroleum compositions is of particular importance in oil forensic studies since they can provide valuable information toward achieving a better characterization and identification of a petroleum sample. The determination of both concentrations and relative distributions of target petroleum hydrocarbons are equally essential to unambiguously identify an oil spill because in some cases, a source can have a similar distribution profile of analytes but significantly different amounts of these compounds [30]. Quantitative analyses of BTEX and PAHs are often required to access the health concern of an oil spill.

The data in this chapter were obtained by using our in-house methods [14, 33–38]. A large number of target analytes are identified and quantified by GC-FID (for *n*-alkanes and isoprenoids) or by characteristic ions from GC-LRMS in SIM mode. These compounds include *n*-alkanes, BTEX and alkylbenzenes, APAH series, aromatic steranes, petroleum biomarkers, diamondoids, and bicyclic sesquiterpanes, and so on. Figure 2.2 depicts the distribution of hydrocarbon groups according to their retention time (generally equivalent to boiling point order) in a typical chromatographic analysis using a nonpolar capillary column. The fingerprinting analyses of these components are discussed in more detail in the following sections.

It is unnecessary to analyze all target compounds in each oil analysis. Appropriate target analytes can be selected based on the type of oil spilled, the particular environmental compartments being assessed, and expected needs for current and future data comparison. The identification of target compounds usually relies on the application of reference oils since it is impractical to apply authentic standards for all target compounds. Reference oils processed as a normal sample also provide quality control for an oil study. For different case studies, different types of reference oils can be applied. The Emergencies Science and Technology Section of Environment and Climate Change Canada established a reference oil (13.1% artificially evaporated Prudhoe Bay crude oil). This oil consists of most of the common target compounds and at appropriate abundance. Other oils or blend oils such as NIST SRM 2779 (crude oil, Gulf of Mexico) can be used as reference oils as long as they meet the requirement as reference materials.

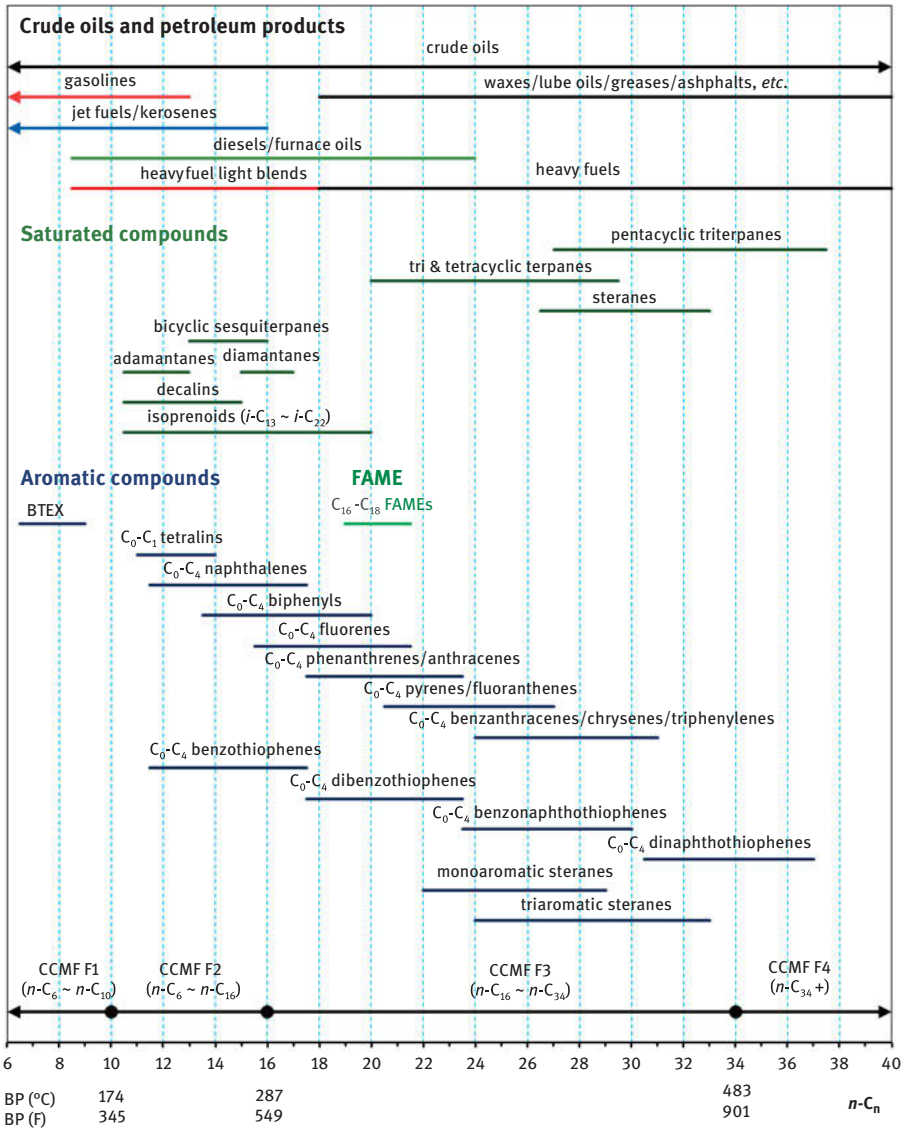

Figure 2.2: Distribution of target compounds for oil fingerprinting analysis.

Quantitative analyses of individual compounds are not always necessary and very time-consuming. Quantitative analysis requires either external or internal standard compounds. Most target compounds especially APAHs, biomarkers, and bicyclic sesquiterpanes, are not commercially available or extremely costly. Quantitation of these analytes is usually based on the relative response factor (RRFs) of their corresponding alternatives rather than authentic standards relative to the internal standards. APAHs

are usually quantified by using their parent unsubstituted PAHs instead of authentic APAH standards, except for few groups such as C_1-N, C_2-N, and C_3-N. As more alkyl-PAH are commercially available now, some are used for APAH quantitation. Yang et al. investigated the variation in RRFs of different APAH isomers and selected a suite of authentic APAH standard materials as representative compounds to accurately quantify APAHs [38]. By using the APAH standard, this could result in a 10–20% difference compared with that by using parent PAHs as quantitation standards. Many oil analytical methods are similar with subtle differences between the actual experimental procedures, while some methods differ considerably. Each lab has its specific oil analytical methodology (i.e., different quantitative standards are used), thereby quantitation discrepancy for the same sample can occur.

For forensic oil fingerprinting analysis, the relative distribution of target compounds is somewhat more important than their real-world concentration, hence quantitation using alternative standards is still meaningful for oil characterization and identification. Table 2.1 tentatively summarizes the overall distribution of these chemical components in various crude oils and refined products. It is important to note, based on our experience and knowledge from analyses of limited oil samples thus far, that the information presented may not be representative in some cases. For each petroleum fuel mixture, the table displays the approximate carbon number range of predominant hydrocarbons and the relative abundance of common target petroleum hydrocarbons in these oils. Their chemical fingerprints are described in more detail later in this chapter.

2.4 GC-FID-detectable petroleum hydrocarbons

As mentioned above, typically, the first step in forensic oil fingerprinting is screening the petroleum hydrocarbons in the sample, identifying the oil type, and evaluating the weathering extent [10, 13, 15, 17, 20]. Incorrect identification of oil type could misdirect subsequent tiered analysis, eventually leading to incorrect results. The physical appearance such as color and odor is helpful to preliminarily identify the type of oil samples. However, to unambiguously identify the oil, dedicated instrumental analysis is important, particularly to those samples that may lead to legal issues.

Generally, preliminary identification of the oil type and weathering can be readily achieved from their GC-FID traces. Measurement of TPH and other hydrocarbon groups (including the total saturates, the total aromatics, the total resolved peaks, and UCM) in oil samples, GC-FID chromatograms provide a distribution pattern of petroleum hydrocarbons (e.g., carbon range and profile of UCM).

To address the diversity of petroleum contamination types, the GC-detectable petroleum hydrocarbons are divided into four broad physicochemical subfractions

Table 2.1: Relative abundance of chemical components in crude oils and refined petroleum products.

Oil types	Approximate carbon range	Aliphatic					Aromatic			
		n-Alkanes	Branched alkanes	Bicyclic sesquiterpanes	Diamondoids	Tri- to penta-cyclic terpanes	BTEX	PAHs	PASHs	Aromatic steranes
Crude oils										
Light or medium crude oil	C_1 to C_{40}	High	High	Variable	Variable	Variable	Variable	Variable	Variable	Variable
Heavy crude/ bitumen	C_{10} to >C_{40}	Low or trace	Low	Low	Low	High	No or trace	Low in naphthalenes	High	High
Petroleum products										
Gasoline	C_4 to C_{12}	Low	High	Trace	Trace	No	High	Medium	No or trace	No or trace
Kerosene	C_6 to C_{16}	High	Lower	Low	Low	No	Low	Low	No or trace	Low
Jet A	C_8 to C_{16}	High	Low	High	High	No	Low	Low	No or trace	No or trace
Diesel no. 2 (on-road)	C_8 to C_{24}	High	Low	High	High	Trace tricyclic	Low	High	No or trace	Low
Diesel (off-road)	C_8 to C_{28}	High	Low	High	High	Low	Low	High	Low	Low
Fuel no. 5/ bunker B	C_8 to C_{40}	High	Medium	High	Medium	High	Low	High	High	Variable
Fuel no. 6/ bunker C	C_{12} to C_{34}	High	High	Low	Low	High	Low	High	High	Variable
Lubricating oil	C_{18} to C_{34}	Low	Low	Low	Low	Variable	No or trace	Trace or low	No or trace	Low

according to the Canadian Council of Ministers of the Environment (CCME) methods [39]. However, the oil analysis described herein could be very different from the CCME methodology. Fraction 1 (smaller than C_{10}) represents the volatile fraction of most hydrocarbon mixtures and consists of the aliphatic and aromatic subfractions. Fractions 2 and 3 represent the semivolatile fraction and comprise saturated and aromatic subfractions in the ranges of C_{10} to C_{16} and C_{16} to C_{34}, respectively. These two fractions make up the most proportion of GC-detectable petroleum hydrocarbons in crude oils and petroleum products. Most of the target compounds fall within these two fractions. PAHs with more than three rings are generally found in fraction 3. Fraction 4 encompasses compounds of $>C_{34}$ up to C_{50}+, having low mobility (volatility and solubility). Petroleum hydrocarbons within this range often represent a significant proportion of heavy crude oils such as Alberta oil sand bitumen (24.4%) and refined products such as lubricating oil 10W-30 (15.2%).

The GC-FID chromatograms of petroleum hydrocarbons in representative crude oils are shown in Figure 2.3, illustrating the difference of these crudes in the chromatographic profiles, carbon range, and UCM distribution patterns. The data in Table 2.2 reports TPHs at a range of ~ *n*-C_8 to *n*-C_{50} determined by GC-FID. These results do not include those components lighter than *n*-C_8, which are lost during sample preparation or co-eluted with solvent peaks (DCM and/or hexane) during GC analysis. This explains why some light oils containing high amounts of small hydrocarbons have smaller TPH values reported than some heavier oil samples. Heavy oils contain heavy substances, which either are retained on the silica gel fractionation column or are uneluted from GC capillary column, resulting in low TPH value for these oils.

The gross chemical composition of crude oils varies greatly, not only among geological sources but also among samples from a single deposit. In general, saturated compounds and UCM dominate GC-detectable TPHs in crude oils. The extra light Scotia crude (API = 53.2°, Nova Scotia, Canada) contains a large proportion of light components with nearly half of the resolved peaks, in which $<C_{16}$ hydrocarbons account for about 70% of TPHs while $>C_{34}$ account for only 0.6%. In addition, TSHs in this crude make up 95.3% of TPH value, obviously higher than in any other oils presented in Table 2.2. The heavy Platform Elly crude oil (API = 15.8°, US west coast, California) contains about 87% of UCM contents, and $>C_{16}$ fractions contribute to over 75% of GC-detectable TPHs. As the heaviest form of petroleum, oil sand bitumen has a pronounced chromatographic UCM hump eluting between *n*-C_{10} and *n*-C_{40}, indicating significant biodegradation of their original crudes. Normal alkanes and isoprenoid alkanes have been steadily depleted by biodegradation and/or water washing in this bitumen. A few resolved peaks eluted between *n*-C_{27} and *n*-C_{31} on the shoulder of the main UCM hump, which is contributed by high boiling point biomarker compounds. Albian Heavy Synthetic (AHS) is a partially upgraded dilbit. It is a blend of sweet Premium Albian Synthetic (API ~ 34°) upgraded from oil sand bitumen with the unconverted residue. The abundance and distribution of TPHs in AHS are significantly different from those of oil sand bitumen. Since Premium Albian Synthetic consists

Table 2.2: GC-FID-detectable petroleum hydrocarbons in representative crude oils and petroleum products.

Oil samples	Crude oils						Petroleum products					
	Scotia Light (ScL)	Bakken crude	Prudhoe Bay	Troll	Platform Elly (PlE)	Alberta oil sand bitumen	>Diesel no. 2	>Marine diesel	>IFO-180	>Bunker B (fuel no. 5)	>Bunker C (fuel no. 6)	>Lubricating oil 10W-30 (10W-30)
	(API = 53.2, Nova Scotia, Canada)	North Dakota, USA	(API = 26.7, Alaska, USA)	(API = 28.4, North Sea)	(API = 15.8, US West-Coast)	(Alberta, Canada)*	(Ottawa, Canada)	(Burnaby, BC)	(Canada, 2004)	(USA, 2002)	(Canada, 2002)	(motor oil, Ottawa, 2004)
TPH (mg/g)**	577	691	549	723	436	302	957	904	463	476	370	808
~n-C_8 to n-C_{10} (%)	9.8	9.3	8.9	6.9	5.3	0.1	6.3	2.9	1.2	0.92	1.85	ND
n-C_{10} to n-C_{16} (%)	59.5	30.4	24.5	25.0	18.1	9.5	54.5	39.5	21.8	12.8	13.3	0.1
n-C_{16} to n-C_{34} (%)	30.1	48.1	55.0	59.3	57.9	65.9	39.1	56.6	71.3	67.5	63.8	84.7
≥n-C_{34} (%)	0.6	12.2	11.6	8.8	18.7	24.4	ND	1.0	5.7	18.8	21.1	15.2
TSH/TPH (%)	95.3	77.3	68.2	71.6	51.8	57.4	89.8	82.5	52.7	63.1	47.6	94.9
TAH/TPH (%)	4.7	22.7	31.8	28.4	48.2	42.5	10.2	17.5	47.3	36.9	52.4	5.1
GC-UCM/GC-TPH (%)	52.3	73.0	77.9	84.4	87.0	97.5	77.7	74.4	80.6	74.7	72.3	95.9
Total n-alkanes (mg/g)	172	53.2	63.0	35.6	21.5	ND***	128	54.2	42.3	46.4	29.1	ND

* The concentration is based on TSEM of DCM extract from raw oil sands.

** Petroleum hydrocarbons are determined by GC-FID at a range of ~ n-C_8 to n-C_{50}.

*** ND represents nondetectable.

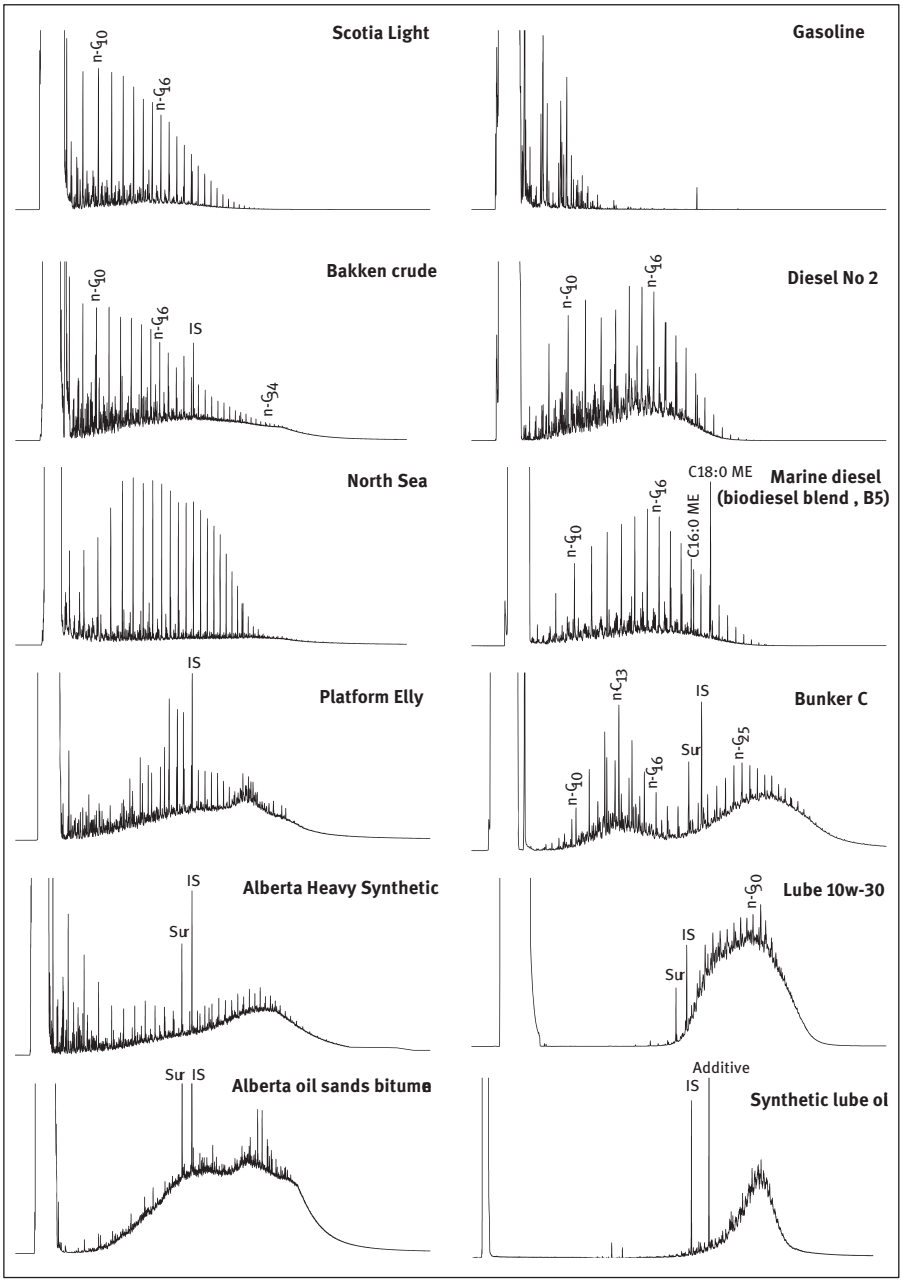

Figure 2.3: GC-FID chromatograms of petroleum hydrocarbons in crude oils and petroleum products.

mostly of light hydrocracking hydrocarbons and is absent of vacuum residue, the UCM contents are mainly constituted by the heavier portion of residues.

As observed from Figure 2.3 and Table 2.2, refined petroleum products vary significantly with type to type and oil to oil in the carbon range, hydrocarbon distribution pattern, and UCM profiles. The distinguishable characteristics for various types of products are attributed to parent crude oil feedstocks, refining processes, and the materials added in the products for specific purposes. Light distillates such as gasoline are generally products of light-end-resolved hydrocarbons nearly without any UCM content. The chemical composition of light distillate is relatively simple and has been well characterized. The composition of gasoline generally includes a majority of light PIANO compounds (paraffins, isoparaffins, aromatics, naphthenes, and olefins) and a small portion of additives (such as alcohols).

Diesel fuel, a mid-range distillate, generally has a carbon range from C_8 to C_{28}. In some regions, diesel is often blended with lighter components for winter use. Its GC-FID chromatogram presents prominent *n*-alkanes in the GC-resolved peaks over a single bell-shaped UCM hump. MDO contains a wider carbon range than on-road diesel. In the analysis of diesel blended with biofuels, additional FAME peaks eluted after *n*-C_{19} and one co-eluted with *n*-C_{21} in the GC-FID chromatograms were readily observed [24]. It is notable that in a biodiesel blend methyl palmitate (C16:0 ME) peak elutes after *n*-C_{19} and methyl stearate (C18:0 ME) and methyl oleate (*cis*-9, C18:1 ME) co-elute with *n*-C_{21} in the GC-FID chromatograms.

HFO are often burned in furnaces to generate heat or in maritime (such heavy fuel is called bunker fuel) or industrial boilers to generate power. Typical marine fuels include lighter fuel no. 5 (Bunker B) and heavier fuel no. 6 (Bunker C). These fuel oils are mainly heavy distillate residue blended by lighter distillates to reduce oil viscosity; therefore, these oils are characterized by two or more obvious chromatographic UCM humps and particular *n*-alkane distribution. HFOs could have a wide carbon range, and some HFOs have similar chromatographic features with weathered crude oils. Their unambiguous identification and differentiation need to rely on the comparison of their fingerprint details from GC-MS analysis.

Commercial lubricating oil is either mineral-based or synthetic, and mineral-based lube oils are most commonly used. The applications of lube oil are very diverse. Lube oil can be classified into various categories such as motor oil and transmission oil according to specific applications. Lubricating oil is distinguishable from other refined products by its unique chromatographic profile. They generally consist of high boiling point hydrocarbons ranging from *n*-C_{20} to *n*-C_{50} eluted as a characteristic UCM hump. GC-resolved peaks only account for a very small portion of TPHs in lubricating oil, for example, lubricating 10W-30 motor oil contains about 96% of UCM content (Table 2.2). As shown in Figure 2.3, the synthetic lube oil has typical GC-chromatographic features of regular lube oil: high UCM content but very little *n*-alkanes and resolved peaks. One high sharp peak over the UCM hump is attributed to additives such as antioxidants

(phenols and amines). It is impossible to differentiate this type of synthetic lube oil from conventional mineral-based lube oils using GC-FID analysis alone.

The analyses of oils in environmental samples can be much more difficult and complex than the analysis of pure oil. The oil in the environment is subjected to various weathering processes and mixed with background substances, which alter oil characteristics and complicate identification. Figure 2.4 shows the GC-FID chromatograms of hydrocarbons in some petroleum-impacted environmental samples. The background soil contains very little UCM, although nonpetroleum UCM content is detectable if not properly removed by a silica-gel column cleanup procedure [40]. This sample has a predominance of odd carbon numbers over even carbon number *n*-alkanes in C_{21} to C_{35} range, indicating hydrocarbon inputs from natural organic matter, plants, and bacteria. The petroleum hydrocarbons in the vessel bilge clearly consist of primarily a diesel range fuel and a slight amount of lubricating oil. More than two UCM humps are noticeable in the river sediment, indicating multiple sources of contamination. Two UCM humps ranging from *n*-C_{20} to *n*-C_{30} and *n*-C_{30} to *n*-C_{50} were detected for the waste lube oil, indicating that the waste oil is mainly a mixture of 10W-30 and 20W-50 lube oils [24]. Prominent odd *n*-alkanes were detected over the UCM hump, indicating that the main hydrocarbons in the sediment from a water treatment plant are mainly attributed to petroleum contamination and the contribution of biogenic sources. The waste lube oil also contains a small portion of *n*-alkanes between *n*-C_{12} to *n*-C_{26} and about 5.0% resolved peaks of TPH, which are certainly attributable to diesel fuel.

It is impossible to identify or quantify the petroleum biomarkers and PAHs through GC-FID analysis alone, which are at relatively low concentrations but of interest to forensic oil analysis. The GC-MS analysis provides data on the "source-specific" markers including a suit of saturated and aromatic target compounds. These analyses provide detailed information from each class of petroleum hydrocarbons to support the findings from GC-FID analysis.

2.5 Saturated hydrocarbons in petroleum

Saturated petroleum fraction consists of aliphatic hydrocarbons such as *n*-alkanes, branched alkanes, and cyclic hydrocarbons. Normal alkanes and branched alkanes are typically attributed to the major resolved peaks in gas chromatograms of the saturated fraction from light to medium crude oils and distillates.

Saturated cyclic hydrocarbons (naphthenes) comprise the most desirable petroleum hydrocarbons for the oil fingerprinting approach. Tables 2.3 summarizes the target saturated hydrocarbons frequently used for oil analysis including decalins, bicyclic sesquiterpanes, diamondoids, polycyclic terpanes, and polycyclic steranes [10, 12, 13, 15, 16, 20, 27, 29]. In brief, the most commonly used fragment ions are *m*/*z* 191 for tri- to penta- cyclic terpanes and *m*/*z* 217 and 218 for steranes. Bicyclic sesquiterpanes are

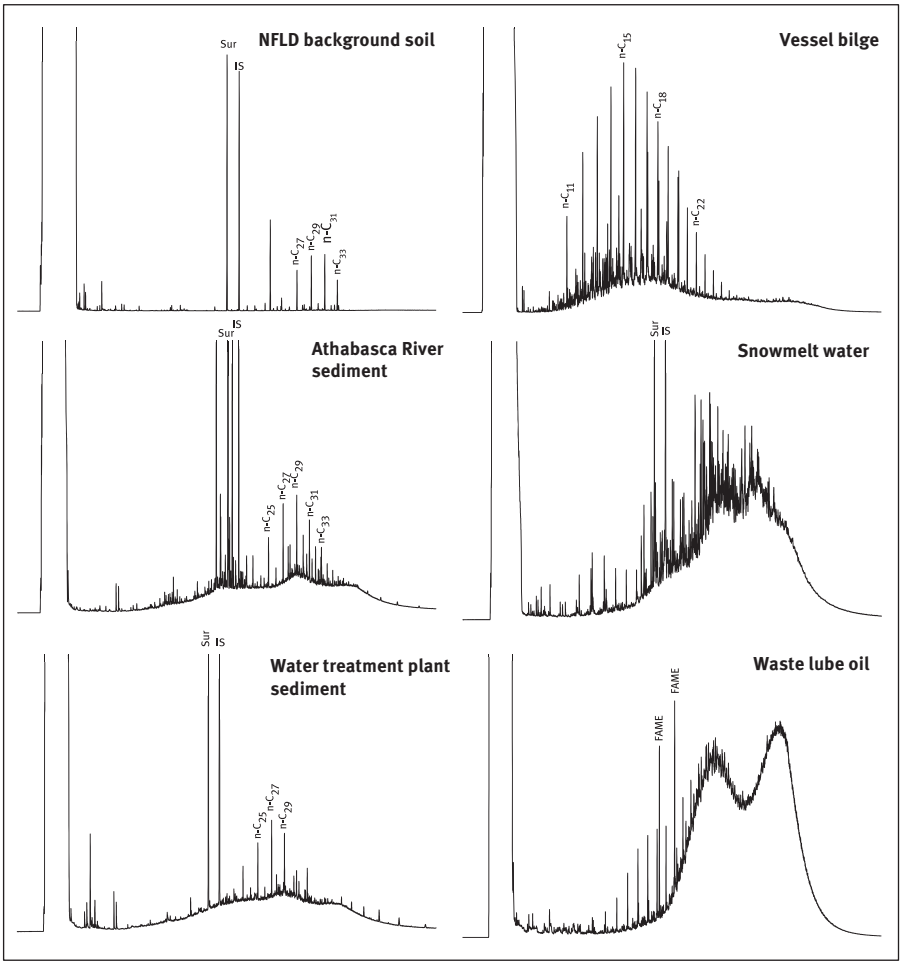

Figure 2.4: GC-FID chromatograms of hydrocarbons in environmental samples.

determined at m/z 123 and confirmed by ions of m/z 179, 193, and 207. The ions for diamondoid analysis include m/z 135, 136, 149, 163, and 177 for adamantanes and m/z 187, 188, 201, and 215 for diamantanes.

Some compounds in crude oils retain all or part of molecular structures from their original biological molecules produced by organisms. These molecular fossils are often called biological markers, or simply biomarkers. These compounds are resistant to biodegradation relative to other hydrocarbons. Their analyses have played an important role in exploring the depositional environment of crude oil and tracking the genesis, maturation, migration, and biodegradation of petroleum. The information from the analysis of backbone petrogenic compounds has been widely used to investigate the source and history of petroleum-derived environmental contaminants.

Table 2.3: Target saturated hydrocarbons frequently used for oil fingerprinting analysis.

Compounds	Code	Empirical formula	Molecular weight	Target ions
Normal alkanes				
n-Alkanes (*n*-C_{10} to *n*-C_{44})	*n*-C_n	C_nH_{2n+2}	14 n + 2	85, 71, 57
Acyclic isoprenoids				
(*i*-C_{13} to *i*-C_{20})				
Norpristane	Norpri	$C_{18}H_{38}$	254	85, 113
Pristane	Pri	$C_{19}H_{40}$	268	85, 113
Phytane	Phy	$C_{20}H_{42}$	282	85, 113, 183
Alkylated cyclopentanes		C_nH_{2n}	14 n	69, 83
Alkylated cyclohexanes		C_nH_{2n}	14 n	83, 97
Bicyclic alkanes				
Decalin	DE	$C_{10}H_{18}$	138	138
C_1-Decalins	C1DE	$C_{11}H_{20}$	152	152
C_2-Decalins	C2DE	$C_{12}H_{22}$	166	166
C_3-Decalins	C3DE	$C_{13}H_{24}$	180	180
Bicyclic sesquiterpanes				
C_4-Decalin	BS1	$C_{14}H_{26}$	194	123, 179
C_{14}-Sesquiterpane	BS2	$C_{14}H_{26}$	194	123, 179
C_{15}-Sesquiterpane	BS3	$C_{15}H_{28}$	208	123, 193
C_{15}-Sesquiterpane	BS4	$C_{15}H_{28}$	208	123, 193
8β(H)-Drimane	BS5	$C_{15}H_{28}$	208	123
C_{15}-Sesquiterpane	BS6	$C_{15}H_{28}$	208	123
C_{16}-Sesquiterpane	BS7	$C_{16}H_{30}$	222	123
C_{16}-Sesquiterpane	BS8	$C_{16}H_{30}$	222	123, 193
C_{16}-Sesquiterpane	BS9	$C_{16}H_{30}$	222	123, 193
8β(H)-Homodrimane	BS10	$C_{16}H_{30}$	222	123, 207
Adamantanes				
Adamantane	A	$C_{10}H_{16}$	136	136
1-Methyladamantane	1-MA	$C_{11}H_{18}$	150	135
1,3-Dimethyladamantane	1,3-DMA	$C_{12}H_{20}$	164	149
1,3,5-Trimethyladamantane	1,3,5-TMA	$C_{13}H_{22}$	178	163
1,3,5,7-Tetramethyladamantane	1,3,5,7-TeMA	$C_{14}H_{24}$	192	177
2-Methyladamantane	2-MA	$C_{11}H_{18}$	150	135
1,4-Dimethyladamantane, *cis*	1,4-DMA, *cis*	$C_{12}H_{20}$	164	149
1,4-Dimethyladamantane, *trans*	1,4-DMA, *trans*	$C_{12}H_{20}$	164	149
1,3,6-Trimethyladamantane	1,3,6-TMA	$C_{13}H_{22}$	178	163
1,2-Dimethyladamantane	1,2-DMA	$C_{12}H_{20}$	164	149
1,3,4-Trimethyladamantane, *cis*	1,3,4-TMA, *cis*	$C_{13}H_{22}$	178	163
1,3,4-Trimethyladamantane, *trans*	1,3,4-TMA, *trans*	$C_{13}H_{22}$	178	163
1,2,5,7-Tetramethyladamantane	1,2,5,7-TeMA	$C_{14}H_{24}$	192	177
1-Ethyladamantane	1-EA	$C_{12}H_{20}$	164	135
1-Ethyl-3-methyladamantane	1-E-3-MA	$C_{13}H_{22}$	178	149
1-Ethyl-3,5-dimethyladamantane	1-E-3,5-DMA	$C_{14}H_{24}$	192	163
2-Ethyladamantane	2-EA	$C_{12}H_{20}$	164	135

Table 2.3 (continued)

Compounds	Code	Empirical formula	Molecular weight	Target ions
Diamantanes				
Diamantane	D	$C_{14}H_{20}$	188	188
4-Methyldiamantane	4-MD	$C_{15}H_{22}$	202	187
4,9-Dimethyldiamantane	4,9-DMD	$C_{16}H_{24}$	216	201
1-Methyldiamantane	1-MD	$C_{15}H_{22}$	202	187
1,4 and 2,4-Dimethyldiamantane	1,4 and 2,4-DMD	$C_{16}H_{24}$	216	201
4,8-Dimethyldiamantane	4,8-DMD	$C_{16}H_{24}$	216	201
Trimethyldiamantane	TMD	$C_{17}H_{26}$	230	215
3-Methyldiamantane	3-MD	$C_{15}H_{22}$	202	187
3,4-Dimethyldiamantane	3,4-DMD	$C_{16}H_{24}$	216	201
Biomarker terpanes				
C_{19} tricyclic terpane	TR19	$C_{19}H_{34}$	262	191
C_{20} tricyclic terpane	TR20	$C_{20}H_{36}$	276	191
C_{21} tricyclic terpane	TR21	$C_{21}H_{38}$	290	191
C_{22} tricyclic terpane	TR22	$C_{22}H_{40}$	304	191
Biomarker terpanes				
C_{23}-Tricyclic terpane	TR23	$C_{23}H_{42}$	318	191
C_{24}-Tricyclic terpane	TR24	$C_{24}H_{44}$	332	191
C_{25}-Tricyclic terpane (a), (b)	TR25A, TR25B	$C_{25}H_{46}$	346	191
Triplet: C_{24} tetracyclic + C_{26} (*S* + *R*) tricyclic terpanes terpanes	TET24 + TR26(A + B)	$C_{24}H_{42}$ + $C_{26}H_{48}$	330, 374	191
C_{28}-Tricyclic terpane (a), (b)	TR28A, TR28B	$C_{28}H_{52}$	388	191
C_{29}-Tricyclic terpane (a), (b)	TR29A, TR29B	$C_{29}H_{54}$	402	191
18α(H)-22,29,30-Trisnorhopane	Ts	$C_{27}H_{46}$	370	191
17α(H),18α(H),21β(H)-25,28,30-Trisnorhopane	TH27	$C_{27}H_{46}$	370	191, 177
17α(H)-22,29,30-Trisnorhopane	Tm	$C_{27}H_{46}$	370	191
C_{30}-Tricyclic terpane 1 and 2	TR30A,TR30B	$C_{30}H_{56}$	416	191
17α(H),18α(H),21β(H)-28,30-bisnorhopane	H28	$C_{28}H_{48}$	384	191
17α(H),21β(H)-25-Norhopane	NOR25H	$C_{29}H_{50}$	398	191, 177
17α(H),21β(H)-30-Norhopane	H29	$C_{29}H_{50}$	398	191
18α(H),21β(H)-30-Norneohopane	C29Ts	$C_{29}H_{50}$	398	191
17α(H)-Diahopane	DH30	$C_{30}H_{52}$	412	191
17β (H),21α(H)-30-Norhopane (normoretane)	M29	$C_{29}H_{50}$	398	191
18α(H) and 18β(H)-Oleanane	OL	$C_{30}H_{52}$	412	191, 412
17α(H),21β(H)-Hopane	H30	$C_{30}H_{52}$	412	191
17α(H)-30-nor-29-Homohopane	NOR30H	$C_{30}H_{52}$	412	191
17β(H),21α(H)-Hopane (moretane)	M30	$C_{30}H_{52}$	412	191
22*S*-17α(H),21β(H)-30-Homohopane	H31S	$C_{31}H_{54}$	426	191
22 *R*-17α(H),21β(H)-30-Homohopane	H31R	$C_{31}H_{54}$	426	191
Gammacerane	G	$C_{30}H_{52}$	412	191, 412

Table 2.3 (continued)

Compounds	Code	Empirical formula	Molecular weight	Target ions
22*S*-17α(H),21β(H)-30,31-Bishomohopane	H32S	$C_{32}H_{56}$	440	191
22*R*-17α(H),21β(H)-30,31-Bishomohopane	H32R	$C_{32}H_{56}$	440	191
22*S*-17α(H),21β(H)-30,31,32-Trishomohopane	H33S	$C_{33}H_{58}$	454	191
22*R*-17α(H),21β(H)-30,31,32-Trishomohopane	H33R	$C_{33}H_{58}$	454	191
22*S*-17α(H),21β(H)-30,31,32,33-Tetrakishomohopane	H34S	$C_{34}H_{60}$	468	191
22*R*-17α(H),21β(H)-30,31,32,33-Tetrakishomohopane	H34R	$C_{34}H_{60}$	468	191
22*S*-17α(H),21β(H)-30,31,32,33,34-Pentakishomohopane	H35S	$C_{35}H_{62}$	482	191
22*R*-17α(H),21β(H)-30,31,32,33,34-Pentakishomohopane	H35R	$C_{35}H_{62}$	482	191
Biomarker steranes				
C_{20} 5α(H),14α(H),17α(H)-Sterane	S20	$C_{20}H_{34}$	274	217, 218
C_{21} 5α(H),14β(H),17β(H)-Sterane	S21	$C_{21}H_{36}$	288	217
C_{22} 5α(H),14β(H),17β(H)-Sterane	S22	$C_{22}H_{38}$	302	217
C_{27} 20*S*-13β(H),17α(H)-Diasterane	DIA27S	$C_{27}H_{48}$	372	217
C_{27} 20*R*-13β(H),17α(H)-Diasterane	DIA27R	$C_{27}H_{48}$	372	217
C_{27} 20*S*-13α (H),17β (H)-Diasterane	DIA27S2	$C_{27}H_{48}$	372	217
C_{27} 20*R*-13α (H),17β (H)-Diasterane	DIA27R2	$C_{27}H_{48}$	372	217
C_{28} 20*S*-13β(H),17α(H)-Diasterane	DIA28S	$C_{28}H_{50}$	386	217
C_{28} 20*R*-13β(H),17α(H)-Diasterane	DIA28R	$C_{28}H_{50}$	386	217
C_{29} 20*S*-13β(H),17α(H)-Diasterane	DIA29S	$C_{29}H_{52}$	400	217
C_{29} 20*R*-13α(H),17β(H)-Diasterane	DIA29R	$C_{29}H_{52}$	400	217
C_{27} 20*S*-5α(H),14α(H),17αH)-Cholestane	C27ααS	$C_{27}H_{48}$	372	217
C_{27} 20*R*-5α(H),14β(H),17β(H)-Cholestane	C27ββR	$C_{27}H_{48}$	372	217, 218
C_{27} 20*S*-5α(H),14β(H),17β(H)-Cholestane	C27ββS	$C_{27}H_{48}$	372	217, 218
C_{27} 20*R*-5α(H),14α(H),17α(H)-Cholestane	C27ααR	$C_{27}H_{48}$	372	217
C_{28} 20*S*-5α(H),14α(H),17α(H)-Ergostane	C28ααS	$C_{28}H_{50}$	386	217
C_{28} 20*R*-5α(H),14β(H),17β(H)-Ergostane	C28ββR	$C_{28}H_{50}$	386	217, 218
C_{28} 20*S*-5α(H),14β(H),17β(H)-Ergostane	C28ββS	$C_{28}H_{50}$	386	217, 218
C_{28} 20*R*-5α(H),14α(H),17α(H)-Ergostane	C28ααR	$C_{28}H_{50}$	386	217

Table 2.3 (continued)

Compounds	Code	Empirical formula	Molecular weight	Target ions
C_{29} 20*S*-5α(H),14α(H),17α(H)-Stigmastane	C29ααS	$C_{29}H_{52}$	400	217
C_{29} 20*R*-5α(H),14β(H),17β(H)-Stigmastane	C29ββR	$C_{29}H_{52}$	400	217, 218
C_{29} 20*S*-5α(H),14β(H),17β(H)-Stigmastane	C29ββS	$C_{29}H_{52}$	400	217, 218
C_{29} 20*R*-5α(H),14α(H),17α(H)-Stigmastane	C29ααR	$C_{29}H_{52}$	400	217
C_{30}-Steranes	C30ααS	$C_{30}H_{54}$	414	217

The commonly analyzed HMW petroleum biomarkers are polycyclic triterpanes and steranes. These conventional biomarker compounds are eluted after *n*-C_{21}, indicating their high boiling points, which occur within the residual range (Figure 2.2). Smaller cyclic hydrocarbons such as diamondoids and bicyclic sesquiterpanes in light to medium carbon range have attracted increasing attention due to their potential forensic applications especially for lighter oils and products [19, 33–36, 41–44]. These compounds have been detected in most crude oils and in a variety of distilled petroleum products, which makes them particularly applicable to the analysis of lighter refined products such as diesel fuels that lack suitable alternatives. In these refined products, HMW biomarkers have been removed during the refining processes.

2.5.1 Normal alkanes and acyclic isoprenoids

Normal and branched alkanes comprise a substantial portion of most crude oils and certain types of petroleum products. These compounds can be readily separated into resolved peaks by capillary GC columns. Normal alkanes in crude oil and petroleum usually occur in high concentrations, which enables them to be quantitatively analyzed by GC-FID. However, if their concentrations in heavy oils and environmental samples are too low or subject to interferences to obtain accurate analysis, GC-MS analysis can be an alternative fingerprinting technique.

Normal alkanes in crude oils often vary significantly in their concentrations and distributions (Table 2.2 and Figure 2.3). Total *n*-alkanes in Scotia Light crude oil are as high as 172 mg/g, whereas only 21.5 mg/g in the Platform Elly crude oil and almost no *n*-alkane are detected in Alberta oil sand bitumen. As shown in Figure 2.2, *n*-alkanes could account for about 25% of GC-detectable TPHs and over half of the resolved peaks in the high wax crude oil.

Refined petroleum products generally have their distinctive abundance and carbon range in their *n*-alkane profiles. Diesel consists of high levels of C_8 to C_{28} *n*-

alkanes and alkyl-cyclohexanes. The properties of a given diesel are largely a fraction of the crude oil feedstock. Diesel no. 2 has a high concentration of *n*-alkanes of 128 mg/g, and its GC chromatogram has a nearly normal distribution with maxima around *n*-C_{11} to *n*-C_{14}. The GC-TPHs are dominated by the central UCM hump, totally accounting for 77.7%. Heavy bunker fuels such as Bunker C generally contain lower *n*-alkanes, whereas lubricating oils generally contain a very trace amount of long-chain *n*-alkanes.

Normal C_{10}–C_{40} alkanes, with a marked predominance of odd-numbered hydrocarbons in the span of *n*-C_{23} to *n*-C_{35}, are identified in higher plants (concentrations of *n*-C_{27}, *n*-C_{29}, and *n*-C_{31} hydrocarbons are especially high) and soil, river, and marine sediments (see Figure 2.4). This characteristic is particularly useful to distinguish biogenic sources from petrogenic sources in environmental samples.

Some branched alkanes in petroleum are genetically related to acyclic isoprenoids and norisoprenoids. These isoprenoids are composed exclusively of "head-to-tail" links of isoprene units, whereas irregular isoprenoids have a "tail-to-tail" link. Compared to other alkanes, these hydrocarbons are characterized by their structural stability and preservation of genetic features, which are inherited from peculiarities of the original organic matter and the conditions of its transformation into petroleum hydrocarbons. Barakat et al. detected a suite of acyclic isoprenoids from C_{13} to C_{20} except C_{17} in the crude oils from the Gulf of Suez region of Egypt [45]. The most abundant acyclic isoprenoids in oil include farnesane (*i*-C_{15}: 2,6,10-trimethyl-dodecane), 2,6,10-trimethyl-tridecane (*i*-C_{16}), norpristane (*i*-C_{18}: 2,6,10-trimethyl-pentadecane), pristane (*i*-C_{19}: 2,6,10,14-tetramethyl-pentadecane), and phytane (*i*-C_{20}: 2,6,10,14-tetramethyl-hexadecane). The acyclic isoprenoids of pristane and phytane are widely assumed diagenetic products of the phytyl side chain of chlorophyll, although alternative sources of precursors have been suggested. Branched alkanes normally exhibit lower melting points and boiling points than those *n*-alkanes with the same carbon numbers; therefore, they tend to elute earlier than their normal isomers during GC analysis. Pristane and phytane are eluted closely with *n*-C_{17} and *n*-C_{18} into two pairs of characteristic peaks in chromatographic analysis. They are often investigated together with *n*-alkane analysis. Crudes with the same geological origin have similar pristane/phytane ratios.

2.5.2 Diamondoids

Diamondoids and their various substituents are widely found in crude oils, intermediate petroleum distillates, and finished petroleum products [33, 34, 46–49]. Diamondoids are a class of cage-like cyclic hydrocarbons and consist of three-dimensionally fused cyclohexane rings, resulting in a diamond-like structure. Diamondoids have the general molecular formula $C_{4n+6}H_{4n+12}$. The simplest diamondoid is adamantane ($C_{10}H_{16}$), followed by its homologues of diamantane ($C_{14}H_{20}$), triamantane, tetramantane,

pentamantane, and hexamantane. Figure 2.5 illustrates a suite of adamantanes and diamantanes identified in crude oils and petroleum products. Adamantane and its C_1- to C_4-substituents are eluted between *n*-C_{10} and *n*-C_{13} (boiling point range: 180–230 °C), while diamantane series are eluted between *n*-C_{15} and *n*-C_{17} (boiling point range: 270–300 °C) at given chromatographic conditions (Figures 2.2).

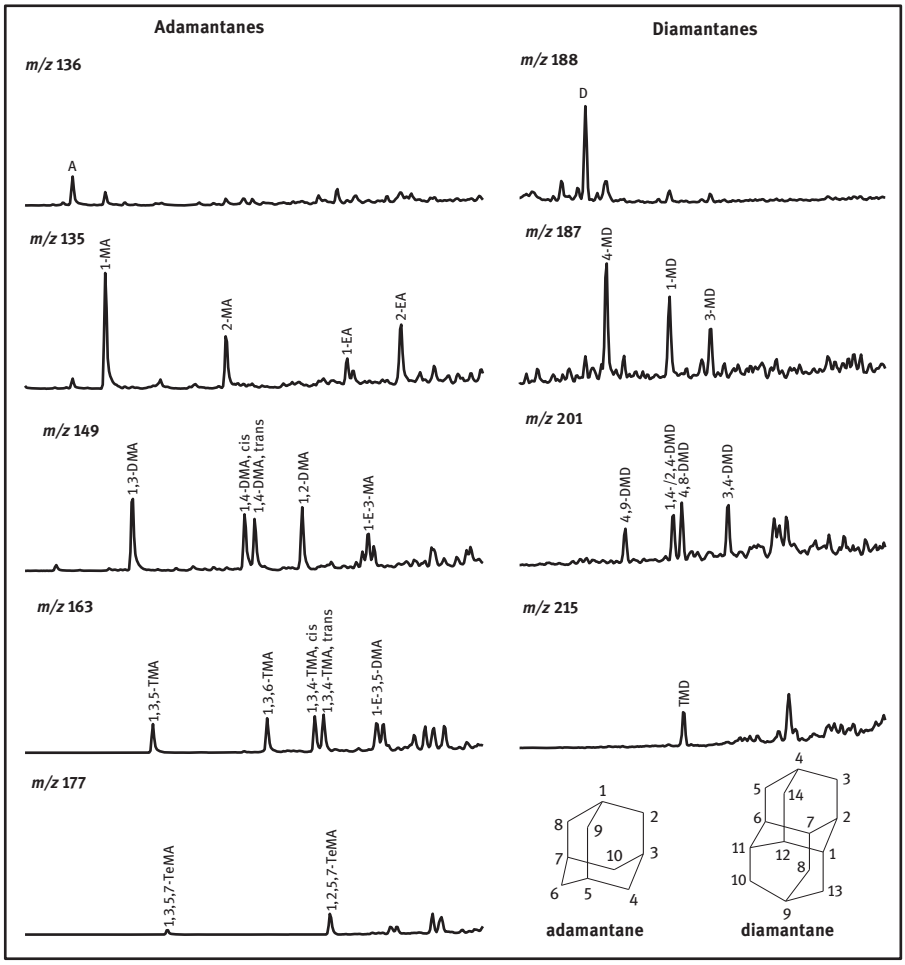

Figure 2.5: Adamantanes (at *m/z* 136, 149, 163, and 207) and diamantanes (at *m/z* 188, 187, 201, and 215) identified in crude oils and petroleum products.

A series of petroleum polymantanes were determined in a gas condensate produced from a very deep petroleum reservoir located in the U.S. Gulf Coast [50]. Dahl et al. reported successful separation of a wide variety of the higher diamondoids containing 4–11 (undecamantane) diamond-crystal cages from petroleum [51]. Diamondoid

compounds in petroleum are believed to be the result of carbonium ion rearrangements of suitable cyclic precursors (such as multiringed terpene hydrocarbons) on clay superacids in the source rock during oil generation [48, 52, 53]. The higher homologues of diamondoids are considered to be formed from lower homologues under extreme temperature and pressure [54].

Diamondoids are common in reservoir fluids and have been considered a problem due to their deposition during production and transportation of natural gas, gas condensates, and light crude oils. The naturally occurring diamondoid compounds are thermodynamically stable [49, 54, 55], and therefore, they are particularly useful in oil-source correlation and differentiation. Environmental scientists have applied the multiple criteria approach with the characterization of more than one suite of analytes, including fingerprinting the diamondoid hydrocarbons for oil spill correlation and identifications. Diamondoid analysis is particularly meaningful for those cases where the conventional tri- to pentacyclic biomarker terpanes and steranes are absent due to removal during the refining processes [34, 36, 41].

***Diamondoids in crude oils*:** GC-MS chromatograms of adamantanes and diamantanes were determined in various crude oils from light South Louisiana crude oil to extra heavy Alberta oil sand bitumen are displayed [36]. The concentration of adamantane, diamantane, and their alkyl-homologues in these crude oils are shown in Table 2.4. Overall, the one-cage adamantanes are much more abundant than the two-cage diamantanes.

As shown in Table 2.4, the concentrations of individual adamantane and its alkylated derivatives are in the range of ~1–30 μg/g for most crude oils, except ~ 1–300 μg/g for the corresponding individual diamondoids in Troll (North Sea, Norway) and South Louisiana (37.2° API, Louisiana, USA) crude oils. Among the detected adamantanes, the principal dominant adamantanes are A, 2-MA, 1-MA, 2-EA, 1,2-DMA, and 1,3-DMA, together accounting for about 50% of all detected adamantanes. Either 1-MA (bridgehead-substituted) or 2-MA is the most abundant homologue in all oil samples. Tri- and tetra-methylated diamondoids have much lower relative abundance compared to methyl- and dimethyl-homologues. Among the adamantane series, 1,3,5,7- tetramethyl-adamantane has the lowest concentration probably due to its relatively poor thermal stability; it has four methyl groups, which could spatially interfere with each other and cause the molecular structure to be strained.

The dominant diamantane compounds in crude oils are D, 4-MD, 1-MD, 3-MD, and 3,4-DMD. The concentrations of individual diamantanes range from undetected levels to 10 μg/g for most crude oil samples and up to 10–53 μg/g for the South Louisiana oil. The California Platform Elly heavy oil has the lowest concentration of adamantanes among the surveyed oils. Cook Inlet (Southern Alaska, USA) crude oil has a low concentration of diamantanes (9.10 μg/g), even though its adamantanes are at a relatively high concentration of 209 μg/g.

Table 2.4: Concentrations of diamondoids in crude oils and petroleum products.

Compounds	SoL	ANS	Troll	ArH	PlE	Oil sands*	Fed	Fed (174–287°C) 287oC)	Fed (287–481°C) 287oC)	JetA	Diesel No. 2	BkC	10W-30
A	126	19.3	48.6	6.80	0.77	3.16	8.25	31.9	0.08	181	63.3	5.19	0.08
1-MA	288	33.9	68.0	12.0	2.04	7.46	12.7	43.2	0.14	222	118	7.53	0.19
1,3-DMA	226	26.2	38.0	9.34	4.23	6.00	11.2	43.8	0.35	174	144	4.40	0.21
1,3,5-TMA	84.3	7.82	10.3	3.19	0.98	2.59	3.65	13.6	0.06	49.8	60.3	0.90	0.06
1,3,5,7-TeMA	13.7	1.28	1.50	0.90	0.19	0.52	0.72	2.7	0.02	7.44	5.85	0.03	0.01
2-MA	190	32.5	81.5	9.96	1.45	9.16	15.7	52.4	0.22	264	85.4	6.53	0.18
1,4-DMA, *cis*	109	17.1	32.2	5.97	1.81	4.84	9.57	38.7	0.33	140	54.3	2.61	0.12
1,4-DMA, *trans*	110	15.8	32.7	4.80	5.05	4.76	7.30	31.1	0.17	112	54.3	2.39	0.10
1,3,6-TMA	79.3	9.25	18.0	3.15	2.20	3.64	4.19	16.7	0.11	64.2	42.7	1.05	0.07
1,2-DMA	112	18.1	34.8	5.01	7.35	6.77	10.1	43.1	0.23	127	49.2	2.27	0.09
1,3,4-TMA, *cis*	76.7	9.36	17.5	2.69	1.33	4.99	4.74	16.3	0.16	52.5	32.0	0.92	0.06
1,3,4-TMA, *trans*	82.6	10.6	20.6	3.30	3.24	4.54	6.05	25.1	0.21	70.2	40.0	1.60	0.07
1,2,5,7-TeMA	55.5	5.28	9.50	1.88	1.65	3.33	3.25	12.0	0.16	31.5	32.3	0.47	0.05
1-EA	56.2	8.38	16.1	2.54	2.26	3.63	4.72	17.9	0.54	63.3	30.5	2.47	0.05
1-E-3-MA	94.1	14.1	20.7	4.91	3.30	6.87	6.56	22.4	0.29	75.0	71.4	2.75	0.07
1-E-3,5-DMA	89.5	10.9	21.5	2.67	1.34	7.97	7.77	26.2	0.34	76.4	31.9	1.28	0.07
2-EA	88.3	23.3	56.2	8.76	2.88	4.33	13.3	49.4	0.43	193	61.3	2.22	0.09
ΣAdamantanes (µg/g)	**1880**	**263**	**528**	**87.8**	**42.1**	**84.6**	**130**	**487**	**3.85**	**1904**	**977**	**44.6**	**1.58**
D	53.3	9.00	9.31	6.28	1.06	2.43	3.46	5.07	5.61	10.6	14.0	1.66	0.09
4-MD	36.5	5.19	4.46	5.22	4.38	1.87	2.89	5.70	6.24	4.50	9.43	1.05	0.06
4,9-DMD	11.7	1.17	0.98	1.02	0.09	ND	0.67	1.33	1.87	1.52	2.94	0.13	0.02
1-MD	22.8	3.82	5.06	2.99	0.69	ND	1.98	5.09	5.88	2.34	9.96	1.92	0.06
1,4- and 2,4-DMD	13.8	1.78	2.34	1.59	1.02	0.65	1.02	1.67	2.73	1.29	4.04	0.34	0.03
4,8-DMD	14.5	1.47	1.70	1.41	1.59	0.52	0.72	0.75	2.38	0.38	2.65	0.21	0.04
TMD	10.6	0.83	0.89	1.05	0.00	0.46	0.43	0.48	1.41	0.12	2.37	0.07	0.04

3-MD	15.4	2.13	3.53	1.44	1.08	1.22	1.03	1.40	9.52	1.14	4.43	0.59	0.04
3,4-DMD	16.3	2.13	3.38	1.65	0.46	1.85	1.26	1.88	3.84	1.14	3.78	0.39	0.04
ΣDiamantanes (µg/g)	**195**	**27.5**	**31.6**	**22.8**	**10.4**	**8.99**	**13.5**	**23.4**	**39.5**	**23.0**	**53.6**	**6.36**	**0.41**

* Concentration: µg/g of TSEM of Alberta oil sands DCM extract.

The concentrations of diamondoids do not appear to be dependent on the densities (or derived API gravities) of the crude oils. Diamondoids in oils from different sources have dissimilar signatures of both absolute concentrations and relative distribution patterns [34, 36]. These diamondoid fingerprints, as well as their molecular ratios particularly from adamantanes, may be useful for oil source identification.

***Diamondoids in petroleum products*:** The concentrations of diamondoids in refined products are significantly influenced by the crude oil feedstocks used in the production and the distillation cutpoint of the petroleum products. During the simulated laboratory distillation of crude oils, the medium distillate fraction (174–287 °C) accounted for >93% of all the adamantanes from the original crude oil. Diamantanes were found mainly in the fractions of 174–481 °C, accounting for about 90% of their total and were rarely found in the lightest fraction (initial boiling point to 174 °C) [36]. These temperature ranges for diamondoid partitioning are consistent with the observations based on GC chromatograms of *n*-alkanes and diamondoids.

Table 2.4 compares adamantanes and diamantanes measured in representative refined products including gasoline, diesel fuel, Bunker C, lubricating oil, and two distillate fractions of the Federated crude oil. The absolute concentrations and distribution patterns of diamondoids differ widely in petroleum products. As shown in Table 2.4, adamantanes were found in all fuel oil samples. As expected, little or no diamantanes were detected in light fuel and heavy-end lubricating oils. Generally, the overall distribution pattern of individual diamondoid compounds in petroleum products are comparable to that in crude oils, in which 1-MA and 2-MA, and D and 4-MD dominate the adamantanes and diamantanes, respectively.

2.5.3 Bicyclic sesquiterpanes

Bicyclic sesquiterpanes with drimane skeletons ($C_{15}H_{28}$) consist of two fused cyclohexane rings (decahydronaphthalene), with various methyl-, dimethyl-, ethyl-, or longer side chains [42, 56–58]. These compounds probably have a microbiological source and are produced from the biodegradation of bigger terpanes or are formed directly from bicyclic compounds of the same carbon framework.

Ten bicyclic sesquiterpanes commonly analyzed in petroleum fingerprinting elute between *n*-C_{13} and *n*-C_{16} (boiling points: 235–287 °C), compared with conventional polycyclic terpanes and steranes eluted between *n*-C_{21} and *n*-C_{37} (boiling points: 345–500 °C) (see Figure 2.2). These terpanes are identified as C_{14} (BS1 and BS2), C_{15} (BS3 to BS6) and C_{16} (BS7 to BS10) sesquiterpanes with molecular weights being 194, 208, and 222 atomic mass units (amu), respectively (Table 2.3). These compounds are determined at their characteristic ions at *m*/*z* 123 ($C_9H_{15}^+$), and confirmation can be conducted using other prominent ions such as *m*/*z* 179, 193, and 207 [35].

Due to the commercial unavailability of sesquiterpane standards, two hydrocarbons with a bicyclic molecular structure, *cis*-decalin and 1-methyldecalin, are applied as alternative standards for the quantitation of bicyclic sesquiterpanes [33, 35]. In our in-house method, the response factor for *cis*-decalin and 1-methyldecalin is determined relative to the internal standard of decalin-d_{18}. The average RRF of *cis*-decalin and 1-methyldecalin is then used to determine the concentrations of each target sesquiterpane compound [35]. Therefore, the quantitation results by this means do not necessarily represent real-world concentrations in the oil samples. Nevertheless, this method offers a quantitative comparison of bicyclic sesquiterpanes in various oils.

Crude oils from different sources and different petroleum products have varied signatures of both the absolute concentrations and relative distribution patterns of sesquiterpanes [33, 35]. Bicyclic sesquiterpanes are resistant against slight to medium weathering, particularly biodegradation [33, 35, 42, 59]. Early studies on sesquiterpanes have mainly focused on geological application in the maturity, depositional environment, and the origin of oils. Recently, they have become a special interest in oil-source correlation and differentiation of refined products with high ring number biomarkers removed during refining processes [20, 33, 35, 42–44]. Stout et al. have reported a successful forensic fingerprinting study of middle distillate fuels in the environment using sesquiterpanes [42]. Wang et al. have presented two real-world spill case studies using unique sesquiterpanes for fingerprinting and identifying mystery diesel spills [33]. However, it is recommended that the absence of bicyclic sesquiterpanes should be used cautiously as an indicator of biodegradation rank because there is a high potential for their alteration by water washing [59].

Bicyclic sesquiterpanes in crude oils: Bicyclic sesquiterpanes are ubiquitous components of ancient sediments, coal, and crude oils [33, 35, 56, 57, 60]. Yang et al. reported a quantitation of bicyclic sesquiterpanes in many crude oils and refined petroleum products collected from various sources [35]. Their relative concentrations in crude oils vary considerably from oil to oil. GC-MS chromatograms of sesquiterpanes for representative crude oils and petroleum products are compared in Figure 2.6. Figure 2.7 compared the total concentrations of ten target sesquiterpanes and normalized percentages of major sesquiterpanes in crude oils.

Bicyclic sesquiterpanes occur in all of the crude oils studied. Their abundance is likely independent of the densities of the crude oils [35]. In general, the GC-MS chromatograms of sesquiterpanes at m/z 123 are often characterized by the dominance of BS1, BS3, BS5, and BS10, with BS5 or BS10 being the most abundant. BS2, BS7, BS8, and BS9 have much lower relative abundance. As shown in Table 2.5, the dominant sesquiterpanes BS1, BS3, BS5, and BS10 together account for about 50–75% of the sum of ten target sesquiterpanes. Bicyclic sesquiterpanes were also detected in extremely heavy oils such as Alberta oil sand bitumen despite the depletion of *n*-alkanes by biodegradation [58, 61]. Bulk concentrations of target sesquiterpanes in oil sand bitumen are at the same level as many other crude oils. The selected ion chromatograms at m/z

123 show distribution patterns of BS10 > BS5 > BS1 for Alberta oil sand bitumen. It is evident that bicyclic sesquiterpanes have been partially biodegraded in these heavy oil samples. 8β(H)-Homodrimane is likely the most abundant homologue in oil sand bitumen, which suggests that this compound has the least degradability among all ten sesquiterpanes.

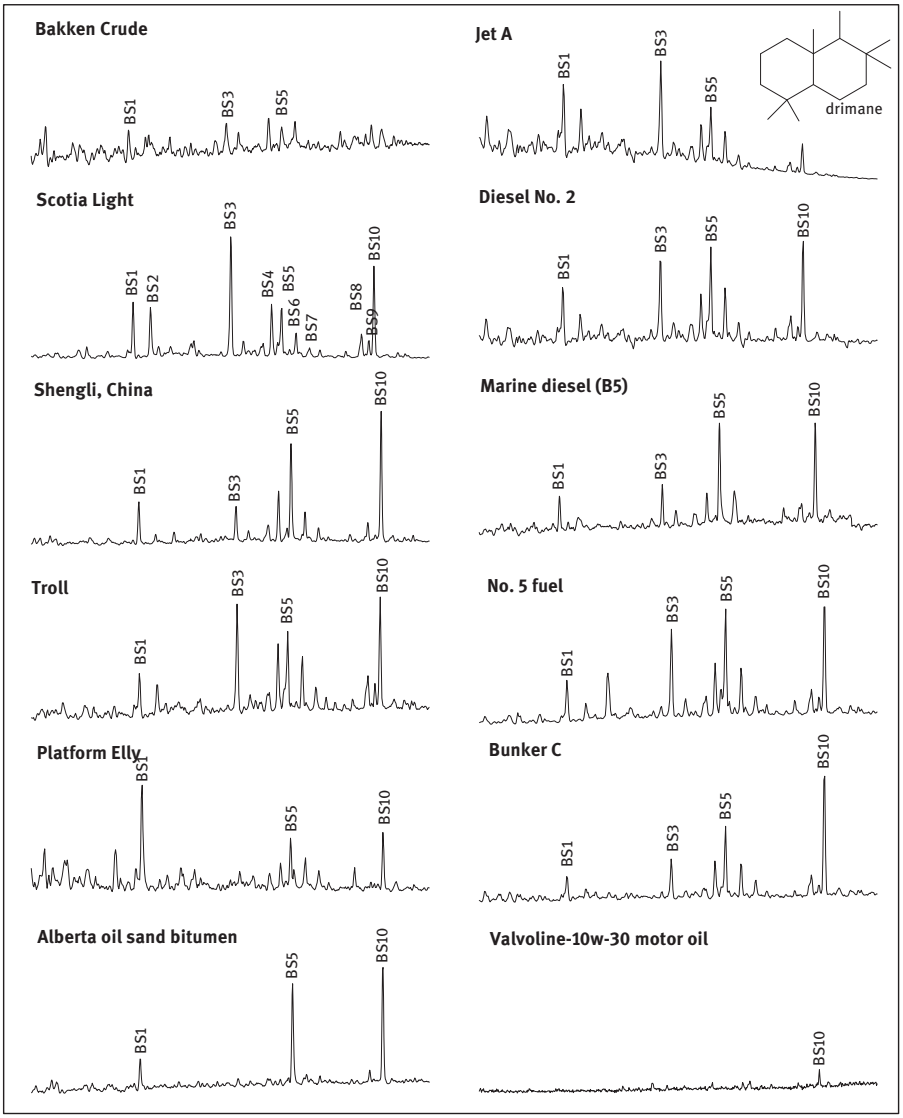

Figure 2.6: GC-MS chromatograms of bicyclic sesquiterpanes (*m*/*z* 123) in crude oils and refined petroleum products.

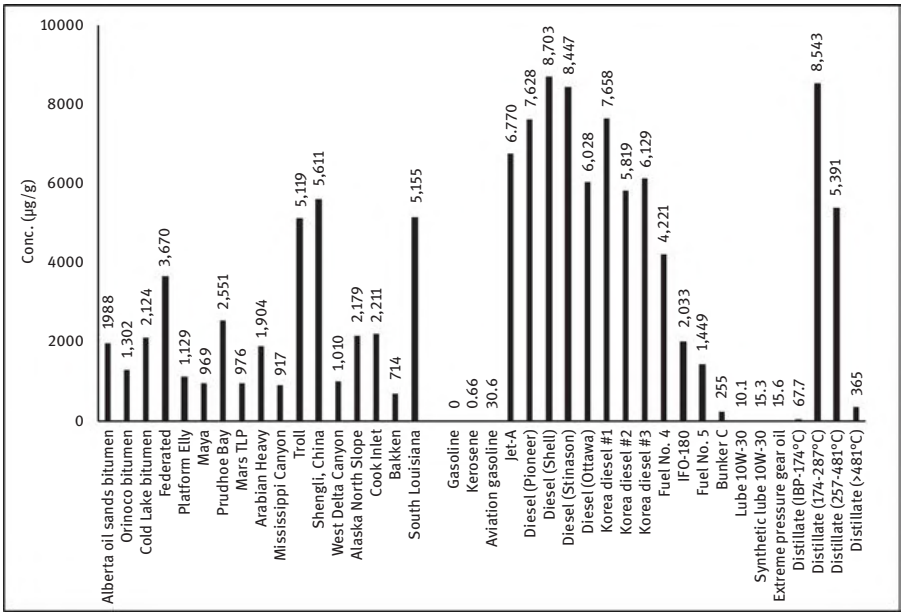

Figure 2.7: Bicyclic sesquiterpanes in crude oils and refined petroleum products.

Bicyclic sesquiterpanes in refined products: Bicyclic sesquiterpanes are widely found in intermediate petroleum distillates and finished petroleum products. The abundances and distribution patterns of sesquiterpanes differ widely in petroleum products, which are attributable to differences in the crude oil feedstocks and the refining processes. Analyses of simulated laboratory distillates of crude oils show that bicyclic sesquiterpanes were largely found in the 174–481 °C distillation fraction of the crude oil. The concentrations of sesquiterpanes in this fraction are at the same level as that found in mid-range fuels [33, 35]. Most of BS1 to BS7 from the feedstock oil entered into the 174–287 °C fraction. About 55% of BS7, to about 95% of BS1, were found in this fraction. It was also observed that in this fraction, all ten target sesquiterpanes were concentrated up to approximately fivefold compared to its parent crude oils. BS10 was found mainly in the 287–481 °C fraction, accounting for about 62% of their total amount. For this fraction, only BS4 to BS10 were concentrated to varying extent. Sesquiterpanes were in low concentration in the lightest fraction and were rarely found in the heaviest fraction.

The abundances of sesquiterpanes in various petroleum products are shown in Figure 2.7. Bicyclic sesquiterpanes were found in most fuel oil samples at various concentrations. In general, these compounds are abundant in most mid-range fuels but relatively low in heavy residual fuels. Understandably, none to trace amounts of sesquiterpanes was detected in gasoline and lubricating oils. However, light biomarkers including bicyclic sesquiterpanes and diamondoids are typically evident in

the used lube oil from diesel engine vehicles [24]. Overall, the distribution pattern of individual sesquiterpane compounds in mid-range distillates is similar to that of crude oils. BS3, BS5 and BS10 are the most dominant, while BS8 and BS9 often show the lowest abundances. It is also noted that the dominance of 8β(H)-homodrimane (BS10) is obvious in mid-range distillates and heavy residual fuels, and among ten common bicyclic sesquiterpanes, BS10 is detected in 10W-30 motor oil.

2.5.4 Biomarker terpanes and steranes

Two groups of petroleum biomarkers (i.e., polycyclic terpanes and steranes) have been extensively investigated and reported by geochemists and environmental chemists [13, 15, 59, 61–66]. These hydrocarbons have played an important role to explore the depositional environment of crude oil and track the genesis, maturation, migration, and biodegradation of petroleum. The information from biomarker analysis is also used to investigate the source and history of petroleum in the determination of petroleum-derived environmental contaminations. Peters et al. discussed the basic principles of biomarkers and their applications to studies on the origin, geological age, and environmental conditions of oil formation [59]. Compared to acyclic alkanes, those cyclic hydrocarbons are characterized by their structural stability and preservation of genetic features, which are inherited from peculiarities of the original organic matter and the conditions of its transformation into petroleum hydrocarbons. For example, the ubiquitous pentacyclic hopanes are triterpenoids derived from cell membranes of prokaryotes (heterotrophic bacteria) and phototrophic cyanobacteria [64, 66].

Biomarker abundances differ greatly from oil to oil and from oil type to type. Biomarker concentrations in crude oils largely depend on the geological source of the oils, while their concentrations in refined petroleum products vary with the feedstocks and the oil types [10, 12, 59].

***Biomarker terpanes*:** Crude oils usually have a wide distribution of triterpanes with a dominance of tricyclic and pentacyclic terpanes (Table 2.3 and Figure 2.8). These traditional biomarkers are eluted between *n*-C_{20} and *n*-C_{38} in GC analysis (equivalent to boiling points 343–500 °C) (Figure 2.2). Pentacyclic triterpanes include C_{30} hopane ($C_{30}H_{52}$) and its homologues ranging from C_{27} trinorhopane to C_{35} homohopanes. A series of hopanes beyond C_{40} were reported in crude oils and source rock extracts [67, 68]. As shown in Figure 2.8, the hopane series have a skeleton of 21 carbon atoms with four fused cyclohexane rings and one cyclopentane ring (E-ring). Gammacerane (G) and oleanane, the structural isomers of hopane, have a cyclohexane E-ring in its molecular structure. These irregular triterpanes can be very useful in oil correlation when they are detected in relatively high abundance. There are generally six methyl substituents on the ring system, of which four methyls are positioned at the ring junctions of C-8, C-10, C-14, and C-18, respectively. The molecular structure has two

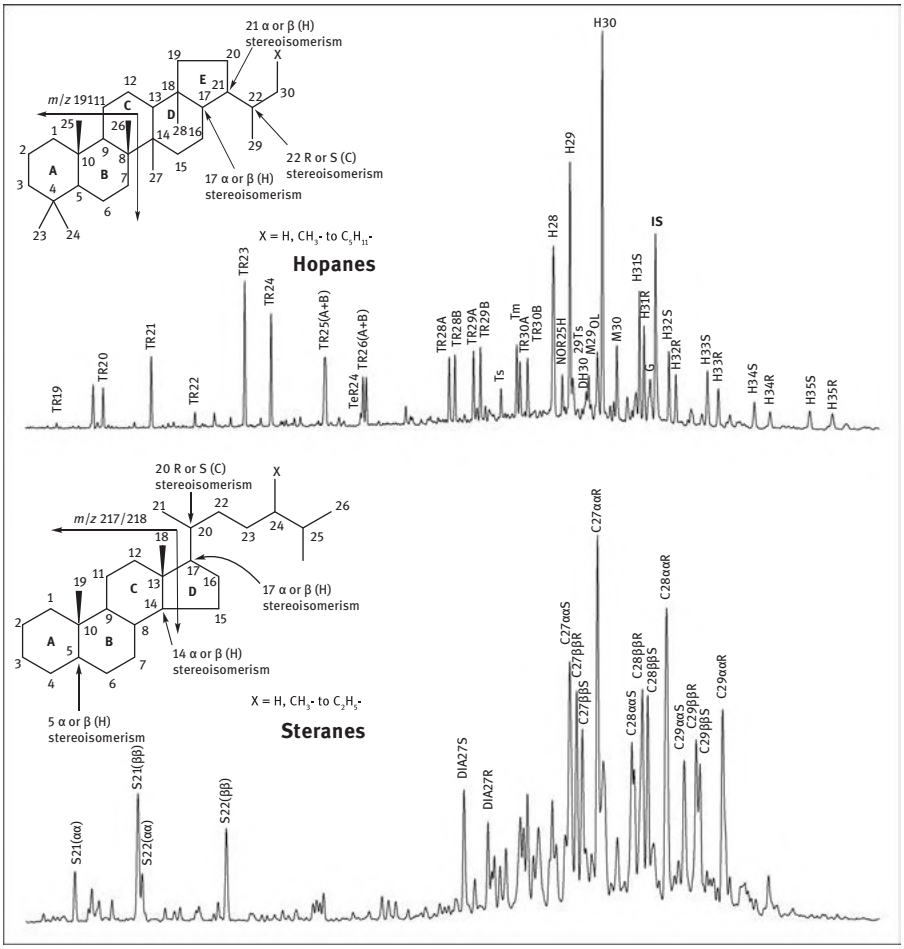

Figure 2.8: Biomarker terpanes and steranes identified in a crude oil.

asymmetric carbons at C-17 and C-21. Atoms attached to the chiral centers in the molecular structure are bonded together in the same sequence but the different orientations of the atoms in space. Common homohopanes (C_{31} to C_{35}) have an extended side chain at C-21 of the pental ring (E-ring). For cyclic biomarkers, α- and β-nomenclature is used to describe asymmetric carbons at the ring, while the R- and S-nomenclature is used for asymmetric centers out of the ring [13]. An additional asymmetric center at C-22 of the side chain results in two stereoisomers with 22R and 22S configurations.

Each biomarker terpane has many potential isomers and stereoisomers. C_{30} hopane has four stereoisomers: 17α(H),21α (H)-, 17α(H),21β(H)- (in petroleum), 17β(H),-21β(H)- (the biological configuration), and 17β(H),21α(H)-hopane (moretane). These

hopane isomers have a decreasing order of thermodynamic stability: 17α(H),21β(H) > 17β(H),21α (H) > 17α(H),21αH) > 17β(H),21β(H) [59]. Therefore, the C_{27}–C_{35} hopane series in crude oils are dominated by the 17α(H),21β(H) stereoisomers. C_{30} 17α(H),21β(H)-hopane widely occurs in crude oil at high abundance, whereas 17β(H),21α(H)-hopane occurs in relatively low concentration. It was found that C_{30} 17α(H),21α(H)-hopane occurs in low concentration in a ratio of typically 0.02–0.04 relative to C_{30} 17α(H),21β(H)-hopane in crude oils and mature sediments [69]. C_{30} 17β(H),21β(H)-hopane is thermodynamically unstable and naturally absent in petroleum, making it a desirable internal standard for quantitative biomarker analysis [10–15]. The C-22 position in the molecular structure is a chiral center resulting in R- and S-configuration epimers for the C_{31}–C_{35} homohopane series. The 22S epimers exist at a slightly higher concentration than their 22R epimers. 25-Norhopanes are a series of C_{26}–C_{34} compounds that are structurally equivalent to the regular hopanes, except for the absence of a methyl group at the A/B ring junction.

These saturated biomarker terpanes are determined at their characteristic base ions at m/z 191 ($C_{14}H_{23}^+$), which are derived from the cleavage of carbon bonds 9–11 and 8–14 in ring C of the molecule to form (A + B) ring or (D + E) fragment, respectively (Figure 2.8). The most intensive ion in the mass spectra of norhopanes, such as 17α(H),21β(H)-25-norhopane, is m/z 177 due to one less methyl group (CH_3-, 15 amu) in their molecular structures.

Biomarker steranes: Steranes represent another important group of biological marker compounds. Steranes and sterenes are believed to be principally derived from C_{27} to C_{30} sterol precursors from the cell membranes of eukaryotes, mainly algae and higher plants [70, 71]. These sterols generate a series of sterane homologs during diagenesis, which inherit the carbon skeletons from biological precursors and only differ by the addition of a sequence of CH_2- units to a certain place in the molecule.

Regular steranes have a tetracyclic androstane skeleton with a methyl at the ring junctions of the A/B ring and C/D ring and a side chain at carbon C-17 of the pental ring (D-ring). As shown in Figure 2.8, steranes have three asymmetric carbon centers at C-5, C-14, and C-17 on the ring structure, and another two asymmetric centers at the C-20 and C-24 on the extended chained attached to C-17, respectively. Chiral center at the C-20 position in the molecular structure results in R- and S-configuration epimers. Therefore, each sterane has many potential isomers. For instance, four isomers of cholestane ($C_{27}H_{48}$) including 20*S*-5α(H),14α(H),17α(H)-, 20*R*-5α(H),14β(H),17β(H)-, 20*S*-5α(H),14β(H),17β(H)-, and 20*R*-5α(H),14α(H),17α(H)-are determined from crude oils. Besides regular steranes, petroleum also contains a family of rearranged steranes of diasteranes (C_{26}–C_{30}). Diasteranes are likely formed during diagenesis and catagenesis of biological precursors.

The typical ions for biomarker steranes are m/z 217 ($C_{16}H_{25}^+$) and m/z 218 ($C_{16}H_{26}^+$) for GC-MS analysis, which are products of (A + B + C) ring due to the cleavage at junction carbon bonds 13–17 and 14–15 of the C/D ring under electron impact (Figure 2.8).

For all epimers with *cis*-C/D-connection, the intensity of the *m*/*z* 218 ions is greater than that of the *m*/*z* 217 ions. The *βαα* and *ααα* steranes have a base peak at *m*/*z* 217, whereas the base peak of *αββ* steranes is at *m*/*z* 218. The distribution profile of C_{27} to C_{29} steranes is of interest for oil exploration and oil forensic study, although it is more or less the same in most crude oils.

Biomarkers in crude oils: Biomarkers in crude oils have been extensively investigated and reported by geochemists and environmental chemists. Different crude oils often have highly distinguishable chemical fingerprints of their biomarkers, varying in both concentration and distribution patterns (Figure 2.9 and Table 2.5).

In fresh crude oils, C_{23} and C_{24} tricyclic terpanes and C_{29} αβ and C_{30} αβ hopanes are generally the most abundant triterpanes (Figure 2.9). C_{30} αβ hopane is usually at a higher concentration than C_{29} αβ norhopane in most crude oils; however, a reverse feature was observed for some crude oils such as Arabian Heavy crude (a Middle East crude oil). In Sockeye crude, a California heavy oil, H28, is even more abundant than C_{29} and C_{30} αβ-hopanes. The homohopanes in Alberta oil sand bitumen account for about 40% of the total 1,519 μg/g of target biomarker terpanes, while in the Bakken crude oil they are very low and even undetectable (Table 2.5).

Some geologically rare acyclic alkanes (i.e., C_{30} 17α(H)-diahopane, C_{30} 18α(H)-hopane, gammacerane, 4-methyl steranes, etc.) are found only in certain oils and therefore used as unique markers for specific oil spill identification. As shown in Figure 2.9, the presence of C_{28}-bisnorhopane and gammacerane is evident in oil sand bitumen and AHS. The occurrence of gammacerane may suggest a saline depositional environment of the original oil in the Alberta oil sands. The abundance of C_{31}–C_{35} homohopanes generally decrease with the increase of carbon numbers, *i.e.*, H31 > H32 > H33 > H34 > H35, and the S-configuration epimer is more common than its R-epimer. One specific feature of H34S < H35S and H34R < H35R is noticed for homohopanes in some crude oils such as Alberta oil sand bitumen, which suggests that these oils were derived from source rocks deposited under anoxic conditions [61]. C_{29} 17α(H),21β(H)-norhopane and $C_{31–35}$ homohopanes, especially C_{35} homohopanes are depleted in southeast Asian crude oils, whereas these compounds are abundant in the Middle East crude oils [72].

C_{27}, C_{28}, and C_{29} steranes are referred to as cholestane, ergostane (24-methylcholestane), and sitostane (or stigmastane, 24-ethylcholestane), respectively. The relative abundances of C_{27} to C_{29} steranes in crude oils are controlled by the types of photosynthetic organisms that contributed to the organic matter. A dominance of C_{27} steranes is usually associated with marine organisms [73]. C_{27} ββ-, C_{28} ββ-, and C_{29} ββ-steranes in crude oils generally have a relative abundance in an overall "V-shaped" distribution pattern. Unlike most of the other crude studied, the Platform Elly crude oil has a reverse V-shaped steranes distribution with a particular abundant C_{28} ββ-steranes. As observed from Figure 2.9, the Bakken crude and the Scotia Light crude oil contain very low biomarker compounds. In contrast, the California Sockeye crude oil particularly

contains a high concentration of biomarker steranes, which account for a large portion of determined biomarkers.

Biomarkers in refined petroleum products: Biomarker terpanes and steranes are found almost entirely in heavier fractions of the distillates of crude oil [15]. These biomarker compounds all exclusively come from their feedstock crude oil as they are unlikely produced in distillation and refining processes.The biomarker fingerprint of a refined oil may be totally or partially the same as that of its original feedstock crude.

Figure 2.10 presents the GC-MS chromatograms of biomarkers in representative refined petroleum products from diesel to lubricating oil. Clearly, the abundances and distribution of biomarkers vary greatly from oil to oil and from type to type (Table 2.5 and Figure 2.10). For lighter petroleum products, refining processes have removed most HMW biomarkers from the corresponding crude oil feedstocks. In general, biomarker compounds are undetectable in light fuels such as gasoline. The lower boiling C_{19}- to C_{24}-tricyclic terpanes are eluted before n-C_{24} during chromatographic analysis. These smaller biomarkers are within the carbon range of automobile diesel and marine diesel and are present in these medium fuel oils at a considerable level. Typically, the higher boiling point biomarkers are not present in light fuel. It is quite common for refineries to add light cycle oil (LCO) to the distilled light oil fraction. LCO is the diesel boiling range material that is produced in a catalytic cracker and contains mainly aromatic compounds and a low concentration of biomarkers [20].

Most triterpanes and steranes remain in the residual fraction during distillation. Therefore, they are detected in heavy residual fuels in equivalent or higher concentrations than their feedstock crude oil. Lubricating oils are rich in terpanes and steranes but contain relatively low lighter tricyclic terpanes (C_{21}–C_{24}). The target biomarker terpanes and steranes in 10W-30 motor oil are as high as 3,652 and 1,666 μg/g, respectively. These biomarker compounds are undetectable or at a trace amount in synthetic lube oils.

2.5.5 Diagnostic criteria of saturated hydrocarbons

Forensic oil–oil correlations are based on the concept that the target components investigated in spilled oils are source-specific and do not significantly differ from those in the source oils. Some of the petroleum compounds in spill samples, in particular those biomarker compounds, show little or no changes in their relative abundance. The abundance ratios between these target analytes serve as important diagnostic criteria for many aspects of oil studies. Diagnostic ratios have been widely applied by geochemists for oil–source rock correlation and oil–oil correlation, determination of organic input and depositional environment, assessment of thermal maturity, and evaluation of oil biodegradation. Environmental chemists frequently use them for the

Table 2.5: Concentrations of target biomarker terpanes and steranes in crude oils and petroleum products.

	Crude oils						Petroleum products					
Oil samples	**Bakken**	**SoL**	**Troll**	**PlE**	**AOS***	**Fed**	**Fed (287–481 °C)**	**Fed (>481 °C)**	**Diesel no. 2**	**Marine diesel**	**Bunker C**	**Lube 10W-30**
Biomarker terpanes												
TR21	2.46	9.43	7.81	20.1	36.2	11.5	33.5	ND	3.11	26.2	3.10	11.6
TR22	0.97	3.53	2.96	4.32	16.9	4.48	12.7	ND	1.42	9.43	1.38	15.2
TR23	5.09	14.8	11.1	41.3	109	26.1	73.8	ND	3.85	45.6	11.0	68.2
TR24	3.71	10.7	9.14	33.9	56.7	15.2	46.2	ND	1.39	18.6	5.97	25.5
Ts	1.97	20.3	34.1	13.2	27.2	22.8	48.8	27.4	ND	1.70	26.1	148
Tm	1.44	29.6	23.3	55.9	91.7	21.3	41.1	27.0	ND	2.13	2.46	215
H29	2.20	74.6	56.6	107	219	36.7	52.1	75.9	ND	3.41	31.9	864
H30	5.68	100	126	216	256	71.0	83.1	184	ND	2.71	59.0	718
H31S	1.66	26.4	44.3	64.6	114	24.6	22.1	70.2	ND	0.88	36.4	385
H31R	1.31	21.5	34.5	52.5	83.5	18.0	17.7	57.0	ND	0.69	25.2	305
H32S	1.42	15.2	30.4	43.0	72.6	18.1	14.3	60.4	ND	1.11	24.8	238
H32R	0.97	9.94	22.0	32.2	53.2	13.4	9.52	42.5	ND	0.28	19.6	164
H33S	ND	8.96	26.7	35.2	54.5	12.9	7.90	41.0	ND	0.27	17.3	140
H33R	ND	5.48	16.3	28.5	36.3	9.88	5.33	31.3	ND	ND	12.9	91.7
H34S	ND	4.65	16.4	20.0	36.7	8.14	4.29	31.0	ND	ND	10.9	77.6
H34R	ND	2.78	9.54	15.1	23.4	4.29	1.73	17.1	ND	ND	6.68	51.6
H35S	ND	3.33	12.4	22.1	39.0	5.73	1.91	22.5	ND	ND	9.94	85.7
H35R	ND	2.27	8.73	20.9	36.2	3.40	1.09	12.3	ND	ND	7.75	47.6
Biomarker steranes												
C27αββ	22.1	89.3	172	649	25.4	113	257	78.3	ND	9.16	87.8	525
C28αββ	10.6	67.4	125	754	62.6	48.6	92.4	57.0	ND	4.48	58.8	363
C29αββ	24.5	89.8	179	466	45.8	113	199	193	ND	3.95	82.9	778
Total (µg/g)	**86.1**	**610**	**968**	**2695**	**1519**	**603**	**1026**	**1028**	**9.77**	**131**	**542**	**5318**

* Concentration: µg/g of TSEM of Alberta oil sands DCM extract.

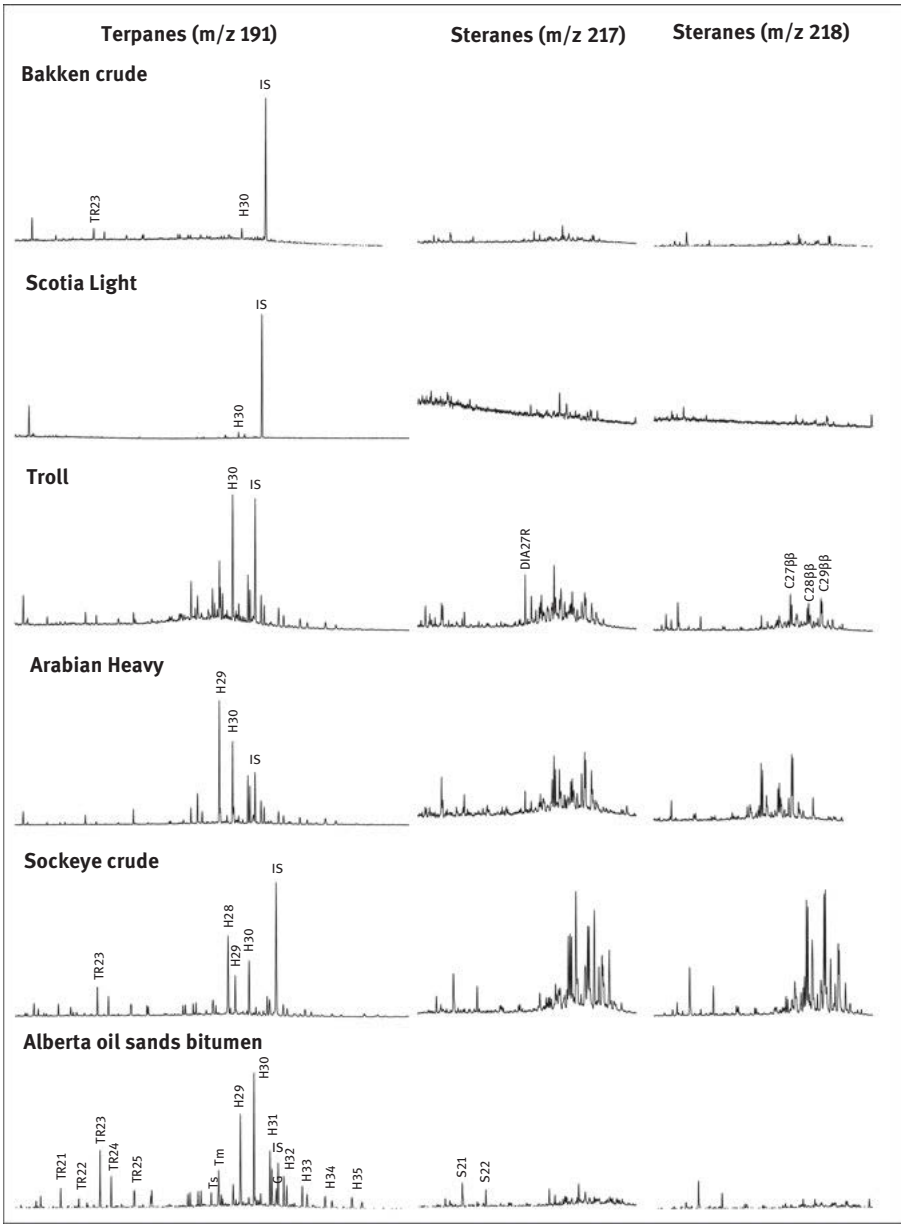

Figure 2.9: GC-MS chromatograms of biomarker terpanes and steranes in crude oils.

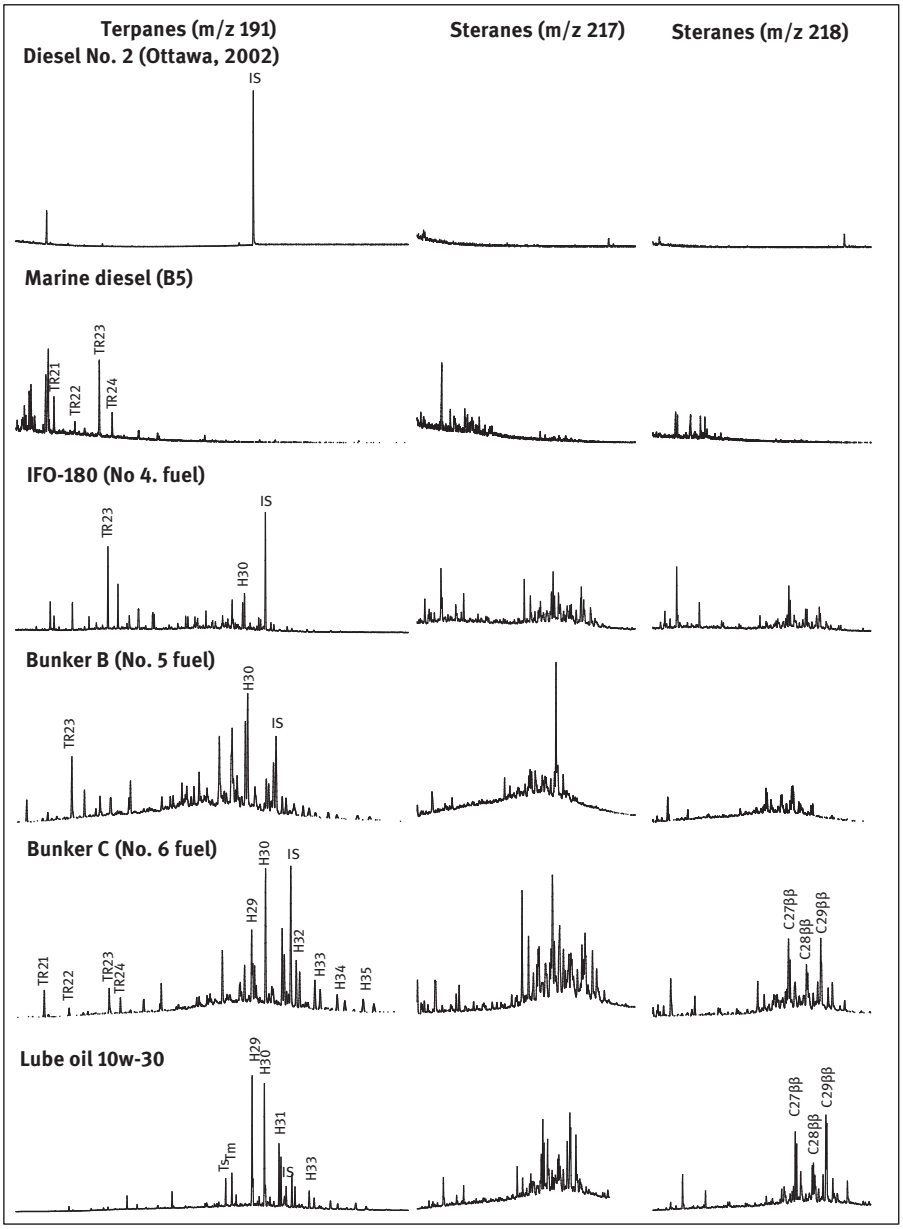

Figure 2.10: GC-MS chromatograms of biomarker terpanes and steranes in petroleum products.

identification, correlation, differentiation of spilled oil, and investigation of its spill history. An important benefit of employing diagnostic ratios in oil identification is to minimize the concentration effects. In addition, the use of ratios tends to induce a self-normalizing effect on the data since variations due to the fluctuation of day-to-day instrument operating conditions, operator, and matrix effects are minimized. Therefore, the comparison of diagnostic ratios reflects more directly differences in biomarkers of samples. However, it should be cautioned that diagnostic ratios are not only oil-dependent but also change with the method used for oil analysis; therefore, for the same oil, the ratio values could vary from different data sources. Because of low abundance or poor peak separation, the ratios of certain compounds can be heavily affected by the measurement errors.

Numerous diagnostic ratios from petroleum compounds have been proposed as molecular markers to identify the source of oil spills [12, 20, 74]. Diagnostic ratios should be used in combination to avoid erroneous conclusions. It is impossible and unnecessary to include ratios from all target analytes. It is essential to select source-specific representative and weathering-resistant diagnostic ratios for forensic oil analysis. Herein, we only select some diagnostic ratios frequently used for detailed discussion.

N-alkane and isoprenoid ratios: These ratios of *n*-alkane and isoprenoids are generally based on results from GC-FID analysis or selected ion of GC-MS analysis if these compounds are in very low concentration in weathered environmental samples. The diagnostic ratios often used from the *n*-alkane analysis include *n*-C_{16}/norpristane *n*-C_{17}/pristane, *n*-C_{18}/phytane, and pristane/phytane. These *n*-alkane and isoprenoid indices are source-specific, and the pristane/phytane ratio is widely used to assess the environmental conditions of deposition of source rock. It was discovered that crudes with the same geological origin have similar pristane/phytane ratios. In addition, *n*-C_{17}/pristane and *n*-C_{18}/phytane elute in two close pairs during chromatographic analysis. The ratios of *n*-C_{17}/pristane and *n*-C_{18}/phytane remain relatively constant through evaporation, but their values decrease remarkably in biodegraded oil due to the preferential depletion of *n*-alkanes. The ratio of pristane/phytane is relatively stable when oil is subject to a certain degree of evaporation and biodegradation.

Carbon preference index (CPI) is the ratio of odd versus even carbon numbered *n*-alkanes. The ratio of *n*-C_{17}/*n*-C_{31} is a simplified parameter indicating relative contributions from aquatic/marine and terrestrial sources. This ratio is used to estimate of the thermal maturity of crude oil and to identify the source of hydrocarbons in an environmental sample. The even and odd numbers of *n*-alkanes are generally equally abundant in high maturity petroleum resulting in a CPI of 1.0 for these oils. CPI values significantly above (odd preference) or below (even preference) 1.0 indicates low thermal maturity. A CPI value below 1.0 for low-maturity oils or bitumens suggests a typical carbonate or hypersaline environment [59]. CPI is a key diagnostic parameter

to determine the relative importance of biogenic and anthropogenic alkane sources to the ambient environment [75].

For the practice of environmental oil analysis, *n*-alkanes are examined within their full span (generally from *n*-C_8 to *n*-C_{44}). CPI is particularly useful in an environmental approach involving biogenic contribution. C_{23-33} *n*-alkanes, and especially those from *n*-C_{27} to *n*-C_{33}, originate from waxes typical of terrestrial higher plants, whereas anthropogenic sources, including fossil fuel combustion, show no enrichment of odd carbon alkanes [76]. A strong odd-to-even predominance with a CPI value ≫1 discloses predominant biogenic contribution from terrestrially derived components in an environmental sample (e.g., soil and sediment). When petroleum is the main contaminant, the CPI can be calculated from the sum of odd divided by the sum of even carbon numbered *n*-alkanes. A CPI value of near 1.0 suggests a mainly petrogenic source of hydrocarbons. The CPI values of biodiesel blends are also around 1.0 since *n*-alkanes are attributable to the petroleum components [24].

Biomarker diagnostic parameters have been long established and are widely used by geochemists for oil correlation (oil–source rock correlation and oil–oil correlation); determination of organic input and precursors, and depositional environment; assessment of thermal maturity; and evaluation of oil in-reservoir biodegradation. Many diagnostic biomarker ratios currently used in oil spill studies and environmental forensics originate from geochemistry.

Ratios of diamondoids and bicyclic sesquiterpanes are of special importance for the analysis of light petroleum. Like traditional biomarker ratios, these ratios originate from geochemical investigation. Diamondoid hydrocarbon ratios, such as methyl adamantane index and methyl diamantane index were applied to evaluate the maturation and evolution of crude oils and to determine the thermal maturity of thermogenic gas and condensate [46, 49, 77]. The ratio of methyladamantanes to adamantanes rises with increasing biodegradation. The ratio changes significantly at extreme levels, showing that diamondoids can be indicators of petroleum biodegradation especially when most other hydrocarbons have been removed. Wang et al. studied many possible diagnostic ratios and found that many diamondoids ratios, such as 1-MA/2-EA, 1-MA/1,2-DMA, 1-MA/1,3,4-TMA, and 1-MA/1,2,5,7-TeMA, are likely more sensitive and reliable parameters for correlation and differentiation of oils and petroleum products [34]. Diamantane isomers generally occur in crude oils only in relatively low abundance. High measurement uncertainty could be evident in oil analysis, particularly when column fractionation of oil sample is not performed prior to GC analysis. Therefore, diagnostic ratios associated with diamantanes should be used cautiously as criteria [32, 74].

Diagnostic ratios of selected sesquiterpanes were developed and calculated from a large number of oils and petroleum products. Diagnostic ratios vary greatly between oils from different regions. Most of these diagnostic ratios are robust for correlation and differentiation of lightly to moderately weathered oil samples. This implies that the sesquiterpane ratios, in combination with other fingerprinting data, may be

used to discriminate different oils and to identify the source of spill samples. However, for heavily weathered samples, the early-eluted lower molecular weight C_{14} sesquiterpanes could be preferentially depleted to certain degrees, resulting in some changes in their corresponding diagnostic ratios [33, 35, 41].

As shown in Figure 2.8, crude oil contains many biomarker terpanes and steranes in a wide carbon range. In theory, their analyses could derive a large number of diagnostic ratios. Diagnostic ratios of these compounds include TR21/TR22, TR23/TR24, H29/H30, Ts/Tm, H31S/H31, H32S/H32R, C27ββ/C29ββ, and C28ββ/C29ββ, as well as ratios compared H30 with other petroleum hydrocarbons. These ratios are regarded as source ratios for oil identification, among which the ratio TR21/TR22, H29/H30, Ts/Tm, and C27ββ/C29ββ are the most commonly used as source tracers [10, 12, 15, 20, 32]. Due to significant differences in boiling points, the ratios between lighter C_{21-24} tricyclic terpanes and C_{30} 17α(H),21β(H)-hopane can provide a useful tool to distinguish the refined oil type and to investigate the weathering level. Ratios of certain unique biomarker compounds (*i.e.*, C_{30} 17α(H)-diahopane, C_{30} 18α(H)-hopane, gammacerane, and 4-methyl steranes, *etc.*) relative to C_{30} 17α(H),21β(H)-hopane can provide exceptional diagnostic information in oil analysis.

Cross-plots (i.e., a plot of one diagnostic biomarker ratio vs. another ratio) are frequently used in oil geochemistry for oil–oil correlation and determination of oil source and depositional environment [72, 78]. Zakaria et al. used the cross-plots of H29/H30 ratio versus the homohopane index Σ(H31–H35)/H30 as key biomarker indicators and successfully distinguished a large number of tarball samples originated from Southeast Asian crude oil sources from those of Middle East sources [72]. Furthermore, the ratios of biomarkers with other classes of hydrocarbons can be proposed as weathering ratios. The abundances of full-range targeted compounds relative to C_{30} 17α(H),21β(H)-hopane are plotted against boiling points (in practice, GC retention time of analytes) providing a criterion where a spilled oil is weathered compared with source oil [15, 20].

2.6 Aromatic hydrocarbons in petroleum

Aromatic hydrocarbons generally make up a smaller proportion of crude oils in comparison with aliphatic hydrocarbons. However, certain refined products can contain an extremely high concentration of these substances. For example, an oil product designed for the preservation of wood products such as utility poles, cross-arms, and railway ties can possess aromatic content as high as 80% [15]. Aromatic hydrocarbons in petroleum can be classified into three main groups according to their molecular structures, including monocyclic aromatic hydrocarbons (MAHs), PAHs, and naphthenoaromatic hydrocarbons. Petrogenic aromatics are generally dominated by

the derivatives of one or more aliphatic substituents, and the alkylated homologues usually occur in significantly higher concentrations than their parent PAHs.

Tables 2.6 summarizes the target petroleum aromatic compounds frequently used for forensic oil fingerprinting analysis [10, 12, 13, 15, 16, 20, 27, 29]. PAH series can be determined by GC-MS with a suit of parent molecular ions, for example, m/z 128, 142, 156, 170, and 184 for C_0- to C_4-naphthalenes; and m/z 178, 192, 206, 220, and 234 for C_0- to C_4-henanthrenes, and so on. Aromatic steranes are determined at m/z 231 for triaromatic steranes (TASs) and at m/z 253 for monoaromatic steranes (MASs).

2.6.1 BTEX and alkylbenzenes

BTEX (benzene, toluene, ethylbenzene, and *o*-, *m*-, and *p*-xylenes) are the major MAHs in petroleum. BTEX are classified as priority pollutants regulated by many environmental organizations around the world. These small aromatics are the most water-soluble and volatile fraction of petroleum. They frequently enter the air, soil, sediments, and groundwater, due to accidental oil spills, leakage of gasoline and other petroleum fuels from underground storage tanks and pipelines, and improper oil-related waste disposal [79]. Because of their potential acute toxicity and health hazard, BTEX are often monitored whenever a hydrocarbon fuel is suspected to have been spilled (especially in relatively confined areas).

Benzene and its C_7–C_{10} homologues have been thoroughly investigated in many crude oils. Wang et al. identified a large number of alkyl-substituted benzene components in Alberta Sweet Mixed Blend (ASMB) [79]. They also reported a quantitative analysis of the individual BTEX compounds and C_3-benzene isomers in various crude and weathered oils. Quantitative analyses of these highly volatile MAHs are usually separated from the analyses of other hydrocarbons. To avoid the loss of light-boiling BTEX during sample preparation, the oil sample is dissolved in *n*-pentane for direct GC analysis. The use of *n*-pentane as solvent also precipitates heavy asphaltenes content, thereby reducing column contamination. Accordingly, mass spectra of alkylated benzenes are characterized by the presence of m/z 91 for methylbenzene, m/z 105 for C_2-benzenes, and m/z 119 for C_3-benzene, similarly isomers with larger alkylation can be determined using the characteristic $(M\text{-}15)^+$ ion.

Concentrations of BTEX and selected C_3- ~ C_6-alkylbenzenes in different crude oils and refined products are presented in Table 2.7. The total concentration of monocyclic aromatics studied in crude oil is at the mg/g level, and varies between oils. Overall, BTEX and C_3-benzenes make up most of the determined monoaromatics. In general, 1,2,4-trimethylbenzene is the most abundant C_3-benzene isomer followed by 3- /4-ethyltoluene and 1,3,5-trimethylbenzene. Unlike in conventional crude oils, these light aromatics are barely detectable in extra heavy oils like Alberta oil sand bitumen.

Table 2.6: Target aromatic analytes frequently used for oil fingerprinting analysis.

Compounds	Code	Empirical formula	Molecular weight	Target ions
BTEX and alkylbenzenes				
Benzene	B	C_6H_6	78	78,77
Toluene	T	C_7H_8	92	91,92
Ethylbenzene	E	C_8H_{10}	106	91,106
Xylenes (*p*-, *m*-, *o*-)	X	C_8H_{10}	106	91,106
C_3-Benzenes	C3B	C_9H_{12}	120	105,120
C_4-Benzenes	C4B	$C_{10}H_{14}$	134	91,105,134
C_n-Benzenes	CnB	C_nH_{2n-6}		91,92,105
Unsubstituted PAHs				
Two-ring PAHs				
Naphthalene	N	$C_{10}H_8$	128	128
Biphenyl	Bph	$C_{12}H_{10}$	154	154
Three-ring PAHs				
Acenaphthylene	Acl	$C_{12}H_8$	152	152
Acenaphthene	Ace	$C_{12}H_{10}$	154	154
Fluorene	F	$C_{13}H_{10}$	166	166
Phenanthrenes	P	$C_{14}H_{10}$	178	178
Anthracene	An	$C_{14}H_{10}$	178	178
Four-ring PAHs				
Fluoranthene	Fl	$C_{16}H_{10}$	202	202
Pyrene	Py	$C_{16}H_{10}$	202	202
Benz[*a*]anthracene	BaA	$C_{18}H_{12}$	228	228
Triphenylene	TP	$C_{18}H_{12}$	228	228
Chrysene	C	$C_{18}H_{12}$	228	228
Five-ring PAHs				
Benzo[*b*]fluoranthene	BbF	$C_{20}H_{12}$	252	252
Benzo[*k*]fluoranthene	BkF	$C_{20}H_{12}$	252	252
Benzo[*e*]pyrene	BeP	$C_{20}H_{12}$	252	252
Benzo[*a*]pyrene	BaP	$C_{20}H_{12}$	252	252
Perylene	Pe	$C_{20}H_{12}$	252	252
Dibenz[*a,h*]anthracene	DA	$C_{22}H_{14}$	278	278
Six-ring PAHs				
Indeno[1,2,3-*cd*]pyrene	IP	$C_{22}H_{12}$	276	276
Dibenzo[*g,h,i*]perylene	BP	$C_{22}H_{12}$	276	276
Alkylated PAHs				
C_1-Naphthalenes	C1N	$C_{11}H_{10}$	142	142
C_2-Naphthalenes	C2N	$C_{12}H_{12}$	156	156
C_3-Naphthalenes	C3N	$C_{13}H_{14}$	170	170
C_4-Naphthalenes	C4N	$C_{14}H_{16}$	184	184
C_1-Biphenyls	C1Bph	$C_{13}H_{12}$	168	168
C_2-Biphenyls	C2Bph	$C_{14}H_{14}$	182	182
C_3-Biphenyls	C3Bph	$C_{15}H_{16}$	196	196
C_4-Biphenyls	C4Bph	$C_{16}H_{18}$	210	210
C_1-Fluorenes	C1F	$C_{14}H_{12}$	180	180

Table 2.6 (continued)

Compounds	Code	Empirical formula	Molecular weight	Target ions
C_2-Fluorenes	C2F	$C_{15}H_{14}$	194	194
C_3-Fluorenes	C3F	$C_{16}H_{16}$	208	208
C_4-Fluorenes	C4F	$C_{17}H_{18}$	222	222
C_1-Phenanthrenes/anthracenes	C1P	$C_{15}H_{12}$	192	192
C_2-Phenanthrenes/anthracenes	C2P	$C_{16}H_{14}$	206	206
C_3-Phenanthrenes/anthracenes	C3P	$C_{17}H_{16}$	220	220
C_4-Phenanthrenes/anthracenes	C4P	$C_{18}H_{18}$	234	234
C_1-Pyrenes/fluoranthenes	C1Py	$C_{17}H_{12}$	216	216
C_2-Pyrenes/fluoranthenes	C2Py	$C_{18}H_{14}$	230	230
C_3-Pyrenes/fluoranthenes	C3Py	$C_{19}H_{16}$	244	244
C_4-Pyrenes/fluoranthenes	C4Py	$C_{20}H_{18}$	258	258
C_1-Benzanthracenes/ chrysenes/triphenylenes	C1C	$C_{19}H_{14}$	242	242
C_2-Benzanthracenes/ chrysenes/triphenylenes	C2C	$C_{20}H_{16}$	256	256
C_3-Benzanthracenes/ chrysenes/triphenylenes	C3C	$C_{21}H_{18}$	270	270
C_4-Benzanthracenes/ chrysenes/triphenylenes	C4C	$C_{22}H_{20}$	284	284
Triaromatic steranes				
C_{20} TA-sterane	C20TA	$C_{20}H_{20}$	260	231
C_{21} TA-sterane	C21TA	$C_{21}H_{22}$	274	231
C_{22} TA-sterane	C22TA	$C_{22}H_{24}$	288	231
C_{26} TA-cholestane (20S)	SC26TA	$C_{26}H_{32}$	344	231
C_{26} TA-cholestane (20 R)	RC26TA	$C_{26}H_{32}$	344	231
C_{27} TA-ergostane (20S)	SC27TA	$C_{27}H_{34}$	358	231
C_{28} TA-stigmastane (20S)	SC28TA	$C_{28}H_{36}$	372	231
C_{27} TA-ergostane (20 R)	RC27TA	$C_{27}H_{34}$	358	231
C_{28} TA-stigmastane (20 R)	RC28TA	$C_{28}H_{36}$	372	231
Monoaromatic steranes				
C_{21} MA-sterane	C21MA	$C_{21}H_{30}$	282	253
C_{22} MA-sterane	C22MA	$C_{22}H_{32}$	296	253
C_{23} MA-sterane	C23MA	$C_{23}H_{34}$	310	253
C_{27} 5β(H) MA-cholestane (20S)		$C_{27}H_{42}$	366	253
C_{27} MA-diacholestane (20S)		$C_{27}H_{42}$	366	253
C_{27} 5β(H) MA-cholestane (20 R)		$C_{27}H_{42}$	366	253
C_{27} MA-diacholestane (20 R)		$C_{27}H_{42}$	366	253
C_{27} 5α(H) MA-cholestane (20S)	SC27MA	$C_{27}H_{42}$	366	253
C_{28} 5β(H) MA-ergostane (20S)		$C_{28}H_{44}$	380	253
C_{28} MA-diaergostane (20S)		$C_{28}H_{44}$	380	253
C_{27} 5α(H) MA-cholestane (20 R)		$C_{27}H_{42}$	366	253
C_{28} 5α(H) MA-ergostane (20S)		$C_{28}H_{44}$	380	253
C_{28} 5β(H) MA-ergostane (20 R)		$C_{28}H_{44}$	380	253
C_{28} MA-diaergostane (20 R)		$C_{28}H_{44}$	380	253

Table 2.6 (continued)

Compounds	Code	Empirical formula	Molecular weight	Target ions
C_{29} 5β(H)MA-stigmastane(20S)		$C_{29}H_{46}$	394	253
C_{29}MA-diastigmastane (20S)		$C_{29}H_{46}$	394	253
C_{29} 5α(H) MA-stigmastane (20S)	SC29MA	$C_{29}H_{46}$	394	253
C_{28} 5α(H) MA-ergostane (20 R)	RC28MA	$C_{28}H_{44}$	380	253
C_{29} 5β(H) MA-stigmastane (20 R)	RC29MA	$C_{29}H_{46}$	394	253
C_{29} 5α(H) MA-stigmastane (20 R)	RC29MA	$C_{29}H_{46}$	394	253
C_{30} 5β(H) MA-sterane (20S)	C30MA	$C_{30}H_{48}$	408	253
Other naphthenoaromatics				
Tetralin	Te	$C_{10}H_{12}$	132	104,132
C_1-Tetralins	C1Te	$C_{11}H_{14}$	146	104,146
Tetrahydrophenanthrene	THP	$C_{14}H_{14}$	182	182,154
PASHs				
Benzothiophene	BT	C_8H_6S	134	134
C_1-Benzothiophenes	C1BT	C_9H_8S	148	148
C_2-Benzothiophenes	C2BT	$C_{10}H_{10}S$	162	212
C_3-Benzothiophenes	C3BT	$C_{11}H_{12}S$	176	176
C_4-Benzothiophenes	C4BT	$C_{12}H_{14}S$	190	190
Dibenzothiophene	DBT	$C_{12}H_8S$	184	184
C_1-Dibenzothiophenes	C1DBT	$C_{13}H_{10}S$	198	198
C_2-Dibenzothiophenes	C2DBT	$C_{14}H_{12}S$	212	212
C_3-Dibenzothiophenes	C3DBT	$C_{15}H_{14}S$	226	226
C_4-Dibenzothiophenes	C4DBT	$C_{16}H_{16}S$	240	240
Benzo[b]naphthothiophenes	BNT	$C_{16}H_{10}S$	234	234
C_1-Benzo[b]naphthothiophenes	C1BNT	$C_{17}H_{12}S$	248	248
C_2-Benzo[b]naphthothiophenes	C2BNT	$C_{18}H_{14}S$	262	262
C_3-Benzo[b]naphthothiophenes	C3BNT	$C_{19}H_{16}S$	276	276
C_4-Benzo[b]naphthothiophenes	C4BNT	$C_{20}H_{18}S$	290	290
Dinaphthothiophenes	DPT	$C_{20}H_{12}S$	284	284
C_1-Dinaphthothiophenes	C1DPT	$C_{21}H_{14}S$	298	298
C_2-Dinaphthothiophenes	C2DPT	$C_{22}H_{16}S$	312	312
C_3-Dinaphthothiophenes	C3DPT	$C_{23}H_{18}S$	326	326
C_4-Dinaphthothiophenes	C4DPT	$C_{24}H_{20}S$	340	340

Gasoline usually consists of a high concentration of small MAHs; for example, according to Table 2.7, a fresh gasoline sample has 375 mg/g of monoaromatics. In comparison, residual fuels contain a very low concentration of these components, which are attributable to the portion of blended light fuels. MAHs barely occur in fresh lubricating oils, but these compounds are found in used lube oils from gasoline and diesel engines [24], which are attribute to unburned fuels.

The plots of the concentrations of BTEX and C_n-benzenes versus weathering percentages were used to estimate the weathering extent of weathered oil samples, especially for short-term weathered oils in which loss of BTEX and C_n-benzenes is significant [79]. For forensic oil spill analysis, these volatile aromatics are of little

Table 2.7: BTEX and alkylbenzenes in crude oils and petroleum products.

Oil samples	Bakken	Fed	Troll	PlE	Oil sand bitumen*	CLWB	Gasoline #87	Diesel no. 2	Marine diesel	Bunker C	Lube 10w-30
Benzene	3.28	2.65	0.70	0.16	ND	1.47	5.62	0.07	0.04	0.03	0.005
Toluene	4.47	6.33	2.53	0.82	0.012	4.15	140	1.03	0.62	0.19	0.009
Ethylbenzene	0.90	1.32	1.43	0.50	0.001	0.41	18.8	0.57	0.35	0.12	0.001
m- and *p*-Xylene	6.24	5.76	5.03	0.74	0.006	3.91	63.4	2.38	1.30	0.50	0.003
o-Xylene	1.99	2.31	1.30	0.55	0.002	1.01	23.3	1.13	0.59	0.24	0.001
ΣBTEX	**16.9**	**18.4**	**11.0**	**2.77**	**0.022**	**10.9**	**251**	**5.19**	**2.90**	**1.08**	**0.019**
Isopropylbenzene	0.28	0.34	0.43	0.18	ND	0.08	2.85	0.38	0.14	0.03	ND
Propylbenzene	0.44	0.40	0.61	0.39	0.001	0.13	7.28	0.62	0.38	0.18	ND
3- and 4-Ethyltoluene	1.93	1.73	1.97	0.56	0.005	0.76	35.4	2.17	1.49	1.12	0.001
1,3,5-Trimethylbenzene	1.29	1.49	1.22	0.19	0.003	0.64	12.6	1.02	0.47	0.45	0.002
2-Ethyltoluene	0.45	0.51	0.67	0.35	0.002	0.16	9.52	0.82	0.45	0.31	ND
1,2,4-Trimethylbenzene	4.14	2.12	2.09	0.53	0.008	1.31	49.1	4.13	1.86	1.99	0.002
1,2,3-Trimethylbenzene	0.24	0.17	0.37	0.14	0.001	0.34	0.46	0.72	0.67	0.04	ND
ΣC_3-Benzenes	**8.76**	**6.76**	**7.36**	**2.34**	**0.020**	**3.43**	**117**	**9.87**	**5.49**	**4.12**	**0.005**
Isobutylbenzene	0.07	0.11	0.11	0.02	0.001	0.04	0.37	0.22	0.05	0.03	ND
1-Methyl-2-isopropylbenzene	0.03	0.05	0.07	0.02	0.001	0.02	0.24	0.08	0.05	0.03	ND
1,2-Dimethyl-4-ethylbenzene	0.59	0.38	0.46	0.17	0.002	0.08	4.69	1.42	0.43	0.58	ND
Amylbenzene	0.08	0.04	0.06	0.08	0.005	0.01	1.04	1.31	0.43	0.26	ND
n-Hexylbenzene	0.04	0.03	0.05	0.06	0.006	0.02	0.06	0.45	0.24	0.09	ND
ΣC_4–C_6 alkyl benzenes	**0.80**	**0.61**	**0.75**	**0.35**	**0.014**	**0.17**	**6.39**	**3.48**	**1.19**	**0.99**	ND
Total (mg/g)	**26.4**	**25.7**	**19.1**	**5.46**	**0.056**	**14.5**	**375**	**18.5**	**9.58**	**6.18**	**0.02**

* Concentration: mg/g of TSEM of Alberta oil sands DCM extract. CLWB: Cold Lake bitumen winter blend.

importance or interest. Alkyl-benzenes in crude oil are not so source-specific informative as PAHs and biomarker compounds, and these small aromatics are highly volatile and susceptible to weathering; therefore, forensic oil identification and correlation usually do not rely on them. However, chemical fingerprints of alkylbenzenes and alkyltoluenes are still useful for a specific case involving gasoline as other forensic information are not applicable in this situation [20, 80].

2.6.2 PAHs

PAHs have two or more fused benzene rings and their structural stability results from concomitant electron pair delocalization. PAHs with three or more rings have various structural isomers due to different ring fusions, for example, phenanthrene and anthracene for $C_{14}H_{10}$; and chrysene, triphenylene, benz[*a*/*b*]anthracene, benzo[*c*] phenanthrene, naphthacene, and acepyrene for $C_{18}H_{12}$. Moreover, PAHs can have structural isomers with various alkylated groups. Some or all of the isomers and their alkylated derivatives could occur in petroleum. The occurrence of one specific isomer in petroleum can be much lower than others. PAHs are relatively persistent in the environment and are toxic, carcinogenic, and mutagenic.

PAHs have a fused ring structure and exhibit high stability due to the conjugated effect. Under typical mass spectral 70 eV collision energy (EI source), these compounds generally produce intensive molecular ions. Therefore, PAHs are normally determined by using their prominent molecular ions, although other less intensive fragmentograms can be used for confirmation [38]. Similar to unsubstituted PAH analysis, APAHs are generally determined using their prominent parent ions. Other fragmentograms such as $(M\text{-}1)^+$, $(M\text{-}15)^+$, and $(M\text{-}29)^+$ can be applied for confirmation.

PAHs are ubiquitous in the environment and generally originate from three main sources: petrogenic, pyrogenic, and biogenic. Petrogenic PAHs are related to crude oils and refined petroleum products and are generated from geochemical alteration of organic matter. Pyrogenic PAHs, particularly HMW PAHs ranging from benzo(a)anthracene to coronene, are prevalent contaminants resulting from heavy anthropogenic and industrial activities such as incomplete combustion of fuel, industrial petrochemical practices, residential wood burning, vehicular emissions, and power plant emissions. At high temperatures, the more reactive APAHs tend to be destroyed. This explains why homologue groups in pyrogenic assemblages are dominated by nonalkylated, parent compounds, with subsequently lower alkyl members as the degree of alkylation increases [81, 82]. It has been reported that the PAHs found in tire pyrolysis oil consist largely of alkylated naphthalenes, fluorenes, and phenanthrenes, meanwhile the concentrations of individual five-ring benzo(a)pyrene ranged from <10 to 600 ppm [83]. Biogenic PAHs are produced by organisms or formed during the early stage of diagenesis in sediments. Unlike petrogenic and pyrogenic PAHs, biogenic PAHs in the environment are non-anthropogenic, which are believed to be

formed during the bacteriological breakdown of organic matter in marine sediments by a process called early diagenesis. These compounds are generally found individually or in very simple mixtures, such as perylene, retene, and alkylated and partially aromatized tetra- and penta-cyclic derivatives of chrysene and picene [84, 85]. Perylene is one of the most abundant biogenic PAHs, and it is often used as an indicator to identify the biogenic contribution.

PAHs in crude oils: Crude oils and refined products generally contain significant amounts of PAHs, in particular the alkylated homologues of naphthalene, phenanthrene, fluorene, and chrysene. Although many unsubstituted PAHs occur naturally, only a selection of two- to six-ring PAHs are monitored as priority pollutants due to their relatively high toxicity and wide occurrence in the environment. The abundance and distribution profiles of these compounds in crude oils vary with the nature of the original organic matter and the geological conditions of formation. These APAHs are particularly useful for source identification because they occur in all crude oils and most the refined petroleum products in considerable concentrations. Their relative concentrations also vary significantly between different oils making them source-specific.

Table 2.8 summarizes the quantitative analytical results of petroleum-characteristic APAHs homologous series and 15 individual unsubstituted PAHs in crude oil samples. As shown in Table 2.8, the total concentration of unsubstituted PAHs in crude oils spans from tens to hundreds of ppm. It is noted that the Platform Elly heavy crude contains 30.2 μg/g of perylene, significantly more abundant than other four- to six-ring PAHs. The PAHs determined in heavily biodegraded Alberta oil sand bitumen are composed of relatively higher three- to five-ring compounds than conventional crudes, particularly light crude oils. In the market, some synthetic crude oils such as AHS (Alberta, Canada), are blended with hydrocracking residues, in which extremely high content of unsubstituted PAHs was detected with a total concentration of 624 μg/g [61].

The concentrations of target PAH alkylated homologues are roughly two orders of magnitude higher than the total concentration of the unalkylated PAHs. APAH concentrations in seven crude oils vary widely from 2,300 μg/g for Alberta oil sand bitumen to 16,670 μg/g for Troll crude. Light crude oil does not necessarily contain high concentrations of APAHs. In fresh crude oils, total APAHs are largely constituted by naphthalene and phenanthrene series. Therefore, it is understandable that the predominance of two- to three-ring PAHs including naphthalenes, fluorenes, and phenanthrenes generally implies fresh petroleum pollution.

The overall distribution of APAHs (generally refer to C_0- to C_4-) in fresh crudes usually have a characteristic bell-shaped profile, due to the different degree of alkylation. C_1- to C_3-naphthalenes are often the most abundant in fresh crude oils but are readily removed in the formation of heavy oils, resulting in a very low concentration. A distribution profile of C_0- < C_1- < C_2- < C_3- in nearly all five oil-characteristic APAH series of Alberta oil sand bitumen is very apparent. This can be explained by the fact

Table 2.8: PAHs in oils.

Samples	Bakken	SoL	Shengli	Troll	ArH	PlE	AOS*	Gasoline	Diesel no. 2	Marine diesel	Bunker C	Lube 10W-30
C0N	159	806	137	967	140	85.8	ND	1,259	933	98.0	342	0.39
C1N	1,112	2,026	566	2,900	616	377	ND	1,198	3,614	328	1,231	0.78
C2N	2,833	2,920	1,017	3,646	1,262	744	11.5	422	6,328	1,211	1,857	1.17
C3N	2,892	2,563	940	2,837	1,625	882	103	130	6,077	1,810	1,665	1.01
C4N	1,853	1,544	594	1,677	1,096	820	240	33.8	3,078	1,236	970	0.79
ΣN	**8,849**	**9,858**	**3,254**	**12,027**	**4,738**	**2,909**	**355**	**3,042**	**20,030**	**4,683**	**6,064**	**4.14**
C0P	98.6	145	104	269	55.8	27.3	10.1	5.60	359	47.3	445	0.22
C1P	396	396	332	585	169	91.4	95.5	16.7	1,081	306	1,837	2.27
C2P	651	460	399	640	280	137	214	11.6	1,041	510	2,653	10.0
C3P	619	371	332	543	224	109	274	3.96	564	454	2,297	9.51
C4P	409	229	180	410	140	95.6	198	0.78	203	226	1,672	5.27
ΣP	**2174**	**1601**	**1347**	**2448**	**868**	**460**	**791**	**38.7**	**3248**	**1544**	**8,903**	**27.2**
C0F	30.3	58.9	40.8	161	29.2	10.2	1.55	4.83	316	45.7	104	0.65
C1F	141	178	85.9	347	80.5	38.5	23.7	11.6	775	223	265	1.04
C2F	291	300	127	484	169	80.5	77.7	9.43	992	547	451	2.13
C3F	335	273	112	396	277	78.7	128	5.60	775	773	510	6.19
ΣF	**798**	**809**	**365**	**1,388**	**555**	**208**	**231**	**31.5**	**2,858**	**1,589**	**1,330**	**10.0**
C0C	13.7	8.07	26.0	40.3	10.3	10.5	15.9	0.11	2.58	2.29	277	0.13
C1C	50.3	23.3	47.6	77.3	21.9	19.7	40.3	0.27	5.65	7.90	1,017	ND
C2C	89.5	31.1	89.1	119	39.1	33.0	84.6	ND	4.72	10.9	1,372	ND
C3C	100	24.0	76.9	71.8	33.9	24.4	75.9	ND	ND	8.44	1,097	ND
ΣC	**254**	**86.6**	**240**	**309**	**105**	**87.6**	**216.6**	**0.38**	**13.0**	**29.6**	**3763**	**0.13**
ΣAPAHS (µg/g)	**12,437**	**12,844**	**5,506**	**16,670**	**8,498**	**4,226**	**2,305**	**3,112**	**26,602**	**7,846**	**21,875**	**70.8**
Bph	51.6	153	20.5	288	23.1	5.77	ND	9.96	489	142	26.1	0.11
Acl	8.11	15.9	6.78	16.4	7.65	8.56	ND	ND	40.1	6.64	12.3	ND
Ace	7.87	13.6	13.9	53.7	4.42	6.01	2.94	3.74	84.4	27.9	48.4	ND
An	1.86	3.64	2.62	2.96	1.75	0.60	ND	1.96	ND	4.09	63.1	0.03

Fl	1.66	3.27	3.60	12.6	1.89	1.57	3.02	0.66	7.05	14.6	33.8	ND
Py	9.75	4.83	15.2	16.3	4.01	3.81	10.4	0.96	29.1	86.8	160	0.08
BaA	1.32	2.67	3.71	7.75	2.11	2.43	2.03	0.20	0.45	0.46	139	0.10
B(b + k)F	1.13	2.17	4.07	10.6	2.33	2.87	4.31	ND	ND	0.30	67.8	ND
BeP	3.30	1.45	12.0	11.1	2.70	3.55	5.93	ND	ND	0.53	95.7	ND
BaP	0.38	0.59	1.43	3.15	1.33	1.32	2.22	ND	ND	0.13	59.9	ND
Pe	ND	21.2	2.41	4.70	0.97	30.2	4.83	ND	ND	0.11	26.5	ND
IP	ND	ND	1.60	1.40	0.31	ND	1.30	ND	ND	ND	12.2	ND
DA	0.68	0.23	2.09	1.50	0.37	ND	1.53	ND	ND	ND	23.2	ND
BP	ND	0.70	1.91	3.61	1.42	1.48	2.61	ND	ND	ND	11.8	ND
ΣPAHs (μg/g)	**87.7**	**223**	**91.7**	**434**	**54.4**	**68.1**	**41.1**	**17.5**	**650**	**283**	**780**	**0.32**

* AOS: Alberta oil sand bitumen, DCM extract.

that susceptibility to microbial degradation decreases as the alkylation level increases in each APAH family. Sometimes, a heavy crude like bitumen is mixed with diluent to facilitate easy transportation; therefore, it is not surprising that C_0- to C_3-naphthalene isomers can be detected in appreciable concentrations [61].

PAHs in petroleum products: Compared with crude oils, a certain types of refined oil products can contain much higher concentrations of unsubstituted PAHs, while some petroleum products such as lubricating oil only contain trace amounts. Table 2.8 summarizes the quantitative analytical results of petroleum-characteristic APAHs homologous series and 15 individual unsubstituted PAHs in representative petroleum products. In general, PAHs in light-distillate fuels are only limited to small two- and three-ring compounds; however, obvious increments of four- to six-ring PAHs attributed to refining processes are found in residual fuels. For instance, four- to six-ring PAHs in total comprise nearly 90% of parent PAHs in Bunker C, these high boiling point PAHs are low in diesel and undetectable levels in gasoline.

APAHs in refined products are partially derived from feedstock crude oil and are generated in the manufacturing processes. The distillation and refining process often alters their abundance and distribution profile. Compared to conventional crudes, many refined oil products, except for gasoline and lubricating oil, have higher contents of APAHs with the predominance of naphthalene and phenanthrene series. These compounds are extremely high in diesel fuels. For example, the concentrations of total APAHs in diesel no. 2 are as high as 26,602 μg/g. The small PAH compounds in these heavy fuels are usually attributed to blended light products. PAHs in gasoline are dominated by naphthalene and its alkyl homologues with a decreasing profile of C_0- > C_1- > C_2- > C_3-. Alkylated chrysene series are hardly detectable in these light fuels such as gasoline and diesel; in contrast, the residual fuels such as Bunker C usually contain them in relatively high amounts.

Waste or used oils are usually mixtures of different types of oils and other non-petroleum material. Used and waste lube oils are mixtures of lube oils, unburned diesel, and combustion exhaust of oils. Used lube oil from a diesel engine retains some characteristics of diesel fuel while having some characteristics of additional pyrogenic PAHs [24].

PAHs in environmental samples: The distribution of PAHs in environmental samples is very important for decoding contamination sources. Most PAHs do not dissolve easily in water and their hydrophobicity generally increases with increasing molecular mass. Consequently, these compounds tend to deposit and accumulate in the river and marine beds, resulting in long-term hazards to the environment.

Figure 2.11 shows PAH distributions in some representative environmental samples including snowmelt water from an Alberta oil sands development site, a vessel bilge, a recreational pond sediment, sediment from the oil industry affected river, and a sediment from water treatment plant. Besides five series of determined APAHs

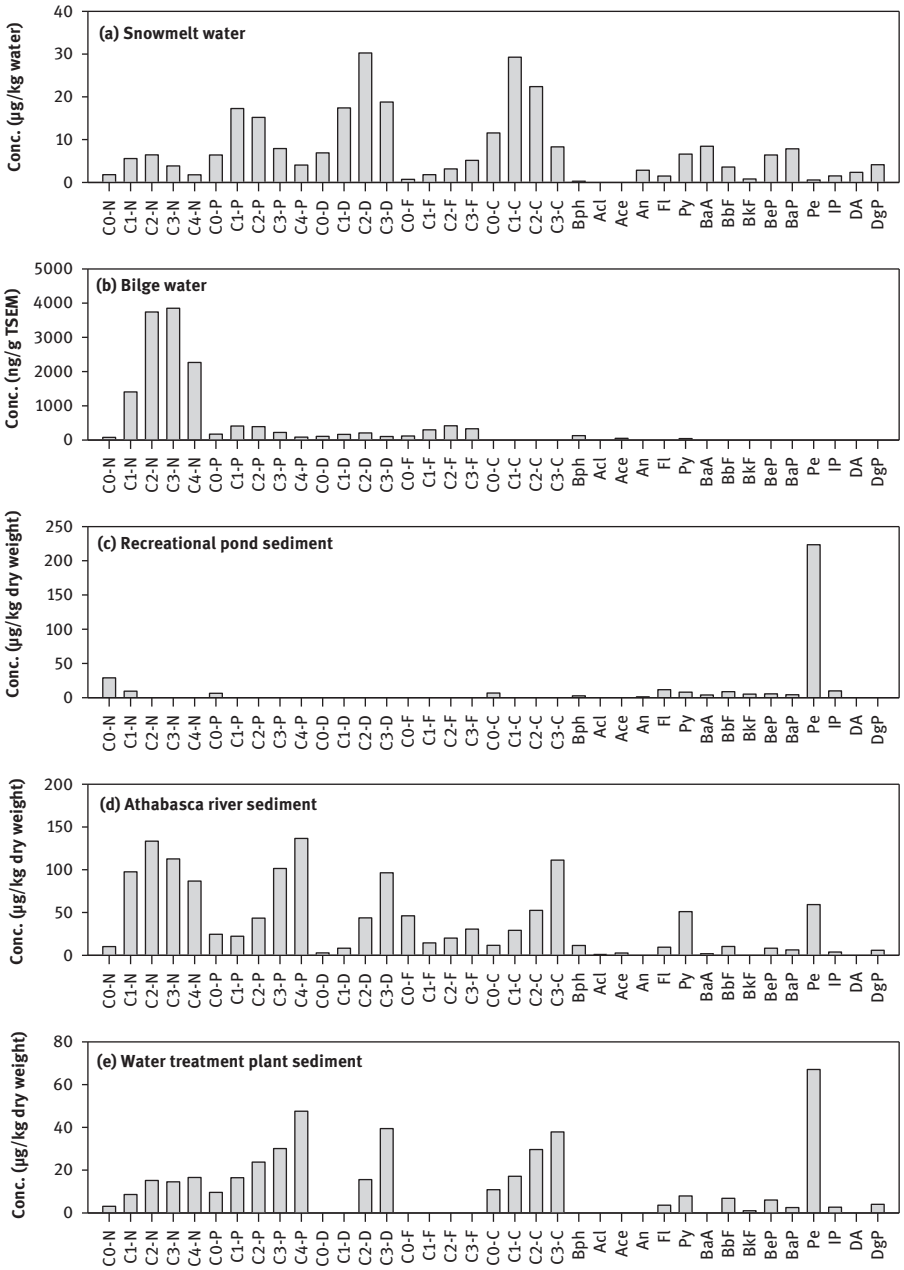

Figure 2.11: PAHs in environmental samples.

as clear evidence of petroleum contamination (oil sands particulate), the high amount of four- to six-ring parent PAHs suggests other contribution sources of contamination in the snowmelt water sample. In the filter, a high percentage of four- to six-ring parent PAHs predominate the total determined unsubstituted PAHs. This typical PAH distribution pattern indicates a contribution from pyrogenic sources, such as runoff from high levels of automobile emissions, which are known to contain a greater amount of larger molecular PAHs relative to others. Perylene only accounts for 3.0% of the total five5-ring PAHs suggesting only a minor biogenic contribution to the detected PHCs in the sample.

The total PAHs were determined to be 14,613 μg/g TSEM with a predominance of APAHs and no detection of the HMW alkylated chrysenes among target APAH homologous series in the bilge. Unsubstituted PAHs are dominated by low molecular weight (LMW) PAHs with two and three rings. This is a typical feature in the chemical composition of light diesel fuels. It has been well known that, in general, PAH concentrations are high in diesels while lube oils only contain trace amounts of APAHs [15, 24]. Therefore, it can be expected that the portion of lube oil in a mixture of diesel and lube oil would only have minimal effects on the PAH distribution pattern and profile. In addition, biogenic and pyrogenic contribution to the bilge sample was not observed from PAH fingerprinting analysis.

As shown in Figure 2.11, only traces of unsubstituted PAHs plus C_1-naphthalenes were detected without other petroleum-characteristic APAH homologues in the recreation pond sediment. These PAHs in trace amount are probably attributed to anthropogenic inputs such as runoff and atmospheric deposition. Perylene in this sample is at an unusually high concentration compared with other five-ring PAHs, accordingly resulting in a high perylene index of 90.5%, which is far higher than the pyrogenic input criteria of 10%. Therefore, the contribution of the natural biogenic sources to the hydrocarbons in the sediment is evident.

PAHs in the Athabasca River sediment in Figure 2.11 are dominated by APAHs. Except for the naphthalene series, the APAH families show an overall decreasing distribution pattern of $C_0 < C_1 < C_2 < C_3$, which is consistent with the typical PAH distribution of the oil sand bitumen [61, 86]. Meanwhile, alkylated naphthalenes are highly abundant and in a bell-shaped distribution profile. This may indicate some anthropogenic contribution of oil hydrocarbons from lighter petroleum products, in addition to oil sand bitumen contribution to the sample [86]. Among target unsubstituted PAHs, perylene is the most abundant component, accounting for about 34.6% of the sum of unsubstituted PAHs and over 70% of total five-ring PAHs, clearly indicating a contribution of biogenic input to this sediment. Excluding the outstanding contribution of biogenic perylene, other unsubstituted PAHs are relatively more abundant than those in common oils and refined products. It may indicate a certain contribution of PAHs from pyrogenic sources (such as emission particulates) to the sediment sample.

2.6.3 Aromatic steranes

A series of bicyclic, tricyclic, and tetracyclic naphthenoaromatics are common in refined petroleum products but also occur in crude oil. These include indane, tetralin, tetrahydrophenanthrene, aromatic steranes, and their alkyl derivatives. These naphthenoaromatic hydrocarbons possess mixed structures of aromaticand alicyclic rings (mostly hexyl or pentyl), as well as aliphatic side chains.

Tetracyclic aromatic steroids (also known as aromatic steranes) are detected in most crude oils [37, 87, 88]. Aromatic steranes in the aromatic fraction have highly similar skeletons to saturated biomarker steranes. These compounds have 17 carbons to form a skeleton consisting of four fused rings and range from C_{20} to C_{30} homologs. MASs are composed of four fused rings in their molecular structure including two cyclohexane rings (A + B), an aromatic ring (C-ring), and one cyclopentane ring (D-ring). TASs have a similar molecular structure as MASs. The cyclohexane A and B rings in TAS are replaced by aromatic rings. Aromatic sterane isomers have a characteristic configuration of C-17 and C-20 chiral centers. Each aromatic sterane is usually represented by two epimers (20R and 20S) with different concentrations. Due to the aromatization of C-ring in monoaromatic and (A + B + C) rings in TASs, these compounds have fewer substituents on the ring skeleton and have much fewer constitutional isomers and stereoisomers than their saturated sterane analogs [37].

In a GC-MS analysis, MASs elute between *n*-C_{23} and *n*-C_{30}, while TASs elute slightly later between *n*-C_{24} and *n*-C_{34}, similar to the elution range for biomarker terpanes in GC-MS analysis (see Figure 2.2). The base peak of TASs is *m*/*z* 217 ($C_{17}H_{13}^{+}$) for the nucleus alone and *m*/*z* 231 ($C_{18}H_{15}^{+}$) if with a single methyl group. C_{26} TA-cholestane (20 R) and C_{27} TA-ergostane (20S) are co-eluted and present as the highest peaks in *m*/*z* 231 chromatograms. A cluster of TA-cholestanes (C_{26}), TA-ergostane (C_{27}), and TA-stigmastanes (C_{28}) are the most distinguishable aromatic steranes in most oil samples. It was also observed that a cluster of peaks (at *m*/*z* 231) elute in the boiling point range of C_{20} and C_{21} TASs, making it impossible to accurately identify and quantify these triaromatic compounds in heavy fuels. This cluster is probably attributed to PAHs and/or naphthenoaromatic hydrocarbons produced in refining processes and their presence could be used as evidence of cracked heavy components. MASs can be identified by their characteristic fragmentograms at *m*/*z* 253 ($C_{19}H_{25}^{+}$), due to loss of the alkyl group attached on C-17. Quantitative analysis of MASs often encounters serious interference at *m*/*z* 253 by saturated hydrocarbons if the oil sample is not fractionated prior to instrumental analysis, and sometimes insufficient abundance of these compounds can hinder reliable measurement [37].

Aromatic steranes in crude oils: These aromatic steranes widely occur in various crude oils and shales and are of utmost importance in petroleum chemistry and geochemistry. In catagenesis, MASs are transformed into triaromatic hydrocarbons via degradation of the aliphatic side chains. The aromatization of the B-ring in MASs

(aromatic C-ring) occurs at a slow pace, but once completed, subsequent A-ring aromatization proceeds with considerable speed, which results in low concentrations of diaromatic steranes (B- and C-rings) in crude oil [59, 62]. The abundance of MASs relative to TASs is used in various geochemical correlations, particularly in evaluating crude oil maturity [59, 87].

Figure 2.12 illustrates the GC-MS chromatograms of TASs in crudes and refined petroleum products. Aromatic steranes are widely detected in all of the crude oils, but their abundances are very low relative to the total concentration of five APAH series [37]. It is obvious from Figure 2.12 that crude oils from different sources and various petroleum products have unique characteristics of aromatic steranes. The abundances of aromatic steranes in crude oils vary significantly. Overall, aromatic steranes in heavier crude oils are likely more abundant than in lighter oils. These compounds occur only at low concentrations in light crude oils such as the Scotia Light and the Bakken crude oils but high concentrations in the heavy California Platform Elly crude oil [37].

Aromatic steranes in petroleum products: The abundance and distribution profiles of petroleum hydrocarbons in refined products are often altered by the distillation and refining process of their original feedstock. In general, TASs are undetectable to very low concentrations in many refined oil products, although these oils probably contain a high concentration of other APAHs. Predictably, these aromatic steranes with relatively high boiling points are barely found in light and middle distillate fuels such as volatile gasoline and light diesel. If simply based on the boiling point range of petroleum products, the heavy fuels and lubricating oils should have a high content of these aromatic steranes; however, in general, aromatic steranes are only at trace levels in these oils. The absence of TASs in combination with the presence of the hopanes confidently indicates the presence of lubricating oil [20]. This is due to the hydrogenation and hydrocracking during the refining process removing most aromatic hydrocarbons including the steranes, from the base oil [37]. As a result, aromatic steranes and PAHs are absent or at a low abundance in the unused lubricating oils (Figure 2.12).

2.6.4 Polycyclic aromatic sulfur heterocycles

Other than PAHs, petroleum also contains a large amount of heterocyclic N-, S-, O-containing analogues of PAHs. As the third most abundant element in crude oil, sulfur occurs in various forms and wide molecular weight fractions. Organosulfur compounds commonly identified in fossil fuels and crude oil include thiols, thioethers, disulfides, thiophenes, benzothiophenes, dibenzothiophenes, and benzonaphthothiophenes [89–93]. Among these organosulfur compounds, the most abundant group of compounds are analogues of PAHs, namely PASHs or thiaarenes. Similar to PAHs, three- to five-

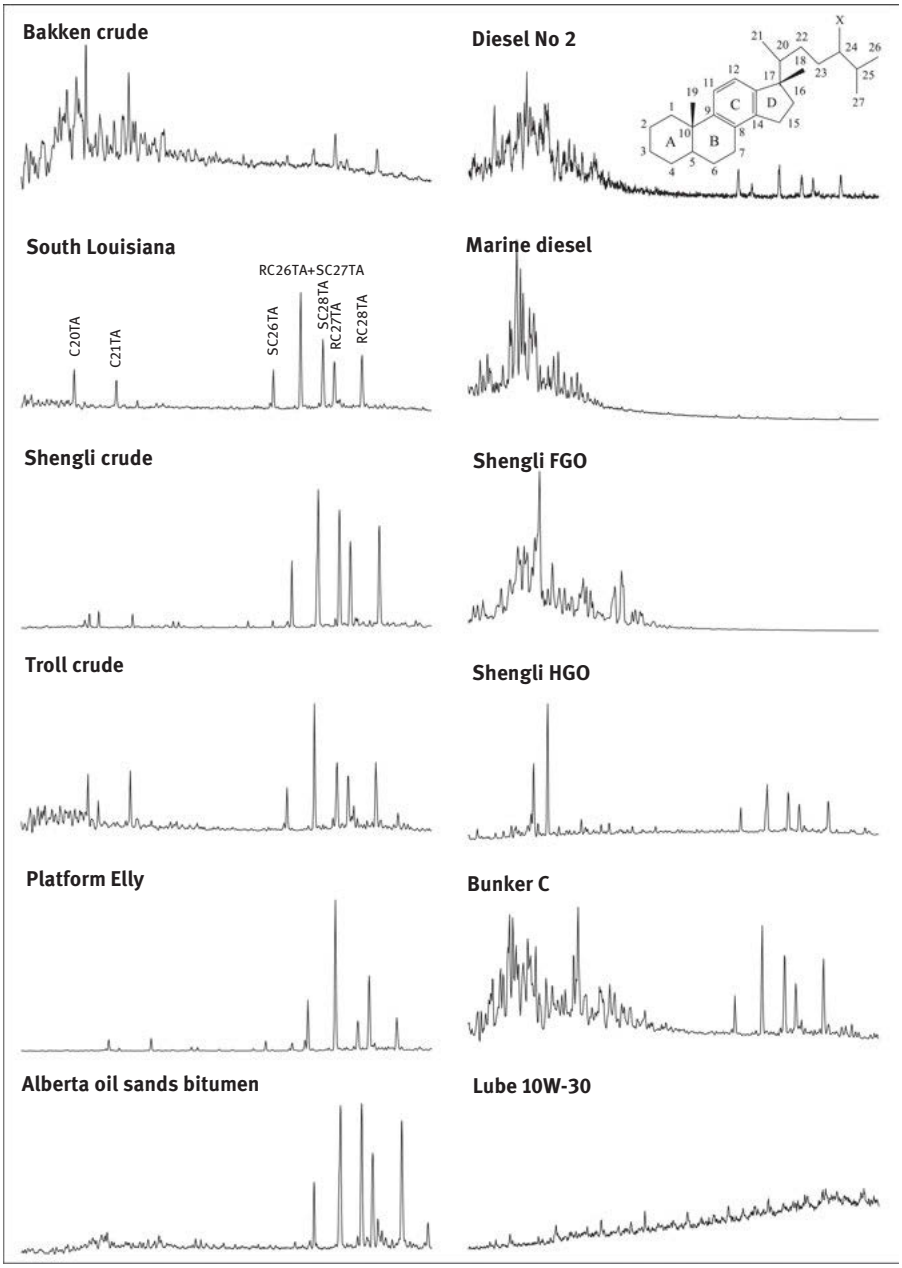

Figure 2.12: GC-MS chromatograms of triaromatic steranes in crude oils and petroleum products.

ring PASHs have various structural isomers, for example, benzo[b]naphtha[2,1-*d*] thiophene, benzo[*b*]naphtha[1,2-*d*]thiophene, and benzo[b]naphtha[2,3-*d*]thiophene for $C_{16}H_{10}S$; Some or all of these isomers and their alkylated homologues could occur in petroleum but are usually difficult to chromatographically differentiate [29].

PASHs have not been as intensively investigated as PAHs, but such studies may lead to a great deal of information not available through the study of PAHs [94]. PASHs are of great interest to environmental monitoring, especially in relation to oil spills and combustion emissions of hard coal. PASHs generally have very similar chemical properties and may exhibit similar carcinogenicity and mutagenicity as their PAH analogues. Eastmond et al. compared a series of PASH with their sterically and structurally similar PAHs for toxicity and biotransformations [95]. Benzo[b]thiophene and benzo[*b*]naphtho[2,1-*d*]-thiophene were bioconcentrated to a greater extent than naphthalene and chrysene, respectively. It was reported that benzo[2, 3] phenanthro[4,5-*bcd*]thiophene exhibited outstanding mutagenic activity exceeding even that of its homocyclic benzo[a]pyrene [96].

Accurate characterization and measurement of these sulfur species are very meaningful for unambiguous identification and differentiation of type and age of petroleum products. PASHs generally concur with other PAHs and their large number of possible alkyl-substituted isomers in crude oil [15, 92, 94]. During a chromatographic analysis, PASHs are usually present at close retention time with PAHs. Moreover, some PASHs by chance have the same nominal masses as other petroleum hydrocarbons, for example, 184 amu for both C_4-naphthalenes and dibenzothiophene, and 234 amu for both C_4-phenanthrenes/anthracenes and benzo[*b*]naphthothiophenes. PAHs and PASHs could interfere with each other's identification and quantitation. Their identification and quantitation can be improved by using high-resolution and high-mass accuracy MS [29, 32].

Sulfur-containing compounds are removed from certain refined petroleum products as undesirable content. With deep desulfurization, the sulfur concentration in refined products is lowered and the analysis of the remaining PASHs becomes increasingly difficult in the presence of the PAHs, whose concentration is unaffected by the refining processes.

PASHs in crude oils: Sulfur-containing compounds occur in the majority of crude oils and certain refined petroleum products. Table 2.9 summarizes the quantitative analytical results of four petroleum-characteristic PASH series and four PAH analogues (C_0- to C_4-naphthalenes, phenanthrenes, chrysenes, and benzopyrenes) in representative light to heavy crude oils. The distributions of APASHs (generally referring to C_0- to C_4-) in fresh crudes usually demonstrate a characteristic bell-shaped profile, which is similar to the profiles of other carbocyclic analogues.

PASH concentrations in seven crude oils vary widely from 405 μg/g for the Bakken crude to 4,825 μg/g for Alberta oil sands extract (bitumen). Among these PASH groups, tricyclic dibenzothiophenes are the most abundant, followed by tetracyclic

Table 2.9: PASHs in crude oils, refined petroleum products, and environmental samples.

Compounds	Crude oils					Petroleum products					Environmental samples		
	Bakken	Federated	South Louisiana	Shengli	Oil sands extract	Diesel (2002)	Diesel (2021)	IFO-180	Bunker C	Shengli distillated diesel	Snowmelt water	Athabasca River sediment	Pond sediment
	(μg/g)	(μg/g)	(μg/g)	(μg/g)	(μg/g)	(μg/g)	(μg/g)	(μg/g)	(μg/g)	(μg/g)	(μg/kg)	(μg/kg)	(μg/kg)
C_0-BT	0.10	0.10	0.83	0.93	ND[a]	1.94	ND	37.7	32.7	8.86	2.72	0.80	1.50
C_1-BT	0.17	5.26	7.67	7.75	0.84	9.66	ND	264	142	58.8	5.83	5.90	1.07
C_2-BT	2.39	97.1	79.6	44.7	52.7	93.7	ND	621	286	304	7.88	36.6	1.63
C_3-BT	6.81	153	103	70.1	210	105	ND	457	182	452	4.15	112	1.63
C_4-BT	11.2	127	97.2	87.2	371	71.4	ND	271	108	551	1.62	145	1.41
Σ BTs	**20.7**	**382**	**288**	**211**	**635**	**282**	**ND**	**1,651**	**751**	**1,374**	**22.2**	**300**	**7.24**
C_0-DBT	7.82	95.8	42.7	16.0	7.89	42.6	ND	153	105	106	9.24	30.6	6.00
C_1-DBT	41.0	282	218	93.5	269	120	ND	573	420	585	31.36	193	7.00
C_2-DBT	87.7	384	403	148	832	106	ND	900	739	794	47.98	417	14.0
C_3-DBT	85.0	241	312	108	868	39.6	ND	834	662	256	24.67	917	13.0
C_4-DBT	45.9	129	177	83.6	657	12.7	ND	561	419	31.0	9.79	1,071	9.00
Σ DBTs	**267**	**1,132**	**1,153**	**449**	**2634**	**321**	**ND**	**3,021**	**2,345**	**1,772**	**123**	**2,629**	**49.0**
C_0-BNT	2.76	19.7	10.2	11.8	63.4	0.19	ND	206	175	ND	16.9	97.4	20.0
C_1-BNT	14.2	78.8	43.7	42.9	251	0.37	ND	783	686	ND	42.6	531	18.0
C_2-BNT	29.9	122	82.7	59.5	388	0.22	ND	1,067	901	ND	30.6	1,436	25.0
C_3-BNT	31.1	101	79.0	52.1	361	ND	ND	825	712	ND	11.5	2,130	31.0
C_4-BNT	19.3	61.0	52.6	34.4	240	ND	ND	413	388	ND	3.58	1,391	21.0
ΣBNTs	**97.3**	**383**	**268**	**201**	**1,303**	**0.78**	**ND**	**3,294**	**2,862**	**ND**	**105**	**5,585**	**115**
C_0-DNT	1.20	7.71	2.33	7.86	20.6	ND	ND	58.0	63.0	ND	32.3	148	22.0
C_1-DNT	2.56	26.8	6.29	12.2	63.1	ND	ND	185	197	ND	50.9	275	22.0
C_2-DNT	5.55	38.6	10.0	17.4	101	ND	ND	263	272	ND	46.5	462	31.0
C_3-DNT	5.60	31.3	12.0	16.8	92.7	ND	ND	214	200	ND	24.0	460	31.0

(continued)

Table 2.9 (continued)

Compounds	Crude oils					Petroleum products					Environmental samples		
	Bakken	Federated	South Louisiana	Shengli	Oil sands extract	Diesel (2002)	Diesel (2021)	IFO-180	Bunker C	Shengli distillated diesel	Snowmelt water	Athabasca River sediment	Pond sediment
C4-DNT	4.33	33.6	7.88	11.6	74.5	ND	ND	138	164	ND	8.47	341	18.0
ΣDNTs	**19.2**	**138**	**38.5**	**65.9**	**352**	**ND**	**ND**	**858**	**896**	**ND**	**162**	**1,686**	**124**
ΣPASHs	**405**	**2,035**	**1,747**	**927**	**4,924**	**603**	**ND**	**8,824**	**6,853**	**3,146**	**413**	**10,200**	**295**
ΣPASHs/ΣPACs	**0.05**	**0.14**	**0.17**	**0.15**	**0.57**	**0.02**	**0.00**	**0.21**	**0.22**	**0.14**	**0.33**	**0.57**	**0.18**

benzonaphthothiophenes. Light bicyclic benzothiophenes and heavy pentacyclic dinaphthothiophenes were both detected, but in relatively lower concentrations in all studied crude oils. PASHs concentrations are lower overall than their corresponding PAH analogues in most studied oils, while Alberta oil sand bitumen contains very high concentrations of PASHs. Four groups of PASHs collectively account for only 4.6% of eight PAC families in the Bakken crude oil, compared to 57.1% for the Alberta oil sand bitumen. Considering that PASHs have similar toxicities with their PAH analogues, the impact of oil contamination will be significantly underestimated without the determination of these sulfur-containing compounds.

PASHs in petroleum products: Sulfur oxide emissions from the combustion of fuels containing sulfur compounds pose an environmental threat. Stringent limits on sulfur levels in gasoline and vehicular diesel fuel were created to allay increasing concern on the environmental impacts. In the last few decades, sulfur levels in vehicular and marine diesel fuels dropped significantly. Marine fuel oil has been condemned for its abundance of sulfur. The International Maritime Organization has required that from January 1, 2015, fuel with less than 0.1% sulfur content is used for vessels operating in the sulfur emission control areas or the emission control areas (ECAs), unless the vessel is fitted with equipment such as scrubbers to reduce the sulfur in exhaust fumes, or is operating on alternative fuel such as liquefied natural gas, or has a dispensation conferred. From January 1, 2020 onward, the limit for sulfur in fuel oil used on ships operating outside designated ECAs will be reduced to 0.50% by weight. Low sulfur (LSFO, sulfur content ≤1%) and ultra-low sulfur fuel oils (ULSFO, sulfur content ≤ 0.1%) have become popular nowadays [97].

The abundance and distribution profile of components in oils are often altered by the distillation and refining process. The high-sulfur diesel fuel contained a larger proportion of PASHs with one or two rings [93]. PASH concentrations in selected refined petroleum products vary significantly from type to type. The higher boiling fractions contain a relatively high content of sulfur species, explaining why HFOs are usually rich in sulfur-containing compounds. Because PASHs are deliberately removed by refining processes, their profiles in refined products could be different from those of their PAH analogues, where all bi- to penta-cyclic PASHs could be very low or even undetectable in certain light petroleum products. Accurate analyses of PASHs in these fuels become very difficult, making GC-HRAM-MS more and more necessary to undertake these tasks [29]. PASHs in diesel produced from different generations probably change significantly. As given in Table 2.9, the no. 2 diesel (Ottawa, 2002) contains 282 μg/mL of benzothiophenes and 321 μg/mL of dibenzothiophenes, while PASHs are barely detectable in automobile diesel obtained in 2021 (Ottawa, ON). With implementing strict environmental regulations, it is expected that PASHs are detected at much lower concentrations or even undetectable in future marine fuel oils.

2.6.5 Diagnostic criteria of aromatic compounds

PAHs in oils have been thoroughly investigated and are widely used for forensic oil analysis. Certain PAH diagnostic ratios have been widely used in oil differentiation or contamination source identification. To reduce the influence of weathering processes, diagnostic ratios are traditionally restricted to parent PAHs with the same molecular weight and similar properties or to ratios of alkylated versus parent PAHs. Various PAH ratios between individual compounds or groups of compounds have been described extensively and used to compare oil samples [15, 20]. Some PAH ratios can often be diagnostic in crude oils, but can or may not have a similar diagnostic significance in refined products in which their distributions can be affected by refinery processes (e.g., cracking, reforming, and hydrotreatment) [20].

Excluding perylene and dibenz(*a*,*h*)anthracene, nine four- to six-ring higher molecular PAHs (refer to Table 2.6) were classified as combustion PAHs. The ratios derived from less stable versus thermodynamically stable PAH isomers, such as fluoranthene to pyrene (Fl/Py), phenanthrene to anthracene (Ph/An), and methylphenanthrenes to phenanthrene (C_1P/C_0P), are often used to investigate petrogenic contamination against pyrogenic input in environmental samples [98–103]. In contrast to pyrogenic sources, petrogenic sources are characterized by high ratios of Ph/An > 15 and $C_1P/C_0P > 2$ in association with lower ratios of fluoranthene/pyrene (Fl/Py < 1) and benzo(a)anthracene/chrysene (BaA/CHR < 0.4) [102]. Yunker et al. reported that the ratio of IP/(IP + BgP) < 0.20 likely implies petroleum; between 0.20 and 0.50 liquid fossil fuel (vehicle and crude oil) combustion; and over 0.50 imply grass, wood, and coal combustion [101, 102]. Refining processes often altered the profile of aromatic compounds in the stock crudes, particularly resulting in less standardized patterns of C_1-phenanthrenes and C_1-pyrene in heavy fuels [20].

Wang et al. proposed the "Pyrogenic Index," which is defined as the sum of three- to six-ring unsubstituted PAHs (see Table 2.8) over the sum of the five APAH homologues (Σ3– 6-ring EPA priority PAHs/Σ5 series APAHs) [99]. The unsubstituted PAHs used PI measurement, including three-ring (acenaphthylene, acenaphthene, anthracene), four-ring (fluoranthene, benz(a)anthracene, pyrene), five-ring (benzo(*b*)fluoranthene, benzo(*k*)fluoranthene, benzo(*e*)pyrene, benzo(*a*)pyrene, perylene, dibenz(*ah*)anthracene), and six-ring (indeno(1,2,3-cd)pyrene, benzo(ghi)perylene). The APAH series include C_0–C_4 naphthalenes, C_0–C_4 phenanthrenes, C_0–C_3 fluorenes, C_0–C_3 dibenzothiophenes, and C_0–C_3 chrysenes. This ratio is a robust quantitative indicator for the identification of pyrogenic PAHs and for differentiating pyrogenic and petrogenic PAHs. Lighter petroleum products and most crude oils show ratios smaller than 0.01, while heavy oils and heavy fuels show significantly higher ratios in the range of 0.01–0.05. The ratios for the oil-burn soot can be as high as 2.0 [99].

Perylene comes primarily from diagenesis of biogenic precursors and partially from petroleum or pyrolytic processes [84, 99]. Perylene index, defined as the

concentration of perylene divided by the total of five-ring PAHs, is a very useful tool to distinguish biogenic from pyrogenic hydrocarbons. This ratio is effective in differentiating and characterizing biogenic sources from others in environmental samples. Perylene indices greater than 10% often indicate diagenetic (biogenic) inputs, whereas those <10% indicate a pyrogenic or petrogenic origin.

Ratios derived from APAHs are of special use for forensic oil identification. Methylated PAHs are present in crude oils and refined products in high concentrations. These C_1-PAHs are well separated in the chromatographic analysis due to their small number of isomers. The ratios among their isomers are often employed for oil analysis, including 2-naphthalene and 1-naphthalene at *m*/*z* 142, 4-, 2-/3-, and 1-methyl dibenzothiophene, and (3- + 2-methyl-phenanthrene) to (4-/9- + 1-methyl-phenanthrene). Relative abundance of five APAHs, ΣN:ΣP:ΣD:ΣF:ΣC, is an important ratio to distinguish oil from oil and type from type. The relative distribution profile C_0-:C_1-:C_2-:C_3-:C_4- of each APAH family is often used to differentiate petrogenic source from other sources, and to investigate the weathering effect.

Among the five APAH series, tricyclic phenanthrenes are frequently applied for forensic oil analysis. These compounds are detected in considerable abundance in crude oils; in addition, they remain relatively stable under weathering and therefore are widely applied to distinguish oils and investigate weathering. As an isomer of phenanthrene, anthracene has three fused benzene rings in a straight linear arrangement. Methylanthracenes are generally absent in most conventional crude oils, with some present in low concentrations relative to methylphenanthrenes. 2-Methylanthracene (2-MAn) is eluted between two pairs of methylphenthrarene isomers (2- and 1-, 4-/9- and 3-, *m*/*z* 192) in variable concentration in different types of oils. A relatively high presence of 2-MAn in the oil sample generally indicates cracking. Based on our experience in analyzing a large number of crude oils and petroleum products, the ratio of 2-MAn relative to the total of methyl-phenanthrenes ranges from 0 to 0.03 for most crude oils, diesels, and lube oils studied, while this ratio is generally greater than 0.03 for heavier refined petroleum products such as Bunker C. In addition, another aromatic cluster at *m*/*z* 216 (methyl-fluoranthenes and methyl-pyrenes) has proven to be relatively stable and especially suitable for comparing light fuel oil samples.

Although aromatic steranes are in relatively low concentrations in oils, their specific fingerprints and high weathering resistance make them desirable biomarkers for forensic investigation [20, 37, 59, 88]. Most parent PAHs and APAHs are susceptible to microbial degradation; however, aromatic steranes are highly resistant to physical weathering and biodegradation, other than the usual biomarker terpanes and steranes. These features make them suitable candidates for forensic oil analysis, particularly when the oils involved are heavily weathered. The relevant diagnostic ratios associated with aromatic steranes are robust for oil-to-oil correlation and oil source tracking.

PASHs have been extensively used as critical criteria for forensic oil analysis, particularly for oil-type recognition. These compounds are particularly useful in oil

spill source identification in a wide variety of weathering conditions such as evaporation, photo-oxidation, and biodegradation [9, 94, 96, 104, 105]. It has been established that, among the PASH markers, the ratios of methylated dibenzothiophenes (C_1-DBTs) vary widely with the source of petroleum. C_1-DBT isomers are present in crude oils at relatively high concentrations, and their distribution profiles vary significantly. Their relative distributions are subject to little interference from evaporative weathering in a short term but are altered by biodegradation. Thereby, the chemical profile of PASHs can be distinctively used as an indication of microbial degradation of oils. For instance, bunker fuels have a 2-/3- to 4-methyldibenzothiophene (MDBT) ratio around 1.0, which is unusually high compared to most crude oils [104]. The presence of a clear V-pattern (4-methyl > 2- + 3-methyl < 1-methyl) for the MDBTs is generally associated with oils from predominantly carbonate source rocks, while a stair-step pattern (4-methyl > 2 + 3-methyl > 1-methyl) is associated with predominantly siliciclastic source rocks or advanced maturity (late- to post-oil window) oils from carbonate sources. The MDBTs are also used as biodegradation indicators. 2- and 3-MDBT are biodegraded at a higher rate, as shown by the strong decrease of their ratio to 4-MDBT, while 1-MDBT is slightly more resistant to biodegradation than 4-MDBT, indicated by an increase of the ratio 1-MDBT/4-MDBT [106].

2.7 Weathering effect on oil chemical composition

Once oil enters the environment, it is immediately subject to natural weathering. Weathering is termed as the combination of a series of physical, chemical, or biological processes that affect the composition and change the physicochemical properties of spilled oil in the environment. Oil weathering processes have an extensive influence on the behavior, effects, and ultimate fate of an oil spill and have therefore been the topic of much research to inform spill-response activities. These processes highly depend on the nature of the oil spilled and the weather conditions during and after the spill (e.g., temperature, wave movement, wind speed, and sun incidence).

Numerous studies have been conducted to study the effects of weathering on oil components [8, 20, 30, 35–37, 107–110]. These weathering processes to spilled oil include spreading, evaporation, dispersion, dissolution, and emulsification in the early stage, following the longer processes of sedimentation, oxidation, and biodegradation. Multiple weathering processes can occur simultaneously and influence each other. Herein we only selectively stress three weathering processes of evaporation, photodegradation, and biodegradation. These processes often significantly alter the physical and chemical properties of spilled oil, which bring challenges to oil identification. However, weathered oil could retain the unique characteristics of some weathering-resistant components, which enables the potential to identify the source oil. Variations of certain analytes that are susceptible to specific weathering processes

could be used as particular indicators of these weatherings, for instance, depletion of *n*-alkanes suggesting oil biodegradation.

2.7.1 Evaporation

In the short term after an oil spill, among the potential physical weathering processes, evaporation is usually one of the dominant weathering processes [8]. The evaporation effect is particularly significant on the oil remaining on land or water surface after a spill. Evaporation simply transports part or all oil mass from its bulk to the surrounding air. The evaporation speed of a specific oil mainly depends on its composition and weathering conditions such as the ambient temperature.

Evaporation in sequence removes components from an oil according to their boiling points, but in fact, the molecular interaction of the complex hydrocarbon mixtures could affect their evaporation. In theory, the oil loses lighter compounds with low boiling points first. As GC separation is based mainly on boiling points of the components, a plot of relative abundance of target compounds in evaporated oil and source oil against the retention time on the *x*-axis shows a sine-curve shape [20]. For lightly evaporated petroleum, most mass loss is attributable to low-boiling point compounds such as BTEX, alkylated benzenes, and alkanes. By this means, evaporation reduces the acute toxicity of the remained oil. An oil with a high amount of light compounds evaporates faster than one with a large proportion of heavier components. Gasoline evaporates completely in a few hours, while diesel range oil evaporates more gradually. Since heavy oils have generally been severely weathered in their formation, evaporation has little effect on their chemical composition. Fingas indicated that, on the land, ongoing oil evaporation could be considerably slowed down due to the "crust" on the oil surface formed by resin and waxes [8]. Evaporation of crude oil leaves heavier and viscous components, resulting in the formation of floating patches of oil and tarballs (or tarmats) or sinking in freshwater [8, 20, 111]. Tarballs could be eventually found on shorelines hundreds of miles away. Stranded tarballs are very persistent in the marine environment and could preserve essential information to determine the extent of oil spillages and to trace the source of an oil spill [112–114].

Slight to medium evaporative weathering has little effect on distribution patterns of most target petroleum hydrocarbons. Most target hydrocarbons were concentrated in proportion with the increase of the weathered percentages [15]. Heavier weathering could lead to a significant reduction in abundances of light *n*-alkanes, all adamantanes, and light sesquiterpanes in some oils [35, 36]. If evaporation continues and has affected the *n*-alkanes beyond *n*-C_{13}, then a relative depletion of the lower boiling $C_{14}H_{26}$ sesquiterpanes would be expected [42]. In a forensic investigation, the concentration reduction of the low boiling components and the buildup of the high boiling components relative to the smaller *n*-alkanes could indicate that the oil has been significantly weathered, even though its *n*-alkanes are not completely

lost [78]. The distributions of target hydrocarbons, particularly biomarker terpanes and steranes, high PAH compounds, and TASs, remain consistent through the evaporation process. In addition, evaporation does not remove significant UCM content, resulting in an increased UCM proportion for evaporated oils.

In summary, the main chemical composition changes caused by evaporative weathering include [8, 13, 20, 104]:

- Evaporation is a physical weathering process. It does not cause preferential loss of one isomer over another.
- Evaporation progressively reduces the abundances of the lower boiling compounds then to heavier components.
- The concentrations of HMW components relatively increase due to the loss of LMW components.
- Evaporation results in an increased UCM proportion in weathered oils
- The CPI values remain virtually unchanged through the entire evaporation process.
- The distribution profiles of HMW terpanes, steranes, and aromatic steranes are unaffected while they are concentrated during evaporative weathering. Relative ratios of these compounds demonstrate great consistency.

2.7.2 Photodegradation

Besides physical weathering processes, oil spilled is also subjected to other destructive chemical weatherings such as oxidative photodegradation or photooxidation. It is established that solar irradiation is an important effect for the alteration or removal of petroleum from water surface and on the land, especially in tropical and subtropical latitudes under conditions of intensive solar radiation and in oligotrophic waters when nutrients needed for biodegradation may be limited [115–122]. Photodegradation is generally not considered as an important process for the degradation of oils in soils or deep-water sediments.

Photooxidation is a slow chemical process and only gradually breaks down spilled oil. The speed and extent of photooxidation are dependent on the thickness of the oil slick as well as sun exposure. Sunlight (particularly short wavelength light <300 nm) directly or indirectly oxidizes petroleum compounds into more polar ketones, aldehydes, carboxylic acids, esters, and so on. Because these products are more soluble in water, photooxidation enhances the overall solubilization of intact petroleum. In contrast, photooxidation may also result in HMW products through the condensation of peroxide intermediates, ultimately leading to tar and gum-like residues [111, 115]. Moreover, photochemical processes are probably also important to oil dissolution and the subsequent biological consumption of oil [117].

Oil photodegradation was not thoroughly studied and less understood by environmental scientists in comparison with evaporation and biodegradation. The studies

on photodegradation of petroleum mainly focused on polycyclic compounds in petroleum due to their high concentrations and potential high environmental impact. Nicodem et al. reported the photochemical weathering of crude oil as a film over seawater by sunlight [118]. The fluorescence emission intensity of the crude decreases rapidly and is only two-fifths of its initial intensity after 100 h of irradiation. It is believed that the reduction of fluorescence intensity is due to the formation of oxygenated derivatives, which are less fluorescent. Ali et al. used a laboratory photodegradation apparatus, incorporating a calibrated xenon lamp, controlled temperature unit, and quartz reaction cells to simulate natural irradiation by sunlight [120]. They reported a pseudo-first-order photodegradation constant (k) of phenanthrene in seawater at 25 °C.

Photooxidation affects different groups of petroleum composition in different degrees. Andersson reported lower losses of sulfur heterocycles than phenanthrene series when oil was exposed to sunlight irradiation [119]. Their photodegradation follows a declining order: phenanthrene > 1-methylphenanthrene = DBT > 2-methylphenanthrene > 4-methyl-DBT > l-methyl-DBT > 2- + 3-methyl-DBT > 3,4-dimethyl-DBT > 1, 7-dimethyl-DBT > 3,7-dimethyl-DBT. Jacquot et al. [115] found that naphthalene and its alkylated homologues in petroleum spilled in the marine environment were severely altered by photooxidation whereas, phenanthrenes, dibenzothiophenes, and their alkylated homologues were rather recalcitrant. Furthermore, methyl derivatives were more degraded than their parent molecules. The degradation of methylated phenanthrenes (MP) follows a decreasing order of 2-MP < 1-MP < 3-MP < 9-MP. It was reported that the photosensitivity of petroleum hydrocarbons increased with increasing aromaticity and alkylation [122]. Photooxidation significantly affects a series of PAHs, that is, methyl anthracene, methyl pyrenes, C_4-phenanthrenes, and methyl chrysenes. Pronounced photodegradation of TASs was also observed although these compounds are traditionally considered robust at medium- to long-term environmental exposure. In particular, the chromatographic patterns of C_1-pyrenes and C_2-pyrenes are easily affected by sunlight, which can serve as markers to disclose photooxidation. Observed from many real oil spills, the reduction of methyl-pyrenes by photodegradation follows an order of 1-MPy > 4-MPy > 2-MPy [20, 123].

It was also reported a preferential alteration of branched alkanes rather than straight alkanes [115]. The distribution of biomarkers such as drimanes, hopanes, and steranes remain stable in photodegradation. Therefore, the diagnostic ratios of these biomarker compounds are still applied to oil identification when oil is exposed to photodegradation.

In summary, the main effect of photodegradation on spilled oil [13, 115, 116]:

- Photochemical degradation yields a variety of oxidized compounds that are more soluble in water than the starting compounds, enhancing the overall solubilization of intact petroleum.
- Generation of the persistent residue by photooxidation may also result in the formation of tarballs.

- Photooxidation affects different groups of petroleum composition in different degrees.
- APAHs are oxidized faster than their parent molecules.

2.7.3 Biodegradation

Oil biodegradation occurs during the formation of crude oils under geological conditions. Natural biodegradation plays an important role in the cleanup of oil spilled into the environment and recovery of the impacted ecosystem. Biodegradation is a long-term oil weathering process, while its effect is not significant in the immediate aftermath of a spill. Besides the physical and chemical properties of the oils, many other environmental factors including the nature of the environmental media (e.g., oxygen concentrations, temperature, salinity, and pressure), the content of nutrient and hazardous contaminant, the characteristics of the microbial population, and so on could greatly affect the rate and extent of oil biodegradation [111]. The biodegradation of petroleum can also be simulated in the laboratory under controllable conditions; however, the process in a laboratory environment could be significantly different from a spill site. Many oil spill incidents around the world have offered scientists great opportunities to study oil biodegradation.

Biodegradation can considerably affect the composition of oil released into the environment. One of the significant differences between biodegradation and physical weathering processes is that the former selectively reduces an individual compound or a group of petroleum compounds. Initial or mild biodegradation readily removes LMW *n*-alkanes, which can be easily observed on whole-oil gas chromatograms. Moderate biodegradation is marked by a nearly total loss of *n*-alkanes and the reduction of alkylcyclohexanes, alkylbenzenes, and acyclic isoprenoid alkanes.

Different classes of petroleum hydrocarbons have different susceptibilities to biodegradation. There are many discussions in the literature about the biodegradation order of petroleum hydrocarbons [15, 30, 59, 124, 125]. Some researchers tried to rank oil biodegradation based on the depletion of petroleum hydrocarbon classes [59, 124, 125]. In general, the biodegradation effects on the oil composition can be summarized in the following patterns [126, 127]: 1) smaller hydrocarbons are degraded faster than larger hydrocarbons; 2) straight-chain *n*-alkanes are degraded faster than branched alkanes; 3) GC-resolved compounds are degraded more than GC-unresolved complex hydrocarbons; 4) small aromatics are degraded faster than HMW aromatics; 5) increase in alkylation level within their alkylated homologous families significantly decreases susceptibility to microbial attack; 6) microbial degradation is often isomer specific. Biodegradation of specific petroleum hydrocarbons generally follows an overall declining order of *n*-alkanes > benzene > toluene > isoalkanes and anteisoalkanes > cyclohexylalkanes and/or methylcyclopentylalkanes > acyclic isoprenoids ≫ naphthalene > phenanthrene ≫ PAHs > C_{27-29} steranes > C_{30-35} hopanes > diasteranes

> C_{27-29} hopanes > C_{21-22} steranes > tricyclic terpanes [30, 59, 124, 128]. However, this sequence does not imply complete removal of one class before another is degraded and does not necessarily always apply to all oil biodegradation.

Biodegradation of biomarkers: Small biomarker compounds such as diamondoids and bicyclic sesquiterpanes are resistant to slight to medium weathering, particularly from biodegradation [33, 35, 59]. These compounds are determined in significant abundance in extra-heavy oil sand bitumen despite the depletion of *n*-alkanes by biodegradation [58, 61, 129]. It was reported that adamantanes are more susceptible to biodegradation than diamantane analogues [36]. Williams et al. found that a series of diamondoid compounds demonstrated resistance to biodegradation in a severely degraded crude oil, in which pentacyclic triterpanes were almost completely demethylated [47]. The degradation resistance of adamantanes is at least as strong as that of tricyclic terpanes and that the adamantine series should therefore be useful for correlating severely biodegraded oils. Grice et al. investigated the effect of biodegradation on diamondoid distribution in a series of crude oil reservoirs in two Australian sedimentary basins [54]. They reported variable susceptibility to microbial degradation for different diamondoids. Wei et al. reported that the concentration of total diamondoids tends to decrease as the biodegradation rank of oil deposits increases [130].

High boiling point biomarkers of steranes and triterpanes, which are relatively resistant to biodegradation, have been used extensively for the correlation of biodegraded crudes [128]. Although terpanes and steranes are highly resistant to biodegradation, several studies have shown that they can be degraded to a certain degree under severe weathering conditions (i.e., extensive microbial degradation) [124, 131]. Studies on oil spills have demonstrated the degradation of C_{23} and C_{24} tricyclic terpanes in intensive weathering [78, 104]. Microbial alteration and removal of the regular steranes and 4α-methylsteranes from petroleum occur after the complete removal of C_{15}–C_{20} isoprenoids, and before or after the hopanes depending on the circumstance.

As mentioned above, terpanes and steranes have many constitutional isomers and stereoisomers. Certain molecular configurations could obstruct microbial degradation. Wang et al. found that 17α(H),21β(H)-22,29,30-trisnorhopane (Tm) is degraded faster relative to 18α(H),21β(H)-22,29,30-trisnorhopane (Ts), resulting in an increase of the Ts/Tm ratio for heavily degraded oil samples [78]. In general, sterane susceptibility to microbial degradation is as follows: ααα 20R > αββ 20R > ααα 20S > αββ 20S > diasteranes. The susceptibility of steranes to biodegradation typically decreases with increasing carbon number for each isomeric configuration $C_{27} > C_{28} > C_{29} > C_{30}$. Diasteranes are particularly resistant to biodegradation. Evidence suggests that the C_{27}–C_{29} steranes are depleted before diasterane alteration. Pregnane and homopregnane have high resistance to biodegradation, comparable to diasteranes [59].

Biodegradation of aromatics: aromatic hydrocarbons comprise a large percentage of crude oil and refined oil products. Many studies have been conducted to investigate their biodegradation. George et al. studied the biodegradation of a suite of oils. The breakdown of aromatic compounds by ring cleavage is an essential biochemical step in the natural carbon cycle and is performed by several kinds of microorganisms [132]. There are three main controls on the susceptibility to biodegradation of cyclic, branched, and aromatic LMW hydrocarbons: carbon skeleton, degree of alkylation, and position of alkylation. The rate of degradation of PAHs decreases with the increase of the number of rings in the PAH molecules. Among APAH homologues, two-ring naphthalene homologues were the most susceptible to biodegradation, while the alkyl homologues of four-ring chrysene were the most resistant to biodegradation. In addition, within each APAH class, the degradation rate tends to decrease with the increase of alkylation level, resulting in a trend of $C_1 \sim > C_2 > C_3 > C_n$ [78, 126].

The positions of alkyl substituents also strongly affect the rate of biodegradation. The biodegradation of methylphenanthrenes is in a decreasing order of 3-MP or 2-MP > 1-MP ≫ 9-/4-MP [61, 126]. 2-/3-Methyl dibenzothiophene biodegrades at the fastest rate within all four isomeric series. In heavy oil sand bitumen, the most refractory isomers of the *m*/*z* 216 cluster appear to be 4-methyl-pyrene (4-MPy) and 1-methyl-pyrene (1-MPy), while other isomers were degraded in different degrees. The C_{26-28} isomers of TASs are very resistant to biodegradation and only degraded under extreme conditions [124]. Preferential depletion of C_{20}–C_{22} TAS isomers is found for the severely biodegraded oils. Aromatic steranes changed slightly in their abundance and distribution pattern in the *m*/*z* 231 fragmentograms, even though most aromatics including methylphenanthrenes and methyldibenzothiophenes were nearly depleted.

In summary, biodegradation affects the oil composition in the following patterns [13, 59, 126, 127, 131]:

- small hydrocarbons degrade faster than large hydrocarbons;
- straight-chain *n*-alkanes degrade faster than branched alkanes;
- GC-UCM in petroleum oil is more resistant to biodegradation than the GC-resolved compounds;
- small aromatics are more susceptible to biodegradation than HMW aromatics;
- increased alkylation level of PAHs significantly decreases susceptibility to microbial degradation;
- microbial degradation is often isomer-specific, and the positions of the alkyl substituents also strongly affect the rate of biodegradation;
- biomarker compounds such as diamondoids, bicyclic sesquiterpanes, triterpanes, steranes, and aromatic steranes are resistant to biodegradation.

References

[1] DPRA. Formation of crude oil and natural gas. In: The Origin and Chemistry of Petroleum, http://www.dpra.com/index.cfm/m/158, accessed on May 16, 2011.

[2] Irwin RJ, van Mouwerik M, Stevens L, Seese MD, Basham W. Environmental contaminants encyclopedia: Fuel oil number 4 entry, National Park Service, Water Resources Division. Fort Collins, CO, 1997.

[3] Speight JG. The chemistry and technology of petroleum (4th ed.). CRC Press, Boca Raton, FL, 2007.

[4] Ancheyta J, Speight JG. Hydroprocessing of heavy oils and residua. CRC Press, Boca Reton, FL, 2007.

[5] Curiale JA, Frolov EB. Occurrence and origin of olefins in crude oils. A critical review. Org Geochem, 1998, 29, 397–408.

[6] Schmidt PF. Fuel oil manual (4th ed.). Industrial Press Inc., New York, NY, 1986.

[7] Speight JG. Petroleum asphaltenes. Part I: Asphaltenes, resins and the structure of petroleum. Oil Gas Sci Technol Rev IFP, 2004, 59, 467–477.

[8] Fingas M. The basics of oil spill cleanup (3rd ed.). CRC Press, Taylor Francis Publishers, Boca Rayon, FL, 2012.

[9] Hegazi AH, Andersson T. Limitations to GC-MS determination of sulfur-containing polycyclic aromatic compounds in geochemical, petroleum, and environmental investigations. Energ Fuel, 2007, 21, 3375–3384.

[10] Wang ZD, Fingas M, Page DS. Oil spill identification. J Chromatogr A, 1999, 843, 369–411.

[11] Wang ZD, Fingas M. Development of oil hydrocarbon fingerprinting and identification techniques. Mar Pollut Bull, 2003, 47, 423–452.

[12] Wang ZD, Fingas M, Yang C, Christensen HJ. Crude oils and refined products fingerprinting: Principles. In: Morrison RD, Murphy BL, eds. Environmental forensics: Contaminant specific guide. Elsevier, New York, NY, 2006, 339–407.

[13] Wang ZD, Yang C, Yang ZY, Brown CE, Hollebone BP, Stout SA. Petroleum biomarker fingerprinting for oil spill characterization and source identification. In: Stout SA, Wang ZD, eds. Standard handbook of oil spill environmental forensics. Elsevier, London, UK, 2016, 131–254.

[14] ESTS. Determination of total petroleum hydrocarbons, n-alkanes, polycyclic aromatic hydrocarbons, and selected biomarkers in oil and petroleum products, ESTS Method No. ESTD-OR-20, Ottawa, ON, 2006.

[15] Yang C, Wang ZD, Hollebone B, Brown CE, Yang ZY, Landriault M. Chromatographic fingerprinting analysis of crude oil and petroleum products. In: Fingas M, ed. Handbook of oil spill science and technology. Jon Wiley & Sons, Inc., Hoboken, NJ, 2015, 95–163.

[16] Daling PS, Faksness LG, Hansen AB, Stout SA. Improved and standardized methodology for oil spill fingerprinting. Environ Forensics, 2002, 3, 263–278.

[17] Hansen AB, Daling PS, Faksness LG, Sorheim KR, Kienhuis P, Duus R. Emerging CEN methodology for oil spill identification. In: Wang ZD, Stout SA, eds. Oil spill environmental forensics: Fingerprinting and source identification. Academic Press, Burlington, MA, 2007, 229–256.

[18] Kienhuis P, Hansen AB, Faksness L, Stout SA, Dahlmann G. CEN methodology for oil spill identification. In: Stout SA, Wang ZD, eds. Standard handbook of oil spill environmental forensics. Elsevier, London, UK, 2016, 685–728.

[19] Malmborg J, Kooistra K, Kraus UR, Kienhuis P. Evaluation of light petroleum biomarkers for the 3rd edition of the European Committee for Standardization methodology for oil spill identification (EN15522-2). Environ Forensics, 2020, 22, 10.1080/15275922.2020.1850558.

[20] CEN (European Committee for Standardization). Oil spill identification – Petroleum and petroleum related products – Part 2: Analytical method and interpretation of results based on GC-FID and GC-low resolution-MS analyses. EN 15522-2_2020 v9, 2020.
[21] MassDEP (the Massachusetts Department of Environmental Protection). Division of Environmental Analysis, Office of Research and Standards, Bureau of Waste Site Cleanup, Method for the Determination of Extractable Petroleum Hydrocarbons (EPH) Revision 1.1, May 2004.
[22] Alzaga R, Montuori P, Ortiz L, Bayona JM, Albaigés J. Fast solid-phase extraction-gas chromatography-mass spectrometry procedure for oil fingerprinting application to the Prestige oil spill. J Chromatogr A, 2004, 1025, 133–138.
[23] Yang ZY, Yang C, Wang ZD, Hollebone B, Landriault M, Brown CE. Oil fingerprinting analysis using commercial solid phase extraction (SPE) cartridge and gas chromatography-mass spectrometry (GC-MS). Anal Methods, 2011, 3, 628–635.
[24] Yang C, Yang ZY, Zhang G, Hollebone B, Landriault M, Wang ZD. Lambert P and Brown C. Characterization and differentiation of chemical fingerprints of virgin and used lubricating oils for identification of contamination or adulteration sources. Fuel, 2016, 163, 271–281.
[25] Yang C, Zhang G, Serhan M, Koivu G, Yang Z, Hollebone B, Lambert P, Brown CE. Characterization of naphthenic acids in crude oils and refined petroleum products. Fuel, 2019, 255, 115846.
[26] Zhang G, Yang C, Serhan M, Koivu G, Yang Z, Hollebone BP, Lambert PG, Brown CE. Characterization of nitrogen-containing polycyclic aromatic heterocycles (PANHs) in crude oils and refined petroleum products. Adv Mar Biol, 2018, 81, 59–96.
[27] Wang ZD, Fingas M, Li K. Fractionation of ASMB oil, identification and quantitation of aliphatic, aromatic and biomarker compounds by GC/FID and GC/MSD. J Chromatogr Sci, 1994, 32, 361–366, (Part I) and 367–82 (Part II).
[28] ASTM. Standard test methods for comparison of waterborne petroleum oils by gas chromatography, ASTM Method D3328-06, ASTM International, West Conshohocken, PA, 2020.
[29] Yang C, Lambert P, Nguyen M, Yang Z, Hollebone BP, Fieldhouse B, Brown CE. Application of gas chromatography-high resolution quadrupole time-of-flight mass spectrometry in fingerprinting analysis of polycyclic aromatic sulfur heterocycles. J Chromatogr A, 2020, 1630, 461577.
[30] Wang ZD, Fingas M, Owen EH, Sigouin L, Brown C. Long-term fate and persistence of the spilled Metula oil in a marine salt marsh environment degradation of petroleum biomarkers. J Chromatogr A, 2001, 926, 275–290.
[31] Peterson AC, Hauschild JP Jr, Quarmby ST, Krumwiede D, Lange O, Lemke R, Grosse-Coosmann F, Horning S, Donohue TJ, Westphall MS, Coon JJ, Griep-Raming J. Development of a GC/Quadrupole-Orbitrap mass spectrometer, Part I: Design and characterization. Anal Chem, 2014, 86, 10036–10043.
[32] Yang C, Kim M, Brown CE, Wang ZD, Yang ZY, Hollebone BP, Lambert P. Oil fingerprinting analysis using gas chromatography-quadrupole time-of-flight (GC-QTOF). In: Stout SA, Wang ZD, eds. Standard handbook of oil spill environmental forensics. Elsevier, London, UK, 2016, 450–480.
[33] Wang ZD, Yang C, Fingas M, Hollebone BP, Landriault M, et al.. Characterization, weathering, and application of sesquiterpanes to source identification of spilled petroleum products. Environ Sci Technol, 2005, 39, 8700–8707.
[34] Wang ZD, Yang C, Hollebone B, Fingas M. Forensic fingerprinting of diamondoids for correlation and differentiation of spilled oil and petroleum products. Environ Sci Technol, 2006, 40, 5636–5646.

[35] Yang C, Wang ZD, Hollebone BP, Brown CE, Landriault M. Characteristics of bicyclic sesquiterpanes in crude oils and petroleum products. J Chromatogr A, 2009, 1216, 4475–4484.
[36] Yang C, Wang ZD, Hollebone B, Peng X, Fingas M, et al.. GC/MS quantitation analysis of diamondoid compounds in crude oils and petroleum products. Environ Forensics, 2006, 7, 377–390.
[37] Yang C, Wang ZD, Li Y, Liu YR, Shah K, et al.. Aromatic steroids in crude and refined oils and their application in forensic oil spill identification. Environ Forensics, 2005, 14, 278–293.
[38] Yang C, Zhang G, Wang ZD, Yang ZY, Hollebone B, Landriault M, Shah K, Brown CE. Development of methodology for accurate quantitation of alkylated polycyclic aromatic hydrocarbons in petroleum and oil contaminated environmental samples. Anal Methods, 2014, 6, 7760–7771.
[39] CCME (Canadian Council of Ministers of the Environment). Reference method for the Canada-wide standard for petroleum hydrocarbons in soil – Tier 1 Method, ISBN 1896997-01-5, Publication No. 1310, 2008.
[40] Wang ZD, Yang C, Kelly-Hooper F, Hollebone B, Peng X, *et al*.. Forensic differentiation of biogenic organic compounds from petroleum hydrocarbons in biogenic and petrogenic compounds cross-contaminated soils and sediments. J Chromatogr A, 2009, 1216, 1174–1191.
[41] Stout SA, Douglas GS. Diamondoid hydrocarbons application in the chemical fingerprinting of natural gas condensate and gasoline. Environ Forensics, 2004, 5, 225–235.
[42] Stout SA, Uhler AD, McCarthy KJ. Middle distillate fuel fingerprinting using drimane-based bicyclic sesquiterpanes. Environ Forensics, 2005, 6, 241–251.
[43] Yang C, Wang ZD, Hollebone BP, Brown CE, Landriault M, Fieldhouse B, Yang ZY. Application of light petroleum biomarkers for forensic characterization and source identification of spilled light refined oils. Environ Forensics, 2012, 13, 298–311.
[44] Malmborg J, Nordgaard A. Forensic characterization of mid-range petroleum distillates using light biomarkers. Environ Forensics, 2016, 17, 244–252.
[45] Barakat AO, Mostafa AR, EL-Gayar MS, Omar MF. Organic geochemical characterization of crude oils based on alkanes and acyclic isoprenoids distribution. Petro Sci Technol, 2019, 37, 243–254.
[46] Bender AO, Said EZ, Abdulsada AK. Gas chromatographic identification of adamantanes in some Iraqi crude oils. Analyst, 1986, 111, 575–576.
[47] Williams JA, Bjoroy M, Dolcater DL, Winters JC. Biodegradation in South Texas Eocene oils-effects on aromatics and biomarkers. Org Geochem, 1986, 10, 451–461.
[48] Wingert WS. GC-MS analysis of diamondoid hydrocarbons in smackover petroleums. Fuel, 1992, 71, 37–43.
[49] Schulz LK, Wilhelms A, Rein E, Steen AS. Application of diamondoids to distinguish source rock facies. Org Geochem, 2001, 32, 365–375.
[50] Lin R, Wilk ZA. Natural occurrence of tetramantane ($C_{22}H_{28}$), pentamantane ($C_{26}H_{32}$) and hexamantane ($C_{30}H_{36}$) in a deep petroleum reservoir. Fuel, 1995, 74, 1512–1521.
[51] Dahl JE, Liu SG, Carlson RMK. Isolation and structure of higher diamondoids, nanometer-sized diamond molecules. Science, 2003, 299, 96–99.
[52] Chen J, Fu J, Sheng G, Liu D, Zhang J. Diamondoid hydrocarbon ratios: Novel maturity indices for highly mature crude oils. Org Geochem, 1996, 25, 179–190.
[53] Dahl JE, Moldowan JM, Peters KE, Claypool GE, Rooney MA, Michael GE, Mello MR, Kohnen ML. Diamondoid hydrocarbons as indicators of natural oil cracking. Nature, 1999, 399, 54–57.
[54] Grice KR, Alexander R, Kagi RI. Diamondoid hydrocarbons as indicators of biodegradation in Australian crude oils. Org Geochem, 2000, 31, 67–73.

[55] Wei ZB, Moldowan JM, Paytan A. Diamondoids and molecular biomarkers generated from modern sediments in the absence and presence of minerals during hydrous pyrolysis. Org Geochem, 2006, 37, 891–911.
[56] Alexander R, Kagi R, Noble RA. Identification of bicyclic sesquiterpanes drimane and eudesmane in petroleum. J Chem Soc Chem Commun, 1983, 5, 226–228.
[57] Alexander R, Kagi R, Noble RA, Volkman JK. Identification of some bicyclic alkanes in petroleum. Org Geochem, 1984, 6, 63–72.
[58] Dimmler A, Cyr TD, Strausz OP. Identification of bicyclic terpenoid hydrocarbons in the saturate fraction of Athabasca oil sand bitumen. Org Geochem, 1984, 7, 231–238.
[59] Peters KE, Walters CC, Moldowan JM. The biomarker guide (2nd ed.). Cambridge University Press, Cambridge, UK, 2005.
[60] Weston RJ, Phlip RP, Sherppard CM, Woolhouse AD. Sesquiterpanes, diterpanes and other higher terpanes in oils from the Taranaki basin of New Zealand. Org Geochem, 1989, 14, 405–421.
[61] Yang C, Wang ZD, Yang ZY, Hollebone B, Brown C, et al.. Chemical fingerprints of Alberta oil sands bitumen and related petroleum products. Environ Forensics, 2011, 12, 173–188.
[62] Petrov AA. Petroleum hydrocarbons. Springer-Verlag, Berlin, Germany, New York, 1987.
[63] Philp RP, Lewis CA. Organic geochemistry of biomarkers. Ann Rev Earth Planet Sci, 1987, 15, 363–395.
[64] Ourrison G, Rohmer M, Poralla K. Prokaryotic hopanoids and other polyterpenoid sterol surrogates. Ann Rev Microbiol, 1987, 41, 301–333.
[65] Requjo AG, Hieshima GB, Hsu CS, McDonald TJ, Sassen R. Short-chain (C_{21} and C_{22}) diasteranes in petroleum and source rocks as indicators of maturity and depositional environment. Geochim Cosmochim Acta, 1997, 61, 2653–2667.
[66] Prahl FG, Dymond J, Sparrow MA. Annual biomarker record for export production in the Central Arabian Sea. Deep-Sea Res II, 2000, 47, 1581–1602.
[67] Rullkötter J, Philip P. Extended hopanes up to C_{40} in Thornton bitumen. Nature, 1981, 292, 616–618.
[68] Wang P, Li M, Larter SR. Extended hopanes in crude oils and source rock extracts from the Liaohe Basin, N.E. China. Org Geochem, 1996, 24, 547–551.
[69] Nytoft HP, Bojesen-Koefoed JA. 17a(H),21a(H)-hopanes: Natural and synthetic. Org Geochem, 2001, 32, 841–856.
[70] Volkman JK. A review of sterol markers for marine and terrigenous organic matter. Org Geochem, 1986, 9, 83–89.
[71] Volkman JK, Barrett SM, Blackburn SI, Mansour MP, Silkes EL, Gelin F. Microalgal biomarkers: A review of recent research developments. Org Geochem, 1998, 29, 1163–1179.
[72] Zakaria MP, Horinouchi A, Tsutsumi S, Takada H, Tanabe S, Ismail A. Oil pollution in the Straits of Malacca, Malaysia: Application of molecular markers for source identification. Environ Sci Technol, 2000, 34, 1189–1196.
[73] Grantham PJ, Wakefield LL. Variations in the sterane carbon number distributions of marine source rock derived crude oils through geological time. Org Geochem, 1988, 12, 61–73.
[74] Yang C, Wang ZD, Hollebone BP, Brown CE, Landriault M Application of statistical analysis in the selection of diagnostic ratios for forensic identification of an oil spill source. Proceeding of the International Oil Spill Conference 2008, Savannah, GA, 2008. 297–310.
[75] Yue ZW, Fraser MP. Polar organic compounds measured in fine particulate matter during TexAQS 2000. Atmos Environ, 2004, 38, 3253–3261.
[76] Simoneit B. Organic matter of the troposphere-III. Characterization and sources of petroleum and pyrogenic residues in aerosols over the Western United States. Atmos Environ, 1984, 18, 51–67.

[77] Li JG, Philip P, Cui MZ. Methyl diamantane index (MDI) as a maturity parameter for kower palaeozoic carbonate rocks at high maturity and overmaturity. Org Geochem, 2000, 31, 267–272.
[78] Wang ZD, Fingas M, Sergy G. Study of 22-year-old Arrow oil samples using biomarker compounds by GC/MS. Environ Sci Technol, 1994, 28, 1733–1746.
[79] Wang ZD, Fingas M, Landriault M, Sigouin L, Xu N. Identification of alkylbenzenes and direct determination of BTEX and (BTEX + C_3-benzenes) in oils by GC/MS. Anal Chem, 1995, 67, 3491–3500.
[80] Albaigés J, Jimenez N, Arcos A, Domínguez C, Bayona JM. The use of long-chain alkylbenzenes and alkyltoluenes for fingerprinting marine oil wastes. Chemosphere, 2013, 91, 336–343.
[81] Stout SA, Uhler AD, McCarthy KJ. A strategy and methodology for defensibly correlating spilled oil to source candidates. Environ Forensics, 2001, 2, 87–98.
[82] Boehm PD, Burns WA, Page DS, Bence AE, Mankiewicz PJ, Brown JS, Douglas GS. Total organic carbon, an important tool in holistic approach to hydrocarbon source fingerprinting. Environ Forensics, 2002, 3, 243–250.
[83] Williams PT, Taylor DT. Aromatization of tire pyrolysis oil to yield polycyclic aromatic hydrocarbons. Fuel, 1993, 72, 1469–1474.
[84] Venkatesan MI. Occurrence and possible sources of perylene in marine sediments – A review. Mar Chem, 1988, 25, 1–27.
[85] Wakeham SG, Canuel EA. Biogenic polycyclic aromatic hydrocarbons in sediments of the San Joaquin River in California (USA), and current paradigms on their formation. Environ Sci Pollut Res, 2016, 23, 10426–10442.
[86] Wang ZD, Yang C, Parrott JL, Frank RA, Yang Z, Brown CE, et al.. Forensic source differentiation of petrogenic, pyrogenic, and biogenic hydrocarbons in Canadian oil sands environmental samples. J Hazard Mater, 2014, 271, 166–177.
[87] Seifert WK, Moldowan JM. Application of steranes terpanes and monoaromatics to maturation, migration and source of crude oils. Geochim Cosmochim Acta, 1978, 42, 77–95.
[88] Barakat AO, Qian Y, Kim M, Kennicutt MC. Compositional changes of aromatic steroid hydrocarbons in naturally weathered oil residues in Egyptian Western Desert. Environ Forensics, 2002, 3, 219–225.
[89] Galpern GD. Thiophenes occurring in petroleum, shale oil and coals. In: Gronowitz S, ed. Thiophene and its derivatives. John Wiley and Sons, Inc., New York, 1985, 325–352.
[90] Kropp KG, Fedorak PM. A review of the occurrence, toxicity, and biodegradation of condensed thiophenes found in petroleum. Can J Microbiol, 1998, 44, 605–622.
[91] Mössner SG, Wise SA. Determination of polycyclic aromatic sulfur heterocycles in fossil fuel-related samples. Anal Chem, 1999, 71, 58–69.
[92] Hua R, Wang J, Kong H, Liu J, Lu X, Xu G. Analysis of sulfur-containing compounds in crude oils by comprehensive two-dimensional gas chromatography with sulfur chemiluminescence detection. J Sep Sci, 2004, 27, 691–698.
[93] Liang F, Lu M, Birch ME, Keener TC, Liu Z. Determination of polycyclic aromatic sulfur heterocycles in diesel particulate matter and diesel fuel by gas chromatography with atomic emission detection. J Chromatogr A, 2006, 1114, 145–153.
[94] Andersson JT, Hegazi AH, Roberz B. Polycyclic aromatic sulfur heterocycles as information carriers in environmental studies. Anal Bioanal Chem, 2006, 386, 891–905.
[95] Eastmond DA, Booth GM, Lee ML. Toxicity, accumulation, and elimination of polycyclic aromatic sulfur heterocycles in Daphnia magna. Arch Environ Con Tox, 1984, 13, 105–111.
[96] Karcher W, Nelsen A, Depaus R, van Eijk J, Claude P, Jacob J. New results in the detection, identification and mutagenic testing of heterocyclic polycyclic aromatic hydrocarbons. In:

Cooke M, Dennis AJ, eds. Chemical analysis and biological fate: Polynuclear aromatic hydrocarbons. Batelle Press, Columbus, 1981, 317–327.
[97] Daling P, Sørheim KR Characterization of low sulfur fuel marine fuel oils (LSFO). SINTEF Report No. OC2020 A-106, Trondheim, Norway, 2020.
[98] Barrick RC, Prahl FG. Hydrocarbon geochemistry of the Puget Sound Region-III. Polycyclic aromatic hydrocarbons in sediments. Estuar Coast Shelf Sci, 1987, 25, 175–191.
[99] Wang ZD, Fingas M, Shu YY, Sigouin L, Landriault M, Lambert P. Quantitative characterization of PAHs in burn residue and soot samples and differentiation of pyrogenic PAHs from petrogenic PAHs – The 1994 mobile burn study. Environ Sci Technol, 1999, 33, 3100–3109.
[100] Yunker MB, Macdonald RW, Brewer R, Vingarzan R, Mitchell RH, Goyette D, Sylvestre S. PAHs in the Fraser River basin: A critical appraisal of PAH ratios as indicators of pah source and composition. Org Geochem, 2002, 33, 489–515.
[101] Yunker MB, Macdonald RW, Goyette D, Paton DW, Fowler BR, *et al*.. Natural and anthropogenic inputs of hydrocarbons to the Strait of Georgia. Sci Total Environ, 1999, 225, 181–209.
[102] Benlahcen KT, Chaoui A, Budzinski H, Bellocq J, Garrigues P. Distribution and sources of polycyclic aromatic hydrocarbons in some Mediterranean coastal sediments. Mar Pollut Bull, 1997, 34, 298–305.
[103] Grimalt JO, van Drooge NL, Ribes A, Fernandez P, Appleby P. Polycyclic aromatic hydrocarbon composition in soils and sediments of high altitude lakes. Environ Pollut, 2004, 131, 13–24.
[104] Wang ZD, Fingas M. Use of methyldibenzothiophenes as markers for differentiation and source identification of crude and weathered oils. Environ Sci Technol, 1995, 29, 2842–2849.
[105] McCarry BE, Allan LM, Legzdins AE, Lundrigan JA, Marvin CH, Bryant DW. Thia-arenes as pollution source tracers in urban air particulate. Polycycl Aromat Comp, 1996, 11, 75–82.
[106] Wang ZD, Fingas M, Blenkinsopp S, Sergy G, Landriault M, et al.. Comparison of oil composition changes due to biodegradation and physical weathering in different oils. J Chromatogr A, 1998, 809, 89–97.
[107] Wang ZD, Hollebone B, Yang C, Fieldhouse B, Fingas M, et al.. Oil composition and properties for oil spill modelling (US EPA Order No.: 3D-6152-NAFX), Environment Canada, Ottawa, ON, 2004.
[108] ESTS. Environment Canada crude oil and petroleum product database. Emergencies Science and Technology Section (ESTS), Environment and Climate Change Canada (ECCC), Ottawa, ON, 2021. https://open.canada.ca/data/en/dataset/53c38f91-35c8-49a6-a437-b311703db8c5.
[109] Douglas GS, Bence AE, Prince RC, McMillen SJ, Butler EL. Environmental stability of selected petroleum hydrocarbon source and weathering ratios. Environ Sci Technol, 1996, 30, 2332–2339.
[110] Short JW, Heintz RA. Identification of Exxon Valdez oil in sediments and tissues from Prince William Sound and the Northwestern Gulf of Alaska based on a PAH weathering model. Environ Sci Technol, 1997, 31, 2375–2384.
[111] National Research Council. Oil in the sea III: Inputs, fates, and effects (review). National Academies Press (US), Washington, DC, 2003.
[112] Zakaria MP, Okuda T, Takada H. PAHs and hopanes in stranded tar-balls on the coast of peninsular Malaysia: Applications of biomarkers for identifying source of oil pollution. Mar Pollut Bull, 2001, 12, 1357–1366.
[113] Warnock AM, Hagen SC, Passeri DL. Marine tar residues: A review. Water Air Soil Pollut, 2015, 226, 68.

[114] Emsbo-Mattingly S, Litman E. Forensic identification of historical and ongoing tar oil releases in nearshore environments. In: Stout SA, Wang ZD, eds.. Case Studies in Oil Spill Environmental Forensics. Academic Press, Oxford, UK, 2017, 785–826.
[115] Jacquot F, Guiliano M, Doumenq P, Munoz D, Mille G. In vitro photooxidation of crude oil maltenic fractions: Evolution of fossil biomarkers and polycyclic aromatic hydrocarbons. Chemosphere, 1996, 33, 671–681.
[116] Garrett PM, Pickerring IJ, Haith CE, Prince RC. Photooxidation of crude oils. Environ Sci Technol, 1998, 32, 3719–3723.
[117] Nicodem DE, Fernandes M, Guedes C, Correa RJ. Photochemical processes and the environmental impact of petroleum spills. Biogeochem, 1997, 39, 121–138.
[118] Nicodem DE, Guedes C, Correa RJ. Photochemistry of petroleum I. Systematic study of a Brazilian intermediate crude oil. Mar Chem, 1998, 63, 93–104.
[119] Andersson JT. Polycyclic aromatic sulfur heterocyclic iii. Photochemical stability of the potential oil pollution markers phenanthrenes and dibenzothiophenes. Chemosphere, 1993, 27, 2097–2102.
[120] Ali LN, Mantourab RF, Rowland SJ. The dissolution and photodegradation of Kuwaiti crude oil in seawater. Part 2: A laboratory photodegradation apparatus and photodegradation kinetics of a model seawater soluble hydrocarbon (phenanthrene). Mar Environ Res, 1995, 40, 319–335.
[121] Stepnowski P, Siedlecka EM, Behrend P, Jastorff B. Enhanced photodegradation of contaminants in petroleum refinery wastewater. Water Res, 2002, 36, 2167–2172.
[122] Radovic JR, Aeppli C, Nelson RK, Jimenez N, Reddy CM, Bayona JM, Albaiges J. Assessment of photochemical processes in marine oil spill fingerprinting. Mar Pollut Bull, 2014, 79, 268–277.
[123] Albaigés J, Bayona JM, Radović JR. Photochemical effects on oil spill identification. In: Stout SA, Wang ZD, eds. Standard handbook oil spill environmental forensics. Elsevier, London, UK, 2016, 917–960.
[124] Volkman JK, Alexander R, Kagi RI. Biodegradation of aromatic hydrocarbons in crude oils from the Barrow Sub-basin of Western Australia. Org Geochem, 1984, 6, 619–632.
[125] Wenger LM, Isaksen GH. Control of hydrocarbon seepage intensity on level of biodegradation in sea bottom sediments. Org Geochem, 2002, 33, 1277–1292.
[126] Wang ZD, Fingas M, Blenkinsopp S, Sergy G, Landriault M, Sigouin L, Lambert P. Study of the 25-year-old Nipisi oil spill: Persistence of oil residues and comparisons between surface and subsurface sediments. Environ Sci Technol, 1998, 32, 2222–2232.
[127] Leahy JG, Colwell RR. Microbial degradation of hydrocarbons in the environment. Microbiol Rev, 1990, 53, 305–315.
[128] Connan J. Biodegradation of crude oils in reservoirs. In: Brooks J, Welte DH, eds. Advances in petroleum geochemistry (Vol. 1). Academic Press, New York, 1983, 299–335.
[129] Strausz OP, Morales-Izquierdo A, Kazmi N, Montgomery DS, Payzant JD, et al.. Chemical composition of Athabasca bitumen: The saturate fraction. Energ Fuel, 2010, 24, 5053–5072.
[130] Wei ZB, Moldowan JM, Peters KE, Wang Y, Xiang W. The Abundance and distribution of diamondoids in biodegraded oils from the San Joaquin Valley: Implications for biodegradation of diamondoids in petroleum reservoirs. Org Geochem, 2007, 38 1910–1926.
[131] Prince RC, Elmendorf DL, Lute JR, Hsu CS, Haith CE, et al.. 17α(H),21β(H)-Hopane as a conserved internal marker for estimating the biodegradation of crude oil. Environ Sci Technol, 1994, 28, 142–145.
[132] George SC, Boreham CJ, Minifie SA, Teerman SC. The effect of minor to moderate biodegradation on C_5 to C_9 hydrocarbons in crude oils. Org Geochem, 2002, 33, 1293–1317.

Ian J. Vander Meulen, Rory P. Downham, Latifa Alostad,
Kerry M. Peru, Dena W. McMartin, Mark P. Barrow,
John V. Headley

3 Advances in Fourier transform mass spectrometry forensic tools for naphthenic acid fraction compounds in oil sand environmental samples and crude oil

Abstract: During the past decade, there has been sustained interest in papers published on naphthenic acids (NAs) and the broader class of naphthenic acid-fraction compounds (NAFCs) as part of environmental and petroleomic studies. This increase attention in part reflects that NAs and related NAFCs are principal toxicants in oil sands process-affected water (OSPW). Furthermore, NAFCs are of industrial concern because they cause infrastructure scaling and corrosion during petroleum transport and processing. Many analytical strategies have therefore been developed for the detection and characterization of NAFCs, but Fourier transform mass spectrometry (FTMS)-based methods provide powerful molecular-level insights into these complex mixtures. This review focuses on the exceptional utility of ultrahigh resolving power FTMS applications to environmental forensics of NAFCs and crude oils. Highlighted are applications of Fourier transform ion cyclotron resonance mass spectrometry and Orbitrap mass spectrometry as ultrahigh resolution methods for (a) molecular-level measurement of environmental occurrence and fate of NAFCs across the Athabasca oil sands region, Canada; (b) improvement of understanding

Ian J. Vander Meulen, Department of Civil, Geological and Environmental Engineering, University of Saskatchewan, 57 Campus Drive, Saskatoon, Saskatchewan, S7N 5A9, Canada; Watershed Hydrology and Ecology Research Division, Water Science and Technology Directorate, Environment and Climate Change Canada, 11 Innovation Boulevard, Saskatoon, Saskatchewan, S7N 3H5, Canada
Rory P. Downham, Latifa Alostad, Mark P. Barrow, Department of Chemistry, University of Warwick, Coventry, CV4 7AL, United Kingdom
Kerry M. Peru, Watershed Hydrology and Ecology Research Division, Water Science and Technology Directorate, Environment and Climate Change Canada, 11 Innovation Boulevard, Saskatoon, Saskatchewan, S7N 3H5, Canada
Dena W. McMartin, Department of Civil, Geological and Environmental Engineering, University of Saskatchewan, 57 Campus Drive, Saskatoon, Saskatchewan, S7N 5A9, Canada; Office of the Vice President (Research), University of Lethbridge, 4401 University Drive West, Lethbridge, Alberta, T1K 3M4, Canada
John V. Headley, Watershed Hydrology and Ecology Research Division, Water Science and Technology Directorate, Environment and Climate Change Canada, 11 Innovation Boulevard, Saskatoon, Saskatchewan, S7N 3H5, Canada, e-mail: John.headley@canada.ca

https://doi.org/10.1515/9783110694529-003

of molecular mechanisms of NAFC-related toxicity in aquatic environments; (c) assessment of treatment outcomes for OSPW; along with (d) compelling data visualizations of organic components in crude oils. Advances in instrumental technology and data processing continue to improve resolution and sensitivity across the mass range. The processing of data generated by these methods can be challenging, but offers unparalleled levels of insight into NAFC composition. Future studies are encouraged to further combine traditional petroleomic data visualization techniques with multivariate ordination methods. Such applications would be particularly useful for matching molecular characteristics with physical properties and with processes, such as toxicity, corrosion, as well as the environmental behaviour and fate of these compounds.

3.1 Introduction

Bitumen extraction operations, such as those in the Athabasca region of Alberta, Canada, require large volumes of water. As a result of substantial water use, large volumes of oil sand process-affected water (OSPW) are generated. OSPW is acutely toxic to a broad variety of aquatic organisms [1–3]. Discharge of OSPW has not yet been permitted, so OSPW is retained in tailings ponds. As of 2018, tailings ponds covered an estimated 220 km^2 and contained approximately 1.2 billion m^3 of water [4]. OSPW is a complex mixture, which includes dissolved salts, fine suspended clay, residual hydrocarbons, and naphthenic acid fraction compounds (NAFCs), including classical naphthenic acids (NAs). NAs are typically described as aliphatic and alicyclic petroleum-carboxylic acids, following the general formula $C_nH_{2n+Z}O_2$, where n denotes the number of carbon atoms, and z is a negative even integer denoting the unsaturation of a particular NA [5] (Figure 3.1). Additional complexity arises when further mixture components such as the broader class of other acid-extractable organic compounds (i.e., NAFCs) are considered; NAFCs include NAs, as well O_x–, N–, and S-containing organic compounds [6, 7]. These definitions for NAs and NAFCs include many compounds that would not normally be considered "naphthenic," including unsaturated and/or aromatic organic acids. Aromatic organic acids are of special concern as potential environmental toxicants, acting as potential endocrine disruptors or affecting overall acute toxicity [8, 9]. Aromatic organic acids are also present in NA fractions collected from OSPW, leading to their inclusion as NAFCs despite the fact that aromatic compounds are, by definition, not "naphthenic."

Despite the compositional complexity of OSPW, NAs and other components of NAFCs have been consistently identified as principal toxicants in the mixture [10–12]. Given the complexity inherent to the measurement of such mixture components, there are a myriad of methods available to test petroleum and petroleum-affected samples for NAFCs. Such methods include Fourier transform (FT) infrared spectroscopy [13, 14], gas chromatography time-of-flight mass spectrometry (GC-TOFMS) [15–18], liquid

chromatography-tandem mass spectrometry [19], and others, which have been reviewed elsewhere [6, 20–22]. Such methods can be useful, but cannot generate data with comparable volume or accuracy. This review focuses specifically on ultrahigh resolving power FT mass spectrometry (FTMS) applications to environmental forensics of NAFCs and crude oils. Herein, we highlight the utility of FT ion cyclotron

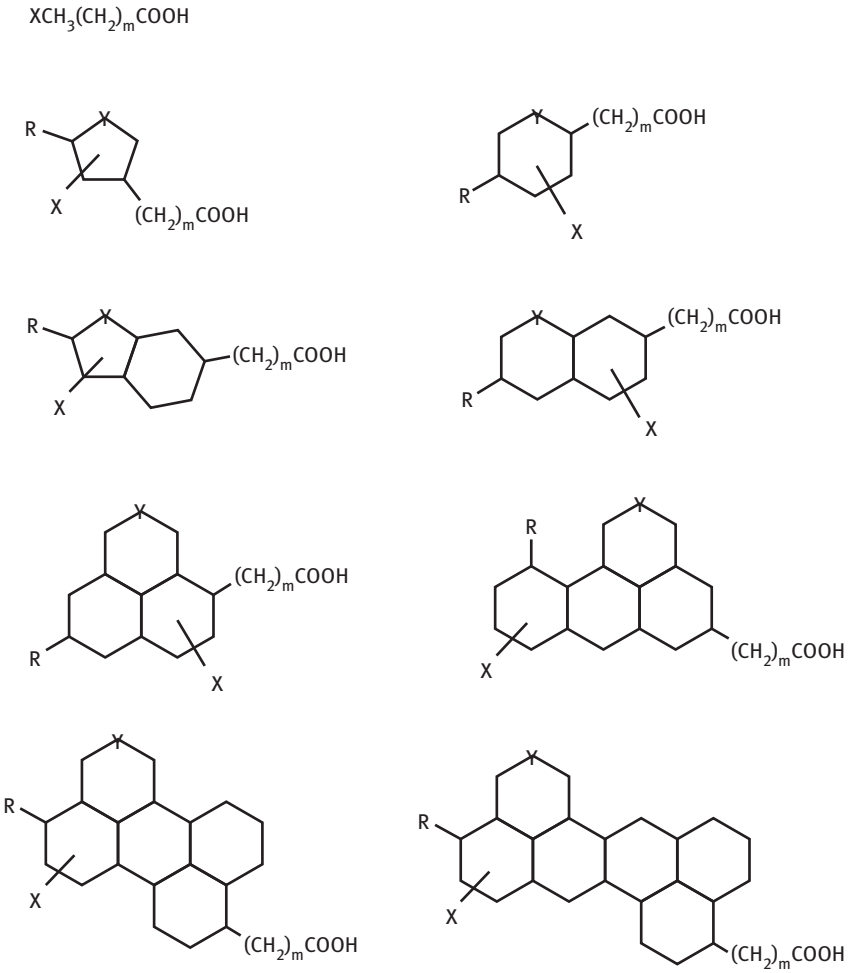

Figure 3.1: Reproduced from Headley et al. [34], with permission. Generic structures to represent OSPW naphthenic acid fraction components.

resonance mass spectrometry (FTICR MS) and Orbitrap mass spectrometry (Orbitrap MS) for (a) characterization of NAFCs in natural waters from the Athabasca oil sand region (AOSR), (b) molecular-level characterizations of NAFCs before and after treatment of OSPW, (c) contributions to toxicity-directed analysis of OSPW, and (d) data visualization and interrogation techniques empowered by ultrahigh-resolution mass spectral data. The characterization of NAs and NAFCs in crude oils is of importance to petroleum producers, as the acidic content of crude oil can result in corrosion problems [23–32], and the environmental impact of naphthenic acids is also of concern [33]. The characterization of petroleum-related samples using mass spectrometry, in particular ultrahigh-resolution mass spectrometry, has been referred to as a field known as "petroleomics" and developments in this area have also directly led to advances in the characterization of NAFCs in the environment.

3.2 FTMS instruments and performance

The term "FTMS" is typically used in reference to FT ion cyclotron resonance and Orbitrap mass spectrometers. In the 1970s, Marshall and Comisarow were the first to utilize a FT in combination with ion cyclotron resonance spectrometry [35–37]. FTICR MS offers the highest performance of all mass spectrometers and is based upon ions orbiting (cyclotron motion) within a cell that is housed within a magnetic field [38]. The cell is typically a cylinder of a few centimeters in diameter and in length, which is maintained at ultrahigh vacuum to minimize collisions between the ions and gases during the cyclotron motion. The Lorentz force, arising due to the motion of ions within a magnetic field, serves as the centripetal force and results in the ions' orbits. As the ions pass the detection plates of the ICR cell during these orbits, an image current is induced; the motions of all the ions are detected together, rather than individually. This composite signal is known as the "transient" or "FID" (free induction decay) and is recorded with respect to time (time domain data), and then a FT is used to convert this data to the frequency domain. In effect, the FT is used to determine the frequencies of the waveforms that comprise the complex time domain data that was recorded. As the frequency of each waveform detected is inversely proportional to the mass-to-charge ratio (m/z), a calibration equation is used to convert from the frequency domain to a mass spectrum, where signal intensity is plotted as a function of m/z. The Orbitrap mass spectrometer, first reported in the literature in 2000 [39], is another instrument based upon the measurement of ion motion followed by the application of the FT. Unlike FTICR mass spectrometers, Orbitrap instruments do not use magnetic fields, but rather ions orbit about a spindle-shaped electrode while oscillating back and forth between a pair of outer electrodes [40]. Whereas orbital motion is detected during FTICR MS experiments, oscillation back and forth between the outer electrodes is

detected during Orbitrap MS experiments. As with FTICR instruments, an FT is used to convert the time domain data to the frequency domain and then calibration is used to produce a mass spectrum. The principles of FTMS are explained in greater detail elsewhere in the literature [37, 38, 41, 42].

FTMS techniques are well known for their ultrahigh resolving power (narrow peaks, making them well-suited to complex samples) and their mass accuracy (accurate measurement of m/z to multiple decimal places). Accordingly, these technologies are capable of assigning elemental compositions at molecular levels in complex mixtures such as crude oils, bio-oils, and oil sand environmental samples, given that analyses follow well-established formulae assignment rules [43]. The ultrahigh resolving power and mass accuracy afford greater detail when characterizing complex samples through confident assignment of thousands of molecular formulas. The assignment of these molecular formulae, however, does not constitute full structural information. For that purpose, FTMS instruments would need to utilize tandem mass spectrometry experiments (fragmentation of prior selected species) or combination with orthogonal separation methods, such as chromatography, particularly where isomers may be present. FTMS instruments can produce broadband mass spectra of complex mixtures with mass errors below the parts-per-million (ppm) level, and even as low as parts-per-billion [44, 45], provided that sufficient resolving power is achieved. It should be noted that small mass error values are desirable because they afford higher confidence of assignments of molecular formulae. On the other hand, large resolution values are desirable, as higher resolving power denotes narrower peaks and therefore a greater number of components can be observed within a complex sample. Figure 3.2 shows a broadband spectrum of a NIST crude oil acquired using FTICR MS, with enlargements down to a 14 mDa window. The resolving power in this example allows for species with well-known mass splits, such as C_4 versus $^{13}CH_3S$, to be separated [42]. For species composed of C, H, N, O, and S atoms, unambiguous molecular formulae assignments are possible up to approximately 500 Da when using traditional methods [42, 46]. In petroleomics, the difficulty in making high-confidence assignments above ~500 Da was overcome by deploying the Kendrick mass scale; a treatment which sets the mass of CH_2 to exactly 14 Da [47–49]. This rescaling approach enables easy identification of molecules belonging to the same homologous series, and thus higher mass molecular compositions can be more confidently assigned as part of a series [48, 49]. The use of this homologous series principle for molecular assignments extends beyond petroleum and is now being used to assist in the analysis of other natural complex mixtures [50, 51].

FTICR MS was first implemented in the analysis of samples derived from oil sands in 2004 [52]. The study concluded that FTICR MS provided greater insights into the compositions of the oil sand samples by achieving unique assignments, including those of higher hydrogen deficiency [52], where hydrogen deficiency (z) is typically a negative, even integer per $C_cH_{2c+z}O_o$. The first utilization of an Orbitrap mass spectrometer to the characterization of oil sand NAs was in 2011, where oil sand NAs were characterized in plant tissue samples [53].

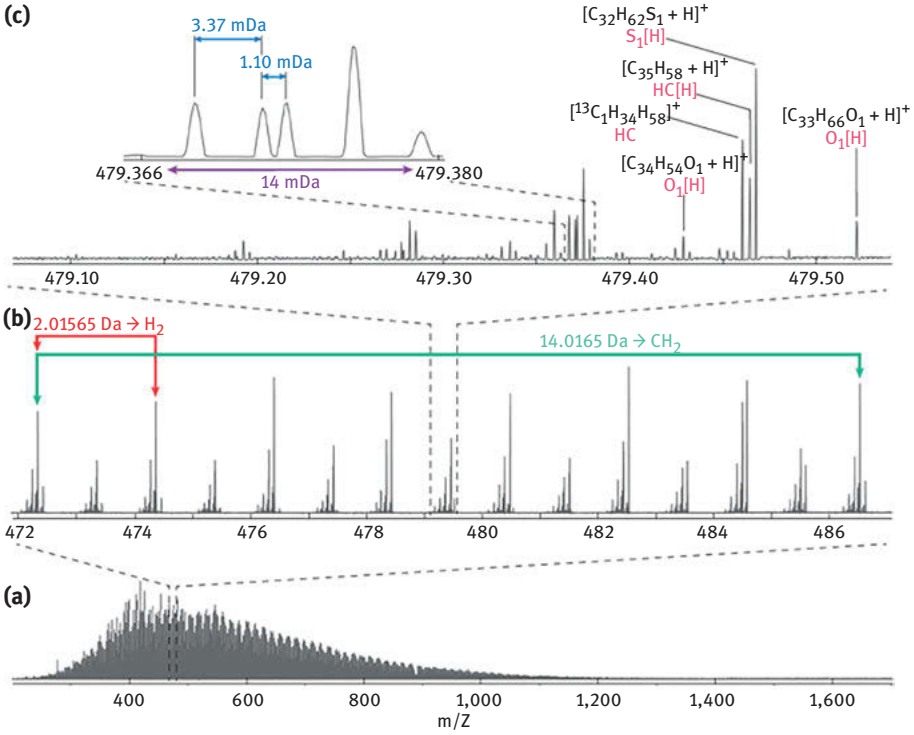

Figure 3.2: Reproduced from Palacio Lozano et al. [42], with permission. Diagrams of (a) NIST crude oil broadband mass spectrum obtained via FTICR MS (using atmospheric pressure photoionization and positive-ion mode). (b) Enlargement showing peak clustering and the typical species separation gaps relating to CH_2 and H_2 units. (c) Further enlargement to demonstrate peak resolution within half a Dalton window, with some peak assignments and compound class designations shown. The indicated mass differences of 1.10 mDa and 3.37 mDa correspond to common mass splits; C_4 versus $^{13}CH_3S$ and C_3 versus H_4S, respectively.

3.3 Contributions to informative data visualizations and interrogation techniques

The acronym "NAFCs" loosely ties together a diverse variety of organic components, grouped as such due to their common extraction during reverse-phase extraction of acidified samples. Much attention has been given to approaches for visualization of spatial or temporal trends for such complex mixtures. Indeed, the task of creating effective data visualizations has long been recognized as a challenge in environmental forensics. An early application of ultrahigh-resolution mass spectrometry to environmental forensics used FTICR MS for accurate formula assignments to compare

commercial mixtures of NAs to OSPW from the Athabasca oil sands [52]. This paper demonstrated the capability of FTICR MS methods to accurately assign molecular formulae comprising complex mixtures, showing clear differences between technical mixtures of NAs and OSPW-derived NAs. Technical mixtures of NAs contained more straight-chain saturated NA species, whereas OSPW-derived NAs were largely unsaturated.

Barrow et al. [54] described an approach for visualization of large datasets of ultrahigh-resolution mass spectrometry data. For example, as is shown in Figure 3.3, raw mass spectra are complex and difficult to interpret without software tools to aide in the identification of compound classes and data processing.

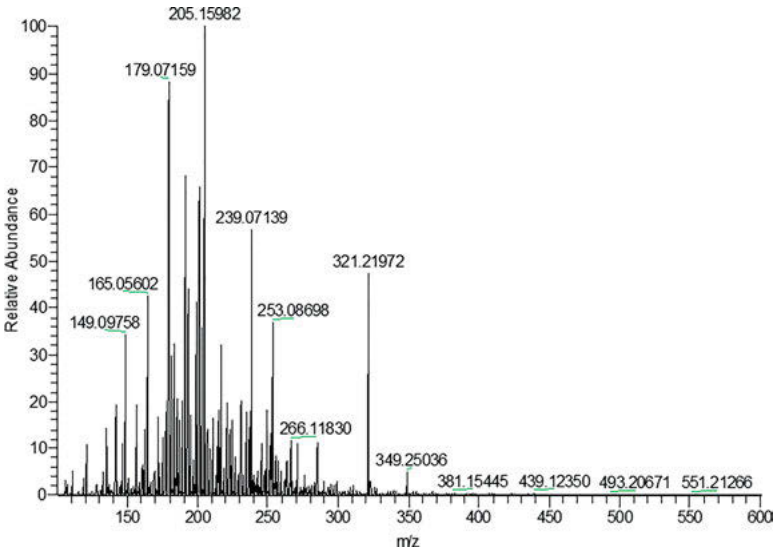

Figure 3.3: An example ultrahigh-resolution mass spectrum collected using Orbitrap mass spectrometry describing water-soluble organic compounds from a simulated oil spill (unpublished data).

As introduced above, the use of homologous series, which extends the range of reliable molecular formulae assignments, can be enabled by use of the Kendrick mass scale and by calculating the Kendrick mass defect (KMD) for molecular compositions [47–49] (eqs. (3.1) and (3.2)). Plots of KMD versus nominal mass allow for homologous series to be readily visualized, as members of a homologous series have the same KMD [49]. By determining series within complex mass spectra, it is possible to greatly accelerate data analysis by determining the molecular formula for one member of a series and then using automatically-determined formulae for the remaining species within a series, rather than performing the molecular assignment process individually for thousands of peaks:

$$\text{Exact Kendrick mass} = \text{IUPAC mass} \times 14.00000/14.01565 \quad (3.1)\ [48, 55]$$

$$\text{KMD} = [\text{nominal Kendrick mass}] - [\text{exact Kendrick mass}] \quad (3.2)\ [48, 55]$$

Once molecular formulae are assigned, the results may be organized and visualized. Petroleum compounds can be categorized by: heteroatom class (sometimes also called "compound class"), double bond equivalents (DBE), and carbon number. The heteroatom class is derived from the atoms that are available within the composition, for example, the hydrocarbon (HC) and single sulfur atom (S_1) classes. DBE signifies the saturation of the compound by calculating the rings and double bonds present within the carbon framework of the composition:

$$\text{DBE} = c - \frac{h}{2} + \frac{n}{2} + 1 \quad (3.3)\ [48]$$

Carbon number relates simply to the number of carbon atoms present in a molecule. It is common to plot DBE versus carbon number as a useful visualization tool in petroleomics-related research (Figure 3.4). Carbon number further enables the identification of homologous series, where compositions have the same heteroatom content and same number of DBE but are separated by CH_2 units (alkylation). The alkylation series of a composition having the same DBE and class will differ with 14.01565 Da [42, 48, 55].

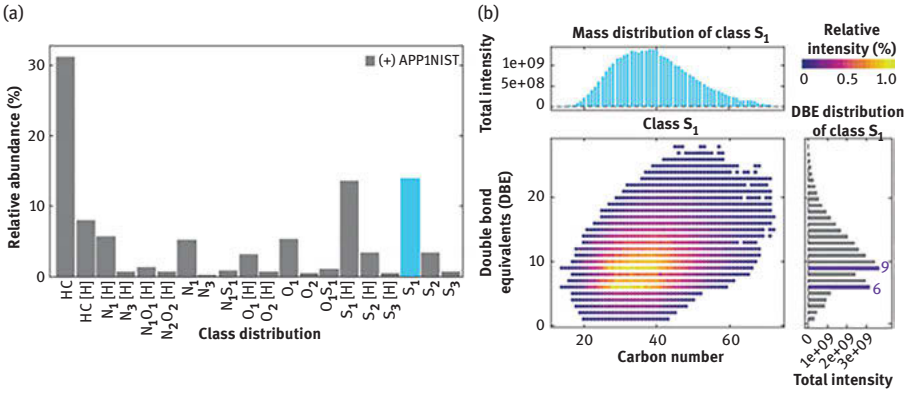

Figure 3.4: Reproduced from Palacio Lozano et al. [42], with permission. Data visualizations for a mass spectrum of a NIST crude oil obtained via atmospheric pressure photoionization FTICR MS. (a) Distribution plot showing the relative abundance of all heteroatom classes in the sample. (b) A DBE versus carbon number plot, with separate intensity distribution plots of DBE and carbon number, all for the S_1 heteroatom class.

The van Krevelen diagram [56–58] is another well-established and important visualization tool for complex mixture analysis, especially for natural organic matter and related samples [42, 59, 60]. Modern van Krevelen diagrams are scatter plots, typically of elemental ratios of H/C versus O/C, although other variants are also employed

[60]. Biogeochemical compound classes are associated with characteristic elemental ratios, and hence the regions of van Krevelen diagrams can be used tentatively to infer the presence of certain species in complex mixtures [58]. Three-dimensional van Krevelen diagrams are also used, whereby the third dimension represents peak intensities or a third molar ratio of elements (e.g., N/C) [42]. Such plots are typically used to visualize results for samples where oxygen contents are observed [61, 62].

Visualization strategies described by Barrow et al. [54] further include dimensional reduction techniques such as principal component analysis (PCA) [Figure 3.5] which can helpfully cluster similar data, and separate dissimilar data. Barrow et al. also highlighted relative abundance line plots, and heat maps which help highlight particular points of interest within a given dataset. These visualizations exploit the advantages of ultrahigh-resolution mass spectrometry, underscoring the importance of unequivocal formula assignment offered by FTMS technologies.

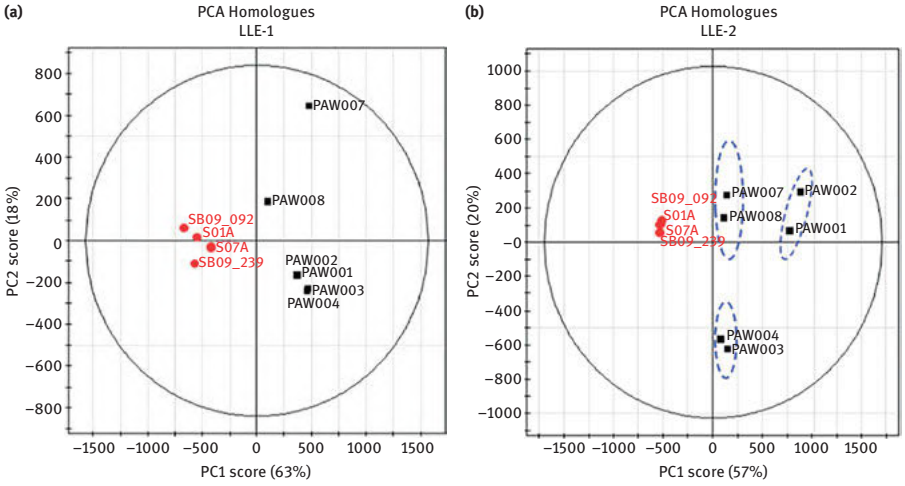

Figure 3.5: Reproduced from Yi et al. [63], with permission. PCA score plots of homologous series showing the compositional differences between OSPW (black) and environmental samples (red). (a) PCA score plots of the results from acidic extraction analyzed in negative ionization mode (LLE-1), and (b) PCA score plot of results from basic extraction analyzed in positive ionization mode (LLE-2).

As was briefly mentioned earlier, studies of OSPW have typically focused on acid-extractable components of OSPW due to the consistent association of NAFCs with acute toxicity [11, 12, 64]. NAFCs are acutely toxic and therefore frequently the focus of study, so visualization of the characterization of different fractions of the mixture can add complementary forensic compositional information. Yi et al. [63] made use of both acid- and base-adjusted liquid–liquid extractions to gather information about the complementarity of each of these OSPW fractions under negative and positive electrospray ionization (ESI) conditions, respectively. This work found that

when acidic and basic fractions (analyzed by negative-ion and positive-ion ESI, respectively) were separately analyzed with PCA, the basic fraction analyzed in positive-ion mode successfully distinguished OSPW from environmental samples and was further able to distinguish different sources of OSPW from one another. Basic-extracted organics were more abundant in S_nO_x compounds, whereas the acid-extracted organics (i.e., NAFCs) had abundant O_x compounds. These analyses generated sufficient data for preliminary source distinction, demonstrating the benefits of such analyses to future environmental forensic studies.

As an analytical tool, FTMS is also helpful as a validation step for techniques that use lower resolution mass spectrometry, such as where time-of-flight mass spectrometry (TOF-MS) instruments are used. For example, Huang et al. [65] used FTICR MS to add information about the relative abundance of S- and N-containing compounds from NAFCs, as resolving these peaks requires mass resolution higher than 120,000 [66]. The additional information allowed the authors to attempt a broader suite of analyses, adding plots wherein data were screened according to unique heteroatom inclusions prior to PCA, shown in Figure 3.6. Unfortunately, additional data from FTICR MS analysis did not consistently separate all sample data from one another. Nonetheless, this approach to subsetting compositional data according to unique formulaic heteroatom inclusions should prove useful in future analyses by greatly reducing noise in the data, leading to principal components that explain high overall percentages of variation therein. Thus, differences observed in the PCA plots should highlight distinct differences between samples, as is seen in Figure 3.6b, where the first principal component (PC1) from analysis of O_3S-NAFCs explained 97% of variation between samples in that subset of the data.

Helpful visualizations of complex datasets can also arise when traditional techniques are combined in compelling ways. For example, Ajaero et al. [67] collected samples from a laboratory-scale constructed treatment wetland system (CWTS) wherein OSPW recirculated through the system for 27 days. Samples were extracted by weak anion-exchange SPE, then analyzed by negative-ion ESI Orbitrap MS. Data were analyzed by PCA, which indicated that gradual changes were happening over time in the treatment wetland, and data separated accordingly from one end of the PCA plot to the other. To investigate which specific factors were contributing to differences between samples, factor loadings from the PCA were color coded over a Kendrick plot to show how formulae of varying molecular weights and unsaturation contributed to sample separation over principal component 1, shown in Figure 3.7. This figure had predictive value, as shifts in NAFC distributions were concentrated among the highest m/z unsaturated components, highlighted by the color-coding of Figure 3.7.

Similar strategies have been applied for natural wetland environmental samples. For example, Vander Meulen et al. [68] employed similar strategies analyzing NAFCs detectable across two Athabasca oil sand wetlands. One wetland in this study had a clear flow pathway from north to south, interrupted by beaver dams throughout, and a suspected contamination point source at the north end of the wetland. The second

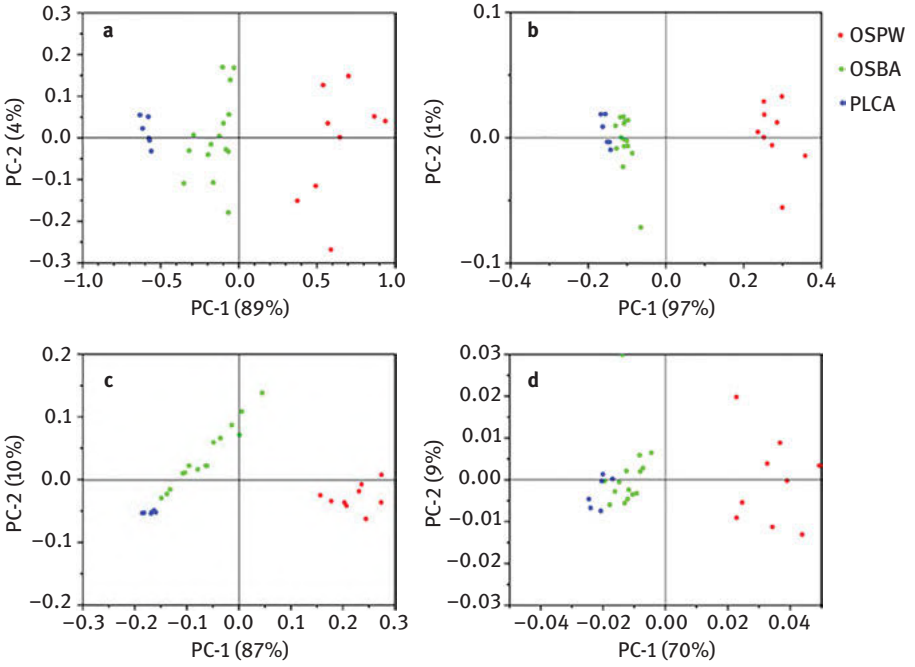

Figure 3.6: Reproduced from Huang et al. [65], with permission. Score plots for PCA analysis of distribution profiles (calibrated intensity in terms of carbon and Z numbers obtained via FTICR MS analysis) of (a) O_2S-NAFCs, (b) O_3S-NAFCs, (c) O_2N-NAFCs, and (d) O_3N-NAs in oil sand process-affected water (OSPW) samples, oil sands basal aquifer samples (OSBA, $n = 15$), and Pleistocene channel aquifer samples (PLCA, $n = 9$) collected from ten sites at three time points. The percentages along with PC-1 or PC-2 indicate their respective contribution to total variance in PCA analysis.

wetland was an opportunistic wetland on overburden with unclear hydrology. Changes in NAFC composition were examined and compared across the span of both wetlands. Instead of a conventional PCA plot, sampling locations were mapped and color-coded according to sample scores along the first principal component in each wetland, shown in Figure 3.8. The sample maps were paired with Kendrick plots color-coded similarly to those generated in Ajaero et al. [67], highlighting differences observed across one wetland (Gateway Wetland, Figure 3.8a) similar to compositional changes previously observed under controlled conditions. The most substantial changes in spatial distributions of NAFCs were again observed among the highest-molecular weight saturated compounds, and a simultaneous increase in the relative abundance of low-molecular weight unsaturated species.

The data visualizations techniques described here are helpful tools for effectively communicating diagnostic features for environmental forensics. Future work in visualization methods may combine van Krevelen and Kendrick plots with multivariate

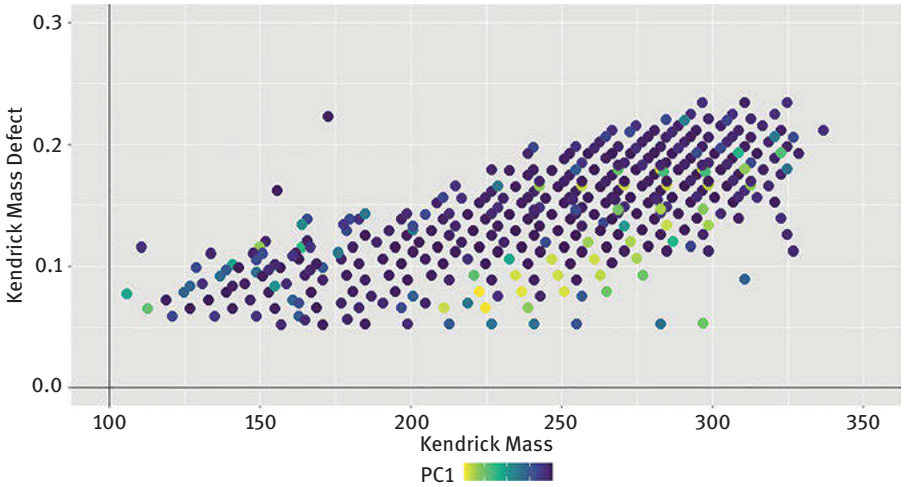

Figure 3.7: Reproduced from Ajaero et al. [67], under Creative Commons 4.0 License (https://creativecommons.org/licenses/by/4.0/legalcode). A Kendrick plot of all formulae used to calculate sample distribution in a PCA of samples from a constructed wetland treatment system (CWTS). Formulae are color-coded according to factor loadings along the first principal component (PC1).

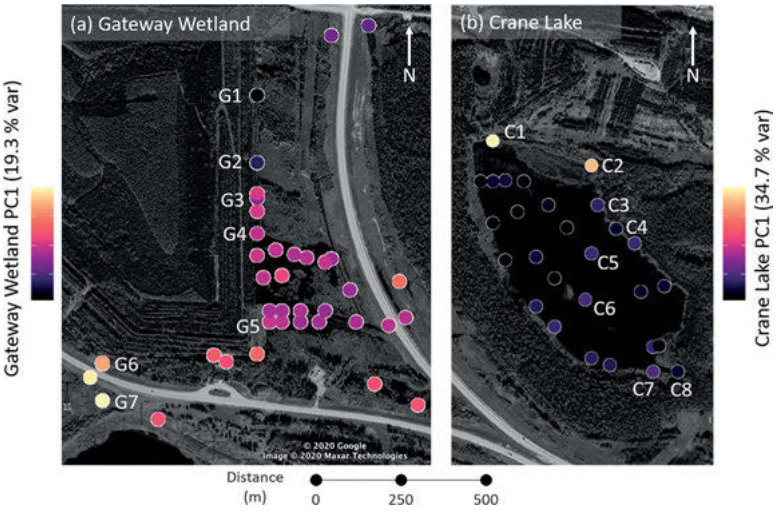

Figure 3.8: Reproduced from Vander Meulen et al. [68] under a Creative Commons 4.0 License (https://creativecommons.org/licenses/by/4.0/legalcode). Sampling maps, color coded according to scores along principal component 1 from the individual principal component analyses (PCA) of (a) Gateway wetland, which has a well-defined north-to-southwest flow pathway, and (b) Crane Lake, which does not have well-characterized hydrology.

data ordination techniques such as principal component analysis, nonmetric multidimensional scaling, correspondence analysis, and detrended correspondence analysis.

3.4 Experimental design considerations

Experiments using FTMS analyses benefit from the inclusion of sample fractionation steps prior to or during mass spectrometric analysis. Such separatory steps include solid-phase extraction (SPE) [5, 69], extract fractionation [11, 70, 71], and chromatography [72–74]. However, the addition of separatory techniques to complement FTMS methods can also introduce complications in data analyses. For example, choosing different SPE methods to extract NAFCs from water (i.e., weak anion exchange versus polydivinylbenzene reverse-phase adsorption) will selectively enrich particular varieties of NAFCs [69]. Differing solvent-extraction procedures will also selectively enhance extraction of particular NAFC components, influencing apparent sample composition [75]. In particular, the pH of the extraction solvent has been demonstrated to influence OSPW component characterizations via FTICR MS [76]. These off-line extraction procedures are also influenced by matrix effects, such as sample salinity, which can decrease the apparent proportion of more highly nonpolar NAFCs [34]. Influences from different extraction procedures will therefore lead to disparate mass spectra, even when a procedure starts with identical samples.

Such concerns are equally applicable to analyses with alternative ionization strategies, including studies employing direct analysis in real time (DART) ionization [77, 78] or matrix-assisted laser desorption ionization (MALDI) [79]. Studies have demonstrated that DART is capable of producing stable ion signals suitable for FTMS instruments and can be used in petroleum [78] and naphthenic acid analyses [77]. NAFC spectra collected using DART-FTICR MS are somewhat similar to ESI spectra for petroleum samples with fewer dimers and less sample preparation [78]. However, negative-ion DART selectively enriches classical NAs in NAFC analysis, and positive-ion DART selectively enriches N- and SO-containing NAFCs [77]. Direct comparisons between sample data derived from different ionization and/or extraction methods must therefore do so with caution, acknowledging the selectivity of different methods.

Online separations, such as high-performance liquid chromatography (HPLC), may be used as an alternative or addition to offline separations. The use of chromatographic techniques like HPLC can aide in minimizing potential ion-suppression effects in ESI [80, 81]. However, discrimination can still result from different solvent composition at the ionization source for particular NAFC components [81]. Likewise, ionization efficiencies of NAFCs are dependent on the pH of the gradient elution and polarity, which can substantially affect the apparent abundance of particular formulae [80]. In general, the multiple factors affecting the relative abundance and distribution of NAFCs limit FTMS analyses and data interpretation to semiquantitative measurements.

Hyphenating chromatographic systems with FTMS systems effectively multiplies sample data volume and complexity. Combining gas chromatography (GC) to FTICR MS utilizing atmospheric pressure chemical ionization (APCI) can be useful to ionize the sample of interest with minimal fragmentation. APCI ionizes species with lower polarity and molecular weight than those analyzed by ESI. GC-APCI-FTICR MS has been used to characterize an OSPW sample and two groundwater samples from the Athabasca River Basin, Alberta, Canada [74]. As mentioned previously, FTMS affords powerful approaches for characterizing complex mixtures and assigning molecular formulae, but ultrahigh resolving power and mass accuracy alone cannot provide full structural information. The hyphenation of ultrahigh-resolution mass spectrometry and chromatography holds potential for identifying isomers present within complex oil sand samples, shown in Figure 3.9. Isomeric information should empower more precise descriptions of sources and mechanisms of oil sand NAFC-derived toxicity [42, 74].

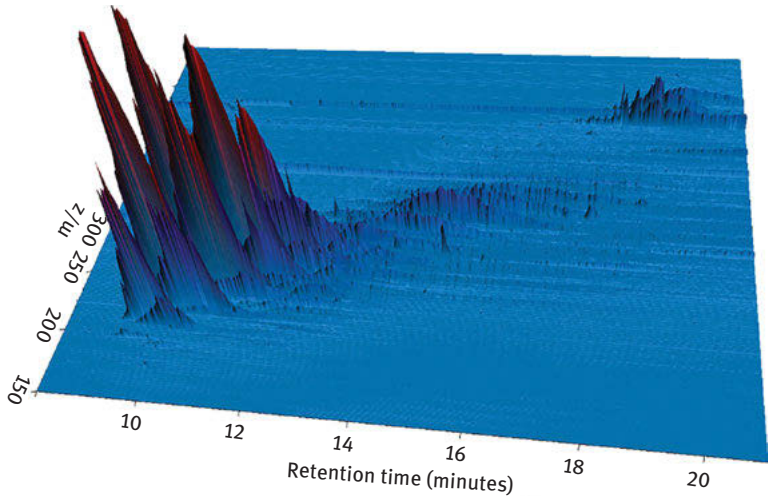

Figure 3.9: Reproduced from Barrow et al. [74], with permission. Three-dimensional representation of m/z versus retention time for an OSPW sample.

The total ion chromatogram was manually divided into segments of 2 min each, in the range of 9–21 min. For each segment, the associated mass spectrum was produced and analyzed prior to the results being visualized. Figure 3.10 shows examples of DBE plots for the O_2, O_3, and O_4 classes associated with the OSPW sample. The predominant species within the O_4 class were typically 1 DBE higher than the predominant species within the O_2 class, which aligns with the hypothesis that the O_4 class includes dicarboxylic acids. The study deduced that the use of GC-APCI FTICR MS offers experimental advantages, as the combination of chromatography and ultrahigh resolving power mass spectrometry can resolve co-eluted species and to determine isomeric

contributions, improving understandings of toxicity from OSPW and related environmental samples [74]. Advances in data processing methods will contribute to increasing nuance in the analysis of these complex sample types [82].

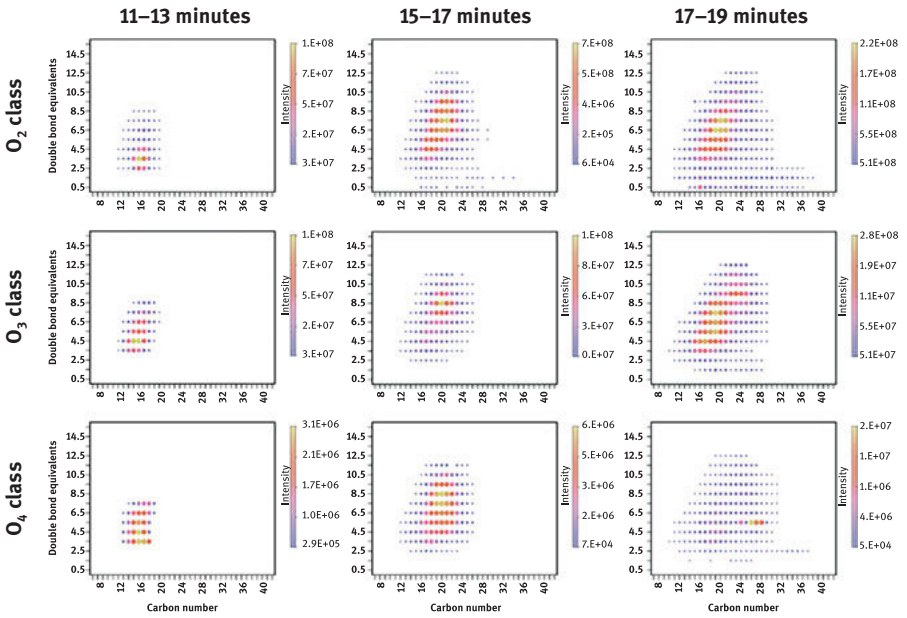

Figure 3.10: Reproduced from Barrow et al. [74], with permission. Plots of DBE versus carbon number for the OSPW sample shown as a function of time.

When the acid-extractable organic components from OSPW (i.e., NAFCs) are characterized using multiple ionization methods with FTMS, sample complexity becomes more apparent [83]. OSPW and related samples have traditionally been analyzed using negative-ion electrospray ionization (ESI) to specifically target NAFCs. In 2010, OSPW-derived NAFCs were analyzed by positive-mode ESI, negative-mode ESI, positive mode atmospheric pressure photoionization (APPI), and negative-mode APPI, and resulting spectra were recorded and compared. The study by Barrow et al. emphasizes the complementary nature of data generated from different ionization modes, as well as the importance of choosing the optimal ionization mode for analysis of particular analytes of interest. For example, negative-mode ESI promotes the ionization of classic NAs (i.e., O_2-NAFCs), but negative-mode APPI further enhances the ionization of aromatic and nonpolar NAFCs. In addition, positive-ion ESI promotes the ionization of NO_x species. Positive-ion APPI further promotes the ionization of neutral nonpolar organic NAFCs, N-, S-, and NO_x-NAFCs, and leads to the widest variety of total detectable peaks among all possible ionization methods, as shown in Figure 3.11. The complexity of the acidic polar organic fraction of OSPW was thus revealed by

complementary ionization modes [83]. Such a finding is of paramount importance for monitoring purposes and reinforces the improved coverage and characterization of NAFCs with different ionization methods.

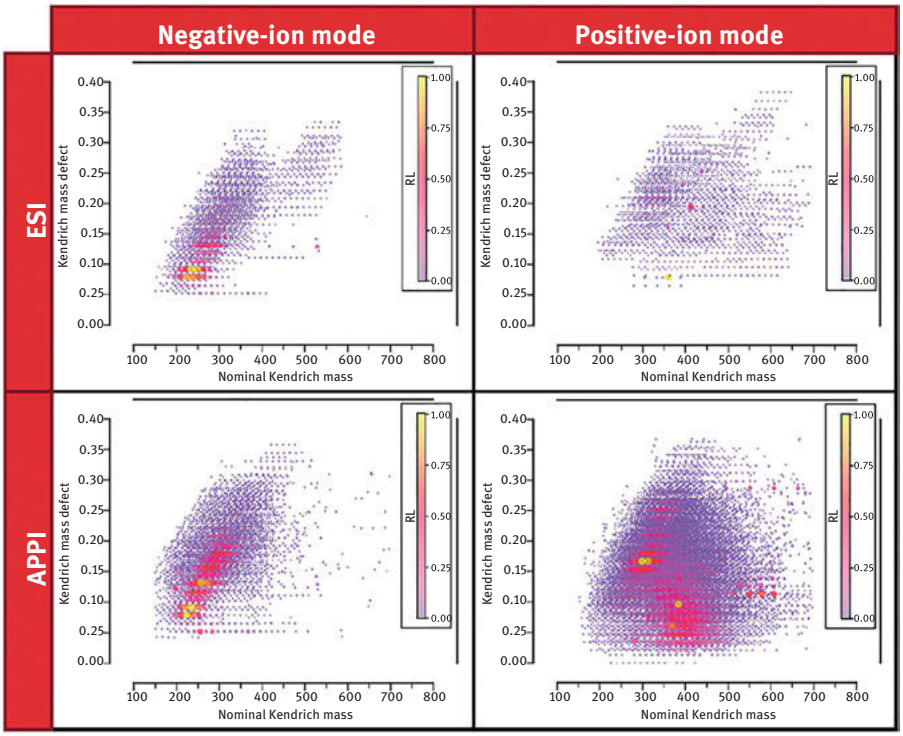

Figure 3.11: Figure reproduced from Barrow et al. [83], with permission. Plots of Kendrick mass defect versus nominal Kendrick mass for four mass spectra in various ionization modes.

In view that measurements of concentrations of NAFCs are semiquantitative, caution must be exercised for comparisons of values reported for different methods, including factors such as extraction techniques, sample preparation prior to analysis, chromatographic separations, and ionization methods. The FTMS methods described here are best suited for comparison of relative trends for a given sample set. For example, if NAFC distributions and amounts differ across a well-defined sample series, meaningful results can be inferred from trends or relative changes of NAFCs. Thus, relative trends in NAFC concentrations and abundance can be readily compared for different studies reported in the literature, even though absolute values of individual samples usually cannot.

3.5 Characterization of NAFCs in natural waters of the Athabasca oil sand region

As was alluded to earlier, classical NAs and other classes of NAFCs are toxicologically relevant contaminants of concern in the Athabasca oil sand region (AOSR) and have therefore been characterized in a number of studies. Both Orbitrap MS and FTICR MS have empowered insights into the molecular characteristics of NAs and NAFCs from in the AOSR.

The Athabasca River and its tributaries run through naturally occurring oil sand deposits, so there is a need to be able to distinguish these natural inputs from potential anthropogenic sources. A preliminary study used FTICR MS to distinguish natural and anthropogenic sources of bitumen-derived NAFCs [7]. Samples in this preliminary study were taken from across the AOSR, including tailings ponds, interceptor wells, groundwater, the Athabasca River, tributaries, and lake surface waters. The FTICR MS data clearly differentiated OSPW from natural water bodies, showing that O_2-NAFCs (i.e., NAs) and O_4-NAFCs dominated mass spectra collected in negative-mode electrospray ionization (ESI). No particular heteroatom type could be implicated as a tracer of anthropogenic versus natural polar organic inputs, but principal component analysis of the ultrahigh-resolution dataset suggested that such differentiation should be possible with more extensive sampling and data analyses [7].

Steps to trace natural versus anthropogenic bitumen-derived inputs in the AOSR have continued in earnest. In a later study from Frank et al., data from loop-injection ultrahigh-resolution Orbitrap MS was used to complement data from comprehensive two-dimensional gas chromatography-time of flight mass spectrometry (GCxGC-TOF-MS) [84]. These data indicated that NAFCs from OSPW have a distinct character distinguishable from natural bitumen-derived inputs at high concentrations. Although multiple techniques suggested that ratios of O_2:O_4-NAFCs from negative ESI-FTMS may be an indicator of OSPW-derived NAFCs, later work found the ratio is not diagnostic for environmental forensics [80, 85–87].

A study reported by Sun et al. characterized NAFCs across the AOSR, including samples from the Athabasca River, tributaries, and groundwater using SPE-HPLC-Orbitrap MS [85]. This study revealed that while NA (i.e., O_2-NAFC) concentrations were elevated in tributaries to the Athabasca River, the presence of these NAs could not be definitively attributed to industrial activity. In addition, O_2:O_4-NAFC ratios did not consistently associate with known industrial inputs; groundwater far from industrial activity had high O_2:O_4-NAFC ratios, similar to OSPW, limiting the usefulness of this ratio. The extensive data set generated by HPLC-Orbitrap MS of organic acid extracts was used to conduct PCA, illustrated in Figure 3.12. PCA of negative-ion ESI data revealed that separated OSPW from other samples, based primarily on the total abundance of O_2^- species, whereas other samples had a greater diversity among NAFCs.

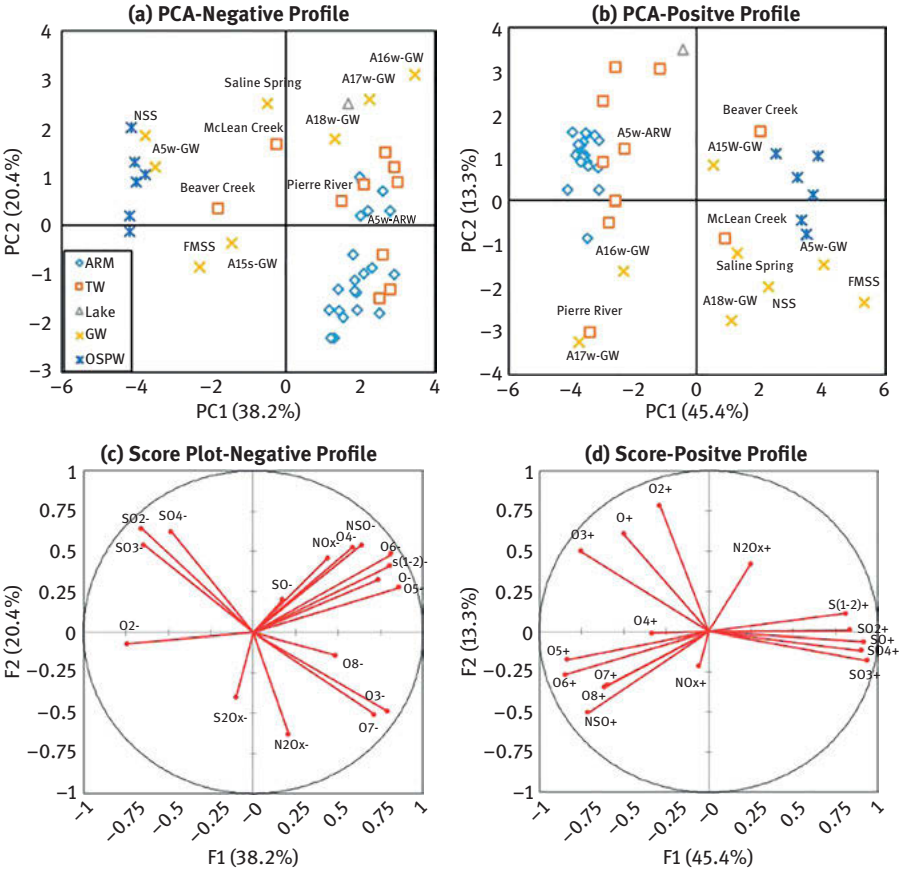

Figure 3.12: Reproduced from Sun et al. [85], with permission. A principal component analysis of heteroatomic profiles in various Athabasca River waters (ARW), tributary waters (TW), groundwaters (GW), lake water (lake), and OSPW samples. A loadings plot (a) and scores plot (c) in negative ionization mode, and loadings plot (b) and scores plot (d) in positive ionization mode are shown.

Likewise, for the PCA of positive-ion ESI data, OSPW also separated away from natural water samples and most tributary sample data, but overlapped with some groundwater sample data. Further work would be needed to attribute the presence of bitumen-derived organics in groundwater and tributaries to natural or anthropogenic sources.

More recent work used ultrahigh-resolution Orbitrap MS data in tandem with other methods (i.e., isotope geochemistry) to help characterize water samples from the AOSR for tracers of anthropogenic versus natural inputs by characterizing the acid-extractable organics (here referred to as NAFCs). In work by Ahad et al. [88], both ultrahigh-resolution Orbitrap MS and stable isotope mass spectrometry were employed to characterize water samples. Samples were initially screened by conducting

PCA on log-transformed relative abundance data describing the percent abundances of all heteroatom-containing NAFC classes detected. This initial PCA screen separated data from McMurray Formation Groundwater (MFGW), seep-pipe samples, and OSPW from other sample types; factor analysis of PCA eigenvectors suggested that the separation was attributable primarily to relative abundances of O_2 and S_nO_x-containing NAFCs. By comparing $\delta^{13}C$ abundance with the percent relative abundance of O_2– plus S_nO_x-containing NAFCs, a strong correlation between these two metrics was identified (0.76), suggesting that C-containing compounds from other sources are more ^{13}C-depleted than NAFCs from OSPW. In addition, this plot helped effectively visualize that although the relative abundances of $O_2 + O_xS_y$-NAFC species from MFGW are similar to those of OSPW, MFGW is statistically ($p < 0.05$) more C^{13}-deplete than OSPW in their dataset. Useful insights such as source discrimination can therefore be gained by pairing FTMS data with alternative methods such as stable isotope analyses.

Further environmental forensic work of AOSR waters was reported that paired HPLC-TOF-MS and supercritical fluid chromatography-Orbitrap MS (SCF-Orbitrap MS) to identify conservative tracers by which to differentiate natural bitumen-derived inputs from OSPW-derived inputs [89]. In this comparison study of the two MS methods, samples included OSPW, OSPW-affected groundwater, and natural bitumen-influenced groundwater. HPLC-TOFMS was used as an initial screening technique, and subsequent analyses of representative samples by HPLC-Orbitrap MS and SCF-Orbitrap MS results verified unambiguous formula assignments. To enhance separation, a long column was used with SCF-Orbitrap MS to identify the presence of structural isomers. Structural characterization of potential tracers was then investigated using ultrahigh-resolution (240,000 at m/z 400) HPLC-MS/MS during product-ion scanning mode. This strategy identified four potential tracers unique to OSPW, and SCF-Orbitrap MS was used to investigate the presence of numerous isomers of one tracer. Although this work successfully identified four potential OSPW tracers, the product ion spectra have not been compared to synthesized authentic standards, so the structural analyses are considered tentative. Nonetheless, these findings report a helpful strategy for building weight-of-evidence for tracing seepage of OSPW to groundwater.

Addressing seasonal variability for environmental monitoring of the Athabasca River is of key importance, as accounting for this variability may assist in differentiating between natural and anthropogenic sources of NAs. In 2007, specialists investigated the spread of toxicants arising from bitumen-related sources in the Athabasca River and its surrounding regions. A field expedition was organized in 2008 to collect samples from the river after 4 months of snow accumulation 50 km away from the main contamination sources. The analysis of the samples revealed that a wide range of toxic impurities within the snow samples affecting the contaminant intake within the river system. It was also stated that erosion may be ascribed with the spread of the pollutants [90].

Kelly et al. studied the loadings of polycyclic aromatic compounds (PAC) to the Athabasca River and its tributary creeks, as well as the Athabasca Delta and Lake Athabasca [91]. In 2008, water samples were collected in two periods: February to March and June to August. Sampling sites upstream and downstream of oil sand industrial activity were chosen, coinciding with erosion of the McMurray geological formation.

Figure 3.13 illustrates the concentrations of PACs in samples collected over two seasons from six tributaries: upstream, midstream, and downstream. The PAC concentrations detected intensified from upstream to downstream, and were also greater in summer than winter. Variations in PAC concentrations were closely linked to sampling locations rather than seasonality in most cases. Nonetheless, the highest PAC concentration was detected downstream during the summer; PAC concentrations in the upstream and midstream were comparatively minor. Figure 3.13 shows a consistent increase in PAC concentrations everywhere due to seasonal differences. Much of this increase may be attributable to increased land disturbance from oil sand expansion between 2006 and 2008. Dissolved PAC concentrations during winter and summer at the Athabasca River, Athabasca Delta, and Lake Athabasca are shown in Figures 3.13C and 3.13D. Greater dissolved PAC concentrations were found in summer than in winter [91]. Seasonality should therefore also be carefully considered in future regional studies characterizing distributions of NAFCs, as seasons are likely to similarly affect environmental dynamics of NAFCs.

Wetlands are key ecosystems in the AOSR, and comprise approximately 50% of the landscape [92]. Mature reclaimed wetlands (i.e., >7 years old) are less toxic to amphibians than immature reclaimed wetlands [93]. It was also observed that the molecular characteristics of industrially sourced bitumen-derived NAFCs are consistent with lesser toxicity to biota in mature wetlands than in young wetlands [86]. Orbitrap MS was therefore used to characterize molecular differences in NAFCs extracted from a variety of wetlands on an active Athabasca oil sand mine lease to characterize this phenomenon [86]. In this exploratory analysis, natural and naturalized off-lease wetlands were differentiable from on-lease wetlands by PCA. Two wetlands were experimental sites that originated from oil sand processed materials (OSPM), and both wetlands segregated from other wetlands during PCA. As shown in Figure 3.14, water from an opportunistic wetland supplemented with OSPM (OWO) was indistinguishable from OSPW, whereas water from an experimental constructed wetland with OSPM (CWO) was substantially different. As follow-up to PCA results, relative proportions of heteroatomic NAFC components were examined, which revealed that NAFCs in CWO contained substantially greater amounts of O_x species (where $x > 2$), suggesting that oxidation and/or breakdown may be occurring in that particular wetland. Future investigations are warranted to unravel the different biogeochemical processes in such wetlands driving toxicity reduction to aquatic organisms, as has been the focus of other studies [94–97].

Environmental samples in the AOSR containing NAFCs are complex, and can be influenced by spatial and temporal sources of variability. The variability in samples can be masked or exaggerated by matrix effects, making data trends difficult to

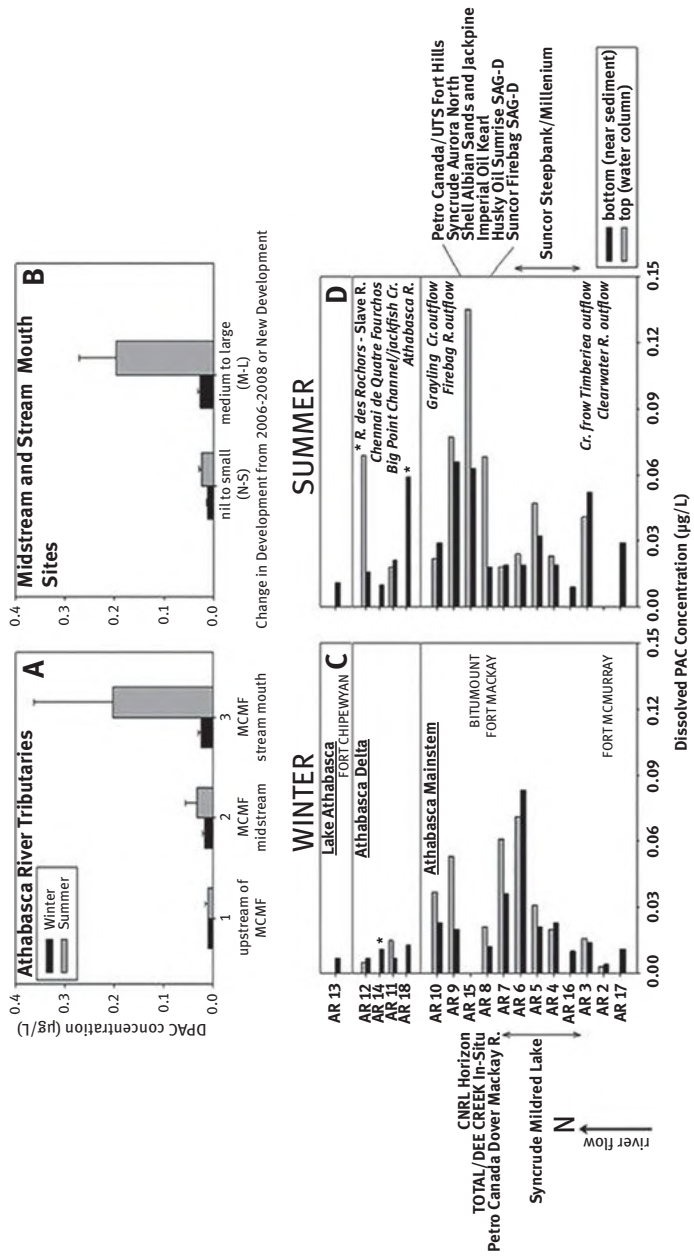

Figure 3.13: Reproduced from Kelly et al. [91], with permission. Dissolved PAC concentrations in µg/L. (A) Tributaries. (B) Development and changes from 2006 to 2008 in midstream and stream mouth sites in Athabasca River and its side creeks the Athabasca Delta and Lake Athabasca. (C) Dissolved PAC concentration in winter. (D) Dissolved PAC concentration in summer. N.B. MCMF: McMurray formation.

decipher. However, FTMS technologies such as FTICR MS and Orbitrap MS allow for the characterization of subtle differences in spatial and temporal samples. FTMS data has provided forensic evidence to support the presence and/or absence of anthropogenic and/or natural bitumen-derived NAFCs in flowing water and in wetlands. Further, these techniques have provided detailed semiquantitative descriptions of the fate and behavior of NAFCs therein that would likely not have been possible with lower resolution instruments. Such data will continue to support environmental monitoring and help improve reclamation techniques and technologies to protect aquatic ecosystems.

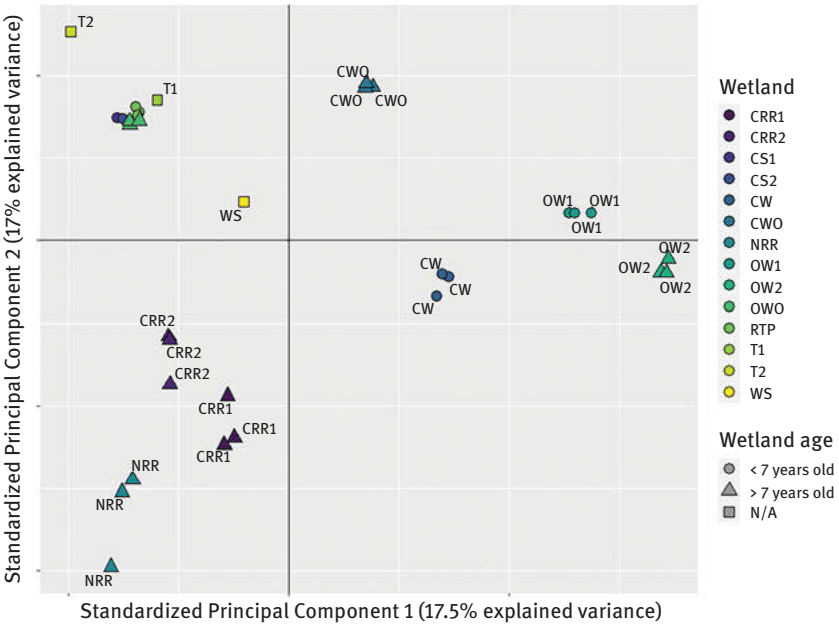

Figure 3.14: Reproduced from Vander Meulen et al. [86] under Creative Commons 4.0 License (https://creativecommons.org/licenses/by/4.0/legalcode). A PCA plot based on Orbitrap MS data from each sample extract. Sampling location replicates are highlighted by common color, and wetland age is highlighted by common shapes. Sites included are tailings pond 1 (T1); tailings pond 2 (T2); collection system 1 (CS1); collection system 2 (CS2); reclaimed tailings pond (RTP); water source used to fill RTP (WS); opportunistic wetland with OSPM (OWO); constructed wetland with OSPM (CWO); opportunistic wetland 1 (OW1); opportunistic wetland 2 (OW2); constructed wetland (CW); constructed regional reference wetland 1 (CRR1); constructed regional reference wetland 2 (CRR2); natural regional reference wetland (NRR).

3.6 Molecular-level characterization of treated OSPW

There is active ongoing work assessing the treatment of NAFCs from the AOSR. Examples of OSPW treatment strategies include the use of engineered wetlands, and buoyant photocatalysts, which contribute to changes in the molecular characteristics of NAFCs in water. However, as a complex mixture, it is difficult to characterize the efficiency of a given treatment based on reduction in the total NAFC concentration and changes in the molecular distributions. The power of FTMS ultrahigh resolving power and mass accuracy is well-suited to meeting this challenge, examples of which are highlighted below.

One study evaluated dynamics of NAFCs in a CWTS wherein samples were taken over the course of 27 days to measure the kinetics of NAFC degradation in the system [98]. Samples were extracted using weak anion exchange (WAX) SPE cartridges, then analyzed by negative-ion ESI-Orbitrap MS using loop injection. Using data from the Orbitrap MS analysis, it was concluded that after the 26 days of treatment the relative abundance of classical NAs was substantially reduced, whereas O_3, O_4, O_5, and O_6-NAFCs all increased in relative abundance. In addition, this laboratory study used the ultrahigh-resolution data to examine the relationship of NA unsaturation to degradation/removal kinetics by plotting progressive snapshots of estimated analyte concentrations at 5 time points across the experiment, shown in Figure 3.16. The visualization of the results in Figure 3.4 demonstrated that NAs concentrations decreased across the range of possible unsaturation values (i.e., double bond equivalents ranging from 1 to 8), with the highest reduction for saturated NAFCs.

Additional efforts have aimed to more completely characterize the fate and behavior of OSPW-derived NAFCs in a broad suite of CWTS configurations [99]. Empowered by ultrahigh-resolution mass spectra describing NAFCs, nonmetric multidimensional scaling (NMDS) analysis was applied to NAFC heteroatom abundance data to interrogate sources of difference in the data, shown in Figure 3.16a. This NMDS, paired with a plot of component vectors of the analysis, visually demonstrates that system A (a CWTS with gravel and vertical up-flow planted with Sedge, or *Carex aquatilis*) was significantly different from other systems tested, as evidenced by a permutational multivariate analysis of variance. Although the results of these systems are statistically different, when changes in the NMDS coordinates of sample data, plotted over time, are superimposed with factor vectors, shown in Figure 3.16b, it is clear that these systems are still similar, driven in a similar direction by similar factors. The authors subsequently examined relative proportions of major O_x-NAFCs (i.e., O_2, O_3, and O_4-NAFCs), and found that NAFCs in all systems decreased total concentrations, and relative abundances of O_2-NAFCs decreased in all systems, with corresponding increases in O_3 and O_4-NAFCs. There were corresponding decreases in acute toxicity to Fathead minnows

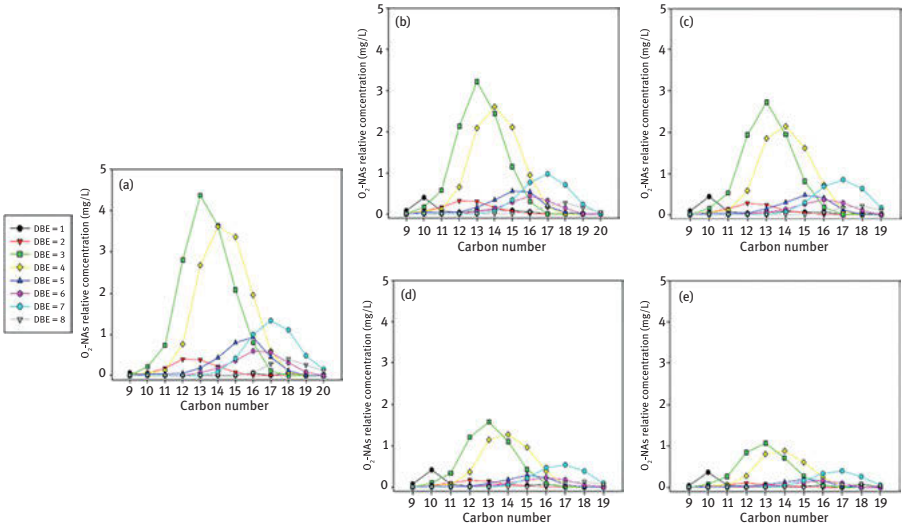

Figure 3.15: Reproduced from Ajaero et al. [98], with permission. The distribution of O2-NAs based on carbon number and DBE values: (a) untreated OSPW on day 0 and in the nonaerated treatment wetland, (b) on day 7 (c), on day 14, (d) on day 21, and (e) on day 27. Concentration data were corrected for evapotranspiration.

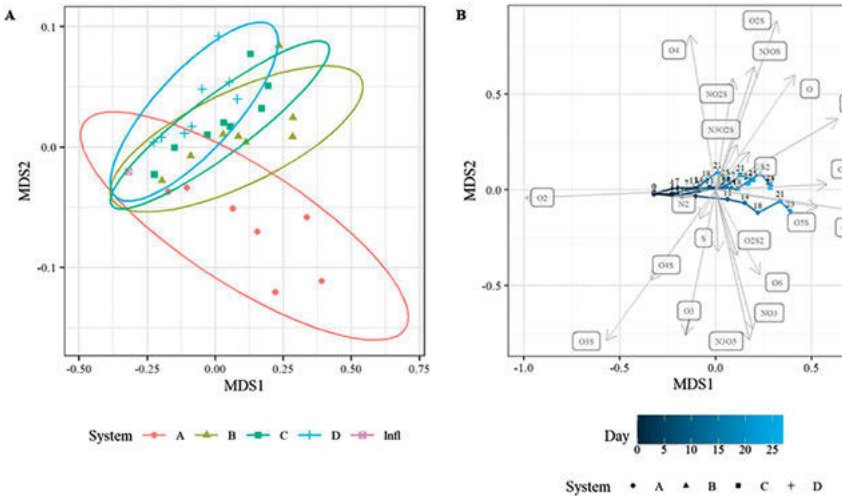

Figure 3.16: Reproduced from Simair et al. [99], with permission. An NMDS analysis was performed using all the NAFC species to assess bulk changes in NAFC chemistry over the treatment period within the CWTSs operated with OSPW as a closed loop over time. In (A) a permutational multivariate analysis of variance (PERMANOVA) was used to determine statistical significance of beta-diversity values. The overall NAFC distribution for system A was the most different relative to systems B, C, and D. As an extension of NMDS analysis in (A), the component vectors (NAFC classes) are shown in (B) and cells within a given system are linked to show change over time in relation to the NAFC classes.

(*Pimephales promelas)*. In addition, the CWTSs planted with sedge (*Carex aquatilis*) reduced O_2-NAFCs and NAFC-related acute toxicity most quickly compared to other CWTS investigated. This exploratory work on CWTS optimization empowered by FTMS demonstrated the relative importance of plant selection in engineering a CWTS for treatment of NAFCs.

Ultrahigh-resolution mass spectrometry has also made substantial contributions to helping understand the molecular dynamics of photocatalytic treatment strategies. One team treated OSPW with buoyant TiO_2 photocatalysts and examined apparent kinetic rates of detectable dissolved organic components in basic, neutral, and acidic fractions, ionized in both positive and negative modes [100]. Lab-scale photocatalysis experiments were conducted, and samples were collected throughout the duration to examine the treatment kinetics. Subsamples were pH-adjusted to acidic (pH < 2), neutral (pH 7), and basic (pH 10.5) conditions, then liquid-liquid extracted prior to analysis by ultrahigh-resolution Orbitrap MS applying both positive and negative ESI. By using exact-mass data, empirical rate constants were determined for the removal and/or emergence of new O_2-containing components, shown in Figure 3.17. Oxidative degradation of OSPW-derived organic species was observed across different heteroatomic classes. For example, O_2^-, SO^+-, and NO^+-NAFCs were consistently oxidized, decreasing quickly in relative concentration. Photocatalysis degraded the heaviest and most unsaturated O_2-containing formulae, and this was consistent across most extraction and ionization conditions, shown in Figure 3.17. The authors postulated that lower-molecular weight compounds emerged as a result of bond scission in higher-molecular weight mixture components; this observation was supported by related work evaluating the reaction kinetics and mechanics of photocatalytic degradation using model compounds [101]. Such an experiment simultaneously evaluating degradation rate constants of a voluminous number of analytes would not be feasible without ultrahigh-resolution mass spectrometry.

Photocatalytic treatment is thus a promising technique for toxicity reduction of OSPW. The question arises as to the effectiveness of naturally occurring rates of photolysis of bitumen-derived water-soluble organics in OSPW, and effects thereof on fate and behavior of these complex organic components in aquatic systems. Challis et al. subjected whole OSPW, acid-extractable organic (AEO) (i.e., NAFCs), and base-extractable organic (BEO) samples to simulated sunshine under controlled conditions, and examined gradual changes to the composition of whole OSPW, AEOs, and BEOs, as characterized by both positive- and negative-mode ESI-Orbitrap MS [102]. The investigation demonstrated that natural photolysis can take place in OSPW, and that whole OSPW was the most susceptible to photolysis, as compared to either AEO or BEO fractions. Because this study used ultrahigh-resolution mass spectral data, it was possible to observe that O_2^- containing species from OSPW with the highest double bonding equivalents (i.e., most unsaturated) were preferentially photodegraded, shown in Figure 3.18. The authors use this data to estimate half-lives of OSPW-derived AEOs at approximately

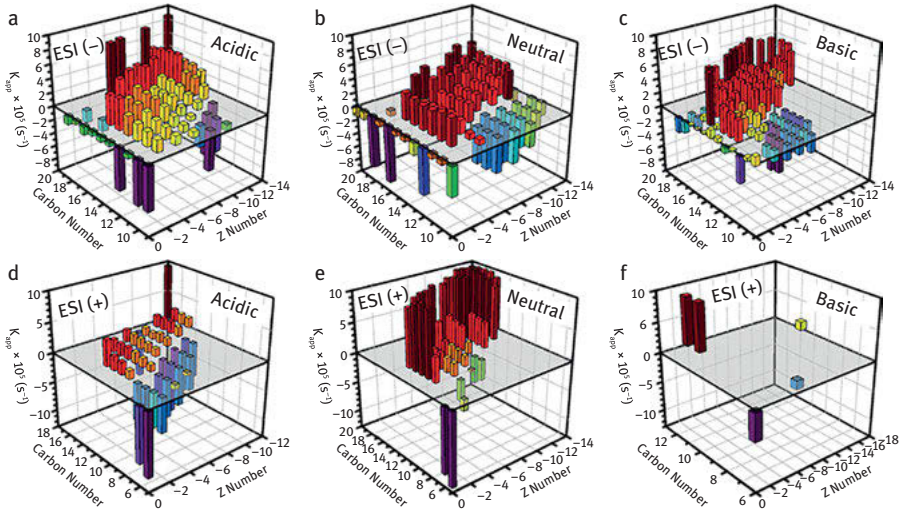

Figure 3.17: Reproduced from Leshuk et al. [100], with permission. Estimates of pseudo-first-order rate constants (k_{app}) of photocatalytic degradation of (a)–(c) O_2^- and (d)–(f) O_2^+ species in the (a) and (d) AEO, (b) and (e) NEO, and (c) and (f) BEO fractions. Positive k_{app} values indicate rates of disappearance, while rates of appearance of new species are plotted as negative values of k_{app}.

122–384 days, depending on seasonal light intensity. The authors emphasized that whole OSPW is usually turbid, effectively preventing photolytic degradation from occurring, making improvements in OSPW water clarity an important subobjective to accelerate degradation of organic contaminants therein.

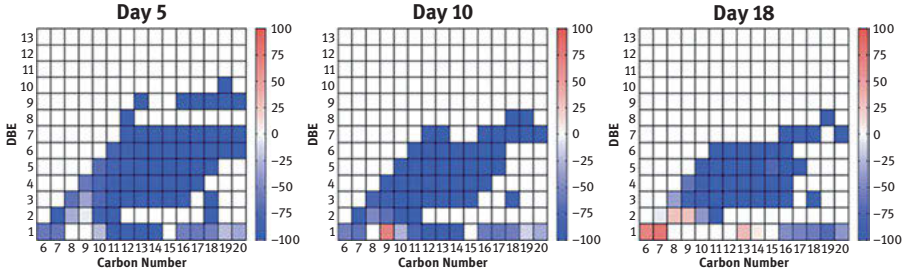

Figure 3.18: Reproduced from Challis et al. [102], with permission. Heat maps of percent change relative to day 0 for O_2^- species in whole OSPW after 5, 10, and 18 days of irradiation.

These studies collectively add to improve understanding of dynamics of NAFCs, and related compounds in degradation studies. Ultrahigh-resolution Orbitrap MS helped describe the results of pilot-scale treatment wetland experiments, showing that these systems were capable of decreasing constituent concentrations in treatment

systems across a wide range of compound classes [98]. In addition, similar studies using multivariate ordination techniques demonstrated the capability of wetlands to alter the makeup of NAFCs by preferentially increasing/decreasing particular heteroatomic classes of NAFCs, which correspondingly decreased acute toxicity to fathead minnows (*Pimephales promelas*). Further insights into the mechanism of photodegradation were also achieved [100–102], emphasizing the descriptive utility of FTMS techniques for describing degradation of OSPW-NAFCs.

3.7 Contributions to toxicity-directed analysis of OSPW for identification of principal organic components

It is difficult to attribute causes of toxicity in a mixture such as OSPW, which contains many thousands of organic components, including polar and nonpolar organic species, as well as suspended and dissolved solids, salts, and metals. Nonetheless, the acidic fraction from OSPW has been consistently implicated as the primary source of acute toxicity [12, 103, 104]. The particular mechanism(s) by which acidic organic components cause toxicity is not fully established.

One study compared toxicity assay results from fractionated OSPW to data from HPLC-Orbitrap mass spectrometry [11]. Morandi et al. subjected OSPW to three sequential rounds of fractionation under neutral (F1-NE), acidic (F1-AEO), and basic conditions (F1-BEO), and evaluated 96 h acute toxicity in fathead minnows (*Pimephales promelas*) and in Microtox assays to help identify specific sources of acute toxicity. The F1-BEO fraction (i.e., the compounds extractable from OSPW in the final sequential fractionation at pH > 11) was the least toxic in both assays; F1-NE was the most toxic, followed by F1-AEO. By examining profiles of dissolved components characterized by negative-ion ESI Orbitrap MS, the authors found that the initial extraction (i.e., F1-NE) had extracted most of the classical NAs, and so subsequent rounds of extract fractionation were carried out to separate NAs and/or other organic acids from the neutral organic species present in F1-NE, shown in Figure 3.19. The secondary fractionation procedure generated two fractions, where one should have contained nonpolar organic species (F2-NE1), and the other fraction should have contained organic acids (F2-NE2). To further characterize the effects of the acidic organic fraction, F2-NE2 was subfractionated chromatographically using repeated isocratic HPLC elutions, generating a highly polar fraction (F3-NE2a), and a fraction of everything else that remained (F3-NE2b), which should have contained polar neutral compounds. An intriguing result of this fractionation was that the final two tertiary fractions (F3-NE2a and F3-NE2b) were more toxic when recombined than when tested separately, suggesting at least two separate toxicity mechanisms, which was supported by the

ultrahigh-resolution mass spectrometry data; only F3-NE2a contained O^- compounds and the most O_2^- organic acids (i.e., classical NAs), whereas only F3-NE2b contained O^+ compounds, suggesting polar neutral compounds therein. The characteristics of NAs in each of these fractions are remarkably different from one another, as shown in Figure 3.19. These findings reinforce that although O_2^- organic acids are responsible for the bulk of acute toxicity, polar neutral compounds also contribute meaningfully to acute toxicity in fathead minnows. Overall, this application is an excellent example of the utility of FTMS for providing insights on the mechanisms of toxicity of OSPW-NAFCs, which would not otherwise be apparent.

Other studies have demonstrated the advantages of ultrahigh-resolution FTMS for measuring chemical dynamics of NAFCs during biological treatment. One such study by Yue et al. used ultrahigh-resolution Orbitrap MS to investigate the dynamics of NAFCs in a continuous-flow biofilm reactor. Both treated and untreated OSPW were fractionated by the use of SPE [105]. Estrogenic fractions, and those fractions which had the greatest decrease in estrogenicity after treatment were further fractionated by semipreparative reverse-phase HPLC. Results from this experiment demonstrated that the biofilm reactor removed about 40% of total NAs as compared to an abiotic control, and a corresponding decrease of 73%, and 22% decrease in estrogenicity, as measured using a Microtox assay. The biotreatment apparently increased the proportion of O_2-NAFCs, suggesting that O_3- and O_4-NAFCs are more readily biodegraded than O_2-NAFCs. Furthermore, NAs with a DBE < 5 degraded most readily, highlighting the recalcitrance of highly cyclic and/or aromatic compounds to biological treatment, consistent with previous studies [106]; the relative abundance of most unsaturated NA species were observed to increase over the course of treatment. The residual toxicity measured after treatment was most likely attributable to recalcitrant NAs with DBE ≥ 5. This work highlights the utility of biotreatment, the need to better understand the biodegradation of aromatic compounds where possible, and the limitations of biofilm treatment of aromatic and/or polyaromatic NAs.

There is a significant need for reference standards to generate representative, replicable results when assessing OSPW-related toxicity. One study sought to contribute to addressing this need by assessing whether or not commercially available mixtures of NAFCs could serve as representative surrogates of OSPW-derived NAFC-related toxicity. In vivo toxicity testing was carried out on three different model organisms (*Hyalella azteca*, *Allivibrio fischeri*, and *Lampisilus cardium*), and samples were characterized with ultrahigh-resolution Orbitrap MS [107]. The investigators characterized samples of fresh OSPW (i.e., from tailings discharge or from active tailings ponds) and aged OSPW (i.e., from an experimental pond) for both toxicity and mass spectrometric characteristics for comparison. Mass spectrometric analysis showed that O_2-NAFCs (i.e., classical NAs) were the predominant mixture component detected in all cases, but that OSPW-derived NAFCs have much greater underlying diversity of subclasses of NAFCs (i.e., species other than O_2-NAFCs) than did

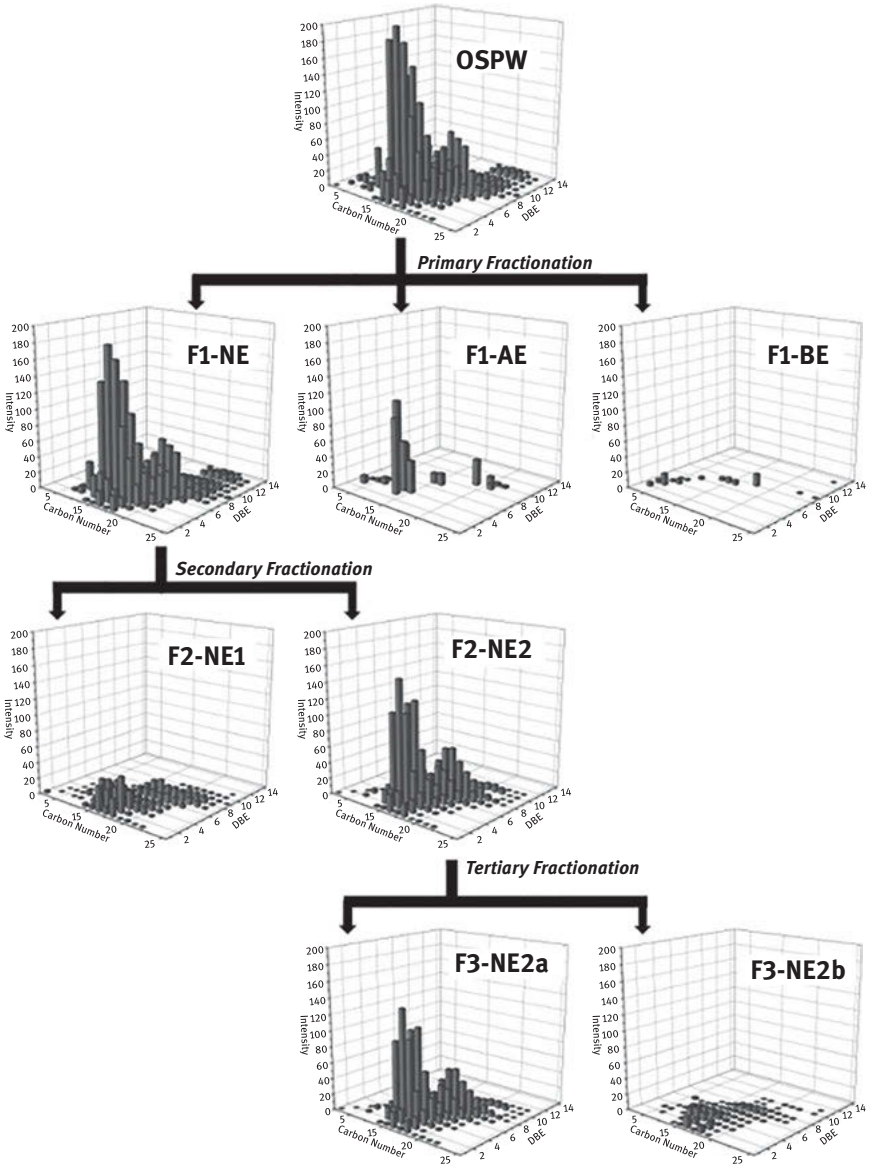

Figure 3.19: Reproduced from Morandi et al. [11], with permission. Profiles of naphthenic acids (O_2^- class) by carbon number and double bond equivalents in each OSPW fraction, compared to unfractionated OSPW. Intensity has been normalized to the response in unfractionated OSPW.

commercially available NA mixtures. Commercial mixtures of NAFCs contained similar amounts of O_2-NAFCs when compared to fresh OSPW, but commercial mixtures of NAs contained a greater proportion of saturated, straight-chain NAs, relative to OSPW-derived NAFCs. Further, aged OSPW contained a lesser proportion of O_2-NAFCs relative to fresh OSPW and commercially sourced mixtures. Commercially sourced NAFC mixtures were generally more toxic than OSPW-derived NAFCs, and aged OSPW was more toxic to *Lampsilis cardium* than were any of the fresh OSPW samples, shown in Figure 3.20. The toxicity endpoints illustrated in Figure 3.20 are environmentally relevant, as NAFC concentrations in OSPW can range from 20 to 120 mg/L [108], and $LC_{50}/IC_{50}/EC_{50}$ values measured ranged from approximately 1–100 mg/L. This work demonstrates that commercially available NA mixtures are dissimilar to OSPW-derived NAs/NAFCs, implying that work intended to assess Athabasca OSPW-derived toxicity ought to be derived from Athabasca oil sand OSPW.

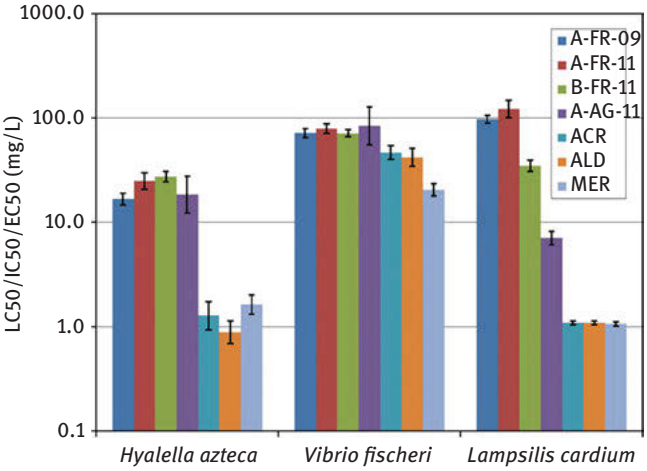

Figure 3.20: Reproduced from Bartlett et al. [107], with permission. Sensitivity of three aquatic species when exposed to naphthenic acid fraction components (NAFCs) extracted from four sources of oil sand process-affected water (OSPW) and three commercial naphthenic acid (NA) mixtures. The four NAFCs are 2009 Industry A Fresh (A-FR-09), 2011 Industry A Fresh (A-FR-11), 2011 Industry B Fresh (B-FR-11), and 2011 Industry A Aged (A-AG-11). The three commercial NA mixtures are Acros (ACR), Aldrich (ALD), and Merichem (MER). The three test species are *Hyalella azteca* (freshwater amphipod), *Vibrio fischeri* (marine bacterium, Microtox® assay), and *Lampsilis cardium* (freshwater mussel larvae). Data from NAFC tests are concentrations measured in exposure waters from *Hyalella azteca* tests (mg/L). Data from commercial NA tests are concentrations measured gravimetrically in stock solutions (mg/L). Toxicity endpoints were determined using nonlinear regression methods. Error bars are 95% confidence intervals.

Despite the fact that the toxicity of OSPW has long been understood to be strongly associated with the dissolved acidic organic fraction [103, 104], it is still difficult to definitively prove the toxicity of specific mixture components within the acidic fraction. As mentioned above, studies have sought to understand the toxicity of OSPW fractions with characterization by ultrahigh-resolution FTICR MS or Orbitrap MS. One study sought to systematically account for the contributions of acidic and other constituents to the toxicity of OSPW using rainbow trout (*Oncorhynchus mykiss*) for a toxicity identification evaluation (TIE) on different fractions of OSPW [12]. As a baseline evaluation, trout fry were exposed to OSPW concentrations from 6.25% to 100% v/v, and a negative control of dechlorinated municipal tap water. The authors of this study took great care to account for potential interferences from metals, volatile organic components, suspended particulates, and salinity. The conclusions of this study were largely in-line with previous findings, as metals, salinity, and suspended particulates did not significantly contribute to acute toxicity in rainbow trout. Furthermore, extraction of OSPW with a C_8-functionalized SPE cartridge removed all acute toxicity; adding the eluent from the SPE cartridge back to the water reintroduced toxicity, demonstrating that the primary toxicants of concern were retained during SPE. The molecular characteristics of NAFCs from were measured by Orbitrap MS using additional C_8-adsorbent SPE extractions sequentially eluted in methanol:water with increasing proportions of methanol to elute increasingly nonpolar fractions. Elevated mortality was observed in SPE fractions eluted with 70–90% methanol; the 50% methanol fraction had an NA concentration similar to the 85% methanol fraction but did not cause any acute toxicity. A PCA procedure was used to nonspecifically characterize similarity or differences between fractions. Plotting percent mortality data against PC1 scores revealed a strong relationship between NAFC molecular characteristics and percent mortality. Loading scores from the PCA revealed that O_2-NAFCs (i.e., classical NAs) were strongly associated with more toxic fractions. Further, structure–toxicity relationships of individual NAs were modeled following the work of Scarlett et al. [109] investigating the relationship between acute potency NA carbon number. When modeled toxicities were compared to relative abundances of different NAs, it was shown that increasing toxicity corresponded to decreasing polarity and increasing molecular size.

The aforementioned study by Hughes et al. [12] used rainbow trout (*Oncorhynchus mykiss*) as a model organism for TIE testing because of the rainbow trout's known sensitivity to the acutely toxic effects of OSPW. Another study used ultra-high -performance chromatography with ultrahigh-resolution Orbitrap MS to investigate toxic mechanisms by examining uptake of NAFCs during an in vitro experiment using a rainbow trout gill cell line, RTgill-W1 [110]. The authors hypothesized that they would observe pH-dependent cytotoxicity as an elevated pH would prevent ionizable organics such as NAFCs from partitioning across cell membranes, making them less bioavailable. This study therefore assessed the dynamics of model compounds, as well as technical mixtures, and OSPW with the trout gill cell line. After an initial in vitro toxicity assessment, samples were extracted, and ionizable organic components

were assessed by Orbitrap MS, only the acidic fraction of OSPW was observed to cause cytotoxicity, consistent with prior studies, To further assess the effect of pH on mixture components crossing the gill epithelium, cells were cultured in permeable 0.4 μm pore diameter inserts suspended in 24-well plates; toxicants were loaded into the upper (apical) chamber, and samples were taken from both the apical and lower (basal) chamber of the well plates [110]. Mass spectrometric characterization of technical NA mixtures and OSPW fractions from apical and basal chamber samples showed that weak acid permeability was highly pH-dependent, being inversely proportional to pH with single compounds and technical mixtures. It was suspected that NAFCs may be retained within cells or membranes. At pH 8.5, cell extracts were relatively rich in NAFCs, despite elevated pH, which suggested active transport and uptake of ionized compounds. To investigate the role of active transport in uptake of NAFCs, the assay was repeated with the addition of cyclosporin A to inhibit active transport proteins. The results of this assessment are illustrated in Figure 3.21. After the addition of an inhibitor, the relative abundance of OSPW-derived compounds was substantially lower, seeming to suggest that an active transport mechanism is required for uptake of OSPW-derived toxicants. These results were compared to 96 h in vivo tests of rainbow trout fry with 10% v/v raw OSPW. The trout fry produced results seeming to contradict in vitro testing, as the whole-body loadings of OSPW-derived NAFCs were observed in order of pH 7.4, 6, then 8.5. In contrast, gill cell loadings of NAFCs were observed, to be greatest at pH 8.5, 7.4, then lowest at pH 6. In addition to having the highest concentration of observed NAFCs, gill cells at pH 8.5 also contained the highest number of unique molecular species of NAFCs, as identified by Orbitrap MS. These collective findings suggest that ionized organic acids, such as NAFCs are retained in the gills at higher pH, or are actively transported into tissues, in contrast to the hypothesis that NAFCs would permeate cells to a greater extent at lower pH.

The studies highlighted herein all benefit from the use of ultrahigh-resolution Orbitrap MS for characterization of NAFCs in complex scenarios. The analyses presented here demonstrate the improved insights to toxic modes of action that may have not otherwise been possible without detailed molecular characterization.

3.8 Examples from petroleum analysis

In addition to being contaminants of environmental concern in the Athabasca oil sand region of Alberta, NAFCs are also a concern for petroleum processing infrastructure due to their contributions to corrosion [23, 54]. There are therefore reviews detailing methods to manage and remove acidic content from petroleum products prior to added-value processing [111]. Oil with a low total acid number (TAN, which describes the amount of solid KOH required in [mg KOH]/[g oil] to neutralize acidic

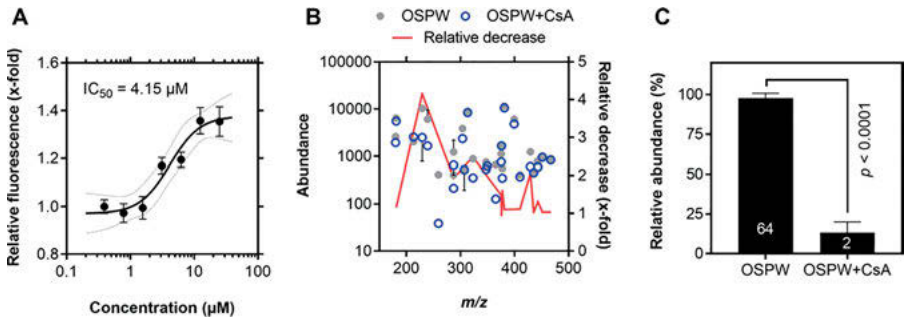

Figure 3.21: Reproduced from Brinkmann et al. [110], with permission. Inhibition of calcein AM efflux in RTgill-W1 cells (A) and reduction of the abundance of various chemical species from OSPW in basal media (B, C) following exposure to the active transport inhibitor cyclosporin A (CsA) at pH 8.5. (A) Data points represent mean values, error bars the standard deviation of $n = 6$ technical replicates. A four-parameter logistic model was used to fit experimental data (solid lines) and 95% confidence intervals computed (shaded areas). (B) Data represent the mean ± standard deviation of raw abundances (areas) of $n = 2$ replicate inserts. Only those chemicals present in both treatments are shown. The solid red line indicates the x-fold reduction in chemical abundance following CsA treatment compared to OSPW alone. (C) Data represent the mean ± standard error of the mean and were normalized to the mean of the group with the greatest relative abundance. The respective number of chemicals with the greatest permeability in each group is provided within the bars. Relative abundance in basal media was significantly lesser following CsA treatment compared to OSPW alone (paired Student's t-test).

components in the oil), is inherently more valuable than oil with a higher TAN, owing to the need for additional capital expenditure to process acidic oil.

In some cases, extraction techniques contribute to the final NAFC concentrations and characteristics in crude oil. As an example, NAFCs may be generated by in situ combustion (ISC) oil recovery techniques [112]. ISC is a recently developed petroleum production technique for heavy oil recovery where burning is induced within the reserve by injecting oxygen gas and igniting the mixture. By allowing partial combustion of petroleum products, the deposit is heated, easing flow without the use of solvents or steam; this heat can also "crack" some components to lower molecular weight, further easing the recovery of oil from heavy petroleum deposits [113]. One study by Zhang et al. [112] used FTICR MS to characterize lab-generated samples and to demonstrate how ISC recovery may contribute to loads of NAFCs in oil. Zhang et al. compared oil put through simulated ISC to oil produced using typical steam-recovery methods. The oil processed by ISC had a notably lower average m/z when analyzed by negative-ion ESI FTICR MS, but little apparent difference when analyzed by positive-ion APPI FTICR MS. In addition, heteroatomic NAFC species were characterized by negative-ion ESI, which showed that O_2-NAFCs, as well as O- and O_3-NAFCs to a lesser extent, increased in relative abundance over the course of ISC. The unsaturation and molecular weight of these components also shifted, as was communicated by carbon number versus DBE plots, shown in Figure 3.22.

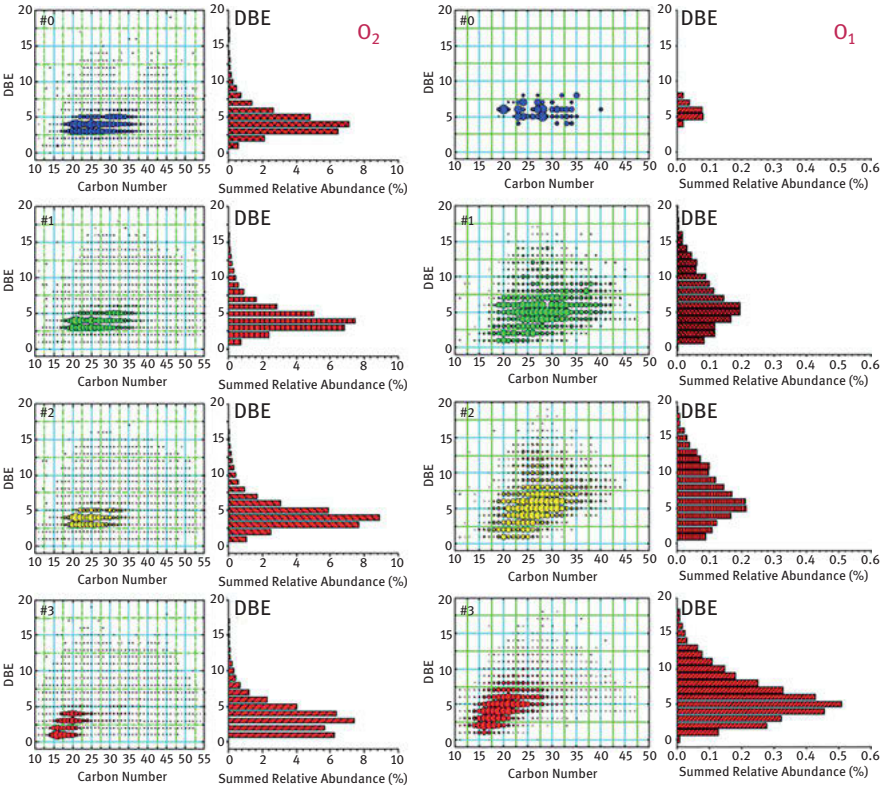

Figure 3.22: Reproduced from Zhang et al. [112], with permission. Double bond equivalents values versus carbon number plots of the O_2 (left) and O_1 (right) species by negative-ion ESI FTICR MS, progressing from top to bottom in order of least-to-most processed by simulated in situ combustion. Dot size is representative of relative abundance of each component formula.

For complex crude oil, it is useful to understand how components biodegrade, and to elucidate particular mechanisms of biodegradation. Liu et al. used FTICR MS to characterize the generation or degradation of polar organic compounds, including NAFCs during biodegradation of crude oil [106]. Two bacterial strains endogenous to the region where the oil was extracted were used to biodegrade the oil under aerobic conditions for 90 days. After degradation, polar organic compounds in the crude oil were liquid–liquid extracted and analyzed by negative-ion ESI on a 9.4 T FTICR MS. One strain of native bacteria (*Pseudomonas aeruginosa* XJ16) degraded the oil to a greater extent than the other (*Acinetobacter lwoffii* XJ19) across almost every category. Nonetheless, both strains successfully degraded *n*-alkanes, *n*-alkylcyclohexanes, and dicyclic sesquiterpanes. These strains affected polar organic species differently, where *P. aeruginosa* slightly increased the amount of NO-, NO_2-, O-, and O_3-containing species relative to raw crude, and slightly decreased N-, O_2-, and O_4-containing components. In

comparison, *A. lwoffii* substantially decreased the relative abundance of N- and O-containing components. Notably, polar organic components became more compositionally complex after treatment by either bacterial cultures, as degraded oils contained higher relative abundances of unsaturated molecular formulae as compared to crude oil, shown in Figure 3.23 [114]. These observations are similar to trends observed in treatment wetlands, as treatment wetlands preferentially degrade saturated high-molecular weight compounds, which leads to increasing relative abundances of more highly unsaturated NAFCs [67, 98, 115], suggesting potentially common degradation mechanisms between wetland treatment systems and bacterial treatment.

FT-based mass spectrometry technologies therefore continue to offer powerful insights for the characterization of polar components in petroleum, such as NAFCs. These techniques provide data that helps characterize the fate of NAFCs through processing, as well as in biodegradation. As instrumentation continues to be further developed, it is reasonable to anticipate improvements in data processing capabilities and enhanced insights for molecular characterization of crude oils.

3.9 Further advancements in FTMS

The challenges faced by the field of petroleomics help to drive advances in FTMS instrumentation and data processing [42, 116], offering improvements to a variety of complex mixture analyses, including analyses of OSPW and NAFCs.

Improvements in Orbitrap technology have resulted in resolving power as high as 1,000,000 at m/z 200 [117]. Until such recent innovations, FTICR MS was typically required for molecular level characterization of complex crude oil samples. Some work has sought to assess whether improvements to Orbitrap technology have been able to provide adequate resolving power to characterize components of crude oil [118]. Oil samples were dissolved in methanol and toluene and analyzed for polar organic components under both negative and positive-ion ESI using an Orbitrap Elite instrument, a "MegaOrbitrap," and a 7.2 T FTICR MS for comparison. Sample data were compiled from stitched mass transients. This work found that for all mass spectrometers tested, resolution was sufficient for assignment of formulae to negative-ion ESI data; in contrast, during positive-ion ESI, the 7.2 T FTICR MS and MegaOrbitrap MS detected the widest varieties of formulae. Overall, the performance of a MegaOrbitrap MS was similar to the 7.2 T FTICR MS, with lower transient times, and similar formula assignment, shown by Figure 3.24**.** However, this technology has yet to be commercially available, while there have also been advances in commercially available FTICR instrumentation in the meantime.

Improvements to FTICR MS instrument performance have also recently been afforded by ongoing analyser cell innovations and higher magnetic field strengths. The dynamically harmonized ICR cell, introduced in 2012, enables longer ion

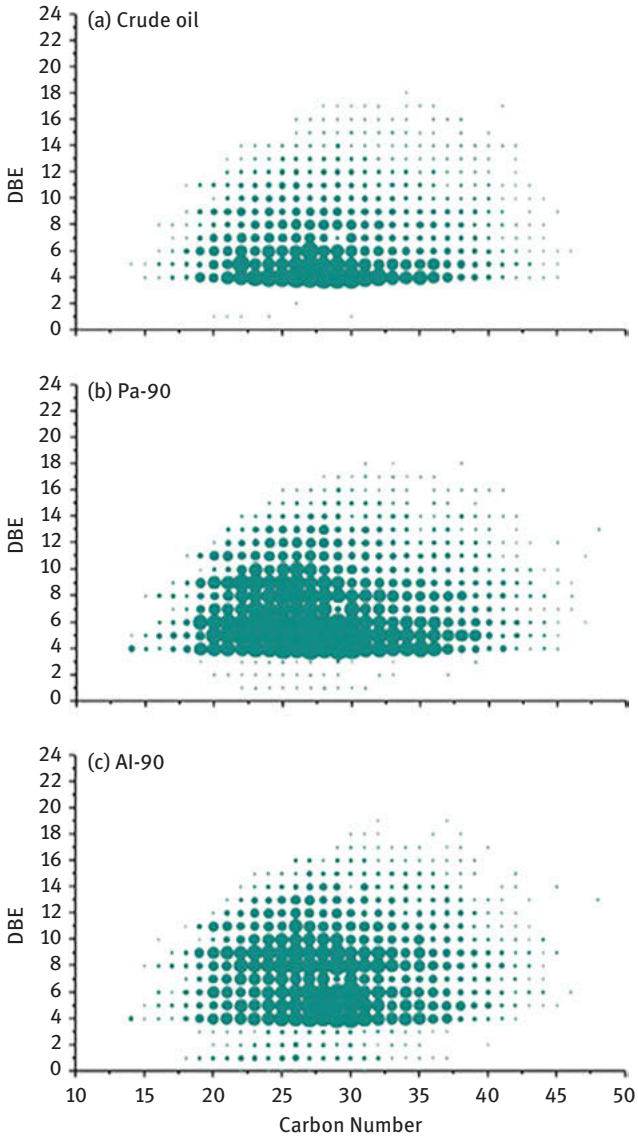

Figure 3.23: Reproduced from Liu et al. [114], with permission. Iso-abundance plots of DBE versus carbon number for the O-class in the original oil, and oils degraded for 90 days by *Pseudomonas aeruginosa* (Pa-90) and *Acinetobacter lwoffii* (Al-90).

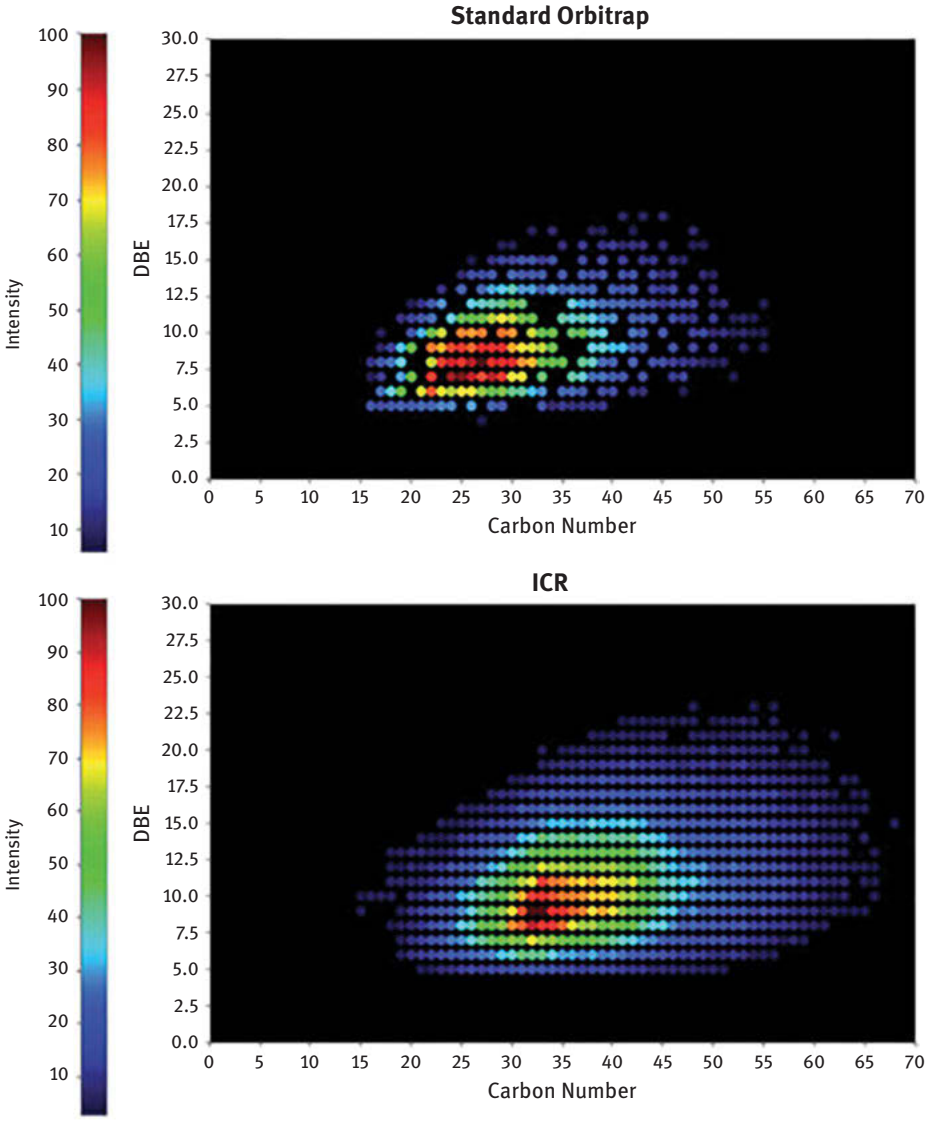

Figure 3.24: Reproduced from Schmidt et al. [118], funder a Creative Commons 3.0 license (https://creativecommons.org/licenses/by/3.0/legalcode). Carbon number versus DBE for the N-class of petroleum compounds as determined by positive-ion ESI data as collected with a standard Orbitrap, a 7.2 T FTICR MS, and a MegaOrbitrap.

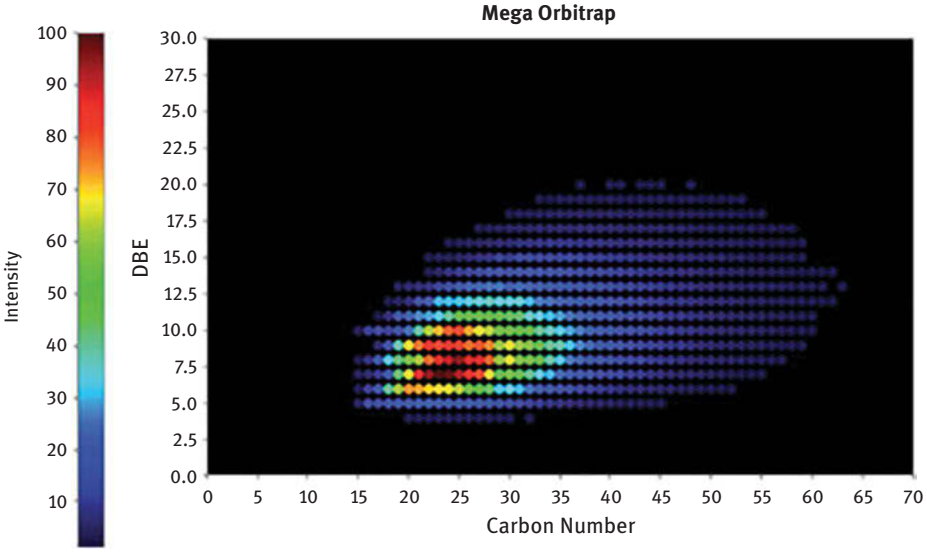

Figure 3.24 (continued)

detection times by compensating for magnetic field inhomogeneities, resulting in significantly increased resolving power [119]. ICR analyser cells may also be designed to provide quadrupolar detection (2 ω) utility, offering either a twofold increase in resolving power for the same acquisition time or else the same resolution but at twice the speed [120, 121]. The latter mode of operation is suitable to hyphenation with GC, as recently demonstrated for the analysis of petroleum-contaminated sediment extracts from Staten Island [121]. Suwannee River fulvic acid and petroleum samples were recently analyzed using a FTICR mass spectrometer with a 21 Tesla magnet, demonstrating improvements to mass accuracy and resolving power, and greater numbers of molecular assignments compared to a lower field FTICR MS instrument [122].

A major innovation in data processing of FTICR MS data is the use of "stitched" spectra, wherein mass spectra with limited ranges can be collected in series to improve resolving power, and then the full mass range of a reconstituted spectrum can be stitched together from the smaller scans [123–125]. This technique minimizes space-charge effects in FTICR instruments, increasing dynamic range, maximizing the number of detectable peaks, and mass accuracy of peak assignments. In one example, a South American vacuum residue sample was analyzed by a 12 T FTICR MS with positive-ion APPI across a detection range of m/z 250–3,000, and a broadband spectrum was compared to a mass spectrum which was produced by stitching segments using the novel algorithm, Rhapso [123]. As part of the processing, the algorithm corrected the abundances at the edges of the segments due to the influences of the isolation steps. As is shown in Figure 3.25, the Rhapso-reconstituted mass spectrum detected a wider mass range of components with greater sensitivity, as compared to a broadband

spectrum. This technique also led to peak assignments with lower overall mass error across most of the mass spectrum versus a broadband spectrum.

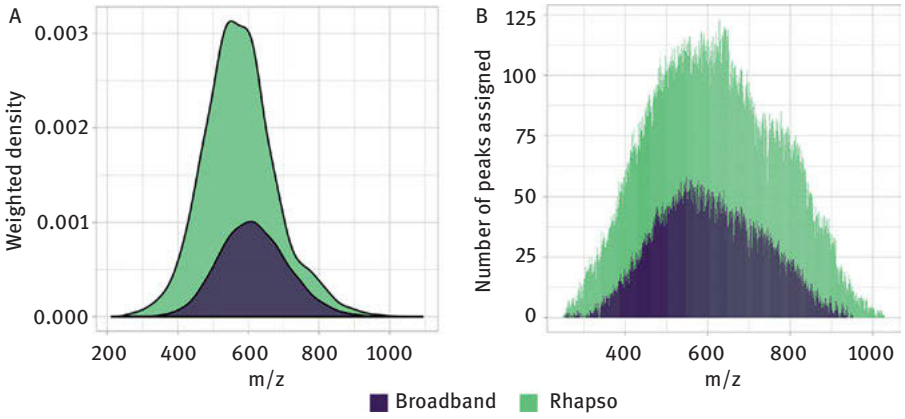

Figure 3.25: Reproduced from Gavard et al. [123], with permission. (A) A density plot based on all the *m/z* measured in both broadband and stitching mode. The plot shows the broader peak distribution in stitching mode due to the increased number of peaks in the low intensity regions. (b) Comparison of the number of assignments per *m/z* width of using both techniques.

The spectral stitching approach and Rhapso algorithm were recently employed in combination with a new experimental approach to provide a new mode of operation for FTMS instruments: operation at constant ultrahigh resolution (OCULAR) [45]. This workflow was developed to overcome some of the challenges to complex mixture analysis via conventional broadband FTICR MS, namely limitations of dynamic range and the well-known decrease in resolving power with increasing mass-to-charge ratio for a given experiment. Importantly, the classic spectral stitching approach was modified to increase the time domain signal length for each subsequent spectral window, enabling operation at constant ultrahigh resolving power across the full *m/z* range. The effectiveness of this workflow was demonstrated for a nondistillable fraction of a vacuum residue of a South American crude oil; this particular sample was so complex that it could not be analyzed via a traditional FTICR MS broadband experiment. Analyzing this sample via OCULAR, the authors demonstrated a complexity of up to 300 individual peak assignments per nominal *m/z* (Figure 3.26), establishing a new world record of 244,779 unique molecular assignments for a single sample [45].

In addition to improvements to instrumentation and workflow approaches, complex sample mass spectra may be enhanced through refined data processing [126]. For decades, data output from FTMS instruments has been in the form of a magnitude mode spectrum, which is "phase-independent" and so more easily calculated, but the performance is lower than could potentially be achieved [127]. More recent advances have led to the ability to apply phase-correction to obtain absorption mode spectra [35,

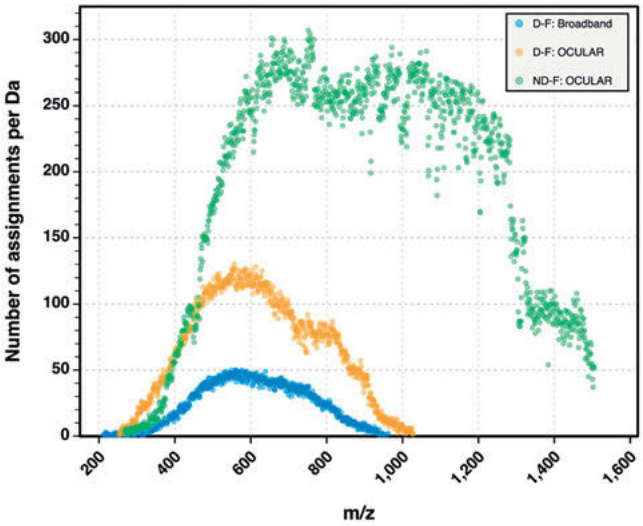

Figure 3.26: Reproduced from Palacio Lozano et al. [45], with permission. Number of peak assignments per nominal Dalton for the mass spectrum of a nondistillable fraction (ND-F) of crude oil, processed using the OCULAR workflow (green profile). Assignments per nominal Dalton also shown for the mass spectra of a distillable fraction (D-F) of crude oil obtained using OCULAR (orange profile) and via a traditional broadband experiment (blue).

127, 128]. A phase-corrected spectrum is improved over the magnitude mode spectrum with increased signal-to-noise ratio, and up to a twofold increase in resolving power. Commercial software packages now offer absorption mode (also known as "phasing") data processing for FTMS data.

Other notable data handling developments include the use of the aromaticity index (AI), developed by Koch and Dittmar, which indicates the density of the carbon–carbon double bonds in a specified molecule. AI is uniquely calculated from the exact molecular masses of a NOM component [129]. The AI was modified (AI_{mod}) to offer improvements such as for the consideration of carbonyl groups. This AI_{mod} parameter can only be calculated with further bulk sample data, however. To describe a compound as aromatic, the AI_{mod} values should be ≥0.5; for nonaromatic compounds, the AI_{mod} is <0.5. For the purpose of data visualization, color coded AI factor is used in parallel with van Krevelen plots to distinguish compositional profiles [42].

The application of statistical techniques to complex FTMS dataset analysis continues to progress. Recently, the volcano plot was applied by Hur et al. to petroleomics data [130]. The volcano plot is a scatterplot obtained by plotting the negative log of statistical significance (p-value) versus the log of fold change, representing the magnitude of change. The fold change will have positive values where peaks are more intense in the second sample compared to the first. The significant peaks can then be categorized following filtering, and the peaks of the desired category can be

represented visually with DBE versus carbon number plots and van Krevelen plots. Statistical analysis can also be used for improved data processing of replicated data arrays. Gavard et al. used batch processing with the Themis algorithm [131]. The algorithm recognizes anomalous replicates, normalizes peak magnitudes, identifies peak configuration throughout the replicates, and eliminates peaks that are inconsistent across replicates to provide a single peak list for subsequent analysis [42].

Languages such as Python and R are increasingly being used for advanced data processing. These data processing and analysis tools are combined with visualization tools, such as interactive plots. In metabolomics and proteomics data analysis, a kit of selected R packages, called bioconductor, is used to obtain visualization outlines [132]. An i–van Krevelen data analysis website was created by Kew et al. in Python to develop interactive visualizations [60]. The tool generates centroid mass spectra, van Krevelen diagrams, DBE versus carbon number plots, and modified AI versus carbon number plots. Connecting several interactive plots simultaneously by highlighting the same selected data in different plots facilitates prompt assessments within different outlines. UltraMassExplorer is an online tool developed using R, providing a comprehensive data assessment by assigning molecular compositions. Two-dimensional and 3D interactive van Krevelen plots can be generated with the options of free rotation and data focusing, and a library-based approach depending on rules recommended by Kind and Fiehn was employed to assign the elemental compositions [42].

3.10 Conclusions

Ultrahigh-resolution FTMS mass spectrometry methods such as FTICR MS and Orbitrap MS allow for the observation of data sets, generating unique insights for environmental forensics in unparalleled detail. With carefully designed experiments using nontargeted mass spectrometric methods, it is now possible to make novel advances in the environmental forensics, such as highlighting geographic differences in NAFCs across the Athabasca oil sands. In addition, these analytical tools have enriched our understanding of particular molecular mechanisms of NAFC-related toxicity in aquatic environments. Furthermore, the molecular insights offered by FTMS methods also now allow for helpful assessment of treatment outcomes for OSPW, especially in relation to the aforementioned characterizations and identifications of the most toxic components of NAFCs. It is worth remembering that data generated by the different varieties of mass spectrometers, including FTMS instruments, will be influenced by a number of experimental parameters. These include the choice of sample extraction methods, preparation of the sample prior to analysis (including the choice of solvents and of pH), the ionization method selected, and the instrument tuning. As a result, there are limitations to the interpretation due to the semiquantitative nature of the

data, which can be partly addressed by combining the methods with chromatography and the use of authentic standards to represent all isomers. Regardless of these considerations, however, FTMS methods afford data of greater volume and far greater detail, when compared to other methods. The sheer volume of information generated by ultrahigh-resolution mass spectrometry presents management and interpretational challenges, but also offers the opportunity for the creation of compelling data visualizations from these data. In addition, FTMS methods continue to empower unique insights into the character of polar organic components of petroleum samples, and this usefulness may expand as FT-based mass spectrometry technology continues to develop. Future studies are encouraged to continue finding ways to combine traditional petroleomic data plotting methods with multivariate statistical and data ordination methods to highlight similarities and/or differences between samples. Such applications would be particularly useful for monitoring programs examining temporal and spatial trends in NAFCs.

References

[1] Kinley CM, McQueen AD, Rodgers JH. Comparative responses of freshwater organisms to exposures of a commercial naphthenic acid. Chemosphere, 2016, 153, 170–178.

[2] Hagen MO, Garcia-Garcia E, Oladiran A, et al. The acute and sub-chronic exposures of goldfish to naphthenic acids induce different host defense responses. Aquat Toxicol, 2012, 109, 143–149.

[3] Li C, Fu L, Stafford J, Belosevic M, Gamal El-Din M. The toxicity of oil sands process-affected water (OSPW): A critical review. Sci Total Environ, 2017, 601–602, 1785–1802.

[4] Alberta Energy Regulator. State of fluid tailings management for mineable oil, 2018 [Internet]. Calgary, Alberta: 2019. Available from: https://www.aer.ca/documents/oilsands/2018-State-Fluid-Tailings-Management-Mineable-OilSands.pdf

[5] Headley JV, Peru KM, McMartin DW, Winkler M. Determination of dissolved naphthenic acids in natural waters by using negative-ion electrospray mass spectrometry. J AOAC Int, 2002, 85 (1), 182–187.

[6] Grewer DM, Young RF, Whittal RM, Fedorak PM. Naphthenic acids and other acid-extractables in water samples from Alberta: What is being measured?. Sci Total Environ, 2010, 408(23), 5997–6010.

[7] Headley JV, Barrow MP, Peru KM, et al. Preliminary fingerprinting of Athabasca oil sands polar organics in environmental samples using electrospray ionization Fourier transform ion cyclotron resonance mass spectrometry. Rapid Commun Mass Spectrom, 2011, 25(13), 1899–1909.

[8] Reinardy HC, Scarlett AG, Henry TB, et al. Aromatic naphthenic acids in oil sands process-affected water, resolved by GCxGC-MS, only weakly induce the gene for vitellogenin production in zebrafish (danio rerio) larvae. Environ Sci Technol, 2013, 47(12), 6614–6620.

[9] Bauer AE, Frank RA, Headley JV, Peru KM, Farwell AJ, Dixon DG. Toxicity of oil sands acid-extractable organic fractions to freshwater fish: Pimephales promelas (fathead minnow) and Oryzias latipes (Japanese medaka). Chemosphere Internet 2017, 171, 168–176. Available from http://dx.doi.org/10.1016/j.chemosphere.2016.12.059

[10] Headley JV, McMartin DW. A review of the occurrence and fate of naphthenic acids in aquatic environments. J Environ Sci Heal – Part A Toxic/Hazardous Subst Environ Eng, 2004, 39(8), 1989–2010.
[11] Morandi GD, Wiseman SB, Pereira A, et al. Effects-directed analysis of dissolved organic compounds in oil sands process-affected water. Environ Sci Technol, 2015, 49(20), 12395–12404.
[12] Hughes SA, Mahaffey A, Shore B, et al. Using ultrahigh-resolution mass spectrometry and toxicity identification techniques to characterize the toxicity of oil sands process-affected water: The case for classical naphthenic acids. Environ Toxicol Chem, 2017, 36(11), 3148–3157.
[13] Ripmeester MJ, Duford DA. Method for routine "naphthenic acids fraction compounds" determination in oil sands process-affected water by liquid-liquid extraction in dichloromethane and Fourier-Transform Infrared Spectroscopy. Chemosphere, 2019, 233, 687–696.
[14] Meshref MNA, Ibrahim MD, Huang R, et al. Fourier transform infrared spectroscopy as a surrogate tool for the quantification of naphthenic acids in oil sands process water and groundwater. Sci Total Environ, 2020, 734, 139191.
[15] Bowman DT, Warren LA, Slater GF. Isomer-specific monitoring of naphthenic acids at an oil sands pit lake by comprehensive two-dimensional gas chromatography–mass spectrometry. Sci Total Environ, 2020, 746, 140985.
[16] Bowman DT, Warren LA, McCarry BE, Slater GF. Profiling of individual naphthenic acids at a composite tailings reclamation fen by comprehensive two-dimensional gas chromatography-mass spectrometry. Sci Total Environ, 2019, 649, 1522–1531.
[17] Zhang L, Zhang Y, Gamal El-Din M. Integrated mild ozonation with biofiltration can effectively enhance the removal of naphthenic acids from hydrocarbon-contaminated water. Sci Total Environ, 2019, 678, 197–206.
[18] Abdalrhman AS, Zhang Y, Arslan M, Gamal El-Din M. Low-current electro-oxidation enhanced the biodegradation of the recalcitrant naphthenic acids in oil sands process water. J Hazard Mater, 2020, 398(January), 122807.
[19] Woudneh MB, Coreen Hamilton M, Benskin JP, Wang G, McEachern P, Cosgrove JR. A novel derivatization-based liquid chromatography tandem mass spectrometry method for quantitative characterization of naphthenic acid isomer profiles in environmental waters. J Chromatogr A, 2013, 1293, 36–43.
[20] Ajaero C, Headley JV, Peru KM, McMartin DW, Barrow MP. Forensic studies of naphthenic acids fraction compounds in oil sands environmental samples and crude oil (2nd ed.). Internet. Elsevier Inc., 2016. Academic Press, Cambridge, Massachusetts. Available from http://dx.doi.org/10.1016/B978-0-12-803832-1/00007-6
[21] Hughes SA, Huang R, Mahaffey A, et al. Comparison of methods for determination of total oil sands-derived naphthenic acids in water samples. Chemosphere, 2017, 187, 376–384.
[22] Headley JV, Peru KM, Mohamed MH, et al. Chemical fingerprinting of naphthenic acids and oil sands process waters-A review of analytical methods for environmental samples. J Environ Sci Heal – Part A Toxic/Hazardous Subst Environ Eng, 2013, 48(10), 1145–1163.
[23] Jin P, Bota G, Robbins W, Nesic S. Analysis of oxide scales formed in the naphthenic acid corrosion of carbon steel. Energy Fuels, 2016, 30(8), 6853–6862.
[24] Dzidic I, Somerville AC, Raia JC, Hart HV. Determination of Naphthenic Acids in California Crudes and Refinery Wastewaters by Fluoride Ion Chemical Ionization Mass Spectrometry. Anal Chem, 1988, 60(13), 1318–1323.
[25] Fan TP. Characterization of naphthenic acids in petroleum by fast atom bombardment mass spectrometry. Energy Fuels, 1991, 5(3), 371–375.

[26] Hsu CS, Dechert GJ, Robbins WK, Fukuda EK. Naphthenic acids in crude oils characterized by mass spectrometry. Energy Fuels, 2000, 14(1), 217–223.
[27] Barrow MP, McDonnell LA, Feng X, Walker J, Derrick PJ. Determination of the nature of naphthenic acids present in crude oils using nanospray Fourier transform ion cyclotron resonance mass spectrometry: The continued battle against corrosion. Anal Chem, 2003, 75 (4), 860–866.
[28] Rudzinski WE, Oehlers L, Zhang Y, Najera B. Tandem mass spectrometric characterization of commercial naphthenic acids and a Maya crude oil. Energy Fuels, 2002, 16(5), 1178–1185.
[29] Baugh T, Wolf N, Mediaas H, Vindstad J, Grande K. Characterization of a calcium naphthenate deposit – The arn acid discovery. Abstr Pap Am Chem Soc, 2004, 228, U172–U172.
[30] Laredo GC, López CR, Álvarez RE, Cano JL. Naphthenic acids, total acid number and sulfur content profile characterization in Isthmus and Maya crude oils. Fuel, 2004, 83(11–12), 1689–1695.
[31] Mapolelo MM, Rodgers RP, Blakney GT, Yen AT, Asomaning S, Marshall AG. Characterization of naphthenic acids in crude oils and naphthenates by electrospray ionization FT-ICR mass spectrometry. Int J Mass Spectrom, 2011, 300(2–3), 149–157.
[32] Qian K, Edwards KE, Dechert GJ, Jaffe SB, Green LA, Olmstead WN. Measurement of Total Acid Number (TAN) and TAN boiling point distribution in petroleum products by electrospray ionization mass spectrometry. Anal Chem, 2008, 80(3), 849–855.
[33] Headley JV, Peru KM, Barrow MP. Advances in mass spectrometric characterization of naphthenic acids fraction compounds in oil sand environmental samples and crude oil – A review. Mass Spectrom Rev, 2016, 35, 311–328.
[34] Headley JV, Barrow MP, Peru KM, Derrick PJ. Salting-out effects on the characterization of naphthenic acids from Athabasca oil sands using electrospray ionization. J Environ Sci Heal – Part A Toxic/Hazardous Subst Environ Eng, 2011, 46(8), 844–854.
[35] Comisarow MB, Marshall AG. Selective-phase Ion Cyclotron Resonance Spectroscopy. Can J Chem, 1974, 52(10), 1997–1999.
[36] Amster IJ. Fourier Transform Mass Spectrometry. J Mass Spectrom, 1996, 31(12), 1325–1337.
[37] Marshall AG, Hendrickson CL, Jackson GS. Fourier transform ion cyclotron resonance mass spectrometry: A primer. Mass Spectrom Rev, 1998, 17(1), 1–35.
[38] Marshall AG, Hendrickson CL. High-resolution mass spectrometers. Annu Rev Anal Chem, 2008, 1(1), 579–599.
[39] Makarov A. Electrostatic axially harmonic orbital trapping: A high-performance technique of mass analysis. Anal Chem, 2000, 72(6), 1156–1162.
[40] Hu Q, Noll RJ, Li H, Makarov A, Hardman M, Cooks RG. The Orbitrap: A new mass spectrometer. J Mass Spectrom, 2005, 40(4), 430–443.
[41] Barrow MP, Burkitt WI, Derrick PJ. Principles of Fourier transform ion cyclotron resonance mass spectrometry and its application in structural biology. Analyst, 2005, 130(1), 18–28.
[42] Palacio Lozano DC, Thomas MJ, Jones HE, Barrow MP. Petroleomics: Tools, challenges, and developments. Annu Rev Anal Chem, 2020, 13, 405–430.
[43] Kind T, Fiehn O. Seven Golden Rules for heuristic filtering of molecular formulas obtained by accurate mass spectrometry. BMC Bioinform, 2007, 8, 1–20.
[44] McKenna AM, Williams JT, Putman JC, et al. Unprecedented ultrahigh resolution FT-ICR mass spectrometry and parts-per-billion mass accuracy enable direct characterization of nickel and vanadyl porphyrins in petroleum from natural seeps. Energy Fuels, 2014, 28(4), 2454–2464.
[45] Palacio Lozano DC, Gavard R, Arenas-Diaz JP, et al. Pushing the analytical limits: New insights into complex mixtures using mass spectra segments of constant ultrahigh resolving power. Chem Sci, 2019, 10(29), 6966–6978.

[46] Kim S, Rodgers RP, Marshall AG. Truly "exact" mass: Elemental composition can be determined uniquely from molecular mass measurement at ~0.1 mDa accuracy for molecules up to ~500 Da. Int J Mass Spectrom, 2006, 251(2-3SPEC. ISS.), 260–265.
[47] Hughey CA, Hendrickson CL, Rodgers RP, Marshall AG, Qian K. Kendrick mass defect spectrum: A compact visual analysis for ultrahigh-resolution broadband mass spectra. Anal Chem, 2001, 73(19), 4676–4681.
[48] Marshall AG, Rodgers RP. Petroleomics: Chemistry of the underworld. Proc Natl Acad Sci U S A, 2008, 105(47), 18090–18095.
[49] Rodgers RP, Schaub TM, Marshall AG. Petroleomics: MS returns to its roots. Anal Chem, 2005, 77, 1.
[50] D'Andrilli J, Foreman CM, Marshall AG, McKnight DM. Characterization of IHSS pony lake fulvic acid dissolved organic matter by electrospray ionization fourier transform ion cyclotron resonance mass spectrometry and fluorescence spectroscopy. Org Geochem, 2013, 65, 19–28.
[51] Qi Y, Hempelmann R, Volmer DA. Shedding light on the structures of lignin compounds: Photo-oxidation under artificial UV light and characterization by high resolution mass spectrometry. Anal Bioanal Chem, 2016, 408(28), 8203–8210.
[52] Barrow MP, Headley JV, Peru KM, Derrick PJ. Fourier transform ion cyclotron resonance mass spectrometry of principal components in oilsands naphthenic acids. J Chromatogr A, 2004, 1058(1–2), 51–59.
[53] Headley JV, Peru KM, Janfada A, Fahlman B, Gu C, Hassan S. Characterization of oil sands acids in plant tissue using Orbitrap ultra-high resolution mass spectrometry with electrospray ionization. Rapid Commun Mass Spectrom, 2011, 25(3), 459–462.
[54] Barrow MP, Headley JV, Peru KM, Derrick PJ. Data visualization for the characterization of naphthenic acids within petroleum samples. Energy Fuels, 2009, 23(5), 2592–2599.
[55] Marshall AG, Rodgers RP. Petroleomics: The Next Grand Challenge for Chemical Analysis. Acc Chem Res, 2004, 37(1), 53–59.
[56] Van Krevelen DW. Graphical-statistical method for the study of structure and reaction processes of coal. Fuel, 1950, 29, 269–284.
[57] Van Krevelen DW. Organic geochemistry-old and new. Org Geochem, 1984, 6(C), 1–10.
[58] Kim S, Kramer RW, Hatcher PG. Graphical method for analysis of ultrahigh-resolution broadband mass spectra of natural organic matter, the Van Krevelen diagram. Anal Chem, 2003, 75(20), 5336–5344.
[59] Wu Z, Rodgers RP, Marshall AG. Two- and three-dimensional van Krevelen diagrams: A graphical analysis complementary to the Kendrick mass plot for sorting elemental compositions of complex organic mixtures based on ultrahigh-resolution broadband Fourier transform ion cyclotron resonance. Anal Chem, 2004, 76(9), 2511–2516.
[60] Kew W, Blackburn JWT, Clarke DJ, Uhrín D. Interactive van Krevelen diagrams – Advanced visualisation of mass spectrometry data of complex mixtures. Rapid Commun Mass Spectrom, 2017, 31(7), 658–662.
[61] Niyonsaba E, Manheim JM, Yerabolu R, Kenttämaa HI. Recent advances in petroleum analysis by mass spectrometry. Anal Chem, 2019, 91(1), 156–177.
[62] Barrow MP. Petroleomics: Study of the old and the new. Biofuels, 2010, 1(5), 651–655.
[63] Yi Y, Han J, Jean Birks S, Borchers CH, Gibson JJ. Profiling of dissolved organic compounds in the oil sands region using complimentary liquid–liquid extraction and ultrahigh resolution Fourier transform mass spectrometry. Environ Earth Sci, 2017, 76(24), 1–13.
[64] Rogers VV, Liber K, MacKinnon MD. Isolation and characterization of naphthenic acids from Athabasca oil sands tailings pond water. Chemosphere, 2002, 48(5), 519–527.

[65] Huang R, Chen Y, Meshref MNA, et al. Monitoring of classical, oxidized, and heteroatomic naphthenic acids species in oil sands process water and groundwater from the active oil sands operation area. Sci Total Environ, 2018, 645, 277–285.
[66] Pereira AS, Bhattacharjee S, Martin JW. Characterization of oil sands process-affected waters by liquid chromatography orbitrap mass spectrometry. Environ Sci Technol, 2013, 47(10), 5504–5513.
[67] Ajaero C, Vander Meulen IJ, Simair MC, et al. Developments in molecular level characterization of naphthenic acid fraction compounds degradation in a constructed wetland treatment system. Environ – MDPI, 2020, 7(10), 89–105.
[68] Vander Meulen IJ, Schock DM, Parrott JL, et al. Transformation of bitumen-derived naphthenic acid fraction compounds across surface waters of wetlands in the Athabasca Oil Sands region. Sci Total Environ Internet, 2021, 806, 150619. Available from https://doi.org/10.1016/j.scitotenv.2021.150619.
[69] Ajaero C, McMartin DW, Peru KM, et al. Fourier transform ion cyclotron resonance mass spectrometry characterization of Athabasca oil sand process-affected waters incubated in the presence of wetland plants. Energy Fuels, 2017, 31(2), 1731–1740.
[70] Morandi G, Wiseman S, Sun C, Martin JW, Giesy JP. Effects of chemical fractions from an oil sands end-pit lake on reproduction of fathead minnows. Chemosphere, 2020, 249, 126073.
[71] Bauer AE, Frank RA, Headley JV, Peru KM, Hewitt LM, Dixon DG. Enhanced characterization of oil sands acid-extractable organics fractions using electrospray ionization-high-resolution mass spectrometry and synchronous fluorescence spectroscopy. Environ Toxicol Chem, 2015, 34(5), 1001–1008.
[72] Han J, Yi Y, Lin K, Birks SJ, Gibson JJ, Borchers CH. Molecular profiling of naphthenic acids in technical mixtures and oil sands process-affected water using polar reversed-phase liquid chromatography–mass spectrometry. Electrophoresis, 2016, 37(23–24), 3089–3100.
[73] Ortiz X, Jobst KJ, Reiner EJ, et al. Characterization of naphthenic acids by gas chromatography-fourier transform ion cyclotron resonance mass spectrometry. Anal Chem, 2014, 86(15), 7666–7673.
[74] Barrow MP, Peru KM, Headley JV. An added dimension: GC atmospheric pressure chemical ionization FTICR MS and the athabasca oil sands. Anal Chem, 2014, 86(16), 8281–8288.
[75] Headley JV, Peru KM, Fahlman B, Colodey A, McMartin DW. Selective solvent extraction and characterization of the acid extractable fraction of Athabasca oils sands process waters by Orbitrap mass spectrometry. Int J Mass Spectrom Internet 2013, 345–347, 104–108. Available from http://dx.doi.org/10.1016/j.ijms.2012.08.023
[76] Barrow MP, Peru KM, McMartin DW, Headley JV. Effects of extraction pH on the Fourier transform ion cyclotron resonance mass spectrometry profiles of Athabasca oil sands process water. Energy Fuels, 2016, 30(5), 3615–3621.
[77] Ren L, Han Y, Zhang Y, Zhang Y, Meng X, Shi Q. Spray injection direct analysis in real time (DART) ionization for petroleum analysis. Energy Fuels, 2016, 30(6), 4486–4493.
[78] Lobodin VV, Nyadong L, Ruddy BM, et al. DART Fourier transform ion cyclotron resonance mass spectrometry for analysis of complex organic mixtures. Int J Mass Spectrom Internet, 2015, 378, 186–192. Available from http://dx.doi.org/10.1016/j.ijms.2014.07.050.
[79] Valencia-Dávila JA, Blanco-Tirado C, Combariza MY. Analysis of naphthenic acids by matrix assisted laser desorption ionization time of flight mass spectrometry. Fuel, 2017, 193, 168–177.
[80] Peru KM, Thomas MJ, Palacio Lozano DC, McMartin DW, Headley JV, Barrow MP. Characterization of oil sands naphthenic acids by negative-ion electrospray ionization mass spectrometry: Influence of acidic versus basic transfer solvent. Chemosphere, 2019, 222, 1017–1024.

[81] Headley JV, Peru KM, Barrow MP, Derrick PJ. Characterization of naphthenic acids from athabasca oil sands using electrospray ionization: The significant influence of solvents. Anal Chem, 2007, 79(16), 6222–6229.
[82] Gavard R, Jones HE, Palacio Lozano DC, et al. KairosMS: A new solution for the processing of hyphenated ultrahigh resolution mass spectrometry data. Anal Chem, 2020, 92(5), 3775–3786.
[83] Barrow MP, Witt M, Headley JV, Peru KM. Athabasca oil sands process water: Characterization by atmospheric pressure photoionization and electrospray ionization Fourier transform ion cyclotron resonance mass spectrometry. Anal Chem, 2010, 82(9), 3727–3735.
[84] Frank RA, Roy JW, Bickerton G, et al. Profiling oil sands mixtures from industrial developments and natural groundwaters for source identification. Environ Sci Technol, 2014, 48(5), 2660–2670.
[85] Sun C, Shotyk W, Cuss CW, et al. Characterization of naphthenic acids and other dissolved organics in natural water from the athabasca oil sands region, Canada. Environ Sci Technol, 2017, 51(17), 9524–9532.
[86] Vander Meulen IJ, Klemish JL, Peru KM, Chen DDYDY, Pyle GG, Headley JV Molecular profiles of naphthenic acid fraction compounds from mine lease wetlands in the Athabasca Oil Sands Region. Chemosphere [Internet] 2021;272:129892. Available from: https://doi.org/10.1016/j.chemosphere.2021.129892
[87] Yi Y, Gibson J, Birks J, Han J, Borchers CH. Comment on “profiling oil sands mixtures from industrial developments and natural groundwaters for source identification. Environ Sci Technol, 2014, 48(18), 11013–11014.
[88] Ahad JME, Pakdel H, Gammon PR, et al. Distinguishing natural from anthropogenic sources of acid extractable organics in groundwater near oil sands tailings ponds. Environ Sci Technol, 2020, 54(5), 2790–2799.
[89] Milestone CB, Sun C, Martin JW, et al. Non-target profiling of bitumen-influenced waters for the identification of tracers unique to oil sands processed-affected water (OSPW) in the Athabasca watershed of Alberta, Canada. Rapid Commun Mass Spectrom 2020;
[90] Schindler D. Tar sands need solid science. Nature, 2010, 468(7323), 499–501.
[91] Kelly EN, Short JW, Schindler DW, et al. Oil sands development contributes polycyclic aromatic compounds to the Athabasca River and its tributaries. Proc Natl Acad Sci U S A, 2009, 106(52), 22346–22351.
[92] Volik O, Elmes M, Petrone R, et al. Wetlands in the athabasca oil sands region: The nexus between wetland hydrological function and resource extraction. Environ Rev, 2020, 28(3), 246–261.
[93] Hersikorn BD, Smits JEG. Compromised metamorphosis and thyroid hormone changes in wood frogs (Lithobates sylvaticus) raised on reclaimed wetlands on the Athabasca oil sands. Environ Pollut, 2011, 159(2), 596–601.
[94] Yu X, Lee K, Ulrich AC. Model naphthenic acids removal by microalgae and Base Mine Lake cap water microbial inoculum. Chemosphere Internet 2019, 234, 796–805. Available from https://doi.org/10.1016/j.chemosphere.2019.06.110
[95] Miles SM, Asiedu E, Balaberda AL, Ulrich AC. Oil sands process affected water sourced Trichoderma harzianum demonstrates capacity for mycoremediation of naphthenic acid fraction compounds. Chemosphere Internet 2020, 258, 127281. Available from https://doi.org/10.1016/j.chemosphere.2020.127281
[96] Huang J, Nemati M, Hill G, Headley J. Batch and continuous biodegradation of three model naphthenic acids in a circulating packed-bed bioreactor. J Hazard Mater, 2012, 201–202, 132–140.

[97] Kinley CM, Gaspari DP, McQueen AD, et al. Effects of environmental conditions on aerobic degradation of a commercial naphthenic acid. Chemosphere Internet 2016, 161(July), 491–500. Available from http://dx.doi.org/10.1016/j.chemosphere.2016.07.050
[98] Ajaero C, Peru KM, Simair M, et al. Fate and behavior of oil sands naphthenic acids in a pilot-scale treatment wetland as characterized by negative-ion electrospray ionization Orbitrap mass spectrometry. Sci Total Environ, 2018, 631–632, 829–839.
[99] Simair MC, Parrott JL, Le Roux M, et al. Treatment of oil sands process affected waters by constructed wetlands: Evaluation of designs and plant types by multiple lines of evidence. Sci Total Environ, 2021, 772, 145508. Available from http://dx.doi.org/10.1016/j.scitotenv.2021.145508
[100] Leshuk T, Peru KM, de Oliveira Livera D, et al. Petroleomic analysis of the treatment of naphthenic organics in oil sands process-affected water with buoyant photocatalysts. Water Res, 2018, 141, 297–306.
[101] de Oliveira Livera D, Leshuk T, Peru KM, Headley JV, Gu F. Structure-reactivity relationship of naphthenic acids in the photocatalytic degradation process. Chemosphere, 2018, 200, 180–190.
[102] Challis JK, Parajas A, Anderson JC, et al. Photodegradation of bitumen-derived organics in oil sands process-affected water. Environ Sci Process Impacts, 2020, 22(5), 1243–1255.
[103] Verbeek AG, Mackay WC, MacKinnon MD Acute toxicity of oil sands wastewater: A toxic balance [Internet]. In: 20th Annual Aquatic Toxicity Workshop. Quebec City, PQ, Canada: 1993. p. 196–207. Available from: https://ecotoxcan.ca/about/past-proceedings/
[104] Frank RA, Kavanagh R, Kent Burnison B, et al. Toxicity assessment of collected fractions from an extracted naphthenic acid mixture. Chemosphere, 2008, 72(9), 1309–1314.
[105] Yue S, Ramsay BA, Wang J, Ramsay JA. Biodegradation and detoxification of naphthenic acids in oil sands process affected waters. Sci Total Environ, 2016, 572, 273–279.
[106] McKenzie N, Yue S, Liu X, Ramsay BA, Ramsay JA. Biodegradation of naphthenic acids in oils sands process waters in an immobilized soil/sediment bioreactor. Chemosphere, 2014, 109, 164–172.
[107] Bartlett AJ, Frank RA, Gillis PL, et al. Toxicity of naphthenic acids to invertebrates: Extracts from oil sands process-affected water versus commercial mixtures. Environ Pollut, 2017, 227, 271–279.
[108] Holowenko FM, MacKinnon MD, Fedorak PM. Characterization of naphthenic acids in oil sands wastewaters by gas chromatography-mass spectrometry. Water Res, 2002, 36(11), 2843–2855.
[109] Scarlett AG, Reinardy HC, Henry TB, et al. Acute toxicity of aromatic and non-aromatic fractions of naphthenic acids extracted from oil sands process-affected water to larval zebrafish. Chemosphere, 2013, 93(2), 415–420.
[110] Brinkmann M, Alharbi H, Fuchylo U, et al. Mechanisms of pH-dependent uptake of ionizable organic chemicals by fish from oil sands process-affected water (OSPW). Environ Sci Technol, 2020, 54(15), 9547–9555.
[111] Wu C, De Visscher A, Gates ID. On naphthenic acids removal from crude oil and oil sands process-affected water. Fuel, 2019, 253, (March):1229–46.
[112] Zhao R, Sun J, Fang Q, et al. Evolution of Acidic Compounds in Crude Oil during in Situ Combustion. Energy Fuels, 2017, 31(6), 5926–5932.
[113] Zhang X, Liu Q, Fan Z, Liu Q. An in situ combustion process for recovering heavy oil using scaled physical model. J Pet Explor Prod Technol, 2019, 9(4), 2681–2688.
[114] Liu Y, Wan YY, Zhu Y, Fei C, Shen Z, Ying Y. Impact of biodegradation on polar compounds in crude oil: Comparative simulation of biodegradation from two aerobic bacteria using ultrahigh-resolution mass spectrometry. Energy Fuels, 2020, 34(5), 5553–5565.

[115] Ajaero C, Peru KM, Hughes SA, et al. Atmospheric pressure photoionization Fourier transform ion cyclotron resonance mass spectrometry characterization of oil sand process-affected water in constructed wetland treatment. Energy Fuels, 2019, 33(5), 4420–4431.
[116] Cho Y, Ahmed A, Islam A, Kim S. Developments in FT-ICR ms instrumentation, ionization techniques, and data interpretation methods for petroleomics. Mass Spectrom Rev, 2015, 34 (2), 248–263.
[117] Michalski A, Damoc E, Lange O, et al. Ultra high resolution linear ion trap orbitrap mass spectrometer (orbitrap elite) facilitates top down LC MS/MS and versatile peptide fragmentation modes. Mol Cell Proteomics, 2012, 11(3), 1–11.
[118] Schmidt EM, Pudenzi MA, Santos JM, et al. Petroleomics: Via Orbitrap mass spectrometry with resolving power above 1=000=000 at m/z 200. RSC Adv, 2018, 8(11), 6183–6191.
[119] Kostyukevich YI, Vladimirov GN, Nikolaev EN. Dynamically harmonized FT-ICR cell with specially shaped electrodes for compensation of inhomogeneity of the magnetic field. Computer simulations of the electric field and ion motion dynamics. J Am Soc Mass Spectrom, 2012, 23(12), 2198–2207.
[120] Cho E, Witt M, Hur M, Jung MJ, Kim S. Application of FT-ICR MS equipped with quadrupole detection for analysis of crude oil. Anal Chem, 2017, 89(22), 12101–12107.
[121] Thomas MJ, Collinge E, Witt M, et al. Petroleomic depth profiling of Staten Island salt marsh soil: 2ω detection FTICR MS offers a new solution for the analysis of environmental contaminants. Sci Total Environ, 2019, 662, 852–862.
[122] Smith DF, Podgorski DC, Rodgers RP, Blakney GT, Hendrickson CL. 21 Tesla FT-ICR mass spectrometer for ultrahigh-resolution analysis of complex organic mixtures. Anal Chem, 2018, 90(3), 2041–2047.
[123] Gavard R, Palacio Lozano DC, Guzman A, Rossell D, Spencer SEF, Barrow MP. Rhapso: Automatic stitching of mass segments from Fourier transform ion cyclotron resonance mass spectra. Anal Chem, 2019, 91(23), 15130–15137.
[124] Southam AD, Payne TG, Cooper HJ, Arvanitis TN, Viant MR. Dynamic range and mass accuracy of wide-scan direct infusion nanoelectrospray fourier transform ion cyclotron resonance mass spectrometry-based metabolomics increased by the spectral stitching method. Anal Chem, 2007, 79(12), 4595–4602.
[125] Gaspar A, Schrader W. Expanding the data depth for the analysis of complex crude oil samples by Fourier transform ion cyclotron resonance mass spectrometry using the spectral stitching method. Rapid Commun Mass Spectrom, 2012, 26(9), 1047–1052.
[126] Qi Y, O'Connor PB. Data processing in Fourier transform ion cyclotron resonance mass spectrometry. Mass Spectrom Rev, 2014, 33(5), 333–352.
[127] Qi Y, Thompson CJ, Van Orden SL, O'Connor PB. Phase correction of Fourier transform ion cyclotron resonance mass spectra using matlab. J Am Soc Mass Spectrom, 2011, 22(1), 138–147.
[128] Qi Y, Barrow MP, Van Orden SL, et al. Variation of the Fourier transform mass spectra phase function with experimental parameters. Anal Chem, 2011, 83, 8477–8483.
[129] Koch BP, Dittmar T. From mass to structure: An aromaticity index for high-resolution mass data of natural organic matter. Rapid Commun Mass Spectrom, 2006, 20(5), 926–932.
[130] Hur M, Ware RL, Park J, et al. Statistically significant differences in composition of petroleum crude oils revealed by volcano plots generated from ultrahigh resolution fourier transform ion cyclotron resonance mass spectra. Energy Fuels, 2018, 32(2), 1206–1212.
[131] Gavard R, Rossell D, Spencer SEF, Barrow MP. Themis: Batch preprocessing for ultrahigh-resolution mass spectra of complex mixtures. Anal Chem, 2017, 89(21), 11383–11390.
[132] Gatto L, Breckels LM, Naake T, Gibb S. Visualization of proteomics data using R and Bioconductor. Proteomics, 2015, 15(8), 1375–1389.

M. R. Yakubov, G. R. Abilova, S. G. Yakubova, D. V. Milordov,
N. A. Mironov

4 Heavy oil resin composition and their influence on asphaltene stability

Abstract: This chapter shows the features of vanadium and nickel content changes in the resins of heavy oils, characteristics of their structural and group composition, the content of heteroatomic (N, S, O) compounds, which indicates the relationship of aromatic and aliphatic structures with vanadyl complexes. The composition of vanadyl porphyrins in resins of heavy oils with increased vanadium content was also investigated. The influence of different fractions of resins as well as concentrates of heteroatomic (N, S, O) compounds with increased content of nitrogen, vanadium, and vanadyl porphyrins on the stability of asphaltenes has been determined.

4.1 Introduction

Resin and asphaltene contents are the most important factors, which affect the difference in petroleum characteristics. Composition of resins and asphaltenes have much in common due to their structural similarity [1–3]. Heavy oils (HOs) are characterized by the increased resin and asphaltene contents which are the main reason for their increased viscosity and usually high content of undesirable heteroatomic (S, N, O) compounds. In addition, HOs often possess high vanadium and nickel contents, which may amount to 0.1 wt% [4, 5].

Formation of heavy oils is associated with ancient or modern hypergenesis, during which physical weathering, oxidation, biodegradation, and sulfurization of oils occur as a result of biochemical or chemical oxidation. Mentioned processes influence not only the hydrocarbon composition of oils and their physicochemical properties, but also metal content. As a result of secondary alteration of oils during ascending migration of fluids, giant and largest deposits of HOs and natural bitumens were formed in the hypergenesis zone in Western Canadian (Peace River, Cold Lake, Athabasca, and other deposits), Eastern Venezuelan (Ofisina, Temblador, Cerro Negro, and other deposits), and Western Venezuelan (Mara, Tia Juana, Bochakero, and other deposits) oil-and-gas bearing basins (OGBs), as well as a large number of deposits in the United States, Russia, Kazakhstan, and others [6–9].

M. R. Yakubov, G. R. Abilova, S. G. Yakubova, D. V. Milordov, N. A. Mironov, Arbuzov Institute of Organic and Physical Chemistry, FRC Kazan Scientific Center, Russian Academy of Sciences, Kazan, Russia

https://doi.org/10.1515/9783110694529-004

In Russia, mainly in the Volga-Ural OGB, more than 100 HO deposits are being developed. All the recovered HO is high in sulfur and has vanadium content of more than 0.01 wt% [10], which largely restricts the potential of conventional processes for upgrading such raw material. It is necessary to have the data on the content and distribution of metals in petroleum components for optimal choice of the schemes of processing or upgrading of HO, which is particularly important for the choice of catalytic processes [11–14]. Deasphaltization is one option to eliminate metal from heavy petroleum, as a result of which asphaltenes and resins with organometallic compounds are separated upon dilution by light alkanes [15]. As a result, most vanadium and nickel content in the form of metalloporphyrins and their counterparts remains in the nontarget residual fraction (asphalt). The asphalt from HO with the increased vanadium content can be considered as a source for the production of metalloporphyrins with the aim of their further use as a basis for dyes, catalysts, drugs, and semiconductors. However, the absence of effective methods for concentration and purification of porphyrins from petroleum residues does not allow for the evaluation of their practical potential [16]. The quantitative distribution of heteroatomic (S, N, O) components between asphaltenes and resins can differ remarkably in the oils from various deposits [13, 17–19]. At present, chemical composition of petroleum resins is investigated using physicochemical methods of analysis, such as infrared and ultraviolet spectroscopy, nuclear and paramagnetic resonance, X-ray analysis, electron microscopy, and mass spectrometry [20]. Molecular mass of resins determined by various methods on average is always lower than that of asphaltenes recovered from the same oils [1, 21]. Fourier IR spectroscopy could evaluate features of structural–group composition of petroleum resins according to the relative content of various functional groups [22–24]. One example is that the presence of ethers and esters in the resins of HO of Usinskoe deposit was shown by IR spectra in [25]. The presence of carbonyl groups in the resins from vacuum residues of HO was also shown using Fourier IR spectroscopy [26]. Comparison of IR spectra of resins and asphaltenes from the same oil showed that there is a higher content of carbonyl groups in resins [27]. It was discovered in article [28] that there are C–O bonds that link polycyclic aromatic hydrocarbons and heterorganic compounds in the molecules of the resins of heavy oils, whereas C–S bond is more common in the resins of light oil. In works by various authors [29–32], analysis of various petroleum fractions using electrospray ionization mass spectrometry (ESI-MS), chromatograph mass spectrometry, X-ray absorption spectroscopy (XAS) showed that there are various sulfur-containing (sulfoxides, sulfides, sulfones, and thiophenes) and nitrogen-containing (amides, pyridines, quinolines, and carbazoles) compounds and structural groups in resins. It was determined that nitrogen is mainly represented by organonitrogen bases (OBs) in the molecules of resins (pyridine and its homologues), and neutral compounds (pyrrole compounds) and porphyrin metallocomplexes [33]. Preliminary concentration of heteroatomic compounds from petroleum resins provides more accurate study of their composition

and structural features. An original methodology was developed in the Institute of Petroleum Chemistry of the Siberian Branch of the Russian Academy of Sciences [25] for the recovery of OBs concentrates from resins through their preliminary treatment with gaseous hydrogen chloride and acetic acid solution of sulfuric acid (H_2SO_4:CH_3COOH:H_2O = 25:60:15) with subsequent exposure to diethylamine with the aim of recovering additional quantities of nitrogen compounds [34]. Nitrogen in resins was also studied in detail within oil porphyrins [35–38].

The ability to provide colloidal stability of asphaltenes is an important characteristic of petroleum resins [39–41]. However, there are yet scattered data on the effect of heteroatomic S-, N-, and O-containing components in resins, which determine their different solubilizing effectiveness toward asphaltenes. For this reason, their effect on the stability of asphaltenes should firstly be investigated, in particular, in the resins with the increased content of vanadium metallocomplexes and heteroatomic compounds, with the aim to increase the effectiveness of recovery and refining of HO [42–46].

In [47], the model for stabilization of asphaltenes with resins was suggested, according to which the process can be divided into four stages:

- adsorption of resins on the asphaltene surface;
- penetration of resins into microporous structure of asphaltenes;
- degradation of asphaltene micropores with resins;
- diffusion of resin–asphaltene particles into solvent.

The resins from various oils are distinguished by the inhibition activity of asphaltene precipitation. It was determined in [48] that the adsorption behavior of two heavy high-viscous oils on the asphaltene surface corresponds to the Freundlich adsorption model. It was shown that the sorption of resins is governed by their polarity and aromaticity.

Alcazar-Vara et al. [49] investigated the effect of resins from light and heavy Mexican oils on the inhibition of asphaltene precipitation. The effectiveness of the resins from two oils as asphaltene precipitation inhibitors was better at the resin-to-asphaltene ratio close to unity.

In [50], the resins from the HO residues of the oilfields of Venezuela and Canada were separated using column chromatography into two fractions, more specifically, light and heavy resins. The fraction of heavy resins is structurally similar to asphaltenes. As a result of the study of the effect of the fractions of resins on the asphaltene precipitation using dynamic light scattering, it was shown that heavy resins are more effective inhibitors of asphaltene precipitation. However, at a particular concentration of heavy resins, the aggregate sizes of asphaltenes increased. Some works also mention the inability of resins to stabilize asphaltenes and they could even precipitate them. One example is that isothermal microcalorimetry revealed [51] that resins and asphaltenes interact only through weak van der Waals forces. This interaction cannot avoid flocculation and precipitation of asphaltenes. It was also reported by

Goual and Firoozabadi [52] that the mass of asphaltene precipitate increased with the addition of resins. This controversy could be rationalized by an alternative model of repulsion/adhesion of resins, where the adsorbed layer of resin molecules could self-aggregate and further increase the particle size of asphaltenes [53].

In petroleum resins with high vanadium content, vanadyl porphyrins can have a particular effect on the stability of asphaltenes [54, 55]. Vanadyl porphyrins, which contain paramagnetic vanadyl ion and alkyl substituents at ring periphery, can significantly affect flocculation of asphaltenes. For example, it was shown by Yakubov et al. [56] that addition of vanadyl porphyrins to resins enhances their inhibition activity toward asphaltene precipitation.

Thus, there are currently scattered data on the features of content and distribution of vanadium and vanadyl porphyrins, as well as heteroatomic (N, S, O) compounds in the resins of heavy oils. No relationship between resin characteristics and their structural–group and elemental composition and content of various chemical compounds was investigated. Results of the studies on the effect of the composition of resins on their effectiveness toward colloidal stabilization of asphaltenes in oil products are contradictory. Investigations in this field are critical for the development of fundamental and applied aspects of petroleum chemistry. There are unique perspectives from the determination of the features of the relationship between structural–group and elemental composition of the resins of heavy oils and the increased vanadium content along with the evaluation of the potential of the production of new valuable products for the development and improvement of processes in oil recovery and upgrading.

4.2 Materials and methods

HOs from various deposits of Russia and Kazakhstan were studied. Most HO deposits are related to Permian and Carboniferous. There is reducing medium in the HOs in Carboniferous deposits, as well as most deposits of conventional oils. There is evidence of oxidizing medium and biodegradation processes in the HOs of Permian deposits due to their shallow depth (80–350 m).

All HO specimens were dehydrated on a centrifuge at 2,000 rpm. Asphaltenes were separated from HO using a 40:1 v:v ratio of hexane to crude oil at ambient temperature for 24 h. The precipitated asphaltenes were then washed from coextracted maltenes using Soxhlet apparatus up to full decoloring of the effluent solvent (Figure 4.1). Then, asphaltenes were washed out with benzene and after evaporation of solvent were dried to a constant weight in vacuum furnace at 80 °C. Maltenes were separated into oils (hydrocarbons) and resins using chromatography column with silica gel of ASKG brand as a stationary phase and *n*-hexane as an eluent of oils. After separating of oils, the resins (R_0) were eluted using the benzene–isopropyl alcohol mixture (50:50 v/v). After that, the fraction of the resins was fractionated again into benzene

(R_1) and alcohol–benzene (R_2) using chromatography column. Benzene was used as an eluent for the fractions of resins R_1, while the benzene–isopropyl alcohol mixture (50:50 v/v) was used for fraction R_2. All the specimens of resins and their fractions were dried in vacuum 80 °C up to a constant weight after evaporation of solvent [57].

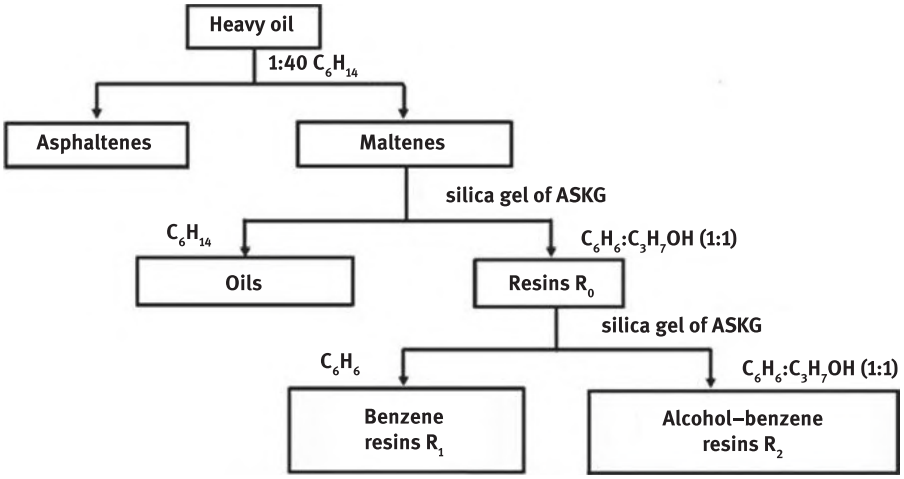

Figure 4.1: Diagram of recovery and fractioning of the resins.

Sulfur content was evaluated using X-ray fluorescent method using a Spectroscan MAKS-GV X-ray spectrometer according to ASTM D 4294–98. Vanadium content was determined through atomic-absorption spectrometry with electrothermal atomization on an MGA-1000 spectrometer. The liquid shot was transferred to the graphite cuvette of the spectrometers using adjustable microdispensers. Calibration plots were recorded using organovanadium standards on a hydrocarbon matrix.

IR spectra of the resins and their fractions were recorded on a JFS-183 V Bruker infrared Fourier spectrometer in the range of 4,000–400 cm^{-1} and processed using the OPUS special program.

The content of vanadyl porphyrins (VPs) was determined on a PE 5400 UV–vis spectrophotometer. For this purpose, the specimen under study was dissolved in toluene of "chemically pure" brand (for spectroscopy) up to the necessary concentration in such a way that the absorbance of the solution would in the minimum error range (0.4–0.8). The concentration of vanadyl porphyrins was calculated at 570 nm, the long-wave band α.

4.3 Features of concentration of heteroatomic components in heavy oil resins with the increased vanadium content

In order to study the features of vanadium content in HO resins, a total of 27 HO specimens from various deposits were analyzed, where the asphaltene content varies in the range of 3.5–21.2 wt%, whereas the resin content varies from 21.3 to 38.6 wt% (Table 4.1). HOs of Permian deposits differ in composition by the lower content of light (I.B.P. – 200 °C) fractions and on average higher total content of resins and asphaltenes, which is the reason for their higher density values.

Table 4.1: Density and component composition of heavy oils of Carboniferous and Permian deposits.

No.	Deposit, well no.	Density, g/cm^3	Content, wt%			
			Fractions i.b.p.-200 °C	Oils	Resins	Asphaltenes
Carboniferous deposits						
1	Adelyakovskoe, 8688	0.936	6.7	63.0	21.9	8.4
2	Aksenovskoe, 4	0.938	6.9	50.9	32.3	10.0
3	Bulatovskoe, 8	0.932	8.5	48.2	33.3	9.9
4	Bulatovskoe, 9	0.932	7.4	50.1	32.9	9.6
5	Bulatovskoe, 10	0.934	7.9	44.7	37.0	10.4
6	Zarechenskoe, 26	0.926	5.4	49.5	38.6	6.5
7	Zyuzeevskoe, 942	0.922	8.3	55.7	29.1	6.9
8	Kazakovskoe, 40	0.936	8.0	45.3	35.7	11.0
9	Kazakovskoe, 50	0.932	6.8	49.1	32.9	11.2
10	Lugovoe, 4	0.923	3.8	48.0	36.5	11.8
11	Maiorovskoe, 58	0.931	4.0	47.3	37.0	11.7
12	Maiorovskoe, 59	0.935	8.0	49.3	34.6	8.0
13	Maiorovskoe, 133	0.932	6.2	55.5	28.9	9.4
14	Maiorovskoe, 600	0.929	6.1	50.1	35.7	7.6
15	Mar'inskoe, 64	0.924	6.9	47.9	35.0	10.3
16	Smorodinskoe, 502	0.947	6.1	47.9	34.2	11.9
17	Smorodinskoe, 254	0.952	7.7	44.2	29.7	18.4

Table 4.1 (continued)

No.	Deposit, well no.	Density, g/cm^3	Content, wt%			
			Fractions i.b.p.-200 °C	Oils	Resins	Asphaltenes
18	Strelovskoe, 83	0.929	8.3	41.2	38.0	12.5
19	Strelovskoe, 92	0.938	6.2	46.0	37.5	10.2
20	Yuganskoe, 100	0.945	9.1	45.4	31.3	14.2
21	Yuganskoe, 403	0.922	7.7	53.8	33.2	5.3
Permian deposits						
22	Ashal'chinskoe, 232	0.973	2.5	55.4	36.6	5.5
23	Gorskoe, 134	0.992	1.3	42.8	34.7	21.2
24	Ekaterinovskoe, 6072	0.972	3.1	48.8	35.0	13.1
25	Karazhanbas, 2139	0.979	2.3	67.0	21.3	9.4
26	Mordovo-Karmal'skoe, 177	0.962	7.7	53.9	32.5	5.9
27	Yaregskoe, 2	0.921	5.1	53.9	37.5	3.5

The V content in HOs varies in the broad range of 0.004–0.084 wt%. There is a clear differentiation in the V content in resins between HO of Permian and Carboniferous deposits; the variation range of V is 0.087–0.140 wt% in HOs of Carboniferous deposits and this range is 0.006–0.063 wt% for HO resins of Permian deposits (Figure 4.2).

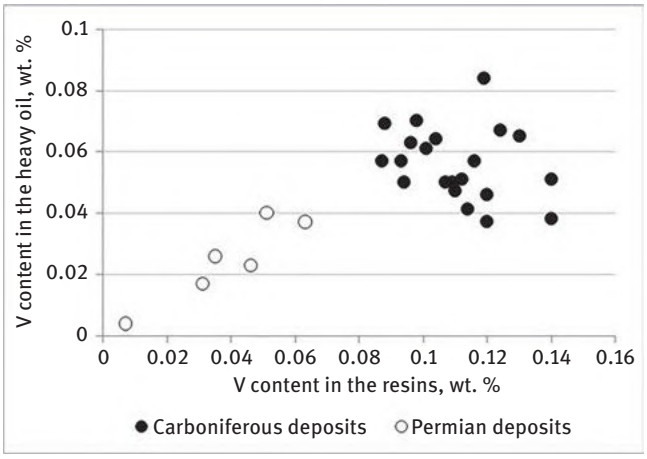

Figure 4.2: Variation of vanadium content in HO with the change of vanadium content in resins.

In order to reveal features of vanadium distribution in the fractions of HO resins, a total of four objects from Carboniferous and Permian deposits were chosen with the assumption of the mean value of vanadium content in resins. The resins were separated using column chromatography on silica to give benzene (R1) and alcohol–benzene (R2) fractions. As a result, it was shown for HOs that the fraction of benzene resins is always higher and, accordingly, the mean value of R1/R2 is 1.73 in the case of HOs of Carboniferous deposits and 1.35 in the case of HOs of Permian deposits.

Results of the determination of V content using atomic-absorption spectroscopy and spectrophotometric determination of the concentration of vanadyl porphyrins (VPs) according to the intensity of the absorption band at 575 ± 5 nm (Figure 4.3) reveal for the HOs regardless of the specific producing complex that V and VPs are concentrated in benzene resins (Table 4.3).

Table 4.2: Content of vanadium and vanadyl porphyrins in fractions of resins (R1, R2).

No.	Deposit, well no.	Content			
		V, wt%		VP, mg/100 g	
		R1	R2	R1	R2
Carboniferous deposits					
1	Adelyakovskoe, 8688	0.160	0.058	598.9	137.4
2	Kazakovskoe, 50	0.150	0.056	579.4	110.1
3	Maiorovskoe, 133	0.119	0.088	314.9	138.1
4	Yuganskoe, 403	0.140	0.087	418.7	283.2
Permian deposits					
5	Ashal'chinskoe, 232	0.054	0.031	153.2	69.2
6	Gorskoe, 134	0.055	0.025	98.3	41.0
7	Ekaterinovskoe, 6072	0.038	0.023	139.2	84.5
8	Karazhanbas	0.029	0.021	81.1	30.0

It was determined from the intensity ratio of the absorption bands at 570 nm (α-band) and 530 nm (β-band) in the absorption spectra of resins (Figure 4.3) that vanadyl porphyrins of etio type are more common than those of deoxophylloerythroetio type (DPEP) (Figure 4.4).

The HO resins of Smorodinskoe deposit (well no. 254) with the high V content were used as the object of study for separation and study of the concentrates of heteroatomic compounds. Concentration of OBs was carried out from the solution of the resins in *n*-hexane following the procedure of the Institute of Petroleum Chemistry of

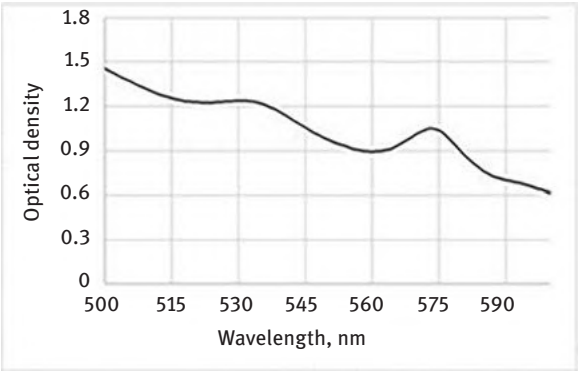

Figure 4.3: Absorption spectrum of HO resins of Adelyakovskoe deposit.

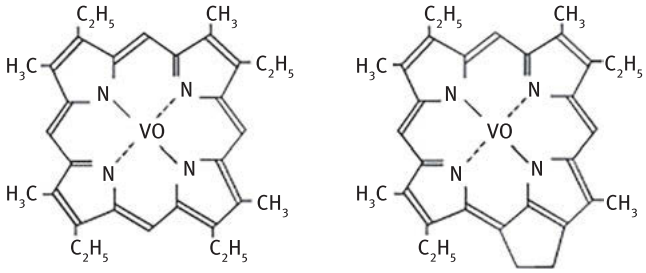

Figure 4.4: Chemical structure of main types of oil VP.

the Siberian Branch of the Russian Academy of Sciences (scheme in Figure 4.5) with subsequent separation of high-molecular OBs using hot *n*-hexane into soluble and insoluble parts.

Main fraction of the OBs extracted from resins is represented by high-molecular-weight bases K-1, the yield of which is 10 wt% of the amount of initial resins. The yield of high-molecular-weight OBs K-2 and low-molecular-weight OBs K-3 is significantly lower and corresponds to less than 1 wt%. Using chromatography-mass spectrometry, C4–C10-qionolines (*m*/*z* 185, 199, 213, 227, 241, 255, 269), C2–C5-benzoquinolines (*m*/*z* 207, 221, 235, 249,), C4–C7-azapyrenes (*m*/*z* 259, 273, 287, 301), as well as C1–C7-thiophenoquinolines (*m*/*z* 199, 213, 227, 241, 255, 269, 283) were identified in low-molecular-weight OBs K-3. In hexane-soluble high-molecular OBs (K-1 GR), C3–C7-benzoquinolines, C4–C8-azapyrenes, and C3–C9-thiophenoquinolines were identified.

Derived from the intensity of intrinsic absorption bands in IR spectra, spectral coefficients, which characterize structural–group composition of OB concentrates, were calculated [58]. *Aliphaticity* (Al) shows the total content of methylene and methyl groups relative to aromatic C=C bonds (D720 + 1380/D1600). *Aromaticity* (Ar) represents the

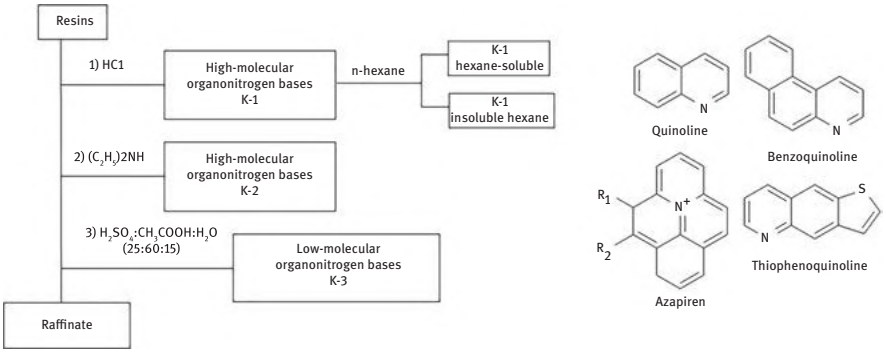

Figure 4.5: Diagram of separation and fractioning of organonitrogen bases from resins.

fraction of C=C-bonds in aromatic fragments relative to C–H-bonds in aliphatic structures (D1600/D720 + 1380). *Condensation degree* (Cn) shows the fraction of C=C-bonds in aromatic fragments relative to C-H-bonds in aromatic structures (D1600/D740 + 860). *Oxidation degree* (Ox) shows the fraction of carbonyl groups R–C=O (when there is OH-group) relative to C=C bonds in aromatic fragments (D1700/D1600). *Sulfonation degree* (S1) reflects the fraction of S=O bonds in sulfoxide fragments relative to aromatic C=C-bonds (D1030/D1600). Analysis of the composition of OBs and raffinate of the resins without OBs according to spectral characteristics and V and VP contents (Table 4.3) showed that K-1 is intrinsic for the maximum aromaticity and condensation degree, as well as the maximum content of V and VPs. Raffinate of the resins is intrinsic for the minimum aromaticity and condensation degree; however, it is characterized by the increased content of carbonyl and sulfoxide groups. In the case of K-3, the V and VP contents are several times as low as those in K-1 and raffinate of the resins.

Table 4.3: Characteristics of the concentrates of organonitrogen bases and raffinate from the heavy oil resins of Smorodinskoe deposit.

Object	Al	Ar	Cn	Ox	S1	Content	
						V, wt%	VP, mg/100 g
K-1	1.38	0.61	1.36	0.43	0.55	0.26	516.3
K-3	1.32	0.59	1.20	0.67	0.74	0.03	62.3
Raffinate of resins	2.75	0.29	0.82	0.76	1.16	0.11	337.9

Recovery and comparison of the concentrate of oxygen-containing compounds (OCs) from resins were performed on the samples of two HOs of Smorodinskoe (well no. 254) and Ashal'chinskoe (well no. 232) deposits with various vanadium contents. Method for recovery of OCs is based on the treatment of the solution of resins in

benzene with aqueous solution of potassium hydroxide followed by oxidation of the extract with sulfuric acid and extraction of water-insoluble oxygen-containing organic compounds with petroleum ether 40–70. As a result, the concentrate of OCs and the residue after treatment of resins with aqueous solution of potassium hydroxide were obtained. The yield of OCs from HO resins of Smorodinskoe deposit (0.3 wt%) with the higher vanadium content is significantly lower as compared to the HO resins of Ashal'chinskoe deposit (2.5 wt%).

Fourier IR spectra of OCs show the absorption bands of carboxyl groups at 1, 700–1,740 cm^{-1}; –C=O groups of chelate complexes, diketones, and ketoesters at 1, 630–1,638 cm^{-1}; and absorbance of ether bonds at 1,170 cm^{-1} along with the absorption bands of aliphatic and aromatic structures. In addition, there is a strong absorption band of free and associated hydroxyl groups at 3,100–3,600 cm^{-1} as compared to initial resins (Figure 4.6b).

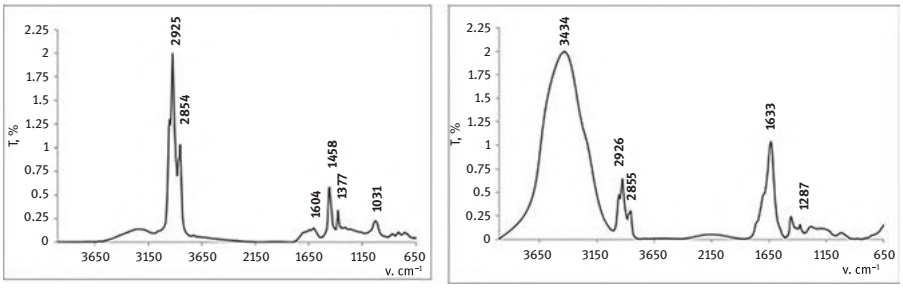

Figure 4.6: Fourier IR spectra of (a) initial resins and (b) OCs of HOs of Ashal'chinskoe deposit.

Analysis of structural–group composition using spectral coefficients showed that the concentrates of OCs differ from initial resins of the HOs by the increased aromaticity, condensation degree, and oxidation degree (Table 4.4).

Recovery and comparison of the concentrate of sulfur-containing compounds from resins were also carried out on the example of two HOs of Smorodinskoe (well no. 254) and Ashal'chinskoe deposits. The procedure of concentration of sulfur-containing compounds was performed in analogy to the procedure developed by the Institute of Petroleum Chemistry of the Siberian Branch of the Russian Academy of Sciences employed for oils and deasphaltizates. The procedure is based on the liquid adsorption chromatography on silica modified with 5% $NiCl_2$, where benzene and, then, ethanol–chloroform (1:1 v/v) mixture were used as eluents. As a result, aromatic (AF) and polar (PF) fractions were recovered from the resins, whose ratio varied among the chosen targets. In the case of the HO of Smorodinskoe deposit, the main fraction is represented by AF (81.5 wt%), whereas in the case of the HO of Ashal'chinskoe deposit the AF content is significantly lower (30.6 wt%). Comparison of

Table 4.4: Characteristics of resins and concentrates of oxygen-containing compounds from heavy oils resins of various deposits.

Object	Al	Ar	Cn	Ox	S1
Smorodinskoe deposit					
Resins	1.47	0.46	0.91	0.54	0.13
OC	0.67	1.24	3.05	0.79	0.22
Ashal'chinskoe deposit					
Resins	1.71	0.45	0.93	0.91	1.44
OC	0.47	1.55	3.39	1.36	0.63

structural–group composition of the fractions of resins was performed on the basis of spectral coefficients in IR spectra with the S2 coefficient, which reflects the fraction of S = O-bonds in sulfonate fragments with respect to aromatic C=C bonds (D1160/D1600) (Table 4.5).

Table 4.5: Characteristics of the fractions of sulfur-containing compounds from heavy oils resins.

Object	Al	Ar	Cn	Ox	S1	S2	Content		
							V, wt%	VP, mg/100 g	S, wt%
Smorodinskoe deposit									
AF	0.70	1.27	1.38	0.45	0.60	0.30	0.14	3971	5.5
PF	2.08	0.49	0.90	0.88	0.81	0.81	0.09	739	2.3
Ashal'chinskoe deposit									
AF	1.00	0.56	1.07	0.81	0.51	0.31	0.056	2489	4.8
PF	2.00	0.39	0.81	1.40	1.60	1.90	0.037	539	1.9

Thus, it was shown that there is concentration of sulfur-containing compounds in PF, where the maximum content of C=O and S=O bonds in sulfoxide and sulfonate groups are indicated along with an increased sulfur content. The AF fraction from resins is characterized by the increased aromaticity and condensation degree, as well as the higher V and VP contents.

4.3 Concentration of vanadyl porphyrins from heavy oil resins

High catalytic activity of natural metalloporphyrins motivated chemists to develop catalytic processes on the basis of their synthetic representatives and the porphyrins recovered from crude oil. A sufficiently high cost of synthetic porphyrins including their closest counterparts, such as phthalocyanines, is a limiting factor for their extensive incorporation in commercial catalytic processes. The porphyrins from heavy oil crude with the increased vanadium content is a promising alternative to expensive synthetic porphyrins.

Study of the variants of concentration and recovery of VPs from resins is exemplified by two HOs of Smorodinskoe (well no. 254) and Ashal'chinskoe (well no. 232) deposits with various vanadium contents. Comparison of the extraction concentration of VPs by various polar solvents (acetone, isopropyl alcohol, acetonitrile, and dimethylformamide (DMF)) was performed on the example of the resins and their fractions (benzene R1 and alcohol-benzene R2). The maximum yield of the extract in all objects was achieved when using DMF as extractant, whereas the yield of the extract was minimum in the case of acetonitrile (Figure 4.7).

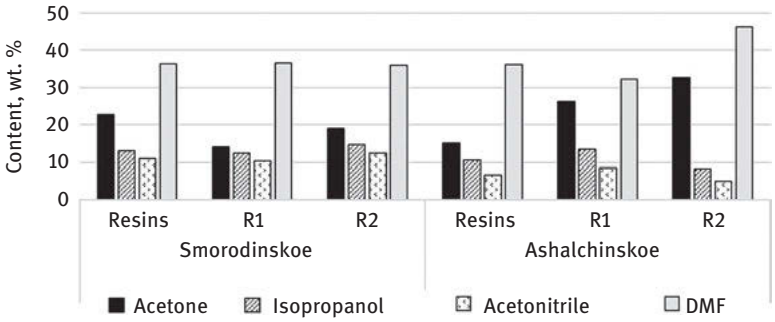

Figure 4.7: Yield of extracts from resins and their fractions (R1) and (R2) for HOs of various deposits.

It was determined from the comparison of the V distribution between extracts and the residues from the resins and their fractions that V is usually concentrated in the residues from resins (47.9–97.4 wt%). Main fraction of VPs is also concentrated in the residues from resins when using acetonitrile, acetone, and isopropyl alcohol as extractants (57.8–94.0 wt%). The maximum content of VPs from resins and fractions of resins is achieved using DMF as extractant (57.8–91.2 wt%); therefore, further studies were carried out with DMF extract.

A fundamentally different approach to the recovery of VPs from oil objects is based on the ability of metalloporphyrins to react with electrophilic addends and

form molecular complexes, which are insoluble in hydrocarbon systems [59–62]. Various metal halides are used as complexing agents, more specifically, $NiCl_2$, $SnCl_4$, $TiCl_4$, and $FeCl_3$. The centers of localization of the bond of metal ion with organic matrix in the complexes are represented by the fragments of molecules containing heteroatoms, free stable radicals, and vanadium (IV).

In order to evaluate the degree of concentration of VPs through complexation under various conditions, DMF extract from HO resins of Smorodinskoe deposit (well no. 254) was studied as initial object. This method is based on the dilution of the mixture of the solution of specimen in benzene with the solution of metal halide in a polar solvent (ethanol or DMF) at the salt-to-N molar ratio in DMF extract of resins of 1:1 or 2:1 (calculated from elemental analysis data) with aliphatic hydrocarbons. As a result, filtrate (F) and residue (R) are obtained after purification from $NiCl_2$ with the mixture of chloroform with water.

Distribution of VPs in filtrate and residue without complexing agent was evaluated at 25°C (Table 4.6). With the aim of preliminary control of the purity of filtrate, the coefficient (K) was introduced, which characterizes the degree of purity of VPs from the impurities of heteroatomic non-porphyrin structure. The coefficient (*K*) was calculated from the recorded spectrum as the intensity ratio of the absorption band at 280–350 nm (absorption band of heteroatomic structures) to 409 ± 2 nm (Soret band of porphyrins) excluding background absorption. The lower the magnitude of the coefficient K, the lower the content of coextracted heteroatomic compounds in the VP concentrate.

Table 4.6: Results of extraction with ethanol and DMF without complexing agent.

Solvent	Yield of filtrate, wt%	VP content, mg/100 g		Fraction of VP in filtrate, wt%	K
		Residue	Filtrate		
Ethanol	92.8	569.2	936.4	95.5	1.73
DMF	89.3	668.8	814.0	90.8	1.91

Thus, it was shown that the main fraction of VP is extracted into filtrate when there is no complexing agent. A series of experiments with $NiCl_2$ complexing agent under various conditions provided the optimal parameters of production of VP concentrate with the minimum fraction of coextracted heteroatomic compounds. The effective concentration of VP from DMF extract of resins using $NiCl_2$ under various temperature conditions is mentioned when using ethanol as solvent (the fraction of VP in filtrate is 92.0–98.4 wt%) (Table 4.7).

It was determined that the coefficient *K* in filtrates is lower as compared to the blank experiment during reaction of heteroatomic components of the object under study with complexing agent. The yield of filtrates in the presence of $NiCl_2$ is higher

Table 4.7: Results of recovery of vanadyl porphyrins (VP) concentrates from DMF extract of resins in the presence of complexing agent in ethanol and DMF under various conditions.

Solvent	$NiCl_2$-to-N ratio (mol:mol)	Yield of filtrate, wt%	VP content in filtrate, mg/100 g	Fraction of VP in F, wt%	K	
					R	F
$T = 6$ °C						
Ethanol	1:1	97.7	1,230.5	98.3	1.13	1.33
	2:1	93.3	1,151.3	93.5	1.20	1.27
DMF	1:1	95.4	1,097.5	98.5	1.15	1.36
	2:1	92.1	930.3	98.0	1.33	1.31
$T = 25$ °C						
Ethanol	1:1	94.6	1,165.4	98.4	1.10	1.29
	2:1	92.7	1,380.6	96.6	1.22	1.27
DMF	1:1	90.0	866.2	95.1	1.26	1.38
	2:1	88.7	941.4	97.7	1.33	1.34
$T_b = 78$ °C						
Ethanol	1:1	91.9	1,231.2	94.6	0.82	1.31
Ethanol	2:1	89.8	1,206.8	92.0	0.87	1.30
$T_b = 153$ °C						
DMF	1:1	89.1	839.2	86.4	0.88	1.49
	2:1	86.4	1,177.8	88.7	0.89	1.49

than 86 wt% under various conditions. As a result of the studies, the lowest magnitude of coefficient K was recorded for residues. Assuming coefficient K, employment of ethanol as a solvent for salt at the temperature of 25 °C represent favorable conditions for the concentration of VP from the DMF extract of resins using $NiCl_2$.

Column chromatography with sulfocationite as a solid phase is one of the variants of purification of VP concentrates from coextracted heteroatomic compounds. Idea of chromatographic purification in this case is based on the ability of polar components with heteroatomic sulfur-, oxygen-, and nitrogen-containing groups to react with sulfo groups of cationite. As a result, heteroatomic compounds are retained in the column, while vanadyl porphyrins do not react with acidic centers of cationite, because nitrogen atoms are protected by chelated by vanadium. This work was not previously carried out; therefore, optimization of chromatography conditions for the isolation of the fractions with the maximum content of vanadyl porphyrins and the minimum

content of impurities was the main problem. As a result, gradient elution of VP concentrate (A0) with a gradual increase in the polarity of eluent was carried out at the first stage, which gave the fractions A1–A10 according to the diagram in Figure 4.8. Vanadyl porphyrin concentrate A0 was obtained from the resins through their adsorption-chromatographic separation on silica (Figure 4.8). Sulfocationite CU-2-8 (analog of Amberlite IR120), which represents a sulfonated copolymer of styrene and divinylbenzene, was used as a sulfocationite after being crushed into fine powder.

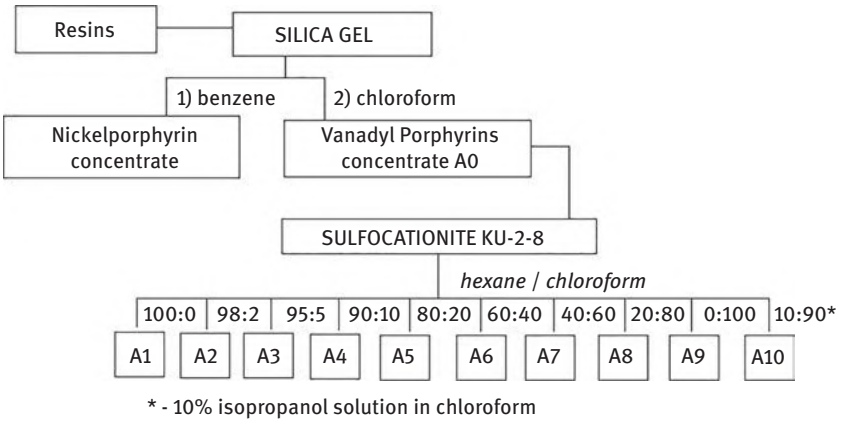

Figure 4.8: Diagram of preparation of vanadyl porphyrin (VP) concentrate from resins and its fractioning via gradient elution through sulfocationite.

In order to evaluate VP distribution into fractions, UV–vis absorption spectra were analyzed (Figure 4.9). The fractions can be divided into two main groups: A1–A4 containing the lowest amount of impurities and A5–A10, in which the absorption bands from impurities (~300 nm) exceed the Soret band intensity (409 ± 2 nm). Each UV–vis absorption spectrum was processed using MS Excel 2010 program. Summation of the heights of Soret bands in the fractions A1–A4 and A5–A10 states that there are ca. 65% of vanadyl porphyrins in A1–A4 fractions and remaining content is in the fractions A5–A10.

As a result of the revealed features of distribution of VPs by fractions, an express approach to the recovery of vanadyl porphyrins from primary concentrate with the retention of the maximum purity of porphyrin fractions was suggested. Three stages of gradient elution were carried out within the improved procedure for VP concentration: 10% chloroform solution in hexane (fraction B1), pure chloroform (fraction B2), and 10% isopropyl alcohol solution in chloroform (fraction B3), which significantly accelerates the process and reduces solvent consumption.

During recovery of VPs according to the improved procedure, fractions B1–B3 were isolated, whose color could be distinguished without preliminary evaporation of solvent and varies from magenta to yellow and yellow-brown. In spite of slight changes

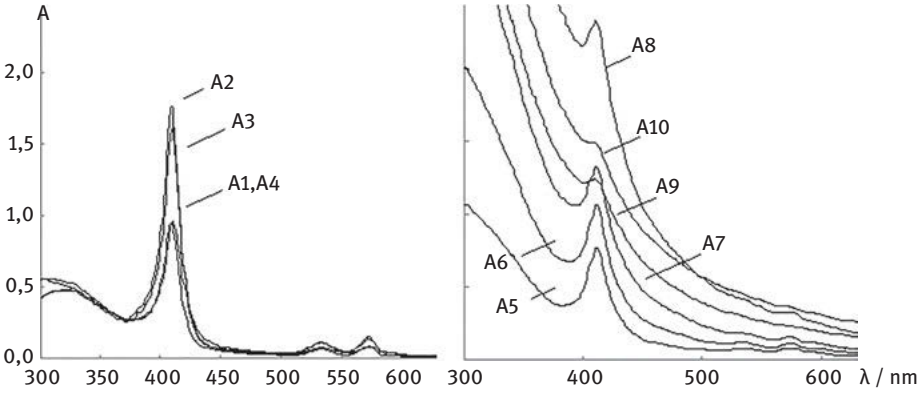

Figure 4.9: UV–vis absorption spectra of the fractions obtained after gradient elution of vanadyl porphyrin (VP) concentrate.

of chromatography conditions, quantitative distribution of VPs by fractions calculated from their absorption spectra remained nearly constant: 66% for the first fraction and 34% for the sum of two other fractions.

In this regard, the result is novel, because there are yet no data on analogous experimental methods, which provide two-stage concentration of nearly 70% of vanadyl porphyrins of such a high spectral purity from oil object. Spectra of the so-formed fractions B1, B2, and B3 are given in Figure 4.10.

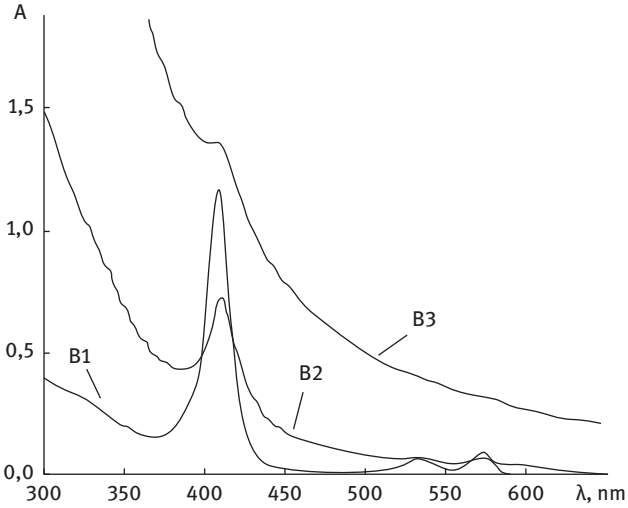

Figure 4.10: Absorption spectra of the fractions obtained after gradient elution of vanadyl porphyrin (VP) concentrate according to optimized procedure.

The achieved degree of purification of vanadyl porphyrins allowed us to record a MALDI-TOF mass spectrum of fraction B1 using *p*-nitroaniline as matrix (Figure 4.11).

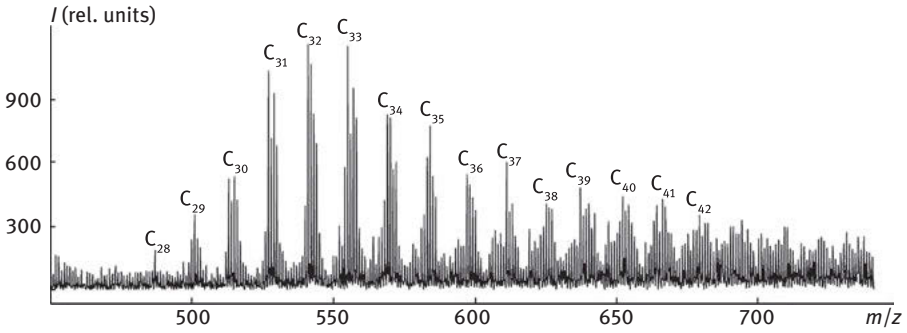

Figure 4.11: MALDI-TOF mass spectrum of fraction B1.

The peaks of homologues C28–C42 of two most common types of oil vanadyl porphyrins were identified in the mass spectrum of fraction B1: etio- and DPEP. The maximum content of both types is represented by the homologue C33 ($m/z = 557.18$ and 555.14 [M] + for etio and DPEP types, respectively), structure of which is given in Figure 4.12. It was also shown that the fraction of etio-VP is slightly lower than that of DPEP-VP (ΣDPEP/ΣETIO = 1.18). A significant complication of the spectrum at higher masses is presumably caused by impurities.

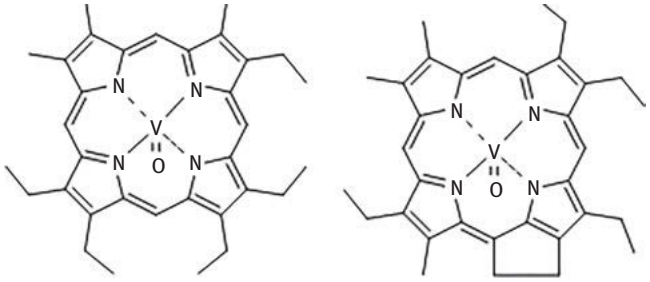

Figure 4.12: Proposed structure of C33 homologue of vanadyl porphyrin (VP) of (a) etio and (b) DPEP types.

Thus, the possibility of recovery of high-purity vanadyl porphyrins from the heavy oil resins through successive extraction concentration and adsorption-chromatographic purification using sulfocationite based on CU-2-8, was demonstrated for the first time. This fact would further extend opportunities of analysis of the structure and

characteristics of oil metalloporphyrins via physicochemical methods of study and form basis for the development of industrial methods for the preparation of porphyrin concentrates from oil crude.

4.4 Spectrophotometric evaluation of the effect of heteroatomic components of resins on the stability of heavy oils to asphaltene precipitation

During the recovery and transport of heavy oil, it is necessary to use more expensive technologies due to the increased instability of such oil systems. Change of pressure and temperature in the deposit may result in precipitation and formation of asphaltene sediments, which decreases the permeability of collector in the bottom-hole zone and downhole pumping equipment. Raw material is diluted with hydrocarbon solvents in the technologies of heavy oil transport in order to decrease viscosity and mix the products of various deposits. If the oils are incompatible, their mixing can give rise to the sediment formation in pipelines and significantly complicate flow processes. To solve this problem, precipitation inhibitors (stabilizers) of asphaltenes are sometimes employed in oil industry. Inhibitors of asphaltene precipitation can kinetically slow down the formation of the solid phase of asphaltenes; thus, stability of oils and oil objects is provided during their recovery, transport, and processing. The components in the oil resins acting as natural asphaltene stabilizing agents are of particular interest. One example is that vanadyl porphyrins in resins can alter asphaltene stability.

Investigation of resins as natural asphaltene stabilizers was carried out on the example of the HOs of Smorodinskoe (well no. 254) and Ashal'chinskoe (well no. 232) deposits. The resins recovered from oils according to the general procedure as well as the concentrates of resins in the form of heavy deasphaltizate residue (HDR) after distillation of the fractions up to 500 °C were used as the inhibitors of asphaltene precipitation (Table 4.8). The yield of HDR corresponds to 31–39.5 wt%, which is slightly higher than the resin content.

Comparison of the composition of resins and HDR revealed that there is a nearly double difference in the V content for each HO (Table 4.8). The VP content in HDR is 2.5 and 4.5 times as low as that in the resins (in the case of HOs of Smorodinskoe and Ashal'chinskoe deposits, respectively). Simultaneously with the extracts from resins (yield of which is given in Figure 4.7), the V and VP content in the extracts from HDR were recovered and analyzed for VP. The V and VP contents in the extracts from resins are larger than those in the extracts from HDR for each HO. The V and VP contents for the extracts from resins and HDR for HO of Smorodinskoe

Table 4.8: Content of V and vanadyl porphyrins (VPs) in resins, heavy deasphaltizate residue (HDR), and corresponding extracts.

Object		Deposit			
		Smorodinskoe		Ashal'chinskoe	
		Content			
		V, wt%	VP, mg/100 g	V, wt%	VP, mg/100 g
Resins		0.140	350.9	0.043	142.4
HDR		0.062	119.6	0.022	31.1
Resin extracts					
Solvent	Acetone	0.130	691.2	0.036	160.8
	Isopropyl alcohol	0.098	490.7	0.021	150.6
	DMF	0.158	790.8	0.047	219.5
HDR extracts					
Solvent	Acetone	0.059	499.1	0.017	61.7
	Isopropyl alcohol	0.038	293.8	0.009	43.1
	DMF	0.074	588.8	0.034	92.0

deposit are higher than those of the HO of Ashal'chinskoe deposit. The maximum content of V and VPs was determined for DMF extracts of all HOs.

Effect of resins and HDR on asphaltene precipitation was investigated through the analysis of variation of absorbance (light absorption coefficient, Kla) of oil upon dilution with *n*-heptane. In this case, there is colloidal destabilization of oil and asphaltene precipitation at a particular solvent-to-*n*-heptane precipitator ratio (40:1). As a result, there is particular decrease in absorbance, which would evaluate the amount of asphaltene precipitate upon dilution of oil with *n*-heptane and, accordingly, effectiveness of various substances that alter this process. Results of comparison of stabilizing effect of resins, HDR, and extracts from them are given in Figure 4.13.

Analysis of the results showed that an increased V and VP contents in the oil resins, HDR, and extracts from them is an important criterion for the effectiveness of inhibition of asphaltene precipitation. One example is that DMF extract from resins showed a comparable result according to the effectiveness of inhibition of asphaltene precipitation with synthetic nonylphenol.

In order to reveal features of asphaltene precipitation, the kinetics of their flocculation in the solvent/precipitator system can be analyzed. This method provides extra information on the asphaltene stability and could test various substances as inhibitors of their precipitation due to the possibility to form various model systems.

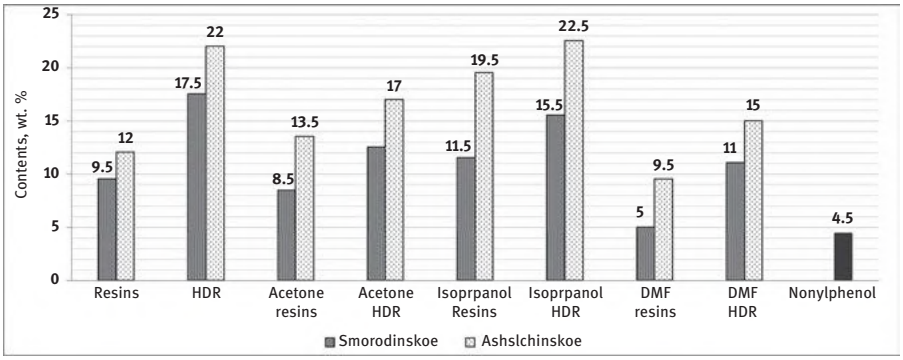

Figure 4.13: Results of determination of minimum amounts of asphaltene precipitation inhibitors.

Example series of experiments of the asphaltenes from Ashal'chinskoe deposit on the UV–vis spectrophotometer evaluated the change of absorbance in kinetic mode for asphaltene solutions in the precipitator/solvent system with the additives of concentrates of N- and S-containing components. The spectra were recorded from the onset of asphaltene flocculation (destabilization of the system) until asphaltene precipitation (steady state) [63–65]. Various fractions of resins were evaluated as additives for inhibition of asphaltene precipitation: OBs (high-molecular-weight OBs K-1 and low-molecular-weight OBs, such as K-3 and raffinate of resins after OB recovery), as well as S-containing (AF and PF). Dynamics of variation of absorbance at 610 nm for toluene solutions of asphaltenes (2 g/L) without/with additives of resins and recovered fractions from resins with the concentration of 3 g/L upon dilution with *n*-heptane (*n*-heptane/toluene = 1.9) over period of 3,600 s is given in Figure 4.14.

As a result, features of the effect of various concentrates of heteroatomic compounds from resins on the aggregation stability of asphaltenes in the solvent/coagulator system were determined. It was shown that the inhibition activity of the concentrates of N-containing components toward asphaltene precipitation increases with an increase in the content of basic nitrogen, vanadium, and vanadyl porphyrins. A series of experiments for the fraction of high-molecular-weight OBs (K-1) revealed the maximum inhibition of asphaltene precipitation, which exceeds that of initial oil resins. It was also discovered on the example of the fractions of resins with various content of S-containing components that the effectiveness of inhibition of asphaltene precipitation increases with an increase in the vanadium and vanadyl porphyrin contents. In this case, an increase in the content of C=O and S=O groups in the fractions of resins does not alter their inhibition activity toward asphaltene precipitation.

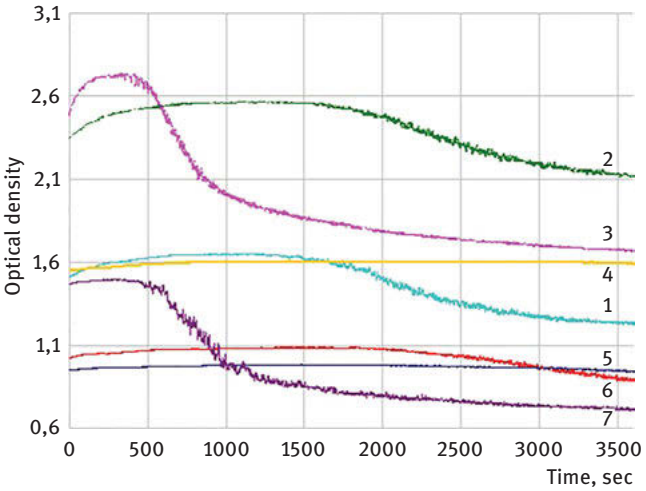

Figure 4.14: Dynamics of variation of absorbance of asphaltene solutions (2 g/L) in toluene after addition of (1) *n*-heptane without additives and with addition of concentrates of N- and S-containing components in *n*-heptane (3 g/L): (2) AF, (3) PF, (4) K-1, (5) resins R_0, (6) raffinate of resins without OB, and (7) K-3.

4.5 Results

1. It has been shown using the example of heavy oils from various deposits that the vanadium content in resins is proportional to the vanadium content in oils. The vanadium content in the resins of the oils of Carboniferous deposits is 1. 5–3.0 times as large as that in initial oils and 1.1–1.9 times as large as that in the resins of the oils of Permian deposits. An increased vanadium content in the resins of oils of Carboniferous deposits as compared to Permian deposits is associated with a larger content of benzene fractions of resins and a higher vanadium content in these fractions.
2. Analysis of the products after chromatographic and extraction fractioning of the resins has shown that vanadium and vanadyl porphyrins are concentrated in benzene resins, which are characterized by the decreased content of aromatic and oxygen-containing structures. The maximum content of vanadyl porphyrins in the extracts from benzene resins is achieved using *N*,*N*-dimethylformamide as extractant, 57.8–84.6% out of their potential content in initial resins.
3. Fourier IR spectroscopy technique has revealed features of structural–group composition of the concentrates of heteroatomic (N, S, O) compounds from heavy oil resins with the increased vanadium content. It has been shown that the concentrates of OBs in the form of alkyl and naphthene derivatives of quinoline, benzoquinoline, azapyrene, and thiophenoquinoline are characterized

by the decreased fraction of carbonyl and sulfo groups. The maximum aromaticity and condensation degree are indicated in the concentrates of oxygen-containing compounds from resins, whereas these values are lowest in the case of the concentrates of polar sulfur-containing compounds.

4. Preparation of purified vanadyl porphyrins from heavy oil resins with the high vanadium content has been demonstrated. Methods for recovery and purification of vanadyl porphyrins are based on their successive extraction-chromatography concentration using sulfocationite at the final stage.
5. Comparison of various fractions of resins has revealed a stabilizing effect of vanadyl porphyrin extracts and concentrates of OBs on the asphaltene precipitation stability of heavy oils. It has been shown that the inhibition of asphaltene precipitation among fractions of resins increases with an increase in the content of basic nitrogen, vanadium, and vanadyl porphyrins.

Funding: This work was performed as part of the state assignment (no. AAAA-A18 -118032690290-1) of the Kazan Scientific Center, Russian Academy of Sciences (studying the features of the influence of concentrates of heteroatomic compounds from resins on the aggregate stability of asphaltenes) and was supported by a grant of the Russian Science Foundation (project no. 19-13-00089) (studying the vanadium distribution in resins and production of purified vanadyl porphyrin concentrates).

References

[1] Speight JG. Petroleum asphaltenes. Part 1. Asphaltenes, resins and the structure of petroleum. Oil & gas science and technology. Rev IFP, 2004, 59(5), 467–477.
[2] Mullins OC, Sheu EY, Hammami A, Marshall AG. Asphaltenes, heavy oils and petroleomics. Springer, New York, 2007.
[3] Mullins OC. The asphaltenes. Annu Rev Anal Chem, 2011, 4, 393–418.
[4] Sugihara JM, Okada T, Branthaver JF. Reductive desulfuration on vanadium and metalloporphyrin contents of fractions from boscan asphaltenes. J Chem Eng Data, 1965, 10(2), 190–194.
[5] Yakubov MR, Milordov DV, Yakubova SG, Borisov DN, Gryaznov PI, Mironov NA, Abilova GR, Borisova YY, Tazeeva EG. Features of the composition of vanadyl porphyrins in the crude extract of asphaltenes of heavy oil with high vanadium content. Petrol Sci Technol, 2016, 34(2), 177–183.
[6] Punanova SA. Supergene transformed naphthides: Peculiarities of trace-element composition. Geochem Int, 2014, 52, 57–67.
[7] Gol'dberg IS. Natural bitumens of USSR (regularities in formation and distribution. Nedra, Leningrad, 1981. (in Russian).
[8] Meyer RF, Attanasi ED, Freeman PA. Heavy oil and natural bitumen resources in geological basins of the world: U.S. Geological Survey Open-File Report 2007-1084, 2007. (available online at http://pubs.usgs.gov/of/2007/1084/).

[9] Head IM, Jones DM, Larter SR. Biological activity in the deep subsurface and the origin of heavy oil. Nature, 2003, 426(20), 344–352.
[10] Dechaine G, Gray M. Chemistry and association of vanadium compounds in heavy oil and bitumen, and implications for their selective removal. Energy Fuels, 2010, 24, 2795–2808.
[11] Speight JG. Heavy and extra–heavy oil upgrading technologies. Gulf Professional Publishing, 2013.
[12] Jenifer AC, Sharon P, Prakash A, et al. A review of the unconventional methods used for the demetallization of petroleum fractions over the past decade. Energy Fuels, 2015, 29(12), 7743–7752.
[13] Liu H, Wang Z, Guo A, et al. The distribution of Ni and V in resin and asphaltene subfractions and its variation during thermal processes. Petrol Sci Technol, 2015, 33(2), 203–210.
[14] Yakubov MR, Borisov DN, Maganov NU, et al. Novel approaches and prospects for upgrading of extra-viscous oil via thermolysis under various conditions. Neftyanoe Khozyaystvo – Oil Ind, 2016, 5, 74–76.
[15] Ancheyta J. In «Problems during Upgrading and Refining of Heavy Petroleum». CRC, 2013, ch. 1.5, pp. 34–41.
[16] Mironov NA, Abilova GR, Borisova YY, et al. Comparative study of resins and asphaltenes of heavy oils as sources for obtaining pure vanadyl porphyrins by the sulfocationite-based chromatographic method. Energy Fuels, 2018, 32(12), 12435–12446.
[17] Yakubov MR, Sinyashin KO, Abilova GR, et al. Differentiation of heavy oils according to the vanadium and nickel content in asphaltenes and resins. Petrol Chem, 2017, 57(10), 849–854.
[18] Gao YY, Shen BX, Liu JC. Distribution of nickel and vanadium in Venezuela crude oil. Petrol Sci Technol, 2013, 31(5), 509–515.
[19] Espinosa PM, Manjarréz A, Campero A. Distribution of vanadyl porphyrins in a Mexican offshore heavy crude oil. Fuel Process Technol, 1996, 46, 171–182.
[20] Yakubov MR, Abilova GR, Yakubova SG, Mironov NA. Composition and properties of heavy oil resins. Petrol Chem, 2020, 60(6), 637–647.
[21] Mullins OC. The modified Yen model. Energy Fuels, 2010, 24(4), 2179–2207.
[22] Andersen SI, Speight JG. Petroleum resins: Separation, character, and role in petroleum. Petrol Sci Technol, 2001, 19(1-2), 1–34.
[23] Boukir A, Aries E, Guiliano M, et al. Subfractionation, characterization and photooxidation of crude oil resins. Chemosphere, 2001, 43(3), 279–286.
[24] Shenghua L, Liu C, Que G, et al. A study of the interactions responsible for colloidal structures in petroleum residua. Fuel, 1997, 76(14–15), 1459–1463.
[25] Cheshkova TV, Kovalenko EY, Gerasimova NN, et al. Composition and structure of resinous components of heavy oil from the field. Petrol Chem, 2017, 57(1), 31–38.
[26] Peralta-Martínez MV, Vázquez-Ramírez R, Blass-Amador G, et al. Determination of functional groups in Mexican vacuum residua. Petrol Sci Technol, 2008, 26(1), 91–100.
[27] Christy AA, Dahl B, Kvalheim OM. Structural features of resins, asphaltenes and kerogen studied by diffuse reflectance infrared spectroscopy. Fuel, 1989, 68(4), 430.
[28] Cheshkova TV, Sergun VP, Kovalenko EY, et al. Resins and asphaltenes of light and heavy oils: Their composition and structure. Energy Fuels, 2019, 33(9), 7971–7982.
[29] Porter DJ, Mayer PM, Fingas M. Analysis of petroleum resins using electrospray ionization tandem mass spectrometry. Energy Fuels, 2004, 18(4), 987–994.
[30] Sudipa MK, Mullins OC, Ralston CY, et al. Determination of sulfur species in asphaltene, resin, and oil fractions of crude oils. Appl Spectrosc, 1998, 52(12), 1522–1525.
[31] Rudzinski WE, Aminabhavi TM. A Review on extraction and identification of crude oil and related products using supercritical fluid technology. Energy Fuels, 2000, 14(2), 464–475.

[32] Zhang J, Tian Y, Qiao Y, et al. Structure and reactivity of Iranian vacuum residue and its eight group-fractions. Energy Fuels, 2017, 31(8), 8072–8086.
[33] Gal'pern GD. Heteroatomic components of petroleum . Russ Chem Rev, 1976, 45(8), 701. (in Russian).
[34] Beiko OA, Golovko AK, Gorbunova LV, et al. Chemical composition of oils in Western Siberia. Nauka, Novosibirsk, 1988. (in Russian).
[35] Baker EW, Palmer SE. Geochemistry of porphyrins. In: Dolphin D, eds. The porphyrins. Academic Press, New York, vol. 1, 1978, 486–552.
[36] Mironov NA, Milordov DV, Abilova GR, Yakubova SG, Yakubov MR. Methods for studying petroleum porphyrins. Petrol Chem, 2019, 59(10), 1077–1091.
[37] Zhao X, Liu Y, Xu C, et al. Separation and characterization of vanadyl porphyrins in Venezuela Orinoco heavy crude. Energy Fuels, 2013, 27, 2874–2882.
[38] Zhao X, Xu C, Shi Q. Porphyrins in heavy petroleums: A review: In structure and modeling of complex petroleum mixtures. Springer, 2015, 39–70.
[39] Sedghi M. Role of Resins on Asphaltene Stability. / M.Sedghi, L. Goual. Energy & Fuels. – 2010. – V. 24. – P. 2275–2280.
[40] Soorghali F, Zolghadr A, Ayatollahi S. Effects of native and non-native resins on asphaltene deposition and the change of surface topography at different pressures: An experimental investigation. Energy Fuels, 2015, 29(9), 5487–5494.
[41] Franco CA, Lozano MM, Acevedo S, Nassar NN, Cortés FB. Effects of resin I on asphaltene adsorption onto nanoparticles: A novel method for obtaining asphaltenes/resin isotherms. Energy Fuels, 2016, 30(1), 264–272.
[42] Larichev YV, Kovalenko EY, Mart'yanov ON. Effect of nitrogen bases on the structure of primary asphaltene clusters and dynamics of aggregation of heavy oil fractions. Petrol Chem, 2019, 59(11), 1195–1200.
[43] Chen L, Bertolini A, Dubost F, et al. Yen–mullins model applies to oilfield reservoirs. Energy Fuels, 2020, 34(11), 14074–14093.
[44] Ovalles C, Rogel E, Moir M, et al. Characterization of heavy crude oils, their fractions, and hydrovisbroken products by the asphaltene solubility fraction method. Energy Fuels, 2012, 26(1), 549–556.
[45] Rogel E, Vien J, Morazan H, et al. Subsurface upgrading of heavy oils via solvent deasphalting using asphaltene precipitants. preparative separations and mechanism of asphaltene precipitation using benzoyl peroxide as precipitant. Energy Fuels, 2017, 31(9), 9213–9222.
[46] Guzmán R, Ancheyta J, Trejo F, et al. Methods for determining asphaltene stability in crude oils. Fuel, 2017, 188, 530–543.
[47] Leon O, Contreras E, Rogel E, et al. Adsorption of native resins on asphaltene particles: A correlation between adsorption and activity. Langmuir, 2002, 18, 5106–5112.
[48] Ren T, Wang Y, Zhang G. Influence of the properties of resins on the interactions between asphaltenes and resins. Petrol Sci Technol, 2017, 35(14), 1481–1486.
[49] Alcazar-Vara LA, Zamudio-Rivera LS, Buenrostro-Gonzalez E. Effect of asphaltenes and resins on asphaltene aggregation inhibition, rheological behavior and waterflood oil-recovery. J Dispers Sci Technol, 2016, 37(11), 1544–1554.
[50] Liu H, Liu Z, Guo A, et al. Peptizing effect of the native heavy resin fraction on asphaltenes. Energy Fuels, 2018, 32(3), 3380–3390.
[51] Marques LCC, Pereira O, Bueno AD, et al. A study of asphaltene-resin interactions. J Braz Chem Soc, 1880, 2012(23).
[52] Goual L, Firoozabadi A. Effect of resins and DBSA on asphaltene precipitation from petroleum fluids. Am Inst Chem Eng J, 2004, 50(2), 470–481.

[53] Pereira JC, López I, Salas R, et al. Resins: The molecules responsible for the stability/instability phenomena of asphaltenes. Energy Fuels, 2007, 21, 1317–1321.
[54] Rytting BM, Harper MR, Edmond KV, et al. High-purity vanadyl petroporphyrins: Their aggregation and effect on the aggregation of asphaltenes. Energy Fuels, 2020, 34, 164–178.
[55] Rytting BM, Harper MR, Edmond KV, et al. Interfacial phenomena of purified petroporphyrins and their impact on asphaltene interfacial film formation. Energy Fuels, 2020, 34, 5444–5456.
[56] Yakubov MR, Abilova GR, Sinyashin KO, et al. Inhibition of asphaltene precipitation by resins with various content of vanadyl porphyrins. Energy Fuels, 2016, 30, 8997–9002.
[57] Demirbas A, Taylan O. Removing of resins from crude oils. Petrol Sci Technol, 2016, 34(8), 771–777.
[58] Taheria Z, Dehaghani AS, Ayatollahi S, et al. new insight to the assessment of asphaltene characterization by using Fortier transformed infrared spectroscopy. J Petrol Sci Eng, 2021, 205, 108824.
[59] Plusnin AN, Khokhlova GP, Kryazhev YG, et al. Fractionation of resinous asphaltene substances of oil by titanium tetrachloride. Petrol Chem, 1976, 16(4), 635–639. (in Russian).
[60] Antipenko VR, Pevneva GS, Zemtseva LI. Composition of the products of reaction of the components of residual petroleum fractions with ferric chloride. Petrol Chem, 1994, 34(1), 84–96. (in Russian).
[61] Khokhlova GP, Plusnin AN, Kryazhev YG. Complexation of some synthetic polymers, modeling structural fragments of asphaltenes, with titanium tetrachloride. Petrol chem. 1979, 19, 148–156. (in Russian).
[62] Khokhlova GP, Plusnin AN. Separation of oil residues by complex formation with TiCl4. Petrol Chem, 1983, 23, 419–423. (in Russian).
[63] Andersen SI. Flocculation onset titration of petroleum asphaltenes. Energy Fuels, 1999, 13(2), 315–322.
[64] Petrova LM, Abbakumova NA, Borisov DN, et al. Interrelation of flocculation, precipitation, and structure of asphaltene fractions. Chem Technol Fuels Oils, 2013, 49(1), 25–31. (in Russian).
[65] Borisova YY, Tazeeva EG, Mironov NA, et al. Role of vanadylporphyrins in the flocculation and sedimentation of asphaltenes of heavy oils with high vanadium content. Energy Fuels, 2017, 31(12), 13382–13391.

Yunlong Zhang, Bruno Schuler, Fang Liu, Yosadara Ruiz-Morales,
Leo Gross, Andrew E. Pomerantz, Vincent Pauchard,
Sanjoy Banejee, Oliver C. Mullins

5 Asphaltenes: structures and applications

Abstract: Asphaltenes are complex chemical mixtures which represent a solubility fraction of crude oil and of carbonaceous materials, typically defined as toluene soluble and *n*-heptane insoluble. Almost every chemical attribute of asphaltenes has been the subject of significant literature debate, especially asphaltene molecular weight. This debate was resolved ultimately with agreement among many mass spectrometric techniques and also molecular diffusion measurements. Artifacts in some molecular weight measurements, especially colligative techniques and some mass spectrometric methods associated with asphaltene aggregation, have been identified. Asphaltene molecular architecture had been less well resolved; however, recent extensive studies of direct molecular imaging using atomic force microscopy (AFM) and scanning tunneling microscopy confirm early findings of the dominance of the "island" molecular structure and have led to definitive conclusions regarding dominant molecular structural motifs of asphaltenes, thereby resolving this important issue. In addition, AFM has proven to be a valuable probe of other related materials and the corresponding reaction chemistry. The distribution of asphaltene molecular structures and characterization of molecular species at lower concentrations is also of interest. In addition, species present in low concentrations exhibit atypical structures and can have measurable impact of some asphaltene properties. Nevertheless, the effective centroids of the molecular and colloidal distributions are important and indeed required for some applications such as thermodynamic modeling. The Yen–Mullins model specifies these molecular and hierarchical nanocolloidal centroids, and when combined with the Flory–Huggins–Zuo equation of state accounts for asphaltene gradients in oilfield reservoirs. The molecular structure from the Yen–Mullins model combined with the Langmuir equation of state accounts for

Yunlong Zhang, ExxonMobil Research and Engineering Company, Annandale, NJ 08801, USA
Leo Gross, IBM Research – Zurich, 8803 Rueschlikon, Switzerland
Bruno Schuler, IBM Research – Zurich, 8803 Rueschlikon, Switzerland; Empa, Swiss Federal Laboratories for Materials Science and Technology, 8600 Dübendorf, Switzerland
Fang Liu, Vincent Pauchard, Sanjoy Banejee, Energy Institute and Department of Chemical Engineering, City College of New York, New York, NY 10031, USA
Yosadara Ruiz-Morales, Instituto Mexicano del Petróleo, Eje Central Lázaro Cárdenas Norte 152, México, D.F. 07730, México
Andrew E. Pomerantz, Oliver C. Mullins, Schlumberger-Doll Research, Cambridge, MA 02139, USA

https://doi.org/10.1515/9783110694529-005

many interfacial properties of lower concentrations of asphaltene solutions. Nevertheless, accounting for more subtle effects of interfacial properties requires more than a single representative structure of asphaltenes. The interplay between basic science measurements of asphaltene properties and of important oilfield applications of these properties provides a stringent test platform and validation for these advances in asphaltene science.

5.1 Introduction

"If you want to understand function, study structure," instructs the Nobel laureate Francis Crick, an axiom he exemplified with elucidation of the structure of DNA. The most important attribute of a chemical is its elemental composition. There is no debate about the measurement of elemental constituents of asphaltenes. Atomic composition of petroleum asphaltenes is dominated by roughly equal amounts of carbon and hydrogen with percent levels of sulfur, nitrogen, and oxygen and trace vanadium and nickel. There is some variability in elemental composition depending on the source materials (virgin (unprocessed) crude oil, resid, coal-derived materials, immature source rock bitumen, etc.) as well as on the choice of precipitating solvent, typically *n*-heptane but sometimes *n*-pentane [1, 2]. Herein, the term "asphaltenes" refers to those compounds obtained from virgin crude oil, unless otherwise specified. In addition, from a practical point of view, some studies are performed on carbonaceous materials that have been constrained to precipitate in *n*-heptane but without the constraint of dissolution in toluene; such materials can possess larger molecules than actual asphaltenes. Table 5.1 lists the elemental composition for a few asphaltenes obtained from black oils. The dominant elements are carbon and hydrogen along with lesser and variable amounts of sulfur, nitrogen, and oxygen. The Yen model [3] proposed that the primary chemical moieties are aliphatic and aromatic carbon as confirmed repeatedly with NMR and IR spectroscopies [4, 5]. In addition, ^{13}C NMR spectroscopy shows that roughly half of the asphaltene carbon is aromatic and half is aliphatic [4–9].

The heteroatoms will be discussed subsequently in more detail in Section 5.7. The most significant heteroatom is generally sulfur; x-ray absorption near-edge structure (XANES) determinations of asphaltene sulfur show that thiophene and sulfide sulfur dominate and occasionally sulfoxide contributes [10, 11]. Nitrogen XANES studies show that all asphaltene nitrogen is aromatic with pyrrolic nitrogen that is present more than pyridinic nitrogen [12]. Oxygen moieties include a substantial phenolic component [13] and a lesser carbonyl component which can include organic acids especially for biodegraded crude oils [4, 5, 14].

Table 5.1: Elemental composition for selected *n*-heptane asphaltenes from black oil.

Asphaltene	C	H	N	S	O	H/C atomic
CAL	82.91	8.55	2.32	2.6	3.75	1.24
FRA	90.79	7.53	0.54	0.68	1.11	1.00
KUW1	79.2	7.82	0.98	7.61	2.45	1.18
KUW2	81.34	7.57	0.85	8.84	0.87	1.12
KUW3	83.28	8.04	0.95	7.76	0.98	1.16
CAN	84.3	8.12	0.91	5.82	1.42	1.16

5.1.1 The Yen–Mullins model

A summary of many results across a multitude of techniques applied to asphaltenes is summarized in the Yen–Mullins model. This model was introduced in 2010 showing the dominant molecular structure of asphaltenes and the two hierarchical nanocolloidal structures that can exist in solution and in crude oil for geologic time [15, 16]. This model, originally called the modified Yen model [15], was built upon the Yen model introduced by Professor Teh Fu Yen in 1967 that captured specific chemical moieties in asphaltenes but could not identify specifics of molecular colloidal structures [17]. The Yen–Mullins model and its predecessor, the Yen model, are designed to provide an overview of the most important structures in asphaltenes but are not intended to capture the incredible range of structures and properties of asphaltenes. Nevertheless, for some purposes, such as modeling gravitational gradients of asphaltenes in oilfield reservoirs, the centroids of each of the three species of the Yen–Mullins model are required; otherwise, the effects of gravity are indeterminate. This is discussed in the section 5.8 in this chapter, *Flory–Huggins–Zuo equation of state (FHZ EoS)*. Indeed, this modeling of reservoir crude oils is very useful and has led to the development of the new technical discipline, "reservoir fluid geodynamics," as described in the eponymous chapter in this book [18]. In addition, the molecular structure of the Yen–Mullins model has found utility with modeling interfacial properties of asphaltene solutions by utilizing the Langmuir equation as discussed in Section 5.2.8 [19, 20]. The applications of the Yen–Mullins model with bulk and interfacial thermodynamic modeling with minimum parameters validate these related results.

The Yen–Mullins model provides the centroid of three species of asphaltenes that are routinely found in crude oils and in laboratory solvents [15, 16, 18]. At low concentrations, such as light oils, asphaltenes are present as true molecular solutions. At moderate concentrations such as in black oils asphaltenes are present as

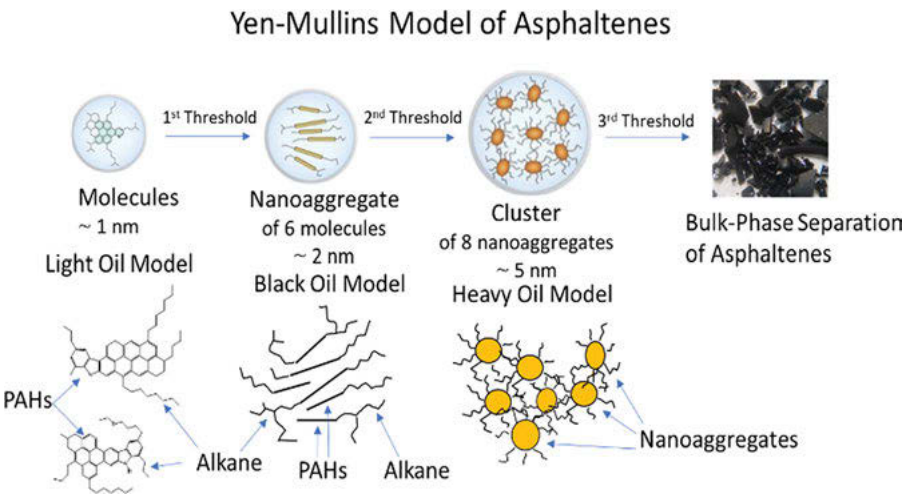

Figure 5.1: The Yen–Mullins model of asphaltenes consisting of approximations of the centroids or most probable molecular structure and two hierarchical nanocolloidal species, the nanoaggregate and the cluster [15, 16]. This model provides an overview of important features of asphaltene science. In addition, such a model is required for the gravity and other terms for some applications such as modeling asphaltene gradients in reservoir crude oils [18]. In addition, to the centroids, this chapter emphasizes the range of molecular structures found in asphaltenes.

nanoaggregates, and at high concentrations such as found in heavy oils, asphaltenes are found as clusters of nanoaggregates. This model clarifies key features of asphaltenes that have been the subject of literature debates, especially molecular weight and molecular architecture. This chapter emphasizes recent key findings on these topics. Other previous controversies such as aggregation concentrations and aggregation numbers are also discussed, and their relationship to hindering accurate determinations of molecular properties are clarified.

5.2 Asphaltene molecular weight and molecular structure

The second most important attribute of a chemical compound after elemental composition is molecular weight. There was a substantial debate regarding asphaltene molecular weight [21]. Popular colligative methods for molecular weight determination of other crude oil components such as vapor pressure osmometry (VPO) gave variable and typically large values of asphaltene molecular weights. Subsequent analysis proved that aggregation thresholds for asphaltenes [22, 23] were below concentrations used for VPO; consequently, the weight of the aggregate species were

determined. Specifically, the existence of two nanocolloidal aggregation thresholds (cf. Figure 5.1) caused significant confusion. VPO measurements were often performed at concentrations below the higher threshold and led to the belief that a molecular dispersion had been achieved; it had not. These experiments were performed at concentrations above the lower nanoaggregation threshold [21]. Indeed, these VPO studies often obtained molecular weights too high by a factor of ~6, thereby providing a preview of nanoaggregate aggregation numbers.

Moreover, a then popular mass spectrometric method for asphaltene molecular weight determination, laser desorption–ionization mass spectrometry (LDI MS), was also subsequently shown to suffer from aggregation effects as well [21, 24–26]. This unfortunate "confirmation" of artifactually high asphaltene molecular weights led to proposals of the "archipelago" molecular structure of asphaltenes with many polycyclic aromatic hydrocarbon (PAH) units cross-linked with aliphatic bridges within single molecules [27].

5.2.1 Asphaltene molecular weight and structure from molecule diffusion

In a series of experiments, the first molecular diffusion measurements by time-resolved fluorescence depolarization (TRFD) obtained strikingly different results [6, 28–34]. These experiments are performed with dilute to very dilute solutions obviating concern of aggregation effects. Figure 5.2A shows the concepts of the TRFD experiment. A polarized laser electronically excites a dilute solution of asphaltenes, and the electric polarization vector is fixed within the molecular framework. Molecular rotational diffusion proceeds, which reorients the polarization direction. At some point, fluorescence emission takes place characterized by the reoriented polarization direction. For an ensemble of molecules, polarization reorientation yields an ensemble depolarization; the rotational diffusion constant is obtained by measuring the decay rate of the polarization [6, 28–33]. The rotational correlation time, τ, the time it takes the polarization vector to displace one radian, is given by eq. (5.1) for a sphere, where η is viscosity, V is the volume of the sphere, k is Boltzmann's constant, and T is temperature:

$$\tau_{sp} = \frac{V\eta}{kT} \tag{5.1}$$

By keeping the wavelength difference between the excitation laser and the detected fluorescence emission to a minimum (~40 nm), a subset of asphaltene molecules were selected that have their HOMO–LUMO gap at that excitation energy (HOMO–LUMO is the highest occupied molecular orbital–lowest unoccupied molecular orbital). By utilizing many pairs of excitation and emission wavelengths always with small differences, the entire population of fluorescent asphaltene molecules can be interrogated. Figure 5.1B shows typical TRFD data for asphaltenes. Asphaltenes are characterized by

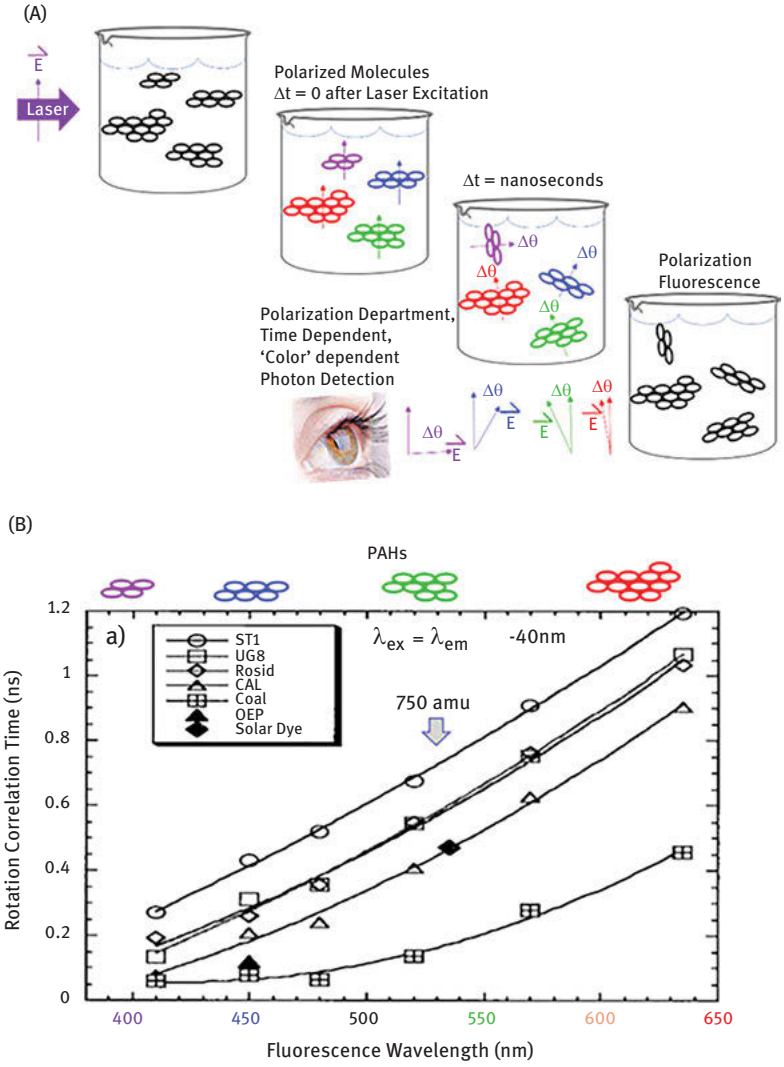

Figure 5.2: (A) Concepts of TRFD for determination of rotational diffusion rates [6, 28–35]. (B) TRFD data obtained for asphaltenes. Rapid rotational rates are obtained, indicating asphaltene molecules are small. A large dispersion is obtained because small, blue emitting chromophores rotate much faster the large, red-emitting chromophores. Thus, these chromophores are not cross-linked in asphaltenes; asphaltene molecules consist predominantly of molecules with a single PAH. The increased fluorescence wavelength for increasing an increasing number of rings is depicted. These TRFD experiments represented the birth of the island molecular model for asphaltenes [6, 28–33]. Reprinted with permission from the American Chemical Society.

rapid rotational diffusion, and, in comparison with model compounds, an average molecular weight of 750 g/mol was obtained for petroleum asphaltenes, and a much smaller molecular weight was obtained for coal-derived asphaltenes.

The very large dispersion exhibited by asphaltene correlation times is in accord with the "quantum-particle-in-a-box." Larger PAHs generally have redshifted spectra associated with the increased length scale of the molecular orbital (MO) wave functions. The geometry of the ring systems also plays a very large role in the energy of electronic transitions of PAHs [36]. Careful accounting of the number and geometry of PAH rings confirms that indeed the results in Figure 5.2B for the dispersion of the rotational correlation time for asphaltenes are consistent with expectations from "quantum-particle-in-a-box" considerations [37–42]. Figure 5.2B indicates that asphaltene molecules contain predominantly a single PAH per molecule. The molecules with a single blue-emitting PAH rotate ten times faster than the asphaltene molecules with a single red-emitting PAH. Cross-linking multiple PAHs into a single molecule would preclude such a large dispersion effect of a factor of 10 [6, 28–33, 35]. The optical spectral analysis of asphaltenes compared to model compounds and to MO calculations of over 500 PAHs is consistent with the average asphaltene PAH possessing seven rings [37, 39–42]. As will be discussed in the atomic force microscopy (AFM) and scanning tunneling microscopy (STM) sections, this assessment closely matches observations obtained in direct molecular imaging of asphaltenes [35, 43, 44].

There is consistency between the determinations of the average asphaltene molecular weight being 750 g/mol for asphaltenes and the average asphaltene PAH ring system containing 7 rings with half of the asphaltene carbon being aromatic and half being aliphatic. The PAH size gives a molecule with roughly 50 carbon atoms with other elemental constituents; this brings the total weight to about 750 g/mol. Certainly, multiple PAHs are inconsistent with 750 g/mol. Several other diffusion measurements are consistent with the TRFD results, including NMR [45], fluorescence correlation spectroscopy [46–49], and Taylor dispersion [50].

5.2.2 Asphaltene molecular weight from mass spectrometry

The divergent results obtained from VPO and some LDI MS studies, on the one hand, and the molecular diffusion measurements, on the other hand, spurred substantial interest in many mass spectrometry groups, and a broad agreement has been obtained with ~750 g/mol with distribution width of 500–1,000 g/mol. The methods that contributed to the resolution of asphaltene molecular weight include electrospray ionization (ESI) and Fourier-transform ion cyclotron resonance mass spectroscopy (FT-ICR MS) [51–55]. This ultrahigh resolution method is capable of assigning a unique elemental composition to each peak, a tremendous capability. However, this method has substantially variable cross sections for different molecular types and has difficulties associated with asphaltene aggregation as well [54], so

other mass spectrometric methods are important for validation purposes. The problems with LDI MS methods for asphaltenes were identified in large part associated with high plasma densities; at low plasma densities, LDI MS results for asphaltenes are consistent with all other techniques [24–26]. Other important methods applied to asphaltenes gave consistent results and include laser-induced acoustic desorption mass spectroscopy (LIAD MS), [56] tandem mass spectrometry [57, 58], atmospheric pressure chemical ionization mass spectrometry (APCI MS) [59], and laser desorption–laser ionization mass spectrometry (L^2MS) [60–65].

L^2MS suppresses aggregation and fragmentation and is characterized by a relatively flat ionization cross section for different classes of asphaltene molecules, thereby giving accurate mass distributions [62, 64, 66, 67]. In L^2MS, the volatilization of the asphaltene is achieved with an IR laser, which yields no ionization. L^2MS applied to very strongly aggregating compounds such as caffeic acid with its organic acid and two phenoxy groups exhibits no aggregation in the mass spectrum [67]. In addition, with the very rapid heating achieved with the IR laser (10^8 K/s), fragmentation is suppressed [68]. At a controllable time after desorption, a UV laser performs ionization. A combination of low power of the UV laser and a delay between desorption and ionization avoids plasma formation, thereby suppressing aggregation.

Figure 5.3 shows the asphaltene molecular weight distribution obtained by L^2MS. The distribution is independent of surface concentration of asphaltenes and of the laser powers, factors which are known to strongly affect LDI MS results on asphaltenes [24–26]. In addition, the distribution is independent of the timing between laser pulses showing that the desorption (neutral) plume density is not introducing artifacts. The molecular weight distributions are consistent with many other mass spectrometric determinations. Little controversy remains regarding asphaltene molecular weight determination. This former controversy in the field of asphaltene science had been particularly pernicious because the determination of structure–function relationships requires reasonably accurate molecular weights.

It is important to note that there is a dependence of asphaltene molecular weight for very different source materials. All petroleum samples exhibit similar molecular weight distributions. However, asphaltenes have been obtained from the process of (1) coal liquefaction via hydrogenation followed by (2) distillation of coal liquids and then (3) separating asphaltenes from the resulting resid [34]. These CAs contain a much smaller fraction of aliphatic carbon than petroleum asphaltenes [6]. All comparisons of these CAs show that they have a molecular weight on order one half of those of petroleum asphaltenes [6, 26, 29, 33, 34, 48, 58, 69]. A broad agreement across many experimental techniques for differences in petroleum asphaltenes versus CAs is important for validation of all these results.

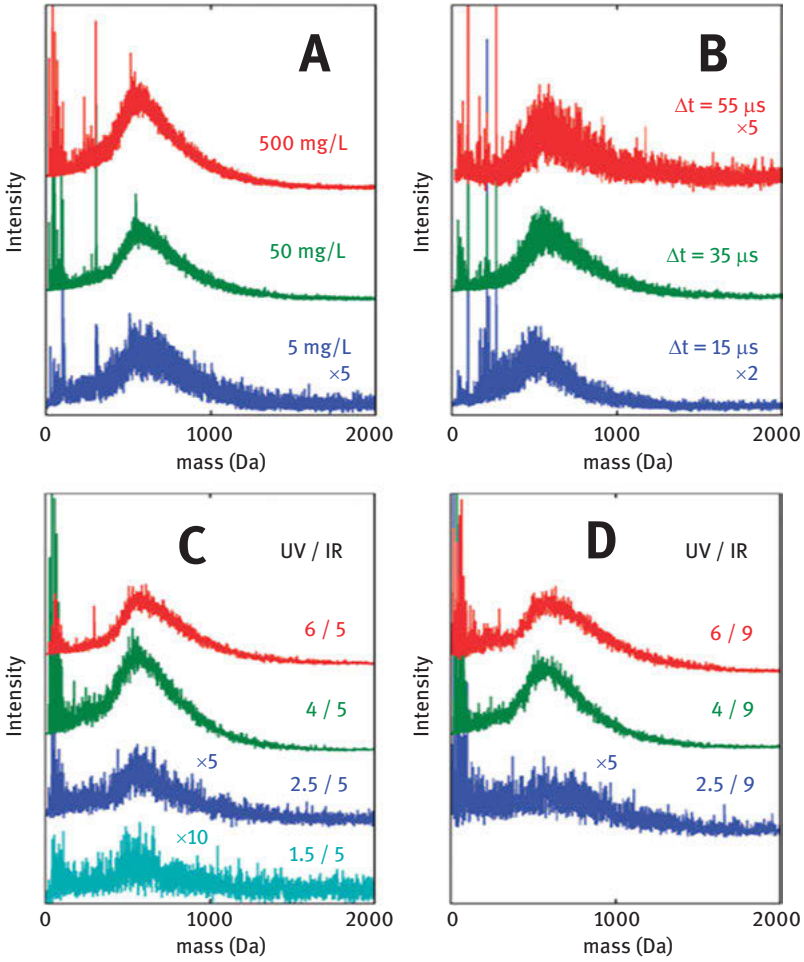

Figure 5.3: Typical L^{2}MS data for asphaltenes shows that the measured molecular weight distribution is independent of (A) asphaltene surface concentration, (B) time between pulses, and (C and D) IR and UV laser power. Artifacts of aggregation and fragmentation at various higher laser powers are evidently not occurring; the asphaltene mass distribution is accurate [60]. Reprinted with permission from the American Chemical Society.

5.2.3 Asphaltene molecular structure from L^{2}MS

As noted above, TRFD gave rise to the first results that indicated asphaltene molecular architecture is dominated by the "island" structure with predominantly a single PAH ring system per molecule. The smaller molecular weights now broadly accepted are incompatible with a large number of PAH per molecule that had previously been accepted. Nevertheless, it is important to utilize methods that have

relatively flat cross sections for virtually all potential classes of molecular structures of asphaltenes. TRFD detects only fluorescent molecules. While there is no reason a priori to expect a bias with TRFD, it remains important to establish the molecular structure with methods utilizing invariant or flat cross sections.

L^2MS has been established to have relatively flat cross section for different asphaltene molecular types [67]. The only type of asphaltene molecule excluded in typical L^2MS studies is those with no PAH, thus high ionization threshold. Consequently, L^2MS is a good candidate to obtain bulk asphaltene information. Moreover, as noted above, L^2MS methods do not suffer from aggregation effects of molecules such as caffeic acid with strong intermolecular interactions [67]. In addition, a lower energy laser desorption method than L^2MS, surface-assisted LDI MS (SALDI MS), shows that asphaltene aggregates can be preserved only at the lowest desorption energies; thus, L^2MS is not expected to have any aggregation concerns [62, 69]. SALDI MS on asphaltenes is discussed in greater detail in the section 5.6.4. Many mass spectrometric methods do not involve flat cross sections. For example, ESI and atmospheric pressure ionization methods such as APPI (atmospheric pressure photoionization) and APCI are widely acknowledged to have huge variations of cross section.

L^2MS has been used to probe the asphaltene molecular architecture [63]. As noted in the L^2MS data for asphaltenes presented in Figure 5.3, the desorbing IR and ionizing UV laser powers can of be independently controlled. If higher powers are used for the ionizing laser pulse, then in some cases molecular fragmentation can result. This fragmentation can be represented as a reduction of the average molecular weight at higher laser powers. Figure 5.3 shows L^2MS applied to asphaltenes and 23 model compounds at various ionization laser powers.

Figure 5.4 shows powerful evidence that asphaltenes are dominated by island architecture with a single PAH per molecule. Asphaltenes and all 13 island model compounds remain stable and resist fragmentation at higher ionization laser powers while all 10 archipelagos are less stable and fragment at higher ionization laser powers. This instability of archipelago compounds might account for why they are not found in crude oil asphaltenes that have survived for geologic time. To be precise, one of the "island" model compounds (I-4 in Figure 5.4) is actually more accurately referred to as an aryl-linked core [35] even though it behaves like an island compound in its resistance to fragmentation. In any event, the data in Figure 5.3 is a strong indicator that the island structure dominates asphaltenes. The flat cross section of $L2^2MS$ and the clear distinction between island and archipelago model compounds in Figure 5.4 are compelling. Nevertheless, a direct method of determination of asphaltene molecular architecture is highly desirable to resolve this long-standing debate of island and archipelago and more importantly to characterize the different classes and distributions of molecular types.

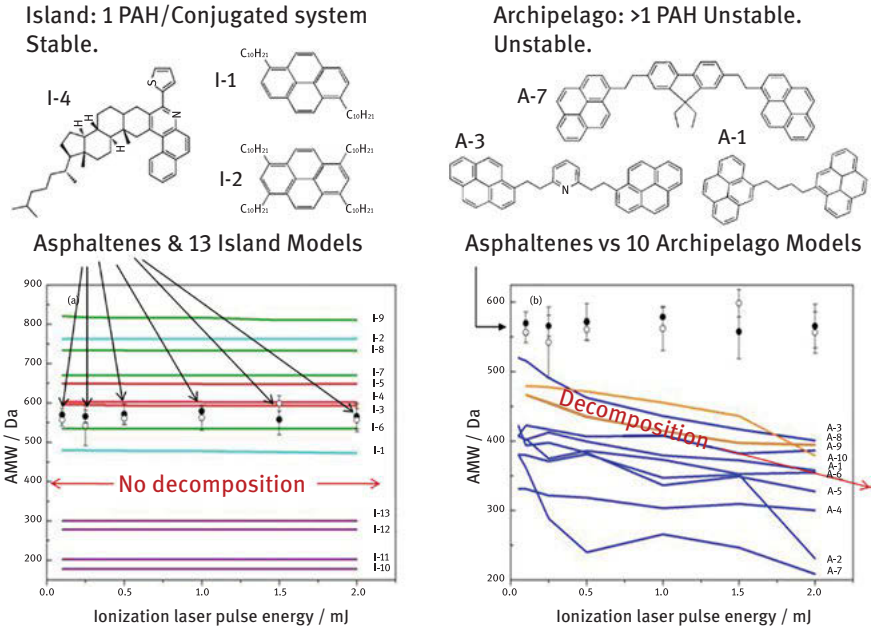

Figure 5.4: Average molecular weight (AMW) versus laser power for 23 model compounds and asphaltenes [63]. The structures of several island and archipelago model compounds are shown at the top and were evaluated by L^2MS. (Left) At higher UV laser power, island molecules and asphaltenes remain stable. (Right) However, under these same conditions, archipelago molecules with more than one PAH cross-linked with aliphatic linkers, fragment; thus, their AMW decreases. This behavior is in contrast to asphaltenes. These results indicate that asphaltenes are dominated by island molecular architecture [63]. Note that a molecule with a direct aryl linkage (I-4) is defined here as an island structure because of its single network of sp^2 hybridized carbon. Reprinted with permission from the American Chemical Society.

5.3 Single-molecule imaging applied to asphaltenes and related materials

5.3.1 Atomic force microscopy

The ability to obtain a real-space, atomically resolved image of a single molecule was first accomplished about a decade ago when the group led by Gerhard Meyer and Leo Gross at IBM Research – Zurich recorded the five-ring structure of pentacene by noncontact AFM (nc-AFM) using a CO-functionalized tip [70]. Since then, this technique has emerged as a new interdisciplinary research field interfacing chemistry, condensed matter physics, nanotechnology, and materials and energy sciences. Single-molecule imaging enables new opportunities to address various

open challenges in chemistry (summarized in Table 5.2), such as (a) structural characterization of synthetic or natural molecules [70–74]; (b) studying reactive intermediates [75–80]; (c) accessing molecular properties such as bond order [81–83], charge distribution or the charge state [84, 85], adsorption geometry [86], and MO densities [87]; and (d) on-surface synthesis of new structures and atomic manipulation of molecules [80, 88–92].

In particular, AFM is a powerful tool for studying complex mixtures like petroleum [93–104], because isolation and purification of individual compounds required for conventional analysis are nearly impossible. The focus of this review will specifically survey the research progress made in applying nc-AFM to study petroleum-related molecular mixtures [77, 94–98, 100–107]. We would also like to highlight recent reviews on nc-AFM-based molecular structural elucidation by Gross et al. [108] and on on-surface synthesis by Clair and de Oteyza [109].

5.3.2 Structure characterization of petroleum asphaltenes with nc-AFM

The first study on petroleum asphaltenes with atomically resolved AFM images was reported in 2015 [93]. Both STM and nc-AFM images were used for a detailed characterization of structures in coal-derived asphaltenes and petroleum-derived asphaltenes which have been studied previously with other methods [9, 115]. The coal-derived asphaltene sample studied was the toluene-soluble and hexane-insoluble fraction obtained from a soxhlet extraction of a distilled residue from liquefaction (450–465 °C) of Tanito Harum coal (H/C 0.74) [115]. The petroleum-derived asphaltene sample studied was the *n*-heptane insoluble fraction (40/1 v/w) obtained from a UG8 crude oil (H/C 1.05) [8, 9, 93]. Over 100 molecules were imaged for coal-derived asphaltenes (Figure 5.5) and 14 images for petroleum-derived asphaltenes (Figure 5.6). AFM imaging yielded more results on coal-derived asphaltenes than on petroleum-derived asphaltenes because the coal-derived asphaltene structures were mostly PAHs or PAH with short aliphatic substituents. The petroleum-derived asphaltene molecules were more complex and more challenging to image than coal-derived asphaltenes because of more and larger aliphatic moieties, and the assignment of their chemical structures was more challenging.

The observed AFM structures for coal-derived asphaltenes are in excellent agreement with a size of 1.2–1.4 nm and an approximate shape of a prolate ellipsoid is obtained from hydrodynamic measurements in organic solvents [115]. The average molecular weight of the imaged molecules (430 g/mol) is also in reasonable agreement with the number averaged molecular weight of 400 g/mol from LDI MS [116]. The overall H/C ratio of over 30 chemical structures assigned by AFM is ~0.6, which is in excellent agreement with the elemental composition of 0.74, considering the fact that the alkyl R groups identified from AFM images were counted as

Table 5.2: STM/AFM has emerged as a versatile toolbox for single-molecule-resolved characterization of the molecular structure, electronic properties, chemical reactivity, and surface chemistry summarized here by some representative examples.

Stable compounds	Reactive intermediate	Molecular properties	On-surface reaction
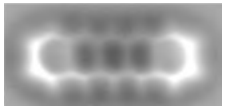 Gross et al. [70]	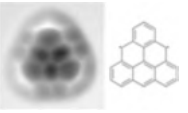 Pavlicek et al. [79]	 Repp et al. [87]	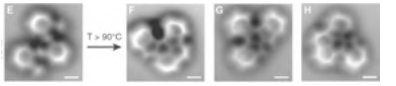 de Oteyza et al. [89]
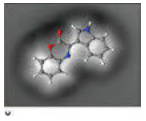 Gross et al. [110]	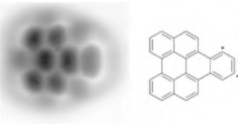 Pavlicek et al. [111]	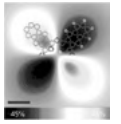 Mohn et al. [84]	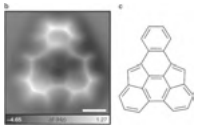 Kawai et al. [112]
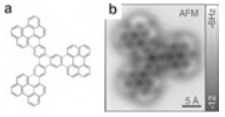 Schuler et al. [113]	 Pavliček et al. [76]	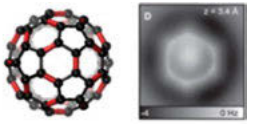 Gross et al. [82]	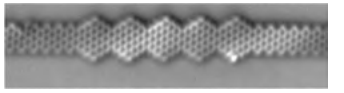 Gröning et al. [114]
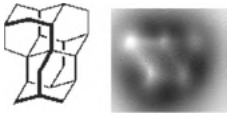 Ebeling et al. [72].	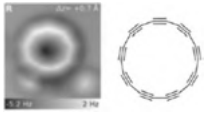 Kaiser et al. [80]	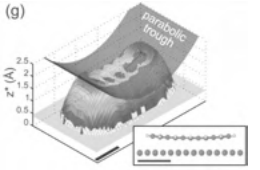 Schuler et al. [86]	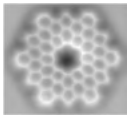 Fan et al. [90]

methyls which necessarily led to an underestimation of the H/C ratio from AFM structures. It is important that the coal-derived asphaltene has a much smaller H/C ratio than petroleum asphaltenes.

Very few chemical structures could be resolved exactly for petroleum-derived asphaltenes because of a higher degree of uncertainties of certain structural moieties, but the aliphatic and aromatic moieties can be distinguished because of a significantly different contrast. Heteroatoms were not easily recognized from AFM images of either coal-derived asphaltenes or petroleum-derived asphaltenes. Based on elemental analysis, it can be estimated that each coal-derived asphaltene molecule contains one heteroatom on average, including 0.6 N, 0.2 O, and 0.2 S atoms. Each petroleum-derived asphaltene molecule is expected to contain multiple heteroatoms on average, including 1.4 S, 0.4 N, and 0.5 O atoms [9].

This work ushered a new era in providing chemical structures of real physical molecules in a complex mixture, rather than relying on virtual or averaged structures deduced from conventional ensemble measurements like NMR and MS in the petroleum field. Nevertheless, this work showed that petroleum structures are indeed very complex and challenging also for AFM, and hence more detailed studies were desired.

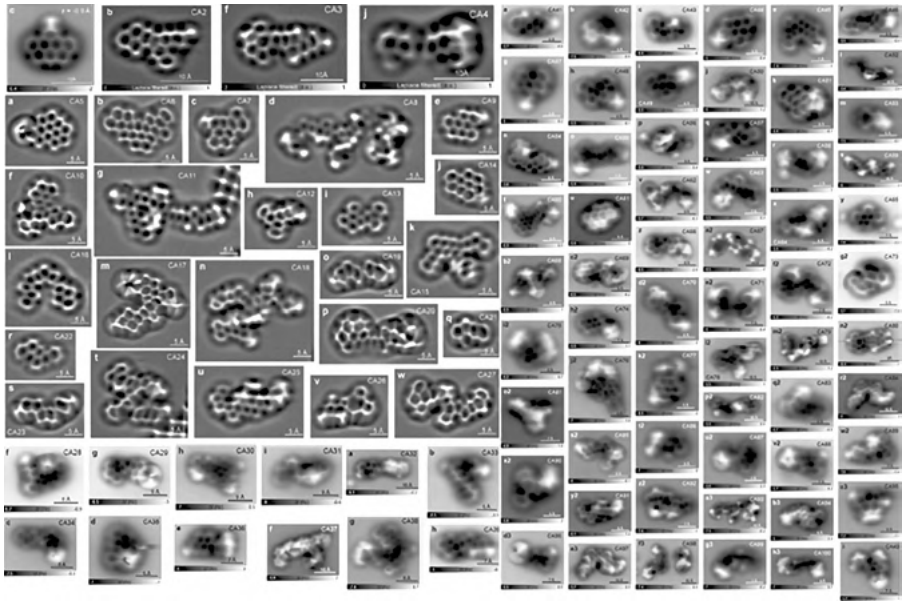

Figure 5.5: AFM images of coal-derived asphaltenes. Reprinted with permission from the American Chemical Society [93].

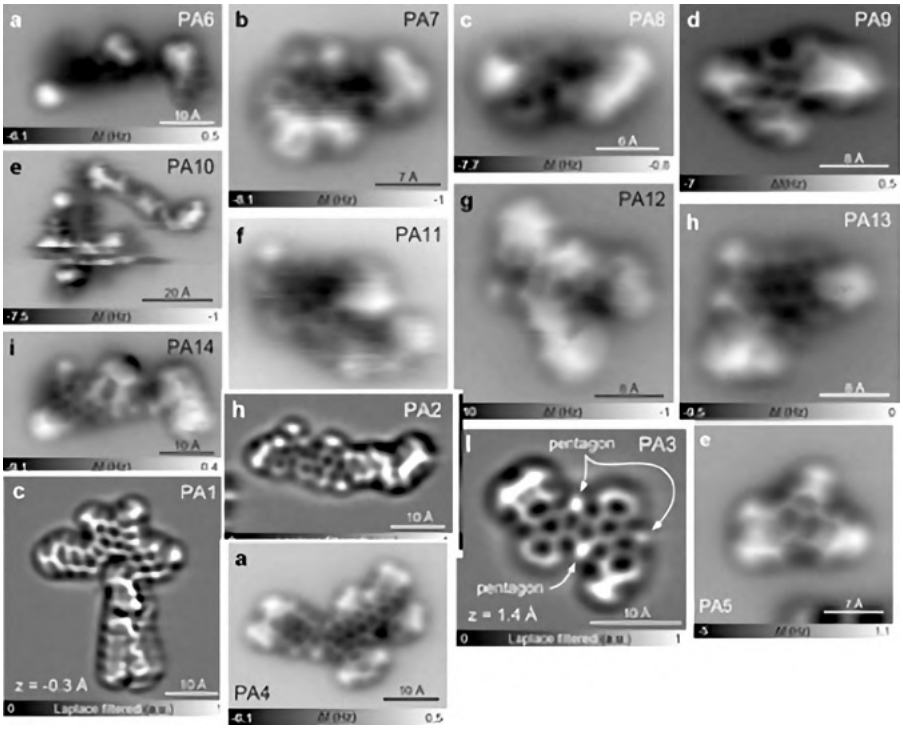

Figure 5.6: AFM images of petroleum-derived asphaltenes (PA1–PA14). Reprinted with permission from the American Chemical Society [93].

A comprehensive investigation focused on petroleum asphaltenes and heavy oils was conducted by a cross-disciplinary team composed of industrial and academic researchers from IBM Research – Zurich, ExxonMobil, Schlumberger, Shell, Chevron, Bruker, and the University of Santiago de Compostela [94]. This study was designed to address different practical challenges in heavy oil production and processing that have been ascribed to molecular structures. A total of four sample pairs were selected with different precipitation behaviors, molecular architectures, maturity, or applied hydroconversion processing (Table 5.3). AFM molecular imaging of more than 400 constituents in these samples revealed characteristic differences in molecular structures that can be ascribed to their different origin or treatment.

In the first set of samples, asphaltenes (A1) were obtained from a medium crude oil (API gravity 33.0) with a yield of 1.7% when compared to *n*-heptane asphaltenes (A2) extracted from an oilfield deposit from the same crude oil to decipher the structural basis contributing to asphaltene aggregation and deposition. A1 was heptane-insoluble asphaltenes isolated with a modified ASTM D6560 method (heptane at 80 °C). A2 was isolated by isocratic elution from a PTFE (Teflon) column with 100% CH_2Cl_2 (third fraction). Sixty-five molecules were imaged with atomic-

Table 5.3: Research samples and analysis of petroleum asphaltenes and heavy oils studied with nc-AFM (adapted with permission from [94], Copyright 2017 American Chemical Society).

		Yield (% wt)	MW (g/mol)	Elemental analysis (wt%)						Metal (ppm)		Density (g/mL)
				C	H	S	N	O	H/C	V	Ni	
A1	Asphaltene isolated from a crude oil	1.7	676 (200–1,500)	88.0	6.8		0.6		0.9			1.23
A2	Asphaltene from deposit from A1 oilfield	67	703 (200–1,500)	88.3	6.3	3.1	0.7		0.8	41	89	1.26
B1	Asphaltene from a vacuum resid before hydroprocessing	10.5	442 (200–700)	80.5	7.7	7.5	1.4	2.6	1.1	1085	406	1.12
B2	Asphaltene from bottom after hydroconversion of vacuum resid in B1	11.7	462 (200–800)	87.6	5.6	1.7	1.2	0.8	0.8	577	504	1.27
C1	Asphaltene from steam cracked tar	24.1	457 (155–896)	89.0	5.9	3.2	0.2	0.2	0.79			
C2	Aromatic fraction in vacuum resid after asphaltene removal	13.7	696 (309–1,154)	82.2	8.8	5.6	0.7	1.6	1.28			
D1	Asphaltene from Green River shale oil		392	66.6	7.6	3.4	1.8		1.36			
D2	Asphaltene from Eagle Ford shale oil		528	73.3	8.5	9.7	1.7	6.5	1.4			1.15

resolution AFM in A1 (Figure 5.7) and 62 in A2 (Figure 5.8). In general, molecules in A2 are more aromatic compared to A1, consistent with its lower average H/C ratio (0.85) than A1 (0.9) and previous studies [117].

A method to estimate the molecular weight from STM images was proposed, and the molecular weights obtained were compared with FT-ICR MS data. The isoabundance plot shows that double bond equivalent (DBE) and carbon number distribution of molecules imaged are consistent with the molecules ionized by ESI MALDI and detected by FT-ICR MS [94].

The second set of samples B1 and B2 compared *n*-heptane asphaltenes before and after hydroconversion [118]. B1 is C_7 asphaltenes from Athabasca vacuum residue extracted with hot heptane, filtered, and soxhlet extracted with a yield of ~10 wt%. This sample was from a feed of a commercial LC-Fining unit [118]. B2 was asphaltenes isolated in the product after severe hydroconversion (80% of conversion), and the isolation yield of asphaltenes in the bottom of the converted vacuum residue was ~10 wt%.

About 49 molecules in B1 and 34 molecules in B2 were imaged. It was found that the molecules of the feed B1 showed a higher degree of aromaticity than the molecules in product B2. The hydroprocessed sample B2 contained more bulky aliphatic groups at the expense of the aromatic fraction, which is consistent with hydrogenation of PAHs. However, it should be noted that although about four of five asphaltene molecules were converted into nonasphaltenes at 80% conversion, asphaltenes isolated from the product might not necessarily represent the converted molecules because the most refractory molecules might remain intact during hydroconversion and hence be isolated and imaged by AFM. On the other hand, asphaltenes will become nonasphaltenes (soluble in heptane) after conversion. Thus, most converted molecules may not be in asphaltenes isolated for AFM imaging, and only some partially converted (and unconverted) molecules will remain the product asphaltenes. Therefore, caution should be taken in direct comparison of structures in this pair of samples.

The sample C1 was analyzed to address the molecular architecture of asphaltenes. The comparison samples C1 and C2 identify the structural differences between asphaltenes and nonasphaltenes. Both samples were highly aromatic.

Asphaltenes C1 were isolated with a 10/1 precipitation method using *n*-heptane on a steam-cracked tar residue, and the yield was 24.1 wt%. It was previously believed that archipelago structures were predominant (min. 80%) based on the literature and other characterizations [119].

C2 was isolated with chromatographic methods [120] from a North American heavy crude oil. Asphaltenes (30.6 wt%) were removed first by *n*-heptane precipitation, and the maltenes were chromatographically fractionated into saturate, aromatic, polar, and sulfide fractions. The aromatic fraction was further separated into several aromatic fractions. The last aromatic fraction C2 (13.7 wt%) obtained was the heaviest aromatic fraction in maltenes. Their molecular structures were expected to

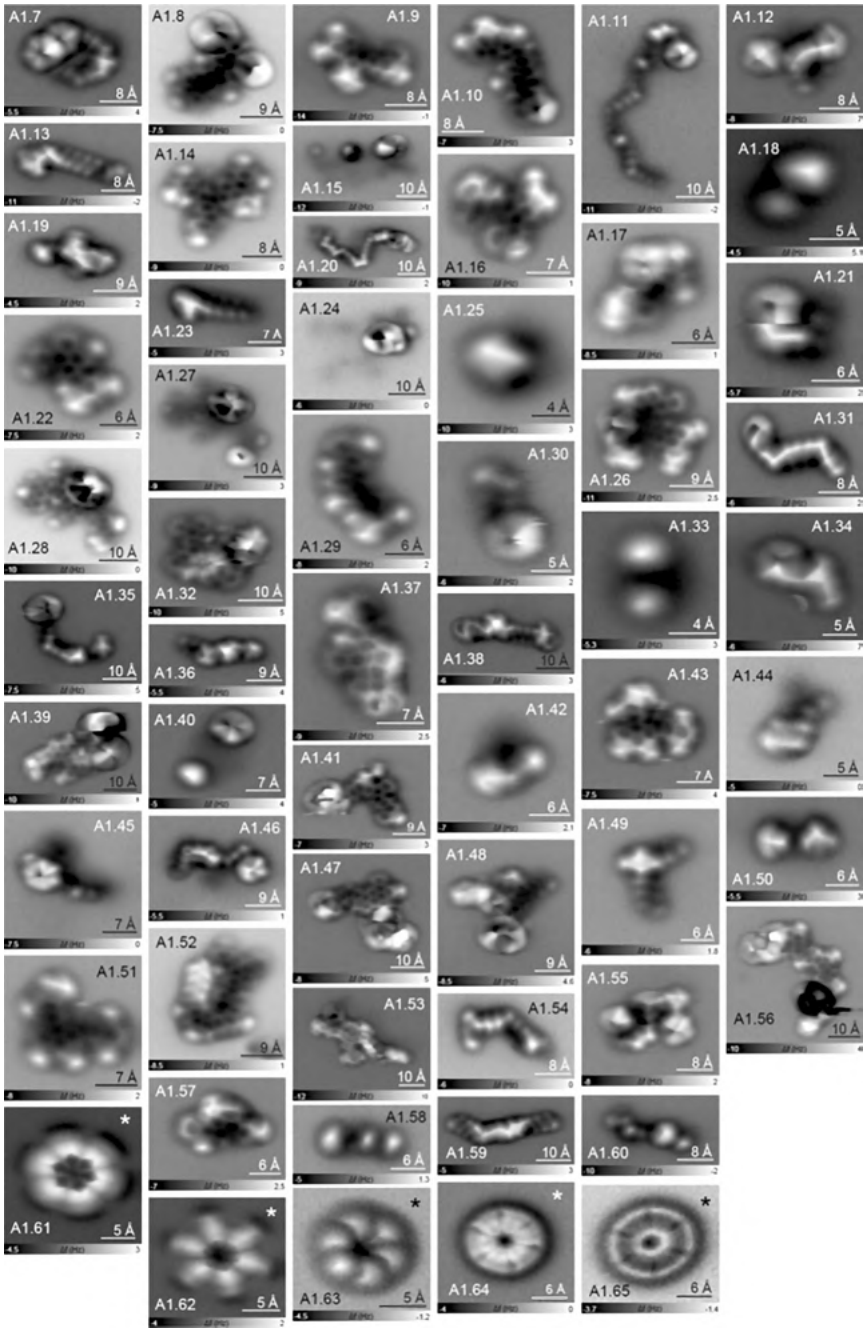

Figure 5.7: AFM images of petroleum asphaltene sample (A1) isolated from crude oil [94]. The asterisk indicates a manipulation image where the molecule rotates around a pinning site Reprinted with permission from the American Chemical Society.

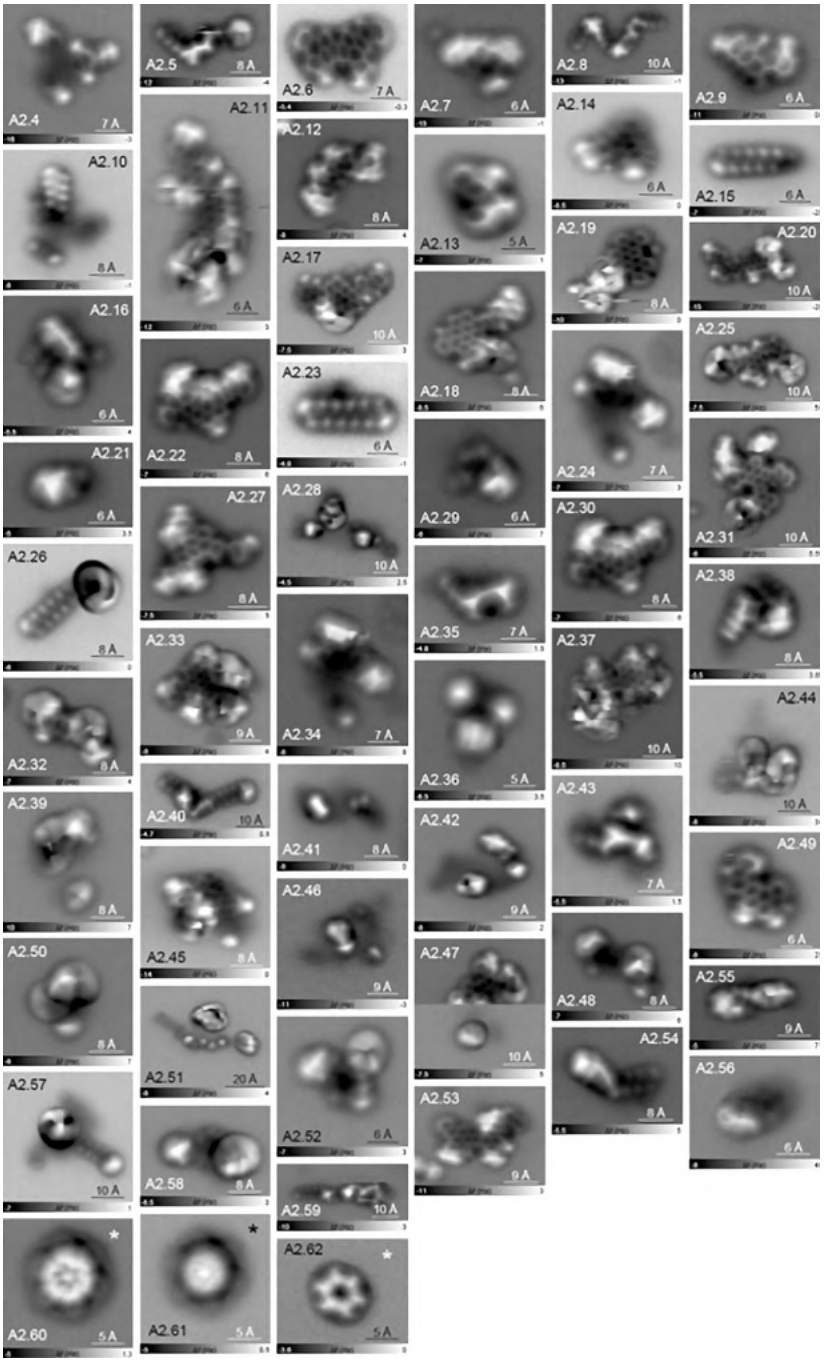

Figure 5.8: AFM images of petroleum asphaltene sample (A2) isolated form deposit from the same crude oil as A1 [94]. Reprinted with permission from the American Chemical Society.

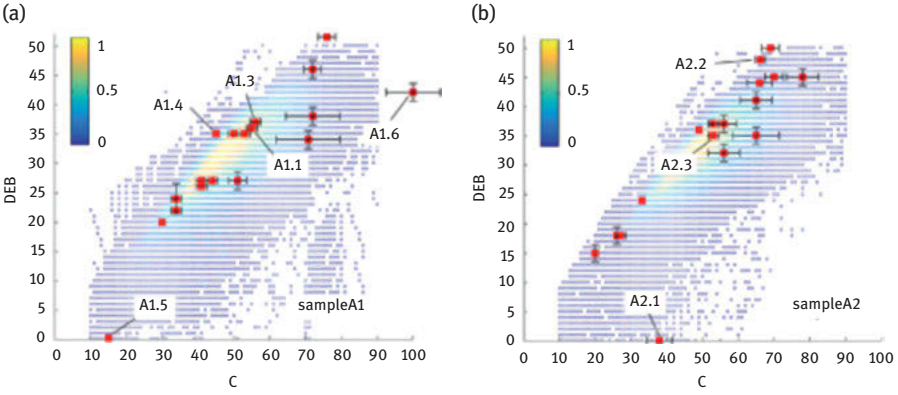

Figure 5.9: ESI MALDI FT-ICR MS spectra of petroleum asphaltenes A1 and A2 and compared with molecules detected by nc-AFM [94]. The molecules imaged by AFM correspond to high abundance locations in the mass spectra plots. Reprinted with permission from the American Chemical Society.

be very similar to asphaltenes, but not exactly asphaltenes by definition, due to the continuum of petroleum composition and structures. This sample was chosen to reveal the structural differences between asphaltenes and nonasphaltenes. In addition, this fraction had been expected to be enriched with archipelago structures (>70%) based on detailed analyses, such as chemically induced dissociation in conjunction with FT-ICR MS [121–124]. The size of aromatic cores was believed to be pyrenes or larger PAHs. The overall molecular weight was measured to be 440–970 g/mol by MS.

A total of 68 molecules in C1 and 30 molecules in C2 were imaged. AFM could resolve the structures of C1 very well because these molecules were predominantly flat aromatic structures. However, all resolved structures were PAHs with short alkyl substituents, with very few (if any) archipelago structures discovered in this sample, contrary to the predominant archipelago structures expected based on other characterization methods [119].

For the C2 sample, AFM could resolve fewer structures than for C1. Most imaged molecules were found to contain unbranched long aliphatic side chains. However, these aromatic moieties were not the anticipated pyrenes or larger PAHs. Some of the structures seemed to contain alicyclic moieties since these structures were nonplanar, and it was difficult to resolve their exact structures and conformations. However, it could be clearly concluded that the predominant molecules found were not the classical archipelago structures with several aromatic cores connected by aliphatic linkers [92]. A few structures could be described as archipelago-like structures, such as aryl–aryl-linked structures; however, they appeared only in low abundance, contrary to the expectation.

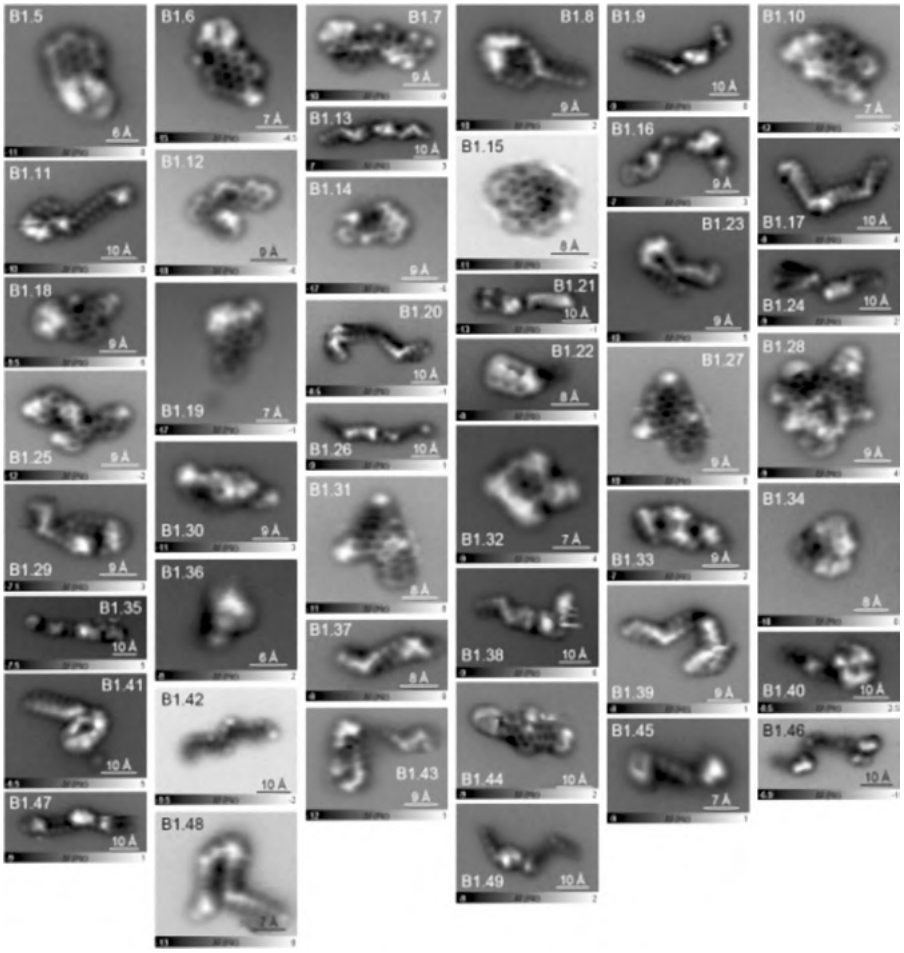

Figure 5.10: AFM images of petroleum asphaltene sample (B1) isolated from a feed before severe hydroconversion [94]. Reprinted with permission from the American Chemical Society.

These results showed that there can be dramatic differences between the structures resolved by nc-AFM imaging of individual molecules and the average structures deduced from conventional chemical analysis.

The fourth set of samples (D1 and D2) compared two asphaltene samples isolated from shale oils of different maturities. D1 is from Green River and D2 is from Eagle Ford. A total of 35 molecules of D1 and 38 molecules of D2 molecules were resolved by AFM. These molecules were found to be about 20% smaller compared to other asphaltene molecules, with smaller aromatic moieties.

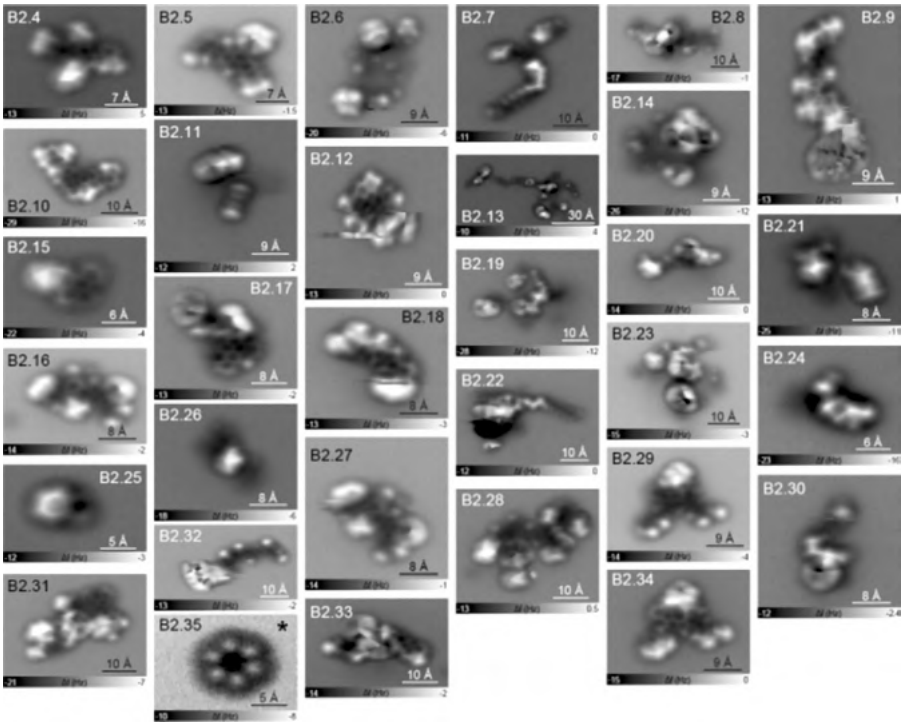

Figure 5.11: AFM images of petroleum asphaltene sample (B2) isolated from a product after severe hydroconversion (80%) [94]. The asterisk indicates a manipulation image where the molecule rotates around a pinning site under the influence of the AFM tip. Reprinted with permission from the American Chemical Society.

About 100 chemical structures derived from about 400 AFM images obtained on 8 petroleum samples are consolidated and shown in Figure 5.16 [98]. Readers are encouraged to refer to the original paper [94] on additional details and information on these molecules and samples.

Overall, a wide range of diverse aromatic PAHs with various degrees of heteroatom and aliphatic substitutions has been observed [94, 98]. Very few classic archipelago structures (e.g., B1.7, B1.25) composed of two similar aromatic cores connected by aliphatic linkers have been observed among the eight samples of this study, including a few with small aromatic substituents (phenyl or naphthyl), and only the aryl–aryl connection was observed by AFM [101]. Many of the observed PAHs have never been reported in the literature. While most PAHs are alternant benzenoids (composed of benzenes or only six-membered rings), a significant fraction of nonalternant PAHs containing five-membered rings was observed [98]. In particular, two kinds of motifs containing five-membered rings were observed: fully conjugated structures (as in fluoranthene) and the nonconjugated structures containing a CH_2 in a five-membered

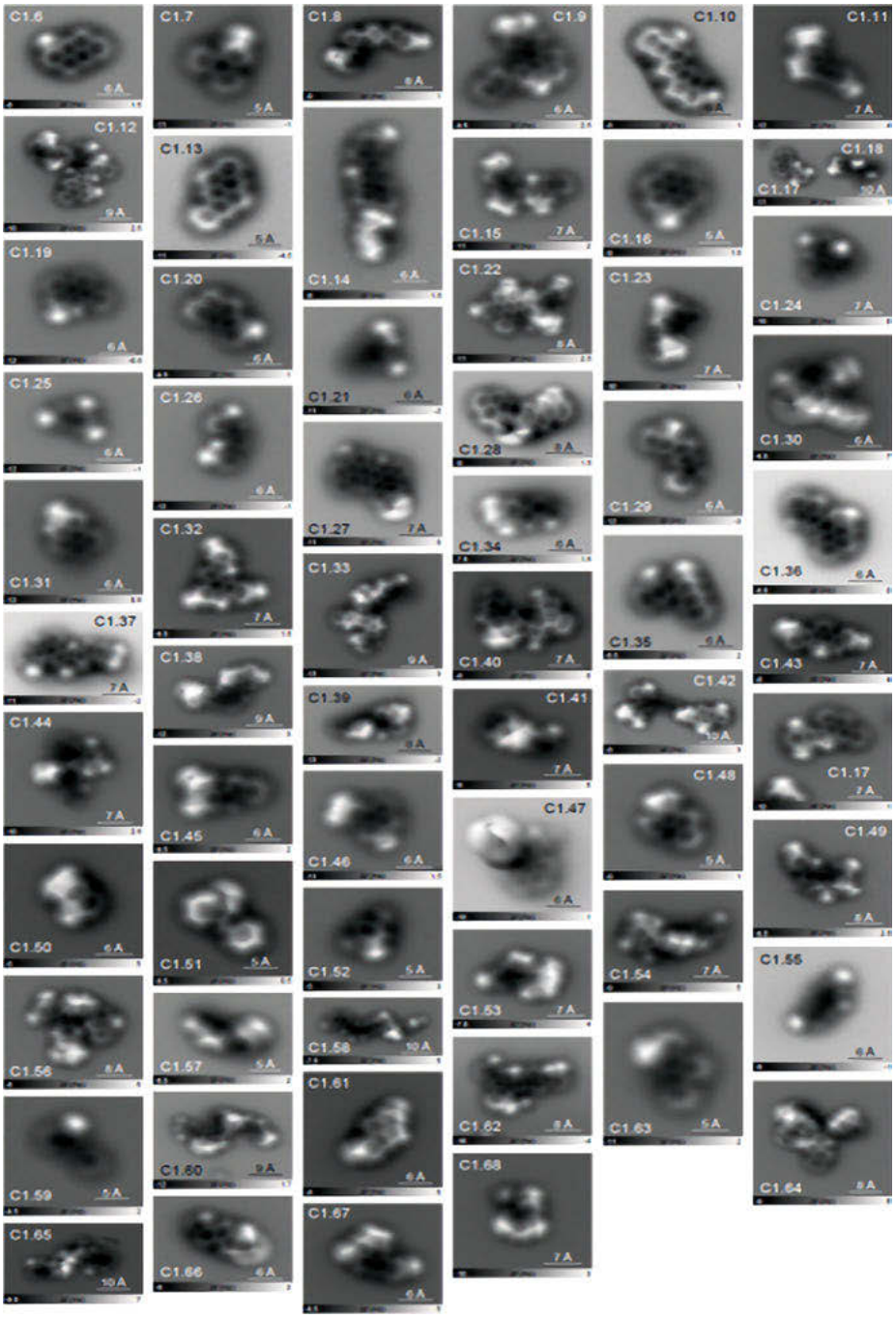

Figure 5.12: AFM images of asphaltene sample (C1) isolated from a product after severe steam cracking [94]. Reprinted with permission from the American Chemical Society.

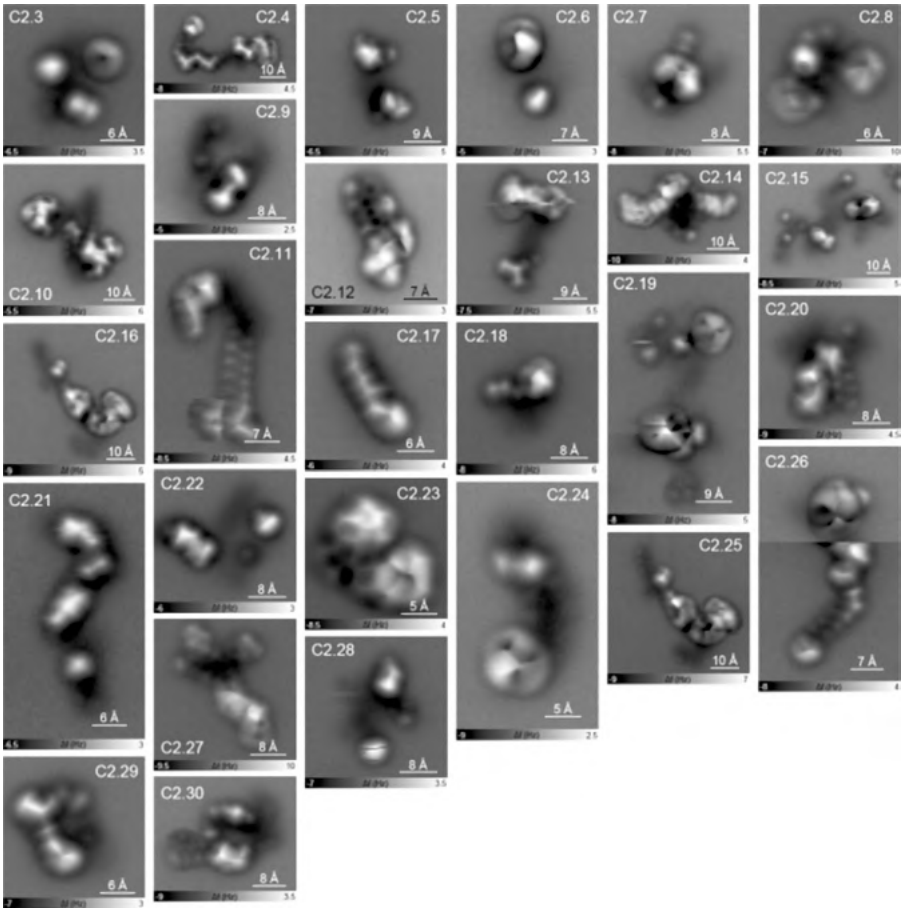

Figure 5.13: AFM images of sample (C2) fraction isolated from chromatographic of maltenes [94]. Reprinted with permission from the American Chemical Society.

ring (as in fluorene). Computation of aromaticity index (NICS) predicts that the aromaticity is decreased at the center of five-membered rings, indicating a charge separation within nonalternant PAHs [98]. The majority of structures contain a highly condensed PAH, but few are the most stable type of PAHs composed of sextets only [125, 126]. Sextets and isolated double bonds are used here within the Clar's representation of PAHs [36]. Most structures contain isolated or hidden "double bonds" within the PAHs, which can be computed using the natural bond order index [98]. Thus, reactivities and behaviors of petroleum asphaltenes can be predicted and identified based on computational studies of AFM-derived structures. Most aliphatic side chains observed are quite short (e.g., methyl), although also longer aliphatic chains were observed, either as side substituents to aromatic groups, or more commonly as separate paraffin (wax) molecules. Most of the long aliphatic moieties are unbranchedchains.

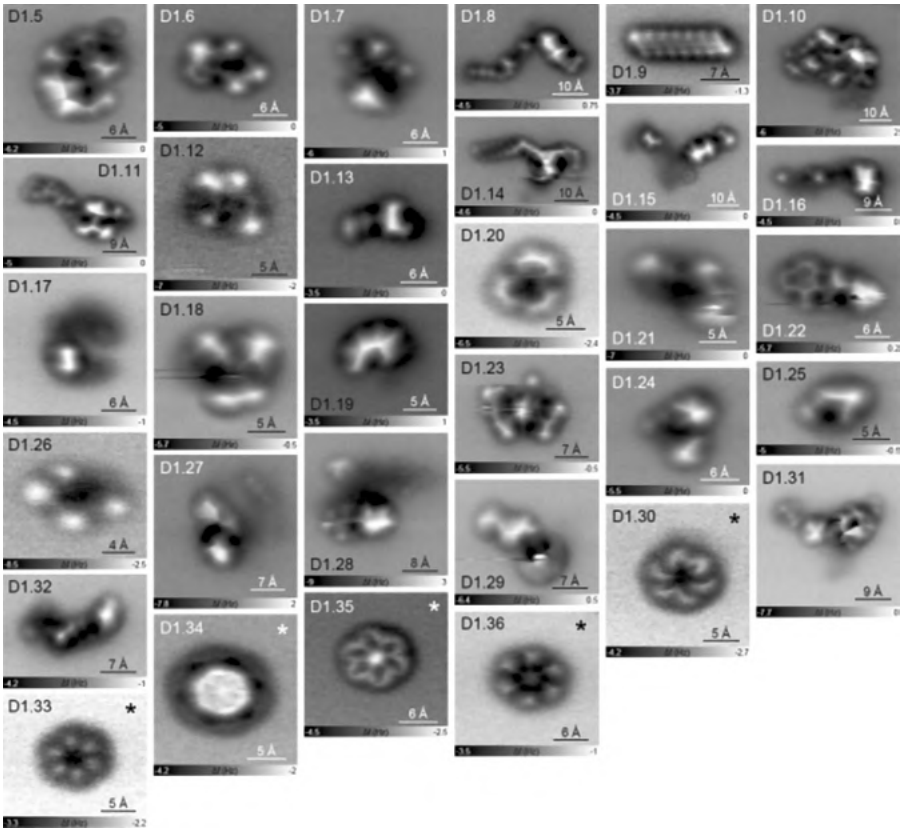

Figure 5.14: AFM images of asphaltene molecules from sample (D1) isolated from Green River shale asphaltenes [94]. The asterisk indicates a manipulation image where the molecule rotates around a pinning site. Reprinted with permission from the American Chemical Society.

Branches (as in isoprenoids) or chiral centers expected from biological precursors were not observed in this study. Nevertheless, the structures of many of the larger aliphatic substituents were not entirely resolved and are indicated in the figures as "R."

From this study, some challenges for nc-AFM molecular imaging of diverse petroleum mixtures can be recognized that need to be addressed to fully understand and valorize the implications of these experimental results: (1) translating AFM images of unknown molecules in petroleum into intelligible chemical structures; (2) assessing the effects of sample preparation and sampling on the representativeness of the imaged structures; (3) dealing with nonplanar adsorption geometries of various structures or architectures; (4) identifying heteroatoms, metals, and other trace components expected for petroleum molecules; (5) comparing and verifying AFM imaging results with other advanced characterization techniques; and (6) expanding the imaging database by applying nc-AFM to other systems including both

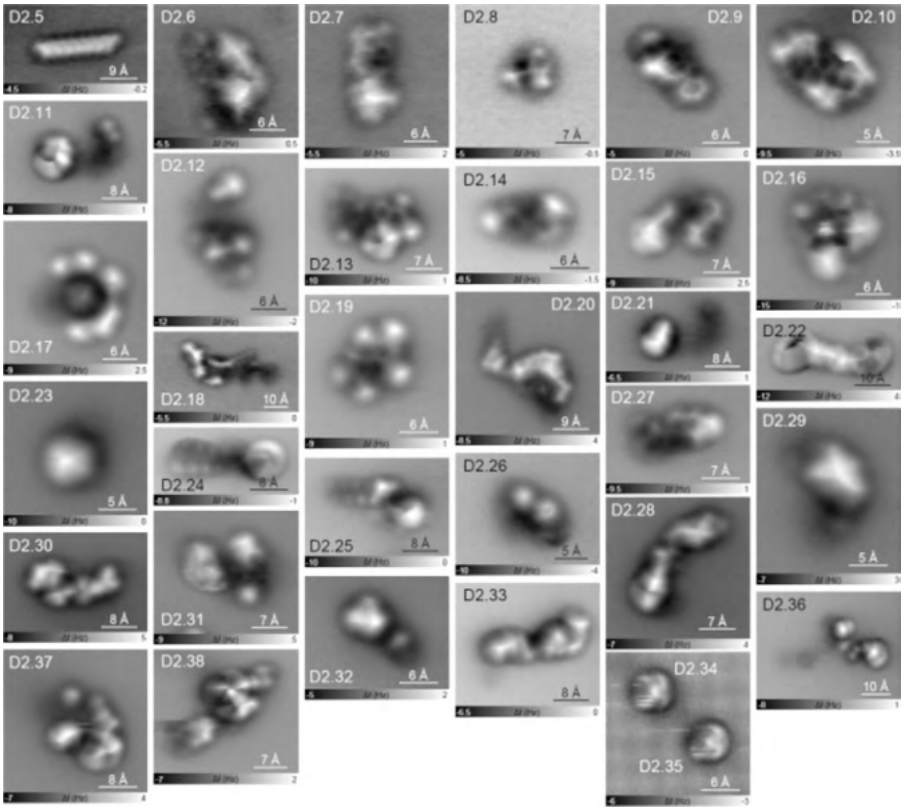

Figure 5.15: AFM images of asphaltene molecules from sample (D2) isolated from Eagle Ford shale asphaltenes [94]. Reprinted with permission from the American Chemical Society.

natural and synthetic compounds. A few recent works aimed to address some of these challenges and will be surveyed next.

5.3.3 The correlation of AFM images with molecular structures

CO-tip nc-AFM images of some aromatic molecules look almost like their schematic structure drawings found in every chemistry textbook [89, 127]. Because of their striking similarities, it is easy to forget that the underlying imaging mechanism is nontrivial, and in turn, molecular structure drawings are an abstraction layer in our chemical language [128, 129]. The frequency shift (Δf) displayed in nc-AFM images originates mainly from interactions between the CO molecule at the tip and the adsorbed molecules on the surface [70]. In a crude approximation, the frequency shift could be interpreted as being proportional to the total electron density at a given scan height. This electron density, which is mostly localized near atoms and covalent bonds, is affected by the

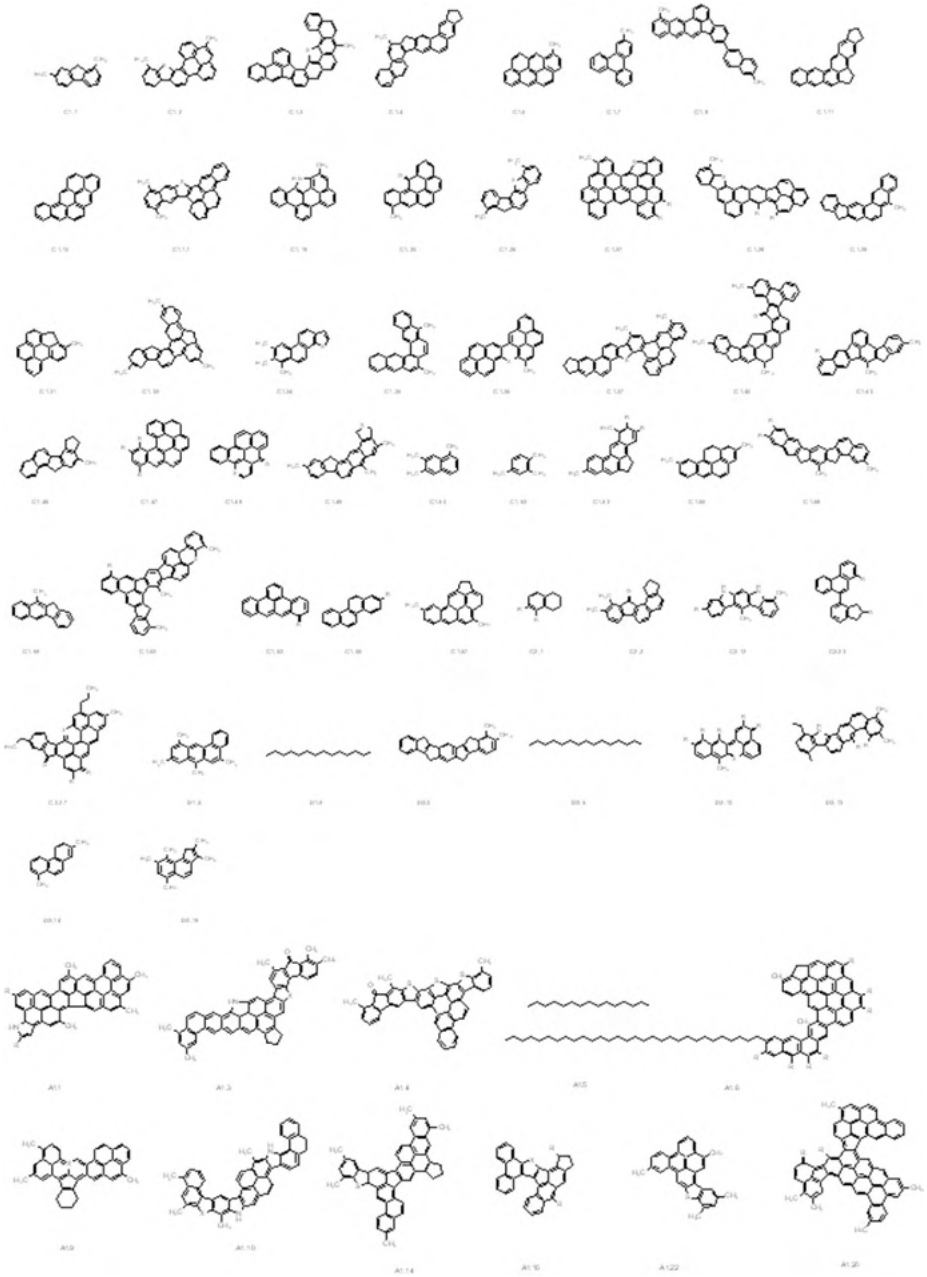

Figure 5.16: Assigned chemical structures from AFM images of eight petroleum asphaltene or heavy oil samples. X and R represent unknown heteroatom and alkyl substituents, respectively. Reprinted with permission from the American Chemical Society.

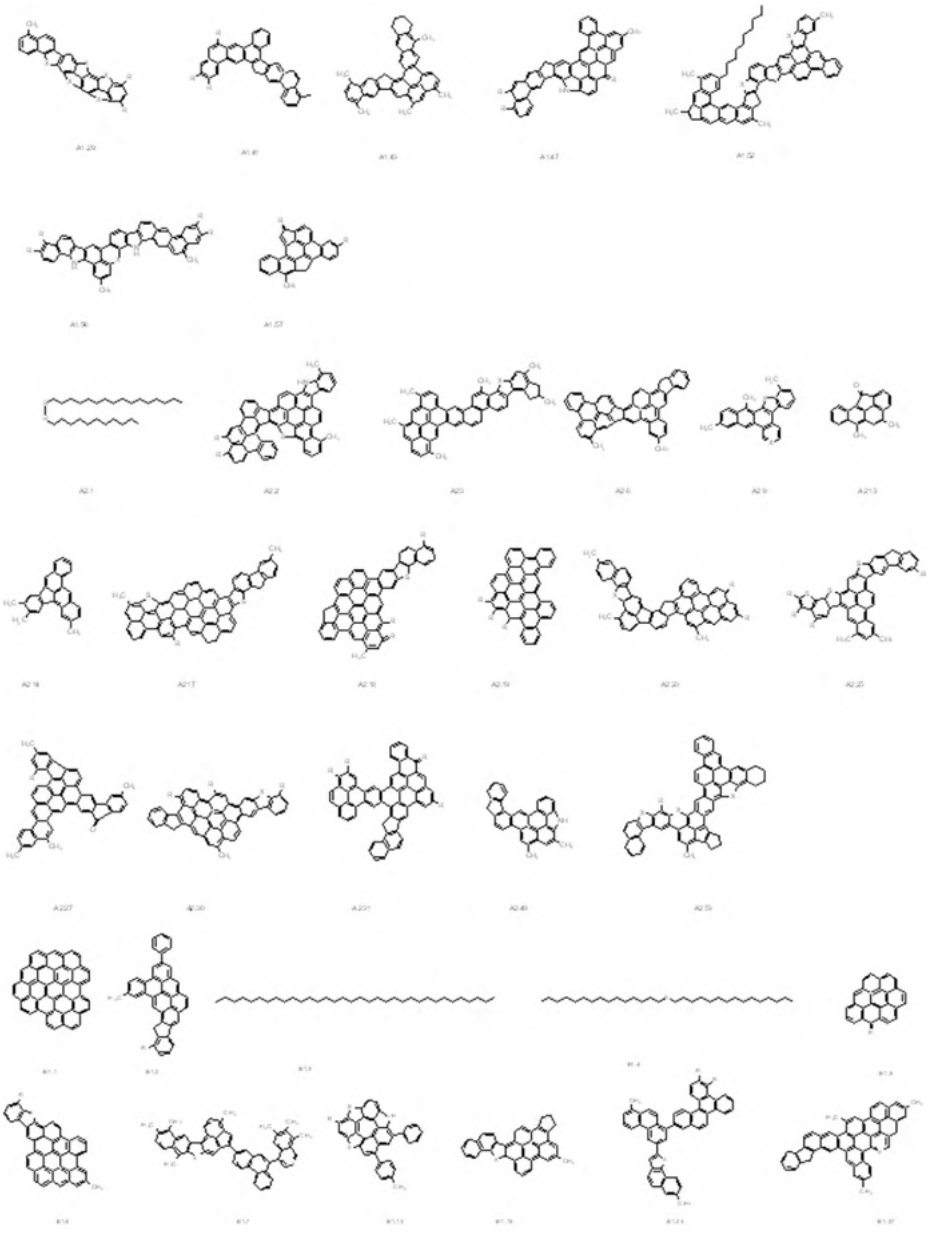

Figure 5.16 (continued)

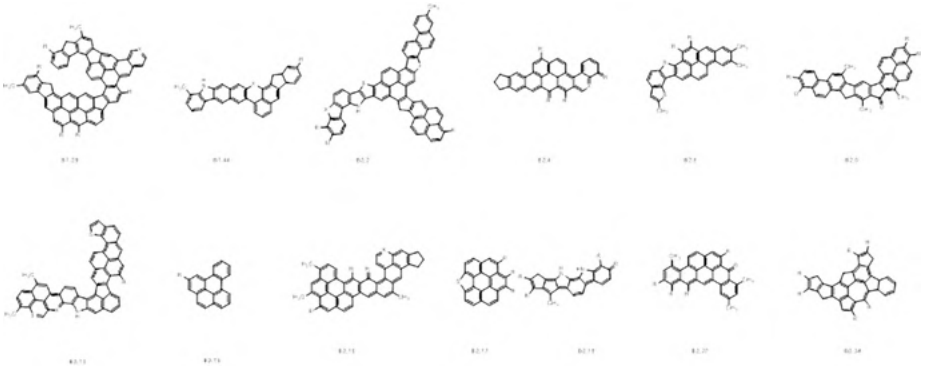

Figure 5.16 (continued)

coordination of atoms and type of bonds (e.g., bond order [82]) and the adsorption geometry [86]. Therefore, it is important to consider the three-dimensional molecular geometry adapted on the surface and its conformational variations that may lead to multiple possible appearances of the same molecule [88]. Some examples (cf., AFM images of tetramantane [72] and C_{60}[82]) shown in Table 5.1 clearly demonstrated this.

Identification of structures from AFM images of an a priori unknown mixture is not straightforward. However, a significant progress has been made in understanding the origins of the imaging contrast [74, 82, 129–131], and different methods have been developed to simulate atomically resolved AFM images [129, 130, 132–138]. In particular, occurrence of apparent bonds has been widely recognized [81, 130, 132, 134, 138]. A recent example is the image distortion due to charge distribution related to nitrogen heteroatoms in six-membered rings (Figure 5.17) [138]. An accurate simulation model is important not only for a better understanding of AFM contrast mechanisms but also for identifying unknown molecules in complex mixtures. Another approach is to study model compounds and compare images with their structures to identify features associated with certain structural moieties [95–97, 103]. Both strategies have been adopted to address the challenge of identifying structures from AFM images. In addition, machine learning approaches are developed to perform this task [139].

5.3.4 Imaging of synthetic archipelago compounds

After more AFM investigations on petroleum asphaltenes and heavy oil mixtures had been published [94], some researchers raised concerns on the lack of archipelago structures, and a few interpreted it as a limitation for AFM [140–142]. It was argued that these architectures might be too difficult to image by AFM of too difficult to prepare for AFM. One argument is that the strong aggregation due to many

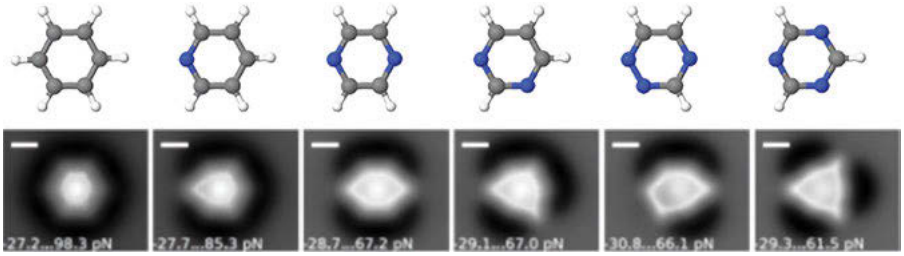

Figure 5.17: Simulated AFM images of six-membered rings with N heteroatoms. Reprinted with permission from the American Chemical Society.

complex interactions in the archipelago structures may cause problems in the flash evaporation process [143]. Others raised concerns on the volatility of asphaltenes and the potential thermal cracking in the AFM sample preparation conditions [142].

For the sample preparation step, a tiny amount, typically on the order of micrograms, of sample material is deposited on a piece of inert silicon wafer, which is resistively heated in ultrahigh vacuum conditions. The molecules are thermally sublimed from the silicon wafer onto the cold (about 10 K) sample. The Si wafer is heated rapidly (typically on the order of 1 s) to a temperature high enough to sublime most of the molecules (typically about 900 K) [101]. The flash heating technique enhances volatility by favoring evaporation and suppressing competitive fragmentation, as demonstrated for various compounds [144–146]. Rapid heating has also been employed to enhance the volatility of various molecules in mass spectrometry [147]. Furthermore, free radicals, if produced from thermal cracking, would be stable at the low temperatures (5 K) and be identified by STM orbital imaging as demonstrated by many studies [75, 79]. Although a few radicals can be detected in some petroleum samples [93], they were far from major. Moreover, persistent native free radicals in petroleum have been detected by EPR since the late 1950s [100, 148]. The number of free radicals observed by nc-AFM was also in reasonable agreement with the spin concentrations measured by EPR [100]. Nonetheless, a precise understanding of the effect of sample preparation specifically on archipelago structures was unclear. Therefore, a series of model compounds mimicking archipelago structures was designed to address these questions (Figure 5.18) [95, 96, 103, 149].

It should be pointed out that these compounds comprise various types of aliphatic linkers, from aryl–aryl (C_0), methylene (-CH_2- or C_1), ethylene (-CH_2CH_2- or C_2), propylene (-$CH_2CH_2CH_2$- or C_3), $C_{10}H_{20}$ (C_{10}) to $C_{20}H_{40}$ (C_{20}) linkers between two aromatic cores. In terms of bond strength, this series covers most conceivable linkers in the hydrocarbon structure space. For example, the aryl–aryl linkage is expected to be the strongest linker due to the strong sp^2–sp^2 CC single bond. On the other hand, an ethylene (C_2) linker is one of the weakest CC single bonds possible due to the formation of two benzylic radicals, and it hence acts like an internal "molecular thermometer" for the impact of flash heating method. The methylene (C_1)

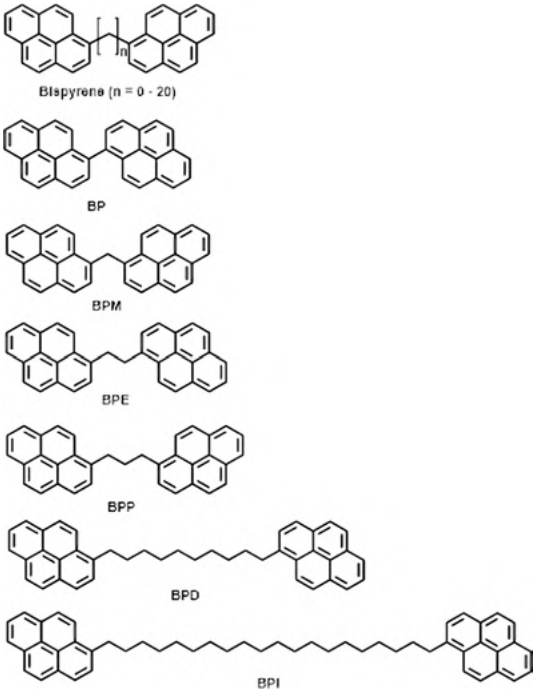

Figure 5.18: Molecular structures of a series of bispyrene model compounds mimicking the basic archipelago structures of asphaltenes (without considering the heteroatoms).

linker contains two relatively strong sp^2–sp^3 CC single bonds. Lastly, the C_3, C_{10}, and C_{20} linkers are of typical strength by referencing to most aliphatic side chains or paraffins and vary mainly by molecular weights and boiling points.

These molecules were designed to have high molecular weight, and hence relatively high boiling points, to mimic asphaltene molecules. High-temperature GC measurements verified that their boiling points are all above 530 °C (or >1,000 °F). Most asphaltenes are obtained from petroleum vacuum resids which have a nominal boiling point of >565 °C (or 1,050 °F). Hence, these molecules meet the criteria of heavy molecules in asphaltenes. The molecular weight of the model compounds (400–700 Da) also overlaps with the molecular weight spectra of asphaltenes (300–800 Da) detected for MS. The aromatic parts are represented by two pyrenes to facilitate synthesis, and pyrene is one of the most common four-ring aromatic compounds (other possibilities include chrysene, tetracene, and benzofluoranthenes). A total of eight aromatic rings is also reasonably consistent with asphaltenes based on NMR data, and the H/C ratio (0.56–1.12) from most elemental analysis of asphaltenes (0.5–1.1) [150, 151]. Overall, these compounds can be considered as possible model compounds of asphaltenes based on the many known criteria to mimic the structures and behaviors of asphaltenes. Indeed, bispyrene (BP) compounds with C_2 linkers have been studied

as model compounds for asphaltenes before [152–154]. An AFM study of these compounds was used as a control experiment to verify the volatility of similar molecules in asphaltenes under the same preparation and imaging conditions.

Table 5.4: Series of bispyrene compounds studied by nc-AFM.

Name	Compounds	Formula	Mol. wt.	H/C	Purity (wt%)	B.P., °C (°F)
BP	1,1′-Bipyrene	$C_{32}H_{18}$	402.50	0.56	99.5	538 (1,000)
BPM	Di(pyren-1-yl)methane	$C_{33}H_{20}$	416.52	0.61	96.1	553 (1,027)
BPE	1,2-Bis-(1-pyrenyl)ethane	$C_{34}H_{22}$	430.55	0.65	97.3	555 (1,031)
BPP	1,3-Bis-(1-pyrenyl)propane	$C_{35}H_{24}$	444.58	0.69	98.3	571 (1,059)
BPD	1,10-Bis-(1-pyrenyl)decane	$C_{42}H_{38}$	542.77	0.90	95.0	592 (1,098)
BPI	1,20-Bis-(1-pyrenyl)icosane	$C_{52}H_{58}$	683.04	1.12	96.3	638 (1,180)

AFM results of three of these compounds are shown in Figure 5.19 [96]. It demonstrated that these molecules, despite containing a flexible linker with various strengths, can be imaged intact and that no fragmentation was observed after flash heating. Various conformations are adapted because of the flexibility of the linkers; however, the molecules can be imaged intact and reliably assigned. Moreover, even trace impurities present in some samples were detected (Figure 5.20), and their abundance is largely consistent with the purity assay (~96 wt%) by HPLC.

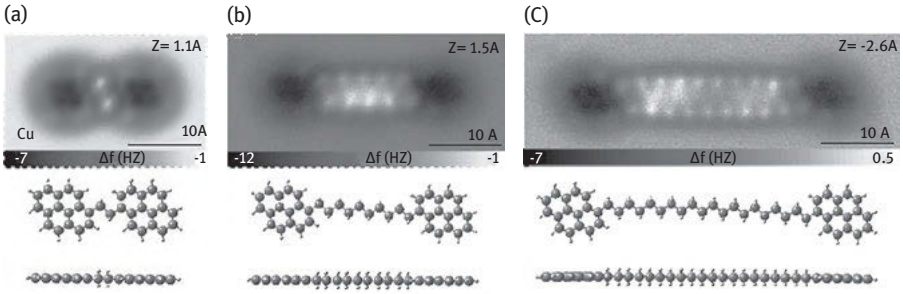

Figure 5.19: The AFM images of some bispyrene compounds [96]. Reprinted with permission from the Royal Society of Chemistry.

Three additional compounds with aryl–aryl (C_0), methylene (C_1), and propylene (C_3) linkers were studied with nc-AFM due to their possible presence in petroleum asphaltenes, and the results are shown in Figure 5.21 [103]. Two conformations were identified for the aryl–aryl-linked BP, and four conformations for di(pyren-1-yl)methane with a methylene linker, and eight conformations were identified for a three-carbon-linked 1,3-bis-(1-pyrenyl)propane. An increase in the number of conformations was expected with an increase in the number of flexible sp^3 carbon atoms of the linker.

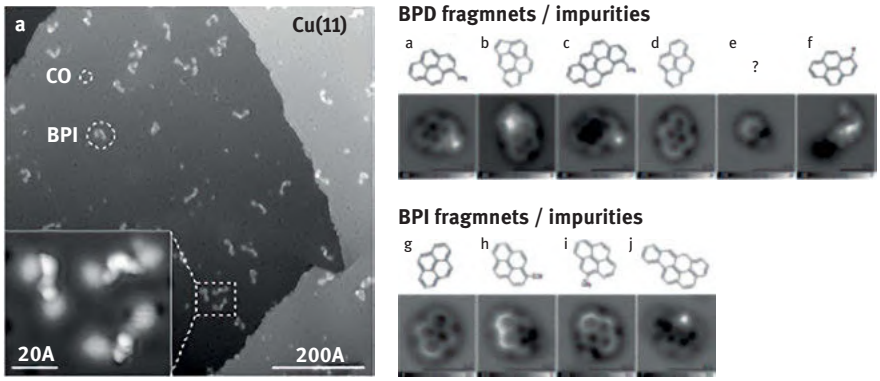

Figure 5.20: STM image of a random area and images of the impurities found by AFM in the samples. Reprinted with permission from the Royal Society of Chemistry.

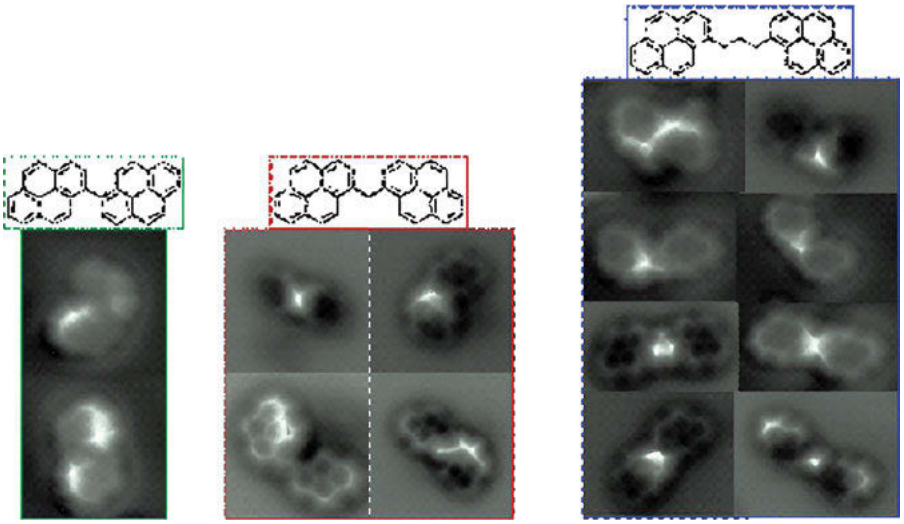

Figure 5.21: AFM imaging to various conformations of nonplanar bispyrene compounds. Reprinted with permission from the American Chemical Society.

The control experiments with archipelago model compounds showed that AFM, using the flash heating method for preparation, would resolve structures as the tested BP compounds, if they were present in petroleum asphaltenes or heavy oils. In addition, these results verified the results obtained on the steam-cracked tar asphaltene sample (C1) and aromatic heavy fraction C2 sample. C1 asphaltene was predicted to contain predominantly ethylene linkers between aromatic cores based on detailed analysis using traditional methods [119]. The results based on 1,2-bis-(1-pyrenyl)ethane unambiguously showed that these archipelagos with ethylene linkers would have

been detected by AFM. Furthermore, molecular species detected by APPI FT-ICR MS are consistent with molecules imaged by nc-AFM (Figure 5.22). These studies revealed the dramatic difference between "hypothetic structures" or "average structures" deduced from bulk analysis and exact structures imaged in real space by nc-AFM. This should not be surprising by considering the huge diversity of structures, which is a tremendous challenge for traditional chemical analysis. nc-AFM can now be used to directly address this challenge and verify molecular structures.

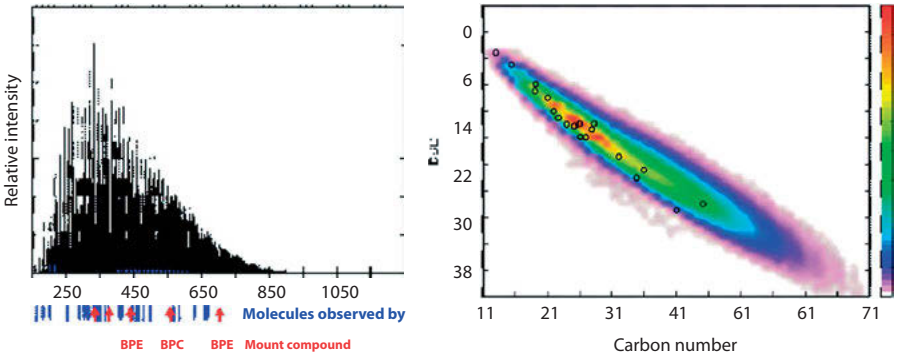

Figure 5.22: Comparison of AFM molecules with FT-ICR MS steam-cracked tar asphaltenes. Reprinted with permission from the American Chemical Society.

5.3.5 Imaging of heteroatoms, metals, and alicyclic moieties

Carbon and hydrogen are the predominant components (>80%) of asphaltene molecules, and they can be further classified into aromatic and aliphatic moieties (olefins are generally very rare in virgin crude oils). In addition to hydrocarbon, many asphaltene molecules also contain heteroatoms (N, S, O), or metal atoms (V, Ni) as in petroporphyrins. AFM imaging and identification of these heteroatom moieties and components are important in structure characterization of petroleum. In a recent study, Zahl and Zhang studied three aromatic heteroatom-containing model compounds to address this need [97]. The S-containing compound dibenzothiophene, and two N-containing compounds, carbazole and acridine, were imaged with nc-AFM, to distinguish these heteroatoms (Figure 5.23). S was relatively straightforward to identify because of its large size as a third-row element. Nevertheless, it was found that S was pulled closer to the metal surface (Au) due to the preferred interaction between S and metal. It can be deduced that similar adsorption occurs during hydroprocessing when S-containing compounds are approaching a catalytic surface.

The discrimination of N from C is more challenging. A few features were identified with nc-AFM experiments and simulations, such as the fainted C–H bond, atomic size, and relative mobility on the surface. Additional N-containing moieties and

a priori unknown molecules with N-containing moieties were characterized in a recent work studying analogs of Titan's haze with AFM [155]. These works provided some guidance for identifying heteroatoms in petroleum asphaltenes.

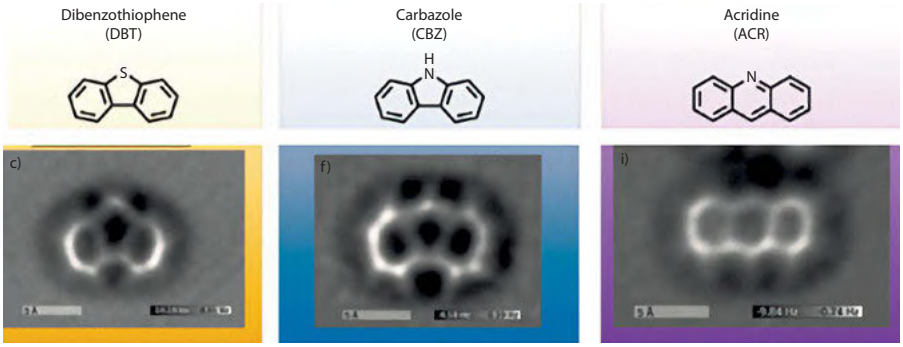

Figure 5.23: Discrimination of heteroatoms in aromatic model compounds with nc-AFM. Reprinted with permission from the American Chemical Society.

Continental petroporphyrins are known to be present in petroleum since their discovery by Treibs in 1930s as a proof of the biogenic hypothesis of petroleum formation [156]. Later, it was shown that porphyrins in petroleum contain V and Ni, rather than Mg and Fe of the biological precursors. Many porphyrins have been discovered from petroleum and they are collectively termed as petroporphyrins since the 1960s. Most petroporphyrins are enriched in the heavy fractions in petroleum, and especially in asphaltenes. In the previous studies on eight samples, no petroporphyrins were detected by nc-AFM. This is probably due to the low concentration of petroporphyrins (a few hundred to a few thousand ppm). Therefore, isolation is needed to study their structures in order to decipher the geochemical pathways from biological precursors.

An nc-AFM study on an isolated vanadyl petroporphyrin fraction was conducted (Figure 5.24) [104]. It was found that petroporphyrins have two conformations on the surface, with V=O facing up or facing down, with about equal probability. Among the molecules with VO facing down, the macrocyclic structure of porphyrin can be identified. It was discovered that some of the petroporphyrins lack a substituent at the β-position, in striking contrast to their biological precursors. This observation is also consistent with FT-ICR MS data based on the detection of C27 species. This presence of β-H indicates the dominance of dealkylation over transalkylation during the diagenesis pathways in geochemistry.

Another widely recognized but so far undetected moiety in petroleum asphaltenes is the naphthenic (or cycloalkano) moiety. Model compounds with five-membered and six-membered cycloalkano moieties attached to aromatic hydrocarbons have

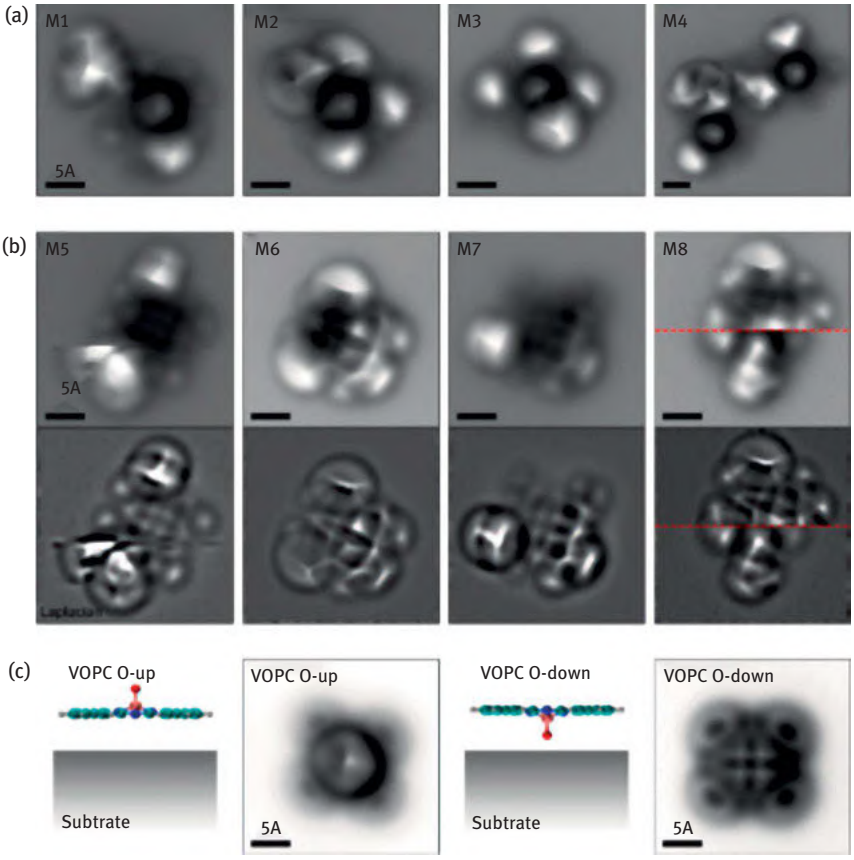

Figure 5.24: Characterization of petroporphyrins with nc-AFM [104]. (a) and (b) AFM images of various petroporphyrins. (C) The dependence of the AFM image on the orientation of the VO direction with respect to the surface. Reprinted with permission from the American Chemical Society.

been studied [96]. The nc-AFM images (Figure 5.21) reveal that these model compounds are prepared intact, and the cycloalkanes can be clearly differentiated from aromatic rings. The molecules adapt different adsorption conformations on the surface.

Figure 5.25: nc-AFM imaging of aromatic molecules with naphthenic moieties with different height sensitivities and different substrates. Reprinted with permission from the Royal Society of Chemistry.

5.3.6 Application of nc-AFM to petroleum pitches

Petroleum pitch M-50 is an important carbonaceous material and has been studied over half a century with multiple advanced techniques [157]. Various average structures have been proposed based on elemental analysis, MS, and NMR analysis [119, 158–165]. However, a direct validation of these proposed hypothetical structures with nc-AFM is valuable to exploit this important source material.

nc-AFM imaging of M-50 pitch was conducted (Figure 5.26) in comparison with NMR and FT-ICR MS analyses [102]. It was found that most molecules are PAHs with short alkyl side chains (mostly methyl groups). Most PAHs are cata-condensed rings, and very few peri-condensed rings. These results were validated by comparing with NMR and FT-ICR MS data.

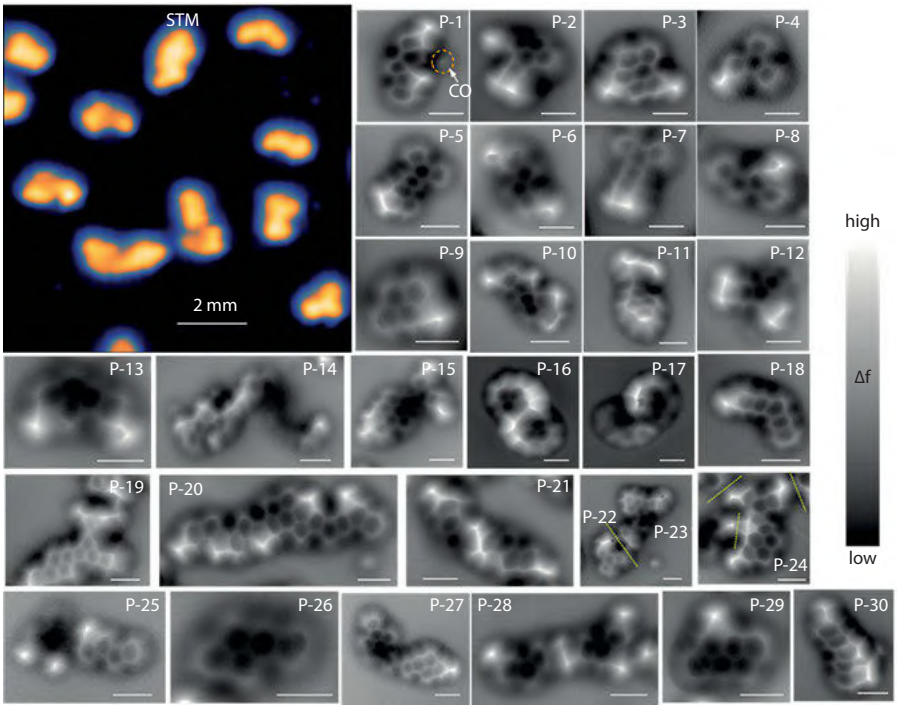

Figure 5.26: nc-AFM imaging of M-50 pitches. Reprinted with permission from Elsevier.

To understand the mechanism of molecular weight growth in M-50 pitch, a model compound (2,7-dimethylpyrene, DMPY) was designed to mimic the key structural features observed in M-50 pitch, namely, the aromatic rings and methyl substituents. DMPY was thermally treated in a similar fashion like M-50 pitch, and a black tar material was obtained. Chemical analysis with TGA, NMR, GC-MS, and FT-ICR MS on the

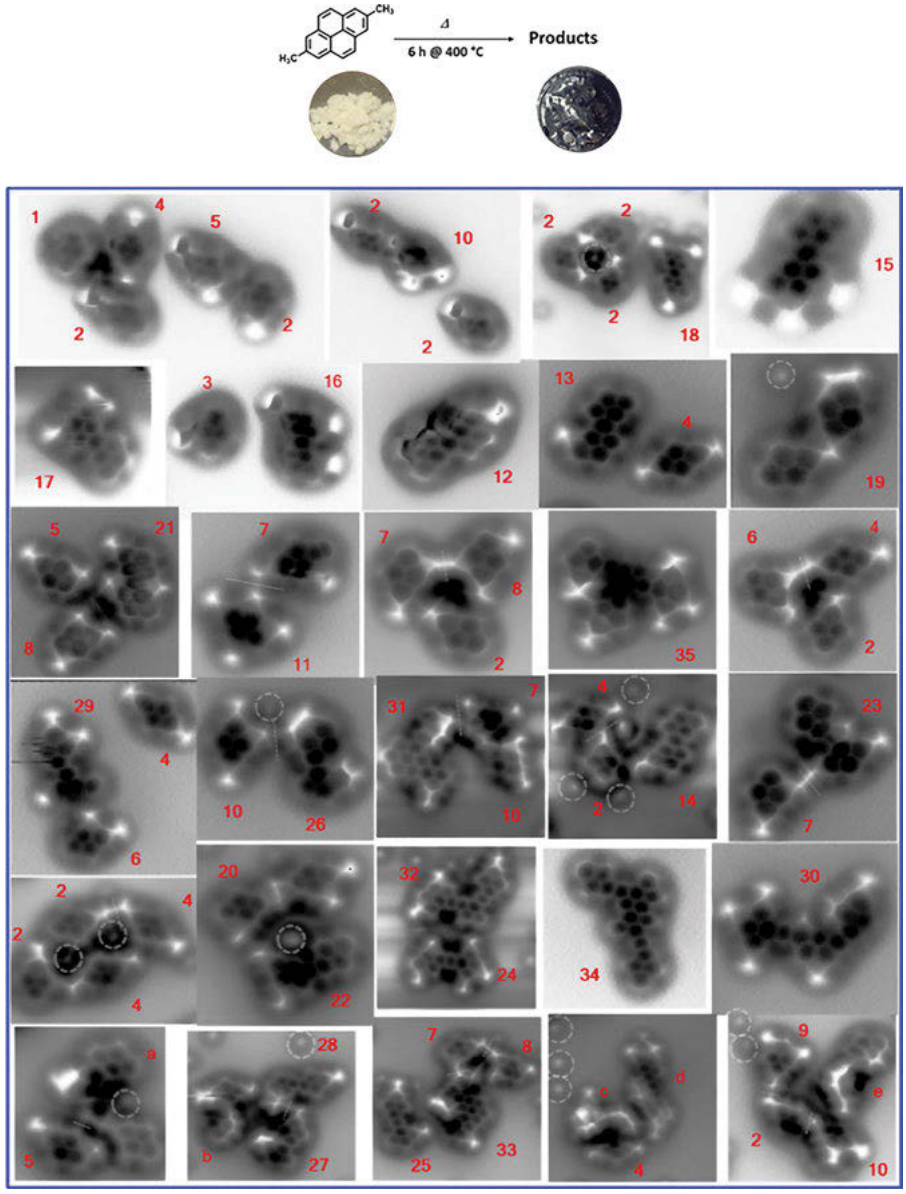

Figure 5.27: nc-AFM images of molecules obtained after thermal treatment of 2,7-dimethylpyrene. Reprinted with permission from the American Chemical Society [99].

products showed the molecular weight growth and polymerization reaction of the products, but their molecular structures were challenging to characterize because ~65% of mass was insoluble in organic solvents (e.g., dichloromethylene). Hence, nc-AFM was carried out to image the structures of products formed (Figure 5.27) [99].

A wide range of structures were identified from about 70 molecules imaged, and classified as monomers, dimers, trimers, and tetramers. In addition to methyl transfers observed on most aromatic molecules, direct condensation between two pyrene units via a six-membered ring was also frequently observed. On the contrary, the anticipated predominant products containing a CH_2-linked five-membered ring formed via the attack of the initial benzylic radicals were rarely observed. Moreover, deformation in the aromatic structure was also evident, which is unexpected for this relatively mild thermal treatment. These unexpected reactions demonstrated by this study improved our understanding on the initial mechanisms in molecular weight growth of aromatic hydrocarbons under thermal conditions.

5.3.7 AFM summary and outlook of applying AFM molecular imaging in studying petroleum mixtures

In summary, nc-AFM imaging of single molecules has been successfully applied to a variety of heavy petroleum compounds and derivatives, such as asphaltene fractions from different origins and treatments. All results indicate that asphaltenes are an incredibly diverse and complex mixture. While this is a widely accepted fact, visualizing the range of their actual constituents, atomically resolving and identifying some of the asphaltene molecules, has added a different perspective on this multifaceted compound. Despite the structural diversity, we identified one PAH with various aliphatic or heteroatom substituents as the most common structural motif. Rarely, molecules contain two or more PAHs connected by aliphatic linkers, as in the classic archipelago structure, except for a few containing aryl–aryl bonds or smaller aromatic substituents (benzene or naphthalene) [101]. Model compounds have been utilized to understand the effects of sample preparation and to identify certain molecular motifs or architectures (e.g., linker or heteroatoms) in nc-AFM images. Although we cannot rule out the existence of archipelago structures in petroleum or predict the abundance of such structures in other samples, results indicated that such molecules would be detected by AFM, if they were present in significant abundances in the samples studied. These results have also been supported by applying nc-AFM to other molecular mixtures, such as thermally processed petroleum pitches [102], synthetic product mixtures [99], fuel pyrolysis products [166], combustion soots [167, 168], marine dissolved organic carbon [169], and tholins [155].

One of the most important advantages of real-space molecular imaging by nc-AFM is the single-molecule sensitivity. While other advanced characterization techniques (e.g., x-ray crystallography, NMR, and MS) allow us to determine the structure of almost any molecule, they rely on the assumption that almost all molecules in the sample are identical (high purity). However, for petroleum, which is inherently a supercomplex molecular mixture [170], composed of hundreds of thousands or even millions of species [171], the concept of an average structure disguises the overwhelming diversity of molecules present in petroleum compounds. Designated "average," "centroid," or "representative" molecular structure(s) may oversimplify the true complexity of the mixture and its diverse phase behavior. Nevertheless, the utility of centroids depends on applications; thermodynamic applications *require* the centroid of the distribution. In contrast, AFM provides real-space molecular images of individual molecules in a physical sample. It provides a first look into actual petroleum molecules, which was unthinkable before. These AFM-derived realistic structures are especially crucial as a basis for modern predictive computational models.

Despite the significant progress in nc-AFM-based molecular structure elucidation, many challenges remain in order to apply this complementary technique more broadly on petroleum mixtures. Expanding the imaging database by measurement or simulation of synthetic model compounds will continue to help identify characteristic fingerprints of common molecular moieties in a priori unknown mixtures. Integrating such fingerprints in image recognition software will be critical to transition from a user-centric interpretation scheme restricted to trained experts, to a more general and comprehensive knowledgebase accessible to nonexperts. Similarly, fully or semi-automated data collection would massively increase adoption of this technique and expand the sampling from hundreds to thousands of molecules. For both data collection and interpretation, machine learning approaches currently developed by different groups [139] may play a critical role in the future.

It is clear, however, that for an extremely complex and diverse mixture like petroleum, combining complementary insights from many characterization methods will always remain essential. Bringing together different puzzle pieces from molecular imaging to macroscopic phase behaviors will enable a holistic view on molecular structures, their interactions, and dynamics that ultimately govern the physical and chemical properties of these incredibly heterogeneous materials. We hope that many researchers in the field will be inspired by our early studies and apply the results and the technique to a broad range of materials to address open questions in organic (geo)chemistry, interface science, catalysis, synthetic chemistry, and chemical processing.

5.4 Molecular orbital (MO) calculations

5.4.1 Aromaticity and fused ring distribution in the PAH core of asphaltenes

Computational chemistry approaches have revolutionized our understanding of the structure and reactivity of molecules, and it has become the third apex of the triangle of science, with experiment and theory representing the other two apexes. Electron spectra of asphaltenes, especially optical absorption spectra are easily and routinely obtained. This offers the opportunity to constrain allowed PAH distributions of asphaltenes. MO computations coupled with the universal optical electron spectra of asphaltenes have been used to identify the fused ring distribution and size of the aromatic PAH core of asphaltenes by virtue of understanding their electron structure. These results compare favorably with the measured PAH distributions obtained by AFM. In addition, these computational simulations, based on ZINDO/S calculations and on density functional theory, have been used to conclude on the number of PAHs per asphaltene molecule [37, 39–42, 172, 173].

In order to understand the chemistry and physics of asphaltenes, it has been essential to elucidate the size and structure of their fused aromatic ring (FAR) systems. The FAR region in island asphaltenes is similar to PAHs; the FAR region may contain heteroatoms and the asphaltene molecule can also have peripheral alkyl chains. To address the question of how many fused rings are in the PAH region of asphaltenes and their spatial arrangement, that is, their structural distribution, the approach was taken to evaluate the HOMO–LUMO transition for a very large number of PAHs by MO calculations. This provides an index of molecular size and structure for PAHs, by comparison of the measured optical transitions of the PAH region in asphaltenes [37, 39–42].

5.4.2 Predicted and measured electron spectra of asphaltenes

The chemical polydispersity in asphaltenes (i.e., how many FARs are in the PAH region, their spatial arrangement, and possible structural isomers) has been addressed by MO calculations [37, 41]. Thus, the effect on the HOMO–LUMO energy gap due to the successive addition of aromatic rings and their different distributions, that is, isomers, in the PAH core of asphaltenes has been analyzed [37, 39–42]. The HOMO–LUMO energy gap has been calculated for many PAHs containing 4–15 FARs, 4 FAR–15 FAR, containing different number of Y-carbons (internal aromatic carbon atom at the junction of three fused rings or also known as Y-carbons [37, 41, 43, 174], C_Y, for being in the vertex of what looks like a Y-letter), different number of double bridgehead aromatic carbons, different carbon and hydrogen content, different spatial arrangement of the fused rings, different percentage of compactness, different

stoichiometry, and different number of resonant sextet in the structure (this last characteristic is explained in more detail in the text below). From the comparison between the calculated HOMO–LUMO energy gap and the experimental HOMO–LUMO energy gaps of asphaltenes, which is obtained from the 0–0 band fluorescence emission experiments, it has been concluded that the magnitude of the HOMO–LUMO gap in PAHs and in PAHs in asphaltenes is related to the PAH stability, to the number of FARs (nFAR), to the spatial arrangement of the fused rings, to the percentage of compactness of the structure, and to the number and location of resonant sextets in the structure. It has been found that the PAH core in asphaltenes is not linear, zigzag, or fully resonant, and the possible presence of large peri-condensed PAHs, with up to 35 fused aromatic rings, 35FAR, and in a highly compact shape, has been postulated [37, 41]. Combining the HOMO–LUMO energy gap results with weight and size arguments, it has been concluded that the most abundant PAH size in the asphaltene PAH core is 5–10 FARs (5FAR–10FAR) [37, 41] with a predominance of 7FAR [39, 40, 42, 172].

In addition, it has been possible to obtain structural topological parameters of PAH chromophores whose HOMO–LUMO energy gap falls inside the experimental fluorescence emission range of asphaltenes, thus making it possible to conclude the most likely average structural candidates of the PAH region in asphaltenes from chemical structural analysis [37, 41, 173, 174]. The structural topological parameters that are allowed for asphaltene–PAH cores in asphaltenes have been used to postulate most likely asphaltene–PAH structures [41, 42, 173, 174]. For example, the fluorescence emission of a mixture containing 523 postulated PAH chromophores, with 3FAR to 15FAR (where 7FAR has the highest distribution) and with heteroatom substitution, has been simulated using the semiempirical ZINDO/S method. The obtained simulated fluorescence emission spectrum agrees very well with the experimental data of asphaltenes [42, 172]. Singlet–singlet transitions (HOMO–LUMO transitions) for asphaltenes have been analyzed using both experiment and MO theory. MO computations have also been performed to treat triplet–triplet transitions from the ground triplet state for 103 PAHs, and the qualitative comparisons with the corresponding triplet–triplet transition experimental measurements for asphaltenes have reinforced the conclusion that a single, relatively large PAH per asphaltene molecule is the predominant asphaltene molecular architecture. [172]

In Figure 5.28, the experimentally measured emission spectra of several asphaltenes and one condensate, Figure 5.28(a), are compared with the simulated fluorescence emission spectrum, Figure 5.28(b), obtained from the sum of the calculated spectra of 523 PAHs that are examples of asphaltene–PAH cores, and that were obtained using the structural topological parameters that are allowed for asphaltene–PAH cores in asphaltenes and whose HOMO–LUMO energy gap falls inside the experimental fluorescence emission range of asphaltenes [37, 39–42]. The PAH distribution and its weighting used to obtain the simulated spectra shown in Figure 5.28(b) is presented in Figure 5.28(c). On top of each bar, the number of compounds with different nFAR is given. The PAH distribution spans from 3 to 15 FARs (3–15FAR), where 7FAR

is considered as most probably (weighting in the distribution of 1), in accordance with previous studies [39–41]. As shown in Figure 5.28, the obtained simulated fluorescence emission spectrum agrees very well with the experimental emission spectra of asphaltenes [42].

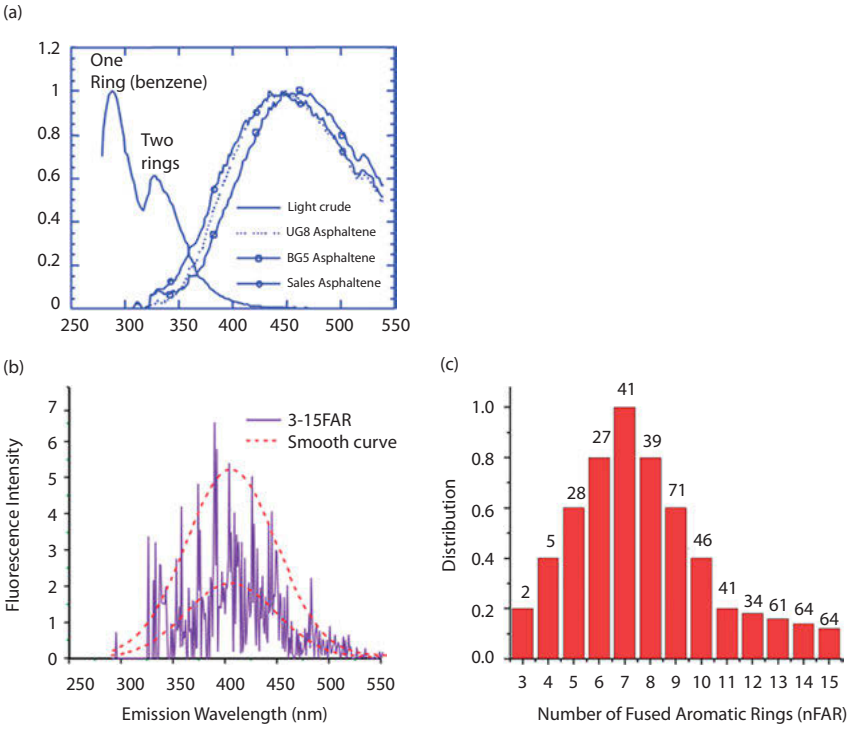

Figure 5.28: (a) Experimentally measured emission spectra of several asphaltenes and one condensate [42]. (b) Simulated fluorescence emission spectrum obtained from the sum of the calculated spectra of 523 postulated asphaltene–PAH cores with 3–15 fused aromatic rings (3–15FAR) and the corresponding smoothed curve. (c) The PAH distribution and its weighting (bar chart) used to obtain the simulated spectra. On top of each bar, the number of compounds used with that number of fused aromatic rings is provided [42]. Reprinted with permission from the American Chemical Society.

In Figure 5.29, the measured optical absorption spectra of four petroleum asphaltenes is shown together with the calculated optical absorption spectrum composed of the spectra of 523 postulated PAH–asphaltene cores, which were weighted as shown in Figure 5.29(c). As it can be seen in general, there is good agreement between the measured and the simulated spectra [42]. As shown in Figure 5.29(c), large PAHs have to be used to account for the important NIR absorption of asphaltenes. In addition, the use of 523 PAH chromophores to simulate the spectra recognizes that there is a substantial chemical polydispersity in asphaltenes.

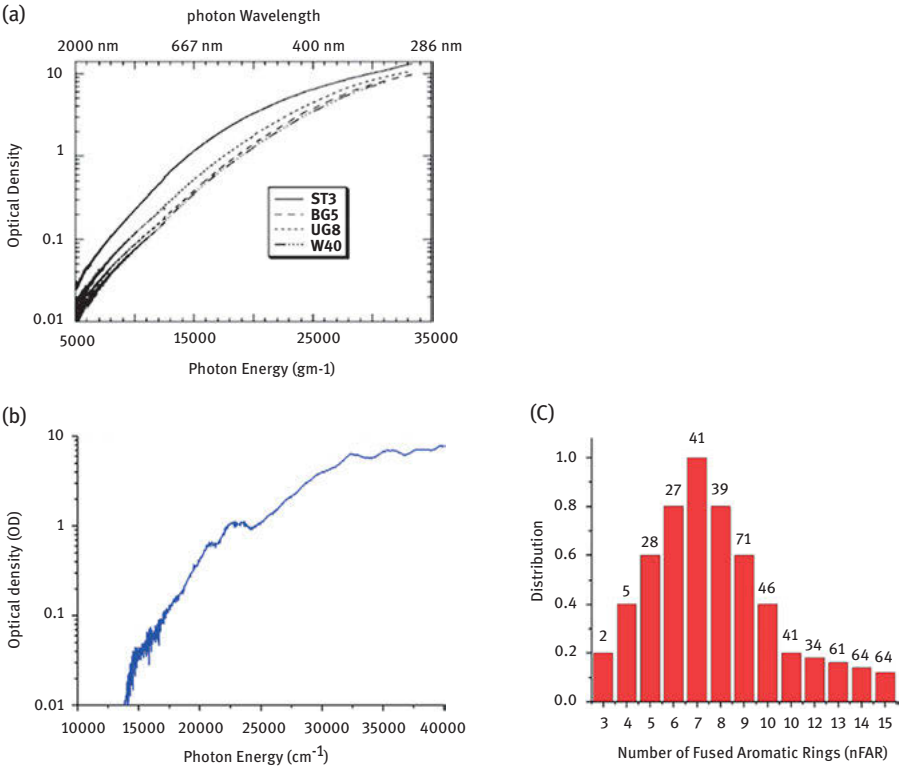

Figure 5.29: (a) Experimental measured absorption spectra (or optical density), on logarithmic scale, of four petroleum asphaltenes. (b) Simulated absorption spectrum obtained from the sum of the calculated spectra of 523 postulated asphaltene–PAH cores with 3–15 fused aromatic rings (3–15FAR). (c) The PAH distribution and its weighting used to obtain the simulated spectra. On top of each bar, the number of compounds used with that number of fused aromatic rings is provided [42]. Reprinted with permission from the American Chemical Society.

5.4.3 Predicted and measured triplet manifold electron spectra of asphaltenes

MO computations have also been performed to treat triplet–triplet transitions from the ground triplet state for 103 PAHs, and the qualitative comparisons with the corresponding triplet–triplet transition experimental measurements for asphaltenes have reinforced the conclusion that a single, relatively large PAH per asphaltene molecule is the predominant asphaltene molecular architecture [172]. In Figure 5.30, the measured nanosecond pump probe T_1–T_n absorption spectra of UG8 asphaltene diluted in benzene are presented together with the MO calculations of the T–T transitions of PAHs with 4–11 FARs (4–11FAR). A total of 103 PAHs were calculated. The MO calculations are consistent with measurements of the triplet electronic states of

asphaltenes. The MO calculations show that there is a significant redshift of the transition energies for the triplet states, compared to the singlet states. As nFARs increases, there is also an overall redshift in the transition wavelengths. Figure 5.30 shows the importance of large PAHs in particular around 7FAR to have a good agreement with the experimental T_1–T_n absorption spectra of UG8 asphaltene [172].

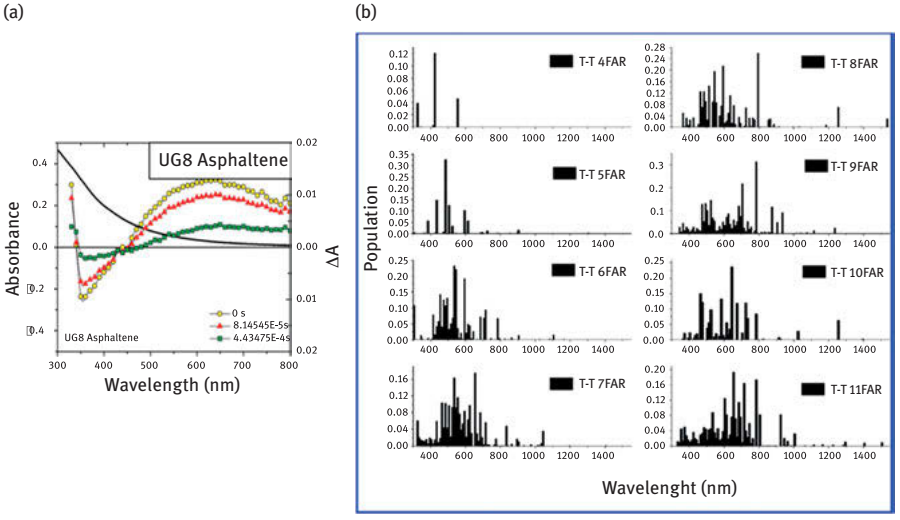

Figure 5.30: (a) The measured experimental nanosecond pump probe T_1–T_n absorption spectra of UG8 asphaltene diluted in benzene. These experiments correspond to exciting triplet states from the ground singlet state. There is "hole burning" (negative ODs) near the excitation wavelength of 355 nm associated with depletion of ground triplet state by the probe laser. (b) The molecular orbital (MO) calculations of the T_1–T_n transitions of PAHs with 4–11 fused aromatic rings (4–11FAR); these spectra are consistent with measurements in (a) [172]. Reprinted with permission from the American Chemical Society.

Schuler et al. found the presence of large numbers of 9-ring PAHs in asphaltenes and some with 18-ring PAHs and larger by using AFM [43, 44]. (Some of these large ring systems might be present because not all samples were constrained to be toluene soluble, instead to be only *n*-heptane insoluble.) These authors combined atomic resolution imaging and STM, to study more than 100 asphaltene molecules [43, 44] and found that a single aromatic core with peripheral alkyl chains is the dominant architecture. In addition, many asphaltene samples from different origins were also analyzed with AFM, finding only island-type structures of asphaltenes. Archipelago molecular structures, where two or more PAH cores are connected by an alkane chain, were not observed. However, a small percentage of archipelago structures with a direct aryl linkage between two PAHs were found in few samples [43, 44]. The PAH cores observed in the AFM studies of asphaltenes are consistent

with those previously predicted by HOMO–LUMO gap theoretical calculations combined with stability arguments [37, 39–42, 172].

In the study of the number of PAHs per asphaltene molecule, computational simulations have also been used. The HOMO–LUMO gap calculations of 3,264 PAH dimer systems in island and archipelago architectures have been carried out at the semiempirical ZINDO method and at the density functional theory–optimized dimer structures [173]. The PAHs were chosen using the structural parameters that are allowed for the PAH region in asphaltenes [37, 41]. The calculated HOMO–LUMO energy gaps were compared to the experimental 0–0 band fluorescence emission of asphaltenes, yielding insight about the most likely architecture of asphaltenes. It has been concluded that asphaltene–PAH cores directly bonded by an aryl linkage would be identified as a single chromophore (given favorable geometry), that is, as an island, by optical spectroscopy methods. Archipelago structures would not be identified as single core by diffusion measurement methods such as TRFD [28, 29]; or by single-molecule decomposition studies. Parallel displacement or skewed π–π stacking has been found as the structure of the stacked island PAH dimmers [173].

Structural topological parameters of PAH chromophores whose HOMO–LUMO gap falls inside the experimental fluorescence emission of asphaltenes have been determined, making it possible to elucidate most likely average structural candidates of the PAH region in asphaltenes, and to postulate PAH asphaltene structures from chemical structural analysis [174]. In addition, it has been concluded that the PAH region in asphaltenes has an intermediate stability for PAHs, which is directly associated with an intermediate number of resonant sextets present in the distribution of the π-electrons [37, 41]. A resonant sextet represents six π-electrons such as in benzene. The π-electron density is distributed in certain number of resonant sextets, which are located in specific rings of the PAH region in asphaltenes, and the remaining π-density is distributed in localized double bonds [37, 39–42, 172]. The higher the number of resonant sextets in a PAH structure, the higher its stability [37, 41], and each resonant sextets confers 36 kcal/mol of stability. Carbon x-ray Raman studies have resolved that the bulk of asphaltene aromatic carbon is aromatic sextet carbon [175, 176].

The Y-rule is used to characterize the π-electron density in resonant sextets and localized double bonds in PAHs, and therefore from the π-electron distribution to elucidate the localization and the number of resonant sextets in peri-condensed benzenoid PAHs [37, 38, 41, 177, 178] in peri-condensed cyclo-pentafused PAHs [178], in the PAH core of asphaltenes [37, 41], and also in the case of cata-condensed systems (extended Y-rule) [179]. The distribution of the π-electron density in resonant sextets and double bonds in PAHs is known as aromaticity [38]. The aromaticity in the asphaltene–PAH region is accountable of electronic properties such as stability, fluorescence emission, and aggregation. The Y-rule is an improvement of the Clar's rule [37, 180], and it has been useful in concluding that the PAH region in asphaltenes contains an intermediate number of resonant sextets. Thus, PAH isomers with

the lowest or highest number of resonant sextets in the structure are not candidates of the PAH region of asphaltenes [37, 174]. In addition, the Y-rule is also important in the rectification of the extended abuse of the use of the circle notation to represent aromaticity in PAHs, where the circle notation is drawn in each fused ring [38]. To summarize, the Y-rule states that the resonant sextets are located in the hexagons that contain the Y-carbons (see text above), C_Y. When distributing the π-electron density, all of the C_Y carbons have to be incorporated into sextets. When there is more than one possibility to locate the sextets, the possibility that provides the higher number of sextets and symmetry is the most probable. The remaining π-electrons are located in localized double bonds but attention must be taken of not overcoming the carbon atoms valence of four. When two π-electron distributions are obtained using the Y-rule, the final distribution is attained by the superposition of these two structures [38, 177, 178].

To elucidate most likely average structural candidates of the PAH region in asphaltenes and to postulate PAH asphaltene structures from chemical structural analysis that involves the use of the combination ^{13}C SPE NMR/^{1}H NMR/^{13}C DEPT and the structural topological parameters of PAH chromophores whose HOMO–LUMO gap falls inside the experimental fluorescence emission [37, 41, 174], it is necessary to know the characteristic NMR ranges for the different carbon and hydrogen types that compose the PAH core. The ^{13}C NMR chemical shift spectral ranges for structural aromatic carbons in PAHs and in asphaltene–PAH cores have been determined by combining calculated ^{13}C NMR chemical shifts, at the GIAO-DFT level, with liquid-state measured experimental ^{13}C NMR chemical shifts [181]. Andrews et al. [9] have shown the importance of performing DEPT NMR experiments in order to accurately determine the relative amount of nonprotonated and protonated carbon in the PAH core. Not utilizing DEPT NMR leads to an underestimation of bridgehead aromatic carbon content, which in turns leads to a lower aromatic ring size in asphaltene structure determination [9, 181].

5.5 Asphaltene components in lesser mass fractions

5.5.1 Pyrolysis GC-MS of asphaltenes

Sensitive techniques such as pyrolysis GC-MS can detect asphaltene molecular fragments that are present in small mass fractions. Figure 5.31 examines the GC-MS results for different samples of the LH crude oil. Corresponding samples of the oil and the asphaltene pyrolysates are compared for three levels of biodegradation as given by the Peters–Moldowan rank (PM) rank [183] 2, 5, and 8, respectively, mild, moderate, and severe. Figure 5.31A examines the results when integrating the total ion signal; fragments of *n*-alkanes dominate in the asphaltene pyrolysates independent of

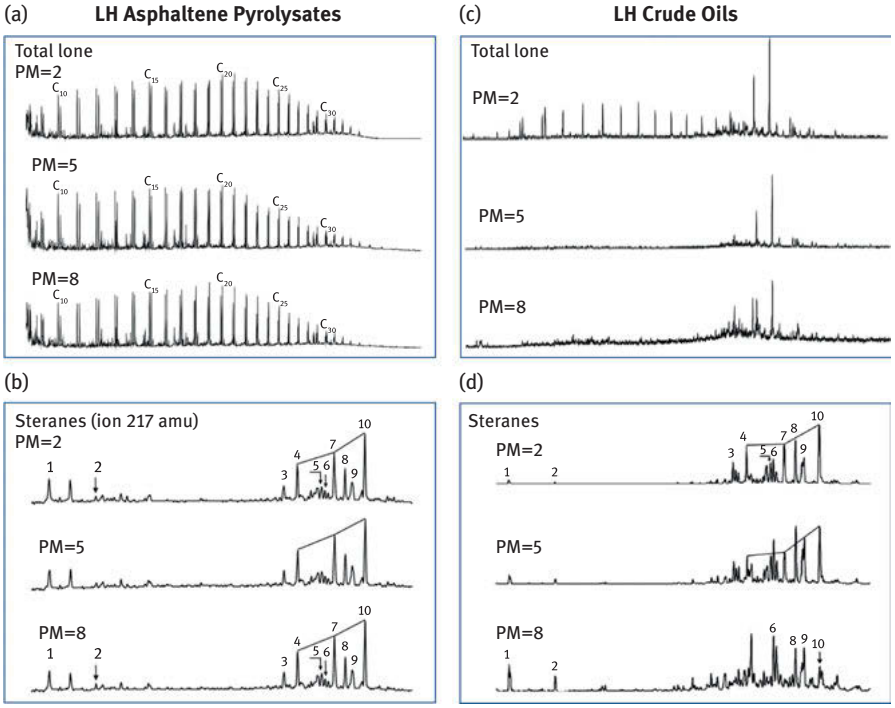

Figure 5.31: GC-MS results from (A and B) asphaltene pyrolysates and corresponding (C and D) LH crude oils as a function of Peters–Moldowan rank of biodegradation; PM = 2 (mild), 5 (moderate), and 8 (severe) [182]. (A) For asphaltene pyrolysates, *n*-alkanes dominate in all cases and are invariant. (B) Steranes can be detected by GC-MS in asphaltene pyrolysates and again are independent of the biodegradation of the oil. (C) For crude oils, the *n*-alkanes are sharply reduced by increased biodegradation. (D) Crude oil steranes are impacted somewhat at PM = 5 and strongly impacted at PM = 8. Comparison of GC-MS from asphaltene pyrolysates and crude oils shows that *n*-alkanes and also steranes are (1) covalently bonded in asphaltene molecules and are not trapped in the precipitation process, and (2) not available for biodegradation in asphaltenes, and (3) as expected, in crude oil, steranes are more resistant to biodegradation than *n*-alkanes [182]. Reprinted with permission from Elsevier.

the extent of biodegradation of the oil [182]. In contrast, Figure 5.31C shows that *n*-alkanes dominate only for the crude oil that has undergone mild biodegradation. For more severe biodegradation, the microbes have preferentially digested the *n*-alkanes reducing their signal relative to other components [183]. There are two important implications: (1) the *n*-alkanes are covalently linked within asphaltene molecules and are not obtained by occlusion in the asphaltene precipitation process and (2) these *n*-alkanes of the asphaltenes are not available for biodegradation [182].

In addition to detecting dominant components, GC-MS methods can be adjusted to detect components in small mass fraction. By setting the detector to the 217 amu molecular cation fragment, families of steranes can be detected; [185] these

compounds are present in crude oils and asphaltenes at very low concentration [183]. Figure 5.31B shows the detection of steranes in asphaltene pyrolysates; such constituents have never been imaged in asphaltenes in the AFM studies of asphaltene molecules because their population is far too low, but they are readily detected by pyrolysis GC-MS applied to asphaltenes. In addition, the sterane composition of the pyrolysates is independent of the extent of biodegradation of the crude oil [182]. In contrast, Figure 5.31D shows that the steranes in the oil are perturbed in PM = 5 and are strongly altered at PM = 8; this is as expected [183]. The comparison of steranes in asphaltene pyrolysates versus crude oils corroborates conclusions obtained for the analysis of *n*-alkanes: (1) the steranes are covalently linked within asphaltenes and are not occluded in the precipitation process and (2) the steranes in the asphaltenes are not available for biodegradation [182]. In addition, these pyrolysis results about dominant straight chain alkane fragments (Figure 5.31A) are consistent with AFM image analysis of asphaltenes [184]. Figure 5.31B shows the signal for m/z = 217, thereby detecting 10 steranes which are identified in Table 5.5 [182]. While detectable, the authors note that the biomarkers from asphaltene pyrolysates are of small quantity even compared to the crude oil, where the biomarkers have a low concentration [182].

Table 5.5: Steroids and terpenoids in Figure 5.31B and D [182].

No.	Compound
1	C_{21} 5α(H)-Sterane
2	C_{22} 5α(H)-Sterane
3	C_{27} 5α(H),14α(H),17α(H)-Cholestane (20*S*)
4	C_{27} 5α(H),14α(H),17α(H)-Cholestane (20*R*)
5	C_{28} 5α(H),14β(H),17β(H)-Ergostane (20*R*)
6	C_{28} 5α(H),14α(H),17α(H)-Ergostane (20*S*)
7	C_{28} 5α(H),14α(H),17α(H)-Ergostane (20*R*)
8	C_{29} 5α(H),14α(H),17α(H)-Stigmastane (20*S*)
9	C_{29} 5α(H),14β(H),17β(H)-Stigmastane (20*R* + 20*S*)
10	C_{29} 5α(H),14α(H),17α(H)-Stigmastane (20*R*)

Figure 5.32 shows two ratios of different isomers of stigmastane, as listed in Table 5.5, for asphaltene pyrolysates and for the liquid phase of crude oil [182]. The insert shows stigmastane and other steroids in Table 5.5 have different substituents on carbon 17. In Figure 5.32A and B, the ratios are shown as a function of the extent of biodegradation using the PM rank of the crude oils. Both these ratios are used as thermal maturity

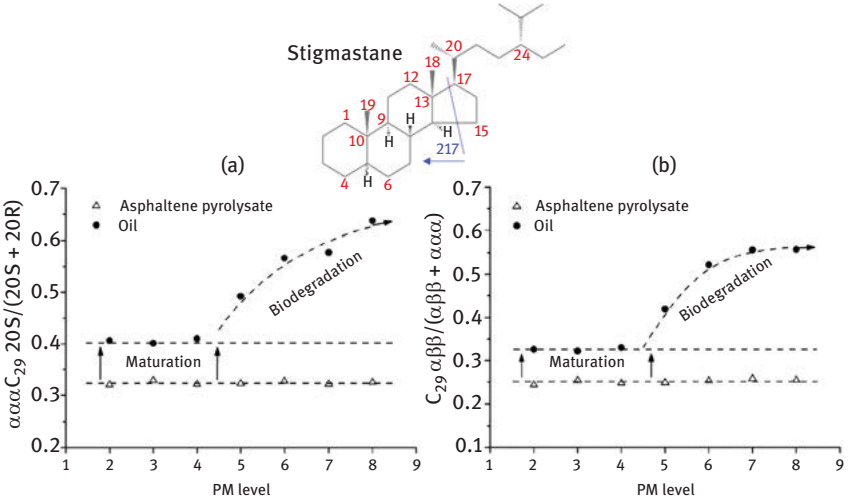

Figure 5.32: Ratios of different isomers of stigmastane (structure in the inset, and 217 *m*/*z* fragment indicated) as identified in Table 5.5 for crude oil liquids and their asphaltene pyrolysates as a function of biodegradation ranging from PM rank 2 to PM rank 8 [182]. Both these stigmastane ratios in (a) and (b) are used as thermal maturity markers. In both plots (a) and (b), the biomarker ratios from asphaltene pyrolysates differ and are of lower maturity than those from the liquid phase of the crude oil. This is expected because asphaltene content is higher in lower maturity crude oils. In addition, in both cases, the biomarker ratios of the asphaltene pyrolysates show no sensitivity to biodegradation, while the biomarker ratios from the liquid phase of the crude oil show increasing dependence on biodegradation. These observations indicate that the stigmastane biomarkers in the asphaltenes are not trapped liquid phase molecules in phase-separated asphaltenes but instead are covalently linked within asphaltene molecules [182]. Reprinted with permission from Elsevier.

markers (unless the ratio is perturbed by biodegradation). Both ratios in Figure 5.32 show that (1) the asphaltenes pyrolysates exhibit a lower maturity than the corresponding crude oil and (2) the biomarker ratios of the asphaltene pyrolysates show no dependence on the extent of biodegradation while these biomarker ratios from the liquid phase of the crude oil show significant effects from biodegradation above PM rank 4 [182]. These observations indicate that the biomarkers from asphaltene pyrolysates are not exchanging with those of the liquid phase biomarkers in geologic time. Instead, the biomarkers in the pyrolysates are covalently linked within asphaltene molecules. The lower maturity of the biomarkers in the asphaltene pyrolysates suggests that thermal isomerization of biomarkers within asphaltene molecules is impeded when compared to the same biomarkers present as a true molecular solution in the crude oil liquid. Other biomarkers in asphaltene pyrolysates exhibit the same ordering of maturity. The fact that the asphaltene biomarkers exhibit a lower thermal maturity than the corresponding marker in the crude oil is consistent with the fact that asphaltenes are concentrated in lower maturity crude oils. In addition, Figure 5.32

also indicates that ratios of thermal maturity markers within asphaltene molecules are being changed by the pyrolysis process; if the ratios were altered, then pyrolysis should correspond to higher maturity for asphaltene pyrolysates than the corresponding crude oil.

The authors were careful to note that the biomarker concentration in the asphaltene pyrolysates is quite low [182]. Indeed, not a single sterane nor hopane subunit was detected in the AFM investigations of many asphaltenes in spite of the tremendous imaging capabilities of AFM [43, 44, 184, 186, 187]. This is expected because AFM methods of investigating individual molecules are generally limited to species present at the few percent level. Nevertheless, it is often quite useful to detect species present at low mass fraction.

5.5.2 Asphaltene archipelago and aryl-linked core molecules

There has been literature debate on the contribution of the archipelago molecular structure for a long time. The term "archipelago" originally referred to molecules with distinct aromatic groups linked by an aliphatic bridge and we use this definition. Molecules with a one or more aryl linkages between two aromatic groups have been termed both island and archipelago in the literature. This third class of structures (in addition to island and archipelago) is now referred to as aryl-linked core molecules, where "core" refers to all contributing aromatic carbon; we use this terminology. TRFD studies on many asphaltenes indicated the dominance of island structures, but this technique requires molecular fluorescence [28–30]. L^2MS studies showed dominance of island structures using a method of relatively invariant cross section for virtually all molecular types in asphaltenes [63].

The most compelling analysis of asphaltene molecular architecture is the actual imaging of asphaltene molecules using AFM and STM as presented above. AFM studies of ten diverse asphaltene samples form crude oil, various process streams, source rock bitumen, and distillation resid from coal liquefaction obtained from ExxonMobil, Shell, Chevron and Schlumberger proves that the results are general [43, 44]. Not even one archipelago molecule with two aromatic groups linked with an aliphatic group was found in the diverse asphaltene samples from this industry study. AFM has unity detection cross section; that is, every molecule in the field of view is analyzed [35, 43, 44]. Asphaltene aggregates, if any, would also be easily detected. There were no asphaltene aggregates on the transfer plate for AFM molecular imaging in any of the asphaltene samples. The aromatic component of the molecules lies in plane on the surface of the cold plate and is readily imaged. In addition, if questions arise as to what is aromatic or what aromatic groups are conjugated, then STM is then used in these asphaltene studies to determine the aromatic and conjugated portion of the molecule by detection of PAH MOs. As noted above, the transfer process of asphaltene molecules from the heated filament to the cold plate was performed with several

model archipelago compounds with no fragmentation [35, 43, 44, 184]. One of the model compounds used is 1,2-dipryene-1-yl ethane, which has a very low carbon–carbon single bond energy of 65 kcal/mol [184]. Thus, if flash thermal desorption would result in fragmentation, this weakly bound molecule should fragment; yet it did not fragment confirming that archipelago model compounds are readily transferred and imaged. Moreover, a small fraction of archipelagos are found in a different carbonaceous sample, a pitch, confirming the ability to detect archipelago structures within complex molecular mixtures [186]. The conclusion from AFM and STM imaging matches the L2MS results and the TRFD results; archipelago structures represent a small mass fraction of asphaltene at most.

5.5.2.1 Ultrahigh-resolution mass spectrometry dissociation studies

Recent studies employing APPI FT-ICR MS coupled with infrared multiphoton dissociation (IRMPD) have explored asphaltene molecular weight and architecture [188–190]. The relationship of these studies to other studies presented above has been discussed elsewhere [18]. The molecular weights obtained in these and other ultrahigh resolution studies are broadly consistent with those obtained by a suite of other methods. These measurements also rule out dominance of the archipelago molecular structure of the sort originally proposed with molecular weights in excess of 6,000 amu [188-190]. Moreover, the ultrahigh resolution studies are also consistent with a substantial fraction of island structures in asphaltenes. Nevertheless, these studies also found a fraction of asphaltene molecules that have what the authors termed “archipelago” structures which explicitly include a variety of structures including molecules with a possible aryl-linked core and molecules with alkyl-linked PAHs [188-190]. These different structural classes were not differentiated in these studies. Figure 5.33 shows an example of these findings.

Figure 5.33 shows results from an ultrahigh resolution mass spectral analysis of asphaltenes [190]. The methods utilized here have very high sensitivity to detection of components present even if in very small quantities [191]. These ultrahigh resolution methods can detect more than 10,000 components in crude oil, so are very sensitive and able to detect components in tiny mass fraction (<100 ppm). However, the authors note that these methods employed have extreme sensitivity to aggregation with very large variations in cross section of different molecular components of a factor of 50 or more for reasons of uncertain origin [188-190]. In addition, ICR methods have inherent cross-sectional variability especially for organic matter [192]. Consequently, quantitative mass fraction assessment is hindered.

The type of binding of the fragments in the initial molecule was not established in these studies [188-190]. No differentiation was made whether the fragments were originally linked with an aliphatic group (archipelago) or with a direct aryl bond (aryl-linked core) [35]; thus, these studies lumped the very different structures of

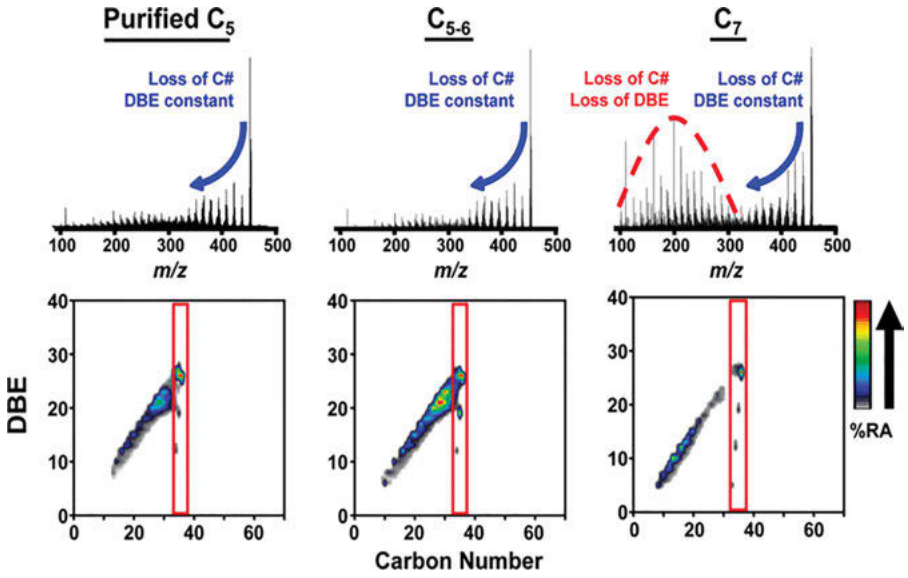

Figure 5.33: Infrared multiphoton dissociation (IRMPD) of "purified" or fractionated asphaltenes (where a fraction of predominantly island molecules were removed) [190]. For the asphaltenes isolated with *n*-pentane, there is little loss of DBE, double bond equivalent, which is defined as double bonds plus rings, after IRMPD; aromatic moieties are high in DBE. For these "purified" asphaltenes, there is a fraction of population (as shown) where, upon IR irradiation, the molecule cleaves into two fractions of roughly equal mass and where each fragment has lower DBE than the original molecule. This result indicates separation of aromatic moieties upon dissociation, consistent with the presence of two aromatic moieties in the molecule. Two questions remain: (1) what structures give rise to this signal? and (2) what is the magnitude of this fraction? Reprinted with permission from the American Chemical Society.

aryl-linked core and archipelago. The data in Figure 5.33 shows a splitting of molecules into roughly two equal parts, but not, for example, 5 parts. Indeed, the small molecular weight of the original molecular population (~400 amu) is not compatible with fragmentation into many parts of an archipelago; asphaltenes are not made of polystyrene.

The molecular AFM imaging of asphaltenes and the model compounds alkyldipyrenes addresses exactly the case of archipelago molecules that can naturally fragment into two roughly equal parts [184]. The mass range of 400 amu for asphaltenes and 200 amu for fragments in Figure 5.33 is well within the molecular weight range for efficient transfer and detection by AFM. Figures 5.19 and 5.21 show excellent sensitivity of AFM and STM imaging for detection of alkyl–dipyrene archipelago molecules with two pyrene PAHs cross-linked by an alkane chain. Specifically, di-pyrene compounds would fragment to an alkylpyrene; pyrene has a molecular weight of 202 amu. Thus, the AFM imaging of Figures 5.19 and 5.21, and thus of the asphaltenes, exactly matches requirements if the fragmentation data in Figure 5.33 corresponds to an archipelago.

However, the AFM and STM studies of 10 diverse asphaltene samples showed no evidence of such archipelago molecules. Given this fact, then the interpretation of the data in Figure 5.33 is that the fragmenting molecules, if present in any significant quantity, are not likely to have two PAHs cross-linked by an aliphatic group (archipelago) but are plausibly from an aryl-linked core. The 50× variation in cross section of the APPI FT-ICR MS studies makes direct comparisons somewhat uncertain [188-190]. The large, flat cross section and high efficiency of the AFM and STM imaging for detection of specific structures is a significant benefit for interpretation results of wide-ranging methods.

5.5.2.2 Re–Os dating of carbonaceous materials

Asphaltenes are known to contain V and Ni at low and highly variable concentrations often in the range of 10–1,000 pm. These metals are known to be contained largely if not entirely in various porphyrin structures in part by the appearance of the porphyrin Soret band. The Soret bands of asphaltenes are generally too small to account for all of the V and Ni in asphaltenes but x-ray spectroscopy methods indicate that these metals are contained within porphyrin-type structures [193]. Mass spectrometry methods have resolved metalloporphyrins in asphaltenes [194, 195]. At much lower concentrations, crude oils and especially asphaltenes contain Re and Os. These concentrations of these metals are correlated to those of V and Ni in different petroleum fractions, indicating possible residence in porphyrin organometallics [196].

The presence of Re and Os in crude oils and asphaltenes enables the ability to employ the geochronology method of ^{187}Re β^- decay (half-life 43 billion years) to ^{187}Os, where the stable ^{188}Os is used for normalization [197, 198]. Re–Os dating was used to obtain the timing of emplacement of giant oil sands in Alberta, Canada, of 112 Mya, tightly constraining the petroleum systems analysis and source rock identification [198]. Re–Os dating has also been used to constrain the timing of tar mat formation in reservoirs with multiple incompatible charges [199]. Nevertheless, there are complexities associated with the partitioning of Re and Os into different components of crude oil [196]. Re–Os dating offers new insights to petroleum systems as well as reservoir fluid geodynamics providing the timing of processes unavailable by any other methods.

5.5.2.3 Organic acids

Crude oils can contain organic acids that may or may not partition to the asphaltene solubility fraction [200]. Biodegraded oils are especially prone to containing organic acids [201]. Hopanoic acids are identified as a possible product of biodegradation

[201], helping to explain how thermal maturity markers can be disrupted by biodegradation. Different crude oils with multiple charges have organic acid content in accord with the mixture [14]. In general, the organic acids can play a significant role in emulsion stability. Organic acids that can have a significant effect on oil production are those with four acid moieties (tetrameric acids) in single molecules, the so-called ARN acids in the C80 range [200, 202]. These acids can form calcium naphthenates that can be but are not necessarily very problematic in oil production [203].

5.6 Colloidal structure of asphaltenes

Asphaltenes have hierarchical nanocolloidal structures that have been reviewed in detail elsewhere [1, 15, 16]. Here, we provide a brief review of older and compelling results regarding aggregation numbers, aggregate structures, concentrations of aggregation, and the hierarchical nanoaggregation of asphaltenes. Most importantly, the aggregates discussed here are found in reservoir crude oils at elevated temperatures (~100 °C) and are stable for geologic time. Larger aggregates are also observed in destabilized asphaltenes and for slight instabilities, asphaltene destabilized particles are initially only slightly larger than the stable clusters of the Yen–Mullins model [204–207].

5.6.1 Nanoaggregates: the critical nanoaggregate concentration (CNAC)

There had been a long-standing perspective that asphaltenes aggregate. However, there were many significant literature disagreements regarding asphaltene aggregation in part because of the then unrecognized hierarchical nature of asphaltene nanoaggregation. It became imperative to resolve the concentration at which asphaltenes first aggregate, the critical nanoaggregate concentration (CNAC). Initial indications of asphaltene aggregation at low concentrations came from fluorescence studies of asphaltenes [208]. High-Q ultrasonic studies then determined the CNAC and also indicated that nanoaggregates reached a certain size and quit growing over a limited concentration range [22, 23]. The results were quickly confirmed by DC-conductivity [209–211], centrifugation [211], and NMR [19, 45].

Figure 5.34 shows data from three very different methods on three different asphaltenes, yet all results are fairly similar. High-Q ultrasonic measurements rely on the ability to resolve speed of sound to a few parts in a million. The speed of sound $u = \sqrt{1/\rho\beta}$, where ρ is density and β is compressibility. Upon nanoaggregate formation, the density, an integral quantity, is rather invariant but compressibility, a differential quantity, changes. For surfactant micelles in water, the change in

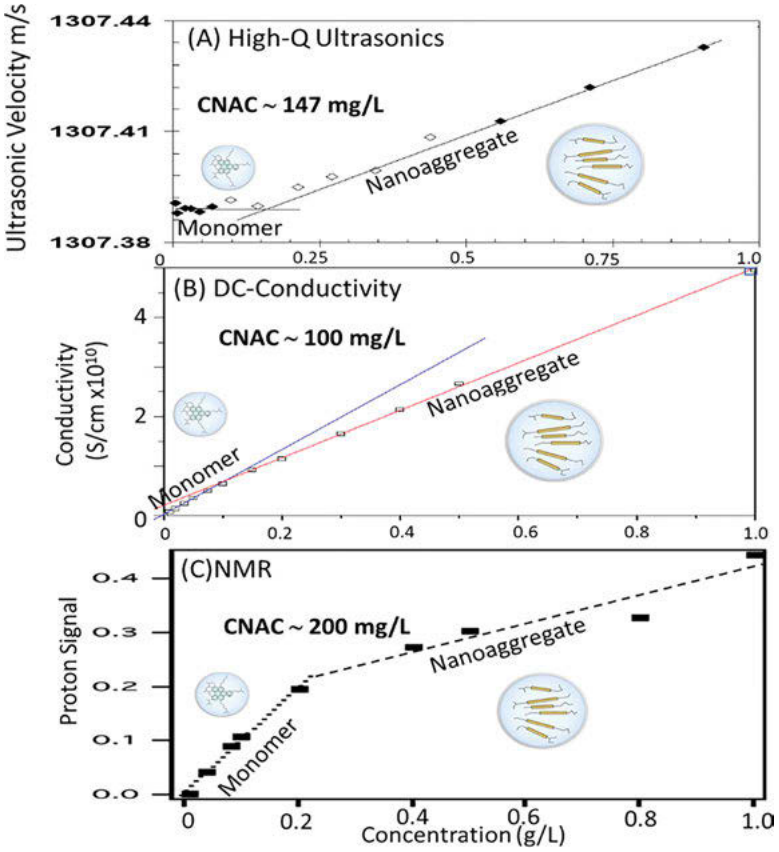

Figure 5.34: Critical nanoaggregate aggregation concentration (CNAC) as measured by (A) high-Q ultrasonics [22, 23], (B) conductivity [210], and (C) NMR [45] for three different asphaltenes. All CNAC values are roughly 2×10^{-4} mass fraction. Each method shows two linear sections, one corresponding to molecules and the other corresponding to nanoaggregates. The CNAC is at the intersection of the straight-line segments. Reprinted with permission from the American Chemical Society.

compressibility upon micelle formation is large and high-Q ultrasonics is readily used to measure critical micelle formation [22]. However, for asphaltenes in toluene, both solute and solvent are essentially alkyl-aromatics and the changes are more subtle, nevertheless, detectable as shown in Figure 5.34A [22]. Reprinted with permission from the American Chemical Society.

The measurement of DC conductivity uses the very small molecular fraction of asphaltene that is charged in toluene (~10^{-5}); thus, the ion acts like a tracer [210]. When neutral molecules attach to the ion, Stokes drag (F_d) increases and the conductivity per unit mass of asphaltenes is diminished, as shown in Figure 5.34B. Equation (5.2) gives the force of Stokes drag for a sphere of radius R and for viscosity η and

particle velocity v [19, 45]. In these experiments, Stokes drag equals the electric field E multiplied by charge q:

$$F_d = qE = 6\pi\eta Rv \tag{5.2}$$

Figure 5.34C shows that NMR measurements also give CNAC. Upon formation of the nanoaggregate, the restricted diffusion of the alkane chains causes a decrease in rotational averaging, thereby reducing the magnitude of the NMR signal per unit mass of asphaltene [19, 45].

5.6.2 Aggregation number of nanoaggregates

The aggregation number of nanoaggregates is not large. The change in slope in the DC conductivity from molecule to nanoaggregate is not large; the cube of this difference gives the effective aggregation number of ~6 with some uncertainty [210]. For comparison purposes, the aggregation number of the sodium dodecyl sulfate (SDS) micelles in water is 63 and increases significantly at higher ionic strength [212]. The small variation of the nanoaggregate aggregation number is not so important; the key conclusion is that this aggregation number is quite small.

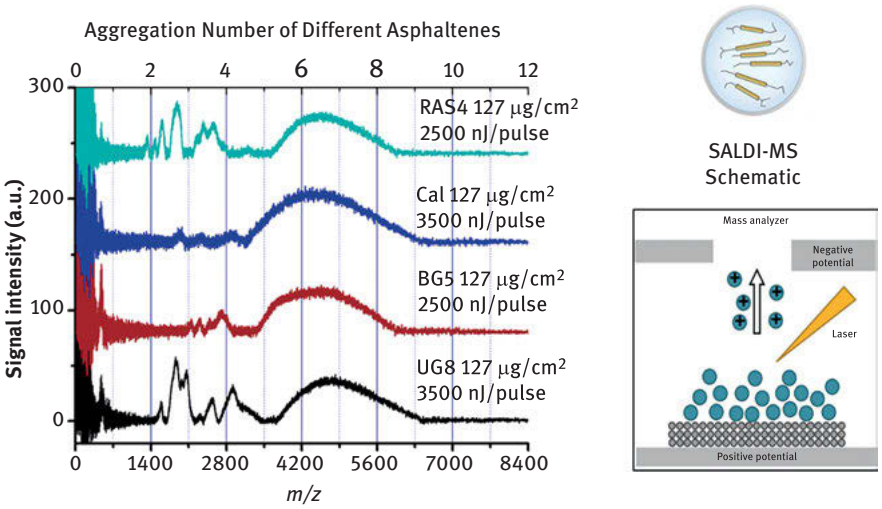

Figure 5.35: SALDI-MS data showing the mass of the nanoaggregate on the bottom x-axis scale [62, 65, 69]. By dividing this nanoaggregate mass by the molecular mass obtained from L^2MS, the aggregation number is obtained. For all asphaltenes measured, the aggregation numbers of about 6 or 7 are obtained. Reprinted with permission from the American Chemical Society.

SALDI-MS measurements were also used to obtain asphaltene nanoaggregation numbers [62, 65, 69].These measurements rely on a gentle laser desorption of asphaltene solids on a SALDI-MS substrate. Figure 5.35 shows that again aggregation numbers of about 6 are obtained independent of the type of asphaltene, including petroleum asphaltenes, coal-derived asphaltenes, and immature source rock asphaltenes. The implication is that the solubility classification of asphaltenes also defines their aggregation numbers, a property of solvation for asphaltene classes that have different elemental composition and C/H atomic ratios.

As noted above, regarding VPO and some mass spectrometric methods, asphaltene aggregation has been observed to introduce important artifacts in measurement and interpretation. Nevertheless, it has been conclusively established that the methods of asphaltene sample transfer in AFM studies are not impacted by asphaltene aggregation since no aggregates have been detected. It is important to establish that laser desorption techniques do not suffer from asphaltene aggregation, especially since the L^2MS measurements have been so important in establishing both asphaltene molecular weight and architecture. The laser desorption method "SALDI-MS" is less energetic than L^2MS. In L^2MS, there is a direct heating of the asphaltenes with the laser, whereas in SALDI-MS, the heating is indirect, the laser heats the surface upon which asphaltenes are placed, and this heating causes desorption.

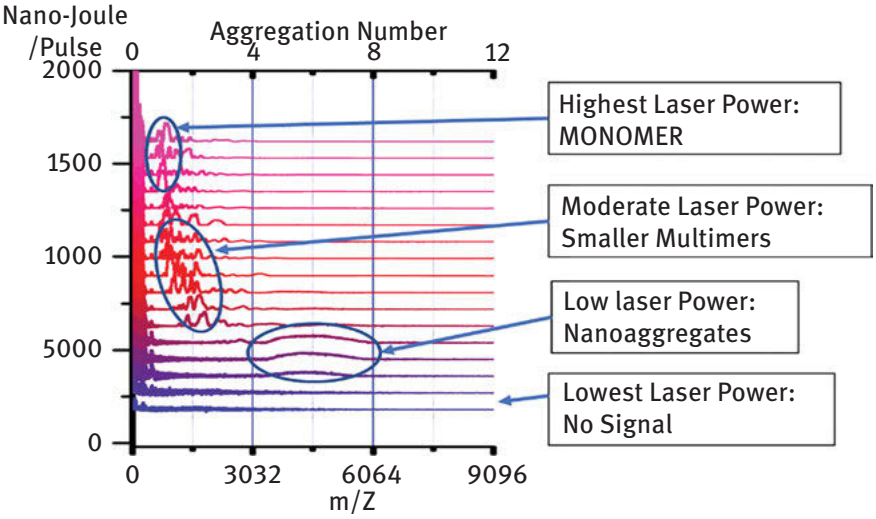

Figure 5.36: SALDI-MS data for asphaltenes versus laser power (see Figure 5.35 for a schematic of the apparatus) [62]. At the lowest laser powers, there is no signal. At low laser powers, nanoaggregates are preserved; an expanded view of such signals is shown in Figure 5.35. At moderate laser powers, small multimers (dimers and trimers) are obtained. At the highest laser powers, monomers are obtained [62]. Reprinted with permission from the American Chemical Society.

Figure 5.36 establishes that laser heating of asphaltenes can readily disaggregate nanoaggregates without difficult. This result confirms that L^2MS results are not affected by nanoaggregates; thus, the important L^2MS results on asphaltene molecular weight [60–62] and on the dominance of island architecture [63] are valid.

5.6.3 Binding energy of nanoaggregates

An estimate of the binding energy of nanoaggregates in solution is obtained with eq. (5.3) from the critical micelle concentration for nonionic surfactants [213]:

$$\Delta G = -RT\ln(\mathrm{CMC}); \quad \Delta G = -RT\ln(\mathrm{CNAC}) \tag{5.3}$$

For a CNAC of 150 mg/L ~ 2×10^{-4} M, ΔG ~ 5 kcal/mol. This is a low binding energy and consistent with the results shown in Figure 5.36 from SALDI-MS:

$$\mathrm{CNAC} = \exp\left\{-\frac{\Delta G}{\mathrm{RT}}\right\} = \exp\left\{-\frac{\Delta H - T\Delta S}{RT}\right\} = \exp\left\{-\frac{\Delta H}{RT}\right\}\exp\left\{-\frac{\Delta S}{R}\right\} \tag{5.4}$$

The asphaltene CNAC has been measured to have a relatively small temperature dependence [45, 211], which helps explain why nanoaggregates are routinely found in reservoir crude oils at temperatures in excess of 100°C [18, 214, 215]. As indicated in eq. (5.4), the limited temperature dependence of the CNAC formation indicates that a substantial fraction of the Gibb's free energy of nanoaggregate formation is due to entropy increase at CNAC. Upon asphaltene aggregation, the entropy of the solvent increases by more than that of the asphaltenes decreases. Similar findings are well known for micelle formation in aqueous systems [216]. For micelles formed with charged surfactants, micelle formation is accompanied by a concentration of like charges in the micelle that are not entirely offset by the counterion binding to the micelle [213]. The growth of micelles with increasing ionic strength is associated with better charge cancellation [217]. The enthalpy of formation of charged micelles can be positive especially at lower temperatures [213, 218, 219] for which case entropy changes must cause micelle formation.

5.6.4 Structure of asphaltene nanoaggregates

Various studies have shown the existence of a disordered PAH stack at the length scale approaching that of the graphite sheet spacing [17, 220]. Asphaltene intermolecular binding is discussed in some detail in Section 5.7; the primary conclusion is that the dominant asphaltene intermolecular interaction is from polarizability, thus primarily from aromatic carbon [221]. Considering the island structure of asphaltenes, the nanoaggregate naturally have an interior core of aromatic carbon, with

peripheral aliphatic substituents. Exactly, this structure has been shown in a series of studies comparing the absolute cross sections of SAXS and SANS measurements of asphaltenes [222–224].

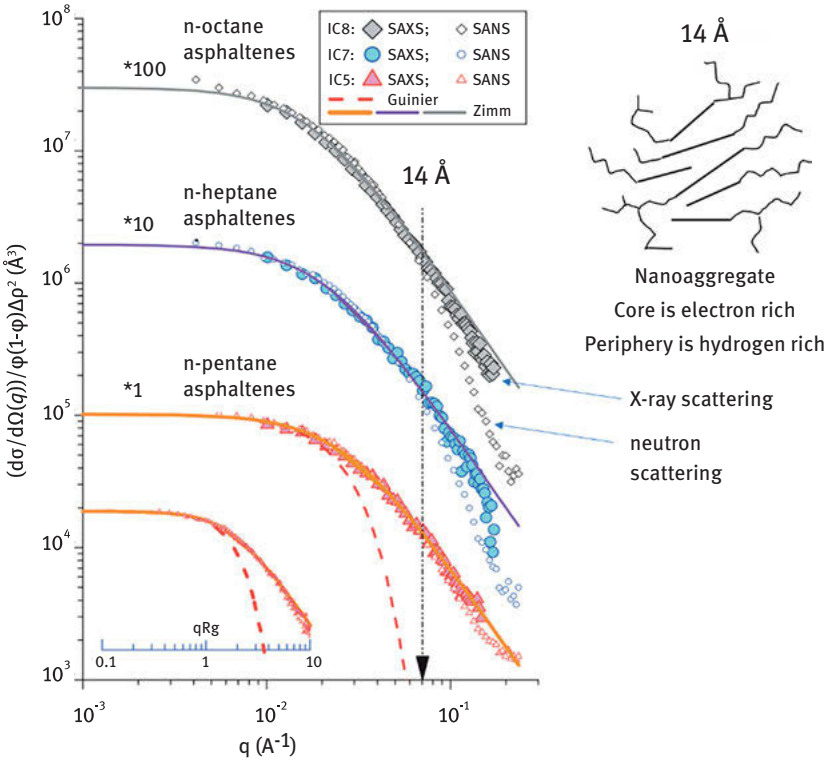

Figure 5.37: Comparison of SAXS and SANS spectra: variations in the normalized cross sections $I(q)/\varphi\Delta\rho 2$ as a function of the wave scattering vector q for solutions of different asphaltenes in toluene. The asphaltenes were obtained by insolubility in *n*-octane (iC8), *n*-heptane (iC7), and *n*-pentane (iC5) [222]. φ is asphaltene fraction and $\Delta\rho$ is density contrast. The dotted and solid lines represent different approximations in the small q domain. The scattering vector q, defined as $4\pi\sin\theta/\lambda$, where 2θ is the scattering or deviation angle and λ is the incident wavelength of the x-ray or neutron and acts as an inverse length scale (thus units of 1/Å). Separation of the SAXS and SANS cross sections shows the fundamental separation of the aromatic and saturate portions of the nanoaggregates [222–224]. Reprinted with permission from the American Chemical Society.

X-rays are scattered preferentially by electrons; the aromatic core of the nanoaggregate is enriched in electrons. Neutrons scatter preferentially by hydrogen; the peripheral alkanes of the nanoaggregate are enriched in hydrogen. Thus, for electron and neutron wavelengths at the length scale of the nanoaggregate and smaller, the SAXS and SANS cross sections will separate *if* the nanoaggregate structure consists of a (disordered) PAH stack in the interior with peripheral alkane [222–224]. Figure 5.37

shows that this nanoaggregate structure is confirmed. The length scale of this structure of the nanoaggregate is 14 Å. Nanoaggregate models with substantial void space and lacking a PAH stack are not consistent with these observations. Such void space is also inconsistent with the dominance of polarizability as the dominant intermolecular interaction.

Molecular dynamic simulations show nanoaggregate structures for three kinds of asphaltenes [225] with very different aromatic to alkane carbon fractions; all have been shown to have essentially the same aggregation number of their nanoaggregates by SALDI-MS [226].

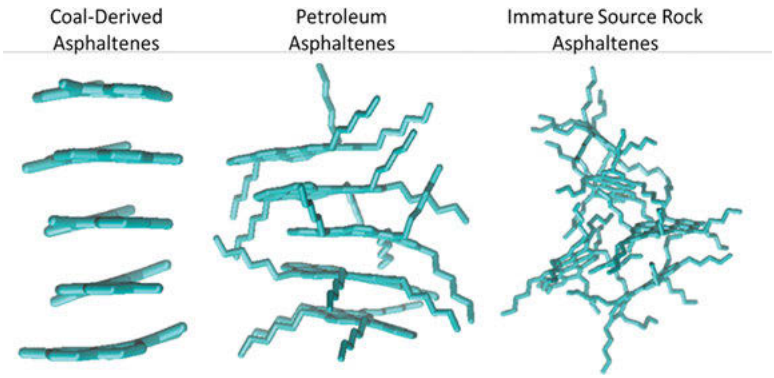

Figure 5.38: The role of aliphatic substituents in the structure of the nanoaggregate as shown by molecular dynamics calculations for three diverse asphaltenes [225, 226]. The coal-derived asphaltenes, with a small alkane fraction (25%), exhibit order in the PAH stack. Petroleum asphaltenes with their substantial, peripheral alkane fraction (~50%) exhibit a disordered PAH stack. The asphaltenes from immature source rock with their dominant alkane fraction (75%) do not exhibit PAH stacking. These three types of asphaltenes all have essentially the same aggregation number as shown by SALDI-MS and, of course, all adhere to the solubility definition of asphaltenes [226]. Reprinted with permission from the American Chemical Society.

Figure 5.38 explores the role of steric disruption of PAH stacking by using three types of asphaltenes that differ significantly in their alkane fraction [225, 226]. The PAHs engage in stronger intermolecular interactions than the alkanes, and the PAHs can also orient and stack in preferred configurations to maximize favorable energetics. Alkanes do engage in attractive intermolecular interactions but due to their typically random orientations, they interfere with each other and with PAHs; this steric repulsion causes disorder or can even preclude PAH stacking. The decrease of order in the PAH stack with increasing alkane fractions is evident in Figure 5.38. Nevertheless, the three types of asphaltenes are all toluene soluble and *n*-heptane insoluble, and they have all been shown to have roughly the same aggregation number of the nanoaggregate. Evidently, the solubility constraint of asphaltenes from the different source materials is sufficient to produce similar aggregation numbers of the nanoaggregates.

5.6.5 Clusters of nanoaggregates

Well-established literature studies are briefly reviewed in this section regarding asphaltene clusters [35]. There is a second concentration threshold of nanoaggregation of asphaltenes; this second threshold results in the formation of clusters of nanoaggregates. Similar to nanoaggregates, clusters can be stable in crude oil for geologic time [227]. Thus, asphaltenes exhibit hierarchical nanoaggregation. There is no third threshold of aggregation known for asphaltenes that results in stable colloids, nor is there likely to be. Colloidally unstable asphaltenes have been shown to have particle sizes down to 10 nm, almost the size of clusters [204–207]. In reservoir crude oils, particles of this size or bigger would settle onto surfaces and would not be suspended in the oil, thus would not be part of the produced crude oil. Phase-separated asphaltenes are common in oilfield reservoirs and result from various reservoir fluid processes [18, 228–230]. Similar to nanoaggregates, key properties of the asphaltene clusters include the critical cluster concentration (CCC), the aggregation number of the clusters, the binding energy of the clusters and the structure of the clusters. Clusters are less strongly bound than nanoaggregates as they form at higher concentrations and represent the second threshold of aggregation of asphaltenes with both factors making cluster characterization more difficult. Nevertheless, clusters have been reasonably well characterized by many different experimental techniques.

5.6.6 Critical cluster concentration (CCC)

Evidence for a change in the (nano)colloidal description of the asphaltenes in toluene was obtained by dynamic light scattering (DLS) experiments that tracked the formation of flocs after addition of *n*-heptane to toluene solutions of asphaltenes [231, 232]. DLS, also known as the photon correlation spectroscopy, directly measures the Brownian motion of particles suspended in solution and, if the kinetics are slow enough, enables one to monitor the particle growth. In this method, the light scattering pattern is measured at a point in time. At later points in time, the light scattering pattern is obtained and compared (or autocorrelated) with the original scattering pattern. The decay rate of the autocorrelation value from 1 to 0 with time occurs via diffusion and gives the translation diffusional correlation time. From this, the diffusion constant can be determined which is related to the size of the asphaltene particle by the Stokes–Einstein equation.

There is a distinction between cluster–cluster aggregation as opposed to aggregate growth from adherence of monomers to a cluster [233, 234]. For colloidal instability as described herein, the appropriate description is cluster–cluster aggregation (both above and below the CCC) [233, 235, 236]. Formerly, the diffusion-limited aggregation (DLA) of cluster–cluster aggregation was called diffusion-limited colloidal

aggregation (DLCA) as opposed to DLA of individual molecules/particles sticking to a colloidal species. The distinction is important because the physical description is different, and the fractal dimensions are different. Likewise, the corresponding nomenclature applies to reaction-limited colloidal aggregation (RLCA) versus reaction-limited aggregation (RLA) [233, 235–237]. There is confusion because many, including the authors who performed DLS on asphaltenes, used the language DLA for DCLA and RLA for RCLA. We keep the designation of the original work of DLS on asphaltenes but we note the work related to colloidal instability, thus actually DLCA and RLCA.

For two dimensions, 2D (such as in a Hele–Shaw cell), for aggregate growth, the fractal dimension d for DLCA is $d \sim 1.45$ [238] and for DLA is $d \sim 1.7$ [233]. For 2D, the fractal dimension for RLCA, $d \sim 1.56$ [238], thus larger than that of DLCA and more space filling and compact. For 3D aggregate growth, the fractal dimension d for DCLA is $d \sim 1.7$ [233, 235, 236], whereas for DLA $d \sim 2.5$ [237]. For 3D, the fractal dimension of RLA $d \sim 2.5$ [233], while for RLCA $d \sim 2.1$ for low concentrations but increases to 2.5 for high concentrations corresponding to the percolation threshold [234, 239]. The reason that the fractal dimension in DLCA is lower (less space filing) than in the case of DLA is because particle growth is dendritic and the large clusters have less access to the "fjords" between the dendritic trees due to their larger particle size [233]. Even for initially smooth surfaces, a roughening of surfaces will magnify similar to the Mullins–Sekerka instability [233, 240].

There is confusion beyond the same name used for two different physics processes (e.g., DLA used for DLA and DLCA); the fractal dimension of 2D aggregate growth for DLA is the same as the fractal dimension for 3D growth of DLCA, $d \sim 1.7$ [236, 239]. For the work below on asphaltenes, cluster–cluster aggregate growth in 3D applies; thus, 3D DLCA ($d \sim 1.7$) and 3D RLCA ($d \sim 2.1$) apply (even though the names "DLA" and "RLA" are used).

Generally, an aggregation process may involve two characteristic times: a diffusion time τ_D and a reaction time τ_R. There are two limiting cases of aggregation, DLA and RLA. If $\tau_D \gg \tau_R$, the aggregation kinetics are controlled by diffusion and referred to as DLA. In the case, when $\tau_R > \tau_D$, the aggregation kinetics are determined by the rate of the "reaction" and referred to as RLA. The equations employed by the authors [231, 232] to determination which aggregation process applied are:

$$\text{DLA}: \; R = R_o(1 + t/\tau_D)^{1/d_f} \tag{5.5}$$

$$\text{RLA}: \; R = R_o \exp\left(t/\tau_R d_f\right) \tag{5.6}$$

where R_o is the initial value of R and d_f is the fractal dimension of the particle. [231, 232]

Figure 5.39 shows a transition from DLA to RLA for asphaltene floc growth when changing the initial concentration of asphaltenes in toluene from 1 to 10 g/L. This indicates a change in the nanocolloidal state of asphaltenes in this concentration

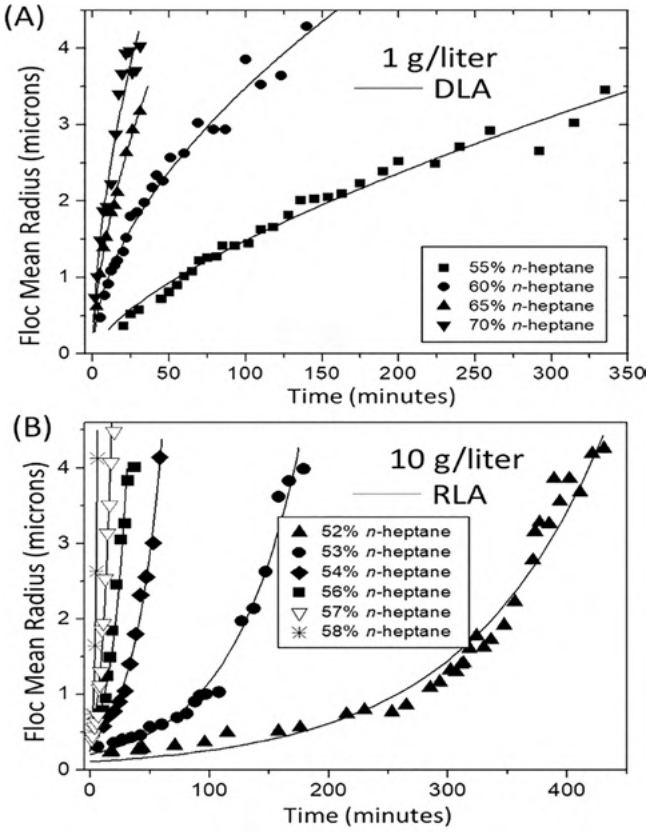

Figure 5.39: Kinetics of floc growth from the so-called cluster–cluster aggregation [234–236] for asphaltenes in toluene destabilized by *n*-heptane addition [231, 232]. (A) For 1 g/L asphaltene in toluene, the kinetics are consistent with diffusion-limited aggregation (DLA or really DLCA) [231, 232]. The fractal dimension is 1.7, which matches expectations for DLA of a destabilized colloidal system. (B) For 10 g/L asphaltenes in toluene, the kinetics are consistent with reaction-limited aggregation (RLA or really RLCA). A fractal dimension of 2 was used for RLA. The change in floc kinetics from DLA to RLA indicates a change in the nanocolloidal state of asphaltenes in going from 1 to 10 g/L [231, 232]. Reprinted with permission from the American Chemical Society.

range. The cross-over concentration was determined to be ~5 g/L [231, 232]. As the authors clarified, once the high-*Q* ultrasonics work identified the CNAC, it was evident that the aggregation detected by these kinetic studies corresponds to a higher level of aggregation, now called cluster formation from nanoaggregates.

RLA reaction kinetics can occur when a morphological change is needed in order for particles to stick. Clusters are likely fractal in nature with some dendritic character and could require such a morphological change for strong adherence at the interface between particles. This might explain the RLA reaction kinetics of clusters.

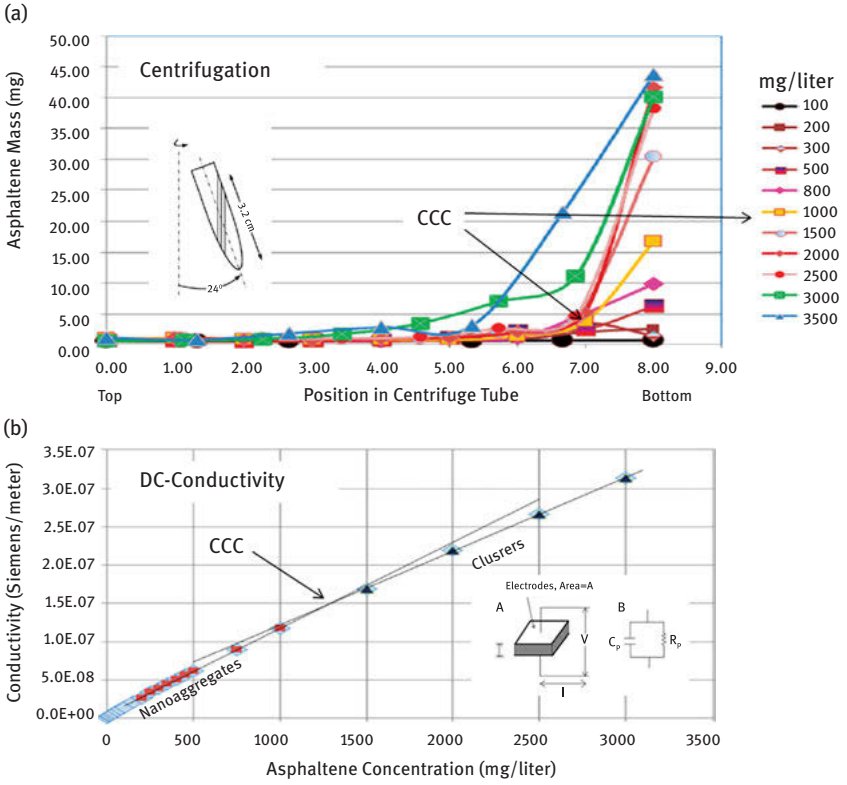

Figure 5.40: Measurement of the critical cluster concentration (CCC) [209]. (A) For centrifugation, spin durations are employed, which are too short to collect nanoaggregates but are sufficient to collect clusters of equivalent sphere 5 nm diameter at the base of the centrifuge tube. Asphaltene accumulation at the bottom of the centrifuge tube occurs at ~1.2 g/L [209]. (B) A very small fraction of asphaltene nanoaggregates are charged. Upon cluster formation of a charged nanoaggregate with neutral nanoaggregates, the Stokes' drag increases, reducing the conductivity per unit mass of asphaltene. For the same asphaltene, the CCC is ~1.3 g/L [209]. Reprinted with permission from the American Chemical Society.

Centrifugation and DC conductivity were both used to detect the CCC just as they were the CNAC [209]. Figure 5.40 shows the CCC to be slightly more than 1 g/L, thus somewhat less that was obtained by the kinetics of floc formation. Possibly, the different asphaltene samples played a role in the CCC difference. In any event, the detection of a second aggregation threshold is confirmed by very different techniques.

5.6.7 Cluster aggregation number/size

To measure CCC, both centrifugation and DC conductivity rely on the change in the hydrodynamic radius r upon cluster formation from nanoaggregates. Both analyses yield cluster sizes smaller than 10 nanoaggregates [209]. The relevant equation (5.7) and discussion for DC conductivity for clusters is the same as for the nanoaggregate. In centrifugation, the force of the asphaltene particle is proportional to the acceleration (g) and the volume of the particle (thus, the cube of the radius), and density contrast between the asphaltene and crude oil, $\Delta\rho$. Stokes' drag of the particle is proportional to r (cf. eq. (5.2)). Thus, the sedimentation velocity v_s is

$$v_s = {}^{2r^2\Delta\rho g}/_{9\eta} \tag{5.7}$$

where η is viscosity. With this equation, centrifugation g-forces and durations can be designed to collect 5 nm clusters at the base of the centrifuge tube, but not 2 nm nanoaggregates, as shown in Figure 5.34A. Similar successful centrifugation experiments were performed to collect nanoaggregates, but not molecules for analysis of the CNAC. NMR studies of asphaltenes also obtained similar aggregation numbers for the cluster of about six nanoaggregates by analysis of the relaxation rates of nanoaggregate alkane chains [7]. Similar cluster sizes have been obtained in other NMR measurements [241].

The combined SAXS and SANS studies yield the structure of the nanoaggregate with a PAH core and peripheral alkyl substituents for the nanoaggregate. These studies also obtained hierarchical nanoaggregates and clusters with aggregation numbers of ~12 [222–224]. Field studies of asphaltene gradients in oilfield reservoirs show a cluster size (equivalent diameter of a sphere) of 5 nm. All of these studies yield similar results. Indeed, a 5 nm diameter of the cluster was proposed in 2010, and in 2013 it was found to match the gravity gradient of clusters in dramatic fashion where the asphaltene gradient ranges from 4% to 35% over a 100 km periphery of a giant oilfield [227]. The cluster size of 5 nm is used in the Yen–Mullins model.

No larger stable, colloidal species of asphaltenes have been observed in reservoir crude oils. For reservoir crude oils of low gas–oil ratio (GOR), the FHZ EoS reduces predominantly to the gravity term shown in eq. (5.8). Gradients of asphaltenes in crude oils of these low GOR crude oils are determined predominantly by the gravity term which consists of the Archimedes buoyancy of the asphaltene particle in the Boltzmann distribution where Conc(h) is the asphaltene concentration at height h in the reservoir, V is the volume of the asphaltene species, $\Delta\rho$ is the density contrast between the asphaltene and bulk oil, g is earth's gravitation attraction, k is Boltzmann's constant, and t is temperature [214, 242, 243]:

$$\frac{\text{Conc}(h)}{\text{Conc}(0)} = \exp\left\{-\frac{V\Delta\rho g h}{kT}\right\} \tag{5.8}$$

This simple equation has been shown to work routinely in oilfield reservoirs [18]. In particular, this equation describes the variation of asphaltene concentration of a factor of 10 over a height of 60 m over the 100 km periphery of a four-way sealing anticline [227]. The asphaltene chemical composition remained invariant [65, 244] in the crude oil but the concentration varied by a factor of 10 confirming the application of eq. (5.8) using asphaltene clusters from the Yen–Mullins model [227]. The half-height of asphaltene concentration given by the exponential of eq. (5.8) was 20 m. For light oils, the half-height is naturally less because the density contrast increases [245]. If a larger asphaltene species existed in reservoir crude oil, then it would have a smaller half-height in accord with its increase size. If a third nanocolloidal particle remained stable in a reservoir crude oil, and had twice the radius compared to a cluster, then it would have a half-height of 2 m. Thus, almost none of the crude oil in the reservoir would have contain larger particles.

Laboratory measurements of destabilized asphaltenes in toluene solutions and crude oils show that the asphaltene nanocolloidal particles approach the size of clusters as the instability is reduced [204–207]. This observation is in accord with the exponentially increasingly slow kinetics of floc formation with decreasing destabilization of asphaltenes [204–207].

5.6.8 Cluster binding energy

By using eq. (5.3) with 5 g/L for the CCC, the binding energy is calculated to be 3 kcal/mol of clusters in toluene solution. There is no other determination of this energy to cross-check. In any event, the CCC is much higher in concentration than the CNAC, thus, the cluster biding energy must be appreciably smaller than that of the nanoaggregate.

The CCC was determined over a limited range to be basically temperature independent [209]. As discussed above for the CNAC involving eq. (5.4), this lack of temperature dependence indicates that cluster formation is predominantly entropy driven. This also explains why clusters that are so weakly bound are found in reservoirs that are 100 °C.

5.6.9 Cluster structure

Unlike the nanoaggregate with its PAH stack, the cluster is unlikely to have a preferred axis. The combined SAXS and SANS study and other SANS studies found that the clusters are fractal [222–224]. It is important to note that clusters can exist in crude oils for geologic time (the same as nanoaggregates).

5.7 The Hansen solubility parameters and asphaltene intermolecular interactions

To improve the understanding of the intermolecular interactions and solubility of organic compounds such as asphaltenes, it is useful to consider the Hansen solubility parameters [246]. The Hildebrand solubility parameter can be decomposed into three orthogonal constituent solubility parameters accounting for the three dominant intermolecular interactions of organic compounds: polarizability (known as the dispersion force) δ_D, polarity δ_P, and hydrogen bonding δ_H. This is shown as follows:

$$\delta = \sqrt{\delta_D^2 + \delta_P^2 + \delta_H^2} \tag{5.9}$$

Polarizability is the dominant intermolecular interaction in crude oils and asphaltenes. The π-electron clouds of the PAH core of asphaltene molecules are deformable and polarizable. The purification action associated with carbon filters relies on this principle as well as on their pore structures. The alkanes lack π-electrons and their σ-electron clouds are more rigid and have lower polarizability. Teflon has even a lower polarizability, thus it is not at all chemically sticky. Helium atoms have almost no polarizability which is why helium does not liquefy until a temperature of 4 K. Polarizability of helium atoms requires incorporation of the $n = 2$ electron shell which has an excitation energy of 26 eV, which results in negligible polarizability.

Polarity refers to molecules that have a permanent dipole moment. Carbon and hydrogen have nearly equal electronegativity, so compounds made of these two elements are nonpolar. Alkanes and aromatic compounds (without heteroatoms) have no dipole moment with rare exception (such as azulene). In contrast, oxygen and hydrogen have very different electronegativity so bonds made of these two elements are quite polar (e.g., water). Asphaltenes contain dominantly carbon and hydrogen and the primary heteroatom is sulfur which is typically in nonpolar groups, thiophenes, and sulfides. Asphaltenes might contain a few percent nitrogen and oxygen, which give asphaltenes a bit of polarity.

H-bonding (or hydrogen bonding) is a relatively strong interaction and always involves hydrogen in bonds to very electronegative atoms such as oxygen or nitrogen. Water molecules form strong hydrogen bonds and consequently water remains liquid at unusually high temperatures for compounds of such a small mass. All compounds that form hydrogen bonds are polar but the converse is much less often the case [246].

The projection of the Hildebrand solubility parameter into three orthogonal Hansen solubility parameters is shown in Figure 5.41. The chemical axiom “like dissolves like” is specified clearly with the Hansen parameters; the condition of two compounds being mutually soluble is that their Hildebrand solubility parameters

should be similar. Moreover, each component of their respective Hansen solubility parameters should also be similar.

In Figure 5.41, this condition of similar solubility parameters is graphically represented by a sphere centered on the solubility parameter of a given compound. Points inside the sphere represent similar solubility parameters to the given compound, thus are soluble. Points outside the sphere are insoluble in/with the given compound.

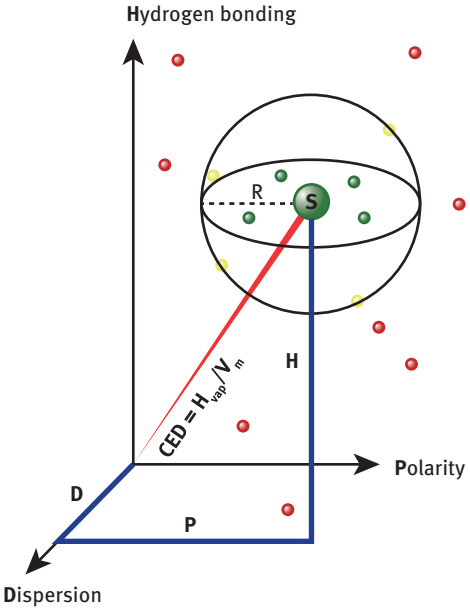

Figure 5.41: Graphical representation of the Hildebrand solubility parameter (*S*) for a given compound projected into the three Hansen components, dispersion or polarizability (D), polarity (P), and hydrogen bonding (H). The chemistry axiom "like dissolves like" dictates that only compounds within the sphere of radius *R* shown centered on *S* will be soluble with the given compound [246].

Green points in Figure 5.41 represent compounds that are soluble in the given compound (inside the sphere) with similar Hansen solubility parameters. Red points represent compounds with very different Hansen components; thus, they are insoluble with the given compound [246]. In the application of Figure 5.41 to indicate solubility between two compounds, the square of difference of polarizabilities is often multiplied by four emphasizing the importance of very similar polarizability for solubility. The distance *R* between the two compounds is represented as in eq. (5.10), where the prime represents the second compound:

$$R = \sqrt{4\left(\delta_D - \delta_D'\right) + \left(\delta_P - \delta_P'\right) + \left(\delta_H - \delta_H'\right)} \tag{5.10}$$

With greater R, the solubility is reduced. Note the factor of 4 in the dispersion term. Small differences in this polarizability term are equivalent to large differences in the other two terms, that is, solubility is sensitive to small differences in the dispersion term.

A table of Hildebrand and Hansen solubility parameters is instructive. Teflon (and other perfluorocarbons) are known to have very low intermolecular interactions, which is why Teflon is a preferred coating in cookware; nothing sticks to it. A value of 12.4 $(MPa)^{1/2}$ for Teflon in Table 5.6 is seen to correspond to such a low intermolecular interaction (not shown but almost entirely the polarizability component). In contrast, Table 5.6 shows that water with its strong intermolecular interaction has a Hildebrand solubility parameter of 47.8 $(MPa)^{1/2}$. Teflon and water establish the range of Hildebrand parameters from very weak 12 $(MPa)^{1/2}$ to very strong 48 $(MPa)^{1/2}$ for condensed phase. Moreover, the solubility parameter of water is dominated by H-bonding, a strong and spatially directional bond. Alkanes, the dominant component of crude oil, are seen to have Hildebrand parameters 16 $(MPa)^{1/2}$ somewhat above Teflon, and those of aromatics are somewhat above the alkanes. Moreover, Table 5.6 shows that the alkanes and the aromatics are dominated by the simple, weak polarizability forces.

Table 5.6 shows that the solubility parameter of asphaltenes is dominated by the polarizability term [221, 247]. The somewhat large asphaltene PAHs impart this property, and the asphaltene peripheral alkanes also contribute. To obtain these entries in Table 5.1 in units of $(cal/cm^3)^{1/2}$, divide by ~2.

The solubility parameters of the asphaltenes are fairly similar to those of aromatics [221, 247]. Indeed, asphaltenes are defined to be toluene soluble and thus must have solubility parameters similar to that of toluene. Note that the difference between the solubility parameters of asphaltenes and alkanes is sufficient to dictate no solubility of asphaltenes in alkanes. The solubility parameters of toluene and asphaltenes are dominated by the weak and simple polarizability component. The asphaltenes do have a component of polarity and H-bonding, but these contributions are fairly small.

Methane has low intermolecular interaction but is not listed in Table 5.6 because the molar volume is very dependent on temperature and pressure making the numeric value of solubility parameter somewhat arbitrary. Nevertheless, addition of methane to crude oil results in a decrease in solubility parameter because both the density decreases and methane has low intermolecular interaction.

To help understand the secondary impact of polarity and H-bonding on asphaltene intermolecular interactions, the heteroatom content of asphaltenes is briefly reviewed. The heteroatom moieties have been addressed by a variety of measurements and are dependent on the source material of the asphaltenes. The heteroatom content

Table 5.6: Hildebrand and Hansen solubility parameters [246].

Compound	Hildebrand δ (MPa$^{1/2}$)	Hansen parameter (MPa$^{1/2}$)		
		$\delta_{Disp.}$	δ_{Pol}	δ_{H}
Alkanes				
n-Butane	14.1	14.1	0	0
n-Pentane	14.5	14.5	0	0
n-Hexane	14.9	14.9	0	0
n-Heptane	15.3	15.3	0	0
n-Dodecane	16.0	16.0	0	0
Aromatics				
Benzene	18.6	18.6	0	2.0
Toluene	18.2	18.0	0	2.0
Naphthalene	20.3	19.2	2.0	5.9
Hetero compounds				
Acetone	20.0	15.5	10.4	7.0
Ethyl alcohol	26.5	15.8	8.8	19.4
Phenol	24.1	18.0	5.9	14.9
Acetic acid	21.4	14.5	8.0	13.5
Carbon disulfide	20.5	20.5	0	0.6
Acetonitrile		15.3	18.0	6.1
Teflon	12.4	–	–	–
C8F18	12.6	–	–	–
Asphaltenes [247]	20.4	19.5	4.7	4.2
Water	47.8	15.6	16.0	42.3

can vary considerably even for asphaltenes sourced from petroleum. Sulfur is typically the most abundant heteroatom by weight (typically several percent) and might be present in a quantity roughly equivalent to one sulfur atom per asphaltene molecule on average, again with substantial variability. As shown by x-ray spectroscopy, specifically, XANES, sulfur is typically found in thiophene and sulfide moieties both of which are nonpolar [10]. Occasionally, sulfoxide is found to be a significant fraction of the sulfur content [11]. Sulfoxide has a large dipole moment of roughly 4 debye so that it can introduce a site of polarity in an asphaltene molecule. Nitrogen is found at lower mass fractions than sulfur in asphaltenes and, similar to sulfur, is quite variable

in content and can occur at roughly one nitrogen atom per two molecules on average. Nitrogen XANES studies of asphaltene nitrogen show that it is found in pyrrolic and pyridinic moieties, both of which are aromatic groups [12]. Pyridinic nitrogen is somewhat basic with a dipole moment of ~2.2 debye while pyrrolic nitrogen is somewhat acidic with a dipole moment of ~1.8 debye; thus, nitrogen introduces some limited charge separation in a sphaltene molecules. Oxygen is present in small quantities, perhaps on average every other molecule has an oxygen atom. Asphaltene oxygen is found in hydroxyls, carbonyls, ethers, and occasional carboxylic acids [13]. Most of these functions also impart some charge separation in asphaltenes and help give rise to the modest contribution of polarity and H-bonding in asphaltene intermolecular interactions.

5.8 Asphaltene thermodynamics

5.8.1 Bulk asphaltene thermodynamics

The understanding of asphaltene molecular and nanocolloidal fundamentals has helped spur a renaissance in asphaltene thermodynamics. For the thermodynamics of bulk phase asphaltenes, there are two primary predictions: asphaltene gradients in solution, for example, in oilfield reservoirs; and asphaltene phase behavior. For asphaltene gradients in solution phase, the FHZ EoS [242, 243, 248] is used with the Yen–Mullins model [15, 16] to account for asphaltene gradients in oilfield reservoirs [18]. This methodology has had substantial success in accounting for a wide variety of observations and is described in detail in chapter 6 in this book.

A modified Flory–Huggins theory is used to characterize gradients of asphaltenes; a gravity term is added with Archimedes buoyancy in the argument of the Boltzmann distribution term (cf. eq. (5.9)). The resulting FHZ EoS , eq. (5.11), is used for modeling gradients [242, 243, 248]. The ratio of asphaltene content is expressed as a ratio of optical density (OD) at two heights, h_i, in the reservoir:

$$\frac{\mathrm{OD}(h_2)}{\mathrm{OD}(h_1)} = \exp\left(\frac{v_a g \Delta\rho (h_2 - h_1)}{RT} + \left(\frac{v_a}{v}\right)_{h_2} - \left(\frac{v_a}{v}\right)_{h_1} - \frac{v_a\left[(\delta_a - \delta)^2_{h_2} - (\delta_a - \delta)^2_{h_1}\right]}{RT}\right) \quad (5.11)$$

where v_a and v are the molar volume of the asphaltene species and oil, respectively, g is Earth's gravity, $\Delta\rho$ is the density difference between the oil and asphaltenes, R is the ideal gas constant, T is temperature, δ_a and δ are the Hildebrand solubility parameters of the asphaltene species and oil, respectively (see Table 5.6). The FHZ EoS theory is fairly simple; there is a single chemical interaction parameter which is the Hildebrand solubility parameter. In eq. (5.11), the first term in the argument of the exponential is

the gravity term, the next two terms account for the Flory–Huggins entropy. The last term incorporates the solubility parameters of the oil and asphaltenes.

For oilfield reservoirs, the key question is whether the contained oil is or is not in equilibrium; thus, this is not an exercise in curve fitting measured gradients with an equilibrium model [18]. In particular, a theory that is to resolve whether or not reservoir fluids are equilibrated cannot have many parameters; otherwise, the theory could fit anything. The few parameters of the FHZ EoS make this theory very attractive. For asphaltene phase behavior, the Flory–Huggins theory has been used [249]. Nevertheless, the predictive capability regarding phase behavior has not been fully developed. PC SAFT modeling has been used for asphaltene phase behavior [250–252]. The cubic EoS has been used for phase behavior modeling asphaltene phase behavior particularly for gas injection into crude oil; this acknowledges that the solvent, where the cubic has utility, controls much of the asphaltene phase behavior [253].

5.8.2 Asphaltene interfacial properties

In addition to modeling bulk solution properties, interfacial properties of asphaltene solutions of moderate or low concentration can also be modeled using simple equations along with the centroid of asphaltene molecular properties [19, 20, 254]. The concentration range of applicability includes the CNAC and lower. The specific molecular properties can be compared to that in Figure 5.1 of the Yen–Mullins model. The Langmuir equation of state (EoS) accounts for the effect of asphaltenes on the interfacial tension (IFT) and is given below:

$$\gamma(\Gamma) = \gamma_o + kT\Gamma_\infty \ln\left(1 - {}^{\Gamma}/_{\Gamma_\infty}\right) \tag{5.12}$$

where $\gamma(\Gamma)$ is the IFT, γ_o is the clean surface IFT, Γ is the surface coverage, Γ_∞ is the maximum surface coverage, k is the Boltzmann constant, and T is the temperature. The Langmuir EoS is perhaps the simplest equation that can be used to fit IFT data as shown in Figure 5.42. There are two adjustable parameters: a reference surface coverage Γ and the size of the molecular footprint of the surfactant on the surface ($1/\Gamma_\infty$). If the asphaltene concentration in the solution is high, this simple description is insufficient to account for the IFT [255].

The IFT can be measured by the pendant drop method. The shape of a drop at equilibrium suspended in a second phase is given by the interplay of interfacial and gravitational forces. The balance of these two forces is given by the Bond number $B = \Delta\rho g L^2/\gamma$, where $\Delta\rho$ is the density difference between the two fluids, g is the gravity acceleration, L is the drop size, and γ is the IFT [256].

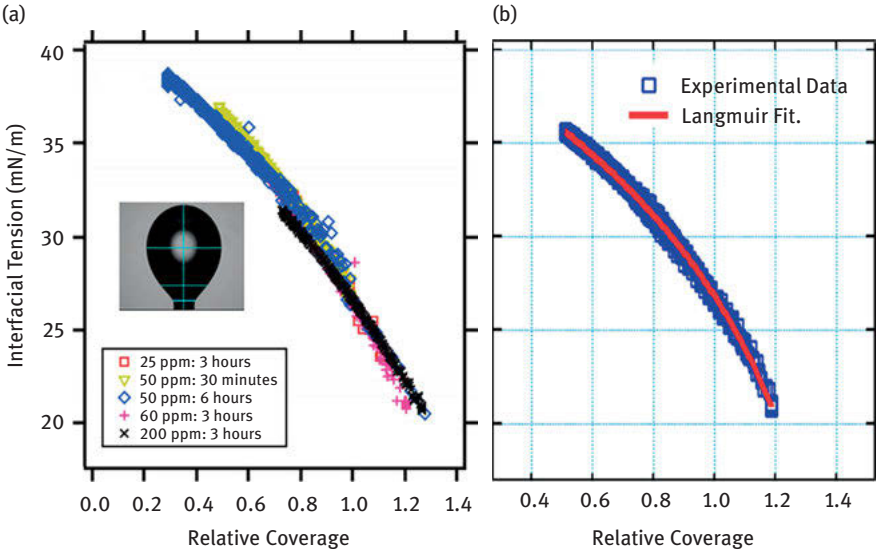

Figure 5.42: The interfacial tension (IFT) between an asphaltene solution and water measure with the pendant drop technique [19]. (A) A universal curve is obtained at low-to-moderate concentrations for all conditions including variable concentrations and aging times. (B) The Langmuir EoS accounts for the asphaltene IFT curve with a minimum number of parameters. Reprinted with permission from the American Chemical Society.

The fit to the IFT data in Figure 5.42 yields a value of the asphaltene molecular footprint equal to a nominal six-ring PAH which applies to the universal curve shown in Figure 5.42B [19]. The corresponding characteristic PAH size is remarkably close to the molecular structure shown in Figure 5.1 in the Yen–Mullins model [19]. This analysis and interpretation require that the asphaltene PAH is in-plane in the oil–water interface and that the alkyl groups are out-of-plane. Exactly this configuration has been measured for asphaltenes in Langmuir–Blodgett films by sum frequency generation (SFG) [257]. In addition, these studies also show that PAHs with peripheral oxygen functions orient such that the PAHs are transverse to the interface [257]. These results are consistent with the finding that asphaltene intermolecular interactions are dominated by polarizability of the PAH in solution studies [221]. Alkylated hexabenzocoronene is also oriented with the PAH in-plane at the oil–water interface [20].

Figure 5.42 shows that the IFT measurements for many experimental conditions reduce to a universal curve that is fit by the Langmuir equation [19, 20, 254]. The excellent fit of the Langmuir equation with its minimum number of parameters to the universal curve lends validity to this analysis. In addition, the concentrations used to obtain the universal curve included values below and above the CNAC; in these experiments, the CNAC was determined by NMR. This indicates that the nanoaggregates

are not surface active in this concentration range; the surfactant contact area at the interface in the Langmuir equation analysis remained molecular and was unaffected by the presence of nanoaggregates in the bulk solution. Otherwise, IFT data from concentrations in excess of the CNAC would diverge from the universal curve. The nanoaggregate has peripheral alkyl substituents as shown in Figure 5.1 and as measured by combined SAXS and SANS experiments [222–224]. The different attraction to the interface of the asphaltene PAH versus alkane groups is shown in the SFG experiments [257] and is also obtained in coarse grained modeling [258]. Consequently, the IFT of asphaltene solutions with water is consistent with the Langmuir equation coupled with the Yen–Mullins model over a wide range of experimental conditions.

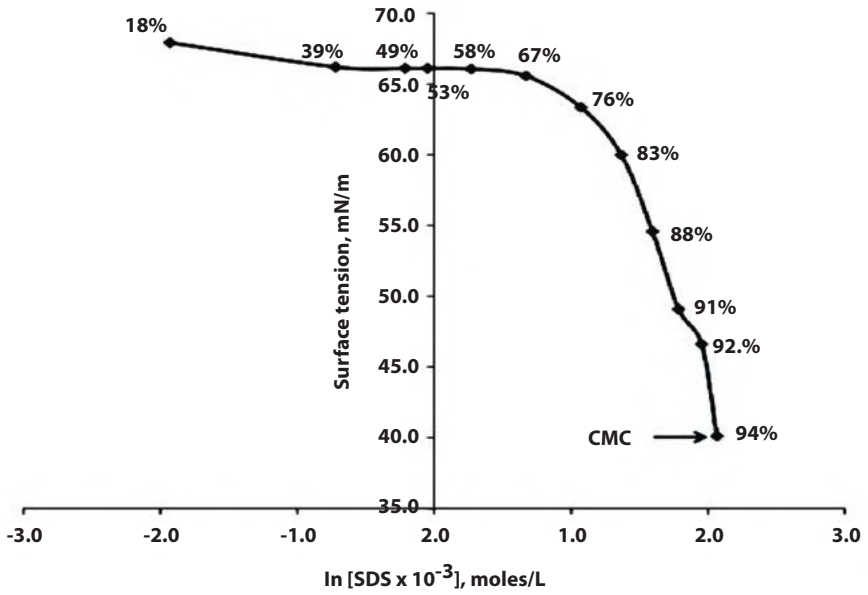

Figure 5.43: Plot of surface tension versus ln[SDS] for pre-CMC concentrations with the percent coverage written for each point [259]. For small surface coverage, large changes in coverage result in modest IFT changes. In contrast, at high surface coverages, small changes in surface coverage give rise to large IFT changes. Reprinted with permission from the American Chemical Society.

Figure 5.43 frames important aspects of IFT behavior as exhibited by static measurements of a solution of SDS [259]. The observation is that there is a relatively small change in IFT up to roughly 80% surface coverage. At higher coverages, there is a large decrease in IFT with even incremental increases in surface coverage. As the authors note, "the tensiometer senses an altered air/water interface chiefly when the packing density exceeds 80% saturation. SDS progressively fills the remaining 20%

of the interfacial loci as the bulk SDS concentration increases all the way up to and beyond the CMC. It is the late stage occupancy of the interface that causes the steep decline in surface tension" [259].

5.8.3 Time dependence of asphaltene IFT

It has often been observed that upon the preparation of an interface involving a solution with surfactants, there is an initial rapid decline of the IFT which is consistent with surfactant diffusing to the interface, thereby reducing the IFT. Indeed, for crude oil–water systems such a reduction is observed and successfully modeled presuming diffusion. For interfaces involving asphaltene solutions and water, there are some similarities but also differences compared to standard surfactants. With known surfactants of a single component and at long times, the IFT asymptotically approaches a fixed value without further reduction of IFT. In contrast, asphaltene solution–water interfaces exhibit continuous long-term declines [260, 261]. The observation that the IFT of crude oil and asphaltene solutions decreases at long times in contrast to solutions with single surfactants suggests that asphaltenes have more than a single interfacially active component.

An oft-repeated observation of asphaltene IFT is best explained by incorporating more than just the centroid of the asphaltene molecular distribution [262]. Figure 5.42 shows that the bulk of asphaltene IFT can be accounted for by relative coverage of the surface independent of surface aging times. However, a more detailed examination of the asphaltene IFT versus aging time shows that there is a small yet readily measurable continuous decline [260, 261]. This is in contrast to the adsorption behavior of standard single-component surfactant.

Figure 5.44 plots the IFT data for asphaltene solutions and shows that there is a large drop of IFT at short times, and that the IFT continues to decline at long times [260]. This data is consistent with other studies of the IFT between water and toluene-asphaltene solutions [261]. At short times, diffusion delivers surfactant to the interface. For a single surfactant, as time progresses, the surface becomes saturated with surfactant and the IFT ceases to change [263]. For a second component of higher interfacial activity but lower concentration, it will take longer to diffuse to the interface, but once it arrives, it can displace the first component. The higher interfacial activity of the second component impacts the IFT via a slightly higher surface coverage in accordance with the results in Figure 5.43 [259]. At high surface coverage, which is obtained at long times, it takes only a small increase of surface coverage to yield a measurable decrease in IFT. This binary model accounts for most the measured data. More components improve the fitting but at the expense of more parameters.

Recent modeling implemented a ternary mixture model for diffusion-limited adsorption at water–oil interface [263]. As observed in Figure 5.45, the smallest fraction,

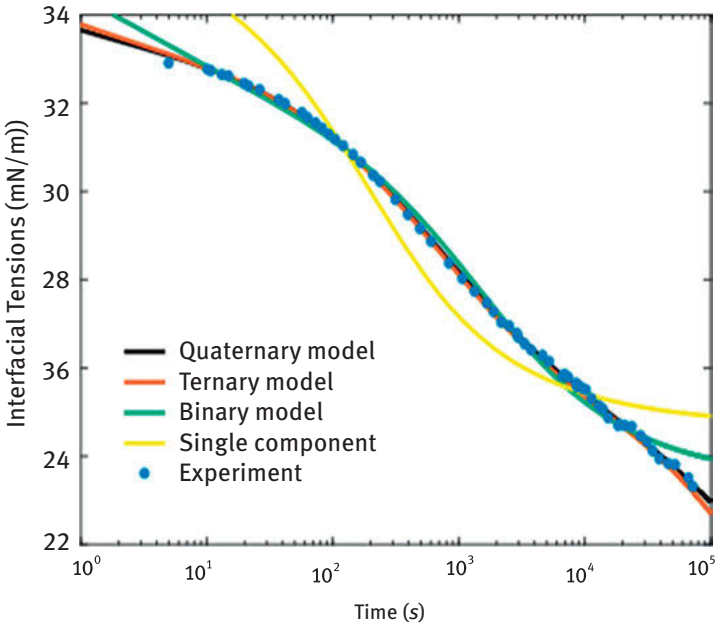

Figure 5.44: Experimental data for 0.005% asphaltenes in toluene–water interface showing long-term, continuous decrease of IFT [260]. Numerical IFT curves generated using different numbers of components: 1 (yellow), 2 (green), 3 (orange), and 4 (black) [263]. Reprinted with permission from the American Chemical Society.

that is, pseudo-component 1, (<0.5%) is largely responsible for the long-term IFT decay. The adsorption of the most abundant but less surface-active components (pseudo-component 3) quickly reached the maximum coverage within several decades of seconds, indicating that it is the main contributor to the initial fast decrease of IFTs. In contrast, the tiny fraction with the highest surface activity (pseudo-component 1) exhibits a slow and prolonged adsorption process. After reaching the maximum surface coverage, the less surface-active components that had adsorbed onto the water–oil interface started to gradually be replaced by the more surface-active but less numerous components [263]. The most surface-active component did not to reach the maximum surface coverage within the simulated time of around 27 h. The result obtained by this model indicates that the presence of a very small fraction of extremely surface-active asphaltenes components could explain both the long-term IFT decay observed and the apparent irreversibility of adsorption during washout experiments.

The analytical solution for this diffusion-controlled adsorption model with a linear isotherm has been worked out as [264]

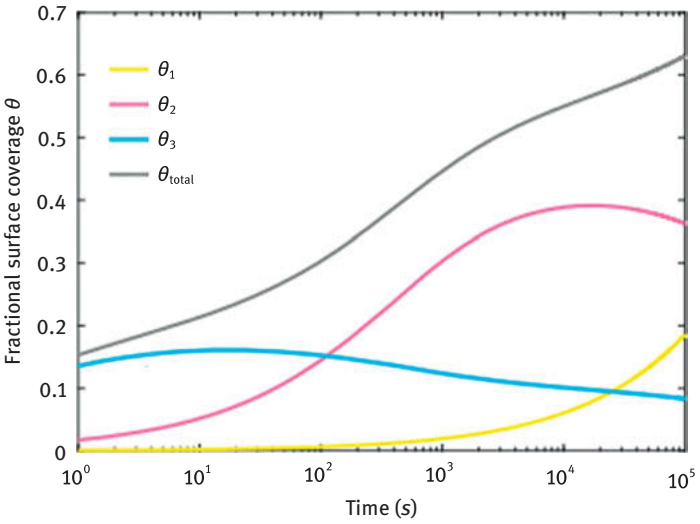

Figure 5.45: Evolution of the fractional surface coverage for each of the three components in the model with a ternary mixture shown in Figure 5.44. Pseudo-component 1 (yellow) is the most surface active but least abundant, pseudo-component 3 (blue) is the least interfacially active but most abundant. The total fraction coverage of the model (gray) increases with time [263]. Reprinted with permission from the American Chemical Society.

$$\Pi = \Delta\gamma_{eq}\left[1 - \exp\left(\frac{\tau}{\tau_D}\right)\mathrm{erfc}\left(\sqrt{\frac{\tau}{\tau_D}}\right)\right. \tag{5.12}$$

where Π is surface pressure, the reduction of surface tension at equilibrium $\Delta\gamma_{eq} = RTK_HC_b$ with R being the gas constant, T the temperature, K_H the Henry's law constant, and C_b the bulk concentration, τ is the time, and the characteristic diffusion time $\tau_D = \frac{K_H^2}{D}$ with D being the diffusion constant.

In the mixture case of Langmuir-type adsorption, the surface excess coverage $\Gamma_\infty$is assumed to be (almost) the same for all the components and the fractional surface coverage θ_i of the ith component becomes [262]

$$\theta_i = \frac{k_iC_{si}}{1 + k_jC_{sj}} \tag{5.13}$$

where k_i is the adsorption constant of component i (the ratio of adsorption rate constant over desorption rate constant), and C_{si} is the subsurface concentration of component i. The binary model employed in Figure 5.44 uses two species with different interfacial activity. Nevertheless, both species are presumed to have the same molecular contact area at the interface [262]. This is consistent with the comparison of asphaltenes for bulk samples vs the most interfacially active components [265]. At

high coverage, only a small change of surface coverage induced by the second component beyond that of the first is needed to cause a significant change of IFT [259]. In addition, this treatment helps keep the number of adjustable parameters to a minimum. This assumption is also consistent with measurement of different surfactant species in asphaltenes [265, 266]. With a third component of even higher interfacial activity and even lower concentration is present in asphaltenes, Figure 5.44 shows that the predicted reduction of surface tension with time occurs for very long times [263].

As with bulk phase distributions of asphaltenes, modeling the IFT sometimes can proceed with consideration only of the centroid of the molecular distribution. For other applications, greater complexity of the distribution of the molecular or colloidal components of asphaltenes must be considered. A minimum number of parameters help reveal the proper chemistry and physics of the system as opposed to providing merely curve fitting of data.

5.8.4 Reversibility and irreversibility of asphaltene processes

There has been persistent debate as to the extent of reversibility of various asphaltene processes. The production of oil from reservoirs is greatly impeded if asphaltenes precipitate in production tubing or worse in the reservoirs themselves as a consequence of pressure reduction during production. Consequently, it is important to obtain oil samples from reservoirs prior to production to measure potential instability conditions of asphaltenes. If these subsurface oil samples obtained for evaluation reach ambient surface temperatures and thus, undergo substantial pressure reduction, then subsequent measurement of asphaltene onset pressure (AOP) in the laboratory is often very inaccurate with much less asphaltene instability measured than actual [267]. That is, the asphaltenes that precipitate in the sample bottles cannot be totally restored to reservoir conditions even at elevated pressures and temperatures [267]. This observation has led to the use of pressurized sample retrieval bottles in the field which limits asphaltene precipitation prior to restoration of the sample in the laboratory. However, these sample bottles are not heated; thus, often some asphaltene precipitation occurs even in pressurized bottles due to temperature reduction.

One factor affecting whether the asphaltenes can be reversibly redissolved in the crude oil is that oilfield sample bottles often contain some quantity of solids (clays, sands, and drilling solids) and water in addition to live crude oil. If the precipitated asphaltene becomes strongly associated with water and/ or with clays and other solids, it is unlikely that they would reversibly redissolve under reservoir conditions of pressure and temperature. Some other metric is required to determine the reversibility of asphaltene flocculation in a more controlled setting. In addition, the measurement of AOP downhole in oil wells is preferred to avoid restoration problems. Measurement of AOP downhole can now be achieved routinely [268]. To date, the pressure measurement of AOP downhole always exceeds that measured in the

lab for the same sample when identical temperatures prevail; the implication is that some restoration problems remain even with use of pressurized bottles [269].

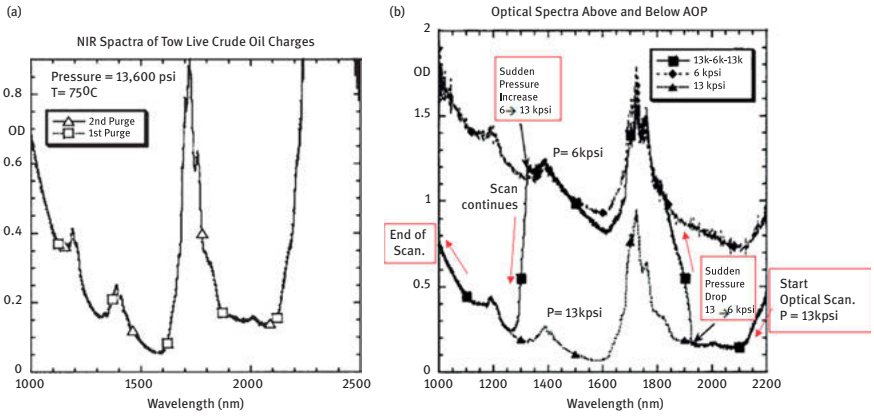

Figure 5.46: Optical spectra of a live crude oil [270]. (A) Replicate sample charging and measurement of a live crude oil with an AOP of ~8 kpsi showing excellent reproducibility. (B) Three optical spectra of the same crude oil: one sample at 13 kpsi with no precipitated asphaltenes, the second sample at 6 kpsi with large flocs (~1 μm), and third sample starting at 13 kpsi with the wavelength at 2,200 nm. A rapid pressure reduction during the optical scan when the wavelength was 1,925 nm precipitated the asphaltenes increasing light scattering. As the optical scan progressed in time, a rapid pressure increase occurred when the wavelength was 1,300 nm; this caused the precipitated asphaltenes to dissolve (to particles much small than 1 μm). This data shows that asphaltene precipitation yielding small flocs is rapidly reversible as long as the asphaltenes do not collect in a tar layer [270]. Reprinted with permission from the American Chemical Society.

Figure 5.46 shows the optical spectra of a live crude oil under different conditions [270]. The peaks at 2,300, 1,725, 1,400, and 1,200 nm are the CH stretch-plus-bend, two-stretch, two-stretch-plus-bend, and three-stretch, respectively. The broad increase OD with shorter wavelengths corresponds to electron absorption of PAHs [39]. The spectra in Figure 5.46A exhibit no optical light scattering with the oil sample at 13 kpsi. Figure 5.46B shows three spectra; the spectrum for the sample at 13 kpsi again shows no optical light scattering (no scattering offset of OD) with the spectrum in 46A [270]. The spectrum for the sample at 6 kpsi is 2 kpsi below AOP and shows a large scattering offset. A new charge of sample was loaded into the cell. The pressure for the third spectrum was changed twice during the optical scan. The optical scan started with a pressure of 13 kpsi and a wavelength of 2,200 nm. The wavelength was continuously reduced; this scan overlays the previous high-pressure scan. When the wavelength reached 1,925 nm, the pressure was suddenly reduced to 6 kpsi which is 2 kpsi below the AOP (at 75 oC) of 8 kpsi. Immediately, asphaltenes flocculated producing about 0.8 OD units of offset. The resulting spectrum largely overlies the previous spectrum for the

oil sample at 6 kpsi. The scan continued with wavelength reduction until 1,325 nm was reached. At this point, the pressure was rapidly increased to 13 kpsi. Very quickly in the minutes time frame, the ODs reduced until no more optical light scattering was evident. This indicates that asphaltene flocculation is reversible at least to the extent measured optically (with a ~1 μm resolution) [270]. This result is consistent with movies of reversibility of asphaltene precipitation with decreases and increases of pressure [271].

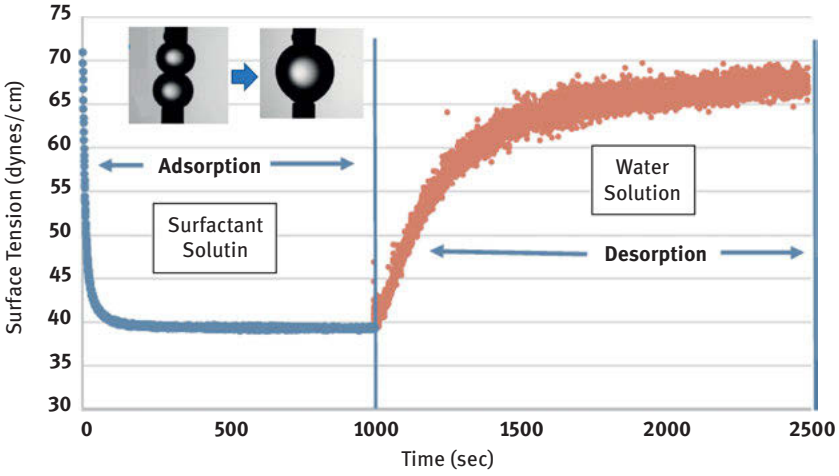

Figure 5.47: A novel experiment enables measurement of IFT while also enabling exchange of the liquid in the drop [256]. Two drops, each on a syringe, are brought together forming a single drop; the fluid in the resulting single drop can be replaced with continuous measurement of surface tension. Upon drop formation with a solution of the nonionic surfactant pentaethylene glycol dodecyl ether (C12E5), the IFT is reduced with increasing coverage on the surface. At 1,000 s, freshwater is introduced into the drop causing desorption of the surfactant and restoration of the IFT close to that of water, thus proving reversibility of adsorption of this surfactant [256]. Measurement of the IFT for the bridging droplet is related to a detailed shape analysis and is described elsewhere and applies especially for low Bond numbers (<0.1) [256]. Reprinted with permission from Elsevier.

Figure 5.47 shows a method to measure the IFT of solutions with adjustable concentrations of surfactant. Two syringes are seen in the insert in Figure 5.47. As the drops are brought together, coalescence occurs. The solution of the resulting bridging drop can be replaced by controlling flow into and out of this drop [256]. Thus, the extent of reversibility of adsorption of surfactant at the interface can be determined for example by flushing the surfactant solution with pure solvent. Figure 5.47 shows that upon drop formation, the IFT decreases up to 1,000 s associated with increasing surfactant diffusing and adsorbing onto the interface. At 1,000 s, the solution in the bridging drop is rinsed with pure water and the IFT responds immediately and eventually increases to that close to pure water in air as flushing continues. Thus, this nonionic surfactant adsorption is reversible [256].

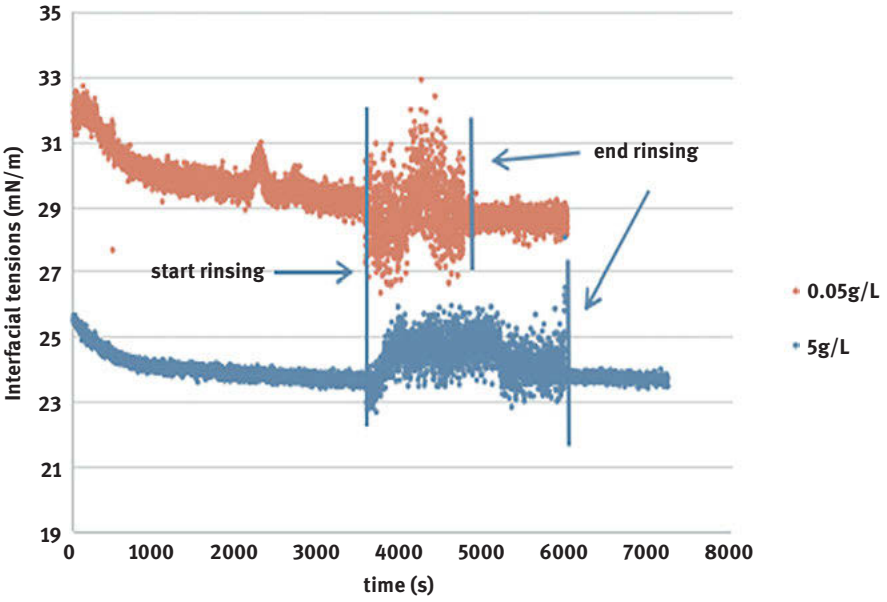

Figure 5.48: IFT versus time for brine–asphaltene solution interfaces. The toluene rinsing started after 3,500 s and stopped 1,500 s later for the 0.05 g/L solution and 2,500 s later for the 5 g/L solution [256]. Asphaltene adsorption at the interface is irreversible under these conditions. Reprinted with permission from Elsevier.

Asphaltene adsorption at a toluene–brine interface is not reversible by rinsing with pure toluene [256]. Figure 5.48 shows the IFT vs time for two different asphaltenes solutions initially in contact with brine, with concentrations 0.05 and 0.5 g/L. At 3,500 s, the asphaltene toluene solution in the bridging drop was flushed with pure toluene. At the end of flushing, the solution was almost pure toluene and the surface tension did not increase for either concentration; under these conditions, asphaltene adsorption is irreversible [256]. Similar experiments involving flushing of prepared surfaces with pure solvent obtained similar results but exhibit some reversibility with pH = 8 aqueous solutions [260]. It is known that asphaltenes are more interfacially active with acidic aqueous solutions and protonation of basic nitrogen.

5.8.5 Surface compression

The use of the Langmuir EoS to analyze the IFT isotherm (Figure 5.42) proved robust enough to predict the relationship between the surface pressure and dilatational modulus when measured at a high frequency as shown in Figure 5.49 [20]. Such analysis has been further confirmed on different asphaltenes including coal-derived, petroleum-originated, and synthetic types of a known core size [20].

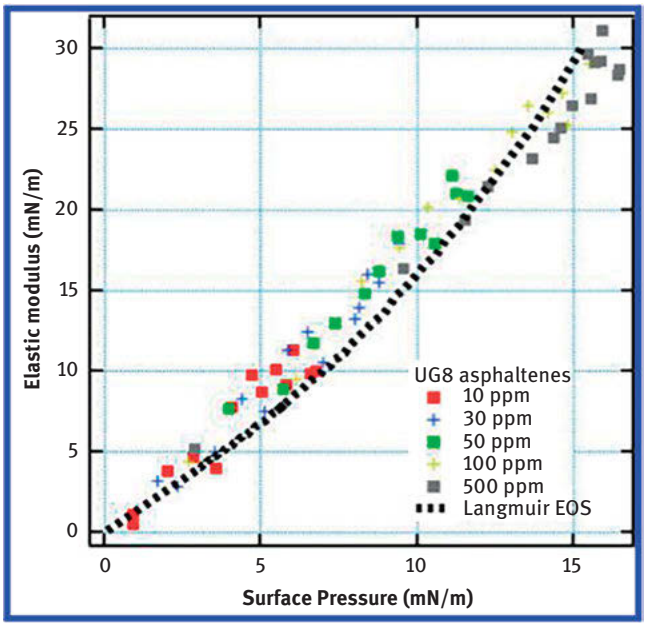

Figure 5.49: Limiting elasticity versus surface pressure for UG8 asphaltene solution–water interface and the parametric curve from the Langmuir EoS (Γ = 3.1 molecules/nm^2 or a six-ring PAH) [20]. Reprinted with permission from the American Chemical Society.

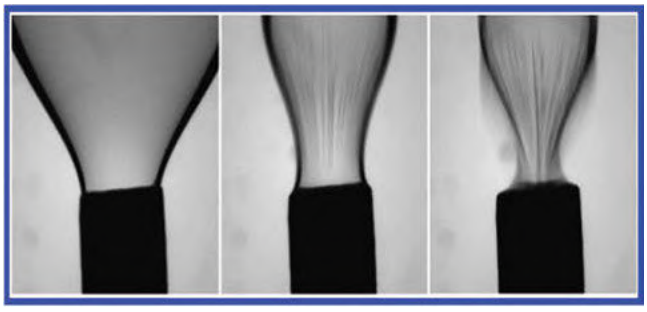

Figure 5.50: Droplet contracted by a factor of 10 in volume (45 s absorption 100 ppm asphaltenes in 86–15% heptane–toluene solution) [272]. Reprinted with permission from the American Chemical Society.

To extend asphaltene experiments past the nominal surface packing limit of 85%, a series of experiments were performed utilizing rapid contractions and contraction–expansions of asphaltene-laden interfaces using the pendant drop experiments to emulate a Langmuir trough [272]. This simulates the rapid increase in interfacial asphaltene concentration that occurs during droplet coalescence events.

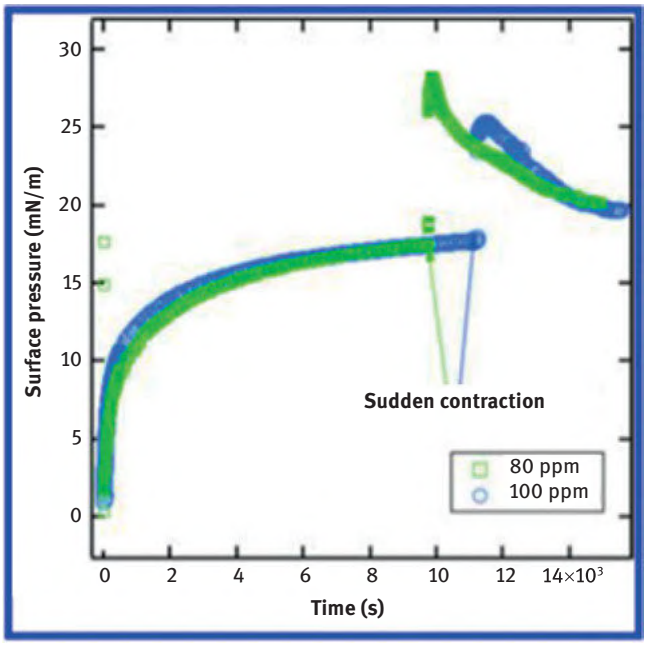

Figure 5.51: Recovery curves of contraction experiments. Variable asphaltene concentration in Nexbase 2002. Variable contraction ratio [272]. Reprinted with permission from the American Chemical Society.

For the contraction of droplets aged in asphaltene solutions, deviation from the EoS consistently occurs at a surface pressure value ~21 mN/m corresponding to a surface coverage ~80%. At this point droplets lose the shape required for validity of the Laplace–Young equation, indicating solid like surface behavior [272]. As shown in Figure 5.50, on further contraction, wrinkles appear, and these disappear when the droplet is held at constant volume over an hour time frame. Figure 5.51 shows that after an initial increase upon contraction, surface pressure also decreases down to an equilibrium value near that measured for slow adsorption experiments. This behavior appears to be due to a transition to a glassy interface on contraction past the packing limit, followed by relaxation toward equilibrium by desorption at constant volume. Thus, asphaltene adsorption appears to be reversible in these conditions of significant surface compression [272].

In a recent study on interfacial activity of asphaltenes studied by performing multiple cycles of compression–expansion experiments in a Langmuir trough, the authors observed that the variations in the maximum surface pressure and the maximum interfacial coverage were negligible, which indicates no loss of asphaltenes to the subphase and no irreversible aggregates formed [273].

By measuring the interfacial rheology, it was found that the dilatational modulus and the shear modulus are monotonically increasing with surface coverage,

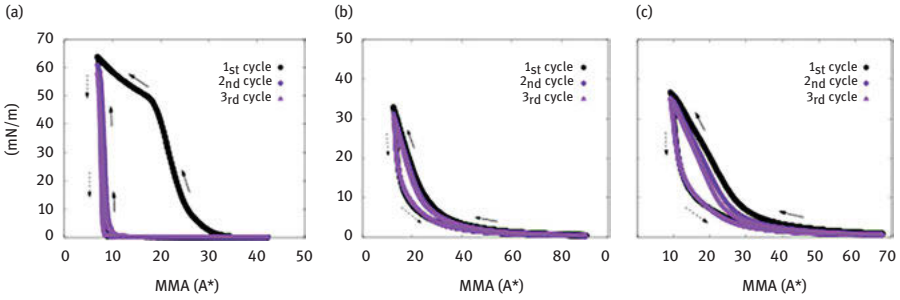

Figure 5.52: Multiple compression–expansion experiments in the Langmuir trough of whole asphaltene at (A) air–water surface and (B, C) oil–water interfaces starting at different initial coverages [273]. Reprinted with permission from the American Chemical Society.

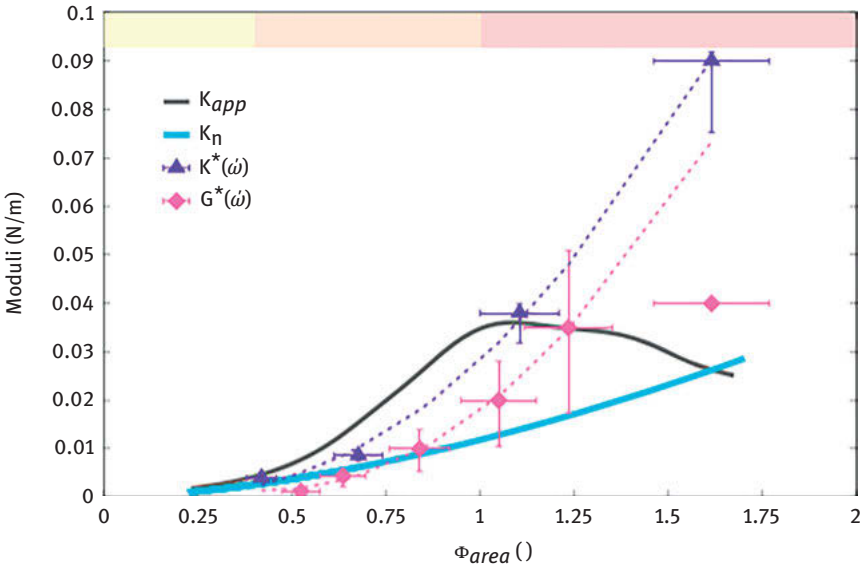

Figure 5.53: Summary of measured moduli as a function of surface coverage $ø_{area}$ for the whole asphaltenes at the water–hexadecane interface. The intrinsic dilatational (K_i^*) and shear (G_i^*) interfacial moduli are both monotonically increasing functions of surface area fractions. The thermodynamic compressibility, "Gibbs elasticity" (K_Π), represents only a small fraction of the elastic modulus. The apparent modulus K_{app} obtained by compression in a Langmuir trough shows a nonmonotonic behavior due to the occurrence of complex deformations and buckling. The *y* error bars represent the frequency dependency of the moduli values, while the *x* error bars account for a ±2 Å in the estimation of nanoaggregate monolayer coverage. The shaded colored bar on the top of the plot reflects the same regions in Figure 5.52 [273]. Reprinted with permission from the American Chemical Society.

which is consistent with the dependency of emulsion stability on increasing coverage. When the surface coverage goes beyond the monolayer coverage, the authors observed a broad distribution of relaxation times and the viscoelastic response of the interface that agree well with a dense packing layer instead of a physical gel. Above the monolayer coverage, the interface seems to become a stronger dense-packed layer with significant viscoelastic response and higher moduli due to the formation of multilayers.

5.9 Conclusions

Petroleomics promises to provide structure–function relationships that are so important in the production and processing of crude oil. Asphaltenes are very important components of crude oils, inordinately important for creating high viscosities, bulk phase transitions, emulsion stability, and surface wettability among other properties. Recent AFM results definitively establish asphaltene molecular structure, proving dominance of the "island" structure with many differing PAHs, greatly empowering the discipline of petroleomics. Asphaltene molecular and nanocolloidal structures can be incorporated into first-principles modeling of many interfacial properties of asphaltene solutions and with considerations of the chapter on reservoir fluid geodynamics, first-principles modeling of bulk thermodynamic properties of asphaltenes applicable in oilfield reservoirs at the 100 km length scale. In addition, asphaltenes can retain geochemical signatures of their origins which can be protected from deleterious processes such as microbial degradation of the corresponding oil. Asphaltenes have now joined their gas and liquid phase brethren of crude oils with established structure–function relations with remarkable impact on practicalities of the oil industry.

Abbreviations

AFM	Atomic force microscopy
AOP	Asphaltene onset pressure
APCI MS	Atmospheric pressure chemical ionization mass spectrometry
APPI MS	Atmospheric pressure photoionization mass spectrometry
CCC	Critical cluster concentration
CNAC	Critical nanoaggregate concentration
DBE	Double bond equivalent
DLA	Diffusion-limited aggregation (often used when DLCA is meant)
DLCA	Diffusion-limited cluster aggregation
ESI	Electrospray ionization
FAR	Fused aromatic ring

FHZ EoS	Flory–Huggins–Zuo equation of state
FT-ICR MS	Fourier-transform ion-cyclotron-resonance mass spectrometry
GOR	Gas–oil ratio
IFT	Interfacial tension
L^2MS	Laser desorption/laser ionization mass spectrometry
LIAD MS	Laser-induced acoustic desorption mass spectrometry
MALDI MS	Matrix-assisted laser desorption–ionization mass spectrometry
nc-AFM	Noncontact atomic force microscopy
PAH	Polycyclic aromatic hydrocarbon
RLA	Reaction-limited aggregation (often used when RLCA is meant)
RLCA	Reaction-limited cluster aggregation
SALDI MS	Surface-assisted laser desorption–ionization mass spectrometry
SANS	Small-angle neutron scattering
SAXS	Small-angle x-ray scattering
SFG	Sum frequency generation
STM	Scanning tunneling microscopy
TRFD	Time-resolved fluorescence depolarization
VPO	Vapor pressure osmometry

References

[1] Mullins OC, Sheu EY, Hammami A, Marshall AG, *Asphaltenes, Heavy Oils, and Petroleomics*. Springer: New York, **2007**.

[2] Mullins OC, Sheu EY, *Structures and dynamics of asphaltenes*. Springer Science & Business Media: **2013**.

[3] Yen TF, Chilingarian GV, *Asphaltenes and asphalts, 2*. Elsevier: **2000**.

[4] Calemma V, Iwanski P, Nali M, Scotti R, Montanari L, Structural characterization of asphaltenes of different origins. *Energy Fuels* 1995, *9*, (2), 225–230. DOI: 10.1021/ef00050a004

[5] Scotti R, Montanari L, Molecular structure and intermolecular interaction of asphaltenes by FT-IR, NMR, EPR. In: *Structures and Dynamics of Asphaltenes*, Springer: 1998, pp 79–113.

[6] Buenrostro-Gonzalez E, Groenzin H, Lira-Galeana C, Mullins OC, The overriding chemical principles that define asphaltenes. *Energy Fuels* 2001, *15*, 972–978.

[7] Dutta Majumdar R, Gerken M, Mikula R, Hazendonk P, Validation of the Yen–Mullins model of Athabasca oil-sands asphaltenes using solution-state 1H NMR relaxation and 2D HSQC spectroscopy. *Energy Fuels* 2013, *27*, (11), 6528–6537. DOI: 10.1021/ef401412w

[8] Dutta Majumdar R, Bake KD, Ratna Y, Pomerantz AE, Mullins OC, Gerken M, Hazendonk P, Single-core PAHs in petroleum- and coal-derived asphaltenes: size and distribution from solid-state NMR spectroscopy and optical absorption measurements. *Energy Fuels* 2016, *30*, (9), 6892–6906. DOI: 10.1021/acs.energyfuels.5b02815

[9] Andrews AB, Edwards JC, Pomerantz AE, Mullins OC, Nordlund D, Norinaga K, Comparison of coal-derived and petroleum asphaltenes by 13C nuclear magnetic resonance, DEPT, and XRS. *Energy Fuels* 2011, *25*, (7), 3068–3076. https://DOI:org10.1021/ef2003443

[10] George GN, Gorbaty ML, Sulfur K-edge X-ray absorption spectroscopy of petroleum asphaltenes and model compounds. *J Am Chem Soc* 1989, *111*, 3182–3186.

[11] Waldo GS, Mullins OC, Penner-Hahn JE, Cramer SP, Determination of the chemical environment of sulphur in petroleum asphaltenes by X-ray absorption spectroscopy. *Fuel* 1992, *71*, 53–57.
[12] Mitra-Kirtley S, Mullins OC, van Elp J, George SJ, Chen J, Cramer SP, Determination of the nitrogen chemical structures in petroleum asphaltenes using XANES spectroscopy. *J Am Chem Soc* 1993, *115*, 252–258.
[13] Moschopedis SE, Speight JG, Oxygen functions in asphaltenes. *Fuel* 1976, *55*, (4), 334–336. DOI:https://doi.org/10.1016/0016-2361(76)90035-1
[14] Pomerantz AE, Ventura GT, McKenna AM, Cañas J, Auman J, Koerner K, Curry D, Nelson RK, Reddy CM, Rodgers RP, Marshall AG, Peters KE, Mullins OC, Combining biomarker and bulk compositional gradient analysis to assess reservoir connectivity. *Org Geochem* 2010, *41*, 812–821.
[15] Mullins OC, The Modified Yen Model. *Energy Fuels* 2010, *24*, 2179–2207.
[16] Mullins OC, Sabbah H, Eyssautier J, Pomerantz AE, Barré L, Andrews AB, Ruiz-Morales Y, Mostowfi F, McFarlane R, Goual L, Advances in asphaltene science and the Yen–Mullins model. *Energy Fuels* 2012, *26*, (7), 3986–4003. https://DOI.org/10.1021/ef300185p
[17] Dickie JP, Yen TF, Macrostructures of the asphaltic fractions by various instrumental methods. *Anal Chem* 1967, *39*, (14), 1847–1852.
[18] Mullins OC, *Reservoir Fluid Geodynamics and Reservoir Evaluation*. Schlumberger: Houston, TX, **2019**.
[19] Rane JP, Pauchard V, Couzis A, Banerjee S, Interfacial rheology of asphaltenes at oil-water interfaces and interpretation of the equation of state. *Langmuir: ACS J Surf Colloids* 2013, *29*, (15), 4750–4759. https://DOI:10.1021/la304873n
[20] Rane JP, Zarkar S, Pauchard V, Mullins OC, Christie D, Andrews AB, Pomerantz AE, Banerjee S, Applicability of the Langmuir equation of state for asphaltene adsorption at the oil–water interface: coal-derived, petroleum, and synthetic asphaltenes. *Energy Fuels* 2015, *29*, (6), 3584–3590. https://DOI:10.1021/acs.energyfuels.5b00179
[21] Mullins OC, Martínez-Haya B, Marshall AG, Contrasting Perspective on Asphaltene Molecular Weight. This Comment vs the Overview of A. A. Herod, K. D. Bartle, and R. Kandiyoti. *Energy Fuels* 2008, *22*, 1765–1773.
[22] Andreatta G, Bostrom N, Mullins OC, High-Q ultrasonic determination of the critical nanoaggregate concentration of asphaltenes and the critical micelle concentration of standard surfactants. *Langmuir: ACS J Surf Colloids* 2005, *21*, 2728–2736.
[23] Andreatta G, Goncalves CC, Buffin G, Bostrom N, Quintella CM, Arteaga-Larios F, Pérez E, Mullins OC, Nanoaggregates and structure–function relations in asphaltenes. *Energy Fuels* 2005, *19*, (4), 1282–1289.
[24] Hortal AR, Martínez-Haya B, Lobato MD, Pedrosa JM, Lago S, On the determination of molecular weight distributions of asphaltenes and the aggregates in laser desorption ionization experiments. *J Mass Spectrom*. 2006, *41*, 960–968.
[25] Martínez-Haya B, Hortal AR, Hurtado P, Lobato MD, Pedrosa JM, Laser desorption/ionization determination of molecular weight distributions of polyaromatic carbonaceous compounds and their aggregates. *J Mass Spectrom*. 2007, *42*, 701–713.
[26] Hortal AR, Hurtado P, Martínez-Haya B, Mullins OC, Molecular weight distributions of coal and petroleum asphaltenes from laser desorption/ionization experiments. *Energy Fuels* 2007, *21*, 2863–2868.
[27] Strausz OP, Mojelsky TW, Lown EM, The molecular structure of asphaltene: an unfolding story. *Fuel* 1992, *71*, (12), 1355–1363.
[28] Groenzin H, Mullins OC, Asphaltene molecular size and structure. *J Phys Chem A* 1999, *103*, (50) 11237–11245. https://doi.org/10.1021/jp992609w

[29] Groenzin H, Mullins OC, Molecular size and structure of asphaltenes from various sources. *Energy Fuels* 2000, *14*, (3) 677–684. doi:org/10.1021/ef990225z
[30] Groenzin H, Mullins OC, Molecular size and structure of asphaltenes. *Pet Sci Technol*. 2001, *19*, (1-2), 219–230.
[31] Buch L, Groenzin H, Buenrostro-Gonzalez E, Andersen SI, Lira-Galeana C, Mullins OC, Molecular size of asphaltene fractions obtained from residuum hydrotreatment. *Fuel* 2003, *82*, (9), 1075–1084.
[32] Groenzin H, Mullins OC, Eser S, Mathews J, Yang M-G, Jones D, Molecular size of asphaltene solubility fractions. *Energy Fuels* 2003, *17*, (2), 498–503.
[33] Groenzin H, Mullins OC, Asphaltene molecular size and weight by time-resolved fluorescence depolarization. In: *Asphaltenes, heavy oils, and petroleomics*, Springer: 2007, pp 17–62.
[34] Badre S, Carla Goncalves C, Norinaga K, Gustavson G, Mullins OC, Molecular size and weight of asphaltene and asphaltene solubility fractions from coal, crude oil, and bitumen. *Fuel* 2006, *85*, 1–11.
[35] Schuler B, Zhang Y, Liu F, Pomerantz AE, Andrews AB, Gross L, Pauchard V, Banerjee S, Mullins OC, Overview of asphaltene nanostructures and thermodynamic applications. *Energy Fuels* 2020, 10.1021/acs.energyfuels.0c00874.https://DOI:10.1021/acs.energyfuels.0c00874
[36] Clar E, *The Aromatic Sextet*. John Wiley & Sons: London, 1972, p 128.
[37] Ruiz-Morales Y, HOMO-LUMO gap as an index of molecular size and structure for polycyclic aromatic hydrocarbons (PAHs) and asphaltenes: a theoretical study. I J Phys Chem A 2002, *106*, (46), 11283–11308. https://doi.org/10.1021/jp021152e
[38] Ruiz-Morales Y, The Agreement between Clar structures and nucleus-independent chemical shift values in pericondensed benzenoid polycyclic aromatic hydrocarbons: an application of the Y-rule. *J Phys Chem A* 2004, *108*, (49), 10873–10896. https://doi.org/10.1021/jp040179q
[39] Ruiz-Morales Y, Wu X, Mullins OC, Electronic absorption edge of crude oils and asphaltenes analyzed by molecular orbital calculations with optical spectroscopy. *Energy Fuels* 2007, *21*, (2) 944–952. https://doi.org/10.1021/ef0605605
[40] Ruiz-Morales Y, Mullins OC, Polycyclic aromatic hydrocarbons of asphaltenes analyzed by molecular orbital calculations with optical spectroscopy. *Energy Fuels* 2007, *21*, (1), 256–265. https://doi.org/10.1021/ef060250m
[41] Ruiz-Morales Y, Molecular orbital calculations and optical transitions of PAHs and asphaltenes. In: *Asphaltenes, Heavy Oils, and Petroleomics*, Springer: 2007, pp 95–137.
[42] Ruiz-Morales Y, Mullins OC, Measured and simulated electronic absorption and emission spectra of asphaltenes. *Energy Fuels* 2009, *23*, (3), 1169–1177. https://doi.org/10.1021/ef800663w
[43] Schuler B, Meyer G, Pena D, Mullins OC, Gross L, Unraveling the molecular structures of asphaltenes by atomic force microscopy. *J Am Chem Soc* 2015, *137*, (31), 9870–9876. DOI: 10.1021/jacs.5b04056
[44] Schuler B, Fatayer S, Meyer G, Rogel E, Moir M, Zhang Y, Harper MR, Pomerantz AE, Bake KD, Witt M, Peña D, Kushnerick JD, Mullins OC, Ovalles C, van den Berg FGA, Gross L, Heavy oil based mixtures of different origins and treatments studied by atomic force microscopy. *Energy Fuels* 2017, *31*, (7), 6856–6861. DOI: 10.1021/acs.energyfuels.7b00805
[45] Lisitza NV, Freed DE, Sen PN, Song Y-Q, Study of asphaltene nanoaggregation by nuclear magnetic resonance (NMR). *Energy Fuels* 2009, *23*, 1189–1193.
[46] Andrews AB, Guerra RE, Mullins OC, Sen PN, Diffusivity of asphaltene molecules by fluorescence correlation spectroscopy. *J Phys Chem A* 2006, *110*, 8093–8097.
[47] Schneider MH, Andrews AB, Mitra-Kirtley S, Mullins OC, Asphaltene molecular size by fluorescence correlation spectroscopy. *Energy Fuels* 2007, *21*, 2875–2882.

[48] Guerra RE, Ladavac K, Andrews AB, Mullins OC, Sen PN, Diffusivity of coal and petroleum asphaltene monomers by fluorescence correlation spectroscopy. *Fuel* 2007, *86*, 2016–2020.
[49] Andrews AB, Shih W-C, Mullins OC, Norinaga K, Molecular size determination of coal-derived asphaltene by fluorescence correlation spectroscopy. *Appl Spectrosc*. 2011, *65*, (12), 1348–1356.
[50] Wargadalam VJ, Norinaga K, Iino M, Size and shape of coal asphaltene studied by viscosity and diffusion coefficient measurement. *Fuel* 2002, *81*, 1403–1407.
[51] Klein GC, Kim S, Rodgers RP, Marshall AG, Yen A, Mass Spectral Analysis of Asphaltenes. II. Detailed Compositional Comparison of Asphaltenes Deposit to Its Crude Oil Counterpart for Two Geographically Different Crude Oils by ESI FT-ICR MS. *Energy Fuels* 2006, *20*, 1973–1979.
[52] Klein GC, Kim S, Rodgers RP, Marshall AG, Yen A, Asomaning S, Mass spectral analysis of asphaltenes. I. Compositional differences between pressure-drop and solvent-drop asphaltenes determined by electrospray ionization Fourier transform ion cyclotron resonance mass spectrometry. *Energy Fuels* 2006, *20*, 1965–1972.
[53] Marshall AG, Rodgers RP, Petroleomics: Chemistry of the underworld. *Proc Natl Acad Sci* 2008, *105*, (47), 18090–18095.
[54] McKenna AM, Donald LJ, Fitzsimmons JE, Juyal P, Spicer V, Standing KG, Marshall AG, Rodgers RP, Heavy petroleum composition. 3. Asphaltene aggregation. *Energy & fuels* 2013, *27*, (3), 1246–1256.
[55] Rodgers RP, Marshall AG, Petroleomics: Advanced characterization of petroleum-derived materials by Fourier transform ion cyclotron resonance mass spectrometry (FT-ICR MS). In: *Asphaltenes, heavy oils, and petroleomics*, Springer: 2007, pp 63–93.
[56] Pinkston DS, Duan P, Gallardo VA, Habicht SC, Tan X, Qian K, Gray M, Müllen K, Kenttämaa HI, Analysis of Asphaltenes and Asphaltene Model Compounds by Laser-Induced Acoustic Desorption/Fourier Transform Ion Cyclotron Resonance Mass Spectrometry. *Energy Fuels* 2009, *23*, (11), 5564–5570. DOI: 10.1021/ef9006005
[57] Borton D II, Pinkston DS, Hurt MR, Tan X, Azyat K, Tykwinski R, Gray M, Qian K, Kenttämaa HI, Molecular Structures of Asphaltenes Based on the Dissociation Reactions of Their Ions in Mass Spectrometry. *Energy Fuels* 2010, *24*, 5548–5559.
[58] Hurt MR, Borton DJ, Choi HJ, Kenttämaa HI, Comparison of the structures of molecules in coal and petroleum asphaltenes by using mass spectrometry. *Energy Fuels* 2013, *27*, (7), 3653–3658.
[59] Cunico RL, Sheu EY, Mullins OC, Molecular Weight Measurement of UG8 Asphaltene Using APCI Mass Spectrometry. *Pet Sci Technol* 2004, *22*, 787–798.
[60] Pomerantz AE, Hammond MR, Morrow AL, Mullins OC, Zare RN, Asphaltene Molecular-Mass Distribution Determined by Two-Step Laser Mass Spectrometry. *Energy Fuels* 2009, *23*, 1162–1168.
[61] Pomerantz AE, Hammond MR, Morrow AL, Mullins OC, Zare RN, Two-Step Laser Mass Spectrometry of Asphaltenes. *J Am Chem Soc* 2008, *130*, 7216–7217.
[62] Pomerantz AE, Wu Q, Mullins OC, Zare RN, Laser-Based Mass Spectrometric Assessment of Asphaltene Molecular Weight, Molecular Architecture, and Nanoaggregate Number. *Energy Fuels* 2015, *29*, (5), 2833–2842. DOI: 10.1021/ef5020764
[63] Sabbah H, Morrow AL, Pomerantz AE, Zare RN, Evidence for Island Structures as the Dominant Architecture of Asphaltenes. *Energy Fuels* 2011, *25*, 1597–1604.
[64] Sabbah H, Pomerantz AE, Wagner M, Müllen K, Zare RN, Laser Desorption Single-Photon Ionization of Asphaltenes: Mass Range, Compound Sensitivity, and Matrix Effects. *Energy Fuels* 2012, *26*, (6), 3521–3526. DOI: 10.1021/ef3002313

[65] Wu Q, Seifert DJ, Pomerantz AE, Mullins OC, Zare RN, Constant Asphaltene Molecular and Nanoaggregate Mass in a Gravitationally Segregated Reservoir. *Energy Fuels* 2014, *28*, (5), 3010–3015. DOI: 10.1021/ef500281s

[66] Sabbah H, Morrow AL, Pomerantz AE, Mullins OC, Tan X, Gray MR, Azyat K, Tykwinski RR, Zare RN, Comparing Laser Desorption/Laser Ionization Mass Spectra of Asphaltenes and Model Compounds. *Energy Fuels* 2010, *24*, 3589–3594.

[67] Wu Q, Pomerantz AE, Mullins OC, Zare RN, Minimization of Fragmentation and Aggregation by Laser Desorption Laser Ionization Mass Spectrometry. *J Am Soc Mass Spectrom* 2013, *24*, 1116–1122. DOI: 10.1007/s13361-013-0636-7

[68] Maechling CR, Clemett SJ, Engelke F, Zare RN, Evidence for thermalization of surface-desorbed molecules at heating rates of 10^8 K/s. *J Chem Phys*. 1996, *104*, 8768–8776.

[69] Wu Q, Pomerantz AE, Mullins OC, Zare RN, Laser-Based Mass Spectrometric Determination of Aggregation Numbers for Petroleum- and Coal-Derived Asphaltenes. *Energy Fuels* 2014, *28*, 475–482.

[70] Gross L, Mohn F, Moll N, Liljeroth P, Meyer G, The Chemical Structure of a Molecule Resolved by Atomic Force Microscopy. *Science* 2009, *325*, 1110–1114. DOI: 10.1126/science.1176210

[71] Pavlicek N, Gross L, Generation, manipulation and characterization of molecules by atomic force microscopy. *Nat Rev Chem* 2017, *1*, (1), 0005. DOI: 10.1038/s41570-016-0005

[72] Ebeling D, Sekutor M, Stiefermann M, Tschakert J, Dahl JEP, Carlson RMK, Schirmeisen A, Schreiner PR, Assigning the absolute configuration of single aliphatic molecules by visual inspection. *Nat Commun* 2018, *9*, (1), 2420. DOI: 10.1038/s41467-018-04843-z

[73] Kawai S, Takahashi K, Ito S, Pawlak R, Meier T, Spijker P, Canova FF, Tracey J, Nozaki K, Foster AS, Meyer E, Annulene C and Radialene Structures in a Single Anti-Aromatic Molecule Studied by High-Resolution Atomic Force Microscopy. *ACS Nano* 2017, *11*, (8), 8122–8130. DOI: 10.1021/acsnano.7b02973

[74] Pavliček N, Fleury B, Neu M, Niedenführ J, Herranz-Lancho C, Ruben M, Repp J, Atomic Force Microscopy Reveals Bistable Configurations of Dibenzo [a,h]thianthrene and their Interconversion Pathway. *Phys Rev Lett* 2012, *108*, (8), 086101. DOI: 10.1103/PhysRevLett.108.086101

[75] Schuler B, Fatayer S, Mohn F, Moll N, Pavlicek N, Meyer G, Pena D, Gross L, Reversible Bergman cyclization by atomic manipulation. *Nat Chem* 2016, *8*, (3), 220–224. DOI: 10.1038/nchem.2438

[76] Pavliček N, Gawel P, Kohn DR, Majzik Z, Xiong Y, Meyer G, Anderson HL, Gross L, Polyyne formation via skeletal rearrangement induced by atomic manipulation. *Nat Chem* 2018, *10*, (8), 853–858. DOI: 10.1038/s41557-018-0067-y

[77] Fatayer S, Albrecht F, Zhang Y, Urbonas D, Peña D, Moll N, Gross L, Molecular structure elucidation with charge-state control. *Science* 2019, *365*, (6449), 142. DOI: 10.1126/science.aax5895

[78] Pavlicek N, Schuler B, Collazos S, Moll N, Perez D, Guitian E, Meyer G, Pena D, Gross L, On-surface generation and imaging of arynes by atomic force microscopy. *Nat Chem* 2015, *7*, (8), 623–628. DOI: 10.1038/nchem.2300

[79] Pavlicek N, Mistry A, Majzik Z, Moll N, Meyer G, Fox DJ, Gross L, Synthesis and characterization of triangulene. *Nat Nanotechnol*. 2017, *12*, (4), 308–311. DOI: 10.1038/nnano.2016.305

[80] Kaiser K, Scriven LM, Schulz F, Gawel P, Gross L, Anderson HL, An sp-hybridized molecular carbon allotrope, cyclo [18]carbon. *Science* 2019, *365*, 1299–1301. DOI: 10.1126/science.aay1914

[81] Zhang J, Chen P, Yuan B, Ji W, Cheng Z, Qiu X, Real-space identification of intermolecular bonding with atomic force microscopy. *Science* 2013, *342*, 611–614.

[82] Gross L, Mohn F, Moll N, Schuler B, Criado A, Guitian E, Pena D, Gourdon A, Meyer G, Bond-Order Discrimination by Atomic Force Microscopy. *Science* 2012, *337*, 1326–1329. DOI: 10.1126/science.1225621

[83] Han Z, Czap G, Chiang C-L, Xu C, Wagner PJ, Wei X, Zhang Y, Wu R, Ho W, Imaging the halogen bond in self-assembled halogen benzenes on silver. *Science (Washington, DC, United States)* 2017, *358*, (6360), 206–210. DOI: 10.1126/science.aai8625

[84] Mohn F, Gross L, Moll N, Meyer G, Imaging the charge distribution within a single molecule. *Nat Nanotechnol* 2012, *7*, (4), 227–231. DOI: 10.1038/nnano.2012.20

[85] Gross L, Mohn F, Liljeroth P, Repp J, Giessibl Franz J, Meyer G, Measuring the charge state of an adatom with noncontact atomic force microscopy. *Science* 2009, *324*, (5933), 1428–1431.

[86] Schuler B, Liu W, Tkatchenko A, Moll N, Meyer G, Mistry A, Fox D, Gross L, Adsorption geometry determination of single molecules by atomic force microscopy. *Phys Rev Lett* 2013, *111*, (10), 106103. DOI: 10.1103/PhysRevLett.112.129902

[87] Repp J, Meyer G, Stojković SM, Gourdon A, Joachim C, Molecules on Insulating Films: Scanning-Tunneling Microscopy Imaging of Individual Molecular Orbitals. *Phys Rev Lett* 2005, *94*, (2), 026803. DOI: 10.1103/PhysRevLett.94.026803

[88] Schuler B, Liu W, Tkatchenko A, Moll N, Meyer G, Mistry A, Fox D, Gross L, Adsorption geometry determination of single molecules by atomic force microscopy. *Phys Rev Lett*. 2013, *111*, (10), 106103/1–106103/5. DOI: 10.1103/PhysRevLett.111.106103

[89] de Oteyza DG, Gorman P, Chen Y-C, Wickenburg S, Riss A, Mowbray DJ, Etkin G, Pedramrazi Z, Tsai H-Z, Rubio A, Crommie MF, Fischer FR, Direct Imaging of Covalent Bond Structure in Single-Molecule Chemical Reactions. *Science* 2013, *340*, (6139), 1434–1437. DOI: 10.1126/science.1238187

[90] Fan Q, Martin-Jimenez D, Werner S, Ebeling D, Koehler T, Vollgraff T, Sundermeyer J, Hieringer W, Schirmeisen A, Gottfried JM, On-Surface Synthesis and Characterization of a Cycloarene: C108 Graphene Ring. *J Am Chem Soc*. 2020, *142*, (2), 894–899. DOI: 10.1021/jacs.9b10151

[91] Riss A, Paz AP, Wickenburg S, Tsai H-Z, De Oteyza DG, Bradley AJ, Ugeda MM, Gorman P, Jung HS, Crommie MF, Rubio A, Fischer FR, Imaging single-molecule reaction intermediates stabilized by surface dissipation and entropy. *Nat Chem* 2016, *8*, (7), 678–683. DOI: 10.1038/nchem.2506

[92] Pavliček N, Gross L, Generation, manipulation and characterization of molecules by atomic force microscopy. *Nat Rev Chem* 2017, *1*, (1), 0005. DOI: 10.1038/s41570-016-0005

[93] Schuler B, Meyer G, Pena D, Mullins OC, Gross L, Unraveling the Molecular Structures of Asphaltenes by Atomic Force Microscopy. *J Am Chem Soc* 2015, *137*, (31), 9870–9876. DOI: 10.1021/jacs.5b04056

[94] Schuler B, Fatayer S, Meyer G, Rogel E, Moir M, Zhang Y, Harper MR, Pomerantz AE, Bake KD, Witt M, Pena D, Kushnerick JD, Mullins OC, Ovalles C, van den Berg FGA, Gross L, Heavy Oil Based Mixtures of Different Origins and Treatments Studied by Atomic Force Microscopy. *Energy Fuels* 2017, *31*, (7), 6856–6861. DOI: 10.1021/acs.energyfuels.7b00805

[95] Zhang Y, Schuler B, Fatayer S, Gross L, Harper MR, Kushnerick JD, Understanding the Effects of Sample Preparation on the Chemical Structures of Petroleum Imaged with Noncontact Atomic Force Microscopy. *Ind Eng Chem Res* 2018, *57*, (46), 15935–15941. DOI: 10.1021/acs.iecr.8b03962

[96] Schuler B, Zhang Y, Collazos S, Fatayer S, Meyer G, Perez D, Guitian E, Harper MR, Kushnerick JD, Pena D, Gross L, Characterizing aliphatic moieties in hydrocarbons with atomic force microscopy. *Chem Sci* 2017, *8*, (3), 2315–2320. DOI: 10.1039/c6sc04698c

[97] Zahl P, Zhang Y, Guide for Atomic Force Microscopy Image Analysis To Discriminate Heteroatoms in Aromatic Molecules. *Energy Fuels* 2019, *33*, (6), 4775–4780. DOI: doi.org/10.1021/acs.energyfuels.9b00165
[98] Zhang Y Identify Similarities in Diverse Polycyclic Aromatic Hydrocarbons of Asphaltenes and Heavy Oils Revealed by Noncontact Atomic Force Microscopy: Aromaticity, Bonding, and Implications in Reactivity. In *Chemistry Solutions to Challenges in the Petroleum Industry*; Eds., Vol. 1320; American Chemical Society, 2019; pp 39–65.
[99] Chen P, Fatayer S, Schuler B, Metz JN, Gross L, Yao N, Zhang Y, The Role of Methyl Groups in the Early Stage of Thermal Polymerization of Polycyclic Aromatic Hydrocarbons Revealed by Molecular Imaging. *Energy Fuels* 2021, *35*, (3), 2224–2233. DOI: 10.1021/acs.energyfuels.0c04016
[100] Zhang Y, Siskin M, Gray MR, Walters CC, Rodgers JR, Mechanisms of Asphaltene Aggregation: Puzzles and a New Hypothesis. *Energy Fuels* 2020, *34*, (8), 9094–9107.
[101] Schuler B, Zhang Y, Liu F, Pomerantz AE, Andrews AB, Gross L, Pauchard V, Banerjee S, Mullins OC, Overview of Asphaltene Nanostructures and Thermodynamic Applications. *Energy Fuels* 2020, *34*, (12), 15082–15105. DOI: 10.1021/acs.energyfuels.0c00874
[102] Chen P, Metz JN, Mennito AS, Merchant S, Smith SE, Siskin M, Rucker SP, Dankworth DC, Kushnerick JD, Yao N, Zhang Y, Petroleum pitch: Exploring a 50-year structure puzzle with real-space molecular imaging. *Carbon* 2020, *161*, 456–465. DOI: https://doi.org/10.1016/j.carbon.2020.01.062
[103] Chen P, Joshi YV, Metz JN, Yao N, Zhang Y, Conformational Analysis of Nonplanar Archipelago Structures on a Cu (111) Surface by Molecular Imaging. *Energy Fuels* 2020, *34*, (10), 12135–12141. DOI: 10.1021/acs.energyfuels.0c01861
[104] Zhang Y, Schulz F, Rytting B, Walters C, Kaiser K, Metz J, Harper M, Merchant S, Mennito A, Qian K, Kushnerick J, Kilpatrick P, Gross L, Elucidating the Geometric Substitution of Petroporphyrins by Spectroscopic Analysis and AFM Molecular Imaging. *Energy Fuels* 2019, *33*, (7), 6088–6097. DOI: https://doi.org/10.1021/acs.energyfuels.9b00816
[105] Chen P, Fan D, Selloni A, Carter EA, Arnold CB, Dankworth DC, Rucker SP, Chelikowsky JR, Zhang Y, Yao N, Breaking a Chemical Bond with Atomic Force Microscopy. *submitted* 2020, *submitted*.
[106] Rahimi P, Ovalles C, Zhang Y, Adams J, *Chemistry Solutions to Challenges in the Petroleum Industry*. Am Chem Soc: **2019**.
[107] Zhang Y, Nonalternant aromaticity and partial double bond in petroleum molecules revealed: theoretical understanding of polycyclic aromatic hydrocarbons obtained by non-contact atomic force microscopy. *Energy Fuels* 2018, *33*, (5), 3816–3820. DOI: 10.1021/acs.energyfuels.8b03284
[108] Gross L, Schuler B, Pavlicek N, Fatayer S, Majzik Z, Moll N, Pena D, Meyer G, Atomic force microscopy for molecular structure elucidation. *Angew Chem Int Ed Engl* 2018, *57*, (15), 3888–3908. DOI: 10.1002/anie.201703509
[109] Clair S, de Oteyza DG, Controlling a chemical coupling reaction on a surface: tools and strategies for on-surface synthesis. *Chem Rev* 2019, *119*, (7), 4717–4776. DOI: 10.1021/acs.chemrev.8b00601
[110] Gross L, Mohn F, Moll N, Meyer G, Ebel R, Abdel-Mageed WM, Jaspars M, Organic structure determination using atomic-resolution scanning probe microscopy. *Nat Chem* 2010, *2*, (10), 821–825. DOI: 10.1038/nchem.765
[111] Pavlicek N, Majzik Z, Collazos S, Meyer G, Perez D, Guitian E, Pena D, Gross L, Generation and Characterization of a meta-Aryne on Cu and NaCl Surfaces. *ACS Nano* 2017, *11*, (11), 10768–10773. DOI: 10.1021/acsnano.7b06137

[112] Kawai S, Haapasilta V, Lindner BD, Tahara K, Spijker P, Buitendijk JA, Pawlak R, Meier T, Tobe Y, Foster AS, Meyer E, Thermal control of sequential on-surface transformation of a hydrocarbon molecule on a copper surface. *Nat Commun* 2016, *7*, (1), 12711. DOI: 10.1038/ncomms12711

[113] Schuler B, Collazos S, Gross L, Meyer G, Perez D, Guitian E, Pena D, From perylene to a 22-ring aromatic hydrocarbon in one-pot. *Angew Chem, Int Ed*. 2014, *53*, (34), 9004–9006. DOI: 10.1002/anie.201403707

[114] Gröning O, Wang S, Yao X, Pignedoli CA, Borin Barin G, Daniels C, Cupo A, Meunier V, Feng X, Narita A, Müllen K, Ruffieux P, Fasel R, Engineering of robust topological quantum phases in graphene nanoribbons. *Nature* 2018, *560*, (7717), 209–213. DOI: 10.1038/s41586-018-0375-9

[115] Wargadalam VJ, Norinaga K, Iino M, Size and shape of a coal asphaltene studied by viscosity and diffusion coefficient measurements. *Fuel* 2002, *81*, (11), 1403–1407. DOI:https://doi.org/10.1016/S0016-2361(02)00055-8

[116] Norinaga K, Iino M, Evaluation of the Thermoplasticity of Upper Freeport Coal and Its Extracts Using Dynamic Viscoelasticity. *Energy Fuels* 2000, *14*, (4), 929–935. DOI: 10.1021/ef000049q

[117] Rogel E, Miao T, Vien J, Roye M, Comparing asphaltenes: Deposit versus crude oil. *Fuel* 2015, *147*, 155–160. DOI: https://doi.org/10.1016/j.fuel.2015.01.045

[118] Powers DP, Characterization and asphaltene precipitation modeling of native and reacted crude oils. 2014.

[119] Seshadri KS, Bacha JD, Albaugh EW, Structural characterization of fractions of petroleum pitch and ethylene pyrolysis tar by proton and carbon-13 NMR spectroscopy. *Fuel* 1982, *61*, (11), 1095–1100. DOI:10.1016/0016-2361(82)90192-2

[120] Chawla B, Green LA Multi-dimensional high performance liquid chromatographic separation technique (STAR7) for quantitative determinations of 7 fractions in heavy petroleum streams boiling above 550 degrees F. US8114678B2, **2010**.

[121] Qian K, Edwards KE, Mennito AS, Freund H, Saeger RB, Hickey KJ, Francisco MA, Yung C, Chawla B, Wu C, Kushnerick JD, Olmstead WN, Determination of Structural Building Blocks in Heavy Petroleum Systems by Collision-Induced Dissociation Fourier Transform Ion Cyclotron Resonance Mass Spectrometry. *Anal Chem* 2012, *84*, (10), 4544–4551. DOI: 10.1021/ac300544s

[122] Qian K, Edwards KE, Mennito AS, Saeger RB Generation of model-of-composition of petroleum by high resolution mass spectrometry and associated analytics. US20120153139A1, **2012**.

[123] Wittrig AM, Fredriksen TR, Qian K, Clingenpeel AC, Harper MR, Single Dalton Collision-Induced Dissociation for Petroleum Structure Characterization. *Energy Fuels* 2017, *31*, (12), 13338–13344. DOI: 10.1021/acs.energyfuels.7b02478

[124] Jaffe SB, Freund H, Olmstead WN, Extension of Structure-Oriented Lumping to Vacuum Residua. *Ind Eng Chem Res* 2005, *44*, (26), 9840–9852. DOI: 10.1021/ie058048e

[125] Clar E, *The Aromatic Sextet*. Wiley: New York, **1972**.

[126] Randić M, Aromaticity of Polycyclic Conjugated Hydrocarbons. *Chem Rev* 2003, *103*, (9), 3449–3606. DOI: 10.1021/cr9903656

[127] Schuler B, Mohn F, Moll N, Gross L, Meyer G, Visualization of chemical bonds. *Phys Unserer Zeit* 2013, *44*, (1), 6–7. DOI: 10.1002/piuz.201390011

[128] Gross L, Mohn F, Meyer G, Textbook images of a molecule. *Europhys News* 2010, *41*, (2), 15–18. DOI: 10.1051/epn/2010202

[129] Moll N, Gross L, Mohn F, Curioni A, Meyer G, The mechanisms underlying the enhanced resolution of atomic force microscopy with functionalized tips. *New J Phys* 2010, *12*, (12), 125020. DOI: 10.1088/1367-2630/12/12/125020

[130] Hapala P, Kichin G, Wagner C, Tautz FS, Temirov R, Jelinek P, Mechanism of high-resolution STM/AFM imaging with functionalized tips. *Phys Rev B* 2014, *90*, (8), 085421–085429. DOI: 10.1103/PhysRevB.90.085421
[131] van der Lit J, Di Cicco F, Hapala P, Jelinek P, Swart I, Submolecular resolution imaging of molecules by atomic force microscopy: the influence of the electrostatic force. *Phys Rev Lett.* 2016, *116*, (9), 096102/1–096102/5. DOI: 10.1103/PhysRevLett.116.096102
[132] Hamalainen SK, van der Heijden N, van der Lit J, den Hartog S, Liljeroth P, Swart I, Intermolecular contrast in atomic force microscopy images without intermolecular bonds. *Phys Rev Lett* 2014, *113*, (18), 186102. DOI: 10.1103/PhysRevLett.113.186102
[133] Hapala P, Temirov R, Tautz FS, Jelinek P, Origin of High-Resolution IETS-STM Images of Organic Molecules with Functionalized Tips. *Phys Rev Lett* 2014, *113*, (22), 226101. DOI: 10.1103/PhysRevLett.113.226101
[134] Iwata K, Yamazaki S, Mutombo P, Hapala P, Ondracek M, Jelinek P, Sugimoto Y, Chemical structure imaging of a single molecule by atomic force microscopy at room temperature. *Nat Commun* 2015, *6*, 7766–7773. DOI: 10.1038/ncomms8766
[135] Sakai Y, Lee AJ, Chelikowsky JR, First-Principles Atomic Force Microscopy Image Simulations with Density Embedding Theory. *Nano Lett.* 2016, *16*, (5), 3242–3246. DOI: 10.1021/acs.nanolett.6b00741
[136] Chelikowsky JR, Fan D, Lee AJ, Sakai Y, Simulating noncontact atomic force microscopy images. *Phys Rev Mater* 2019, *3*, (11), 110302. DOI: 10.1103/PhysRevMaterials.3.110302
[137] Fan D, Sakai Y, Chelikowsky JR, Discrimination of Bond Order in Organic Molecules Using Noncontact Atomic Force Microscopy. *Nano Lett.* 2019, DOI: 10.1021/acs.nanolett.9b02097
[138] Ellner M, Pou P, Pérez R, Molecular Identification, Bond Order Discrimination, and Apparent Intermolecular Features in Atomic Force Microscopy Studied with a Charge Density Based Method. *ACS Nano* 2019, *13*, (1), 786–795. DOI: 10.1021/acsnano.8b08209
[139] Alldritt B, Hapala P, Oinonena N, Urtev F, Krejci O, Federici Canova F, Kannala J, Schulz F, Liljeroth P, Foster AS, Automated Structure Discovery in Atomic Force Microscopy. *Science Adv* 2019, *6*, (9), eaay6913. DOI: 10.1126/sciadv.aay6913
[140] Law JC, Headen TF, Jiménez-Serratos G, Boek ES, Murgich J, Müller EA, Catalogue of Plausible Molecular Models for the Molecular Dynamics of Asphaltenes and Resins Obtained from Quantitative Molecular Representation. *Energy Fuels* 2019, *33*, (10), 9779–9795. DOI: 10.1021/acs.energyfuels.9b02605
[141] Neumann A, Chacón-Patiño ML, Rodgers RP, Rüger CP, Zimmermann R, Investigation of Island/Single-Core- and Archipelago/Multicore-Enriched Asphaltenes and Their Solubility Fractions by Thermal Analysis Coupled with High-Resolution Fourier Transform Ion Cyclotron Resonance Mass Spectrometry. *Energy Fuels* 2020, 10.1021/acs.energyfuels.0c03751. DOI: 10.1021/acs.energyfuels.0c03751
[142] Chacón-Patiño ML, Rowland SM, Rodgers RP, Advances in Asphaltene Petroleomics. Part 3. Dominance of Island or Archipelago Structural Motif Is Sample Dependent. *Energy Fuels* 2018, *32*, (9), 9106–9120. DOI: 10.1021/acs.energyfuels.8b01765
[143] Rüger CP, Neumann A, Sklorz M, Schwemer T, Zimmermann R, Thermal Analysis Coupled to Ultrahigh Resolution Mass Spectrometry with Collision Induced Dissociation for Complex Petroleum Samples: Heavy Oil Composition and Asphaltene Precipitation Effects. *Energy Fuels* 2017, *31*, (12), 13144–13158. DOI: 10.1021/acs.energyfuels.7b01778
[144] Beuhler RJ, Flanigan E, Greene LJ, Friedman L, Proton transfer mass spectrometry of peptides. A rapid heating technique for underivatized peptides containing arginine. *J Am Chem Soc* 1974, *96*, (12), 3990–3999. DOI: 10.1021/ja00819a043

[145] Rapenne G, Grill L, Zambelli T, Stojkovic SM, Ample F, Moresco F, Joachim C, Launching and landing single molecular wheelbarrows on a Cu(100) surface. *Chem Phys Lett* 2006, *431*, (1-3), 219–222. DOI: 10.1016/j.cplett.2006.09.080
[146] Grill L, Rieder K-H, Moresco F, Jimenez-Bueno G, Wang C, Rapenne G, Joachim C, Imaging of a molecular wheelbarrow by scanning tunneling microscopy. *Surf Sci* 2005, *584*, (2-3), L153–L158. DOI: 10.1016/j.susc.2005.03.062
[147] Beuhler RJ, Flanigan E, Greene LJ, Friedman L, Proton transfer mass spectrometry of peptides. Rapid heating technique for underivatized peptides containing arginine. *J Am Chem Soc*. 1974, *96*, (12), 3990–3999. DOI: 10.1021/ja00819a043
[148] Gutowsky HS, Ray BR, Rutledge RL, Unterberger RR, Carbonaceous Free Radicals in Crude Petroleum. *J Chem Phys* 1958, *28*, (4), 744–745. DOI: 10.1063/1.1744250
[149] Lawrence J, Mohammed MSG, Rey D, Aguilar-Galindo F, Berdonces-Layunta A, Peña D, de Oteyza DG, Reassessing Alkyne Coupling Reactions While Studying the Electronic Properties of Diverse Pyrene Linkages at Surfaces. *ACS Nano* 2021, DOI:10.1021/acsnano.0c09756
[150] Moir ME Asphaltenes, What Art Thou? In: *The Boduszynski Continuum: Contributions to the Understanding of the Molecular Composition of Petroleum*; Ovalles C, Moir M, Eds.; ACS Symposium Series, Vol. 1282; American Chemical Society, 2018; pp 3–24.
[151] Moir ME The Quantum Mechanics of Asphaltene Aggregation. In: *Chemistry Solutions to Challenges in the Petroleum Industry*; Parviz R, Ovalles C, Adams J, Zhang Y, Eds.; ACS Symposium Series, Vol. 1320; American Chemical Society, 2019; pp 89–111.
[152] Sabbah H, Morrow AL, Pomerantz AE, Mullins OC, Tan X, Gray MR, Azyat K, Tykwinski RR, Zare RN, Comparing Laser Desorption/Laser Ionization Mass Spectra of Asphaltenes and Model Compounds. *Energy Fuels* 2010, *24*, (6), 3589–3594. DOI: 10.1021/ef100402g
[153] Morimoto M, Fukatsu N, Tanaka R, Takanohashi T, Kumagai H, Morita T, Tykwinski RR, Scott DE, Stryker JM, Gray MR, Sato T, Yamamoto H, Determination of Hansen solubility parameters of asphaltene model compounds. *Energy Fuels* 2018, *32*, (11), 11296–11303. DOI: 10.1021/acs.energyfuels.8b02661
[154] Qian K, Edwards KE, Mennito AS, Freund H, Saeger RB, Hickey KJ, Francisco MA, Yung C, Chawla B, Wu C, Kushnerick JD, Olmstead WN, Determination of structural building blocks in heavy petroleum systems by collision-induced dissociation Fourier transform ion cyclotron resonance mass spectrometry. *Anal Chem* 2012, *84*, (10), 4544–4551. DOI: 10.1021/ac300544s
[155] Schulz F, Maillard J, Kaiser K, Schmitz-Afonso I, Gautier T, Afonso C, Carrasco N, Gross L, Imaging Titan's organic haze at atomic scale. *Astrophys J* 2021, *908*, (1), L13. DOI: 10.3847/2041-8213/abd93e
[156] Treibs A, Organic minerals. III. Chlorophyll and hemin derivatives in bituminous rocks, petroleums, mineral waxes and asphalts. Origin of petroleum. *Justus Liebigs Ann Chem* 1934, *510*, 42–62.
[157] Smith WE, Horne OJ Jr., Napier B Jr. *Characterization and reproducibility of petroleum pitches*; United States,1974-03-01, **1974**.
[158] Dickinson EM, Structural analysis of petroleum fractions by proton and carbon-13 NMR spectroscopy. *Ext Abstr Program - Bienn Conf Carbon* 1979, *14*, 417–418.
[159] Dickinson EM, Structural comparison of petroleum fractions using proton and 13C n.m.r. spectroscopy. *Fuel* 1980, *59*, (5), 290–294. DOI:https://doi.org/10.1016/0016-2361(80)90211-2
[160] Dickinson EM, Average structures of petroleum pitch fractions by proton/carbon-13 NMR spectroscopy. *Fuel* 1985, *64*, (5), 704–706. DOI:10.1016/0016-2361(85)90058-4
[161] Kershaw JR, Black KJT, Structural characterization of coal-tar and petroleum pitches. *Energy Fuels* 1993, *7*, (3), 420–425. DOI: 10.1021/ef00039a014

[162] Burgess WA, Thies MC, Molecular structures for the oligomeric constituents of petroleum pitch. *Carbon* 2011, *49*, (2), 636–651. DOI: https://doi.org/10.1016/j.carbon.2010.10.011
[163] Hutchenson KW, Roebers JR, Thies MC, Fractionation of petroleum pitch with supercritical toluene. *J Supercrit Fluids* 1991, *4*, (1), 7–14. DOI:https://doi.org/10.1016/0896-8446(91)90025-2
[164] Edwards WF, Jin L, Thies MC, MALDI-TOF mass spectrometry: Obtaining reliable mass spectra for insoluble carbonaceous pitches. *Carbon* 2003, *41*, (14), 2761–2768. DOI:https://doi.org/10.1016/S0008-6223(03)00386-5
[165] Burgess WA, Pittman JJ, Marcus RK, Thies MC, Structural identification of the monomeric constituents of petroleum pitch. *Energy Fuels* 2010, *24*, (8), 4301–4311. DOI: 10.1021/ef1002556
[166] Fatayer S, Poddar NB, Quiroga S, Schulz F, Schuler B, Kalpathy SV, Meyer G, Perez D, Guitian E, Pena D, Wornat MJ, Gross L, Atomic force microscopy identifying fuel pyrolysis products and directing the synthesis of analytical standards. *J Am Chem Soc* 2018, *140*, (26), 8156–8161. DOI: 10.1021/jacs.8b02525
[167] Commodo M, Kaiser K, De Falco G, Minutolo P, Schulz F, D'Anna A, Gross L, On the early stages of soot formation: Molecular structure elucidation by high-resolution atomic force microscopy. *Combust Flame* 2019, *205*, 154–164. DOI: https://doi.org/10.1016/j.combustflame.2019.03.042
[168] Schulz F, Commodo M, Kaiser K, De Falco G, Minutolo P, Meyer G, D`Anna A, Gross L, Insights into incipient soot formation by atomic force microscopy. *Proc Combust Inst* 2019, *37*, (1), 885–892. DOI: https://doi.org/10.1016/j.proci.2018.06.100
[169] Fatayer S, Coppola AI, Schulz F, Walker BD, Broek TA, Meyer G, Druffel ERM, McCarthy M, Gross L, Direct visualization of individual aromatic compound structures in low molecular weight marine dissolved organic carbon. *Geophys Res Lett* 2018, *45*, (11), 5590–5598. DOI: 10.1029/2018gl077457
[170] Panda SK, Andersson JT, Schrader W, Characterization of supercomplex crude oil mixtures: what is really in there? *Angew Chem Int Ed*. 2009, *48*, (10), 1788–1791. DOI: 10.1002/anie.200803403
[171] Rodgers RP, Mapolelo MM, Robbins WK, Chacón-Patiño ML, Putman JC, Niles SF, Rowland SM, Marshall AG, Combating selective ionization in the high resolution mass spectral characterization of complex mixtures. *Faraday Discuss*. 2019, *218*, (0), 29–51. DOI: 10.1039/C9FD00005D
[172] Ruiz-Morales Y, Mullins OC, Singlet–triplet and triplet–triplet transitions of asphaltene PAHs by molecular orbital calculations. *Energy Fuels* 2013, *27*, (9), 5017–5028. https://doi.org/10.1021/ef400168a
[173] Alvarez-Ramírez F, Ruiz-Morales Y, Island versus archipelago architecture for asphaltenes: polycyclic aromatic hydrocarbon dimer theoretical studies. *Energy Fuels* 2013, *27*, (4), 1791–1808. https://doi.org/10.1021/ef301522m
[174] Ruiz-Morales Y, Miranda-Olvera AD, Portales-Martínez BN, Domínguez J, Experimental and theoretical approach to determine the average asphaltene structure of a crude oil from the Golden Lane (Faja de Oro) of Mexico. *Energy Fuels* 2020, *34*, (7), 7985–8006. https://doi.org/10.1021/acs.energyfuels.0c00593
[175] Bergmann U, Mullins OC, Cramer S, X-ray Raman spectroscopy of carbon in asphaltene: light element characterization with bulk sensitivity. *Anal Chem* 2000, *72*, (11), 2609–2612. https://doi.org/10.1021/ac990730t
[176] Bergmann U, Groenzin H, Mullins OC, Glatzel P, Fetzer J, Cramer S, Carbon K-edge X-ray Raman spectroscopy supports simple, yet powerful description of aromatic hydrocarbons

and asphaltenes. *Chem Phys Lett* 2003, *369*, (1-2), 184–191. https://doi.org/10.1016/S0009-2614(02)02003-1

[177] Gutman I, Ruiz-Morales Y, Note on the Y-rule in Clar theory. *Polycycl Aromat Compd* 2007, *27*, (1), 41–49.

[178] Ruiz-Morales Y, Aromaticity in pericondensed cyclopenta-fused polycyclic aromatic hydrocarbons determined by density functional theory nucleus-independent chemical shifts and the Y-rule—Implications in oil asphaltene stability. *Can J Chem* 2009, *87*, (10), 1280–1295.

[179] Ona-Ruales JO, Ruiz-Morales Y, Extended Y-rule method for the characterization of the aromatic sextets in cata-condensed polycyclic aromatic hydrocarbons. *J Phys Chem A* 2014, *118*, (51), 12262–12273. DOI: 10.1021/jp510180j

[180] Solà M, Connecting and combining rules of aromaticity. Towards a unified theory of aromaticity. *WIREs Comput Mol Sci* 2019, *9*, (4), e1404. DOI: https://doi.org/10.1002/wcms.1404

[181] Ruiz-Morales Y, Miranda-Olvera AD, Portales-Martínez BN, Domínguez JM, Determination of 13C NMR Chemical Shift Structural Ranges for Polycyclic Aromatic Hydrocarbons (PAHs) and PAHs in Asphaltenes: An Experimental and Theoretical Density Functional Theory Study. *Energy Fuels* 2019, *33*, (9), 7950–7970. DOI: 10.1021/acs.energyfuels.9b00182

[182] Pan Y, Liao Y, Sun Y, The characteristics of bound biomarkers released from asphaltenes in a sequence of naturally biodegraded oils. *Org Geochem* 2017, *111*, 56–66. DOI: https://doi.org/10.1016/j.orggeochem.2017.06.007

[183] Peters KE, Walters CC, Moldowan JM, *The Biomarker Guide*. 2 ed.; Cambridge University Press: Cambridge, 2005; Vol. 1.

[184] Schuler B, Zhang Y, Collazos S, Fatayer S, Meyer G, Pérez D, Guitián E, Harper MR, Kushnerick JD, Pena D, Characterizing aliphatic moieties in hydrocarbons with atomic force microscopy. *Chem Sci* 2017, *8*, (3), 2315–2320.

[185] Wang Z, Stout SA, Fingas M, Forensic Fingerprinting of Biomarkers for Oil Spill Characterization and Source Identification. *Environ Forensic* 2006, *7*, (2), 105–146. DOI: 10.1080/15275920600667104

[186] Zhang Y, Schuler B, Fatayer S, Gross L, Harper MR, Kushnerick JD, Understanding the Effects of Sample Preparation on the Chemical Structures of Petroleum Imaged with Noncontact Atomic Force Microscopy. *Ind Eng Chem Res* 2018, *57*, (46), 15935–15941. DOI: 10.1021/acs.iecr.8b03962

[187] Ebeling D, Šekutor M, Stiefermann M, Tschakert J, Dahl JEP, Carlson RMK, Schirmeisen A, Schreiner PR, Assigning the absolute configuration of single aliphatic molecules by visual inspection. *Nat Commun* 2018, *9*, (1), 2420. DOI: 10.1038/s41467-018-04843-z

[188] Chacón-Patiño ML, Rowland SM, Rodgers RP, Advances in Asphaltene Petroleomics. Part 3. Dominance of island or archipelago structural motif is sample dependent. *Energy Fuels* 2018, *32*, (9), 9106–9120.

[189] Chacón-Patiño ML, Rowland SM, Rodgers RP, Advances in asphaltene petroleomics. Part 2: selective separation method that reveals fractions enriched in island and archipelago structural motifs by mass spectrometry. *Energy Fuels* 2018, *32*, (1), 314–328.

[190] Chacón-Patiño ML, Rowland SM, Rodgers RP, Advances in asphaltene petroleomics. part 1: asphaltenes are composed of abundant island and archipelago structural motifs. *Energy Fuels* 2017, *31*, (12), 13509–13518.

[191] Hughey CA, Rodgers RP, Marshall AG, Resolution of 11 000 compositionally distinct components in a single electrospray ionization Fourier transform ion cyclotron resonance mass spectrum of crude oil. *Anal Chem*. 2002, *74*, (16), 4145–4149.

[192] Kew W, Blackburn JW, Uhrín DA, Response to comment on "laser desorption/ionization coupled to FTICR mass spectrometry for studies of natural organic matter". *Anal Chem*. 2018, *90*, (9), 5968–5971.
[193] Zhao X, Xu C, Shi Q, Porphyrins in heavy petroleums: a review. *Struct Model Complex Petr Mix* 2015, 39–70.
[194] Qian K, Edwards KE, Mennito AS, Walters CC, Kushnerick JD, Enrichment, Resolution, and Identification of Nickel Porphyrins in Petroleum Asphaltenes by Cyclograph Separation and Atmospheric Pressure Photoionization Fourier Transform Ion Cyclotron Resonance Mass Spectrometry. *Anal Chem* 2010, *82*, 413–419.
[195] McKenna AM, Purcell JM, Rodgers RP, Marshall AG, Identification of vanadyl porphyrins in a heavy crude oil and raw asphaltene by atmospheric pressure photoionization Fourier transform ion cyclotron resonance (FT-ICR) mass spectrometry. *Energy Fuels* 2009, *23*, (4), 2122–2128.
[196] DiMarzio JM, Georgiev SV, Stein HJ, Hannah JL, Residency of rhenium and osmium in a heavy crude oil. *Geochim Cosmochim Acta* 2018, *220*, 180. DOI: 10.1016/j.gca.2017.09.038
[197] Selby D, Creaser RA, Re–Os geochronology of organic rich sediments: an evaluation of organic matter analysis methods. *Chem Geol* 2003, *200*, (3-4), 225–240.
[198] Selby D, Creaser RA, Direct radiometric dating of hydrocarbon deposits using rhenium-osmium isotopes. *Science* 2005, *308*, (5726), 1293–1295.
[199] Georgiev SV, Stein HJ, Hannah JL, Di Primio R, Timing and origin of multiple petroleum charges in the Solveig oil field, Norwegian North Sea: A rhenium-osmium isotopic study. *Am Assoc Pet Geol Bull* 2021, *105*, (1), 109–134.
[200] Mapolelo MM, Rodgers RP, Blakney GT, Yen AT, Asomaning S, Marshall AG, Characterization of naphthenic acids in crude oils and naphthenates by electrospray ionization FT-ICR mass spectrometry. *Int J Mass Spectrom* 2011, *300*, (2), 149–157. DOI: https://doi.org/10.1016/j.ijms.2010.06.005
[201] Meredith W, Kelland SJ, Jones DM, Influence of biodegradation on crude oil acidity and carboxylic acid composition. *Org Geochem* 2000, *31*, (11), 1059–1073. DOI:https://doi.org/10.1016/S0146-6380(00)00136-4
[202] Simon S, Gao B, Tofte S, Sjöblom J, Passade-Boupat N, Palermo T, Rondon-Gonzalez M, Influence of Asphaltenes on Gelation of Tetrameric Acid with Calcium Ion at the Oil/Water Interface under Flow-Model Condition. *Energy Fuels* 2020, *34*, (5), 5846–5855. DOI: 10.1021/acs.energyfuels.0c00829
[203] Eke WI, Victor-Oji C, Akaranta O, Oilfield metal naphthenate formation and mitigation measures: a review. *J Pet Explor Prod Technol* 2020, *10*, (2), 805–819. DOI: 10.1007/s13202-019-00797-0
[204] Maqbool T, Raha S, Hoepfner MP, Fogler HS, Modeling the aggregation of asphaltene nanoaggregates in crude oil– precipitant systems. *Energy Fuels* 2011, *25*, (4), 1585–1596.
[205] Fávero CVB, Maqbool T, Hoepfner M, Haji-Akbari N, Fogler HS, Revisiting the flocculation kinetics of destabilized asphaltenes. *Adv Colloid Interface Sci* 2017, *244*, 267–280.
[206] Yang Y, Chaisoontornyotin W, Hoepfner MP, Structure of Asphaltenes during Precipitation Investigated by Ultra-Small-Angle X-ray Scattering. *Langmuir* 2018, *34*, (35), 10371–10380. DOI: 10.1021/acs.langmuir.8b01873
[207] Hoepfner MP, Fogler HS, Multiscale scattering investigations of asphaltene cluster breakup, nanoaggregate dissociation, and molecular ordering. *Langmuir: ACS J Surf Colloids* 2013, *29*, (49), 15423–15432. DOI: 10.1021/la403531w
[208] Goncalves S, Castillo J, Fernández A, Hung J, Absorbance and fluorescence spectroscopy on the aggregation behavior of asphaltene–toluene solutions. *Fuel* 2004, *83*, (13), 1823–1828. DOI: https://doi.org/10.1016/j.fuel.2004.03.009

[209] Goual L, Sedghi M, Zeng H, Mostowfi F, McFarlane R, Mullins OC, On the formation and properties of asphaltene nanoaggregates and clusters by DC-conductivity and centrifugation. *Fuel* 2011, *90*, (7), 2480–2490.
[210] Zeng H, Song Y-Q, Johnson DL, Mullins OC, Critical nanoaggregate concentration of asphaltenes by direct-current (DC) electrical conductivity. *Energy Fuels* 2009, *23*, 1201–1208.
[211] Goual L, Sedghi M, Mostowfi F, McFarlane R, Pomerantz AE, Saraji S, Mullins OC, Cluster of asphaltene nanoaggregates by DC conductivity and centrifugation. *Energy Fuels* 2014, *28*, (8), 5002–5013. DOI: 10.1021/ef5010682
[212] Almgren M, Lo J-E, Determination of micelle aggregation numbers and micelle fluidities from time-resolved fluorescence quenching studies. *J Colloid Interface Sci* 1981, *81*, (2), 486–499.
[213] Chatterjee A, Moulik S, Sanyal S, Mishra B, Puri P, Thermodynamics of micelle formation of ionic surfactants: a critical assessment for sodium dodecyl sulfate, cetyl pyridinium chloride and dioctyl sulfosuccinate (Na Salt) by microcalorimetric, conductometric, and tensiometric measurements. *J Phys Chem B - J Phys Chem B* 2001, *105*. DOI: 10.1021/jp0123029
[214] Mullins OC, Betancourt SS, Cribbs ME, Dubost FX, Creek JL, Andrews AB, Venkataramanan L, The collodial structure of crude oil and the structure of oil reservoirs. *Energy Fuels* 2007, *21*, 2785–2794.
[215] Betancourt SS, Ventura GT, Pomerantz AE, Viloria O, Dubost FX, Zuo J, Monson G, Bustamante D, Purcell JM, Nelson RK, Nanoaggregates of asphaltenes in a reservoir crude oil and reservoir connectivity. *Energy Fuels* 2009, *23*, (3), 1178–1188.
[216] Chen L-J, Lin S-Y, Huang -C-C, Chen E-M, Temperature dependence of critical micelle concentration of polyoxyethylenated non-ionic surfactants. *Colloids Surf A Physicochem Eng Asp* 1998, *135*, (1), 175–181. DOI:https://doi.org/10.1016/S0927-7757(97)00238-0
[217] Turro NJ, Yekta A, Luminescent probes for detergent solutions. A simple procedure for determination of the mean aggregation number of micelles. *J Am Chem Soc* 1978, *100*, (18), 5951–5952. DOI: 10.1021/ja00486a062
[218] Opatowski E, Kozlov MM, Pinchuk I, Lichtenberg D, Heat evolution of micelle formation, dependence of enthalpy, and heat capacity on the surfactant chain length and head group. *J Colloid Interface Sci* 2002, *246*, (2), 380–386. DOI: 10.1006/jcis.2001.8050
[219] Volpe PLO, Filho EAS, Calorimetric study of SDS micelle formation in water and in NaCl solution at 298 K. *Thermochim Acta* 1995, *257*, 59–66. DOI:https://doi.org/10.1016/0040-6031(94)02208-6
[220] Sharma A, Groenzin H, Tomita A, Mullins OC, Probing order in asphaltenes and aromatic ring systems by HRTEM. *Energy Fuels* 2002, *16*, 490–496.
[221] Redelius PG, Solubility parameters and bitumen. *Fuel* 2000, *79*, 27–35.
[222] Eyssautier J, Levitz P, Espinat D, Jestin J, Gummel J, Grillo I, Barre L, Insight into asphaltene nanoaggregate structure inferred by small angle neutron and X-ray scattering. *J Phys Chem B* 2011, *115*, (21), 6827–6837. DOI: 10.1021/jp111468d
[223] Eyssautier J, Hénaut I, Levitz P, Espinat D, Barré L, Organization of asphaltenes in a vacuum residue: a small-angle X-ray scattering (SAXS)–viscosity approach at high temperatures. *Energy Fuels* 2012, *26*, (5), 2696–2704. DOI: 10.1021/ef201412j
[224] Eyssautier J, Espinat D, Gummel J, Levitz P, Becerra M, Shaw J, Barré L, Mesoscale organization in a physically separated vacuum residue: comparison to asphaltenes in a simple solvent. *Energy Fuels* 2012, *26*, (5), 2680–2687. DOI: 10.1021/ef201411r
[225] Bake KD, Craddock PR, Bolin TB, Abdallah W, Mitra-Kirtley S, Andrews AB, Mullins OC, Pomerantz AE, Structure-solubility relationships in coal, petroleum, and immature source-rock-derived asphaltenes. *Energy Fuels* 2020, 10.1021/acs.energyfuels.0c01960. DOI: 10.1021/acs.energyfuels.0c01960

[226] Wang W, Taylor C, Hu H, Humphries KL, Jaini A, Kitimet M, Scott T, Stewart Z, Ulep KJ, Houck S, Luxon A, Zhang B, Miller B, Parish CA, Pomerantz AE, Mullins OC, Zare RN, Nanoaggregates of diverse asphaltenes by mass spectrometry and molecular dynamics. *Energy Fuels* 2017, *31*, (9), 9140–9151. DOI: 10.1021/acs.energyfuels.7b01420
[227] Mullins OC, Seifert DJ, Zuo JY, Zeybek M, Clusters of Asphaltene Nanoaggregates Observed in Oilfield Reservoirs. *Energy Fuels* 2013, *27*, (4), 1752–1761. DOI: 10.1021/ef301338q
[228] Mishra VK, Zuo JY, Dumont H, Mullins OC In *Permeable tar mat formation described within context of novel asphaltene science*, SPE Kuwait international petroleum conference and exhibition, SPE 163292, KIPCE, Kuwait **2012**.
[229] Seifert DJ, Zeybek M, Dong C, Zuo JY, Mullins OC In *Black oil, heavy oil and tar in one oil column understood by simple asphaltene nanoscience*, Abu Dhabi International Petroleum Conference and Exhibition, SPE 161144, Society of Petroleum Engineers: **2012**.
[230] Mullins OC, Pomerantz AE, Zuo JY, Andrews AB, Hammond PS, Dong C, Elshahawi H, Seifert DJ, Rane JP, In BS *Asphaltene nanoscience and reservoir fluid gradients, tar mat formation and the oil-water interface*, SPE Annual Technical Conference and Exhibition, SPE 166278, Society of Petroleum Engineers: **2013**.
[231] Anisimov M, Yudin I, Nikitin V, Nikolaenko G, Chernoutsan A, Toulhoat H, Frot D, Briolant Y, Asphaltene aggregation in hydrocarbon solutions studied by photon correlation spectroscopy. *J Phys Chem* 1995, *99*, (23), 9576–9580.
[232] Yudin IK, Anisimov MA, Dynamic light scattering monitoring of asphaltene aggregation in crude oils and hydrocarbon solutions. In *Asphaltenes, Heavy Oils, and Petroleomics*, Springer: 2007, pp 439–468.
[233] Sander LM, Diffusion-limited aggregation: a kinetic critical phenomenon? *Contempo Phys* 2000, *41*, (4), 203–218.
[234] Lin MY, Lindsay HM, Weitz DA, Ball RC, Klein R, Meakin P, Universality in colloid aggregation. *Nature* 1989, *339*, 360–362.
[235] Lin M, Lindsay H, Weitz D, Ball R, Klein R, Meakin P, Universal reaction-limited colloid aggregation. *Physical review A* 1990, *41*, (4), 2005.
[236] Weitz DA, Oliveria M, Fractal structures formed by kinetic aggregation of aqueous gold colloids. *Phys Rev Lett* 1984, *52*, (16), 1433–1436. DOI: 10.1103/PhysRevLett.52.1433
[237] Halsey TC, Diffusion-limited aggregation: a model for pattern formation. *Phys Today* 2000, *53*, (11), 36–41.
[238] González AE, Martínez-López F, Moncho-Jordá A, Hidalgo-Alvarez R, Two-dimensional colloidal aggregation: concentration effects. *J Colloid Interface Sci* 2002, *246*, (2), 227–234. DOI: 10.1006/jcis.2001.7973
[239] Jungblut S, Joswig J-O, Eychmüller A, Diffusion- and reaction-limited cluster aggregation revisited. *Phys Chem Chem Phys* 2019, *21*, (10), 5723–5729. DOI: 10.1039/C9CP00549H
[240] Mullins WW, Sekerka RF, Morphological stability of a particle growing by diffusion or heat flow. *J Appl Phys* 1963, *34*, (2), 323–329.
[241] Korb JP, Louis-Joseph A, Benamsili L, Probing structure and dynamics of bulk and confined crude oils by multiscale NMR spectroscopy, diffusometry, and relaxometry. *J Phys Chem B* 2013, *117*, (23), 7002–7014. DOI: 10.1021/jp311910t
[242] Freed DE, Mullins OC, Zuo JY, Theoretical treatment of asphaltene gradients in the presence of GOR gradients. *Energy Fuels* 2010, *24*, (7), 3942–3949. DOI: 10.1021/ef1001056
[243] Zuo JY, Mullins OC, Freed D, Elshahawi H, Dong C, Seifert DJ, Advances in the Flory–Huggins–Zuo equation of state for asphaltene gradients and formation evaluation. *Energy Fuels* **2013**, *27*, 1722-1735. DOI: 10.1021/ef301239h

[244] Pomerantz AE, Seifert DJ, Bake KD, Craddock PR, Mullins OC, Kodalen BG, Mitra-Kirtley S, Bolin TB, Sulfur chemistry of asphaltenes from a highly compositionally graded oil column. *Energy Fuels* 2013, *27*, (8), 4604–4608. DOI: 10.1021/ef400773f
[245] Chen L, Meyer J, Campbell T, Canas J, Betancourt SS, Dumont H, Forsythe JC, Mehay S, Kimball S, Hall DL, Applicability of simple asphaltene thermodynamics for asphaltene gradients in oilfield reservoirs: The Flory-Huggins-Zuo Equation of State with the Yen-Mullins model. *Fuel* 2018, *221*, 216–232.
[246] Hansen CM, *Hansen solubility parameters: a user's handbook*. CRC press: **2002**.
[247] Acevedo SC, Castro A, Vásquez E, Marcano F, Ranaudo MAA, Investigation of physical chemistry properties of asphaltenes using solubility parameters of asphaltenes and their fractions A1 and A2. *Energy Fuels* 2010, *24*, (11), 5921–5933. DOI: 10.1021/ef1005786
[248] Freed DE, Mullins OC, Zuo JY, Heuristics for equilibrium distributions of asphaltenes in the presence of GOR gradients. *Energy Fuels* 2014, *28*, (8), 4859–4869. DOI: 10.1021/ef500680v
[249] Buckley JS, Wang J, Creek JL, Solubility of the least-soluble asphaltenes. In: *Asphaltenes, Heavy Oils, and Petroleomics*, Mullins OC, Sheu EY, Hammami A, Marshall AG, Eds. Springer: New York, 2007, pp 401–438.
[250] Gonzalez DL, Ting PD, Hirasaki GJ, Chapman WG, Prediction of asphaltene instability under gas injection with the PC-SAFT equation of state. *Energy Fuels* 2005, *19*, (4), 1230–1234. DOI: 10.1021/ef049782y
[251] Vargas FM, Gonzalez DL, Creek JL, Wang J, Buckley J, Hirasaki GJ, Chapman WG, Development of a general method for modeling asphaltene stability. *Energy Fuels* 2009, *23*, (3), 1147–1154. DOI: 10.1021/ef800666j
[252] Panuganti SR, Vargas FM, Chapman WG, Modeling reservoir connectivity and tar mat using gravity-induced asphaltene compositional grading. *Energy Fuels* 2012, *26*, (5), 2548–2557. DOI: 10.1021/ef201280d
[253] Abutaqiya MIL, Sisco CJ, Khemka Y, Safa MA, Ghloum EF, Rashed AM, Gharbi R, Santhanagopalan S, Al-Qahtani M, Al-Kandari E, Vargas FM, Accurate modeling of asphaltene onset pressure in crude oils under gas injection using Peng–Robinson equation of state. *Energy Fuels* 2020, *34*, (4), 4055–4070. DOI: 10.1021/acs.energyfuels.9b04030
[254] Rane JP, Harbottle D, Pauchard V, Couzis A, Banerjee S, Adsorption kinetics of asphaltenes at the oil-water interface and nanoaggregation in the bulk. *Langmuir: ACS J Surf Colloids* 2012, *28*, (26), 9986–9995. DOI: 10.1021/la301423c
[255] Langevin D, Argillier J-F, Interfacial behavior of asphaltenes. *Adv Colloid Interface Sci* 2016, *233*, 83–93. DOI: https://doi.org/10.1016/j.cis.2015.10.005
[256] Cagna A, Esposito G, Quinquis A-S, Langevin D, On the reversibility of asphaltene adsorption at oil-water interfaces. *Colloids Surf A Physicochem Eng Asp* 2018, *548*, 46–53. DOI: https://doi.org/10.1016/j.colsurfa.2018.03.038
[257] Andrews AB, McClelland A, Korkeila O, Demidov A, Krummel A, Mullins OC, Chen Z, Molecular orientation of asphaltenes and PAH model compounds in Langmuir– Blodgett films using sum frequency generation spectroscopy. *Langmuir: ACS J Surf Colloids* 2011, *27*, (10), 6049–6058.
[258] Ruiz-Morales Y, Mullins OC, Coarse-grained molecular simulations to investigate asphaltenes at the oil–water interface. *Energy Fuels* 2015, *29*, (3), 1597–1609. https://doi.org/10.1021/ef502766v
[259] Menger FM, Rizvi SA, Relationship between surface tension and surface coverage. *Langmuir* 2011, *27*, (23), 13975–13977.
[260] Freer E, Radke C, Relaxation of asphaltenes at the toluene/water interface: diffusion exchange and surface rearrangement. *J Adhes* 2004, *80*, (6), 481–496.

[261] Sztukowski DM, Yarranton HW, Rheology of asphaltene– toluene/water interfaces. *Langmuir: ACS J Surf Colloids* 2005, *21*, (25), 11651–11658.
[262] Liu F, Understanding Asphaltenes Adsorption at Liquid-Liquid and Liquid-Solid Interfaces. PhD Thesis CCNY, **2020**.
[263] Liu F, Pauchard V, Banerjee S, Modeling the multicomponent compositional effects of asphaltenes on interfacial phenomena. *Energy Fuels* 2020, *34*, (11), 13673–13685. DOI: 10.1021/acs.energyfuels.0c02421
[264] Daniel RC, Berg JC, A simplified method for predicting the dynamic surface tension of concentrated surfactant solutions. *J Colloid Interface Sci*. 2003, *260*, (1), 244–249.
[265] Stanford LA, Rodgers RP, Marshall AG, Czarnecki J, Wu XA, Compositional characterization of bitumen/water emulsion films by negative- and positive-ion electrospray ionization and field desorption/ionization fourier transform ion cyclotron resonance mass spectrometry. *Energy Fuels* 2007, *21*, (2), 963–972. DOI: 10.1021/ef060291i
[266] Yang F, Tchoukov P, Dettman H, Teklebrhan RB, Liu L, Dabros T, Czarnecki J, Masliyah J, Xu Z, Asphaltene subfractions responsible for stabilizing water-in-crude oil emulsions. Part 2: Molecular representations and molecular dynamics simulations. *Energy Fuels* 2015, *29*, (8), 4783–4794.
[267] Hammami A, Ratulowski J, Precipitation and Deposition of Asphaltenes in Production Systems: A Flow Assurance Overview. 2007, 10.1007/0-387-68903-6_23pp 617–660.
[268] Dumont H, Zuo JY, Mullins OC, Garcia G, Mishra VK, Harrison C, Fukagawa S, Sullivan M, Chen L, Montesinos J. In *Asphaltene and Saturation Pressure Detection with DFA While Pulling out of Hole on Wireline*, SPWLA 57th Annual Logging Symposium, Society of Petrophysicists and Well-Log Analysts: **2016**.
[269] Dumont H, Garcia G, Mullins OC, Nighswander J, Mishra VK, El-Khoury J, Chen L, Lake P. In *Asphaltene Onset Pressure Uncertainty and Other Asphaltene Issues in Field Development Planning*, Offshore Technology Conference, Offshore Technology Conference: **2017**.
[270] Joshi NB, Mullins OC, Jamaluddin A, Creek J, McFadden J, Asphaltene precipitation from live crude oil. *Energy Fuels* 2001, *15*, (4), 979–986.
[271] Hammami A, Phelps CH, Monger-McClure T, Little TM, Asphaltene precipitation from live oils: an experimental investigation of onset conditions and reversibility. *Energy Fuels* 2000, *14*, (1), 14–18. DOI: 10.1021/ef990104z
[272] Pauchard V, Rane JP, Banerjee S, Asphaltene-laden interfaces form soft glassy layers in contraction experiments: a mechanism for coalescence blocking. *Langmuir* 2014, *30*, (43), 12795–12803. DOI: 10.1021/la5028042
[273] Alicke A, Simon S, Sjöblom J, Vermant J, Assessing the interfacial activity of insoluble asphaltene layers: interfacial rheology versus interfacial tension. *Langmuir* 2020, *36*, (49), 14942–14959. DOI: 10.1021/acs.langmuir.0c02234

Oliver C. Mullins, Jesus A Cañas, Soraya S. Betancourt,
Andrew E. Pomerantz

6 Asphaltene equation of state and oilfield reservoirs

Abstract: In general, reservoir crude oils consist of dissolved gases, liquids and dissolved or suspended solids, the asphaltenes. As in all disciplines, thermodynamic modeling is a powerful method to improve efficiencies and understanding. Indeed, application of a modified van der Waals equation of state (EoS) to model the gas and liquid components of crude oil became an immediate success when introduced by Peng and Robinson in 1976. However, thermodynamic modeling of asphaltene gradients in oil reservoirs has only recently been accomplished. The Yen–Mullins model gives the requisite solution to the asphaltene particle size, thus resolving the gravity term, among others, for thermodynamic modeling. A modified polymer solution theory, the Flory–Huggins–Zuo EoS, has been established as the method of choice to model asphaltene gradients in reservoirs. One powerful benefit to this approach is the small number of adjustable parameters, in some cases, no adjustable parameters, to model oilfield asphaltene gradients. This modeling is powerful for understanding wide-ranging issues such as viscous oil and viscosity gradients, tar mats, aquifer support, reservoir connectivity, and asphaltene onset pressure as many oilfield case studies establish. In addition, this newly developed ability to identify equilibrium versus nonequilibrium distributions of reservoir fluids has enabled the development of a new technical discipline, "reservoir fluid geodynamics" (RFG) which fulfills the sole missing component of modeling and understanding the evolution of reservoirs over geologic time. The resulting comprehensive rock and fluid geodynamic approach represents a powerful, new methodology to address oilfield reservoirs.

6.1 Introduction

Thermodynamic modeling is ubiquitously used in a wide variety of disciplines for a plethora of objectives. Correspondingly, when modifications to the van der Waals EoS were introduced to treat the gas and liquid components in crude oils by Peng and Robinson [1], all manners of applications followed. Other variants of this approach have been introduced and are referred to as cubic equations of state (EoS). Virtually all compositional reservoir simulators use a cubic EoS for predicting

Oliver C. Mullins, Jesus A Cañas, Soraya S. Betancourt, Andrew E. Pomerantz, Schlumberger-Doll Research

https://doi.org/10.1515/9783110694529-006

phase behavior and compositional gradients. The general approach for modeling crude oils is to use some form of lumping of components generating pseudo-components with corresponding parameters. Asphaltenes have been treated using these methods; however, using a variant of the ideal gas law, the cubic EoS, to treat solids is less than ideal. Moreover, this approach does not account for asphaltene molecular and colloidal structure in crude oils which is required if there is to be a first principles approach to resolving the gravity term and other terms in thermodynamic modeling of fluid gradients. In addition, many reservoirs contain fluids that are not in thermodynamic equilibrium [2]. Instead, thermodynamic modeling must be employed to determine whether the fluids are equilibrated. Cubic EoS methods generally are not capable of making this assessment. The gradients of solution gas or gas-oil ratio (GOR) are too small, the errors in determining GOR are too big, and the cubic EoS has too many parameters for determining whether reservoir fluids are equilibrated. Likewise, geochemical methods are also generally not sufficient to make this assessment [2]. There is no thermodynamics attached to traditional geochemical methods of crude oil evaluation. In addition, ratios of nearly equivalent biomarkers are frequently used for example such as the hopanes Ts and Tm, and these ratios are invariant at equilibrium [3]. Measurement of homogeneity of a trace parameter with unknown initial conditions does not provide the extent of disequilibrium.

Modeling of phase behavior of asphaltenes is far more sensitive to the variations of solution properties than asphaltene chemistry; thus, the more traditional cubic EoS approaches to modeling asphaltene phase behavior have had some successes. Nevertheless, for addressing reservoir concerns, it is far more important to address asphaltene gradients than partially addressing the modeling of phase behavior. For example, in an industry wide study of 28 Gulf of Mexico reservoirs, 75% of reservoirs underperformed in production rates and/or overall recovery; the number one culprit in this underperformance was unrecognized compartmentalization [4]. The ability to determine equilibrium of reservoir fluids through EoS modeling of asphaltene gradients provides a powerful new approach to address this enormous reservoir concern [2, 5–12]. Naturally, modeling of asphaltene gradients through asphaltene EoS modeling can account for viscosity gradients, another huge reservoir concern [2, 5, 9, 13–20], since crude oil viscosity depends so strongly on asphaltene content, even more than exponential, once asphaltene content exceeds a few percent [21]. These methods work for reservoirs that are not in equilibrium when diffusive processes can be identified and modeled [2, 16, 22–25]. Great insights to tar mat formation, thus potential aquifer support, can also be obtained from asphaltene gradient analysis [2, 13, 14, 24–29].

6.2 Asphaltene gradient thermodynamic treatment

6.2.1 Asphaltene nanostructures

Chapter 5 reviews many significant developments that have resolved major uncertainties in asphaltene science and shows examples of how the understanding of asphaltene structures gives rise to tremendous improvements in modeling and understanding of asphaltene behavior. The Yen–Mullins model captures many of these advances and provides centroids of the structures which are required for thermodynamic modeling of reservoir crude oils where gravity plays such an important role [30, 31]. That is, the size of asphaltene molecules and nanocolloids is required; otherwise, the gravity term is indeterminant. This chapter starts with the Yen–Mullins model (cf. Figure 6.1) as a foundation for the thermodynamics modeling of asphaltene gradients in reservoir crude oils.

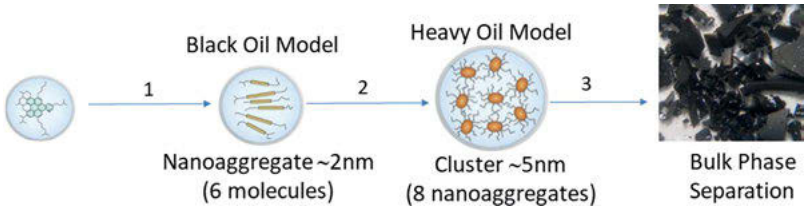

Figure 6.1: The Yen–Mullins model of asphaltenes consists of centroids or most probable structures for molecules and the hierarchical nanocolloidal species, nanoaggregates, and clusters [30, 31]. This model accounts for three solubility thresholds, not just one. For low concentration such as in light crude oils, asphaltenes are dispersed as molecules. For moderate asphaltene concentrations such as in black oils, asphaltenes are dispersed as nanoaggregates. For high asphaltene concentrations such as in heavy oils, asphaltenes are dispersed as clusters.

6.2.2 Asphaltene gradient theory

Utilizing the size from the Yen–Mullins, standard polymer solution theory, the Flory–Huggins theory, can be utilized for developing an equation of state for modeling asphaltene gradients [16, 17, 19]. The Flory–Huggins theory has previously been used to account for asphaltene solubility and phase behavior [32]. By adding the gravity term, eq. (6.1), the Flory–Huggins–Zuo (FHZ) EoS, is obtained [16, 17, 19]. The ratio of asphaltene content is expressed as a ratio of optical density (OD) at two heights, h_i, in the reservoir:

$$\frac{\mathrm{OD}(h_2)}{\mathrm{OD}(h_1)} = \exp\left(\frac{v_a g \Delta\rho (h_2 - h_1)}{\mathrm{RT}} + \left(\frac{v_a}{v}\right)_{h_2} - \left(\frac{v_a}{v}\right)_{h_1} - \frac{v_a\left[(\delta_a - \delta)^2_{h_2} - (\delta_a - \delta)^2_{h_1}\right]}{\mathrm{RT}}\right) \quad (6.1)$$

where v_a and v are the molar volume of the asphaltene species and oil respectively, g is earth's gravity, $\Delta\rho$ is the density difference between the oil and asphaltenes, R is the ideal gas constant, T is temperature, δ_a and δ are the Hildebrand solubility parameters of the asphaltene species and oil respectively. The Flory–Huggins theory is well suited for oilfield applications in that there are few adjustable parameters. In particular, there is one chemical interaction parameter for the solute and one chemical interaction parameters for the solvent, the respective Hildebrand solubility parameters. As described in Chapter 5, the Hildebrand solubility parameter can be expressed in terms of three constituent Hansen solubility parameters accounting for polarizability, polarity, and hydrogen bonding. Nevertheless, because the crude oil solvent and even the asphaltenes, albeit to a lesser degree, are dominated by the polarizability term, then the Hildebrand parameter can be used for asphaltene gradient modeling without the need for inclusion of additional parameters.

6.2.3 Asphaltene gradient measurement

Equation (6.1) shows the asphaltene gradients are measured in oilfield reservoirs by measuring the "oil color" or optical density (OD) at a suitable wavelength and at different heights h_i in the reservoir. Optical density OD = $-\log(I/I_o)$, where I_o is the incident light intensity and I is the transmitted light intensity as shown in the inset in Figure 6.2.

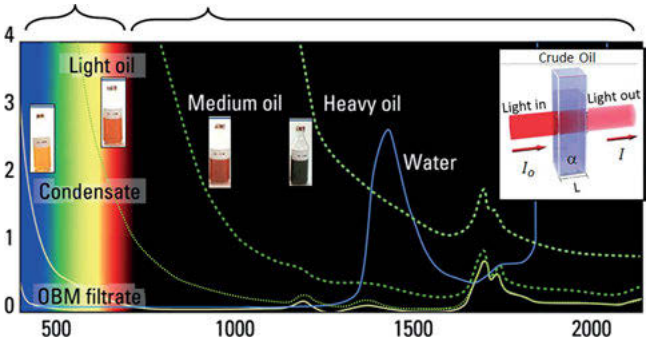

Figure 6.2: Optical spectra of various dead crude oils and water. There are huge differences in the coloration of the different oils depending on asphaltene content [33, 34] and oil based mud (OBM) filtrate. Specific oilfield tools can extract formation fluids from permeable zones and measure the visible-near-infrared spectrum [33]. By performing this spectral measurement at various points in the reservoir, vertical and lateral fluid gradients are determined.

The monotonically increasing absorption at shorter wavelengths of the spectra in Figure 6.2 corresponds to electronics transitions of asphaltenes and other aromatic molecules [35–40]. These electronic absorption bands display the Urbach tail, a result familiar in solid state physics [41, 42]. The discrete peaks in the crude oil spectra are dominated by combination bands and overtones of aliphatic groups; the spectral differences among the methylene, methyl, and methane peaks can be used to obtain the GOR of live crude oils [43–45].

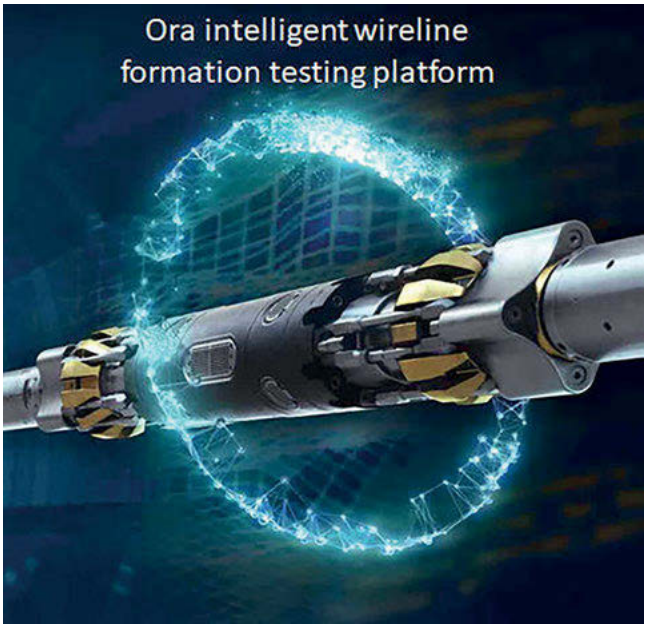

Figure 6.3: The dual-flowline, multiport probe of the Ora intelligent wireline formation testing platform [46]. This new probe allows crude oil sample acquisition in a huge array of borehole conditions.

The acquisition of crude oil samples from subsurface formations is critically important for designing production strategies and facilities especially in the exploration and appraisal phases of reservoir exploitation. Wireline tools such as the Ora platform in Figure 6.3 descend in the well to the target zone prior to installation of casing at this zone to acquire samples under environmental extremes of 35,000 psi pressures and 200 °C temperatures. The size of the tool cannot get too large in order to minimize risk of tool sticking in wells that can exceed 30,000 feet depth. The contained hydrocarbon can vary from tar to natural gas. The rock formation properties can vary from unconsolidated sand to fractured basement, with permeabilities ranging over many orders of magnitude. In addition, at this stage, the borehole contains drilling fluids at pressures greater than formation pressures to prevent blowouts, and the

solids and clay constituents of the drilling fluids set up a “mudcake” on the permeable zones. This must be breached by crude oil sample acquisition tools. Finally, fluid pumping out of the formation and into the wireline tool must proceed long enough to acquire clean formation fluids without OBM filtrate contamination. The Ora platform is the culmination of superior design and execution in this enormously demanding setting [46].

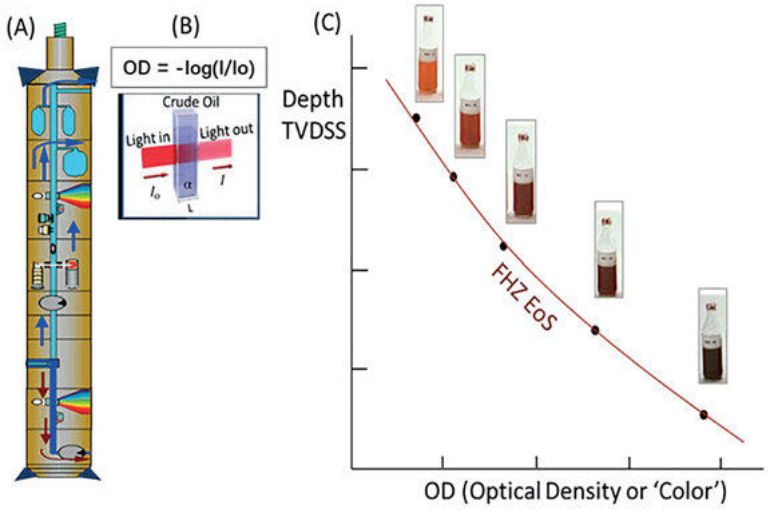

Figure 6.4: Measurement and analysis of asphaltene gradients [47]. (A) A wireline tool with optical spectrometers on board is used to make spectral measurements in situ in oil wells on fluids extracted from permeable formations. The optical density (OD) is measured; in the absence of scattering, the OD is simple the optical absorbances. (C) The OD plotted versus true vertical depth, subsea (TVDSS). These measurements can be within a single well or across a field in multiple wells. The thermodynamic evaluation is dependent only on depth, not on lateral position.

Figure 6.4 shows the essentials of measuring asphaltene gradients. Wireline or possible while-drilling tools with spectrometers are used to provide accurate gradient measurements. The ability to measure the optical spectra of crude oils in situ in oil wells has enabled the characterization of subtle fluid gradients in the reservoir; this capability is referred to as downhole fluid analysis (DFA). First, many systematic errors cancel when measuring fluid gradients in a well with the same tool, same operator, same calibration, same time and same temperature [47]. Second, the crude oil is at its reservoir temperature and pressure and has not undergone any alteration associated with tripping the tool out of the well such as gas evolution and asphaltene instability due to pressure and temperature reduction. Third, any surprising result associated with the spectrum can be checked in real time, as the tool is still in the well. Fourth, obtaining these oilfield samples is associated with a cost, real time analysis is critically important for optimizing efficiency within cost-benefit considerations. Fifth,

oil wells are frequently drilled with oil-based muds (OBM) and some of the filtrate from these muds leaks into permeable formations. Measurements of flowline spectra in the sample acquisition tools as a function of pumping time enables determination of the extent of OBM filtrate contamination [48–50]. For all these reasons, downhole analysis of reservoir fluids is routinely used worldwide.

The asphaltene gradient depicted in Figure 6.4 is shown to represent an equilibrated crude oil column. As such, there is no lateral gradient. The measurement points depicted in Figure 6.4 can be performed within a single well with little lateral distance or can be across a field with lateral extent of tens of kilometers. Indeed, the RFG case studies to date have included this range of lateral displacement in the measurement and analysis of asphaltene gradients. Equation (6.1) has a height dependence but not a lateral dependence. Consequently, a lateral gradient measured in a reservoir indicates some fluid complexity which likely represents disequilibrium [2]. Such lateral gradients can readily occur in reservoirs which have a process occurring in one flank of the reservoir, thus is asymmetric. For example, if the oil reservoir is a tilted sheet and has an oil–water contact in one flank only, then any process such as biodegradation that occurs at the oil–water contact will necessarily introduce lateral gradients which are in disequilibrium [23, 51–53].

6.3 A new discipline: reservoir fluid geodynamics (RFG)

With the development of the FHZ EoS, it is now possibly to determine whether reservoir fluids are equilibrated. Naturally, disequilibrium is now also recognized routinely, and with it, reservoir fluid processes that preclude equilibrium have been catalogued [2]. A collection of these fluid processes constitutes the new technical discipline “reservoir fluid geodynamics” (RFG) [2]. Figure 6.5 frames RFG within common workflows for reservoir evaluation.

For reservoir evaluation, the depositional setting as well as post-deposition alterations of rock formations is always considered. Figure 6.5 depicts a few important depositional settings as well as “structural geodynamics” or post-depositional alterations of rock formations. For example, all structural traps of reservoirs result from structural geodynamics. In contrast, until now, reservoir crude oils had not been subjected to the same degree of rigor. Petroleum systems analysis accounts for trap filling, which is the analogue of deposition. However, there had been little accounting of what happens to reservoir fluids during and post charge (trap filling). With the development of thermodynamic modeling of asphaltene gradients, the evaluation of the evolution of reservoir fluids in geologic time is enabled. Because fluids respond to their container, variations in the reservoir rock structure in geologic time can be recorded in the fluid compositional distribution. Consequently,

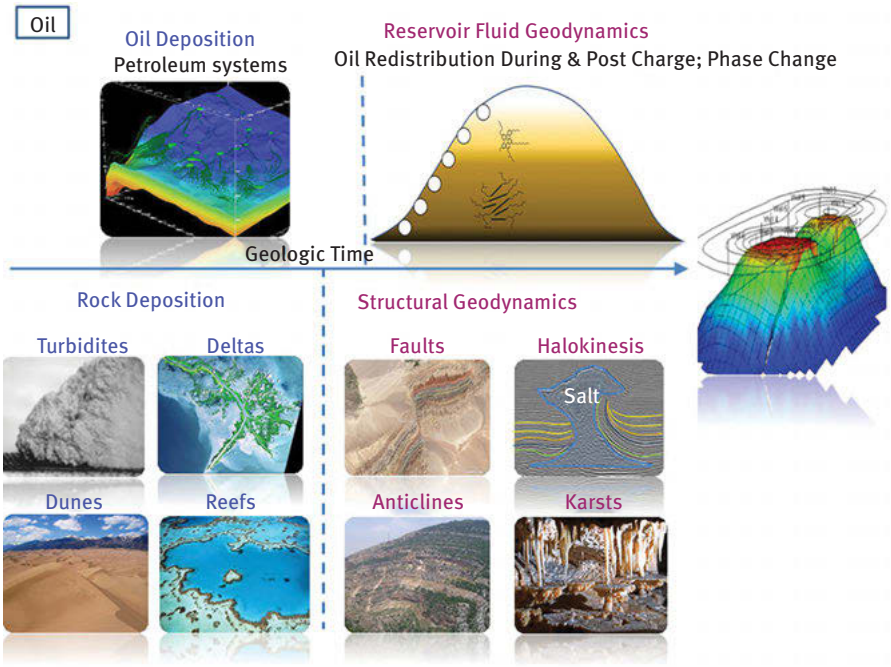

Figure 6.5: In the evaluation of oilfield reservoirs, both the rock depositional setting (lower left) and post-deposition alterations (lower right) are always considered [2, 54–56]. Petroleum systems analysis (upper left) accounts for filling the reservoir with oil among other tasks [57]. The new discipline based on asphaltene thermodynamics, reservoir fluid geodynamics (upper right), accounts for fluid processes acting from trap filling to present day enabling comprehensive reservoir evaluation [2].

the advent of RFG enables a comprehensive fluid geodynamics approach to be employed. Understanding the origins of complexities is a powerful means to elucidate reservoir complexities of the present-day reservoir [2]. The literature is replete with such examples [2, 4, 5, 8, 10, 11, 16, 29, 52, 54, 58–71].

6.4 RFG oilfield case studies; equilibrated reservoir fluids

The application of thermodynamic modeling to determine the extent of equilibrium of reservoir crude oils had not been robustly tested until the development of the FHZ EoS. Indeed, virtually all reservoir simulators presume at the outset that reservoir crude oils are equilibrated. Essentially, this condition has been presumed to mean asphaltene homogeneity in the reservoir. Asphaltene and viscosity gradients

are known in reservoirs, but there was no asphaltene equation of state to use to interpret these gradients. Occasionally, a GOR gradient in reservoir fluids was sufficiently well characterized to enable determination of the extent of equilibration of this gradient [72]. The invention of downhole fluid analysis greatly expanded this capability from the measurement perspective [47]. Nevertheless, GOR gradients are often small, which is generally the case for low GOR oils. In addition, the errors of GOR measurement tend to be large and cubic EoS modeling has too many parameters. The FHZ EoS with constraints provided by the Yen–Mullins model enable determination of the extent of asphaltene equilibration over a wide range of fluids, specifically light oil, black oil and heavy oil with very few, sometimes no adjustable parameters. This is a powerful extension of thermodynamic modeling into reservoir crude oils. Examples of reservoir fluid equilibration follow up to the length scale of 100 km. Obviously, such processes mandate convection, not just diffusion. Consequently, these thermodynamic methods give rise to exacting analysis of mass transport in reservoirs providing increased insight into the fluid history in geologic time [2, 67, 73–76]. Demonstrations of these overarching principles follow for specific reservoirs.

6.4.1 Case study #1: equilibration of light crude oil

Figure 6.6 shows the cross section of the Ivar Aasen reservoir, offshore Norway, intersected by six wells. The numbered DFA stations are shown in the wells. This reservoir consists of fluvial sandstones of the Late Triassic to Middle Jurassic in the Skagerrak and Sleipner Formations and shallow marine sandstones in the Middle Jurassic Hugin Formation. Figure 6.7 shows a cross section of these different formations across the field. The Hugin and Sleipner formations are homogeneous and high net to gross in this field. However, the Skagerrak formations which contain roughly half of the oil in place in this field are characterized by medium to low net to gross, thereby increasing the concern about reservoir connectivity. DFA evaluation of connectivity is even more important in complex reservoirs that have lower net-to-gross pay.

Figure 6.6 shows a much deeper GOC in the west and a much shallower GOC in the east. This means that the solution gas is not equilibrated laterally in this field and might be explained by lack of connectivity. However, this disequilibrium is not detected in the compositional analysis of the oil samples across the field. As such, the effect of this disequilibrium is subtle regarding composition while dramatic regarding differing GOCs. The asphaltene gradients are very informative regarding the extent of equilibrium in the liquid phase across the field. Figure 6.8C shows the DFA-measured asphaltene gradient and Figure 6.8A shows the relation of the data points to the location in the field.

The equilibrium asphaltene gradient shown in Figure 6.8C is quite small (little variation of asphaltene content with height) [2, 8, 29, 69]. The gravity term predicts very small gradients of asphaltenes dispersed as molecules which are expected for light oils

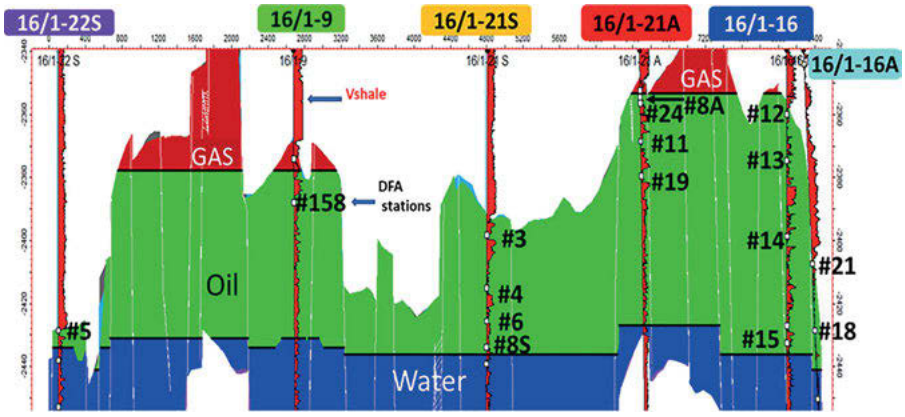

Figure 6.6: Cross section of the Ivar Aasen oilfield with six appraisal wells shown, on the Gudrun terrace of the continental shelf of Norway [2, 8, 29, 69]. The numbered DFA stations are indicated for each well. The question of reservoir connectivity is paramount. Green is oil; red is gas; and blue is water. There is a deeper gas-oil contact (GOC) in the west than in the east. This is a consequence of structural highs near the charge point preferentially charging with phase-separated gas. Published with permission from the Society of Petroleum Engineers.

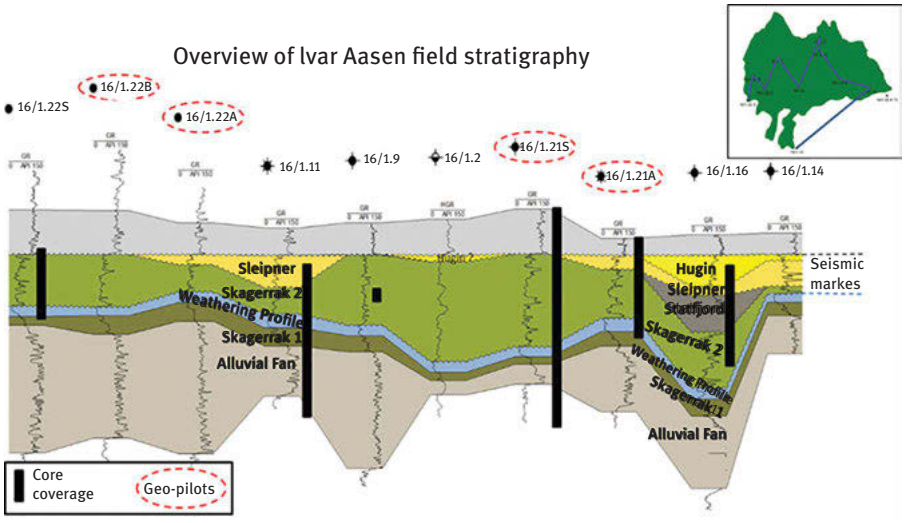

Figure 6.7: The stratigraphy across the Ivar Aasen oilfield. The Hugin and Spleipner formations are homogeneous and high net to gross. The Skagerrak formations (and the Weathering Profile) are medium to low net to gross thereby elevating concern about reservoir connectivity. Published with permission from the Society of Petroleum Engineers.

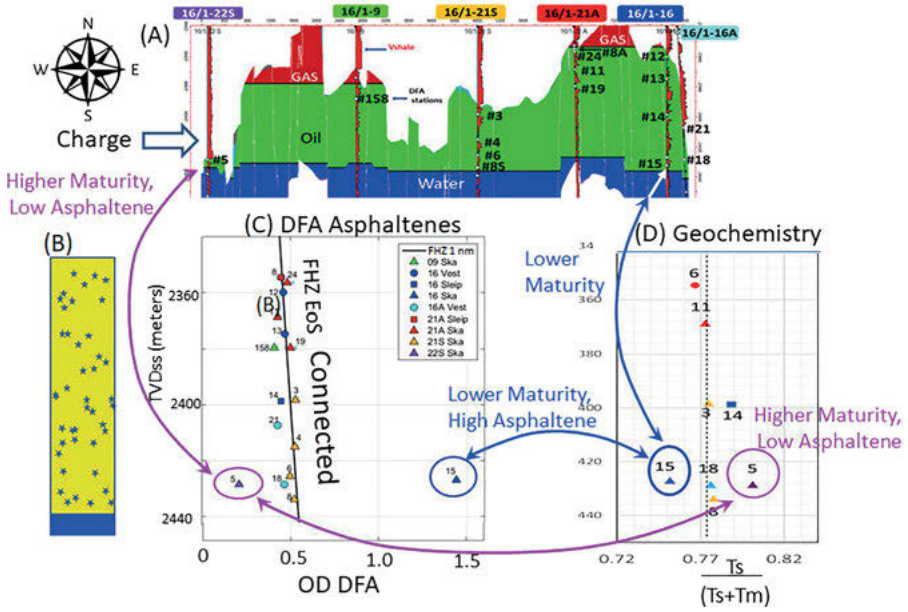

Figure 6.8: (A) Field map. (B) Schematic of the oil column in this field with asphaltenes (stars) dispersed as molecules. (C) DFA-measured asphaltene gradient; OD is optical density, here at a wavelength of 815 nm. Almost all of the DFA stations in the reservoir fall on the "light oil model" equilibrium curve predicting connectivity. DFA station #5 on the western flank of the field has half the asphaltene content and is likely not connected. DFA station #15 on the eastern flank of the field has triple the asphaltene content and is also likely not connected. (D) Thermal maturity indicator; in the connected part of the field, the thermal maturity ratio is equilibrated. DFA #5 is high maturity, DFA #15 is low maturity. The connectivity prediction from DFA matches one year of production data to date [2, 8, 29, 69]. Published with permission from the Society of Petroleum Engineers.

(the "light oil model"). In addition, the GOR is relatively small due to the relatively low pressure of the reservoir, excess gas has flashed out of the oil. Crude oils with small GORs have small GOR gradients. Thus, the solubility term changes little from the top to the bottom of the column, thereby giving a small asphaltene gradient from the solubility term of the FHZ EoS. The third term of the FHZ EoS is the entropy term which is small and tends to homogenize the oil column.

The general rule is that equilibrated asphaltenes predict reservoir connectivity; [2, 5] the asphaltene equilibrium gradient found here is quite consistent with extensive connectivity in the reservoir. The two outliers which are quite removed from the asphaltene equilibrium curve appear to be disconnected, samples #5 and #15. Sample #15 has three times the asphaltene content and sample #5 has half the asphaltene content compared to the bulk of the reservoir oil. This difference relates directly with thermal maturity as seen in Figure 6.8D. Sample #15 is seen to be lower maturity that the bulk of the oil, and sample #5 is seen to be higher thermal

maturity. The asphaltene content variation is a factor of 6 while the difference in thermal maturity is only 6%; asphaltene gradients are a far more sensitive indicator to detect fluid variations. Outliers which are understandable "prove the rule" and validate the basic understanding of the fluid gradients [2, 8, 69].

Other factors that might produce variations in asphaltene content are ruled out below. Thus, the asphaltene content of the charge fluid varied by a factor of 6. Consequently, significant flow or mass transport had to occur in the reservoir to achieve equilibrium of the asphaltenes, which in this case corresponds to variations in asphaltenes much smaller than the factor of 6 in charge fluids. This equilibration process requires excellent reservoir connectivity. The actual asphaltene content of well under 1% obtained in the lab is consistent with a high-maturity fluid, Ts/(Ts +Tm) ~ 0.8 [2, 8, 29, 69].

The observables in this RFG analysis are consistent with simple petroleum systems concepts. The crude oil in Ivar Aasen is sourced from the Viking graben in the west. In this subsiding basin, the first charge to enter the reservoir is the lowest maturity; some of this crude oil was trapped in the eastern flank farthest from the charge point and corresponds to Sample #15. The last charge to enter the field is the highest maturity; some of this crude oil was trapped in the western flank nearest to the charge point and corresponds to sample #5. The charge fluids broke into two phases prior to entering the reservoir. The liberated gas becomes trapped in structural highs in the reservoir near the charge point in the west while oil sweeps across the reservoir. Consequently, the GOC in the west is much deeper than in the east. This expected charge scenario is consistent with the observed differing GOCs in Figure 6.6. A variety of measurements discussed below validate these simple concepts.

The evaluation of the asphaltene content and thermal maturity of sample #15 shows that it is quite different from all other samples. It is important to validate that sample #15 is really isolated from the rest of the reservoir. Figure 6.9 shows the sealing fracture that confirms the isolation of sample #15 in agreement with its different asphaltene content and thermal maturity [2, 8, 29, 69].

Samples #12, #13, #14, and #15 were all obtained in well 16/1-16. As emphasized in Figure 6.9A, the crude oils from the top three stations, #12, #13, and #14 all fall on the equilibrium curve while sample #15 has three times the asphaltene content. Figure 6.9C shows whole core through an interval separating samples #14 and #15. The sealing fracture is circled in red; there is light oil with high UV fluorescence above the fracture and no light oil below the fracture, it is sealing. The whole core images capture the sealing fracture between samples #14 and #15 validating the lack of connectivity found by asphaltene gradients and thermal maturity evaluation [2, 8, 29, 69].

Figure 6.10 shows the excess pressure plot and the GOR gradient. Because these flashed crude oils are within the same pressure regime, the reservoir oil throughout flashed until the saturation pressure matched the reservoir pressure. More specifically, the crude oils that charged into the reservoir were all increasing in maturity and decreasing in density. As geologic time proceeded, these crude oils with decreasing density continued to enter the reservoir and density stack at the

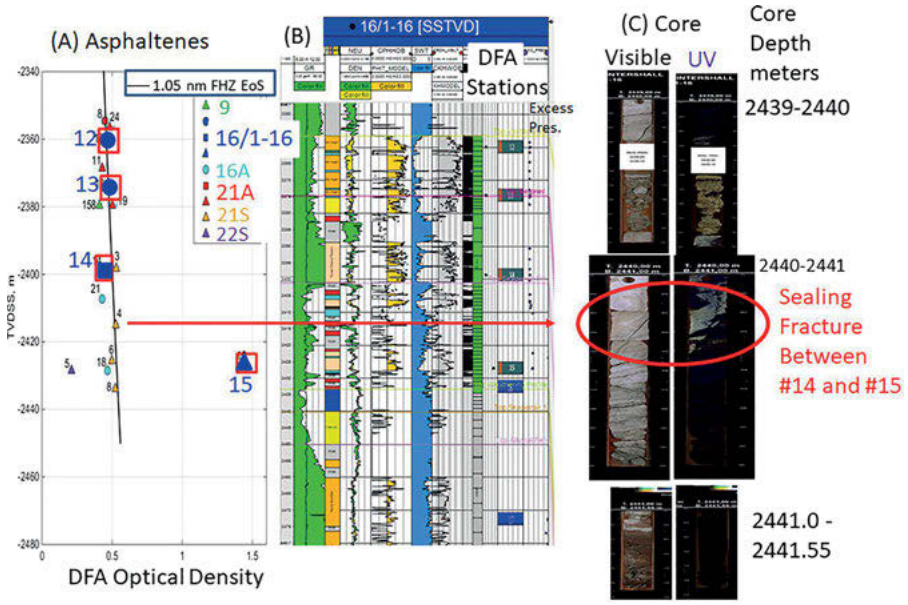

Figure 6.9: Evaluation of crude oils, petrophysics, and selected whole core from well 16/1-16. (A) Asphaltene content of four DFA stations with oil (#12, #13, #14, and #15) in this well showing sample #15 is isolated from the others. (B) DFA station locations are indicated by horizontal bars; green is oil, yellow is methane, orange is C2-C5 gases and blue is water. (C) Whole core from well 16/1-16 shows the fracture isolating #15 circled in red. The fracture is evident in visible light illumination of the whole core (left core image). UV illumination of whole core (right core image) isolates a lighter oil (higher UV fluorescence) above the fracture with a heavier oil (low UV fluorescence) below the fracture [2, 8, 29, 69]. Published with permission from the Society of Petroleum Engineers.

GOC [77]. The first charge fluids experienced the lowest reservoir pressure, and the smallest gas cap yielding a low saturation pressure and low GOR. With subsidence, new charge fluids also density stacked to the GOC which increased with depth due to reservoir subsidence and growth of the gas cap. Thus, these new charge fluids retained more solution gas with a higher saturation pressure and GOR [77]. The evolving gradient from charge history is indistinguishable from equilibrium. This is true for connected crude oils *and* for isolated crude oils provided the isolated samples are in the same pressure regime as is the case here. In addition, the error bars in GOR measurements are significant. Consequently, the GOR gradient roughly matching the cubic EoS is not a stringent constraint establishing connectivity. Samples #5 and #15 that are clearly outliers in the asphaltene gradient (Figure 6.8C) are barely outside of error bar in the GOR plot. Nevertheless, the pressure measurement and the GOR gradient is consistent with connectivity [2, 8, 29, 69].

Figure 6.11A shows that gas–liquid compositional analysis is consistent with equilibrium even for the disconnected samples #5 and #15 which are plotted in this

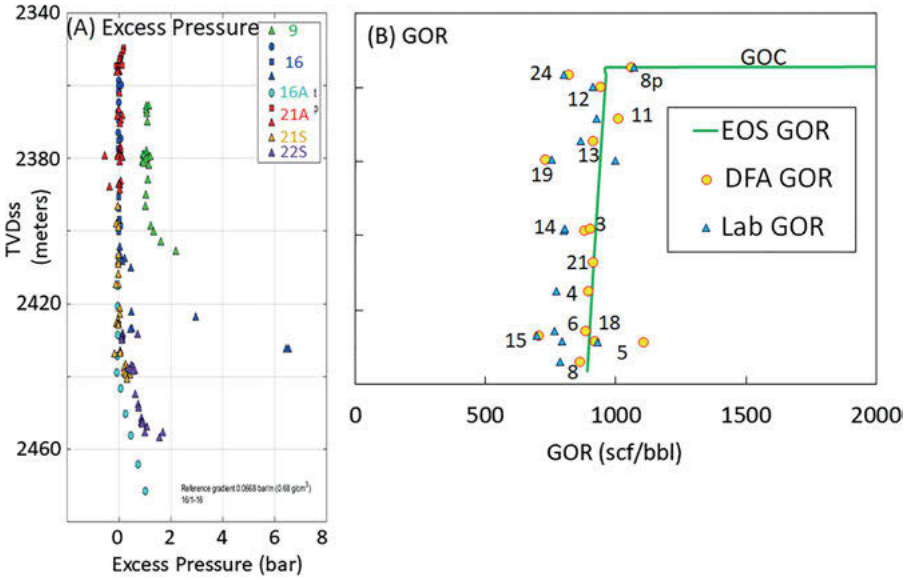

Figure 6.10: (A) Excess pressure plot showing almost all the wells are in the same pressure regime. The pressure measurement in one well is offset by 1 bar but is within possible error when comparing pressure from different wells. Thus, pressure measurements do not prove compartmentalization and are consistent with connectivity. (B) The GOR gradient (from DFA and Lab) is consistent with equilibration, thus consistent with connectivity. Nevertheless, GOR measurements are associated significant error [2, 8, 29, 69]. Published with permission from the Society of Petroleum Engineers.

figure. Figure 6.11B shows that the CO_2 content in the crude oil is small and consistent with equilibrium. The origin of this lack of sensitivity of compartmentalization to gas–liquid analysis is discussed in the preceding paragraph and limits the utility of the corresponding thermodynamic analysis of gas–liquid distribution. Consequently, the asphaltene gradient analysis of Figure 6.8 is even more important in such cases of oil reservoirs with (1) gas caps and (2) single pressure regimes [2, 8, 29, 69].

Figure 6.6 shows that there is a large variation of GOC across the field. For a connected reservoir (with no lateral thermal gradient), this necessarily means that the there is a lateral disequilibrium in GOR. Yet, Figures 6.10 and 6.11 show that GOR and gas–liquid composition are roughly equilibrated. The lateral variation of GOR and gas–liquid composition are subtle and smaller than corresponding error bars. In addition, the lateral difference in GOCs across the field can be sustained for very long geologic time. The large distances across the field coupled with the very small compositional differences limit the mass flux required to equilibrate the different GOCs, whether by convective or diffusive processes [2, 8, 29, 69].

When differences of asphaltene content are measured such as in Figure 6.8C, it is important to determine if biodegradation played a role in these differences, especially

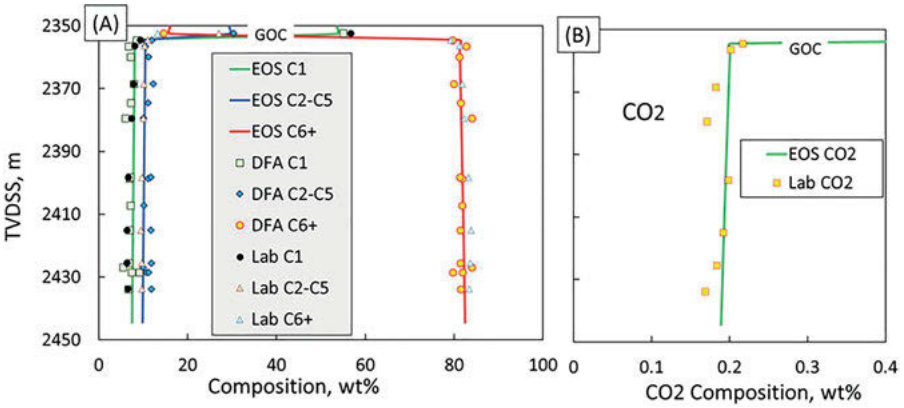

Figure 6.11: (A) The gas–liquid compositional analyses of all Ivar Aasen samples are consistent with equilibrium even for isolated samples #5 and #15 (which are in this plot). Flashed samples in the same pressure regime are constrained by their nearly equivalent saturation pressures. (B) CO_2 content in the live crude oil is small and consistent with equilibrium. Published with permission from the Society of Petroleum Engineers.

in oil provinces such as the North Sea where biodegradation is common. In the process of biodegradation, microbes can consume about 2/3 of the crude oil [78, 79]. The microbes do not eat asphaltenes (or at most, a tiny fraction), thus, as the crude oil goes from nonbiodegraded to severely biodegraded, the asphaltene content can triple.

Figure 6.12 shows that the intermediate alkane population is very similar for the different samples, thus, evidently largely equilibrated. In addition, the reduction of *n*-alkane peaks in the C7 range below that of others such as cyclohexane and methylcyclohexane indicates that all samples are mildly biodegraded. The current reservoir temperature is 100 °C, well above the limiting temperature of biodegradation of 80 °C. The oil does contain a small quantity of CO_2, which sometimes is an indicator of in-reservoir biodegradation. However, the quantity of CO_2 is quite small, 0.2% in the reservoir fluid and its origin is not clear. The fact that the isolated sample #15 near the OWC has a similar extent of biodegradation as samples far from the OWC suggests that the oil that charged into the reservoir was already biodegraded. Biodegradation occurs at the OWC; if biodegradation proceeded in this reservoir, then sample #15 would be more biodegraded; it would not mix diffusively with nonbiodegraded oil higher in the oil column due to its isolation. Indeed, sample #15 has more asphaltene and different Ts/(Ts+Tm) ratio than the other crude oils proving it did not mix diffusively. Likewise, the isolated sample #5 is also near the OWC and is also biodegraded to an extent similar to all other crude oils analyzed. Again, the conclusion is that the crude oil must have been biodegraded prior to entry into this reservoir [2, 8, 29, 69].

Figure 6.13 quantifies the extent of biodegradation and also compares one source rock parameter. All crude oils are mildly biodegraded, with some limited variation. The Halpern index TR2 (*n*-heptane/1,1-dimethylcyclopentane) is very sensitive to

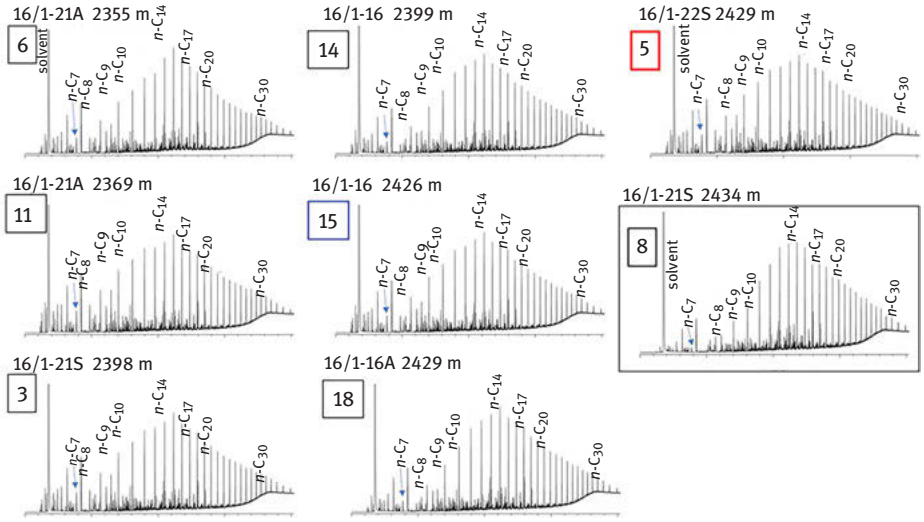

Figure 6.12: Conventional gas chromatograms (GCs) for the Ivar Aasen oil samples. The plots are very similar which is expected for equilibrium. The relative reduction of n-alkanes in the C7 range indicates all samples underwent mild biodegradation. Sample #8, closest to the OWC shows slightly greater biodegradation. The isolated samples #5 (red square, hot catagenesis) and #15 (blue square, cold catagenesis) are biodegraded to a similar extent of all other oil samples; biodegradation did not cause the observed asphaltene differences [2, 8, 29, 69]. Published with permission from the Society of Petroleum Engineers.

biodegradation. Microbes prefer to consume *n*-alkanes especially in the C7 range as opposed to branched, cyclic alkanes. The value for this index is typically above 20 for nonbiodegraded crude oils and is less than 1 for moderate biodegradation. Values in Figure 6.13A indicate mild biodegradation. It is not clear why there is variation in this index. The variation does not correlate with asphaltene content or thermal maturity. Comparison of Figure 6.13A and B shows that the Halpern TR3 index, 3-methylheptane/1,1-dimethylheptane, is consistent with the Halpern TR2 index. It is important not to be overly concerned with a single data set that is mostly in agreement with the generally theme but which exhibits some subtle differences. Figure 6.13C plots pristane/*n*C17, no biodegradation is indicated in this range. Examination of the GC plots in Figure 6.12 shows that the loss of *n*-alkane which is evident in the *n*C7 range terminates at about *n*C14 and is consistent with no biodegradation in the *n*C17 range. Analysis of phytane/*n*-C18 is consistent with this analysis [2, 8, 29, 69].

Figure 6.13D shows the source rock parameter Halpern C1, a complex ratio of seven carbon alkanes, is the same for all samples including the isolated samples. Differences in thermal maturity variation Ts/(Ts+Tm) are recorded when comparing this isolated samples. The source rock components are formed at the same time as the thermal maturity markers, which is at the time of kerogen catagenesis. The

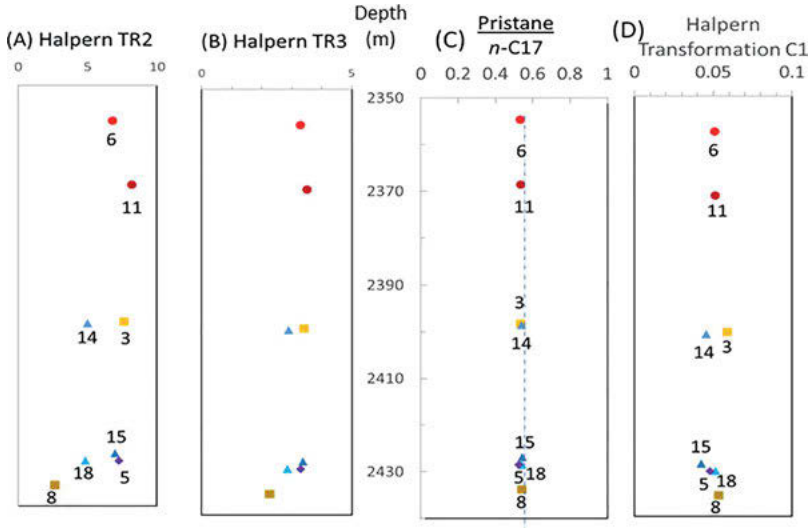

Figure 6.13: Comparison of various geochemical ratios for selected Ivar Aasen crude oils [2, 8, 29, 69]. (A) Halpern TR2 equals *n*-heptane/1-1,dimethylcyclopentane, a biodegradation index. All crude oils are mildly biodegraded and some variations are seen. (B) Halpern TR3 equals 3-methylhexane/1-1,dimethylcycloheptane, a biodegradation index. In agreement with Halpern TR2, the crude oils are all mildly biodegraded with some limited variations. (C) Pristane/n-C17, no biodegradation is indicated in this carbon-number range, and the crude oils are all very similar. Halpern C1 source correlation comprised of a complex ratio of seven carbon saturates. This parameter is the same within error for all crude oils including the isolated samples that have preserved thermal maturity variations. No indication of variations in source rock is seen. Published with permission from the Society of Petroleum Engineers.

source rock parameters for the isolated samples did not equilibrated with the other crude oils in the same way that their asphaltene content and thermal maturity did not equilibrated. There is no evidence that there is variation in the source rock for these crude oils. Analysis of other source rock parameters, Halpern C2 and Halpern C3, yields the same conclusion [2, 8, 29, 68].

The timing of the formation of the fracture which isolates sample #15 can be determined. Figure 6.6 shows that sample #15 is at the base of the oil just above the OWC. The last part of the reservoir to fill with oil is the base of the reservoir. Consequently, it is evident that the sealing fracture seen in whole core in Figure 6.9 occurred *after* the reservoir charge was complete. This fracture must have occurred fairly quickly after reservoir charging; otherwise, oil mixing would have caused sample #15 to be similar to the other oils in terms of asphaltene content and thermal maturity markers. Thus, we can conclusively say that (1) fracture formation occurred shortly after reservoir charging and (2) biodegradation occurred in this oil prior to its emplacement in Ivar Aasen.

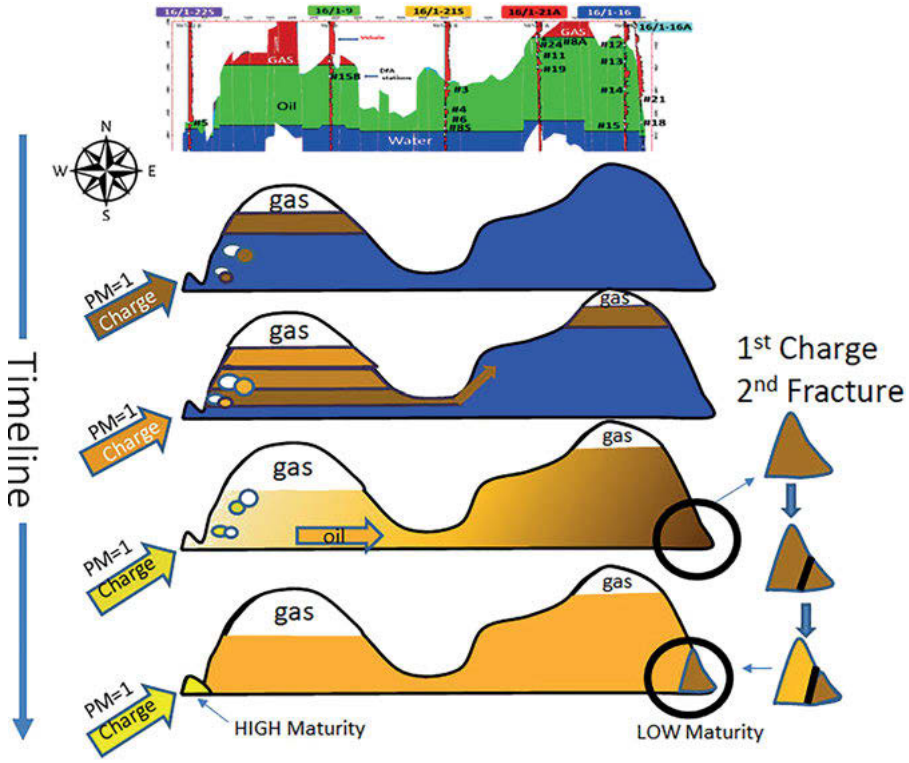

Figure 6.14: Geo-scenario of coevolution of fluid and rock in the reservoir [2, 8, 29, 68]. Cross section of Ivar Aasen. The reservoir charged from the west. The color shading in the oil in the schematics indicates asphaltene content. The low pressure of the reservoir caused gas and oil to break into two phases. The oil charging into the reservoir was mildly biodegraded, PM rank~1. The gas remained trapped in structural highs near the charge point. The later oil generation and charge increased in maturity during subsidence. The heavier crude oil initially swept toward the east across the spill point and eventually, at the bottom of the oil column. A fracture occurred after charge isolating low maturity, heavy oil at the bottom of the eastern flank. The bulk of the reservoir density stacked (by convection) and equilibrated. A more recent, high-maturity oil became trapped in the western flank.

Figure 6.14 shows in schematic fashion the key RFG processes the occurred in this reservoir. The oil that charged into Ivar Aasen was mildly biodegraded, thus in a separate trap that overfilled. This charge scenario and the current high temperature of this field (100 °C) help to constrain the petroleum system analysis of the field, and basin. The relatively low pressure of the reservoir caused liberation of the solution gas which became trapped in structural highs near the charge point. Initially, the heavy oil pooled at the bottom of the eastern flank. A fracture formed shortly after charge isolating some of the heavy oil. Eventually, convection and diffusion caused fluid equilibration in most of the reservoir which is known to be

connected from production data. The highest maturity oil, the most recent charge, became trapped in the western edge of the field. The trapping of heavier oil in the east and lighter oil in the west is consistent with the influence of lateral sweep on fluid properties [2, 25, 28, 80]. That is, lateral sweep can create lateral variations in fluid properties. Subsequent equilibration processes can remove lateral differences if the crude oils are in communication, not trapped. This overall understanding of the reservoir is very useful for optimization of this reservoir, for field extension and local basin analysis.

6.4.2 Case study #2: equilibration of black oil

Black oil reservoirs are very common and many of the RFG evaluations are for black oil reservoirs. Typical black oils contain asphaltenes dispersed as nanoaggregates of the Yen–Mullins model. This invokes the "black oil model" of asphaltenes with a diameter of ~2 nm. A case study of the Tornado field, deepwater Gulf of Mexico, with comprehensive data sets shows the value of asphaltene gradient analysis in revealing a sequence of specific RFG processes that occurred in the reservoir [2, 5, 10, 29, 59, 81].

Figure 6.15 shows various data sets for the Tornado reservoir where connectivity analysis had been key [2, 5, 10, 29, 59, 81]. The oilfield is a middle Pliocene turbidite with no overhanging salt canopy; consequently, seismic analysis is relatively good. The very young age assures there is not too much overlying sediment which is helpful for seismic imaging. Asphaltene gradient analysis, seismic isopach image analysis, and 1.5 years of production to date are all consistent. Seismic imaging with its many meters of resolution cannot establish connectivity since thin barriers below seismic resolution are well known to cause compartmentalization. Nevertheless, agreement of seismic analysis with asphaltene gradient analysis with their very different physics indicates that the conclusions are robust. The fact that this combined analysis was made prior to production and now matches years of production to date validates the RFG evaluation workflow, especially with its reliance on asphaltene gradient analysis from DFA.

Figure 6.16 shows that there is a significant GOR gradient, this is part of the reason why there is a large asphaltene gradient. The higher GOR oil at the top of the column is a worse solvent for asphaltenes than the lower GOR oil at the base of the column. The color scales linearly with asphaltene concentration and is independent of the extent of nanocolloidal aggregation. Consequently, the solubility term of the FHZ EoS adds to the gravity term creating an asphaltene gradient. Both the GOR variation and the asphaltene variation create the observed variation in viscosity. These other gradients are consistent with the connectivity interpretation of the asphaltene gradients but lack the resolution to a robust interpretation analysis themselves.

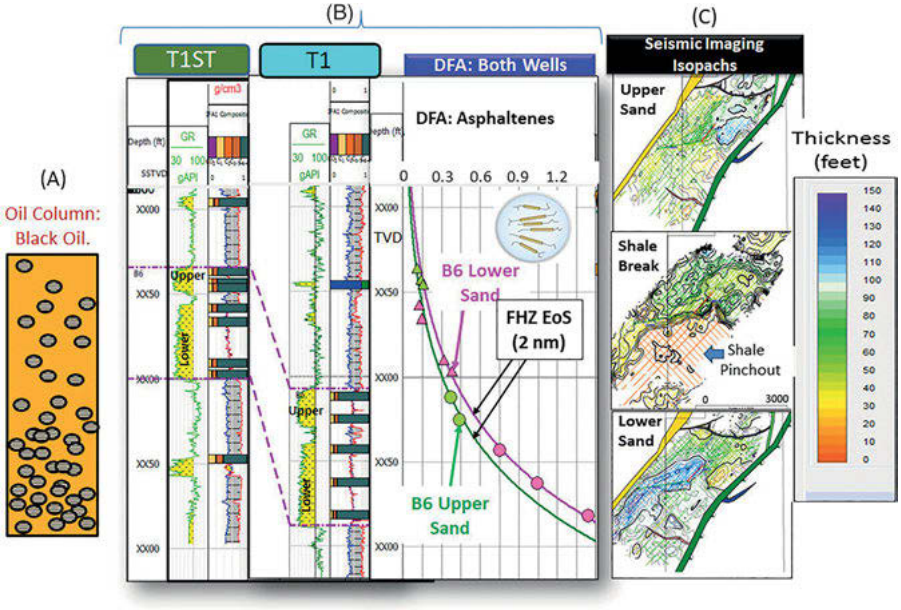

Figure 6.15: The Tornado oilfield [2, 5, 10, 29, 59, 81]. Evaluation of two stacked sands in a reservoir fairway bounded by two faults. (A) The schematic shows an asphaltene gradient in a black oil, comprised of an increasing nanoaggregate concentration lower in the oil column. (B) Wireline data obtained in each of the two wells. DFA stations are indicated with horizontal bars; yellow is methane; orange is other hydrocarbon gases; green is oil; and blue is water. The upper and lower sands are indicated in the yellow shaded sections of the gamma ray log. The sands show a small separation in density and neutron logs, while the shales show a large separation. There is a clear intervening shale between the sands in both wells. The DFA-measured asphaltene gradients are shown for the upper sand (green curve) and lower sand (pink curve). The crude oil in each sand is equilibrated showing lateral connectivity. The pink and green asphaltene curves are offset from each other showing that the shale break is either a regional baffle or barrier. About 1.5 years of production to date are consistent with this analysis. (C) Isopach formation thickness maps are consistent with the asphaltene gradient analysis. The upper sands and lower sand are seen to be quite thick and laterally extensive. The intervening shale is shown to be a regional baffle or perhaps a barrier. The subseismic "pinchout" observed in seismic imaging might act as a substantial baffle if not a barrier. Published with permission from the Society of Petroleum Engineers.

The thermal maturity marker ratio Ts/(Ts+Tm) shows no variation within error and is not very useful for connectivity analysis as seen here [2, 5, 10, 29, 59, 81]. Geochemical analyses have been used in the past for connectivity analysis [2]. Many RFG case studies show that a better use of geochemistry is to confirm RFG thermodynamic analyses, and in turn, the RFG analysis can be used to assess connectivity [2]. Here, the primary utility of the thermal maturity marker is to show lateral equilibration supporting the conclusions that the asphaltenes are laterally equilibrated. The slight difference in Ts/(Ts+Tm) between the upper sand (0.40)

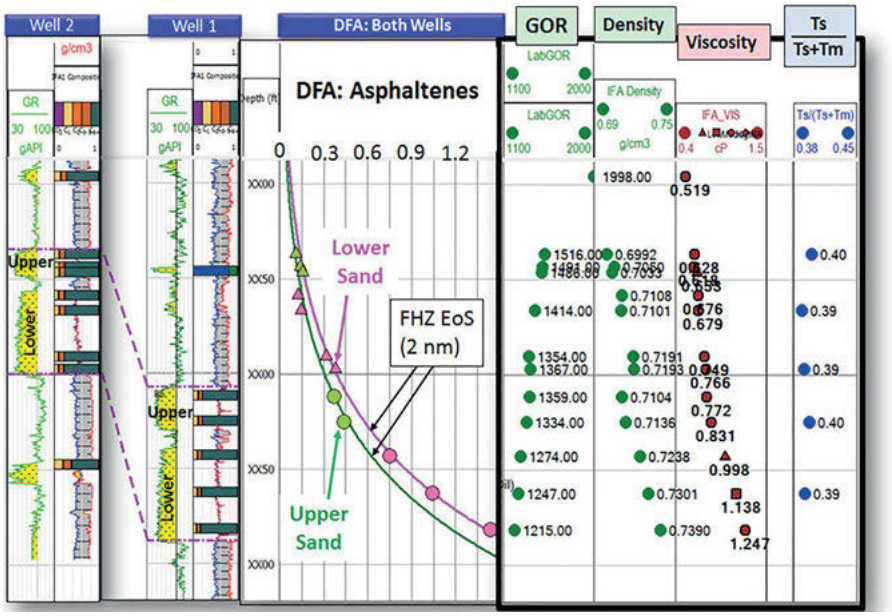

Figure 6.16: Many fluid measurements for the same reservoir shown in Figure 6.15 [2, 5, 10, 29, 59, 81]. GOR (scf/bbl) from lab measurements, fluid density (g/cc) and viscosity (cP) from DFA and the thermal maturity marker Ts/(Ts+Tm) are all consistent with the DFA asphaltene gradient analysis. However, no other fluid measurement gives the clarity of lateral connectivity and vertical baffling. Published with permission from the Society of Petroleum Engineers.

versus the lower sand (0.39) is suggestive of and consistent with the subtle asphaltene difference observed between the upper and lower sands, and the slightly higher asphaltene content is associated with slightly lower thermal maturity. However, the difference in thermal maturity is within error, even for the case of all samples being analyzed in the same batch run as performed here.

RFG including fault block migration. For the reservoir depicted immediately above, a new well, T2, was drilled on the other side of the fault on the eastern flank. Seismic imaging and well log correlation showed that the fault throw is ~380 feet, with the lower block in the east. Figure 6.17 shows that the same two sands are found on both sides of the "green" fault. Moreover, the DFA data in the T2 well shows that the upper sand has slightly less asphaltene and that the lower sand has the same gradient as observed in the central fairway [2, 5, 10, 29, 59, 81].

The data presented in Figures 6.17 and 6.18 are dramatic. The asphaltene content measured by DFA in the T2 well interpolates in both the upper and lower sands obtained from the two wells in the central fairway when shifted up by the fault throw of 380 feet. This indicates that asphaltene equilibration in this reservoir preceded the

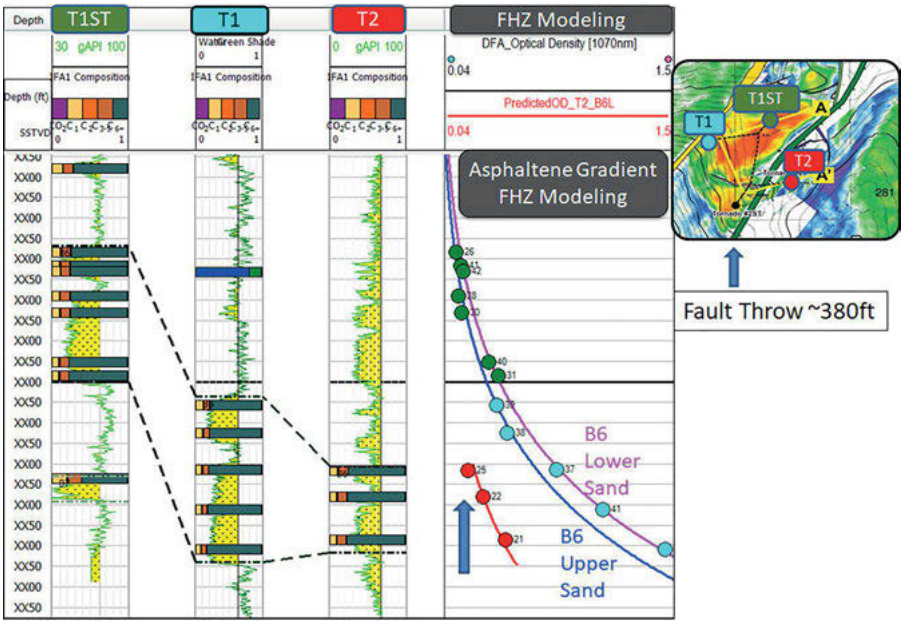

Figure 6.17: The T2 well drilled on the other side of the east "green" fault shows the same two sands as in the central fairway. Seismic imaging and well correlation show that the fault throw is ~380 feet. The following figure shows the asphaltene gradient data shifted up by this fault throw – a data treatment indicated by the vertical blue arrow [2, 5, 10, 29, 59, 81]. Published with permission from the Society of Petroleum Engineers.

fault throw. It is very important to validate the RFG scenario. It is important to analyze other fluid properties to determine consistency with this observation.

Figure 6.20 shows that a vertical shift by the fault throw of the fluid data in the T2 well in the downthrown block yields consistency across the reservoir for asphaltene content and API gravity. As noted for Figure 6.19, this is consistent with asphaltene and fluid equilibration across the field. However, the methane isotope ratios of the T2 crude oils are heavier than that of the central fairway. This indicates that the central fairway crude oils have more primary biogenic gas. Likewise, the GORs of the T2 oils are lower than those of the central fairway crude oils. Both these observations are consistent with the RFG process of a primary biogenic charge entering the upper block of the central fairway *after* the fault throw.

Figure 6.21 shows various geochemical markers which all show consistency across the entire field, specifically across the fault. This homogeneous distribution of these ratios of very similar compounds is consistent with equilibration of the crude oils across the field prior to the fault throw depicted in Figures 6.16–6.20. Moreover, the geochemical analysis of these markers does not indicate any fluid complexity beyond that discussed above with respect to the primary biogenic gas

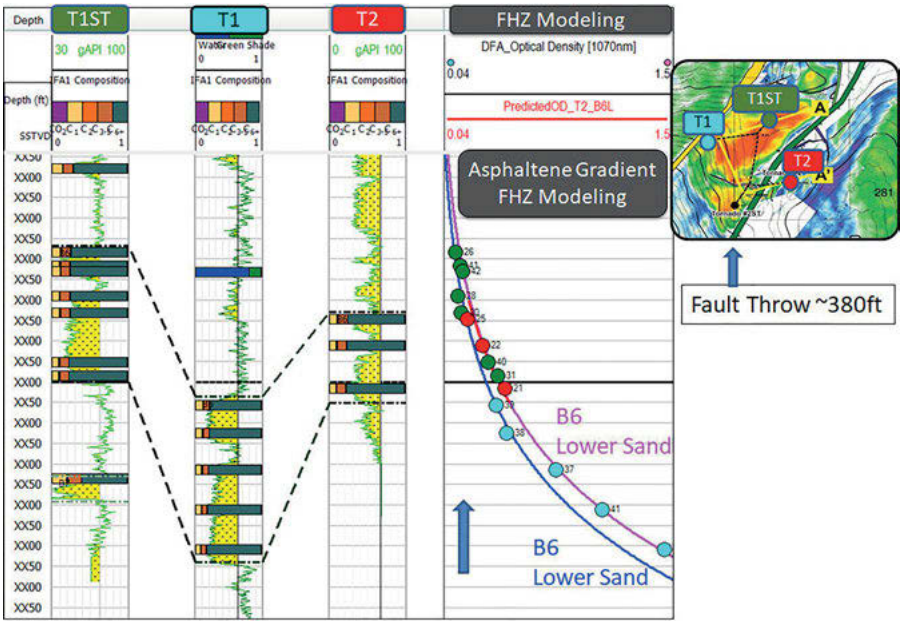

Figure 6.18: The data presented in Figure 6.17 with the DFA asphaltene data from the T2 well shifted vertically by 380 feet, the fault throw. The asphaltene data from the T2 well interpolates into the asphaltene gradient data from the T1ST and T1 wells. The implication is that in the geologic history of the reservoir, the asphaltenes equilibrated across the entire reservoir prior to the fault throw [2, 5, 10, 29, 59, 81]. Published with permission from the Society of Petroleum Engineers.

charge. Consequently, the RFG scenario proposed for this reservoir is consistent with the geochemical analysis. The value of the Halpern TR1 index, toluene/1,1-dimethylcyclopentane, is consistent with no water washing. The value of the Halpern TR2 index, *n*-heptane/1,1-dimethylcyclopentane, is consistent with no biodegradation. The value of the Hapern-C1 index, a ratio incorporating many saturated C7 compounds, shows no source variation. The hopane thermal maturity marker, Ts/(Ts+Tm), shows no thermal maturity variation and exhibits typical values for black oil. Unlike Case Study #1, this field does not have preserved charge. Thus, it remains unknown what the range was of asphaltene content and thermal maturity for charge fluids entering the reservoir; they are all equilibrated at now.

Figure 6.22 shows the geo-scenario of the RFG and rock formation processes that took place in this Middle Pliocene reservoir. The anticline formed associated with halokinesis underneath the field. The anticline filled with oil, and the asphaltenes and all other fluid components equilibrated. With continuing stress of anticline growth, a fault occurred, splitting off a fault block containing part of the reservoir, with a displacement of 380 feet. Equilibrated crude oils were preserved in both the upper and lower fault blocks. Subsequent to the fault throw, the upper block charged preferentially

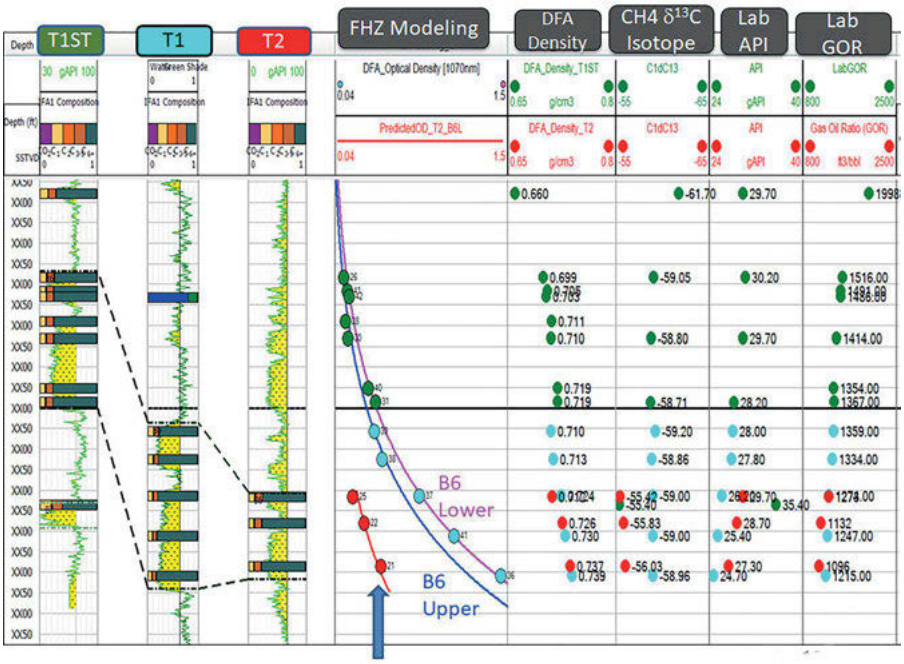

Figure 6.19: Comparison of fluid properties for the three wells in the reservoir. The asphaltene content is not aligned when plotted on actual depth. The fluid properties, methane isotope, API gravity, and GOR are also not aligned when plotted on actual depth [2, 5, 10, 29, 59, 81]. Published with permission from the Society of Petroleum Engineers.

with primary biogenic methane. That is, both the upper and lower blocks have primary biogenic methane mixed with the crude oil as gleaned by the light carbon isotope of methane. But the upper fault block had more primary biogenic methane ($\delta^{13}C$ ~ −59‰) compared to the lower fault block ($\delta^{13}C$ ~ −56‰). Moreover, as shown in Figures 6.18 and 6.20, the methane isotope values of all the different oil samples within each of the blocks are about the same, but differ from one block to the next. This means that after the thermogenic gas entered the upper block, the methane equilibrated throughout both the upper and lower sands. This case study proves that reservoir fluids can equilibrated rapidly; almost certainly convective processes contribute to this.

Finally, the T1ST well has two DFA stations in different sands than the target reservoir. The deepest DFA station in T1ST shows a very heavy carbon isotope of methane meaning the least biogenic gas charge of all. In addition, the API gravity is the highest of all, meaning that this is the lightest oil charge. It is common for higher maturity fluids to get trapped deeper with increasing subsidence because (1) subsidence can seal migration to shallower formations and (2) spill-fill preferentially retains lighter fluids deeper. The shallowest DFA station shows the lightest carbon

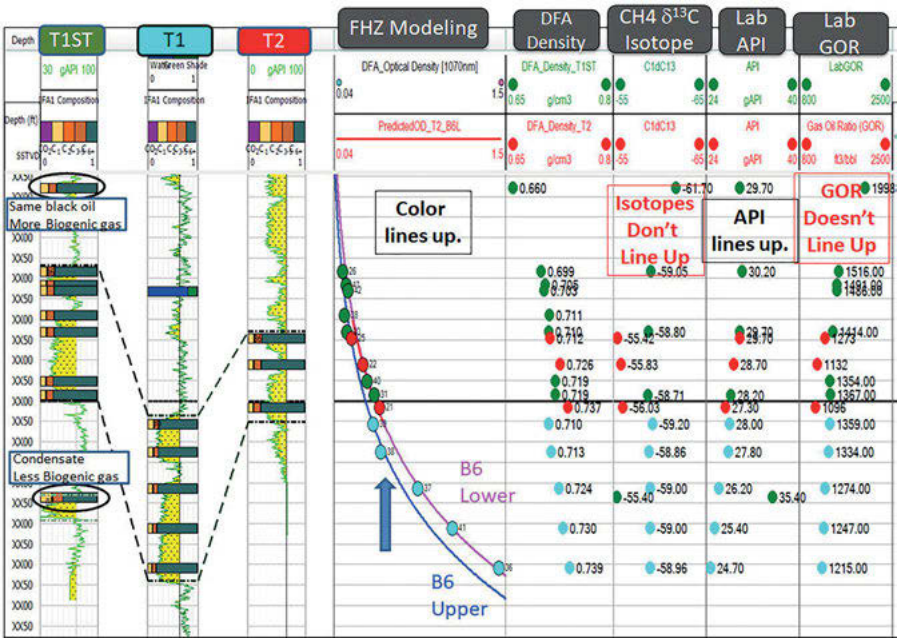

Figure 6.20: Comparison of fluid properties of the three wells after shifting vertically the T2 well fluid data by 380 feet, which equals the fault throw. As noted in Figure 6.19, the asphaltene gradient data interpolates in both the upper and lower sand. The API gravity also interpolates reasonably well in both sands. However, both the methane isotope data and the GOR do not line up with the previous two wells. Specifically, the methane isotope of the upper block is lighter indicating a greater content of primary biogenic gas. In addition, the GOR of the upper block oil is higher indicating a greater gas content. Since the API gravities, a flashed oil property, do line up, the implication is that after the fault throw, the upper block preferentially received a new charge of primary biogenic gas [2, 5, 10, 29, 59, 81]. Published with permission from the Society of Petroleum Engineers.

isotope of methane meaning it has the highest fraction of biogenic methane. This oil API gravity is similar to the almost all others yet its GOR is the highest. Thus, the sand has a similar oil charge as the main reservoir but has a higher biogenic gas fraction. These other sands help illustrate charge complexities that can occur.

There are two origins of biogenic methane with distinct carbon isotope ratios [79]. Primary biogenic methane corresponds to microbial digestion of organic matter in shale and other sediments. The conversion efficiency in this process from organic carbon to methane is very low; consequently, the smaller activation energies of carbon 12 (due to zero-point energy dependence on mass) are important, thereby yielding preferential light carbon in the methane with $\delta^{13}C \sim -70\%$. Secondary biogenic methane corresponds to microbes consuming oil. The conversion efficiency of this process is high; thus, the produced methane is constrained to have more similar isotopic ratios as the oil, thus $\delta^{13}C \sim -50\%$ [79]. Thermogenic methane has an

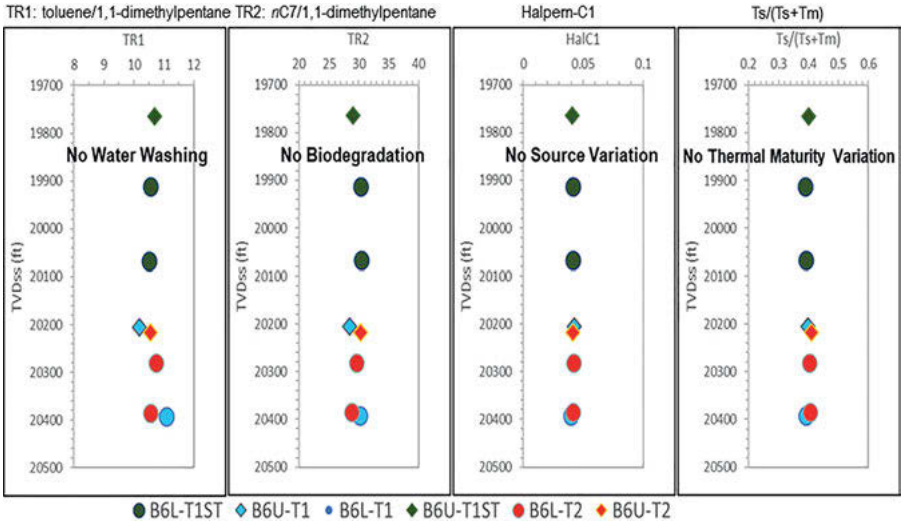

Figure 6.21: Geochemical analyses of many biomarkers show the same values for all samples in the T1, T1ST, and T2 wells. Halpern TR1 shows no water washing, TR2 shows no biodegradation, Halpern-C1 shows no source variation and Ts/(Ts+Tm) indicates a typical black oil maturity. The homogeneous distributions of these geochemical ratios are consistent with fluid equilibration [2, 5, 10, 29, 59, 81]. Moreover, the lack of fluid complexities reinforces use of the simple FHZ EoS formalism. Published with permission from the Society of Petroleum Engineers.

Figure 6.22: Geo-scenario of the key RFG and rock formation processes in this Pliocene reservoir. First, the anticline formed and filled with oil. The asphaltenes and other oil components equilibrated. Second, with continuing growth of the anticline, a fault occurred cleaving the reservoir into an upper block and lower block, each with equilibrated fluids. Third, a primary biogenic gas charge then entered the upper block and again the fluid equilibrated.

isotope ratio roughly of $\delta^{13}C \sim -40‰$ but with some variability associated with different parameters. Also, the ratio of methane to ethane generally exceeds 1,000 for biogenic gas while much smaller ratios are obtained with thermogenic processes; the exact ratio depends greatly on maturity.

6.4.3 Case study #3: equilibration of heavy oil

Heavy oils are characterized by high asphaltene content which causes asphaltenes to form clusters of nanoaggregates in the oil, the largest nanocolloidal particles of asphaltenes that are stable in crude oil over geologic time. These clusters with 5 nm diameter are the largest of the stably suspended asphaltene particles and accumulate toward the base of the oil column creating a large gravity gradient of asphalt. When this gradient equilibrates, this is referred to as the "heavy oil model" of the FHZ EoS. Since viscosity is highly correlated with asphaltene content, heavy oils often are characterized by large viscosity and large viscosity gradients. In addition, because the asphaltene concentration is high in heavy oils, asphaltenes are often near their solubility limit in heavy oils. Any increase in asphaltene concentration beyond this limit causes asphaltene phase separation often yielding a tar mat.

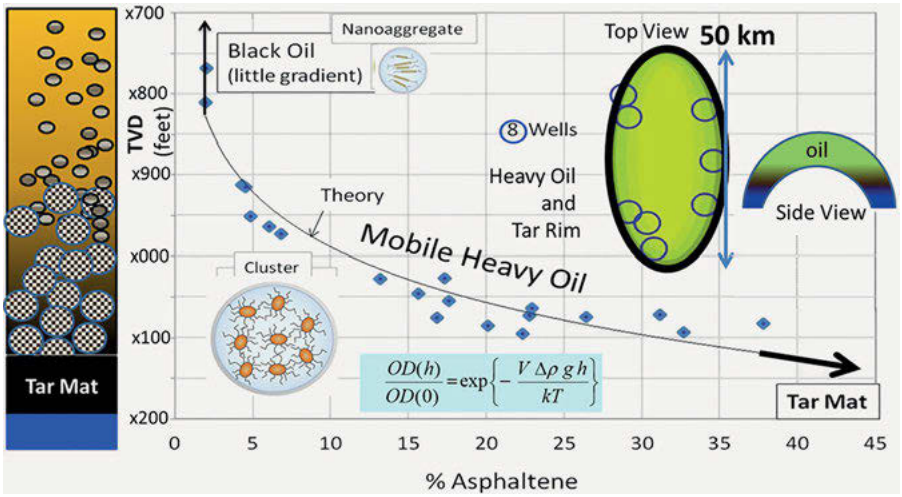

Figure 6.23: A large, four-way sealing anticlinal oilfield with a black oil in the crest and a rim of heavy oil underlain by a tar mat; a schematic of this oil column is on the left [9, 20, 27, 60, 82, 83]. The factor of 10 increase in asphaltene content in the heavy oil matches the FHZ EoS with asphaltene clusters, with no adjustable parameters, around the entire 100 km rim. The asphaltene content of 37% at the base of the heavy oil is the solubility limit for asphaltenes; the underlying tar mat has phase-separated asphaltenes clogging any permeability. Published with permission from the Society of Petroleum Engineers.

Figure 6.23 shows a giant reservoir with an oil column that is startling in its simplicity [9, 20, 27, 60, 82, 83]. The reservoir was initially placed into production for a limited time and is known to be well connected. Moreover, the asphaltenes are equilibrated throughout this field. All other fluids properties examined are consistent with this finding of fluid equilibration but only the asphaltene gradients are

useful to *predict* connectivity. And of course, asphaltene analysis is required to understand crude oil viscosity. There is a black oil in the crest with a small gradient of asphaltenes; the GOR is low; thus, there is no variation of GOR to create a solubility gradient contribution for the asphaltene gradient. For the black oil section of the field toward the crest, the asphaltenes are present in the crude oil as nanoaggregates and the black oil model of the FHZ EoS applies with its relatively small asphaltene gravity gradient. The magnitude of the gravity gradients also scales with the contrast in density between asphaltenes and the oil; for this low API oil, this density difference is not large thereby reducing the magnitude of the asphaltene gradient.

With depth below the crest the asphaltene content increases on this mild black oil gradient. At a concentration of a few percent, the asphaltenes form clusters which cause the asphaltene gradient to become very large and then conform to the heavy oil model of the FHZ EoS. This heavy oil model applies over the entire 100-km rim of this field; the 10× gradient in asphaltene concentration over 60 m of height matches the FHZ EoS prediction for asphaltene clusters [9, 20, 27, 60, 82, 83]. The only term of appreciable size is simply the gravity term for this column. The only adjustable parameter in the gravity term is the asphaltene particle size. The asphaltene gradient is accounted for with a particle size of 5.1 nm which is nearly identical to the nominal 5.0 nm cluster size published years before this study [30]. Essentially, this means there is no adjustable parameter; the fit of the data to the theory with clusters is nearly exact. This is an amazing success and validates the theoretical formalism of the FHZ EoS and validates the existence of asphaltene clusters in heavy oils. This 10× asphaltene gradient corresponds to a 1,000× gradient in viscosity, from a few cP to a few thousand cP under downhole conditions and is critically important in field development planning.

Injection of water into the aquifer for sweep and pressure support is precluded by the tar mat which is described below. Injection of water into the base of the heavy oil column is ineffective because the viscosity ratio of water to the viscous oil is 1,000. Oil to water viscosity ratios in excess of 10 lead to fingering of injection water into the oil column as opposed to aquifer sweep of the oil. In addition, injected water into this heavy oil would cause stable emulsion formation which would resist flow through porous media. Consequently, water injection for pressure support and sweep must be performed above the heaviest oil in the column; understanding the detailed nature of the gradients of asphaltene content and viscosity is important for production planning.

There is a roughly 10-m vertical tar mat underlying the heavy oil; this tar zone seals the aquifer from the oil. It is obvious that whatever mechanism produced this tar, it had nothing to do with water; (much) less than 1 m of tar would seal the aquifer; the formation of the next 9 m of tar above this 1-m tar layer cannot involve the aquifer [9, 20, 27, 60, 82, 83].

Figure 6.24 shows a plausible mechanism for the formation of the heavy oil and tar mat at the base of the anticline shown in Figure 6.23. First, the reservoir received

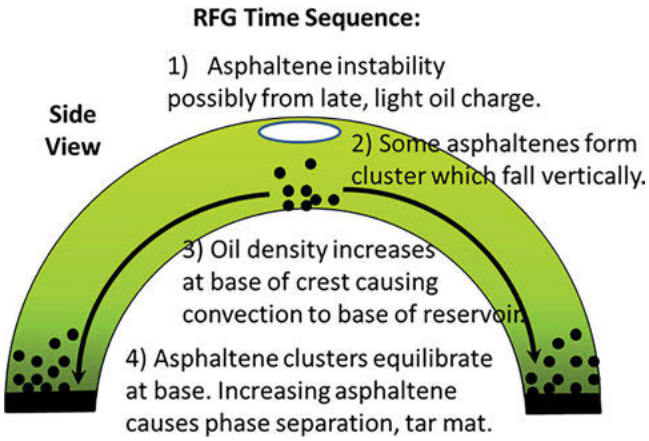

Figure 6.24: Proposed RFG mechanism for formation of heavy oil and the underlying tar mat in the field depicted in Figure 6.23. (1) The first and large charge into the field was a heavy oil. This was followed by a charge of a much lighter oil. Asphaltenes were destabilized by this mixture at the interface of the two charges. (2) Asphaltenes migrated downwards likely in the form of asphaltene clusters. (3) The increase in asphaltenes at the base of the crest caused this oil to be higher density than the oil in the flank. Convection followed. In colloidal instability of this nature, this convection proceeds by the well-known "Boycott effect" [84]. (4) Clusters at the base of the reservoir equilibrated in part by diffusion locally. As asphaltene accumulation at the base continued, the asphaltene concentration exceeded their solubility limit leading to asphaltene phase separation. The asphaltenes coated surfaces until any permeability was vanquished trapping heavy oil in the tar mat.

a large, somewhat heavy oil charge. Subsequent to this, the reservoir received a lighter oil charge. For the most part, the charge fluids do not mix during charging except at and near the charge point [77]. Instead, the charge fluids' density stacks away from the charge point [77], but can exhibit lateral sweep near the charge point [25, 80]. At the interface of the different, density-stacked charge crude oils, the asphaltenes are destabilized. Instead of undergoing bulk phase separation, the asphaltenes form clusters which naturally migrate down toward the base of the crest (or base of the formation interval). This oil at the base of the interval, and newly enriched in asphaltenes, is more dense than the oil toward the top of the interval but down-structure in the formation. This process is similar to the "Boycott effect" (after Professor Boycott), associated with colloidal instability and convection in fluids in tilted containers [84]. Convection follows with speeds that can easily reach 30 km/million years, thus very fast [85].

The asphaltenes transported to the base of the reservoir then equilibrated at least by diffusion rather quickly as the length scales are small. The gradient of clusters is large, thereby resulting in large concentrations of asphaltenes at the base of the heavy oil column. With continued incompatible charge, asphaltene migration to and accumulation at the base of the reservoir continues. There, asphaltene equilibration

(of clusters) corresponds to the heavy oil model which produces large asphaltene gradients at the base of the oil column. The asphaltene concentration at the lowest part of the oil column, at the oil–water contact, can become larger than the solubility limit for asphaltenes in crude oil; for this crude oil in Figure 6.23, the limit is about 37%. The excess concentration causes bulk phase separation of the asphaltenes resulting in an asphaltene-enriched coating on rock surfaces. Once permeability is reduced to zero, this is referred to as a tar mat. First, the heavy oil column is reviewed in detail, then the tar zone is treated.

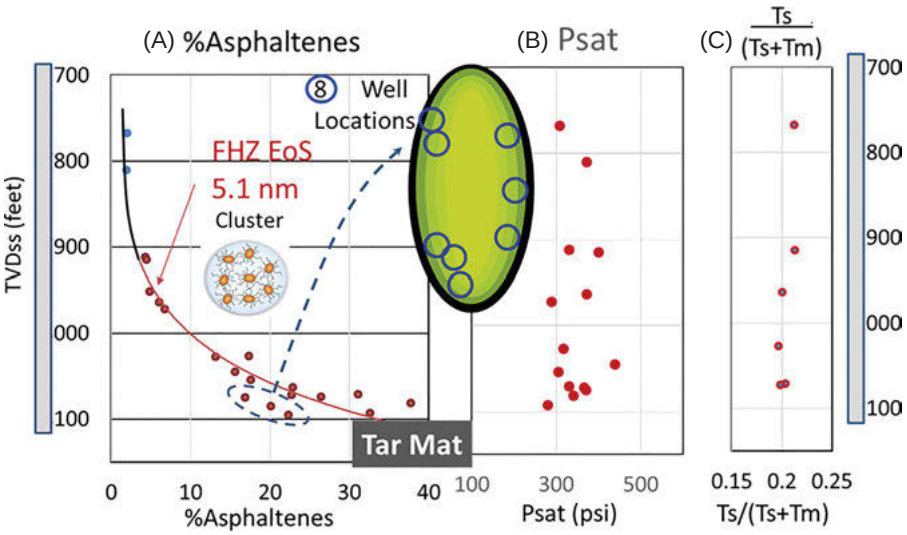

Figure 6.25: (A) The asphaltene gradient is very large and creates a viscosity gradient of a factor of 1,000. There is no gradient in (B) saturation pressure (Psat), nor in the (C) thermal maturity index Ts/(Ts+Tm). The thermal maturity of this crude oil is quite low which is consistent with a large asphaltene fraction in this oil [9, 20, 27, 60, 82, 83]. Published with permission from the Society of Petroleum Engineers.

Heavy oil and tar are largely defined by their asphaltene content [86, 87]. Naturally, understanding the asphaltene distribution is key to understand these materials. In particular, the large gradient of asphaltenes in the heavy oil column is seen to result from simply a gravity gradient of asphaltene clusters; this corresponds to the heavy oil model of the FHZ EoS. Figure 6.25 shows that other fluid properties are not very useful in understanding this gradient. The saturation pressure is homogeneous as expected for low GOR crude oils. There is no hint of the 1,000× variation of viscosity in the saturation pressure profile. Once again, the cubic EoS is of limited use to understand crude oil equilibration. In contrast, the asphaltene gradient analysis with the FHZ EoS accounts for the key concerns in this reservoir, viscosity gradients, tar mats and aquifer support [9, 20, 27, 60, 82, 83].

Figure 6.25C shows that the low thermal maturity of this crude oil (Ts/(Ts+Tm)~ 0.2) is consistent with the large asphaltene content of this crude oil. The asphaltene gradient in Figure 6.25A is consistent with equilibrium in accordance with the heavy oil model of the FHZ EoS. Nevertheless, other possible origins of the gradient must be considered. The thermal maturity gradient is very small; the gradient of the heavy oil column is not due to a density-stacked maturity variation of charge fluids. In any event, such an explanation does not make sense. If the gradient shown in Figure 6.25A is due to a maturity variation, then the lowest maturity "fluid" would be the tar which underlays the oil column. The concept would be that the tar charged first into the crest of the reservoir, then as lighter charge fluids entered the reservoir, the tar would be pushed downward. First, this tar is immobile; it does not migrate in the reservoir. Second, this tar is a two-phase system, it is not a single-phase system, the latter being expected for a low maturity charge fluid [9, 20, 27, 60, 82, 83].

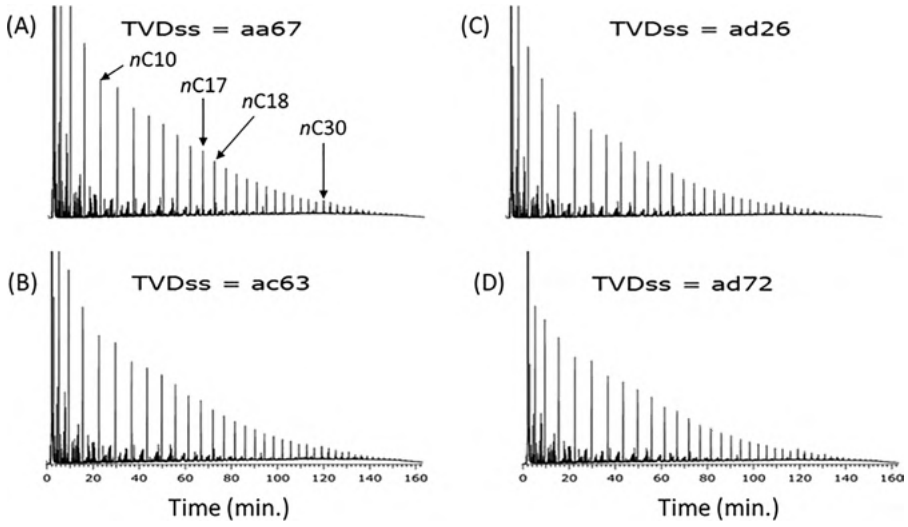

Figure 6.26: Conventional GC analysis of four samples from the heavy oil column of Figures 6.23 and 6.25 [20]. These GC chromatograms are essentially equivalent consistent with reservoir fluid equilibration. The nC18 is much larger than the phytane peak to its immediate right and the light n-alkanes are present in abundance precluding any appreciable biodegradation. Published with permission from the American Chemical Society.

Figure 6.26 shows that the liquid phase *n*-alkane content is large and essentially homogeneous as expected for an equilibrated reservoir fluid. In addition, there is no evidence of biodegradation. For all samples measured, the lighter *n*-alkanes appear unaltered, the pristane/*n*C17 ratio is ~0.17 and the phytane/*n*C18 ratio is ~0.45 confirming the lack of biodegradation and consistent with equilibration. For severe

biodegradation, the microbes can digest 2/3 of the crude oil [78, 79], thereby tripling the asphaltene content [23, 88]. Thus a gradient from biodegradation can create at most a factor of three gradients in asphaltenes. Here, there is no evidence of even mild biodegradation, let alone a difference of biodegradation in the column, and the asphaltene gradient is a factor of 10. Biodegradation did not contribute to the asphaltene gradient in this reservoir.

Figure 6.25A shows three points (circled with a dashed line) are somewhat low in asphaltene content and were obtained in the north part of the field. While the schematics shown in Figures 6.23 and 6.25 show two-fold rotational symmetric anticline, in fact, the oilfield is asymmetric (but accurate field maps are proprietary). The crest of the oilfield is toward the south, and the dip angle away from the crest is much steeper going south than north. Consequently, the asphaltene-enriched convective currents that are shown schematically in Figure 6.24 preferentially flowed south causing greater asphaltene accumulation in the south. Convective flows north could proceed but were over much greater distances yielding less asphaltene in the base of the oil column in the north. Thus, the asphaltene content in the oil column in the north is somewhat deficient in asphaltene content as indicated by the three circled data points in Figure 6.25A. In addition, the actual tar mat is much thicker in the south than in the north. This asymmetry represents a first-order correction to the zeroth-order model of total reservoir fluid equilibration. Understanding these first-order corrections is also important for field development planning and well placement [9, 20, 27, 60, 82, 83].

6.4.3.1 FHZ EoS treats heavy oil, cubic EoS fails

Thermodynamics applied to crude oils predicts two main properties, phase behavior and gradients. Both Flory–Huggins theory and cubic EoS have been used to address phase behavior. Both these methods are naturally parametric and depend on matching measurements of phase behavior such as the asphaltene onset pressure (AOP). For asphaltene gradient analysis, the FHZ EoS utilizes the Yen–Mullins model of nanocolloidal structures of asphaltenes, thereby providing treatment of size-dependent terms such as the gravity term. In contrast, common Cubic EoS methods utilize pseudo-components to address fluid complexities, and each pseudo-component is associated with a variety of parameters such as molecular weights, interaction parameters, critical constants and acentric factors, giving flexibility in fitting data. For asphaltene gradients, it is important to determine the theoretical methods that best represent the chemistry of crude oils and asphaltenes. The heavy oil column shown in Figures 6.23 and 6.25 offers a test to determine whether traditional cubic EoS methods or the FHZ EoS methods are correct. The excellent fit of the gradient to the FHZ EoS indicates that the FHZ EoS is superior to treat asphaltene gradients over cubic EoS methods. In

addition, analytical chemistry methods can be utilized to predict the superior theoretical treatment.

The clusters of the Yen–Mullins model used with the FHZ EoS presume that the chemical description of the asphaltenes in this oil is invariant. The same asphaltene molecular components comprise the nanaoaggregates and clusters at the top and the base of the heavy oil column. In contrast, traditional cubic EoS methods to treat such a huge asphaltene gradient would utilize different asphaltene pseudo-components; each asphaltene pseudo-component would have its own molecular weight, interaction parameters, and critical constants. With so many variables, any gradient can be "fit." However, the chemistry and physics of such an approach can be nonphysical and in error. It is straightforward to test whether the chemical properties of asphaltenes vary or are fixed in this oil column.

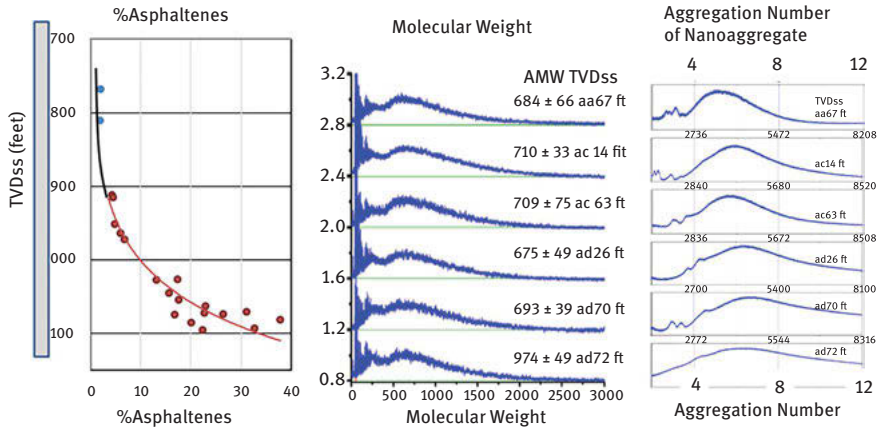

Figure 6.27: The molecular weight and the aggregation number of the nanoaggregate are determined for asphaltene samples throughout the heavy oil column [89]. In spite of the large gradient of asphaltenes, the asphaltene molecular weight and aggregation number are invariant. Use of the Yen–Mullins model and the FHZ EoS is supported. Use of different asphaltene pseudo-components in a cubic EoS treatment is contradicted. Published with permission from the American Chemical Society.

Figure 6.27 plots the molecular weight and aggregation number of asphaltene nanoaggregates for asphaltene samples throughout the oil column also plotted in Figures 6.23 and 6.25. The conclusion is that there is no variation of either property in the heavy oil column. Consequently, the basic assumption of the Yen–Mullins model is reinforced, the asphaltenes are chemically invariant, what is changing in the oil column is the nanocolloidal description based on asphaltene concentration and solvency. The application of the FHZ EoS with its reliance on the Yen–Mullins is similarly reinforced as being chemically valid. The results in Figure 6.27 show that any presumption of multiple pseudo-components for the asphaltenes in a

cubic EoS treatment is chemically invalid. Consequently, such an approach would correspond to curve fitting, but not correspond to any true chemical analysis of the oil column. Merely curve fitting is not predictive and is not of interest [2].

The molecular weight of any chemical species is fundamentally important. In addition, for asphaltenes, the aggregation properties as determined from the aggregation number of asphaltene nanoaggregates are also fundamentally important. Asphaltene molecular weight had been a topic of significant controversy in the past but is now resolved [82, 86, 90–109]. Arguably the best method for determination of asphaltene molecular weight is laser desorption, laser ionization mass spectrometry (L2MS) [82, 89, 96, 102, 106, 107, 110, 111]. This method is sensitive to nearly all of the asphaltene sample, has nearly uniform cross section, is unaffected by aggregation, and has minimal fragmentation. The molecular weight data shown in Figure 6.27 is from L2MS, and shows the molecular weight is invariant in this heavy oil column [89].

Asphaltene nanoaggregates are weakly bound and difficult to preserve in mass spectrometry studies; from the critical nanoaggregate concentration, binding energies of nanoaggregates in toluene are estimate to 5 kcal/mol of nanoaggregates [2, 112]. Surface-assisted laser desorption ionization mass spectrometry (SALDI-MS) utilizes a rapid, indirect heating method to loft asphaltene nanoaggregates from the solid state into the vacuum. Clusters are even more weakly bound and do not survive volatilization. As with the molecular weight, Figure 6.27 shows there is no variation of the aggregation number of nanoaggregates from (solid) asphaltene samples throughout the heavy oil column [102].

Another sensitive chemical metric to detect possible changes in chemical composition is the analysis of sulfur speciation of asphaltenes [83, 113–118]. Sulfur chemical analysis of asphaltenes can discriminate between invariant chemical composition of asphaltenes as presumed by the Yen–Mullins model or if varied, support multiple pseudo-components for the treatment of asphaltenes. There can be many different, resolvable sulfur species in organic compounds as shown in Figure 6.28A [83]. The sulfoxide group is characterized by very large polarity (~4 Debyes), and could affect intermolecular interactions significantly. In addition, the fraction of aromatic sulfur (thiophenic) to saturated sulfur (sulfide) is known to vary considerable in different asphaltenes [83, 113, 114, 116, 118, 119].

Figure 6.28 shows application of x-ray absorption near edge structure (XANES) on the sulfur chemistry. Figure 6.28A shows that the energy of the main peak for each compound, the sulfur k-edge (1s-3p transition), is highly dependent on the specific chemical form of sulfur. This energy is very dependent on the oxidation state of sulfur; the k-edge of more oxidized sulfur is at higher energy. This fact makes the different sulfur species resolvable by XANES methods.

Figure 6.28B shows that the asphaltenes throughout the heavy oil column in Figure 6.23 (in blue) and even samples from a different stacked, reservoir (in red) are all very similar and all dominated by thiophene sulfur [83]. The asphaltene sulfur speciation is invariant throughout the heavy oil column and this invariance

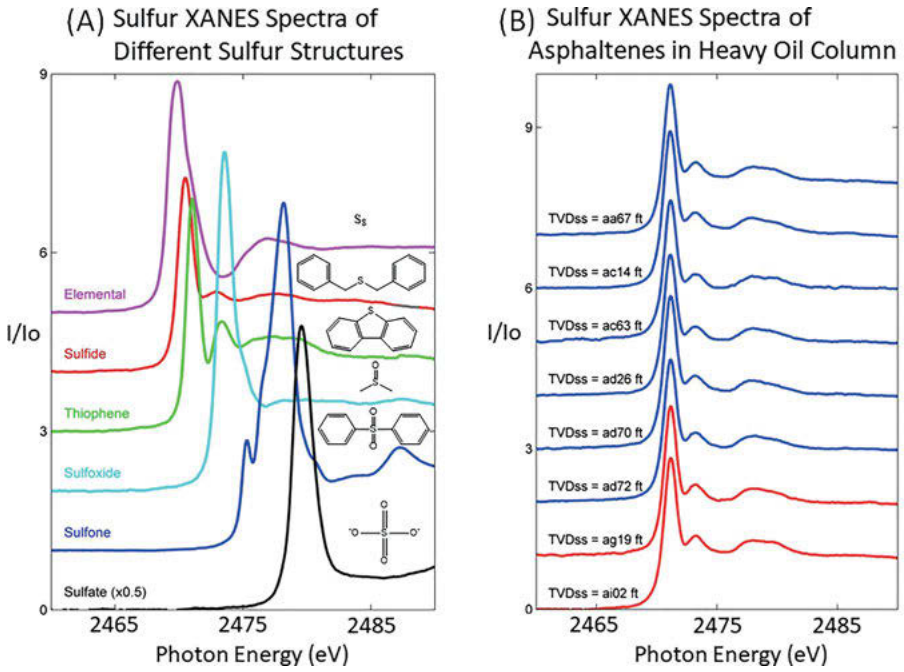

Figure 6.28: (A) Sulfur XANES spectra showing excellent differentiation of different chemical forms of sulfur (B) Sulfur XANES spectra of many asphaltenes samples throughout the heavy oil column of Figures 6.23 and 6.25 (in blue) as well as those from a different, stacked reservoir (red) [83]. All these sulfur XANES spectra of the different asphaltenes in (B) are very similar and dominated by thiophene sulfur. Spectra are offset for clarity of presentation and arranged in order of depth (shallowest at the top and deepest at the bottom). For the asphaltene gradient in the heavy oil column, use of the Yen–Mullins model and FHZ EoS is validated; the Cubic EoS method with different asphaltene pseudo-components is contradicted [2]. Published with permission from the American Chemical Society.

even extends into a different stacked reservoir. It is known that asphaltenes from different reservoirs can show significant variation in their sulfur chemistry. The invariance observed here is consistent with the Yen–Mullins model and its utilization in the FHZ EoS. This invariance contradicts utilization of different pseudo-components for asphaltenes in the Cubic EoS approach for describing asphaltene gradients [2].

The stable isotopic compositions of three asphaltene samples from the heavy oil column in Figure 6.23 were measured for both carbon and hydrogen; the results are shown in Table 6.1 [20]. These values are similar to those obtained from kerogen and bitumen. The different asphaltenes have the same stable isotopic composition within error for the two dominant elements of asphaltenes, carbon and hydrogen, which is consistent with invariance of the asphaltene chemistry and of equilibration.

Table 6.1: Isotope composition of three asphaltene samples from the heavy oil column in Figure 6.23 [20].

Sample ID	$\delta\,^{13}$C ‰ vs VPDB[a]	$\delta\,^{2}$H vs VSMOW[b]
MC7-21130 asphaltene	−27.93	−84
MC7-23477 asphaltene	−27.97	−81
MC7-20860 asphaltene	−27.94	−83

(a) VPDB carbon isotope reference Vienna Pee Dee Belemnite.
(b) VSMOW hydrogen isotope reference Vienna Standard Mean Ocean Water.

6.4.3.2 Tar mat under a nonbiodegraded heavy oil

The terms "tar" and "bitumen" have been widely used in the oilfield to account for a variety of carbonaceous materials of various origins [14, 18, 25, 27, 29, 120–122]. Tar and bitumen are both characterized by high asphaltene content and as such are either very high viscosity liquids or solids. The term "tar mat" is often used to signify a tar layer at the OWC that seals the aquifer from the oil thereby precluding aquifer sweep and even pressure support during production. There are a variety of mechanisms that can form viscous or immobile tar layers at the base of the reservoir. Most importantly, at the transition from the oil column to the tar mat, there can be either a continuous or a discontinuous increase in asphaltene content. If the asphaltene content is continuous, then the dominant process forming the tar mat is asphaltene addition to the base of the column from upstructure as depicted in Figure 6.24. Asphaltene addition to the heavy oil column at the base of the reservoir is compensated by asphaltene deposition out of the oil once the solvency capacity of the oil is exceeded by the asphaltene concentration. In this case, the carbonaceous material that deposits is rather pure asphaltene [120]. Tar mats associated with a discontinuous increase of asphaltenes result from a process where the solvent becomes a worse solvent for the asphaltene [25, 28, 121, 123]. For example, gas diffusion into the oil from upstructure decreases the capacity of the crude oil to dissolve asphaltene. In this case the asphaltene undergoes phase separation [25, 28, 121, 123]. With further increases in solution gas, the discontinuity of the asphaltene gradient between the oil and the tar mat can become very large. Thus, tar mats exhibit the two primary controls of solubility (in addition to temperature), concentration of the solute, and solvency capacity of the solvent.

In this anticlinal structure, the tar is generally deeper than the oil column, and with the small dip angle of the anticline, the tar extends further laterally than the oil. Six tar wells were drilled with whole core acquired in the tar zone. Core plugs were obtained from whole core at known heights in the column. The organics were extracted from these core plugs and the SARA content was obtained for each extracted

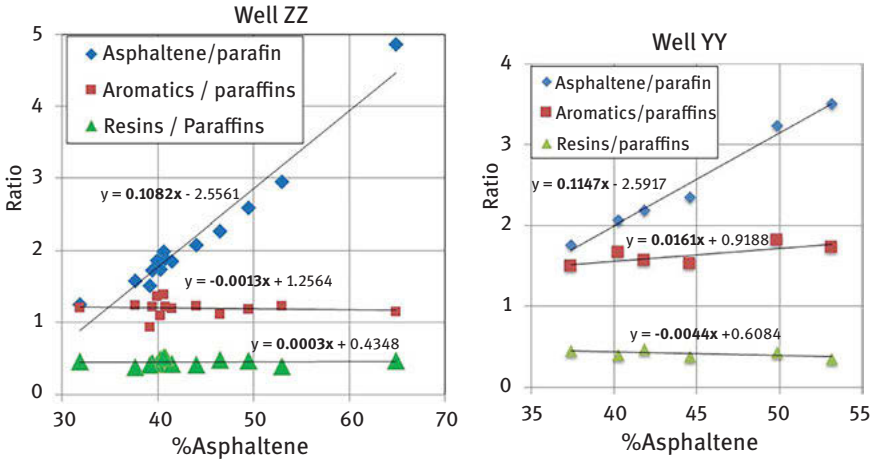

Figure 6.29: SARA ratios of many of core plugs taken from whole core from two wells (ZZ and YY) obtained in the tar mat (with no oil column). The is a huge range of the asphaltenes/paraffins where there is almost no variation of aromatics/paraffins and resins/paraffins. This data is consistent with (1) the tar mat is a two phase system with a carbonaceous deposit and an trapped oil and (2) the carbonaceous phase is pure asphaltene with no resin [120]. Published with permission from the Society of Petroleum Engineers.

sample. Figure 6.29 shows the analysis of core plugs from whole core from the tar zone in wells that intersected only the tar zone, not the oil column; these wells were drilled for tar analysis providing an excellent platform for analysis of the tar mat. In some cases, the thickness of the tar mat exceeded 10 m. This strongly implies that the tar did not form as a consequence of oil–water interaction. One meter of tar easily seals the aquifer from the oil column, if water is necessary to form tar, then how did the other 9 m of tar form? The tar mat is a two organic phase systems, a solid carbonaceous material and a trapped heavy oil. The ratio of SARA components can be plotted to determine exactly what is the carbonaceous phase. Figure 6.29 shows that neither the resins not the aromatics scale with asphaltenes (all normalized by the saturates). In other words, only asphaltenes are depositing, but not resins. At first, this might seem surprising. However, the asphaltenes constitute the material that is colloidally suspended in crude oil, and, in this case, only asphaltenes are being added to the base of the reservoir. Thus, it is the increase in asphaltene concentration, and only the asphaltene concentration, at the base of the oil column that causes asphaltene deposition at the base.

The tar mat underneath the oil column in Figure 6.23 exhibits a largely continuous increase in asphaltene content. However, the asphaltene fraction in the core plugs from the tar zone do not exhibit an extension of the FHZ EoS curve obtained in the oil column as shown in Figure 6.30. The tar mat corresponds to asphaltene deposition in the core. Once permeability is sealed in some reservoir volume, then there is

no more compositional change in this sealed volume. The sealed volume might represent a pore if all pore throats leading to the pore are sealed by deposited asphaltenes. Nevertheless, the sealed volume could present a cubic meter if the sealed volume is capped by a tight carbonate streak that itself is plugged by deposited asphaltenes. The reservoir sections below the tight streak might retain some limited volume that retains some permeability. This explains why wells drilled in the tar zone fill with oil.

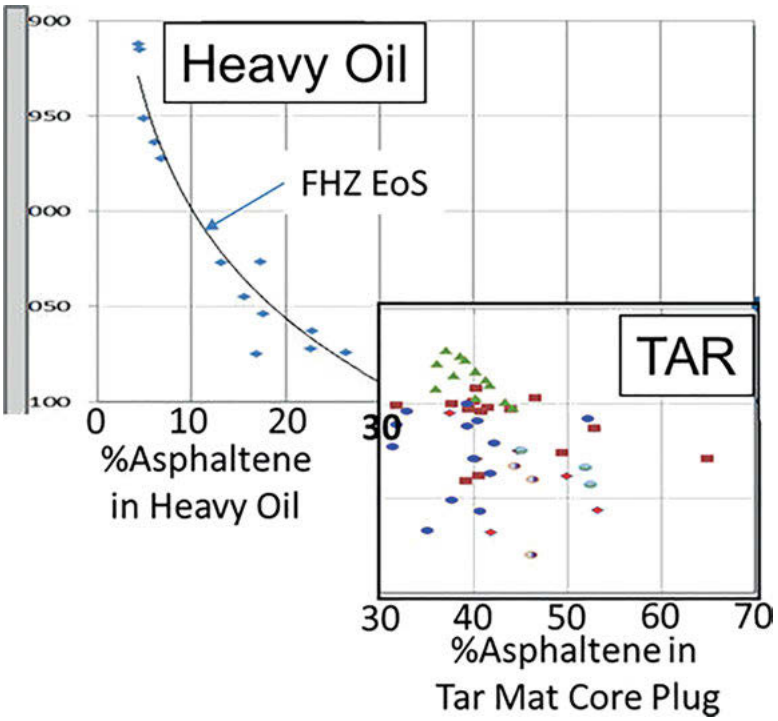

Figure 6.30: Comparison of asphaltene content in heavy oil samples and in tar extracted from core plugs in the tar mat [120]. Data from six tar wells are plotted; each symbol is a specific well (green triangle, blue circle, etc.). The high asphaltene content of the oil grades roughly continuously into the higher asphaltene content in the tar zone. However, while the oil column shows a gravity gradient of asphaltenes matching the FHZ EoS, asphaltene content in the extracted tar is always high but varies randomly with depth in each of the tar wells. Published with permission from the Society of Petroleum Engineers.

The asphaltene content from the core plugs from six tar wells are plotted in Figure 6.30; each different symbol refers to a specific tar well. The tar well with the green triangles in Figure 6.30 corresponds to the tar well which is the farthest upstructure in the anticline, thus, the tar plugs are at shallower depths than those of other tar wells. Unlike the oil column above the tar, where the asphaltene content largely matches a gravity gradient of asphaltene clusters, the tar zone exhibits

random variations of the asphaltene content with depth; the tar zone does not exhibit an extension of the FHZ EoS to higher asphaltene content. This may seem surprising as the core plugs are in close spatial proximity within a given tar well, however, the asphaltene content is far from the equilibrium FHZ EoS curve. In addition, Figure 6.30 shows that the asphaltene content in the core plugs varies significantly from 30% to 65%; at 30% to 35% the material is a very viscous oil (~2,000 cP) while at 55% to 65% asphaltenes, the material has the rheology of coal [9, 21]. The tar mat is not a uniform material, and the asphaltene content and rheology of the material do not vary systematically with depth.

The lack of equilibration of the tar mat asphaltene content even over a tiny length scale of meters and the lack of homogeneity of the material within the tar mat are both explained by the fact that the tar mat consists of two organic phases: one phase is a viscous oil of about 30% asphaltene content; the other phase is a solid asphaltene deposit which appears to be 100% asphaltene by the analysis of Figure 6.29. With continued asphaltene migration to the base of the oil column, the asphaltene content eventually exceeds the solvency concentration of asphaltenes in the oil. Specifically, the asphaltene in the crude oil above the tar mat at the base can diffusively equilibrate over the small vertical intervals (many tens of meters). Thus, the asphaltene content at the very bottom of the oil column is highest. When this concentration is greater than 37%, asphaltene deposition occurs. Once permeability is sealed due to clogging of permeability with solid asphaltenes, then the oil column has a new higher base. By this means, a thick tar deposit can be built with increasing thickness over time. This process precludes any equilibrium of asphaltenes in the tar mat. Consequently, even over the short distance of meters length scale, the asphaltene content cannot match the FHZ EoS heavy oil model. With no permeability, any porosity that is occupied by the viscous oil remains trapped. For a core plug, the ratio of trapped viscous oil versus asphaltene deposit determines the asphaltene content of the extracted organics. If more trapped oil is obtained in the core plug, then the core plug asphaltene content is closer to 30%. If more asphaltene deposit is obtained in the core extract, then the asphaltene content is closer to 60%. The deposited asphaltenes and the trapped viscous oil have very different responses in pyrolysis of cores and cuttings. The deposited asphaltenes behave as a refractory material similar to pyrobitumen while the viscous oil behaves similarly to black oils. The refractory nature of asphaltenes has also been noted in analysis of refining resid.

Figure 6.31 shows a thin section from a tar mat in a condensate oilfield [124]. For condensates, there is no question that the deposited tar is a separate organic phase. The 2-meter tar mat consists of trapped condensate and a phase-separated tar. This tar mat in Figure 6.31 represents a discontinuous increase in asphaltene content in transitioning from the condensate to the tar [124]. The deposited tar is enriched in asphaltene and has very low mobility. There is porosity but no permeability in this tar zone. The blue in Figure 6.31 corresponds to epoxy that has been forced into the

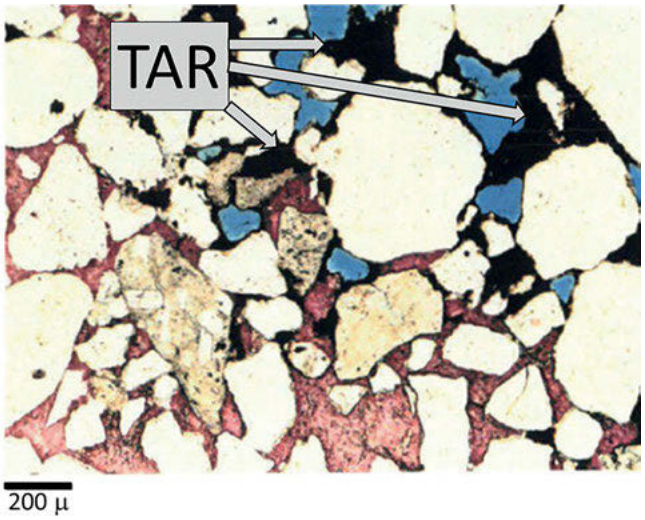

Figure 6.31: Thin section of a tar mat from a condensate oilfield [124]. The 2-m tar mat consists of two organic phases. The thick, black coating on mineral surfaces is an asphaltene-enriched, phase-separated tar. The blue is epoxy from thin section preparation and corresponds to displaced condensate which is trapped within the tar mat. The white grains are sandstone and the pink is cement. Published with permission from the Society of Petroleum Engineers.

core plug displacing condensate for preparation of thin sections. This tar mat was deposited on a cemented sandstone, the tar formation has nothing to do with water.

6.5 RFG oilfield case study; disequilibrium reservoir fluid

6.5.1 Case study #4: Diffusive gradient and quasi-equilibrium

A common occurrence is a gas charge into an oil reservoir (or an oil charge into a gas reservoir). Figure 6.32 shows a reservoir with this condition of a recent charge. It is not clear which fluid is the recent arrival, the gas or oil. From a practical matter in this reservoir, it does not matter; however, from a standpoint of basin analysis, the timing and order of charge fluids do matter. The important point is that the second hydrocarbon charged into the reservoir with a relatively short duration and that a gas was density stacked over an undersaturated oil. In some cases, the order of charge fluids can be established, often a late primary biogenic gas charge enters an oil reservoir [12, 59, 70]. The discussion below presumes a recent gas charge entered an oil reservoir, but the charge order might be reversed.

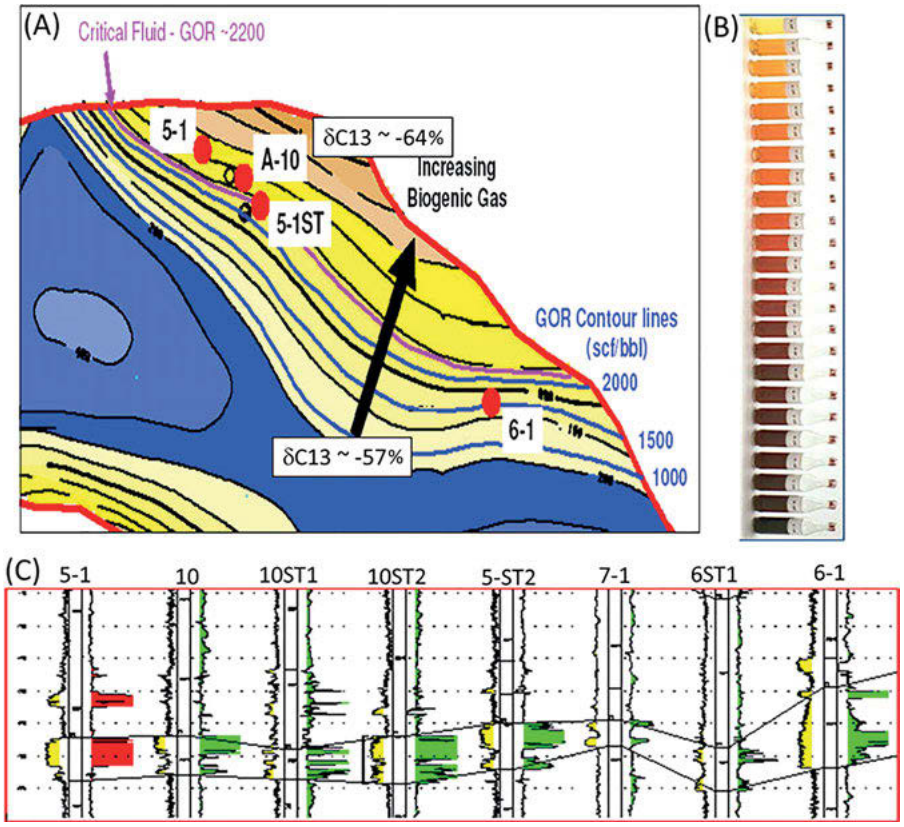

Figure 6.32: Deepwater Gulf of Mexico reservoir with a relatively recent, charge of primary biogenic gas into an undersaturated black oil (or oil into gas) in a single reservoir [2, 62, 67, 124]. (A) Contour map of the field indicating fluid gradients of GOR and isotopic composition of methane. (B) A series of dead oil samples visually showing an enormous variation of asphaltene content (courtesy, Hani Elshahawi, Shell). (C) Petrophysical log data gamma ray and resistivity, identifying the producing sand lobe in various wells. Published with permission from the Society of Petroleum Engineers.

Figure 6.32 shows a deepwater reservoir that experienced an oil charge and a primary biogenic gas charge [2, 62, 67, 124]. The tilted sheet sandstone reservoir is an amalgamated fan lobe that is known from production to be well connected [62]. Figure 6.32A shows a contour map of the field; variations in GOR and in methane isotopic composition are indicated. Figure 6.32B shows a series of dead oils commonly referred to as the "Hani Bottles" showing the enormous variation in asphaltene content in this field (*courtesy, Hani Elshahawi, Shell*). Figure 6.32C shows petrophysical logs identifying this lobe system in many wells. Good production performance and pressure depletion measurements confirmed excellent connectivity in this reservoir.

This case study and its visual proof of compositional variation in a connected reservoir was an important milestone in the general recognition that reservoirs can contain compositionally graded crude oils and that such gradients can impact field development planning. Prior to this time, there had been a perspective within the industry that compositional variation of reservoir fluids could be largely ignored in field development planning. Subsequent to this case study and the ubiquitous appearance of the "Hani Bottles" (from Hani Elshahawi) in many publications, widespread recognition has grown substantially regarding the importance of compositional grading and fluid complexities for production concerns. At this juncture, RFG exploits compositional variations of any sort of varying magnitudes to address a broad range of reservoir concerns [2].

During the charge process, there is very little mixing of the original and new charge fluids except in and near the charge points of the reservoir [77]. Away from the charge point, the fluids' density stacks. The crude oil in the reservoir is undersaturated, in part due to the high pressure for this and other deepwater reservoirs. The only way for this density-stacked gas to mix with the oil is by diffusion of the gas downward into the oil column.

Figure 6.33 shows a giant diffusive gradient of solution gas in the upper half of the oil column going from 8,000 scf/bbl to 2,200 scf/bbl in 150 feet of height. The lower half of the oil column shows a much smaller GOR gradient going from 2,200 scf/bbl to 1,800 scf/bbl in 200 feet of height. It might appear surprising to have such a giant gradient in rather limited height of the upper half of the oil column. However, on closer inspection this observation is quite reasonable. The actual direction of the diffusive flux is mostly lateral within the reservoir in this tilted sheet sand of small dip angle. Thus, a limited height difference corresponds to an extended lateral distance. Detailed analysis shows that this GOR gradient meets expectations for a Late Miocene gas charge into this oil reservoir [2, 62, 67, 124].

The GOR gradient in the lower half of the oil column is labeled, "quasi-equilibrium"; quasi means "seemingly or apparently but not really." With continuing geologic time, the diffusive flux of gas would extend lower in the column, so the bottom half of the oil column is not really equilibrated but would change in time. Nevertheless, if *only* the bottom half of the oil column is analyzed, the GOR gradient is consistent with equilibrium [2].

The high solution gas toward the top of the column is incompatible with dissolution of much asphaltene as shown by measurement (Figure 6.33C) and visually in the dead oil samples (Figure 6.33B). The question arises, "where did the asphaltenes go?" Figure 6.33C shows that the asphaltenes migrated to the base of the reservoir increasing the concentration of asphaltenes there in this high GOR black oil. The gradient of asphaltenes at the base exhibits a quasi-equilibrium distribution of asphaltene clusters. Clusters formed because of the relatively high concentration of asphaltenes and relative high solution gas (~2,000 scf/bbl). The term "quasi-equilibrium" is used because if (geologic) time progressed, the solution gas would

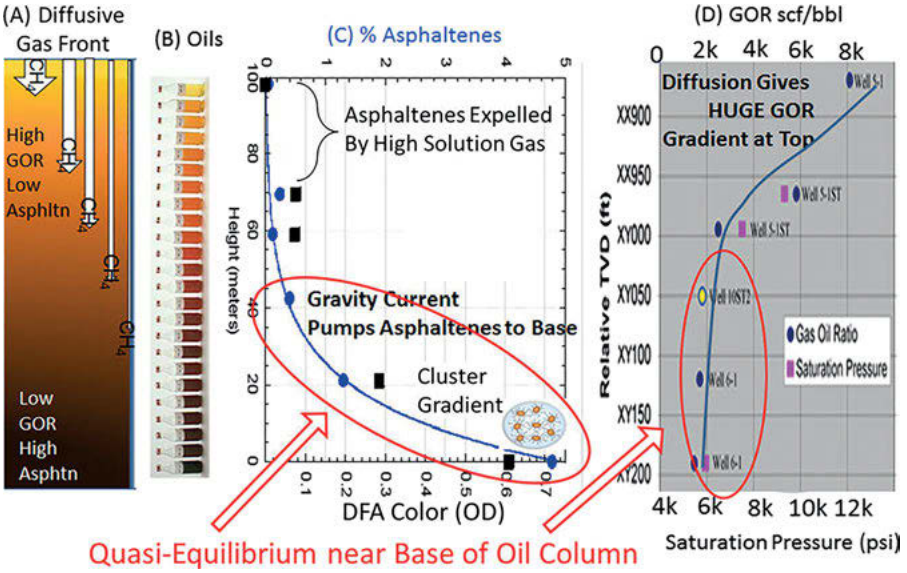

Figure 6.33: Oil column for the reservoir in Figure 6.32 with a relatively recent mixed charge of primary biogenic gas into oil (or oil into gas) [2, 62, 67, 124]. (A) RFG schematic showing the diffusive flux of gas into oil. At and near the original GOC, the solution gas increases significantly expelling asphaltenes. (B) Dead crude oil samples showing the huge asphaltene gradient. The color variation of the crude oils which is very visually evident is quantified by DFA measurements. (C) Lab asphaltene content (blue circles) and DFA color (black squares). The asphaltenes are being expelled from the top of the column by the increasing solution gas. The asphaltenes at the base of the column exhibit a gradient consistent with a quasi-equilibrium distribution of asphaltene clusters. (4) Lab GOR (blue circles) and saturation pressure (Psat, pink squares) showing a diffusive gradient at the top of the column and a quasi-equilibrium at the base of the column. Published with permission from the American Chemical Society.

increase at the base of the reservoir expelling the asphaltenes, ultimately in bulk phase separation. Thus, the asphaltene cluster gradient is time dependent violating a necessary condition for equilibrium. Nevertheless, if only the bottom half of the oil column is analyzed, it is consistent with an equilibrated gradient of asphaltene clusters. This quasi-equilibrium condition exists because the flux of asphaltenes from upstructure is not high, limited by the diffusion of gas lower in the oil column that causes further asphaltene expulsion and migration. Since most of the net diffusive displacement is lateral, the rate of downward diffusive flux is quite low. Consequently, the relatively small flux of newly added asphaltenes toward the base of the oil column does not significantly perturb equilibration of asphaltene clusters at the base of the column. The asphaltenes at the base of the column can be diffusively equilibrated over reasonable times, due to the limited spatial extent [2].

Figure 6.34 shows that a diffusive gas flux associated with a Late Miocene gas charge into a reservoir with undersaturated black oil can account for the dominant

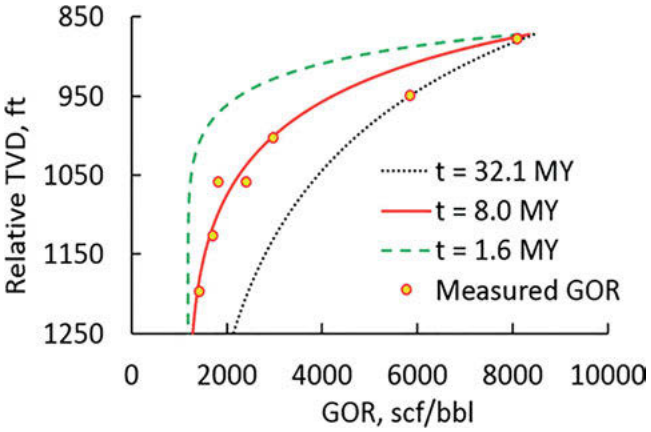

Figure 6.34: Diffusive GOR gradients versus elapsed time for the initial condition gas over undersaturated crude oil. The data in Figure 6.33C is consistent with an ongoing diffusive process since the Late Miocene. The diffusion model employs the error function solution to the diffusion equation which is arguably the simplest solution. Published with permission from the American Chemical Society.

observations associated with the GOR gradient shown in Figure 6.33C. The primary features of a very large decrease in GOR toward the top of the column and a much smaller decrease of GOR toward the base of the column are readily reproduced by the diffusive model. The exact timing of the gas charge into the oil reservoir is not expected to be accurate because of uncertainties in the diffusion constant. A rough timing of a Late Miocene charge of gas is quite reasonable. Figure 34 shows that the diffusive GOR gradient changes dramatically with over geologic times.

Figure 6.35 shows that the methane isotope ratio is not equilibrated in this oilfield [2, 62, 124]. Toward the top of the column, there is a substantial increase in the fraction of methane which is primary biogenic. Estimates of the fraction of methane that is primary biogenic versus thermogenic are given in the figure. At equilibrium, there would be a single isotopic composition; the observed disequilibrium is consistent with the diffusive gradient depicted in Figure 6.33. The significantly greater fraction of biodegradation gas at the top of the column is also consistent with the concept of a recent stacking of primary biodegradation gas over an undersaturated oil followed by the process of diffusive mixing. The exact fraction of biogenic to thermogenic gas depends on the presumed isotopic composition of methane from each source. For the fractions listed in Figure 6.35, primary biogenic methane is presumed to be −70‰ and thermogenic methane is presumed to be −45‰.

One point of uncertainty is why there is so much primary biogenic gas at the base of the oil column. The analysis in Figure 6.35 shows that the methane at the base of the column is 50% primary biogenic methane, while the diffusive model shows that the diffusive addition of methane to the base of the column should be

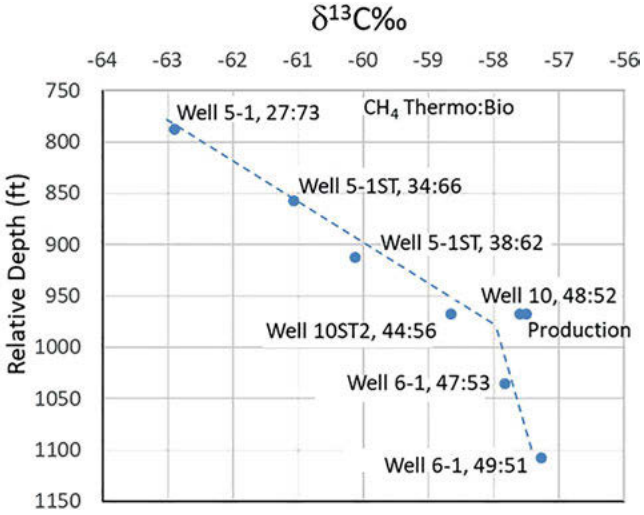

Figure 6.35: Methane carbon isotope analysis indicating a greater contribution of primary biogenic gas upstructure. Notation X/Y means X% of thermogenic gas, Y% of biogenic gas [2, 62, 124]. Published with permission from the Society of Petroleum Engineers.

much less. Nevertheless, one effect of this excess solution gas is likely why asphaltenes are in the cluster form as opposed to nanoaggregates that would be expected in low GOR black oils. It is likely that this excess primary biogenic gas arrived at the base of the column by a mechanism that is not strictly from a recent diffusive process. Perhaps there was some mixing during charge; such a process is known to occur near charge points [25, 80]. Perhaps there was a more complicated entry of oil and primary biogenic gas into the reservoir with some overlapping charge. In any event, the primary observations in the field are consistent with a simple diffusive model, but some observations imply some additional complexities. This is often the case with applications of simple models to describe earth science with its many contingencies.

6.6 Conclusions

At long last, chemical structure-function relations have been established for asphaltenes with direct applications in the oilfield. The resolution of molecular and the hierarchical nanocolloidal structure of asphaltenes in the Yen–Mullins model is enables resolution of the gravity and other terms in equation of state modeling. The regular solution theory Flory–Huggins theory can be modified with the gravity term giving the FHZ EoS for modeling asphaltene gradients in oilfields. The FHZ EoS

with the Yen–Mullins model can be used to determine whether reservoir crude oils are or are not in thermodynamic (compositional) equilibrium. With the three species of the Yen–Mullins model, there are three types of asphaltene gradients applicable for light oil, black oil and heavy oil. When reservoir fluids are equilibrated, then reservoir connectivity is likely. This addresses perhaps the biggest risk factor in deepwater reservoirs. Examples of reservoir fluid equilibration even at the 100 km length scale are reviewed herein. In addition, the equilibration process has many implications regarding petroleum systems and reservoir attributes. If reservoir fluids are not equilibrated, then frequently, one or more processes can be identified acting on the reservoir fluids that preclude equilibration. A collection of these processes, including reservoir fluid equilibration processes constitutes a new technical discipline, "reservoir fluid geodynamics." With the incessant demand to increase efficiency, RFG provides a major improvement in reservoir evaluation. A simple example is the common occurrence of gas charge into reservoirs of undersaturated oil. In such cases density stacking of charge fluids is followed by diffusive mixing of gas and oil. The simplest solution to the diffusion equation, the error function solution, can be employed to model this process with a small number of parameters. Moreover, the increase in solution gas expels asphaltenes, and they can migrate many kilometers by convective flows conceptually matching the Boycott effect yielding high asphaltene content and even tar mats at the base of the reservoir. Such an example is reviewed herein matching enormous solution gas and asphaltene gradients. With the resolution of asphaltene structures, the application of a host of fundamental chemical principles is now being applied successfully to oilfield reservoirs to address all manners of reservoir concerns. The chemical sciences offer powerful means to exploit even extremely complex chemical systems such as reservoir crude oils in enigmatic earth science settings.

References

[1] Peng D-Y, Robinson DB. A new two-constant equation of state. Ind Eng Chem Fundam, 1976, 15, 59–64.

[2] Mullins OC. *Reservoir Fluid Geodynamics and Reservoir Evaluation*. 2019, Houston, TX: Schlumberger, https://www.slb.com/resource-library/book/reservoir-fluid-geodynamics-and-reservoir-evaluation.

[3] Peters KE, Walters CC, Moldowan JM. The biomarker guide. 2nd ed, vol. 1, Cambridge University Press, Cambridge, 2005.

[4] Mishra VK, Cañas JA, Betancourt SS, Dumont H, Chen L, De Santo I, Pfeiffer T, Achourov V, Hingoo N, Zuo JY. DFA connectivity advisor: a new workflow to use measured and modeled fluid gradients for analysis of reservoir connectivity. In: Offshore technology conference. Offshore Technology Conference, 2014.

[5] Mullins OC, Dumont H, Mishra VK, Gomez A, Wilkinson T, Winkelman B, Primio RD, Uchytil S, Nagarajan N, Strauss S. The critical role of asphaltene gradients and data integration in

reservoir fluid geodynamics analysis. In: SPE annual technical conference and exhibition. SPE 187277, 2017.
[6] Mullins OC, Cribbs ME, Betancourt SS, Dubost FX. Asphaltene gradient in a deepwater oil reservoir as determined by downhole fluid analysis. In: International symposium on oilfield chemistry. Society of Petroleum Engineers, 2007.
[7] Betancourt SS, Ventura GT, Pomerantz AE, Viloria O, Dubost FX, Zuo J, Monson G, Bustamante D, Purcell JM, Nelson RK. Nanoaggregates of asphaltenes in a reservoir crude oil and reservoir connectivity. Energy Fuels, 2009, 23(3), 1178–1188.
[8] Johansen YB, Rinna J, Betancourt SS, Forsythe JC, Achourov V, Canas JA, Chen L, Zuo JY, Mullins OC. Asphaltene gradient analysis by DFA coupled with geochemical analysis by GC and GCxGC indicate connectivity in agreement with one year of production in a norwegian oilfield. In: SPE annual technical conference and exhibition, SPE 191490. 2018.
[9] Mullins OC, Seifert DJ, Zuo JY, Zeybek M. Clusters of asphaltene nanoaggregates observed in oilfield reservoirs. Energy Fuels, 2013, 27(4), 1752–1761.
[10] Chen L, Forsythe JC, Wilkinson T, Winkelman B, Meyer J, Canas JA, Xu W, Zuo JY, Betancourt SS, Shan D. A study of connectivity and baffles in a deepwater gulf of mexico reservoir linking downhole fluid analysis and geophysics. In: SPE annual technical conference and exhibition, SPE 187231. 2017.
[11] Dong C, Hows MP, Cornelisse PM, Elshahawi H. Fault block migrations inferred from asphaltene gradients. In: SPWLA 54th annual logging symposium. New Orleans, LA, 2013.
[12] Chen L, Meyer J, Campbell T, Canas J, Betancourt SS, Dumont H, Forsythe JC, Mehay S, Kimball S, Hall DL. Applicability of simple asphaltene thermodynamics for asphaltene gradients in oilfield reservoirs: The Flory-Huggins-Zuo equation of state with the Yen-Mullins model. Fuel, 2018, 221, 216–232.
[13] Zuo JY, Elshahawi H, Mullins OC, Dong C, Zhang D, Jia N, Zhao H. Asphaltene gradients and tar mat formation in reservoirs under active gas charging. Fluid Phase Equilib, 2012, 315, 91–98.
[14] Mullins OC, Seifert DJ, Zuo JY, Zeybek M, Zhang D, Pomerantz AE, Asphaltene gradients and tar mat formation in oil reservoirs. In: World heavy oil conference. Aberdeen, Scotland, 2012.
[15] Pastor W, Garcia G, Zuo JY, Hulme R, Goddyn X, Mullins OC. Measurement and EOS modeling of large compositional gradients in heavy oils. In: SPWLA 53rd annual logging symposium. Society of Petrophysicists and Well-Log Analysts, 2012.
[16] Zuo JY, Mullins OC, Freed D, Elshahawi H, Dong C, Seifert DJ. Advances in the flory–huggins–zuo equation of state for asphaltene gradients and formation evaluation. Energy Fuels, 2013, 27, 1722–1735.
[17] Freed DE, Mullins OC, Zuo JY. Theoretical treatment of asphaltene gradients in the presence of GOR gradients. Energy Fuels, 2010, 24(7), 3942–3949.
[18] Mullins OC, Pomerantz AE, Zuo JY, Andrews AB, Hammond PS, Dong C, Elshahawi H, Seifert DJ, Rane JP, Banerjee S. Asphaltene nanoscience and reservoir fluid gradients, tar mat formation and the oil-water interface. In: SPE annual technical conference and exhibition, SPE 166278. Society of Petroleum Engineers, 2013.
[19] Freed DE, Mullins OC, Zuo JY. Heuristics for equilibrium distributions of asphaltenes in the presence of GOR gradients. Energy Fuels, 2014, 28(8), 4859–4869.
[20] Forsythe JC, Pomerantz AE, Seifert DJ, Wang K, Chen Y, Zuo JY, Nelson RK, Reddy CM, Schimmelmann A, Sauer P, Peters KE, Mullins OC. A geological model for the origin of fluid compositional gradients in a large saudi arabian oilfield: An investigation by two-dimensional gas chromatography (GC × GC) and asphaltene chemistry. Energy Fuels, 2015, 29(9), 5666–5680.

[21] Lin MS, Lunsford KM, Glover CJ, Davidson RR, Bullin JA, The effects of asphaltenes on the chemical and physical characteristics of asphalt. In: Sheu EY, Mullins OC, eds. Asphaltenes: Fundamentals and applications. Plenum Press, New York, 1995, 155–176.
[22] Zuo JY, Elshahawi H, Dong C, Latifzai AS, Zhang D, Mullins OC. DFA asphaltene gradients for assessing connectivity in reservoirs under active gas charging. In: SPE annual technical conference and exhibition, SPE 145438. Denver, Colorado, USA, 2011.
[23] Zuo JY, Jackson R, Agarwal A, Herold B, Kumar S, Santo ID, Dumont H, Ayan C, Beardsell M, Mullins OC. Diffusion model coupled with the flory–huggins–zuo equation of state and yen–mullins model accounts for large viscosity and asphaltene variations in a reservoir undergoing active biodegradation. Energy Fuels, 2015, 29(3), 1447–1460.
[24] Mullins OC, Primio RD, Uchytil S, Zuo JY, Dumont H, Mishra V, Pfeiffer T, Achourov V. Bitumen and tar deposition and tar mat formation accounted for by multiple charging, trap filling and fluid geodynamics. In: SPE ATCE 181535, ATCE Dubai. Society of Petroleum Engineers, 2016.
[25] Pfeiffer T, DiPrimio R, Achourov V, Mullins OC. TAR MAT formation on baffles in the middle of the oil column. In: SPWLA 57th Annual Logging Symposium. Society of Petrophysicists and Well-Log Analysts, 2016.
[26] Zuo JY, Mullins OC, Mishra V, Garcia G, Dong C, Zhang D. Asphaltene grading and tar mats in oil reservoirs. Energy Fuels, 2012, 26(3), 1670–1680.
[27] Qureshi A, Zuo JY, Seifert DJ, Zeybek M, Mullins OC. Mobile heavy oil and tar mat characterization within a single oil column utilizing novel asphaltene science. In: SPE Kuwait international petroleum conference and exhibition. Society of Petroleum Engineers, 2012.
[28] Pfeiffer T, Di Primio R, Achourov V, Mullins OC. Scanning electron micrographs of tar-mat intervals formed by asphaltene phase transition. Petrophysics, 2017, 58(02), 141–152.
[29] Mullins OC, Dumont H, Forsythe JC, Chen L, Achourov V, Meyer J, Johansen YB, Rinna J, Winkelman B, Wilkinson TW. Asphaltene gradients and connectivity analysis in reservoirs, asphaltene onset pressure, bitumen and tar mats all treated within a simple, unified chemistry treatment. In: SPE annual technical conference and exhibition. Society of Petroleum Engineers, 2018.
[30] Mullins OC. The modified yen model. Energy Fuels, 2010, 24, 2179–2207.
[31] Mullins OC, Sabbah H, Eyssautier J, Pomerantz AE, Barré L, Andrews AB, Ruiz-Morales Y, Mostowfi F, McFarlane R, Goual L. Advances in asphaltene science and the Yen–Mullins model. Energy Fuels, 2012, 26(7), 3986–4003.
[32] Buckley JS, Wang J, Creek JL. Solubility of the least-soluble asphaltenes. In: Mullins OC et al, eds. Asphaltenes, heavy oils, and petroleomics. Springer, New York, 2007, 401–438.
[33] Mullins OC. Physics of Reservoir Fluids. Schlumberger, Houston, TX, 2008.
[34] Kharrat AM, Indo K, Mostowfi F. Asphaltene content measurement using an optical spectroscopy technique. Energy Fuels, 2013, 27(5), 2452–2457.
[35] Ruiz-Morales Y, Wu X, Mullins OC. Electronic absorption edge of crude oils and asphaltenes analyzed by molecular orbital calculations with optical spectroscopy. Energy Fuels, 2007, 21, 944–952.
[36] Ruiz-Morales Y, Mullins OC. Polycyclic aromatic hydrocarbons of asphaltenes analyzed by molecular orbital calculations with optical spectroscopy. Energy Fuels, 2007, 21, 256–265.
[37] Ruiz-Morales Y. Molecular orbital calculations and optical transitions of PAHs and asphaltenes. In: Asphaltenes, heavy oils, and petroleomics. Springer, 2007, 95–137.
[38] Ruiz-Morales Y, Mullins OC. Measured and simulated electronic absorption and emission spectra of asphaltenes. Energy Fuels, 2009, 23(3), 1169–1177.
[39] Ruiz-Morales Y, Mullins OC. Singlet–triplet and triplet–triplet transitions of asphaltene PAHs by molecular orbital calculations. Energy Fuels, 2013, 27(9), 5017–5028.

[40] Ruiz-Morales Y. HOMO-LUMO gap as an index of molecular size and structure for polycyclic aromatic hydrocarbons (PAHs) and asphaltenes: A Theoretical Study. I. J Phy Chem A, 2002, 106, 11283–11308.
[41] Mullins OC, Zhu Y. First observation of the Urbach tail in a multicomponent organic system. Appl Spectrosc, 1992, 46(2), 354–356.
[42] Mullins OC, Mitra-Kirtley S, Zhu Y. The electronic absorption edge of petroleum. Appl Spectrosc, 1992, 46, 1405–1411.
[43] Mullins OC, Daigle T, Crowell C, Groenzin H, Joshi NB. Gas-oil ratio of live crude oils determined by near-infrared spectroscopy. Appl Spectrosc, 2001, 55(2), 197–201.
[44] Fujisawa G, Van Agthoven MA, Jenet F, Rabbito PA, Mullins OC. Near-infrared compositional analysis of gas and condensate reservoir fluids at elevated pressures and temperatures. Appl Spectrosc, 2002, 56(12), 1615–1620.
[45] Van Agthoven MA, Fujisawa G, Rabbito P, Mullins OC. Near-infrared spectral analysis of gas mixtures. Appl Spectrosc, 2002, 56(5), 593–598.
[46] Partouche A, Edmundson S, Tao C, Chen H, Nelson K, Sawaf T, Yang B, Xu L, Dindia D, Pfeiffer T. Applications of wireline formation testing – a technology update. OTC 30879, Houston, TX, 2020.
[47] Mullins OC. The physics of reservoir fluids: Discovery through downhole fluid analysis. Schlumberger, Houston, TX, 2008.
[48] Mullins OC, Schroer J. Real-time determination of filtrate contamination during openhole wireline sampling by optical spectroscopy. In: SPE annual technical conference and exhibition. Society of Petroleum Engineers, 2000.
[49] Mullins OC, Schroer J, Beck GF. Real-time quantification of OBM filtrate contamination during openhole wireline sampling by optical spectroscopy. In: SPWLA 41st annual logging symposium. Society of Petrophysicists and Well-Log Analysts, 2000.
[50] Dong C, Hegeman PS, Elshahawi H, Mullins OC, Fujisawa G, Kurkjian A. Advances in downhole contamination monitoring and GOR measurement of formation fluid samples. In: SPWLA 44th Annual Logging Symposium. Society of Petrophysicists and Well-Log Analysts, 2003.
[51] Forsythe JC, Martin R, De Santo I, Tyndall R, Arman K, Pye J, De Nicolais N, Nelson RK, Pomerantz AE, Kenyon-Roberts S. Integrating comprehensive two-dimensional gas chromatography and downhole fluid analysis to validate a spill-fill sequence of reservoirs with variations of biodegradation, water washing and thermal maturity. Fuel, 2017, 191, 538–554.
[52] Mullins OC, Johansen YB, Rinna J, Meyer J, Kenyon-Roberts S, Chen L, Forsythe JC, Achourov V, Jackson R, Betancourt SS. Diverse fluid gradients associated with biodegradation of crude oil. In: SPWLA 60th annual logging symposium. Society of Petrophysicists and Well-Log Analysts, 2019.
[53] Forsythe JC, Kenyon-Roberts S, O'Donnell M, Betancourt SS, Masurek N, Gisolf A, Bennett B, Nelson RK, Canas JA, Reddy CM. Biodegradation and water washing in a spill-fill sequence of oilfields. Fuel, 2019, 237, 707–719.
[54] Chen L, Bertolini A, Dubost F, Achourov V, Betancourt S, Cañas JA, Dumont H, Pomerantz AE, Mullins OC. Yen–Mullins model applies to oilfield reservoirs. Energy Fuels, 2020, 34(11), 14074–14093.
[55] Schuler B, Zhang Y, Liu F, Pomerantz AE, Andrews AB, Gross L, Pauchard V, Banerjee S, Mullins OC. Overview of asphaltene nanostructures and thermodynamic applications. Energy Fuels, 2020, 34(12), 15082–15105.

[56] Mullins OC, Zuo JY, Pomerantz AE, Forsythe JC, Peters K. Reservoir fluid geodynamics: the chemistry and physics of oilfield reservoir fluids after trap filling. Energy Fuels, 2017, 31(12), 13088–13119.
[57] Tissot B, Welte D. Petroleum formation and occurrence. 2nd ed, Springer, 1984.
[58] Bertolini AC, Monteiro J, Canas JA, Betancourt SS, Mullins OC, Colacelli S, Polinski RK. Reservoir fluid geodynamics in Brazilian presalt carbonate field. In: SPE middle east oil and gas show and conference, SPE 194841. Society of Petroleum Engineers, 2019.
[59] Chen L, Winkelman B, Wilkinson T, Meyer J, Mullins OC, Forsythe JC, Hayden RS, Xu W, Shan D, Canas JA. Using formation testing and asphaltene gradient modeling to guide g&g modeling and field development-a fault block migration study. In: SPE annual technical conference and exhibition, SPE 191499. 2018.
[60] Seifert DJ, Zeybek M, Dong C, Zuo JY, Mullins OC. Black oil, heavy oil and tar in one oil column understood by simple asphaltene nanoscience. In: Abu Dhabi international petroleum conference and exhibition, SPE 161144. Society of Petroleum Engineers, 2012.
[61] Dong C, Elshahawi H, Mullins OC, Venkatramanan L, Hows MP, McKinney DE, Flannery M, Hashem MN. Improved interpretation of reservoir architecture and fluid contacts through the integration of downhole fluid analysis with geochemical and mud gas analyses. In: Asia pacific oil and gas conference and exhibition. Society of Petroleum Engineers, 2007.
[62] Elshahawi H, Hows MP, Dong C, Venkatramanan L, Mullins OC, McKinney DE, Flannery M, Hashem MN. Integration of geochemical, mud gas and downhole fluid analyses for the assessment of compositional grading-case studies. In: SPE annual technical conference and exhibition, SPE 109684, 2007.
[63] Zuo JY, Mullins OC, Mishra V, Garcia G, Zhang D, Dong C. Advanced reservoir and tar mat evaluation using downhole fluid analysis and asphaltene Flory-Huggins-Zuo EoS. In: IPTC 16649. 2013.
[64] Wang K, Kauerauf AI, Zuo JY, Chen Y, Dong C, Elshahawi H, Mullins OC. Differing equilibration times of GOR, asphaltenes and biomarkers as determined by charge history and reservoir fluid geodynamics. Petrophysics, 2015, 56(5), 440–456.
[65] Mullins OC, Wang K, Kauerauf A, Zuo JY, Chen Y, Dong C, Elshahawi H. Evaluation of coexisting reservoir fluid gradients of GOR, asphaltene and biomarkers as determined by charge history and reservoir fluid geodynamics. In: SPWLA 56th annual logging symposium. Society of Petrophysicists and Well-Log Analysts, 2015.
[66] Betancourt S, Mishra V, Clinch S, Guo G, Malik M, Cañas JA, Chen L, Mullins OC. Understanding fluid complexity and reservoir connectivity using downhole fluid analysis in wilcox formation Gulf of Mexico. In: Offshore technology conference. Offshore Technology Conference, 2016.
[67] Zuo JY, Pan S, Wang K, Mullins OC, Elshahawi H, Canas JA, Chen L, Dumont H, Mishira VK, Garcia G. A quantitative study on the evolution of the asphaltene distribution during gas charge processes. In: SPE annual technical conference and exhibition. Society of Petroleum Engineers, 2017.
[68] Dumont H, Garcia G, Mullins OC, Nighswander J, Mishra VK, El-Khoury J, Chen L, Lake P. Asphaltene onset pressure uncertainty and other asphaltene issues in field development planning. In: Offshore technology conference. Offshore Technology Conference, 2017.
[69] Betancourt SS, Johansen YB, Forsythe JC, Rinna J, Christoffersen K, Skillingstad P, Achourov V, Canas J, Chen L, Pomerantz AE, Zuo JY, Mullins OC. Gravitational gradient of asphaltene molecules in an oilfield reservoir with light oil. Energy Fuels, 2018, 32(4), 4911–4924.
[70] Chen L, Gan Y, Gao B, Chen J, Canas JA, Jackson R, EI-Khoury J, Mullins OC. Reservoir fluid geodynamics, a new way to evaluate the reservoir connectivity and crude oil alteration with late gas charge. In: International petroleum technology conference. SPE IPTC 19472, 2019.

[71] Chen Q, Kristensen M, Johansen YB, Achourov V, Betancourt SS, Mullins OC. Analysis of lateral fluid gradients from dfa measurements and simulation of reservoir fluid mixing processes over geologic time. In: SPWLA 61st annual logging symposium-online. Society of Petrophysicists and Well-Log Analysts, 2020.
[72] Ratulowski J, Fuex AN, Westrich JT, Sieler JJ. Theoretical and experimental investigation of isothermal compositional grading. SPE Reservoir Eval Eng, 2003, SPE 84777, 168–175.
[73] Zuo JY, Chen Y, Pan S, Wang K, Mullins OC. Investigation of density inversion induced by gas charges into oil reservoirs using diffusion equations. Energy, 2016, 100, 199–216.
[74] Pan S, Zuo JY, Wang K, Chen Y, Mullins OC. A multicomponent diffusion model for gas charges into oil reservoirs. Fuel, 2016, 180, 384–395.
[75] Zuo Y, Lehne E, Sirimongkolkitti S, Pan S, Mullins OC. Methods for reservoir evaluation employing non-equilibrium compositional gradients. *US Patent* 9,322, 2016, 268.
[76] Zuo JY, Mullins OC, Achourov V, Pfeiffer T, Pan S, Wang K, Kollien T, Di Primio R. Fluid distributions during light hydrocarbon charges into oil reservoirs using multicomponent Maxwell-Stefan diffusivity in gravitational field. Fuel, 2017, 209, 211–223.
[77] Stainforth JG. New insights into reservoir filling and mixing processes. In: Cubitt JM, England WA, Larter SR, eds. Understanding petroleum reservoirs: Towards an integrated reservoir engineering and geochemical approach, Geological Society, London, 2004, 115–132.
[78] Head IM, Jones DM, Larter SR. Biological activity in the deep subsurface and the origin of heavy oil. Nature, 2003, 426, 344–352.
[79] Jones D, Head I, Gray N, Adams J, Rowan A, Aitken C, Bennett B, Huang H, Brown A, Bowler B. Crude-oil biodegradation via methanogenesis in subsurface petroleum reservoirs. Nature, 2008, 451(7175), 176–180.
[80] Uchytil S, Mishra VK, Betancourt SS, Guthrie J, Huang J, Teerman S, Nguyen A, Evans S, Nagarajan N, Mullins OC. Impact of a secondary condensate charge into an oil reservoir evaluated by downhole fluid analysis, core analysis, and production. In: Offshore technology conference. OTC 27240, Houston, TX, 2016.
[81] Mullins OC, Forsythe JC, Pomerantz A, Wilkinson T, Winkelman B. Downhole fluid analysis and gas chromatography; a powerful combination for reservoir evaluation. Petrophys – SPWLA J Formation Eval Reservoir Description, 2018, 59, 649–671.
[82] Pomerantz AE, Seifert DJ, Qureshi A, Zeybek M, Mullins OC. The molecular composition of asphaltenes in a highly compositionally graded column. Petrophysics, 2013, 54(5), 427–238.
[83] Pomerantz AE, Seifert DJ, Bake KD, Craddock PR, Mullins OC, Kodalen BG, Mitra-Kirtley S, Bolin TB. Sulfur chemistry of asphaltenes from a highly compositionally graded oil column. Energy Fuels, 2013, 27(8), 4604–4608.
[84] Boycott AE. Sedimentation of blood corpuscles. Nature, 1920, 104(2621), 532–532.
[85] Chen Y, Wang K, Zuo JY, Mullins OC. Dynamics of tar mat formation due to asphaltenes accumulation under gas charge in reservoirs. In: Offshore technology conference. 2015.
[86] Mullins OC, Sheu EY, Hammami A, Marshall AG. Asphaltenes, heavy oils, and petroleomics. Springer, New York, 2007.
[87] Sheu EY, Mullins OC. Structures and dynamics of asphaltenes. Plenum Press, 1998.
[88] Jackson RR, Zuo JY, Agarwal A, Herold BH, Kumar S, De Santo I, Dumont H, Ayan C, Mullins OC. Mapping and modeling large viscosity and asphaltene variations in a reservoir undergoing active biodegradation. In: SPE annual technical conference and exhibition. Society of Petroleum Engineers, 2014.
[89] Wu Q, Seifert DJ, Pomerantz AE, Mullins OC, Zare RN. Constant asphaltene molecular and nanoaggregate mass in a gravitationally segregated reservoir. Energy Fuels, 2014, 28(5), 3010–3015.

[90] Groenzin H, Mullins OC. Molecular size and structure of asphaltenes from various sources. Energy Fuels, 2000, 14, 677–684.
[91] Groenzin H, Mullins OC. Molecular size and structure of asphaltenes. Petrol Sci Technol, 2001, 19(1–2), 219–230.
[92] Rodgers RP, Marshall AG. Petroleomics: Advanced characterization of petroleum-derived materials by Fourier transform ion cyclotron resonance mass spectrometry (FT-ICR MS). In: Asphaltenes, heavy oils, and petroleomics. Springer, 2007, 63–93.
[93] Hortal AR, Hurtado P, Martínez-Haya B, Mullins OC. Molecular weight distributions of coal and petroleum asphaltenes from laser desorption/ionization experiments. Energy Fuels, 2007, 21, 2863–2868.
[94] Groenzin H, Mullins OC. Asphaltene molecular size and weight by time-resolved fluorescence depolarization. In: Asphaltenes, heavy oils, and petroleomics. Springer, 2007, 17–62.
[95] Mullins OC. Petroleomics and structure–function relations of crude oils and asphaltenes. In: Asphaltenes, heavy oils, and petroleomics. Springer, 2007, 1–16.
[96] Pomerantz AE, Hammond MR, Morrow AL, Mullins OC, Zare RN. Two-step laser mass spectrometry of asphaltenes. J Am Chem Soc, 2008, 130, 7216–7217.
[97] Mullins OC. Review of the molecular structure and aggregation of asphaltenes and petroleomics. Spe J, 2008, 13(01), 48–57.
[98] Pinkston DS, Duan P, Gallardo VA, Habicht SC, Tan X, Qian K, Gray M, Müllen K, Kenttämaa HI. Analysis of asphaltenes and asphaltene model compounds by laser-induced acoustic desorption/fourier transform ion cyclotron resonance mass spectrometry. Energy Fuels, 2009, 23(11), 5564–5570.
[99] Mullins OC. Rebuttal to Strausz et al. regarding time-resolved fluorescence depolarization of asphaltenes. Energy Fuels, 2009, 23(5), 2845–2854.
[100] Hurtado P, Gámez F, Martínez-Haya B. One- and two-step ultraviolet and infrared laser desorption ionization mass spectrometry of asphaltenes. Energy Fuels, 2010, 24(11), 6067–6073.
[101] Borton II D, Pinkston DS, Hurt MR, Tan X, Azyat K, Tykwinski R, Gray M, Qian K, Kenttämaa HI. Molecular structures of asphaltenes based on the dissociation reactions of their ions in mass spectrometry. Energy Fuels, 2010, 24, 5548–5559.
[102] Wu Q, Pomerantz AE, Mullins OC, Zare RN. Minimization of fragmentation and aggregation by laser desorption laser ionization mass spectrometry. J Am Soc Mass Spectrom, 2013, 24, 1116–1122.
[103] Hurt MR, Borton DJ, Choi HJ, Kenttämaa HI. Comparison of the structures of molecules in coal and petroleum asphaltenes by using mass spectrometry. Energy Fuels, 2013, 27(7), 3653–3658.
[104] Chacón-Patiño ML, Rowland SM, Rodgers RP. Advances in asphaltene petroleomics. part 1: Asphaltenes are composed of abundant island and archipelago structural motifs. Energy Fuels, 2017, 31(12), 13509–13518.
[105] Bake KD, Craddock PR, Bolin TB, Abdallah W, Mitra-Kirtley S, Andrews AB, Mullins OC, Pomerantz AE. Structure-solubility relationships in coal, petroleum, and immature source-rock-derived asphaltenes. Energy Fuels, 2020.
[106] Pomerantz AE, Hammond MR, Morrow AL, Mullins OC, Zare RN. Asphaltene molecular-mass distribution determined by two-step laser mass spectrometry. Energy Fuels, 2009, 23, 1162–1168.
[107] Sabbah H, Morrow AL, Pomerantz AE, Zare RN. Evidence for island structures as the dominant architecture of asphaltenes. Energy Fuels, 2011, 25, 1597–1604.

[108] Pomerantz AE, Mullins OC, Paul G, Ruzicka J, Sanders M. Orbitrap mass spectrometry: A proposal for routine analysis of nonvolatile components of petroleum. Energy Fuels, 2011, 25(7), 3077–3082.
[109] Mullins OC, Martínez-Haya B, Marshall AG. Contrasting perspective on asphaltene molecular weight. This comment vs the overview of A. A. Herod, K. D. Bartle, and R. Kandiyoti. Energy Fuels, 2008, 22, 1765–1773.
[110] Sabbah H, Pomerantz AE, Wagner M, Müllen K, Zare RN. Laser desorption single-photon ionization of asphaltenes: Mass range, compound sensitivity, and matrix effects. Energy Fuels, 2012, 26(6), 3521–3526.
[111] Wu Q, Pomerantz AE, Mullins OC, Zare RN. Laser-based mass spectrometric determination of aggregation numbers for petroleum- and coal-derived asphaltenes. Energy Fuels, 2014, 28, 475–482.
[112] Schuler B, Zhang Y, Liu F, Pomerantz AE, Andrews AB, Gross L, Pauchard V, Banerjee S, Mullins OC. Overview of asphaltene nanostructures and thermodynamic applications. Energy Fuels, 2020.
[113] George GN, Gorbaty ML. Sulfur K-Edge X-ray absorption spectroscopy of petroleum asphaltenes and model compounds. J Am Chem Soc, 1989, 111, 3182–3186.
[114] Mullins OC. Sulfur and nitrogen molecular structures in asphaltenes and related materials quantified by XANES spectroscopy. In: Sheu EY, Mullins OC, eds. Asphaltenes: Fundamentals and applications. Plenum Press, New York, 1995.
[115] Mitra-Kirtley S, Mullins OC, Ralston CY, Sellis D, Pareis C. Determination of sulfur species in asphaltene, resin, and oil fractions of crude oils. Appl Spectrosc, 1998, 52, 1522–1525.
[116] Mitra-Kirtley S, Mullins OC, Ralston CY, Pareis C. Sulfur characterization in asphaltene, resin, and oil fractions of two crude oils. In: ACS National Conference, New Orleans, 1999.
[117] Mitra-Kirtley S, Mullins OC. Sulfur chemical moieties in carbonaceous materials. In: Asphaltenes, heavy oils, and petroleomics. Springer, 2007, 157–188.
[118] Pomerantz AE, Bake KD, Craddock PR, Kurzenhauser KW, Kodalen BG, Mitra-Kirtley S, Bolin T. Sulfur speciation in kerogen and bitumen from gas and oil shales. Org Geochem, 2014, 68, 5–12.
[119] Waldo GS, Carlson RMK, Moldowan JM, Peters KE, Penner-Hahn JE. Sulfur speciation in heavy petroleums: Information from X-ray absorption near-edge structure. Geochimica Et Cosmochimica Act, 1991, 55, 801–814.
[120] Seifert DJ, Qureshi A, Zeybek M, Pomerantz AE, Zuo JY, Mullins OC, Heavy oil and tar mat characterization within a single oil column utilizing novel asphaltene science. In: KIPCE SPE 163291. Kuwait, 2012.
[121] Mishra VK, Zuo JY, Dumont H, Mullins OC. *Permeable tar mat formation described within context of novel asphaltene science*. In: SPE Kuwait international petroleum conference and exhibition. SPE 163292, KIPCE, Kuwait, 2012.
[122] Mullins OC, Primio RD, Zuo JY, Uchytil S, Mishra VK, Dumont H, Pfeiffer T, Achourov VV, Pomerantz AE, Forsythe J. Reservoir fluid geodynamics; the link between petroleum systems and production concerns relating to fluids and tar distributions in reservoirs. In: SPE annual technical conference and exhibition. SPE ATCE 181535, 2016.
[123] Achourov V, Pfeiffer T, Kollien T, Betancourt SS, Zuo JY, Di Primio R, Mullins OC. Gas diffusion into oil, reservoir baffling and tar mats analyzed by downhole fluid analysis, pressure transients, core extracts and DSTs. Petrophysics, 2015, 56(04), 346–357.
[124] Elshahawi H, Latifzai AS, Dong C, Zuo J, Mullins OC. Understanding reservoir architecture using downhole fluid analysis and asphaltene science. In: SPWLA 52nd annual logging symposium. Society of Petrophysicists and Well-Log Analysts, 2011.

Chuanyuan Wang, Shijie He, Zixuan Zhang

7 Molecular distributions and geochemical implications of pyrrolic nitrogen compounds in crude oils

Abstract: A suite of oils from the Tarim Basin, Qaidam Basin, Ordos Basin, and Liaohe Basin, China was characterized geochemically to clarify factors other than lateral migration that can affect the concentrations and distributions of pyrrolic nitrogen compounds (PNCs) in crude oils. Except for oil fractionation during migration, facies and depositional environment and maturity also affect the distribution of PNCs. The relative distribution of pyrrole isomers may vary with the depositional environment. The isomers with high shielding degree are relatively enriched with the increase of maturity, which is consistent with the principle of thermodynamic equilibrium. Biodegradation is another factor which can alter PNCs behavior in oils. Partially shielded dimethylcarbazole isomers appear to be more susceptible to biodegradation than their exposed counterparts. Benzo[c]carbazole seems to show a higher ability to resist biodegradation than benzo[a]carbazole in heavily biodegraded oils. It was determined that PNCs have potential significance in evaluating oil migration, paleo environment, thermal maturity, and the degree of biodegradation. The PNCs could provide another useful diagnostic means for spill source identification at their lightly to moderately weathered stages.

Key words: carbazole, benzocarbazole, paleoenvironment, maturity, biodegradation

Acknowledgments: This study was co-supported by Key Projects in the Ocean Mega-Research of Science, Chinese academy of science (COMS2019J05), Shandong Key R&D Program (Public Welfare Project) (2019GSF109081), and Yantai Science and Technology Pillar Program (2018ZHGY079).

Chuanyuan Wang, Key Laboratory of Coastal Environmental Processes and Ecological Remediation, Yantai Institute of Coastal Zone Research, Chinese Academy of Sciences, Yantai 264003, P.R. China
Shijie He, School of Resource and Environmental Engineering, Ludong University, Yantai 264025, China
Zixuan Zhang, Key Laboratory of Coastal Environmental Processes and Ecological Remediation, Yantai Institute of Coastal Zone Research, Chinese Academy of Sciences, Yantai 264003, P.R. China; University of Chinese Academy of Sciences, Beijing 100049, China

https://doi.org/10.1515/9783110694529-007

7.1 Introduction

Molecular markers based on aliphatic and aromatic hydrocarbons have proven to be suitable for the characterization of crude oils and source rocks, and are indicators of thermal maturity level, degree of preservation, and migration. On the other hand, hetero-compounds (nitrogen, oxygen, and sulfur; NSO compounds) that make up a small portion of most crude oils have significant implications in terms of petroleum exploration due to their greater structural diversity [1]. Nitrogen is a common element in petroleum, mainly in the form of heterocyclic aromatic structures in low abundance [2]. Aromatic heterocyclic N compounds in petroleum include two main groups: neutral pyrrolic compounds, including pyrrole and higher alkylated and benzylated analogues, and basic pyridinic compounds, comprising pyridine and higher alkylated and benzylated components. Among the two groups, the neutral pyrrolic species contribute the major proportion of the N compounds, evincing interest via studies of potential applications to petroleum migration [3–7]. Because of their high polarity, pyrrolic nitrogen compounds (PNCs) exhibit a stronger absorption/adsorption in the interactions between organic nitrogen compounds and solid organic/mineral phases and/or higher solubility in water [8, 9]. On the other hand, the differences in absorptive intensity among different kinds of PNCs can lead to their geological chromatographic fractional effect. Thus, enrichments of benzo[c]carbazole in crude oils relative to benzo[a]carbazole, the N-H shielded to N-H exposed alkylcarbazoles and higher to lower homologues with increasing migration distance are observed [3, 4, 10]. Based on simulation experiments and case studies, PNCs (carbazole, benzocarbazoles, dibenzocarbazoles and their alkyl derivatives) have been proposed as molecular tracers for monitoring petroleum migration [3, 4, 11]. Actually, the nitrogen compounds in geological structure body derived mainly from amino acid of sedimentary organism, and the formation and distribution of nitrogen compounds are closely related to sedimentary facies and the evolvement of organic matter.

Carbazoles and benzocarbazoles (Figure 7.1) are common constituents of rock extracts or crude oils. As a common component of non-hydrocarbons in crude oils, organic nitrogen compounds have been proposed to exert a positive function on the adsorption of petroleum on reservoir rocks, leading to petroleum compounds variation during the petroleum migration, production, and refining [12, 13]. Fractionation effects related to migration have been observed both empirically in case studies and experimentally in laboratory simulations [3, 4, 14]. However, recent studies have also shown that the distributions of PNCs can be also affected by paleo environment [3, 15, 16], organic source inputs [17, 18] and thermal maturity [16, 19–21]. Biodegradation is another factor which can alter carbazoles behavior in oils. Huang et al. [22] successively studied the content and distribution of neutral nitrogen compounds in degraded crude oil in the Lengdong area of Liaohe Oilfield, and obtained some important understandings [22]. They believed that the content of nitrogen-

containing compounds of crude oil with medium biodegradation is gradually reduced. Moreover, benzo[b]carbazole has the highest ability to resist biodegradation among benzocarbazole isomers, and with the increase of biodegradation, the ratio of benzo[a] carbazole/benzo[b]carbazole showed a decreasing trend [22, 23].

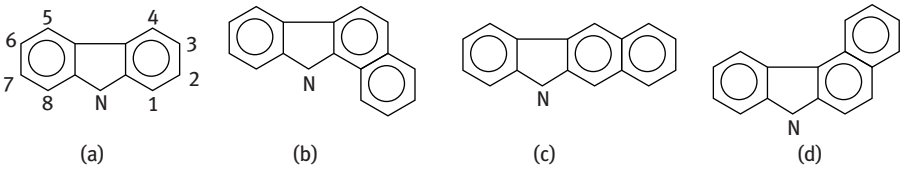

Figure 7.1: Chemical structures of carbazole compounds (a) and benzo[a]carbazole (b), benzo[c] carbazole (c), benzo[b]carbazole (d).

Table 7.1: Geochemical and geological information of all samples.

Sedimentary basins	Well no.	Oilfield	Reservoir age	Strata	Depth (M)	Density (g/cm^3)
Tarim Basin (Marine Facies)	LN2	Lunan	Triassic	T	4,499–4,528	0.8919
	LN4	Lunan	Triassic	T	4,787–4,793	0.8450
	LN5	Lunan	Triassic	T	4,563–4,570	0.8453
	TD2-32	Tadong	Ordovician	O1	4,917	0.8369
	TZ4	Tazhong	Carboniferous	CII	3,532–3,548	0.5782
Qaidam Basin (Saline Lake Facies)	Q13-6	Qigequan	Neogene	N;	839–1,318	–
	QD1	Qidong	Paleogene	E32	2,790–2,825	–
	Hong110	Hongliuquan	Paleogene	E31	2,833–2,891	–
	Shizhong10	Shizigou	Neogene	N1	829–1,258	–
	Youzhong1	Youyuangou	Neogene	N1	1,272	–
	Shazhong90	Yuoshashan	Neogene	N21	262–263	–
	Shaxi7	Shaxi	Neogene	N1-N21	2,266–2,706	–
	Yue133	Yuejin Ⅰ	Neogene	N1-N21	1,686–1,759	–
	Yue17-27	Yuejin Ⅰ	Paleogene	E31	3,657–3,856	–
	Yue10-8	Yuejin Ⅰ	Paleogene	E31	3,232–3,283	–
	Yue2-2	Yuejin Ⅰ	Paleogene	E31	3,472–3,529	–
	Yue341	Yuejin Ⅰ	Neogene	N1-N21	1,737–2,048	–
	Yue41	Yuejin Ⅰ	Neogene	N1-N21	1,932–2,132	–

Table 7.1 (continued)

Sedimentary basins	Well no.	Oilfield	Reservoir age	Strata	Depth (M)	Density (g/cm^3)
Ordos Basin (Freshwater Lacustrine Facies)	Ding210-10	Jiyuan	Triassic	Y10	–	–
	Yuan215	Jiyuan	Triassic	Y10	–	–
	Ding382	Jiyuan	Triassic	Y9	–	–
	Sha106	Jiyuan	Triassic	Y9	–	–
	An48	Jiyuan	Triassic	Y9	–	–
	Ding124-2	Jiyuan	Triassic	Y9	–	–
	Yan18-14	Jiyuan	Triassic	Y8	1,800	–
	Yan16-20	Jiyuan	Triassic	Y8	–	–
	A17	Jiyuan	Triassic	Y7	1,380	–
	Yuan222	Jiyuan	Triassic	C4 + 5	–	–
	Yuan220	Jiyuan	Triassic	C4 + 5	1,985	–
	Xin70-67	Jiyuan	Triassic	C4 + 5	–	–
	Yuan91	Jiyuan	Triassic	C4 + 5	–	–
	Yuan213	Jiyuan	Triassic	C4 + 5	1,960	–
	Yan102	Jiyuan	Triassic	C2	–	–
	Geng115	Jiyuan	Triassic	C6	2,290	–
	Geng130	Jiyuan	Triassic	C2	–	–
	An47-3	Jiyuan	Triassic	C2	1,810	–

Note: "–" mean the data not available.

PNCs have been applied to the study of oil-gas migration in continental petroliferous basins in China [5, 14, 23]. However, the distribution characteristics and heterogeneity of PNCs in crude oil depend on a variety of geological or geochemical factors. Due to the different bacteria species and physical and chemical conditions of reservoir, the variation trend of PNCs in biodegradable crude oil is different, especially in the distribution of alkyl carbazole isomers [13, 23, 24], which leads to some changes in isomer parameters, indicating that this topic needs to be further explored. At present, the research on PNCs focusses on the influence of oil-gas migration on the distribution, and the understanding of their distribution characteristics and various influencing factors in crude oil is not enough. Therefore, in order to confirm the validity and reliability of nitrogen compounds as oil-gas migration indicators and oil source correlation parameters, it is necessary to conduct a comprehensive and in-depth analysis on the basic geochemical characteristics and controlling factors of PNCs. Although PNCs have found increasing application in petroleum exploration and refining in recent years, there have been few reports of use of these compounds for forensic oil spill investigations.

Therefore, the main goals of this paper were to determine the influence of source material, sedimentary environment and maturity on PNCs in a suit of crude oils from China. In addition, the effects of biodegradation on PNCs distributions are quantitatively investigated. Finally, a number of diagnostic indices of PNCs with high values

of diagnostic power are developed for correlation and differentiation of oils. The results are helpful to understand the facies, depositional environment and biodegradation influence and mechanism of PNCs, and provide a scientific basis for advancing the fingerprinting techniques associated with oil spills.

7.2 Samples and analytical methods

7.2.1 Oil samples

In order to study the influence of sedimentary facies and maturity on the distribution of PNCs, some crude oil samples derived from different source rocks deposited in different environments, thermal maturity, were collected from various oilfields in Tarim Basin Marine Facies [25], Western Qaidam Basin Saline Lake Facies [26], and Ordos Basin Freshwater lacustrine facies [27] China (Table 7.1). The Liaohe Basin is an important oil-producing basin in China. The petroleum geological setting has been described in detail by Huang [22]. The Lengdong oilfield is located in a complicated faulted anticline block on the steep eastern slope of the Western Depression of the Liaohe basin [22]. A set of biodegraded crude oils are taken from Lengdong oilfield. The crude oil viscosity ranges from 95 to 16,890 mPa · s (50 °C). Heavy oil in this area is mainly formed by microbial degradation, and crude oil viscosity is closely related to microbial degradation. The samples were kept frozen after collection.

7.2.2 Analytical methods

The experimental has been reported previously [1, 23, 26]. Briefly, the extracts were deasphaltened and then separated into saturate, aromatics and non-hydrocarbons fractions by way of column chromatography. Pyrrolic nitrogen compounds in the non-hydrocarbons were further isolated via column chromatography with 2 g of silicic acid by the elution of *n*-hexane/toluene (1:1 (v/v), 50 mL). The neutral alumina (l00–200 mesh) and silicic acid were activated at 110 °C before use.

Gas chromatograph–mass spectrometric analyses of these compounds were performed using a Finngan SSQ710 instrument at China University of Petroleum–Beijing (CUPB). A capillary column (30 m 0.32 mm i.d.) coated with HP-5 (film thickness 0.25 μm) was used with Helium as carrier gas. The oven temperature was programmed from 80 to 150 °C at 2 °C/min, and from 150 °C to 310 °C at 3 °C/min, then held at this temperature for 25 min. The mass spectrometer was operated in EI mode at 70 eV.

Identification of individual PNCs was based on comparison with authentic standards and literature data [9]. Quantification was performed using *N*-phenylcarbazole

as an internal standard and taking into account all significant fragment ions of the target compounds. Quantification of the isomeric compounds was calculated using the peak areas in the corresponding molecular-ion chromatograms. Twenty percent real samples were selected randomly and analyzed in parallel three times every batch ($n = 3$). Linearity was evaluated through the coefficient of determination (R^2) of calibration curves. Accuracy was expressed as recovery. In this study, a certain amount of deuterated carbazole was added and collected into a conical flask after column chromatographic separation, and then 9-phenylcarbazole was added to calculate the yield of deuterated carbazole. In this study, recoveries averaged 86 ± 12%.

7.3 Results and discussion

7.3.1 Occurrence and distribution of PNCs

Extracted ion chromatograms displaying the distribution of carbazole (m/z 167 + 14i, $i = 0–6$), benzocarbazole (m/z 217 + 14i, $i = 0–5$) and dibenzocarbazole (m/z 267 + 14i, $i = 0–4$) in samples are displayed in Figure 7.2 and Table 7.2. The crude oils studied contain abundant PNCs with total concentrations (W) in the range of 8–94 μg/g. GC-MS analysis of the pyrrolic fraction reveals that carbazole and its alkylated derivatives are in high abundance in all the samples. Among the C_0–C_5-carbazoles, high molecular weight isomers (C_3- and C_4-carbazoles, TMC, TeMC) are often present in very high abundance relative to the low molecular weight homologues (carbazole (C) and C_1-carbazoles (MC)), originally proposed by Clegg et al. [20], and Bakr and Wilkes [28] was observed.

7.3.2 Influence of sedimentary facies and maturity on the distribution of PNCs

Migration-related fractionation effects have been observed both empirically in case studies and experimentally in laboratory simulations [3, 4, 15, 23]. However, recent studies have also shown that the distributions of PNCs can be also affected by sedimentary environment, organic source inputs, and maturity [20, 28]. Biodegradation has a great influence on the content and distribution of PNCs in crude oil. In order to determine the influence of source material, sedimentary environment, and maturity on carbazoles and benzocarbazoles in a suit of crude oils, the crude oil samples from Liaohe Basin were not discussed in this part.

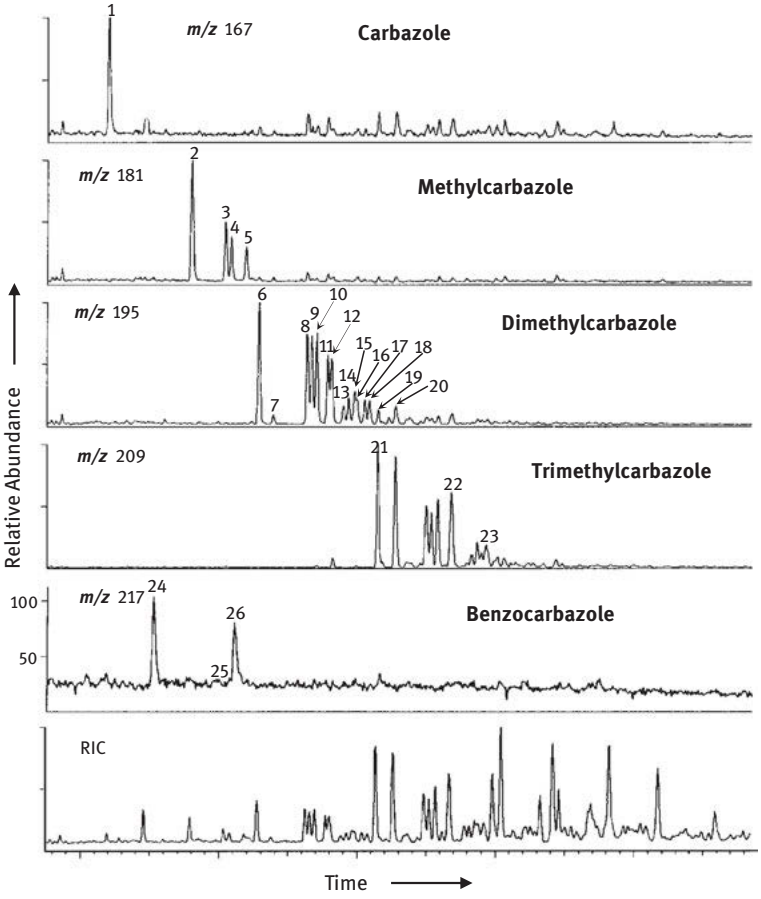

Figure 7.2: Mass chromatogram showing the distribution characteristics of PNCs in crude oils. Note: 1. carbazole, 2. 1-methyl carbazole, 3. 3- methyl carbazole, 4. 2- methyl carbazole, 5. 4-methyl carbazole, 6. 1,8-dimethyl carbazole, 7. 1-ethyl carbazole, 8. 1,3-dimethyl carbazole, 9. 1,6-dimethyl carbazole, 10. 1,7-dimethyl carbazole, 11. 1,4-dimethyl carbazole, 12. 1,5-dimethyl carbazole, 13. dimethyl carbazole, 14. 2,6-dimethyl carbazole, 15. 2,7-dimethyl carbazole, 16. 1,2-dimethyl carbazole, 17. 2,4-dimethyl carbazole, 18. 2,5-dimethyl carbazole, 19. 2,3-dimethyl carbazole, 20. 3,4-dimethyl carbazole, 21. methyl-carbazole(A), 22. methyl-carbazole(B), 23. methyl-carbazole (C), 24. benzo[a]carbazole, 25. benzo[b]carbazole, 26. benzo[c]carbazole.

7.3.2.1 Influence of sedimentary facies on the distribution of PNCs

As already mentioned in Section 7.3.1, methylcarbazoles were predominant in crude oils. However, there are obvious difference for the distribution of methylcarbazoles from crude oils in Tarim Basin (Marine Facies), Western Qaidam Basin (Saline Lake Facies) and Ordos Basin (Freshwater lacustrine facies, Figure 7.3). In this study, we

Table 7.2: Extracted ion chromatograms displaying the distribution of PNCs in samples.

Peak no.	Molecular formula	M^+ *m/z*	Compounds	Abbreviations	Types
1	$C_{12}H_9N$	167	Carbazole	C	Shielded
2	$C_{13}H_{11}N$	181	1-Methylcarbazole	1-MC	Semishielded
3	$C_{13}H_{11}N$	181	3-Methylcarbazole	3-MC	
4	$C_{13}H_{11}N$	181	2-Methylcarbazole	2-MC	Shielded
5	$C_{13}H_{11}N$	181	4-Methylcarbazole	4-MC	
6	$C_{14}H_{13}N$	195	1,8-Dimethylcarbazole	1,8-DMC	Shielded
7	$C_{14}H_{13}N$	195	1-Ethylcarbazole	1-EC	
8	$C_{14}H_{13}N$	195	1,3-Dimethlycarbazole	1,3-DMC	
9	$C_{14}H_{13}N$	195	1,6-Dimethlycarbazole	1,6-DMC	
10	$C_{14}H_{13}N$	195	1,7-Dimethlycarbazole	1,7-DMC	Semishielded
11	$C_{14}H_{13}N$	195	1,4-Dimethylcarbazole	1,4-DMC	
4E	$C_{14}H_{13}N$	195	4-Ethylcarbazole	4-EC	
12	$C_{14}H_{13}N$	195	1,5-Dimethylcarbazole	1,5-DMC	
16	$C_{14}H_{13}N$	195	1,2-Dimethylcarbazole	1,2-DMC	
14	$C_{14}H_{13}N$	195	2,6-Dimethylcarbazole	2,6-DMC	
15	$C_{14}H_{13}N$	195	2,7-Dimethylcarbazole	2,7-DMC	Exposed
17	$C_{14}H_{13}N$	195	2,4-Dimethylcarbazole	2,4-DMC	
18	$C_{14}H_{13}N$	195	2,5-Dimethylcarbazole	2,5-DMC	
24	$C_{16}H_{11}N$	217	Benzo[a]carbazole	BaC	Semishielded
25	$C_{16}H_{11}N$	217	Benzo[b]carbazole	BbC	Shielded
26	$C_{16}H_{11}N$	217	Benzo[c]carbazole	BcC	Shielded

found that the contents carbazole and benzo [c] carbazole were the lowest in freshwater lacustrine facies, and were predominant in depositional environments (saline lake fFacies) under regressive conditions of higher salinity. Zhu et al. [29] reported that the abundance of carbazoles and benzocarbazoles in marine oil is much higher than that in lacustrine oil [29]. In the crude oils from Tarim Basi, a strong predominance of the higher homologous (TMC%: 66–72%) is observed. The relative amounts of C_2-carbazoles (DMC) in the second position covered a range from 15% to 23%. In contrast, the relative contents of DMC and TMC are close to each other for the crude oil in Ordos Basin. As can be seen in Figure 7.3, the oil samples with Saline Lake Facie from the Western Qaidam Basin show an enhanced abundance of MC compared with other Basins.

As can be seen in Figure 7.4, the ratio of TMC/DMC and C/(C + BC) may have strong environment dependence. The value of C/(C + BC) in freshwater lacustrine crude oil is low, while that in marine and salt lacustrine crude oil is relatively high, indicating that continental crude oil may be relatively enriched in benzocarbazole series. In addition, the value of TMC/DMC in marine crude oil is high, while that in freshwater lacustrine and salt lacustrine crude oil is relatively low, indicating that continental crude oil may be relatively enriched in TMC.

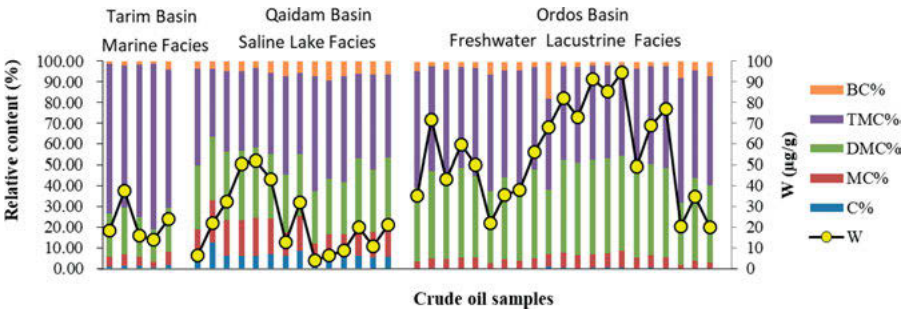

Figure 7.3: The total concentration (*W*) and relative content of PNCs in crude oils.

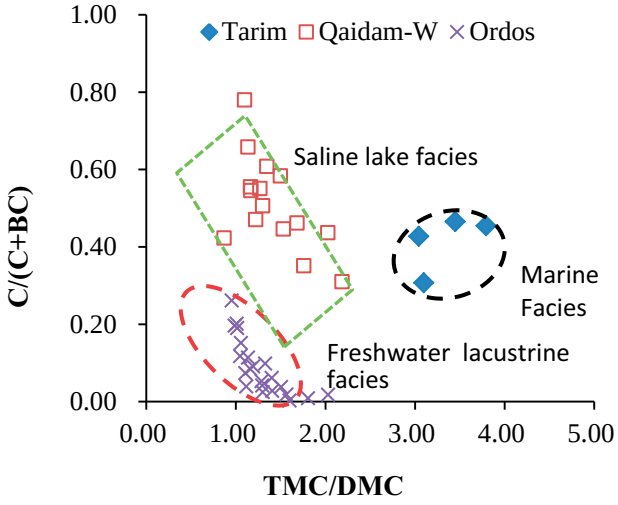

Figure 7.4: Cross plot of C/(C + BC) versus TMC/DMC.

The abundances of isomers of methylcarbazole compounds are different in different types of crude oils. In general, the relative content of 1-MC, 3 -, 2-and 4-MC showed a "V" shape. As for the methylcarbazoles, much variability is found for the triangular diagram representing the 1-,3- and 4-DMC isomers among crude oils under different depositional environment. Data points in triangular diagram are scattered together (Figure 7.5a). For marine facies and freshwater lacustrine facies crude oils, the relative content of 1-MC was higher, followed by 4-MC, and the relative content of 3-MC was the lowest. The relative content of 4-MC in saline lake facies crude oils was higher, followed by 1-MC, and the relative content of 3-MC was the lowest. Considering the variations in methylcarbazole, the cross plot of 3-/4-MC versus 1-4-MC (Figure 7.6a) can well show the facies and depositional environment of crude oils. It can be seen that methylcarbazole compounds are distributed

in different intervals among different types of crude oils. The sedimentary environment of crude oil in Ordos Basin is low salinity, while that of Tarim Basin and Western Qaidam Basin is high salinity. Salinity may be one of the factors affecting carbazole methylation, so it can be inferred that the differences in the distribution of methyl carbazole compounds are due to the sedimentary environment.

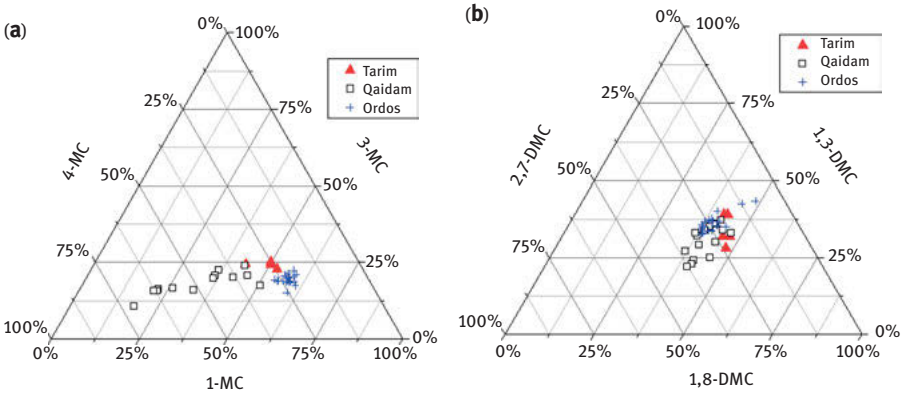

Figure 7.5: Triangular diagrams displaying the distribution of MC isomers (a) and DMC isomers (b).

As for the dimethylcarbazoles, not much variability is found for the triangular diagram representing the 1,3-, 1,8-, and 2,7-DMC isomers among crude oils under different depositional environment. Data points in Figure 7.5b are clustered together. The relative content of 1,8-DMC (41.29% ± 3.08%) was higher, followed by 1,3-DMC (33.76% ± 4.66%), and the relative content of 2,7-DMC (24.95% ± 5.71%) was the lowest. For these three types of sedimentary environment, their distribution difference is small. However, the cross plot of 1,8-/2,7-DMC versus 1,3-/2,7-DMC (Figure 7.6b) cannot well show the sedimentary facies of crude oils. It appeared that the depositional environments have weaker influence on the distribution of dimethylcarbazole isomers.

7.3.2.2 Influence of thermal maturity on the distribution of PNCs

The source input and depositional environment have considerable impact on the occurrence and distributions of PNCs in oils and sedimentary organic matter [20, 28]. Thermal maturity may have some effect on the abundance and distribution of PNCs, but its influence mode and degree need further study. Clegg et al. [20] provided convincing evidence of source maturity control on alkylcarbazole and benzocarbazole concentrations and distributions in petroleum from the Sonda de Campeche area, Gulf of Mexico [20]. Similarly, Li et al. [19] demonstrated this for the Duvernay

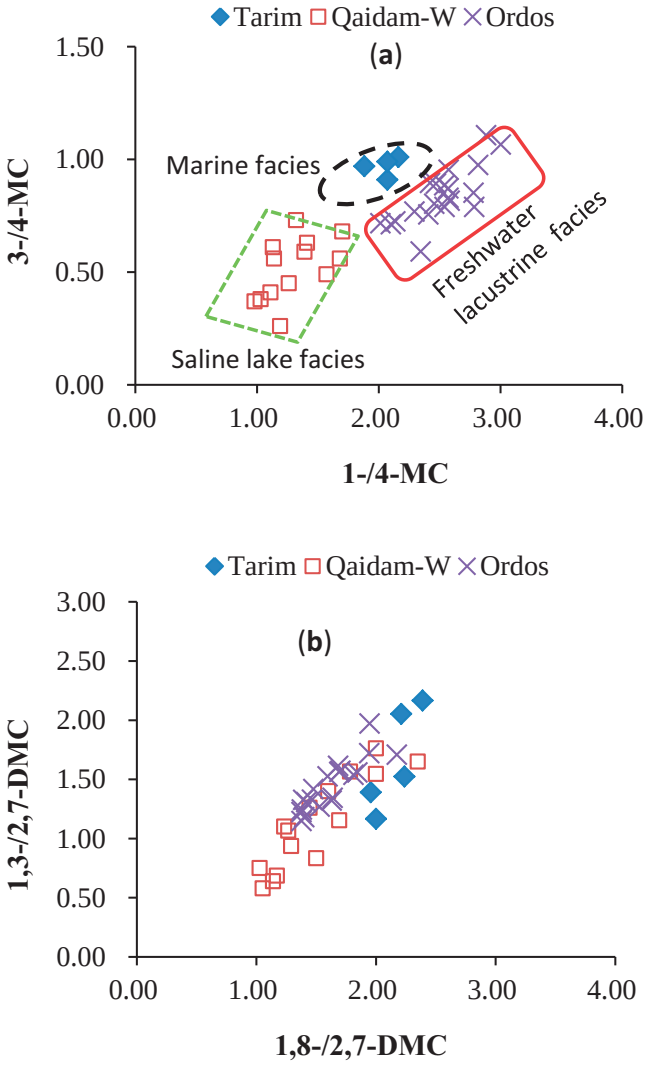

Figure 7.6: Cross plot of 1-/4-MC versus 3-/4-MC (a) and 1,8-/2,7-DMC versus 1,3-/2,7-DMC (b).

Formation of the Western Canada Basin [15]. The value of C_{29} sterane 20*S*/(20*S* + 20*R*) can well indicate the maturity of crude oil. The ratios of C_{29} sterane 20*S*/(20*S* + 20*R*) greater than 0.4 are related to mature oils, corresponding to a vitrinite reflectance of 0.8% [30, 31]. It can be seen that 1,8/2,4-DM increased with the thermal maturity enlarging (Figure 7.7). It is preliminarily considered that the isomers with high shielding degree are relatively enriched with the increase of maturity, which is consistent with the principle of thermodynamic equilibrium. The chemical stability of shielded isomers is higher than that of exposed isomers. In addition, benzocarbazole [a]/[c]

isomer ratios, such as [a]/([a] +[c]), increased with the increasing thermal maturity [15, 28]. In this study, the relevant parameters also showed a good correlation between them (Figure 7.7). During oil migration, the more rod-shaped benzo[a]carbazole relative the sub-spherical benzo[c]carbazole is related to selective sorption of benzocarbazoles from the oil onto clay minerals [32]. A significant increase in the [a]/([a] +[c]) has been obtained for studied oils. This also may be related to the different chemical structures of the two compounds. We suggest the [a]/([a] +[c]) versus C_{29}

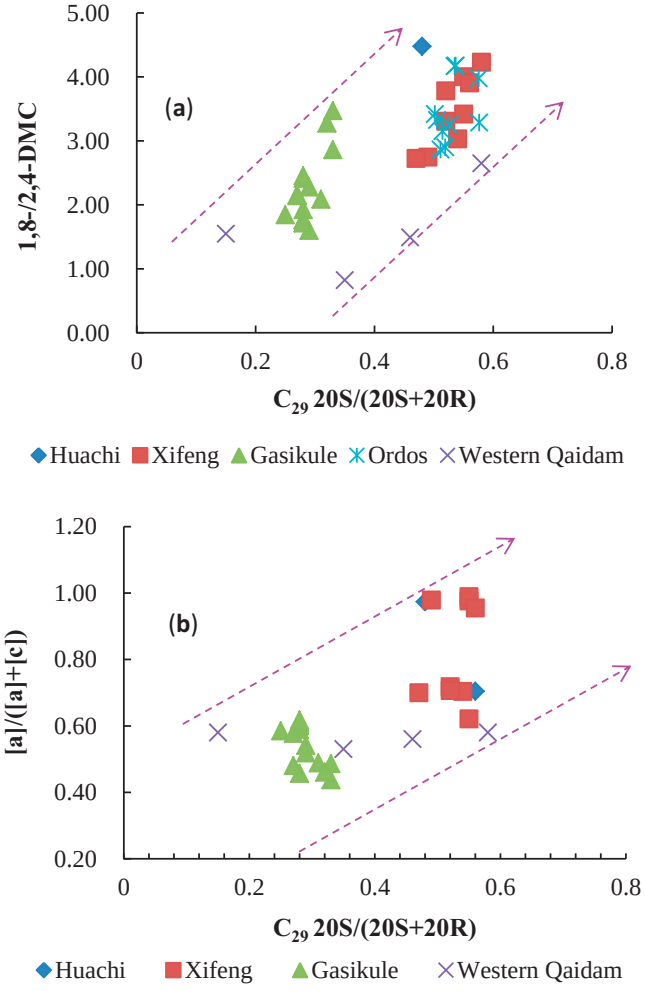

Figure 7.7: Cross plot of 1,8-/2,4-DMC versus C_{29} 20*S*/(20*S* + 20*R*) (a) and [a]/[a] +[c] versus C_{29} 20*S*/(20*S* + 20*R*) (b).
Note: C_{29} 20*S*/(20*S* + 20*R*) = The ααα-20*S* configuration /(ααα-20*S* configuration + ααα-20*R* configuration)-C_{29} sterane ratios; [a]/([a] +[c]) = benzo[a]carbazole/ (benzo[a]carbazole+benzo[c] carbazole).

$20S/(20S + 20R)$ plot can be used as a very sensitive tool for source assessment of crude oils in petroleum systems.

However, compared with the sedimentary environment, maturity may not be the main factor controlling the relative distribution of PNCs in a certain maturity range [10, 15]. Biodegradation is another factor which can alter carbazoles behavior in oils [13, 22, 24]. Moreover, benzo[b]carbazole has the highest ability to resist biodegradation among benzocarbazole isomers [33].

7.3.3 Influence of biodegradation on PNCs distributions in crude oil from the Liaohe Basin, NE China

7.3.3.1 Concentrations of carbazoles and benzocarbazoles

The concentrations of carbazole, methylcarbazoles, C_2-carbazoles, C_3-carbazoles and benzocarbazoles show systematic variations within increasing levels of biodegradation in our sample set samples (Figure 7.8). The C_0–C_2 alkylcarbazoles concentrations firstly increase in the least degraded oil and then decrease gradually at the moderate biodegradation stages. A very sharp decrease of concentrations is then observed in samples at heavy biodegradation levels. Additionally, results from Zhang et al. [33] and Song et al. [13] also support the observation that the concentrations of carbazoles in oils sharply decrease at severe biodegradation levels in the same basin [13, 33]. Alkylcarbazoles and benzocarbazoles are generally resistant to biodegradation at light to moderate biodegradation levels [22]. The observation of a slight increase in alkylated carbazoles and benzocarbazoles concentrations between no-biodegradation and mild biodegradation stages may be due to the fact that significant carbazole and benzocarbazole degradation has not yet begun in these samples and their relative enrichment is the result of depletion of other components (e.g., hydrocarbons). Their sharp decrease in abundance in the lower part of the column may be the result of biodegradation.

The normalization treatment of carbazole, methylcarbazole, C_2-carbazole and C_3-carbazole showed that the relative percentages of the three compounds did not change significantly in the undegraded, lightly degraded and moderately degraded crude oils (Figure 7.9). It is suggested that the microbial effect on the above three kinds of compounds may be consistent in these degradation stages. In the heavily degraded crude oils, the relative percentages of carbazole and methylcarbazole decreased significantly, while the relative percentages of C_2- and C_3- carbazole increased significantly. This indicates that C_2- and C_3-carbazole showed stronger anti-microbial degradation than carbazole and methylcarbazole in the heavy degradation stage.

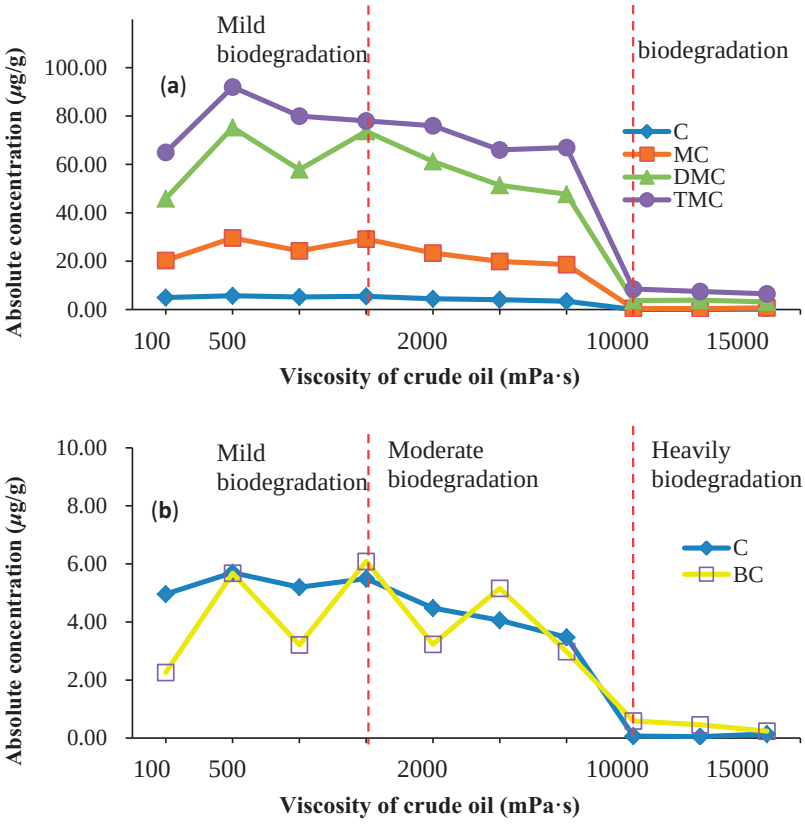

Figure 7.8: Concentrations of the alkylcarbazole homologue groups and benzocarbazoles with increasing levels of biodegradation.

7.3.3.2 Methylcarbazole distribution

For most crude oils and source rocks, 1-methylcarbazole is the predominant component among the methylcarbazoles [19, 20]. 1-Methylcarbazole is overall the most abundant of the four methylcarbazole isomers, except for the severely biodegraded sample (where 4-methylcarbazole is the dominant isomer). Our results clearly show that the abundances of 2- and 3-methylcarbazoles decrease significantly with increasing degree of biodegradation relative to 1- and 4-methylcarbazoles in the biodegraded oils (Figure 7.10). 2- and 3-methylcarbazoles are more susceptible to biodegradation than the 1- and 4-methylcarbazoles. Moreover, the ratio of 1-/4-methylcarbazole increased slightly, followed by decreasing with progressively higher levels of biodegradation. From Figure 7.11, it can be seen that 1-/(2- + 3-MC) showed the same pattern. 4-/(2- + 3-MC)) show the opposite rule. These data suggest

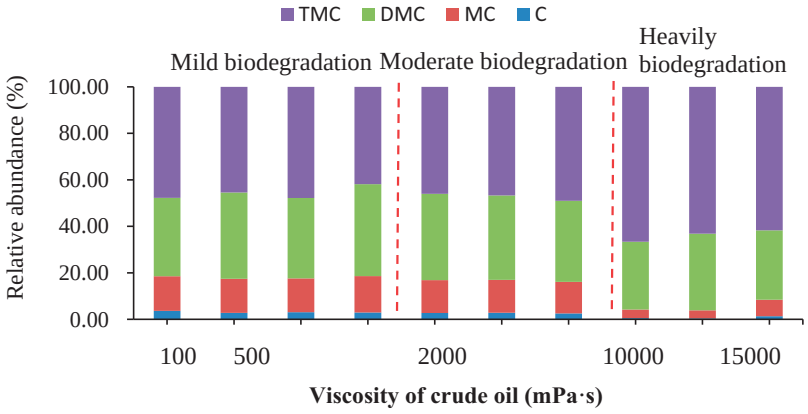

Figure 7.9: Relative abundance of the alkylcarbazole homologue groups and benzocarbazoles with increasing levels of biodegradation.

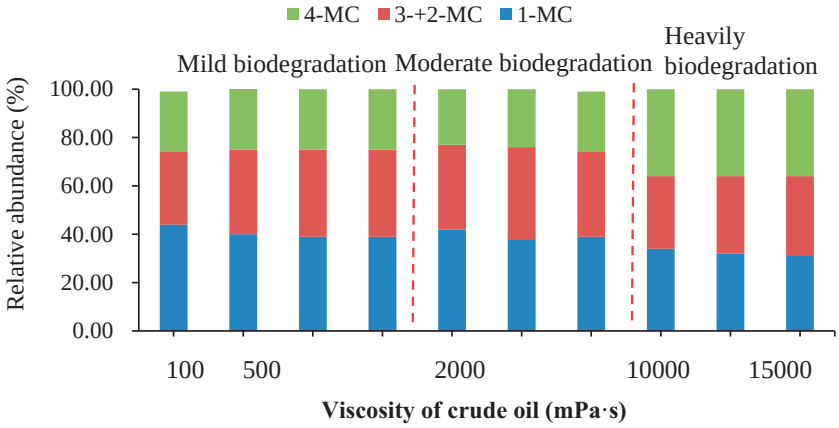

Figure 7.10: Relative abundance of the methylcarbazole isomers to total with increasing levels of biodegradation.

that among the methylcarbazoles, the 4-MC isomer is the most susceptible to biodegradation. Positive correlations between these ratios (Figure 7.11) indicates that both of can be applied to assess the degree of biodegradation. Similar features were reported by Song et al. [13] for the crude oils from the Bongor Basin, Chad [13].

7.3.3.3 Dimethylcarbazole distribution

Dimethylcarbazoles can be classified into three isomer groups; N-H shielded isomers (SNs), N-H partially shielded isomers (PSNs), and N-H exposed isomers (ENs),

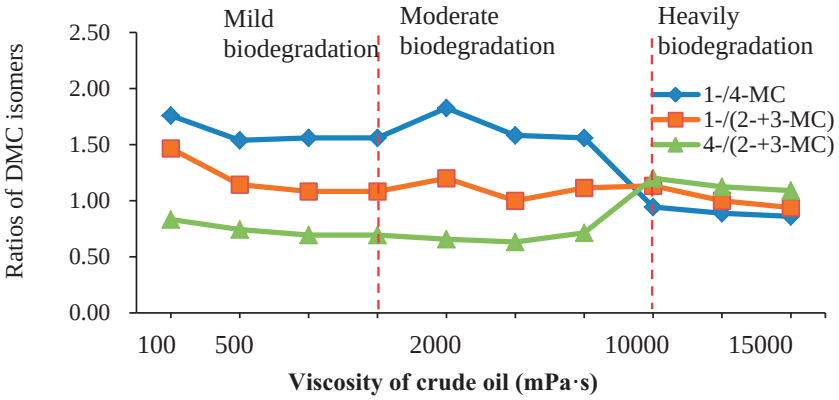

Figure 7.11: Ratios of methylcarbazoles isomers with increasing levels of biodegradation.

according to the present positions of the methyl group. The shielded isomers have two methyl groups, at the 1- and 8- positions; partially shielded isomers have one of the alkyl groups present at the 1-position; and exposed isomers have no substitution at the 1-position or 8-position. The samples display a strong predominance of the N-H partially shielded over N-H exposed isomers. For the light or moderately degraded crude oil, the relative composition of the three isomers changed little. At the same time, the relative abundance of partially shielded isomers decreased noticeably and the relative abundance of shielded isomers and exposed isomers increase slightly (Figure 7.12). These results imply that the shielded dimethylcarbazole isomer (1,8-dimethylcarbazole) is more resistant to biodegradation. The ratios of SNS/ENS and SNS/PSNs display a sharper decrease (Figure 7.12), indicating that the former is more difficult to degrade. Furthermore, the ratio of PSNS/ENS and PSNS/SNS decreased in heavily degraded oils, which means that the degradation rate of N-H semishielded isomer was higher than that of N-H shielded isomer and N-H exposed isomer. The degradation rates of different isomers were significantly different. The degradation rates of semishielded isomers (e.g., 1,6-DMC, 1,4-DMC) were higher than that of shielded isomers (1,8-DMC). It is worth noting that the two exposed isomers (2,4-DMC and 2,6-DMC) have great differences in anti-biodegradation ability. The 2,4-DMC with methyl distributed on the same benzene ring has much higher anti-biodegradation ability than other isomers in PM4 to PM5 [PM biodegradation scale [34]], and the relative content of 2,4-DMC with methyl distributed on different benzene rings is significantly increased, The degradation rate of 6-DMC is similar to that of semi sheltered structure [35].

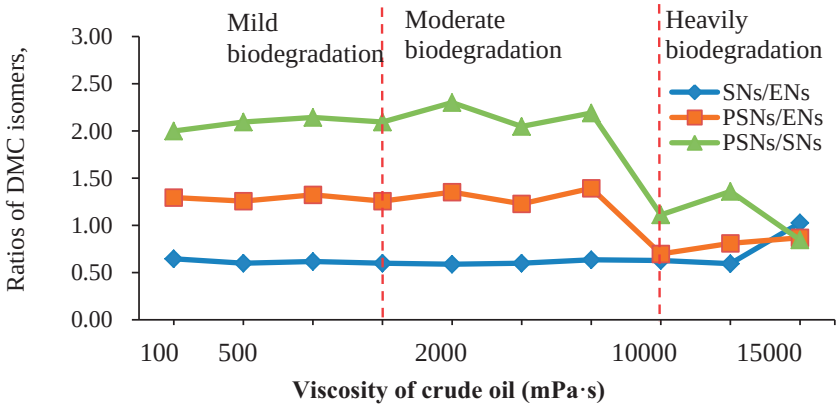

Figure 7.12: Ratios of dimethylcarbazoles isomers with increasing levels of biodegradation.

7.3.3.4 Benzocarbazole distribution

Benzocarbazole has three isomers: benzo[a]carbazole, benzo [b]carbazole, and benzo[c]carbazole. The Liaohe oils in this study are characterized by uniform benzocarbazole distributions dominated by benzo[a]- and benzo[c]-carbazole, with the benzo[b] isomer being present in minor abundance. The [a] benzene ring in benzo-[a]carbazole is in the same side of the N-H group in carbazole, and has a certain shielding effect on this group; and benzo[c]carbazole is far away from carbazole N-H group in [c] position, making it completely bare. The relative abundance of benzo[a]carbazole seems to decrease compared to benzo[c]carbazole in heavily degraded oils (Figure 7.13). The ratio of [a]/([a] +[c]) benzocarbazole (B[a]C/(B[a]C + B[c]C) has been used as indicator of oil migration distance [3]. It has also been noted that this ratio is influenced to some extent by maturity [13, 15, 20], organic source [26, 36], and biodegradation [22].

In petroleum geochemistry, parameters such as 1-MC/4-MC, 1,8-DMC/2,6-DMC, and B[a]C/(B[a]C + B[c]C) (BCR) can be used to trace crude oil and study migration distance [3, 5]. The results also imply that the PNCs could provide another useful diagnostic means for spill source identification at their lightly to moderately weathered stages.

7.3.3.5 Degradation mechanism of nitrogen compounds

Relatively little work has been done on the mechanisms of carbazole compound biodegradation, and most of it has been carried out under aerobic conditions. It appears that under aerobic conditions there are three different modes of initial oxidation:

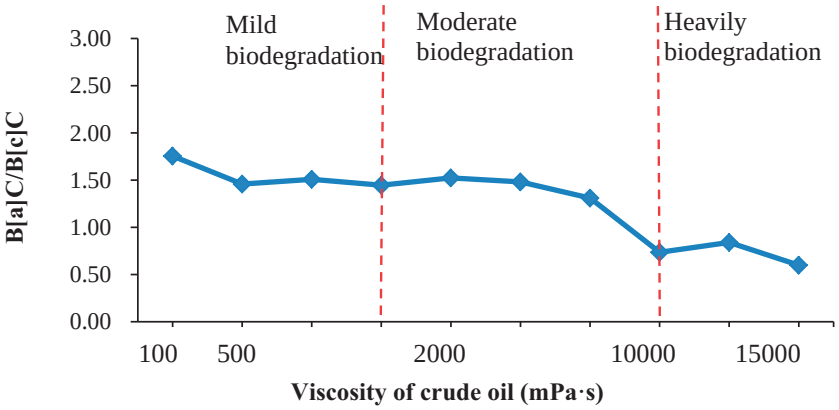

Figure 7.13: Ratios of B[a]C/B[c]C with increasing levels of biodegradation.

(i) a naphthalene-like attack, in which one of the aromatic rings is oxidized to a dihydrodiol; (ii) an angular dioxygenase attack, in which the carbon bonded to the nitrogen and the adjacent carbon in the aromatic ring are both oxidized; and (iii) a five-membered ring attack, in which the nitrogen atom is directly oxidized [37, 38]. Some details are known; for example, in an angular dioxygenase attack, the initial enzymatic degradation of carbazoles is considered to give a dihydroxylated intermediate which is spontaneously converted to 2′-aminobiphenyl-2,3-diol (an unstable intermediate) [22]. In the anaerobic environment, the degradation mechanism of carbazole compounds is mainly through the breaking of aromatic rings or nitrogen-containing

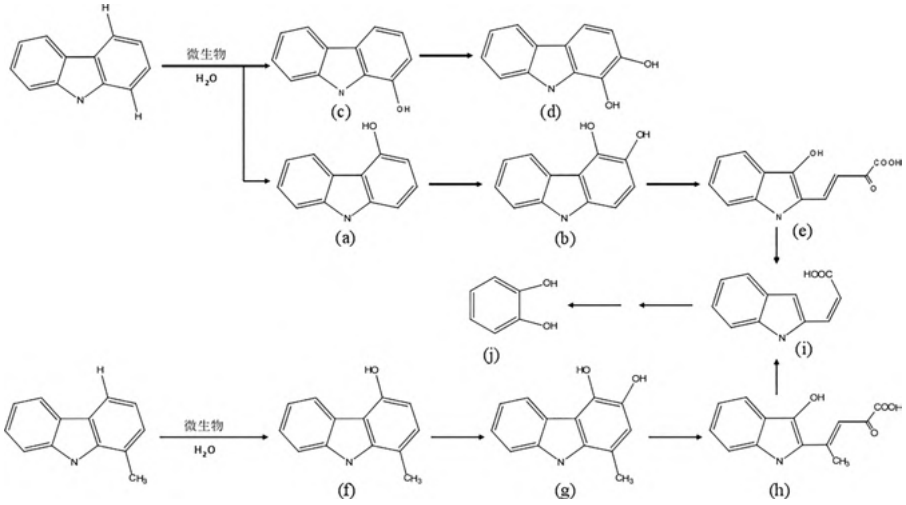

Figure 7.14: Possible biodegraded pathways of carbazole and methylcarbazoles [35].

aromatic rings, the substitution of N groups by OH or CO groups, and the formation of intermediates containing no groups in this process [39]. Based on the results observed in the actual samples, Shi et al. [35] proposed a degradation pathway of less alkyl substituted carbazole homologues as shown in Figure 7.14. For carbazole substituted by dimethyl or more alkyl group, the process may be more complicated due to the influence of substituents. Further research is needed in this field. In general, the biodegradation of carbazole is more likely to be accomplished by attacking the carbon or nitrogen in or near the five-membered ring.

7.4 Conclusion

The results suggest that the depositional environment and thermal maturity have some impact on the geochemical characteristics of the pyrrolic nitrogen compounds. Similar to hydrocarbon compounds, the distribution characteristics of pyrrolic nitrogen compounds in crude oil are controlled by a variety of geochemical factors, such as depositional environment, biogenic parent material, thermal maturity, and oil and gas migration. The abundance of carbazoles and benzocarbazoles in marine oil is much higher than that in lacustrine oil. Carbazoles (C_0–C_2) in source rocks are related to the maturity level. The isomers with high shielding degree are relatively enriched with the increase of maturity, which is consistent with the principle of thermodynamic equilibrium. It is possible to obtain information from PNCs that indicates the maturity, origin, migration, and deposition environments, thereby demonstrating the role of these species as geochemical markers. Biodegradation is another factor which can alter carbazoles' behavior in oils. The degradation rates of carbazole, alkyl carbazole and benzocarbazole in crude oil samples from high to low are C > MC > DMC > TMC > BCS. The degraded rates of four methylcarbazoles are in order as followed, 2-MC > 3-MC > 4-MC > 1-MC, dimethylcarbazole isomers as followed, partly shield > shield > exposed, and benzocarbazoles as followed, B[a]C > B[b]C > B[c]C. The biodegradation rate of carbazole compounds is different, which is reflected in the selectivity of microbial degradation to isomers. The effects of facies, depositional environment, maturity, and biodegradation need to be constrained carefully when PNCs used as indicators of secondary migration. Obviously, these findings can also be applied for correlation and differentiation of spilled oils at their lightly to moderately weathered stages.

References

[1] Dias LC, Bahia P, Amaral D, Machado ME. Nitrogen compounds as molecular markers: An overview of analytical methodologies for its determination in crude oils and source rock extracts. Microchem J, 2020, 157, 105039.
[2] Tissot BP, Welte DH. Petroleum formation and occurrence. Springer Verlag, Berlin, 1984.
[3] Larter SR, Bowler BFJ, Li M, Chen M, Brincat D, Bennett B, Noke K, Donohoe P, Simmons D, Kohnen M, Allan J, Telnaes N, Horstad I. Molecular indicators of secondary oil migration distances. Nature, 1996, 383, 593–597.
[4] Li MW, Osadetz KG, Yao H, Obermajer M, Fowler MG, Snowdon LR, Christensen R. Unusual crude oils in the Canadian Williston Basin, southeastern Saskatchewan. Org Geochem, 1998, 28, 477–488.
[5] Wang T, Li S, Zhang S. Oil migration in the Lunnan region, Tarim Basin, Chian based on the pyrrolic nitrogen compound distribution. J Petrol Sci Eng, 2004, 41, 123–134.
[6] Zhang CM, Li ST, Yang JM, Yang SK, Wang JR. Petroleum migration and mixing in the Pearl River Mouth Basin, South China Sea. Mar Petrol Geol, 2004, 21, 215–224.
[7] Ziegs V, Noah M, Poetz S, Horsfield B, Hartwig A, Rinna J, Skeie JE. Unravelling maturity- and migration-related carbazole and phenol distributions in Central Graben crude oils. Mar Petrol Geol, 2018, 94, 114–130.
[8] Dorban M, Schrnjtter JM, Garrigues P, Ignatiadis I, Ewald M, Arpino P, Guiochon G. Distribution of carbazole derivatives in petroleum. Org Geochem, 1984, 7, 111–l20.
[9] Bowler BFJ, Larter SR, Clegg H, Wilkes H, Horsfield B, Li M. Dimethylcarbazoles in crude oils: Comment on “liquid chromatographic separation schemes for pyrrole and pyridine nitrogen aromatic heterocyclic fractions from crude oils suitable for rapid characterization of geochemical samples”. Anal Chem, 1997, 69, 3128–3129.
[10] Han JH, Guo XW, Dong T, He S, Wang YS, Wang XJ, Hua YQ, Zhao W, Chen JX. Oil origin and secondary migration pathway in the Bonan sag, Bohai Bay Basin, China. Mar Petrol Geol, 2020, 122, 104702.
[11] Abrakasa S, Onojake MC, Ukaegbu V, Nwankwoala HO. Carbazoles and benzocarbazoles confirm migration of leaked petroleum through caprocks and overlaying formations of Valhall Well 2/8-8 in the North Sea. Acta Geochim, 2018, 37, 537–545.
[12] Clegg H, Wilkes H, Horsfield B. Carbazole distributions in carbonate and clastic source rocks. Geochim Cosmochim Ac, 1997, 61, 5335–5345.
[13] Song HX, Wen ZG, Bao JP. Influence of biodegradation on carbazole and benzocarbazole distributions in oils from the Bongor Basin, Chad. Org Geochem, 2016, 100, 18–28.
[14] Guo XW, Liu KY, Jia CZ, Song Y, Zhao MJ, Zhuo QG, Lu XS. Hydrocarbon accumulation processes in the dabei tight-gas reservoirs, Kuqa subbasin, Tarim basin, northwest China. AAPG (Am Assoc Pet Geol) Bull, 2016, 100, 1501–1521.
[15] Li SM, Wang TG, Zhang AY. Geochemical characteristics and significance of the pyrrnlic compounds in petroleum. Acta Sedimentologica Sinica, 1999, 17, 312–317. (In Chinese with English Abstract).
[16] Bechtel A, Gratzer R, Linzer HG, Sachsenhofer RF. Influence of migration distance, maturity and facies on the stable isotopic composition of alkanes and on carbazole distributions in oils and source rocks of the alpine foreland basin of Austria. Org Geochem, 2013, 62, 74–85.
[17] Bennett B, Lager A, Christopher A, Russell CA, Love GD, Larter SR. Hydropyrolysis of algae, bacteria, archaea and lake sediments: Insights into the origin of nitrogen compounds in petroleum. Org Geochem, 2004, 35, 1427–1439.

[18] Mohamed MYB, Heinz W. The influence of facies and depositional environment on the occurrence and distribution of carbazoles and benzocarbazoles in crude oils: A case study from the Gulf of Suez, Egypt. Org Geochem, 2002, 33, 561–580.
[19] Li MW, Yao H, Stasiuk LD, Fowler MG, Larter SR. Effect of maturity and petroleum expulsion on pyrrolic nitrogen compound yields and distributions in duvernay formation petroleum source rocks in central Alberta, Canada. Org Geochem, 1997, 26, 731–744.
[20] Clegg H, Wilkes H, Santamaria-Orozco D, Horsfield B. Influence of maturity on carbazole and benzocarbazole distributions in crude oils and source rocks from the Sonda de Campeche, Gulf of Mexico. Org Geochem, 1998, 29, 183–194.
[21] Li SM, Wang TG, Zhang AY. Effect of maturity on pyrrolic nitrogen compounds. Scientia Geologica Sinica, 2000, 9, 227–236. (In Chinese with English Abstract).
[22] Huang HP, Bowler BFJ, Zhang ZW, Oldenburg TBP, Later SR. Influence of biodegradation on carbazole and benzocarbazole distributions in oil columns from the Liaohe basin, NE China. Org Geochem, 2003, 34, 951–969.
[23] Duan Y, Yuan YD, Qian RR. Migration features of crude oil in fluvial deposits of maling oilfield in ordos basin, China. Org Geochem, 2013, 58, 78–85.
[24] Dyreborg S, Arvin E, Broholm K. Biodegradation of NSO-compounds under different redox-conditions. J Contam Hydrol, 1997, 25, 177–197.
[25] Zhang S, Huang H. Geochemistry of Palaeozoic marine petroleum from the Tarim Basin, NW China: Part 1. Oil family classification. Org Geochem, 2005, 36, 1204–1214.
[26] Zhang CM, Zhang YQ, Zhang M, Zhao HJ, Cai CF. Carbazole distributions in rocks from non-marine depositional environments. Org Geochem, 2008, 39, 868–878.
[27] Duan Y, Wang CY, Zheng CY, Wu BX, Zheng GD. Geochemical study of crude oils from Xifeng oilfield of Ordos Basin, China. J Asian Earth Sci, 2008, 31, 341–356.
[28] Baker MMY, Wilkes H. The influence of facies and depositional environment on the occurrence and distribution of carbazoles and benzocarbazoles in crude oils: A case study from the Gulf of Suez, Egypt. Org Geochem, 2002, 33, 561–580.
[29] Zhu YM, Fu JM, Sheng GY, Xiang TS, Mei BW. Geochemical significance of pyrrolic nitrogen compounds in various kinds of crude oils from the tarim basin. Chin Sci Bull, 1998, 43, 1366–1370.
[30] Huang DF, Li JC, Zhang DJ, Huang XM, Zhou ZH. Maturation sequence of tertiary crude oils in the Qaidam Basin and its significance in petroleum resource assessment. J Southeast Asian Earth Sc, 1991, 5, 359–366.
[31] Duan Y, Zheng CY, Wang ZP, Wu BX, Wang CY, Zhang H, Qian YR, Zheng GD. Biomarkers of geochemistry of crude oils from the Qaidam Basin, NW China. J Petrol Geol, 2006, 29, 175–188.
[32] Li M, Wang TG, Shi S, Liu K, Ellis GS. Benzo[b]naphthothiophenes and alkyl dibenzothiophenes: Molecular tracers for oil migration distances. Mar Petrol Geol, 2014, 57, 403–417.
[33] Zhang C, Mei B, Later RS, Marting PK, Xiao Q. Effects of biodegradation on the distribution of alkylcarbazoles in crude oils. Chin J Geochem, 2002, 22, 140–146.
[34] Peters KE, Moldowan JM. The biomarker guide. In: Interpreting molecular fossils in petroleum and ancient sediments. Englewood Cliffs Nj Prentice Hall, 1993, 63.
[35] Shi SB. The biodegradation effect and mechanism of nitrogen compounds in crude oils, Linpan Oilfield (D). China University of Petroleum. Beijing, 2019, 119–120.
[36] Zhang CM, Zhang YQ, Cai CF. Maturity effect on carbazole distributions in source rocks from the saline lacustrine settings, the western Qaidam Basin, NW China. J Asian Earth Sci, 2011, 42, 1288–1296.

[37] Bressler DC, Fedorak PM. Bacterial metabolism of fluorene, dibenzofuran, dibenzothiophene and carbazole. Can J Microbiol, 2000, 46, 397–409.
[38] Shi S, Qu Y, Zhou H, Ma Q, Ma F. Characterization of a novel cometabolic degradation carbazole pathway by a phenol-cultivated *Arthrobacter* sp. W1. Bioresource Technol, 2015, 193, 281–287.
[39] Kim S, Stanford LA, Rodgers RP, Marshall AG, Walters CC, Qian KN, Wenger LM, Mankiewicz P. Microbial alteration of the acidic and neutral polar NSO compounds revealed by fourier transform ion cyclotron resonance mass spectrometry. Org Geochem, 2005, 36, 1117–1134.

Roman S. Borisov, Vladimir G. Zaikin

8 Analysis of petroleum-related samples by soft ionization/high-resolution mass spectrometry

Abstract: This chapter considers the achievements in applying the various methods of "soft" ionization in high- and ultrahigh-resolution mass spectrometry to investigate polar, low-volatility nonpolar, and high molecular petroleum components for refining and further their processing into useful products. High-resolution method is of particular importance as it allows determining the mass of ions with very high accuracy and establishing the elemental composition of the detected compounds. In turn, "soft" ionization methods operating at atmospheric pressure or permitting the desorption/ionization of solid samples are very suitable for the analysis of heavy petroleum fractions. The capabilities and disadvantages of existing approaches and instrumental techniques are discussed.

8.1 Introduction

Mass spectrometry is the most effective structural-analytical tool for the analysis of such a complex mixture as petroleum. The fundamental knowledge on the petroleum compositions serves as the basis for creating standardized approaches to determining the origin of oils, routes of their transformation in nature during migration and catagenesis. Such knowledge is particularly necessary for the development of oil refining processes in industry.

To name the emerging trend in petroleum chemistry, the term "petroleomics" was proposed by A. Marshall [1], implying the "comprehensive description of all chemical compounds of crude oil and their interactions." Although the authors of the term introduced it to describe the aggregate of data obtained using ultrahigh-resolution mass spectrometry (uHRMS), its meaning is almost completely consistent with the challenges that petroleum chemistry faces. Thus, these concepts have become practically interchangeable, and the use of mass spectrometry to solve the problems of petroleum – "petroleome" – includes the use of a set of relatively recent and traditional mass spectrometric options. The application of the variety of approaches to such analysis is due to the extraordinary variety of organic compounds present in oil and differing in chemical, physical-chemical properties, as

Roman S. Borisov, Vladimir G. Zaikin, A.V. Topchiev Institute of Petrochemical Synthesis RAS, Moscow

https://doi.org/10.1515/9783110694529-008

well as in the quantitative content in oil. In turn, mass spectrometric ionization techniques have various capabilities and limitations and each of them allows studying only a certain part of the components of petroleum feedstock, but none of them is completely universal. Indeed, at present, there is no single mass spectrometric method by which one could characterize the complete composition of crude oil, usually consisting of hundreds of thousands of compounds of various structures, elemental compositions, volatility, and ionizability (aliphatic, alicyclic, and aromatic hydrocarbons; N- and S-containing hetero-organic compounds; naphthenic acids; asphaltenes; resins; and even organoelemental entities). Therefore, the study of petroleome is usually based on the use of a set of mass spectrometric methods, and this requires the development of approaches for complete interpretation of such huge composite data.

The previous chapter explored the possibilities of mass spectrometry combined with online gas chromatographic separation for oil analysis. However, these methods manage to investigate, although most of the oils, but only its volatile part. At the same time, other mass spectrometry techniques are necessary to investigate polar, low-volatility nonpolar, and high molecular petroleum components for refining and further their processing into useful products.

This chapter is devoted to this issue, where the possibilities of various methods of "soft" ionization, mainly with uHRMS, are considered. This high-resolution method is of particular importance as it allows determining the mass of ions with very high accuracy and, therefore, establishing the elemental composition of the detected compounds. In turn, "soft" ionization methods operating at atmospheric pressure or permitting the desorption/ionization of solid samples are very suitable for the analysis of heavy petroleum fractions. Note that some aspects of application of mass spectrometry to solve the petrochemical problems have been discussed in a number of reviews. Here we note only recent reviews on this issue.

8.2 Soft ionization methods in mass spectrometry of polar and low-volatility nonpolar petroleum compounds

Ionization methods used in the study of petroleum by the uHRMS can be divided into two main types based on "soft"-ionization principles: atmospheric pressure ionization and desorption/ionization. The former method involves spraying and ionizing the analytes in the ion source at atmospheric pressure, and the latter one suggests simultaneous desorption/ionization of molecules from the solid samples. The energy supplied to the analyte molecules in both cases is fairly low and primary ions almost do not undergo fragmentation which is convenient for establishing their molecular weights. Each of the methods considered below has its own advantages and disadvantages,

and unfortunately, as already mentioned, none of them allows one to describe in detail the whole petroleum, consisting of various classes of compounds differing in molecular weights, elemental composition, physical chemical properties, reactivity, and ionization capacity.

8.2.1 Atmospheric pressure ionization

8.2.1.1 Electrospray ionization (ESI)

Electrospray ionization (ESI) is based on the principle developed by M. Dole [2]: if a solution of a nonvolatile compound in a volatile solvent passes through a thin capillary, then charged drops are formed at the capillary end under the action of a strong positive or negative electric field. Upon evaporation of solvent molecules, ions of the analyzed compound are released in a gaseous state and enter the mass spectrometer. A further sharp increase in the popularity of ESI is associated with the work of the Russian research group headed by L.N. Gall' [3] and the later study by J. Fenn [4], who showed the great promise of the method for the analysis of biomacromolecules. At the same time, D. Zhan and J. Fenn [5] were the first who applied ESI-MS to the study of organic matter of fossil fuels and their processing products. They showed that ESI mass spectra of deasphalted oils are a complex superposition of ion peaks of a large number of polar compounds. It should be emphasized that the main ionization mechanisms of ESI are based on primary formation of closed-shell ions owing to protonation (cationization) or deprotonation of analyte molecules. That is why the method is mainly applicable to the detection of polar oil compounds.

As will be shown below, the highest analytical value of ESI-MS manifests itself in experiments with uHRMS (see below) which makes it possible to resolve ions having the same nominal, but different exact mass, allowing one to calculate the elemental composition of the ion. The first works in this area were carried out under the guidance of A. Marshall, who, as already mentioned, proposed the term "petroleomics" [1]. Since only polar substances, mainly nitrogen-, oxygen-, and sulfur-containing (NSO) compounds, are detectable with the use of ESI, it is believed that no more than 15% of oil components can be detected by this method [1]. However, it is these components that make up the most important classes of heteroatomic compounds, which are possible markers for determining the geochemical parameters of oils and oil generation routes and, most importantly, predetermine the choice of the most effective oil refining processes. Note also that most of the polar petroleum compounds have acidic properties, providing deprotonation, and can be analyzed by ESI in the negative ion detection mode, ESI(−). Generally speaking, ESI in conjunction with uHRMS is the most common ionization method owing

to both its easy use and handling and a possibility to effectively ionize the components rising from high to medium polarity.

For ESI-HRMS analysis, the samples are usually injected in the infusion mode. However, the introduction of the samples via high-performance liquid chromatography (HPLC) can be used in a number of cases.

8.2.1.2 Atmospheric pressure chemical ionization (APCI)

Atmospheric pressure chemical ionization (APCI) is the oldest "soft" ionization method in MS. As noted in the previous chapter, APCI is due to secondary ion–molecule interactions of an analyte, which is sprayed in the ion source at atmospheric pressure. Solvent ions, ionized water clusters and dopant ions, formed in a corona discharge, are the main ionized participants in such reactions. During APCI, most petroleum compounds are characterized by the formation of positive ions among which the M^+ and $[M + H]^+$ ions are particularly important. For such investigation, the samples may be introduced into the ion source by direct injection.

The first experiments showed that the sensitivity and universality of APCI method in the detection of oil components are lower than those of ESI [6]. However, by varying the composition of the solvent or adding special dopants, the ionization efficiency of certain classes of compounds can be enhanced. For example, the use of toluene as a solvent significantly increases the signal intensity of aromatic compounds in the APCI mass spectra of a bitumen sample [7]. In this case, however, both $M^{+\cdot}$ and $[M + H]^+$ ions are produced which complicate the interpretation of the data [7]. The situation changes when toluene is replaced by carbon disulfide: in almost all cases, the generation of only $[M + H]^+$ ions was observed [8]. In addition, the use of this approach in combination with tandem mass spectrometry made it possible to conduct a comparative study of petroleum and coal asphaltenes [9]. In particular, the latter were distinguished by significantly shorter chain lengths of substituents and a broader distribution of the number of aromatic rings. Quite interesting is the fact that the use of a low-molecular-weight aliphatic or alicyclic hydrocarbons, and particularly isooctane, as a solvent for analytes can sharply increase the ionization efficiency of paraffin hydrocarbons [10] (Figure 8.1). To explain this unexpected effect, an ionization scheme was proposed, including hydride ion transfer of saturated hydrocarbons from *tert*-butyl carbocations generated from isooctane. Subsequent experiments allowed the authors to propose the use of a mixture of carbon disulfide and isooctane for oil analysis. In addition, the influence of the nature of the gases used in the ion source for spraying and forming a cloud of microdroplets (nitrogen, helium, synthetic air, or their mixtures) was clarified [11]. Other authors [12] suggested using oxygen as the carrier gas that provided recording the APCI mass spectra of paraffin mixtures, revealing intense peaks of the $[M - H]^+$ ions.

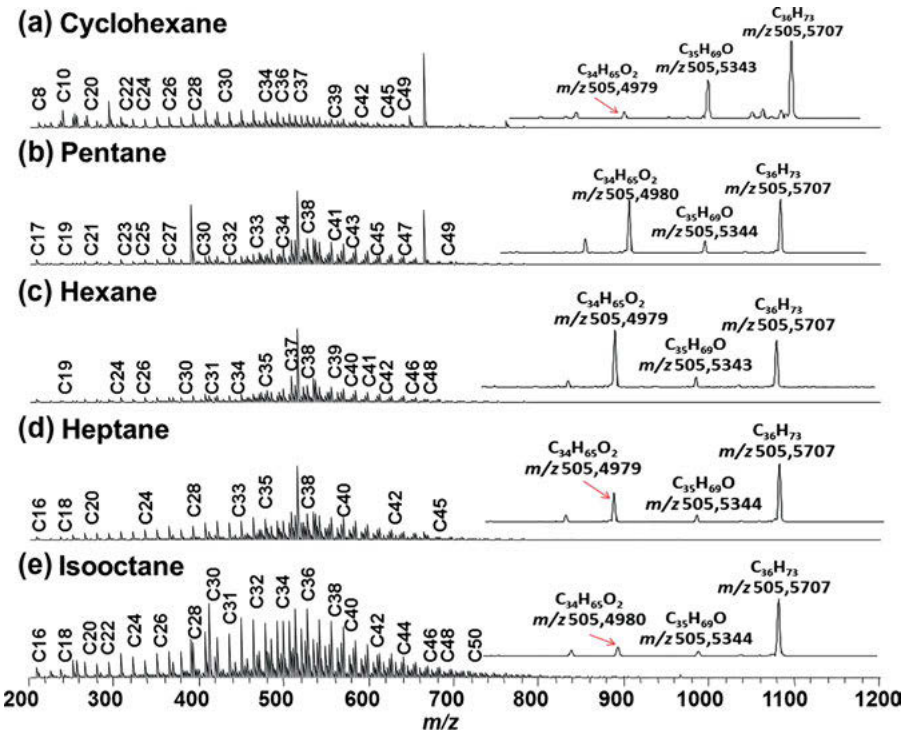

Figure 8.1: APCI(+)FT-ICR mass spectra for a paraffin sample registered using different aliphatic solvents as APCI reagent: (a) cyclohexane; (b) pentane; (c) hexane; (d) heptane; and (e) isooctane. Reprinted from [10] with permission. Copyright (2015) Elsevier.

8.2.1.3 Atmospheric pressure photoionization (APPI) and photochemical ionization (APPCI)

Atmospheric pressure photoionization (APPI) and photochemical ionization (APPCI) techniques are based on the interaction of organic molecules with photons at atmospheric pressure. In both cases, analyte $M^{+\cdot}$ ions along with products of secondary ion–molecule reactions are formed. APPCI version includes additionally the introduction of dopants into the ionization region which gives rise to increasing the probability of secondary ion formation. The APPCI-based version of mass spectrometry involves spraying an analyte solution in the ion source where secondary ion formation processes resulting from the interaction of analyte molecules with ionized solvent molecules under photon irradiation at atmospheric pressure take place. In contrast to ESI and APCI, this ionization technique makes it possible to impart a charge to nonpolar and weakly polar compounds giving rise to molecular cation radicals, protonated, deprotonated molecules and cluster ions. On the other hand, as

for APCI, the introduction of dopant vapors into the ionization region can substantially alter the probability of occurrence of certain ionization processes.

8.2.2 Desorption/ionization

8.2.2.1 Laser desorption/ionization (LDI), matrix-assisted laser desorption/ionization (MALDI), surface-activated laser desorption/ionization (SALDI)

Laser desorption/ionization (LDI), involving the ion formation during pulsed laser irradiation of solid samples, was discovered in the late 1960s and soon showed the ability to investigate nonvolatile polar compounds [13] and polyaromatic hydrocarbons [14]. Being a pulsed technique, LDI is optimally combined with time-of-flight (TOF) mass analyzer, but a relatively low resolving power of the latter does not allow for full-scale analysis of mixtures of polar and low-volatility petroleum compounds. In this regard, the combination of LDI with ultrahigh-resolution analyzer such as FT-ICR is more advantageous. For example, it shows greater sensitivity to organic nitrogen compounds and the possibility of simultaneous detection of aromatic and nonaromatic oxygen-containing compounds [15].

However, LDI has gained the greatest prevalence and popularity owing to the discovery of enhancement of desorption/ionization efficiency in the presence of another compound (matrix) and the creation of the method called matrix-assisted desorption/ionization (MALDI) [16]. Even in combination with conventional medium-resolution TOF mass analyzers, the method is successfully used for the selective detection of certain classes of compounds. Since the efficiency of desorption/ionization of analytes of various structures directly depends on the nature of the matrix used, it is possible to select it in such a way as to achieve a better yield of ions for one class of compounds and their suppression for the other class.

An additional version of LDI, so-called L^2MS, should be noted. In this case, two lasers independently operate in the ion source: an IR laser ensures the desorption of analyte molecules from the target surface, and the UV laser ensures their ionization in the gas phase. This method is particularly efficient in the analysis of asphaltenes.

Another variant of two-stage desorption/ionization is based on using the effect of laser energy transfer as a result of the generation of thermal and acoustic waves (laser-induced acoustic desorption, LIAD). In this case, the analyte is deposited on a metal foil, and the laser beam is directed to its back side. The restructuring of the analyte film surface is accompanied by desorption of molecules that can be ionized by various methods. LIAD is operative at atmospheric pressure and can be attributed to ambient mass spectrometry, which practically does not require a special sample preparation procedure.

8.2.2.2 Direct analysis in real time (DART)

Direct analysis in real time (DART) became one of the first mass spectrometric methods that include ionization in open air and laid the foundation for the creation of a whole series of mass spectrometric methods related to "ambient mass spectrometry." The method is based on the Penning ionization which consists in the formation of ions during the interaction of molecules with excited metastable atoms [17]. Although ion generation processes, in principle, depend on the nature of the used metastable gas (helium, neon, nitrogen, argon), in general, secondary ionic reactions apparently occur when analytes desorbed from a sample surface interact with ionized molecules of air components (water vapor, ammonia, or nitrogen and oxygen). One of the advantages of DART-MS is that it usually requires no special sample preparation.

8.2.2.3 Atmospheric solid analysis probe (ASAP)

Like APCI, atmospheric solid analysis probe (ASAP) mass spectrometry, proposed in 2005, is based on the ionization of analytes via secondary ion–molecule reactions with the primary ions produced in a corona discharge (Figure 8.2) [18]. The sample or sample solution is introduced into the ion source in a tube, the end of which is placed in the ionization region and is blown with a stream of nitrogen at a temperature of 50 to 500°C. In this case, analytes are desorbed and interact with the corona-generated ions from nitrogen and water vapor present in the atmosphere. The method practically does not require the use of sample preparation procedures and relates to ambient mass spectrometry.

The first experiments showed that molecules of petroleum hydrocarbons can be ionized in this mode, with protonated molecules and $[M + N]^+$ ions being formed from aromatic and olefins respectively (in the latter cases, molecular radical ions are additionally formed [19]. It is important to pay attention to the fact that, by varying the gas temperature, the fractionation of the samples can be accomplished, thereby facilitating the interpretation of the obtained spectral data. In particular, the application of this approach to the analysis of crude oils made it possible to separate the components according to their boiling points and to detect a wide range of various compounds [20].

8.2.2.4 Other prospective desorption ionization techniques

In addition to the aforementioned techniques, other versions of ambient MS including the desorption ionization in open air have been tested in the analysis of oil. For example, so-called desorption ESI (DESI) [21] and nanospray DESI [22] can be used

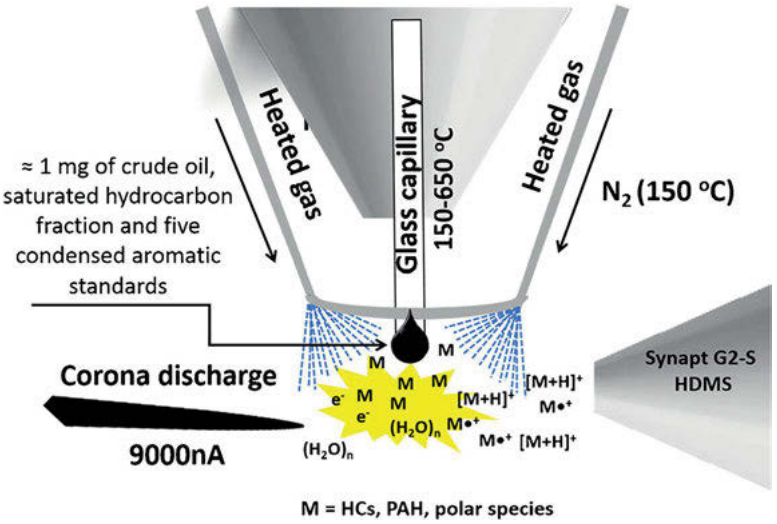

Figure 8.2: ASAP probe scheme and the ionization mechanisms via proton ($[M + H]^+$) and electron ($M^{+\bullet}$) transfers. Reprinted from [20] with permission. Copyright (2017) American Chemical Society.

to obtain mass spectra of petroleum constituents. In these cases, the flow of atomized solvent microdroplets is directed to the surface of the object under study. A significant effect is achieved by the use of solvent spraying at high pressures (ionization by ultrasonic spraying) [23]. In the other case, desorption/ionization by low-temperature plasma was found to be valuable in determining low-molecular-weight nonpolar and weakly polar petroleum components [24]. Aromatic compounds can also be detected with the use of the so-called desorption APCI (DAPCI): in this case, a nitrogen stream passing through a corona discharge area and containing ionized particles is directed to the analyte surface (Figure 8.3) [25]. The same class of compounds was detected using laser-assisted paper spray ionization [26]. The potential application of thermal desorption coupled with APPI to oil analysis was demonstrated [27]. However, despite the obvious advantages of the methods considered, there is still little research describing their application to oil analysis.

8.3 High-resolution mass spectrometry

8.3.1 MS Resolution and mass accuracy

In crude oil analysis, it is necessary to determine an accurate mass for all the compounds present in a sample. This means that a mass spectrometer should provide a high mass resolution throughout the whole recorded mass range. Usually, the mass

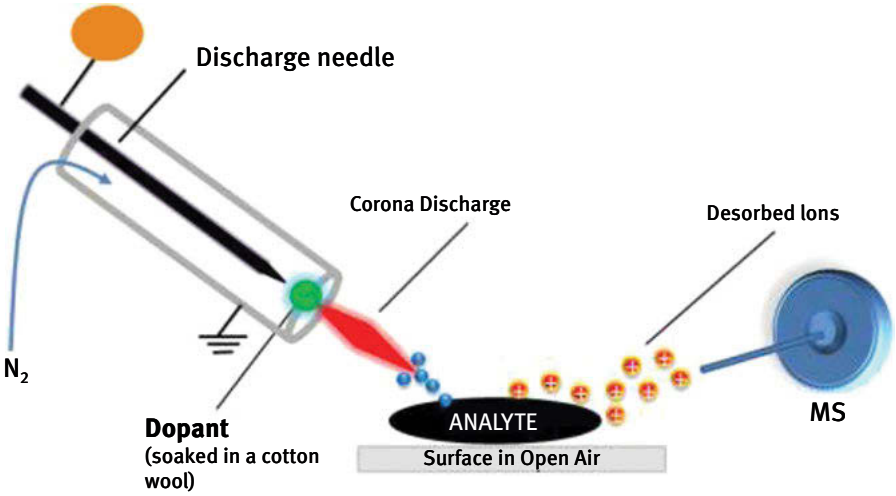

Figure 8.3: Schematic of the DAPCI ion source for analysis of petroleum-related compounds from ambient surfaces. Reprinted from [25] with permission. Copyright (2013) Elsevier.

resolving power (R) is equal to M/ΔM(50%), where ΔM(50%) is full width at half maximum (FWHM).

Mass accuracy indicates the accuracy of the m/z provided by the mass analyzer which is indicated by the difference between the theoretical m/z (m_{theor}) and the measured m/z (m_{measured}) and expressed in millimass units (mmu) or in parts per million (ppm).

8.3.2 FT-ICR-MS

The FT-ICR analyzers determine the m/z ratio according to the cyclotron frequency of an ion in a fixed magnetic field. Corresponding instruments belong to a type of ion trap but unlike a conventional ion trap, they are capable of providing the highest mass resolution of more than 10^7. The principles of FT-ICR MS instrumentation and data interpretation were described in the recent review [28].

Further development of ultrahigh-resolution mass analyzers is associated with the creation of more powerful permanent magnets for FT-ICR-MS. Recently created 21 Tesla FT-ICR mass spectrometer allowed the assignment of molecular formulas for 49,040 compounds versus 29,012 for 9.4 Tesla magnet and extends the identification of previously unresolved O_o, S_sO_o, and NO_o classes [29]. Another direction of FT-ICR-MS development deals with further improving resonance cells to enhance resolution at the same electromagnetic induction values [30].

8.3.3 FT orbitrap MS

Orbitrap mass analyzer is an orbital ion trap [31]. It includes inner and outer electrodes and the ions, generated with the aid of one or another ionization method, are injected into the space between them. Under action of static electric field, the ions orbit around the inner electrode and oscillate along the z-axis (Figure 8.4) [32]. Using Fourier transformation, the m/z values of ions are determined by measuring the frequency of their oscillation. Being rather cheap relative to FT-ICR mass spectrometers, FT-Orbitrap mass spectrometers, providing ultrahigh resolution, have become the most common instruments in analytical practice dealing with the analysis of complex mixtures, and, in particular, with the study of petroleum. Note that A. Pomerantz and co-workers [33] were the first who understood the prospects of using the FT-Orbitrap-MS for routine analysis of nonvolatile components in petroleum.

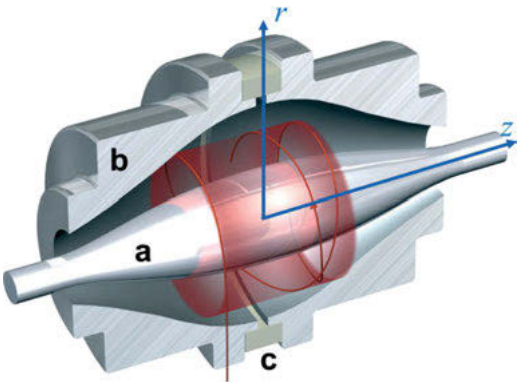

Figure 8.4: A model of the Orbitrap mass analyzer. Ions are moving in spirals around a central electrode (a), an outer electrode (b) is split in half by an insulating ceramic ring (c). Reprinted from [32] with permission. Copyright (2006) John Wiley and Sons.

The mass resolution of the Orbitrap mass spectrometers exceeds 200 000. The high-field FT-Orbitrap mass spectrometers provide the resolution above 400,000 [30]. For example, applied to petroleomics, its resolving power reaches 480,000 at m/z 400 [34]. In addition to the lower cost and the absence of a superconducting magnet, the FT-Orbitrap mass spectrometer has a number of other advantages over FT-ICR-MS.

8.3.4 Multireflection time-of-flight (TOF) mass analyzer

Ultrahigh-resolution multireflection TOF mass analyzer is based on an innovative multireflecting "zig-zag" design (Figure 8.5) [35]. Such mass spectrometers (HRT) are characterized by high speed, simplicity, nondiscriminative mass analysis, and relatively

low costs. Another advantage of HRT is that its resolution power increases with m/z, whereas for FT-ICR and FT-Orbitrap, resolution decreases exponentially with m/z [36].

Another approach allowing to increase flight pass length and, hence, the resolution power is based on a spiral ion trajectory [37]. A mass resolution higher than 55 000 was achieved using such a mass analyzer. Now this type of TOF is mostly used in conjunction with MALDI ion sources.

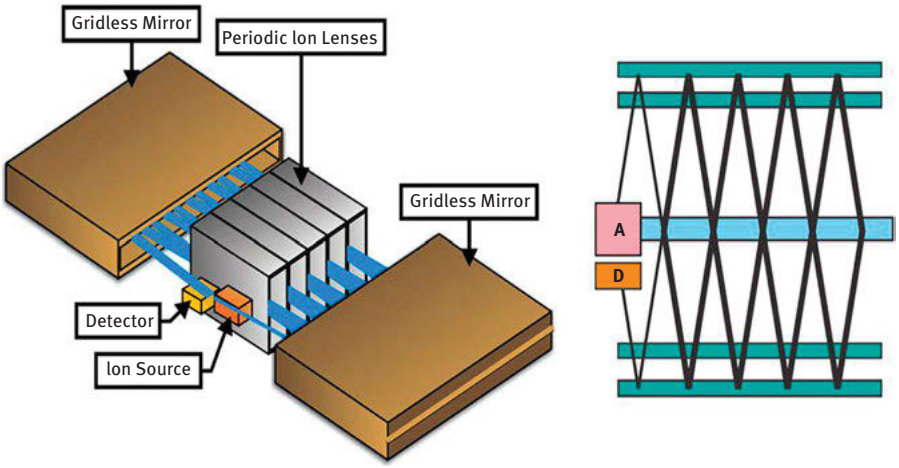

Figure 8.5: Multireflecting TOF with a folded flight path and its ultrahigh resolution mode of operation with two long full passes across the TOF analyzer for a total of 40 m flight. Reprinted from [36] with permission. Copyright (2012) American Chemical Society.

8.4 Visualization and presentation of high-resolution mass spectrometry data

High-resolution mass spectrometry and, particularly, ultrahigh-resolution FT-ICR-MS allows the determination of ion masses with extremely high accuracy which is used for the determination of their elemental composition. Applying to the study of crude oil at a molecular level, such MS methods allow recording mass spectra containing hundreds of thousands of ion peaks with exact m/z values for each oil sample reflecting its complex nature. Such mass spectra are difficult not only for visualization, but especially for interpretation. To simplify and visualize a huge array of data contained in high-resolution mass spectra of oils, processing methods giving rise to the Kendrick mass scale and the Kendrick mass defect (KMD) plots [38] as well as van Krevelen diagrams [39] have been important.

In Kendrick mass scale, the mass of the methylene fragment $^{12}CH_2$ is taken for an integer value of 14.00000 amu instead of 14.01565 amu as in the IUPAC carbon scale

(where the mass of the ^{12}C isotope is taken as 12.00000 amu). For ions recorded in a high-resolution mass spectrum, the IUPAC mass scale can be easily transformed into Kendrick mass scale according to the following equation:

$$\text{Kendrick mass} = \text{IUPAC mass} \times (14.00000 / 14.01565)$$

Thus, in the Kendrick mass scale, all hydrocarbon homologues have the same mass defect, which makes it easy to sort them into separate rows.

Kendrick mass defects (KMD) are determined by the equation:

$$\text{KMD} = \text{Nominal (Integer)Kendrick mass} - \text{Exact Kendrick mass}$$

To visualize and interpret the data of ultrahigh-resolution mass spectra, it is convenient to use plots of the dependence of the KMD values (y-axis) on the nominal Kendrick masses (x-axis). In such plots, the dots aligned in each line parallel to x-axis correspond to elemental compositions differing by $(CH_2)_n$. Relative abundance of peaks can be presented by color or size of dots which provide the third dimension of the Kendrick diagrams [40].

The proposed scale turned out to be extremely convenient for analysis of mixtures of hydrocarbons, in particular, of petroleum origin (petroleomics) by high-resolution mass spectrometry and especially FT-ICR-MS. When comparing the petroleum samples of various origin, the 3D Kendrick plots allow one to observe changes in aromaticity and carbon number. In addition, it should be noted that masses of other groups of atoms (in addition to CH_2) can be taken as integers and involved in Kendrick scale in the detection of ONS-containing petroleum components.

The van Krevelen diagram is another type of presentation of ultrahigh-resolution mass spectra of petroleum heterorganic compounds by plotting the ratio of the number of noncarbon atoms (H, N, S, and/or O) to the number of carbon atoms for each elemental composition. In the usually generated three-dimensional van Krevelen plot, the x-axis is X/carbon ratio (where X is specifically chosen heteroatoms O, N, and S), the y-axis is hydrogen/carbon ratio and z-axis presents colored dots, reflecting the relative abundance of corresponding peak. The 3D van Krevelen plots are complementary to the Kendrick diagrams readily and reflect the changes in aromaticity and carbon number for particular classes and types of compounds (Figure 8.6) [41].

An alternative approach for simultaneous visualization of two- and three-heteroatomic molecules was proposed using a 3D vector space (Figure 8.7). In this case each axis represents nitrogen, oxygen, or sulfur, whereas CH class has zero value at all axes. This approach allows characterizing the entire sample using only some plots [42].

Attention should be paid to an important feature of the analyzed molecule that predicts chemical structure and can be readily obtained from high-resolution mass spectra. It is about the double-bond equivalence (DBE) which characterizes the deficiency of hydrogen and, in other words, shows the total number of double bonds and cycles in the molecule. Knowing the elemental composition of the compound $C_cH_hN_nO_oS_s$, and taking into account the "nitrogen rule," DBE can be calculated

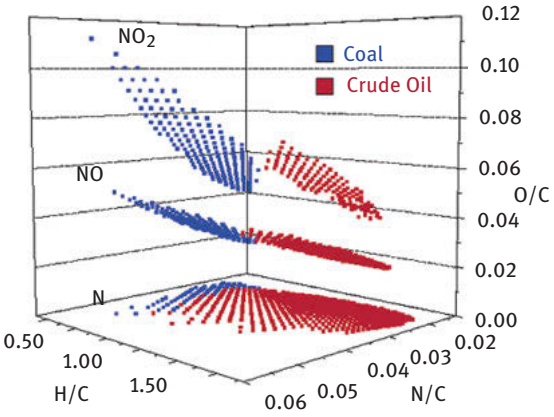

Figure 8.6: Three-dimensional van Krevelen diagram for the same classes (N, NO, NO_2) for two different fossil fuels: coal (blue) and crude oil (red). Reprinted from [41] with permission. Copyright (2012) American Chemical Society.

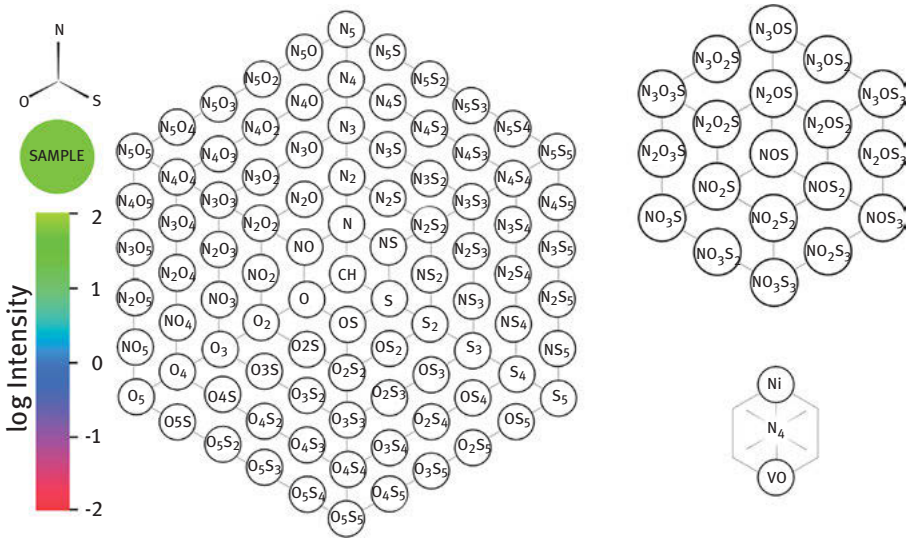

Figure 8.7: Template of hexagonal class representation: includes a hexagon based on the CH and NOS classes as well as provides framework for including metal containing species. Reprinted from [42] with permission. Copyright (2013) American Chemical Society.

using the equation $DBE = c - h/2 + n/2 + 1$. For visualization, the DBE values calculated from elemental formulae may be plotted against carbon number. Such presentation allows observing the distribution of the sets of compounds with identical heteroatom contents by degree of unsaturation [40].

An aromaticity index was proposed for evaluation of unsaturation and aromaticity of heteroatomic compounds [43]. This index can be determined using the following equation:

$$AI = \frac{1 + C - O - S - \frac{1}{2}(N + P + H)}{C - O - N - S - P}$$

When AI value exceeds 0.5 the molecules can be considered as aromatic ones, whereas in cases when AI ≥ 0.67 condensed aromatic structures can be proposed. Modified AI for highly oxygenated compounds was also developed on the basis of the assumption that a half of oxygens in such molecules are σ-bonded [43].

8.5 Particular applications of soft-ionization high-resolution mass spectrometry in the analysis of petroleum-related samples

In the previous chapter, we discussed the unique capabilities and the great potential of hyphenated GC-MS methods for studying the composition of crude oils and refined products at the molecular level. It was emphasized also that these methods are suitable for the analysis of only those oil compounds that can be transferred into a gaseous state at temperatures up to 300 °C, maximum 450 °C. However, oil contains a fairly large amount of polar, low-volatility nonpolar and high-molecular-weight compounds (e.g., resins, asphaltenes, and organometallic compounds) that cannot be analyzed by these combined methods. In addition, it should be noted that this portion of oil is characterized by a significant set of various structure types with different elemental composition and isomerism. Thus, the use of on-line chromatographic separation methods in conjunction with MS is usually much less efficient. In this situation, most of the studies focus on establishing the elemental composition of detectable compounds, which is impossible unless ultrahigh-resolution orbital ion trap (FT-Orbitrap) or Fourier-transform ion-cyclotron resonance (FT-ICR) mass analyzers are used.

The first work in this area was carried out under the guidance of A. Marshall, who, as already mentioned, proposed the term “petroleomics” [1]. Since only polar substances, mainly nitrogen-, oxygen-, and sulfur-containing (NSO) compounds, were detected with the use of FT-ICR-MS (ESI), it was believed that no more than 15% of oil components are amenable to analysis by this method [1]. However, this set includes the most important classes of heteroatomic compounds, which are possible markers for determining the geochemical parameters of oils and, most importantly, predetermine the most effective oil refining processes using catalytic methods.

This is why, this high-resolution ESI-MS versions in both positive and negative ion modes were primarily used for the analysis of large, polar, heteroatom containing

compounds in crude oils and petroleum [6, 44–47]. Only basic compounds (i.e., a small fraction of the entire chemical composition) within crude oils are ionized in ESI conditions. However, the detection of more than 11,100 resolved distinct compounds, of which >75% may be assigned to an elemental composition ($C_cH_hO_oN_nS_s$), in various crude oils in a single run was reported by A. Marshall et al. [48]. To provide the best ionization of nonpolar polyaromatic and nonbasic nitrogen-containing compounds, appropriate solvent compositions and capillary voltage were chosen in the work [45] and the suggestion was made that ESI can be expanded for the analysis of asphaltene and other polyaromatic systems. For the determination of acidic species, negative-ion ESI FT-ICR MS is very convenient. This method, providing mass resolving power ($m/\Delta m(50\%) > 400{,}000$) and high mass accuracy (better than 500 ppb), enable the assignment of an elemental composition to each peak in the spectra of Canadian bitumen and its distilled heavy vacuum gas oil. As a result, acidic species are characterized by heteroatom content in $N_nO_oS_s$ class, DBE equivalence without preliminary acid prefractionation [49]. Recent review [47] discussed new developments in mass spectrometric techniques for detailed characterization of naphthenic acid fraction (all $C_cH_hO_oN_nS_s$ compounds, including heteroatomic and aromatic components in the acid-extractable fraction).

Ultrahigh-resolution ESI mass spectrometry continues to be actively used at present to solve geochemistry problems. For example, analysis of the correlation of the composition of NSO compounds with the origin and maturity of crude oils allowed distinguishing the most informative classes of these compounds. In fact, ESI-MS in combination with chemometric processing methods showed a characteristic difference in the concentration of compounds with one heteroatom (N_1 or O_1) in Brazilian oils formed in oceanic and lacustrine depositional environments (Figure 8.8) [50]. By using FT-ICR-MS in ESI(–) mode, similar results were obtained in [51], where N_1 compounds were shown to prevail in lacustrine oils from China. In addition, it was found that amounts of homologues with a smaller number of substituents and the degree of unsaturation of compounds with N_1 and O_1 atoms increase with increasing the maturity. Oils of the same field were investigated by Ji et al. [52], who suggested new markers for determining maturity and emphasized that data obtained with the use of ESI in some cases provide a more reliable result than the geochemical analysis using GC-EIMS.

FT-ICR-MS in ESI(–) mode was also applied to the analysis of Duverney oils (Canada), which had migrated most likely over long distances [53]. It was found that the relative concentrations of compounds belonging to the N_1, N_1O_1, N_1S_1, and O_1 series vary, depend on the distance traveled, and can be considered as new migration markers. Similar investigations of oils from North Sea (Norway) showed that benzocarbazoles can act as such markers, because the changes in the distribution of the long chains of the substituents in their molecules correlate with the migration parameters [54].

Using FT-ICR-MS(ESI), the pathways of formation of organic sulfur compounds in immature oils were studied [55]. Because no special derivatization was used, only polar sulfur-containing compounds were detected. The authors suggest that their

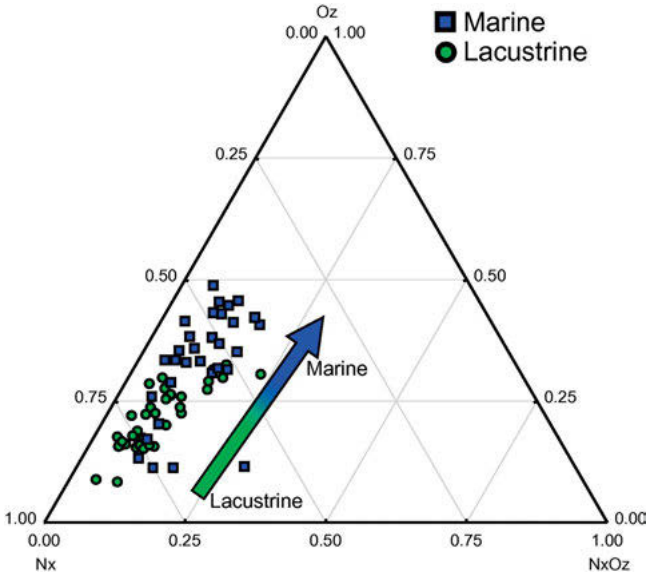

Figure 8.8: Ternary diagram for the most abundant elemental classes assigned on the negative ESI FTICR-MS results for Brazilian oils formed in oceanic and lacustrine depositional environments. Reprinted from [50] with permission. Copyright (2018) Elsevier.

formation was due to intramolecular sulfurization during early diagenesis. This is confirmed by the detection of a set of carotenoid sulfurization products and by the increases in DBEs compared to their nonsulfur counterparts.

Ultrahigh-resolution ESI-MS in various ion polarity modes is a powerful tool for studying the oil generation processes and the biodegradation transformation of crude oils and organic matter of source rocks. In particular, the studies of oils from Colombian [56] and Brazilian fields [57] made it possible to suggest new parameters for assessing the degree of their biodegradation. Negative ion ESI analysis of the products arising during pyrolysis of the organic matter from Barbalha formation rocks (Brazil) in the presence of water showed a decrease in the concentration of sulfur compounds and steranoic and hopanoic acids and an increase in the degree of unsaturation [58].

The study of petroleum refining processes is another important area of application of ESI-MS. In this regard, we note the works where FT-ICR-MS in ESI(−) mode was used to predict the acid number of straight-run petroleum fractions [59], to study the products of sulfonation of crude oil [60] and the thermocatalytic removal of naphthenic acids [61].

The low polarity and proton affinity of some hetero-organic petroleum compounds impede their ESI. One of the examples of such compounds is thiols. To increase their ionization efficiency, preliminary derivatization of sulfhydryl groups in petroleum-based molecules looks rather attractive. One of such approaches is based on the addition reaction with phenyl vinyl sulfone to give sulfides containing sulfone

group that shows much higher ionization efficiency under the positive-ion ESI conditions and ensures low limits of detection of the derivatives [62]. Another approach to the derivatization of thiols involves the introduction of fixed-charged moieties via the successive reactions with *N*-(2-aminoethyl)maleimide trifluoroacetate and tri(2,6-dimethoxyphenyl)carbenium hexafluorophosphate [63]. Corresponding derivatives are highly ionizable in ESI conditions as was demonstrated by the detection of thiols in gas condensate (Figure 8.9).

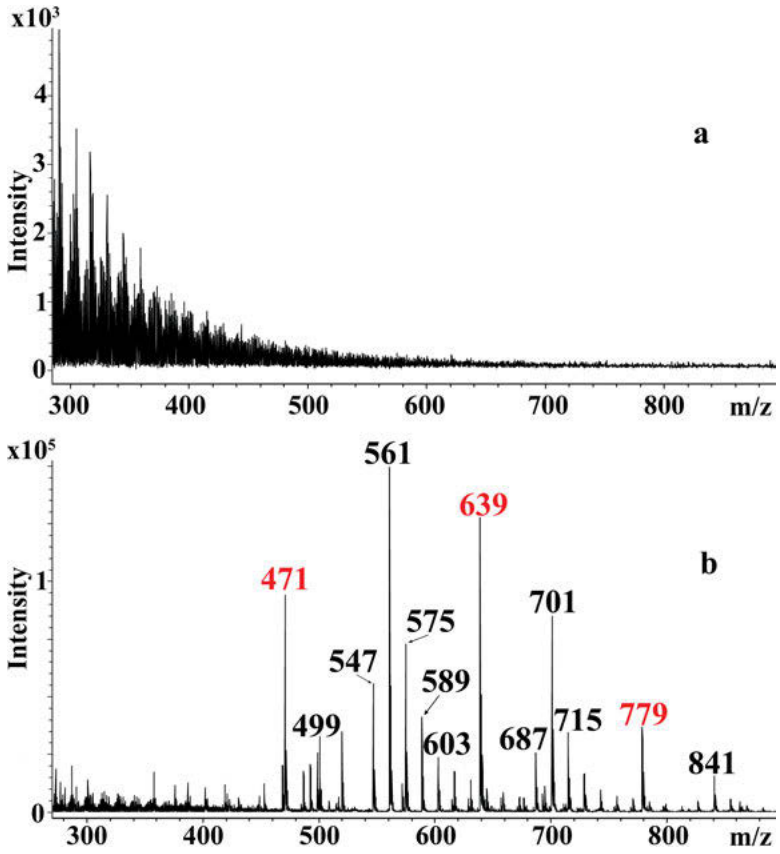

Figure 8.9: LDI mass spectra of gas condensate (a) without derivatization and (b) after derivatization with reagent, produced by reaction of *N*-(2-aminoethyl)maleimide trifluoroacetate and tri(2,6-dimethoxyphenyl)carbenium hexafluorophosphate. Reprinted from [63] with permission of the Royal Society of Chemistry.

A promising charge generation derivatization has been proposed for the analysis of linear and saturated cyclic sulfides in petroleum by the ESI-MS method [64, 65]. It involves the treatment of sulfides with various alkylating agents, giving rise quantitatively to corresponding sulfonium salts whose sulfonium cations are

easily detected by ESI-MS. The mass spectra, recorded by using collision-induced dissociation of cations, reveal a structurally informative set of product ion peaks.

Unlike aliphatic sulfides and saturated thiacyclanes, nonpolar sulfur-containing aromatics do not undergo the same easy S-alkylation. However, such polycyclic aromatic sulfur compounds (PASHs) are widely represented in oil, especially in its high boiling fractions, resins and asphaltenes where their qualitative and quantitative determination is extremely necessary. The most efficient derivatization approach to analysis of such nonpolar sulfur compounds by ESI and MALDI in conjunction with FT-ICR-MS is based on methylation in the presence of $AgBF_4$ (Scheme 8.1) [66] or $AgSbF_6$ [67]. The resulting thiophenium salts are desorbed as sulfonium cations whose mass is determined by FT-ICR-MS with very high accuracy which makes it possible to establish the elemental composition, the number of double bonds and aromatic rings in the molecules of petroleum sulfur aromatics. In fact, the same derivatization approach was further used for determination of PASHs in oil of various origins and its refined products (e.g., [68]). This approach also can be used for isolation of sulfur compounds for their further characterization [69]. Another way to increase ionization efficiencies of sulfur compounds is using strong acids as ionization promoters (Figure 8.10) [70].

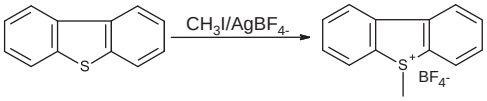

Scheme 8.1: The most efficient methylation of nonpolar polycyclic aromatic sulfur compounds for ESI(+) FT-ICR-MS.

To enhance the generation of positive ions from compounds, containing SxOy elements, chemical modification is unnecessary because the required effect can be achieved by adding a lithium salt to their solution [71]. For instance, such an approach was used to reveal the distribution of such compounds in the oils of North and South America. It should be noted that similar method can be used to detect sulfur compounds that are susceptible to Ag-cation attachment [72]. The addition of ammonium acetate to a solution of compounds under study made it possible to get ionized nonpolar aromatic compounds that hardly form ions under ESI conditions [73]. For quantitative analysis and molecular characterization of reactive and nonreactive sulfur compounds in crude oil, their separation by ligand exchange chromatography on an Ag-modified strong-cation exchange cartridge was suggested [74]. The distribution of reactive and nonreactive sulfur and their molecular characterization in separated fractions were determined by ESI FT-ICR-MS. In all these cases, ESI(+) mode was employed.

An efficient method to enumerate labile hydrogens in all constituents of molecular ensemble of crude oil is based on the use of H/D exchange performing in ESI

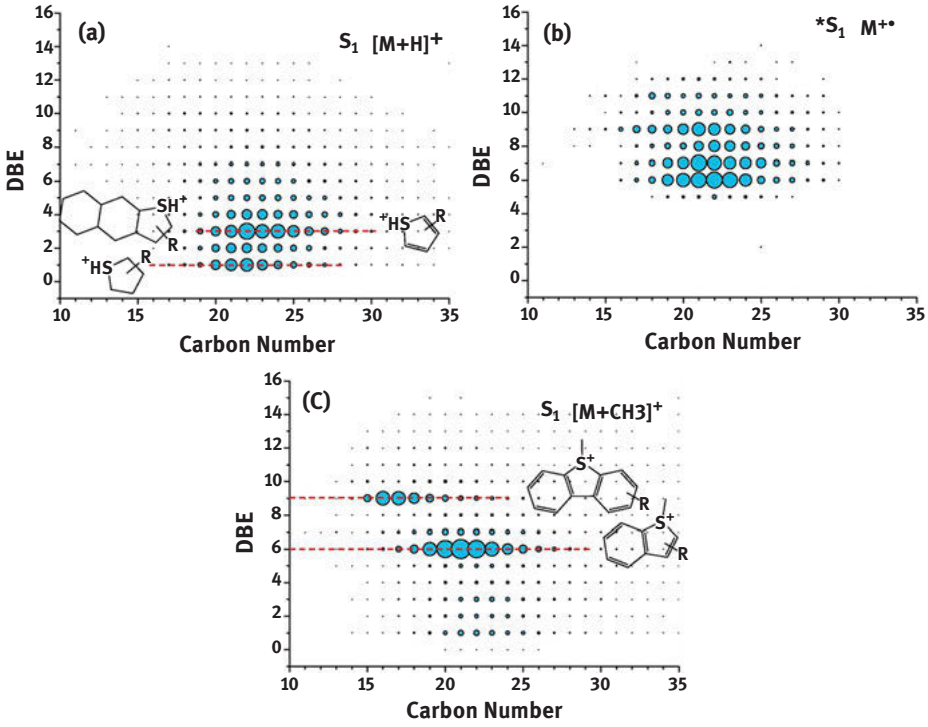

Figure 8.10: Plots of DBE as a function of carbon number for S_1 class species $[M + H]^+$ (a) and $*S_1$ class species M^+ (b) of vacuum gas oil assigned from (+) ESI FT-ICR mass spectrum with HBF_4 promoter and S_1 class species $[M + CH_3]^+$ (c) assigned from (+) ESI FT-ICR mass spectrum of methylated sulfur compounds of vacuum gas oil. Reprinted from [70] with permission. Copyright (2020) Elsevier.

FT-ICR mass spectrometer [75]. It is interesting to note that compounds of Siberian crude oil ionizing in positive-ESI(+) mode do not have labile hydrogens, while compounds ionizing in ESI(-) have one labile hydrogen.

Metalloporphyrins constitute a separate class of oil compounds, the presence of which complicates the processing of heavy oils and this necessitates the development of approaches to their analysis. Owing to low content, their direct detection within hydrocarbon mixtures by ESI-MS is difficult. To overcome the problem, preliminary isolation and concentration procedures are practiced. For example, preliminary chromatography on silica gel was used to detect vanadium and nickel porphyrins in the organic matters of Alberta oil sands (Canada) and Bohai field oil (China) using ESI(+) FT-ICR-MS (Figure 8.11) [76]. In other case, the concentration of porphyrins was achieved by solvent extraction as was accepted in a study of vanadium porphyrins in the vacuum residues of Saudi Arabian oils [77].

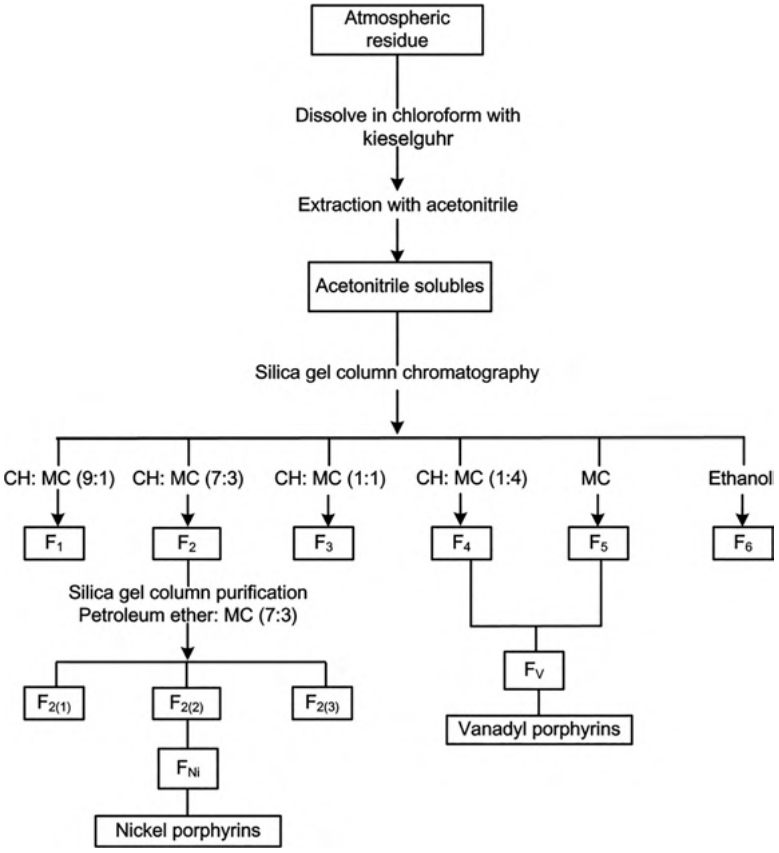

Figure 8.11: Separation scheme of petroporphyrins in feed residues. (CH refers to cyclohexane; MC refers to methylene chloride; F_1–F_6 are the corresponding subfractions eluting with certain solvents from acetontrile extract; $F_{2(1)}$, $F_{2(2)}$, and $F_{2(3)}$ are the three subfractions obtained during further chromatographic purification of F_2. The subfractions abundant with nickel porphyrins and vanadyl porphyrins are labeled as F, Ni and FV, respectively). Reprinted from [76] with permission. Copyright (2015) American Chemical Society.

Assessing limitations and possibilities of the ESI technique as well as the development of alternative and complementary approaches, one should conclude that this pioneering method of petroleomics is still widely used for studying oils. Prospects for the further development of ESI-MS are obviously associated with the improvement of ultrahigh-resolution mass analyzers [29] and the development of new approaches to data processing [78] that can expand the range of differentially detected compounds. In this regard, attention should be paid to the use of ultrahigh-resolution multireflectron TOF mass spectrometers for petroleomic analysis. For example, using various oil samples and ESI(+) mode, it was shown that such instruments with resolution of

100,000 at m/z 400 show the same accuracy of ion mass determination as FT-ICR with resolution 400,000 at m/z 400 [36].

Another "soft" ionization method, namely APCI, is also exploited in the study of oils and petroleum products, also the scope of its application is largely limited by the competitive capabilities of other mass spectrometric soft ionization techniques. Let's pay attention to a rather interesting approach based on the application of this method to a detailed study of nitrogen-containing compounds in oils [79]. In this case, the samples were dissolved in a mixture of dichloromethane and deuteromethanol which should provide an exchange of active hydrogen atoms of the test compounds for deuterium in the ion source for further enumerate labile hydrogens in all constituents of molecular ensemble. The results obtained by APCI-MS together with the subsequent investigation of the double bond equivalence distribution indicated that resins of shale oil contained mostly pyridine-type nitrogen compounds that are unable to undergo such H/D exchange, respectively

APCI-MS is an efficient tool for studying asphaltenes and metalloporphyrins as well. In particular, this technique (carbon disulfide as dopant and tandem MS) was employed to determine the molecular mass distribution of asphaltenes of various deposits [80] and asphaltenes from sediments formed during the extraction and transportation of oil from Wyoming fields (the United States) [81]. For the analysis of metalloporphyrins, APCI-MS (Orbitrap mass analyzer) was coupled with the HPLC separation and this creates the basis for quantifying these compounds in oil [82].

A very fruitful approach to analysis of various heavy oils and asphaltenes is based on their thermal desorption and pyrolysis directly in a FT-ICR mass spectrometer with APCI (Figure 8.12) [83]. The methodology is particularly helpful in the investigation of SARA fractions including maltenes, C7-asphaltenes, aromatics, saturated compounds, and resins. Thermal fractionation and pyrolysis at 300–350 °C allows increasing the number of assigned elemental compositions in the region from m/z 150 to m/z 700.

APPI and APPCI methods belong also to "soft" ionization types and are becoming increasingly popular in the analysis of complex mixtures of organic compounds and, in particular, in the study of crude oil and refined products. These techniques are readily compatible with uHRMS. Unlike ESI, where the need to increase the ionization efficiency sometimes requires the use of preliminary derivatization of analytes, the superiority of APPCI in the versatility in studying the oil components of different polarities is quite obvious [84,85]. Nevertheless, preliminary S-methylation of aromatic sulfur compounds, that was used for the analysis by ESI(+) MS, appeared to provide semiquantitative determination of such analytes [86]. At the same time, it is only with the use of nonderivatization APPCI-MS that the empirical formulas of polyaromatic sulfur compounds can be determined. In the work [87], it was shown that the analysis of APPCI(+) FY-ICR mass spectra of 30 samples of oils of various origins in combination with the principal component analysis for their processing made it

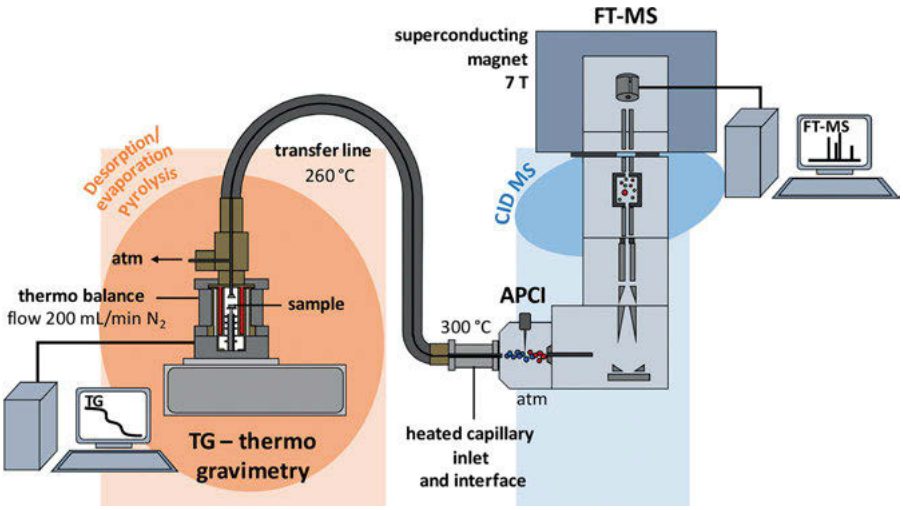

Figure 8.12: A scheme of a hyphenation of thermal analysis to APCI high-resolution mass spectrometry. Reprinted from [83] with permission. Copyright (2017) American Chemical Society.

possible not only to study the distribution of classes of sulfur compounds, but also to propose a procedure for determining the total sulfur content in objects of this kind.

Like other "soft" ionization methods, ordinary APPCI mass spectra provide rather low structural information content. However, the use of collision-activated dissociation tandem mass spectrometry helps to obtain such information [88]. For example, such technique made it possible to characterize the structure of aromatic compounds with one sulfur atom in a sample of Kuwaiti oil. In addition, partial structure information for sulfur [89] and nitrogen compounds in petroleum [90, 91] can be obtained with the aid of APPCI including H/D exchange.

APPCI-FT-ICR-MS is also used to study oil transformation processes. For example, this approach was used to detect products of sunlight-induced oil degradation [92] and shale oil hydrofining products [93].

In the direct analysis of crude oils by APPI and APPCI, suppression of signals of heavy components to be detected by easily ionized compounds can be observed. To increase their sensitivity, preliminary separation of oil samples to be analyzed is very helpful because fractional isolation of certain types of compounds can significantly reduce such "matrix" effect [94]. The addition of dopant also increases the ionization efficiency of particular compound classes. For example, oil analysis by APPCI method involved the addition of toluene as the best dopant [95]. The latter promoted the generation of both negative and positive quasi-molecular ions in addition to molecular radical ions. As a result, the registered mass spectra of the oil samples revealed peaks due to ions of both nonpolar aromatic hydrocarbons and

weakly polar sulfur-containing aromatic compounds, the detection of which with the use of ESI and APCI was difficult.

A rather efficient microprobe for the thermal analysis of crude oil with the aid of APPI(APPCI)-FT-Orbitrap-MS was suggested in [27]. It allowed a thermal desorption from droplet of crude oil placed on the heating element and ionization of vapors by a vacuum UV lamp (Figure 8.13). Experiments performed at different pressure showed that at high pressure protonated CHN compounds dominate in the spectrum, while at the low-pressure CH compounds dominate.

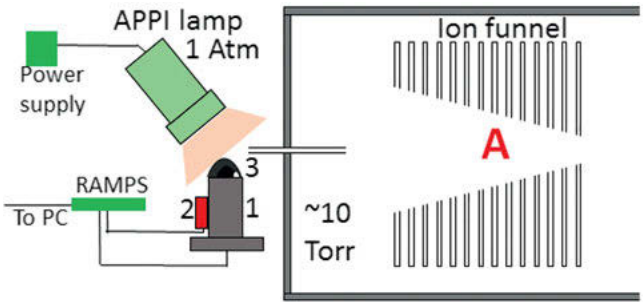

Figure 8.13: Experimental setup for performing thermal analysis of crude oil coupled to APPI FTMS. Reprinted from [27] with permission. Copyright (2018) American Chemical Society.

Having highly aromatic structure, asphaltene molecules can be easily analyzed by APPCI-MS. For example, the method was used in the work [96] to characterize asphaltene extracts from the vacuum residue of Brazilian oil. Additional use of elemental analysis and NMR data allows a comparison of the degrees of aromaticity and distributions of heteroatoms in asphaltenes of various heavy oils [97].

The application of APPCI-MS to the study of the structure of asphaltene molecules is especially important. For this purpose, it turned out to be convenient to use the tandem MS **v**ersion, which includes the activation and decomposition of primary ions by infrared photons followed by the observation of product ions which are due to the "island" and "archipelago" models [98–100]. The results of these works allowed the conclusion to be made that the "island"-type molecules generally prevail. However, the results, obtained using collision activation, suggested that heavier polynuclear entities included in "island" molecules have lower ionization efficiency under APPCI conditions, which may explain the excess of such type molecules over the "archipelagos" [101]. As was shown in [102], high-energy collision activation (FT-Orbitrap) can hardly be used for determining the absolute ratio of the "island" and "archipelago" structures owing to the difference in their ionization efficiencies; however, the approach is suitable for a comparative analysis of various samples.

Having aromatic properties, metalloporphyrins can be easily determined by APPI. This method is advantageous because allows almost direct analysis without using

complicated isolation and concentration procedures, as has been shown for a number of vanadium and nickel-containing compounds [103].

APPI coupled to FTICR MS was used for the study a group of fourteen samples of crude oil coming from different fields around the world [104]. To interpret the complex mass spectra, statistical methods (Principal Component Analysis and hierarchical clustering) were applied which allowed grouping the oils according to the well where they have been extracted and from their geographical origin.

It should be emphasized once again the important advantage of the APPI and APPCI, which lies in the possibility of direct detection of nonpolar and weakly polar, especially sulfur-containing, aromatic petroleum compounds. This predetermines their further developments associated with the appearance of more powerful high-resolution mass analyzers [77, 105] and the elaboration of sensitivity-enhancing methods for recording mass spectra [106].

Moving on to mass spectrometric methods, based on desorption/ionization, we will focus primarily on MALDI and its LDI and SALDI versions. In general, it should be noted that these MS methods has a rather limited potential for oil analysis and for use in petroleomics, which is due to the peculiarities of ion generation. Nevertheless, their use for targeted analysis of some classes of compounds (naphthenic acids, porphyrins, and asphaltenes) has great prospects. It should also be noted that MALDI-MS is practically unsuitable for the analysis of nonpolar compounds (such as various hydrocarbons), which are the main components of oil.

As noted above, MALDI method involves the use of special organic matrices (most often aromatic acids), which provide energy transfer to analyte molecules, as well as proton transfer to or from the analyte under the action of laser radiation. A striking example of MALDI application is the detection of naphthenic acids isolated by solid-phase extraction from high-boiling oil fractions using the highly basic matrix compounds 9-aminoacridine and 1,8-di(dimethylamino)naphthalene [107]. These compounds accomplish the deprotonation of analyte molecules by removing a proton from the carboxyl groups giving rise to negative ions $[M\text{-}H]^-$ with high probability. As a result, a very selective and highly sensitive detection of acid can be achieved even without special fractionation. Due to the use of ultrahigh resolution of FT-ICR mass spectrometer, much greater number of acid components was detected [108]. It is interesting to note that the MALDI mode allowed the detection of 22 classes of compounds whereas ESI(-)-MS analysis gave only six classes for the same sample, with the data acquisition rate being much higher in the case of MALDI.

Asphaltenes are another class of important petroleum compounds that can be investigated using MALDI and LDI mass spectrometry because they are easily ionized under these conditions. Pioneering studies in this realm made it possible to record mass spectra containing ion peaks, presumably due to asphaltenes and even fullerenes [109]. To explain the distribution of peak abundances of ions, observed in the MALDI mass spectra, recorded using various matrices, as well as in the LDI spectra

[110], it was suggested that there were new, previously unknown, types of organic matter [111] or the ionization of noncovalently bound asphaltene aggregates [112].

Further studies made it possible to formulate a well-substantiated hypothesis about the formation of associates of condensed aromatic systems and fullerenes directly during ionization [113]. One of the arguments in favor of this hypothesis was based on the results of using the so-called L^2MS method for analysis of asphaltenes. It is assumed that unlike the case of other LDI techniques, the ionization of asphaltenes occurs not on the target surface and/or in the plume, but by the single photon ionization mechanism after their flying off in a vacuum [114, 115]. These data and the results of SALDI led to the conclusion that monomeric, not aggregated, asphaltene molecules were mostly observed in the case of L^2MS and products with various aggregation numbers were observed in the case of SALDI [116, 117].

Other desorption/ionization method, namely LIAD, was used in combination with APCI and EI (in its vacuum version). In this case, it was possible to record the mass spectra of asphaltenes that revealed no ion peaks responsible for aggregates or condensation products [118]. In the other work [119], LIAD coupled to single photon ionization with variable photon energy made it possible to detect various classes of hydrocarbons.

As has been already mentioned, it is difficult to detect metal porphyrins, because of their low content. However, (matrix-assisted) LDI mass spectrometry is a rather promising method for its analysis owing to the greater ionization efficiency under LDI conditions compared to, e.g., APPI [120]. Usually, such compounds are preliminarily isolated by various solvent extractions and chromatographic purification [121]. As conventional acidic matrices can form adducts with porphyrins, they are inappropriate for MALDI-MS analysis [122] At the same time, dithranol appeared to be suitable [123, 124]. The use of matrices that facilitate the generation of radical ions by electron transfer is equally promising. For example, application of a specially synthesized electron transfer matrix compound – α-cyanophenylenevinylene allowed registering intense peaks of metal porphyrin ions using rather simple sample preparation [125].

It should be noted that derivatization approaches can be used to increase the efficiency of desorption/ionization under (MA) or (SA)LDI conditions. For example, the methods of introducing and generating a fixed charge in thiols and other sulfur compounds developed for ESI analysis were also applied to these desorption/ionization methods [62–64].

Research is gradually expanding to clarify the possibilities of ambient mass spectrometry versions for oil analysis. One of the most common of them, namely DART, which also includes the principle of desorption and ionization, was shown to be efficient in combination with an FT-ICR mass analyzer in the study of deasphalted oils [126]. In this case, the composition of positive ion mass spectra was close to those registered with the use of APPCI. At the same time, negative ion DART spectra made it possible to detect naphthenic acids in residues formed in oil refining processes.

Quite curious are the results demonstrating the fact that the efficiency of ion formation from organic molecules depends on the type of substrate applied to insert the analyte into the ion formation region, the best results being obtained with the use of paper. Most likely, this effect is due to the interaction of polar components with hydroxyl groups of cellulose [127]. In addition, the ion yield was shown to depend on gas temperature (the best results were obtained at 400 °C) but not on its nature (helium or nitrogen). Very interesting results were obtained concerning the analysis of paraffinic hydrocarbons, whose molecules should not be ionized under DART conditions. However, the recorded mass spectra revealed ion peaks corresponding to the products of paraffin oxidation, which apparently occurred as a result of the interaction of paraffin molecules with oxygen-containing radicals in the DART plasma.

To characterize crude oil and its fractions, rather interesting application of DART ionization coupled to FT-ICR-MS (negative- and positive-ion detection) was developed [128]. In this case, crude oil samples dissolved in toluene were directly infused into a spray needle. As a result, a continuous and long-time stable ion current for FT-ICR MS analysis was maintained and the spectra were characterized by a broad dynamic range and high signal-to-noise ratio. Compared with ESI(-), the described DART(-) method demonstrated high selectivity on naphthenic acids and may be suitable for their characterization in petroleum with a low total acid number.

It should also be noted that ionization processes in the DART plasma are similar to those occurring in the APPCI system and, therefore, introduction of dopants into the ionization region increases the probability of similar secondary ion–molecule reactions in the gas phase. In fact, the mass spectra of aromatic compounds of diesel fuel can be recorded using argon as a gas and a toluene/anisole mixture as a dopant, and this opens up new possibilities for using DART-MS in oil analysis (Figure 8.14) [129].

8.6 Complementary methods for comprehensive characterization of crude oils and petroleum products

As noted earlier, due to the specificity and limitations of various ionization methods and to a huge variety of petroleum components that differ in molecular weight, chemical and physicochemical properties, there are currently no universal mass spectrometric method that alone would provide a comprehensive characterization of such a complex object as oil. In order to get a more knowledge about the chemical characteristics of petroleum and crude oils, the samples can be analyzed using two-three different “soft” ionization mass spectrometry methods. For example, only combined application of ESI and APPI coupled to FT-ICR-MS allowed the identification of about 30,000 chemical components in shale oils [130].

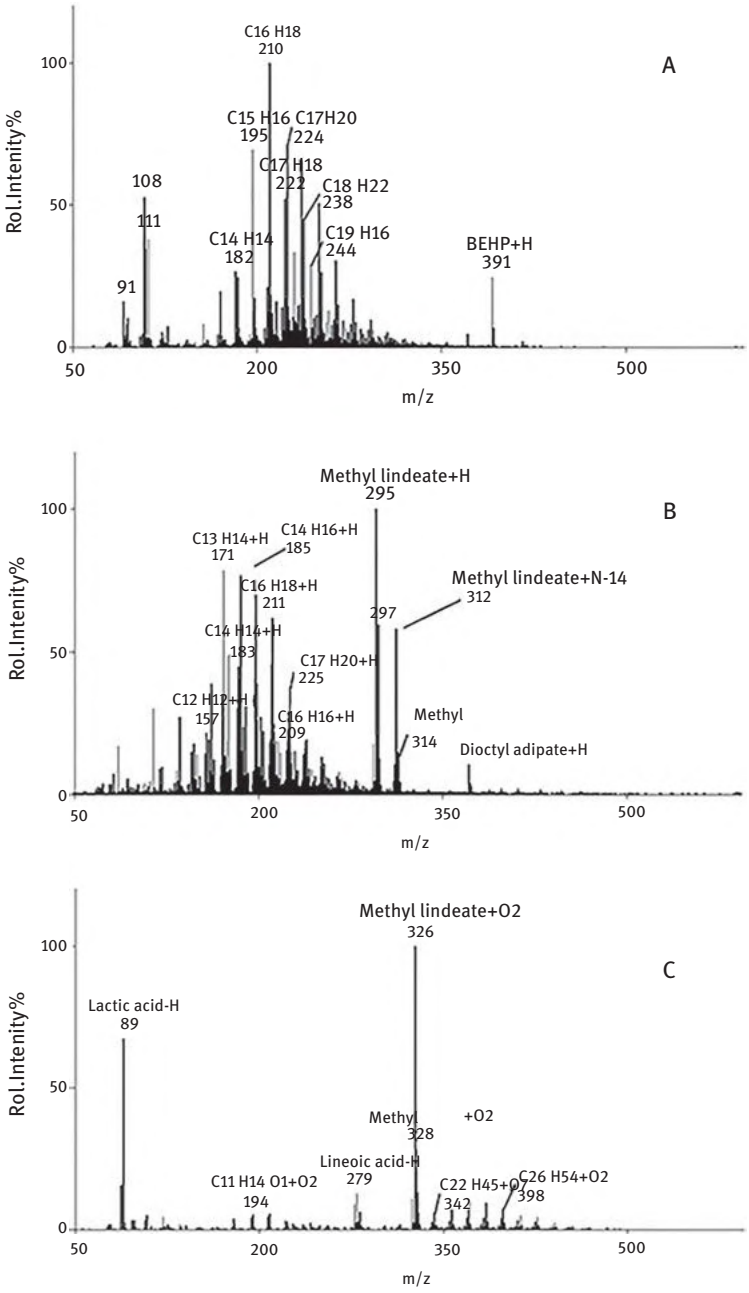

Figure 8.14: Diesel fuel analyzed by (A) argon DART with the toluene/anisole dopant, (B) conventional helium DART, and (C) O_2^--attachment chemical ionization. Reprinted from [129] with permission. Copyright (2016) John Wiley and Sons.

It is quite clear that differences in the mechanisms of ion formation between ESI, APCI, and APPI can provide the detection of interfering, but not completely overlapping sets of organic compounds, with the selectivity for many of them being altered by "matrix" effects [131]. Therefore, the comprehensive characterization of soluble polar and low-volatile nonpolar petroleum compounds requires the use of various combinations of these techniques. For example, the parallel use of these three ionization methods in FT-Orbitrap mass spectrometer allowed a detailed characterization of the saturate fractions (SARA) of different crude oils to be made [132]. The observed results show the high affinity of some specific compounds toward different ionization techniques and the presence of different heteroatom containing classes (i.e., presence of thiophenes, mercaptans, and cyclic sulfides in case of S-containing compounds). In other case, the combination of ESI and APPI with opposite polarities in FT-Orbitrap mass spectrometers resulted in the development of a procedure for the semiquantitative determination of acid compounds in oils [133]. The same methods were proposed for analysis of the degradation products of oils spilled to the environment [134] and the asphaltene oxidation products [135].

To characterize an oak pyrolysis bio-oil, three ionization techniques (ESI, LDI and APPI) in FT-ICR MS was used in parallel [136]. About 4,500 compounds have been attributed CxHyOz compositions. The dependence of DBE on the ion sources used was investigated.

In other cases, oils under study are preliminary separated and the fractions are analyzed in parallel by using GC-MS (GCxGC-MS) techniques (volatile compounds) and at least of two complementary uHRMS method based on "soft" ionization and ion mobility spectrometry (polar, nonpolar semivolatile, and nonvolatile compounds). Obviously, such an investigation gives rise to a huge array of data even for one sample and this requires the development of a special methodology for interpreting the results of the aggregate set of mass spectrometric techniques and separation methods.

Approaches to a fairly detailed description of the composition of oils, their fractions and petroleum products on the experimental basis of GC separation and several mass spectrometric techniques have been developed in a number of works. For example, for the multifaceted characterization of petroleum compounds their preliminary separation into fractions containing certain classes of compounds (saturate hydrocarbons, aromatic hydrocarbons, basic compounds, naphthenic acids and other oxygen containing species, carbazoles, sulfones, and thiophenes), followed by analysis of these fractions by GCxGC-EIMS and uHRMS (Q Exactive Focus Orbitrap LC-MS/MS) operating in ESI(+) or ESI(−) modes (depending on polarity) was utilized [137]. Similar integrated approach including GCxGC-MS(EI) and FT-ICR-ESI(−)MS was used to perform a systematical study of 25 Brazilian oils [138]. As a result, the former method made it possible the identification and semiquantification of various normal and branched alkanes, alkyl-monocyclic alkanes, alkyl-bicyclic alkanes, saturated polycyclic, alkylbenzenes, alkylnaphthalenes, alkylphenanthrenes, alkylchrysene, alkylindanes, alkyl-tetrahydronaphthalenes, pyrenes, fluorenes, whereas the latter method

allowed the detection of various ONS polar and nonvolatile components. For the characterization of resin fractions from vacuum gas oils, complementary methods of high-temperature GCxGC-MS and uHRMS (FT-ICR) operating in positive ESI and APPI modes were efficiently employed [139]. This combination allowed performing a fully comprehensive identification of hydrocarbons, mono-sulfur and mono-nitrogenated polyaromatic compounds. In other case, using GC-EIMS method together with FT-ICR MS operating in both ESI(+) and ESI(−) modes, the transformations of organic sulfur compounds during the biodegradation of crude oils were investigated [140].

It should be noted that GC-MS (GCxGC-MS) and uHRMS can be used in parallel to obtain complementary information on the composition of petroleum-related products. For example, owing to high GC resolution and high dynamic range of m/z of FT-ICR-ESI(−)MS differential identification of polar, volatile and nonvolatile compounds in bio-fuels was achieved [141].

Concluding this section, let us pay attention to the possibilities of the parallel use of uHRMS and MS on the basis of ion mobility spectrometry (IMS-MS) for oil analysis. The IMS method is based on the separation of ions of different spatial structures as a result of difference in velocity of their movement in a gas-filled space. The ions generated from analytes by ionization method are injected into the drift space, where they move under the influence of an electric field. The choice of an ion source for research by IMS-MS is very critical. In this regard, it is worth mentioning the work [142] where four atmospheric pressure ionization methods (ASAP, ESI, APCI, and APPI) were compared. Mass spectrometry of oils showed that the ASAP-MS data are close to those obtained in the APPI mode, although the ASAP ionization mechanism is believed to be closer to that of APCI. On the other hand, APCI, APPI, and ASAP yielded valuable information concerning thiophenic species.

Since the ions experience the resistance of the gas molecules present in the drift region, they are separated depending on the spatial structure. A great advantage of IMS is the ability to separate compounds having the same empirical formula but different structures, and the IMS method has quickly gained popularity. One of its versions, so-called traveling wave ion mobility spectrometry (TW-IMS), looks particularly efficient to resolve and identify a large set of compounds of various classes in the study of oils [143]. For example, the use of TW-IMS and FT-ICR-MS (both in negative ions ESI modes) made it possible to identify two sets of isomeric compounds of the O_2 class in oils and to tentatively classify them with cholanic and phenyl substituted fatty carboxylic acids [144]. In the other work [145], theoretical calculation of the collisional cross sections of isomeric molecule allowed the suggestion of the structure of TW-IMS separated isomers of both unsubstituted aromatic compounds present in oils and aromatics bearing short alkyl substituents. In the recent work [146], high-field asymmetric waveform ion mobility spectrometry (FAIMS) was coupled to a FT-Orbitrap mass spectrometer with a heated ESI source for the analysis of crude oil and respective saturate, aromatic, and resin fractions. Four classes of compounds N_1, N_1S_1, O_1S_1, and O_2S_1 were investigated. In addition, it was noted that preliminary fractionation of oil samples

enabled a higher number of molecular features to be observed in comparison to whole oil for compounds N_1, O_1S_1, and O_2S_1.

It should be noted that the use of various IMS modes significantly increases the analytical capabilities of soft ionization methods. In our opinion, further enhancing the resolving power of IMS cells and developing computational methods for predicting the behavior of molecules in the drift region will ensure a wide use of this approach.

8.7 Conclusions

In this chapter, using a large number of examples, we tried to present the huge opportunities, as well as the significant disadvantages, manifested when using the most modern mass spectrometric methods in the analysis of various petroleum-related objects, such as crude oils, their composites and transformation products. The main attention was paid to "soft"-ionization methods and mostly powerful ultrahigh-resolution mass spectrometry. It was constantly emphasized that today there is no single universal mass spectrometric method that would provide a complete analysis of all components of crude oil. At the same time, the parallel application of complementary ionization methods makes it possible to make comprehensive analysis with the detection, profiling and, if possible, quantification of oil ingredients that differ greatly on the structures, physical and chemical properties. Some important advances in the application of uHRMS combined with soft-ionization methods in petroleum analysis are discussed in recent papers [147–150].

Further development of the MS methods is aimed at reducing the limits of detection of various compounds and increasing the structural and analytical information content of the obtained mass spectral data. Of importance is the development of automated chemometrics, data predictive, and data visualization tools to gain the mass spectral information regarding the chemical compositions and origins of petroleum samples. All this, however, does not exclude the need in some cases to carry out preliminary fractionation of oil samples or products from them. Taking into account the power of uHRMS, further development of comparatively cheap instruments is highly desirable because the need for such devices is observed not only in scientific research but also in petroleum industry.

References

[1] Marshall AG, Rodgers RP. Petroleomics: The next grand challenge for chemical analysis. Acc Chem Res, 2004, 37, 53–59.

[2] Dole M, Mack LL, Hines RL, Mobley RC, Ferguson LD, Alice MB. Molecular beams of macroions. J Chem Phys, 1968, 49, 2240–2249.

[3] Aleksandrov ML, Gall' LN, Krasnov NV, Nikolaev VI, Pavlenko VV, Shurov VA. Extraction of ions from solutions at atmospheric pressure – a new method of mass spectrometric analysis. Dokl Akad Nauk SSSR, 1984, 277, 379–383. (in Russian).
[4] Yamashita M, Fenn JB. Electrospray ion source – Another variation of the free-jet theme. J Phys Chem, 1984, 88, 4451–4459.
[5] Zhan D, Fenn JB. Electrospray mass spectrometry of fossil fuels. Int J Mass Spectrom, 2000, 194, 197–208.
[6] Roussis SG, Fedora JW. Quantitative determination of polar and ionic compounds in petroleum fractions by atmospheric pressure chemical ionization and electrospray ionization mass spectrometry. Rapid Commun Mass Spectrom, 2002, 16, 1295–1303.
[7] Kim YH, Kim S. Improved abundance sensitivity of molecular ions in positive-ion APCI MS analysis of petroleum in toluene. J Am Soc Mass Spectrom, 2010, 21, 386–392.
[8] Owen BC, Gao J, Borton DJ, Amundson LM, Archibold EF, Tan X, Azyat K, Tykwinski R, Gray M, Kenttämaa HI. Carbon disulfide reagent allows the characterization of nonpolar analytes by atmospheric pressure chemical ionization mass spectrometry. Rapid Commun Mass Spectrom, 2011, 25, 1924–1928.
[9] Hurt MR, Borton DJ, Choi HJ, Kenttamaa HI. Comparison of the structures of molecules in coal and petroleum asphaltenes by using mass spectrometry. Energy Fuels, 2013, 27, 3653–3658.
[10] Tose LV, Cardoso FMR, Fleming FP, Vicente MA, Silva SRC, Aquije GMFV, Vaz BG, Romão W. Analyzes of hydrocarbons by atmosphere pressure chemical ionization FT-ICR mass spectrometry using isooctane as ionizing reagent. Fuel, 2015, 153, 346–354.
[11] Souza LM, Tose LV, Cardoso FMR, Fleming FP, Pinto FE, Kuster RM, Filgueiras PR, Vaz BG, Romão W. Evaluating the effect of ion source gas (N2, He, and synthetic air) on the ionization of hydrocarbon, condensed aromatic standards, and paraffin fractions by APCI(+)FT-ICR MS. Fuel, 2018, 225, 632–645.
[12] Jin C, Viidanoja J, Li M, Zhang Y, Ikonen E, Root A, Romanczyk M, Manheim J, Dziekonski E, Kenttämaa HI. Comparison of atmospheric pressure chemical ionization and field ionization mass spectrometry for the analysis of large saturated hydrocarbons. Anal Chem, 2016, 88, 10592–10598.
[13] Vastola FJ, Mumma RO, Pirone AJ. Analysis of organic salts by laser ionization. Org Mass Spectrom, 1970, 3, 101–104.
[14] Balasanmugam K, Viswanadham SK, Hercules DM. Characterization of polycyclic aromatic hydrocarbons by laser mass spectrometry. Anal Chem, 1986, 58, 1102–1108.
[15] Cho Y, Witt M, Kim YH, Kim S. Characterization of crude oils at the molecular level by use of laser desorption ionization fourier-transform ion cyclotron resonance mass spectrometry. Anal Chem, 2012, 84, 8587–8594.
[16] Karas M, Bachmann D, Hillenkamp F. Influence of the wavelength in high-irradiance ultraviolet laser desorption mass spectrometry of organic molecules. Anal Chem, 1985, 57, 2935–2939.
[17] Cody RB, Laramee JA, Durst HD. Versatile new ion source for the analysis of materials in open air under ambient conditions. Anal Chem, 2005, 77, 2297–2302.
[18] McEwen CN, McKay RG, Larsen BS. Analysis of solids, liquids, and biological tissues using solids probe introduction at atmospheric pressure on commercial LC/MS instruments. Anal Chem, 2005, 77, 7826–7831.
[19] Wu C, Qian K, Walters CC, Mennito A. Application of atmospheric pressure ionization techniques and tandem mass spectrometry for the characterization of petroleum components. Int J Mass Spectrom, 2015, 377, 728–735.

[20] Tose LV, Murgu M, Vaz BG, Romão W. Application of atmospheric solids analysis probe mass spectrometry (ASAP-MS) in petroleomics: Analysis of condensed aromatics standards, crude oil, and paraffinic fraction. J Am Soc Mass Spectrom, 2017, 28, 2401–2407.
[21] Wu C, Qian K, Nefliu M, Cooks RG. Ambient analysis of saturated hydrocarbons using discharge-induced oxidation in desorption electrospray ionization. J Am Soc Mass Spectrom, 2010, 21, 261–267.
[22] Eckert PA, Roach PJ, Laskin A, Laskin J. Chemical characterization of crude petroleum using nanospray desorption electrospray ionization coupled with high-resolution mass spectrometry. Anal Chem, 2012, 84, 1517–1525.
[23] Corilo YE, Vaz BG, Simas RC, Lopes Nascimento HD, Klitzke CF, Pereira RCL, Bastos WL, Santos Neto EV, Rodgers RP, Eberlin MN. Petroleomics by EASI(+/-) FT-ICR MS. Anal Chem, 2010, 82, 3990–3996.
[24] Benassi M, Berisha A, Romão W, Babayev E, Römpp A, Spengler B. Petroleum crude oil analysis using low-temperature plasma mass spectrometry. Rapid Commun Mass Spectrom, 2013, 27, 825–834.
[25] Jjunju FPM, Badu-Tawiah AK, Li A, Soparawalla S, Roqan IS, Cooks RG. Hydrocarbon analysis using desorption atmospheric pressure chemical ionization. Int J Mass Spectrom, 2013, 345–347, 80–88.
[26] Basuri P, Sarkar D, Paramasivam G, Pradeep T. Detection of hydrocarbons by laser assisted paper spray ionization mass spectrometry (LAPSI MS). Anal Chem, 2018, 90, 4663–4668.
[27] Kostyukevich Y, Zherebker A, Vlaskin MS, Borisova L, Nikolaev E. Microprobe for the thermal analysis of crude oil coupled to photoionization fourier transform mass spectrometry. Anal Chem, 2018, 90, 8756–8763.
[28] Cho Y, Ahmed A, Islam A, Kim S. Developments in FT-ICR MS instrumentation, ionization techniques, and data interpretation methods for petroleomics. Mass Spectrom Rev, 2015, 34, 248–263.
[29] Smith DF, Podgorski DC, Rodgers RP, Blakney GT, Hendrickson CL. 21 Tesla FT-ICR mass spectrometer for ultrahigh-resolution analysis of complex organic mixtures. Anal Chem, 2018, 90, 2041–2047.
[30] Zhdanova E, Kostyukevich Y, Nikolaev. E static harmonization of dynamically harmonized fourier transform ion cyclotron resonance cell. Eur J Mass Spectrom, 2017, 23, 197–201.
[31] Makarov A. Electrostatic axially harmonic orbital trapping: A high-performance technique of mass analysis. Anal Chem, 2000, 72, 1156–1162.
[32] Scigelova M, Makarov A. Orbitrap mass analyzer – Overview and applications in proteomics. Proteomics, 2006, 6, 16–21.
[33] Pomerantz AE, Mullins OC, Paul G, Ruzicka J, Sanders M. Orbitrap mass spectrometry: A proposal for routine analysis of nonvolatile components of petroleum. Energy Fuel, 2011, 25, 3077–3082.
[34] Zhurov KO, Kozhinov AN, Tsybin YO. Evaluation of high-field orbitrap fourier transform mass spectrometer for petroleomics. Energy Fuel, 2013, 27, 2974–2983.
[35] Verentchikov AN, Yavor MI, Hasin YI, Gavrik MA. Multireflection planar time-of-flight mass analyzer. I: An analyzer for a parallel tandem spectrometer. Tech Phys, 2005, 50, 73–81.
[36] Klitzke CF, Corilo YE, Siek K, Binkley J, Patrick J, Eberlin MN. Petroleomics by ultrahigh-resolution time-of-flight mass spectrometry. Energy Fuels, 2012, 26, 5787–5794.
[37] Satoh T, Tsuno H, Iwanaga M, Kammei Y. A new spiral time-of-flight mass spectrometer for high mass analysis. J Mass Spectrom Soc Jpn, 2006, 54, 11–17.
[38] Kendrick E. A mass scale based on CH_2 = 14.0000 for high resolution mass spectrometry of organic compounds. Anal Chem, 1963, 35, 2146–2154.

[39] van Krevelen DW. Graphical-statistical method for the study of structure and reaction processes of coal. Fuel, 1950, 29, 269–284.
[40] Islam A, Cho Y, Ahmed A, Kim S. Data interpretation methods for petroleomics. Mass Spectrom Lett, 2012, 3, 63–67.
[41] Wu Z, Rodgers RP, Marshall AG. Two- and three-dimensional van Krevelen diagrams: A graphical analysis complementary to the Kendrick mass plot for sorting elemental compositions of complex organic mixtures based on ultrahigh-resolution broadband fourier transform ion cyclotron resonance mass neasurements. Anal Chem, 2004, 2004(76), 2511–2516.
[42] Zhurov KO, Kozhinov AN, Tsybin YO. Hexagonal class representation for fingerprinting and facile comparison of petroleomic samples. Anal Chem, 2013, 85, 5311–5315.
[43] Koch BP, Dittmar T. From mass to structure: An aromaticity index for high-resolution mass data of natural organic matter. Rapid Commun Mass Spectrom, 2006, 20, 926–932.
[44] Hughey CA, Rodgers RP, Marshall AG, Qian K, Robbins WK. Identification of acidic NSO compounds in crude oils of different geochemical origins by negative ion electrospray fourier transform ion cyclotron resonance mass spectrometry. Org Geochem, 2002, 33, 743–759.
[45] Guricza LM, Schrader W. Electrospray ionization for determination of non-polar polyaromatic hydrocarbons and polyaromatic heterocycles in heavy crude oil asphaltenes. J Mass Spectrom, 2015, 50, 549–557.
[46] Schäfer M, Drayß M, Springer A, Zacharias P, Meerholz K. Radical cations in electrospray mass spectrometry: Formation of open-shell species, examination of the fragmentation behaviour in ESI-MSn and reaction mechanism studies by detection of transient radical cations. Eur J Org Chem, 2007, 2007, 5162–5174.
[47] Headley JV, Peru KM, Barrow MP. Advances in mass spectrometric characterization of naphthenic acids fraction compounds in oil sands environmental samples and crude oil – A review. Mass Spectrom Rev, 2016, 35, 311–328.
[48] Hughey CA, Rodgers RP, Marshall AG. Resolution of 11 000 compositionally distinct components in a single electrospray ionization fourier transform ion cyclotron resonance mass spectrum of crude oil. Anal Chem, 2002, 74, 4145–4149.
[49] Smith DF, Schaub TM, Kim S, Rodgers RP, Rahimi P, Teclemariam A, Marshall AG. Characterization of acidic species in Athabasca bitumen and bitumen heavy vacuum gas oil by negative-ion ESI FT-ICR MS with and without acid-ion exchange resin prefractionation. Energy Fuels, 2008, 22, 2372–2378.
[50] Rocha YS, Pereira RCL, Filho JGM. Geochemical characterization of lacustrine and marine oils from off-shore Brazilian sedimentary basins using negative-ion electrospray Fourier transform ion cyclotron resonance mass spectrometry (ESI FTICR-MS). Org Geochem, 2018, 124, 29–45.
[51] Wan Z, Li S, Pang X, Dong Y, Wang Z, Chen X, Meng X, Shi Q. Characteristics and geochemical significance of heteroatom compounds in terrestrial oils by negative-ion electrospray fourier transform ion cyclotron resonance mass spectrometry. Org Geochem, 2017, 111, 34–55.
[52] Ji H, Li S, Greenwood P, Zhang H, Pang X, Xu T, He N, Shi Q. Geochemical characteristics and significance of heteroatom compounds in lacustrine oils of the Dongpu Depression (Bohai Bay Basin, China) by negative-ion fourier transform ion cyclotron resonance mass spectrometry. Mar Pet Geol, 2018, 97, 568–591.
[53] Liu P, Li M, Jiang Q, Cao T, Sun Y. Effect of secondary oil migration distance on composition of acidic NSO compounds in crude oils determined by negative-ion electrospray Fourier transform ion cyclotron resonance mass spectrometry. Org Geochem, 2015, 78, 23–31.

[54] Ziegs V, Noah M, Poetz S, Horsfield B, Hartwig A, Rinna J, Skeie JE. Unravelling maturity- and migration-related carbazole and phenol distributions in central graben crude oils. Mar Pet Geol, 2018, 94, 114–130. 2018.
[55] Liu W, Liao Y, Shi Q, Hsu CS, Jiang B, Peng P. Origin of polar organic sulfur compounds in immature crude oils revealed by ESI FT-ICR MS. Org Geochem, 2018, 121, 36–47.
[56] Vaz BG, Silva RC, Klitzke CF, Simas RC, Nascimento HDL, Pereira RCL, Garcia DF, Eberlin MN, Azevedo DA. Assessing biodegradation in the Llanos orientales crude oils by electrospray ionization ultrahigh resolution and accuracy Fourier transform mass spectrometry and chemometric analysis. Energy Fuels, 2013, 27, 1277–1284.
[57] Martins LL, Pudenzi MA, Da Cruz GF, Nascimento HDL, Eberlin MN. Assessing biodegradation of Brazilian crude oils via characteristic profiles of O1 and O2 compound classes: Petroleomics by negative-ion mode electrospray ionization fourier transform ion cyclotron resonance mass spectrometry. Energy Fuels, 2017, 31, 6649–6657.
[58] Rocha YS, Pereira RCL, Filho JGM. Negative electrospray Fourier transform ion cyclotron resonance mass spectrometry determination of the effects on the distribution of acids and nitrogen-containing compounds in the simulated thermal evolution of a Type-I source rock. Org Geochem, 2018, 115, 32–45.
[59] Terra LA, Filgueiras PR, Pereira RCL, Gomes AO, Vasconcelos GA, Tose LV, Castro EVR, Vaz BG, Romão W, Poppia RJ. Prediction of total acid number in distillation cuts of crude oil by ESI(–) FT-ICR MS coupled with chemometric tools. J Braz Chem Soc, 2017, 28, 1822–1829.
[60] Li S, Peng B, Liu D, Sun C. Resolution and identification of petroleum sulfonate by electrospray ionization Fourier transform ion cyclotron resonance mass spectrometry. Energy Fuels, 2016, 30, 2751–2759.
[61] Dias HP, Gonçalves GR, Freitas JCC, Gomes AO, de Castro EVR, Vaz BG, Aquije GMFV, Romão W. Catalytic decarboxylation of naphthenic acids in crude oils. Fuel, 2015, 158, 113–121.
[62] Wang M, Zhao S, Liu X, Shi Q. Molecular characterization of thiols in fossil fuels by Michael addition reaction derivatization and electrospray ionization fourier transform ion cyclotron resonance mass spectrometry. Anal Chem, 2016, 88, 9837–9842.
[63] Topolyan AP, Belyaeva MA, Slyundina MS, Ilyushenkova VV, Formanovsky AA, Korshun VA, Borisov RS. Novel trityl/acridine derivatization agent for analysis of thiols by (matrix-assisted)(nanowire-assisted) laser desorption/ionization and electrospray ionization mass spectrometry. Anal Methods, 2017, 9, 6335–6340.
[64] Zaikin VG, Kozlov AV, Borisov RS, Shchapin IY. Regio-isomeric effects in tandem mass spectra of sulfonium cations generated from thiacyclane based sulfonium salts under soft ionization conditions. Eur J Mass Spectrom, 2018, 24, 108–115. 24.
[65] Kozlov AV, Borisov RS, Zaikin VG. Soft-ionization mass spectrometric observation of isomeric effects occurring in the synthesis of bis-sulfonium salts from thiacyclanes/xylylene dibromides and collision induced dissociation of bis-sulfonium cations. Int J Mass Spectrom, 2018, 432, 18–25.
[66] Müller H, Andersson JT, Schrader W. Characterization of high-molecular-weights sulfur-containing aromatics in vacuum residues using fourier transform ion cyclotron resonance mass spectrometry. Anal Chem, 2005, 77, 2536–2543.
[67] Ge Y, Wu J, Zhang Y, Liang Y, Shi Q. Characterization of sulfur-containing compounds in petroleum using AgSbF6 as a methylation reagent. Energy Fuels, 2020, 34, 10842–10848.
[68] Dalmaschio GP, Malacarne MM, de Almeida VMDL, Pereira TMC, Gomes AO, de Castro EVR, Greco SJ, Vaz BG, Romão W. Characterization of polar compounds in a true boiling point distillation system using electrospray ionization FT-ICR mass spectrometry. Fuel, 2014, 115, 190–202.

[69] Wang M, Zhao S, Chung KH, Xu C, Shi Q. Approach for selective separation of thiophenic and sulfidic sulfur sompounds from petroleum by methylation/demethylation. Anal Chem, 2015, 87, 1083–1088.
[70] Chen X, Li H, Zhang L, Shi Q, Zhao S, Xu C. Direct sulfur-containing compounds analysis in petroleum via (+) ESI FT-ICR MS using HBF4 as ionization promoter. Fuel, 2020, 278, 118334. doi:https://doi.org/10.1016/j.fuel.2020.118334.
[71] Lobodin VV, Juyal P, McKenna AM, Rodgers RP, Marshall AG. Lithium cationization for petroleum analysis by positive ion electrospray ionization Fourier transform ion cyclotron resonance mass spectrometry. Energy Fuels, 2014, 28, 6841–6847.
[72] Lobodin VV, Juyal P, McKenna AM, Rodgers RP, Marshall AG. Silver cationization for rapid speciation of sulfur-containing species in crude oils by positive electrospray ionization fourier transform ion cyclotron resonance mass spectrometry. Energy Fuels, 2014, 28, 447–452.
[73] Lu J, Zhang Y, Shi Q. Ionizing aromatic compounds in petroleum by electrospray with HCOONH4 as ionization promoter. Anal Chem, 2016, 88, 3471–3475.
[74] Lobodin VV, Robbins WK, Lu J, Rodgers RP. Separation and characterization of reactive and non-reactive sulfur in petroleum and its fractions. Energy Fuels, 2015, 29, 6177–6186.
[75] Kostyukevich Y, Kononikhin A, Popov I, Kharybin O, Perminova I, Konstantinov A, Nikolaev E. Enumeration of labile hydrogens in natural organic matter by use of hydrogen/deuterium exchange Fourier transform ion cyclotron resonance mass spectrometry. Anal Chem, 2013, 85, 11007–11013.
[76] Liu H, Mu J, Wang Z, Ji S, Shi Q, Guo A, Chen K, Lu J. Characterization of vanadyl and nickel porphyrins enriched from heavy residues by positive-ion electrospray ionization FT-ICR mass spectrometry. Energy Fuels, 2015, 29, 4803–4813.
[77] Liu T, Lu J, Zhao X, Zhou Y, Wei Q, Xu C, Zhang Y, Ding S, Zhang T, Tao X, Ju L, Shi Q. Distribution of vanadium compounds in petroleum vacuum residuum and their transformations in hydrodemetallization. Energy Fuels, 2015, 29, 2089–2096.
[78] Gavard R, Rossell D, Spencer SEF, Barrow MP. Themis: Batch preprocessing for ultrahigh-resolution mass spectra of complex mixtures. Anal Chem, 2017, 89, 11383–11390.
[79] Acter T, Cho Y, Kim S, Ahmed A, Kim B, Kim S. Optimization and application of APCI hydrogen–deuterium exchange mass spectrometry (HDX MS) for the speciation of nitrogen compounds. J Am Soc Mass Spectrom, 2015, 26, 1522–1531.
[80] Tang W, Hurt MR, Sheng H, Riedeman JS, Borton DJ, Slater P, Kenttämaa HI. Structural comparison of asphaltenes of different origins using multi-stage tandem mass spectrometry. Energy Fuels, 2015, 29, 1309–1314.
[81] Riedeman JS, Kadasala NR, Wei A, Kenttämaa HI. Characterization of asphaltene deposits by using mass spectrometry and Raman spectroscopy. Energy Fuels, 2016, 30, 805–809.
[82] Woltering M, Tulipani S, Boreham CJ, Walshe J, Schwark L, Grice K. Simultaneous quantitative analysis of Ni, VO, Cu, Zn and Mn geoporphyrins by liquid chromatography-high resolution multistage mass spectrometry: Method development and validation. Chem Geol, 2016, 441, 81–91.
[83] Rüger CP, Grimmer C, Sklorz M, Neumann A, Streibel T, Zimmermann R. Thermal analysis coupled to ultrahigh resolution mass spectrometry with collision induced dissociation for complex petroleum samples: Heavy oil composition and asphaltene precipitation effects. Energy Fuels, 2017, 31, 13144–13158.
[84] Purcell JM, Juyal P, Kim D-G, Rodgers RP, Hendrickson CL, Marshall AG. Sulfur speciation in petroleum: Atmospheric pressure photoionization or chemical derivatization and electrospray ionization fourier transform ion cyclotron resonance mass spectrometry. Energy Fuels, 2007, 21, 2869–2874.

[85] Santos JM, Pudenzi MA, Wisniewski A Jr, Breitkreitza MC, Eberlin MN. Optimization of atmospheric pressure photoionization for the crude oil analysis using ultra-high resolution mass spectrometry. J Braz Chem Soc, 2019, 30, 819–829.
[86] Muller H, Adam FM, Panda SK, Al-Jawad HH, Al-Hajji AA. Evaluation of quantitative sulfur speciation in gas oils by fourier transform ion cyclotron resonance mass spectrometry: Validation by comprehensive two-dimensional gas chromatography. J Am Soc Mass Spectrom, 2012, 23, 806–815.
[87] Corilo YE, Rowland SM, Rodgers RP. Calculation of the total sulfur content in crude oils by positive-ion atmospheric pressure photoionization fourier transform ion cyclotron resonance mass spectrometry. Energy Fuels, 2016, 30, 3962–3966.
[88] Ha J, Cho E, Kim S. Interpreting chemical structures of compounds in crude oil based on the tandem mass spectra of standard compounds obtained at the same normalized collision. Energy Fuels, 2017, 31, 6960–6967.
[89] Acter T, Kim D, Ahmed A, Ha J-H, Kim S. Application of atmospheric pressure photoionization H/D-exchange mass spectrometry for speciation of sulfur-containing compounds. J Am Soc Mass Spectrom, 2017, 28, 1687–1695.
[90] Cho Y, Ahmed A, Kim S. Application of atmospheric pressure photo ionization hydrogen/deuterium exchange high-resolution mass spectrometry for the molecular level speciation of nitrogen compounds in heavy crude oils. Anal Chem, 2013, 85, 9758–9763.
[91] Kim E, Cho E, Ahmed A, Kim YH, Kim S. Structural elucidation of nitrogen-containing compounds in polar fractions using double bond equivalence distributions and hydrogen–deuterium exchange mass spectra. Fuel, 2017, 194, 503–510.
[92] Griffiths MT, Da Campo R, O'Connor PB, Barrow MP. Throwing light on petroleum: Simulated exposure of crude oil to sunlight and characterization using atmospheric pressure photoionization Fourier transform ion cyclotron resonance mass spectrometry. Anal Chem, 2014, 86, 527–534.
[93] Zhang K, Yu J, Gao S, Li C, Xu G. Understanding shale oil hydrotreatment with composition analysis using positive-ion mode atmospheric pressure photoionization Fourier transform ion cyclotron resonance mass spectrometry. Energy Fuels, 2017, 31, 1362–1369.
[94] Giraldo-Dávila D, Chacón-Patiño ML, Orrego-Ruiz JA, Blanco-Tirado C, Combariza MY. Improving compositional space accessibility in (+) APPI FT-ICR mass spectrometric analysis of crude oils by extrography and column chromatography fractionation. Fuel, 2016, 185, 45–58.
[95] Purcell JM, Hendrickson CL, Rodgers RP, Marshall AG. Atmospheric pressure photoionization Fourier transform ion cyclotron resonance mass spectrometry for complex mixture analysis. Anal Chem, 2006, 78, 5906–5912.
[96] Zorzenão PCS, Mariath RM, Pinto FE, Tose LV, Romão W, Santos AF, Scheer AP, Simon S, Sjöblom J, Yamamoto CI. Asphaltenes subfractions extracted from Brazilian vacuum residue: Chemical characterization and stabilization of model water-in-oil (W/O) emulsions. J Pet Sci Eng, 2018, 160, 1–11.
[97] Pereira TMC, Vanini G, Oliveira ECS, Cardoso FMR, Fleming FP, Neto AC, Lacerda V Jr, Castro EVR, Vaz BG, Romão W. An evaluation of the aromaticity of asphaltenes using atmospheric pressure photoionization Fourier transform ion cyclotron resonance mass spectrometry – APPI(±)FT-ICR MS. Fuel, 2014, 118, 348–357.
[98] Chacón-Patiño ML, Rowland SM, Rodgers RP. Advances in asphaltene petroleomics. Part 1: Asphaltenes are composed of abundant island and archipelago structural motifs. Energy Fuels, 2017, 31, 13509–13518.

[99] Chacón-Patiño ML, Rowland SM, Rodgers RP. Advances in asphaltene petroleomics. Part 2: Selective separation method that reveals fractions enriched in island and archipelago structural motifs by mass spectrometry. Energy Fuels, 2018, 32, 314–328.
[100] Chacón-Patiño ML, Rowland SM, Rodgers RP. Advances in asphaltene petroleomics. Part 3. Dominance of island or archipelago structural motif is sample dependent. Energy Fuels, 2018, 32, 9106–9120.
[101] Wittrig AM, Fredriksen TR, Qian K, Clingenpeel AC, Harper MR. Single Dalton collision-induced dissociation for petroleum structure characterization. Energy Fuels, 2017, 31, 13338–13344.
[102] Nyadong L, Lai J, Thompsen C, LaFrancois CJ, Cai X, Song C, Wang J, Wang W. High-field orbitrap mass spectrometry and tandem mass for molecular characterization of asphaltenes. Energy Fuels, 2018, 32, 294–305.
[103] McKenna AM, Williams JT, Putman JC, Aeppli C, Reddy CM, Valentine DL, Lemkau KL, Kellermann MY, Savory JJ, Kaiser NK, Marshall AG, Rodgers RP. Unprecedented ultrahigh resolution FT-ICR mass spectrometry and parts-per-billion mass accuracy enable direct characterization of nickel and vanadyl porphyrins in petroleum from natural seeps. Energy Fuels, 2014, 28, 2454–2464.
[104] Chiaberge S, Fiorani T, Savoini A, Bionda A, Ramello S, Pastori M, Cesti P. Classification of crude oil samples through statistical analysis of APPI FTICR mass spectra. Fuel Process Technol, 2013, 106, 181–185.
[105] Cho E, Witt M, Hur M, Jung M-J, Kim S. Application of FT-ICR MS equipped with quadrupole detection for analysis of crude oil. Anal Chem, 2017, 89, 12101–12107.
[106] Krajewski LC, Rodgers RP, Marshall AG. 126 264 Assigned chemical formulas from an atmospheric pressure photoionization 9.4 T Fourier transform positive ion cyclotron resonance mass spectrum. Anal Chem, 2017, 89, 11318–11324.
[107] Valencia-Dávila JA, Blanco-Tirado C, MY C. Analysis of naphthenic acids by matrix assisted laser desorption ionization time of flight mass spectrometry. Fuel, 2017, 193, 168–177.
[108] Valencia-Dávila JA, Witt M, Blanco-Tirado C, Combariza MY. Molecular characterization of naphthenic acids from heavy crude oils using MALDI FT-ICR mass spectrometry. Fuel, 2018, 231, 126–133.
[109] Daly TK, Buseck PR, Williams P, Lewis CF. Fullerenes from a fulgurite. Science, 1993, 259, 1599–1601.
[110] Fergoug T, Boukratem C, Bounaceur B, Bouhadda Y. Laser desorption/ionization-time of flight (LDI-TOF) and matrix-assisted laser desorption/ionization – time of flight (MALDI – TOF) mass spectrometry of an Algerian asphaltene. Egypt J Pet, 2017, 26, 803–810.
[111] Rizzi A, Cosmina P, Flego C, Montanari L, Seraglia R, Traldi P. Laser desorption/ionization techniques in the characterization of high molecular weight oil fractions. Part 1: Asphaltenes. J Mass Spectrom, 2006, 41, 1232–1241.
[112] Daaou M, Bendedouch D, Modarressi A, Rogalski M. Properties of the polar fraction of Hassi-Messaoud asphaltenes. Energy Fuels, 2012, 26, 5672–5678.
[113] Santos VG, Fasciotti M, Pudenzi MA, Klitzke CF, Nascimento HL, Pereira RCL, Bastosc WL, Eberlin MN. Fullerenes in asphaltenes and other carbonaceous materials: Natural constituents or laser artifacts. Analyst, 2016, 141, 2767–2773.
[114] Sabbah H, Pomerantz AE, Wagner M, Müllen K, Zare RN. Laser desorption single-photon ionization of asphaltenes: Mass range, compound sensitivity, and matrix effects. Energy Fuels, 2012, 26, 3521–3526.
[115] Wu Q, Pomerantz AE, Mullins OC, Zare RN. Laser-based mass spectrometric determination of aggregation numbers for petroleum- and coal-derived asphaltenes. Energy Fuels, 2013, 28, 475–482.

[116] Pomerantz AE, Wu Q, Mullins OC, Zare RN. Laser-based mass spectrometric assessment of asphaltene molecular weight, molecular architecture, and nanoaggregate Number. Energy Fuels, 2015, 29, 2833–2842.
[117] Wang W, Taylor C, Hu H, Humphries KL, Jaini A, Kitimet M, Scott T, Stewart Z, Ulep KJ, Houck S, Luxon A, Zhang B, Miller B, Parish CA, Pomerantz AE, Mullins OC, Zare RN. Nanoaggregates of diverse asphaltenes by mass spectrometry and molecular dynamics. Energy Fuels, 2017, 31, 9140–9151.
[118] Borton DJ, Amundson LM, Hurt MR, Dow A, Madden JT, Simpson GJ, Kenttämaa HI. Development of a high-throughput laser-induced acoustic desorption probe and raster sampling for laser-induced acoustic desorption/atmospheric pressure chemical ionization. Anal Chem, 2013, 85, 5720–5726.
[119] Chen J, Jia L, Zhao L, Lu X, Guo W, Weng J, Qi F. Analysis of petroleum aromatics by laser-induced acoustic desorption/tunable synchrotron vacuum ultraviolet photoionization mass spectrometry. Energy Fuels, 2013, 27, 2010–2017.
[120] Cho Y, Witt M, Jin JM, Kim YH, Nho N-S, Kim S. Evaluation of laser desorption ionization coupled to Fourier transform ion cyclotron resonance mass spectrometry to study metalloporphyrin complexes. Energy Fuels, 2014, 28, 6699–6706.
[121] Borisova YY, Tazeeva EG, Mironov NA, Borisov DN, Yakubova SG, Abilova GR, Sinyashin KO, Yakubov MR. Role of vanadylporphyrins in the flocculation and sedimentation of asphaltenes of heavy oils with high vanadium content. Energy Fuels, 2017, 31, 13382–13391.
[122] Mironov NA, Sinyashin KO, Abilova GR, Tazeeva EG, Milordov DV, Yakubova SG, Borisov DN, Gryaznov PI, Borisova YY, Yakubov MR. Chromatographic isolation of vanadyl porphyrins from heavy oil resins. Russ Chem Bull, 2017, 66, 1450–1455.
[123] Mironov NA, Abilova GR, Sinyashin KO, Gryaznov PI, Borisova YY, Milordov DV, Tazeeva EG, Yakubova SG, Borisov DN, Yakubov MR. Chromatographic isolation of petroleum vanadyl porphyrins using sulfocationites as sorbents. Energy Fuels, 2018, 32, 161–168.
[124] Mironov NA, Abilova GR, Borisova YY, Tazeeva EG, Milordov DV, Yakubova SG, Yakubov MR. Comparative study of resins and asphaltenes of heavy oils as sources for obtaining pure vanadyl porphyrins by the sulfocationite-based chromatographic method. Energy Fuels, 2018, 32, 12435–12446.
[125] Ramírez-Pradilla JS, Blanco-Tirado C, Hubert-Roux M, Giusti P, Afonso C, Combariza MY. Comprehensive petroporphyrin identification in crude oils using highly selective electron transfer reactions in MALDI-FTICR-MS. Energy Fuels, 2019, 33, 3899–3907.
[126] Lobodin VV, Nyadong L, Ruddy BM, Curtis M, Jones PR, Rodgers RP, Marshall AGDART. Fourier transform ion cyclotron resonance mass spectrometry for analysis of complex organic mixtures. Int J Mass Spectrom, 2015, 378, 186–192.
[127] Romão W, Tose LV, Vaz BG, Sama SG, Lobinski R, Giusti P, Carrier H, Bouyssiere B. Petroleomics by direct analysis in real time-mass spectrometry. J Am Soc Mass Spectrom, 2016, 27, 182–185.
[128] Ren L, Han Y, Zhang Y, Zhang Y, Meng X, Shi Q. Spray injection direct analysis in real time (DART) ionization for petroleum analysis. Energy Fuels, 2016, 30, 4486–4493.
[129] Cody RB, Dane AJ. Dopant-assisted direct analysis in real time mass spectrometry with argon gas. Rapid Commun Mass Spectrom, 2016, 30, 1181–1189.
[130] Bae E, Na JG, Chung SH, Kim HS, Kim S. Identification of about 30 000 chemical components in shale oils by electrospray ionization (ESI) and atmospheric pressure photoionization (APPI) coupled with 15 T fourier transform ion cyclotron resonance mass spectrometry (FT-ICR MS) and a comparison to conventional oil. Energy Fuels, 2010, 24, 2563–2569.

[131] Huba AK, Huba K, Gardinali PR. Understanding the atmospheric pressure ionization of petroleum components: The effects of size, structure, and presence of heteroatoms. Sci Total Environ, 2016, 568, 1018–1025.
[132] Farmani Z, Schrader W. A detailed look at the saturate fractions of different crude oils using direct analysis by ultrahigh resolution mass spectrometry (UHRMS). Energies, 2019, 12, 3455–3467.
[133] Orrego-Ruiz JA, Gomez-Escudero A, Rojas-Ruiz FA. Combination of negative electrospray ionization and positive atmospheric pressure photoionization fourier transform ion cyclotron resonance mass spectrometry as a quantitative approach of acid species in crude oils. Energy Fuels, 2016, 30, 8209–8215.
[134] Huba AK, Gardinali PR. Characterization of a crude oil weathering series by ultrahigh-resolution mass spectrometry using multiple ionization modes. Sci Tot Environ, 2016, 600, 563–564.
[135] Silva RC, Radović JR, Ahmed F, Ehrmann U, Brown M, Ortega LC, Larter S, Pereira-Almao P, Oldenburg TBP. Characterization of acid-soluble oxidized asphaltenes by Fourier transform ion cyclotron resonance mass spectrometry: Insights on oxycracking processes and asphaltene structural features. Energy Fuels, 2016, 30, 171–179.
[136] Hertzog J, Carréa V, Le Brech Y, Mackay CL, Dufour A, Masek O, Aubriet F. Combination of electrospray ionization, atmospheric pressure photoionization and laser desorption ionization fourier transform ion cyclotronic resonance mass spectrometry for the investigation of complex mixtures e application to the petroleomic analysis of bio-oils. Anal Chim Acta, 2017, 969, 26–34.
[137] Robson WJ, Sutton PA, McCormack P, Chilcott NP, Rowland SJ. Class type separation of the polar and apolar components of petroleum. Anal Chem, 2017, 89, 2919–2927.
[138] Vanini G, Pereira VB, Romão W, Gomes AO, Oliveira LMSL, Dias JCM, Azevedo DA. Analytical advanced techniques in the molecular-level characterization of Brazilian crude oils. Microchem J, 2018, 137, 111–118.
[139] Dutriez T, Courtiade M, Ponthus J, Thiébaut D, Dulot H, Hennion M-C. Complementarity of Fourier transform ion cyclotron resonance mass spectrometry and high temperature comprehensive two-dimensional gas chromatography for the characterization of resin fractions from vacuum gas oils. Fuel, 2012, 96, 108–119.
[140] Liu W, Liao Y, Pan Y, Jiang B, Zeng Q, Shi Q, Hsu CS. Use of ESI FT–ICR MS to investigate molecular transformation in simulated aerobic biodegradation of a sulfur-rich crude oil. Org Geochem, 2018, 123, 17–26.
[141] Tessarolo NS, Silva RC, Vanini G, Pinho A, Romão W, de Castro EVR, Azevedo DA. Assessing the chemical composition of bio-oils using FT-ICR mass spectrometry and comprehensive two-dimensional gas chromatography with time-of-flight mass spectrometry. Microchem J, 2014, 117, 68–76.
[142] Farenc M, Corilo YE, Lalli PM, Riches E, Rodgers RP, Afonso C, Giusti P. Comparison of atmospheric pressure ionization for the analysis of heavy petroleum fractions with ion mobility-mass spectrometry. Energy Fuels, 2016, 30, 8896–8903.
[143] Santos JM, Galaverna RDS, Pudenzi MA, Schmidt EM, Sanders NL, Kurulugama RT, Mordehai A, Stafford GC, Wisniewski A Jr, Eberlin MN. Petroleomics by ion mobility mass spectrometry: Resolution and characterization of contaminants and additives in crude oils and petrofuels. Anal Methods, 2015, 7, 4450–4463.
[144] Lalli PM, Corilo YE, Rowland SM, Marshall AG, Rodgers RP. Isomeric separation and structural characterization of acids in petroleum by ion mobility mass spectrometry. Energy Fuels, 2015, 29, 3626–3633.

[145] Ahmed A, Cho Y, Giles K, Riches E, Lee JW, Kim HI, Choi CH, Kim S. Elucidating molecular structures of nonalkylated and short-chain alkyl ($n < 5$, $(CH_2)_n$) aromatic compounds in crude oils by a combination of ion mobility and ultrahigh-resolution mass spectrometries and theoretical collisional cross-section calculations. Anal Chem, 2014, 86, 3300–3307.
[146] Szykuła KM, Wicking C, Whitmarsh S, Creaser CS, Reynolds JC. Characterization of crude oil and its saturate, aromatic, and resin fractions by high-field asymmetric waveform ion mobility spectrometry–high-resolution mass spectrometry. Energy Fuels, 2018, 32, 11310–11316.
[147] Niles SF, Chacón-Patiño ML, Smith DF, Rodgers RP, Marshall AG. Comprehensive compositional and structural comparison of coal and petroleum asphaltenes based on extrography fractionation coupled with Fourier transform ion cyclotron resonance MS and MS/MS analysis. Energy Fuels, 2020, 34, 1492–1505.
[148] Chacón-Patiño ML, Smith DF, Hendrickson CL, Marshall AG, Rodgers RP. Advances in asphaltene petroleomics. Part 4. Compositional trends of solubility subfractions reveal that polyfunctional oxygen containing compounds drive asphaltene chemistry. Energy Fuels, 2020, 34, 3013–3030.
[149] Niyonsaba E, Manheim JM, Yerabolu R, Kenttamaa HI. Recent advances in petroleum analysis by mass spectrometry. Anal Chem, 2019, 91, 156–177.
[150] Borisov RS, Kulikova LN, Zaikin VG. Mass Spectrometry in petroleum chemistry (petroleomics) (Review). Pet Chem, 2019, 59, 1055–1076.

J. R. Radović, R. C. Silva

9 Non-combustion applications of petroleum chemistry

Abstract: Global efforts to reduce CO_2 emissions and limit the associated climate change effects are profoundly transforming our energy system, and likely reducing future markets for petroleum-derived combustibles. On the other hand, the chemical energy stored in petroleum, and the diversity of elements and molecules that it contains, present an opportunity for research and technology development routes to promote novel product streams from petroleum resources, thus extending its economic utility. Some of the innovative, non-combustion applications of petroleum that have been discussed and researched in recent years include clean energy in the form of hydrogen or electricity, sulfur- or carbon-based polymers, and materials for energy storage systems, to name a few. This chapter showcases a selection of future-looking, petroleum-derived product streams, while providing a critical perspective on their feasibility and scalability.

9.1 Introduction

Global energy systems have been dominated by fossil fuels throughout the twentieth and into twenty-first centuries. In 2019, natural gas, crude oil, and coal comprised almost 80% of the primary energy mix, while petroleum resources alone accounted for approximately one-third of primary energy consumption, Figure 9.1. Combustion of fossil fuels emits large amounts of CO_2 to the atmosphere – during 2019, roughly 33 Gt (gigatons) of CO_2 were released from energy-related sources [1]. The transportation sector, as the main end-use for petroleum-derived products, contributes to approximately 20% of total energy-related CO_2 emissions [2].

Over decades, anthropogenic CO_2 has accumulated in the atmosphere, and been recognized as a major driver of rising global temperatures and climate change, due to

Acknowledgments: The authors kindly acknowledge funding support from the Canada First Research Excellence Fund (CFREF) at the University of Calgary (Global Research Initiative in Sustainable Low Carbon Unconventional Resources – GRI). Additional funding came from the PRG group at the Department of Geoscience, University of Calgary. We thank Dr. Stephen Larter and all our colleagues in PRG and GRI for useful discussions and fruitful collaboration that contributed to some of the research showcased in this chapter. Finally, we acknowledge useful and constructive suggestions from the book editor and reviewers of this chapter.

J. R. Radović, R. C. Silva, Department of Geoscience, University of Calgary, T2N1N4 Calgary, Canada, e-mail: Jagos.Radovic@ucalgary.ca

https://doi.org/10.1515/9783110694529-009

its greenhouse effect [3]. The risks of CO_2-driven global climate change have motivated a global policy push to reduce carbon emissions from fossil fuels by, among other things, incentivizing renewable, carbon-free sources of energy, mainly solar and wind. Some recent forecasts estimate that in order to keep the global temperature rise below 1.5 and 2 °C by the year 2050, carbon emissions from energy use would have to be reduced by between 95% and 70%, respectively [4]. To achieve such reductions, liquid fuel consumption would have to fall from current ~ 100 Mb/d (million barrels per day) levels to 55 and 30 Mb/d, in below 2.0 and 1.5 °C scenarios, respectively [4].

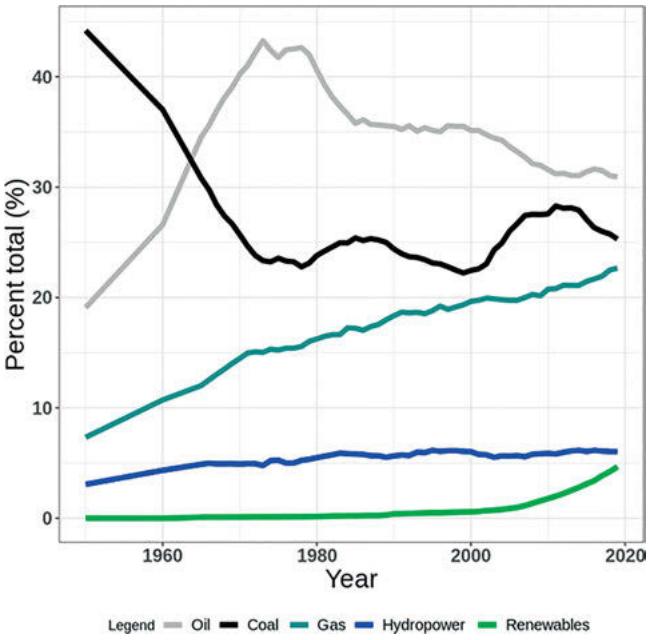

Figure 9.1: Global primary energy consumption by source, from 1950 to 2019 [5, 6].

Since the peak in 1970s, the share of petroleum in the global energy mix has been on a decline (Figure 9.1). If such trend continues in the upcoming decades, the market for combustion end-use of petroleum resources would substantially shrink, potentially stranding an increasing share of global petroleum reserves, currently estimated at approx. 1,500 billion barrels [7]. Countries with economies heavily dependent on the fossil fuels industry are particularly sensitive to this energy transition process. For example, crude exports from oil sands deposits of Western Canadian Sedimentary Basin, that hosts an estimated 300 billion barrels of oil, contribute to more than 6% of Canada's gross domestic product [8, 9].

Currently, crude oil is refined into a plethora of products, mainly liquid fuels such as gasoline, diesel fuel, heating oil, and jet fuel (Figure 9.2). Only a smaller fraction of

petroleum refinery streams is converted to various non-combustion products, such as petrochemical feedstocks, polymers, lubricants, and waxes.

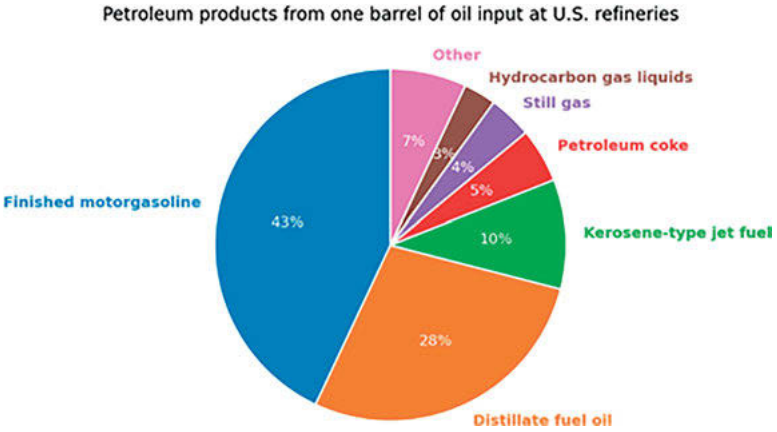

Figure 9.2: Main product streams currently produced from a barrel of petroleum [10].

On the other hand, looking to the future, there is a potential to leverage complex, and diverse chemistry of petroleum in novel, innovative ways, whether to extract clean(er) energy from crude oil, or to use a much larger proportion of petroleum resource as a substrate and feedstock for value-added, non-combustion products. This chapter features a nonexhaustive selection of such possible routes, recently discussed in the academic literature and among petroleum industry stakeholders, while offering our high-level assessment on their feasibility and scalability.

9.2 Petroleum chemistry basics

Petroleum has its origin in ancient terrestrial or marine biomass that incorporated atmospheric CO_2 via photosynthesis into labile biomolecules, e.g., carbohydrates and lipids. After senescence, this ancient biomass was sedimented and buried, and over geological timescales its constituent biomolecules were subjected to transformation, both chemically and thermally, converting them to highly reduced chemical species. The reduced chemical energy stored in petroleum can be readily released by oxidation, such as during combustion or aerobic biodegradation, ultimately releasing CO_2 back to the environment.

Chemically, petroleum is a comprehensive, general term to denote complex subsurface fluids, predominantly comprising molecules containing carbon and hydrogen, that accumulate in suitable geological reservoirs, and can be commercially produced as natural gas, crude oil, or mixtures thereof, by excavation or drilling. Produced crude oil

loses its solution gases, mainly methane and other gaseous hydrocarbons containing up to five carbons, leaving out a liquid mixture of compounds containing from approximately 6 to up to 100 carbons, with an average molecule consisting of 20 carbon atoms.

In addition to hydrocarbons, crude oils can also contain compounds which bear atoms other than carbon and hydrogen, such as nitrogen, sulfur, oxygen (N, S, O), and some trace metals, as nickel and vanadium, Table 9.1. Broadly, these compounds are termed *non-hydrocarbons*.

Table 9.1: Typical abundance ranges of elements present in petroleum [10].

Carbon	83.0–87.0%
Hydrogen	10.0–14.0%
Nitrogen	0.1–2.0%
Oxygen	0.05–1.5%
Sulfur	0.05–6.0%
Metals (Nickel and vanadium)	<1,000 ppm

Defining petroleum fluid by its individual constituents is not a common practice in the oil industry, given the complexity of the mixture. A typical approach to defining the compositional space of crude oil is operational, based on the solubility of different compound classes in organic solvents of different polarities, or boiling point distribution. Figure 9.3 shows a selection of example molecular structures found in crude oils, including: (a) saturated hydrocarbon compounds, such as straight and branched alkanes, and alicyclic compounds, (b) aromatic compounds including polycyclic aromatic hydrocarbons, and (c) some heteroaromatic species, and finally, (d) the resin and asphaltene compound class. Solubility in polar solvents increases from saturates to resins and asphaltenes, which are the most diverse, and still poorly characterized mixture of high-molecular weight (HMW), heteroatom-bearing species. Different sectors of the industry may use other arbitrary schemes to classify petroleum fluids based on their overall composition, thus the many other crude oil adjectives we can find in the literature: *sour*, *waxy*, *heavy*, and so on. We direct readers interested in an exhaustive overview of petroleum chemistry and technology concepts to consult available textbooks on the topic [11, 12].

Novel analytical tools and methods, mainly the advent of ultrahigh-resolution mass spectrometry (Fourier transform ion cyclotron resonance mass spectrometry, FT-ICR-MS) and the field of *petroleomics*, have significantly advanced molecular-level understanding of complex species present in polar, heteroatom-bearing compound classes that are not amenable to conventional analytical tools such as gas chromatography (GC). Petroleomics studies of various crude oils demonstrated that

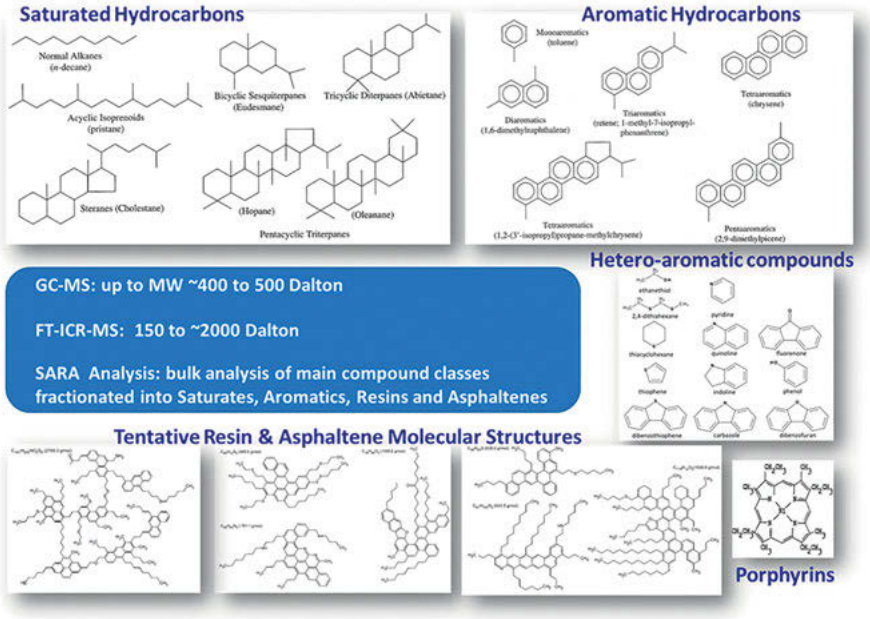

Figure 9.3: Main compound classes present in crude oil, showing some representative molecular structures. Central textbox highlights some of the methods typically used to characterize petroleum. Adapted from Overton, Wade [13] under Creative Commons Attribution 4.0 International License (https://creativecommons.org/licenses/by/4.0/).

more than 60,000 different elemental compositions are present in petroleum molecules, at concentration levels differing by various orders of magnitude [14]. For example, going from light, to medium and heavy crudes, and on to diluted bitumen, the abundance of saturated hydrocarbons decreases 4-fold and the abundance of non-hydrocarbons (resins and asphaltenes) increases 50-fold [15].

Table 9.2 shows the common compositional range of the main compound classes found in crude oils. Conventional crude oils are mainly composed of hydrocarbons. However, in certain unconventional oil types, such as heavy oils and bitumen, the non-hydrocarbon class is enriched due to in-reservoir processes, mainly anaerobic biodegradation, that deplete the lighter hydrocarbons, and produce a dense, viscous material, dominated by HMW and heteroatomic species found within resin and asphaltene fraction. In most extreme cases, resin and asphaltene fractions comprise up to 60% of oil (Table 9.2).

The separation of individual crude oil components is a daunting task, and no stream of pure oil fractions can be easily obtained. On an industrial scale, petroleum fractionation is based on the different boiling points of its components, which is the core concept of a refinery. Nevertheless, the obtained refinery streams are still complex mixtures themselves. Any efforts applied to further fractionate crude oil components,

Table 9.2: Composition of a typical medium crude, compared to heavy oils/ bitumens from Western Canada, showing much higher proportion of resins and asphaltenes in the unconventional oils [16].

	Weight percent (%)			
Oil type	*Saturates*	*Aromatics*	*Resins*	*Asphaltenes*
WTI*	78	15	6	1
Cold Lake	21.5	23.2	39.4	15.6
Athabasca	16.9	18.3	44.8	17.3

*WTI = Western Texas Intermediate.

through solubility or boiling point differences, come with significant challenges, but are not relevant for combustion-driven applications. We expect that breakthroughs on the molecular-level fractionation of crude oil and its derivatives will be needed to achieve some of the higher value-added non-combustion applications.

In sum, thousands of chemical species found in petroleum create a continuum over a wide range of physicochemical properties, in terms of molecular weights, functionalities, phase behavior, and susceptibility to abiotic and biotic alterations. For non-combustion petroleum uses, such chemical diversity is at the same time a challenge, and a promising opportunity.

9.3 Non-combustion applications of petroleum

9.3.1 Zero carbon emission energy recovery from petroleum

Production of zero carbon emission energy from petroleum can be achieved by either subsurface processes, which would leave the carbon in the reservoir while extracting clean energy, or via energy production from extracted petroleum on the surface with concurrent capture of emitted CO_2 and its subsurface sequestration (Figure 9.4).

The latter approach, involving surface combustion of petroleum (or other fossil fuels) for emission-less electricity production, is technically feasible with current carbon capture and storage (CCS) technology, which is relatively mature and being successfully piloted and up scaled. Briefly, CO_2 generated in the power plant is captured at the point of release using scrubbers (e.g., amine-based), followed by the injection of concentrated, supercritical CO_2 into geological formations with suitable caprocks to prevent future CO_2 leakage (Figure 9.4A). A notable example of this approach is the Quest CCS project operating within the oil sands industrial complex in Western Canada, which, to date, stored more than 5 million tons of CO_2, with plans to use the same technology for other large-scale projects globally [17]. The main limitation to scaling up of this route is the presence of suitable subsurface formations for long-

term CO_2 storage. Some estimates suggest that up to 12% of global emissions could be offset in this way [18].

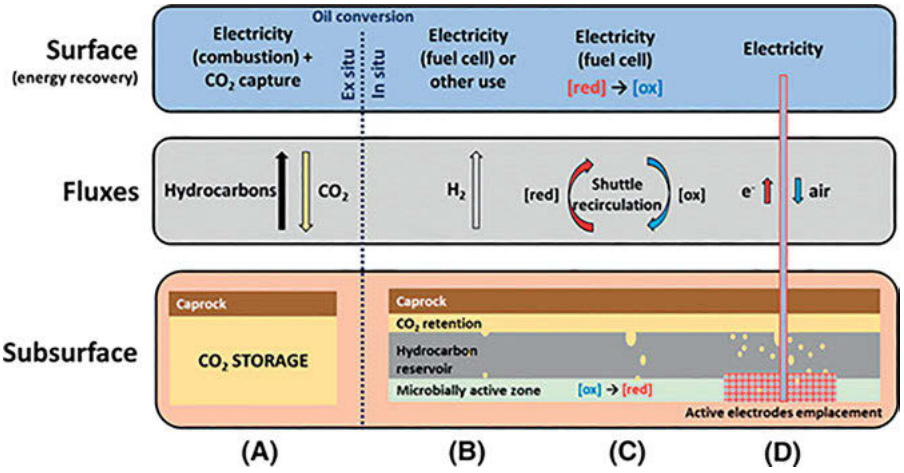

Figure 9.4: Possible routes for zero carbon emission energy extraction from oil reservoirs. (A) Conventional oil or gas production combined with direct power generation and carbon capture and storage. (B) Microbial conversion of hydrocarbons to alternative energy vectors such as hydrogen. Similar processes can be designed using thermal oxidation of hydrocarbons with water. (C) Electron transporter mediated processes, using in-reservoir oil or gas shuttle redox and CO_2 retention. (D) Direct power generation using macroscopic electrodes emplaced in the microbially active zone of a hydrocarbon reservoir. From Novotnik, Nandy [19] with permission.

On the other hand, technologies for in situ conversion of petroleum to zero carbon emission energy vectors are much less mature. Conceptually, they are based on microbiological or thermal conversion of petroleum to hydrogen, electricity, or other energy carries, such as ammonia (Figure 9.4B–D). With any in-reservoir energy extraction technology, petroleum reservoirs with high water saturations are particularly relevant; while not economically viable for conventional petroleum production, they still contain appreciable volumes of oil in place, and feature large surface areas of water/oil interface that are suitable for microbial, and thermochemical reactions.

9.3.1.1 Hydrogen production from oil reservoirs

Thermal conversion routes aimed at recovering energy from oil fields using H_2 as an energy vector (Figure 9.4B) is technologically the most advanced in-reservoir, zero carbon emission energy recovery route. In this embodiment, petroleum is combusted in situ at high temperatures in the presence of reservoir water to generate hydrogen gas, among other products. The process is initiated by injection of oxygen rich stream

via wellbore deep into the reservoir, which stimulates oxidation of surrounding hydrocarbons, and generates heat [20–22]. If needed, additional radiofrequency energy is provided to further the oxidative combustion reaction. Once the combustion is sufficiently advanced, temperatures within the target reservoir zone rise to above 500 °C, which causes the thermal cracking of hydrocarbons and water molecules to generate a complex gaseous mixture of steam, carbon mono- and dioxide, hydrogen, and other gases. The main reaction pathways occurring in this process include low- and high-temperature oxidation, gasification, water gas shift, and methanation (Figure 9.5). The key technology hurdle at this point is to selectively extract the hydrogen rich gas stream while leaving carbon oxides and other reaction products within the reservoirs. Recently, a significant breakthrough was made to that end, by developing a selective, down-hole membrane that can filter out hydrogen from the complex gaseous mixture and bring a pure H_2 to the wellhead [20].

In-reservoir hydrogen production is currently being pilot tested in an orphaned oil well in the western Canadian province of Saskatchewan [23]. If proven feasible in the field, and commercially scalable, hydrogen production from in situ gasification of petroleum could be a game changer that could secure strategic relevance of petroleum resources as a major energy source through the twenty-first century. Some forecasts predict that hydrogen could satisfy approximately 25% of global energy needs by 2050, with a US$700 billion worth annual market [24]. Some of the main challenges that we perceive for scaling up this route is the reaction control and optimization and ensuring long-term subsurface sequestration of large amounts of attendant carbon oxides and other gases produced during gasification, as well as possible issues around gas membrane fouling and longevity.

9.3.1.2 Electricity production from oil reservoirs

Another plausible concept involves electron-transporter-mediated processes, wherein electron shuttle species (e.g., metal ions such as Fe(III) or Mn(IV), sulfide–sulfate ion pair, or organic redox active molecules such as quinones) are injected in the oil reservoir, where they become reduced, as terminal electron acceptors in the reaction of microbial hydrocarbon degradation [19] (Figure 9.4C). Reduced electron shuttles are then recirculated to the surface, where they are re-oxidized in a fuel cell using atmospheric oxygen, while generating electricity. The CO_2 that has been released during petroleum oxidation remains trapped in the reservoir, therefore the electrical energy generated at the surface is zero-emission. Microbial processes of subsurface electron shuttle reduction are favored in oil reservoirs with high water-cut [25] that are typically not economically profitable for oil exploitation. Therefore, this technology concept would allow for repurposing of many currently abandoned oil wells to clean energy generation. To date, this route has only been tested in the laboratory, where production of reduced metal electron carriers during microbial degradation of saturated and

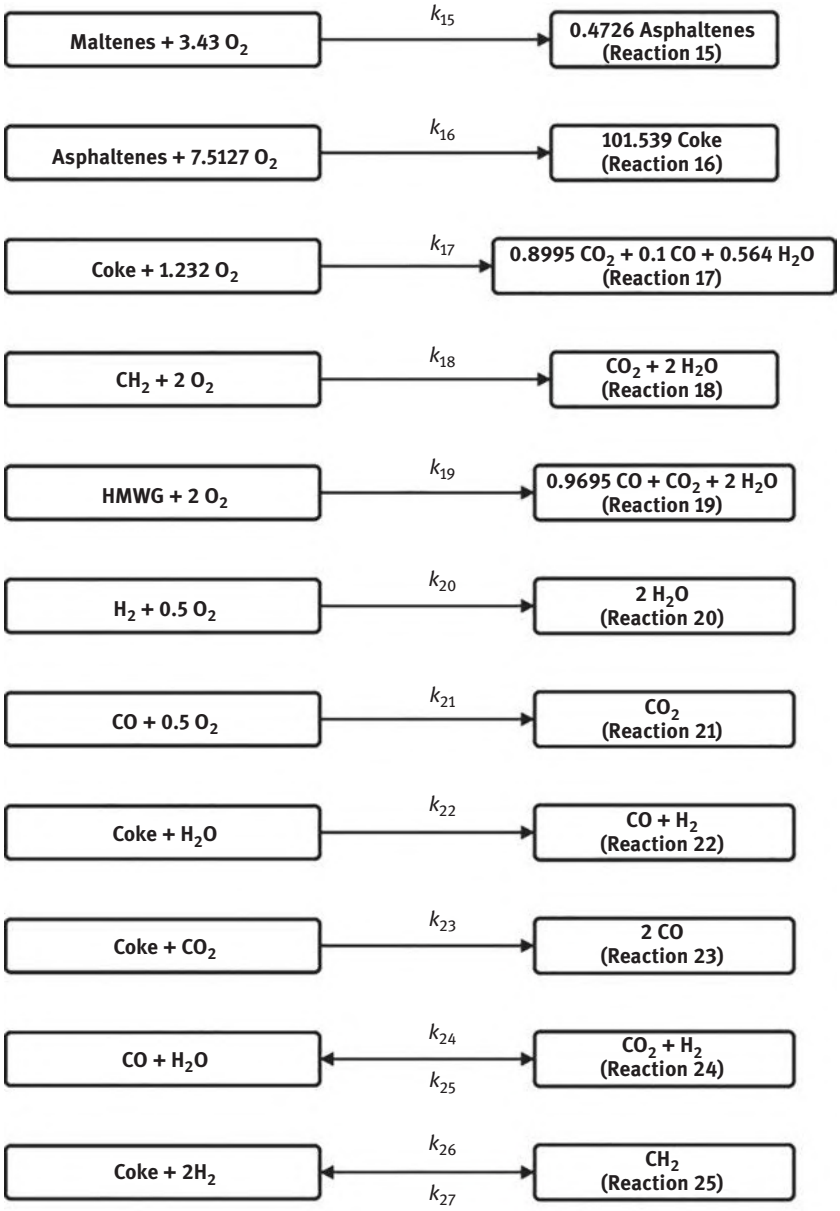

Figure 9.5: Bitumen low temperature oxidation (reactions 15 and 16), high-temperature oxidation (reactions 17–21), coke gasification (reactions 22 and 23), water gas shift (reaction 24), and methanation (reaction 25) reactions. From Kapadia, Wang [22] with permission.

aromatic hydrocarbons, and simpler substrates such as lactate, has been demonstrated [26, 27]. In addition, a lab prototype of auxiliary electrode fuel cell has been developed, that has the capability to handle complex redox configurations (e.g., inorganic–organic electrolytes, air breathing cathode) involved in the electron-shuttle concept [28, 29]. However, major technical challenges have been identified for scaling up of such an electron shuttle technology beyond the laboratory; the main ones including flux limitations for shuttle recirculation within the reservoir, concentration limits of shuttle species in the liquid phase, possible losses of shuttles in the reservoir due precipitation or degradation, and the need to maintain low pH in order to maximize CO_2 retention within the reservoir.

In this context, it is noteworthy to highlight naturally occurring subsurface petroleum oxidation routes that generate mobile, reduced electron shuttles, most importantly H_2S, commonly known as sour gas. Under suitable reservoir conditions, sour gas is produced on rapid timescales (months to years) by sulfate reducing *Bacteria* and *Archaea* present in the reservoir [30]. Alternatively, H_2S generation can be the result of abiogenic, thermochemical sulfate reduction, occurring with slower kinetics than microbial processes, and at temperatures higher than ~ 120 °C, leading to substantial H_2S buildup in the reservoir over long timescales [31]. Historically, the oil and gas industry has been investing significant resources and efforts to prevent H_2S generation, and mitigate its detrimental effects on oilfield assets and humans [32]. On the other hand, one can envision an alternative scenario where the knowledge on bacterial and thermal sulfate reduction is leveraged to develop technologies that would use suitable sulfur species as injectable energy shuttles, acting to promote the subsurface oil oxidation and capture the released chemical energy in the form of reduced sulfur that could then be converted on the surface to clean electricity [33, 34]. Existing technologies and expertise of oil and gas industry to safely manage and control sulfur streams would be highly advantageous to this energy vector route.

Finally, a possible alternative to produce electricity from oil reservoirs is the use of microbial fuel cell (MFC) technology that would be emplaced within the reservoir (Figure 9.4D). One potential embodiment of this approach would involve an air-breathing cathode, serving as a conduit for oxygen from the surface to the reservoir, and taking the electricity generated from microbial hydrocarbon oxidation to the surface [19] (Figure 9.6).

Again, CO_2 generated in oil oxidation stays in the reservoir. The main limitation in this solution is the low power density of MFC, which could be improved by enhancing the microbial electron mechanisms. One way to address the problem of low power density is the emplacement of large number of smaller MFC devices, thus creating an energy generating network. Other challenges to this concept include maintaining electrical and proton connectivity to the reservoir, avoiding undesirable geochemical reactions such as mineral precipitation, and preventing the escape of CO_2 through the electrode oxygen conduits. The latter issue could probably be prevented through the

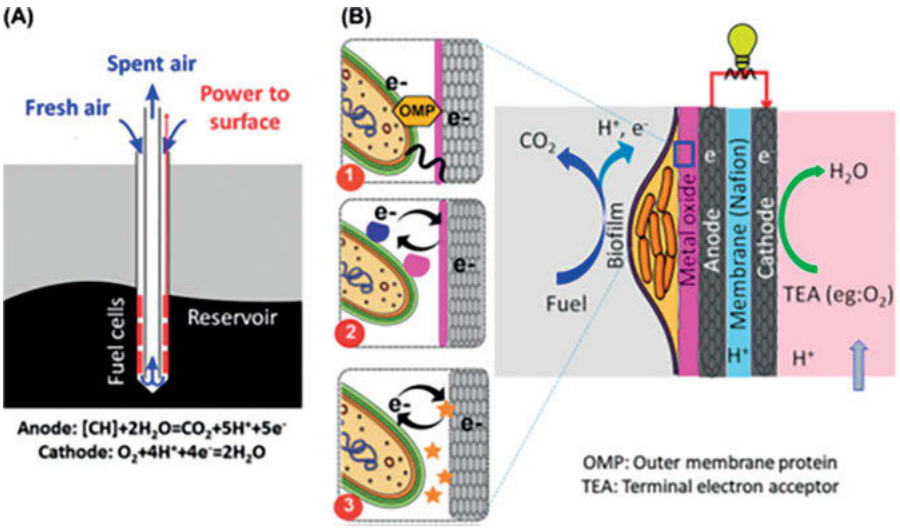

Figure 9.6: (A) Depiction of the operating mechanism of an air breathing microbial fuel cell (MFC). (B) Possible electron transfer mechanisms between microbes and electrodes. From Novotnik, Nandy [19] with permission.

usage of selective membranes, as the ones being applied in the thermal conversion route for H_2 generation described earlier in this section.

Although energetically plausible, at this stage of development, it seems unlikely that electricity production from oil reservoirs can be scaled to practical, grid-power levels (i.e., ≫MW); however, these routes could possibly be used as standalone solutions for supplementing power needs at remote industrial sites, or similar smaller scale applications. Longer-term, new technological breakthroughs, for example related to microbial engineering and advances in subsurface exploration [35], may increase the deployment potential for approaches described in this section.

9.3.2 Energy storage applications

With the rise of intermittent renewable power sources, mainly solar and wind, in the global energy mix (Figure 9.1), there is an increased need for large-scale energy storage solutions to act as a backup when the generating power from renewables is low, or as a longer-term store for any excess power generated. To that end, redox flow batteries (RFB) are often considered as a suitable solution, mainly because of the possibility to up-scale them to the needs of electricity grids, which is not as easily achievable using the competing solid-state battery technology, as well as due to their greater lifetime, safety, and lower cost. RFB consist of two reservoirs containing solutions of suitable electrolytes, with balancing redox chemistries (Figure 9.7). To charge

an RFB, the oxidized form of electrolyte in one reservoir is reduced (i.e., accepts electrons), which is balanced by the oxidation reaction in the anolyte compartment when the stored electricity is used. In an ideal case, these cycles are fully reversible, and can be repeated with high cycling rates; in practice, RFB performance characteristics will be highly dependent on the type of electrolytes, electrode materials, and operating conditions.

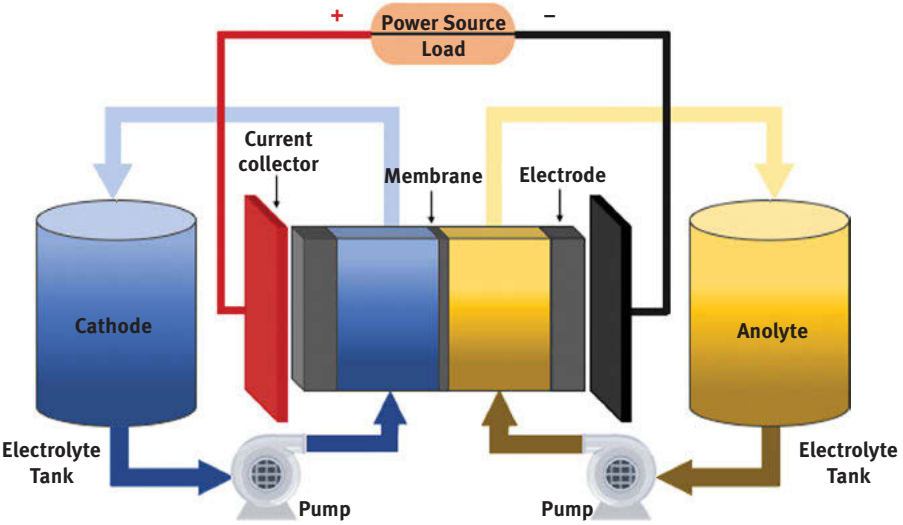

Figure 9.7: Schematic depiction of conventional RFB design. From Clemente and Costa-Castelló [36] under Creative Commons Attribution 4.0 International License (https://creativecommons.org/licenses/by/4.0/).

Most research and technological advances in the past decades have been made with vanadium-based RFB, including commercial applications such as load-levelling, power quality control and renewable coupling in more than 20 large-scale deployments [37]. Conventional vanadium RFB are based on V(II)/V(III) redox couple in the anolyte compartment, and V(IV)/V(V) pair on the catholyte side. The vanadium ions for anolyte and catholyte solutions are typically sourced from the mined salts (e.g., vanadium sulfate, $VOSO_4$; vanadium trichloride, $VOCl_3$) or oxides (e.g., vanadium pentoxide, V_2O_5, and trioxide V_2O_3).

More recently, alternative vanadium sources for RFB have been considered, including soot and ash from combustion of fossil fuels, and the vanadium present in petroleum resources. In that context, heavy oil and bitumen resources as found for example in biodegraded deposits of Western Canada, Venezuela, or Mexico, are of particular interest. Because of their biodegraded nature, they present an elevated abundance of non-hydrocarbon species, including vanadium and nickel metals. For example, Canadian oil sands bitumen can contain up to 200 ppm of vanadium (by

weight), which is often conveniently concentrated in the residual streams of bitumen production, such as fly ash and coke. Therefore, in a presumed scenario of rapid and extensive deployment of renewable power generation, and increased energy storage demand via RFB, there exists a potential economical incentive to extract vanadium metal, whether directly from raw bitumen, or from other fractions along the bitumen value chain, to be used for RFB electrolytes. Currently, no commercially viable technologies exist to that end, and the main challenge to developing them is the need for selective separation of vanadium species, at high purity, from the complex petroleum (or petroleum residue) matrix. Noteworthy metals in crude oils are present in an organic form (Figure 9.8), bound within complex molecules called porphyrins [38, 39], which could possibly be leveraged to develop highly selective extraction/separation technologies, able to generate high purity vanadium streams.

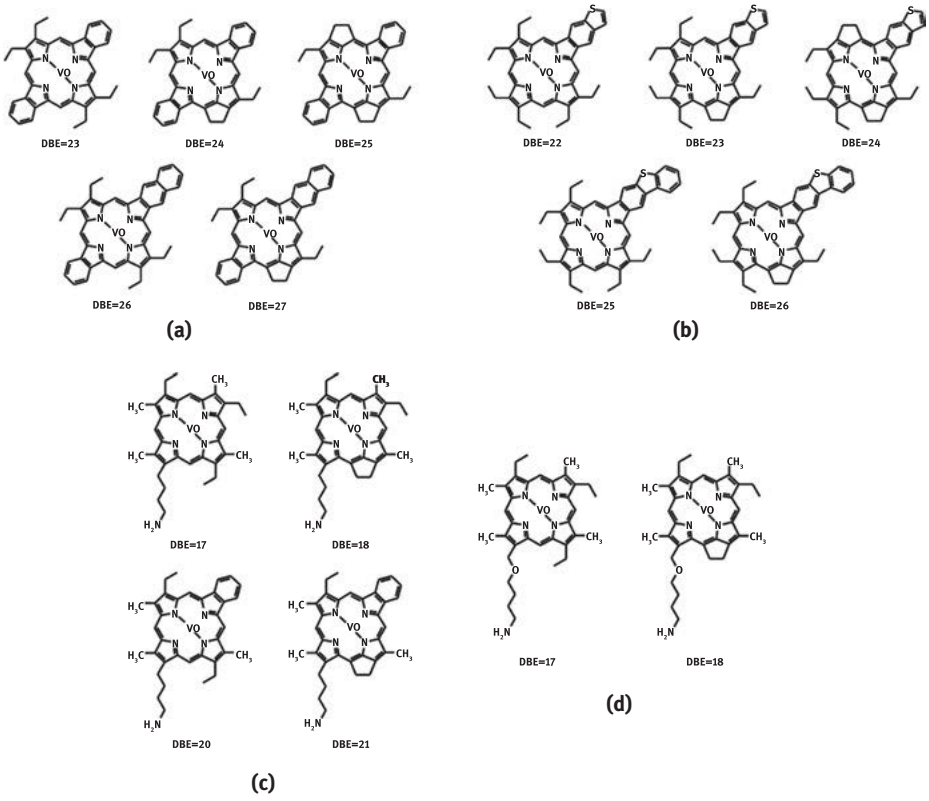

Figure 9.8: Putative structures of vanadium porphyrins in Venezuela Orinoco crude oil detected in purified fractions by FT-ICR-MS analysis. From Zhao, Shi [39] under a Creative Commons Attribution-NonCommercial-NoDerivs 4.0 International License (http://creativecommons.org/licenses/by-nc-nd/4.0/).

In addition to vanadium-based RFB energy storage solutions, in the past few years, organic and organo-metallic redox species have received increased interest because of the wider electrochemical window which can be achieved, compared to metal-based RFB, resulting in higher energy densities. Furthermore, all-organic electrolytes have lower cost, due to their higher abundance in many feedstocks, less environmental impact (e.g., no need for minerals mining), and the advantage of structural diversity, which can be used to tweak their solubility and other properties, such as operating temperature [40]. Poor solubility and limited temperature range (10–35 °C) are some of the main limitations to vanadium RFB electrolytes.

One of the most studied organic electrolytes for RFB applications are the ketone-/quinone-type molecules, such as anthraquinone disulfonic acid, AQDS, and others [40, 41]. Similar oxygen-bearing types of molecules are also found in petroleum, within the resin and asphaltene fractions. The oxygen content of petroleum is typically in the order of 0.1–1.0% by weight, whereas in the case of unconventional oils such as bitumen, concentration of oxygen species can be much higher than that, due to low maturity of oil, and/or in-reservoir biodegradation [42, 43]. Oxygen functionalities in non-hydrocarbon petroleum include hydroxyl groups, ethers, carboxyl groups, sulfur-oxygen functions, but also carbonyl moieties, such as ketones and quinones [42–45]. Ketone and quinone species have been investigated in resin and asphaltene fractions of Athabasca bitumen [44, 45], and some of them, such as 9-fluorenone, selectively extracted and quantified in oil and rock extracts [46]. Recently, similar extraction method has been adapted and applied to oil sands bitumen sample, resulting in a substantial mass fraction enriched in fluorenone, and other ketone-/quinone-type compounds [47]. Fluorenone, and other ketone-/quinone-derivatives have been used as both catholytes and anolytes in all organic and mixed (organic-inorganic) RFB, showing good redox properties and performance [40, 48].

As in the case of vanadium, purity of target organic compounds and/or compound classes derived from crude oil, remain a challenge for their use in electrochemical systems, within current technology constraints. Notwithstanding, if the demand for these types of materials grows in the future, we envision viable routes for technology development that would couple improved separation schemes for electroactive species from crude oil and bitumen streams, and more flexible RFB designs that allow the use of mixed organic and organo-metallic electrolytes [29, 49].

9.3.3 Polymers and other petroleum-derived materials

Synthetic polymers such as polyethylene, polypropylene, nylon, polyester, and polytetrafluoroethylene are some of the main end-uses for petrochemical streams of conventional downstream petroleum processing. Petroleum-based polymers found their applications in a myriad of industrial and consumer products, thanks to many desirable properties, including strength, flexibility, resistivity, chemical inertness, to name

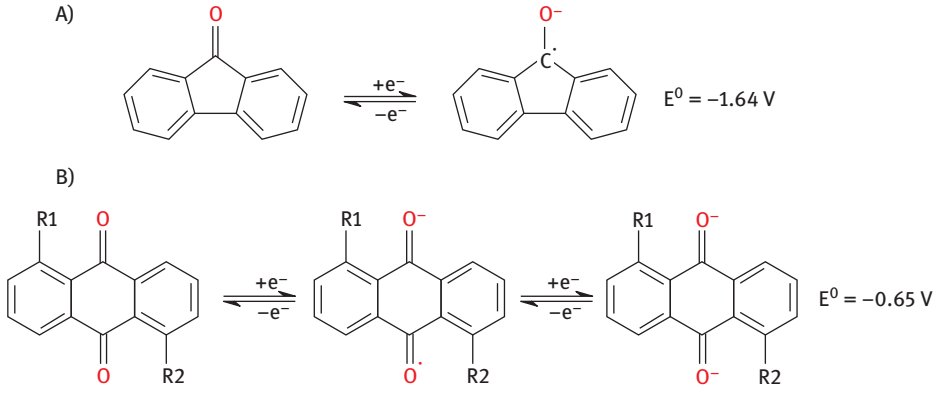

Figure 9.9: A) Fluorenone and B) anthraquinone redox pairs, these compounds have been successfully used as electrolytes in RFBs [40, 48].

a few. Asphalt, and related viscous distillation residues, have been used as binding and waterproofing agents in road and building construction for decades.

More recently, in the context of increased market competition, and more stringent life-cycle emissions criteria, the petroleum industry is looking for novel, value-added, and non-combustion uses for some of its residual, low-value product streams. That is particularly true for unconventional heavy oil and bitumen resources, as found for example in Western Canada, which are typically associated with an increased content of less desirable and valuable petroleum components, such as non-hydrocarbons (resins, asphaltenes), and sulfur.

9.3.3.1 Carbon fibers

Carbon fibers are a class of polymers that have emerged in the past few decades as high-performance materials of superior mechanical, electrical, and thermal properties, which made them suitable for specific, high-end applications in aerospace, construction, defense, and healthcare sector. More recently, promising potential of carbon fiber materials has been recognized in automotive, and renewable energy industry (e.g., wind), especially in the form of carbon fiber reinforced polymer matrix composites [50]. Thanks to these new applications, the demand for carbon fiber materials has been increasing in recent years, growing at ~ 12% annual rate, and is projected to reach up to 200,000 tons per year, by 2024 [51].

Carbon fibers comprise pyrolytic carbon (>90% carbon content) and synthesized from a suitable organic precursor [52]. Typically, high-performance carbon fibers are produced from polyacrylonitrile (PAN) as starting material that is polymerized from acrylonitrile monomers in solvent solution, out of which precursor fibers are extracted,

and then thermally treated. During the stabilization step, the fibers are oxidized at 200–300 °C in air, after which they are thermalized during high temperature (1,000–3,000 °C) carbonization/graphitization in inert atmosphere, involving dehydrogenation and removal of oxygen, nitrogen, and other non-carbon elements (Figure 9.10). Resulting carbon-rich fibers have superior material properties, most importantly higher tensile strength and elastic modulus, compared to some other materials, such as steel, titanium and aluminum alloys, or glass fibers [52, 53].

While historically PAN-based carbon fibers have their niche, high-end applications, their high price in combination with processing costs puts hard constraints to potential uses in rapidly growing, large-volume markets. Significant research and technology development efforts in the recent years have focused on alternative, more-affordable types of carbon fiber feedstocks that would allow for increased production and expanded range of end-uses for this type of materials.

For example, carbon fibers production from pitch has been investigated and commercially deployed since the 1960–1970s. The basic feedstocks for these fibers are dense, viscous, residual distillation/fractionation streams that are generated during petroleum or coal processing, generically termed "pitch." Pitch materials are enriched in non-hydrocarbons, such as asphaltenes, and condensed aromatic fractions, present in variable proportions, depending on the nature of petroleum/coal input, and thermal processing parameters (Table 9.3).

Production of pitch-based carbon fibers is similar to PAN-based process, and involves fiber spinning, heat stabilization in oxidative atmosphere, followed by high-temperature carbonization in inert atmosphere. However, unlike the PAN process that starts with consistent and uniform pure chemical feedstock (acrylonitrile), the quality of the final carbon fiber will be determined by the complex chemical properties of raw pitch materials. Generally, isotropic pitches, in which the aromatic fraction is not spatially oriented, produce a lower quality, general grade carbon fiber. On the other end, condensed aromatic cores in mesophase (also called anisotropic) pitches tend to align when subjected to heating, resulting in superior grade fiber with higher elastic modulus. Notwithstanding, even the best performing carbon fibers from mesophase pitch still lack the tensile strength of PAN-derived fibers [54] but have a much higher modulus.

Some strategies to improve properties of feedstock pitches may include pyrolysis to increase the content of condensed aromatic moieties, and/or solvent treatments that attempt to remove smaller, disordered components from isotropic pitch, while concentrating higher molecular weight, condensed aromatics that can spatially align during heating. These and similar attempts to improve the properties of raw feedstocks still struggle with the issue of residual impurities that detrimentally affect the performance of final produced fibers, both in the form of lower molecular weight hydrocarbon species, occluded within HMW fraction, but also present as heteroatom elements (sulfur and nitrogen) within the structure of highly aromatic, anisotropic molecules such as asphaltenes. This is an active and lively area of research,

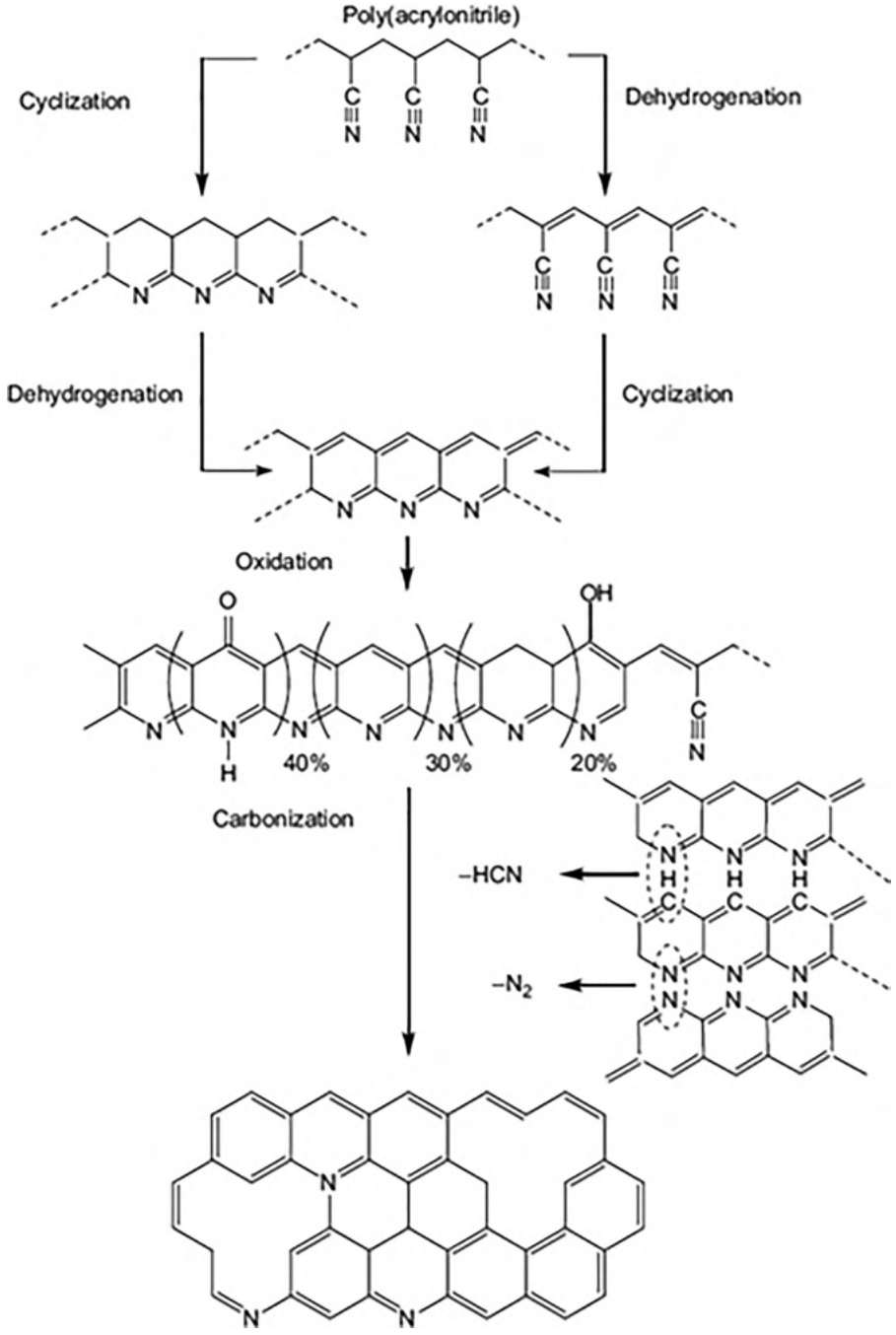

Figure 9.10: Generalized reaction pathway from PAN to a carbon phase. From Frank, Ingildeev [53] with permission.

Table 9.3: Compound class composition of some commercial petroleum pitches [54].

%	Asphaltene	Polar aromatic	Naphthene aromatic	Saturate
EXXON (DAU) bottoms (refinery sludge)	14.5	41.1	18.1	26.3
Ashland 240 petroleum pitch	64.4	8.6	25.4	1.6
Ashland 260 petroleum pitch	82.7	5.9	11.4	0

supported by industry that wants to improve the value of residual components in their value chain, in particular in production zones that rely on heavy petroleum resources [55]. For example, recently, carbon fibers were successfully synthesized from modified asphaltene feedstocks [56, 57], and we recognize a promising potential, with further technology breakthroughs in this area, to produce fibers of suitable strength and strain-to-failure properties from bitumen and similar heavy petrogenic resources. This would be a game changer because of the much lower cost of input materials that would unlock many of the high-volume applications which are currently limited due to high price of PAN-based fibers.

9.3.3.2 Sulfur-based, inverse vulcanization polymers

Elemental sulfur is produced in large amounts during petroleum refining. A main source of elemental sulfur in petroleum production is hydrogen sulfide (H_2S), a toxic gas that is present natively in crude petroleum feedstocks, but also generated during refining, in the catalytic hydrodesulfurization process which removes sulfur covalently bound within petroleum molecules as H_2S. By-product H_2S gas is then converted to elemental sulfur in the two-step Claus process, involving oxidation to SO_2, and its subsequent reaction with excess H_2S to produce elemental sulfur and water vapor [58]:

$$H_2S + 0.5\,O_2 \rightarrow SO_2 + H_2O$$

$$2H_2S + SO_2 \rightarrow 2\,H_2O + 3\,S$$

The resulting elemental sulfur can be present in various allotropic forms – S_2, S_6, and S_8, the latter being the most prevalent one.

Over the years, petroleum refining became one of the largest sources of elemental sulfur, driven by the evolving, increasingly stringent regulations of SO_x emissions from transportation fuels. At present, approximately 70 million tons of residual sulfur are generated every year globally [59]. While some of this by-product sulfur finds its end-use in the fertilizer and chemical industries, the production is still outpacing the demand, leading to increasing stockpiles of unused sulfur. The problem is particularly

notable in regions that produce heavy, sulfur-rich petroleum (Western Canada, Venezuela), and is only to become exacerbated, as additional low-sulfur fuel benchmarks are introduced to global marine shipping sector [60].

In that context, an increased research interest in recent years has been directed toward finding novel, non-combustion uses for residual elemental sulfur from petroleum production. Particularly promising is the inverse vulcanization process, in which the molten elemental sulfur is reacted with organic molecules, producing copolymers with diverse physicochemical properties that can be leveraged for various value-added applications [61]. Contrary to conventional vulcanization, wherein a small amount of sulfur acts as a crosslinker for bulk organic feedstock (polyisoprene or styrene–butadiene) to produce synthetic rubber, in the inverse vulcanization process, the opposite happens – excess elemental sulfur (50–90 wt%) reacts with a smaller fraction of polyene organic compound via free radical reaction mechanism to create thermoplastic, sulfur-dense copolymer, Figure 9.11.

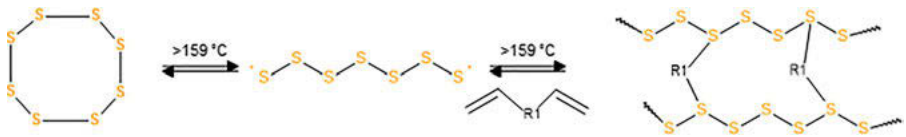

Figure 9.11: Inverse vulcanization reaction of elemental sulfur (in excess) with polyunsaturated organic cross-linker.

While free-radical sulfur (co)polymerization reactions have been reported before, they suffered from the issue of poor material stability due to depolymerization [59]. The first demonstration of inverse vulcanization reaction producing stable copolymer was achieved in 2013 using di-iso-propylbenzene (DIB) as organic cross-linker, in a solvent-free system [62]. Depending on the content of DIB in the starting mixture, the resulting polymers showed semi-crystalline (0–15% DIB) or amorphous structure (20–65% DIB) [59]. This discovery started a whole new field of material/polymer science that is booming in the past few years, and resulting in reports of novel, alternative organic cross-linkers, improved reaction chemistries (e.g., catalyzed), and new potential applications for this emerging class of sulfur-based materials [63].

In addition to sulfur, other residual petroleum streams could be thought of as feedstocks for inverse vulcanization polymerization. If needed, radiolytic and (thermo) chemical reactions can be leveraged to modify the molecular composition of petroleum fractions (e.g., increase the content of carbon–carbon double bonds), so as they become more amenable to co-polymerization with sulfur [64, 65].

In terms of promising applications of inverse vulcanization materials, one of the highly researched areas is the development of novel cathode materials for lithium-sulfur batteries (Li-S). These are a potential alternative to incumbent lithium-ion

technology, particularly for large-scale energy storage, because of much lower cost of sulfur, and higher energy density of Li-S batteries [66]. On the other hand, the main limitation to wider adoption of Li-S batteries are the detrimental material properties of elemental sulfur, such as brittleness, poor solubility, and electrical insulation. Thus, the advent of novel inverse vulcanization materials offers an opportunity to overcome many of the issues associated with elemental sulfur, through strategic design of inverse vulcanization materials that can (a) facilitate electrode fabrication via melting or solution processing, (b) improve key battery parameters including charge conductivity by incorporating conductive organic cross-linkers, (c) improve capacity retention and cycling efficiency by doping with metals and metalloids [63, 67–69].

Another interesting property of inverse vulcanization polymers is their high index of optical refraction, and transmissivity to near-infrared and mid-infrared light wavelengths [70]. This enables diverse applications in technologies such as infrared spectroscopy analytics, night vision, thermal imaging, and remote sensing, to name a few [59]. As in the case of electrode materials, lower cost of sulfur-based polymers, and their malleability are advantageous in comparison to incumbent optical materials and technologies.

In our view, bio-based inverse vulcanization polymers are particularly interesting because of their potential for large-volume applications. They are prepared from sulfur and appropriate biomaterials or other residual organic feedstocks that are either natively rich in polyunsaturated organic compounds (e.g., unsaturated oils) or can be pre-treated to increase the amount of carbon–carbon double bonds in the molecules. Some applications of bio-based sulfur polymers include construction materials from woody, or other lignocellulosic biomass [71], remediation agents that can sorb heavy metals or crude oil residues from polluted waters or soils [72], and controlled-release fertilizers [73].

One of the main limitations of inverse vulcanization process is the formation temperature of sulfur radical species at temperatures >160 °C, which constrains the selection of possible organic comonomers that do not volatilize and/or degrade at those temperatures. This can be circumvented to some extent by application of catalysts enabling efficient reactions at temperatures as low as 95–110 °C [61, 74]. Lower reaction temperatures also reduce the possibility for generation of toxic H_2S during inverse vulcanization. For large-scale applications such as construction, agriculture, environmental remediation, a better understanding of the long-term fate of inverse vulcanization materials will be needed: their material stability, potential to generate corrosive or otherwise harmful degradation products, volatilization of S-species, or their leaching to water resources, and others.

9.3.3.3 Asphalt

Asphalt is a viscous and dense bituminous material primarily used as binder (cement) mixed with construction aggregates such as gravel, sand, stone, and others to produce material suitable for road paving. A smaller portion, up to 20% of global asphalt production is consumed as waterproofing agent in building construction [75]. Asphalt is a well-established, conventional product; notwithstanding, we discuss it in this chapter, because it is expected to be a growing non-combustion end-use of petroleum resources, in particular the heavy, bituminous reserves, as found in Western Canada and elsewhere. According to some estimates, it is predicted that the size of global asphalt market will increase in the coming years, to reach about 180 million tons in 2030 [75], mainly driven by growing economies in Asia and the booming construction sector in that region.

The term "asphalt" is an operational definition for a specific heavy, residual cut produced during petroleum refining processes; typically, residuum from the atmospheric distillation is subjected to secondary, vacuum distillation to yield a product of suitable consistency to be used as asphalt [76]. Chemically, asphalt comprises a complex mixture of hydrocarbons, and should not be confused with the specific compound class of asphaltenes, as defined in the Section 2. While asphaltenes are present in asphalts, they account only for up to 20–25% (by weight) of the mixture, while the rest is made up from saturated hydrocarbons, naphthenic aromatic, and polar, heteroaromatic compounds, present in different proportions, depending on the source crude oil, Table 9.3 [76–78].

Table 9.3: Compound class composition of some petroleum asphalts and their material properties; modified from Corbett [76].

	Asphalt type		
Compound class composition (wt%)	**A**	**C**	**E**
Saturates	12	10	8.5
Naphthene aromatics	48.9	38.7	30.3
Polar aromatics	30.8	36.3	41.5
Asphaltenes	8	14.6	19.1
Asphalt properties			
Viscosity @60 °C, Poises	2,000	2,000	2,000
Viscosity @135 °C, Poises	352	445	540
Penetration @25 °C	50	85	130
Penetration ratio (4–25 °C)	24	30	41
Softening point, °C	46.1	47.2	52.2

Mechanical properties of asphalts, such as hardness, will depend on the chemical composition of different compound classes (Table 9.3) and are mainly driven by the physicochemical processes involving molecular moieties such as condensed aromatics, reactive carbon–carbon bonds, and polar, heteroatom-bearing functional groups [77, 79]. In the environment, these complex interactions are dynamically changing with seasonal temperature variations, and oxidative weathering of asphalt components, leading to progressive deterioration of paving material over time [79].

To that, research looking into improving physical and mechanical properties of asphalts is an active area of investigation. In our view, particularly relevant examples include the use of synthetic and bio-based asphalt additives [80–82] that promote co-polymerization and crosslinking processes, such as the ones involving sulfur, as discussed in the previous section. In this area of technological development, streams derived from unconventional petroleum resources that are enriched in heteroatoms and functionalized chemical species could be particularly suitable for production of advanced asphalt materials.

9.4 Conclusion and perspectives

Energy markets are rapidly moving toward a low-emissions future, driven by environmental and societal pressures of global change. Combustion hydrocarbon fuels are facing increased scrutiny and demands for improved life-cycle performance, as it relates to carbon emissions and other environmental impacts. Producers of unconventional, emissions-intensive resources, the likes of heavy oil and bitumen in Western Canada, are already experiencing difficulties to fund new developments, and access global markets. In the context of expected declining demand for petroleum-based fuels in the upcoming decades, there is an increased interest to re-think petroleum resources from a non-combustion perspective, that looks at the complex chemistry of petroleum as an opportunity to develop radically different product streams and technologies that would generate value, but without CO_2 and other negative emissions. In this chapter, we provided a high-level, nonexhaustive overview of some of those technology development routes that we have been working on, or find particularly promising, including in-reservoir energy vector approaches, production of materials used in large-scale, renewable energy storage systems, and materials with diverse applications ranging from automotive industry, and optical sensing, to construction, remediation, or agriculture. Most of them are still quite early on technology readiness scale, and may depend on other emerging, adjacent technology trends including cheaper renewable electricity, robotics, nanotechnology, and novel chemical separation technologies such as membranes, molecular adsorbents, and molecular sieves. Notwithstanding, any breakthroughs in discussed development routes could contribute to fundamental transformation of petroleum complex into a more sustainable, future-oriented sector.

References

[1] IEA. Global CO2 emissions in 2019. International energy agency, Paris, 2020.
[2] IPCC. Climate change 2014: Mitigation of climate change. contribution of working group iii to the fifth assessment report of the intergovernmental panel on climate change. Cambridge University Press, New York, NY, 2014.
[3] Parmesan C, Yohe G. A globally coherent fingerprint of climate change impacts across natural systems. Nature, 2003, 421, 37–42.
[4] BP. Energy outlook: 2020. Edition, BP plc, London, UK, 2020.
[5] BP. Statistical review of world energy. 2020, 69th ed, BP plc, London, UK, 2020.
[6] Smil V. Energy transitions: Global and national perspectives: ABC-CLIO. Santa Barbara, CA, 2016.
[7] OPEC. Annual statistical bulletin. organization of the petroleum exporting countries. OPEC, Vienna, Austria, 2019.
[8] NRC. Energy markets fact book – 2014–2015. National Resources Canada, Ottawa, Ontario, Canada, 2014.
[9] CAPP. Canadian Economic Contribution. Canada's Oil & Natural Gas Producers, Calgary, AB, Canada, 2020.
[10] US EIA. Petroleum supply annual: U.S. energy information administration. US EIA, Washington, DC, 2020.
[11] Speight JG. The chemistry and technology of petroleum. CRC press, Boca Raton, FL, 2006.
[12] Speight JG. Handbook of petroleum product analysis. John Wiley & Sons, Hoboken, NJ, 2015.
[13] Overton EB, Wade TL, Radović JR, Meyer BM, Miles MS, Larter SR. Chemical composition of Macondo and other crude oils and compositional alterations during oil spills. Oceanography, 2016, 29, 50–63.
[14] Marshall AG, Rodgers RP. Petroleomics: Chemistry of the underworld. Proceedings of the National Academy of Sciences, 2008;105:18090–18095.
[15] NAS. Spills of diluted bitumen from pipelines: A comparative study of environmental fate, effects, and response: National academies of sciences, engineering, medicine. National Academies Press., 2016.
[16] Radović JR, Oldenburg TBP, Larter SR. Chapter 19 – environmental assessment of spills related to oil exploitation in canada's oil sands region. In: Stout SA, Wang Z, eds, Oil spill environmental forensics case studies. Butterworth-Heinemann, 2018, 401–417.
[17] Rock L, O'Brien S, Tessarolo S. et al., The quest CCS project: 1st year review post start of injection. Energy Procedia, 2017, 114, 5320–5328.
[18] Rogelj J, Popp A, Calvin KV. et al., Scenarios towards limiting global mean temperature increase below 1.5 °C. Nat Clim Chang, 2018, 8, 325–332.
[19] Novotnik B, Nandy A, Venkatesan SV. et al., Can fossil fuel energy be recovered and used without any CO2 emissions to the atmosphere?. Rev Environm Sci Bio/Technol, 2020, 19, 217–240.
[20] Gates ID, Wang J. In-situ process to produce hydrogen from underground hydrocarbon reservoirs. In: Google patents. 2019.
[21] Kapadia PR, Kallos MS, Gates ID. Potential for hydrogen generation from in situ combustion of Athabasca bitumen. Fuel, 2011, 90, 2254–2265.
[22] Kapadia PR, Wang J, Kallos MS, Gates ID. Practical process design for in situ gasification of bitumen. Appl Energy, 2013, 107, 281–296.
[23] Bramadat-Willcock M. Saskatchewan pilots hydrogen to fuel the future. Canada's National Observer, Vancouver, BC, Canada, 2020.

[24] Van de Graaf T, Overland I, Scholten D, Westphal K. The new oil? The geopolitics and international governance of hydrogen. Energy Res Soc Sci, 2020, 70, 101667.
[25] Larter S, Wilhelms A, Head I. et al., The controls on the composition of biodegraded oils in the deep subsurface – part 1: Biodegradation rates in petroleum reservoirs. Org Geochem, 2003, 34, 601–613.
[26] Novotnik B, Radovic J, Nandy A, Larter SR, Strous M. Microbial metal dependent conversions of hydrocarbons for zero CO2 emission energy extraction. In: 7th international symposium on applied microbiology and molecular biology in oil systems (ISMOS-7). Halifax; 2019.
[27] Novotnik B, Zorz J, Bryant S, Strous M. The effect of dissimilatory manganese reduction on lactate fermentation and microbial community assembly. Front Microbiol, 2019, 10, 1007.
[28] Venkatesan S. An auxiliary electrode mediated membrane-free redox electrochemical cell for energy storage. Sustainable Energy Fuels, 2020, 4, 2149–2152.
[29] Venkatesan SV, Karan K, Larter S, Thangadurai V, Radovic JR. Auxiliary electrode mediated membrane-free redox electrochemical cell for energy storage. In: Google patents. 2021.
[30] Basafa M, Hawboldt K. Reservoir souring: Sulfur chemistry in offshore oil and gas reservoir fluids. J Pet Explor Prod Technol, 2019, 9, 1105–1118.
[31] Dembicki H. Practical petroleum geochemistry for exploration and production. Elsevier, Amsterdam, Netherlands, 2016.
[32] Goodwin MJ, Musa OM, Steed JW. Problems associated with sour gas in the oilfield industry and their solutions. Energy Fuels, 2015, 29, 4667–4682.
[33] Jin X, Wu J, Silva RC. et al., Alternate routes to sustainable energy recovery from fossil fuels reservoirs. Part 1. Investigation of high-temperature reactions between sulfur oxy anions and crude oil. Fuel, 2021, 302, 121050.
[34] Uzun D, Razkazova–Velkova E, Petrov K, Beschkov V. H2S/O2 fuel cells using hydrogen sulfide from Black Sea waters. J Appl Electrochem, 2016, 46, 943–949.
[35] De La Fuente J, Shor R, Larter S. Single actuator peristaltic robot for subsurface exploration and device emplacement. In: 2020 IEEE International Conference on Robotics and Automation (ICRA); 2020 31 May-31 Aug. 2020; 2020. p. 8096–8102.
[36] Clemente A, Costa-Castelló R. Redox flow batteries: a literature review oriented to automatic control. Energies, 2020, 13, 4514.
[37] Leung P, Li X, Ponce de León C, Berlouis L, Low CTJ, Walsh FC. Progress in redox flow batteries, remaining challenges and their applications in energy storage. RSC Adv, 2012, 2, 10125–10156.
[38] McKenna AM, Williams JT, Putman JC. et al., Unprecedented ultrahigh resolution FT-ICR mass spectrometry and parts-per-billion mass accuracy enable direct characterization of nickel and vanadyl porphyrins in petroleum from natural seeps. Energy Fuels, 2014, 28, 2454–2464.
[39] Zhao X, Shi Q, Gray MR, Xu C. New vanadium compounds in venezuela heavy crude oil detected by positive-ion electrospray ionization fourier transform ion cyclotron resonance mass spectrometry. Sci Rep, 2014, 4, 5373.
[40] Winsberg J, Hagemann T, Janoschka T, Hager MD, Schubert US. Redox-flow batteries: from metals to organic redox-active materials. Angew Chem Int Ed, 2017, 56, 686–711.
[41] Yang B, Murali A, Nirmalchandar A, Jayathilake B, Prakash GKS, Narayanan SR, Durable A. Inexpensive and scalable redox flow battery based on iron sulfate and anthraquinone disulfonic acid. J Electrochem Soc, 2020, 167, 060520.
[42] Speight JG. Chapter 6 – refining shale oil. In: Speight JG ed, Shale oil production processes. Boston, Gulf Professional Publishing, 2012, 139–163.
[43] Oldenburg TBP, Jones M, Huang H. et al., The controls on the composition of biodegraded oils in the deep subsurface – Part 4. Destruction and production of high molecular weight non-

hydrocarbon species and destruction of aromatic hydrocarbons during progressive in-reservoir biodegradation. Org Geochem, 2017, 114, 57–80.
[44] Moschopedis SE, Fryer JF, Speight JG. Investigation of the carbonyl functions in a resin fraction from Athabasca bitumen. Fuel, 1976, 55, 184–186.
[45] Moschopedis SE, Speight JG. Oxygen functions in asphaltenes. Fuel, 1976, 55, 334–336.
[46] Bennett B, Larter SR. The isolation, occurrence and origin of fluorenones in crude oils and rock extracts. Org Geochem, 2000, 31, 117–125.
[47] Radović J, Venkatesan S, Mannan P, Thangadurai V, Larter S. Redox active organic compounds sourced from bitumen for next generation energy systems. In: Suncor academic forum. Calgary, Canada, 2018.
[48] Wei X, Xu W, Huang J. et al., Radical compatibility with nonaqueous electrolytes and its impact on an all-organic redox flow battery. Angew Chem Int Ed, 2015, 54, 8684–8687.
[49] Lee W, Park G, Kwon Y. Alkaline aqueous organic redox flow batteries of high energy and power densities using mixed naphthoquinone derivatives. Chem Eng J, 2020, 386, 123985.
[50] Zhang J, Chevali VS, Wang H, Wang C-H. Current status of carbon fibre and carbon fibre composites recycling. Composites Part B: Eng, 2020, 193, 108053.
[51] Das S, Warren J, West D. Global Carbon Fiber Composites Supply Chain Competitiveness Analysis, Clean Energy Manufacturing Analysis Center, 2016 Archived (PDF) from the original on 29 March 2017. In: Retrieved; 2017.
[52] Endo M. Carbon fiber. In: The society of fiber S, Techno J eds, High-performance and specialty fibers: Concepts, technology and modern applications of man-made fibers for the future. Tokyo, Springer Japan, 2016, 327–342.
[53] Frank E, Ingildeev D, Buchmeiser MR. 2 – High-performance PAN-based carbon fibers and their performance requirements. In: Bhat G ed, Structure and properties of high-performance fibers. Oxford, Woodhead Publishing, 2017, 7–30.
[54] Aldosari SM, Khan M, Rahatekar S. Manufacturing carbon fibres from pitch and polyethylene blend precursors: A review. J Mat Res Technol, 2020, 9, 7786–7806.
[55] FP. Creating Carbon Fibre from Bitumen $5 Million to support Phase II of the Carbon Fibre Grand Challenge. Financial Post 2021.
[56] Ni G, Jiang W, Shen W. Chemical modification of asphaltene with SEBS as precursor for isotropic pitch-based carbon fiber. ChemistrySelect, 2019, 4, 3690–3696.
[57] Qin F, Jiang W, Ni G. et al., From coal-heavy oil co-refining residue to asphaltene-based functional carbon materials. ACS Sustain Chem Eng, 2019, 7, 4523–4531.
[58] Higman C, van der Burgt M. Gasification. Elsevier Science, Amsterdam, Netherlands, 2003.
[59] Griebel JJ, Glass RS, Char K, Pyun J. Polymerizations with elemental sulfur: A novel route to high sulfur content polymers for sustainability, energy and defense. Prog Polym Sci, 2016, 58, 90–125.
[60] Cuong NM, Hung PV. An analysis of available solutions for commercial vessels to comply with IMO strategy on low sulphur. J Internatl Marit Saf, Environl Aff Ship, 2020, 4, 40–47.
[61] Wu X, Smith JA, Petcher S. et al., Catalytic inverse vulcanization. Nat Commun, 2019, 10, 1–9.
[62] Chung WJ, Griebel JJ, Kim ET. et al., The use of elemental sulfur as an alternative feedstock for polymeric materials. Nat Chem, 2013, 5, 518–524.
[63] Chalker JM, Worthington MJH, Lundquist NA, Esdaile LJ. Synthesis and applications of polymers made by inverse vulcanization. In: Jiang X ed, Sulfur Chemistry. Cham, Springer International Publishing, 2019, 125–151.
[64] Silva RC, Snowdon LR, Huang H, Larter S. The dating of petroleum fluid residence time in subsurface reservoirs. Part 2: Tracking effects of radiolysis on crude oil by comprehensive molecular analysis. Org Geochem, 2021, 152, 104142.

[65] Xu W-w P, Rosini G, Krogh-Jespersen K. et al., Thermochemical alkane dehydrogenation catalyzed in solution without the use of a hydrogen acceptor. Cheml Commun, 1997, 23, 2273–2274.
[66] Ji X, Nazar LF. Advances in Li–S batteries. J Mater Chem, 2010, 20, 9821–9826.
[67] Chang A, Wu Q, Du X. et al., Immobilization of sulfur in microgels for lithium–sulfur battery. Cheml Commun, 2016, 52, 4525–4528.
[68] Dirlam PT, Park J, Simmonds AG. et al., Elemental sulfur and molybdenum disulfide composites for Li–S batteries with long cycle life and high-rate capability. ACS Appl Mater Interfaces, 2016, 8, 13437–13448.
[69] Gomez I, Mantione D, Leonet O, Blazquez JA, Mecerreyes D. Hybrid sulfur– selenium co-polymers as cathodic materials for lithium batteries. ChemElectroChem, 2018, 5, 260–265.
[70] Griebel JJ, Namnabat S, Kim ET. et al., New infrared transmitting material via inverse vulcanization of elemental sulfur to prepare high refractive index polymers. Adv Mater, 2014, 26, 3014–3018.
[71] Lauer MK, Karunarathna MS, Tennyson AG, Smith RC. Recyclable, sustainable, and stronger than portland cement: A composite from unseparated biomass and fossil fuel waste. Mater Adv, 2020, 1, 590–594.
[72] Crockett MP, Evans AM, Worthington MJ. et al., Sulfur-limonene polysulfide: A material synthesized entirely from industrial by-products and its use in removing toxic metals from water and soil. Angew Chem Int Ed, 2016, 55, 1714–1718.
[73] Mann M, Kruger JE, Andari F. et al., Sulfur polymer composites as controlled-release fertilisers. Org Biomol Chem, 2019, 17, 1929–1936.
[74] Zhang B, Gao H, Yan P, Petcher S, Hasell T. Inverse vulcanization below the melting point of sulfur. Mater Chem Front, 2020, 4, 669–675.
[75] Alberta Innovates. Bitumen beyond combustion – phase 2 report: Stantec consulting. Stantec Consulting, Edmonton, AB, Canada, 2017.
[76] Corbett LW. Refinery processing of asphalt cement. Transp Res Rec, 1984, 999, 1–6.
[77] Halstead WJ. Relation of asphalt chemistry to physical properties and specifications. Virginia Transportation Research Council, Charlottesville, VA, 1984.
[78] Manolis S. Engineering properties of asphalt cement binders and their relation to pavement performance: royal military college of Canada. Coco Paving Inc., Kingston, Ontario, Canada, 2014.
[79] Liu M. The effects of asphalt fractional composition on properties. Texas A&M University, Texas, 1996.
[80] Bao D-X, Yu -Y-Y, Zhao Q-M. Evaluation of the chemical composition and rheological properties of bio-asphalt from different biomass sources. Road Mater Pavement Des, 2020, 21, 1829–1843.
[81] Jiang X, Li P, Ding Z, Wang A, Bing H, Zhang J. Thermochemical liquefaction of wheat straw and its effectiveness as an extender for asphalt binders: Characterization of liquefied products and potential opportunities. Constr Build Mater, 2021, 305, 124769.
[82] Zhang F, Hu C. Physical and rheological properties of crumb rubber/ styrene–butadiene–styrene compound modified asphalts. Polym Compos, 2017, 38, 1918–1927.

R. Paul Philp, Gregory T. Connock

10 Biomarkers in crude oils

Abstract: Biomarkers have played a critical role in hydrocarbon exploration and production for the better part of the past half century. Their evolution can be traced to the development of analytical techniques that started to become commercially available in the late 1960s to early 1970s. These techniques, based on gas chromatography and mass spectrometry, permitted separation and identification of an ever-increasing number of biomarkers awaiting determination. Developments in this area have continued to this day and now provide the ability to demonstrate the presence of hydrocarbons ranging up to C_{120} in crude oils and a wide variety of polar compounds containing O, S, and/or N atoms. Not all of these compounds may be authentic biomarkers that can be traced back to a functionalized precursor occurring in a living system, but they may still provide information of use in unraveling the origin and history of a crude oil.

Biomarkers can provide information on the nature of source, maturity, depositional environments, biodegradation, geologic age, and migration pathways. This type of information is useful to the explorationist when obtained from a crude oil since it then permits the nature of the source rock to be established and develop a framework for the petroleum system. Furthermore, biomarker fingerprints provide critical information used in oil/oil and oil/source rock correlations.

In this chapter, major families of biomarkers in crude oils will be described. It is not meant to be an exhaustive review but rather a document that provides an overview to the interested geologist, geophysicist, or engineer of the power biomarkers possess when applied to petroleum system problems. While biomarkers in source rocks are not discussed in this chapter, the presence of biomarkers in source rocks may be comparably interpreted and applied.

10.1 Introduction

Crude oils are complex mixtures of varying proportions of hundreds of thousands of organic, as well as certain organometallic compounds such as metalloporphyrins. In 1927, prior to development of the sophisticated analytical techniques available today, an extensive project (API Project 6) was launched to study and identify hydrocarbon constituents of a representative petroleum from the Brett No. 6 well (Ponca City, Oklahoma). This ambitious project required exhaustive fractionation,

R. Paul Philp, Gregory T. Connock, School of Geosciences, University of Oklahoma, Norman, OK 73019, e-mail: pphilp@ou.edu

https://doi.org/10.1515/9783110694529-010

including five forms of distillation, two forms of extraction, four forms of adsorption, two forms of crystallization, and two forms of separation using molecular sieves. By the time the project ended in the mid-1960s, 295 compounds had been identified but hundreds of thousands of compounds remained unidentified and still do today despite new and sophisticated technology[1]. Currently, the most commonly used technique for the identification of organic compounds, and more specifically biomarkers, is gas chromatography-mass spectrometry (GCMS) or related techniques. GCMS emerged as a commercially available technique in the 1970s following many years of development work, particularly in the laboratories of Biemann [2] at MIT and Burlingame at University of California[3]. The technique has evolved significantly since the mid-1960s/early 1970s, but despite continued development it still involves separation (GC) and identification (MS). More recent techniques have evolved, such as Fourier transform ion cyclotron resonance mass spectrometry (FTICRMS) that has elucidated previously uncharacterized molecular compositions of a large number of high-molecular-weight polar compounds [4–7]. FTICRMS may permit the molecular compositions of many new compounds to be determined but positively identifying the structures of every compound is an exhausting and almost impossible task. The problem is further exacerbated by multiple isomeric structures for a given molecular formula. While isomers increase the complexity of the oils or extracts, they also increase the quantity of available geochemical information available related to maturity or mixing of oils from different sources. Lower carbon number compounds may only have two or three isomeric structures, but it was shown many years ago that as the carbon number of a molecule increases so does the number of possible isomers as summarized below. Not all of these isomers will exist, but this clearly indicates the nature and extent of the problem in comprehensive compound delineation in a crude oil.

- C1- 1 isomer
- C2- 1 isomer
- C6- 5 isomers
- C10- 75 isomers
- C20- 366,319 isomers
- C30- 4,111,846,763 isomers
- C40- 62,491,178,805,831 isomers

Another significant analytical advance in recent years has been the combination of 2D gas chromatography coupled with time-of-flight (TOF) mass spectrometry which has provided further evidence for the complexity of crude oils, particularly the “hump,” or unresolved complex mixture (UCM), present in so many oils and readily apparent

in heavily weathered oils [8, 9]. Even if it was possible to identify all the compounds in one crude oil, valuable insight may not be readily forthcoming since crude oil compositions are quite variable and dependent upon the nature of the source material deposited millions of years ago.

Despite the lack of identity of the majority of compounds in crude oils, many families of compounds have been identified that are of significant use in areas related to exploration and production. From a geochemical perspective, in much of the work related to exploration and determination of the source, maturity, depositional environment, or geological age of the oil, oftentimes a compound of interest may remain unidentified for several years. However, if a specific compound can be associated with a specific source of organic matter, its presence in another oil is taken to indicate a similar input of organic matter, even if the compound remains unidentified.

The purpose of this chapter is relatively specific in that it will primarily review compounds present in crude oils that are referred to as biomarkers. Biomarkers are compounds in crude oils (and source rocks) with carbon skeletons that can be related back to their functionalized precursor molecules present in the original source material deposited in a sedimentary environment many millions of years ago. A classic example would be the relationship between a sterol and sterane. The precursor being the sterol which is converted into the sterane following diagenesis and maturation of the organic matter.

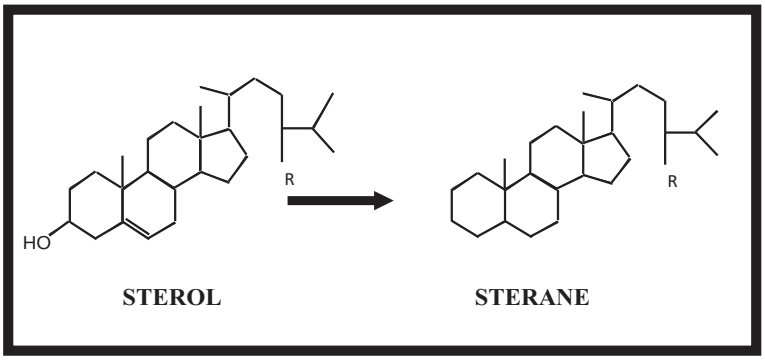

Detection, identification, and utilization of these compounds have become an important part of any exploration effort [10] as well as in reservoir characterization and production [11–13]. Biomarkers can provide information related to source materials responsible for generation of a crude oil, maturity, level of biodegradation, depositional environments, migration pathways, geologic age of an oil, and oil/oil and oil/source rock correlations [10]. This information is a very important part of any exploration study since most conventional exploration efforts are directed toward finding the oil, not source rocks. In unconventional systems source is even more important since the source rock in many cases is also the reservoir rock. Information that can be

obtained from the biomarkers in crude oils can be used to infer the nature of the source rocks responsible for generating the crude oil. If source rocks can be identified and located, migration pathways can be predicted and additional traps or reservoirs along migration pathways identified.

The majority of organic compounds in crude oils are hydrocarbons and basically fall into two categories, aliphatic and aromatic. Numerous heteroatomic compounds containing N, S, and O atoms, along with organometallic compounds such as porphyrins are also present in relatively lower concentrations [14, 15]. The relative proportions of these compounds reflect the origin and history of the crude oils starting from the distribution of the organic source materials and the nature of the depositional environment into which the organic material was deposited. Following burial, diagenesis and thermal alteration of the organic source material, three major products are possible, namely, crude oil, gas, or coal. (Since the title of this monograph is *Chemistry of Crude Oils and Petroleum Products*, the discussion in this chapter will only cover crude oils and will not discuss characteristics of coals, natural gas or source rocks.) For a crude oil this is simply a starting point in its history. After generation, expulsion, and migration to a reservoir or surface seep, multiple processes, such as migrational fractionation, biodegradation, water washing, thermochemical sulfate reduction, or thermal alteration, can impact the composition of the oil that is ultimately discovered and produced.

As a result of the factors mentioned above, crude oils can have a wide variety of characteristics, or properties, and may range from very light condensate type products to very heavily degraded crude oils dominated by asphaltic material. The ways in which crude oils are characterized have changed significantly over time following the earliest discoveries of crude oils both in the USA and many other countries. It is difficult to accurately pin down when oil was first discovered in the world, but it certainly predated the discovery in this [USA] country in the 1850s. The roots of petroleum geochemistry go back to the nineteenth century, but mankind certainly knew of the occurrence and some forms of petroleum as early as 3800 BC with bitumen blocks from the Dead Sea being used for trading purposes even earlier around 5000 BC [1]. Indigenous people in many countries have used oil from seeps for a variety of purposes, such as sealing baskets or medicinal purposes, for many centuries. Naturally in those ancient times no-one knew, or really cared for that matter, where the oil came from or how it was formed. Early British explorers in Burma discovered a flourishing oil extraction industry in the town of Yenangyaung in 1795 which had over 500 hand dug wells at that time, with oil first exported from Burma in 1853. Many early discoveries were associated with wells that had been dug in the search for water and accidently discovered shallow oil accumulations. The first oil well in Poland was hand dug in 1853 in the village of Bobrka, and for the first time a petroleum derived product originating from that oil was used for the purposes of lighting. Edward Doheny also dug a well by hand on a tar seep, ultimately discovering the Los Angeles City oil field in 1892. The last half of the nineteenth century saw the early development of a petroleum

industry in what became the USSR, particularly in the Baku region of Azerbaijan. The first discovery and production of oil in North America was at Oilsprings, Ontario, Canada, in 1858. Early uses of petroleum included sealants, illuminants, lubricants, and products for medicinal purposes. The US petroleum industry started in 1859 with the drilling of the Drake well at an oil seep near Titusville, Pennsylvania. This well produced about 25 bbl/day from a sandstone reservoir ~ 69.5 ft below the surface [1].

In the late 1800s, changes were afoot once it was realized that products could be obtained from crude oils, by simple distillation processes, that could replace whale oil as a source of heat and light [17]. Early oil exploration and well placement were determined as much by luck as science and the origin of oil was still not understood. Many wells were drilled in areas where seeps had been observed but, as we know today, that certainly did not guarantee success in finding large reserves of crude oil. The introduction of the automobile in the early 1900s undoubtedly fueled the thirst for discovering additional reserves of crude oil from which gasoline could be produced. Early gasolines were straight distillation products from crude oils and, in many cases, very light crude oils, or condensates, were used directly to fuel the automobile. In the same period groundbreaking developments such as seismic reflection surveys greatly increased the exploration success rate [18].

Production from this US industry increased at an astonishing rate, reaching a maximum of 9.6 million bbl/day in 1970 and 13 million bbl/day in 2020. Worldwide oil production was 23.17 million bbl/day in July 2020. Much of the recent increase in US production has resulted from unconventional production which has increased exponentially over the past decade. In an unconventional system the crude is often generated in place and does not migrate significant distances from the source rock as typically happens in a conventional petroleum system. As a result, it is necessary to utilize hydrofracking to release the oil trapped in these rocks, which have very low permeability preventing the oil from being expelled and migrating to conventional reservoirs [16]. Despite this significant difference between conventional and unconventional resources, biomarkers remain paramount in petroleum characterization, as well as confirming the origin and history of the oil.

Despite increasing exploration success in the late 1800s and early 1900s, an understanding of processes involved in formation of crude oils was very limited. Refineries were starting to become more complex, and more exploration companies being formed, major discoveries were being made in the early to mid-1900s, but the origin and history of crude oils were not foremost in most people's minds. Various theories started to appear that discussed the origin of crude oils, such as the abiogenic origin of crude oils strongly favored by various Russian geoscientists [19, 20] and theories such as formation of crude oils in recent sediments without the need for burial or heat [21], a theory that prevailed into the early 1970s in some companies. However, in the 1967 World Petroleum Congress, McIver [22] put forward the revolutionary theory that kerogen was a key intermediate in the formation of crude oils. The term "kerogen" (from the Latin meaning "oil or gas forming") had been

introduced several years previously and referred to the insoluble organic matter in source rocks. Methods of formation of kerogen have been widely discussed in the literature and many mechanisms proposed for its formation [15, 23]. However it is now widely accepted that there is no one well-defined chemical structure for kerogen but rather it is primarily composed of insoluble residues from the organic matter deposited in the original depositional environments and recognizable as macerals (i.e. recognizable and identifiable fragments of organic matter derived from a variety of source such a plants, algae, fungi etc.) under the microscope [24].

Characterization of kerogens through a wide variety of techniques has led to an understanding that the maceral content of kerogen will play a key role in determining the nature of the product(s) that can be generated from the different kerogen types [14, 23, 25]. This has also led to a comprehensive understanding of the role of the depositional environment in preserving organic matter as it is being deposited and buried and undergoing thermal alteration to generate crude oil. In the early 1900s, an understanding of the processes involved in formation of crude oils was improving and more sophisticated exploration techniques were being developed. In addition, methods were starting to evolve that would improve efforts to elucidate the composition of crude oils. Initially much of this development was related to the refinery processes. The value of a crude oil lies in the relative proportions of different products that can be produced from distillation processes at a refinery, with gasoline being the major money-making product. Heavily biodegraded crude oils, such as high asphaltene, high sulfur and high metal content oils, are less valuable than lighter nondegraded crude oils with low sulfur and asphaltene content.

For many years dating back to the early 1900s, it was recognized that there were certain compounds in crude oils that could be associated with certain specific types of organic matter. However, at that time analytical techniques were very limited and it was the remarkable work of Alfred Treibs in the 1920s/1930s that led to the identification of compounds, with very complex tetrapyrrole structures, known as porphyrins in crude oils [26]. He was able to show structural similarities between porphyrins and naturally occurring chlorophylls, revealing the biological origins of crude oil for the first time and ruling out any potential abiogenic formation pathways. After many more years, and based on Treibs's original work, Eglinton and Calvin [28] formally introduced the concept of chemical fossils, which, after several iterations, became known as biomarkers

The study of biomarkers developed exponentially following the early concepts proposed by Eglinton and Calvin [28] as a result of developments in the field of analytical chemistry, particularly gas chromatography (GC) and gas chromatography-mass spectrometry (GCMS). The number of source specific biomarkers identified in crude oils that could be used to indicate the nature of source material responsible for a crude oil increased dramatically [29]. With time, additional uses for these compounds as indicators of maturity, nature of the depositional environment, migration pathways, age dating, and biodegradation became commonplace. Today, widespread

utilization of biomarkers has spread from the major oil companies to many smaller oil companies who have seen the added value of using this approach as part of their exploration programs.

Since these compounds are an integral part of virtually all crude oils, this chapter will review the utilization of many common classes of biomarkers along with some compound classes that may not be true biomarkers. However, unclear or unknown biological origins do not preclude a compound from becoming widely used in petroleum studies as will be highlighted in the coming sections.

10.2 Analytical techniques

It is important to note that developments in analytical techniques have played a major role in the discovery and characterization of biomarkers. The initial commercial availability of the combined GCMS systems in the late 1960s/early 1970s catalyzed the development of the biomarker concept. Biomarkers are generally present in relatively low concentrations and, apart from *n*-alkanes, pristane and phytane, are not detectable by GC alone. GC simply provides a separation mechanism while mass spectrometry provides the identification. All the developed techniques have evolved to improve the degree of separation and the ability to detect and identify compounds at increasingly lower concentrations, as well as more polar compounds and higher molecular weight compounds. Since that time, many developments and advances have occurred in this approach such as gas chromatography-mass spectrometry mass spectrometry (GC-MSMS), 2D gas chromatography-time of flight mass spectrometry (2DGC-TOF), liquid chromatography-mass spectrometry (LC-MS), and, more recently, gas chromatography-inductively coupled plasma-mass spectrometry (GC-ICP-MS), and Fourier transform-ion cyclotron resonance-mass spectrometry (FT-ICR-MS). These developments have enabled the discovery and characterization of a much wider range of biomarkers including polar compounds and high-molecular-weight hydrocarbons (HMWHCs) that can be used to improve our understanding of the origin and history of crude oils. However, in this chapter the focus is not the analytical developments but rather the biomarkers discovered using these techniques. Despite all the significant developments in analytical techniques described above, the vast majority of biomarker analyses are still undertaken using conventional GC-MS and GC-MSMS. The majority of analyses are undertaken in the multiple ion detection mode using ions characteristic of the various biomarker families. These methods are discussed in multiple publications along with the use of GC-MSMS to obtain an additional level of separation and improved structural characterization and identification of biomarkers [30–32].

10.3 Crude oil composition

Crude oils have a wide range of compositions, resulting primarily from their original organic source materials and secondly from processes impacting their composition after expulsion from the source rock. Crude oils from unconventional systems show the same level of variability in composition as conventional crude oils. The major difference between conventional and unconventional oils is related to the generation and accumulation processes. Unconventional oils are generated and accumulate within the source rock [16], whereas in a conventional system the oil is expelled from the source rock and migrates to a reservoir. Tissot and Welte [14] summarized data from a representative worldwide set of over 500 oils and noted a wide range of chemical compositions. A ternary diagram illustrating these variations shows that the compositions can vary from oils that contain very abundant *n*-alkanes to the those that are heavily biodegraded or at low maturity and dominated by the heavier asphaltic fraction (Figure 10.1).

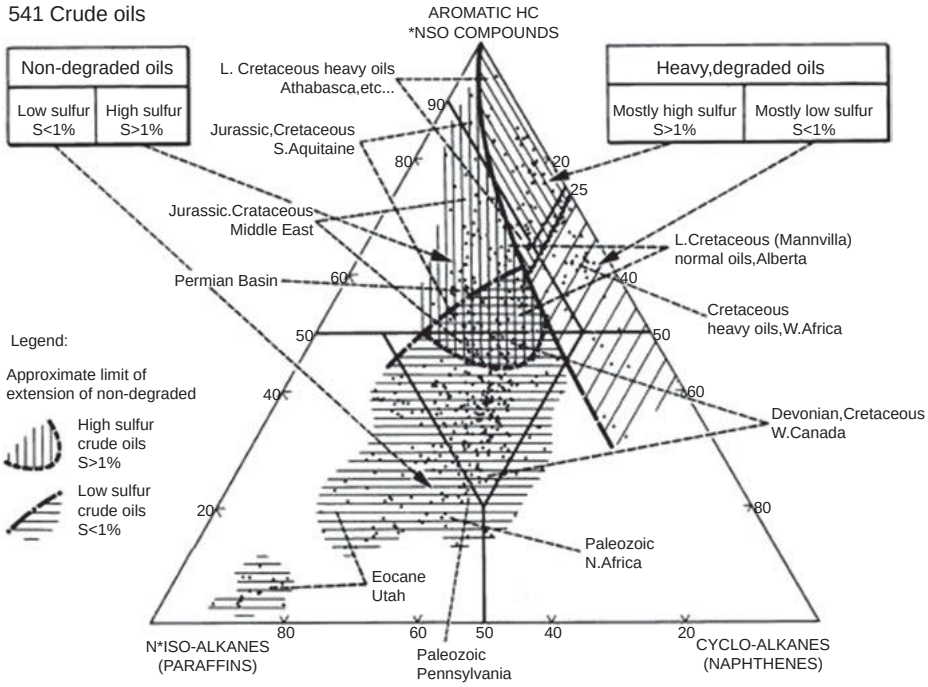

Figure 10.1: The ternary diagram shows the relative proportions of paraffins, naphthenes, and aromatics in 541 oils collected from locations around the world. The purpose of the diagram originally published by Tissot and Welte [14] illustrates the variability of crude oil compositions resulting from a variety of factors including source, maturity, and biodegradation. Reproduced with permission from Tissot and Welte [14].

In general, a large proportion of unaltered crude oils are dominated by *n*-alkanes ranging from methane to alkanes with carbon numbers around C_{40}. However, the higher carbon number, C_{40}, is somewhat misleading since it is primarily limited by analytical techniques, particularly gas chromatographic conditions. In reality, application of appropriate chromatographic conditions will reveal that many oils have hydrocarbons extending to C_{120}, albeit in progressively lower concentrations with increasing carbon number [33–35] (Figure 10.2). At the other extreme are the very light oils, or condensates, that may only contain hydrocarbons in a very narrow range covering a few carbon numbers up to approximately C_{15}. One of the most common factors influencing the alteration of a crude oil is biodegradation. The impact of biodegradation is most commonly manifested by the removal of the *n*-alkanes starting with the lower carbon numbered alkanes and subsequently removing higher carbon numbered compounds leading to heavily degraded oils dominated by an unresolved complex mixture (UCM) of branched and cyclic compounds [36, 37]. As discussed below, it should also be noted that many heavily degraded oils will contain HMWHCs above C_{40} that are often overlooked through the use of conventional analytical methods, yet are readily measured via high-temperature gas chromatography (HTGC). *n*-alkanes above C_{40} are very resistant to biodegradation and their relative concentrations will increase in heavily biodegraded oils [38].

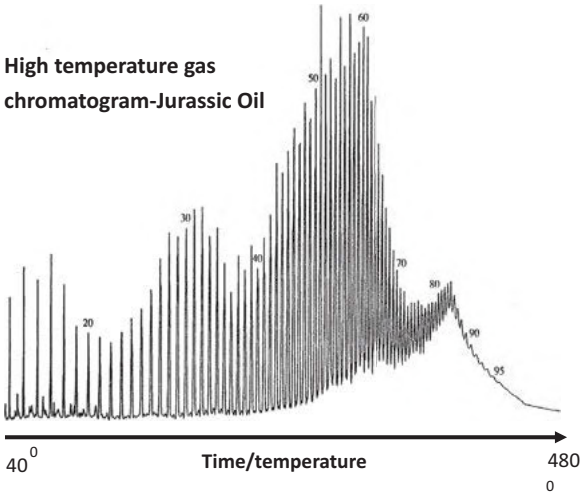

Figure 10.2: The high-temperature gas chromatogram shown here is from a Jurassic carbonate oil from the Middle East. It illustrates the fact that although alkanes in crude oils are often shown to extend to around C_{40}, many oils contain varying proportions of hydrocarbons that extend to at least C_{120} [33–35].

The major focus of this chapter is related to the presence of biomarkers in crude oils and their utilization for providing information on the origin and history of crude oils.

For a conventional crude oil the various classes of biomarkers occur over certain carbon number ranges in the oil as shown in Figure 10.3. As a consequence, it is clear that not all crude oils will contain the complete range of biomarkers. Very light condensates are virtually devoid of all common classes of biomarkers, while lower carbon numbered biomarkers are often absent in very heavy and altered oils will be devoid of the lower carbon numbered biomarkers. It should also be noted that the concentrations of most biomarkers are relatively low in crude oils and will decrease in concentration with increasing maturity [10]. With increasing maturity many biomarkers are thermally degraded to lower carbon numbered analogues or converted to aromatized counterparts. The *n*-alkanes provide a classic example of the thermal cracking process. A conventional crude oil may contain *n*-alkanes dominated by those extending to C_{40} but with increasing maturity these *n*-alkanes will be cracked into lower carbon homologues which in turn can undergo further cracking. With this in mind an oil that was originally a waxy oil dominated by the long chain *n*-alkanes may ultimately be converted into a light oil or condensate dominated by alkanes in the C_1 to C_{15} range.

Many biomarkers are used to monitor maturity, but it should be mentioned that the majority of biomarker maturity parameters are only operative until the middle of the oil window. By that time many have reached equilibrium values and start to undergo degradation or aromatization reactions.

It is also important to add a note of caution related to many of the commonly used maturity parameters that are generally monitored using relative concentrations and not absolute concentrations of individual biomarkers. The 20*S*/20*S* + 20*R* maturity parameter derived from the steranes can be used to illustrate this point. This ratio will increase as a result of increasing maturity until it reaches an equilibrium value [39]. Using relative concentrations, it is commonly assumed the ratio changes as a result of the 20*S* epimer increasing at the expense of the 20*R* epimer. However, in the absence of an internal standard and absolute concentrations, it is impossible to distinguish between that interpretation and an interpretation that results from the 20*R* epimer being degraded more rapidly than the 20*S* sterane. Ideally, internal standards and absolute concentrations should be used when calculating these maturity parameters [40].

10.4 Biomarkers in crude oils

The study of biomarkers expanded exponentially in the late 1960s to 1980s along with a parallel development in the techniques used to monitor their distributions in crude oils and source rocks. The growth in the number of biomarkers discovered and identified in those years was clearly illustrated in an article published by Mackenzie et al. [29] and reproduced in Figure 10.4. Since that time new biomarkers have continued to

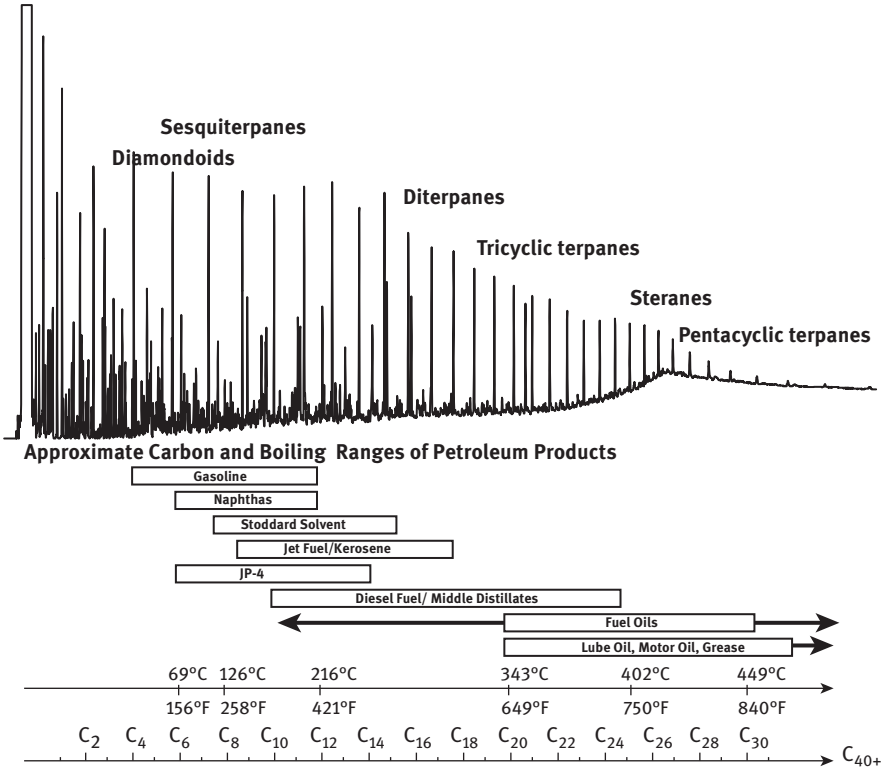

Figure 10.3: A conventional crude oil chromatogram showing the distribution of the *n*-alkanes along with the regions where you expect the common classes of biomarkers discussed herein to elute. Various petroleum products derived from crude oils and their boiling points are also shown at the bottom of the figure.

be identified and applications continue to increase. In exploration studies, biomarkers are used extensively to obtain information related to source input, depositional environments, maturity, age dating, migration, biodegradation, oil/oil, and oil/source rock correlations. Biomarkers also play an important role in environmental investigations in order to determine possible origins of crude oil releases [41]. Furthermore, many refined products also contain partial distributions of biomarkers which can play a role in evaluating the origin of refined product spills.

In the following sections, the major families of biomarkers will be reviewed along with some examples of the most significant information that can be obtained from these and related compounds. It should be mentioned that similar information is also available from the presence of these compounds in source rock extracts. Source rocks will not be discussed in this chapter, but a number of review articles and monographs are available to provide additional information [10].

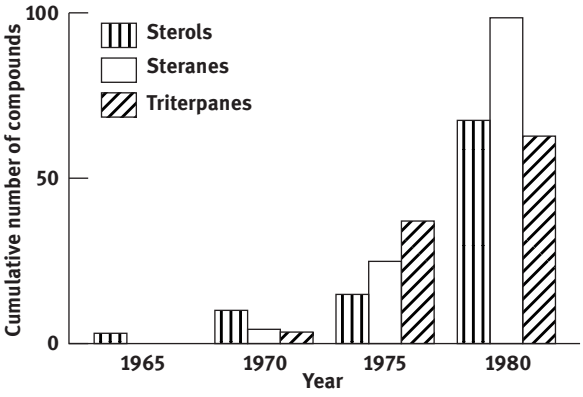

Figure 10.4: A diagram originally by Mackenzie et al. [29] showing the exponential growth in the number of biomarkers that were identified in the 1970s. This rapid growth was directly related to the development and commercial availability of GCMS systems. Reproduced with permission from Mackenzie et al. [29].

10.4.1 Porphyrins

In the light of the historical significance of the finding, it is proposed to initially discuss porphyrins since the discovery and identification of these compounds by Alfred Treibs [26, 27] provided the foundation for contemporary biomarker investigations. These compounds were studied and utilized extensively in the 1970s/1980s but, due to the rather tedious extraction and analytical procedures, lost some of their popularity after that time. More recently with improved analytical techniques there would appear to be a reemergence of these compounds in various aspects of exploration. It should be noted that porphyrins are tetrapyrroles, occurring as either free bases or organometallic compounds (more common in crude oils) containing Ni or V, or other metals in lower concentrations. The metal concentrations are much higher in heavily biodegraded oils and one of the reasons heavily degraded oils are less-desirable products due to the impact of metals on the catalysts used in refining processes.

The porphyrins present in petroleum are predominantly chelated to metals, primarily as VO- or Ni-complexes that form during source rock diagenesis [42] (Figure 10.5) known as metalloporphyrins. The derivation of these metalloporphyrins from chlorophylls was initially proposed by Treibs [26, 27] and later confirmed by observations of chlorophyll degradation [43]. The massive gap in time between these two studies underscores the nature of porphyrin investigations, which are often disconnected in time due to a dependence on analytical advances as previously mentioned. However, porphyrins continue to lag other biomarkers in terms of development due to the extensive preparatory procedures (e.g., processing/purification/isolation) for analysis present to this day. Porphyrins are still not readily analyzed by the commonly used

GCMS methods but typically require some form of liquid chromatography coupled with mass spectrometry for analysis and identification. Furthermore, the porphyrin mixtures in crude oils are very complex mixtures. In addition to the occurrence of Ni and V porphyrins, there are structurally different deoxyphylloerythroetioporphyrins (DPEP), etioporphyrins (ETIO), and bicycloalkanoporphyrin (BiCAP), free-base and metalloporphyrins (e.g., Ni and V, but also Zn, Cu, and other metals), as well as benzoporphyrins. For each individual member of the series there are multiple isomers that are not completely chromatographically resolvable precluding confident identification of alkylation patterns and potential correlations to specific chlorophylls. The porphyrin structure in Figure 10.5 can be used to illustrate this point. The tetrapyrrole rings contain multiple alkyl-substituents which can be arranged in multiple configurations leading to a large number of isomers for any one carbon number. In many of the early publications the porphyrins were assigned the ETIO and DPEP configurations and carbon numbers with no indication of the individual structural isomers present at each carbon number. Despite these challenges, a brief review on the potential applications and significance of porphyrins, primarily in the form of metalloporphyrins, will be provided. When preparatory and/or analytical methods inevitably improve, as well as widely accepted standards being readily available, it will be critical to leverage past investigations to accelerate the application of porphyrins in the petroleum industry.

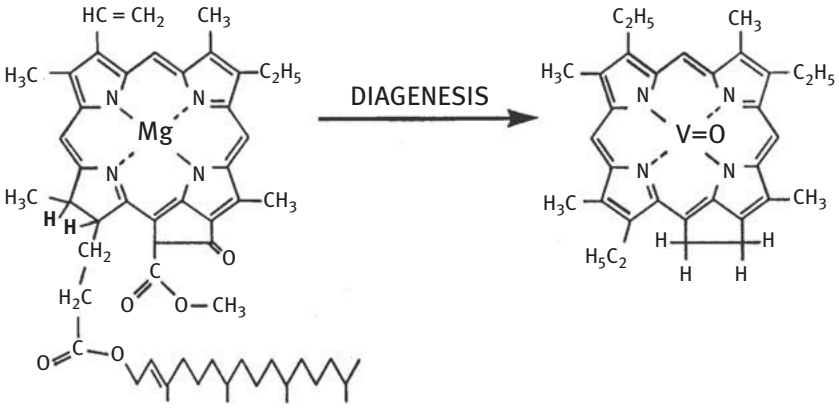

Chlorophyll - a
BIOLOGIC PIGMENT

Vanadyl
Deoxophylloerythro-
etioporphyrin (DPEP)
GEOLOGIC PIGMENT

Figure 10.5: Treibs [26, 27] established the relationship between chlorophyll in biological systems and porphyrins in geological systems. This established the biological origin of crude oils and was the birth of the biomarker concept.

The allure of characterizing the porphyrin contents of a petroleum lies in the fact they are fossil chlorophylls, a record of the main contributors to the organic matter preserved in source rocks. In addition, the redox state of the water column (e.g., oxic vs. anoxic) will influence the availability of certain metals (e.g., V, Ni) for chelation with free base tetrapyrroles during diagenesis [44]. Thus, past efforts attempting to utilize porphyrins as a tool in petroleum applications has relied on leveraging these two relatively well-constrained ideas. For example, a classification scheme was devised by Barwise [45] which employed VO- and Ni-porphyrins, as well as other geochemical parameters. It was found the ratio of V/Ni, primarily comprising metalloporphyrins, was relatively unaltered from source rock to oil, and, thus, a potentially useful tool in oil-source correlations. The V/Ni ratio is still used extensively today both for correlation purposes and also providing information on the redox state of the depositional environment [44]. This is because determination of the V/Ni ratio does not require isolation of the porphyrins from the oil but can be measured by simply combusting a sample of the oil and then measuring the V/Ni ratio in the residual ash. Other studies found variable success with similar applications [46–48], substantiating the fingerprinting capabilities of metalloporphyrins. By comparable logic, later efforts proposed that porphyrin concentrations were also a function of paleoproductivity, with different source rocks deposited under contrasting productivity levels [49]. The extent to which this is preserved in the oil is unconstrained and compounded by known maturity effects on porphyrin species [50, 51, 53]. However, it has been reported porphyrins are more or less decomposed by ~ 0.8 R_o, ultimately limiting their use from early to peak oil window [53]. In spite of the apparent decomposition of the porphyrins by the peak oil window, two maturity parameters were developed based on various porphyrins in the 1980s and used quite extensively at that time. As shown in Figure 10.5, DPEP porphyrins have a 5-membered ring attached to the tetrapyrrole structure, but ETIO porphyrins (not shown) do not have that 5-membered ring. Baker and Louda [42] noted the DPEP/ETIO ratio decreased with increasing maturity. Initially it was assumed that was as a result of the ring opening in the DPEP porphyrins with increasing maturity. However, it was also suggested changes in this ratio may also result from differential stability of the two classes of porphyrins or preferential release of ETIO porphyrins from the kerogen with increasing maturity. The second porphyrin maturity parameter (PMP) was more specific in the sense that it was based on the ratio of C_{28}ETIO/(C_{28}ETIO + C_{32}DPEP) porphyrins [54]. This ratio has a value of 0.2 indicating the onset of oil generation followed by a sharp increase in the value with increasing maturity. The exact mechanism for the increase in this parameter was not determined at the time [49, 50]. Unfortunately as with much of the other porphyrin work in the 1980s progress has virtually stopped primarily due to analytic issues. It is to be hoped that in the future with the availability of many new analytical techniques, more convenient and less time-consuming methods will become more widely available and interest in the porphyrins will be revitalized.

It may be noted that many of the cited works above are limited to the 1980s and 1990s, with a review by Chicarelli and Maxwell [55] reviewing the same potential utility of porphyrins in petroleum applications as discussed here. This reflects a similar gap in analytical abilities that separated the initial hypothesis of porphyrin formation from chlorophylls and its subsequent confirmation decades later. Much study today subjects porphyrins to isotopic analysis (both C and N) as a tool to reconstruct the microbial ecology and biogeochemical cycling at critical points in Earth history [56–58]. However, these investigations are not entirely applicable for leveraging metalloporphyrins in petroleum.

To summarize, metalloporphyrins may serve as useful oil–oil and oil–source correlation tools, proxies to reconstruct the depositional environment of unknown source facies, and as relative indicators of maturity. For example, the presence of intact metalloporphyrins in a petroleum sample, combined with high V/Ni values, will provide critical information pertaining to the source rock. In this instance, the source rock has likely not exceeded a R_o of 0.8 and was deposited in relatively euxinic (i.e., sulfidic) bottom waters. Thus, the porphyrins remain underutilized and poorly understood biomarkers, not for a lack of utility but rather a lack of analytical capability. Until methods are developed that involve comparable, or less, sample preparation and provide the similar ease of identification associated with GC-amenable biomarkers (e.g., steranes), the porphyrins will continue as the one-hit wonder that led to the inception of molecular geochemistry but was unable to keep pace with the more conventional biomarkers that dominate the field today.

10.4.2 Acyclic hydrocarbons

10.4.2.1 C_1–C_7 light hydrocarbons

Hydrocarbons in crude oils start at C_1 (methane) and generally contain an abundance of light hydrocarbons in the C_1–C_7 range in varying concentrations depending on the source and maturity of the crude oil. The individual compounds, up to C_7, while not traditionally thought of as biomarkers, have been used to provide significant information on the history of the oil, particularly thermal history, as well as extensive use in reservoir continuity studies. Care has to be taken in the way in which samples are handled prior to any analytical work since the distributions of these compounds can readily change through evaporation. A typical distribution of the light hydrocarbons in a crude oil is shown in Figure 10.6. Over the years many ratios and cross plots have been developed particularly those based on the work of Thompson [59–62] related to identification of migrational fractionation, Mango [63, 64] on maturity related issues, and Halpern [65] related to reservoir continuity studies. Many of these compounds are not conventional biomarkers but in view of their abundance and widespread use

it is important to mention their significance in an article of this nature (Figures 10.4 and 10.5).

Thompson [61] proposed a number of parameters that could be used to monitor the process of what was initially called evaporative fractionation but more recently referred to as migrational fractionation. This process refers to the presence of condensate-like products in relatively shallow reservoirs in the absence of maturity levels needed to generate such products. Seals in over-pressured reservoirs are breached, with fractionation occurring during leakage and preferential release of *n*-alkanes over aromatic compounds. The escaped products are enhanced in lighter *n*-alkanes and the residual oil enriched in lighter aromatic compounds and the longer chain *n*-alkanes. The released products migrate to reservoirs present at shallower depths where they appear as condensates even in the absence of any mature source rocks in the area. A cross plot of aromaticity versus paraffinicity was developed to assist in recognition of this process and is commonly referred to as the Thompson plot (Figure 10.7). Mango [63, 64] developed a number of maturity parameters which were utilized in crossplots referred to as Mango plots and based on the C_7 hydrocarbons (Figure 10.8). The C_7 compounds exist as many isomers and are widely used since they represent the highest carbon number where all the structural isomers for a particular carbon number can be separated chromatographically (Figure 10.6).

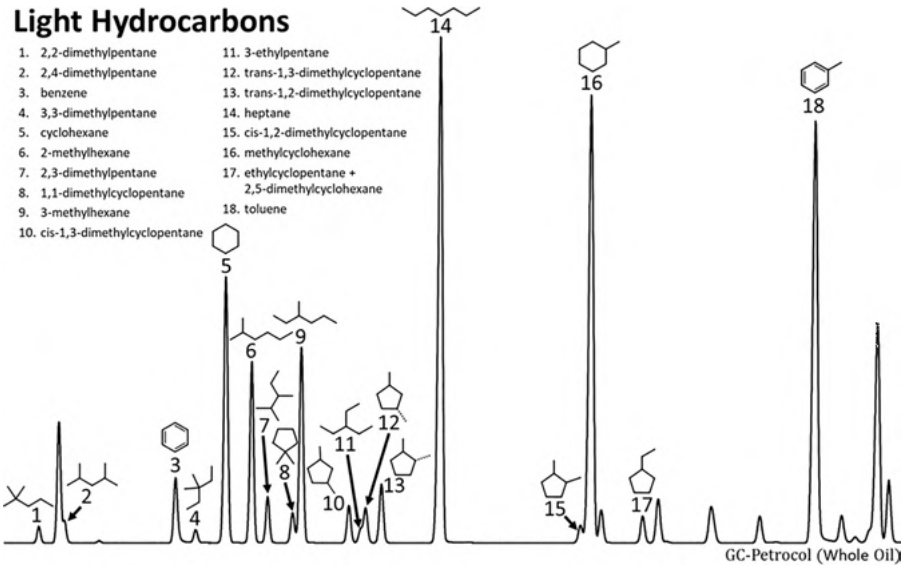

Figure 10.6: Many crude oils are dominated by the light hydrocarbons from C_1 to C_{10}. Of particular interest are the so called C_7 compounds that have been used for a variety of purposes in terms of characterizing the crude oils. C_7 is the highest carbon number where it is possible to separate all of the isomers that exist with seven carbons as shown on this chromatogram.

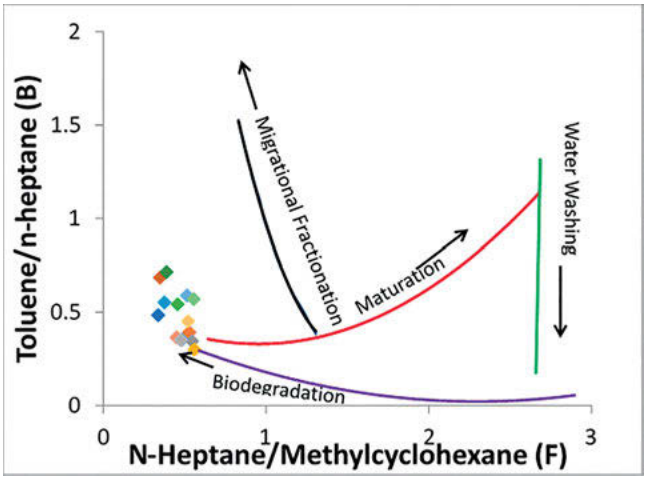

Figure 10.7: The cross plot of aromaticity (toluene/*n*-heptane) versus *n*-heptane/methylcyclohexane is often referred to as the Thompson plot. The plot provides information indicating processes that may have impacted the oil in the reservoir such as biodegradation, migrational fractionation, maturation, and water washing.

Reservoir geochemistry rose to prominence in the 1990s [66]. There were many geochemical applications used in reservoir geochemistry, but a primary application was the use of light hydrocarbons to evaluate whether or not there was continuity between different blocks within a reservoir [67]. For the most part this was based on ratios determined from a random assortment of light hydrocarbons and plotting the ratios on a star diagram. If the plots for two oils from the same reservoir were dissimilar it was concluded those oils were not in communication. Halpern [65] introduced a more formal approach using two sets of known C_7 compounds, one being referred to as correlation parameters and the other transformation ratios. The latter set reflecting changes that might have resulted from alteration effects such as biodegradation or water-washing. Both of these approaches are still widely used today in conventional reservoir continuity studies.

10.4.2.2 *n*C_8–C_{40} alkanes

In the development of petroleum geochemistry starting in the early 1960s, the major analytical tool available was the gas chromatograph. It was rather basic at the time with 3 ft analytical columns compared to the 100 m columns available today or the 30 m columns used for routine analyzes. However, this meant for the most part that the primary groups of compounds that could be analyzed were *n*-alkanes and

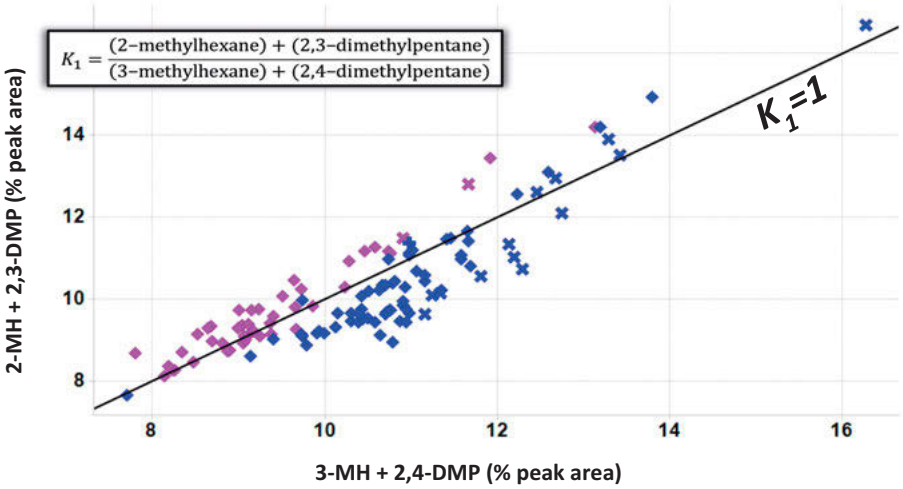

Figure 10.8: This is an example of a Mango plot which illustrates that oils from the same source exhibit invariance in isoheptane ratios. In this example increasing deviation from non-altered oils reflects increasing alteration by thermochemical sulfate reduction (TSR).

isoprenoids, primarily pristane and phytane. Despite this limitation much significant information evolved from those early studies.

Bray and Evans [68] published one of the first papers related to the distribution of *n*-alkanes in crude oils and source rock extracts. It was recognized that very immature samples were dominated by a homologous series of *n*-alkanes ranging basically from C_1 to C_{40}. Distributions of the alkanes were found to vary depending on the nature of the source material. Oils dominated by marine source material were defined by the presence of *n*-alkanes in the lower carbon number range (C_{15}–C_{23}), whereas those with a predominance of higher plant material typically had a waxy distributions of *n*-alkanes in the C_{23}–C_{33} region primarily derived from leaf waxes [69]. Very immature samples contained a predominance of odd numbered *n*-alkanes over even numbered *n*-alkanes as a result of biosynthetic pathways responsible for the formation of these compounds. With increasing maturity it was noted that the relative proportions of odd/even *n*-alkanes trended to a value of 1 leading to the first geochemical maturity parameter, odd/even predominance (OEP) or carbon preference index (CPI), that is still used extensively today [68, 70]. It is now recognized that the *n*-alkane distributions will change as a result of various processes such as biodegradation, maturity, lithology, and, to a lesser degree, migration. Biodegradation preferentially removes the *n*-alkanes, under both aerobic and anaerobic conditions, starting with the lower carbon number compounds [71–73]. Maturity tends to lead to cracking of the longer chain compounds increasing the relative proportion of the shorter chain compounds. Lithology is most noticeable for carbonate derived oils that typically have

a predominance of even numbered alkanes over odd-numbered alkanes for reasons uncharacterized.

10.4.2.3 nC_{40}–C_{120} alkanes and high-molecular-weight hydrocarbons

In general, most papers related to *n*-alkanes report data obtained using conventional gas chromatography columns which limit the range of detectable *n*-alkanes up to approximately C_{40}. However, by using high-temperature GC columns it is possible to extend the range of hydrocarbons to approximately C_{120} [33, 34] (Figure 10.9). These HMWHCs are present in most conventional oils in varying concentrations and can exacerbate production problems resulting from wax accumulation. The HMWHCs can be mixtures of a variety of *n*-alkanes, methylbranched alkanes, alkylcyclopentanes, alkyl-cyclohexanes, alkylbenzenes, and alkyltoluenes. Variations in the distributions of these compounds have been used to provide information of the depositional environment in selected cases [35]. It is also important to note that it has been shown these compounds are far more resistant to biodegradation than the lower carbon number compounds and those above C_{50} appear to be almost totally resistant to biodegradation [38]. Characterization of the HMWHCs is not as widespread as the lower carbon number compounds due to the more restricted use of high-temperature gas chromatographic analyses.

10.4.3 Isoprenoids

The two most widely used isoprenoids, pristane (Pr), and phytane (Ph), were initially determined by GC alone since they were easily detected without the need for mass spectrometry (Figure 10.10). Following their initial discovery, the Pr/Ph ratio was proposed and became the first biomarker ratio related to interpreting the oxicity of depositional environments [75]. This ratio is still widely used today, although additional controls on the ratio have been discovered through time. One of the most significant changes related to the initial misinterpretation of the Pr/Ph ratio assumed that both compounds were derived from a common precursor, namely, chlorophyll. However, it has been subsequently shown that there are other potential sources for both compounds [76] with this confirmed through the use of carbon isotopes [77]. Incorporation of the isotopes into the analytical scheme showed, in some cases, the compounds were isotopically distinct from each other and hence derived from separate sources. Goosens et al. [76] showed, via pyrolysis, that tocopherol was a precursor to pris-1-ene and further work by Rontani et al. [78] substantiated the initial work. Despite these possible complications, the ratio is still used extensively today for correlation purposes as well as interpreting the redox potential of the depositional + environment [74]. One such application involves ratios of Pr/*n*-C_{17} and Ph/*n*-C_{18}, initially proposed

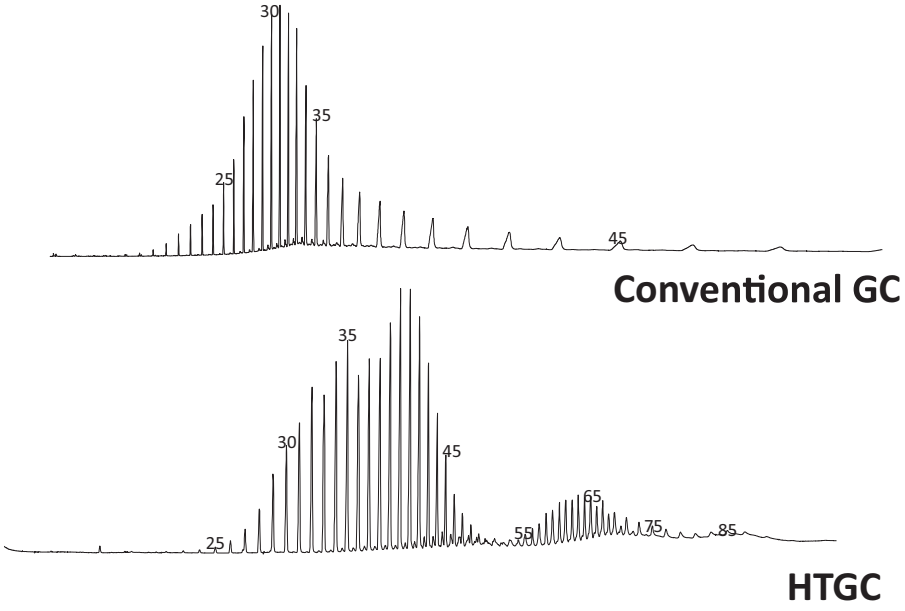

Figure 10.9: A comparison between a sample analyzed by conventional gas chromatography versus the same sample analyzed by high-temperature gas chromatography. These chromatograms illustrate the fact that in many samples, particularly waxy oils, a significant proportion of the higher carbon numbered hydrocarbons may not be determined by conventional GC.

by Shanmugam [79]. The cross plot of these ratios has been not only used for correlation purposes and an indication of whether samples are biodegraded or affected by maturity, but also may provide information pertaining to the kerogen type from which the oil was originally sourced as shown in Figure 10.11.

Pr and Ph can easily be detected by GC, but the remaining biomarkers require the use of GCMS for their detection starting with the higher carbon number isoprenoids. Detection of these and other biomarkers utilizes GCMS through selected ion monitoring of characteristic ions for each compound class. This is now a standard technique and will not be described in detail in this chapter. There are three series of isoprenoids that have been reported in crude oils. The most abundant isoprenoids are the regular head-to-tail series, followed by the head-to-head and tail-to-tail series, with the latter primarily related to pigment degradation/diagenetic products such as carotane and lycopane.

The head-to-tail series of isoprenoids extends to around C_{45} in many oils [80] as does the tail-to-tail series, although the head-to-tail series being most abundant. The higher carbon numbered isoprenoids have not been utilized extensively because of the need to use GCMS to detect these compounds. Variations in the relative proportions of the longer chain isoprenoids result from maturity changes. Moldowan and

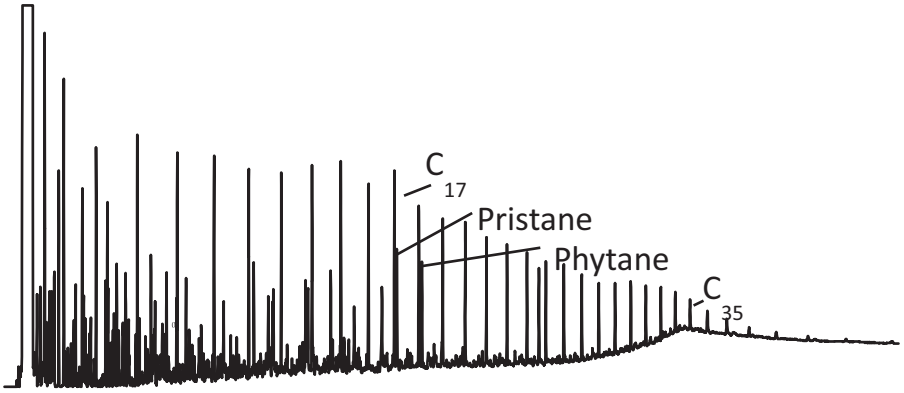

Figure 10.10: A conventional crude oil gas chromatogram. Note the presence of the isoprenoids, pristane and phytane that elute adjacent to the *n*-C_{17} and *n*-C_{18} respectively. The majority of biomarkers cannot be determined by GC alone and require the combination of GCMS for their successful detection and identification.

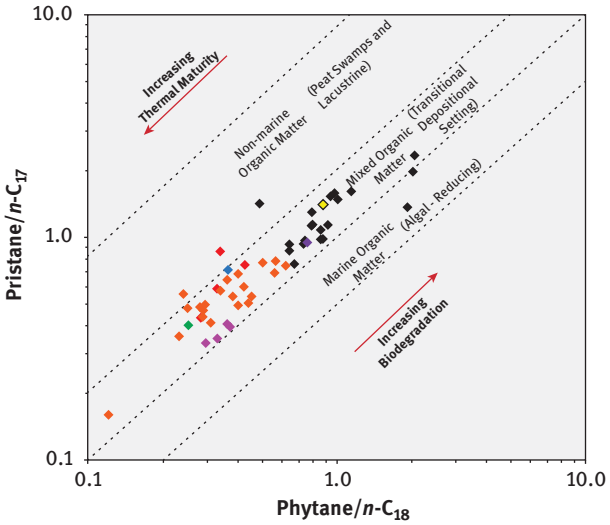

Figure 10.11: The cross plot of Pr/C_{19} versus Ph/C_{18} is commonly used to provide information related to the source of crude oils along with information related to relative levels of biodegradation and influence of maturity[79]. In can also be used to preliminary establish relationships between families of oils.

Seifert [81] originally proposed the higher carbon number head-to-head compounds were derived from archaebacteria (Figure 10.12). The higher carbon number regular isoprenoids are also derived from bacteria but have also been reported to occur in higher plant sources [82, 83].

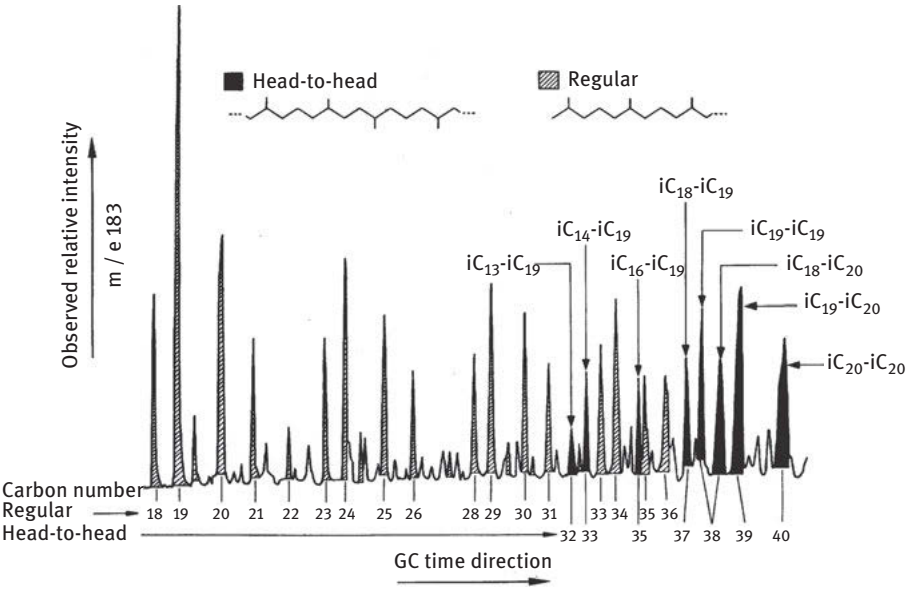

Figure 10.12: The isoprenoids, pristane and phytane, are easily determined by GC. However, use of GCMS and monitoring the *m/z* 183 ion indicates the presence of a mixture of isoprenoids extending to at least C_{40} as illustrated in this diagram [81]. Reproduced with permission from Seifert and Moldowan [81] .

10.4.4 Terpanes

Terpanes are among the most widely studied family of biomarkers present in crude oils. The terpane family includes bicyclic, tricyclic, tetracyclic, pentacyclic, and, to a limited extent, hexacyclic compounds. Each of these exists as a homologous series with varying numbers of members, isomers, and epimers. It is impossible to discuss and review all of these compounds in a chapter of this nature, and therefore a number of key items of information will be included along with a number of important references where additional information can be found.

10.4.4.1 Bicyclic terpanes (i.e., sesquiterpanes)

Sesquiterpanes are bicyclic terpanes in the C_{14}–C_{16} range with a typical distribution shown in Figure 10.13. The majority of these compounds have been identified with the most commonly utilized compounds being the drimanes and eudesmane. The former has been proposed to be derived from microbial sources and the latter from higher plants [84]. These compounds are relatively volatile, and fractionation may lead to

their loss through volatilization, but with care they can also be used for correlation purposes as well as providing limited source related information. Isomers have been detected for the drimanes, but the use of changes in the isomer distributions as a maturity parameter is very limited given one isomer for each compound exists once the oil window is reached. As an example of how novel biomarkers continue to be discovered, a study by Rodriguez and Philp [85] identified a novel sesquiterpene in oil samples from the Aman Trough, Indonesia, whose origin and significance remain to be determined. However, its presence in oils derived from source rocks containing a significantly higher plant content would suggest this novel compound is almost certainly a higher plant indicator.

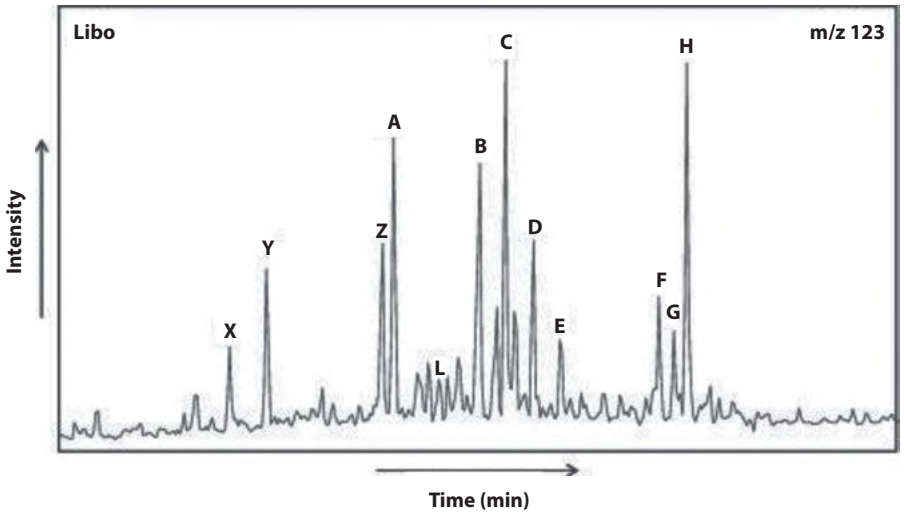

Figure 10.13: Sesquiterpanes are determined by GCMS and monitoring the ion at *m*/*z* 123. This example from an Indonesian oil illustrates the typical mixture commonly observed in many crude oils. The dominant components in many oils are drimane (C) and homodrimane (H) as well as eudesmane (E). In this sample, a previously unreported compound was identified (Z). The structure of this compound remains unknown but can still be used for correlation purposes.

10.4.4.2 Tricyclic terpanes (i.e., cheilanthanes)

Tricyclic terpanes are common constituents of most crude oils, although their relative concentrations are highly variable and depend upon a number of factors. The source(s) of tricyclic terpanes remain enigmatic, although suggestions regarding their origin have been proposed, such as *Tasmanites*, but no precursor molecules have been unambiguously identified to date. The tricyclic terpanes exist as a homologous series from C_{19} with reports [86] showing they could extend to C_{75}, and possibly higher but in most oils tricyclic terpanes to C_{29} are clearly evident and beyond that point they

are overwhelmed by the hopanes (Figure 10.14). The higher carbon number members of the series can be observed either through extensive fractionation [87] or through the use of GCMSMS. In recent years many oils, particularly unconventional oils, have been observed that are dominated by tricyclic terpanes with either no apparent hopane content or very low relative concentrations of hopanes [88] (Figure 10.14). A possible explanation for this involves preferential generation of hopanes over tricyclic terpanes at lower levels of maturity leading to a depletion of residual hopane precursors at higher levels of maturity. This in turn will lead to a predominance of tricyclic terpanes being generated at higher levels of maturity resulting in the terpane fingerprint similar to that shown in Figure 10.15 [88].

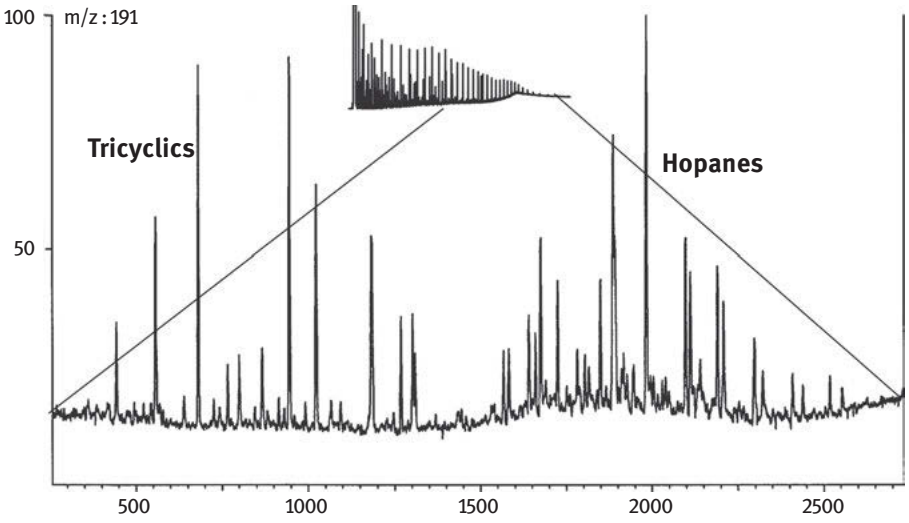

Figure 10.14: The presence of terpanes in crude oils is monitored by the ion at m/z 191. This example shows a typical terpane chromatogram which is generally dominated by tricyclic terpanes and pentacyclic terpanes. Variations in the distributions of the individual compounds will occur as a result of variations in source, depositional environments, maturity and biodegradation .

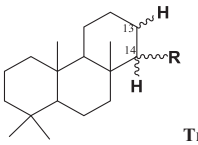

Tricyclic Terpane

Tricyclic terpanes can exist as four possible stereoisomers at C_{13} and C_{14} and multiple optical isomers. The stereochemical configurations are: 13α(H),14α(H); 13α(H),14β(H); 13β(H),14α(H); 13β(H),14β(H). Once the oil window is reached only one of the four series of stereoisomers is found to exist, namely, 13β(H),14α(H). The optical isomers

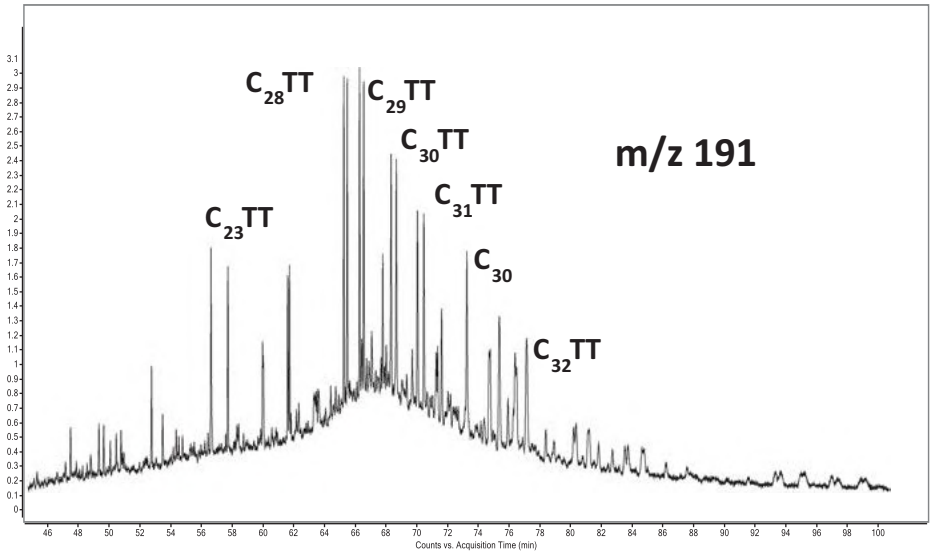

Figure 10.15: There are a relatively small number of reports in the literature that show terpane chromatograms dominated by the tricyclic terpanes. These distributions are thought to result from preferential generation of hopanes at lower levels of maturity leading to a predominance of tricyclic terpanes in oils generated at higher levels of maturity, particularly in unconventional reservoirs.

result from the presence of optically active carbon atoms in the side chain starting with the C_{25} member of the series. The first optically active carbon is C_{22} and then every fifth carbon is an additionally optically active C atom. The absence of a known source(s) precludes the use of these compounds for source determination but variations in relative proportions of individual homologs have been extensively used to obtain information on the nature of the depositional environment and source rock lithology. A comprehensive summary of the tricyclic ratios developed for use in exploration studies can be found in the Biomarker Guide [10]. To illustrate these applications two examples of the cross plots are shown in Figure 10.16a and b. The second plot (Figure 10.16b) depicts a combination of a tricyclic terpane ratio and a hopane ratio. Regions on these plots can be assigned to oils derived from source materials deposited in certain depositional environments. The precursors of the tricyclic terpanes remain elusive, but the divisions on the plots such as these are based on numerous empirical observations involving many oils that have been assigned to certain depositional environments using more source specific biomarkers. This is also important since the source rock is unknown in many exploration investigations, but using information derived from the oils it may grant insight into the nature and characteristics of the source rock.

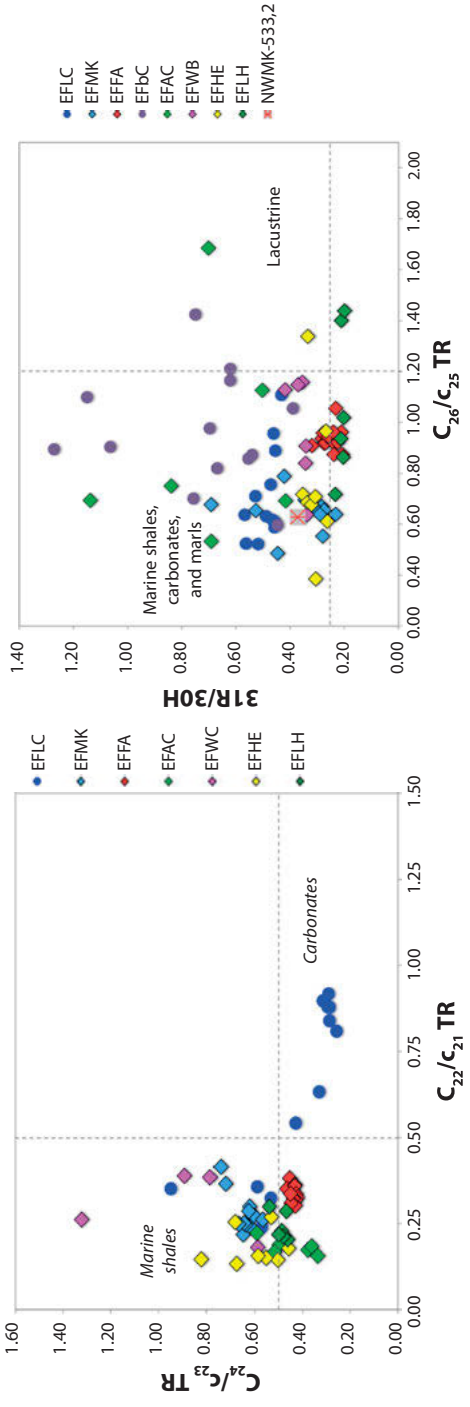

Figure 10.16: There a number of ratios based on tricyclic terpanes as well as combined tricyclic terpane and hopane ratio that used extensively to provide information of the source rock lithology and source material primarily responsible for the oils.

10.4.4.3 Tetracyclic terpanes

Two groups of tetracyclic terpanes are commonly present in crude oils. The most commonly reported tetracyclic terpane is the C_{24} 17,21-secohopane which elutes adjacent to the C_{26} tricyclic terpanes. Initially this compound was thought to be related to terrigenous source material [89] but is now interpreted as being indicative of an oxic/sub-oxic depositional environment. It is also the most abundant member of a homologous series of tetracyclic terpanes from C_{24} to C_{27} with C_{24} being the most abundant and easily observable [90]. The C_{24} tetracyclic terpane can be seen on the chromatograms shown in Figure 10.14, but the higher homologues are typically not visible in the *m/z* 191 chromatograms and require GCMSMS to be observed.

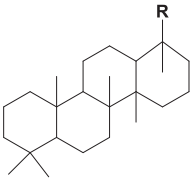

Tetracyclic Terpane

In addition to the secohopanes, several degraded C_{24} terpanes derived from higher plant biomarkers such as oleanane and lupane have been reported in Tertiary age oils that are known to be derived from source rocks containing abundant higher plant source material [91]. Generally, these compounds are not used extensively for source evaluation but in cases where the abundance of oleanane and lupane are relatively low, the presence of these compounds may provide additional evidence for the input of higher plant material.

10.4.4.4 Hopanes (i.e., pentacyclic terpanes)

The hopane family was one of the earliest families of biomarkers studied and utilized in petroleum geochemistry [92]. A typical hopane distribution is shown in Figure 10.14. Generally, the hopanes are dominated by the C_{30} hopane and are present as a series from C_{27} to C_{35}. The C_{30} parent hopane hydrocarbon structure is shown below. It has been firmly established this family of "regular" hopanes is derived from functionalized precursors occurring in bacteria [93, 94]. In addition to the primary series of hopanes, ranging from C_{27} to C_{35}, and in some cases C_{40} [95], there are multiple families of related compounds, including 30-norhopanes, 25-norhopanes, diahopanes, secohopanes, methylhopanes, hexacyclic hopanes, benzohopanes, rearranged hopanes, and others [10]. Not all families of hopanes are present in every oil since their presence will depend on a number of factors primarily related to maturity, depositional environment, and biodegradation. However, since they are all sourced from

precursors present in bacteria, their use as source indicators is limited. Certain families such as 25-norhopanes reflect episodes of biodegradation, 30-norhopanes, and benzohopanes are both associated with carbonate lithologies, diahopanes, and other rearranged hopanes are generally considered to indicate clay-rich shales. In addition, many ratios involving individual hopanes have also evolved, such as the ratio of 18α(H)-trisnorhopane/17α(H)-trisnorhopane (Ts/Tm) which can reflect both maturity and/or depositional environment as well as being a useful correlation parameter [96]; 17α(H)-norhopane(C_{29})/17α(H)-hopane(C_{30}) when >1 is taken to indicate a carbonate source. Within each family of hopanes there are multiple isomers and epimers which have been incorporated into ratios that relative changes in maturity. Hopanes can exist as four possible stereoisomers, but only two of these isomeric structures are commonly observed in crude oils, namely, the dominant 17α(H),21β(H) series and minor series of 17β(H),21α(H) moretanes. The other two series, 17α(H),21α(H) and 17β(H),21β(H), are generally only observed in low maturity or immature source rock extracts, not oils. The most commonly used maturity parameters based on the hopanes are the 22S/22S + 22 R ratio and the ratio of the 17α(H),21β(H)-hopanes/17β(H),21α(H)-moretanes, both of which increase with increasing maturity. Another hopane parameter is commonly referred to as the homohopane index (Figure 10.17), which is the ratio of the 22S and R epimers of each individual extended homohopane to the sum of the total extended homohopanes: i.e., 22*S* + 22*R*-C_{35}-pentakishomohopanes/22*S* + 22*R*-C_{31}–C_{35} extended homohopanes [97]. A comparison of these values can be used to differentiate oils sourced from different organic facies. If the C_{35} homohopane ratio is greater than the C_{34} homohopane ratio it is generally indicative of an oil derived from a marine source rock deposited under highly reducing conditions (Figure 10.17) [98, 99].

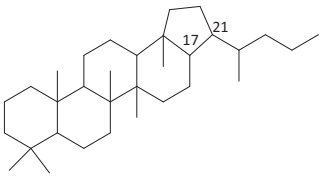

Hopane

The rearranged hopanes are one of the more underappreciated tools at a geochemist's disposal. Four series of rearranged hopanes have been identified since the 1970s (Figure 10.18). The original series of rearranged hopanes, that has been known for many years, would be the 18α(H)-neohopane series.

Originally, only the C_{27} member was identified, but now it is known that this family exists as a homologous series ranging from C_{27} to C_{35} in a manner analogous to the regular hopanes. The ratio of the C_{27}1α(H)/C_{27}17α(H) (Ts/Tm) has long been used as a maturity indicator if it is known the samples under consideration are from a common source (Seifert and Moldowan, 1978). Alternatively, if a series of samples of similar maturity are under investigation, then variations in this value reflect differences in source and depositional environment. Initially only the C_{27} compounds were used

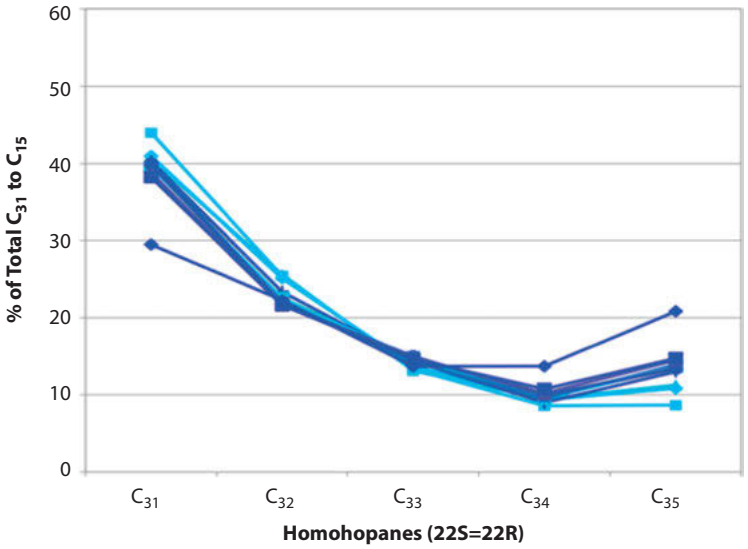

Figure 10.17: The homohopane indices are based on the relative concentration of an extended homohopane relative to the total extended homohopanes. These values as shown can be plotted in this manner to establish correlations within groups of oils. In addition, samples that have elevated values of the C_{35} homohopane index relative to the C_{34} value typically result from organic material deposited in highly reducing depositional environments, typically marine settings.

for this purpose but in recent years the same ratio based on the C_{29} compounds has been used to provide supporting data. The next series of rearranged hopanes to be discovered was the 17α(H)-diahopanes with the C_{30} member being the most abundant and first identified member of the series [89, 100]. As with the Ts series it has now been shown to exist as a homologous series in the same manner as the regular hopanes. The third series of rearranged hopanes has been tentatively identified as 9,15-dimethyl-25,27-bisnohopanes [101] after previously being observed, but not identified, by Farrimond and Telnaes [102] with the C_{30} member again being the most abundant.

The final and generally least abundant family of rearranged hopanes is the 28-norspergulanes (21-methyl-28,30-*dinor*-hopane) identified by Nytoft and others [103]. In this series the C_{29} member is the most abundant member and although the complete homologous series has not been identified, the C_{30} and C_{31} members have also been identified. The 28-norspergulanes are present in a wide variety of oils, particularly oils that also high relatively high concentrations of diahopanes and neohopanes. The 28-norspergulanes have also been observed to be present in relatively high concentrations in lacustrine oils from SE Asia. This series is typically determined by monitoring the ion at m/z 369 rather than m/z 191 that is commonly used for all the other hopane families.

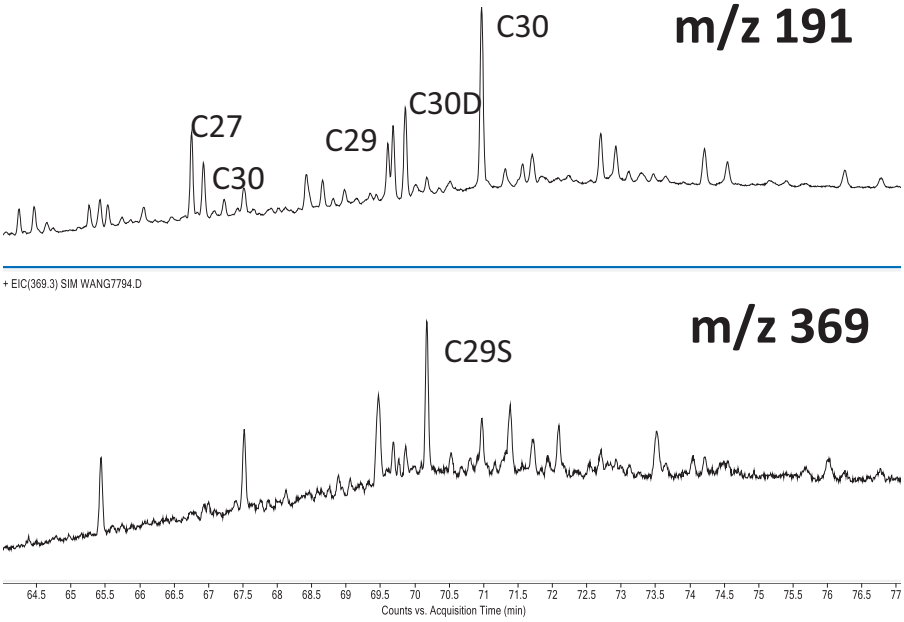

Figure 10.18: Four series of rearranged hopanes have been detected in crude oils in recent years as illustrated in these chromatograms. The four series include the 18α(H)-neohopanes (Ts); the diahopanes (DH), a so-called early eluting series of rearranged hopanes (EE) tentatively identified as 9,15-dimethyl-25,27-bisnohopanes and the 21-methyl-28,30-*dinor*-hopanes (C29S). The first three series can be determined using the ion at mass 191 and the fourth series requires the ion at mass 369 for detection.

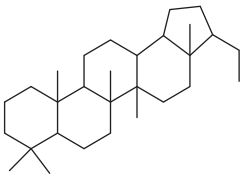

C_{29}Ts

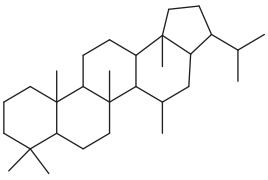

17α(H)-Diahopane

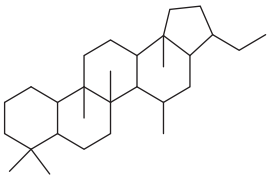

9,15-Dimethyl-25,27-bisnohopane

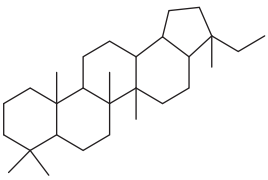

C_{29} 28-norspergulane

For the most part these four series of rearranged hopanes co-occur in crude oils and source rocks. In many oils the 28-norspergulanes are often present in very low concentrations and not readily detectable. The co-occurrence of these families of rearranged hopanes is not exactly surprising since it has been proposed that are probably formed through clay-catalyzed rearrangement reactions. Maturity also plays a role in their presence but, in all probability, not in their actual formation. The rearranged hopanes are more thermally stable than the regular hopanes and with increasing maturity the relative concentrations of the rearranged hopanes will increase as a result of preferential degradation of the regular hopanes. A more recent paper has proposed that these rearranged hopanes are formed under oxic conditions through oxidation of the methyl group at C16 rather than through clay catalyzed rearrangement reactions. This proposal was based on the occurrence of the rearranged hopanes in a section of the Xiamaling Formation, North China Block, which was deposited under relatively oxic conditions but their absence in an overlying unit deposited under highly anoxic conditions [104].

Multiple families of hopanes have been identified in crude oils, with two families briefly described below in view of their widespread utilization. The first of these is the 25-norhopanes. These exist as a series from C_{26} to C_{34} similar to the regular hopane series but with one carbon less as a result of the methyl group having been removed from C10 in the hopane structure [105]. The origin(s) of this series has been debated for many years as far back as the late 1970s. Initially they were associated with biodegraded oils which in itself raised an interesting question as to whether or not these compounds were formed during the biodegradation process. Alternatively, were they a product of relative enhancement, whereby 25-norhopanes were derived directly from the source material, albeit present in low concentrations, which were relatively enhanced as other compounds were removed via biodegradation? Another issue with their formation during in-reservoir biodegradation is the absence of any intermediates. If the C10 methyl group is being removed during biodegradation, that methyl group would initially need to be oxidized to a carboxyl group and subsequently removed via decarboxylation. Only one report has ever documented hopanes with the carboxyl group at the C10 position in crude oils [106]. There have been few reports of 25-norhopanes in source rocks. One study several years ago reported a number of source rock samples containing 25-norhopanes [72] and more recently a significant number of Mississippian samples in the Anadarko Basin, Oklahoma, were reported to contain the 25-norhopanes [107]. Clearly the origin of these compounds has not been resolved. Regardless of their exact origin there is one particularly interesting observation based on these compounds related to mixing of crude oils. There are multiple examples where the initial reservoir charge has been biodegraded leading to an enhanced 25-norhopane fingerprint along with removal of the *n*-alkanes and other biomarkers resulting from biodegradation. Following biodegradation of the initial charge, a second charge of oil from the same or a different source enters the reservoir replenishing the *n*-alkanes as well as the regular hopanes. Hence oils that contain both series of hopanes are commonly assumed to result from mixing of degraded and nondegraded oils (Figure 10.19).

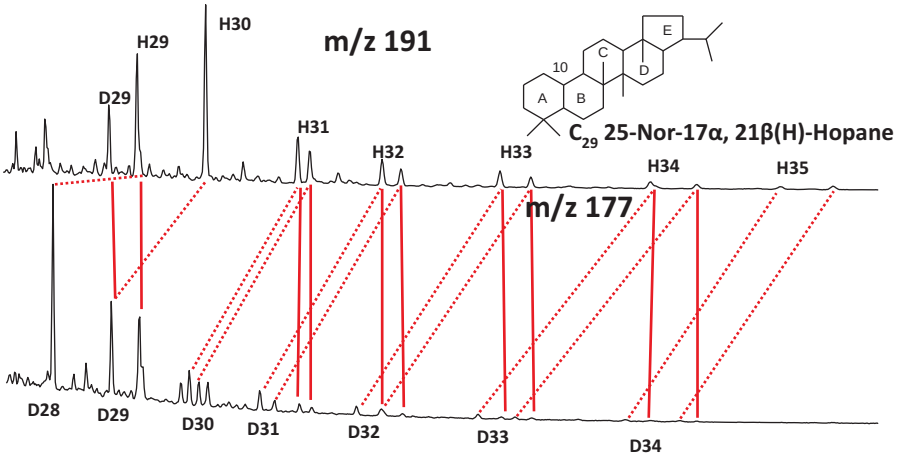

Figure 10.19: 25-Norhopanes are generally associated with biodegraded oils and determined using the ion at mass 177 as a result of the loss of the C25 methyl group at C10.

Methylhopanes are present in many oils, and rock extracts, particularly those associated with carbonates, and occur as complex mixtures of the same isomers and epimers observed for the regular hopanes. In addition, there are four possible series of methylhopanes ranging from C_{28} to C_{36}. The additional methyl group is located in the A ring can be either in the second or third position plus it can either have the α or β stereochemistry leading to a potentially very complex mixture of methylhopanes. The major series is the 2α methyl hopanes which are typically dominant over the 3β series with both series being monitored using the ion at m/z 205 [108]. There are many co-elution issues but generally it is possible to see two major families when present in varying concentrations (Figure 10.20). The presence of these compounds is extremely useful for correlation purposes as a result of their complexity. Also, the methylhopanes generally appear to be present in relatively higher abundance for oils derived from carbonate source rocks. Possible precursors for these compounds, 2β-methyldiplopterol and 3β-methylbacteriohopane have been detected in cyanobacteria and methylotrophic bacteria [109], as well as more recently in α-proteobacteria [110].

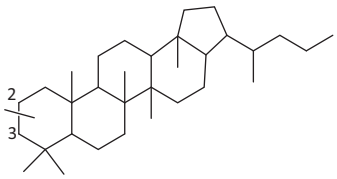

2 or 3-Methylhopanes

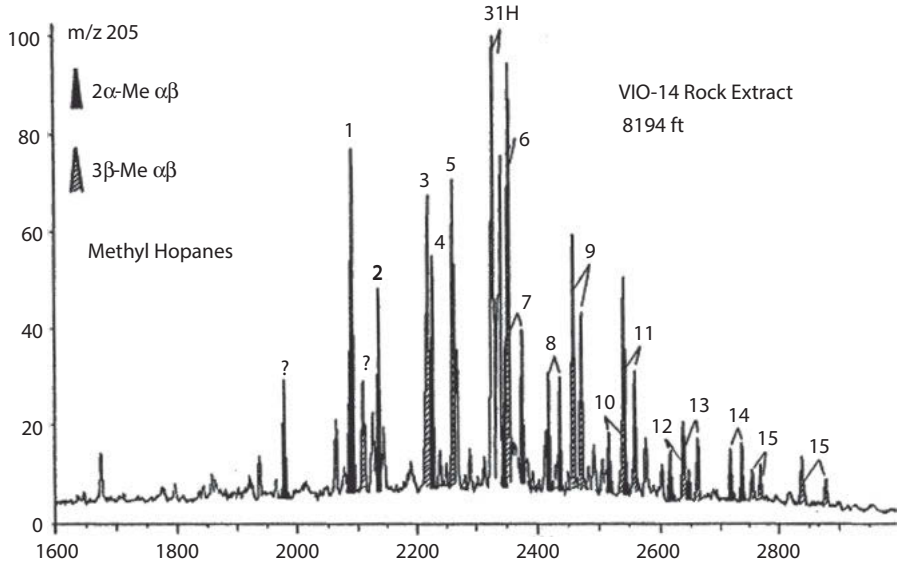

Figure 10.20: Methylhopanes are often present in oils derived from carbonate source rocks and determined through the use of the ion at mass 205. The methylhopanes are typically present as complex mixtures of both the 2α- and 3β-methylhopanes.

10.4.4.5 Other terpanes

The hopanes are the most widely utilized family of biomarkers present in crude oils but it is important to mention two additional biomarkers that are frequently observed, namely, 18α(H)-oleanane and gammacerane. The former has been traditionally associated with a source from higher plants, specifically angiosperms. 18α(H)-Oleanane was one of the first biomarkers recognized as an indicator of higher plant material in source rocks and crude oils [111–113]. Following the identification of 18α(H)-oleanane it was proposed that possible precursors for this compound were present in angiosperms which led to the utilization of 18α(H)-oleanane as an age-dating biomarker as well as a source indicator [114]. Since that time, it has been routinely assumed that the presence of 18α(H)-oleanane can be taken to indicate the age of an oil, or source rock, as Late Cretaceous or Early Tertiary given the coincident expansion and proliferation of angiosperms. There are a few reported occurrences of 18α(H)-oleanane in samples older than Late Cretaceous including: Middle Jurassic marine siltstones of Tyumen Formation from West Siberia, Russia; a Pennsylvanian coal ball from Illinois, USA [114]; a Middle Jurassic Brora coal in Scotland [115]; Upper Permian rock extracts from Guizhou Province, China [116]. More recently 18α(H)-oleanane has been observed in a number of Mississippian and Pennsylvanian age source rocks in the Anadarko Basin, Oklahoma [117]. Explanations for these early occurrences

of 18α(H)-oleanane are generally tentative but possibilities proposed by Moldowan et al. [114] included: (i) a separate lineage leading to the angiosperms, such as stem-angiophytes [118, 119], leaving a chemical signature long before plants with unmistakably angiospermous features were preserved; (ii) related angiosperm sister groups that may have had the capability to produce the precursors to 18α(H)-oleanane. Murray and coworkers noted there are many oils of Late Cretaceous age devoid of oleanane even though it is clear there was significant angiosperm input [120]. The explanation being that in certain depositional environments, particularly marine, the oleanane precursors will aromatize preventing the formation of oleanane. In certain cases, it has been proposed that the presence of 1,2,7-trimethylnaphthalene can be formed from the degradation of oleanane and possibly used to support the angiosperm input [121–124].

Gammacerane is another very specific biomarker that was discovered many years ago and initially proposed as a salinity indicator, particularly for lacustrine environments [125–127]. It has also been observed in many marine oils sourced from carbonate or evaporitic source rocks and is thought to be derived from tetrahymanol [128, 129]. Subsequently, Sinninghe Damste et al. [130] and others proposed that gammacerane was derived from bacterial ciliates which thrive in stratified water columns in marine and non-marine environments commonly resulting from hypersalinity at depth, leading to elevated levels of anoxicity in the water column. Stratified water columns are often associated with elevated levels of salinity, although temperature gradients in the water column may also lead to stratification. However, the presence of gammacerane may still indicate elevated levels of salinity.

10.4.5 Steranes

10.4.5.1 Regular steranes

Alongside the hopanes, the steranes are another family of widely studied biomarkers present in crude oils. It is well documented that steranes are derived from their parent functionalized sterols [29]. Sterols are present in a wide variety of living source materials and hence the steranes are very useful as indicators of source input [131]. Some source specificity is lost during the transformation process (i.e. diagenesis) since sterols from two different sources may simply differ in structure by the position of a double bond. However, when two different sterols, of identical carbon number are reduced to steranes they will share the same hydrocarbon structure/backbone. In spite of this shortcoming steranes can still provide a tremendous amount of source information. In general, it is commonly assumed that C_{27} steranes are primarily derived from phytoplankton or marine algal sources, C_{28} steranes

primarily from lacustrine sources and C_{29} steranes, initially thought to be derived from higher plant sources, were subsequently shown to also have sources related to an algal input [131]. In more recent times, rather than trying to relate sterane distributions to specific source input, more emphasis has been placed on ternary diagrams to show relative proportions of $C_{27}/C_{28}/C_{29}$ steranes for correlation purposes and use the distributions on the plots to get a general idea of major source input (Figure 10.21). Steranes have two important stereochemical centers and can exist as two major series of stereoisomers in crude oils, namely, 14α(H),17α(H) and 14β(H),17β(H), and each of these can exist as the 20*S* and 20*R* epimers. Steranes also exist as diasteranes, or rearranged steranes, which can also exist as a number of stereoisomers and epimers. This leads to the possibility of a very complex mixture of steranes and diasteranes plus isomers and epimers in a crude oil which can be very useful for oil/oil and oil/source rock correlations (Figure 10.21).

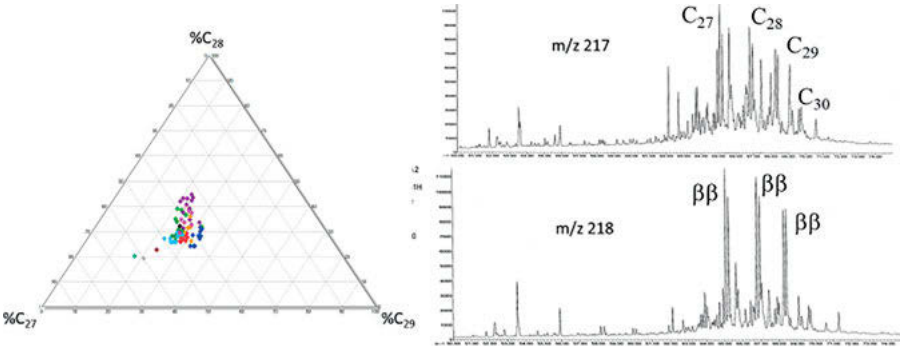

Figure 10.21: Steranes in crude oils are generally dominated by a complex mixture of steranes ranging from C_{27} to C_{30} and detected by monitoring the ions at mass 217 and/or 218. The sterane distributions will vary as a result of differences in source, maturity, depositional environments, and lithology. Ternary diagrams are generally used for correlation purposes as illustrated in this diagram.

As with many families of biomarkers, biodegradation removes individual compounds in a very systematic and reproducible manner. The order of removal is C_{27}, C_{28} and then C_{29} steranes, with each member of the series the 20*R* epimer is removed at a faster rate than the 20*S* epimer and the αα isomers more rapidly than the ββ isomers. The common theme observed with biodegradation of individual biomarkers is that the isomer with the naturally occurring configuration (i.e., 20*R* and αα) is removed more rapidly than those with the configuration obtained after diagenesis and maturation (i.e., 20*S*, ββ and diasteranes). Heavily biodegraded oils are often characterized by an absence of regular steranes and a predominance of diasteranes, which have no naturally occurring precursors. If necessary, the relative proportions of the C_{27}, C_{28},

and then C_{29} diasteranes can also be utilized for source correlation purposes in these heavily degraded oils (Figure 10.22).

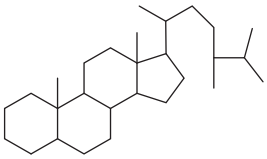

Steranes

In addition to the source information recorded by the C_{27} to C_{29} regular steranes, the 24-*n*-propylcholestanes (C_{30}) are used extensively as unique indicators of marine source input [132]. The lower carbon members of the regular sterane series, pregnanes (C_{20}–C_{22}) are commonly assumed to be formed by side chain cleavage of the C_{27}–C_{29} steranes with increasing maturity. It has also been observed that extracts or oils derived from hypersaline-related sources will often contain relatively high concentrations of the lower carbon numbered steranes along with relatively high concentrations of the ββ steranes even in samples of relatively low maturity [133]. In that situation, the C_{20}–C_{22} steranes are source/depositional environment related rather than maturity related.

The fact that steranes can occur as a number of isomers and epimers means that they can also address questions pertaining to maturity. The two most widely used maturity parameters are generally determined from the C_{29} sterane isomers and epimers since all four of these compounds are completely resolved chromatographically (Figure 10.22) The two ratios are:

$$14\alpha(H),17\alpha(H)20SC_{29}/14\alpha(H),17\alpha(H)(20S + 20R)C_{29} \text{ and}$$

$$14\beta(H),17\beta(H)(20S + 20R)C_{29}/(14\beta(H),17\beta(H) + 14\alpha(H),17\alpha(H))20S + 20RC_{29}.$$

Both of these ratios increase with increasing maturity until they reach their equilibrium values in the middle of the oil window. At that point in some samples a turnover effect has been observed as the ratios actually start to decrease again following the more rapid aromatization of the 20*S* epimer compared to the 20*R* epimer [134]. It is very challenging to relate these molecular maturity parameters to the more conventional and widely used vitrinite reflectance values. Maturity parameters change as a result of very specific chemical reactions which will occur at different rates. Even the increase in vitrinite reflectance is related to a chemical reaction that increases the level of aromatization of the vitrinite maceral and hence its ability to reflect light. These reactions will, in most cases, proceed at different rates and therefore one sample that has a 20*S*/20*S* + 20*R* value of 0.56 and vitrinite reflectance value of 0.7% may not necessarily show the same relationship in a second sample matured to the same level but from a different depositional environment. Caution must be exercised not to over interpret these values. They provide valuable information related to relative

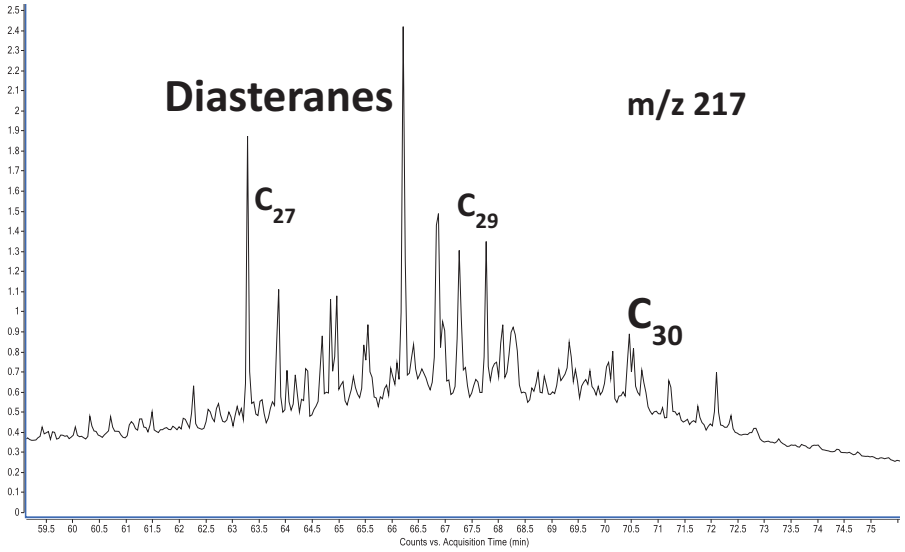

Figure 10.22: Biodegradation of crude oils removes compounds in a very specific manner. For the regular steranes the order of removal is C_{27} then C_{28} then C_{29}. The regular steranes are also removed faster that the rearranged steranes or diasteranes as illustrated in this chromatogram.

maturity levels and also reliable indications as to the maturity level of a sample in terms of whether it is immature or in the oil or gas window.

10.4.5.2 Mono and triaromatic steroid hydrocarbons

The steranes described above are derived, via a few intermediates, directly from sterols occurring in the original source material. Continued diagenesis and maturation will lead to the formation of mono- and triaromatic steroid hydrocarbons. Since these aromatized compounds are formed from the steranes it is natural to assume the relative proportions of the individual compounds will be similar to the relative proportions of the saturate steranes. The use of the sterane ternary diagram to obtain source information was described above and a similar approach can be used based on the relative proportions of the monoaromatic steroid hydrocarbons (Figure 10.23). This approach is preferred in some cases since the aromatization process leads to fewer possible isomers making the resulting mixtures less complex and somewhat easier to interpret. A similar approach is possible with the triaromatics where the number of isomers is even lower producing less complex fingerprints (Figure 10.24). In addition to the "regular" triaromatic steroid hydrocarbons there are a number of additional series of triaromatic steroid hydrocarbons that have been used for a variety of applications. Included in these series are the dinosteroids,

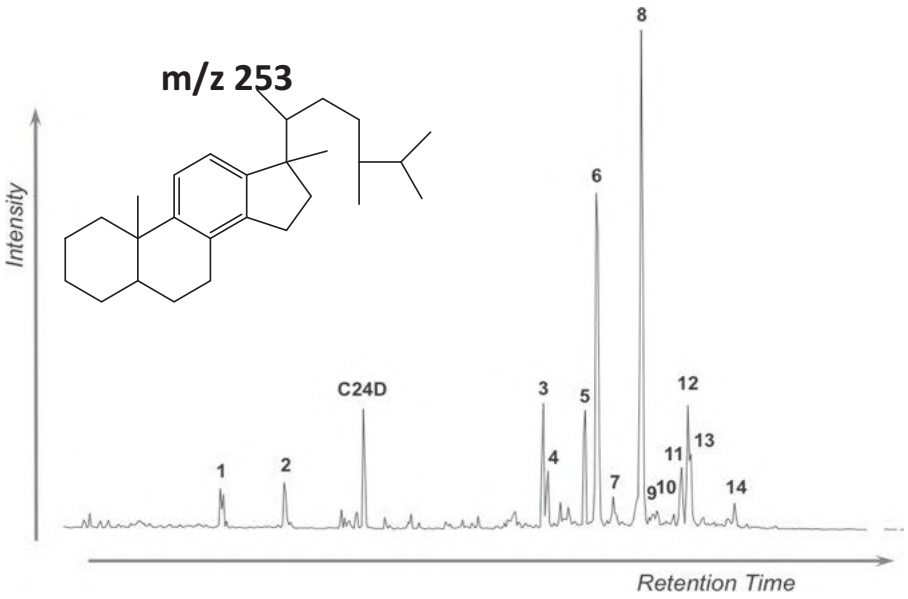

Figure 10.23: Monoaromatic steroid hydrocarbons are detected by the ion at mass 253. These compounds can be used for source correlation based on ternary diagrams similar to those shown for the regular steranes. In addition, the ratio of the lower carbon numbered monoaromatic steroid hydrocarbons (peaks 1 and 2) to the total monoaromatic steroid hydrocarbons (peaks 1–14) concentrations is commonly used as a maturity indicator.

which differ from the conventional triaromatic steroid hydrocarbons in terms of the side chain structure. The dinosteroids are indicators of a source contribution from dinoflagellates and as such these compounds have been widely utilized as age dating biomarkers. The presence of dinosteroid aromatic hydrocarbons paralleled the evolution of the dinoflagellates in the Triassic. Later studies showed the presence of these compounds in Paleozoic rock extracts where it was rationalized they are derived from ancient analogues of dinoflagellates, namely, achritarchs [135–137].

Apart from their use in providing source correlation and age dating information on the ternary plot, an additional application of the mono- and triaromatic steroid hydrocarbons is their use as relative maturity parameters. The aromatized steranes do occur as stereoisomers and epimers with the following isomers typically occurring in most crude oils. The monoaromatic steroid hydrocarbons can occur as the 5α or 5β stereoisomers as well as the 20*S* and 20*R* epimers. There is also an optically active carbon atom at C24 but the *S* and *R* epimers at that carbon center are generally not separated on most commonly used GC columns. For the triaromatic steroid hydrocarbons there are no stereochemical centers remaining as a result of the aromatization and only the possibility of 20*S*, 20*R*, 24*S*, and 24*R* epimers being present. It should be

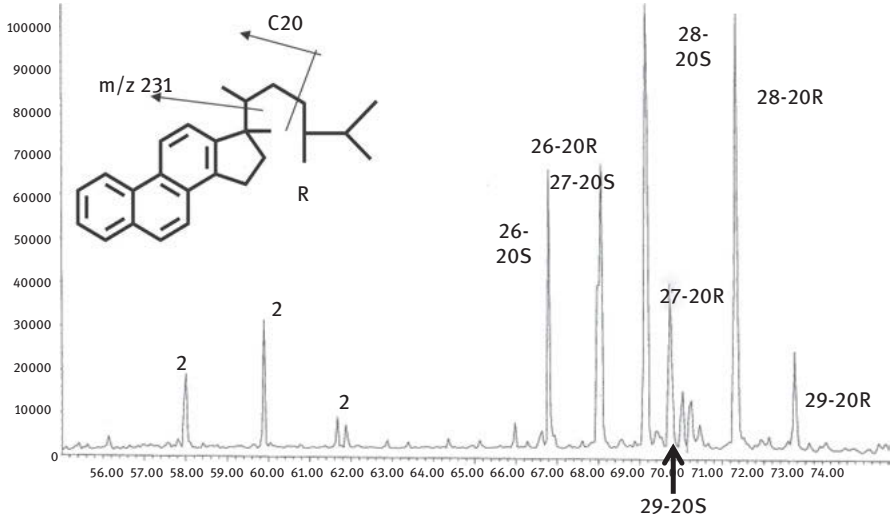

Figure 10.24: The triaromatic steroid hydrocarbons are detected by the mass 231 and the major use of these compounds is as a maturity parameter based on the relative proportions of the C_{20}–C_{22} lower carbon member to the total triaromatic steroid hydrocarbon content (C_{20}–C_{29}).

noted again that as with the monoaromatic steroid hydrocarbons, the 24*S* and 24*R* epimers are generally not separable on commonly used chromatographic columns.

The mono-and triaromatic steroid hydrocarbon maturity parameters are not based on these isomers but are derived from relative proportions of short chain (MAI and TAI) relative to the longer chain components (MAII and TAII). These are based on the concept of side chain cracking where the relative proportions of the shorter chain components will increase with increasing maturity. These maturity parameters are expressed in a similar manner for both the mono (MA)- and triaromatic (TA) components, namely, MAI/(MAI + MAII) and TAI/(TAI + TAII) where MAI and TAI correspond to the shorter chain components and MAII and TAII to the higher carbon number components. As mentioned above, these molecular maturity parameters are challenging to correlate with measured vitrinite reflectance values. They do provide a good indication of the relative maturity levels when evaluating a family of oils, from a common source to determine whether or not there are significant variations in maturity across a field. Such maturity trends could indicate possible fill direction in conventional reservoirs [66]. In a conventional reservoir, it is proposed that reservoirs are initially filled with the lowest maturity oils and as filling continues the continual subsidence of the source rock leads to increased thermal stress and more mature oils. Therefore, in the absence of homogenization in the reservoir, there will be a maturity gradient across the reservoir, with the oils closest to the source kitchen being most mature and those farthest from the kitchen being least mature.

10.4.5.3 Other steranes

In addition to the above-mentioned families of steranes that are used extensively in exploration studies, methylsteranes are another very complex family of biomarkers that occur in oils of all ages in varying proportions and distributions. As with the regular steranes, methylsteranes can also occur with the same variations in stereochemistry and optical isomers and as a homologous series from C_{28} to C_{30}. Adding to the complexity is the presence of the methyl group in the A ring which can be in the second, third, or fourth position as well as in the α or β configuration. The methylsteranes are not used as extensively as the regular steranes but can be used to provide source-related information [126, 139–141].

One C_{30} sterane, which has the additional methyl group not in the A ring but on the side-chain, is dinosterane. This sterane, and its related isomers and epimers, are derived from sterols occurring in dinoflagellates. It has been used as an age dating biomarker and primarily as a marine source input indicator [142].

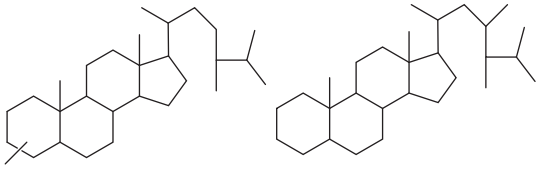

Methylsteranes **Dinosterane**

10.4.6 Methylated chromans

Methyltrimethyltridecylchromans (MTTCs), when present, are typically relatively abundant constituents in the aromatic fractions of source rock extracts and, to a lesser extent, oils. While the presence and distribution of MTTCs is often used as an indicator for elevated paleosalinity and stratification [143–145], there is some evidence MTTC distribution may be partially affected by maturity [146–148].

Methyltrimethyltridecylchromans (MTTCs) comprise a chroman head group and an isoprenoid chain, identical in structure to the tocopherols except the MTTCs lack a hydroxyl group at C-6 as shown in the structures below. Like the tocopherols, the chroman head group may be mono-, di-, or tri-methylated, producing mono-, di-, and tri-methyl MTTCs that exhibit major fragments at *m/z* 121, 135, and 149, respectively. 5, 7, 8-Trimethyl MTTC is typically the most abundant MTTC in source rocks and oils.

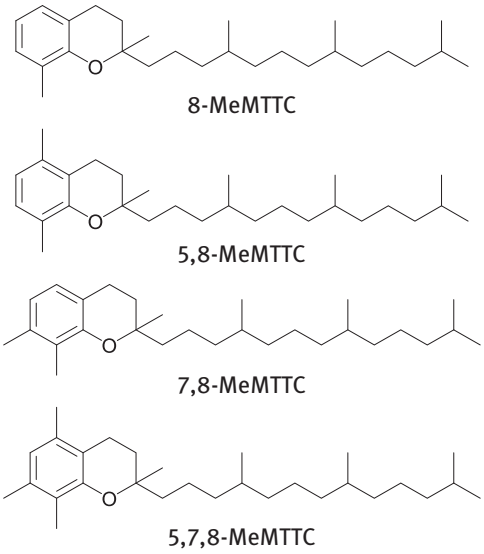

The MTTCs were first identified in a suite of rock/sediment extracts and oils spanning the Permian to Pleistocene, initially suggested to represent paleohypersalinity when dominated by the mono- and dimethyl variants [143]. Over the years, an association with hypersalinity remains, yet it is important to review the supporting evidence for this interpretation given the continued enigmatic origin of these compounds. Naturally, the derivation of MTTCs directly from an organism or the formation of MTTCs from a biological precursor molecule is a function of the depositional environment, so attendant biochemical conditions in hypersaline environments should be kept in mind throughout the following discussion.

Early work associated the MTTCs with hypersalinity by comparing the occurrence and relative proportions of specific MTTCs with other biomarker signatures (e.g., low Pr/Ph, even-odd *n*-alkane predominance, high C_{34} or C_{35} relative to C_{31}–C_{33} homohopanes), which at the time were presumed to be strong indicators for hypersalinity [149] to establish "hypersaline" and "nonhypersaline" conditions [143]. Further observations of the co-occurrence of MTTCs and hypersaline deposits were reported [144, 150], but were purely based on empiricism and somewhat contradictory. This may partly reflect preservation biases inherent to contrasting lithologies, but primarily is an artifact arising from the unknown source of the MTTCs. More recent work continues to develop empirically founded proxies for paleosalinity using the MTTCs [151] and attribute MTTC occurrence and distributions to elevated salinity or density stratification [145, 152].

Understanding the geochemical significance of MTTCs is entirely reliant on empirical observations, as reviewed above, due to the ongoing uncertainties surrounding their origin. When first discovered, the MTTCs were thought to be produced by non-photosynthetic bacteria [143], then revised to originate from photosynthetic

origins, possibly algae [144]. Subsequent work proposed a formation pathway of MTTCs via condensation reactions between phytol and alkyl phenols from higher plants [153], although the occurrence of MTTCs in an early Cambrian crude oil complicates this theory [154]. Carbon isotopic analysis of MTTCs revealed a common source for the mono-, di-, and trimethyl variants, comparable to pristane and phytane carbon isotopic values, but differing from sterane carbon isotopic compositions [155]. Thus, MTTCs are not a true "biomarker," but still retain value in exploratory applications due to an under constrained depositional context (i.e., stratified and/or hypersaline environments [144]), wide temporal distribution (predominantly Permian and younger [143]), and resistance to elevated levels of thermal stress [145, 146, 156].

The utility of MTTCs will primarily lie in oil–source and oil–oil correlations and source facies prediction and delineation. Hydrous pyrolysis (i.e., artificial maturation) of immature samples demonstrated the thermal stability of MTTCs, with increasing concentrations observed throughout the experiments [145]. These experiments, combined with numerous reports of MTTCs in the liquid hydrocarbon phase (i.e., oil), underscore the 'survivability' of these compounds during catagenesis. In addition, MTTCs may serve as a useful age dating tool, albeit relatively broad. Although MTTCs are observed in late Devonian source rocks and oils [145, 157], as well as an isolated occurrence in an early Cambrian oil [154], the majority of MTTC reports range from Permian to Pleistocene [143]. Therefore, it can be presumed any oil possessing MTTCs was likely derived from a source rock of Permian or younger age, but comparison with more robust biomarker age dating proxies (e.g., relative abundance of ergostanes to stigmastanes [158]) is encouraged.

The most valuable aspect of MTTCs as an oil–source and oil–oil correlation tool is the association of these compounds with a specific environmental condition, hypersalinity or density stratification. Comparison with additional geological and/or geochemical proxy data may assist in the refinement of candidate source intervals for a produced oil. If one considers the basin geometry and climatic state required to produce hypersaline conditions, further refinement of potential source rocks comes into focus. The MTTCs, although an orphan biomarker, possess the requisite characteristics to supplement more conventional biomarkers employed in oil–oil and oil-source investigations.

10.4.7 C_{40} aromatic carotenoids

The C_{40} aromatic carotenoids may exhibit variable concentrations in oils depending on the depositional environment and maturity associated with the source. If specific environmental conditions are present (see below), carotenoids may be one of the most dominant compounds in the aromatic fraction, with identification relatively straightforward from a simple GC run due to the late eluting time of carotenoids

relative to other aromatics. However, maturity will adversely affect carotenoid concentrations via degradation to aryl isoprenoids and other breakdown products.

The C_{40} aromatic carotenoids may be composed of two trimethylated aromatic rings linked by a C_{20} isoprenoid chain (e.g., isorenieratane, renieratane, renierapurpurane, paleorenieratane) or a single trimethylated aromatic ring with an isoprenoid tail (e.g., okenane, chlorobactane); all degradation products of the diagnostic pigments (e.g., isorenieratene → isorenieratane) of photoautotrophic sulfur oxidizing bacteria and, in some instances, cyanobacteria (Figure 10.25) [142, 159, 160]. Methylation patterns vary on the aromatic rings, differentiating one carotenoid from another, but this does not affect the predominant, diagnostic fragments of these compounds at *m/z* 133 and 134. Further degradation of the intact C_{40} structure will produce a series of aryl isoprenoids also identified by these fragment ions [142].

As previously mentioned, the C_{40} aromatic carotenoids have been linked to sulfur oxidizing bacteria, such as the *Chromatiaceae* (purple sulfur bacteria, PSB) and *Chlorobiaceae* (green sulfur bacteria, GSB), which conduct anoxygenic photosynthesis in sulfidic (i.e., euxinic) waters [159]. In addition, early work attributed some carotenoids (renieratene and renierapurpurin) to sponges [161–163], but this was later associated with bacterial symbionts [164], specifically cyanobacteria [160]. Therefore, the presence of certain carotenoids (okenane, chlorobactane, isorenieratane) signify the presence of sulfidic waters in the photic zone during deposition (i.e., photic zone euxinia, PZE; Figure 10.25), while other carotenoids (reineratane and renierapurpurane) are likely not indicative of PZE and instead represent the occurrence of cyanobacteria.

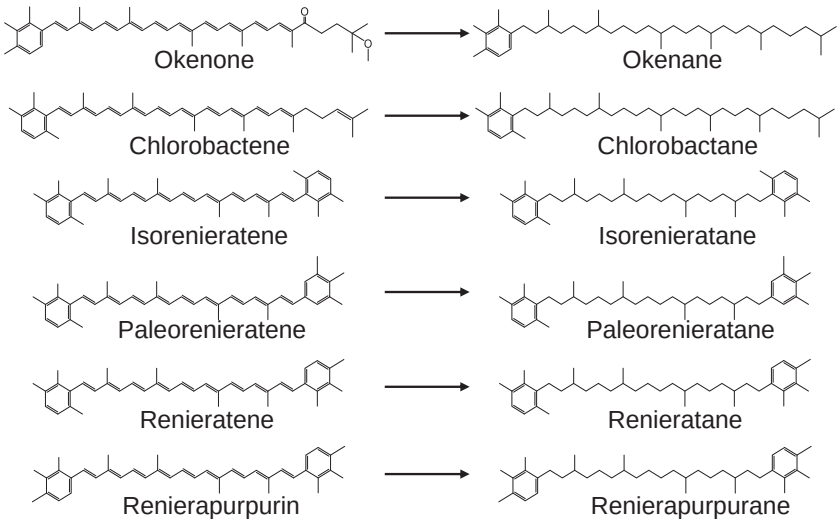

Figure 10.25: Aromatic carotenoids commonly observed in source rocks and oils and biosynthetic precursors.

In correlation assessments, any trait of the depositional environment that can be extracted from the chemical composition of an oil is critical. However, a biomarker or compound related to an environmental phenomenon requiring a specific set of paleoclimatic conditions is a powerful tool. Photic zone euxinia (PZE) is one such phenomenon whereby hydrogen sulfide permeates the euphotic zone, creating the ideal conditions for anoxygenic photosynthesis by sulfur oxidizing bacteria [165]. The relative vertical extent of the chemocline (the boundary between oxygenated and euxinic waters) may be inferred by the occurrence and distribution of certain aromatic carotenoids, specifically okenane, chlorobactene and isorenieratane (Figure 10.26). This is an artifact of the biological associations of these three biomarkers, with okenane derived from PSB that occupy the shallowest depths (i.e., requires the most light) of the three strains, while isorenieratane linked with the brown GSB is indicative of likely deep PZE restricted to the basal euphotic zone or low-light conditions within the upper chemocline [166–169]. Therefore, the sole occurrence of PZE-associated carotenoids in an oil may be sufficient to conduct an oil-source correlation if there is only one known source facies containing these biomarkers. Even if multiple source facies exist possessing evidence for PZE, contrasting carotenoid distributions may still be sufficient to differentiate between each source. This is due to the fact varying carotenoid distributions are indicative of varying chemocline depths sensitive to specific paleoenvironmental factors (basin configuration, water depth, proximity to shoreline, circulation, etc.) that are unique to each source facies. Maturity contrasts between source intervals is not a concern, as increasing maturity will not affect the methylation patterns on the aromatic rings. However, if only trace amounts of isorenieratane are detected alongside high concentrations of renieratane and renierapurpurane, then it is likely the carotenoids are indicative of cyanobacteria and not sulfur oxidizing bacteria [160]; thus, an interpretation of PZE is not appropriate. Recent work by Cui et al. [160] highlighted the ability for cyanobacteria to produce certain aromatic carotenoids, and while this primarily shifted the interpretation of Precambrian oceans, it is important to note given the occasionally high ratios of renieratane + renierapurpurane/isorenieratane observed in the Phanerozoic. Lastly, while paleorenieratane remains an orphan biomarker, the co-occurrence of this aromatic carotenoid with isorenieratane and other carotenoids indicative of PZE, as well as an enriched carbon isotopic composition indicative of reverse TCA (used by the Chlorobiaceae) [170], suggests derivation from an unidentified extant or extinct sulfur oxidizing bacteria [171–173].

The C_{40} aromatic carotenoids, as formerly outlined, possess excellent potential in oil–oil and oil–source correlations. However, simply the detection of these biomarkers in an oil produced from an exploratory well in a frontier basin may suggest the presence of a mature, organic-rich source rock(s). The establishment of PZE will enhance organic matter preservation through sulfurization and a reduction of the oxidizing (i.e., degrading) portion of the water column [174, 175]. While this does not promise the development of a prolific play, it does hint at a source facies characterized by

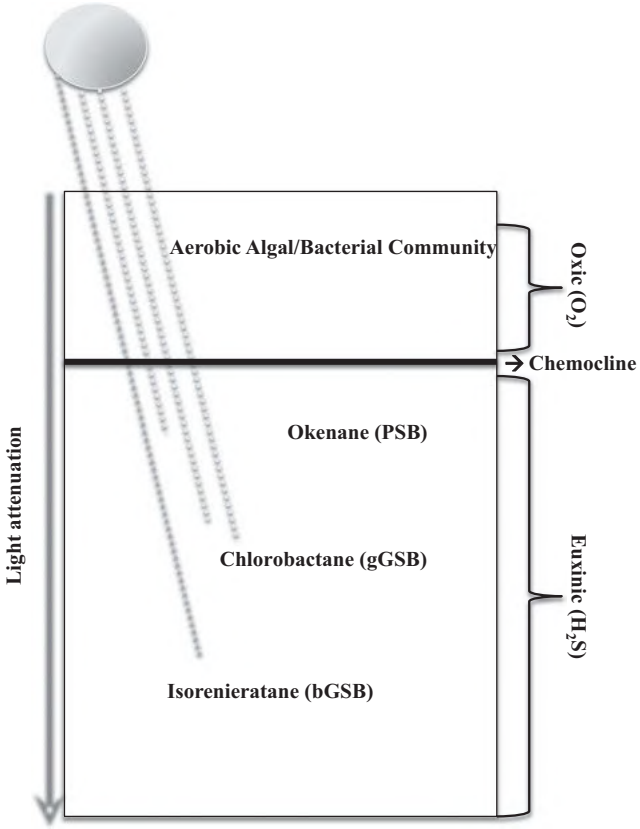

Figure 10.26: Paleoenvironmental significance of aromatic carotenoids preserved in source rocks and oils. Note how carotenoids originate from distinct depths in the water column, enabling a qualitative assessment of the relative depth of the chemocline and vertical extent of photic zone euxinia.

above-average organic carbon sequestration, which may lead to a prolific source rock if other criteria are met (e.g., thickness). The utility of aromatic carotenoids is compromised by increasing maturity though, with carotenoids rarely preserved as C_{40} structures past the early to middle oil window (Figure 10.27), although this could be a result of preferential expulsion [176, 177].

Regardless, it seems beyond the middle oil window the concentrations of aromatic carotenoids decline dramatically, necessitating use of the aryl isoprenoids. Aryl isoprenoids are further degradation products of the original carotenoids produced by photosynthetic bacteria [142]. Compound-specific isotopic analysis (CSIA) is necessary to confirm the origin of aryl isoprenoids, with an enriched signature often indicative of GSB [142, 178]. Therefore, in more mature source rocks and oils, aryl isoprenoids may substitute for the precursor aromatic carotenoids.

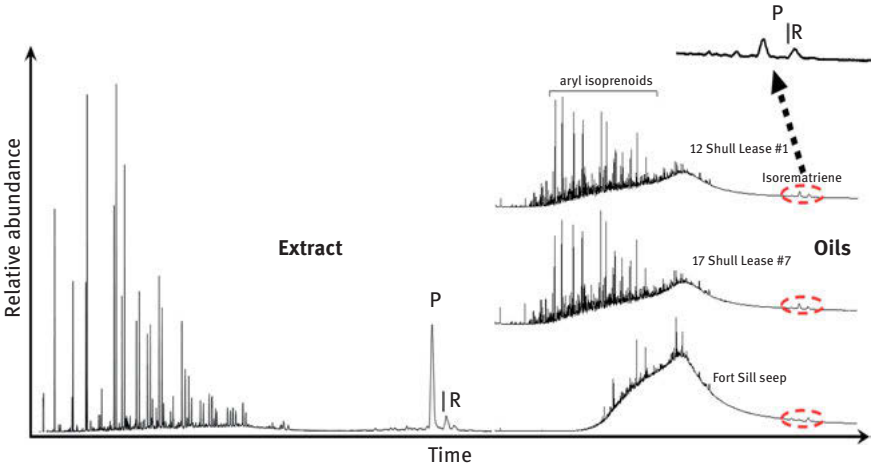

Figure 10.27: Effects of thermal maturity on aromatic carotenoid concentrations. Note how the Woodford Shale extract possesses relatively high concentrations of aromatic carotenoids compared to Woodford oils subjected to varying levels of thermal stress.

10.4.8 Diamondoids

The first diamondoid, adamantane, was discovered in crude oils in the early 1930s[179]. In recent years the range of diamondoids has been extended into higher molecular weight regions [180, 181]. Diamondoids cannot be specifically thought of as authentic biomarkers since they are not directly related to any precursor(s) occurring in living sources of organic matter. It has been previously proposed that these compounds are derived via thermal alteration reactions involving clay minerals and various compounds derived from sterols and triterpenoids [182]. However, their widespread occurrence and utilization in recent years as well as their suspected origin from authentic biomarkers makes it appropriate to include them in a chapter of this nature. In recent years a far more extensive literature has appeared on these compounds due to the ability to detect the compounds by GCMS as well as using GCIRMS to determine the isotopic composition of individual diamondoids. The first compound identified was adamantane but more recent work has shown that members of the homologous series include diamantanes, triamantanes, tetramantanes, pentamantanes, and hexamantanes [183–185]. With increasing carbon number, the number of potential isomers also increases with polymantanes containing 4, 5, and 6 repeated adamantane units have 3, 6, and 17, isomers, respectively [186].

Using 2D gas chromatography coupled to time-of-flight mass spectrometry (GC/GC-TOF-MS), over 100 compounds of adamantane, diamantane, and triamantane have been identified [8, 187]. Each homolog in the series can also occur as multiple isomers, primarily differing the positions of methyl and ethyl substituents located

around the ring structures. The resulting complexity of the diamondoid distributions results in fingerprints that can be used for correlation purposes. These compounds are thermally very stable and very resistant to biodegradation and as a result are often present in relatively high concentrations in very light oils and condensates as well as biodegraded oils.

A number of maturity parameters have been developed based on various lighter members of the series. One of the earliest parameters that was correlated with vitrinite reflectance was proposed to be particularly useful for very mature samples where the majority of more conventional biomarkers had either reached equilibrium or started to be subject to thermal degradation [188]. The two maturity parameters proposed by Chen et al. [188] that have been correlated with vitrinite reflectance are:

Methyl adamantane index I, MAI = 1-MA/(1-MA + 2-MA)

Methyl diamantane index II, MDI = 4-MD/(1-MD + 3-MD + 4-MD)

Diamondoids have also been used to monitor the extent of thermal cracking of a crude oil along with the possibility of determining whether in-reservoir mixing has occurred between thermally cracked oils and conventional uncracked oils. This approach is also referred to as the quantitative diamondoid analyzes (QDA) [189]. Dahl and others [190] developed QDA based on changes in sterane and diamondoid concentrations that occur with increasing maturity. QDA has been used to re-evaluate many basins, particularly deep basins, and has shown in many cases, that oils in those basins are mixtures of thermally cracked oils and conventional oils from deeper sources. It is well documented that steranes concentrations decrease with increasing maturity and Dahl and others [190] noted an increase in diamondoid concentrations with increasing maturity after the sterane concentrations had basically decreased to virtually zero. The cross plot developed from these observations is shown below and the general trend for increasing maturity and cracking is shown (Figure 10.28). If the oils plot off the maturity trend it indicates mixing has occurred and possibly the extent of mixing that has occurred.

In addition to the QDA process described above, Moldowan et al. also introduced another approach referred to as the quantitative extended diamondoid analyzes (QEDA) [188]. This approach uses the quantitative homolog distributions of the higher polymantanes, triamantanes, tetramantanes, and pentamantanes for oil/oil correlations. Such an approach has the advantage over using conventional biomarkers for oil/oil correlations in that it can be applied to oils at maturity levels where conventional biomarkers would be thermally degraded. Differences in the distributions of the polyamantanes result from differences in sources and maturity. If end members are available it will also be possible to determine the extent of mixing in many cases particularly where it is also possible to determine the carbon isotope values for individual polyamantanes [189].

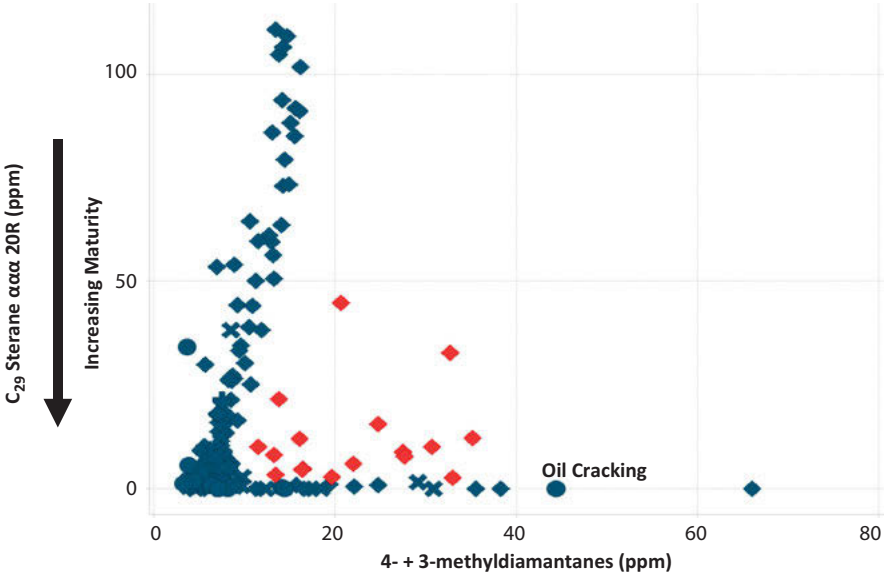

Figure 10.28: The cross plot between stigmastane concentrations and diamondoid concentrations has been used to indicate the extent of cracking of a crude oil. Mixing of unaltered oil and thermally cracked oil can also be detected on this plot, since a mixture of such oils will tend to plot in the region toward the center of the plot depending on the extent of the mixing.[190].

In an earlier application Schulz et al. [191] used the following diamondoid ratios to distinguish between Type II carbonate, Type II marine siliclastic, and Type III organic facies:

$$\text{Dimethyl diamantane index 1(DMDI-1)} = \text{3,4-DMD}/(\text{3,4-DMD} + \text{4,9-DMD})$$

$$\text{Dimethyl diamantane index 2(DMDI-2)} = \text{4,8-DMD}/(\text{4,8-DMD} + \text{4,9-DMD})$$

$$\text{Ethyl adamantane index (EAI)} = \text{2-EA}/(\text{2-EA} + \text{1-EA})$$

These ratios were originally developed using source rocks but were also applied to oils in order to differentiate oils derived from different source facies. A similar approach was proposed by Wilhelms et al. [192].

Based on the distribution of diamondoids from eleven oil samples, Gordadze [193] noted that the relative content of adamantane and alkyl substituted homologues could be used to distinguish marine oils and terrestrial oils as well as geologic age of the oils. Marine oils were observed to have a C_{13} adamantane content below 25%, whereas terrestrial oils contained approximately 15% C_{11} adamantane and approximately 47% C_{12} adamantane. Proterozoic oils were distinguished by low concentrations of C_{13} adamantanes (23%), high concentrations of the C_{12} adamantane (58%) and a relatively high C_{29} sterane concentration relative to total steranes (85%). It does not appear this has been used extensively as a source indicator and caution

needs to be exercised if it is applied due to the fact the original sample set only was only comprised of eleven samples. Finally, it should be mentioned that the diamondoids are very resistant to biodegradation and can be used to correlate biodegraded and nondegraded oils [194]. In the case of oils being impacted by thermochemical sulfate reduction and production of copious quantities of H_2S, it has also been observed that a wide array of thiadiamondoids will be produced and used as indicators that TSR has occurred [9, 195, 196].

10.4.9 Polycyclic aromatic hydrocarbons (PAHs)

10.4.9.1 PAHs as indirect indicators of source input

The majority of compounds mentioned above can be thought of as authentic biomarkers. In other words, there is a clearly defined precursor present in living systems that can be readily related to a hydrocarbon moiety present in the oil. Polyaromatic hydrocarbons (PAHs) may not show a direct structural relationship with functionalized precursors but can be related to specific biomarkers through a series of alteration or aromatization reactions. A classic example of this would be the phenanthrenes. While there are no functionalized precursors of phenanthrenes in the sedimentary record, these compounds are indirectly derived from steranes which, in turn, are derived from sterols. It is well documented that with increasing maturity, steranes will aromatize and initially produce C-ring monoaromatic steroid hydrocarbons, followed by triaromatic steroid hydrocarbons and ultimately phenanthrenes. While specific source information may no longer be available from these second or third level biomarkers, significant information, such as maturity, may still be available [13, 121, 197]. In addition, the fingerprints ranging from the parent compound, such as naphthalene or phenanthrene, along with their alkylated analogues may also provide complex fingerprints that are useful for correlation purposes as illustrated below.

PAHs typically result from diagenetic and catagenetic reactions that transform olefinic and naphthenic precursors into complex mixtures of PAHs [198–200]. Several methylated naphthalenes and phenanthrenes, such as 1,2,5-trimethylnaphthalene, 9-methylphenanthrene, and 1,7-dimethylnaphthalene have been shown to originate from aromatized terpenoids or steroids [172, 201]. PAHs in sediments may also result from incomplete combustion of organic matter during forest fires [202–204], warfare [205], agriculture [206], and human industrialization [207]. PAHs such as benzo(a)pyrene are highly carcinogenic and persistent in the environment as well as in crude oils [208–210]. Several aromatic compounds, notably benzo(a)pyrene, benzo(e)pyrene, and benzo(ghi)perylene, have been linked to paleo-wildfires [211, 212]. Benzo(e)pyrene has also been attributed to reworked algal kerogen [213, 214] but since it generally follows the same distribution as benzo(a)pyrene and benzo(ghi)perylene, it is probably derived from a combustion source. The distributions of benzo(a)pyrene (B

(a)P), benzo(e)pyrene (B(e)P), and benzo(ghi)perylene (B(ghi)Per) can be determined by GCMS and monitoring the ions at $m/z = 252 + 276$ (Figure 10.29).

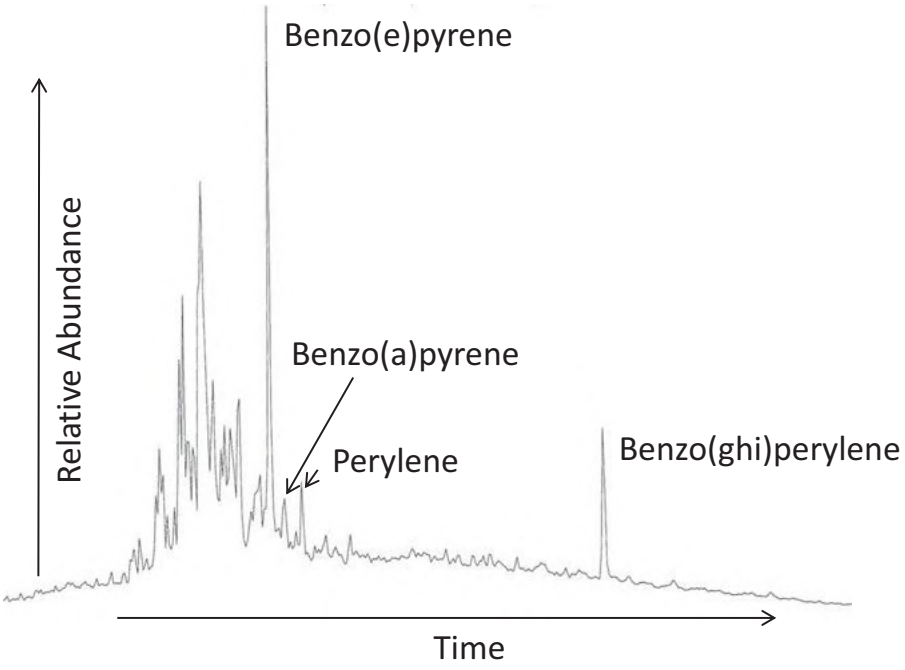

Figure 10.29: PAHs such as benzo(e)pyrene, benzo(a)pyrene, perylene, and benzo(ghi) perylene are shown in this chromatogram having been monitored by the ions at mass 252 and 276.

Perylene is another individual PAH of interest since numerous sources have been proposed for its origin [215]. Possible sources include perylene quinone pigments in modern plants [216], fungi [217], crinoids [218], and insects [219]. Itoh et al. [220] proposed that dihydroxyperylene-3,10-quinone (DHPQ) is the parent compound of perylene and suggested that Cenococcum geophilium Fr. actively produces DHPQ in sediments. While some fungal communities in the marine environment may be contributors of perylene [221], fewer than 2% of fungi are aquatic [222], and are unlikely exclusively produce perylene in marine sediments and related oils.

10.4.9.2 Naphthalenes and phenanthrenes and alkylated derivatives

The complex fingerprints of naphthalenes and phenanthrenes and related alkylated components are useful for correlation purposes and other sources of information. These two families of compounds are often the most abundant aromatic compounds in crude oils and can be readily determined by GCMS. For the naphthalenes the ions

monitored are *m*/*z* 128, 142, 156, 170, 184, 198, and 212 and for the phenanthrenes the corresponding ions are *m*/*z* 178, 192, 206, 220, 234, and 248 (Figure 10.30). Certain individual naphthalenes have been identified as possible degradation products related to oleanane, and various naphthalenes and phenanthrenes have been incorporated into maturity parameters. Furthermore, certain ratios have been linked to samples of specific geologic ages. The ratio of 1,2,8-trimethylphenanthrene/total phenanthrenes was shown to be relatively high in Permian and Devonian extracts compared to carboniferous extracts. A cross plot of the log1,2,5-/1,3,6-trimethylnaphthalenes versus 1,2,7- /1,3,7-trimethylnapthalenes was also of use is distinguishing a number of extracts from a variety of Permian and Carboniferous samples[122]. The relative abundance of 1,2,7-TMN over 1,2,5-TMN indicates an early oil window oil or immature extract [121, 223]. High concentrations of these compounds in younger sediments (Cretaceous-Recent) have been related to aromatization of β-amyrin and oleanane-type triterpenoids in angiosperms [121]. Armstroff et al. [122] suggested a strong presence of 1,2,7-TMN and 1,2,5 TMN may be related to gymnosperm resins [224], hopanoid precursors [172, 225], or both. Relative concentrations of these alkylnaphthalenes have been observed to follow the relative abundance of cadalene reinforcing the notion that these aromatic compounds are possibly related to gymnosperms and terrigenous input to the depositional system during the alternating parasequences [226].

The susceptibility of alkylnaphthalenes to biodegradation typically decreases with increasing number of alkyl substituents [227, 228]. The biodegradation of alkylnaphthalenes can be monitored using three ratios developed by Fisher et al. [229]: dimethylnaphthalenes (DBR; 1,6-dimethyl-naphthalene/1,5-trimethyl-naphthalene), trimethylnaphthalenes (TBR; 1,3,6-tri-methylnaphthalene/1,2,4-trimethyl-naphthalene), and tetramethylnaphthalene (TeBR; 1,3,6,7-tetramethyl-naphthalene/1,3,5,7-tetramethylnaphthalene). According to Fisher et al. [229] all three of these ratios should decrease with additional levels of biodegradation.

In previous studies [230, 231], it was proposed that phenanthrene was derived from combustion of ancient land vegetation. Several specific alkylphenanthrenes have been attributed to alternative sources, such as pimaric acid for 1,7-dimethylphenanthrene [232] and bacteria for tetramethylphenanthrenes [233]. The phenanthrene/methylphenanthrene ratio has been utilized as a proxy for weathering and as a source parameter for PAHs [123, 124, 197]. Hydrocarbons generated from combustion sources would show values greater than 0.5 for this ratio [234, 235]. An increase in methylphenanthrene concentrations could be indicative of paleoweathering if sedimentary methylation is the dominant mechanism for their generation [231, 236].

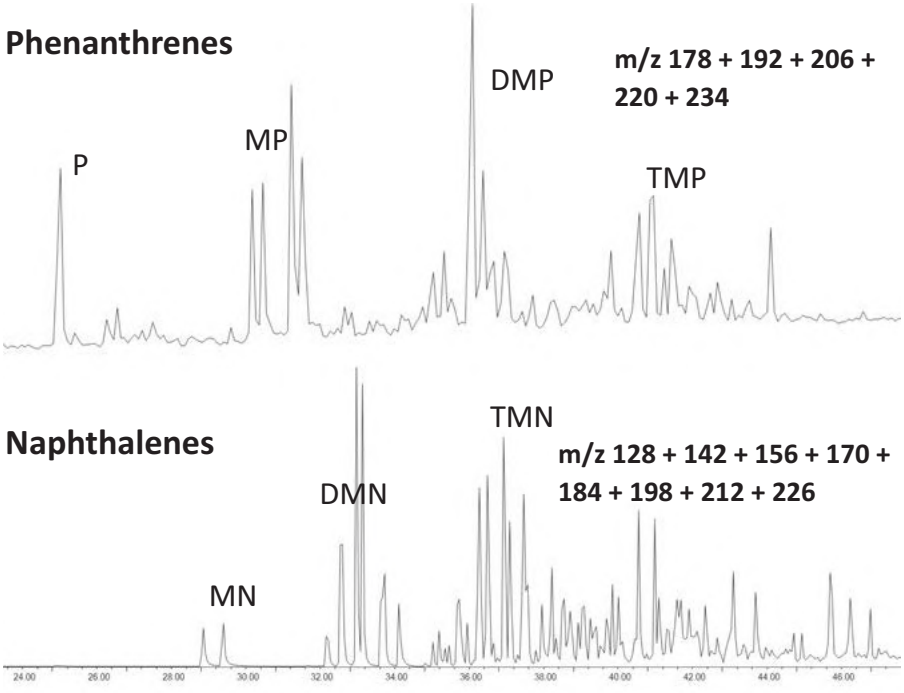

Figure 10.30: Phenanthrenes and naphthalenes exist as complex mixtures of homologues and isomers. They are readily detected by use of a number of ions as shown above.
(P = Phenanthrenes; MP = methylphenanthrenes; DMP = dimethylphenanthrenes;
TMP = trimethylphenanthrenes; MN = methylnaphthalenes; DMN = dimethylnaphthalenes;
TMN = trimethylnaphthalenes).

10.4.9.3 PAHs as maturity indicators

The most widely used maturity parameter derived from the PAHs would be the methylphenanthrene index [197, 237]. Additional maturity parameters have also been derived from the dibenzothiophenes and the alkylnaphthalenes [238, 239]. For oils, these parameters indicate the maximum level of maturity experienced after generation which is not necessarily the same as the maturity level at generation. Caution must be exercised when using the naphthalene parameters in view of the possible loss of the more volatile naphthalenes during sample preparation. The formula used to calculate the MPI is shown below along with that used to calculate the corresponding maturity parameter from the dibenzothiophenes and some examples of the naphthalene parameters. Where individual parameters have been correlated with vitrinite values, the formula to calculate these relationships are also shown.

MPI-1 = 1.89(2MP + 3MP)/(P + 1.26(1MP + 9MP)
Rc = 0.60MPI-1 + 0.4 (for 0.65 to 1.35%Ro)
Rc = – 0.60MPI-1 + 2.30 (for 1.35 to 2.00%Ro)
MNR = 2MN/1MN
ENR = 2EN/1EN
DNR-1 = (2,6-DMN + 2,7-DMN)/1,5-DMN
DNR-2 = 2,7DMN/1,8-DMN
DNR-3 = 2,6DMN/1,8-DMN
DNR-4 = 1,7DMN/1,8-DMN
DNR-5 = 1,6DMN/1,8-DMN
-log(1,8DMN/totalDMN)
(P = Phenanthrene; N = naphthalene; M = methyl; E = ethyl; D = di; R = ratio)

The MPI was initially developed for coals by Radke [240] in 1983 and then extrapolated to Type III kerogens and finally all kerogen types and oils. There have been issues in the past when applying the MPI to samples not related to Type III kerogens. It also needs to be remembered that when converted to vitrinite equivalent reflectance values a high value and a low value can be determined from the calibration plot of Radke [240] and a decision must be made for the value most appropriate for the sample under evaluation. However, despite potential limitations these maturity parameters are extremely useful for obtaining relative maturity values for oils to indicate maximum levels experienced by the oils and hence possible depth of generation. The ability to determine vitrinite equivalent values from oils is important from an exploration point of view since it provides an indication of the maximum maturity level experienced by oil that cannot be determined through the actual measurement of the reflectance of the vitrinite maceral. This information in turn can be translated into approximate depths at which the oil was generated and possibly lead to identification of the potential source rock. One important point in utilizing biomarker parameters for determining maturity is to determine as many biomarker maturity parameters as possible since there are other processes such as source, biodegradation, depositional environment as well as maturity that may influence some parameters more than others. Hence by using a number of parameters it will be relatively simple to determine whether there are any anomalous biomarker maturity proxies.

An interesting use of PAH components in crude oils came from intensive studies undertaken following the Exxon Valdez spill in Alaska in March 1989. Many ratios were developed that were initially used for correlation of degraded residues with the original Exxon Valdez oil. Many of these ratios can be applied in exploration studies to correlate degraded and non-degraded oils. Based on observations carried out several years after the original incident it was noted that various PAHs were degraded at different rates. One important observation was that the C3-alkylphenanthrenes (P3) and C3-dibenzothiophenes (D3) degraded at approximately the same rate. Whereas the C3-alkylchrysenes (C3) degraded faster than either P3 or D3 therefore

it was proposed that the ratio of D3/P3 could be used as a source indicator even in biodegraded oils since that ratio would remain fairly constant with weathering. The second ratio was that of D3/C3 which was introduced as a weathering ratio. When these ratios were applied to a number of oils that were degraded to varying degrees and derived from different sources, it could be clearly seen that the source ratio (D3/P3) clearly separated the oils from different sources despite differing levels of biodegradation [241].

10.4.9.4 Dibenzothiophenes

The primary sulfur-containing compounds in crude oils are thiophenes, benzothiophenes, and dibenzothiophenes and their alkylated analogues, with the latter being the abundant and readily detectable. The dibenzothiophenes are detected by the ions at m/z 184, 198, 212, and 226 which are ions also used to detect naphthalenes (Figure 10.31). The composite chromatogram showing dibenzothiophene (DBT) and alkylated analogues illustrates the typical dominance of dibenzothiophene over the alkylated analogues. Dibenzothiophene has been widely used in a plot developed by Hughes et al. [242] to evaluate the lithology and depositional environment of the source rock responsible for the generation of the oil. The aforementioned plot is the ratio of DBT/PHEN versus the Pr/Ph ratio (Figure 10.32). The theory behind this plot is that the DBT concentration will be higher in a carbonate environment than clay-rich shales. The reason for this is that DBT is formed via the incorporation of an S atom into a PAH molecule. In the absence of iron species that will react with the S atoms, the S is available to be incorporated into the aromatic structures and form DBT. Hence carbonate environments, deficient in iron relative to clastic-dominated sedimentation, will have higher DBT content than shales. In addition, being a fairly reducing environment will mean low Pr/Ph values explaining why you can expect oils derived from carbonates to plot in that region along the *Y*-axis of the plot and oils derived from shales to plot along the higher values of the X axis.

A second application is based on the composite distribution of DBT and the alkylated analogues. It has been shown that these compounds are relatively resistant to biodegradation and therefore of use in correlating degraded oils [237, 239, 243]. Furthermore, the ratios: 4MDBT/4MDBT + 1MDBT and of 4,6-DMDBT/1,4-DMDBT, 2,4-DMDBT/1,4-DMDBT have also been shown to be useful maturity ratios.

10.4.9.5 Benzothiophenes and benzocarbazoles

For many years geochemists have discussed the use of biomarkers as indicators of both absolute and relative migration distances. This is an important issue for conventional petroleum systems in particular since explorationists are searching for oil,

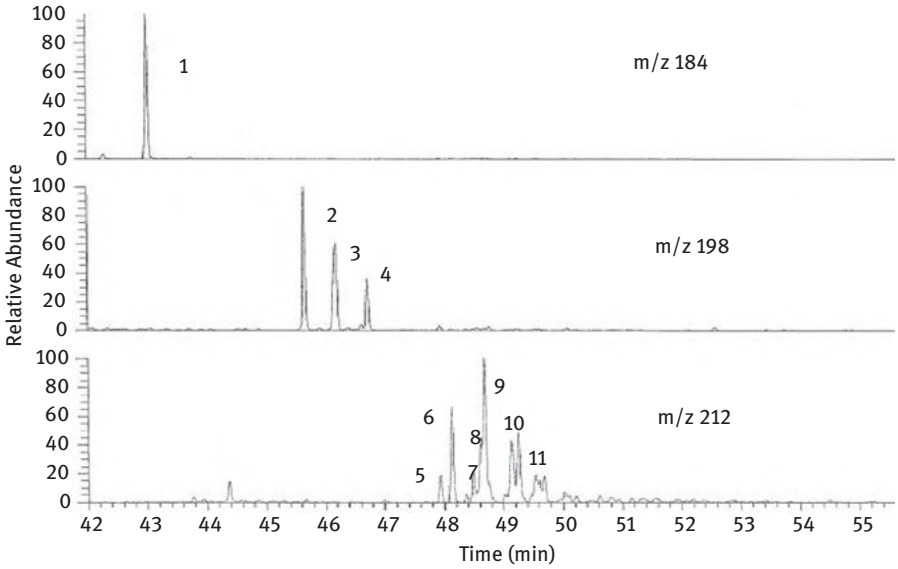

Figure 10.31: Dibenzothiophene and alkylated analogues are readily detected by GCMS and show a mixture of structural isomers which can provide information related to both biodegradation and maturity. (Peak identifications are: 1. Dibenzothiophene (DBT); 2. 4-MethylDBT (4-MDBT); 3. 2 + 3-MDBT; 4. 1-MDBT; 5. 4-EthylDBT (4-EDBT); 6. 4,6-DimethylDBT (4,6-DMDBT); 7. 2,4-DMDBT; 8. 2,6-DMDBT; 9. 3,6-DMDBT; 10. 2,7- + 3,7-DMDBT).

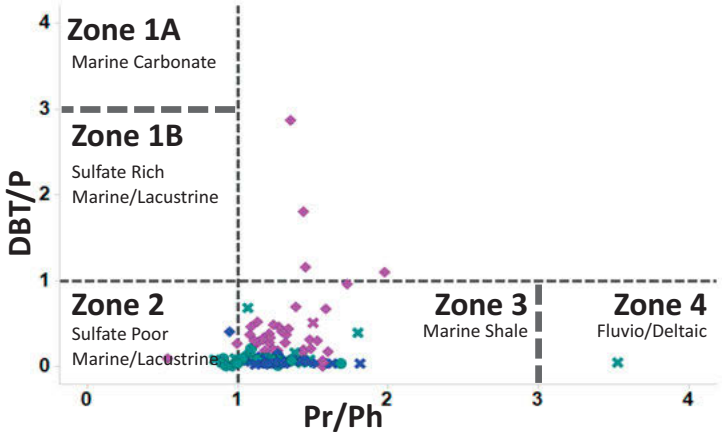

Figure 10.32: The cross plot of dibenzothiophene (DBT)/phenanthrene (PHEN) versus pristane/phytane was developed many years ago by Hughes and coworkers [242] and is used extensively to provide information on source rock lithology.

not source rocks. If absolute migration distances can be determined possible source locations, migration pathways, and additional reservoirs along the migration pathway could be determined. Attempts to quantify migration distances were initially proposed by Seifert and Moldowan [244] in one of the early papers discussing steranes and their use as maturity indicators. The use of the two sterane maturity parameters had been proposed along with the suggestion that these two parameters would change at the same rate. However, a cross plot of the 20*S*/20*R* versus the ββ/αα C_{29} sterane ratios showed a number of samples did not follow the expected relationship. It was proposed that such a discrepancy was related to the differential rate of migration of the different isomers. However, the actual migration distances related to these discrepancies were never quantified at that time.

It was not until many years later when Larter and co-workers introduced a ratio based on benzocarbazoles (BC) that was proposed could be used to quantify absolute migration distances [245]:

$$\text{BC Ratio} = \frac{\text{benzo[a]carbazole}}{\text{benzo[a]carbazole} + \text{benzo[c]carbazole}}$$

This concept was based on the idea that the two benzocarbazoles were structurally identical apart from their shape and any impact on the two isomers by factors such as source, migration, or depositional environment would basically be the same. Any change in the relative proportions of the two isomers could be assumed to result from differences in the migration rates of the two isomers as a consequence of the small differences in the shapes of the molecules. Ideally, oils that have migrated further should have a lower BC ratio due to the preferential loss and possible sorption onto clays during migration of the linear benzo[a]carbazole as compared to the benzo[c]carbazole [245]. Calibration plots were developed for this ratio in a number of basins and used to propose that the ratio would reflect absolute migration distances.

However, the BC ratio was subsequently found to be unreliable as the carbazoles retained maturity and facies information so that the measured migration distance was erroneous [246–248]. Later, Zhang et al. [248] used a new method to better quantify long-distance migration distances using heavy polar compounds to potentially eliminate the contamination of organofacies, maturity, lithology, and biodegradation. This new method suggests a secondary migration fractionation index which used low-abundance polar compounds, such as methyl- and dimethylcarbazoles, from which the relative lateral migration distances could be calculated with the use of a reference point [248]. A number of papers have still appeared in recent years where the benzocarbazole ratio has been used to measure relative migration distances rather than absolute distances [249].

A more recent approach that also appears to have achieved limited success is related to the use of S-containing aromatic compounds. Fang et al. [250] attempted to demonstrate the use of methyldibenzothiophenes (MDBT), dimethyldibenzothiophenes (DMDBT), and benzo[b]naphthothiophene (BNT) to determine relative oil migration

distances and pathways. Benzothiophenes and benzo[b]naphthothiophenes were used since they have a slightly higher electronegativity than hydrocarbons due to the presence of the sulfur atom bonding with hydrogen. When these molecules migrate, a dipole interaction occurs between the thiophene compounds and carrier beds which causes preferential adsorption of thiophene compounds onto clays of the carrier bed (Fang et al., 2016). The use of these sulfur-bearing compounds has been found to work well in determining migration pathways of oils that are genetically related. Lithology, organic matter input, and maturity have little or no effect on these compounds, leaving the oil migration pathway as the only variable [250]. In the study by Fang et al. [250] regular steranes and triaromatic steranes were initially used to show the samples were genetically related. The ratios: 4-/1-MDBT, 4,6/(1,4 + 1,6)-DMDBT, (2,6 + 3,6)/(1,4 + 1,6)-DMDBT, and 2,1/(2,1 + 1,2)-BNT were most efficient in determining migration pathways and filling points over 30 miles in the Tarim Basin. These studies show that a change from a higher ratio to a lower ratio indicates the oil migration pathway(s). A more recent study in the Anadarko Basin, Oklahoma, used these same ratios to demonstrate an overall oil migration pathway that moves from south to north, out of Oklahoma into the Hugoton Embayment, Kansas [251].

10.5 Summary

Biomarkers have played a key role in exploration and production studies over the last half century. Much of this progress has paralleled developments in analytical techniques, particularly GC and GC-MS. Novel biomarkers continue to be identified, albeit at a slower rate than many years ago. Many of the most recent compounds are higher carbon numbered compounds, heteroatomic compounds, and more polar molecules. As is well documented, the "easy" oil has been found and in order to find new reserves every possible technique available will need to be used. Our understanding and interpretation of the biomarker distributions continue to improve. Many of the earlier interpretations have been changed or been modified, but this continues to be an evolving field. As the years pass it is inevitable that new techniques will evolve, new biomarkers will be discovered, and additional and novel interpretations will be made. These compounds will continue to provide information that is of great value to the explorationists and production engineers. The majority of biomarkers discovered to date have been saturate and aromatic hydrocarbons with less than 50 carbon atoms. In the future it is inevitable that novel biomarkers will be found with the polar compounds present in crude oils in the carbon number range above C_{40}. The presence of these compounds will be utilized in the same manner as previously discovered biomarkers and provide additional information on source and depositional environments in both conventional and unconventional petroleum systems.

References

[1] Rossini FD. Hydrocarbons in petroleum. J Chem Ed, 1960, 37, 554–561.
[2] Hites RA, Biemann K. Mass spectrometer-computer system particularly suited for gas chromatography of complex mixtures. Anal Chem, 1968, 40, 1217–1221.
[3] Burlingame AL, Haug PA, Schnoes HK, Simoneit BR. High resolution mass spectrometry in molecular structure studies. XXVII. Fatty acids derived from the green river formation oil shale by extractions and oxidations. A review. Adv Org Geochem, 1969, 85–129.
[4] Marshall AG, Hendrickson CL, Jackson GS. Fourier transform ion cyclotron resonance mass spectrometry: A primer. Mass Spectrom Rev, 1998, 17(1), 1–35.
[5] Marshall AG. Milestones in fourier transform ion cyclotron resonance mass spectrometry technique development. Int J Mass Spect Ion Proces, 2000, 200, 331–356.
[6] Marshall AG, Rodgers RP. Petroleomics: The next grand challenge for chemical analysis. Acc Chem Res, 2004, 37(1), 53–59.
[7] Rodgers RP, Schaub TM, Marshall AG. Petroleomics: MS returns to its roots. Anal Chem, 2005, 77(1), 20A–27A.
[8] Silva R, Silva RSF, Castro EVR, Peters KE, Azevedo DA. Extended diamondoid assessment in crude oil using comprehensive two-dimensional gas chromatography coupled to time-of-flight mass spectrometry. Fuel, 2013, 112(5), 125–133.
[9] Wang G, Shi S, Wang P, Wang TG. Analysis of diamondoids in crude oils using comprehensive two-dimensional gas chromatography/time-off-flight mass spectrometry. Fuel, 2013, 107(5), 706–714.
[10] Peters KE, Walters CC, Moldowan JM. The biomarker guide: biomarkers and isotopes in petroleum exploration and earth history. 2nd edition, Cambridge University Press, New York, 2005.
[11] Larter SR, Wilhems A, Head IM, Koopmans M. The controls on the composition of biodegraded oils in the deep subsurface-Part 1: Biodegradation rates in petroleum reservoirs. Org Geochem, 2003, 34(4), 601–613.
[12] Larter S, Huang H, Adams J, Bennett B, Jokanola O, Oldenburg T, Jones M, Head I, Riediger C, Fowler M. the controls on the composition of biodegraded oils in the deep subsurface: Part II – Geological controls on subsurface biodegradation fluxes and constraints on reservoir-fluid property prediction. Am Assoc Petrol Geol Bull, 2006, 90(6), 921–938.
[13] Larter SR, Huang H, Adams J, Bennet B, Snowdon LR. A practical biodegradation scale for use in reservoir geochemical studies of biodegraded oils. Org Geochem, 2012, 45, 66–76.
[14] Tissot B, Welte DH. Petroleum formation and occurrence. 2nd edition, Springer Verlag, Berlin, 1984.
[15] Hunt JM. Petroleum geochemistry and geology. 2nd edition, Freeman, New York, 1996.
[16] Curiale JA, Curtis JB. Organic geochemical applications to the exploration for source-rock reservoirs – A review. J Unconv Oil Gas Res, 2016, 13, 1–31.
[17] Hunt JM, Philp RP, Kvenvolden KA. Early developments in petroleum geochemistry. Org Geochem, 2002, 33, 1025–1052.
[18] Schriever W. Reflection seismograph prospecting - how it started. Geophysics, 1952, 17(4), 936–942.
[19] Vernadskii VI. Outlines of geochemistry. ONTI Gornogeologie Neft Izd, 1934, 152–153.
[20] Vassoevich NB, Yu I, Korchagina I, Lopatin NV, Chernischev VV. The main stage of petroleum formation. vol. 6, Moscow University, Vestnik, 1969, 3–37. (in Russian). [English translation: Intern Geol Rev 1970,12,1276-96].
[21] Trask PD, Wu CC. Does petroleum form in sediments at time of deposition?. Am Assoc Petrol Geol Bull, 1930, 14, 1451–1463.

[22] McIver RD Composition of kerogen-Clue to its role in the origin of petroleum. Proceedings of the SeventhWorld Petroleum Congress in Mexico City. Elsevier Science, London, 1967, 2, 26–36.
[23] Durand B, ed. Kerogen-insoluble organic matter from sedimentary rocks. Editions Technip, Paris, 1980.
[24] Stach E, Mackowsky M-T, Teichmeuller M, Taylor GH, Chandra D, Teichmeuller R. Textbook of coal petrology. 3rd edition, Bebruder Borntraeger, Berlin, 1982.
[25] Dow WG. Kerogen studiesand geological interpretations. J Geochem Explor, 1977, 7(2), 77–79.
[26] Treibs A. The occurrence of chlorophyll derivatives in an oil shale of the upper triassic. Annalen, 1934, 517, 103–114.
[27] Treibs A. Chlorophyll and hemin derivatives in organic materials. Angewan Chem, 1936, 49, 682–686.
[28] Eglinton G, Calvin M. Chemical fossils. Sci Am, 1967, 216, 32–43.
[29] Mackenzie AS, Brassell SC, Eglinton G, Maxwell JR. Chemical fossils: The geological fate of steroids. Science, 1982, 217, 491–504.
[30] Philp RP, Oung JN. Biomarker, occurrence, formation and detection. Anal Chem, 1988, 60(10), 887A–896A.
[31] Wang Y, Moldowan JM. Molecular and isotopic geochemistry: Technology development and applications to exploration from the present-day to mid-century. Am Assoc Petrol Geol Search Discovery Article #42503, 2020. doi:10.1306/42503Wang202.
[32] French KL, Hallmann C. Comparability and reproducibility of biomarker ratio values measured by GC-QQQ-MS-Organic Geochemistry https://doi.org/10.1016/j.orggeochem.2020.104124.
[33] Del Rio JC, Philp RP. Nature and geochemistry of high molecular weight hydrocarbons (above C_{40}) in oils and solid bitumens. Org Geochem, 1992, 18(4), 541–553.
[34] Philp RP. High temperature gas chromatography for the analysis of fossil fuels. In: The uses of chromatography for analysis of synthetic and fossil fuels. J High Res Chromatog, 1984, 17 (6), 398–406.
[35] Tuo J, Philp RP. Occurrence and distribution of high molecular weight hydrocarbons in selected non-marine source rocks from the Liaohe, Qaidam and Tarim Basins, China. Org Geochem, 2003, 34, 1543–1558.
[36] Milner CWD, Rogers MA, Evans D. Petroleum transformations in reservoirs. J Geochem Explor, 1977, 7, 101–153.
[37] Blanc PH, Connan J. Preservation, degradation and destruction of trapped oil. In: Magoon LB, Dow WG, eds. The petroleum system-from source to trap. AAPG, Tulsa, OK, 1994, 237–247.
[38] Heath DJ, Lewis CA, Rowland SJ. The use of high temperature gas chromatography to study the biodegradation of high molecular weight hydrocarbons. Org Geochem, 1997, 26, 769–785.
[39] Mackenzie AS, McKenzie D. Isomerization and aromatization of hydrocarbons in sedimentary basins formed by extension. Geol Mag, 1983, 120, 417–470.
[40] Requejo AG. Quantitative analysis of triterpanes and sterane biomarkers: Methodology and applications in molecular maturity studies. In: Moldowan JM, Albrecht P, Philp RP, eds. Biological markers in sediments and petroleum. Prentice-Hall, Englewood Cliffs, NJ, 1992, 222–240.
[41] Murphy BL, Morrison RD, eds. Introduction to environmental forensics. Academic Press, Oxford, 2015.
[42] Baker EW, Louda JW. Porphryins in the geological record. Meth Geochem Geophys, 1986, 24, 124–125.

[43] Baker EW, Louda JW. Thermal aspects in chlorophyll geochemistry. Adv Org Geochem, 1983, 1, 401–421.
[44] Lewan MD. Factors controlling the proportionality of vanadium to nickel in crude oils. Geochem Cosmochim Acta, 1984, 48(11), 2231–2238.
[45] Barwise AJ. Role of nickel and vanadium in petroleum classification. Energy Fuels, 1990, 4(6), 647–652.
[46] Filby RH, Van Berkel GJ. Geochemistry of metal complexes in petroleum, source rocks, and coals: An overview. ACS Publications, 1987, 1, 2–39.
[47] Aizenshtat Z, Sundararaman P. Maturation trend in oils and asphalts of the jordan rift: Utilization of detailed vanadylporphyrin analysis. Geochim Cosmochim Acta, 1989, 53(12), 3185–3188.
[48] Xu H, Lesage S. Separation of vanadyl and nickel petroporphyrins on an aminopropyl column by high-performance liquid chromatography. J Chromatog, 1992, 607(1), 139–144.
[49] Sundararaman P, Schoell M, Littke R, Baker DR, Leythaeuser D, Rullkötter J. Depositional environment of Toarcian shales from northern Germany as monitored with porphyrins. Geochem Cosmochim Acta, 1993, 57(17), 4213–4218. CHECKYEARS.
[50] Sundararaman P, Raedeke LD. Vanadyl porphyrins in exploration: Maturity indicators for source rocks and oils. Appl Geochem, 1993, 8(3), 245–254.
[51] Barwise AJ, Roberts I. Diagenetic and catagenetic pathways for porphyrins in sediments. Org Geochem, 1984, 6, 167–176.
[52] Mackenzie AS, Quirke JM, Maxwell JR. Molecular parameters of maturation in the toarcian shales, Paris Basin, France – II evolution of metalloporphyrins. Phy Chem Earth, 1980, 12, 239–248.
[53] Barwise AJ. Use of porphyrins as a maturity parameter for oils and sediments. Geological Soc London Spec Pub, 1983, 12(1), 309–315.
[54] Louda JW, Mongkhonsri P, Baker EW. Chlorophyll degradation during senescence and death-III: 3–10 yr experiments, implications for ETIO series generation. Org Geochem, 2011, 42(6), 688–699.
[55] Chicarelli MI, Maxwell JR. Analysis of ancient porphyrins. Trends Anal Chem, 1987, 6, 158–164.
[56] Higgins MB, Robinson RS, Husson JM, Carter SJ, Pearson A. Dominant eukaryotic export production during ocean anoxic events reflects the importance of recycled NH4+. Proc Nat Acad Sci, 2012, 109(7), 2269–2274.
[57] Kashiyama Y, Ogawa NO, Kuroda J, Shiro M, Nomoto S, Tada R, Kitazato H, Ohkouchi N. Diazotrophic cyanobacteria as the major photoautotrophs during mid-cretaceous oceanic anoxic events: Nitrogen and carbon isotopic evidence from sedimentary porphyrin. Org Geochem, 2008, 39(5), 532–549.
[58] Junium CK, Freeman KH, Arthur A. Controls on the stratigraphic distribution and nitrogen isotopic composition of zinc, vanadyl and free base porphyrins through oceanic anoxic event 2 at demerara rise. Org Geochem, 2015, 80, 60–71.
[59] Thompson KFM. Classification and thermal history of petroleum based on light hydrocarbons. Geochim Cosmochim Acta, 1983, 47(2), 303–316.
[60] Thompson KFM. Fractionated aromatic petroleums and the generation of gas-condensates. Org Geochem, 1987, 11(6), 573–590.
[61] Thompson KFM. Gas-condensate migration and oil fractionation in deltaic systems. Mar Petrol Geol, 1988, 5, 237–246.
[62] Thompson KFM. Light hydrocarbons in subsurface sediments. Geochem Cosmochim Acta, 1979, 43(5), 657–672.

[63] Mango FD. An invariance in the isoheptanes of petroleum. Science, 1987, 237(4814), 514–517.
[64] Mango FD. The origin of light cycloalkanes in petroleum. Geochim Cosmochim Acta, 1990, 54(1), 23–27.
[65] Halpern HI. Development and applications of light-hydrocarbon-based star diagrams. Am Assoc Petrol Geol Bull, 1995, 79(6), 801–815.
[66] England WA. The org geochem of petroleum reservoirs. Org Geochem, 1990, 16, 419–426.
[67] Kaufman RL, Ahmed AS, Elsinger RJ. Gas chromatography as a development and production tool for fingerprinting oils from individual reservoirs: Applications in the Gulf of Mexico. GCSSEPM Found Ninth Ann Res Conf Proc, 1990, 263–282.
[68] Bray EE, Evans ED. Distribution of n-paraffins as a clue to recognition of source beds. Geochim Cosmochim Acta, 1961, 22, 2–15.
[69] Eglinton G, Murphy MTJ, eds. Org geochemistry: Methods and results. Springer Verlag, New York, 1969.
[70] Stevens NP, Bray EE, Evans ED. Hydrocarbons in sediments of the Gulf of Mexico. AAPG Bull, 1956, 40, 975–983.
[71] Winters JC, Williams JA. Microbiological alteration of crude oil in the reservoir. Symposium on petroleum transformation in geologic environments. ACS Div Petrol Chem Paper, 1969, 86, E22–E31.
[72] Blanc PH, Connan J. Origin and occurrence of 25-norhopanes: A statistical study. Org Geochem, 1992, 18(6), 813–828.
[73] Holba AG, Wright L, Levinson R, Huizinga B, Scheihing B. Effects and impact of early-stage anaerobic biodegradation on Kuparuk River Field, Alaska. Geol Soc London Spec Pub, 2004, 237, 53–88.
[74] Didyk BM, Simoneit BRT, Brassell SC, Eglinton G. Organic geochemical indicators of palaeoenvironmental conditions of sedimentation. Nature, 1978, 272, 216–221.
[75] Powell TG, McKirdy DM. Relationship between ratio of pristane to phytane, crude oil composition and geological environment in Australia. Nature, 1973, 243, 37–39.
[76] Gossens J, de Leeuw JW, Schenck PA, Brassell SC. Tocopherols as likely precursors of pristane in ancient sediments and crude oils. Nature, 1984, 312, 440–442.
[77] Ten Haven HL, De Leeuw JW, Damsté JS, Schenck PA, Palmer SE, Zumberge JE. Application of biological markers in the recognition of palaeohypersaline environments. Geological Soc London Spec Pub, 1988, 40(1), 123–130.
[78] Rontani J-F, Nassiry M, Michotey V, Guasco S, Bonin P. Formation of pristane from α-tocopherol under simulated anoxic sedimentary conditions: A combination of biotic and abiotic degradative processes. Geochim Cosmochim Acta, 2010, 74, 252–263.
[79] Shanmugam G. Significance of coniferous rain forests and related organic matter in generating commercial quantities of oil, Gippsland Basin, Australia. Am Assoc Petrol Geol Bull, 1985, 69, 1241–1254.
[80] Albaiges J. Identification and geochemical significance of long chain acyclic isoprenoid hydrocarbons. In: Douglas AG, Maxwell JR, eds. Advances in org geochem 1979. Pergamon, Oxford, 1980, 19–28.
[81] Moldowan JM, Seifert WK. Head to head linked isoprenoids in petroleum. Science, 1979, 204, 169–171.
[82] Lange BM, Rujan T, Martin W, Croteau R. Isoprenoid biosynthesis: The evolution of two ancient and distinct pathways across genomes. Proc Nat Acad Sci, 2000, 97, 13172–13177.
[83] Lichtenthaler HK, Schwender J, Disch A, Rohmer M. Biosynthesis of isoprenoids in higher plant chloroplasts proceeds Vla a mevalonate-independent pathway. Fed Euro Biochem Soc Letts, 1997, 400, 271–274.

[84] Alexander R, Kagi RI, Sheppard PN. 1,8-Dimethylnaphthalene as an indicator of petroleum maturity. Nature, 1984, 308, 442–443.
[85] Rodriguez ND, Philp RP. Productivity and paleoclimate controls on source rock character in the anan trough, north central Sumatra, Indonesia. Org Geochem, 2012, 45, 18–28.
[86] de Grande SMB, Aquino Neto FR, Mello MR. Extended tricyclic terpanes in sediments and petroleum. Org Geochem, 1993, 20, 1039–1047.
[87] Moldowan JM, Seifert WK, Gallegos EJ. Identification of an extended series of tricyclic terpanes in petroleum. Geochim Cosmochim Acta, 1983, 478, 1531–1534.
[88] Philp P, Symcox C, Wood M, Nguyen T, Wang H, Kim D. possible explanations for the predominance of tricyclic terpanes over pentacyclic terpanes in certain oils and rock extracts. Org Geochem, 2021, 155, 104220. doi:https://doi.org/10.1016/j.orggeochem.2021.104220.
[89] Philp RP, Gilbert TD. Biomarker distributions in Australian oils predominantly derived from terrigenous source material. In: Leythauser D, Rulkotter J, eds. Advs. in org. geochem. 1985. Pergamon Press, Oxford, 1986, 73–84.
[90] Aquino Neto FR, Trendel JM, Wrestle A, Connan J, Albrecht PA. Occurrence and formation of tricyclic and tetracyclic terpenes in sediments and petroleums. In: Bjorøy M et al, eds. Advances in organic geochemistry 1981. J. Wiley and Sons, New York, 1983, 659–667.
[91] Woolhouse AD, Oung J-N, Philp RP, Weston RJ. Triterpanes and ring-a degraded triterpanes as characteritic of tertiary oils derived from predominantly higher plant sources. Org Geochem, 1992, 18, 23–31.
[92] Ourisson G, Albrecht P. Hopanoids. 1. Geohopanoids: The most abundant natural products on Earth?. Acc Chem Res, 1992, 259, 398–402.
[93] Ourisson G, Albrecht P, Rohmer M. Predictive microbial biochemistry-from molecular fossils to prokaryotic membranes. Trend Biochem Sci, 1982, 77, 236–239.
[94] Ourisson G, Rohmer M, Porolla K. Prokaryotic hopanoids and other polyterpenoid sterol surrogates. Ann Rev Microbiol, 1987, 411, 301–333.
[95] Rullkotter J, Philp RP. Extended hopanes up to C_{40} in Thornton bitumen. Nature, 1981, 292, 616–618.
[96] Seifert WK, Moldowan JM. Applications of steranes, terpanes and monoaromatics to maturation, migration, and source of crude oils. Geochim Cosmochim Acta, 1978, 42, 77–95.
[97] Peters KE, Clark ME, Das Gupta U, McCaffrey MA, Lee CY. (1995). Recognition of an Infracambrian source rock based on biomarkers in Bagehwala-1 oil, India. Am Assoc Petrol Geol Bull, 1985, 78, 893–909.
[98] Bishop AN, Farrimond P. A new method of comparing extended hopane distributions. Org Geochem, 1995, 23(10), 987–990.
[99] Sinninghe Damsté JS, Van Duin AC, Hollander D, Kohnen ME, De Leeuw JW. Early diagenesis of bacteriohopanepolyol derivatives: Formation of fossil homohopanoids. Geochim Cosmochim Acta, 1995, 59(24), 5141–5157.
[100] Moldowan JM, Fago FJ, Carlson RMK, Young DC, van Duyne G, Clardy J, Schoell M, Pillinger CT, Watt DS. Rearranged hopanes in sediments and petroleum. Geochim Cosmochim Acta, 1991, 55, 3333–3353.
[101] Nytoft HP, Lund K, Kennet T, Jørgensen C, Thomsen JV, Sørensen SW, Lutnæs BF. Identification of an early-eluting rearranged hopane series. Synthesis from hop 17 (21)-enes and detection of intermediates in sediments. Abst Rep -Int Congr Org Geochem, 2007, 23, 1017–1018.
[102] Farrimond P, Telnæs N. Three series of rearranged hopanes in Toarcian sediments (northern Italy). Org Geochem, 1996, 25, 165–177.

[103] Nytoft HP, Lutnaes BE, Johansen JE. 28-Nor-spergulanes, a novel series of rearranged hopanes. Org Geochem, 2006, 37, 772–786.
[104] Wang X, Zhao W, Zhang S, Wang H, Su J, Canfield DE, Hammarlund J. The aerobic diagenesis of mesoproterozoic organic matter. Scient Rep, 2018, 8, 13324.
[105] Moldowan JM, McCaffrey MA. A novel microbial hydrocarbon degradation pathway revealed by hopane demethylation in a petroleum reservoir. Geochim Cosmochim Acta, 1995, 59, 1891–1894.
[106] De Lemos Scofield A Nouveaux marqueurs biologiques de sediments et petroles riches en soufre: identification et mode de formation. PhD Thesis, Universidade Louis Pasteur De Strasbourg. 1990.
[107] Sumer Gorenekli Y. Geochemical characterization of the lower Pennsylvanian Morrow shale in the Anadarko Basin of Oklahoma. M.S. Thesis, U. Oklahoma. 2018, pp. 175.
[108] Summons RE, Janhke LL. Hopenes and hopanes methylated in ring A: Correlation of the hopanoids from extant methylotrophic bacteria with their fossil analogues. In: Moldowan JM, Albrecht P, Philp RP, eds. Biological markers in sediments and petroleum. Prentice-Hall, Englewood Cliffs, NJ, 1992, 182–194.
[109] Summons RE, Jahnke LL, Hope JM, Logan GA. 2-Methylhopanoids as biomarkers for cyanobacterial oxygenic photosynthesis. Nature, 1999, 400, 554–557.
[110] Naafs BDA, Bianchini G, Monteiro FM, Sanchez-Baracaldo P. The occurrence of 2-methylhopanoids in modern bacteria and the geological record. Geobiology, 2021, 1–19.
[111] Whitehead EV. Molecular evidence for the biogenesis of petroleum and natural gas. In: Ingerson E, ed. Proceedings of symposium on hydrogeochemistry and biogeochemistry. vol. II, The Clarke Company, 1973, 158–211.
[112] Whitehead EV. The structure of petroleum pentacyclanes. In: Tissot B, Bienner F, eds. Advances in org geochem 1973. Editions Technip, 1974, 225–243.
[113] Grantham PJ, Posthuma J, Baak A. Triterpanes in a number of far eastern crude oils. In: Bjoroy M, et al eds. Advances in org geochem 1981. Wiley-Haydon, Chichester, 1983, 710–724.
[114] Moldowan JM, Dahl J, Huizinga BJ, Fago FJ, Hickey LJ, Peakman TM, Taylor DW. The molecular fossil record of oleanane and its relation to angiosperms. Science, 1994, 265, 768–771.
[115] Peters KE, Clutson MJ, Robertson G. Mixed marine and lacustrine input to an oil-cemented sandstone breccia from Brora, Scotland. Org Geochem, 1999, 30(4), 237–248.
[116] Taylor DW, Li H, Dahl J, Fago FJ, Zinniker D, Moldowan JM. Biogeochemical evidence for the presence of the angiosperm molecular fossil oleanane in paleozoic and mesozoic non-angiospermous fossils. Paleobiology, 2006, 32(2), 179–190.
[117] Philp P, Wood M, Sumer Gorenekli Y, Nguyen T, Symcox C, Wang H, Kim D. The presence of 18α (H)-oleanane in pennsylvanian and mississippian rocks in the anadarko basin, Oklahoma. Org Geochem, 2021, 152, 104181.
[118] Doyle JA, Donoghue MJ. Phylogenies and angiosperm diversification. Paleobiology, 1993, 19, 141–167.
[119] Crane PR. Time for the angiosperms. Nature, 1994, 366, 631–632.
[120] Murray AP, Sosrowidjojo IB, Alexander R, Kagi RI, Norgate CM, Summons RE. Oleananes in oils and sediments: Evidence of marine influence during early diagenesis?. Geochim Cosmochim Acta, 1997, 61(6), 1261–1276.
[121] Strachan MG, Alexander R, Kagi RI. Trimethylnaphthalenes in crude oils and sediments: Effects of source and maturity. Geochim Cosmochim Acta, 1988, 52, 1255–1264.
[122] Armstroff A, Wilkes H, Schwarzbauer J, Littke R, Horsfield B. Aromatic hydrocarbon biomarkers in terrestrial organic matter of devonian to permian age. Palaeogeog Palaeoclim Palaeoecol, 2006, 240, 253–274.

[123] Marynowski L, Kurkiewicz S, Rakocinski M, Simoneit BRT. Effects of weathering on organic matter: I. Changes in molecular composition of extractable organic compounds caused by paleoweathering of a lower Carboniferous (Tournasian) marine black shale. Chem Geol, 2011a, 285, 144–156.
[124] Marynowski L, Szeleg E, Jedrysek MO, Simoneit BRT. Effects of weathering on organic matter Part II: Fossil wood weathering and implications for organic geochemical and petrographic studies. Org Geochem, 2011b, 42, 1076–1088.
[125] Hills IR, Whitehead EV, Anders DE, Cummins JJ, Robinson WE. An optically active triterpene, gammacerane in green river, colorado, oil shale bitumen. JCS Chem Comm, 1966, 20, 752–754.
[126] Moldowan JM, Seifert WK, Gallegos EJ. Relationship between petroleum composition and depositional environment of petroleum source rocks. Am Assoc Petrol Geol Bull, 1985, 69, 1255–1268.
[127] Fu Jiamo F, Guoying S, Pingan P, Brassell SC, Eglinton G, Jigang J. Peculiarities of salt lake sediments as potential source rocks in China. Org Geochem, 1986, 10, 119–126.
[128] Mello MR, Gaglianone PC, Brassell SC, Maxwell JR. Geochemical and biological marker assessment of depositional environments using Brazilian offshore oils. Mar Petrol Geol, 1988a, 5, 205–223.
[129] Mello MR, Telnaes N, Gaglianone PC, Chicarelli MI, Brassell SC, Maxwell JR. Organic geochemical characterization of depositional paleoenvironments in Brazilian marginal basins. Org Geochem, 1988b, 13, 31–46.
[130] Sinninghe Damste JS, Kenig F, Koopmans MP. Evidence for gammacerane as indicator of water column stratification. Geochim Cosmochim Acta, 1995, 59, 1895–1900.
[131] Volkman JK. A review of sterol markers for marine and terrigenous organic matter. Org Geochem, 1986, 9(2), 83–99.
[132] Moldowan JM, Fago FJ, Lee CY, Jacobson SR, Watt DS, Slougui N, Jeganathan A, Young DC. Sedimentary 24-n-propylcholestanes, molecular fossils diagnostic of marine algae. Science, 1990, 247(4940), 309–312.
[133] Ten Haven HL, de Leeuw JW, Peakman TM, Maxwell JR. Anomalies in steroid and hopanoid maturity indices. Geochem Cosmochim Acta, 1986, 50, 853–855.
[134] Lewan MD, Bjoroy M, Dolcater DE. Effects of thermal maturation on steroid hydrocarbons as determined by hydrous pyrolysis of phosphoria retort shale. Geochim Cosmochim Acta, 1986, 50, 1977–1987.
[135] Barbanti SM, Moldowan JM, Watt DS, Kolaczkowska E. New triaromatic steroids distinguish paleozoic from mesozoic oil. Org Geochem, 2011, 42(4), 409–424.
[136] Moldowan JM, Dahl J, Jacobson SR, Huizinga BJ, Fago FJ, Shetty R, Watt DS, Peters KE. Chemostratigraphic reconstruction of biofacies: Molecular evidence linking cyst-forming dinoflagellates with pre-Triassic ancestors. Geology, 1996, 24(2), 159–162.
[137] Moldowan JM, Jacobson SR, Dahl J, Al-Hajji A, Huizinga BJ, Fago FJ. Molecular fossils demonstrate precambrian origin of dinoflagellates. In: Zhuravlev A, Riding R, eds. Ecology of the Cambrian radiation. Columbia University Press, New York, 2001, 474–493.
[138] Summons RE, Volkman JK, Boreham CJ. Dinosterane and other steroidal hydrocarbons of dinoflagellate origin in sediments and petroleum. Geochem Cosmochim Acta, 1987, 51, 3075–3082.
[139] Goodwin NS, Mann AL, Patience RL. Structure and significance of C30 4-methylsteranes in lacustrine shales and oils. Org Geochem, 1988, 12, 495–506.
[140] Summons RE, Capon RJ. Fossil steranes with unprecedented methylation in ring A. Geochim Cosmochim Acta, 1988, 52, 2733–2736.

[141] Dahl J, Moldowan JM, Summons RE. Extended 3β-alkylsteranes and 3-alkyltriaromatic steroids in crude oils and rock extracts. Geochim Cosmochim Acta, 1995, 59, 3717–3729.
[142] Summons RE, Powell TG. Identification of aryl isoprenoids in source rocks and crude oils: Biological markers for the green sulphur bacteria. Geochem Cosmochim Acta, 1987, 51(3), 557–566.
[143] Sinninghe Damsté JS, Kock-Van Dalen AC, De Leeuw JW, Schenck PA, Guoying S, Brassell SC. The identification of mono-, di-and trimethyl 2-methyl-2-(4, 8, 12-trimethyltridecyl) chromans and their occurrence in the geosphere. Geochem Cosmochim Acta, 1987, 51(9), 2393–2400.
[144] Sinninghe Damsté JS, Keely BJ, Betts SE, Baas M, Maxwell JR, de Leeuw JW. Variations in abundances and distributions of isoprenoid chromans and long-chain alkylbenzenes in sediments of the mulhouse basin: A molecular sedimentary record of palaeosalinity. Org Geochem, 1993, 20(8), 1201–1215.
[145] Tulipani S, Grice K, Greenwood PF, Schwark L, Boettcher ME, Summons RE, Foster CB. Molecular proxies as indicators of freshwater incursion-driven salinity stratification. Chem Geol, 2015, 409, 61–68.
[146] Koopmans MP, Rijpstra WI, de Leeuw JW, Lewan MD, Damsté JS. Artificial maturation of an immature sulfur-and organic matter-rich limestone from the ghareb formation, jordan. Org Geochem, 1998, 28(7-8), 503–521.
[147] Bao J, Zhu C, Ma A. The relationship between methylated chromans and maturity of organic matter in the source rocks from Jianghan hypersaline basin. Sci Chin Ser D: Earth Sci, 2009, 52(1), 34–41.
[148] Jiang K, Lin C, Cai C, Zhang X, Huang S, Fan Z. Current status and challenges of methyltrimethyltridecylchromans research in source rocks and crude oils. ACS Omega, 2019, 4(6), 9835–9842.
[149] Ten Haven HL, de Leeuw JW, Rullkotter J, Sinninghe Damste JS. Restricted use of pristane/phytane ratio as a palaeoenvironmental indicator. Nature, 1987, 330, 641–643.
[150] Schwark L, Püttmann W. Aromatic hydrocarbon composition of the permian kupferschiefer in the lower rhine basin, NW Germany. Advan Org Geochem, 1990, 16, 749–761.
[151] Wang L, Song Z, Yin Q, George SC. Paleosalinity significance of occurrence and distribution of methyltrimethyltridecyl chromans in the upper cretaceous nenjiang formation, songliao basin, China. Org Geochem, 2011, 42(11), 1411–1419.
[152] Bechtel A, Gawlick HJ, Gratzer R, Tomaselli M, Püttmann W. Molecular indicators of palaeosalinity and depositional environment of small scale basins within carbonate platforms: The late triassic hauptdolomite wiestalstausee section near hallein (Northern Calcareous Alps, Austria). Org Geochem, 2007, 38(1), 92–111.
[153] Li M, Larter SR, Taylor P, Jones DM, Bowler B, Bjorøy M. Biomarkers or not biomarkers? A new hypothesis for the origin of pristane involving derivation from methyltrimethyltridecylchromans (MTTCs) formed during diagenesis from chlorophyll and alkylphenols. Org Geochem, 1995, 23(2), 159–167.
[154] Dutta S, Hartkopf-Fröder C, Witte K, Brocke R, Mann U. Molecular characterization of fossil palynomorphs by transmission micro-FTIR spectroscopy: Implications for hydrocarbon source evaluation. Intern J Coal Geol, 2013, 115, 13–23.
[155] Zhang Y, Jiang A, Sun Y, Xie L, Chai P. Stable carbon isotope compositions of isoprenoid chromans in Cenozoic saline lacustrine source rocks from the Western Qaidam Basin, NW China: Source implications. Chin Sci Bull, 2012, 57(9), 1013–1023.
[156] Koopmans MP, De Leeuw JW, Lewan MD, Damste JS. Impact of dia-and catagenesis on sulphur and oxygen sequestration of biomarkers as revealed by artificial maturation of an immature sedimentary rock. Org Geochem, 1996a, 25(5–7), 391–426.

[157] Connock GT, Philp RP. Terrigenoously-induced photic zone euxinia in the late devonian midcontinent of North America. Rocky Mount Geobiol Sympos, 2019.
[158] Grantham PJ, Wakefield LL. Variations in the sterane carbon number distributions of marine source rock derived crude oils through geological time. Org Geochem, 1988, 12(1), 61–73.
[159] Liaaen-Jensen S. Bacterial carotenoids. Acta Chem Scand, 1964, 19, 1025–1030.
[160] Cui X, Liu XL, Shen G, Ma J, Husain F, Rocher D, Zumberge JE, Bryant DA, Summons RE. Niche expansion for phototrophic sulfur bacteria at the Proterozoic–Phanerozoic transition. Proc Nat Acad Sci, 2020, 117(30), 17599–17606.
[161] Liaaen-Jensen S, Renstrøm B, Ramdahl T, Hallenstvet M, Bergquist P. Carotenoids of marine sponges. Biochem Syst Ecol, 1982, 10(2), 167–174.
[162] Yamaguchi M. Renieratene, a new carotenoid containing benzene rings, isolated from a sea sponge. Bull Chem Soc Jap, 1958, 31(6), 739–742.
[163] Yamaguchi M. On carotenoids of a sponge "Reniera japonica". Bull Chem Soc Jap, 1957, 30 (2), 111–114.
[164] Imhoff JF, Trüper HG. Marine sponges as habitats of anaerobic phototrophic bacteria. Micro Ecol, 1976, 3(1), 1–9.
[165] Meyer KM, Kump LR. Oceanic euxinia in earth history: Causes and consequences. Annu Rev Earth Planet Sci, 2008, 36, 251–288.
[166] Trüper HG, Genovese S. Characterization of photosynthetic sulfur bacteria causing red water in Lake Faro (Messina, Sicily) 1. Limnol Oceanog, 1968, 13(2), 225–232.
[167] Overmann J, Cypionka H, Pfennig N. An extremely low-light adapted phototrophic sulfur bacterium from the black sea. Limnol Oceanog, 1992, 37(1), 150–155.
[168] Van Gemerden H, Mas J. Ecology of phototrophic sulfur bacteria. In: Anoxygenic photosynthetic bacteria. Springer, Dordrecht, 1995, 49–85.
[169] Brocks JJ, Schaeffer P. Okenane, a biomarker for purple sulfur bacteria (Chromatiaceae), and other new carotenoid derivatives from the 1640 ma barney creek formation. Geochem Cosmochim Acta, 2008, 72(5), 1396–1414.
[170] Sirevåg R, Ormerod JG. Carbon dioxide fixation in green sulphur bacteria. Biochem J, 1970, 120(2), 399–408.
[171] Connock GT, Nguyen TX, Philp RP. The development and extent of photic-zone euxinia concomitant with woodford shale deposition. Am Assoc Petrol Geol Bull, 2018, 102(6), 959–986.
[172] Grice K, Audino M, Boreham CJ, Alexander R, Kagi RI. Distributions and stable carbon isotopic compositions of biomarkers in torbanites from different palaeogeographical locations. Org Geochem, 2001, 32, 1195–1210.
[173] Hartgers WA, Damsté JS, Requejo AG, Allan J, Hayes JM, Ling Y, Xie TM, Primack J, de Leeuw JW. A molecular and carbon isotopic study towards the origin and diagenetic fate of diaromatic carotenoids. Org Geochem, 1994, 22(3–5), 703–725.
[174] Werne JP, Hollander DJ, Lyons TW, Sinninghe Damsté JS. Organic sulfur biogeochemistry: Recent advances and future research directions. Geol Soc Am Spec Pap, 2004, 379, 135–150.
[175] Burridge DJ. Preservation of organic matter in marine sediments: Controls, mechanisms, and an imbalance in sediment organic carbon budgets?. Chem Rev, 2007, 107, 467–485.
[176] Requejo AG, Allan J, Creaney S, Gray NR, Cole KS. Aryl isoprenoids and diaromatic carotenoids in Paleozoic source rocks and oils from the Western Canada and Williston Basins. Org Geochem, 1992, 19(1–3), 245–264.
[177] Maslen E, Grice K, Gale JD, Hallmann C, Horsfield B. Crocetane: A potential marker of photic zone euxinia in thermally mature sediments and crude oils of Devonian age. Org Geochem, 2009, 40(1), 1–11.

[178] Koopmans MP, Schouten S, Kohnen ME, Damsté JS. Restricted utility of aryl isoprenoids as indicators for photic zone anoxia. Geochem Cosmochim Acta, 1996b, 60(23), 4873–4876.
[179] Landa S, Machacek V. Adamantane, a new hydrocarbon extracted from petroleum. Collect Czech Chem Commun, 1933, 5(1), 1–5.
[180] de Araujo PLB, Mansoori GA, de Araujo ES. Diamondoids: Occurrence in fossil fuels, applications in petroleum exploration and fouling in petroleum production. A review paper. Int J Oil Gas Coal Technol, 2012, 5(4), 316–367.
[181] Ma A. Advancement in application of diamondoids on org geochem. J Nat Gas Geosci, 2016, 1(4), 257–265.
[182] Wei Z, Moldowan JM, Adina Paytan P. Diamondoids and molecular biomarkers generated from modern sediments in the absence and presence of minerals during hydrous pyrolysis. Org Geochem, 2006, 37, 891–911.
[183] Lin R, Wilk ZA. Natural occurrence of tetramantane ($C_{22}H_{28}$), pentamantane ($C_{26}H_{32}$) and hexamantane ($C_{30}H_{36}$) in a deep petroleum reservoir. Fuel, 1995, 74(10), 1512–1521.
[184] Dahl JEP, Moldowan JM, Peakman TM, Clardy J, Cobkovsky E, Olmstead MM, May PW, Davis TJ, Steeds JW, Peters KE, Pepper A, Ekuan A, Carlson RMK. Isolation and structural proof of the large diamond molecule, cyclohexamantane ($C_{26}H_{30}$). Angew Chem Int Ed, 2003b, 42(18), 2040–2044.
[185] Dahl JEP, Liu SG, Carlson RMK. Isolation and structure of higher diamondoids, nanometer-sized diamond molecules. Science, 2003a, 299(11), 96–99.
[186] Schoell M, Carlson RMK. Diamondoids and oil are not forever. Nature, 1999, 399(5), 15–16.
[187] Wang G, Li N, Gao B, Li X, Shi B, Wang T. Thermochemical sulfate reduction in fossil ordovician deposits of the majiang area: Evidence from a molecular-marker investigation. Chin Sci Bull, 2013, 58(33), 3450–3457.
[188] Chen J, Fu J, Sheng G, Liu D, Zhang J. The diamondoid hydrocarbon ratios: Novel maturity indices for over-mature crude oils. Org Geochem, 1996, 25, 179–190.
[189] Moldowan JM, Dahl J, Zinniker D, Barbanti SM. Underutilized advanced geochemical technologies for oil and gas exploration and production. J Petrol Sci Eng, 2015, 126, 87–96.
[190] Dahl JE, Moldowan JM, Peters KE, Claypool GE, Rooney MA, Michael GE, Mello MR, Kohnen ML. Diamondoid hydrocarbons as indicators of natural oil cracking. Nature, 1999, 399, 54–57.
[191] Schulz LK, Wilhelms A, Rein E, Steen AS. Application of diamondoids to distinguish source rock facies. Org Geochem, 2001, 32, 365–375.
[192] Wilhelms A, Rein E, Steen AS. Application of diamondoids to distinguish source facies. Org Geochem, 2001, 32(3), 365–375.
[193] Gordadze GN. Geochemistry of cage hydrocarbons. Pet Chem, 2008, 48(4), 241–253.
[194] Grice K, Alexander R, Kagi RI. Diamondoid hydrocarbon ratios as indicators of biodegradation in Australian crude oils. Org Geochem, 2000, 31(1), 67–73.
[195] Wei Z, Walters CC, Moldowan JM, Mankiewicz PJ, Pottorf RJ, Xiao Y, Maze W, Nguyen PTH, Madincea ME, Phan NT, Peters KE. Thiadiamondoids as proxies for the extent of thermochemical sulfate reduction. Org Geochem, 2012, 44(1), 53–70.
[196] Jiang N, Zhu G, Zhang S, Wang Z. Detection of 2-thiaadamantanes in the oil from well TZ-83 in Tarim Basin and its geological implication. Chin Sci Bull, 2008, 53(3), 396–401.
[197] Radke M, Welte DH, Willsch H. Maturity parameters based on aromatic hydrocarbons: Influence of the organic matter type. Org Geochem, 1986, 10, 51–63.
[198] Albrecht P, Ourisson G. Biogenic substances in sediments and fossils. Angew Chem Int Ed, 1971, 10, 209–225.
[199] Hase A, Hites RA. On the origin of polycyclic aromatic hydrocarbons in recent sediments: Biosynthesis by anaerobic bacteria. Geochim Cosmochim Acta, 1976, 40, 1141–1143.

[200] Radke M. Organic geochemistry of aromatic hydrocarbons. In: Brooks J, Welte D, eds. Advances in petroleum geochemistry 2. Academic Press, New York, 1987, 141–207.
[201] Alexander R, Larcher AV, Kagi RI, Price PL. An oil-source correlation study using age-specific plant-derived aromatic biomarkers. In: Moldowan JM, Albrecht P, Philp RP, eds. Biological markers in sediments and petroleum. Prentice-Hall, Englewood Cliffs, New Jersey, 1992, 201–221.
[202] Baek SO, Field RA, Goldstone ME, Kirk PW, Lester JN, Perry R. A review of atmospheric polycyclic aromatic-hydrocarbons – Sources, fate and behavior. Water Air Soil Poll, 1991, 60, 279–300.
[203] Wilcke W. Global patterns of polycyclic aromatic hydrocarbons (PAHs) in soil. Geoderma, 2007, 141, 157–166.
[204] Estrellan CR, Iin F. Toxic emissions from open burning. Chemosphere, 2010, 80, 193–207.
[205] Moriwaki H, Katahira K, Yamamoto O, Fukuyama J, Kamiura T, Yamazaki H, Yoshikawa S. Historical trends of polycyclic aromatic hydrocarbons in the reservoir sediment core at Osaka. Atmos Environ, 2005, 39, 1019–1025.
[206] Chrysikou L, Gemenetzis P, Kouras A, Manoli E, Terzi E, Samara C. Distribution of persistent organic pollutants, polycyclic aromatic hydrocarbons and trace elements in soil and vegetation following a large-scale landfill fire in northern Greece. Environ Int, 2008, 34, 210–225.
[207] Musa Bandowe BA, Srinivasan P, Seelge M, Sirocko F, Wilcke WA. 2600-year record of past polycyclic aromatic hydrocarbons (PAHs) deposition at Holzmaar (Eifel, Germany). Palaeogeog Palaeoclim Palaeoecol, 2014, 401, 111–121.
[208] Mastral MA, Callen MS. A review on polycyclic aromatic hydrocarbons (PAH) emissions from energy generation. Environ Sci Technol, 2000, 34, 3051–3057.
[209] Bostrom CE, Gerde P, Hanberg A, Jernstrom B, Johansson C, Kyrklund T, Rannug A, Torngvist M, Victorin K, Westerholm R. Cancer risk assessment, indicators, and guidelines for polycyclic aromatic hydrocarbons in the ambient air. Environ Health Persp, 2002, 110, 451–488.
[210] Choi SD. Time trends in the levels and patterns of polycyclic aromatic hydrocarbons (PAHs) in pine bark, litter, and soil after a forest fire. Sci Tot Environ, 2014, 470–71, 1441–1449.
[211] Simoneit BRT. Biomass burning – A review of organic tracers for smoke from incomplete combustion. Appl Geochem, 2002, 17, 129–162.
[212] Marynowski L, Simoneit BRT. Widespread Upper Triassic to Lower Jurassic wildfire records from Poland: Evidence from charcoal and pyrolytic polycyclic aromatic hydrocarbons. Palaios, 2009, 24, 785–798.
[213] Grice K, Nabbefield B, Maslen E. Source and significance of selected polycyclic aromatic hydrocarbons in sediments (Hovea-3 well, Perth Basin, Western Australia) spanning the permian-triassic boundary. Org Geochem, 2007, 38, 1795–1803.
[214] Grice K, Lu H, Atahan P, Asif M, Hallmann C, Greenwood P, Maslen E, Tulipani S, Williford K, Dodson J. New insights into the origin of perylene in geological samples. Geochim Cosmochim Acta, 2009, 73, 6531–6543.
[215] Kawamura K, Ishiwatari R, Ogura K. Early diagenesis of organic matter in the water column and sediments: Microbial degradation and resynthesis of lipids in Lake Haruna. Org Geochem, 1987, 4, 251–264.
[216] Britton G. The biochemistry of natural pigments. Cambridge University Press, 1983.
[217] Hashimoto T, Tahara S, Takaoka S, Tori M, Asakawa Y. Structures of a novel binaphthyl and three novel benzophenone derivatives with plant-growth inhibitory activity from the fungus Daldinia concentrica. Chem Pharm, 1994, 42, 1528–1530.

[218] De Riccardis F, Iorzzi M, Minale L, Riccio R, De Forges BR, Debitus C. The gymnochromes: Novel marine brominated phenanthroperylene-quinone pigments from stalked crinoid Gymnocrinus richeri. J Org Chem, 1991, 56, 6781–6787.
[219] Cameron DW, Cromartie RIT, Todd L. Colouring matters of the Aphididae. Part XVI. Reconsideration of the structure of the Erythroaphins. J Chem Soc, 1964, 48–50.
[220] Itoh N, Sakagami N, Torimura M, Watanabe M. Perylene in lake Biwa sediments originating from Cenococcum geophilum in its catchment area. Geochim Cosmochim Acta, 2012, 95, 241–251.
[221] Kohlmeyer J, Kohlmeyer E. Marine mycology, the higher fungi. Academic Press, New York, 1979.
[222] Ingold CT, Hudson HJ. The biology of fungi. 6th edn, Chapman & Hall, London, 1993.
[223] Akinlua A, Torto N, Ajayi TR. Oils in the Northwestern Niger Delta: Aromatic hydrocarbons content and infrared spectroscopic characterization. J Petrol Geol, 2007, 30(1), 91–100.
[224] van Aarssen BGK, Bastow TP, Alexander R, Kagi RI. Distributions of methylated naphthalenes in crude oils: Indicators of maturity, biodegradation and mixing. Org Geochem, 1999, 30, 1213–1227.
[225] Villar JH, Puttmann W, Wolf M. Org Geochem and petrography of tertiary coals and carbonaceous shales from Argentina. Org Geochem, 1988, 13, 1011–1021.
[226] Philp RP, Degarmo CD. Woodford shale from the mcalister cemetery quarry, criner hills uplift, ardmore basin, Oklahoma. Mar Petrol Geol, 2019, 112. doi:https://doi.org/10.1016/j.marpetgeo.2019.104078.
[227] Volkman JK, Alexander R, Kagi R, Rowland SF, Sheppard PN. Biodegradation of aromatic hydrocarbons in crude oils from the barrow sub-basin of Western Australia. Org Geochem, 1984, 6, 619–632.
[228] Williams JA, Bjoroy M, Dolcator DL, Winters JC. Biodegradation in South Texas eocene oils-effects on aromatics and biomarkers. Org Geochem, 1986, 10, 451–461.
[229] Fisher SJ, Alexander R, Kagi RI, Oliver GA. Aromatic hydrocarbons as indicators of biodegradation in north Western Australian reservoirs. In: Purcell PG, Purcell RR, eds. Sedimentary basins of Western Australia: West Australian basins symposium. petroleum exploration society of Australia. WA Branch, Perth, Australia, 1998, 185–194.
[230] Jiang C. Polycyclic Aromatic Hydrocarbons and their Geochemical Significance. Application to Sediments from the Northern Carnarvon Basin. Ph.D. Thesis, Curtin University of Technology, Australia, 1998.
[231] Jiang C, Alexander R, Kagi R, Murray AP. Polycyclic aromatic hydrocarbons in ancient sediments and their relationships to palaeoclimate. Org Geochem, 1998, 29, 1721–1735.
[232] Wakeham SG, Schaffner C, Giger W. Polycyclic aromatic hydrocarbons in recent lake sediments – II. Compounds derived from biogenic precursors during early diagenesis. Geochim Cosmochim Acta, 1980, 44, 415–429.
[233] Killops SD. Novel aromatic hydrocarbons of probable bacterial origin in a Jurassic lacustrine sequence. Org Geochem, 1991, 17, 25–36.
[234] Youngblood WW, Blumer M. Polycyclic aromatic hydrocarbons in the environment: Homologous series in soils and recent marine sediments. Geochim Cosmochim Acta, 1975, 39, 1303–1314.
[235] Prahl FG, Carpenter R. Polycyclic aromatic hydrocarbon (PAH)-phase associations in Washington coastal sediment. Geochim Cosmochim Acta, 1983, 47, 1013–1024.
[236] Alexander R, Bastow TP, Fisher SJ, Kagi RI. Geosynthesis of organic compounds: II. Methylation of phenanthrene and alkylphenanthrenes. Geochim Cosmochim Acta, 1995, 59, 4259–4266.

[237] Radke M, Welte DH, Willsch H. Geochemical study on a well in the Western Canada Basin: Relation of the aromatic distribution pattern to maturity of organic matter. Geochim Cosmochim Acta, 1982, 46, 1–10.
[238] Alexander R, Kagi RI, Noble RA, Volkman JK. Identification of some bicyclic alkanes in petroleum. In: Schenck PA, De Leeuw JW, Lijmbach GWM, eds. Advances in org geochem 1983. Pergamon Press, Oxford, 1984.
[239] Wang Z, Fingas M. Use of methyldibenzothiophenes as markers for differentiation and source identification of crude and weathered oils. Environ Sci Technol, 1995, 29, 2842–2849.
[240] Radke M, Welte DH. The methylphenanthrene index (MPI). A maturity parameter based on aromatic hydrocarbons. In: Bjoroy M et al, eds. adv org geochem 1981. J. Wiley and Sons, New York, 1983, 504–512.
[241] Douglas GS, Bence AE, Prince RC, McMillen SJ, Butler EL. Environmental stability of selected petroleum hydrocarbon source and weathering ratios. Environ Sci Technol, 1996, 30(7), 2332–2339.
[242] Hughes WB, Holba AG, Dzou LI. The ratios of dibenzothiophene to phenanthrene and pristane to phytane as indicators of depositional environment and lithology of petroleum source rocks. Geochim Cosmochim Acta, 1995, 59(17), 3581–3598.
[243] Wang Z, Stout SA, Fingas M. Forensic fingerprinting of biomarkers for oil spill characterization and source identification. Environ Forens, 2007, 7, 105–146.
[244] Seifert WK, Moldowan JM. Paleoreconstruction by biological markers. Geochim Cosmochim Acta, 1981, 45, 783–794.
[245] Larter SR, Bowler BF, Li M, Chen M, Brincat D, Bennett B, Noke K, Donohoe P, Simmons D, Kohnen M, Allan J, Telnaes N, Horstand I. Molecular indicators of secondary oil migration distances. Nature, 1996, 383, 593–597.
[246] Clegg H, Wilkes H, Oldenburg T, SantaMaria-Orozco D, Horsefield B. Influence of maturity on carbazole and benzocarbazole distributions in crude oils and source rocks from the Sonda de Campeche, Gulf of Mexico. Org Geochem, 1998, 29(1–3), 183–194.
[247] Bakr MMY, Wilkes H. The influence of facies and depositional environment on the occurrence and distribution of carbazoles and benzocarbazoles in crude oil: A case study from the Gulf of Suez, Egypt. Org Geochem, 2002, 33, 561–580.
[248] Zhang L, Li M, Wang Y, Yin Q, Zhang W. A novel molecular index for secondary oil migration distance. Sci Rep, 2013, 3(2487), 1–9.
[249] Terken JMJ, Frewin NL. The dhahaban petroleum system of Oman. Am Assoc Petrol Geol Bull, 2000, 84, 523–544.
[250] Fang R, Wang TG, Li M, Xiao Z, Zhang B, Huang S, Shi S, Wang D, Deng W. Dibenzothiophenes and benzo[b]naphthothiophenes: Molecular markers for tracing oil filling pathways in the carbonate reservoir of the Tarim Basin, NW China. Org Geochem, 2016, 91, 68–80.
[251] Tamborello BL. Potential sources of oil from Hugoton Embayment reservoirs. MS Thesis, University of Oklahoma 2020, pp. 220.

Christoph Aeppli

11 Photooxidation of crude oil: formation, characterization, and fate of oil photoproducts in the environment

Abstract: Oil photooxidation by natural sunlight is a process that fundamentally affects the composition, properties, and fate of oil residues in the environment, especially after marine oil spills. This chapter summarizes the current knowledge about the mechanism of photochemical petroleum oxygenation, the bulk and molecular characterization of oil photoproducts, and the fate of photooxidized oil in the environment. Furthermore, current knowledge gaps and perspectives for further research are discussed.

11.1 Introduction

When crude oil or petroleum enters the environment, it changes its properties and chemical composition through various oil weathering processes. The main weathering processes occurring during a marine oil spill are physical processes (such as evaporation and dissolution) and chemical processes (such as biodegradation and photooxidation). This chapter focuses on oil photooxidation of crude oil. While the process of photooxidation has been observed for terrestrial and freshwater oil spills [1, 2], most current knowledge has been gained from studying oil photooxidation at sea. Therefore, this chapter will focus on this scenario.

Oil photooxidation is increasingly recognized as a significant fate process of oil constituents after a marine oil spill. Research conducted in the aftermath of the 2010 *Deepwater Horizon* oil spill elevated the importance of oil photooxidation as a fast-acting oil weathering process [3]. However, it is important to recognize that oil photooxidation has been studied for more than 50 years [4–7]. Some of the earliest oil photooxidation studies were conducted in the 1970s and focused on the degradation

Acknowledgments: Funding for developing and writing this chapter was provided by a grant from the Gulf Research Program from the National Academies of Sciences, Engineering, and Medicine (NAS Grant 2000008903). Erin Beirne, Samuel Katz, Deedar Nabi, and Phoebe Keyes (Bigelow Laboratory) are acknowledged for their research contributions to topics presented in this chapter. Three anonymous reviewers are acknowledged for providing helpful comments on an earlier version of this chapter.

Christoph Aeppli, Bigelow Laboratory for Ocean Sciences, East Boothbay, ME 04544, USA, e-mail: caeppli@bigelow.org

https://doi.org/10.1515/9783110694529-011

of saturated compounds [8–10]. Studies conducted in the aftermath of the 1979 IXTOC-I oil spill in the Bay of Campeche (Gulf of Mexico) highlighted the importance of oil photooxidation and showed that oil photoproducts might play an essential role in the fate and effect of oil [11]. A review by Payne and Philipps [4] summarized the state of knowledge of the 1980s.

The 1989 *Exxon Valdez* led to a new wave of oil spill research. Thereby, the establishment of GC/MS as a tool to monitor the fate of petroleum hydrocarbons greatly improved the mechanistic understanding of oil photooxidation. For example, studies of photosensitized degradation of saturated oil compounds [12–14] and aromatic fractions of crude oil [15, 16] were conducted. Reviews by Nicodem et al. [5, 6] detailed the knowledge to this point.

In the 2000s, a number of studies focused on the photochemical degradation of PAHs in the aqueous phase rather than on aliphatic compounds in an oil slick. Progress in the understanding of direct versus indirect photochemical degradation of PAHs was made [17–19]. These reaction mechanisms are described in more detail in Section 11.2.

The *Deepwater Horizon* oil (DWH) spill led to a multitude of research improving the understanding of oil photooxidation research, as reviewed by Ward and Overton [3]. It was realized that the oil photooxidation was acting on oil much faster than previously assumed. An estimated 50% of the mass of oil present in oil slicks was presumably transformed into oxygen-containing oil photoproducts within a timescale of 5 to 30 days of solar irradiation on the sea surface [20, 21]. This fast transformation led to a shift in our understanding of the importance of photooxidation for the fate of oil at sea (Figure 11.1). The resulting photoproducts formed a polar fraction of oil that comprised a complex mixture of oxygen-enriched aliphatic and aromatic compounds. This fraction was similar to the resin or asphaltene fraction of crude oil in that it was mostly non-GC-amenable [20, 22]. Various studies gained new insights into the mechanism of oil photooxidation [23–27]. Biodegradation was found to be less important than photooxidation for the formation of this polar fraction [21]. Novel high-resolution mass spectrometry methods such as Fourier-transform ion cyclotron resonance mass spectrometry (FT-ICR-MS) were able to identify thousands of oxygen-containing molecular formulas that were presumably formed due to photooxidation [28–30].

Studies of the effects of oil photoproducts were also conducted [31, 32], and a number of toxicity studies were conducted with field-weathered oil that was significantly photooxidized [33–36].

In this chapter, the research related to oil photooxidation and resulting oil photoproducts is reviewed. Thereby, the mechanism of oil photooxidation and formation of oil photoproducts, the characterization of oil photoproducts, and the environmental fate of these products will be discussed. Finally, needs for further research will be outlined.

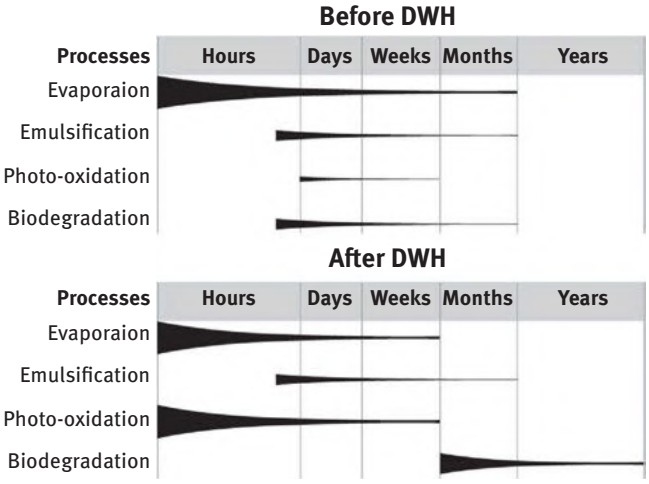

Figure 11.1: Change in the understanding of the importance of oil weathering processes. Photooxidation was thought to be of relatively minor importance [37–40]. More recent research showed that photooxidation significantly affects the fate of oil at sea. Figure reprinted with permission from Ward and Overton (2020) [3]. Copyright 2020 The Royal Society of Chemistry.

11.2 Mechanism of oil photooxidation at sea

As outlined in Section 11.1, there is a large body of literature that investigated the mechanism of oil photooxidation in the environment. This section reviews the current understanding of the mechanism of oil photooxidation.

11.2.1 Direct photochemical transformation of light-absorbing compounds

Direct photochemical transformation of oil hydrocarbons occurs if compounds absorb light that promotes them into excited electronic states. These excited-state compounds can then decay through various pathways, leading to oxygenated products. Only oil compounds that are able to efficiently absorb sunlight in the spectral range relevant on the earth's surface (generally > 280 nm; Figure 11.2B) can undergo direct photooxidation. PAHs are the primary candidates for this reaction. Breaking of a carbon–carbon bond generally requires UV light, and PAH can absorb light in the environmentally relevant UV range (Figure 11.2A). Saturated compounds such as *n*-alkanes are not able to undergo direct photooxidation. Similarly, monoaromatic compounds typically have little light absorption in the solar spectrum relevant for the sea surface. Direct photolysis is generally considered to be responsible

for PAH degradation in dilute aqueous solutions, and the product of photooxidation or PAHs are the corresponding alcohols, aldehydes, ketones, and acids [41–45].

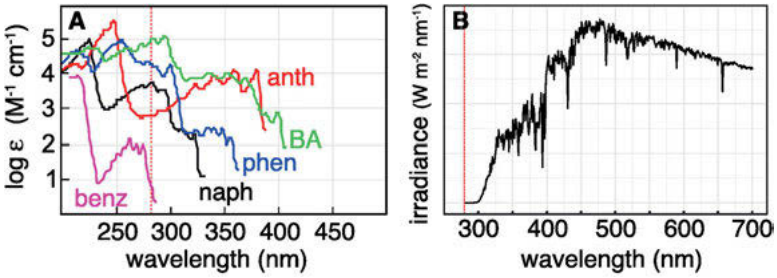

Figure 11.2: Molar absorption spectra of benzene (benz) and the PAHs naphthalene (nap), phenanthrene (phen), anthracene (anth), and benzo(a)anthracene (BA) (source: NIST Chemistry Webbook; webbook.nist.gov). (B) Solar spectrum calculated for the sea surface in the Gulf of Mexico (source: Quick TUV Calculator, www.acom.ucar.edu/Models/TUV). The vertical dotted lines depict 280 nm, which is the lower boundary of the UV-B range.

11.2.2 Indirect degradation of aromatic compounds via singlet oxygen

Indirect photooxidation is a second mechanism for oil degradation. Thereby, sunlight can react with light-absorbing photosensitizers, which can lead to photochemically produced reactive species (PPRIs) that in turn react with oil constituents (Figure 11.3). The irradiation of oil films has been shown to give rise to various PPRIs, such as singlet oxygen ($^1O_2$) [46], hydroxyl radicals ($^{\bullet}OH$) [24], organic triplets [26], and peroxyl radicals [46]. Many of these PPRI are well-known species for the photochemical degradation of pollutants in the environment. Organic triplets and $^1O_2$ are known to degrade a large variety of pollutants and can be formed from multiple sources, including dissolved organic matter (DOM) [47–49].

Since $^1O_2$ reacts with electron-rich substrates such as double bonds, aromatic rings, or sulfur compounds, aromatic oil compounds seem to be efficiently degraded through $^1O_2$. Endo-peroxides are frequently observed as intermediates for photochemical reactions of many PAHs with $^1O_2$ [50]. Various compounds can act as $^1O_2$-producing photosensitizers, including PAHs or compounds in the resins or asphaltene fraction of oil residues [46, 51].

Not all PAHs react efficiently with $^1O_2$ [19, 52]. An alternative pathway based on hydrogen abstraction of excited-state PAHs and the formation of carbon-centered radicals has been proposed (Figure 11.3B) [53, 54]. These radicals react with O_2 to form peroxyl radicals, which can undergo various reactions leading to carbonyl or hydroxyl-containing compounds.

Since PAHs can undergo direct or indirect photochemical degradation, studies investigated the relative importance of these two pathways. It has been suggested that direct photochemical degradation can be substantial for dilute solutions of PAHs in natural waters because PPRIs are efficiently deactivated in natural waters [55, 56]. In oil films, however, indirect photochemical oxidation appears to be the dominant pathway for most PAHs [19, 46].

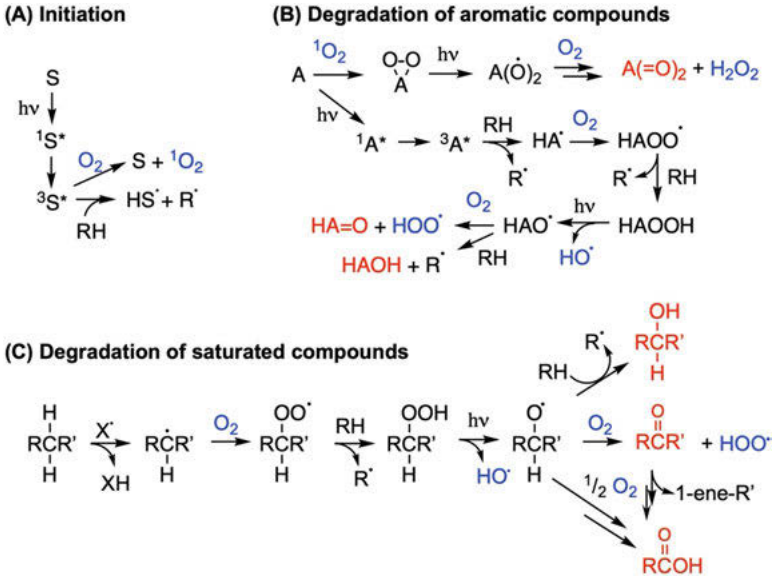

Figure 11.3: General reaction scheme of indirect oil photooxidation. S represents a photosensitizer, A is a singlet oxygen acceptor or aromatic compound, RH is an active hydrogen species, RCH_2R' a saturated compound (e.g., alkane), X• represents a radical species capable of alkane hydrogen abstraction. Species in blue indicate oxygen or reactive oxygen species. Compounds in red are final oil photoproducts commonly observed after oil photooxidation, including alcohols (RCOH, HAOH), ketones (RC = OR', HA = O), and carboxylic acids (RCOOH).

11.2.3 Peroxyl radical–mediated degradation of saturated compounds

A variety of photoproducts, such as long-chain alcohols, ketones, aldehydes, and carboxylic acids, can often be observed in irradiated oil residues [2, 9, 11–14, 57, 58]. Due to their structure, they likely originate from saturated compounds. However, since saturated hydrocarbons would not react with sunlight or $^1O_2$, radical species have to be involved in the degradation of these compounds. Various radical species have been observed during oil photooxidation. For example, excited-state photosensitizers or PAHs can abstract hydrogens from oil constituents, leading to C-centered

radicals that can initiate the degradation of saturated compounds (Figure 11.3A) [13]. Furthermore, hydroxyl radicals can be produced during the photochemical degradation of aromatic compounds discussed above (Figure 11.3B). Hydroxyl radicals can perform hydrogen abstraction from a saturated compound, resulting in C-centered radicals that can react with molecular oxygen to produce peroxyl radicals ($ROO^{\bullet}$). These species, further react to organic hydroperoxides and can undergo multiple reactions leading to alcohols, ketones, aldehydes, and carboxylic acids (Figure 11.3D).

A number of laboratory studies, summarized by Nicodem et al. [6], confirmed the importance of free radicals in oil photooxidation. Generally, saturated oil compounds were irradiated together with free radical generating sensitizers such as naphthalene derivatives, xanthone, and anthraquinone [9, 42, 44, 52, 59, 60]. Singlet oxygen has been hypothesized to play an essential role in the degradation of saturated compounds. This hypothesis was supported by a study that found significantly reduced oil photooxidation in the presence of beta-carotene, a singlet oxygen quencher [10], or a study where hydroxyl radicals were formed under irradiated oil sheens [24]. Based on another set of experiments, the role of the $^1O_2$ in the formation of peroxyl radicals was considered less important [46]. The authors of that study pointed out that the oxygen or light concentration might become limiting in an oil film, and direct photochemical formation of radicals might be initiating the chain reaction. Depending on the oil properties, an oil sheen as thin as 10 μm can absorb most of the light below 400 nm [46]. The environmental importance of $^1O_2$-mediated versus direct photochemical production of radical for oil photooxidation in oil films has yet to be determined.

11.2.4 Source and magnitude of oxygen incorporation

In line with the discussed mechanisms, it has been shown that atmospheric O_2 rather than H_2O is the source of oxygen in the photoproducts. Experiments without oxygen atmosphere showed low oil photooxidation [9, 27] or reduced formation of reactive intermediates [24].

The degree of oil photooxidation can be quantified by measuring the incorporated oxygen into oil. Field studies show that for a light sweet crude oil, the oxygen content can increase from ~ 1% in the crude oil to > 6% in highly oxygenated oil sheens collected from the sea surface after the *Deepwater Horizon* oil spill in the timeframe of days [20, 21]. At the same time, $\Delta^{14}C$ analysis confirmed that the carbon of these samples were of petrogenic and not of recent biological origin [20]. Based on C, H, N, O, and S elemental analysis of oil residues, it was estimated that the polar fraction of photooxidized *Deepwater Horizon* oil that contains the photoproducts ("resins" and "asphaltenes") has an average molecular formula of $C_{5x}H_{7x}O_x$ [20]. This estimation suggests that a compound containing 20 carbons would contain four oxygen atoms,

which would correspond to, for example, a dicarboxylic acid or a di-oxo carbonylic acid. Various oxo-carbonylic acids have been identified in irradiated oil [58].

11.3 Characterization of changes in bulk oil properties

Observing changes in bulk properties of oil often represents the first evidence of oil photooxidation. For example, the combination of bulk oxygen content, carbonyl index, and quantification of bulk saturated, aromatic, and polar fractions (SARA analysis) has been used to identify and quantify photooxidation of oil residues in the aftermath of the *Deepwater Horizon* oil spill [20, 21]. More advanced analyses also include stable isotopes (carbon, oxygen) or radioisotopes [20, 22, 27]. This section will discuss how these bulk analytical methods can be used for the identification of oil photooxidation and oil photoproducts.

11.3.1 Oxygen content

Tracking the oxygen content of oil residues is a direct way of identifying oil photooxidation since oil photooxidation leads to the formation of oxygenated oil photoproducts. Because oxygen-containing compounds already present in the source oil will also be preferentially enriched during evaporative oil weathering, care has to be taken to disentangle contributions from such preferential enrichment and from oil photoproducts. The preferential enrichment can, e.g., be estimated via the degree of evaporation that can be determined from *n*-alkane analysis of an oil residue (assuming no major biodegradation occurred). Furthermore, measurement of oxygen content along with other heteroatoms can help to identify oil photooxidation (Figure 11.4).

The oxygen content of an oil residue can be measured on an elemental analyzer using the Unterzuacher or related methods [61, 62]. This method is based on high-temperature pyrolysis followed by carbon monoxide detection using thermal conductivity detection or mass spectrometry.

11.3.2 Infrared spectroscopy (FT-IR): carbonyl index

Oil photooxidation gives rise to alcohols, ketones, aldehydes, and carboxylic acids. Molecular vibrations associated with these functional groups can be seen using Fourier transform infrared spectroscopy (FT-IR) (Figure 11.5). Carbonyl functional groups have been the main target in FT-IR to identify oil photooxidation [20, 21, 63–66].

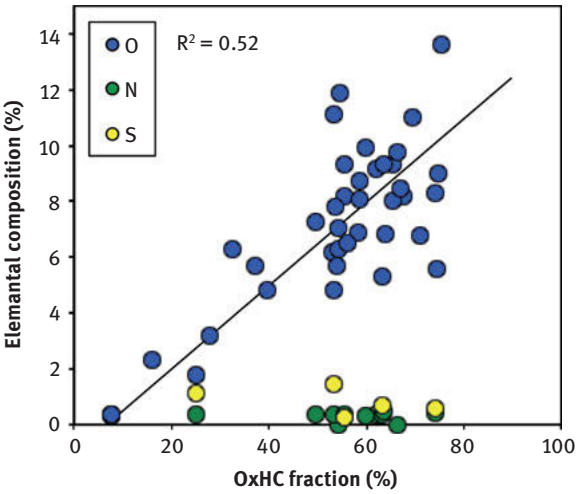

Figure 11.4: Elemental analysis of oxygen, sulfur, and nitrogen in field-weathered *Deepwater Horizon* oil residues versus the amount of OxHC fraction (resins and asphaltene fraction on TLC/FID) as a proxy of photooxidation. The data shows photochemically-induced enrichment of oxygen in oil residues during oil weathering. Data are from Aeppli *et al.* (2012) [20].

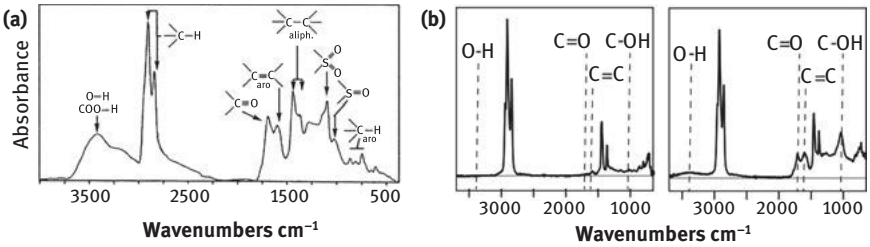

Figure 11.5: FT-IR to identify oxygen-containing functional groups. (A) Assignment of functional groups in oxygenated oil from terrestrial oil spills. Figure reprinted with permission from Charrié-Duhaut et al., (2000) [2]. Copyright 2000 Elsevier Science Ltd. (B) FT-IR spectra of crude *Deepwater Horizon* oil (left) and field-weathered oil (right). Figure reprinted with permission from Aeppli *et al.*, 2012 [20]. Copyright 2012 American Chemical Society.

To quantify degrees of photooxidation, a "carbonyl index" can be calculated as the ratio of the carbonyl vibration (1,800 to 1,670 cm^{-1}) relative to a reference peak. As reference peak, the C–H absorbance at 2,910 cm^{-1} is often used. This carbonyl index is similar to that used to detect aging of plastic and microplastic [67–70].

11.3.3 SARA or TLC-FID analysis

The quantification of polar versus nonpolar fractions in oil residues is a valuable method to estimate the degree of photooxidation in oil residues since during oil photooxidation, saturated and aromatic compounds are transformed into more polar compounds. The polar fraction is sometimes referred to as the "oxygenated hydrocarbon fraction" (OxHC) since it is enriched in oxygenated products from hydrocarbon precursors. For example, samples collected in the aftermath of the *DWH* oil spill showed decreasing amounts of GC-amenable saturated and aromatic fractions, while the non-GC-amenable OxHC fractions increased (Figure 11.6).

The analysis of saturated, aromatic, resin, and asphaltene fractions (SARA) using thin-layer chromatography coupled to flame ionization detection (TLC/FID) has proven to be a superior method compared to traditional open-column SARA analysis since TLC/FID has orders of magnitude smaller sample requirements [15, 71]. Generally, the resin and asphaltene fractions are combined to form the OxHC fraction. Note that resins and asphaltenes present in crude oil will also contribute to the OxHC fraction. Therefore, TLC/FID is especially useful to detect oil photooxidation for light oils where the native asphaltenes will be small compared to the formed fraction of oil photoproducts.

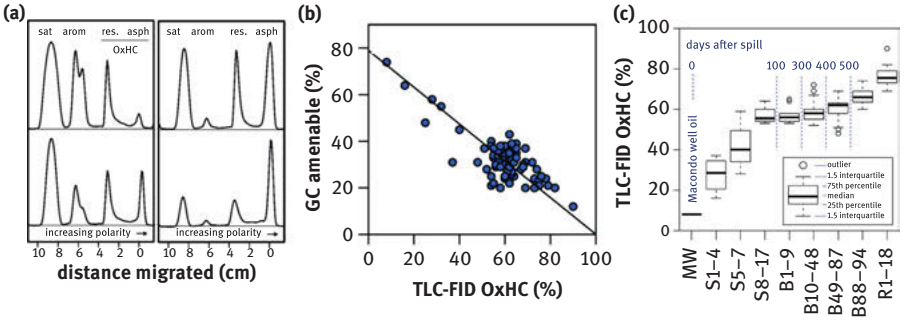

Figure 11.6: TLC-FID to identify photoproduct containing polar fractions. (A) TLC-FID chromatograms of a series of crude and field-weathered *Deepwater Horizon* oil residues with increasing weathering. (B) Correlation between GC amenable fraction and content of TLC-FID OxHC fraction in field-collected *Deepwater Horizon* oil residues. (C) Increase in TLC/FID OxHC with increasing weathering in the field. Figure reprinted with permission from Aeppli *et al.*, 2012 [20]. Copyright 2012 American Chemical Society.

11.3.4 Stable isotopes and radioisotopes to identify oil photoproducts

While stable isotopes ($\delta^{18}O$, $\delta^{13}C$) and radiocarbon ($\Delta^{14}C$) are often not standard tools for oil analysis, they can be powerful in detecting oil photooxidation. Oxygen-18 has been shown to be preferentially incorporated into oil during photooxidation, with a large enrichment from approx. – 1‰ (vs. standard mean ocean water, SMOW) to >+5‰ [27] (Figure 11.7). Furthermore, $\delta^{13}C$ in the asphaltene fraction was a good indicator for oil photooxidation of *DWH* oil residues [22]. Finally, $\Delta^{14}C$ of the OxHC fraction from *DWH* oil residues confirmed that this fraction is of petrogenic and not recent biological origin [20].

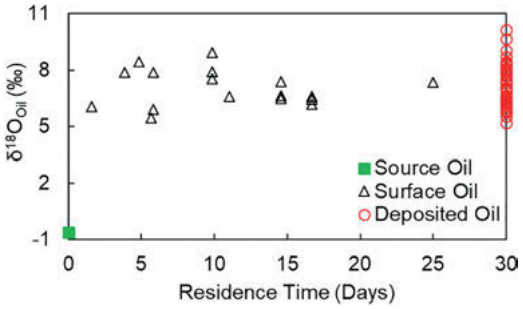

Figure 11.7: Increase in stable oxygen isotopic signature ($\delta^{18}O$) in field-collected *DWH* oil residues during photooxidation. The increase from approx. – 1‰ to approx. + 7 ± 2‰ occurred during photooxidation on the surface. This signature remained after the oil was deposited on the shore (red circles, ≥ 30 days of residence time). Figure reprinted with permission from Ward et al., 2019 [27]. Copyright 2019 American Geophysical Union.

11.4 Characterization of changes in molecular properties

11.4.1 GC/MS-based characterization of photoproducts

Most oil photoproducts are not GC-amenable. The addition of oxygen makes these compounds either too non-volatile or polar for GC analysis. However, a number of aromatic and aliphatic oil photoproducts are detectable on GC/MS, either through direct measurement or after fractionation or derivatization (Figure 11.8). Fractionation is generally performed using silica gel chromatography, which allows separating saturated, aromatic, and heteroatom-containing compounds [2]. Common methods for derivatization include silylation, methylation, or carbonyl-specific reagents [2, 30, 57, 58].

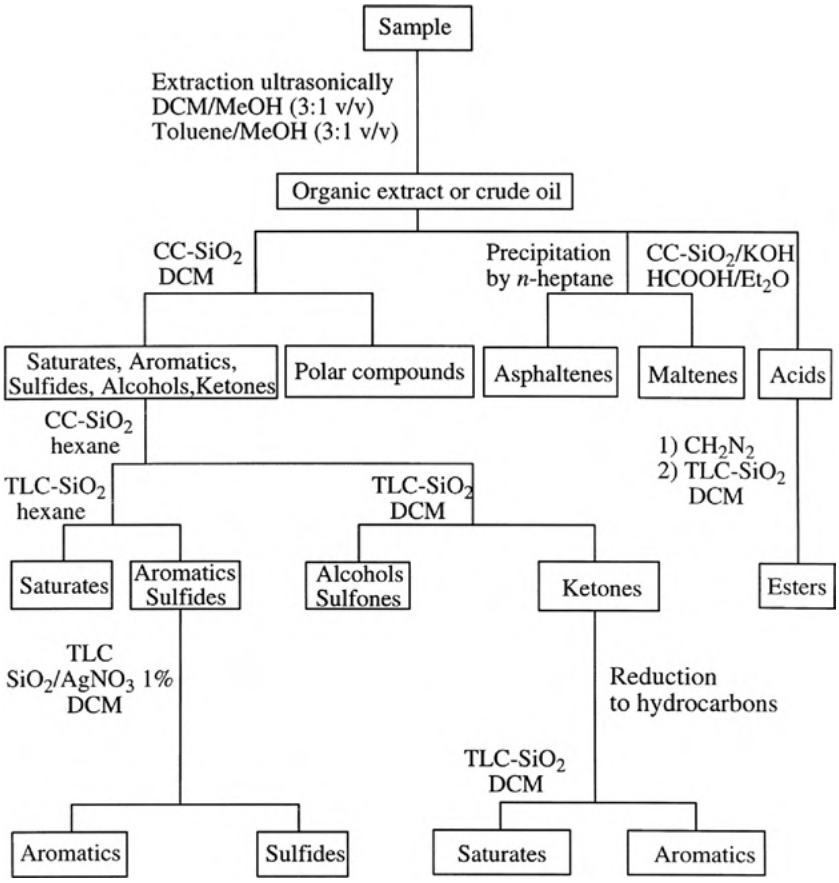

Figure 11.8: Detailed scheme for isolating various fractions of compounds. Figure reprinted with permission from Charrié-Duhaut et al., 2000 [2]. Copyright 2000 Elsevier Science Ltd.

Various oxygenated PAHs have been reported as oil photoproducts [4, 7, 17]. This includes the GC/MS detectable 9-fluorenone, anthraquinone, benz(a)anthraquinone, benzanthrone, and hydroxy fluoranthene. However, GC/MS analysis is not always feasible. Many oxygenated PAHs are thermally labile and cannot be analyzed by GC/MS without prior derivatization [72]. Other compounds, such as alkylated 9-fluorenone congeners, show co-elution and mass overlap with alkylated fluorene congeners.

Aliphatic ketones and aldehydes are photoproducts observed from the photosensitized photooxidation of alkanes [12, 14]. The major products are typically 1-alkanols and 2-ketones with the same carbon number (Figure 11.9). Since the retention times and mass spectra of these photoproducts can overlap with that of their *n*-alkane precursors, a silica gel fractionation step is typically necessary before GC/MS analysis [2]. Series of linear carboxylic acids are frequently found in irradiated

crude oil [13, 20, 57]. These compounds can be detected on GC/MS after transformation into their corresponding silyl esters or methyl esters.

The use of comprehensive two-dimensional gas chromatography (GC × GC) is a powerful tool to overcome chromatographic co-elution resolution limitations of GC/MS in detecting oil photoproducts. For example, aliphatic alcohols, ketones, and carboxylic acids can be resolved (Figure 11.9). Furthermore, alkylated fluorenone and fluorene congeners can be separated chromatographically.

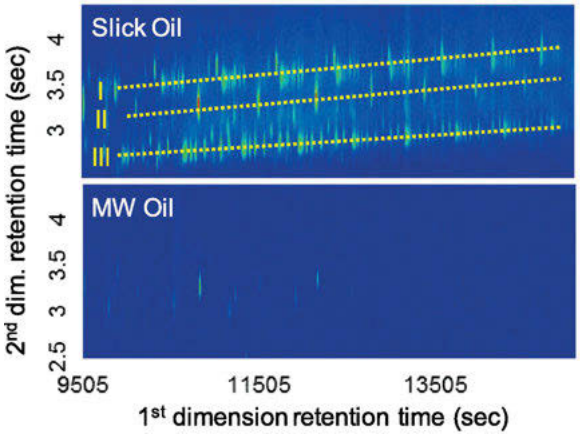

Figure 11.9: GC × GC – time of flight chromatograms (*m/z* 73 and 83 mass traces) to identify ketones (region I), *n*-alkanoic acids (region II), and 1-alkanols (III) in *DWH* slick oil collected from the sea surface ("Slick Oil"). These compounds were absent in non-photooxidized source *DWH* oil ("MW Oil"). Figure reprinted with permission from Aeppli et al. [57]. Copyright 2018 American Chemical Society.

11.4.2 LC-MS/MS-based characterization of photoproducts

Given that many oil photoproducts are too polar for GC analysis, liquid chromatography coupled to mass spectrometry (LC-MS) is in many instances more suitable for the analysis of oil photoproducts. For example, the use of LC-MS/MS with electrospray ionization (ESI(–)) allowed for the detection of photoproducts in irradiated oil residues [58]. A large number of carbonyl-containing compounds were detected after transformation into their hydrazones using 2,4-dinitrophenylhydrazin (DNPH) (Figure 11.10). While no analytical standards were available, the exact identification of compounds and development of quantitative methods was not possible. However, a suite of oxocarboxylic acids was detected. The presence of these compounds (containing at least three oxygen atoms per molecule) demonstrates that oil photooxidation can produce highly oxygenated products. However, although LC-MS is suitable for the detection of oil photoproducts, there is still a lack of standardized analytical methods.

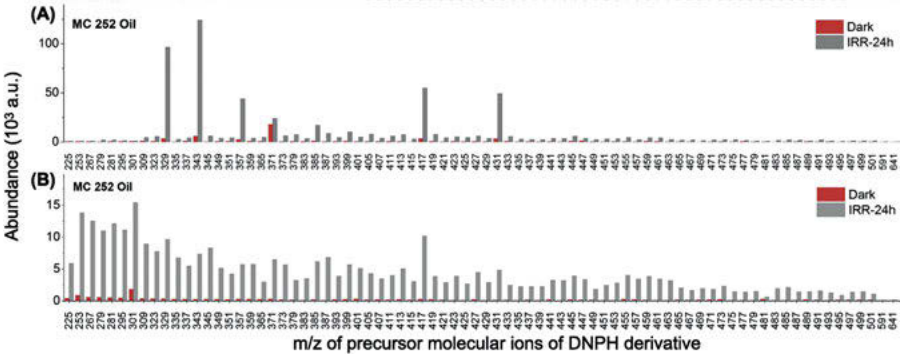

Figure 11.10: LC-MS/MS identification of oil photoproducts formed by irradiation of Macondo Well source oil (MW 525 Oil). (A) Carbonyl compounds identified as 2,4-dinitrophenylhydrazin (DNPH) derivatives. Shown is the intensity of the *m/z* 182 ion for a series of precursor ions in dark (red bars) and 24-h irradiated oil samples (grey bars) (B) Oxo-carboxylic acids, identified from neutral loss of an *m/z* 44 mass fragment from the DNPH derivative in dark (red bars) and 24-h irradiated oil samples (gray bars). Figure reprinted with permission from Cao et al., 2017 [58]. Copyright 2017 American Chemical Society.

11.4.3 Direct infusion high-resolution mass spectrometry

Another strategy to overcome chromatographic limitations of GC/MS (or LC/MS) is by skipping the chromatographic separation step and using direct infusion techniques. In order to identify individual compounds, ultrahigh-resolution mass spectrometry is necessary. This method is based on identifying the exact mass of compounds and assigning molecular formulas to these compounds. The higher the mass resolution, the better this assignment can be performed. Ultrahigh mass resolution can be achieved with Fourier transform ion cyclotron resonance mass spectrometers (FT-ICR-MS) [73]. The currently most powerful FT-ICR-MS has a 21 T magnet and can resolve the mass of an electron (resolving power >2,700,000 at *m/z* 400) [74].

While each molecular formula can represent numerous compounds or isomers, this method allows identifying a large number of compounds as well as classes of compounds. Typically, data are displayed as carbon numbers versus double-bond equivalents for compound classes, such as pure hydrocarbons, O_1 class (molecules containing C, H, and 1 O), O_2 class (molecules containing C, H, and two O), N_1O_1 (containing C, H, one N and one O), etc. The method of ionization determines what kind of compounds are visible. The most commonly used ionization modes are electrospray ionization (ESI, in positive or negative mode) and atmospheric pressure photoionization (APPI, positive or negative mode). Different compounds are preferentially ionized depending on the ionization method [75, 76].

Using FT-ICR-MS, oxygenated compounds were detected from *Deepwater Horizon* oil samples collected on beaches [28] (Figure 11.11). Interestingly, these weathered samples contained more than double the number of peaks (i.e., identifiable molecular formulas) than the original crude oil, and many of these extra peaks contained oxygen (Figure 11.11B). Such oxygenated compounds were also detected in *Deepwater Horizon* oil beached on marshes [29] or in irradiated oil samples [30].

While FT-ICR-MS are superb for their resolution, they are not widely available in laboratories. However, using the more commonly available Orbitrap instrument that has a roughly 20 times lower resolution than the 21-T FT-ICR-MS, similar results can be obtained, showing an increase in oxygen-congaing molecular formulas for more oxygenated oil residues [75, 76].

11.5 Environmental fate and toxicity of oil photoproducts

Due to their polar nature, oil photoproducts have distinct environmental fate and toxicity properties from their hydrocarbon precursors. This section reviews the current understanding of dissolution, biodegradation, bioaccumulation, and toxicity of oil photoproducts.

11.5.1 Dissolution of oil photoproducts

As hydrocarbons become oxygenated, the resulting products are more polar than their precursors. Therefore, photoproducts have a higher water solubility than their precursors. Water-soluble fractions (WSFs) of non-photooxidized oil had higher dissolved organic carbon (DOC) values than WSFs of field-collected photooxidized oil [57]. Increasing DOC values were also observed in the aqueous phase during irradiation of an oil slick [32].

The observation of increased water solubility of photoproducts was supported by estimations of physico-chemical properties of photoproducts [57]. Based on a semi-empirical fragment-based property estimation method (WSKOW and KOWWIN; U.S. EPA [77]), aliphatic, neutral photoproducts were estimated to have water solubilities that were one to four orders of magnitude higher than the putative precursors (Figure 11.12). Other property estimation methods gave similar results [78]. For charged carboxylic acids, this value can even be higher. The increased water solubility of oil photoproducts suggests that oil photoproducts might be preferentially

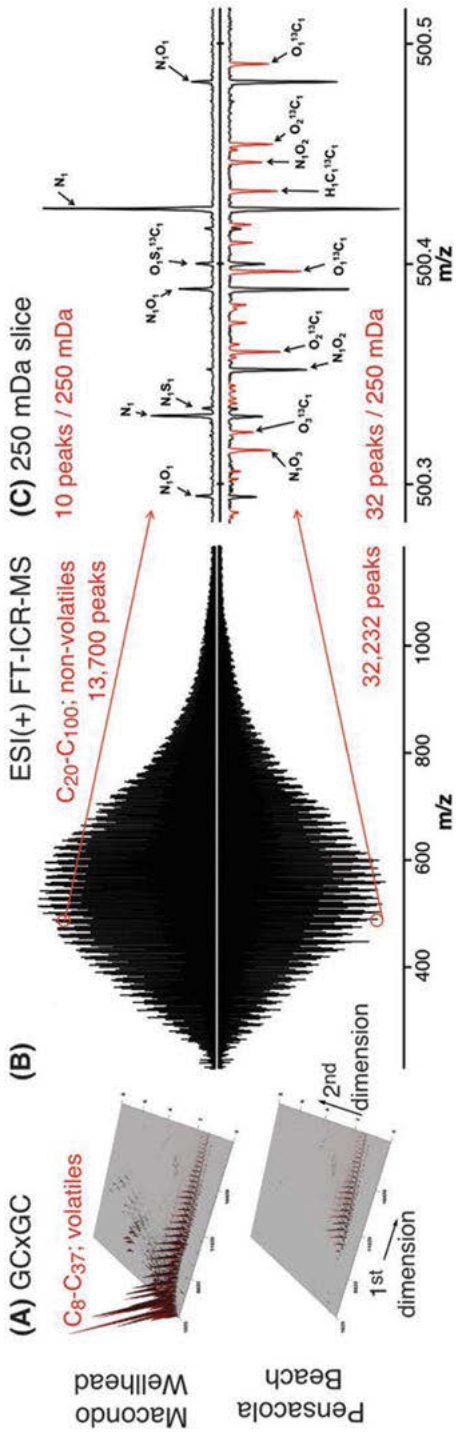

Figure 11.11: FT-ICR-MS analysis of a crude oil (Macondo well oil) and an oxygenated oil residue (Pensacola Beach oil residue). (A) GC × GC chromatograms of the oils show significant weathering of the oxygenated oil residue. (B) Mass spectra of the two oils, showing an increase of features in the oxygenated oil. (C) Sub-section of the mass spectra, showing that the additional features correspond mostly to oxygen-containing molecular formulas. Figure reprinted with permission from Ruddy et al. [28]. Copyright 2014 American Chemical Society.

water-washed and depleted from irradiated oil residues. However, many photoproducts were still detected in *Deepwater Horizon* oil slicks that floated an estimated 10 to 30 days on the water surface before being washed ashore [20, 21, 57], suggesting that some of the oil photoproducts can be hydrophobic and persistent.

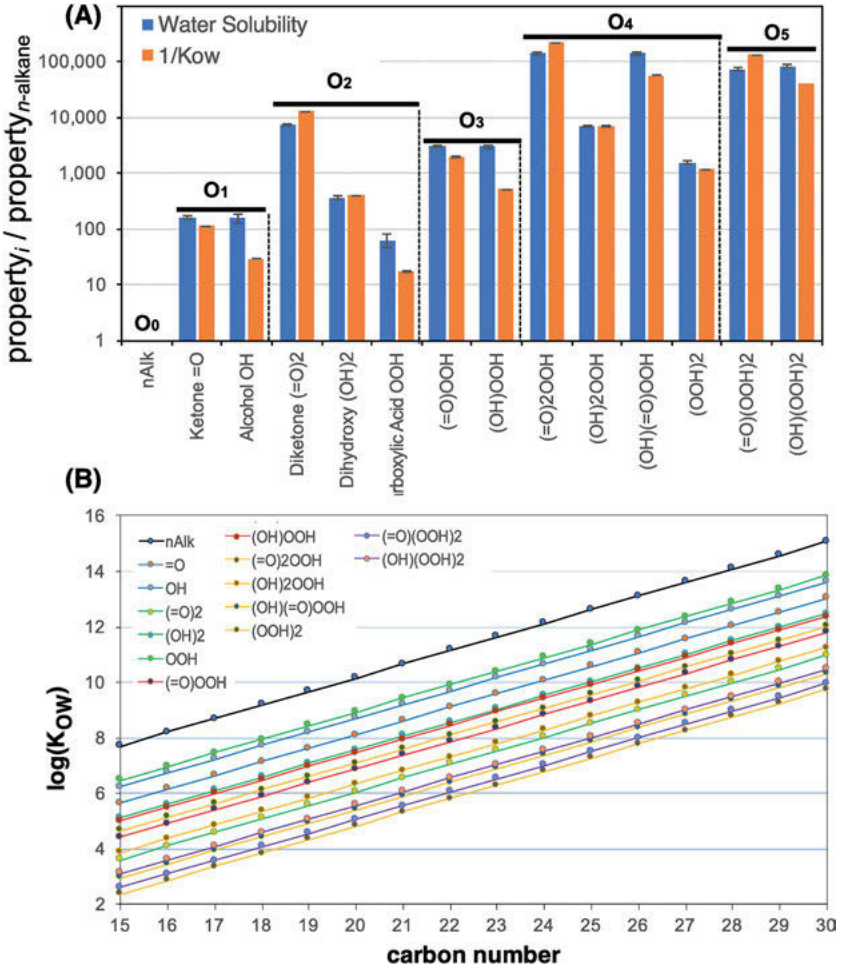

Figure 11.12: Physico-chemical properties of photoproducts. (A) Calculated water solubility (WS; blue bars) and $1/K_{OW}$ values (orange bars) of oxygenated model compounds relative to their saturated precursors. Shown are molecules containing one (O_1) to five oxygen atoms (O_5). Water solubilities are predicted to increase by up to five orders of magnitude upon oxygenation, while K_{OW} values decrease by a similar amount. (B) Calculated K_{OW} values for C_{15} to C_{30} homologous series of *n*-alkanes and oxygenated derivatives. Figure reprinted with permission from Aeppli et al. [57]. Copyright 2018 American Chemical Society.

11.5.2 Biodegradation of oil photoproducts

Given that oil photoproducts have an increased solubility compared to their precursors, one could expect that biodegradation might be an essential fate process of oil photoproducts. Increased aqueous concentrations would translate to higher bioavailability. In contrast, the oxygenated nature of photoproducts reduces the energy that can be gained by microbes from the oxidation of these compounds.

Currently, only a few studies specifically address the issue of oil photoproduct biodegradation. From studies investigating the degradation of compounds biodiesel, it appears that the biodegradation of fatty acid methyl esters occurs at similar rates as that of corresponding *n*-alkanes [79–81]. There is also evidence that photooxidation aids the overall biodegradation of oil. Pre-oxygenation of petroleum hydrocarbons was increased the degree of biomineralization for oil residues [82] and increased the biodegradation of oil-sand-related compounds [83]. Thereby, photooxidation might aid biodegradation by breaking down larger compounds into smaller compounds that are more easily biodegradable.

There are also indications that highly recalcitrant photoproducts are formed during oil photooxidation. We performed a 48-day biodegradation experiment of crude oil in seawater following literature [88], measured the saturated, aromatic, and OxHC fraction (i.e., the combined resin and asphaltene fraction) using TLC/FID, and normalized the fractions to the recalcitrant marker compound C_{30}-hopane (Figure 11.13) [20]. We performed the same hopane normalization with samples subjected to photooxidation (described in ref. [89]) and collected in the aftermath of the *Deepwater Horizon* oil spill (described in ref. [20]]. (Figure 11.13). While the OxHC fraction decreased in the biodegradation experiments, the OxHC fraction increased in the photooxidation experiments and the field-collected *Deepwater Horizon* oil residues. These data suggest that some oil photoproducts formed during oil weathering can be relatively stable in the environment.

11.5.3 Bioaccumulation of oil photoproducts

Bioaccumulation of organic compounds is generally driven by the hydrophobicity of compounds, and the octanol–water partition coefficient (K_{OW}) is a proxy for their hydrophobicity. Due to their more polar nature than their precursors, neutral oil photoproducts generally have lower K_{OW} values than their hydrocarbon precursors (Figure 11.12). We estimated that aliphatic and aromatic oil photooxidation have a bioaccumulation potential between one to five orders of magnitude lower than their hydrocarbon precursors [78].

Contrasting the finding of decreasing bioaccumulation potential with increasing photooxidation are biomimetic extraction (BE) measurements [90]. This technique uses the accumulation of organic compounds on a polydimethylsiloxane

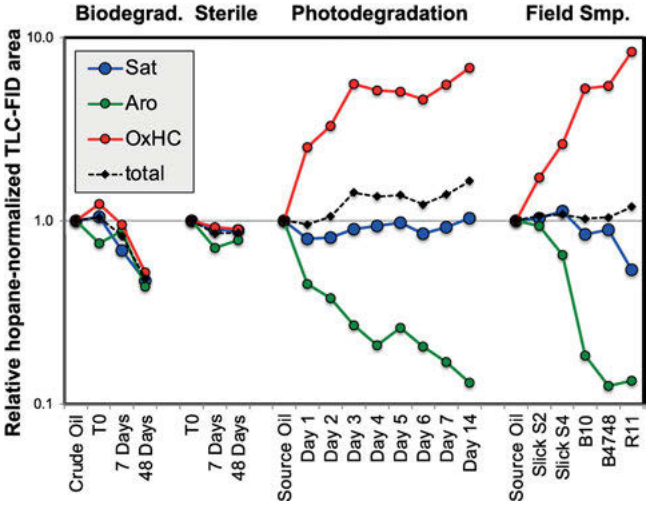

Figure 11.13: Hopane-normalized TLC/FID fractions (Sat: saturated fraction; Aro: aromatic fraction; OxHC: combined resin and asphaltenes fraction), showing their relative increase or decrease during various treatments. The OxHC fraction of a crude oil biodegraded during a 48-day biodegradation experiment ("Biodegr."), but not in the sterile control ("Sterile"). *Deepwater Horizon* field samples collected up to one year after the oil spill showed an increase in OxHC, pointing to the persistence of compounds in the OxHC fraction. A laboratory irradiation experiment ("Photodegradation") showed a similar increase in the OxHC fraction, suggesting that the recalcitrant compounds are formed photochemically. Shown are samples irradiated for 1 to 14 days.

(PDMS) fiber as a proxy for bioaccumulation. We used BE and found that WAFs produced with irradiated oil residues led to higher bioaccumulation than WAFs with non-irradiated oil (Figure 11.14). By modifying the pH during the extraction, carboxylic acid species can be identified [91]. Using this technique, we found that photochemically produced carboxylic acids are the main contributors to this bioaccumulating mass (Figure 11.14A). Carboxylic acids are generally ionized in freshwater or seawater, but they can accumulate in biological membranes [92, 93]. These photochemically produced and bioaccumulative carboxylic acids are likely depleted by dissolution in the environment: using a field-weathered oil slick sample that has a residence time of 5–30 days on the sea surface (sample SO25 described in ref. [21]), we found a much smaller contribution to the bioaccumulation potential of such accumulating carboxylic acids than in freshly photooxidized oil (Figure 11.14B).

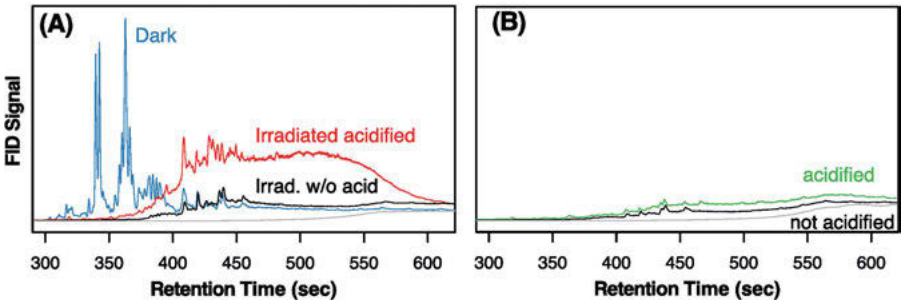

Figure 11.14: Biomimetic extraction based on solid-phase microextraction (SPME) coupled to GC-FID to identify bioaccumulative photoproducts. (A) More material accumulated on SPEM fibers in water-accommodated fractions (WAFs) of laboratory-irradiated oil residues (red GC-FID trace) than in dark-control oils (blue trace). However, this increased response disappeared when the WAF was not acidified (black trace), suggesting that ionized photoproducts, likely carboxylic acids, are formed during photooxidation and can be bioaccumulative. (B) WAFs produced with highly oxygenated *Deepwater Horizon* samples collected from the sea surface did not show a significant increase in GC-FID upon acidification, suggesting that the photoproducts were depleted in these samples due to dissolution.

11.5.4 Toxicity of oil photoproducts

There are currently few studies explicitly focusing on photoproduct toxicity. However, there are some lines of evidence that oil photoproducts can contribute to the overall toxicity of photooxidized oil. First, using a target lipid model that includes estimated water solubility and bioaccumulation of photoproducts and hydrocarbon precursors, we estimated that the process of oil photooxidation likely increases the overall baseline toxicity of an oil residue, as compared to a sample that was only subjected to evaporation but no photooxidation [57, 78]. Second, it is known that oxygenated compounds present in oil sand process water can be toxic to aquatic organisms [94–97]. Such compounds likely share similarities with oil photoproducts, since both types of compounds are derived from hydrocarbons and are oxygenated. Third, toxicity studies performed with field-weathered *DWH* oil residues that were highly oxygenated showed remarkably high toxicities to a number of model organisms [33, 35]. While three-ring PAHs presumably played a role in the observed toxicities, it is likely that oil photoproducts also contributed to the observed effects. Lastly, laboratory-irradiation of oil and subsequent toxicity assays suggest that oil photooxidation led to increased genotoxic effects in fish embryos [31] and an initial toxic response in bioluminescent bacteria [32].

Note that the discussed toxicity of oil photoproducts should not be confused with photoenhanced (or photosensitized) toxicity of oil [98–100]. This latter type of toxicity is based on the formation of reactive photochemical species that are produced in a

transparent organism that has taken up PAHs or other compounds that can be excited by the UV portion of solar light. While both types of toxicity occur in the environment during an oil spill, there is currently a lack of studies evaluating the relative importance of both processes.

11.6 Outlook: future research needs

As outlined in this chapter, a large body of knowledge regarding the photooxidation of oil has been developed during the past five decades. While many key findings were already reported after the 1979 *Ixtoc-I* and the 1989 *Exxon Valdez* oil spills, significant knowledge was gained in research conducted in the aftermath of the 2010 *Deepwater Horizon* oil spill. Nevertheless, some questions brought up 50 years ago are still being debated. These gaps in our understanding of oil photooxidation at sea need to be addressed in ongoing or future research. This section provides recommendations for such future studies.

11.6.1 Mechanistic understanding of oil photooxidation

While research has shown that both aromatic [15, 17, 19], as well as saturated oil compounds [9, 12, 14], can be degraded photochemically, the magnitude of $^1O_2$-mediated degradation of aromatic compounds versus the peroxyl radical–mediated degradation of saturated compounds is not clear yet. Furthermore, it is unclear whether $^1O_2$ [10] or direct photochemical reactions [46] initiate the formation of peroxyl radicals that are ultimately degrading saturated compounds. Future research should address these knowledge gaps.

11.6.2 Understanding the rate of oil photooxidation at sea

Besides questions regarding the mechanism of oil photochemistry, there are challenges in determining and predicting the rate of oil photooxidation at sea. Important factors determining this rate include the solar spectrum and intensity and the oil film thickness. Thereby, the latter is highly dynamic at sea and difficult to predict. For example, a patch of oil could start off as a very thin film (e.g., 10 μm) and exhibit rapid photooxidation since photons penetrate the whole film [46]. Resulting changes in oil viscosity [101] could increase the film thickness (e.g., >100 μm) and thereby reduce the rate of photooxidation due to limitations of light and oxygen availability in the oil film [21, 46]. Besides, an oil sheen at sea is likely not a continuous film for a long duration. Due to the encounter with breaking waves, the oil

will spend some time as submerged droplets in the water phase, where the light availability is different than at the surface. A better understanding of these factors would facilitate extrapolating laboratory irradiation experiments to the kinetics of oil photooxidation at sea.

The formation of water-in-oil emulsions will also significantly affect the oil film thickness and optical properties, thereby slowing down the kinetics of oil photooxidation. Interestingly, oil photooxidation can facilitate the formation of emulsions [102], likely due to the surface-active compounds produced during photooxidation. Future research should address these issues and lead to a better understanding of the interplay between oil photooxidation and the formation of a water-in-oil emulsion.

11.6.3 Analytical challenges

There is a need for a better characterization of oil photoproducts. Although numerous oil photoproducts (or putative molecular formulas thereof) have been identified through GC/MS [2, 57], LC-MS/MS [58], or FT-ICR-MS [28–30], there is still no consensus about the most abundant and relevant oil photoproducts. What is more, there is a lack of generally accepted analytical methods to quantify these products. Much of the oil spill science still relies exclusively on GC/MS-base methods. GC/MS with electron impact (EI) ionization is ideal for hydrocarbon analysis up to a boiling point of approx. tetracontane (n-C_{40}; 523 °C) since it shows little ionization efficiency discrimination between compounds and has a large linear range for quantification. However, GC/MS has its limitation for photoproduct analysis and needs to be complemented with LC-based or direct infusion coupled to high-resolution mass spectrometry (HRMS)-based methods [103].

LC- or HRMS-based methods, however, have their limitations. First, the ionization efficiencies of the ionization methods used for these methods vary substantially between different compounds and matrices [75], requiring multiple runs with different ionization methods for a comprehensive analysis. Second, due to the lack of analytical standards for many of the photoproducts, these methods are generally semi-quantitative rather than quantitative. Lastly, while HRMS methods can produce a large number of molecular formulas for each analyzed oil residue (>10,000), these methods are usually not able to identify the structure of the analytes since one molecular formula can correspond to very different structures. Ion mobility spectrometry – mass spectrometry (IMS/MS) might be a promising method to overcome this limitation [104, 105].

Future research should aim to identify and quantify the most relevant fractions of oil photoproducts. Furthermore, standardized analytical methods for quantification of these photoproducts should be developed, and analytical standards and standard reference materials (SRM) that include oil photoproducts should be

produced. This SRM 2777 from the national institute of standards and technology (NIST) is a good starting point for creating photoproduct-containing standard reference material.

11.6.4 Fate and effect of oil photoproducts

There are knowledge gaps related to the environmental fate of oil photoproducts. For example, since photoproducts are more water-soluble than their precursors, one would expect the photoproduct to be prone to depletion from oil residues due to dissolution. However, many photoproducts are still present in oil residues after years of weathering [57]. Furthermore, the biodegradability of photoproducts is not well studied. Future research should address what structural features make photoproducts labile versus recalcitrant in the environment.

The toxicity of oil photoproducts is also not well understood. While it is known that oxygenation has the potential to increase the toxicity of certain compounds (e.g., oxygenation of PAHs [106–108]), it is not clear under which circumstances photooxidation increases or decreases the overall toxicity of oil residues during environmental weathering [31, 32, 109, 110]. Future research should address this question, taking into account the simultaneous weathering processes that occur at sea, including evaporation, dissolution, biodegradation, and photooxidation.

References

[1] Mackay D. Chemical and physical behaviour of hydrocarbons in freshwater. In: Vandermeulen JH, Hrudey SE, eds. Oil in freshwater: Chemistry, biology, countermeasure technology. Pergamon, 1987, 10–21.
[2] Charrié-Duhaut A, Lemoine S, Adam P, et al. Abiotic oxidation of petroleum bitumens under natural conditions. Org Geochem, 2000, 31, 977–1003.
[3] Ward CP, Overton EB. How the 2010 Deepwater Horizon spill reshaped our understanding of crude oil photochemical weathering at sea: A past, present, and future perspective. Environ Sci Process Impacts, 2020, 22, 1125–1138.
[4] Payne JR, Phillips CR. Photochemistry of petroleum in water. Environ Sci Technol, 1985, 19, 569–579.
[5] Nicodem DE, Guedes CLB, Correa RJ, Fernandes MCZ. Photochemical processes and the environmental impact of petroleum spills. Biogeo chem, 1997, 39, 121–138.
[6] Nicodem DE, Guedes CLB, Conceição M, et al. Photochemistry of petroleum. Prog React Kinet Mech, 2001, 26, 219–238.
[7] Lee RF. Photo-oxidation and photo-toxicity of crude and refined oils. Spill Sci Technol Bull, 2003, 8, 157–162.
[8] Larson RA, Hunt LL, Blankenship DW. Formation of toxic products from a #2 fuel oil by photooxidation. Environ Sci Technol, 1977, 11, 492–496.

[9] Gesser HD, Wildman TA, Tewari YB. Photooxidation of n-hexadecane sensitized by xanthone. Environ Sci Technol, 1977, 11, 605–608.
[10] Larson RA, Hunt LL. Photooxidation of a refined petroleum oil: Inhibition by β-carotene and role of singlet oxygen. Photochem Photobiol, 1978, 28, 553–555.
[11] Overton EB, Laseter JL, Mascarella W. Photo-chemical oxidation of IXTOC-I oil. Proceedings of a Symposium on Preliminary Results From The September 1979 Researcher/Pierce Ixtoc-1 Cruise, Key Biscayne, Florida, 1980, June 9–10, 1980.
[12] Rontani J-F, Giral -PJ-P. Significance of photosensitized oxidation of alkanes during the photochemical degradation of petroleum hydrocarbon fractions in seawater. Int J Environ Anal Chem, 1990, 42, 61–68.
[13] Rontani J-F. Identification by GC/MS of acidic compounds produced during the photosensitized oxidation of normal and isoprenoid alkanes in seawater. Int J Environ Anal Chem, 1991, 45, 1–9.
[14] Guiliano M, El Anba-Lurot F, Doumenq P, et al. Photo-oxidation of n-alkanes in simulated marine environmental conditions. J Photoch Photobio A, 1997, 102, 127–132.
[15] Garrett RM, Pickering IJ, Haith CE, Prince RC. Photooxidation of crude oils. Environ Sci Technol, 1998, 32, 3719–3723.
[16] Prince RC, Garrett RM, Bare RE, et al. The roles of photooxidation and biodegradation in long-term weathering of crude and heavy fuel oils. Spill Sci Technol Bull, 2003, 8, 145–156.
[17] Fasnacht MP, Blough NV. Mechanisms of the aqueous photodegradation of polycyclic aromatic hydrocarbons. Environ Sci Technol, 2003, 37, 5767–5772.
[18] Fasnacht MP, Blough NV. Kinetic analysis of the photodegradation of polycyclic aromatic hydrocarbons in aqueous solution. Aquat Sci, 2003, 65, 352–358.
[19] Plata DL, Sharpless CM, Reddy CM. Photochemical degradation of polycyclic aromatic hydrocarbons in oil films. Environ Sci Technol, 2008, 42, 2432–2438.
[20] Aeppli C, Carmichael CA, Nelson RK, et al. Oil weathering after the Deepwater Horizon disaster led to the formation of oxygenated residues. Environ Sci Technol, 2012, 46, 8799–8807.
[21] Ward CP, Sharpless CM, Valentine DL, et al. Partial photochemical oxidation was a dominant fate of Deepwater Horizon surface oil. Environ Sci Technol, 2018, 52, 1797–1805.
[22] Lewan MD, Warden A, Dias RF, et al. Asphaltene content and composition as a measure of Deepwater Horizon oil spill losses within the first 80days. Org Geochem, 2014, 75, 54–60.
[23] Ray PZ, Chen H, Podgorski DC, et al. Sunlight creates oxygenated species in water-soluble fractions of Deepwater Horizon oil. J Hazard Mater, 2014, 280, 636–643.
[24] Ray PZ, Tarr MA. Petroleum films exposed to sunlight produce hydroxyl radical. Chemosphere, 2014, 103, 220–227.
[25] King SM, Leaf PA, Olson AC, et al. Photolytic and photocatalytic degradation of surface oil from the Deepwater Horizon spill. Chemosphere, 2014, 95, 415–422.
[26] Ray PZ, Tarr MA. Formation of organic triplets from solar irradiation of petroleum. Mar Chem, 2014, 168, 135–139.
[27] Ward CP, Sharpless CM, Valentine DL, et al. Oxygen isotopes (δ 18 O) trace photochemical hydrocarbon oxidation at the sea surface. Geophys Res Lett, 2019, 46, 6745–6754.
[28] Ruddy BM, Huettel M, Kostka JE, et al. Targeted petroleomics: Analytical investigation of macondo well oil oxidation products from pensacola beach. Energy Fuels, 2014, 28, 4043–4050.
[29] Chen H, Hou A, Corilo YE, et al. 4 years after the Deepwater Horizon spill: Molecular transformation of macondo well oil in louisiana salt marsh sediments revealed by FT-ICR mass spectrometry. Environ Sci Technol, 2016, 50, 9061–9069.

[30] Niles SF, Chacón-Patiño ML, Chen H, et al. Molecular-level characterization of oil-soluble ketone/aldehyde photo-oxidation products by fourier transform ion cyclotron resonance mass spectrometry reveals similarity between microcosm and field samples. Environ Sci Technol, 2019, 53, 6887–6894.
[31] Kim D, Jung J-H, Ha SY, et al. Molecular level determination of water accommodated fraction with embryonic developmental toxicity generated by photooxidation of spilled oil. Chemosphere, 2019, 237, 124346.
[32] Zito P, Podgorski DC, Johnson J, et al. Molecular-level composition and acute toxicity of photosolubilized petrogenic carbon. Environ Sci Technol, 2019, 53, 8235–8243.
[33] Brette F, Machado B, Cros C, et al. Crude oil impairs cardiac excitation-contraction coupling in fish. Science, 2014, 343, 772–776.
[34] Faksness LG, Altin D, Nordtug T, et al. Chemical comparison and acute toxicity of water accommodated fraction (WAF) of source and field collected Macondo oils from the Deepwater Horizon spill. Mar Pollut Bull, 2015, 91, 222–229.
[35] Echols B, Smith A, Gardinali PR, Rand GM. Chronic toxicity of unweathered and weathered macondo oils to mysid shrimp (Americamysis bahia) and Inland Silversides (Menidia beryllina). Arch Environ Contam Toxicol, 2016, 71, 78–86.
[36] Alloy M, Baxter D, Stieglitz J, et al. Ultraviolet radiation enhances the toxicity of Deepwater Horizon oil to mahi-mahi (Coryphaena hippurus) Embryos. Environ Sci Technol, 2016, 50, 2011–2017.
[37] Reed M, Johansen Ø, Brandvik PJ, et al. Oil spill modeling towards the close of the twentieth Century: Overview of the state of the art. Spill Sci Technol Bull, 1999, 5, 3–16.
[38] National Research Concil. Oil spill dispersants: Efficacy and effects. The National Academies Press, Washington, DC, 2005.
[39] National Research Council (US) Committee on Oil in the Sea: Inputs, Fates, and Effects. Oil in the sea III: Inputs, fates, and effects. National Academies Press (US), Washington (DC), 2014.
[40] Exxon Mobil Research and Engineering Company. Oil spill response field manual, 6th edition, Exxon Mobil, 2014.
[41] Hansen HP. Photochemical degradation of petroleum hydrocarbon surface films on seawater. Mar Chem, 1975, 3, 183–195.
[42] Sanniez WHK, Pilpel N. Photo-oxidation of floating hydrocarbon oils in the presence of some naphthalene derivatives. J Chem Soc Lond Faraday Trans 1, 1978, 74, 123–130.
[43] Larson RA, Bott TL, Hunt LL, Rogenmuser K. Photooxidation products of a fuel oil and their antimicrobial activity. Environ Sci Technol, 1979, 13, 965–969.
[44] Ehrhardt MG, Weber RR. Sensitized photo-oxidation of methylcyclohexane as a thin film on seawater by irradiation with natural sunlight. Fresenius J Anal Chem, 1995, 352, 357–363.
[45] Ehrhardt MG, Bicego MC, Weber WR. Photo-oxidation of 1-methylnaphthalene dissolved in seawater and exposed to sunlight under quasi-environmental conditions. J Photoch Photobio A, 1997, 108, 253–259.
[46] Lichtenthaler RG, Haag WR, Mill T. Photooxidation of probe compounds sensitized by crude oils in toulene and as an oil film on water. Environ Sci Technol, 1989, 23, 39–45.
[47] Richard C, Canonica S. Aquatic phototransformation of organic contaminants induced by coloured dissolved natural organic matter. In: The handbook of environmental chemistry. Springer Berlin Heidelberg, Berlin, Heidelberg, 2005, 299–323.
[48] Canonica S. Oxidation of aquatic organic contaminants induced by excited triplet states. CHIMIA Intl J Chem, 2007, 61, 641–644.
[49] McNeill K, Canonica S. Triplet state dissolved organic matter in aquatic photochemistry: Reaction mechanisms, substrate scope, and photophysical properties. Environ Sci Process Impacts, 2016, 18, 1381–1399.

[50] Aubry J-M, Pierlot C, Rigaudy J, Schmidt R. Reversible binding of oxygen to aromatic compounds. Acc Chem Res, 2003, 36, 668–675.
[51] Corrêa RJ, Severino D, Souza RDS, et al. The generation of singlet oxygen by petroleum and its fractions. J Photochem Photobiol A Chem, 2012, 236, 9–13.
[52] Ehrhardt M, Petrick G. On the sensitized photo-oxidation of alkylbenzenes in seawater. Mar Chem, 1984, 15, 47–58.
[53] Odum JR, McDow SR, Kamens RM. Mechanistic and kinetic studies of the photodegradation of Benz[a]anthracene in the presence of methoxyphenols. Environ Sci Technol, 1994, 28, 1285–1290.
[54] Wu S-P, Schwab J, Yang B-Y, Yuan C-S. Effect of phenolic compounds on photodegradation of anthracene and benzo[a]anthracene in media of different polarity. J Photochem Photobiol A Chem, 2015, 309, 55–64.
[55] Zepp RG, Wolfe NL, Baughman GL, Hollis RC. Singlet oxygen in natural waters. Nature, 1977, 267, 421–423.
[56] Fasnacht MP, Blough NV. Aqueous photodegradation of polycyclic aromatic hydrocarbons. Environ Sci Technol, 2002, 36, 4364–4369.
[57] Aeppli C, Swarthout RF, O'Neil GW, et al. How persistent and bioavailable are oxygenated Deepwater Horizon oil transformation products?. Environ Sci Technol, 2018, 52, 7250–7258.
[58] Cao X, Tarr MA. Aldehyde and ketone photoproducts from solar-irradiated crude oil-seawater systems determined by electrospray ionization-tandem mass spectrometry. Environ Sci Technol, 2017, 51, 11858–11866.
[59] Ehrhardt M, Petrick G. The sensitized photo-oxidation of n-pentadecane as a model for abiotic decomposition of aliphatic hydrocarbons in seawater. Mar Chem, 1985, 16, 227–238.
[60] Rontani J-F, Giusti G. Photosensitized oxidation of pristane in sea water: Effect of photochemical reactions on tertiary carbons. J Photochem, 1987, 40, 107–120.
[61] Oita IJ, Conway HS. Direct determination of oxygen in organic substances. Anal Chem, 1954, 26, 600–602.
[62] Culmo R. Micro determination of oxygen in organic compounds with an automatic elemental analyzer. Microchim Acta, 1968, 56, 811–815.
[63] Boukir A, Guiliano M, Asia L, et al. A fraction to fraction study of photo-oxidation of BAL 150 crude oil asphaltenes. Analusis, 1998, 26, 358–364.
[64] Boukir A, Aries E, Guiliano M, et al. Subfractionation, characterization and photooxidation of crude oil resins. Chemosphere, 2001, 43, 279–286.
[65] Fernandez-Varela R, Gomez-Carracedo MP, Fresco-Rivera P, et al. Monitoring photooxidation of the Prestige's oil spill by attenuated total reflectance infrared spectroscopy. Talanta, 2006, 69, 409–417.
[66] White HK, Wang CH, Williams PL, et al. Long-term weathering and continued oxidation of oil residues from the Deepwater Horizon spill. Mar Pollut Bull, 2016, 113, 380–386.
[67] Rouillon C, Bussiere P-O, Desnoux E, et al. Is carbonyl index a quantitative probe to monitor polypropylene photodegradation?. Polym Degrad Stab, 2016, 128, 200–208.
[68] Almond J, Sugumaar P, Wenzel MN, et al. Determination of the carbonyl index of polyethylene and polypropylene using specified area under band methodology with ATR-FTIR spectroscopy. E-polymers, 2020, 20, 369–381.
[69] Rodrigues MO, Abrantes N, Gonçalves FJM, et al. Spatial and temporal distribution of microplastics in water and sediments of a freshwater system (Antuã River, Portugal). Sci Total Environ, 2018, 633, 1549–1559.
[70] Prata JC, Reis V, Paço A, et al. Effects of spatial and seasonal factors on the characteristics and carbonyl index of (micro)plastics in a sandy beach in aveiro, portugal. Sci Total Environ, 2020, 709, 135892.

[71] Sharma BK, Sarowha S, Bhagat SD, et al. Hydrocarbon group type analysis of petroleum heavy fractions using the TLC-FID technique. Fresenius J Anal Chem, 1998, 360, 539–544.
[72] Delgado-Saborit JM, Alam MS, Godri Pollitt KJ, et al. Analysis of atmospheric concentrations of quinones and polycyclic aromatic hydrocarbons in vapour and particulate phases. Atmos Environ, 2013, 1994, 77, 974–982.
[73] Marshall AG, Rodgers RP. Petroleomics: Chemistry of the underworld. Proc Natl Acad Sci U S A, 2008, 105, 18090–18095.
[74] Smith DF, Podgorski DC, Rodgers RP, et al. 21 Tesla FT-ICR mass spectrometer for ultrahigh-resolution analysis of complex organic mixtures. Anal Chem, 2018, 90, 2041–2047.
[75] Huba AK, Gardinali PR. Characterization of a crude oil weathering series by ultrahigh-resolution mass spectrometry using multiple ionization modes. Sci Total Environ, 2016, 563–564, 600–610.
[76] Huba AK, Huba K, Gardinali PR. Understanding the atmospheric pressure ionization of petroleum components: The effects of size, structure, and presence of heteroatoms. Sci Total Environ, 2016, 568, 1018–1025.
[77] US EPA. EPI Suite – Estimation Program Interface. In: United States Environmental Protection Agency, 2012. https://www.epa.gov/tsca-screening-tools/epi-suitetm-estimation-program-interface#citing.
[78] Nabi D, Katz S, Aeppli C. Are oxygenated hydrocarbons important oil degradation products after oil spills?. Int Oil Spill Conference Proc, 2017, 2017, 571–588.
[79] DeMello JA, Carmichael CA, Peacock EE, et al. Biodegradation and environmental behavior of biodiesel mixtures in the sea: An initial study. Mar Pollut Bull, 2007, 54, 894–904.
[80] Prince RC, Haitmanek C, Lee CC. The primary aerobic biodegradation of biodiesel B20. Chemosphere, 2008, 71, 1446–1451.
[81] Yassine MH, Wu S, Suidan MT, Venosa AD. Aerobic biodegradation kinetics and mineralization of six petrodiesel/soybean-biodiesel blends. Environ Sci Technol, 2013, 130417133207005.
[82] Dutta TK, Harayama S. Fate of crude oil by the combination of photooxidation and biodegradation. Environ Sci Technol, 2000, 34, 1500–1505.
[83] Abdalrhman AS, Zhang Y, Arslan M, Gamal El-Din M. Low-current electro-oxidation enhanced the biodegradation of the recalcitrant naphthenic acids in oil sands process water. J Hazard Mater, 2020, 398, 122807.
[84] Moran MA, Zepp RG. Role of photoreactions in the formation of biologically labile compounds from dissolved organic matter. Limnol Oceanogr, 1997, 42, 1307–1316.
[85] Benner R, Biddanda B. Photochemical transformations of surface and deep marine dissolved organic matter: Effects on bacterial growth. Limnol Oceanogr, 1998, 43, 1373–1378.
[86] Tranvik LJ, Bertilsson S. Contrasting effects of solar UV radiation on dissolved organic sources for bacterial growth. Ecol Lett, 2001, 4, 458–463.
[87] Lam B, Baer A, Alaee M, et al. Major structural components in freshwater dissolved organic matter. Environ Sci Technol, 2007, 41, 8240–8247.
[88] Prince RC, McFarlin KM, Butler JD, et al. The primary biodegradation of dispersed crude oil in the sea. Chemosphere, 2013, 90, 521–526.
[89] Radović JR, Aeppli C, Nelson RK, et al. Assessment of photochemical processes in marine oil spill fingerprinting. Mar Pollut Bull, 2014, 79, 268–277.
[90] Redman AD, Butler JD, Letinski DJ, et al. Technical basis for using passive sampling as a biomimetic extraction procedure to assess bioavailability and predict toxicity of petroleum substances. Chemosphere, 2018, 199, 585–594.

[91] Redman AD, Parkerton TF, Butler JD, et al. Application of the target lipid model and passive samplers to characterize the toxicity of bioavailable organics in oil sands process-affected water. Environ Sci Technol, 2018, 52, 8039–8049.
[92] Escher BI, Berg M, Mühlemann J, et al. Determination of liposome/water partition coefficients of organic acids and bases by solid-phase microextraction. Analyst, 2002, 127, 42–48.
[93] Escher BI, Abagyan R, Embry M, et al. Recommendations for improving methods and models for aquatic hazard assessment of ionizable organic chemicals. Environ Toxicol Chem, 2020, 39, 269–286.
[94] Scarlett AG, Reinardy HC, Henry TB, et al. Acute toxicity of aromatic and non-aromatic fractions of naphthenic acids extracted from oil sands process-affected water to larval zebrafish. Chemosphere, 2013, 93, 415–420.
[95] Toor NS, Franz ED, Fedorak PM, et al. Degradation and aquatic toxicity of naphthenic acids in oil sands process-affected waters using simulated wetlands. Chemosphere, 2013, 90, 449–458.
[96] Jones D, Scarlett AG, West CE, Rowland SJ. Toxicity of individual naphthenic acids to vibrio fischeri. Environ Sci Technol, 2011, 45, 9776–9782.
[97] Dogra Y, Scarlett AG, Rowe D, et al. Predicted and measured acute toxicity and developmental abnormalities in zebrafish embryos produced by exposure to individual aromatic acids. Chemosphere, 2018, 205, 98–107.
[98] Larson RA, Berenbaum MR. Environmental phototoxicity. Environ Sci Technol, 1988, 22, 354–360.
[99] Marzooghi S, Di Toro DM. A critical review of polycyclic aromatic hydrocarbon phototoxicity models. Environ Toxicol Chem, 2017, 36, 1138–1148.
[100] Marzooghi S, Finch BE, Stubblefield WA, Di Toro DM. Predicting phototoxicity of alkylated PAHs, mixtures of PAHs, and water accommodated fractions (WAF) of neat and weathered petroleum with the phototoxic target lipid model. Environ Toxicol Chem, 2018, 37, 2165–2174.
[101] Ward CP, Armstrong CJ, Conmy RN, et al. Photochemical oxidation of oil reduced the effectiveness of aerial dispersants applied in response to the Deepwater Horizon spill. Environ Sci Technol Lett, 2018, 5, 226–231.
[102] Thingstad T, Pengerud B. The formation of “chocolate mousse” from Statfjord crude oil and seawater. Mar Pollut Bull, 1983, 14, 214–216.
[103] McKenna AM, Rodgers RP, Nelson RK, et al. Expansion of the analytical window for oil spill characterization by ultrahigh resolution mass spectrometry: Beyond gas chromatography. Environ Sci Technol, 2013, 130521150737003.
[104] Fernandez-Lima FA, Becker C, McKenna AM, et al. Petroleum crude oil characterization by IMS-MS and FTICR MS. Anal Chem, 2009, 81, 9941–9947.
[105] Ponthus J, Riches E. Evaluating the multiple benefits offered by ion mobility-mass spectrometry in oil and petroleum analysis. Int J Ion Mobil Spectrom, 2013, 16, 95–103.
[106] Knecht AL, Goodale BC, Truong L, et al. Comparative developmental toxicity of environmentally relevant oxygenated PAHs. Toxicol Appl Pharmacol, 2013, 271, 266–275.
[107] Lundstedt S, White PA, Lemieux CL, et al. Sources, fate, and toxic hazards of oxygenated polycyclic aromatic hydrocarbons (PAHs) at PAH- contaminated sites. Ambio, 2007, 36, 475–485.
[108] Geier MC, Chlebowski AC, Truong L, et al. Comparative developmental toxicity of a comprehensive suite of polycyclic aromatic hydrocarbons. Arch Toxicol, 2017, 35, 330.
[109] Rial D, Radović JR, Bayona JM, et al. Effects of simulated weathering on the toxicity of selected crude oils and their components to sea urchin embryos. J Hazard Mater, 2013, 260, 67–73.
[110] Maki H, Sasaki T, Harayama S. Photo-oxidation of biodegraded crude oil and toxicity of the photo-oxidized products. Chemosphere, 2001, 44, 1145–1151.

Thamina Acter, Nizam Uddin, Sunghwan Kim

12 Molecular structure characterization of crude oil and its products by mass spectrometry

Abstract: Crude oil and its products, including light oils, heavy oils, fuels, tar, asphalt, lubricating oils, heavy oils, spilled oils, and hydrotreated oils, are complex mixtures containing thousands of chemical compounds with diverse structures. The chemical structural identification of crude oil and its products is extremely important for gaining insights into the chemistry of petroleum in the petrochemical industry. Mass spectrometry (MS), particularly ultrahigh-resolution MS (UHR-MS), is considered an important technique for the accurate analysis of the underlying mass and structure of crude oil components. Hydrogen/deuterium exchange (HDX) tandem MS and ion-mobility (IM) spectrometry coupled with HR-MS have attracted significant attention for their application in investigating the molecular structures of petroleum and its products. The most effective HDX technique used for crude oil analysis is atmospheric pressure in-source HDX, which is suitable for the detailed structural identification of complex mixtures, such as crude oil. By combining atmospheric pressure ionization techniques, such as electrospray ionization (ESI), atmospheric-pressure photoionization (APPI), and atmospheric-pressure chemical ionization (APCI), the sample preparation step for HDX MS can be considerably simplified, enabling the attainment of high-quality results and the specification of the heteroatom classes in crude oil. To isolate ions with specific m/z values and, thus, understand the core structures of oil compounds, the fragmentation patterns of the oil compounds are studied by tandem MS with collision-induced dissociation (CID) or infrared multiphoton dissociation coupled with HR-MS. In addition, IM separation with multiple cycles combined with quadrupole selection is considered a powerful technique for isolating ions with specific mobility values during complex mixture analysis. Recently, IM coupled with HR-MS, experimental collision cross-section (CCS) and theoretical CCS values was employed to study the chemical structures of petroleum compounds. Due to the separation of isomeric or isobaric ions in IM cells, improved peak capacities and highly accurate structural assignments of crude oil compounds can be achieved. This chapter

Thamina Acter, Department of Mathematical and Physical Sciences, East West University, A/2, Jahurul Islam Avenue, Aftabnagar, Dhaka 1212, Bangladesh
Nizam Uddin, Department of Nutrition and Food Engineering, Faculty of Allied Health Science, Daffodil International University, 102, Shukrabad, Dhanmondi, Dhaka 1207, Bangladesh
Sunghwan Kim, Department of Chemistry, Kyungpook National University, Daegu, 702–701, Republic of Korea; Green-Nano Materials Research Center, Daegu, 41566, Republic of Korea

https://doi.org/10.1515/9783110694529-012

provides an overview of some of the key applications of HDX, tandem MS, and IM-MS techniques to the structural analysis of crude oil and its products

12.1 Introduction

The current global energy supply is vastly dependent on fossil fuels, particularly heavy crudes, because of the low reserve of light and sweet (low sulfur) crudes and the low availability of sustainable energy resources. Unlike light crudes, heavy crude oil has a naturally complex molecular composition along with a trend continuum of the carbon number, aromaticity, heteroatom content, and molecular motifs [1, 2]. For the efficient valuation and refinery optimization of heavy petroleum fractions in the petroleum industry, their molecular and structural characterizations are of utmost importance. In addition, various refining processes, including hydrotreatments (e.g., hydrodemetallation (HDM), hydrodesulfurization (HDS), and hydrodenitrogenation (HDN)), hydrocracking of large molecules to low-molecular-weight paraffins/isoparaffins, and hydrogenation of aromatics to naphthenes, are performed during the conversion of heavy fractions of crude oil into different oil products [3]. However, the chemical upgrading of crude oil is more challenging due to the presence of various unwanted heteroatoms (nitrogen, sulfur, and oxygen) contained polycyclic aromatic hydrocarbons (PAHs) and metals, which drastically degrade the catalyst activity during the petroleum conversion. Consequently, petroleum refiners and process chemists need to know the specific composition of the feed to recognize the problems of catalyst dysfunction and devise improved process models to optimize the refining process and apply the appropriate treatment methods. Therefore, the quantification and structural analysis of crude oil with a high content of heteroatom-containing compounds are essential [4].

Conventionally, the large groups of chemically diverse compounds present in complex crude oils exhibit a common core structure with different substitution patterns. The average individual structural properties, i.e., the amount and character of carbon atoms in the aliphatic sidechains of crude oil, can be determined by nuclear magnetic resonance (NMR) spectroscopy or through the ruthenium-driven oxidation of aromatic moieties [5]. Conversely, detailed structural information on a significant portion of the analytes can be obtained using MS techniques if the sample pretreatment of individual species is performed. The analysis of either light or heavy petroleum is primarily performed on a molecular basis [2]. Due to the very complex nature of the numerous heteroatom species in heavy crude oil and its products, obtaining detailed structural and compositional information is challenging and, thus, requires the use of more sophisticated high-resolution analytical techniques. Since the early age of the modern analytical society, mass spectrometry (MS), particularly high-resolution mass spectrometry (HR-MS), has been extensively utilized to profoundly understand the chemistry of crude oil and elucidate its elemental composition [6–11].

The molecular analysis of complex crude oil and its products cannot be conducted without HR-MS, i.e., ultrahigh-resolution (UHR) Fourier transform ion cyclotron resonance mass spectrometry (FTICR MS), which affords exhaustive molecular formula characterization [8, 12–14]. Moreover, map-type diagrams can be used as molecular fingerprints for crude oil [11, 15].

Admittedly, the current HR-MS analysis for heavy crude oils based on molecular formula assignments is inadequate for the complete and accurate elucidation of the chemical structures of individual congeners, i.e., the individual side chains (number and length), aromatic core, and different isomers that yield different molecular properties [16]. To access the structural information on the molecular core of the isomeric compounds in crude oil, more reliable analytical methods with enhanced separation capabilities, such as chromatographic separation [17–19], hydrogen/deuterium exchange (HDX) [20–23] tandem MS (MS/MS) by collision-induced dissociation (CID) [24–27], and IM-MS[28–32], have been coupled with the HR-MS platform. In this chapter, the application of recent hyphenated MS techniques, including tandem MS, IM-MS, and HDX MS, for the structural analysis of crude oil and its products is elaborately discussed.

12.2 MS archives

MS is the most common analytical tool with the most potential for studying thermochemical and physical properties, molecular structures, and ion-molecule reaction dynamics in physics, pharmaceutical sciences, and environmental sciences [33]. In MS analysis, the molecular masses of individual compounds are precisely measured using the ions generated via different ionization methods, which undergo ionization and separation subsequently based on their mass-to-charge ratio (m/z), under the effect of an electric or magnetic field.

MS was introduced in 1886 when Eugen Goldstein observed the canal rays, whose deflection through strong electric and magnetic fields was later demonstrated by Wilhelm Wien in 1898. Sir J. J. Thomson of the Cavendish Laboratory of the University of Cambridge is considered the father of modern MS, who measured the m/z ratio of electrons during the analysis of negatively and positively charged cathode rays [34, 35]. The development of MS instruments proceeded during the following two decades [36–38]. In 1943, the MS instrument was commercialized for the first time by the Consolidated Engineering Corporation. From 1946 to 1953, the time-of-flight (TOF) MS, ion cyclotron resonance (ICR) MS, double-focusing HR-MS, quadrupole mass analyzer, and ion traps were introduced simultaneously. After the 1950s, the evolution of MS techniques progressed as researchers began applying them in the field of organic chemistry. In the 1960s, gas chromatography (GC) coupled with MS was developed and applied to the structural analysis of complex mixtures [39]. During

this period, tandem MS [40] and soft ionization techniques, such as chemical ionization (CI) [41], were also developed for structural analysis. In the 1970s, high-performance liquid chromatography (HPLC) was coupled with MS for the first time and subsequently commercialized with atmospheric pressure ionization (API) sources (e.g., electrospray ionization (ESI) and atmospheric pressure photoionization (APPI)) for routine analysis.

In the 1980s, other soft ionization methods, such as fast atom bombardment (FAB) [42], ESI [43], and matrix-assisted laser desorption/ionization (MALDI) [44], were developed, which significantly increased the application range of MS in biology and life sciences. In the 2000s, technical improvements in mass analysis techniques, such as TOF, FTICR, orbitrap, and linear quadrupole ion trap (LIT), were observed. Most importantly, the increased resolving power, mass resolution, and mass accuracy of the FTICR MS technique developed by Professor Alan Marshall and coworkers have expanded the application of MS. The strength of the applied magnetic field in the FTICR MS methods is still undergoing improvement to achieve the best MS results.

12.3 Evolution of MS for petroleomics

The comprehensive characterization of crude oil and its products at the molecular level by MS is known as petroleomics [10, 45]. MS was first explored as an analytical tool to monitor petroleum refining processes in the 1940s. Although the MS technology has long evolved into a tool for elucidating the composition of petroleum, the first hyphenated MS technique, such as GC/MS, was developed in the 1950s and 1960s to analyze complex mid-light distillates [46]. In 1958, low-voltage EI was developed by Lumpkin to minimize fragmentation and analyze a much wider molecular-weight range [47]. The MS platform, interfaced with high-voltage (70 eV) electron ionization (EI) and field desorption (FD)/EI, was employed to characterize the low-boiling-point nonpolar species, middle distillates and residues of petroleum until the 1990s. Most importantly, ASTM Standards based on these methods are practiced until now (e.g., ASTM D2425 – 21). The molecular assignments of petroleum compounds were mainly based on group types, carbon number distributions [46], and structure-oriented lumping [48]. In the 1990s, HR-MS instruments with ultrahigh resolving power were developed [12, 49, 50] based on low-field (~3 T) superconducting magnets; however, these instruments could analyze petroleum distillates only within a narrow mass-spectral range at a time [51]. Thenceforth, the resolving power (above one million) and resolution of HR-MS have advanced with time via the strengthening of the magnetic field to >7 T to achieve a highly accurate analysis and wide m/z range (one kilodalton) in the growing field of petroleomics [8, 9, 45, 50, 52]. The mass spectrum of crude oil obtained using UHR FTICR MS enables the unambiguous identification of crude

oil molecules by providing unique elemental peak listings with approximately 10,000–50,000 molecular formulas.

Since the year 2000, an increasing number of hyphenated MS techniques, including liquid chromatography coupled with MS (LC/MS), tandem MS, IM-MS, and HDX, and promising simple and diverse ionization sources, such as ESI and APPI, have been successfully applied to the analysis of heavy crude distillates containing polar and non-polar species to extract more detailed information on the composition and structure of petroleum.

12.4 Outlook for crude oil and its products

The heavy fractions of crude oil are used for producing paving and roofing materials, fuel oils, asphalt, gasoline, diesel, and jet fuel [3]. Petroleum mainly contains hydrocarbons (C_cH_h, ~85–90%); polar species ($N_nO_oS_s$, ~10–15%) consisting of heteroatoms, such as nitrogen-, sulfur-, and oxygen-containing compounds; and metals (V, Fe, Ni) [3].

Crude oil can be separated into four different fractions: saturates, aromatics, resins, and asphaltenes (SARA), using the SARA fractionation procedure [53]. Heteroatom PAH compounds, such as nitrogen-, sulfur-, and oxygen-containing compounds, can be found in the resin and asphaltene fractions of heavy oils. The polar resin fraction comprises dark brownish-black semisolids. It is a chemically complex mixture, which contains diverse polar chemicals, including nitrogen- (amides, pyridines, quinolines, and carbazoles), sulfur- (sulfoxides, sulfides, sulfones, thiophenes), and oxygen-containing compounds [54]. Therefore, the individual chemical identification of the resin fraction components is difficult. During the production and processing of petroleum, its polar fraction usually causes corrosion, emulsion formation, deposit formation, and catalyst poisoning. Crude oil compounds can be structurally characterized based on the groups and classes of various oil compounds, carbon number distribution, double-bond equivalent (DBE) distribution, and types of heteroatom compounds/aromatics/aliphatic hydrocarbons.

12.4.1 PAHs

PAHs are organic compounds composed of multiple aromatic rings. PAHs can be formed from the pyrolysis and dehydrogenation of compounds containing branched chains, as well as saturated structures. The analogs of PAHs, e.g., oxygen-, nitrogen-, or sulfur-containing PAH compounds, can also be formed.

The PAH compounds present in fossil fuels (petroleum, coal, shale oil, etc.) are extremely complex and rich in alkylated species (e.g., alkylated naphthalenes),

hydroaromatic species (e.g., pentacyclic and tetracyclic aromatic hydrocarbons such as monoaromatic and triaromatic steranes), and heteroatomic compounds (e.g., oxygen-, nitrogen-, or sulfur-containing PAH compounds). The three-dimensional structural range of the PAHs and sulfur-containing PAH compounds is shown in Figure 12.1a and b, where each of the PAH compound types may be present as a continuous homologous series in a given petroleum sample. In addition, the structures such as biphenyl and diphenylmethane, can also be present in petroleum. The compositions of the PAH compounds in coal- and shale-derived oils are more complex compared to those in petroleum. The detailed compositional analysis of the PAH compounds in petroleum can be performed using MS group-type analyses.

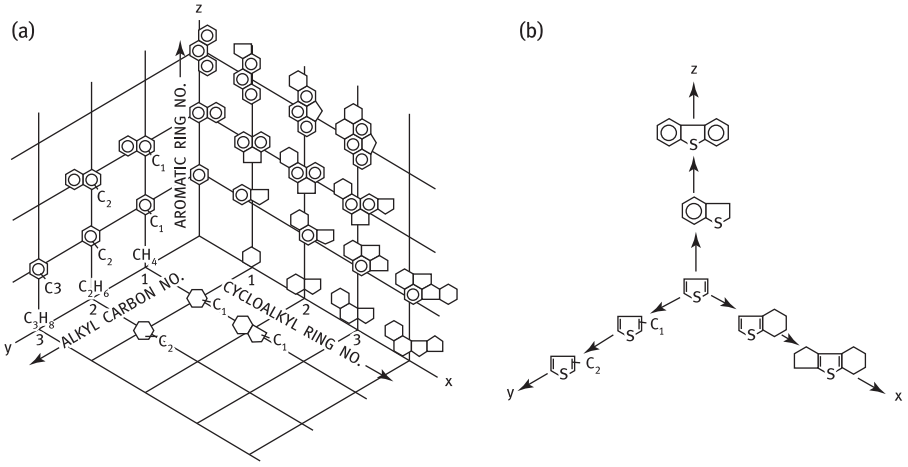

Figure 12.1: Structural range of the petroleum (a) hydrocarbons, (b) sulfur heterocycles [reproduced with permission from L. R. Snyder [200]. Copyright, American Chemical Society].

The PAH compounds present in petroleum have been extensively analyzed by group-type mass-spectral analyses. In the early 1950s, Brown [55] first developed a reliable group-type analysis method for analyzing saturated and unsaturated hydrocarbons, such as paraffins, cycloparaffins, monoolefins, diolefins, and acetylenes, and gasoline using the early commercial low-resolution mass spectrometers. The alkyl homolog plots can be constructed for semiquantitative comparison during the group-type mass-spectral analysis of PAHs, using the graph of the molecular ion abundance versus the carbon number for each parent PAH compound and its alkyl derivatives [56]. Blumer et al. [57] analyzed PAHs isolated from fossil fuels and constructed their alkyl homolog plots, which revealed the three or four carbon alkyl-substituted PAHs with the highest abundance. Besides, Clerc et al. [58] applied group-type analysis to saturated and alkyl- and hydroaromatics. Later, additional group-type analyses of petroleum aromatic fractions were conducted by several

research groups using low-resolution mass spectrometers [59–61]. The conventional low-resolution MS ionization methods, such as low- and high-voltage EI, field ionization (FI), FD, and photoionization (PI), were used primarily for the determination of the molecular-weight distributions (MWDs) of PAHs. In the early 1970s, FI and FD-MS were employed for the analysis of the aromatic fractions of fossil fuels [62], while HR-MS was employed for the group-type analysis of the PAHs in petroleum [63]. To achieve the separation of individual PAH components before mass-spectral identification, hyphenated MS techniques, such as GC/MS, GC/MS/MS [64], CI, metastable-ion, and CID MS, are selected to analyze complex petroleum mixtures containing many structural isomers.

12.4.2 Nitrogen-containing species

Nitrogen compounds constitute approximately 0.01–2% of petroleum during the refining process while more than 15 wt% of most biodegraded (heavy) lacustrine oils. The common nitrogenous compounds in petroleum are aromatic heterocycles with one neutral nitrogen or amine groups [4]. The basic nitrogen-containing compounds present in crude oil are mainly pyridines, while the non-basic nitrogen-containing compounds such as pyrroles, indoles, carbazoles, and benzo-carbazoles may contain alkyl groups in certain isomeric positions. These nitrogen-containing species can significantly affect the refining processes. Since they have a very high absorption capacity at catalytic sites, they act as a poison for the hydrotreating catalysts used in HDS [4]. Therefore, they must be removed by nitrogen hydrotreatment or HDN before performing HDS. However, some nitrogen-containing species are resistant to HDN processes, which are called refractory nitrogen compounds; these compounds must be saturated before initiating the HDN processes. Moreover, the identification of nitrogen-containing species is very important during petroleum refining.

The identification of nitrogen compounds in petroleum can be performed effectively using MS techniques. The existence of basic nitrogen-containing compounds in crude oil, e.g., pyridines and quinolines by Richter et al. using extraction with 5% aqueous hydrochloric acid [65]. Conventionally, ESI is employed to facilitate the selective ionization of polar nitrogen-containing compounds containing basic (e.g., quinoline) or neutral nitrogen (e.g., carbazole) molecules in petroleum samples.

12.4.3 Oxygen-containing species

The polar oxygen-containing compounds present in acidic crude oil may include alcohols, phenols, oxygen heterocycles, and carboxylic acids, collectively denoted as naphthenic acids (NA). Among the oxygen-containing compounds, fatty acids are one of the most important precursor of long chains alkanes in the crude oil while

naphthenic acids are the reservoir biodegradation product of the crude oil [66] The carboxylic acids, collectively denoted as NA, are organic acids mainly composed of polycycloaliphatic acids and aromatic acids with substituents of heteroatoms such as nitrogen, sulfur, and oxygen. The carboxylate functional group (–COOH) is common in the isomers of NAs and aromatic acids of crude oils. They can cause liquid-phase corrosion during crude oil transport and refining processes, emulsion formation, naphthenate deposition, and flow assurance problems [67]. Notably, naphthenates can significantly contribute to petroleum solubilization, aggregation, and emulsion [68, 69]. During naphthenate deposition, metal naphthenates, such as calcium naphthenate solids and sodium naphthenate emulsions, are precipitated by the hydrolysis of naphthenic acid with the inorganic cations (e.g., divalent ions, such as Ca^{2+}, Fe^{2+}, and Mg^{2+}, or monovalent ions, such as Na^{+} and K^{+}) present in the production waters. Crude oils containing high NAs are (by) products of severe biodegradation. New crude oil reservoirs may also be more prone to naphthenate deposition because they contain immature heavy crude oils with a high heteroatom content. Therefore, the structural identification of the oxygen-containing compounds, such as NAs and aromatic acids, in crude oil is very important.

12.4.4 Sulfur-containing species

Crude oil and its products, including gasoline and diesel fuel, may contain abundant sulfur-containing compounds, such as sulfides, polysulfides, thiophenes, and mercaptans (thiols) [4]. The amount of sulfur-containing compounds for crude oil may be more than 10%, while for the products of crude oil, including gasoline and diesel fuel, may be less than 10%. Among the sulfur-containing species, thiols are the most reactive, and they are present in relatively lower amounts compared to thiophenes or sulfides.

The identification of sulfur-containing compounds in petroleum is as important as the identification of nitrogen and oxygen-containing compounds, considering their catalyst-deactivating and corrosion-inducing capabilities in petroleum refineries [4]. Although the absorptive, adsorptive, and reactive properties of sulfur compounds have hindered their identification in petroleum for some time [45], several analytical methods, such as HR-MS [70–72] ESI and CI coupled with GC [73], and APPI [21, 74] have been reported for the molecular-level characterization of sulfur-containing compounds in crude oil. Han et al. reviewed the most recent analytical techniques used for the detection of the sulfur-containing compounds in crude oil [72].

12.4.5 Petroporphyrins

Petroporphyrins consist of four pyrrole units bonded to methine carbons. Ni and V have the highest abundance in petroleum [75]. Their structures remain stable under different geological conditions. Examples of two petroporphyrins found in petroleum are deoxyophyl loerythroetioporphyrins (DPEP) and etioporphyrins (ETIO) (Figure 12.2).

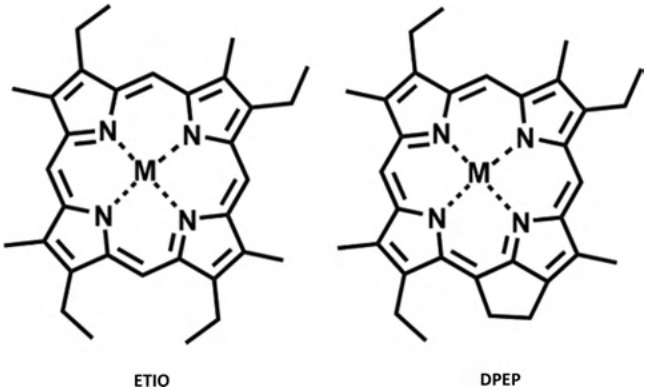

Figure 12.2: The structures of DPEP and ETIO.

In order to deactivate cracking catalysts, reduce furnace corrosion during petroleum refining, establish their potential petroporphyrins as biomarkers, and explore new fuel sources, the compositional and structural identifications of pure porphyrins and complex petroporphyrins are important [76].

Triebs was the first to identify petroporphyrins in petroleum in the 1930s [77]. MS techniques, such as FAB/other desorption techniques, H_2/NH_3 CI, specialized derivatization procedures, and tandem mass spectrometry, can be used for the analysis of petroporphyrins. The major fragment ions observed in previous studies suggest that petroporphyrins comprise mainly pyrrolic structures, which can be formed by cleavage at the bridge positions [78, 79]. The compositional analysis of petroporphyrins is also performed using UHR MS [80, 81]. More recently, Maillard et al. [82] combined trapped ion mobility (TIMS) and FTICR MS to characterize vanadium petroporphyrins present in heavy petroleum fractions.

12.5 Tandem MS/MS

12.5.1 Principle of tandem MS

Tandem MS (MS/MS) is a two-stage MS technique, which involves the simultaneous fragmentation/collisional ionization of the target ion, causing a change in the mass or ion charge; thus, this technique is suitable for the m/z analysis of structurally important fragments or product ions [83]. The concept of building a MS/MS instrument into the MS system was first introduced by J. J. Thomson, who is thought to be the forefather of tandem MS [84].

The tandem MS phenomenon is represented by a general reaction depicted as follows [85]:

$$m_p^+ \rightarrow m_f^+ + m_n \tag{12.1}$$

where m_p^+ is the precursor ion isolated in the first mass analyzer; m_f^+ and m_n are the product ion and neutral fragment, respectively, produced after collisional fragmentation and analyzed by a second mass analyzer.

The basic tandem MS technique progresses in three steps (Figure 12.3) [83]. First, the ion selected for the tandem MS, called the precursor ion, is isolated in the first mass analyzer before fragmentation. To isolate the precursor ion, the MS instruments generally allow a mass window of approximately 1 Da. The isolated precursor ion enters the collision cell placed between the two mass analyzers. Second, an inert gas passes through the collision cell and collides with the precursor ion. In this step, translational energy is transferred to the precursor ion, causing it to disintegrate into fragments; this fragmentation is facilitated by different activation methods (discussed later). Third, the ions produced during the fragmentation are called product ions, whose m/z ratios are measured in the second mass analyzer.

During the MS/MS experiment, the type of product ions observed mainly depends on the ion-activation step [86], and the collision energy can be measured by dissociating 50% of the precursor ion; thus, different classes of compounds can be differentiated. The most important factors controlling the number of ions

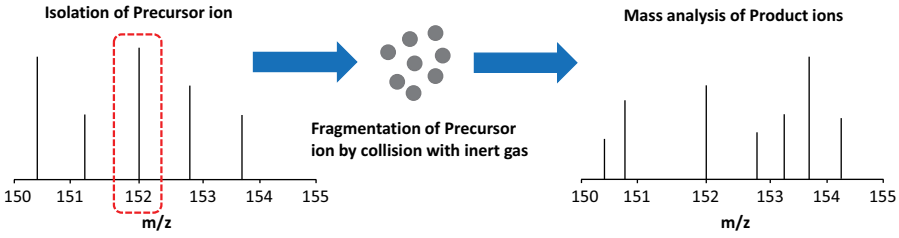

Figure 12.3: Principle of the MS/MS analysis.

undergoing fragmentation and the ion collisional probability are the nature and pressure of the collision gas used in the collision cell [86].

12.5.2 Categories of the MS^n experiment

Tandem MS experiments can be performed using two main categories of instruments operated either in space or through time separation [83]. For the instruments operated in space, such as double-focusing mass spectrometers, and quadrupole mass analyzers [87], at least two mass spectrometers are usually coupled together. For the instruments operated through time separation, such as ion traps [88], FTICR mass spectrometers [7], and orbitrap mass spectrometers, an appropriate sequence of successive fragmentations, generally seven to eight at maximum, occurs in the same instrument. The basic difference in the tandem MS operations of ion trap and FTICR is that the ions are measured at the end of the fragmentation process in ion trap MS, whereas the ions are detected at each step of the tandem process in the FTICR MS [83]. Notably, increasing the number of analyzers in the MS system can yield higher order MS^n spectra; however, this also increases the instrument complexity and cost.

12.5.3 Types of scan modes used for the MS^n experiments

There are four types of scan modes for the tandem MS experiments, proposed by Cooks and coworkers [89] as shown in Table 12.1:

Table 12.1: Types of scan modes used in tandem MS.

Scan modes	Details
Product-ion scan	A precursor ion of a target m/z ratio is selected, and the product ions produced from the tandem process are determined
Precursor-ion scan	The precursor-ion scan mode operates opposite to the product-ion scan mode, where the precursor ions are determined from a given product ion and can only be performed in space-based mass spectrometers
Neutral-loss scan	A neutral fragment is chosen, and the fragmentations leading to such loss are detected; Similar to the precursor-ion scan mode, the neutral-loss scan mode can be performed only in space-based mass spectrometers
Selected-reaction monitoring (SRM) or multiple reaction monitoring (MRM)	A fragmentation reaction is selected by focusing the selected m/z ratios of the first and second mass analyzers; therefore, the MS sensitivity can be increased. This scan mode can be performed in both time- and space-based MS instruments.

12.5.4 Types of activation methods

Ion activation is an important step in tandem MS experiments, which can overcome the activation barrier expressed in eq. (12.1) before the overall fragmentation reaction occurs. Many activation methods exist, including collision-activated/induced dissociation (CAD and CID), infrared multiphoton dissociation (IRMPD), electron capture/electron transfer dissociation (ECD and ETD), and surface-induced dissociation (SID) [84, 85].

12.5.4.1 CID

The most common activation method used in tandem MS is CID or CAD, where inert gas molecules collide with the precursor ion (with high kinetic energy), resulting in the conversion of kinetic energy into internal energy, which leads to the decomposition of the analyzed ion [85, 86, 90]. CID has been applied to study the structures of isolated ions by tandem MS [91].

The CID process can be described as follows:

$$E_{\mathrm{cm}} = \left[N/\left(m_{\mathrm{p}} + N\right)\right] \times E_{\mathrm{Lab}} \tag{12.2}$$

where E_{cm} is the internal energy available for fragmentation, N is the mass of the neutral gas molecule, m_{p} is the mass of the precursor ion, and E_{lab} is the ion kinetic energy. It was reported that the overall CID process depends on the value of N and m_{p}, while the energy conversion (E_{cm}) in the CID process can be improved by increasing m_{p} [84]. Similar to Boltzmann's distributions, the distributions of the internal energy for the parent ions in multiple CIDs are mostly thermal.

The activation mechanism is depicted by the excitation of the precursor ions, followed by fragmentation [86]:

$$m_{\mathrm{p}}^{+} + N \rightarrow m_{\mathrm{p}}^{+\#} \rightarrow m_{\mathrm{f}}^{+} + m_{\mathrm{N}} \tag{12.3}$$

The CID process occurs in two energy ranges: low energy (1–100 eV) and high energy (a few keV). The low-energy CID can be performed in ion traps, quadrupoles (e.g., triple quadrupoles, QqQ), and FTICR instruments, whereas the high-energy CID (HCD) is performed in sectors and TOF instruments employing He or heavier gases (such as Ar or Xe) as the collision gas.

CID-based MS techniques have been employed to study the aromatic core structures of crude oil components because CID can easily break the weakly σ-bonded alkyl chains linked to the aromatic core [92, 93]. The structure of crude oil species has recently been studied using CID coupled to FTICR MS [94].

Another specific CID technique is higher-energy C-trap dissociation, or HCD, which can be performed in high-field Orbitrap instruments with a low collision energy range (<100 eV) by fragmenting ions in a collision cell [95]. The fragmentation

pathways in the HCD process are much wider than those in the low-energy process. Due to its low-mass cut-off, HCD-based FT-ICR MS was applied to study the structures of asphaltenes [96].

Another CID process, called multipole storage assisted dissociation (MSAD), can be used to enhance the fragmentation in the collision cell at certain concentrations [97]. In the MSAD process, the excited ion can be oscillated at relatively high magnitudes in the multipole during the radial spreading of the ions by Columbic force after the ion density reaches the charge limit. Thereafter, the radio frequency (rf) energy of the ions can be converted into high kinetic energy, resulting in the extensive fragmentation of the excited ions in the collision cell during the collision with the gas molecules [96].

12.5.4.2 Infrared multiphoton dissociation (IRMPD)

IRMPD is another ion-activation technique, which involves photon absorption of the precursor ion, followed by photodissociation using different continuous-wave low-energy lasers, such as UV, visible, and IR lasers, at a selected irradiance time (approximately 10–100 ms) [85]. The instruments used for this activation technique are ion traps and FTICR mass spectrometers. The IRMPD process can be explained by two steps:

$$m_{\mathrm{p}}^{+} + N \underset{\rightarrow}{^{nh\nu}} m_{\mathrm{p}}^{+} \underset{\rightarrow}{^{\#K_{\mathrm{dis}}}} m_{\mathrm{f}}^{+} + m_{\mathrm{N}} \tag{12.4}$$

where n is the number of photons absorbed, $h\upsilon$ is the photon energy, and k_{dis} is the photodissociation rate constant. In the first step, IR rays are absorbed, which excite the stored ions. In the second step, the absorbed photon energy dissociates depending on the internal energy and produces fragment ions.

The advantages of this activation process include the high availability of photon energy, good dissociation efficiency at high activation times, and non-use of collisional gas [86]. Conversely, the limitations include its nonselectivity, high cost, and complex collection of fragmentation spectra. IRMPD-based FTICR MS and tandem MS/MS techniques were applied for the comprehensive fragmentation of pentane-insoluble asphaltenes from a de-asphalted oil (DAO) to identify the building blocks for a stable aromatic core [98].

12.5.4.3 ECD

ECD, developed by McLafferty's group [99], is an ion-activation method, wherein the precursor ion of multiply charged cationic species is activated by capturing a beam of low-energy electrons, resulting in charge state reduction and subsequent

fragmentation at the radical site [85]. The mechanism of ECD is governed by radical-ion chemistry, reviewed by Zubarev et al. [100] Only FTICR mass spectrometers are suitable for conducting ECD experiments. The advantages of the ECD method are its fastness, ability to dissociate very large biomolecules, and ability to cleave strong bonds. To facilitate the movement of electrons in the trap instruments, an alternate activation method, named ETD, was developed by Hunt's group [101].

12.5.4.4 SID

SID, developed by Cooks and coworkers [102], is another ion-activation method, wherein the precursor ion (with a high kinetic energy) collides with a solid surface, resulting in the efficient conversion of kinetic energy into internal energy and the consequent decomposition of the analyzed ion [85]. Since the entire surface is used as the collision target in the SID method, the excited ions can distribute the internal energy in a narrow range [103], facilitating the discrimination of the isomers [104]. The instruments used for low-energy SID are triple quadrupoles, ion traps, and FTICR mass spectrometers, whereas TOF mass spectrometers are used for high-energy SID.

12.5.5 Tandem MS chemistry of crude oil

The general chemical formula of a petroleum system is depicted as follows [4]:

$$C_cH_{2C+Z}N_nS_sO_oVNi \tag{12.5}$$

where c, n, s, and o are the numbers of carbon, nitrogen, sulfur, and oxygen atoms present in a crude oil molecule, respectively; V and Ni are the metals present in the crude oil as metalloporphyrins; Z indicates the hydrogen deficiency or degree of unsaturation (a homologous series of a petroleum system containing alkyl chains has one unique Z number and heteroatom combination). The negative Z value highlights the unsaturation of the molecules. The Z values of the alkylated carbazoles ($C_cH_{2c-15}N$), benzothiophenes ($CcH_{2c-10}S$), and alkylated benzenes (C_cH_{2c-6}) are – 15, – 10, and – 6, respectively.

Z can further be described as follows:

$$Z = -2 \times (\mathrm{DBE} - 1) + n \tag{12.6}$$

where DBE indicates the total number of rings and double bonds in the compound with formula (12.5).

During tandem MS experiments, the Z numbers of the parent molecules and the fragments in eq. (12.1) can vary depending on the change in the chemical structure of the crude oil compounds [85]. The parent molecules and the fragments of the tandem MS experiment may have the same Z number or not, as expressed in eq. (12.5).

For a molecule with a single-core structure, dealkylation is expected to occur, whereas for a molecule with multicore structures, dealkylation, as well as the change in the Z number, should occur during the MS^n experiment. Terpenoids and steroids are popular structures in petroleum, and these molecules are more prone to split their core structure instead of the side chains as shown in Figure 12.6. The fragments produced from the parent multicore-structured molecule should have relatively low absolute Z numbers.

Since a crude oil sample contains numerous parent molecule ions, the fragmentation study of petroleum samples is more complicated than that of known standard model compounds. Consequently, a quality control sample is recommended to be analyzed along with the petroleum samples to achieve consistent fragmentation patterns. The important factors affecting the fragmentation chemistry for different core structures include the presence of weak versus strong bonds in the molecules, product distribution, and charge efficiency [85]. The mass and product distributions and ion transmission tandem MS experiments can be significantly affected by different instrument parameters, including the collision energy, collision cell ion density, beam steering, and excitation in the ICR cell [84].

12.5.6 Interpretation of the tandem MS crude oil data

Altgelt [3] summarized the interpretation methods of the tandem MS data under three basic steps: (a) All the fragment ions produced during the tandem MS, belonging to the same parent ions, are identified; (b) all parent ions belonging to the specific fragment ions produced during the tandem MS are identified; and (c) all parent ions resulting in fragment ions through the same neutral-loss (fixed mass) process are identified. Among all the three mentioned interpretation methods, method (a) is the most convenient because of the elimination of isotope effects and the readily interpretable fragmentation patterns obtained from the parent ions in the second MS stage.

Recently, Rodgers's and Zimmermann's research teams differentiated the structural families of petroleum by studying the mapping (DBE as a function of the carbon number) interpreted from the MS/MS spectra [25, 105–107] A mapping is the most common oil-characterization diagram derived from the HR-MS data; this diagram displays the "molecular fingerprint" for a given class of heteroatoms, enabling the visualization and identification of thousands of elemental compositions and structures in a given oil sample [15, 108, 109].

12.5.7 Application of tandem MS in crude oil analysis

Understanding the effect of CID on various class species of different petroleum crudes can help elucidate their molecular structures. Tandem MS has been used to

study the structures of aromatic compounds in heavy petroleum fractions [94, 96, 98, 110], as well as asphaltene [26]. Tandem MS had yielded impressive compositional information on not only heavy crude oils, but also many petroleum distillates, such as gasoline, diesel, and gas oils [111]. A continuum of crude oil species has been distinguished in previous studies based on their boiling points, molecular weights, and unsaturation [3, 98]. Recently, many researchers, including Kekäläinen et al. [112], Wittrig et al. [26], Chacón-Patiño et al. [106, 113–115], and Lalli et al. [116], are focusing on the continuous compositional and structural investigation (heteroatom distribution, structural conformation with single and multiple core motifs) of heavy crude oil fractions, such as VGO, bitumen, and asphaltene.

12.5.7.1 PAHs

Qian et al. [96] applied CID (MSAD in a linear quadrupole)-12 T FTICR MS (ESI and APPI) technology with no isolation prior to fragmentation to determine the aromatic building blocks and their distributions in heavy petroleum fractions, such as vacuum residues (VRs), based on the CID chemistry of a wide range of model compounds having both single-core and multicore structures (e.g., pyridines, pyrroles, hydrocarbons, and sulfides). The most prevalent fragmentation pattern for the model compounds was observed to be dealkylation (breakage of the weak $-CH_2-CH_2-$ bonds on the alkyl side chains); other patterns, such as breaking of the C2 + alkyl linkages and naphthenic ring-openings, were also observed. The single-core-structured compounds showed a reduction in the molecular weight only, while the multicore-structured compounds showed a reduction in both molecular weight and the *Z* number. The higher the condensation efficiency of the aromatic molecule, the lower the molecular mass. The before and after CID results of the VR sample suggested its architecture to be a mixture of single-core and multicore configurations with abundant aromatic ring classes (Figure 12.4). Therefore, the parent petroleum molecules can be reconstructed from the CID product distribution used as the building blocks. The authors stated that the main drawback of this broadband CID experiment is the difficulty in finding a direct parent–product ion correlation, fragmentation patterns, and mechanisms for the analyzed crude oil samples.

12.5.7.2 Nitrogen-containing compounds

Maître et al. [93] identified and characterized nitrogen-containing compounds by analyzing three different VGO fractions of the same oil before and after HDN, using ESI (+) FTICR tandem MS and IM spectrometry. The results obtained from the FTICR MS data provided information on the basic nitrogen compounds, such as quinoline and isoquinoline, with DBEs of 7, 8, and 9. The IM spectrometry data confirmed

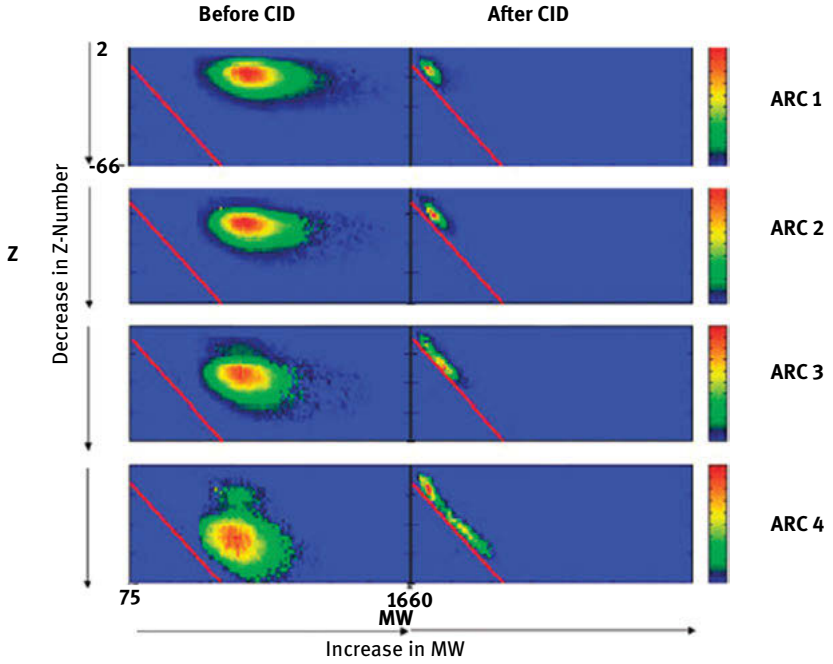

Figure 12.4: Analysis of the aromatic fractions of vacuum residue oil before and after CID coupled with 12 T FTICR MS; *Z*-number versus MW distributions along with the relative abundances (color scheme) of their aromatic ring classes. The stoichiometric limits of the planar polycyclic aromatic hydrocarbons (PAHs) structures are represented by the red lines [reproduced with permission from Qian, K. et al. [96]. Copyright, American Chemical Society].

that the N_1 isomers, which are highly resistant to the HDN process, have long alkyl branches with high CCS values. From the MS/MS data of the protonated precursor ion, the island core structures of the N_1 class compounds were deduced based on the alkane losses as a function of the collision energy.

Maître et al. [117] further examined the efficiency of a vacuum hydrocracking unit in eliminating the neutral nitrogen compounds that are refractory to the HDN processes. For this, they analyzed two petroleum samples: processed VGO and unprocessed VGO, containing 10 w-ppm N, by (–) ESI UHR FTICR tandem MS (CID, collision energy: 60 eV) and TWIMS TOF MS, and they identified the structures of the N_1 compounds by studying their tandem MS fragments. They observed that the structural conformation of the molecular core correlates with the refractory behavior. The fragmentation mechanism obtained from the MS/MS results of the selected precursor ions shows the subsequent loss of small alkyl chains (e.g., methyl, butyl) following the rearrangement of the molecular nuclei. The IM-MS and MS/MS results highlighted that the isomers presenting low CCS values with DBEs of 10 and 13 are the dominant species. Moreover, the benzocarbazole derivatives with small alkyl

branches are suggested to be the aromatic core pattern of the selected refractory precursors, which are considered as highly refractory compounds in this study.

Porter, D. and Mayer, P [24]. demonstrated the usefulness of ESI-triple-quadrupole tandem MS using CID as an activation method for the analysis of petroleum-based chemicals, e.g., polar resin fractions of crude oil (Alberta sweet mix blend, ASMB), fuel oil, and diesel (Summer Diesel). The CID mass spectrum obtained at various collision energies for a model compound, protonated 1,4,5,8,9-pentamethyl carbazole (m/z 238), was very identical to that of the ASMB resin peak at m/z 238. Additionally, the fragmentation patterns of two model carbazole compounds with different alkyl chains ($-CH_2$, 14 mass units larger): 9-methyl carbazole and 9-ethylcarbazole, and resin constituents (m/z 240, 254, and 268) were identical. Finally, the resin constituents in this study were identified as alkyl-substituted carbazoles based on their structures.

Quan and coworkers [110] selectively investigated the bond-dissociation behavior and aromatic ring architecture of the basic nitrogen compounds in a low sulfur crude oil-derived VR, such as Sudan heavy petroleum fraction, using both broadband and quadrupole isolation mode (+) ESI FT-ICR MS coupled with CID techniques. The fragmentation pattern of the VR sample indicated that heterolytic bond cleavages of the protonated parent ions were more common than the homolytic cleavages in the dealkylation process, due to the predominance of odd-electron fragment ions. The trend of iso-abundance plots and the DBE distribution plot highlighted the "island" or single-core structure of the basic nitrogen compounds present in the analyzed oil sample, due to the preservation DBE values after the fragmentation of their parent ions.

Marshall and coworkers [46] confirmed the aggregation tendency of the polar species in Canadian bitumen by ESI MS and suggested their relatively high aggregated multimer structures with masses of 900, 1,500, and 2,000. The results of tandem CID (MS^4) MS demonstrated the low-molecular-weight monomer distribution (below ~800 Da) as a low-mass segment of the original broadband mass spectrum.

12.5.7.3 Oxygen-containing compounds

Cao, X. and Tarr, M. A [118] applied (–) ESI MS/MS (CID) coupled with 2,4-dinitrophenylhydrazine (DNPH) derivatization to identify aldehyde and ketone photoproducts in the aqueous phase under the oil exposed to simulated sunlight. DNPH can selectively react with aldehyde and ketone photoproducts to produce aldehyde/ketone-DNPH derivatives, which can be ionized and fragmented by (–) ESI MS/MS. The MS/MS results confirmed the presence of more than 80 aldehyde and ketone photoproducts in the solar irradiated oil samples. The comparative fragmentation patterns for the aldehyde/ketone photoproducts formed from the irradiated crude oil on sea water and oil on pure water were identical to those of dicarbonyls, hydroxycarbonyls, and oxo-carboxylic acids. The higher abundance

of polar aldehyde and ketone photoproducts in sea water than in fresh water evidenced their transfer into sea water, due to the photo-oxidation of oil, which ultimately represents their biodegradation nature. However, there are also hypotheses that recalcitrant dissolved organic matter pool may be the source of soluble photoproducts [119].

Mapolelo et al. [120] characterized isolated NA from a European calcium naphthenate deposit, commonly known as "ARN" acids, by (–) ESI FT-ICR MS coupled with tandem MS (MS^n), along with CID and IRMPD. The results of the IRMPD and CID fragmentation proposed the structure of the ARN acids to have a tetracarboxylic acid group with a C_{80} hydrocarbon skeleton, attributed to the multiple dehydration and decarboxylation of the carboxylic acid groups without dealkylation (Figure 12.5).

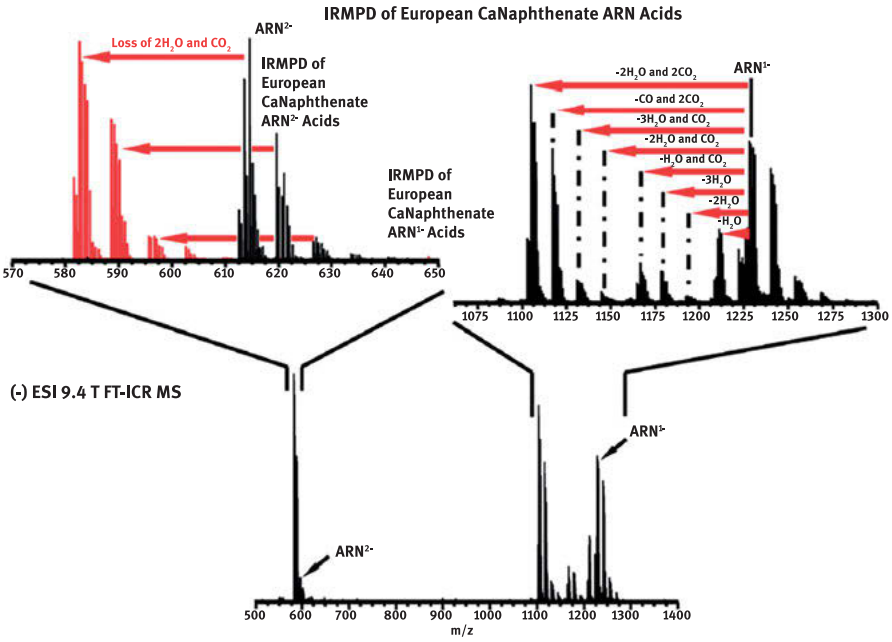

Figure 12.5: Analysis of the ARN acids extracted from a European calcium naphthenate deposit by (–) ESI FT-ICR coupled with IRMPD (low power); bottom: broadband mass spectrum; top: fragmentation of doubly charged (left) and singly charged (right) ARN acids from the same deposit [reproduced with permission from Mapolelo, M. M. et al. [120]. Copyright, Elsevier B. V.].

12.5.7.4 Sulfur-containing compounds

Kim and coworkers [27] proposed an analytical method using CAD tandem MS to analyze a Kuwaiti oil sample; they distinguished the structure of the aromatic compounds with one sulfur atom in the oil sample by comparison with the spectra of model

compounds. Further, they evaluated the potential of a systematic analytical approach by comparing the HR tandem MS spectra (with a normalized collision energy of 50 eV) of crude oil with those obtained from a well-defined set of 25 standard compounds having various functional groups to interpret the chemical structures of the crude oil compounds. The results of the tandem MS analysis showed that the product-ion distributions and fragmentation pattern for S_1 compounds with different DBE values are different, because of their different numbers of alkylation sites. The presence of less abundant alkylated benzothiophene and abundant alkylated dibenzothiophene suggested that dibenzothiophene with DBE values of 9 is the major structural motif for the S_1-class compounds present in the analyzed crude oil. Kim's group summarized their MS/MS findings via the tandem MS analysis of crude oil as follows: (i) a series of peaks differed by CH_2 group masses were generated from isomers with different numbers of alky side chains; (ii) the fragmentation pattern depends on the number and length of the alkyl side chains attached to the aromatic cores; (iii) there is a positive correlation between the number of methyl groups lost during the fragmentation and the molecular branching; (iv) significant fragmentation occurs for the compounds with long alkyl side chains (C_nH_{2n}, $n \geq 5$); (v) archipelago structures with short alkyl side chains C_nH_{2n}, $n \leq 1$) are stable during MS/MS; (vi) compounds with saturated ring structures can lead to a decrease in the DBE value.

Vetere et al. [92] synthesized different individual isomerically compounds with different aromatic cores and various substituents that are presumed to be present in a chromatographically simplified complex VGO mixture. They structurally characterized the compounds by defining their fragmentation mechanisms using (+) ESI or APPI tandem MS in either a triple quadrupole MS or a linear ion trap MS, which was operated in either Q_1 or the product-ion scan mode with an isolation window of 0.3 Da and collision energy of 10–50 eV. The tandem MS results of the standard compounds consisting of an aromatic core with aliphatic side chains, e.g., sulfur-containing compounds and pure hydrocarbons, showed that the fragmentation mechanism is the benzylic cleavage of the aliphatic side chains; thus, the remaining base aromatic core structure can finally be characterized. The tandem MS results of the PASHs from a crude oil sample revealed a series of fragments with a 14 Da spacing, attributed to the presence of multiple structural isomers containing different alkyl substituents in the crude oil sample.

12.5.7.5 Petroporphyrins

Brodbelt et al. [121] used MS/MS in combination with isobutane CI using a Finnigan 4500 triple quadrupole mass spectrometer to characterize the trace porphyrin constituents, such as vanadyl deoxophylloerythroetioporphyrins (DPEP) and vanadyl etioporphyrins (ETIO) species, in West Coast, Gato Ridge, and Boscan petroleum samples. The CI mass spectra confirmed the presence of low-level porphyrins in the

analyzed samples. The total concentration of the porphyrins in the samples was estimated by tandem MS and UV–Vis spectroscopy. The tandem MS experiments performed with CID at a collision energy of 20 eV showed that the fragmentation patterns for the daughter spectra of several suspected vanadyl porphyrin ions in a West Coast crude oil sample having a low signal-to-noise (S/N) ratio were similar to those obtained for the Gato Ridge porphyrin samples. Hexane extraction was conducted to improve the S/N ratio of the fragment ions. The degree of fragmentation and the relative DPEP/ETIO ratio of the analyzed daughter spectra revealed that the West Coast oil sample is as aged as the Gato Ridge and Boscan oils. Petroporphyrin compositional analysis of a heavy crude oil has also been studied by Amy McKenna and others from MagLab [122–124].

12.5.7.6 Petroleum biomarker analysis

Petroleum biomarkers, namely, isoprenoids, terpanes, and steranes, are first and foremost analyzed by conventional GC-MS [125, 126]. As saturate fraction is mostly rich in biomarkers of interest, SARA fractionation prior to GC-MS analysis having lower resolving power may be advantageous. GC coupled to a tandem mass spectrometer (GC-MSn), i.e., GC-multiple reaction monitoring (MRM) can be used for analysis of biomarkers having known composition [127]. The more recent powerful techniques used for biomarker analysis are multidimensional gas chromatography coupled to MS, i.e., GC × GC-FID, and GC × GC-TOFMS [128]. The tandem MS (e.g., MRM) with standard EI can be applied for the traditional petroleum biomarker analysis. To investigate the ion formation of petroleum standards (paraffins, isoparaffins, naphthenes, and aromatic hydrocarbons), Wu et al. [94] applied an atmospheric solid analysis probe (ASAP) to analyze a saturate fraction of petroleum VR and a relatively new technique combining GC with APCI, atmospheric pressure GC (APGC) coupled with tandem MS techniques to characterize the petroleum biomarkers (particularly, naphthenic). In both ASAP and APGC tandem MS experiments, there is no complication of data interpretation by nitrogen fixation, due to the unavailability of this reaction for multiring naphthenic structures generating only molecular ions ($M^{+\cdot}$) with subsequent fragmentation in Q-TOF MS configurations. The APGC tandem MS analysis of the saturate crude oil fraction in the product-ion scan mode produced five parent ions, corresponding to C_{26}–C_{30} sterane biomarkers. The MS/MS spectra characterized the steroidal hydrocarbons by selectively detecting the daughter ion (m/z 217) along with its D-ring fragmentation and separating isomeric diasteranes from regular steranes at different elution times (Figure 12.6).

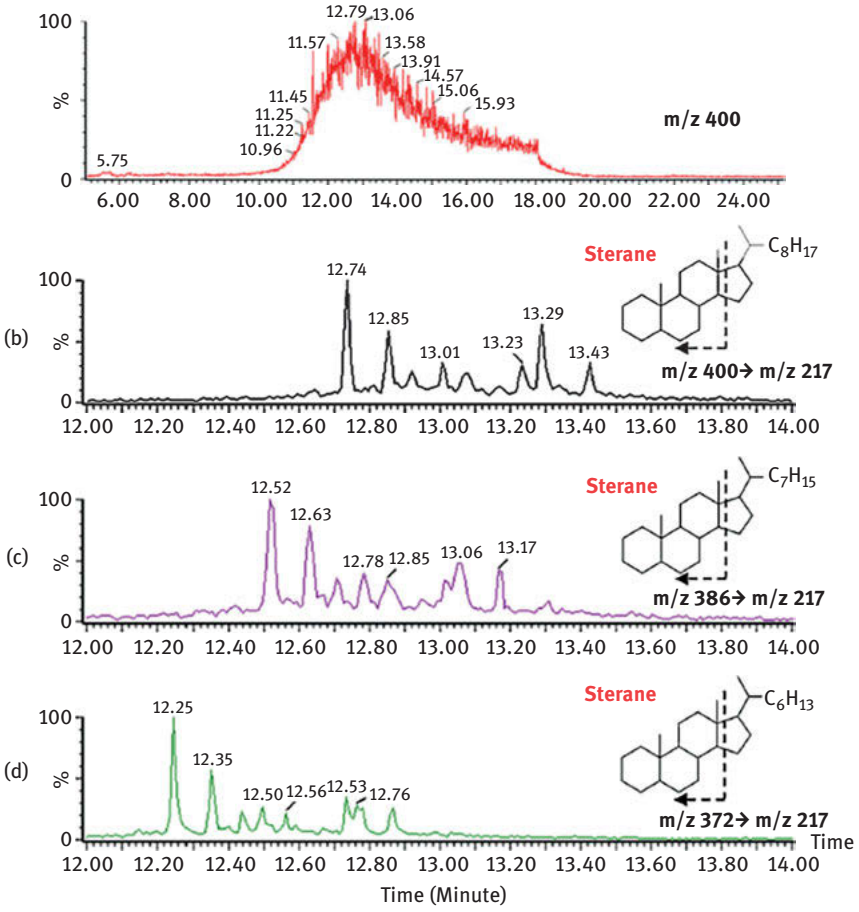

Figure 12.6: Analysis of petroleum biomarkers using atmospheric pressure gas chromatography (APGC) coupled with tandem MS techniques; (a) ion chromatogram for MS/MS of *m/z* 400; (b) selected ion chromatogram for MS/MS of *m/z* 400–217; (c) selected ion chromatogram for MS/MS of *m/z* 386–217; (d) selected ion chromatogram for MS/MS of *m/z* 372–217 [reproduced with permission from Wu, C. et al. [94]. Copyright, Elsevier B. V.].

12.5.7.7 Asphaltenes

There are two models for explaining the structure of asphaltene molecules: the island model and the archipelago model. The former applies to a single aromatic core of asphaltene, while the latter applies to multiple aromatic cores bridged by linkers in the asphaltene molecule. The identification of the aromatic core structure of asphaltene molecules (either single or multiple aromatic cores) is one of the most controversial topics in the petroleum society. The controversy is mainly

due to the support of the island model by MS results and the inconsistency between the island-asphaltene structural motifs and the composition of the products derived from asphaltene pyrolysis/thermal cracking, which are consistent with the coexistence of island and archipelago structures. Tandem MS has been employed to investigate asphaltene structures by several research groups [129, 130].

Rodgers and coworkers [105, 113, 114] performed a series of research to examine the structure of asphaltenes. In the first and second parts of their research [105, 113], they demonstrated that the selective ionization of island compounds by (+) APPI tandem (IRMPD) FTICR MS occurs due to the weak nanoaggregation of large aromatic cores in toluene, resulting in the support of the island structure of asphaltene. Conversely, the (+) APPI tandem (IRMPD) MS method does not ionize the archipelago-dominant fractions effectively because of their high tendency to aggregate. Therefore, they highlighted the urgent need for a separation method based on MS for enhancing the ionization of monomeric ions generated from archipelago asphaltene molecules. In the third part of their research [114], Rodgers and coworkers applied (+) APPI FT-ICR MS coupled with the IRMPD technique to characterize the asphaltenes and asphaltene extrography fractions derived from Wyoming deposit (island dominant) and Athabasca bitumen (archipelago dominant) C_7 asphaltenes. They concluded that the abundance of island or archipelago structures mainly depends on the sample and that all asphaltene samples cannot be described by Yen–Mullins molecular definition of asphaltenes. The FTICR MS results suggest that the Wyoming deposit asphaltenes exhibit island-type asphaltene structures with highly aromatic/alkyl-deficient species, while the more than 40 wt% Athabasca bitumen C_7 asphaltenes contain species with low DBE values and high carbon numbers (up to 60), which are difficult to ionize. The IRMPD results showed that the fragmentation mechanism for the fractions obtained from the Wyoming deposit C_7 asphaltenes is dealkylation without significant loss of aromaticity, which supports the island structures. Contrarily, the IRMPD results obtained from all the Athabasca bitumen-derived fractions correspond to the archipelago structures.

Rodgers and coworkers [98] further implemented the tandem MS (IRMPD) method coupled with APPI FT-ICR MS to reveal the component aromatic core building blocks in a heptane-C_7-deasphalted whole oil (C_7-DAO) heavy distillate cut (AEBP 523°C–593°C) obtained by DISTACT distillation, its pentane soluble/insoluble fractions (C_5-soluble and C_5-insoluble C_7-DAO), and their different ring number fractionations obtained by HPLC-2. The compositional continuum of the "maltenic" and "asphaltenic" species fractionated from the C_7-solubles by HPLC-2 was validated, as predicted by Boduszynski. The FTICR MS results showed a continuous progression in the decrease in the carbon number and increase in DBE (aromaticity) with increasing ring numbers of the aromatic structures. The tandem MS results afforded the structure of the aromatic building blocks of the "maltenic" and "asphaltenic" species (from 1 ring to 5 + ring fractions) to be an increasingly heterogeneous mixture of island and archipelago motifs (Figure 12.7). Additionally, the pentane-

insoluble C_7-DAO fraction was composed of a higher proportion of archipelago structures with higher-order fused ring core structures compared to those in the pentane-soluble C_7-DAO fraction.

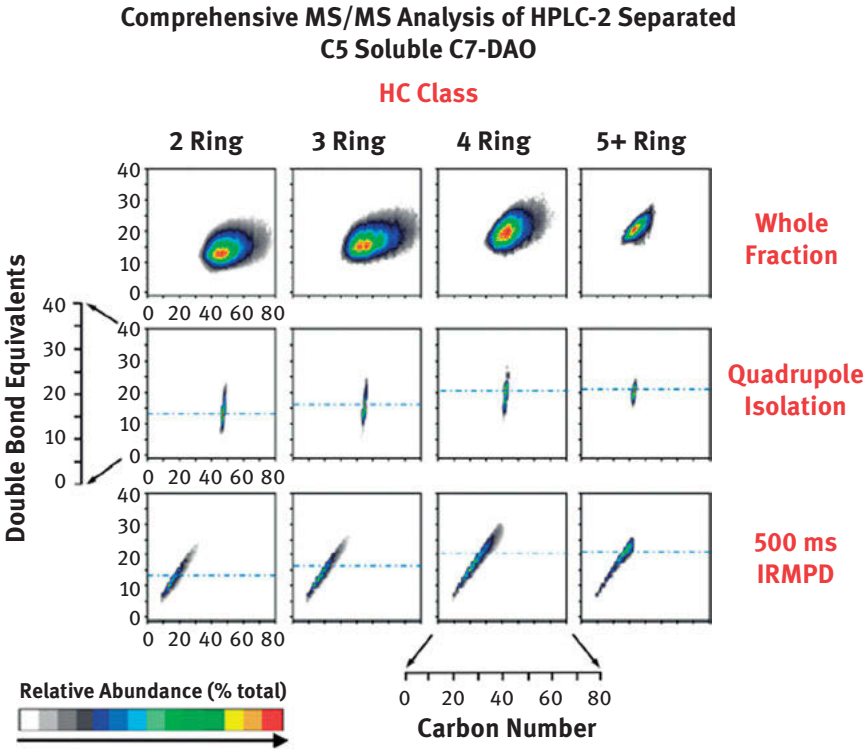

Figure 12.7: DBE versus the carbon number plots for the HC species identified for each ring number fraction (top row), quadrupole mass isolated segments (middle row), and IRMPD fragments of the mass-isolated fragments (bottom row), exposing the aromatic core structures of the C5-soluble C7-DAO fraction. The blue dashed line denotes the highest relative abundance for the DBE distribution for each mass isolated segment (middle in Figure 12.4), and the red dashed line denotes the completely dealkylated fragments (bottom in Figure 12.4) [reproduced with permission from Podgorski, D. C., et al. [98]. Copyright, American Chemical Society].

The asphaltenes in petroleum and coal were comparatively studied by Kenttämaa and coworkers [130], where the aromatic rings and the substituent chain length of the coal asphaltenes were found to be significantly broader and shorter, respectively, than those of the petroleum asphaltenes. To reduce the spectral complication interpreted from the data including both the molecular radicals and protonated ions generated from the petroleum samples, carbon disulfide was used as the solvent instead of toluene in combination with APCI tandem MS, since it generates only molecular

radical ions [131], while toluene generates both molecular radicals and protonated ions [132].

Tang et al. [133] studied the structures of six petroleum asphaltene samples of different geographical origins by the (+) APCI (CS2) method in a LIT mass spectrometer (LQIT) subjected to multistage tandem MS with CAD at the same collision energy. The results showed that the asphaltene samples from the Americas, Europe, and China have similar apparent MWDs, ranging from 200 to 1,450 Da, with apparent average MWs ranging from 570 to 700 Da. Moreover, the number of carbons (ranging from 17 to 41) in all the alkyl chains correlates well with the MWs of the asphaltene molecules (ranging from 500 to 808 Da). The fragmentation patterns obtained from the MS/MS analysis (MS^2 and MS^3) of the eight isolated molecular ions (m/z values ranging from m/z 500 up to m/z 808), derived from the examined asphaltene samples, supported the island structure with the subsequent losses of small alkyl radicals and without the loss of aromatic cores with different numbers of aromatic rings. This study was limited to the identification of compounds in asphaltenes ionized by the APCI (CS2) method.

Nyadong et al. [134] introduced a novel approach based on the high-energy CID (HCD) fingerprints, using the (+) APPI high-field Orbitrap MS platform to fragment six different crude oil asphaltene samples (including those derived from hydrotreated residues) into their constituent stable aromatic cores within narrow mass segments (~1 Da) at normalized collision energies (CE, %) of 35 and 200 eV. Thus, the relative proportions of the island-to-archipelago constituents were determined based on the discrepancy in the DBEs between the precursors and the stable aromatic cores. The results of the high-energy CID analysis showed that the relative proportions of the island-to-archipelago structures decreased as the MW of the analyzed asphaltenes increased and that the hydrotreated asphaltenes contained a higher proportion of island structures compared to the archipelago structures. Figure 12.8 shows that the archipelago-type precursors lead to the formation of product ions, consisting of one, two, three, etc. aromatic rings, which were observed at the lower bound of the HCD. Overall, the boundary between the island- and archipelago-derived product ions presented in the figure reveals that the sum of their product-ion abundances can be considered as a measure of their relative proportions in the asphaltene precursor-ion segment.

To extract more conclusive information on the core structures of the ions, single Dalton CID analysis coupled with APPI 15-T FTICR MS was performed for several aromatic ring class fractions of a heptane deasphalted VR and the associated asphaltene fraction, after simplifying the parent ions of the same nominal mass (isobaric and isomeric ions) via distillation, liquid chromatography, and mass selection (~1 Da) [26]. The main advantage of this single dalton mass isolation CID over broadband CID is the simplification of the reaction products obtained during fragmentation, resulting in an improved understanding of the correlation between the parent and fragment ions. The fragmentation results for the model compounds and

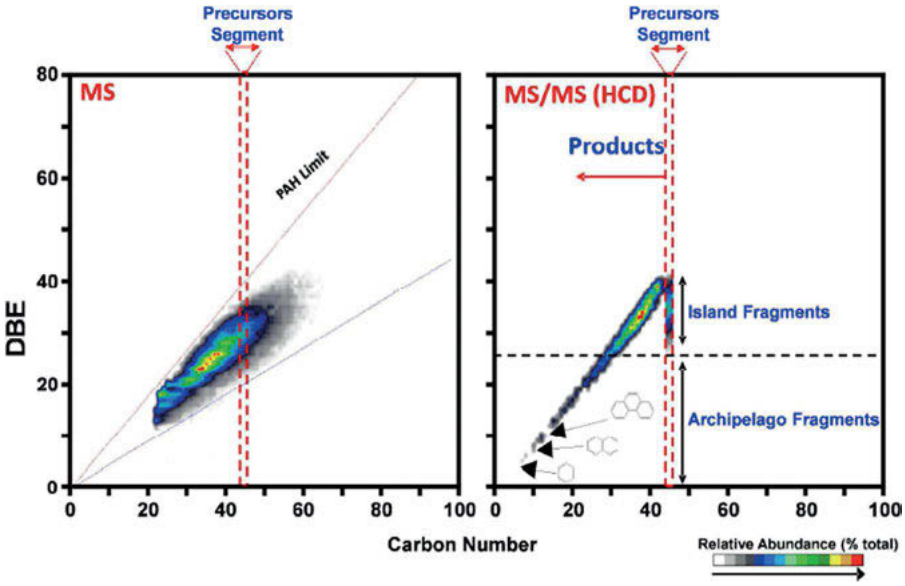

Figure 12.8: Analysis of Eagle Ford Crude Asphaltenes by (+) APPI-orbitrap MS/MS. Left: full MS; right: MS/MS (HCD) isoabundance-contour plots of DBE versus the carbon number for the hydrocarbon class of compounds with m/z in the range of 545–555 [reproduced with permission from Nyadong, L. et al. [134]. Copyright, American Chemical Society].

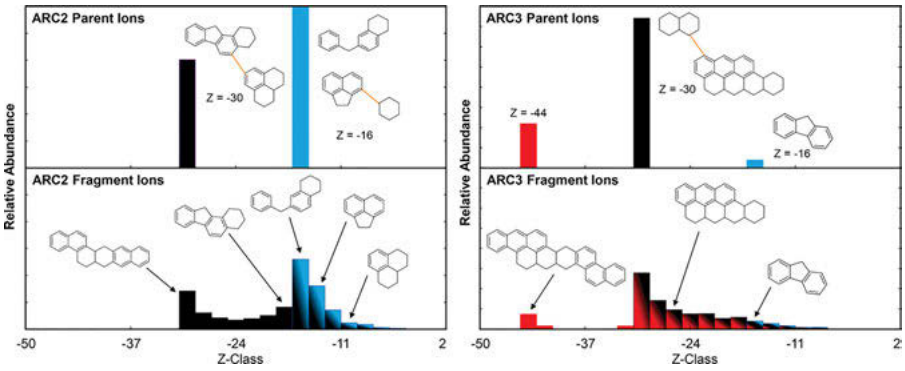

Figure 12.9: Proposed possible structures for the cores of several fragment ions in example *Z* class distributions for the ARC2 (left) and ARC3 (right) fractions, analyzed by single Dalton CID analysis coupled with APPI 15-T FTICR MS. Fragment ion *Z* classes are colored to indicate the parents that can produce those fragments. The orange lines represent some linkage (perhaps C2 + alkyl chains) that breaks on CID [reproduced with permission from Wittrig, A. M. et al. [26]. Copyright, American Chemical Society].

petroleum samples suggested the parent-ion structures of the deasphalted oil (the ARC1 – 4 + fractions) to be both single and multicored and the asphalted oil to be single cored. The molecular structures of the parent ions (Z classes) were proposed based on the assigned elemental formula by adding the fragment structures together (Figure 12.9).

12.6 IM spectrometry coupled to MS (IM-MS)

12.6.1 Principle of IM-MS operation

IM-MS is a gas-phase separation method for separating gas-phase ions according to their size and shape [135]. Due to the ineffective use of traditional on-line chromatography in separating crude oil compounds, the IM-MS separation technique is implemented for separating ions generated during the MS analysis of crude oil mixtures [111]. The IM-IS technique enables the partial separation of the isomers and access to the direct descriptor of the ion's molecular structure (CCS), whereas the ion's peak width at full width at half maximum (FWHM) and its isomeric content are correlated [136, 137].

The main stages of IM-MS analysis are given below (Figure 12.10):

a) The analyte ions having different IMs are formed in the gas phase using different ionization sources.
b) The gas-phase formed ions migrate through a carrier-buffer gas-filled drift tube or IM cell with a distance of L (cm), at a drift time of t_d, generating a voltage gradient or electric field (E, V/cm) from a constant velocity (drift velocity: v_d, cm/s) [138]. The mobility rate of the gas-phase ions (K) is determined by the mobile ions, which have different physicochemical and structural properties, and it depends on their drift velocity and drift time [139], as follows:

$$K = \frac{V_d}{E} = \frac{L}{t_d E} \tag{2.7}$$

c) Subsequently, the mass analyzer separates the ions according to their m/z ratios, and the IM-MS spectra can be obtained as a plot of the m/z versus the drift time.

As the drift time separates ions based on their average CCS and charge, large MW ions move slower than small MW ions [140]. The CCS demonstrates the ability of an ion to collide with other ions. The experimental CCS (Ω) values can be determined by measuring the arrival time distribution of ions, which is directly proportional to Ω. The following Mason–Schamp equation (eq. 12.8) can be used to deduce the experimental CCS value of the ion [141]:

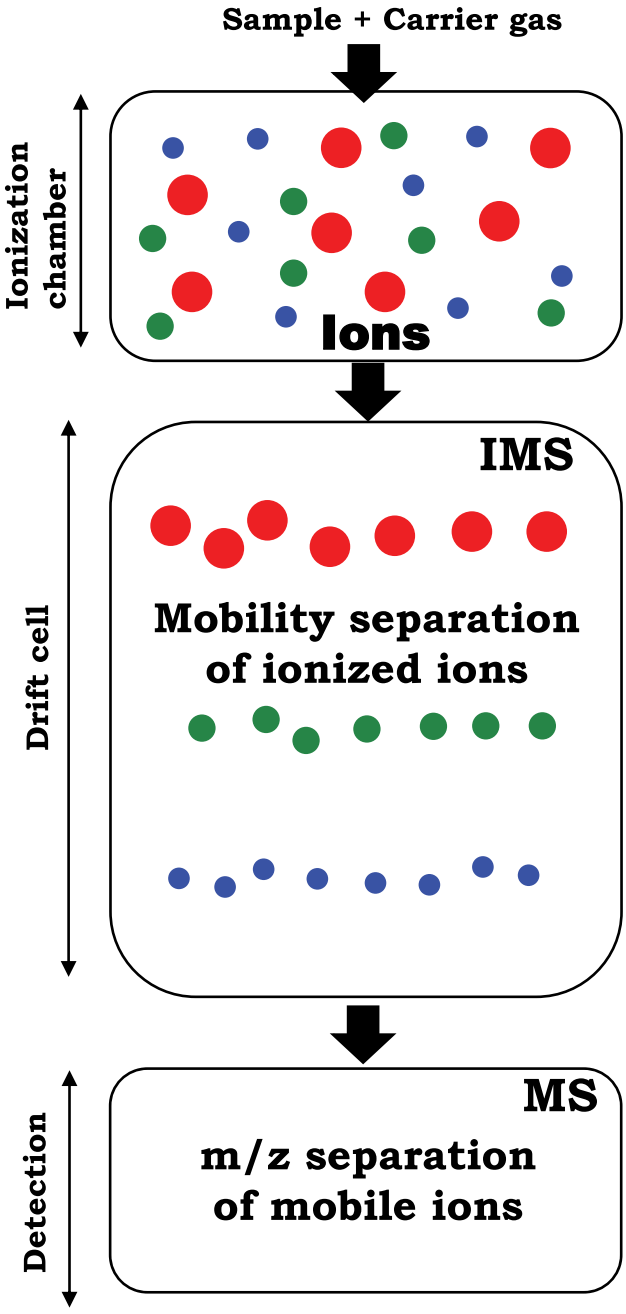

Figure 12.10: Principle of the IM-MS operation.

$$K = \left(\frac{3q}{16N}\right)\left(\frac{2\pi}{kT}\right)^{1/2}\left(\frac{m+M}{mM}\right)^{1/2}\left(\frac{1}{\Omega}\right) \tag{12.8}$$

where K is the mobility rate of ions, q is the charge of the analyte ion, N is the number buffer gas density, k is the Boltzmann's constant, T is the absolute temperature, m is the molecular mass of the buffer gas, and M is the molecular mass of the analyte ion. Equation (12.8) can be used to generate the mass-mobility plot for calibrating the CCS values [28, 142, 143] and describing the structural relationship in complex mixtures, such as crude oils [138].

12.6.2 Types of IM-MS instruments

In an IM-MS instrumentation set-up, different IM-MS cells can be coupled with different mass analyzers, e.g., TOF, quadrupole, ion trap, and FTICR mass spectrometers [135]. For petroleum study, the traditional drift time IMS (DTIMS) operated at ambient pressure has been widely used, where a low-electric field (typically 5–100 V/cm) is applied to separate ions [144]. Differential-mobility spectrometry (DMS) techniques, e.g., the high-field asymmetric-waveform ion-mobility spectrometry (FAIMS) technique, have also been widely used for the analysis of crude oil [145], naphthenic acid [146], and oil additives [147], due to their ability to achieve continual and orthogonal separation of different isomeric species under a sequence of intermediate and high-voltage electric fields [148]. The traveling wave IM cell (TWIM)-MS can also be used for petroleum analysis, where a series of voltages are pulsed in a shape of a traveling wave, called T-wave, by applying a high electric field [149]. The most recent addition to the IMS cell is trapped ion-mobility spectrometry (TIMS), developed by Bruker Daltonics, which consists of ion trap confining ions under the rf potentials [150].

The TOF mass spectrometer can be interfaced with the IMS [IM(TOF)MS] instrument, e.g., Synapt HDMS from Waters and the Agilent ion-mobility Q-TOF MS instrument. The quadrupole mass spectrometers, including triple Q, can be interfaced with ambient-pressure IMS, DMS, and aspiration-type IMS, where the separation of ions is performed within a specific mass range [135]. The ion trap mass spectrometer interfaced with IMS, i.e., DMS (ion trap) MS, can trap ions in a 3D space during their separation. The FTICR MS interfaced with IMS can separate ions under a constant magnetic field; thus, it has been widely used for crude oil analysis due to its significantly high resolving power and mass accuracy [151]. The tandem MS coupled with IMS (IM^n–MS^m)[152] quadrupole-cIM-TOF (Q-cIM-ToF) geometry [153, 154] is one of the post-IMS fragmentation (post-IM CID) MS technique for characterizing and differentiating isomeric ions and functionalities

of complex mixtures, such as crude oil, where the IMS and tandem MS/MS experiments can run in parallel.

The resolving power of IM-MS instruments should be high for crude oil analysis because of the coelution of petroleum isomers, which causes their partial separation. The resolving power of the IM-MS spectrometer can be expressed as follows [155]:

$$R \sim \left(\frac{LEQ}{T}\right)^{\frac{1}{2}}, \tag{12.9}$$

where L is the length of the IM device, E is the electric field applied during the IM separation, Q is the ion charge, and T is the temperature of the carrier-buffer gas. To increase the resolving power of the IM-MS instruments, many technological improvements have been introduced by various researchers [150, 153, 154, 156–159]. More recently, Giles et al. [154] introduced the design and performance of a TW-enabled multipass, high-resolution cyclic ion mobility separator, which was incorporated in a Q-cIM-TOF geometry. Later, Kim and coworkers [153] explored the potential of cIM-MS in petroleum analysis by coupling with MS/MS experiments.

12.6.3 IM-MS data analysis

The visualization of the 2D IM-MS spectra of the drift time versus the m/z images obtained from a petroleum sample is carried out using Kendrick [108] or van Krevelen [160] diagrams, which are also used in MS analysis. The software used for this purpose are Data Analysis (Bruker), OriginPro (OriginLab Corporation), Matplotlib (Michael Droettboom, et al., Matplotlib development team), MasterView (SCIEX), and petroOrg (Bruker). The conventional IM-MS spectra processing software include MassLynx, DriftScope, Analyst TF, HDMS Compare Build, and Software-Assisted Molecular Elucidation. The peak-fitting algorithm is occasionally used to systematically determine the IM peak width of the unresolved or partially resolved species [161, 162]. The peak deconvolution methods have been used by Kim et al. [163] and Lalli et al. [30] to investigate petroleum isomeric compounds.

The calculation of the theoretical CCS values can also help interpret the IMS data to determine the resistance to its movement in the drift cell. The CCS values can be computed by generating the candidate structures (usually PAHs), optimizing their geometries, and calculating the CCS values for the optimized structures. The general software for drawing the structures include Chem3D Ultra (CambridgeSoft Corporation), MacMolPlt (Brett Bode), VMD (University of Illinois at Urbana–Champaign), and Avogadro [164]. The CCS computation software mainly processes quantum-mechanical approaches, e.g., density functional theory and Hartree–Fock (HF) methods.

12.6.4 Application of IM-MS for the analysis of crude oil and its products

IM-MS has been indispensable for the characterization of crude oil and its products. This technique can be used to effectively resolve isomeric species of PAH and polar compounds present in petroleum to predict their molecular structures [165]. The comparison of the theoretical and experimental CCS values and preparation of theoretical trend lines play important roles in achieving more reliable structural assignments of the aromatic compounds in complex mixtures, such as crude oil [28, 31, 116, 137, 142, 163, 166–168]. Several research groups have studied the structures of gas-phase molecules using IM-MS in combination with theoretical CCS calculations [169–171]. Isomeric indicators, e.g., the FWHM and peak deconvolution, have been proposed for determining the isomeric content of complex mixtures [93, 137, 161].

12.6.4.1 Heteroatom-containing hydrocarbons

The IM-MS technique was first implemented on different types of light, medium, and heavy petroleum crude oils by Fernandez-Lima et al. [28] using (+) LDI DTIM (TOF) MS and (+) APPI FTICR MS to characterize the heteroatom-containing hydrocarbons. The heavy crude oils containing heteroatom species (N_1, S_1, O_1, NS, SO_{1-2}, and NO_{1-2}) were suggested to be non-planar based on their mass-reduced mobility (Ko) plot. Later, several research groups implemented IM-MS techniques to analyze heavy crude oils [172–174]. In these works, FAIMS linear trap Q Orbitrap MS and DTIM (dual grid gating) Orbitrap MS were used to effectively separate poorly resolved polar class compounds.

The SARA fractions were characterized by Ponthus et al. [166] and Reynolds and coworkers [145]. In the former work, the resin fraction of Nigerian crude oil was analyzed by ESI TWIMS coupled with orthogonal acceleration Q-TOF MS (oa-QToF MS) for future crude oil mapping during oil data processing. Based on the CCS results, N1 class compounds with three different DBE series obtained from Kendrick plots were correctly assigned. In the latter work, FAIMS coupled with heated ESI HR (Orbitrap) MS was applied to increase the S/N ratio of low-abundant O_2S_1 classes analyzed by HR-MS alone.

A relationship exists between the isomeric diversity and the patterns in alkylation (length, position). The PAH isomers in petroleum samples have been efficiently separated in several studies using IM-MS [30, 163, 175–177]. Hagen separated model PAH isomers using IMS [178]. The PAH compounds in petroleum samples have also been structurally identified by several research groups using IM-MS coupled with theoretical CCS calculations [163, 167, 179, 180]. The structures of PAH compounds containing short and long alkyl chains present in crude oil were subsequently studied by Kim's group [163, 168, 179] using ASAP TWIMS (TOF) MS measurements combined with

theoretical CCS approaches. First, Kim and coworkers [163] analyzed Doba crude oil to compare the experimental and theoretical CCS values, which showed low and high CCS values for the short alkyl-chain PAHs and long alkyl-chain PAHs, respectively. Based on this phenomenon, different structural assignments of a selected hydrocarbon peak were suggested (Figure 12.11). However, a large CCS deviation was observed between the experimental and theoretical values for the PAH compounds containing long alkyl chains. Considering this issue, the theoretical CCS calculating method, i.e., molecular dynamics (MD) simulation, was optimized by Kim's group [168] using various types of internal energy factors. They achieved improved accuracy in the determination of the theoretical CCS at high internal energies by considering the internal degrees of freedom of ions in the flexible long alkyl chains during CCS computation. Besides the high-level theoretical approach, i.e., MD simulation, Kim's group [179] explored the performance of a low-level classical theoretical approach, i.e., molecular mechanics; they calculated the theoretical CCS values for many aromatic compounds with both approaches to improve the IM-MS technique. Their research findings suggested that IM-MS researchers can also use the inexpensive, simple, classical theoretical approach, which was found to be as effective as the high-level theoretical methods for identifying the molecular structures of PAH compounds in petroleum. It should be noted that the low level theoretical approaches such as HF theory means approximation for the determination of the energy of a quantum many-body system in a stationary state where high level means full quantum based on ab initio method like Moller–Plesset theory and/or density functional theory [181, 182].

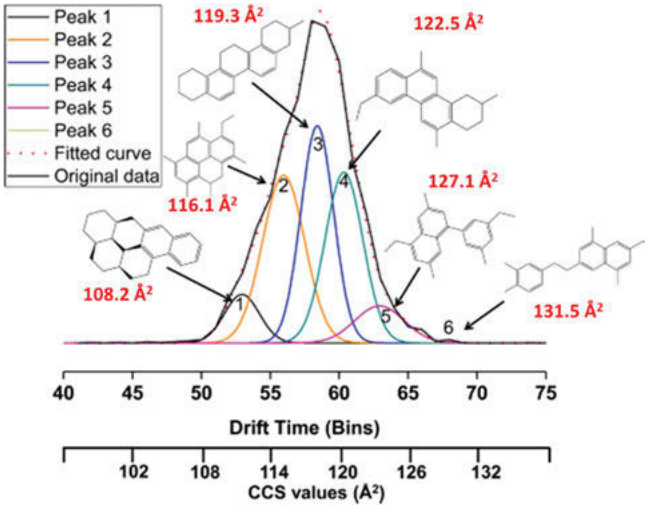

Figure 12.11: Comparison of the theoretical (red text with structures) and experimental CCS values (*x*-axis) for the six different structural assignments of a C23H26 peak observed in Doba crude oil analyzed by ASAP TWIMS TOF MS [reproduced with permission from figure 4, Ahmed, A. et al., Anal. Chem., 86, 7, 3300–3307 (2014). Copyright, American Chemical Society].

Recently, IM coupled with tandem MS methods, with multiple passes [154], was employed by Kim and coworkers [153] for the isomeric separation of HC compounds in crude oil. In their work, a multiple drift tube cycle design (IMS^n) was coupled with MS, named TW cIMS-MS/MS, to isolate the ions based on a 0.1 m/z difference. The small fragmentation pattern of the precursor ions with a high m/z value indicated their reduced aromatic structures.

The model PAH isomers containing nitrogen and oxygen were separated and identified by Laakia et al. [29], utilizing APPI-DTIMS-triple Q MS. The speciation of the refractory nitrogen compounds in crude oil collected during HDN using IM-MS techniques has been performed by several research groups [28, 93, 137, 167, 183]. Farenc et al. [167] used TWIMS TOF MS coupled with four API ionization sources (ESI, APCI, APPI, and ASAP) and theoretical CCS calculations to characterize the N_1 class compounds with alkyl groups in VGO samples. Here, the comparison between the experimental and theoretical CCS values suggests that N_1 compounds with a branched alkyl chain have lower theoretical CCS values than the experimental values and vice versa. Based on this phenomenon, the structure of the $C_{22}H_{32}N^+$ ion was suggested to be derived from highly branched compact type compounds with the three proposed isomeric molecular core structures: benzo[de]isoquinoline, tetrahydrophenanthridine, and phenylpyridine. Farenc et al. [137] further studied the structural changes of the N_1 isomers detected in VGO samples by calculating their isomeric FWHM peaks ($\Delta CCS'1/2$) using (+) ESI TWIM Q TOF MS coupled with tandem MS (CAD MS/MS). The nitrogen removal efficiency of the three different catalysts (catalyst A, C, and A + C) from VGO was examined by Parulkar et al. [183] using ESI TWIMS TOF MS. They suggested the sequential use of two catalysts (A + C) for the effective removal of N_1 species with high and low DBE values (Figure 12.12). Giusti and coworkers [93] analyzed three VGO samples before and after HDN using (+) ESI FTICR tandem MS and ESI TWIMS (TOF) MS to study the structures of N_1 isomeric compounds. The low isomeric dispersity, dealkylation during fragmentation, and unfolded conformations, i.e., long branching isomers with high CCS values, suggested that the polyaromatic quinolone-type compounds with DBE values of 7, 8, and 9 may be present in the analyzed samples.

Maître et al. [117] employed TWIMS TOF MS coupled with (–) ESI FTICR MS and tandem MS to characterize the neutral nitrogen compounds in two VGO samples (containing 10 w-ppm N) before and after HDN. The FTICR MS results showed the highest abundance of nitrogen-containing compounds at DBEs of 10 and 13, as well as the resistance of low DBE molecules to the HDN process. The tandem MS results suggested the molecular core structures of the nitrogen-containing compounds at DBEs of 10 and 13 based on dealkylation. Two descriptors, i.e., the isomeric diversity (FWHM) and the size and shape of species (tD and CCS), were used during the IMS analysis; the DBE 10 series showed a decrease in the FWHM, while the DBE 13 series showed an increase. The IMS data further revealed the resistance of the isomers with low CCS values to the HDN process.

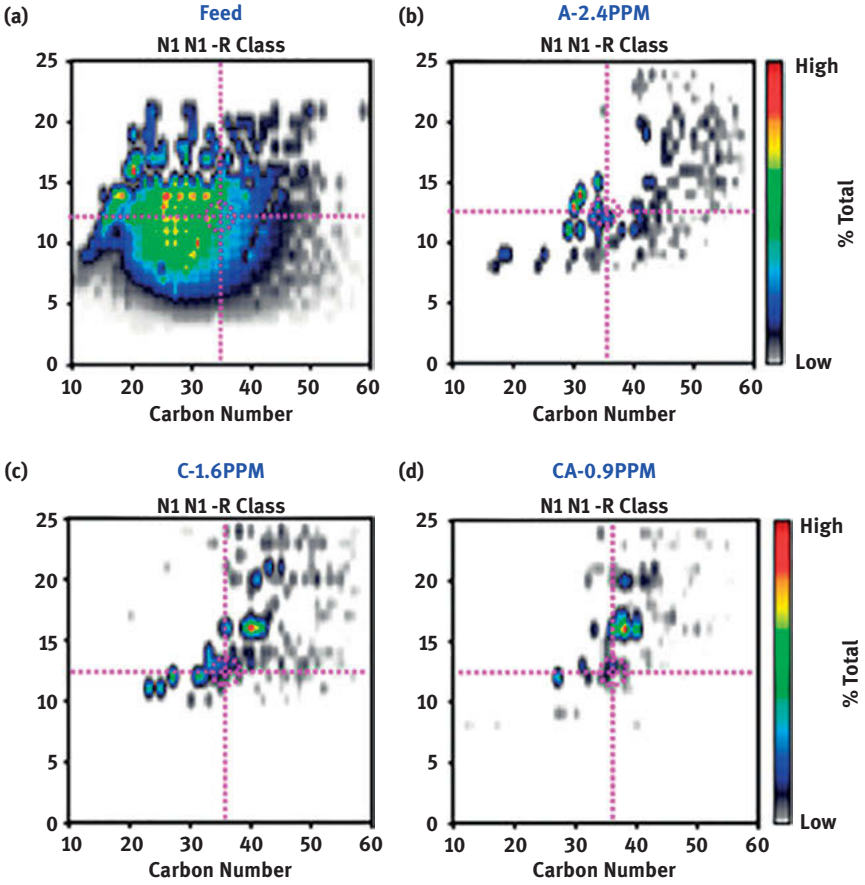

Figure 12.12: Characterization of the N1 species in the VGO sample by ESI TWIMS TOF MS: a) DBE versus the carbon number plot for the VGO (feed) with no catalyst; b) DBE versus the carbon number plot for the VGO treated with catalyst A ($N = 2.4$ ppm); c) DBE versus the carbon number plot for the VGO treated with C ($N = 1.6$ ppm), and d) DBE versus the carbon number plot for the VGO treated with layered bed CA ($N = 0.9$ ppm) [reproduced with permission from figures 3 and 4, Parulkar, A., et al. [183]. Copyright, American Chemical Society].

The IM-MS techniques can also be used for the isomeric separation of the polar oxygen-containing compounds, e.g., NAs, present in acidic crude oil [30, 138, 146, 184]. The standard NAs were analyzed by Fasciotti et al. [138] to find a correlation between their structures and drift time using ESI TWIMS (oa-QTOF) MS, with CO_2 as the drift gas. The results of their IM-MS experiments showed a linear CCS increase for the unsaturated NA and a decrease for the cyclic and aromatic NAs. The three NA fractions separated from the Athabasca bitumen sample by solid-phase extraction (SPE) and their isomeric homologous structures were investigated by Rodgers and coworkers [30] using (–) ESI TWIMS (TOF) MS and FTICR MS. The IM-MS results of the

samples showed that the two isomeric ions of abundant O_2 class compounds with DBE 5 were separated at two different drift times, while the IM-MS results of two standard model compounds confirmed the steranoic acid-type structures of the analyzed NAs (Figure 12.13). The oil sand process-affected water (OSPW) extracts containing the NA fraction components were analyzed by IM-MS to identify their isobars and isomers. Gabryelski et al. [146] used ESI FAIMS (TOF) MS coupled with tandem MS to separate and identify isobaric NA ions from oil sand extracts from the Athabasca tar sand region at different compensation voltages. The isomer distributions of the NA samples were found within only 3 min, during the FAIMS analysis, while the identical NA dissociated ions produced during the tandem MS suggested the NAs to be hydroxycarboxylic acids. Later, Noestheden et al. [184] separated and identified the isomeric NA

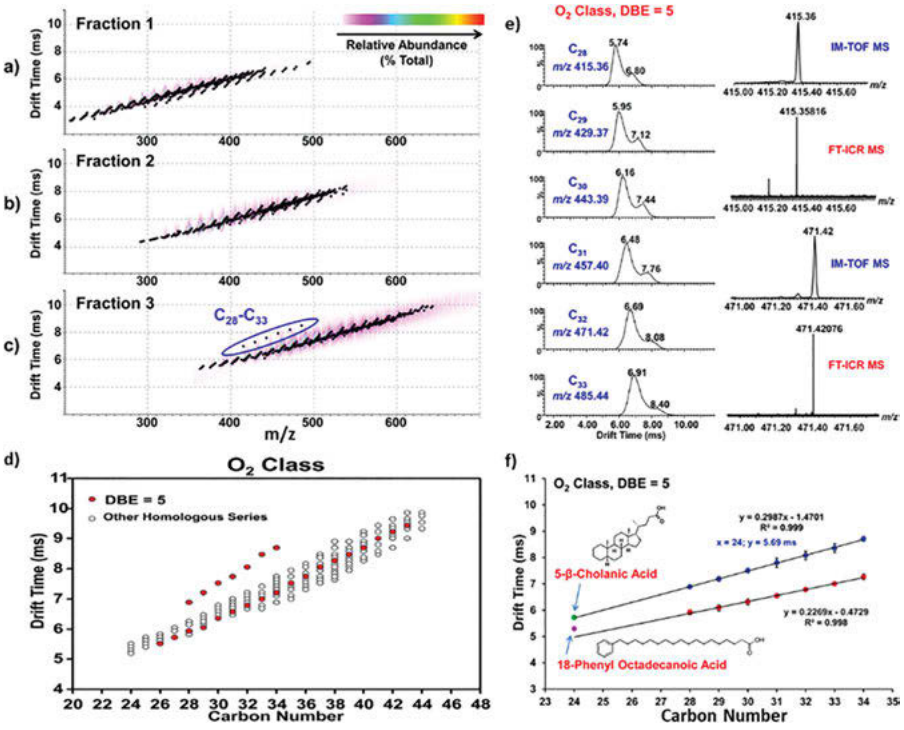

Figure 12.13: Characterization of two isomeric ions obtained from the NA fractions of Athabasca bitumen acids analyzed by (–) ESI IM-TOF MS, followed by SPE (modified aminopropyl silica): (a) IM-MS spectra of three NA fractions; (d) drift time versus carbon number plot for the O_2 species from NA fraction 3; (e) expanded mobiligrams for the selected O_2 peaks with DBE = 5 (C28–C33) (left) and expanded IMMS and FT-ICR mass spectra of the selected nominal *m/z* 415 and 471 (right); (f) extrapolation curve in the drift time versus the carbon number plot for the selected NA series (O2 with DBE = 5) and two standard compounds (both C24) [reproduced with permission from figures 2, 3, 4, 5, Lalli, P. M. et al. [30]. Copyright, American Chemical Society].

ions and their dimers from OSPW extracts in less than 2 min using ESI DMS coupled with hybrid quadrupole linear ion trap (QqLIT) MS or DMS (QTOF) MS.

The sulfur-containing compounds contained in crude oil and its products have recently been studied by IM-MS techniques [32, 167, 173, 175]. Kim and coworkers [142] first utilized the slope of the m/z-mobility plot to elucidate the molecular structures of the sulfur-containing compounds in crude oil, analyzed by ASAP TWIMS TOF MS. The CCS results showed a linear–continual increase for the nonaromatic structures differing in the number of alkyl units and a discontinuous increase for the aromatic structures differing in the number of H atoms. The removal efficiency of the sulfur-containing compounds from crude oil during HDS has been investigated by several research groups using IM-MS techniques [167, 175]. To evaluate the performance of the HDS method for removing sulfur species, Giusti and coworkers [175] first separated and identified two ion series of PASH compounds detected in unprocessed and processed diesel fuel, analyzed using ASAP TWIM QTOF MS coupled with tandem MS (Figure 12.14). The performance of the HDS method for removing thiophenic S_1 species, e.g., alkyl-benzothiophenes, alkyl-dibenzothiophenes, and alkyl-benzonaphthothiophene, from VGO samples was evaluated by Farenc et al. [167] using ESI/ASAP/APCI/APPI TWIM Q TOF MS.

The separation and identification of isomeric hydrocarbons of $C_{22}H_{30}$ (DBE 8) and $C_{21}H_{24}$ (DBE 10), and isomeric sulfur-containing compounds of $C_{21}H_{26}S$ (DBE 9) and $C_{21}H_{20}S$ (DBE 12), in heavy North American crude oil was studied by Vetere et al. [173] using online FAIMS (TOF) MS combined with two PI sources: APPI (1-photon VUV ionization) and APLI (2-photon ionization using laser radiation), at different compensation voltages. Most recently, Maleki et al. [32] applied ESI DTIMS (linear ion trap Q) MS combined with silver ionization, tandem MS CAD methods, and molecular cross-section to characterize Saudi crude oil samples containing sulfur-containing compounds. The S_1, S_2, and S_3 classes with elongated and compact structures at low and high m/z values, respectively, were distinguished from the IM-MS results, based on their most abundant CID peaks and theoretical CCS values (Figure 12.15).

12.6.4.2 Asphaltene structures

The asphaltene structures of crude oil can also be evaluated by IM-MS techniques [185–187]. Russell and collaborators [185] investigated the molecular structures of asphaltenes and deasphalted oils using LDI DTIMS TOF MS and molecular modeling computations, along with model polymeric systems, such as polywax 650, polystyrene 1400, and fullerene. The results of the IMMS experiment and theoretical calculations suggested that the structures of asphaltenes are more condensed with single aromatic rings, either fused or linked to multiple alkyl or heteroatom substituents, due to their high CCS values and high aggregation at high m/z values. However, it is still debatable whether fullerenes are natural constituents of asphaltenes or a laser

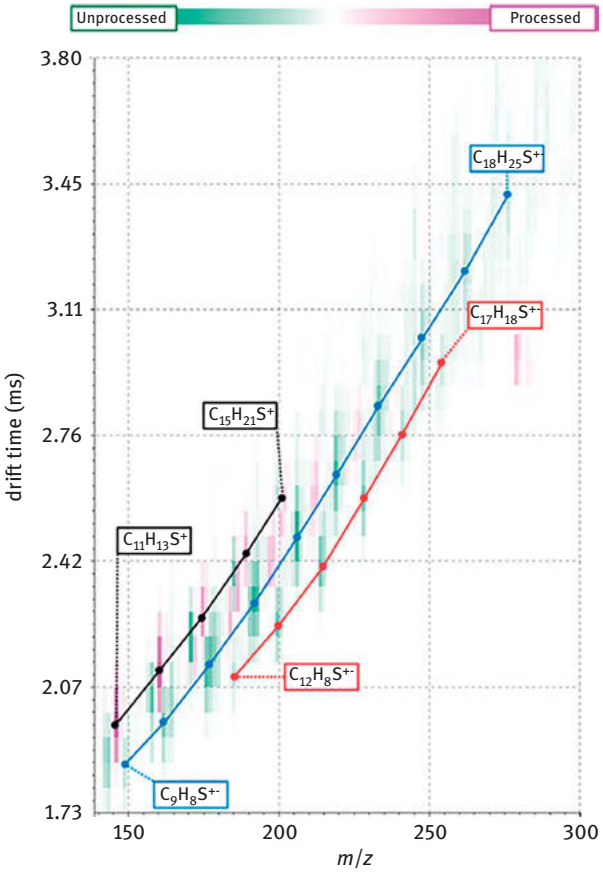

Figure 12.14: Comparative m/z – drift time plot showing the performance of ASAP TWIM Q TOF MS in separating and identifying two ion series of sulfur species: alkyl-benzothiophene (alkyl-BT) and alkyl-dibenzothiophene (alkyl-DBT), in the unprocessed and processed diesel fuels, respectively. The pink and green areas indicate the ions of high intensity in the processed and unprocessed diesel fuels, respectively, while the white area indicates no significant difference between them [reproduced with permission from figure 4, Maire, F. et al. [175]. Copyright, American Chemical Society].

artifact formed during LDI MS analysis of asphaltenes. Santos et al. reviewed the presence of fullerenes in carbonaceous materials and their artifacts formation as laser during LDI MS [188]. Koolen et al. [186] effectively identified the fullerenes in asphaltene samples using LDI TWIM (Q-TOF) MS combined with theoretical CCS calculations. Here, the similarity between the experimental CCS of a selected fullerene peak for the asphaltene sample and the theoretical CCS value of a standard C_{60} fullerene was observed. The IM-MS results confirmed the elution of the sample and standard fullerene at different drift times. Later, Koolen et al. [187] determined the

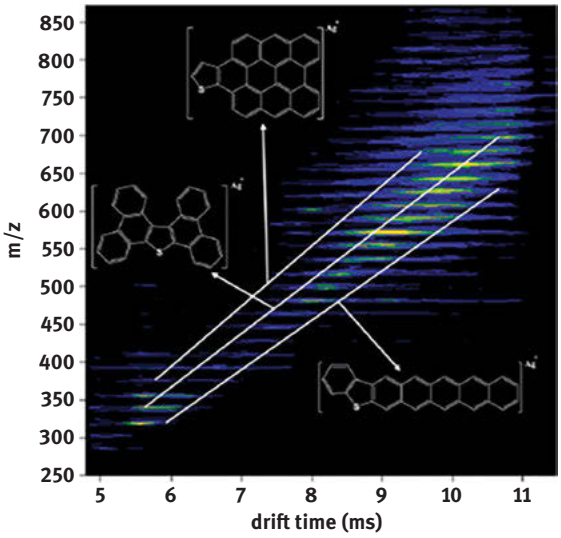

Figure 12.15: Application of ESI DTIMS (linear ion trap Q) MS coupled with silver-ionization for the analysis of sulfur-containing compounds in a Saudi crude oil sample [reproduced with permission from figure 2, Maleki, H. et al. [32]. Copyright, American Chemical Society].

structures of asphaltenes obtained from heavy and light Brazilian oils using a combination of LDI TWIM MS, theoretical calculations, UHRTOF MS, and pyrolysis GC coupled with HR-MS (Py-GC-HR-MS). Based on their preliminary experimental and theoretical CCS comparison, it was assumed that island-type condensed structures, i.e., alkylated coronene-like structures, are present in the sample.

12.6.4.3 Additives and contaminants in crude oil

The additives and contaminants in crude oil can also be analyzed by IM-MS techniques [116, 147, 149, 189–191]. The separation and identification of polar heteroatom compounds, e.g., N_1O_1, O_2, and N_1, in the additives of petrofuels with different polarities were first performed by Fasciotti et al. [149] using ESI TWIM (hybrid Q-TOF) MS with CO_2 as the drift gas and ESI FTICR MS. The unresolved polar N_1, N_1O_1, N_1S_1, and O_2 classes of crude oil contaminants and petrofuels (e.g., gasoline) by HR-MS were effectively separated and identified by Eberlin and coworkers [149, 190] using Agilent ESI IM (hexapole Q-TOF)) MS. The rapid analysis of the additives in lubricants was performed by Barrere et al. [189] using IM-MS. Da Costa et al. [147, 191] applied FAIMS MS using two different ionization sources: ESI and DESI, to investigate the corrosion inhibitors in crude oil at low concentrations. The separation and identification of multiple functional isomers of the O_3S_1 species present in petroleum

emulsion interfacial materials isolated from Athabasca bitumen were performed by Rodgers and coworkers [116] using ESI TWIMS (TOF) MS coupled with subsequent post-IM CID. The IM-MS results showed that the isomers of the O_3S_1 species (DBE 4) were synthetic surfactants (alkylbenzenesulfonates) and naturally occurring NAs. The CID spectra confirmed the identification by exhibiting the formation of the $SO_3^{\bullet-}$ ion and neutral losses, such as CO_2, H_2O, $CO_2 + H_2O$, and the alkyl chain, during fragmentation.

12.6.4.4 WAF of crude oil

The photoirradiated WAF of crude oil was studied by Fernandez-Lima and coworkers [192, 193] using APLI TIMS (FT-ICR) MS. The preparation protocol of the photoirradiated WAFs developed in their first work was applied to investigate the photo-oxidized products of the PAHs in an isomeric complex WAF under sunlight exposure. The IM-MS results revealed the abundant transformation products of the oil components to be O_4–O_5 class compounds with DBE values greater than 9.

12.7 Hydrogen/deuterium exchange coupled to MS (HDX MS)

12.7.1 Principle of HDX MS

HDX is a low-energy chemical exchange reaction, through which an isotopic deuterium atom is inserted in specific places of a compound exposed to deuterated reagents; the deuterium atom replaces the unstable hydrogen atom without causing any transformation of the compound [194]. Generally, not all the hydrogen atoms of a molecule can participate in this exchange reaction. The hydrogen atoms bonded to atoms with lone pairs, such as halogens, oxygen, nitrogen, and sulfur, called "exchangeable," "active," or "labile" hydrogens, are the most acidic hydrogen atoms in an organic molecule; these hydrogens constitute the targets of the deuterium atom during the HDX reaction. The other hydrogen atoms bonded to atoms without lone pairs (e.g., carbon), called non-labile protons, are stable and, thus, have less tendency to participate in the HDX reaction. Non-labile hydrogen atoms, such as the hydrogens in an aromatic ring, can also participate in this exchange under specific experimental conditions, such as at elevated temperatures and pressures and strong acid or base addition [22, 23, 195–199].

In an HDX experiment, the analyte solution is simply mixed with deuterated reagents, such as D_2O, resulting in the instant exchange of the labile hydrogens atoms from the functional groups of the analyte molecule. After the replacement of

the hydrogen atoms (1.007825 Da) by deuterium atoms (2.014102 Da) via the HDX reaction, the deuterium's heavier mass containing a neutron is incorporated into the molecule. Consequently, the resulting mass of the exchanged product increases by exactly 1.006277 Da. HDX is a low-energy chemical exchange reaction that occurs between hydrogen and deuterium when a compound is exposed to deuterated reagents, which enables the evaluation of the intrinsic structure of the ions.

One of the main techniques used for monitoring the mass accurately during the HDX reaction is HR-MS [200]. Many important chemical and structural properties, such as the type and number of active hydrogens in an unknown molecule, isomeric compounds in the molecule, structural features, and thermochemical properties of the molecule, can be extracted using the HDX HR-MS system. If the D-solvent is used in the HDX MS system, not only is the target compound ionized by the mass spectrometer, but also the hydrogen atoms on the target compound are replaced by the deuterium atoms of the D-solvent as well.

During HDX MS analysis using D-solvent as the deuterium reagent, two types of reactions mainly occur: the ionization of analyte and the exchange of labile hydrogen atoms on the analyte with deuterium. Consequently, different ions, such as radical ions, HDX radical ions, and HDX plus deuterium ions, may be observed in a single HDX HR mass spectrum with the following notations [21, 201]:

$$M^{+\cdot};\ (M+H)^{+};\ d_0MD^{+};\ d_n(M^{+\cdot},\ MD^{+}) \tag{12.10}$$

$$M^{-\cdot};\ (M-H)^{-};\ d_n(M-H)^{-} \tag{12.11}$$

where n indicates the number of deuterium atoms incorporated in the ion ($n = 0$, 1, 2, 3, etc.); D indicates the additional deuterium atom attached during ionization. The product ions produced during the positive (+)-mode MS analysis are $M^{+\cdot}$ (molecular ion), $(M + H)^{+}$ (protonated ion), d_0MD^{+} (deuterated ion), $d_nM^{+\cdot}$ (exchanged radical-ion), and d_nMD^{+} (exchanged ion with an additional deuterium atom). The product ions produced during the negative (–)-mode MS analysis are $M^{-\cdot}$ (molecular ion), $(M - H)^{-}$ (deprotonated ion), and $d_n(M - H)^{-}$ (the replacement of n hydrogen atoms by n deuterium atoms after deprotonation).

12.7.2 Mass analyzers used for HDX studies

The mass analyzers usually separate the exchanged ions according to their m/z ratios in space or time after the completion of the exchange reaction. The most common mass analyzers used for HDX studies are trap instruments, such as quadrupole ion trap (QIT) [202] and FTICR mass spectrometers [203], because of their ion-trapping capacity for variable periods during collision between the ions of interest and gaseous deuterium reagents.Quadrupole mass spectrometers, e.g., Orbitrap, usually capture and confine the ions of interest in their collision region by applying

electric fields. Many isomeric aromatic compounds have been studied using QIT instruments [204]. The FTICR MS usually traps the ions of interest in its ICR cell by applying a magnetic field [8]. Increasing the magnetic field strength of the instrument can increase the confinement period of the ion in the ICR cell. It is widely accepted that the FTICR MS instrument has the highest mass resolution among all the mass analyzers; thus, it can be employed to perform simultaneous isolation and high-field HDX of ions without the overlapping of the exchanged ions.

12.7.3 Classification of HDX MS methods

HDX can be accomplished via three methods during MS analysis: in solution, under vacuum, and in-source. In solution HDX occurs when the solution-phase exchange is achieved in the analyte solution mixed with deuterium reagents and MS is used subsequently for the exact mass measurement of the exchanged products. One of the limitations of this HDX method is the reversed replacement of deuterium by hydrogen in the analyte solution due to its dependence on the pH and temperature. The application of solution-phase HDX MS has been reported for several biological complex mixtures, such as proteins and peptides [205, 206]. HDX under vacuum occurs when the gas-phase H/D exchange is performed using collisions with a deuterated reagent gas in the mass analyzer (usually trap instruments) operated under reduced pressure [207, 208]. This was the traditional HDX MS method used for CI MS and CI coupled to GC techniques [209]. The common deuterium reagent gases used in the vacuum HDX MS method are D_2O, ND_3, CD_4, and CH_3OD [210]. The most recent HDX MS method is in-source HDX, where the gas-phase exchange can be achieved using a deuterated solvent or the vapor of a deuterated solvent generated in the ionization source operated at atmospheric pressure (Figure 12.16) [198, 211–213]. The in-source HDX became popular in modern MS society after the introduction of API sources, such as ESI, APCI, and APPI, into the MS interface. Notably, ESI is generally used to ionize polar compounds, while APCI and APPI are used to study a wide range of non-polar compounds. Several experimental designs, such as ESI–APCI dual-spray source with D_2O [211] and MS interface with curtain ND_3 gas in the capillary-skimmer region [214], which are capable of generating saturated deuterated gas in the ionization source, have been proposed. In the ESI source HDX MS, the HDX reactions are better performed inside the desolvating capillary or in the vacuum capillary-skimmer region by the generation of deuterated vapor from the evaporation of a droplet of the D_2O molecule [197, 198, 215].

In the APCI and APPI source HDX, the deuterated reagent is usually premixed with the analyte solution before the experiment [201] or the vapor of the deuterated reagent is continuously generated into the ionization source [216]. In the continuous APPI source HDX MS, a capillary line is inserted into the ionization source used for feeding D_2O continuously to achieve spontaneous HDX reactions. In the case

where the solubility of the analytes is a matter of concern for complex mixtures, such as crude oil, the continuous APPI source HDX MS is preferable. To achieve a high ionization efficiency during the HDX MS experiment, a co-solvent and dopant should be used along with the deuterated reagent in-APCI-HDX and APPI HDX, respectively. The type and amount of cosolvent and dopant used are usually optimized to achieve the best sensitivity during the HDX experiments [21, 201, 213]. As it is well known that different ionization sources have different ionization efficiencies and selectivities for different molecular structures, the use of diverse API sources during the HDX MS experiment is crucial for ionizing the analytes of interest.

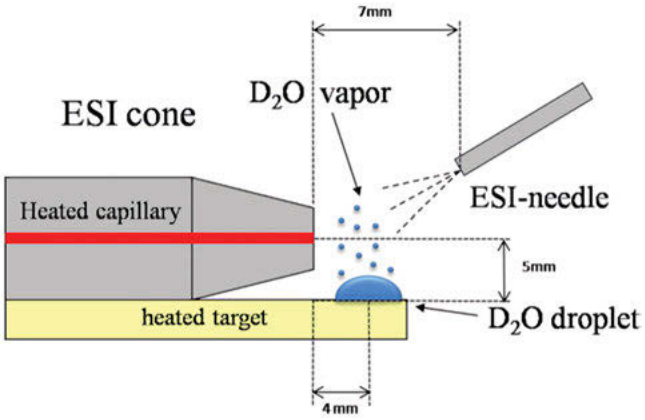

Figure 12.16: Modified ESI source design for the HDX experiments [reproduced with permission from figure 1, Kostyukevich, Y. et al., Anal. Chem., Energy Fuels, 85, 22, 11,007–11,013 (2013). Copyright, American Chemical Society].

12.7.4 HDX MS data analysis for petroleum

Since the HDX MS spectrum can reflect a mixture of ions for a given oil sample containing thousands of peaks, this spectrum is considered to be more complex than the original mass spectrum. To visualize the HDX MS spectra, Kendrick mass, Kendrick mass defect, and DBE are usually employed. The DBE can be calculated according to eq. (12.12) for $C_cH_hD_dN_nO_o$ [20]:

$$\mathrm{DBE} = \mathrm{C} - \frac{h+d}{2} + \frac{n}{2} + 1 \tag{12.12}$$

where c is the number of carbon atoms, h is the number of hydrogen atoms, d is the number of deuterium incorporated into the molecule, and n is the number of nitrogen atoms.

For the general analysis of the HDX MS spectra, the plot of the Kendrick mass defect versus the Kendrick mass can be used to introduce a weighted Kendrik mass defect histogram. Recently, a series of specialized software named "STORM-HDX," written in the C programming language, was developed by Lee et al. [217] for processing complex HDX MS data. "STORM-HDX" denotes the Software Tool used for the interpretation of ORganic Mixtures' spectra–HDX. The application of STORM-HDX software to process the HDX MS data for crude oil samples has been reported by several researchers [20, 21, 213]. The HDX depth can be calculated using the following equation [197]:

$$P = \frac{1\sum_{i=0}^{N} ih_i}{N\sum_{i=0}^{N} h_i} \tag{12.13}$$

where N is the total number of exchangeable hydrogens, and h_i is the intensity of the i_{th} HDX peak (i indicates the number of exchanged hydrogens).

12.7.5 Application of HDX MS to complex mixtures

The isotopic exchange approach, i.e., HDX, is a selective chemical reaction, which is considered a popular analytical tool for identifying the intrinsic chemical structures, properties, composition, conformational dynamics, and chemical/biochemical reaction pathways of individual compounds and molecules in complex natural mixtures [194]. In 1933, Lewis [218] first invented the isotopic exchange reaction. Later, several researchers implemented this technique coupled with NMR to investigate the structures of nitrogen-containing compounds, which had different numbers of labile hydrogens [219–221]. Before 1990, HDX coupled with NMR spectroscopy was employed for the analysis of complex biological systems, such as protein-folding structures. Another method of performing HDX for protein analysis is MS, which gained popularity in the 2000s due to its high sensitivity, ability to analyze very low sample concentrations (~0.1 μM), high MW limit (>25 kDa), and rapid data interpretation. Since the 2000s, the application of HDX coupled with HR-MS has widely been employed for protein analysis to calculate the number of surface labile hydrogen atoms [222–224]. GC was also used to perform HDX reactions on a column. In this case, neutral and basic carbowax are pretreated with D_2O before the HDX analysis [209]. CI MS coupled with HDX was first explored by Hunt et al. in the early 1970s [225]. Here, the number of active hydrogens bonded to heteroatoms in various model compounds, such as alcohols, phenols, carboxylic acids, amines, amides, and mercaptans, is determined accurately. In the 1980s, Hunt and Sethi discovered that the hydrogens attached to aromatic rings, carbons adjacent to aromatic rings, and carbons α to carbonyl groups are most likely to be replaced by deuterium [226]. The recent addition of API sources, such as ESI, APCI, and APPI, to the HR-MS techniques

contributed significantly to their development for the structural analysis of compounds. Consequently, the coupling of API sources, such as ESI [211, 227–229], APCI [211], APPI [21], and MALDI [230], with HDX occurring in solution or in the gas phase has widely expanded their application from individual compounds to complex mixtures, such as proteins, peptides, metabolites, antibiotics, and crude oil.

Recently, GC–ESI MS [231]; SFC MS [232]; tandem MS techniques [233], such as CID, ECD, and ETD; and IM-MS [234] have also been combined with HDX for structural studies. For crude oil studies, various HDX approaches have been implemented to differentiate between pyridinic and pyrrolic structures, alcohols and carboxylic acids, and thiols and thiophenes, as well as to identify the degree of substitution of the aromatic core [194, 235, 236]. Most importantly, considering the extensive applications of HR-MS in analyzing crude oil structures [160, 237–240], the combination of HR-MS with HDX has become a potential analytical technique in recent years for predicting the structure of the individual molecules contained in crude oil simultaneously [194].

12.7.5.1 In-ESI source HDX MS for crude oil

12.7.5.1.1 Nitrogen-containing species

ESI has long been extensively used to ionize polar nitrogen compounds in petroleum by several research groups [12, 43, 241, 242]. The direct HDX (+) ESI HR-MS analysis of petroleum nitrogen-containing compound hydroconversion has recently been reported by Zhang et al. [243], who systematically identified nitrogen-containing compounds with different functional groups (pyridine, aliphatic amine, aniline) in petroleum samples (coker gas oil (CGO) hydrotreated product, heavy petroleum (VRI), heavy petroleum (VRII)) before and after hydrotreatment using HDX coupled with (+) ESI 9.4 T FT-ICR MS. The developed HDX method was optimized using Orbitrap Fusion MS for model nitrogen-containing compounds. The HDX MS spectra of the model compounds showed that the HDX efficiency was significantly enhanced by the addition of deuterated water (D_2O) as the deuterating reagent and formic acid (DCOOD) as the promoter. The HDX FTICR MS spectra of the CGO hydrotreated product revealed the presence of pyridines, cyclic amines, and primary amines, due to the dominance of N_1D_1, N_1D_2, and N_1D_3 peaks, respectively. The HDX FTICR MS results of VRI and VRII and their hydrotreated products confirmed the presence of pyridines in the VRI feedstock and cyclic amines (DBE ≤ 4) and aliphatic amines or anilines (DBE > 4) in their hydrotreated products.

Kostyukevich et al. [197] detected pyridinyl or quinolone fragments of crude oil using (+) ESI HDX MS and ether and ester structural fragments with only 1 acidic proton using (–) ESI HDX MS (Figure 12.17).

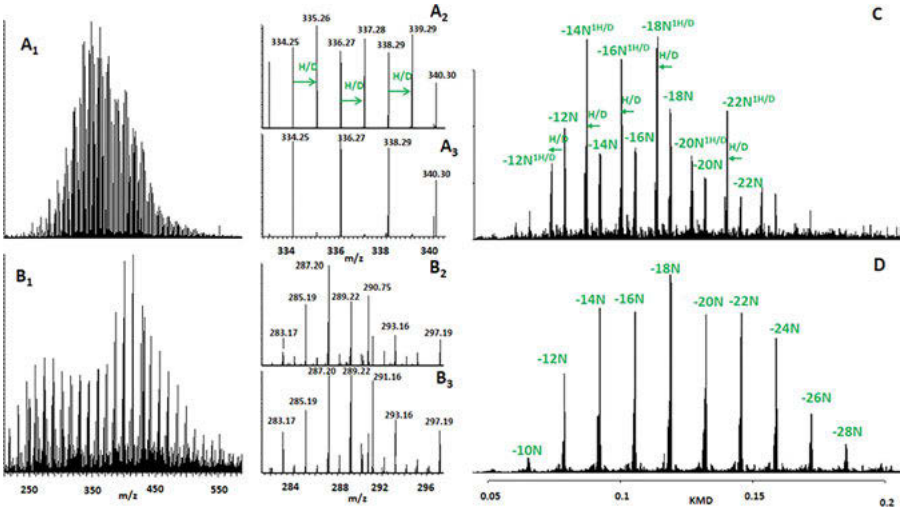

Figure 12.17: The in-ESI source HDX of the crude oil. A1: wide range spectrum of (+) ESI MS, A2: narrow range of the (+) ESI HDX conditions, A3: narrow range of (+) ESI MS. B1: wide range spectrum of (–) ESI MS, B2: narrow range of the (–) ESI HDX conditions, B3: narrow range of (–) ESI MS. C: weighted Kendrick mass defect histogram under the HDX conditions for (+) ESI MS. D: weighted Kendrick mass defect histogram for (+) ESI MS [reproduced with permission from figure 1, Kostyukevich, Y. et al., Anal. Chem., Energy Fuels, 85, 22, 11,007–11,013 (2013). Copyright, American Chemical Society].

12.7.5.1.2 Oxygen-containing species

As ESI MS is suitable for the analysis of polar compounds, the implementation of in-ESI source HDX MS has recently been reported for the structural elucidation of oxygen-containing compounds in crude oil and its products [22, 197].

Kostyukevich et al. [22] investigated and estimated the biodegradation of bitumen present in the Taman peninsula, an ancient (V B.C.) Greek amphora, using in-ESI source HDX FTICR MS. The HDX MS results showed that the number of labile hydrogens in the biodegraded bitumen was higher than that in the nondegraded oil; this is because the oxidation of bitumen was initiated in amphora 2500 years ago.

Recently, it has been reported that superheated water can dissolve even nonpolar compounds, enabling them to participate in the HDX reaction [244, 245]. Nikolaev and coworkers [246] developed a simple (+) and (–) ESI HDX coupled with FTICR MS method for crude oil analysis, where a light Siberian crude oil sample was sealed with D_2O (exchange reagent) in an autoclave and incubated at high temperatures and pressures ($T > 300$ °C, $P > 30$ MPa). The (+) ESI HDX MS results for both the condensed and relatively saturated compounds showed up to 9 HDXs for the low DBE values (DBE < 6) and 4 or at least 3 HDXs for the high DBE values (DBE > 10). The (–) ESI HDX MS results for the acidic compounds revealed the possible occurrence of HDX in α-CH_n

protons and that the low HDX efficiency observed was due to the high pK_a of the CH_2 substituent (Figure 12.18).

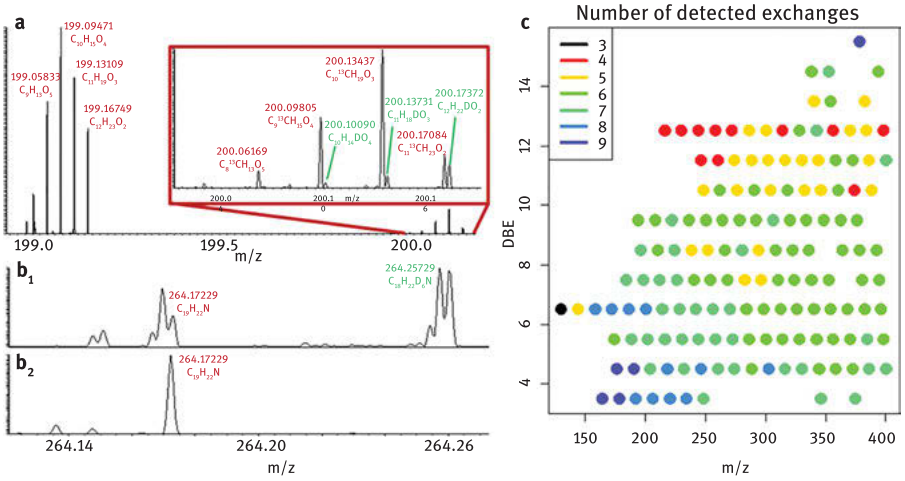

Figure 12.18: ESI HDX FTICR MS method for crude oil analysis using only water as the exchange agent. (a) Weak HDX in (–) ESI MS; (b1) appearance of new peaks in (+) ESI MS; (b2) original oil in (+) ESI MS; (c) double-bond equivalents (DBE) versus *m/z* ratio, where the number of HDX detected is represented by colors [reproduced with permission from figure 1, Kostyukevich, Y. et al., Anal. Bioanal. Chem. 411, 3331–3339 (2019). Copyright, Springer-Verlag GmbH Germany].

12.7.5.1.3 Sulfur-containing species

To specify the sulfur-containing species in crude oil, Wang et al. [247] implemented the deuterium-labeling technique using ESI MS. Here, deuterated alkylating reagents, such as iodomethane-d3 (CD_3I) and iodoethane-d5 (C_2D_5I), were added to the crude oil solution to selectively tag sulfur species by the formation of a coordination complex.

12.7.5.2 In-APCI HDX MS for crude oil

12.7.5.2.1 Nitrogen-containing species

APCI and APPI became as effective as ESI for HDX because of their ability to ionize a wide range of non-polar compounds. Previously, the amino groups in pharmaceuticals [211], as well as monosaccharides [248], were studied by APCI HDX MS to identify their conventional "exchangeable" protons. The HDX of aromatic hydrogen atoms was observed in the substituted nitrogen compounds, e.g., indoles, using APCI HDX MS techniques [249]. The feasibility study of using APCI HDX coupled with 15-T FTICR MS for the investigation of nitrogen-containing compounds in shale oil resins was accomplished by Kim and coworkers [213]. In their work, the mass spectrum of 20 test

compounds showed the replacement of their active hydrogen atoms by deuterium in the APCI source while revealing the exact masses of their corresponding HDX ions. A mixture of dichloromethane and deuteromethanol was used as the solvent to achieve the best HDX sensitivity. The HDX MS spectra of the resin fraction revealed pyridine-type structures lacking the ability to undergo HDX (Figure 12.19).

12.7.5.2.2 Oxygen-containing species

In 2016, both positive and negative modes in-APCI source HDX coupled with quadrupole Orbitrap MS was implemented to investigate 38 model oxygen-containing compounds for HDX [201]. The results of the (+) and (–) APCI HDX MS analyses demonstrated the effectiveness of the method for all types of model oxygen compounds, except PAH compounds bonded to oxygen atoms (oxygen heterocycles) (Table 12.1). The compounds that do not have exchangeable hydrogen atoms are aldehydes, esters, ketones, and oxygen heterocycles. Some of the test compounds showed HDX of non-labile hydrogen atoms, analyzed by both (+) and (–) APCI HDX methods, due to their high energized ionization achieved by applying corona currents [249]. Depending on the HDX pattern, this method can differentiate only alcohols from aldehydes, ketones, and esters. However, this method was unable to differentiate aldehydes, ketones, esters, and oxygen heterocycles.

12.7.5.2.3 Sulfur-containing species

Although the conventional CI HDX MS has been applied for the analysis of model sulfur-containing compounds, e.g., mercaptans [250], there is still no report on the application of APCI HDX MS for characterizing sulfur-containing compounds in crude oil mixtures.

12.7.5.3 In-APPI HDX-MS for crude oil

12.7.5.3.1 Nitrogen-containing species

Similar to the in-APCI source HDX MS method, the in-APPI source HDX MS is effective for the unambiguous determination of the active hydrogen atoms that can be replaced by deuterium atoms to distinguish between isomers containing primary, secondary, and tertiary amines, as well as pyridine and pyrrole functional groups [212]. Kim and coworkers [212] first differentiated the nitrogen isomers of amines using (+) APPI HDX coupled with LCQ Fleet ion trap MS in 2013. Their work suggested that the nitrogen-containing compounds in crude oil can be studied at the molecular level based on the HDX ions produced, which are related to their functional group distributions. Immediately after the analysis of the model nitrogen compounds, Kim and coworkers [20] applied the experimental approach of (+) APPI HDX coupled with 15-T FTICR MS at two different flow rates (250 and 2,000 μL/h) to the resin fractions of Qinhuangdao (QHD)

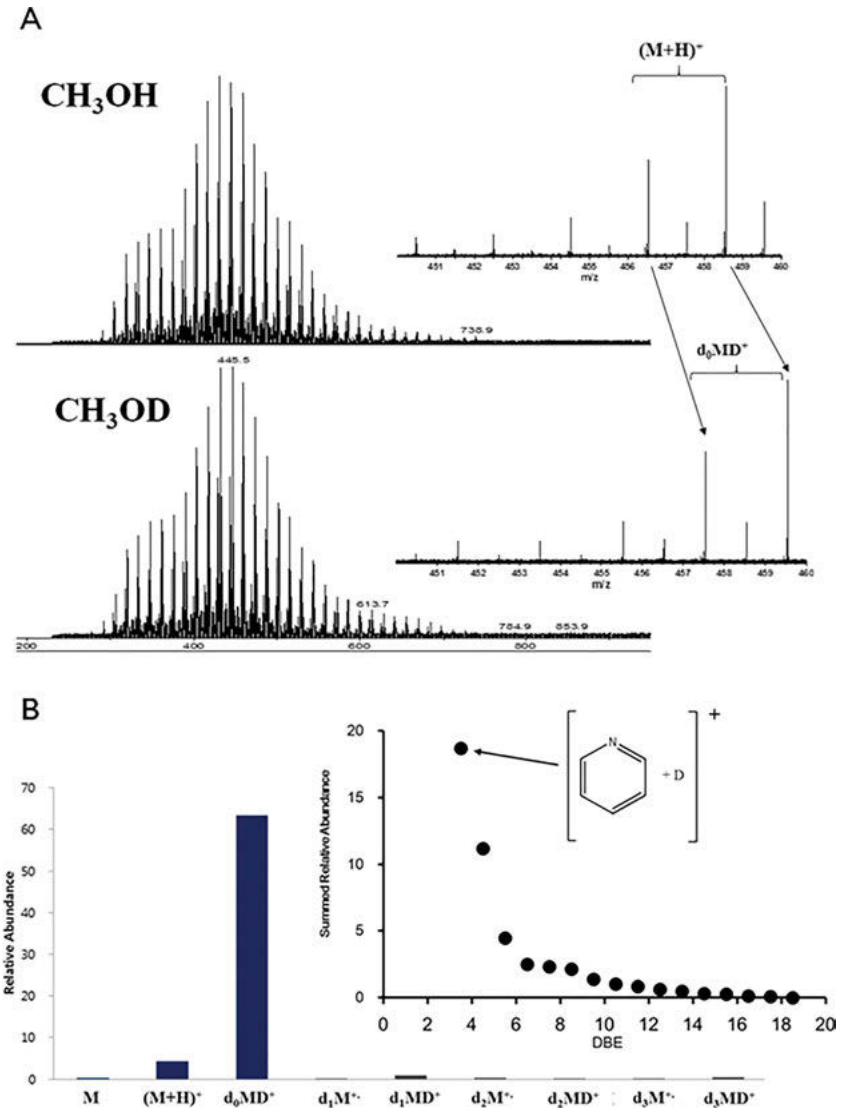

Figure 12.19: Analysis of the shale oil resin by in-APCI source HDX MS: (A) broadband HDX-MS spectra showing peaks with the addition of one deuterium atom instead of performing HDX; (B) type of ions produced during the HDX-MS analysis (inset: double bond equivalence (DBE) distribution for the abundant product ion) [reproduced with permission from Acter et al., J. Am. Soc. Mass Spectrom. 26, 1522–1531 (2015). Copyright, American Society for Mass Spectrometry].

Table 12.2: HDX product-ion patterns for 38 model oxygen-containing compounds analyzed by (+/–) APCI and APPI HDX-MS.

Groups	Compounds	APCI		APPI	
		(+)	(–)	(+)	(–)
I	Alcohols	$d_nM^{+\cdot}/d_nMD^+$	$d_{(n-1)}(M\text{-}H)^-$	$d_nM^{+\cdot}/d_nMD^+$	$d_{(n-1)}(M\text{-}H)^-$
II	Carboxylic acids	d_nMD^+	$d_n(M\text{-}H)^-$		$d_{(n-1)}(M\text{-}H)^-$
III	Aldehydes, esters, ketones	d_0MD^+	$M^{-\cdot}/d_0(M\text{-}H)^-$	d_0MD^+	$M^{-\cdot}/d_0(M\text{-}H)^-$
	Oxygen heterocycles	$M^{+\cdot}$		$M^{+\cdot}$	$d_0(M\text{-}H)^-$

[Reproduced with permission from Table, Acter, T. et al., Anal. Bioanal. Chem., 408, 3281–3293 (2016). Copyright, Springer-Verlag Berlin Heidelberg]

crude oil and Anvil Points Mine (APM) shale oil. The (+) APPI HDX MS spectra for 20 nitrogen-containing compounds obtained from quadrupole Orbitrap MS revealed that the abundant HDX ions produced were $d_2M^{+\cdot}/d_2MD^+$ for primary amines, $d_1M^{+\cdot}/d_1MD^+$ for secondary amines, $M^{+\cdot}/d_0MD^+$ for tertiary amines, d_0MD^+ for pyridines, and $d_1M^{+\cdot}/d_1MD^+$ for pyrroles. The HDX MS spectra for the oil samples suggested the structures of nitrogen-containing species in QHD resin to be tertiary amine-type (e.g., N-alkylated and N-phenyl pyrroles) and secondary amine-type (e.g., C-alkyl and C-phenyl pyrroles), and those in the APM resin to be pyridine-type compounds.

Furthermore, Kim and coworkers [251] analyzed the polar fractions (Polar 1 and Polar 2) of atmospheric pressure residue (AR) maltene samples fractionated by medium-pressure liquid chromatography, utilizing (+) APPI HDX 7-T FTICR MS along with the DBE distributions obtained from (+) APPI MS to characterize the nitrogen-containing compounds. The abundant HDX ions produced for the N_1 class compounds and their original DBE distributions suggested their structures to be pyrrole-type in the Polar 1 fraction and pyridine and N-alkyl pyrrole-type in the Polar 2 fraction (Figure 12.20).

12.7.5.3.2 Oxygen-containing species

Oxygen-containing compounds were identified by HDX and CAD after derivatization with methoxyborane reagents in FTICR MS [252]. Kim and coworkers [201] applied (+) and (–) in-APPI source HDX coupled with quadrupole Orbitrap MS to analyze 38 model oxygen-containing compounds, as well as photodegraded oil rich in oxygen-containing compounds. The results of the APPI HDX MS analysis of the model oxygen compounds revealed that the method in the (–)-mode worked effectively for all types of oxygen functionalities, while the method in the (+)-mode was insensitive to carboxylic acids (Table 12.2). The positive HDX MS spectra for the photo-oxidized (2- and 5-days) oil samples demonstrated that O_2 class compounds have naphthalenedione structures having two ketone groups, which originate from

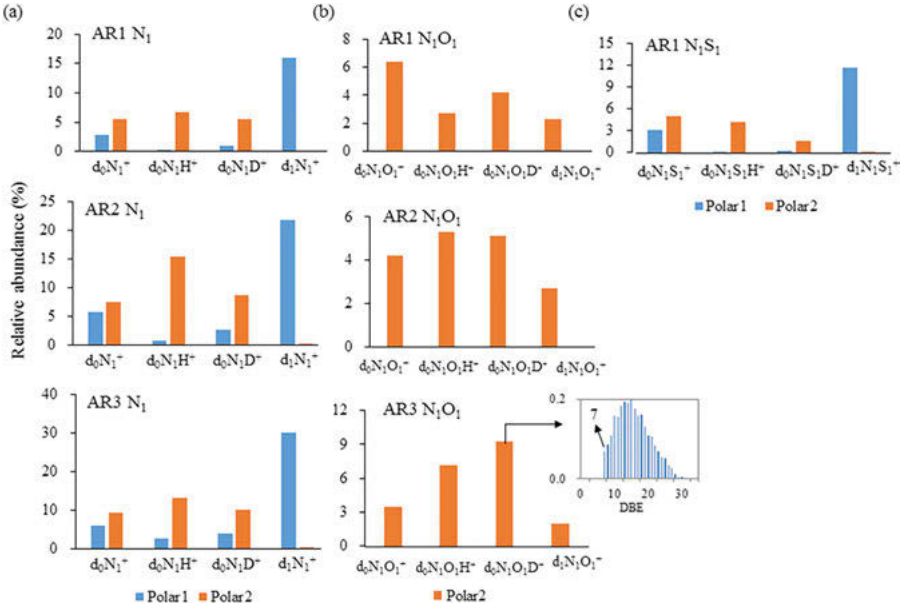

Figure 12.20: Types of HDX ions produced from the polar fractions of the three AR samples analyzed by (+) APPI HDX 7-T FTICR MS: a) N_1 class, b) N_1O_1 class, and c) N_1S_1 class [reproduced with permission from figure, Kim, E. et al., Fuel, 194, 503–510 (2017). Copyright, Elsevier Ltd.].

the oxidation of naphthalene, while O_3 and O_4 class compounds comprise one carboxylic acid group with ketone, aldehyde, or ester groups (Figure 12.21). Similar to the APCI HDX method, APPI HDX MS was unable to differentiate compounds lacking active hydrogen atoms. Kim and coworkers [251] reported the oxygen-containing functional groups of N_1O_1 class compounds observed in the Polar 2 fraction of three AR maltene samples, analyzed by (+) APPI HDX 7-T FTICR MS along with DBE distributions obtained from (+) APPI MS. The suggested oxygen-containing functional groups in the pyridine or pyrrole core structures were aldehyde or ketone groups, attributed to the abundance of d_0MD^+ ions (Figure 12.21).

12.7.5.3.3 Sulfur-containing species

Kim and coworkers [251] suggested the sulfur-containing functional groups of N_1S_1 class compounds observed in the Polar fraction of three AR maltene samples, analyzed by (+) APPI HDX 7-T FTICR MS along with DBE distributions obtained from (+) APPI MS. The suggested sulfur-containing functional group in carbazole and pyridine (and N-alkylated carbazole) was the thiophene ring, attributed to the abundance of d_0MD^+ ions and the 2 DBE difference between the N_1 and N_1S_1 classes in the Polar 1 and Polar 2 fractions, respectively (Figure 12.20). (+) APPI HDX 7-T FTICR MS was also utilized to analyze thiophenes, sulfides, and thiol fractions separated by

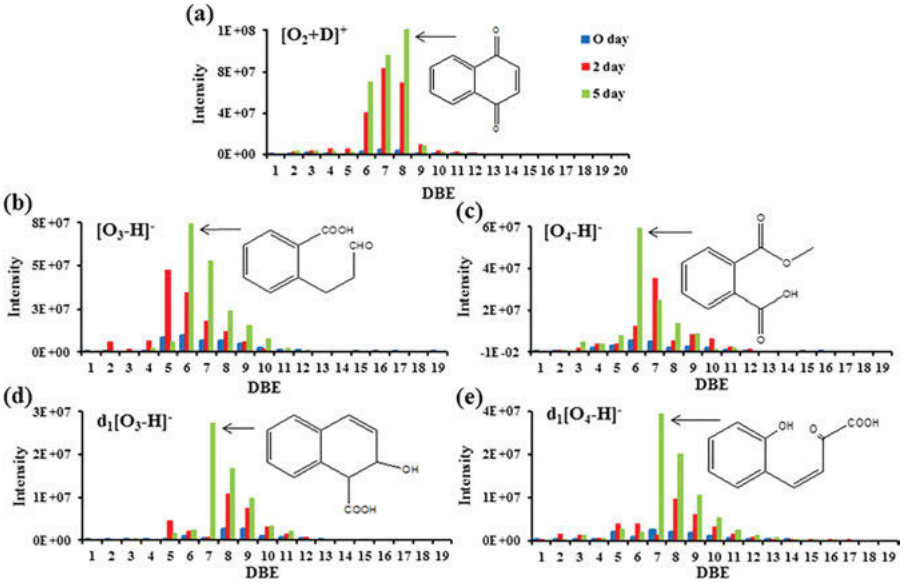

Figure 12.21: DBE distributions of the abundant product ions obtained from the photooxidized oil samples analyzed by (a) (+) APPI HDX MS and (b)–(e) (–) APPI HDX MS [reproduced with permission from table, Acter, T. et al., Anal. Bioanal. Chem., 408, 3281–3293 (2016). Copyright, Springer-Verlag Berlin Heidelberg].

ligand-exchange chromatography from Soroosh crude oil (Iran) enriched with 3.99% sulfur and 30 ppm mercaptans [21]. The HDX MS results obtained from the thiophene and sulfide fractions confirmed their respective structures, which lacked active hydrogen atoms for HDX, while the thiol fraction was suggested to have dithiol groups due to their capacity to produce 2 HDX ions (Figure 12.22).

12.7.5.3.4 Spilled oil

HDX MS has recently been implemented for the analysis of spilled and weathered oil to understand the weathering processes by observing their compositional changes at the molecular level [253]. Here, the resin fractions of three oil spills from the M/V Hebei Spirit oil spill, which occurred on December 7, 2007, on the West Coast of the Republic of Korea, and weathered oils collected at weathering stages II and IV from the oil spill site were analyzed by (+)APPI HDX 15 T FTICR MS. The HDX MS results of this study suggested that the nitrogen-containing compounds, particularly secondary and tertiary amines are more prone to natural weathering and can, thus, gradually produce degraded products (Figure 12.23).

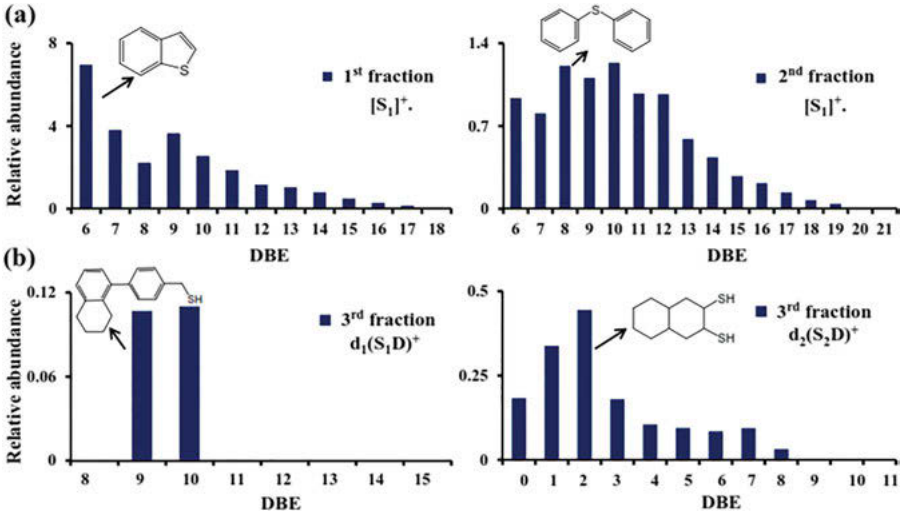

Figure 12.22: DBE distributions plots for the abundant HDX product ions obtained from three different fractions of oil: (a) $[S_1]^{+\cdot}$ ion for the first (left) and second (right) fraction; (b) $d_1(S_1D)^+$ (left) and $d_2(S_2D)^+$ (right) ion for the third fraction [reproduced with permission from figure 4, Acter, T. et al., J Am Soc Mass Spectrom., 28(8):1687–1695 (2017). Copyright, American Chemical Society].

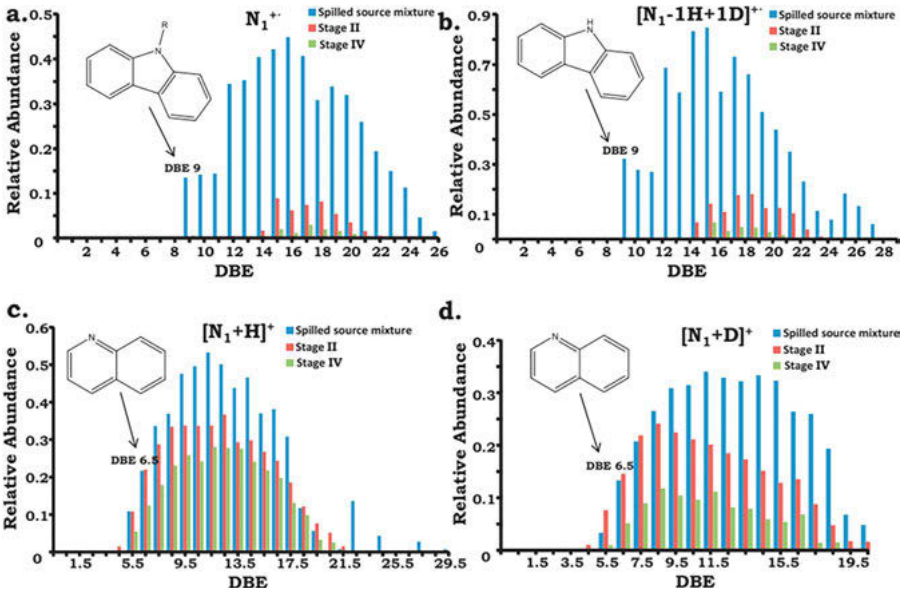

Figure 12.23: DBE distribution plots for the abundant HDX product ions, obtained from the resin fractions of spilled source mixture and weathered oils: (a) $N_1^{\bullet+}$, (b) $[N_1 - H + D]^+$, (c) $[N_1 + H]^+$, and (d) $[N_1 + D]^{\bullet+}$, obtained from the resin fractions of spilled source mixture and weathered oils [reproduced with permission from Islam, A. et al., J. Hazard. Mater., 296, 93–100 (2015). Copyright, Elsevier B.V.].

12.8 Current challenges and future perspectives for crude oil analysis

12.8.1 Tandem MS

Although there are numerous analytical techniques used for the chemical characterization of crude oil and its derived liquids, the application of tandem MS methods for the compositional characterization of crude oil is not prevalent; there are still some challenges associated with their application for crude oil analysis.

a. The results of the tandem MS analysis of crude oil are occasionally useless because of the high complexity of crude oil mixtures, resulting in the simultaneous generation, isolation, and fragmentation of many chemical species (including isomers). Consequently, the structural elucidation of the individual compounds in the fragment spectra is challenging.
b. One of the major challenges of tandem MS for the analysis of crude oil and its products is the unclear fragmentation reaction mechanisms of heavy petroleum fractions, due to the complexity of their isolated precursor ions [92]. There are occasionally conflicting CID reports of crude oil–related compound fragments. Qian et al. [96] suggested that the interpretation of the fragmentation mechanisms for a crude oil mixture may be invalidated as single isomers cannot be generated from single fragments. To overcome this issue, a relatively small isolation window (<0.3 Da) during analysis, accurate mass measurement of the obtained fragments, and multistep fragmentation (MS^n) can be considered [254]. For example, a triple quadrupole mass spectrometer [255] and LTQ-Oribtrap can be used for this purpose.
c. Another challenge of tandem MS experiments, particularly peculiar to scanning-type mass analyzers, is the potential loss of ions during crude oil analysis, resulting in decreased sensitivity. An increase in the S/N ratio and a decrease in the ion loss can be achieved using the selected ion monitoring (SIM) mode during the tandem MS experiments [165]. However, in the case of using only one or several ions for interpreting the fragmentation spectra during SIM, erroneous results may be obtained. To increase the scanning speed of the MS instruments and reduce ion loss, modern quadrupole analyzers, e.g., triple quadrupole mass analyzers, can be used [256].
d. Insufficient detection limits are often encountered during MS/MS analysis, due to the wide variety and low concentration of crude oil compounds.
e. The generation of unwilling reactions during MS/MS experiments occasionally complicates the fragmentation spectra. Tandem CID MS methods performed with ion traps or quadrupole instruments can control the bond-dissociation energy, which can ultimately reduce the occurrence possibility of unwilling reactions.

f. Low-resolution MS instruments used in the analysis of heavy petroleum fractions may cause severe peak overlapping, due to the lack of mass resolution [257]. The use of mass spectrometers with increased resolution, e.g., FT-ICR MS, and distinct ionization sources may widen the scope of tandem MS methods for studying the structures of crude oil compounds [11].

To identify specific classes of crude oil compounds, more ionization techniques coupled with tandem MS techniques should be developed in the future. We expect that tandem MS methods will play a more important role in the characterization of crude oil and its products in the future.

12.8.2 IM-MS

As the IMS technology has proven its analytical capability to differentiate isomeric structures that are difficult to separate by other MS methods, the development of this approach in different perspectives will facilitate its widespread application and enable the improved understanding of the chemistry of the individual compounds present in complex mixtures, such as crude oil, at the molecular level.

a. One of the challenges associated with using the IMS technique for crude oil analysis is that the isobaric species in complex mixtures are occasionally poorly resolved because of the low resolving power of IMS cells [137, 258]. Although significant progress has already been achieved in recent years to enhance the resolving power of IMS instruments [137, 154, 157, 159, 259–261], more advancements in their instrumental design and data-interpretation methods, i.e., IM peak capacity, will ensure the widespread use of this approach for crude oil analysis. To further improve the separation of petroleum isomers, more polarizable drift gases may be selected for IMS cells. CO_2, N_2O, and N_2 are common polarizable drift gases used for petroleum analysis [262–264]. In addition, the coupling of the IM-MS technique with other methods, such as the addition of shifting reagents, derivatization, and complexation, may improve the overall IM peak capacity [31, 32, 265]. Generally, since the use of different ionization sources may increase the sensitivity and selectivity of any MS method, the use of various IMS modes can influence the drift behavior of the isomeric structures in petroleum mixtures [165]. Excluding ESI, APCI, and APPI, the ionization sources recently used in IM-MS experiments are ASAP [266] and APLI [267]. However, the ionization source should be properly selected for the IM-MS analysis of a complex mixture to obtain reliable IMS data.
b. Tandem MS coupled with IMS can solve the mobility-prediction problem of the ions in the drift region. However, the implementation of this combination for crude oil analysis remains challenging, due to the complex fragmentation patterns, lack of a library for the fragmentation patterns of model compounds,

limited information on product ions, low availability of model compounds with different core structures, and use of conventional mass spectrometers for MS/MS experiments. Therefore, researchers should focus on overcoming these issues related to IM tandem MS. Recently, several improvements have been introduced in IM tandem MS instruments, e.g., multipass approaches, named cyclic ion-mobility MS (cIM-MS) [153, 154].

c. The IM-MS data-processing methods are complex and time-consuming, owing to the huge array of data consisting of the m/z values and drift times obtained from IMS and HR-MS analyses [142]. Therefore, data-interpretation methods should be developed for IM-MS techniques to increase the application range of this approach.
d. The structures of crude oils rich in non-/less polar aromatic compounds do not match always with the conventional calibration standard (poly-DL-alanine), which is used for experimental CCS calibration during IM-MS experiments. Recently, more calibration standards, including PAH compounds, have been developed for crude oil analysis [268, 269].
e. Another challenge of the IM-MS technique for crude oil analysis is the application of IM-MS coupled with computational methods, which can play an important role in predicting the molecular behavior in IM cells. Lack of theoretical CCS values for numerous standard compounds, complex and expensive computational software, and limited descriptors for petroleum samples are major hindrances to the advancements in the computational field of IM-MS studies.

12.8.3 HDX MS

The in-API source HDX approach in the gas phase in combination with HR-MS can be employed directly in the ion-source mode for quantitative measurements, enumeration of the functional groups in individual compounds, and speciation of the heteroatomic classes of complex mixtures, such as crude oil. Moreover, this approach simplifies the sample preparation methods. Overall, the HDX MS method is considered a simple, specific, and sensitive tool for the structural analysis of complex mixtures. However, unlike other hyphenated MS methods, the HDX MS method has been minimally applied for crude oil analysis. The following factors may be considered for the future development of HDX MS for crude oil analysis to ensure its widespread application in petroleomics.

a. Need for HR-MS
Although HDX coupled with low-resolution MS work well for the analysis of model heteroatom-containing compounds, the use of HR-MS is a prerequisite for the analysis of complex mixture, such as crude oil and its products, which limits the routine application of the HDX MS method in the MS community for the structural elucidation of

petroleum compounds. If we can ensure the availability of HR-MS in the future, the applications of HDX combined with HR-MS will continue to expand, positioning it as a convenient structural approach in the field of chemistry for analyzing crude oil and its products.

b. HDX versus ionization source
The performance of HDX analysis mainly depends on the ionization source used during the MS experiments. For example, ESI MS and ESI HDX are suitable for polar compounds, while APCI MS/APCI HDX MS and APPI MS/APPI HDX MS are fit for less polar or nonpolar compounds. Therefore, the ionization source design should be improved to optimize the experimental conditions and maximize the HDX efficiency. The ionization behaviors of crude oil compounds with subtle structures are different for different ionization techniques. Therefore, the proper selection of the ionization source is crucial for effective petroleum analysis.

c. Need for the addition of shift reagents
A shift reagent usually forms a stable gas-phase complex with the analyte ion when added to the analyte solution before ionization to increase the S/N ratio and overall peak capacity of the analyzed ions. The HDX MS methods occasionally require the addition of shift reagents before the analysis to identify specific chemical classes, which further complicates the data-interpretation procedures. For example, Acter et al. [270] added Ag salt to a crude oil sample during an LDI HDX MS experiment for the speciation of sulfur-containing compounds.

d. Data-interpretation methods
Predictably, HDX coupled with HR-MS would produce an aggregated dataset of molecular ions and HDX product ions during the ionization of complex crude oil compounds. Only a few software, e.g., STORM-HDX, can process these huge arrays of petroleum HDX data. The development of relatively fast and easily adoptable HDX data-processing software is of urgent significance to ensure the complete utilization of this analytical technique in the petroleum area.

e. Limited application of HDX tandem MS
To enhance the structural characterization capabilities of the HDX method, the coupling of tandem MS with HDX MS might be the best strategy. A library of HDX fragmentation patterns for standards with different core structures may be constructed to improve the CID data interpretation of petroleum samples. However, the application of HDX with tandem MS for petroleum analysis has not yet been implemented.

f. Limited computational studies for HDX MS
The combined approach of HDX MS and theoretical CCS calculations for crude oil analysis needs to be explored to gain further information on oil analysis. An inexpensive,

easily handled, and adoptable computational software for performing HDX reactions should be developed. Excluding the expensive quantum-mechanical methods, the application of inexpensive classical methods for performing theoretical calculations of HDX reactions should also be evaluated.

12.9 Conclusion

The products of crude oil are in high demand in modern society. Petroleomics is a highly interesting process, involving the prediction of the structures of crude oil compounds, of which significant exploitation is still required to evaluate the structure–function relationships. In this book, we have described the most promising approaches for crude oil analysis, including tandem MS, IM-MS, and HDX MS, which can meet the current and future needs of the petroleum refining industry. Despite the difficulty in analyzing extremely complex mixture, the number of research works related to the application of these mass spectrometric methods for crude oil analysis is increasing. To fully utilize these methods in unraveling the chemical structures and reactions in petroleomics, we highly recommended that these methods be implemented along with new and diverse computational tools.

References

[1] Boduszynski MM. Composition of heavy petroleums. 1. Molecular weight, hydrogen deficiency, and heteroatom concentration as a function of atmospheric equivalent boiling point up to 1400.degree.F (760.degree.C). Energy Fuels, 1987, 1(1), 2–11.
[2] Boduszynski MM. Composition of heavy petroleums. 2. Molecular characterization. Energy Fuels, 1988, 2(5), 597–613.
[3] Altgelt KH. Composition and Analysis of Heavy Petroleum Fractions. 1st, CRC Press, Boca Raton, 1993.
[4] Marshall AG, Rodgers RP. Petroleomics: Chemistry of the underworld. Proc Natl Acad Sci U S A, 2008, 105(47), 18090–18095.
[5] Warton B, Alexander R, Kagi RI. Characterisation of the ruthenium tetroxide oxidation products from the aromatic unresolved complex mixture of a biodegraded crude oil. Org Geochem, 1999, 30(10), 1255–1272.
[6] Gross ML. High performance mass spectrometry: Chemical applications; ACS symposium series no. 70. In: Analytical chemistry. University of Nebraska: American Chemical Society, 1980.
[7] Marshall AG, Grosshans PB. Fourier transform ion cyclotron resonance mass spectrometry: The teenage years. Anal Chem, 1991, 63(4), 215A–229A.
[8] Cho Y, et al. Developments in FT-ICR MS instrumentation, ionization techniques, and data interpretation methods for petroleomics. Mass Spectrom Rev, 2015, 34(2), 248–263.
[9] Rodgers RP, Schaub TM, Marshall AG. Petroleomics: MS returns to its roots. Anal Chem, 2005, 77(1), 20 A–27 A.

[10] Palacio Lozano DC, et al. Petroleomics: Tools, challenges, and developments. Annu Rev Anal Chem, 2020, 13(1), 405–430.
[11] Qian K, et al. Resolution and identification of elemental compositions for more than 3000 crude acids in heavy petroleum by negative-ion microelectrospray high-field fourier transform ion cyclotron resonance mass spectrometry. Energy Fuels, 2001, 15, 1505–1511.
[12] Qian K, et al. Reading chemical fine print: Resolution and identification of 3000 nitrogen-containing aromatic compounds from a single electrospray ionization Fourier transform ion cyclotron resonance mass spectrum of heavy petroleum crude oil. Energy Fuels, 2001, 15(2), 492–498.
[13] Cho Y, Abed HN, Kim S. Molecular level investigation of oil sludge at the bottom of oil tank in Ratawi oil field by atmospheric pressure photo ionization ultrahigh-resolution mass spectrometry. Bull Korean Chem Soc, 2020, 41(4), 450–453.
[14] Islam A, et al. Molecular-level evidence provided by ultrahigh resolution mass spectrometry for oil-derived doc in groundwater at Bemidji, Minnesota. J Hazard Mater, 2016, 320, 123–132.
[15] Kim S, Kramer RW, Hatcher PG. Graphical method for analysis of ultrahigh-resolution broadband mass spectra of natural organic matter, the Van Krevelen diagram. Anal Chem, 2003, 75(20), 5336–5344.
[16] Panda SK, Andersson JT, Schrader W. Mass-spectrometric analysis of complex volatile and nonvolatile crude oil components: A challenge. Anal Bioanal Chem, 2007, 389(5), 1329–1339.
[17] Cho Y, et al. Extension of the analytical window for characterizing aromatic compounds in oils using a comprehensive suite of high-resolution mass spectrometry techniques and double bond equivalence versus carbon number plot. Energy Fuels, 2017, 31(8), 7874–7883.
[18] Kim E, et al. Characterization of petroleum heavy oil fractions prepared by preparatory liquid chromatography with thin-layer chromatography, high-resolution mass spectrometry, and gas chromatography with an atomic emission detector. Energy Fuels, 2016, 30(4), 2932–2940.
[19] Kim D, et al. Combination of ring type HPLC separation, ultrahigh-resolution mass spectrometry, and high field NMR for comprehensive characterization of crude oil compositions. Fuel, 2015, 157, 48–55.
[20] Cho Y, Ahmed A, Kim S. Application of atmospheric pressure photo ionization hydrogen/deuterium exchange high-resolution mass spectrometry for the molecular level speciation of nitrogen compounds in heavy crude oils. Anall Chem, 2013, 85(20), 9758–9763.
[21] Acter T, et al. Application of atmospheric pressure photoionization H/D-exchange mass spectrometry for speciation of sulfur-containing compounds. J Am Soc Mass Spectrom, 2017, 28(8), 1687–1695.
[22] Kostyukevich Y, et al. The investigation of the bitumen from ancient Greek amphora using FT ICR MS, H/D exchange and novel spectrum reduction approach. J Mass Spectrom, 2016, 51 (6), 430–436.
[23] Kostyukevich Y, et al. The investigation of the birch tar using ultrahigh resolution Fourier transform ion cyclotron resonance mass spectrometry and Hydrogen/Deuterium exchange approach. Int J Mass Spectrom, 2016, 404, 29–34.
[24] Porter DJ, Mayer PM, Fingas M. Analysis of petroleum resins using electrospray ionization tandem mass spectrometry. Energy Fuels, 2004, 18(4), 987–994.
[25] Rüger CP, et al. Thermal analysis coupled to ultrahigh resolution mass spectrometry with collision induced dissociation for complex petroleum samples: Heavy oil composition and asphaltene precipitation effects. Energy Fuels, 2017, 31(12), 13144–13158.
[26] Wittrig AM, et al. Single dalton collision-induced dissociation for petroleum structure characterization. Energy Fuels, 2017, 31(12), 13338–13344.

[27] Ha J, Cho E, Kim S. Interpreting chemical structures of compounds in crude oil based on the Tandem mass spectra of standard compounds obtained at the same normalized collision energy. Energy Fuels, 2017, 31(7), 6960–6967.
[28] Fernandez-Lima FA, et al. Petroleum crude oil characterization by IMS-MS and FTICR MS. Anal Chem, 2009, 81(24), 9941–9947.
[29] Laakia J, et al. Separation of different ion structures in atmospheric pressure photoionization-ion mobility spectrometry-mass spectrometry (APPI-IMS-MS). J Am Soc Mass Spectrom, 2010, 21(9), 1565–1572.
[30] Lalli PM, et al. Isomeric separation and structural characterization of acids in petroleum by ion mobility mass spectrometry. Energy Fuels, 2015, 29(6), 3626–3633.
[31] Maleki H. *Complex Mixture Analysis Using Ion Mobility Spectrometry-Mass Spectrometry (IMS-MS) and Computational Techniques*, in *Dept. of Chemistry*. West Virginia University, Morgantown, West Virginia, 2017.
[32] Maleki H, et al. Structural assignments of sulfur-containing compounds in crude oil using ion mobility spectrometry-mass spectrometry. Energy Fuels, 2016, 30(11), 9150–9161.
[33] Gross JH. Mass spectrometry: A textbook. Springer International Publishing, 2017.
[34] Thomson JJ. XL. Cathode rays. London Edinburgh Dublin Phil Mag J Sci, 1897, 44(269), 293–316.
[35] Thomson JJ. XLVII. On rays of positive electricity. London Edinburgh Dublin Phil Mag J Sci, 1907, 13(77), 561–575.
[36] Aston FW. LXXIV. A positive ray spectrograph. London Edinburgh Dublin Phil Mag J Sci, 1919, 38(228), 707–714.
[37] Bainbridge KT, Jordan EB. Mass spectrum analysis 1. The mass spectrograph. 2. The existence of isobars of adjacent elements. Phys Rev, 1936, 50(4), 282–296.
[38] Nier AO. A mass spectrometer for routine isotope abundance measurements. Rev Sci Instrum, 1940, 11(7), 212–216.
[39] Ryhage R. Use of a mass spectrometer as a detector and analyzer for effluent emerging from high temperature gas liquid chromatography columns. Anal Chem, 1964, 36(4), 759–764.
[40] Jennings KR. Collision-induced decompositions of aromatic molecular ions. Int J Mass Spectrom Ion Phys, 1968, 1(3), 227–235.
[41] Munson MSB, Field FH. Chemical ionization mass spectrometry. I. General introduction. J Am Chem Soc, 1966, 88(12), 2621–2630.
[42] Barber M, et al. Fast atom bombardment of solids (F.A.B.): A new ion source for mass spectrometry. J Chem Soc Chem Commun, 1981, 7, 325–327.
[43] Fenn JB, et al. Electrospray ionization for mass spectrometry of large biomolecules. Science, 1989, 246(4926), 64.
[44] Karas M, Hillenkamp F. Laser desorption ionization of proteins with molecular masses exceeding 10,000 daltons. Anal Chem, 1988, 60(20), 2299–2301.
[45] Marshall AG, Rodgers RP. Petroleomics: The next grand challenge for chemical analysis. Acc Chem Res, 2004, 37(1), 53–59.
[46] C., O., et al. Asphaltenes, Heavy Oils, and Petroleomics. Springer, New York, NY, 2007.
[47] Lumpkin HE. Low voltage techniques in high molecular weight mass spectrometry. Anal Chem, 1958, 30(3), 321–325.
[48] Quann RJ, Jaffe SB. Structure-oriented lumping: Describing the chemistry of complex hydrocarbon mixtures. Ind Eng Chem Res, 1992, 31(11), 2483–2497.
[49] Comisarow MB, Marshall AG. Fourier transform ion cyclotron resonance spectroscopy. Chem Phys Lett, 1974, 25(2), 282–283.
[50] Marshall AG. Milestones in fourier transform ion cyclotron resonance mass spectrometry technique development. Int J Mass Spectrom, 2000, 200(1), 331–356.

[51] Guan S, Marshall Ag Fau – Scheppele SE, Scheppele SE, *Resolution and chemical formula identification of aromatic hydrocarbons and aromatic compounds containing sulfur, nitrogen, or oxygen in petroleum distillates and refinery streams*. (0003-2700 (Print)).
[52] Son S, et al. Reproducibility of crude oil spectra obtained with ultrahigh resolution mass spectrometry. Anal Chem, 2020, 92(14), 9465–9471.
[53] Akmaz S, et al. The structural characterization of saturate, aromatic, resin, and asphaltene fractions of Batiraman crude oil. Petrol Sci Technol, 2011, 29(2), 160–171.
[54] Rudzinski WE, Aminabhavi TM. A review on extraction and identification of crude oil and related products using supercritical fluid technology. Energy Fuels, 2000, 14(2), 464–475.
[55] Brown R. Compound types in Gasoline by mass spectrometer analysis. Anal Chem, 1951, 23 (3), 430–437.
[56] Mullins OC, et al. Asphaltenes, heavy oils, and petroleomics. 1st ed. , Springer, New York, NY, 2007.
[57] Giger W, Blumer M. Polycyclic aromatic hydrocarbons in the environment. Isolation and characterization by chromatography, visible, ultraviolet, and mass spectrometry. Anal Chem, 1974, 46(12), 1663–1671.
[58] Clerc RJ, Hood A, O'Neal MM. Mass spectrometric analysis of high molecular weight, saturated hydrocarbons. Anal Chem, 1955, 27(6), 868–875.
[59] Swansiger JT, Dickson FE, Best HT. Liquid coal compositional analysis by mass spectrometry. Anal Chem, 1974, 46(6), 730–734.
[60] Robinson CJ, Cook GL. Low-resolution mass spectrometric determination of aromatic fractions from petroleum. Anal Chem, 1969, 41(12), 1548–1554.
[61] Robinson CJ. Low-resolution mass spectrometric determination of aromatics and saturates in petroleum fractions. Anal Chem, 1971, 43(11), 1425–1434.
[62] Scheppele SE, et al. Determination of field-ionization relative sensitivities for the analysis of coal-derived liquids and their correlation with low-voltage electron-impact relative sensitivities. Anal Chem, 1976, 48(14), 2105–2112.
[63] Gallegos EJ, et al. Petroleum group-type analysis by high resolution mass spectrometry. Anal Chem, 1967, 39(14), 1833–1838.
[64] Cha E, et al. Ionization of gas-phase polycyclic aromatic hydrocarbons in electrospray ionization coupled with gas chromatography. Anal Chem, 2018, 90(6), 4203–4211.
[65] Richter FP, et al. Distribution of nitrogen in petroleum according to basicity. Ind Eng Chem, 1952, 44(11), 2601–2605.
[66] Cooper JE, Bray EE. A postulated role of fatty acids in petroleum formation. Geochim Cosmochim Acta, 1963, 27(11), 1113–1127.
[67] Brocart B, Hurtevent C. Flow assurance issues and control with naphthenic oils. J Dispersion Sci Technol, 2008, 29, 1496–1504.
[68] Clingenpeel AC, et al. Fractionation of interfacial material reveals a continuum of acidic species that contribute to stable emulsion formation. Energy Fuels, 2017, 31(6), 5933–5939.
[69] Rogel E, Ovalles C, Moir M. Asphaltene chemical characterization as a function of solubility: Effects on stability and aggregation. Energy Fuels, 2012, 26(5), 2655–2662.
[70] Lobodin VV, et al. Separation and characterization of reactive and non-reactive sulfur in petroleum and its fractions. Energy Fuels, 2015, 29(10), 6177–6186.
[71] Liu L, et al. Structural characterization of sulfur-containing aromatic compounds in heavy oils by FT-ICR mass spectrometry with a narrow isolation window. Fuel, 2019, 240, 40–48.
[72] Han Y, et al. Molecular characterization of sulfur-containing compounds in petroleum. Fuel, 2018, 221, 144–158.
[73] Yang B, et al, *Application of solid-phase microextraction to the determination of polycyclic aromatic sulfur heterocycles in Bohai Sea crude oils*. (1615-9314 (Electronic)).

[74] Purcell JM, et al. Sulfur speciation in petroleum: Atmospheric pressure photoionization or chemical derivatization and electrospray ionization Fourier transform ion cyclotron resonance mass spectrometry. Energy Fuels, 2007, 21(5), 2869–2874.
[75] Singleton MF, et al. Occurrence of biomarkers in Green River shale oil. [Isoprenoids and polycycloalkanes]. In: American Chemical Society national meeting. Seattle, WA, USA, 1983.
[76] Woodle RA, Chandler WB. Mechanism of occurrence of metals in petroleum distillates. Ind Eng Chem, 1952, 44(11), 2591–2596.
[77] Treibs DA. Chlorophyll- und Häminderivate in organischen Mineralstoffen. Angewandte Chemie, 1936.
[78] Wolff GA, et al. Structure analysis of naturally occurring alkyl porphyrins by hydrogen chemical ionisation mass spectrometry. Tetrahedron, 1984, 40(19), 3777–3786.
[79] Baker EW, et al. Mass spectrometry of porphyrins. II. Characterization of petroporphyrins. J Am Chem Soc, 1967, 89(14), 3631–3639.
[80] Ramírez-Pradilla JS, et al. Comprehensive petroporphyrin identification in crude oils using highly selective electron transfer reactions in MALDI-FTICR-MS. Energy Fuels, 2019, 33(5), 3899–3907.
[81] Chen X, et al. Direct nickel petroporphyrin analysis through electrochemical oxidation in electrospray ionization ultrahigh-resolution mass spectrometry. Energy Fuels, 2021, 35(7), 5748–5757.
[82] Maillard JF, et al. Structural analysis of petroporphyrins from asphaltene by trapped ion mobility coupled with Fourier transform ion cyclotron resonance mass spectrometry. Analyst, 2021, 146(13), 4161–4171.
[83] de Hoffmann E, Stroobant V. Mass spectrometry: Principles and applications. 3rd ed., John Wiley & Sons, 2007, 502.
[84] Busch KL, Glish GL, McLuckey SA. Mass spectrometry/mass spectrometry: Techniques and applications of tandem mass spectrometry. New York, VCH, Wiley, 1988.
[85] Prasain JK. Tandem mass spectrometry – Applications and principles. IntechOpen, 2012.
[86] Sleno L, Volmer DA, *Ion activation methods for tandem mass spectrometry*. (1076-5174 (Print)).
[87] Douglas DJ, *Linear quadrupoles in mass spectrometry*. (1098-2787 (Electronic)).
[88] Douglas DJ, Frank D, Mao AF, Mao D, *Linear ion traps in mass spectrometry*. (0277-7037 (Print)).
[89] Schwartz JC, et al. Systematic delineation of scan modes in multidimensional mass spectrometry. Anal Chem, 1990, 62(17), 1809–1818.
[90] Shukla AK, Futrell JH. Tandem mass spectrometry: Dissociation of ions by collisional activation. J Mass Spectrom, 2000, 35(9), 1069–1090.
[91] Mayer PM, Poon C. The mechanisms of collisional activation of ions in mass spectrometry. Mass Spectrom Rev, 2009, 28(4), 608–639.
[92] Vetere A, et al. Studying the fragmentation mechanism of selected components present in crude oil by collision-induced dissociation mass spectrometry. Rapid Commun Mass Spectrom, 2018, 32(24), 2141–2151.
[93] Le Maître J, et al. Structural analysis of heavy oil fractions after hydrodenitrogenation by high-resolution tandem mass spectrometry and ion mobility spectrometry. Faraday Discuss, 2019, 218(0), 417–430.
[94] Wu C, et al. Application of atmospheric pressure ionization techniques and tandem mass spectrometry for the characterization of petroleum components. Int J Mass Spectrom, 2015, 377.
[95] Denisov E, et al. Orbitrap mass spectrometry with resolving powers above 1,000,000. Int J Mass Spectrom, 2012, 325–327, 80–85.

[96] Qian K, et al. Determination of structural building blocks in heavy petroleum systems by collision-induced dissociation Fourier transform ion cyclotron resonance mass spectrometry. Anal Chem, 2012, 84(10), 4544–4551.
[97] Pan C, Hettich RL. Multipole-storage-assisted dissociation for the characterization of large proteins and simple protein mixtures by ESI-FTICR-MS. Anal Chem, 2005, 77(10), 3072–3082.
[98] Podgorski DC, et al. Heavy petroleum composition. 5. Compositional and structural continuum of petroleum revealed. Energy Fuels, 2013, 27(3), 1268–1276.
[99] Zubarev RA, Kelleher NL, McLafferty FW. Electron capture dissociation of multiply charged protein cations. A nonergodic process. J Am Chem Soc, 1998, 120(13), 3265–3266.
[100] Zubarev RA, et al. Towards an understanding of the mechanism of electron-capture dissociation: A historical perspective and modern ideas. Eur J Mass Spectrom, 2002, 8(5), 337–349.
[101] Syka JEP, et al. Peptide and protein sequence analysis by electron transfer dissociation mass spectrometry. Proc Natl Acad Sci U S A, 2004, 101(26), 9528.
[102] Cooks RG, et al. Surface modified mass spectrometry. J Am Chem Soc, 1975, 97(6), 1583–1585.
[103] Wysocki VH, et al. Surface-induced dissociation in tandem quadrupole mass spectrometers: A comparison of three designs. J Am Soc Mass Spectrom, 1992, 3(1), 27–32.
[104] Schaaff TG, et al, *Investigation of the trans effect in the fragmentation of dinuclear platinum complexes by electrospray ionization surface-induced dissociation tandem mass spectrometry*. (1076-5174 (Print)).
[105] Chacón-Patiño ML, Rowland SM, Rodgers RP. Advances in asphaltene petroleomics. Part 2: Selective separation method that reveals fractions enriched in Island and Archipelago structural motifs by mass spectrometry. Energy Fuels, 2018, 32(1), 314–328.
[106] Chacón-Patiño ML, Rowland SM, Rodgers RP. The compositional and structural continuum of petroleum from light distillates to Asphaltenes: The Boduszynski continuum theory as revealedby FT-ICR mass spectrometry. In: The Boduszynski continuum: Contributions to the understanding of the molecular composition of petroleum, American Chemical Society, 2018, 113–171.
[107] Rüger CP, et al. Combination of different thermal analysis methods coupled to mass spectrometry for the analysis of asphaltenes and their parent crude oils: Comprehensive characterization of the molecular pyrolysis pattern. Energy Fuels, 2018, 32(3), 2699–2711.
[108] Hughey CA, et al. Kendrick mass defect spectrum: A compact visual analysis for ultrahigh-resolution broadband mass spectra. Anal Chem, 2001, 73(19), 4676–4681.
[109] Kim E-K, et al. Compositional characterization of petroleum heavy oils generated from vacuum distillation and catalytic cracking by positive-mode APPI FT-ICR mass spectrometry. Mass Spectrom Lett, 2011, 2, 41–44.
[110] Zhang L, et al. Characterization of heavy petroleum fraction by positive-ion electrospray ionization FT-ICR mass spectrometry and collision induced dissociation: Bond dissociation behavior and aromatic ring architecture of basic nitrogen compounds. Sci China Chem, 2013, 56(7), 874–882.
[111] Borisov RS, Kulikova LN, Zaikin VG. Mass spectrometry in petroleum chemistry (petroleomics) (review). Petrol Chem, 2019, 59(10), 1055–1076.
[112] Kekäläinen T, et al. Compositional analysis of oil residues by ultrahigh-resolution Fourier transform ion cyclotron resonance mass spectrometry. Energy Fuels, 2013, 27(4), 2002–2009.
[113] Chacón-Patiño ML, Rowland SM, Rodgers RP. Advances in asphaltene petroleomics. Part 1: Asphaltenes are composed of abundant island and archipelago structural motifs. Energy Fuels, 2017, 31(12), 13509–13518.

[114] Chacón-Patiño ML, Rowland SM, Rodgers RP. Advances in asphaltene petroleomics. Part 3. Dominance of island or archipelago structural motif is sample dependent. Energy Fuels, 2018, 32(9), 9106–9120.
[115] Chacón-Patiño ML, et al. Tracing the compositional changes of asphaltenes after hydroconversion and thermal cracking processes by high-resolution mass spectrometry. Energy Fuels, 2015, 29(10), 6330–6341.
[116] Lalli PM, et al. Functional isomers in petroleum emulsion interfacial material revealed by ion mobility mass spectrometry and collision-induced dissociation. Energy Fuels, 2017, 31(1), 311–318.
[117] Le Maître J, et al. Structural analysis of neutral nitrogen compounds refractory to the hydrodenitrogenation process of heavy oil fractions by high-resolution tandem mass spectrometry and ion mobility–Mass Spectrometry. Energy Fuels, 2020, 34(8), 9328–9338.
[118] Cao X, Tarr MA. Aldehyde and ketone photoproducts from solar-irradiated crude oil–seawater systems determined by electrospray ionization–tandem mass spectrometry. Environ Sci Technol, 2017, 51(20), 11858–11866.
[119] Hansell DA. Recalcitrant dissolved organic carbon fractions. Ann Rev Mar Sci, 2013, 5 (1941–1405), Print), 421–445.
[120] Mapolelo MM, et al. Characterization of naphthenic acids in crude oils and naphthenates by electrospray ionization FT-ICR mass spectrometry. Int J Mass Spectrom, 2011, 300(2), 149–157.
[121] Brodbelt JS, et al. The analysis of metalloporphyrins in petroleum using tandem mass spectrometry. Fuel Sci Technol Int, 1986, 4(6), 683–698.
[122] McKenna AM, et al. Identification of vanadyl porphyrins in a heavy crude oil and raw asphaltene by atmospheric pressure photoionization fourier transform ion cyclotron resonance (FT-ICR) mass spectrometry. Energy Fuels, 2009, 23(4), 2122–2128.
[123] Rodgers R, et al. Molecular characterization of petroporphyrins in crude oil by electrospray ionization Fourier transform ion cyclotron resonance mass spectrometry. Can J Chem, 2011, 79, 546–551.
[124] Putman JC, et al. Chromatographic enrichment and subsequent separation of nickel and vanadyl porphyrins from natural seeps and molecular characterization by positive electrospray ionization FT-ICR mass spectrometry. Anal Chem, 2014, 21(1520–6882), (Electronic). 10708–10715.
[125] El-Sabagh SM, et al. Fingerprinting of biomarker characteristics of some Egyptian crude oils in Northern Western Desert as evidence for organic matter input and maturity level assessment. Egypt J Petrol, 2018, 27(2), 201–208.
[126] Peters KE, et al. *The Biomarker Guide*. Biomarkers and isotopes in petroleum exploration and earth history. Vol. 2. Cambridge University Press, 2005.
[127] Eiserbeck C, et al. Comparison of GC–MS, GC–MRM-MS, and GC×GC to characterise higher plant biomarkers in Tertiary oils and rock extracts. Geochim Cosmochim Acta, 2012, 87, 299–322.
[128] Eiserbeck C, et al. Separation of 18α(H)-, 18β(H)-oleanane and lupane by comprehensive two-dimensional gas chromatography. J Chromatogr A, 2011, 1218(32), 5549–5553.
[129] Pinkston DS, et al. Analysis of asphaltenes and asphaltene model compounds by laser-induced acoustic desorption/Fourier transform ion cyclotron resonance mass spectrometry. Energy Fuels, 2009, 23(11), 5564–5570.
[130] Hurt MR, et al. Comparison of the structures of molecules in coal and petroleum asphaltenes by using mass spectrometry. Energy Fuels, 2013, 27(7), 3653–3658.

[131] Owen BC, et al. Carbon disulfide reagent allows the characterization of nonpolar analytes by atmospheric pressure chemical ionization mass spectrometry. Rapid Commun Mass Spectrom, 2011, 25(14), 1924–1928.
[132] Kim YH, Kim S. Improved abundance sensitivity of molecular ions in positive-ion APCI MS analysis of petroleum in toluene. J Am Soc Mass Spectrom, 2010, 21(3), 386–392.
[133] Tang W, et al. Structural comparison of asphaltenes of different origins using multi-stage tandem mass spectrometry. Energy Fuels, 2015, 29(3), 1309–1314.
[134] Nyadong L, et al. High-field orbitrap mass spectrometry and tandem mass spectrometry for molecular characterization of asphaltenes. Energy Fuels, 2018, 32(1), 294–305.
[135] Kanu AB, et al. Ion mobility–mass spectrometry. J Mass Spectrom, 2008, 43(1), 1–22.
[136] Hupin S, et al. A calibration framework for the determination of accurate collision cross sections of polyanions using polyoxometalate standards. Rapid Commun Mass Spectrom, 2018, 32(19), 1703–1710.
[137] Farenc M, et al. Effective ion mobility peak width as a new isomeric descriptor for the untargeted analysis of complex mixtures using ion mobility-mass spectrometry. J Am Soc Mass Spectrom, 2017, 28(11), 2476–2482.
[138] Fasciotti M, et al. Structure-drift time relationships in ion mobility mass spectrometry. Int J Ion Mobility Spectrom, 2013, 16(2), 117–132.
[139] Eiceman GA, Karpas Z. Ion mobility spectrometry. *second comment*, Taylor & Francis Group, LLC, 20056000 Broken Sound Parkway NW, Suite 300.
[140] Wilkins CL, Trimpin S. Ion mobility spectrometry-mass spectrometry: Theory and applications. Taylor and Francis Group, LLC, 2011.
[141] Revercomb HE, Mason EA. Theory of plasma chromatography/gaseous electrophoresis. Review. Anal Chem, 1975, 47(7), 970–983.
[142] Ahmed A, et al. Application of the Mason–Schamp equation and ion mobility mass spectrometry to identify structurally related compounds in crude oil. Anal Chem, 2011, 83(1), 77–83.
[143] Lim D, et al. Determining collision cross-sections of aromatic compounds in crude oil by using aromatic compound mixture as calibration standard. Bull Korean Chem Soc, 2019, 40 (2), 122–127.
[144] Gutiérrez Sama S, et al. Molecular fingerprints and speciation of crude oils and heavy fractions revealed by molecular and elemental mass spectrometry: Keystone between petroleomics, metallopetroleomics, and petrointeractomics. Energy Fuels, 2018, 32(4), 4593–4605.
[145] Szykuła KM, et al. Characterization of crude oil and its saturate, aromatic, and resin fractions by high-field asymmetric waveform ion mobility spectrometry–high-resolution mass spectrometry. Energy Fuels, 2018, 32(11), 11310–11316.
[146] Gabryelski W, Froese KL. Characterization of naphthenic acids by electrospray ionization high-field asymmetric waveform ion mobility spectrometry mass spectrometry. Anal Chem, 2003, 75(17), 4612–4623.
[147] Da Costa C, et al. Direct analysis of oil additives by high-field asymmetric waveform ion mobility spectrometry-mass spectrometry combined with electrospray ionization and desorption electrospray ionization. Anal Chem, 2016, 88(4), 2453–2458.
[148] Guevremont R. High-field asymmetric waveform ion mobility spectrometry: A new tool for mass spectrometry. J Chromatogr A, 2004, 1058(1), 3–19.
[149] Fasciotti M, et al. Petroleomics by Traveling Wave Ion Mobility–Mass Spectrometry Using CO2 as a drift gas. Energy Fuels, 2013, 27(12), 7277–7286.
[150] May JC, McLean JA. Ion mobility-mass spectrometry: Time-dispersive instrumentation. Anal Chem, 2015, 87(3), 1422–1436.

[151] Marshall AG, Hendrickson CL, Jackson GS. Fourier transform ion cyclotron resonance mass spectrometry: A primer. Mass Spectrom Rev, 1998, 17(1), 1–35.
[152] Le Maître J, et al. Structural analysis of heavy oil fractions after hydrodenitrogenation by high-resolution tandem mass spectrometry and ion mobility spectrometry. Faraday Discuss, 2019, 218, 417–430.
[153] Cho E, et al. Isolation of crude oil peaks differing by m/z ~0.1 via tandem mass spectrometry using a cyclic ion mobility-mass spectrometer. Anal Chem, 2019, 91(22), 14268–14274.
[154] Giles K, et al. A cyclic ion mobility-mass spectrometry system. Anal Chem, 2019, 91(13), 8564–8573.
[155] Moseley JT, et al. Measurement of transport properties of ions in gases; results for K+ ions in N2. Phys Rev, 1969, 178(1), 234–239.
[156] Kirk AT, et al. A compact high resolution ion mobility spectrometer for fast trace gas analysis. Analyst, 2013, 138(18), 5200–5207.
[157] Ujma J, et al. New high resolution ion mobility mass spectrometer capable of measurements of collision cross sections from 150 to 520 K. Anal Chem, 2016, 88(19), 9469–9478.
[158] Giles K, et al. *Comparison of CCS(N2) Measurements obtained from two different T-WAVE IMS Systems with direct measurements using a drift tube IMS*, in *63rd ASMS conference on mass spectrometry and allied topics*. St. Louis, MO, USA, 2015.
[159] Stow SM, et al. An interlaboratory evaluation of drift tube ion mobility–mass spectrometry collision cross section measurements. Anal Chem, 2017, 89(17), 9048–9055.
[160] Stanford LA, et al. Characterization of compositional changes in vacuum gas oil distillation cuts by electrospray ionization fourier transform–ion cyclotron resonance (FT–ICR) mass spectrometry. Energy Fuels, 2006, 20(4), 1664–1673.
[161] Brantley MR, et al. Automated peak width measurements for targeted analysis of ion mobility unresolved species. Anal Chim Acta, 2016, 941, 49–60.
[162] Zekavat B, Solouki T. Chemometric data analysis for deconvolution of overlapped ion mobility profiles. J Am Soc Mass Spectrom, 2012, 23(11), 1873–1884.
[163] Ahmed A, et al. Elucidating molecular structures of nonalkylated and short-chain alkyl (n < 5, (CH2)n) aromatic compounds in crude oils by a combination of ion mobility and ultrahigh-resolution mass spectrometries and theoretical collisional cross-section calculations. Anal Chem, 2014, 86(7), 3300–3307.
[164] Hanwell MD, et al. Avogadro: An advanced semantic chemical editor, visualization, and analysis platform. J Cheminform, 2012, 4(1), 17.
[165] Niyonsaba E, et al. Recent advances in petroleum analysis by mass spectrometry. Anal Chem, 2019, 91(1), 156–177.
[166] Ponthus J, Riches E. Evaluating the multiple benefits offered by ion mobility-mass spectrometry in oil and petroleum analysis. Int J Ion Mobility Spectrom, 2013, 16(2), 95–103.
[167] Farenc M, et al. Comparison of atmospheric pressure ionization for the analysis of heavy petroleum fractions with ion mobility-mass spectrometry. Energy Fuels, 2016, 30(11), 8896–8903.
[168] Lim D, et al. Application of molecular dynamics simulation to improve the theoretical prediction for collisional cross section of aromatic compounds with long alkyl chains in crude oils. Rapid Commun Mass Spectrom, 2019, 33, 650–656.
[169] Clemmer DE, Jarrold MF. Ion mobility measurements and their applications to clusters and biomolecules. J Mass Spectrom, 1997, 32(6), 577–592.
[170] Mesleh MF, et al. Structural Information from ion mobility measurements: Effects of the long-range potential. J Phys Chem, 1996, 100(40), 16082–16086.
[171] Shvartsburg AA, Jarrold MF. An exact hard-spheres scattering model for the mobilities of polyatomic ions. Chem Phys Lett, 1996, 261(1), 86–91.

[172] Schrader W, Xuan Y, Gaspar A. Studying ultra-complex crude oil mixtures by using high-field asymmetric waveform ion mobility spectrometry (FAIMS) coupled to an electrospray ionisation-LTQ-Orbitrap mass spectrometer. Eur J Mass Spectrom, 2014, 20(1), 43–49.
[173] Vetere A, Schrader W. 1- and 2-photon ionization for online FAIMS-FTMS coupling allows new insights into the constitution of crude oils. Anal Chem, 2015, 87(17), 8874–8879.
[174] Ibrahim YM, et al. Development of an ion mobility spectrometry-Orbitrap mass spectrometer platform. Anal Chem, 2016, 88(24), 12152–12160.
[175] Maire F, et al. Identification of ion series using ion mobility mass spectrometry: The example of alkyl-benzothiophene and alkyl-dibenzothiophene ions in diesel fuels. Anal Chem, 2013, 85(11), 5530–5534.
[176] Sun N, et al. Advanced analytical mass spectrometric techniques and bioassays to characterize untreated and ozonated oil sands process-affected water. Environ Sci Technol, 2014, 48(19), 11090–11099.
[177] Benigni P, Marin R, Fernandez-Lima F. Towards unsupervised polyaromatic hydrocarbons structural assignment from SA-TIMS-FTMS data. Int J Ion Mobility Spectrom, 2015, 18(3), 151–157.
[178] Hagen DF. Characterization of isomeric compounds by gas and plasma chromatography. Anal Chem, 1979, 51(7), 870–874.
[179] Lim D, Ahmed A, Kim S. Comparison of theoretical calculation methods for obtaining collisional cross-section of aromatic compounds. Bull Korean Chem Soc, 2018, 39(8), 999–1002.
[180] Castellanos A, et al. Fast screening of polycyclic aromatic hydrocarbons using trapped ion mobility spectrometry – Mass spectrometry. Anall Methods, 2014, 6(23), 9328–9332.
[181] Uddin N, et al. Gauche effects of glucopyranose by QM/MM-MD simulations. Theor Chem Acc, 2015, 134(11), 122.
[182] Uddin N, et al. Comparative proton transfer efficiencies of hydronium and hydroxide in aqueous solution: Proton transfer vs Brownian motion. J Phys Chem B, 2014, 118(47), 13671–13678.
[183] Parulkar A, et al. Improving hydrodenitrogenation catalyst performance through analyzing hydrotreated vacuum gas oil using ion mobility–mass spectrometry. Ind Eng Chem Res, 2018, 57(27), 8845–8854.
[184] Noestheden MR, et al. Rapid characterization of naphthenic acids using differential mobility spectrometry and mass spectrometry. Environ Sci Technol, 2014, 48(17), 10264–10272.
[185] Becker C, Qian K, Russell DH. Molecular weight distributions of asphaltenes and deasphaltened oils studied by laser desorption ionization and ion mobility mass spectrometry. Anal Chem, 2008, 80(22), 8592–8597.
[186] Koolen HHF, et al. Fullerene separation and identification by traveling wave ion mobility mass spectrometry in laser desorption processes during asphaltene analysis. J Mass Spectrom, 2016, 51(3), 254–256.
[187] Koolen HHF, et al. Integrative mass spectrometry strategy for fingerprinting and tentative structural characterization of asphaltenes. Fuel, 2018, 220, 717–724.
[188] Santos VG, et al. Fullerenes in asphaltenes and other carbonaceous materials: Natural constituents or laser artifacts. Analyst, 2016, 141(9), 2767–2773.
[189] Barrère C, et al. Rapid analysis of lubricants by atmospheric solid analysis probe–ion mobility mass spectrometry. J Mass Spectrom, 2014, 49(8), 709–715.
[190] Santos JM, et al. Petroleomics by ion mobility mass spectrometry: Resolution and characterization of contaminants and additives in crude oils and petrofuels. Anall Methods, 2015, 7(11), 4450–4463.

[191] Da Costa C. Applications of desorption electrospray ionisation mass spectrometry and ion mobility spectrometry to petroleomic and lubricant analysis. Loughborough University, Loughborough, U.K, 2015.
[192] Benigni P, et al. Analysis of photoirradiated water accommodated fractions of crude oils using tandem TIMS and FT-ICR MS. Environ Sci Technol, 2017, 51(11), 5978–5988.
[193] Benigni P, et al. Chemical analysis of water-accommodated fractions of crude oil spills using TIMS-FT-ICR MS. J Visualized Exp: JoVE, 2017, 121, 55352.
[194] Kostyukevich Y, et al. Hydrogen/deuterium exchange in mass spectrometry. Mass Spectrom Rev, 2018, 37(6), 811–853.
[195] Zherebker A, et al. High desolvation temperature facilitates the ESI-source H/D exchange at non-labile sites of hydroxybenzoic acids and aromatic amino acids. Analyst, 2016, 141(8), 2426–2434.
[196] Kostyukevich Y, et al, *Enumeration of non-labile oxygen atoms in dissolved organic matter by use of $^{16}O/^{18}O$ exchange and Fourier transform ion-cyclotron resonance mass spectrometry*. (1618–2650 (Electronic)).
[197] Kostyukevich Y, et al. Enumeration of labile hydrogens in natural organic matter by use of hydrogen/deuterium exchange Fourier transform ion cyclotron resonance mass spectrometry. Anal Chem, 2013, 85(22), 11007–11013.
[198] Kostyukevich Y, et al. Simple atmospheric hydrogen/deuterium exchange method for enumeration of labile hydrogens by electrospray ionization mass spectrometry. Anal Chem, 2013, 85(11), 5330–5334.
[199] Kostyukevich Y, Fau – Kononikhin A, et al, *Separation of tautomeric forms of [2-nitrophloroglucinol-H]- by an in-electrospray ionization source hydrogen/deuterium exchange approach*. (1469-0667 (Print)).
[200] Snyder LR. Petroleum nitrogen compounds and oxygen compounds. Acc Chem Res, 1970, 3 (9), 290–299.
[201] Acter T, et al. Optimization and application of atmospheric pressure chemical and photoionization hydrogen-deuterium exchange mass spectrometry for speciation of oxygen-containing compounds. Anal Bioanal Chem, 2016, 408(12), 3281–3293.
[202] Schaaff TG, Stephenson JL, McLuckey SA. Gas phase H/D exchange kinetics: DI versus D2O. J Am Soc Mass Spectrom, 2000, 11(2), 167–171.
[203] Balbeur D, Dehareng D, De Pauw E. Conformationally driven gas-phase H/D exchange of dinucleotide negative ions. J Am Soc Mass Spectrom, 2007, 18(10), 1827–1834.
[204] Chipuk JE, Brodbelt JS. Gas-phase hydrogen/deuterium exchange of dinucleotides and 5′-monophosphate dinucleotides in a quadrupole ion trap. Int J Mass Spectrom, 2009, 287 (1–3), 87–95.
[205] Trabjerg E, et al. Conformational analysis of large and highly disulfide-stabilized proteins by integrating online electrochemical reduction into an optimized H/D exchange mass spectrometry workflow. Anal Chem, 2015, 87(17), 8880–8888.
[206] Mysling S, et al. Electrochemical reduction of disulfide-containing proteins for hydrogen/deuterium exchange monitored by mass spectrometry. Anal Chem, 2014, 86(1), 340–345.
[207] McLafferty FW, et al. Gaseous conformational structures of cytochrome c. J Am Chem Soc, 1998, 120(19), 4732–4740.
[208] Nagy K, Redeuil K, Rezzi S. Online hydrogen/deuterium exchange performed in the ion mobility cell of a hybrid mass spectrometer. Anal Chem, 2009, 81(22), 9365–9371.
[209] Blum W, et al. On-line hydrogen/deuterium exchange in capillary gas chromatography – chemical ionization mass spectrometry (GC-CIMS) as a means of structure analysis in complex mixtures. Tetrahedron Lett, 1976, 17(7), 565–568.

[210] Stone JA. H–D exchange at low energy in a collision cell between protonated aromatic hydrocarbons and D2O, CD3OD and C6D6. Org Mass Spectrom, 1993, 28(10), 1119–1123.
[211] Wolff J-C, Laures AMF. 'On-the-fly' hydrogen/deuterium exchange liquid chromatography/mass spectrometry using a dual-sprayer atmospheric pressure ionisation source. Rapid Commun Mass Spectrom, 2006, 20(24), 3769–3779.
[212] Ahmed A, Kim S. Atmospheric pressure photo ionization hydrogen/deuterium exchange mass spectrometry – A method to differentiate isomers by mass spectrometry. J Am Soc Mass Spectrom, 2013, 24(12), 1900–1905.
[213] Acter T, et al. Optimization and application of APCI hydrogen-deuterium exchange mass spectrometry (HDX MS) for the speciation of nitrogen compounds. J Am Soc Mass Spectrom, 2015, 26(9), 1522–1531.
[214] Hemling ME, et al. Gas phase hydrogen/deuterium exchange in electrospray ionization mass spectrometry as a practical tool for structure elucidation. J Am Soc Mass Spectrom, 1994, 5 (5), 434–442.
[215] Kostyukevich Y, et al. Investigation of bio-oil produced by hydrothermal liquefaction of food waste using ultrahigh resolution Fourier transform ion cyclotron resonance mass spectrometry. Eur J Mass Spectrom, 2017, 24(1), 116–123.
[216] Acter T, et al. Design and validation of in-source atmospheric pressure photoionization hydrogen/deuterium exchange mass spectrometry with continuous feeding of D2O. J Am Soc Mass Spectrom, 2018, 29(1), 85–94.
[217] Lee S, Cho Y, Kim S. Development and application of a software tool for the interpretation of organic mixtures' spectra – hydrogen deuterium exchange (STORM-HDX) to interpret APPI HDX MS spectra. Bull Korean Chem Soc, 2014, 35(3), 749–752.
[218] Lewis GN. A simple type of isotopic reaction. J Am Chem Soc, 1933, 55(8), 3502–3503.
[219] Sheinblatt M. Determination of an acidity scale for peptide hydrogens from nuclear magnetic resonance kinetic studies. J Am Chem Soc, 1970, 92(8), 2505–2509.
[220] Wüthrich K, Wagner G. Nuclear magnetic resonance of labile protons in the basic pancreatic trypsin inhibitor. J Mol Biol, 1979, 130(1), 1–18.
[221] Wagner G, Wüthrich K. Amide proton exchange and surface conformation of the basic pancreatic trypsin inhibitor in solution: Studies with two-dimensional nuclear magnetic resonance. J Mol Biol, 1982, 160(2), 343–361.
[222] Konermann L, Pan J, Liu Y-H. Hydrogen exchange mass spectrometry for studying protein structure and dynamics. Chem Soc Rev, 2011, 40(3), 1224–1234.
[223] Shi X, et al. Hydrogen exchange-mass spectrometry measures stapled peptide conformational dynamics and predicts pharmacokinetic properties. Anal Chem, 2013, 85(23), 11185–11188.
[224] Li KS, et al. Hydrogen-deuterium exchange and hydroxyl radical footprinting for mapping hydrophobic interactions of human bromodomain with a small molecule inhibitor. J Am Soc Mass Spectrom, 2019, 30(12), 2795–2804.
[225] Hunt DF, Russell JW, Torian RL. Chemical ionization mass spectrometry studies: V. Some transition metal organometallic compounds. J Organomet Chem, 1972, 43(1), 163–173.
[226] Hunt DF, Sethi SK. Gas-phase ion/molecule isotope-exchange reactions: Methodology for counting hydrogen atoms in specific organic structural environments by chemical ionization mass spectrometry. J Am Chem Soc, 1980, 102(23), 6953–6963.
[227] Kostyukevich Y, et al. In-ESI source hydrogen/deuterium exchange of carbohydrate ions. Anal Chem, 2014, 86(5), 2595–2600.
[228] Wolf C, et al. Elucidation of the presence and location of t-Boc protecting groups in amines and dipeptides using on-column H/D exchange HPLC/ESI/MS. J Am Soc Mass Spectrom, 2005, 16(4), 553–564.

[229] Katta V, Chait BT. Hydrogen/deuterium exchange electrospray ionization mass spectrometry: A method for probing protein conformational changes in solution. J Am Chem Soc, 1993, 115 (14), 6317–6321.
[230] Mandell JG, Falick AM, Komives EA. Measurement of amide hydrogen exchange by MALDI-TOF mass spectrometry. Anal Chem, 1998, 70(19), 3987–3995.
[231] Jeong ES, et al, *Online Simultaneous Hydrogen/Deuterium Exchange of Multitarget Gas-Phase Molecules by Electrospray Ionization Mass Spectrometry Coupled with Gas Chromatography*. (1520-6882 (Electronic)).
[232] Cho Y, et al. Supercritical fluid chromatography coupled with in-source atmospheric pressure ionization hydrogen/deuterium exchange mass spectrometry for compound speciation. J Chromatogr A, 2016, 1444, 123–128.
[233] Rand KD, Jørgensen TJD. Development of a peptide probe for the occurrence of hydrogen (1H/2H) scrambling upon gas-phase fragmentation. Anal Chem, 2007, 79(22), 8686–8693.
[234] Iacob RE, Murphy Iii JP, Engen JR. Ion mobility adds an additional dimension to mass spectrometric analysis of solution-phase hydrogen/deuterium exchange. Rapid Commun Mass Spectrom, 2008, 22(18), 2898–2904.
[235] Atzrodt J, et al. The Renaissance of H/D Exchange. Angewandte Chem Int Ed, 2007, 46(41), 7744–7765.
[236] Nicholson K. Isotope chemistry. In: Nicholson K, Editor. Geothermal fluids: Chemistry and exploration techniques. Springer Berlin Heidelberg, Berlin, Heidelberg, 1993, 117–137.
[237] Hourani N, et al. Atmospheric pressure chemical ionization Fourier transform ion cyclotron resonance mass spectrometry for complex thiophenic mixture analysis. Rapid Commun Mass Spectrom, 2013, 27(21), 2432–2438.
[238] Purcell JM, et al, *Atmospheric pressure photoionization proton transfer for complex organic mixtures investigated by fourier transform ion cyclotron resonance mass spectrometry*. (1044-0305 (Print)).
[239] Kekäläinen T, et al. Compositional study of polar species in untreated and hydrotreated gas oil samples by electrospray ionization Fourier transform ion cyclotron resonance mass spectrometry (ESI FTICR–MS). Energy Fuels, 2009, 23(12), 6055–6061.
[240] Ruddy BM, et al. Targeted petroleomics: Analytical investigation of Macondo well oil oxidation products from Pensacola Beach. Energy Fuels, 2014, 28(6), 4043–4050.
[241] Rodgers RP, Marshall AG. *Petroleomics: Advanced characterization of petroleum-derived materials by Fourier transform ion cyclotron resonance mass spectrometry (FT-ICR MS)*, in *Asphaltenes, heavy oils, and petroleomics*. Mullins OC, et al Editors, Springer New York, New York, NY, 2007, 63–93.
[242] Zhang T, et al. Transformation of nitrogen compounds in deasphalted oil hydrotreating: Characterized by electrospray ionization Fourier transform-ion cyclotron resonance mass spectrometry. Energy Fuels, 2013, 27(6), 2952–2959.
[243] Zhang Y, et al. Specification of the nitrogen functional group in a hydrotreated petroleum molecule using hydrogen/deuterium exchange electrospray ionization high-resolution mass spectrometry. Analyst, 2020, 145(13), 4442–4451.
[244] Junk T, Catallo WJ. Preparative supercritical deuterium exchange in arenes and heteroarenes. Tetrahedron Lett, 1996, 37(20), 3445–3448.
[245] Smith RM, *Superheated water: the ultimate green solvent for separation science*. (1618-2642 (Print)).
[246] Kostyukevich Y, et al. Speciation of structural fragments in crude oil by means of isotope exchange in near-critical water and Fourier transform mass spectrometry. Anal Bioanal Chem, 2019, 411(15), 3331–3339.

[247] Wang X, Schrader W. Selective analysis of sulfur-containing species in a heavy crude oil by deuterium labeling reactions and ultrahigh resolution mass spectrometry. Int J Mol Sci, 2015, 16(12), 30133–30143.
[248] Choi -S-S, Kim J-C. Deuterium effect on ionization and fragmentation patterns of monosaccharides ionized by atmospheric pressure chemical ionization. Carbohydr Res, 2010, 345(3), 408–413.
[249] Davies NW, et al. Hydrogen/deuterium exchange on aromatic rings during atmospheric pressure chemical ionization mass spectrometry. Rapid Commun Mass Spectrom, 2010, 24 (7), 1105–1110.
[250] Hunt DF, McEwen CN, Upham RA. Determination of active hydrogen in organic compounds by chemical ionization mass spectrometry. Anal Chem, 1972, 44(7), 1292–1294.
[251] Kim E, et al. Structural elucidation of nitrogen-containing compounds in polar fractions using double bond equivalence distributions and hydrogen–deuterium exchange mass spectra. Fuel, 2017, 194, 503–510.
[252] Watkins MA, et al. Ion–molecule reactions for mass spectrometric identification of functional groups in protonated oxygen-containing monofunctional compounds. Anal Chem, 2004, 76 (4), 964–976.
[253] Islam A, et al. Structure-dependent degradation of polar compounds in weathered oils observed by atmospheric pressure photo-ionization hydrogen/deuterium exchange ultrahigh resolution mass spectrometry. J Hazard Mater, 2015, 296, 93–100.
[254] Schrader W, Klein H-W. Liquid chromatography/Fourier transform ion cyclotron resonance mass spectrometry (LC-FTICR MS): An early overview. Anal Bioanal Chem, 2004, 379(7), 1013–1024.
[255] Cho E, et al. Application of FT-ICR MS equipped with quadrupole detection for analysis of crude oil. Anal Chem, 2017, 89(22), 12101–12107.
[256] Qian Y, et al. Multiple reaction monitoring of GC/MS/MS analysis of terpanes and its application to petroleum exploration. Petrol Sci Technol, 2017, 35(2), 134–140.
[257] Hsu CS. Mass resolving power requirement for molecular formula determination of fossil oils. Energy Fuels, 2012, 26(2), 1169–1177.
[258] Li Z, Valentine SJ, Clemmer DE. Complexation of amino compounds by 18C6 improves selectivity by IMS-IMS-MS: Application to petroleum characterization. J Am Soc Mass Spectrom, 2011, 22(5), 817.
[259] Maurer MM, Donohoe GC, Valentine SJ. Advances in ion mobility-mass spectrometry instrumentation and techniques for characterizing structural heterogeneity. Analyst, 2015, 140(20), 6782–6798.
[260] Gabelica V, et al. Recommendations for reporting ion mobility Mass Spectrometry measurements. Mass Spectrom Rev, 2019, 38(3), 291–320.
[261] Giles K, et al. Design and utility of a multi-pass cyclic ion mobility separator. In: 62nd ASMS Conference on mass spectrometry and allied topics. Baltimore, MD, 2014.
[262] Fasciotti M, et al. Separation of isomeric disaccharides by traveling wave ion mobility mass spectrometry using CO2 as drift gas. J Mass Spectrom, 2012, 47(12), 1643–1647.
[263] Lalli PM, et al. Resolution of isomeric multi-ruthenated porphyrins by travelling wave ion mobility mass spectrometry. Rapid Commun Mass Spectrom, 2012, 26(3), 263–268.
[264] Lalli PM, et al. Baseline resolution of isomers by traveling wave ion mobility mass spectrometry: Investigating the effects of polarizable drift gases and ionic charge distribution. J Mass Spectrom, 2013, 48(9), 989–997.
[265] Huang Y, Dodds ED. Ion mobility studies of carbohydrates as Group I adducts: Isomer specific collisional cross section dependence on metal ion radius. Anal Chem, 2013, 85(20), 9728–9735.

[266] Barrère C, et al. Atmospheric solid analysis probe–ion mobility mass spectrometry of polypropylene. Anal Chem, 2012, 84(21), 9349–9354.
[267] Ihlenborg M, et al. A comparative study of APLI and APCI in IMS at atmospheric pressure to reveal and explain peak broadening effects by the use of APLI. Analyst, 2015, 140(22), 7565–7571.
[268] Forsythe JG, et al. Collision cross section calibrants for negative ion mode traveling wave ion mobility-mass spectrometry. Analyst, 2015, 140(20), 6853–6861.
[269] Cho E, et al. Comprehensive lists of internal calibrants for ultrahigh-resolution mass spectrometry analysis of crude oil and natural organic matter and their preparation recipes. J Am Soc Mass Spectrom, 2021, 32(2), 590–596.
[270] Acter T, et al. Application of silver-assisted laser desorption ionization ultrahigh-resolution mass spectrometry for the speciation of sulfur compounds. Anal Bioanal Chem, 2020, 412(1), 243–255.

Kawthar Z. Alzarieni, Hilkka I. Kenttämaa

13 The distillation precipitation fractionation mass spectrometry (DPF-MS) method for molecular profiling of crude oil

Abstract: Crude oil is an exceedingly complex mixture of various hydrocarbons and, to a lesser extent, heteroatom-containing compounds. Their chemical characterization at the molecular level is challenging. Most of the existing chemical analysis methods require fractionation of the crude oil to generate mixtures with less complexity. One of the most commonly used crude oil fractionation methods is a method called SARA, which involves separation of crude oil into four fractions containing predominantly saturated hydrocarbons, aromatic compounds, resins and asphaltenes. The fractions are typically subjected to gravimetric analysis. A limitation of this method is that the fractions contain combinations of different compound classes and therefore are still rather complex mixtures. The distillation precipitation fractionation mass spectrometry (DPF-MS) method, the focus of this review, was developed in 2018 for the molecular-level characterization of crude oil. This method involves the separation of the crude oil into six different fractions containing chemically similar compounds: volatile hydrocarbons, asphaltenes, heavy saturated hydrocarbons, alkyl aromatic hydrocarbons, heteroaromatic compounds, and polar compounds. The gravimetric percentages of all six fractions are determined. After the separation, each fraction is analyzed by utilizing a medium- or high-resolution mass spectrometric method optimized for the types of compounds each fraction contains. This approach enables the ionization of each analyte to yield only one type of an ion that contains the intact analyte molecule, with minimal or no associated fragmentation. Furthermore, the separation enables the ionization of the analytes in each fraction at a similar efficiency, making the method semiquantitative. The high-resolution mass spectrometry data obtained can be used to draw conclusions about the chemical composition of each fraction and of the crude oil as a whole. For example, the gravimetric percentages of specific chemical compound classes can be obtained, such as saturated hydrocarbons, aromatic hydrocarbons, and nitrogen-, oxygen- and sulfur-containing compounds etc. Furthermore, the degree of unsaturation (from the measured ring and double bond equivalent) of the compounds and their average molecular weights can be determined. The DPF-MS method has been used to characterize crude oil samples of different API gravities, ranging from heavy to medium and light crude oil. This

Kawthar Z. Alzarieni, Hilkka I. Kenttämaa, Department of Chemistry, Purdue University, West Lafayette, IN 47907, USA

https://doi.org/10.1515/9783110694529-013

chapter focuses on the development of the DPF-MS method and on its applications in molecular profiling of crude oil and other petroleum products.

13.1 Introduction

Better knowledge on the chemical composition of crude oil samples with different origins would facilitate the development of more efficient and economic recovery and refinery processes [1]. Additionally, this could improve the understanding of the interfacial interactions between the compounds in the crude oil and surfactants with reservoir rocks, which is necessary to improve the currently used crude oil recovery methods [2]. Further, this may facilitate the identification of certain chemical biomarkers that reveal information on the origin and parent materials of the crude oil for better understanding of its geochemical characteristics [3]. However, obtaining molecular-level information on crude oil is challenging due to its extremely complex nature [4]. Mass spectrometry is the only analytical method that can be used to obtain information on specific compounds in such mixtures. However, their complexity causes many problems even for mass spectrometry, and more specifically, for ionization of all the compounds in the mixtures. For example, competition between different compounds for the charge during ionization leads to ionization biases. Further, fragmentation of the generated ions is common, which complicates the data even further. These issues may reduce the ability of detecting a particular group of compounds in favor of detecting another group more efficiently.

The oldest ionization method, electron ionization (EI), has the benefit of being the only universal ionization method in mass spectrometry (all organic compounds get ionized). However, it has the disadvantage of causing extensive fragmentation, and in particular, to aliphatic compounds. Among the milder evaporation/ionization methods available for commercial mass spectrometers, atmospheric pressure chemical ionization (APCI) can be used for the ionization of both polar and nonpolar, thermally stable compounds [5] while atmospheric pressure photoionization (APPI) is commonly used for aromatic compounds [6] and electrospray ionization (ESI) for polar, thermally labile compounds [7]. Some of the limitations of the above ionization methods were illustrated by Kenttämaa et al. [8] when they prepared an equimolar mixture of model compounds representing the main compound types in crude oil, including an alkane (pentadecane), two cycloalkanes (cycloheptane and methylcyclopentane), an alkene (1-decene), an alkyne (1-hexyne) and two alkyl aromatic compounds (*n*-decylbenzene and *n*-hexylbenzene). The mixture was analyzed by using positive-ion mode APCI and APPI under conventional experimental conditions by using a linear quadrupole ion trap mass spectrometer. However, carbon disulfide was chosen as the solvent for the mixture. Unlike common solvents, such as water or methanol, that did not completely dissolve the mixture, the mixture was completely soluble in carbon disulfide. Positive-ion mode APPI and APCI of analytes in carbon

disulfide solvent should generate exclusively molecular radical cations and their fragments. Both APCI and APPI mass spectra (Figure 13.1) show that the linear alkane (pentadecane) had completely fragmented (generating ions of m/z 57, 71, and 85), illustrating the difficulty in obtaining molecular weight (MW) information for linear alkanes when using these ionization methods. For the alkene (1-decene), a stable molecular ion was generated. However, fragmentation was extensive, producing fragment ions of m/z 57 and 70. The fragment ions were as abundant as the molecular ion. A stable molecular ion was also observed for the alkyne but it was associated with only minor fragmentation. The two alkyl aromatic compounds mostly generated stable molecular ions [$M^{+\cdot}$] with minimal fragmentation. The molecular ions obtained for the two compounds were nearly equally abundant for APCI but not APPI, and they were more abundant than those for the alkene and alkyne. The cycloalkanes generated stable

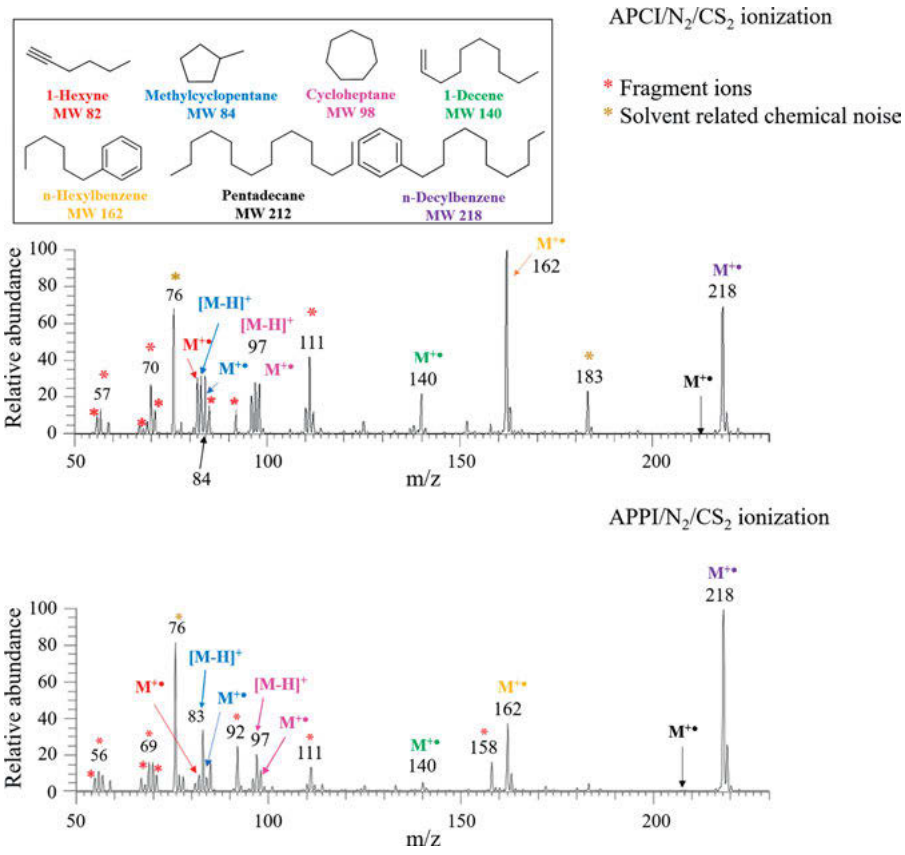

Figure 13.1: A) An APCI/N_2 (with N_2 being the sheath gas)/CS_2 and B) an APPI/N_2/CS_2 mass spectrum measured for an equimolar (1 mM) mixture of seven nonpolar model compounds of the type that are typically present in crude oils [8]. Figure modified from reference [8].

molecular ions and fragment ions of m/z 56 as well as $[M\text{-}H]^+$ molecular ions that had lost a hydrogen radical. The generation of different types of ions for each analyte complicates data analysis. Therefore, accurate characterization of this mixture based on these data would be impossible. Additionally, the compounds that produced abundant molecular ions without extensive fragmentation showed different molecular ion abundances (except for the two aromatic compounds upon APCI) even though the corresponding neutral compounds had the same concentrations in the analyzed solution. Based on these results, the APCI ionization method appears to be a good method for the analysis of aromatic compounds, which has been confirmed in the literature [5, 9, 10], but not for the other types of compounds in the mixture. APPI does not appear to have any advantages over APCI.

The limitations of the ESI method were demonstrated in a study that used positive-ion mode ESI to analyze a mixture that contained tetracosane (a linear alkane), 5-*R*-cholestane (a cyclic alkane), squalane (a branched alkane), coronene (a polyaromatic hydrocarbon), and 2,9-dimethyl-4,7-diphenyl-1,10-phenanthroline (a *N*-heteroaromatic compound) in a linear quadrupole ion trap mass spectrometer (9). ESI only generated ions from 2,9-dimethyl-4,7-diphenyl-1,10-phenanthroline (via protonation), the most polar component in the mixture [11]. None of the other mixture components were detected. Therefore, positive-ion mode ESI has a strong bias toward the most basic compounds in the mixture.

In order to address the above ionization issues, fractionation of the crude oil to simpler mixtures before mass spectrometric analysis is required [12]. The most commonly used method for the fractionation of crude oil is the "saturated hydrocarbons, aromatic compounds, resins and asphaltenes" (SARA) method in which the crude oil is separated into four different fractions [13]. The SARA method is used for gravimetric fractionation and the fractions are typically not further analyzed. This approach starts with the precipitation of asphaltenes. The remaining compounds (maltenes) are chromatographically separated into three fractions called "saturated hydrocarbons," "aromatic compounds," and "resins," to generate a total of four fractions. However, this method does not enable the determination of the amount of volatile hydrocarbons. Furthermore, the generated fractions are still relatively complex mixtures of different types of compounds. For example, the fraction called "saturated hydrocarbons" has been demonstrated to contain a considerable amount of aromatic compounds [8]. Therefore, the weights of the "saturated hydrocarbon" and "aromatic compound" fractions do not provide an accurate estimate for the amount of saturated hydrocarbons and aromatic compounds in the sample. Further, the fraction called resins contains many different types of compounds.

Over the years, several other fractionation methods have been developed for crude oil samples. For example, a preparative high-performance liquid chromatography (HPLC)-based fractionation method was developed by Bissada et al. [10, 11]. This method involved the use of an automated two-dimensional HPLC to separate a crude oil into SARA-like fractions although their ability to separate saturated

hydrocarbons and aromatic compounds from each other was much better than for SARA. The fractions were collected and analyzed by using gas chromatography equipped with a flame ionization detector (GC/FID), gas chromatography equipped with a photoionization detector (GC/PID) and gas chromatography/positive-ion mode electron ionization quadrupole mass spectrometry ((GC/(+) EI quadrupole (Q) MS) to determine the extent of cross contamination between the fractions. However, compound identification was hindered by the inability of the GC method to completely separate the polar compounds in the resin and asphaltenes fractions and by the poor resolution and mass accuracy of the (+) EI Q MS method. Furthermore, no model compounds were used to verify the preliminary identifications. Additionally, the method does not allow quantitation and analysis of volatile hydrocarbons as most of these compounds were lost during processing. Volatile hydrocarbon losses of up to 35% were reported [14].

The distillation precipitation fractionation mass spectrometry (DPF-MS) method was developed in 2018 by Kenttämaa et al. to help alleviate the above problems associated with the molecular-level characterization of crude oil samples [8, 15]. The basic idea behind the DPF-MS method is that different types of compounds need different ionization methods for accurate mass spectrometric analysis, and that there are no universal mass spectrometry methods that would work equally well for all the diverse compound types in crude oil. Therefore, the crude oil should first be fractionated into different compound types so that a different analysis method can then be developed for each compound type [8]. Indeed, the DPF part of the above method involves the fractionation of crude oil samples into six major compound classes depending on the differences in their volatility, solubility, and polarity: volatile hydrocarbons, asphaltenes, heavy saturated hydrocarbons, alkyl aromatic hydrocarbons, heteroaromatic compounds, and polar compounds. These fractions are much simpler than those generated using SARA or similar methods, and they are largely compound specific. Therefore, their mass percentages in the crude oil are also more meaningful. Furthermore, as each fraction contains *predominantly* one compound type, optimization of an ionization method for mass spectrometric analysis of each fraction is now possible.

13.2 Development of the distillation precipitation fractionation (DPF) mass spectrometry (MS) method

The DPF-MS method was developed to achieve a more comprehensive analysis of crude oil than previously possible. Unlike most of the previous crude oil fractionation methods [12, 14, 16], the DPF part of the method included an initial room-

temperature vacuum distillation to separate the volatile hydrocarbons from the crude oil. These compounds are usually lost when using literature methods. After removal of the volatile hydrocarbons, the asphaltenes were precipitated out of the mixture by using a simple and effective methodology that had been developed earlier for this task [17]. In this work, asphaltenes are defined as compounds not soluble in *n*-hexane [18]; therefore, the sample was mixed with *n*-hexane in a 1:10 (v/v) oil:*n*-hexane ratio, and was then sonicated for 20 min. Then it was left undisturbed in a sealed container overnight to allow the asphaltenes to precipitate. The sample mixture was filtered through a membrane filter that retained the asphaltenes. After a crude oil sample was treated in this manner, the soluble portion (maltenes), was then separated based on the polarity of the compounds in it by using flash-column chromatography equipped with both UV and evaporative light scattering (ELS) detectors and by using *n*-hexane, dichloromethane and 2-propanol as the eluents. This treatment yielded three distinct fractions. A typical auto-column chromatogram measured for a crude oil sample is shown in Figure 13.2.

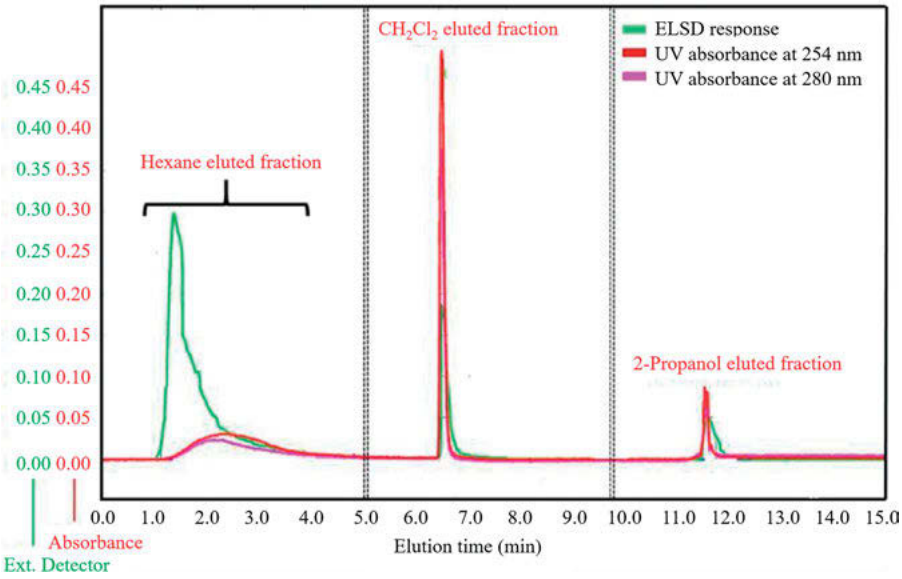

Figure 13.2: A typical auto-column ELSD/UV chromatogram of maltenes indicating their separation into three distinct fractions. The presence of both ELSD and UV signals in the later eluting part of the n-hexane-eluted fraction indicates co-elution of aliphatic (no UV absorption: green trace) and aromatic compounds (UV absorption: red and purple traces) [8]. The strong UV peak (red trace) for the dichloromethane-eluted fraction indicates the presence of aromatic compounds. The most polar compounds eluted last with 2-propanol. Figure modified from reference [8].

The most nonpolar fraction (eluted using *n*-hexane) of the crude oil sample tested when developing the DPF-MS method was discovered to contain both aliphatic and

aromatic compounds as it gave different signals in the two autocolumn detectors: a large signal in the ELS detector for saturated hydrocarbons and a smaller signal on the UV detector, indicating the presence of aromatic compounds (Figure 13.2). This fraction was further analyzed using GCxGC/(+) EI time-of-flight mass spectrometry (Figure 13.3A), which verified the proposal that the fraction contained two different compound classes. Therefore, this fraction was further separated into two different fractions by using solid-phase extraction chromatography based on a Si/CN-S-1.5 g cartridge, from which the heavy saturated hydrocarbons were eluted with *n*-hexane and the alkyl aromatic hydrocarbons with a 3:1 mixture of dichloromethane:*n*-hexane [19]. The GCxGC/(+) EI MS analysis (Figure 13.3B) was performed to verify that the first of these fractions, that obtained using *n*-hexane as the eluent, contained almost exclusively saturated hydrocarbons. After the separation, the solvents were removed from each of the fractions by means of a rotary evaporator and initial analysis of the fractions was performed using IR spectroscopy.

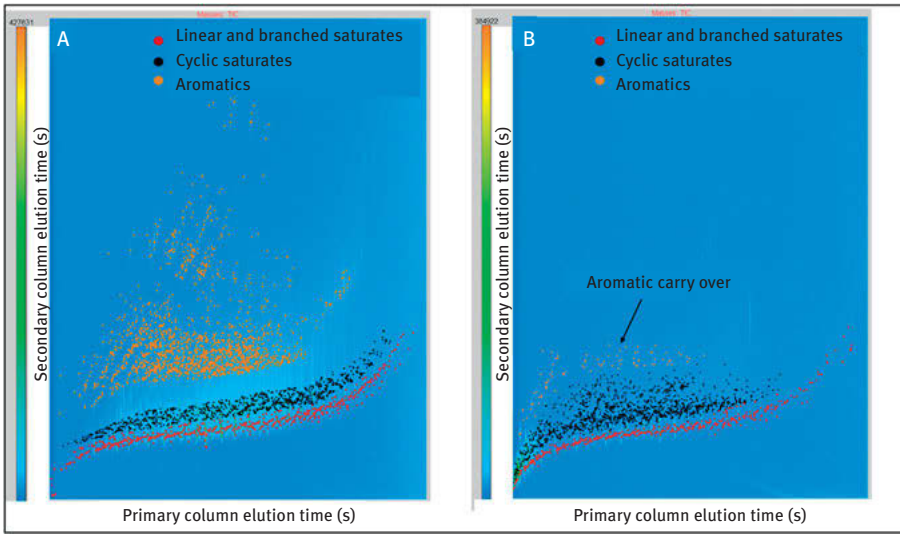

Figure 13.3: A) Total ion chromatogram measured using GCxGC/(+)EI TOF for the hexane-eluted fraction of a crude oil sample before SPE fractionation. B) Heavy saturated compounds separated from the n-hexane-eluted fraction by using solid phase extraction. Eight percent carryover of aromatic compounds into the heavy saturated compound was observed. Linear, branched, and cyclic saturated and aromatic compounds are color-coded. Figure modified from reference [8].

To explore the types of compounds in each of the six fractions, Fourier-transform infrared spectroscopy (FTIR) was used to help identify the predominant compound classes in each fraction (Figure 13.4). Table 13.1 summarizes the absorption frequency bands observed and the corresponding functionalities in the

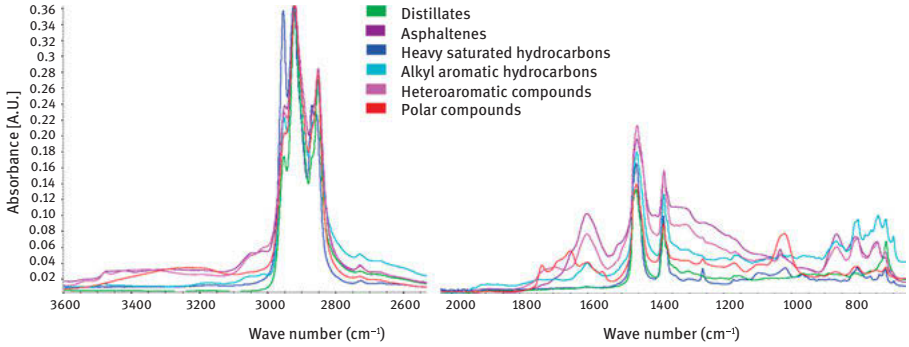

Figure 13.4: FTIR spectra from 3,600–2,600 cm^{-1} (left) and 2,000–600 cm^{-1} (right) measured for the crude oil fractions generated by the DPF method. Figure modified from reference [8].

mixture components. The IR spectra measured for the volatile hydrocarbon and the heavy saturated hydrocarbon fractions indicate that saturated hydrocarbons are predominantly present in these fractions. Spectral analysis of the asphaltenes and the dichloromethane eluted compounds revealed the presence of heteroatoms and significant aromaticity. The spectrum measured for light aromatic hydrocarbons indicated the presence of only alkyl aromatic compounds. The isopropanol-eluted compounds were found to contain heteroatoms and have minimal aromaticity (polar compounds). The generation of the fractions and the types of compounds in each fraction obtained by using the DPF method for the crude oil sample are summarized in Figure 13.5.

Table 13.1: FTIR absorption bands and their functional group assignments.

Functional group	Absorption band (cm^{-1})
C = C-H aromatic stretch	3,020–3,100
CH_3 asymmetric and symmetric stretch	2,950 and 2,872
CH_2 asymmetric and symmetric stretch	2,920 and 2,830
C = O stretch	1,700
NH_2 bending vibrations	1,650–1,550
C = C stretch	1,600
CH_3 or CH_2 deformations	1,460
CH_3 deformation	1,380
C–O stretch	970–1,250
Aromatic C–H deformation (“oop” bands)	900–730

After identification of the different compound classes present in the six crude oil fractions, model compound mixtures were used to optimize a mass spectrometric ionization method for each fraction so that only one type of an ion containing the

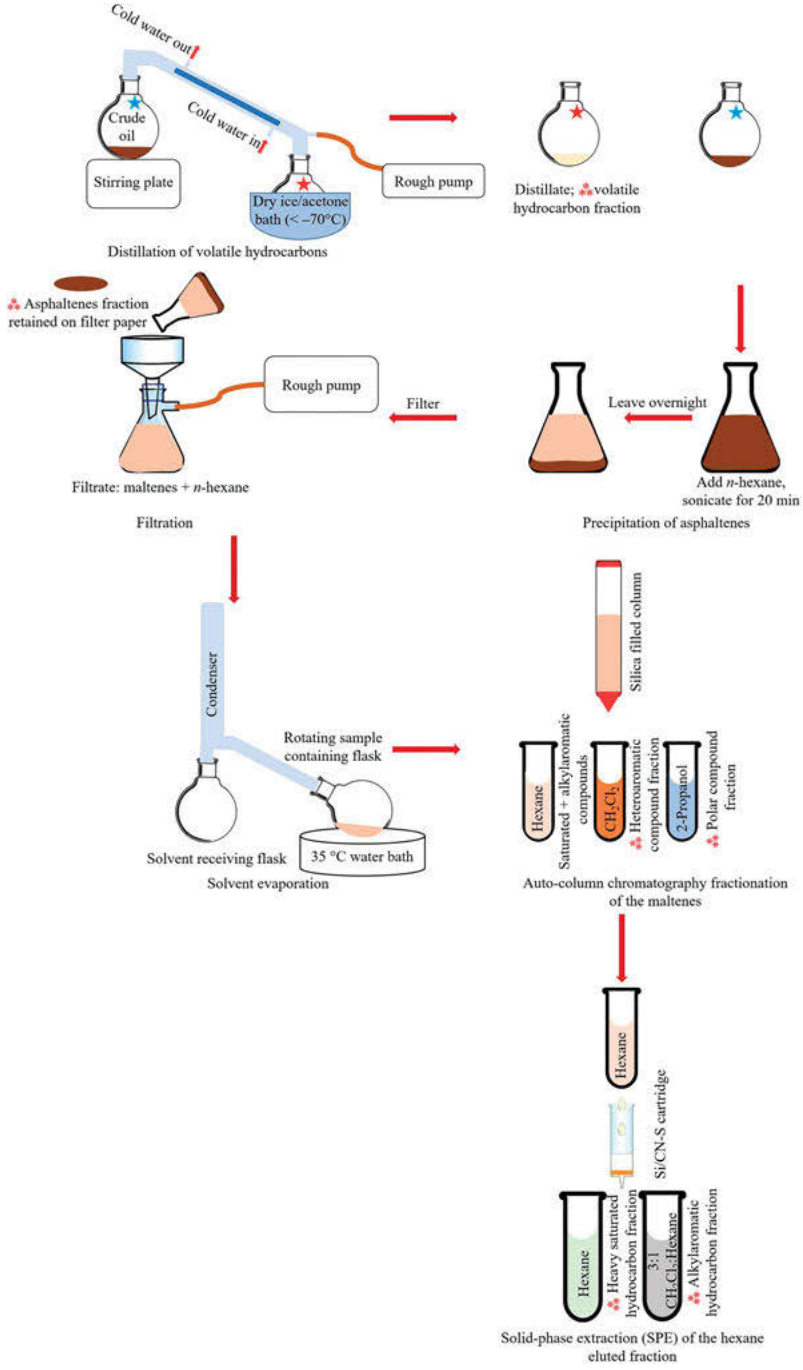

Figure 13.5: Schematic of the work layout of the DPF method. DPF fractions are designated by ⁂.

intact analyte molecule, generated without fragmentation, was formed for each analyte. Different ionization methods and various solvents were tested on model compound mixtures representing each fraction in order to choose the most suitable ionization method and solvent(s) [8].

Two-dimensional gas chromatography (GCxGC) coupled with positive-ion mode electron ionization ((+) EI) medium-resolution time-of-flight mass spectrometry (GC × GC/(+) EI TOF MS) was selected for the analysis of the volatile hydrocarbon fraction due to the great separation power of GCxGC [20] and the ability of the EI method to ionize all organic compounds. The sample was dissolved in high-purity *n*-pentane to a mass ratio of 1.0 wt/wt% [21]. An auto injector was used to introduce 0.5 μL of the sample into a split/splitless injector at a split ratio of 1 to 20 under a constant flow of helium carrier gas (1.25 mL/min) at a temperature of 260 °C. The compounds were separated by using high temperature columns that could withstand temperatures up to 430 °C. The first column was a polar 60 m capillary column (ZB-1HT Inferno, Zebron) and the second a nonpolar 2 m capillary column (ZB-35HT Inferno, Zebron). The primary oven containing the first, polar column was held at 35 °C for one minute. After that, the oven was heated to 55 °C at a rate of 1 °C/min, followed by heating to a maximum temperature of 175 °C at a rate of 3 °C/min. The oven was held at the maximum temperature of 175 °C for 3 min. A quad-jet dual stage thermal modulator consisting of two hot jets and two cold jets was placed between the two columns. Each stage had one hot and one cold jet pair. The modulator focuses the bands of the compounds eluting from the first column and introduces them sequentially into the second column. Liquid nitrogen was used for cooling the cold jets and heated nitrogen gas was used for the hot jets. A total modulation time of 3.5 s was split equally between the two stages (1.75 s each), 0.6 s of which was used for the hot jet pulse and 1.15 s for the cold jet pulse. A modulator temperature 80 °C greater than the temperature of the secondary oven containing the nonpolar column was used. The secondary oven offset was 10 °C greater than that of the primary oven and it was subjected to the same temperature program as the primary oven. The transfer line between the GC × GC and the TOF MS was held at 300 °C throughout the analysis. The MS ion source was heated to 250 °C. The eluting compounds were ionized by (+) EI with 70 eV electron kinetic energy. All ions were transferred into the TOF MS for medium-resolution analysis (25,000 resolution at m/z 219). The availability of extensive EI mass spectral libraries allowed the identification of many of the compounds in the volatile hydrocarbon fraction of the crude oil studied. Most of the detected compounds in the volatile hydrocarbon fraction of the crude oil analyzed by Kenttämaa et al. were found to be alkanes and cycloalkanes containing 7–10 carbons [8, 21].

The ability to use the above method for the identification of volatile hydrocarbons and determination of their elemental composition as well as their semiquantitative analysis has been evaluated earlier by using a model compound mixture [22]. The mixture consisted of 25 compounds that represented all major categories of compounds

found in jet fuels. The model compound mixture was dissolved in high-purity *n*-hexane to achieve a concentration of 10 mM for each mixture component. GCxGC was able to fully resolve all mixture components. The quantitative analysis of the mixture components was based on the GCxGC peak area of each compound relative to the sum of all detected peak areas. Data processing and analysis were performed via LECO Visual Basic Scripting (VBS) software, ChromaTOF version 5.10.58.0.52262. The software automatically provided the peak areas that were extracted to a Microsoft Excel sheet for further analyses.

Linear quadrupole ion trap/high-resolution Orbitrap mass spectrometry (LQIT/Orbitrap HRMS) coupled with atmospheric pressure chemical ionization in the positive ion mode ((+) APCI) was used to optimize the ionization for the remaining five fractions as this method can be used to successfully ionize a wide variety of analytes. Optimization was accomplished using different sheath gases and solvents or solvent systems and tested by using model compound mixtures [8].

For asphaltenes and alkyl aromatic hydrocarbon and heteroaromatic compound fractions, carbon disulfide was selected as the solvent and APCI reagent and nitrogen as the sheath and auxiliary gas as this combination had been demonstrated in the literature to be suitable for the ionization of aromatic compounds, as discussed above. These compounds are ionized at similar efficiencies and they predominantly generate stable molecular cations [$M^{+\bullet}$] with minimal fragmentation [5], as illustrated in Figure 13.6 for a mixture of aromatic model compounds [8]. The use of other solvents besides carbon disulfide did not lead to equally good results (Figure 13.6).

Different solvent systems and sheath gases were tested for the heavy saturated hydrocarbon fraction and the polar compound fraction in order to identify an optimal ionization method for each. The APCI/N_2/CS_2 method is not suitable for the heavy saturated hydrocarbon fraction as it results in significant fragmentation and has a different ionization efficiency for different saturated hydrocarbons (Figure 13.7B) [8]. Instead, *n*-hexane was used as the solvent and APCI reagent while oxygen was employed in place of nitrogen as the nebulizing gas (for safety precautions, please see the publication). These conditions are known to predominantly produce $[M\text{-}H]^+$ ions [23] with minimal fragmentation for saturated hydrocarbons, as demonstrated in Figure 13.7A.

A model compound mixture of nonaromatic oxygen-, nitrogen-, or sulfur-containing polar compounds was used to simulate the behavior of the polar compound fraction. For this mixture, APCI with 3:1 methanol:*n*-hexane solvent system and nitrogen as the sheath and auxiliary gases were found to be the optimal ionization method. This approach predominantly generates stable $[M + H]^+$ ions with similar relative abundances for these analytes (Figure 13.8) [8].

The optimal APCI conditions for each compound class (fraction) are shown in Table 13.2. The high-resolution mass spectrometry instruments and the optimized ionization methods used for each crude oil fraction are summarized in Figure 13.9.

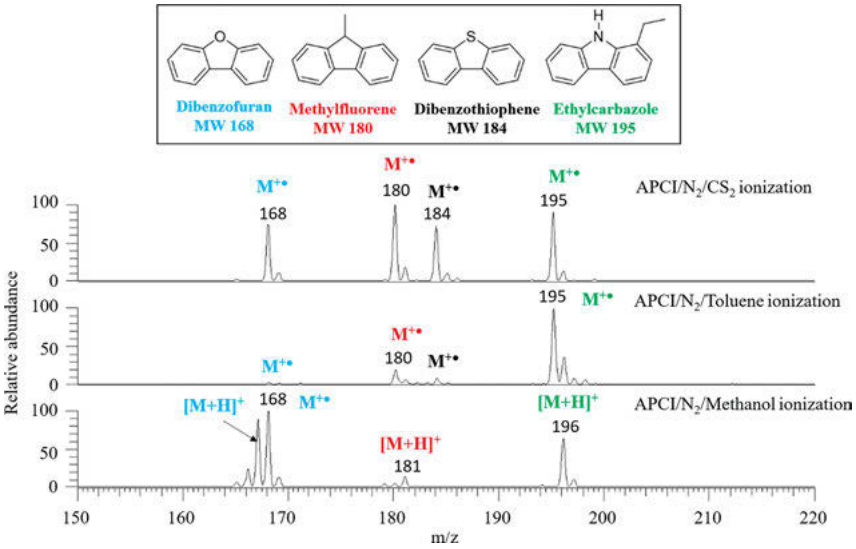

Figure 13.6: (+) APCI/N_2/CS_2, (+) APCI/N_2/toluene and (+) APCI/N_2/methanol mass spectra measured for an equimolar mixture (1 mM) of aromatic and heteroaromatic model compounds. While (+) APCI/N_2/CS_2 successfully generated stable molecular radical cations for all four model compounds in the mixture at roughly equal efficiencies, the other two methods did not. Figure modified from reference [8].

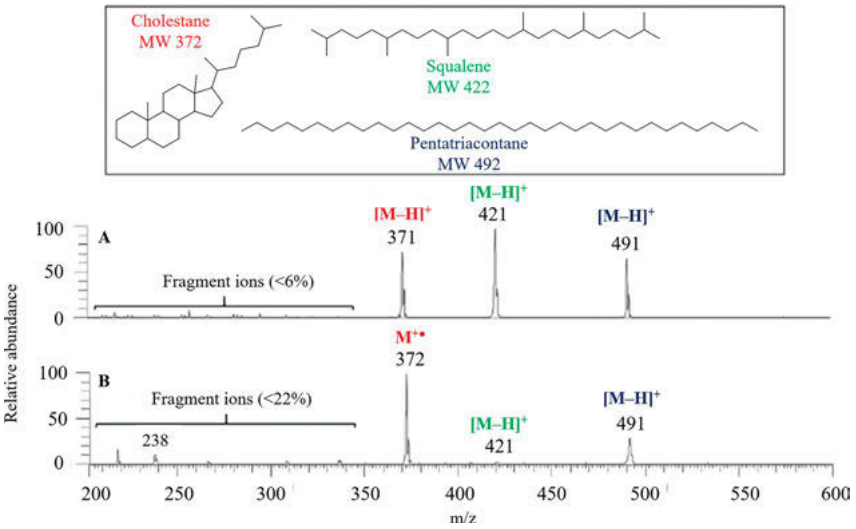

Figure 13.7: A) APCI/O_2/n-hexane mass spectrum measured for an equimolar mixture (1 mM) of three saturated hydrocarbon model compounds. All compounds were ionized at a similar efficiency. B) APCI/N_2/CS_2 mass spectrum measured for the same mixture (no ions were observed below m/z 200). Figure modified from reference [8].

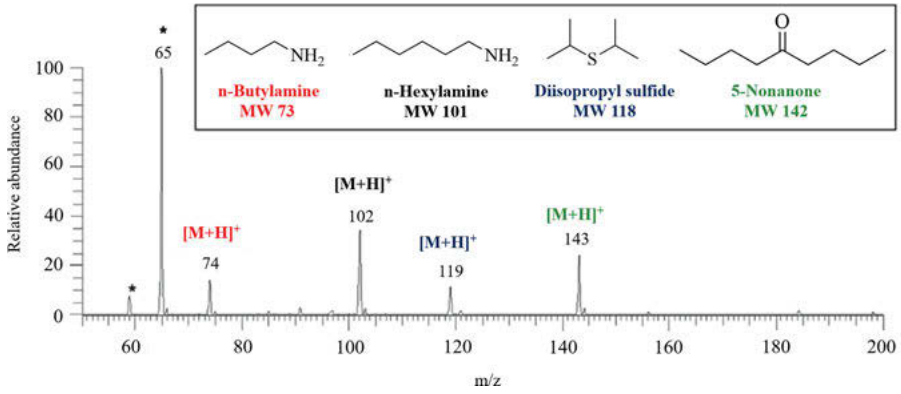

Figure 13.8: APCI/N_2/n-hexane, methanol mass spectrum measured for an equimolar mixture (1 mM) of four nonaromatic polar compounds (* denotes solvent peaks). Figure modified from reference [8].

Table 13.2: Optimal ionization methods and ion source parameters for high-resolution mass spectrometry analysis of crude oil fractions generated by using the DPF method [8].

	Asphaltenes fraction	Saturated hydrocarbon fraction	Alkyl aromatic hydrocarbon fraction	Heteroaromatic compound fraction	Polar compound fraction
Ionization mode and method	(+) APCI	(+) APCI	(+) APCI	(+) APCI	(+) APCI
Solvents	CS_2	*n*-Hexane	CS_2	CS_2	Methanol, *n*-hexane (3:1)
Predominant type of ions produced	$[M^{+\bullet}]$	$[M\text{-}H]^+$	$[M^{+\bullet}]$	$[M^{+\bullet}]$	$[M + H]^+$
Sample concentration (mg/mL)	1	1	0.5	0.5	1
Flow rate (µL/min)	5	10	3	3	1
Sheath and auxiliary nebulization gas	N_2	O_2	N_2	N_2	N_2
Vaporizer temperature (°C)	400	150	300	300	300
Sheath gas flow rate (AU)	40	60	20	20	40
Auxiliary gas flow rate (AU)[a]	20	30	10	10	20

Table 13.2 (continued)

	Asphaltenes fraction	Saturated hydrocarbon fraction	Alkyl aromatic hydrocarbon fraction	Heteroaromatic compound fraction	Polar compound fraction
Capillary temperature (°C)	350	50	275	275	275
Discharge current (mA)	4.7	4.5	4.5	4.5	4.5
Capillary voltage (V)	35	10	25	25	30
Tube lens voltage (V)	50	20	50	50	50

[a] AU = arbitrary units

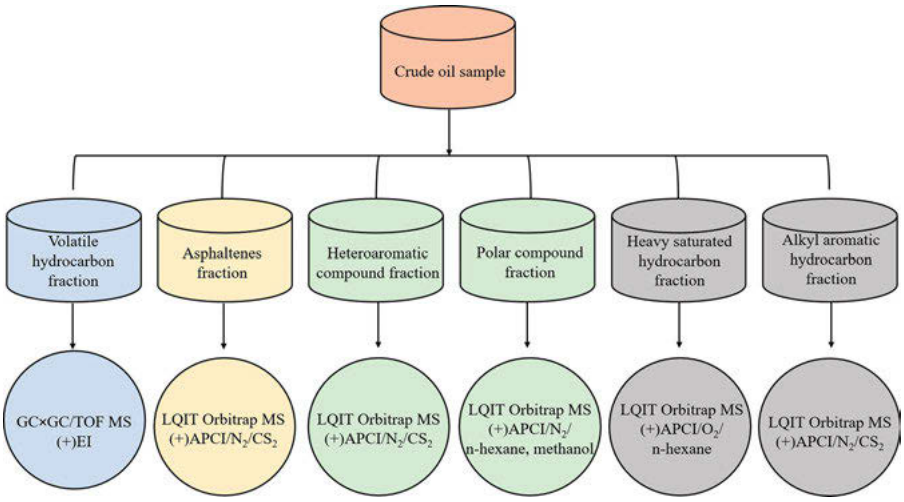

Figure 13.9: High-resolution mass spectrometry instruments and ionization methods selected for the analysis of the six crude oil fractions generated by the DPF method. Figure modified from reference [8].

13.3 Determination of the average gravimetric percentages of the different compound classes in crude oil samples

As described above, the DPF method allows the separation of a crude oil into six fractions, each containing a different class or classes of compounds. Therefore, the mass percentage of each fraction can be easily determined relative to the mass of

the original sample subjected to fractionation. The mass difference between the crude oil sample before and after distillation is used to determine the gravimetric weight percentage of volatile hydrocarbons. The difference in the mass of the membrane filter before and after filtration can be utilized to determine the gravimetric weight percentage of asphaltenes. The fractions obtained using flash chromatography are weighed for the determination of the gravimetric percentages of each fraction (and hence the different compound classes). The gravimetric percentages of the DPF generated compound fractions for a crude oil sample determined by Kenttämaa et al. were 8%, 1%, 44%, 21%, 9%, and 8% for the volatile hydrocarbon, asphaltenes, and heavy saturated hydrocarbon, alkyl aromatic hydrocarbon, heteroaromatic compound, and polar compound fractions, respectively. The method achieved about 92% recovery of the original crude oil sample. Sample losses in the range of (8–17%) were reported in the literature [8, 15]. Potential reasons for sample loss during processing include compounds that may not have completely eluted from the auto column system or the solid-phase cartridge with the solvents used. In the future, the DPF method will be improved to reduce sample loss.

The DPF-MS method has been used also to examine crude oils of different densities ranging from heavy to medium and light in order to determine whether a correlation can be found between their density (or API gravity) and the average gravimetric mass percentages of their different compound classes [21]. The dominant fraction in the medium and light crude oils was the heavy saturated hydrocarbon fraction. The gravimetric percentages of the heavy saturated hydrocarbon fraction in the medium and light crude oils ranged from 36% up to 49%. The dominant fraction in the heavy crude oil was the heteroaromatic compound fraction at a mass percentage of 37%. The mass percentage of the polar compound fraction in the heavy crude oil was more than twice the mass percentage of the polar compound fraction in the medium and light crude oil samples. The mass percentage of volatile hydrocarbons increased gradually with the decrease in crude oil density, going from none in the heavy crude oil to about 8% in light crude oils. A correlation was found between the mass percentage of heteroaromatic compounds and the API gravity; as the weight percent of compounds in the heteroaromatic compound class increased, the API gravity decreased [21].

13.4 Determination of the elemental compositions of compounds in each fraction by using medium- or high-resolution mass spectrometry

As the crude oil fractions predominantly contain just one compound type, they can be analyzed both qualitatively and semiquantitatively by using the optimized medium- or high-resolution mass spectrometric methods. The obtained data provide a

variety of information, including the elemental compositions of the detected ions, approximate weight percentages of compounds with different consolidated elemental compositions, the degree of unsaturation of the compounds and their average molecular weights [8, 21]. This information can be obtained for each fraction and for the crude oil as a whole by combining the data obtained for each fraction [21].

The measured high-resolution accurate-mass data can be used to assign the elemental compositions for the detected ions. The general formula used for the determination of the elemental compositions of the compounds of interest is $C_cH_hN_nO_oS_s$ where *c* and *h* are positive nonzero integers while *n*, *o*, and *s* are any positive integer numbers or zero. In these analyses, the maximum allowed number of carbon and hydrogen atoms was not limited while the number of nitrogen, oxygen, and sulfur atoms was set between zero and five [21]. Most of the ions detected for the polar and heteroaromatic compound fractions were assigned chemical formulas that contained heteroatoms (N, O, and/or S). The approximate weight percentages of compounds with specific consolidated elemental compositions in a fraction can be determined from the ratio of the abundance of the ions of a specific elemental composition to the total abundance of all ions detected in that fraction. This information should be of high importance to crude oil industries and refineries as it helps in determining which fraction contains most of the compounds of interest.

Kenttämaa et al. found that in the heteroaromatic compound class of light, medium and heavy crude oil samples fractionated and analyzed by using the DPF-MS method, the weight percentage of the nitrogen-containing compounds with the elemental composition C_cH_hN inversely correlated with the API gravity of the samples [21]. The majority of the compounds in the heteroaromatic compound class had the elemental composition C_cH_hN for all studied crude oils. Other correlations between chemical compositions of the crude oils and API gravity were not identified in this study.

Further, the examination of the chemical compositions of the compound classes in the above crude oil samples revealed that most of the abundant sulfur-containing compounds with the elemental composition C_cH_hS in the medium heavy crude oils (with API gravities of 25.5 and 31.0°; 12–18% weight percentage in the whole crude oils) were sulfur-containing compounds in the alkyl aromatic compound fraction [21]. The class containing the second-highest amount of sulfur compounds in the medium heavy crude oils was the heavy saturated hydrocarbon class [21]. These findings may lead to better ways to remove sulfur from medium-heavy crude oils that were found to contain most of the sulfur among the studied crude oil samples [21]. Further, the abundant compounds with the elemental composition $C_cH_hO_o$ in the lightest crude oil studied (17% of weight of the whole crude oil) were found to belong to the heavy saturated hydrocarbon compound class [21].

In addition to the above information, accurate mass measurements enable the determination of the ring and double bond equivalent (RDBE), which represents the degree of unsaturation and/or number of rings in the compounds, according to eq. (13.1),

wherein c, h, and n are the number of carbon, hydrogen and nitrogen atoms in the ion, respectively:

$$\mathrm{RDBE} = c - \frac{h}{2} + \frac{n}{2} + 1 \tag{13.1}$$

Determination of RDBE values enabled Kenttämaa et al. to confirm that most of the hydrocarbons detected in the volatile and heavy saturated hydrocarbon fractions in a crude oil were saturated compounds with RDBE values between one and two [8], as opposed to the compounds in the alkyl aromatic hydrocarbon and heteroaromatic compound fractions that had RDBE values equal to or greater than four [8]. Comparison of the RDBE values determined for light, medium, and heavy crude oil samples revealed that the average RDBE value of compounds in the heteroaromatic compound class correlated with the API of the samples. This finding suggests that the aromatic core size for compounds in the heteroaromatic compound class may be larger for the heavier crude oils than the lighter crude oils [21]. Figure 13.10 illustrates the distribution of heteroatoms as a function of the number of carbons in the

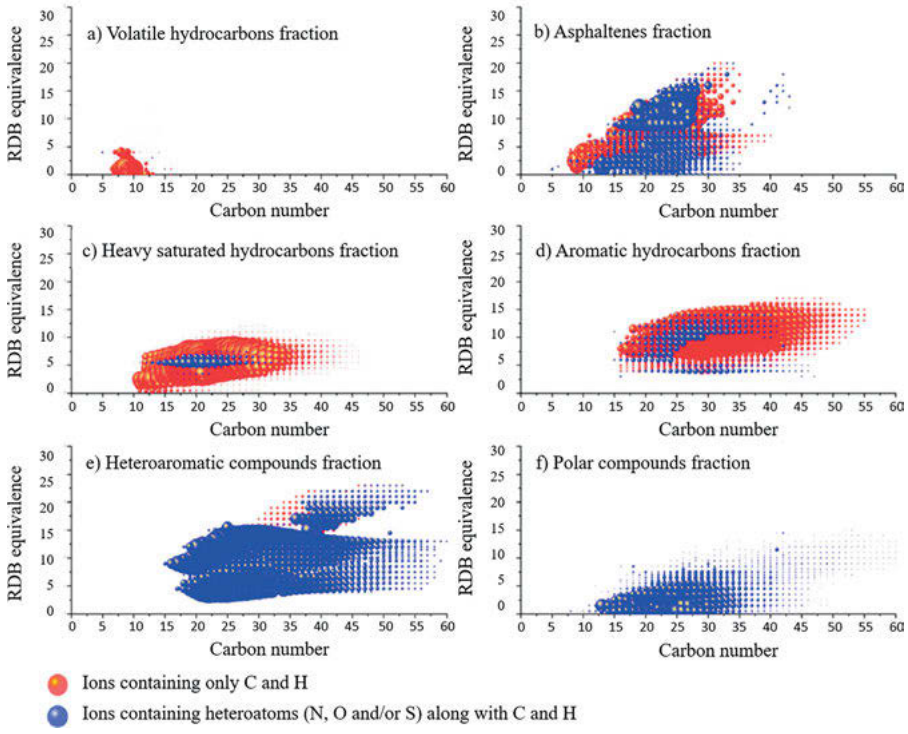

Figure 13.10: Colored bubble plots of ring and double bond (RDBE) equivalent versus carbon number for ionized compounds derived for each of the six fractions of a crude oil obtained by using DPF. Figure modified from reference [8].

compounds in the fractions of a crude oil sample analyzed by Kenttämaa et al. [8]. Oxygen-, nitrogen-, and sulfur-containing compounds are illustrated using blue bubbles. The larger the bubble size, the greater the abundance of the compound type. Based on these data, no heteroatom containing compounds were present in the volatile hydrocarbon fraction. The majority of the compounds detected in the heavy saturated and the alkyl aromatic hydrocarbon fractions were hydrocarbons. Only minor amounts of heteroatom-containing compounds were detected in these fractions. All compounds in the polar compound fraction contained heteroatoms, and almost all compounds in the heteroaromatic compound fraction contained heteroatoms, with only a few exceptions.

13.5 Determination of the consolidated weight percentages of compounds with different elemental compositions in the crude oil as a whole

Figure 13.11 shows typical high-resolution mass spectra generated by using the optimized ionization/mass spectrometry methods for each fraction obtained using the DPF method from a crude oil sample. The consolidated elemental compositions of compounds with a certain chemical formula of interest can be determined for the entire crude oil by using eq. (13.2), which utilizes the gravimetric weight percentage of individual fractions and their compound class distributions:

The (consolidated) weight percentage of compounds with different elemental compositions =

$$\sum_{x=1}^{6} \frac{\Sigma i_x \text{abundance}}{\Sigma x \text{abundance}} \times \text{wt\%}(x) \tag{13.2}$$

where x is one of the six compound fractions derived from the crude oil, i is a specific elemental composition type of an ionized compound, Σx abundance is the total ion abundance for all compounds in each fraction, and wt%(x) is the gravimetric weight percentage of the compounds in that fraction in the crude oil sample. The consolidated weight percentages of compounds of different elemental compositions in crude oils of different densities were determined previously for the sake of examining how they correlate with the API gravity of the crude oils [21]. However, no correlations were found between the amounts of compounds with different elemental compositions in the whole crude oils tested and their API gravities.

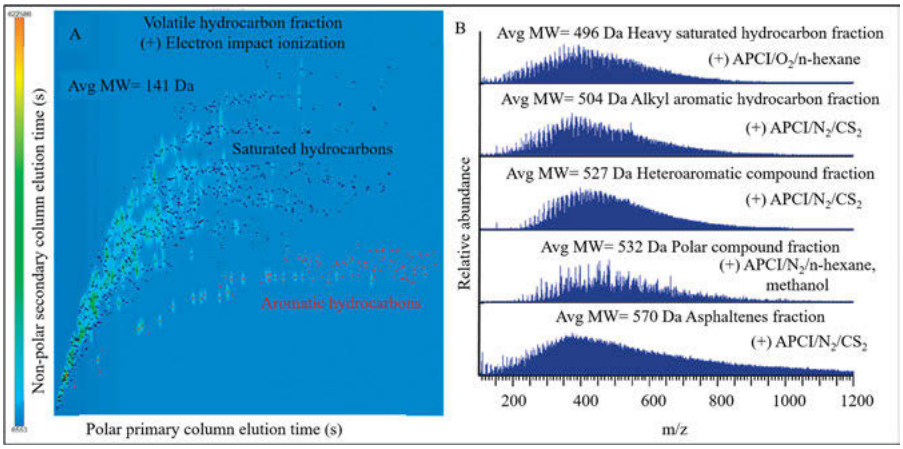

Figure 13.11: A) GCxGC/((+)EI medium-resolution TOF total ion chromatogram measured for the volatile hydrocarbon fraction of a crude oil. The aromatic hydrocarbons are color-coded in red and saturated hydrocarbons in black. B) (+) APCI high-resolution LQIT Orbitrap mass spectra measured for the five nonvolatile crude oil fractions. Avg MW denotes the weighted average molecular weight. Figure modified from reference [8].

13.6 Determination of the average molecular weight of compounds in crude oil

It is important for crude oil industries and refineries to be able to determine the molecular weight distributions of the different compound classes in a crude oil [24], as refinery processes are chosen based on the chemical composition of each crude oil sample [25]. The ability to accurately estimate the average molecular weight of all compounds in crude oil may further facilitate the optimization of the refinery processes [26]. This knowledge would allow a better estimation of the amount of reagents required for chemical reactions used to modify compounds in crude oil, such as alkylation, dimerization, cracking, and/or hydrotreating [26]. Additionally, the average molecular weight of compounds in hydrocarbon oils is thought to determine many of their physical properties, including the density and viscosity [27].

Since optimized mass spectrometric ionization methods with minimal fragmentation are utilized in the DPF-MS method, the method can be used to accurately determine the average molecular weight of the compounds in the fractions as well as in the entire crude oil. Indeed, data obtained by applying the DPF-MS on mixtures of model compounds demonstrated that the method is highly accurate, with errors less than 3% for most of the model compound mixtures; the greatest error observed was at 7% for a mixture of alkyl benzenes with long alkyl side chains [8].

The experimental average molecular weight for compounds in each fraction of a crude oil was determined based on the equations below; slightly different equations were applied for each fraction based on the predominantly formed stable ions. Equation (13.3) was used to determine the average molecular weight of heteroaromatic compounds and alkyl aromatic hydrocarbons ionized using CS_2 as the solvent and APCI reagent and nitrogen as the sheath and auxiliary gas because these conditions generate stable molecular ions for aromatic compounds. On the other hand, eq. (13.4) was used for the heavy saturated hydrocarbons (M) ionized by using *n*-hexane as the solvent and APCI reagent and oxygen as the nebulizing gas, because this ionization method predominantly generates stable $[M\text{-}H]^+$ ions from saturated hydrocarbons. Finally, eq. (13.5) was utilized to determine the experimental average molecular weight of polar compounds (M) analyzed by using 3:1 methanol:*n*-hexane as the solvent and APCI reagent and nitrogen as the sheath and auxiliary gas as this ionization method predominantly generates stable $[M + H]^+$ ions from polar nonaromatic compounds [8].

$$\text{Experimental Avg MW} = \frac{\sum((\text{ion } m/z) \times \text{abundance})}{\sum \text{all abundances}} \tag{13.3}$$

$$\text{Experimental Avg MW} = \frac{\sum(((\text{ion } m/z) + 1) \times \text{abundance})}{\sum \text{Abundances}} \tag{13.4}$$

$$\text{Experimental Avg MW} = \frac{\sum(((\text{ion } m/z) - 1) \times \text{abundance})}{\sum \text{Abundances}} \tag{13.5}$$

The average MW of the volatile hydrocarbons analyzed by using GC × GC/(+)EI TOF MS can be determined by using the following equation:

$$\text{Experimental Avg MW} = \frac{\sum(\text{molecular ion } m/z \times \text{GC peakarea})}{\sum^{\text{GC peak area}}} \tag{13.6}$$

The average molecular weight of each fraction and its gravimetric percentage can be used to determine the average molecular weight of the entire crude oil based on the following equation:

$$\text{Overall Avg MW of compounds in a crude oil} = \frac{\sum(\text{Average MW of compounds in each individual fraction} \times \text{wt}\%)}{\sum(\text{wt}\%)} \tag{13.7}$$

It is worth noting that the fragmentation caused by EI may sometimes hinder the determination of the MW of a compound, which can lead to an underestimation of the average molecular weight for compounds in the volatile hydrocarbon fraction. However, this was not the case in a study where DPF-MS was used to determine the average molecular weights of five model compound mixtures representing each DPF generated fraction, except the asphaltenes. The model compound mixture that

simulated the volatile hydrocarbon fraction contained small cyclic, linear and aromatic compounds and was analyzed by using GC × GC/(+)EI TOF MS. The theoretical average molecular weight of the compounds in the mixture was only one Dalton greater than the experimentally determined average molecular weight; the experimental error reported was 1%.

The m/z value of the molecular ions used in eq. (13.6) is based on the identification of the compound by using the EI mass spectral library match. Fragmentation of the volatile hydrocarbons in a crude oil studied did not significantly affect the results obtained because the gravimetric percentage of the volatile hydrocarbon fraction was only about 8%, which is much smaller than the percentage of the other fractions [8]; therefore, it did not significantly affect the determined overall average molecular weight of the crude oil studied [8]. However, this might be different for other crude oils.

Other methods commonly used for the determination of the average molecular weight of compounds in crude oil include the measurement of freezing point depression and GC simulated distillation [28, 29]. These methods have been found to substantially underestimate the average molecular weight of model compound mixtures compared to the DPF-MS method [8]. The average molecular weight values obtained by freezing point depression, GC simulated distillation, and the DPF-MS method on a crude oil sample were 230 Da, 339 Da, and 473 Da, respectively [8].

13.7 Conclusions

The distillation precipitation fractionation mass spectrometry (DPF-MS) method is a separation and analysis method that was recently developed for the characterization of crude oil at the molecular level. The DPF part of the method involves separation of the crude oil into six fractions containing different types of compounds. The first fraction contains volatile hydrocarbons that are mostly saturated hydrocarbons, but light aromatic hydrocarbons may also be present. The second fraction contains asphaltenes, which are predominantly highly condensed (low H/C ratio) aromatic and heteroaromatic compounds. The third fraction contains heavy saturated hydrocarbons, including linear, branched, and cyclic hydrocarbons. The fourth fraction contains light aromatic hydrocarbons, which are predominantly alkyl aromatic compounds. The fifth fraction contains heteroaromatic compounds, which are mostly heavy nonpolar aromatic compounds. The sixth fraction contains nonaromatic polar compounds.

The above fractions are analyzed by using different medium- or high-resolution mass spectrometry methods. An optimized ionization method has been developed for each fraction in order to ionize all of its components with similar efficiency and to generate only one type of ions, either molecular radical cations, protonated molecules, or cations that formally correspond to hydride abstraction from the analyte

molecule. While (+) EI ionization method coupled with GCxGC/TOF is a suitable method for the analysis and characterization of the volatile hydrocarbon fraction, (+) APCI approaches with different nebulization gases and solvent systems coupled to linear quadrupole ion trap mass spectrometer are used for the nonvolatile fractions. Besides accurate gravimetric information, DPF-MS provides semiquantitative molecular-level information that includes elemental compositions and molecular weights of the compounds. These data can be further processed to obtain accurate average molecular weights, ring, and double bond equivalent values and the percentage abundances of different compound classes in the different fractions. This method excels over previous methods by including the weight percentages of all compounds, including volatile hydrocarbons. Additionally, the gravimetric weight percentage of compounds of certain elemental compositions can be determined for each fraction and the crude oil, thus allowing for data consolidation (data obtained from different fractions consolidated into one data set). The DPF-MS method provides comprehensive analysis of the crude oil, including average molecular weight, heteroatom content, and weight percentage of compounds in different compound classes.

References

[1] Tang G-Q, Morrow NR. Influence of brine composition and fines migration on crude oil/brine/rock interactions and oil recovery. J Pet Sci Eng, 1999, 24, 99–111.
[2] Sayyouh MH, Hemeida AM, Al-Blehed MS, Desouky SM. Role of polar compounds in crude oils on rock wettability. J Pet Sci Eng, 1991, 6, 225–233.
[3] Zhang X, He J, Zhao Y, Wu H, Zeqiang R. Geochemical characteristics and origins of the crude oil of triassic Yanchang formation in southwestern Yishan slope, Ordos basin. Int J Anal Chem, 2017, 2017, 1–12.
[4] Ansari TM. Occupational exposures in petroleum refining; crude oil and major petroleum fuels. IARC, Lyon, France, International Agency for Research on Cancer, 1989.
[5] Owen BC, Gao J, Borton DJ. et al., Carbon disulfide reagent allows the characterization of nonpolar analytes by atmospheric pressure chemical ionization mass spectrometry. Rapid Commun Mass Spectrom, 2011, 25, 1924–1928.
[6] Chiaberge S, Fiorani T, Savoini A. et al., Classification of crude oil samples through statistical analysis of APPI FTICR mass spectra. Fuel Process Technol, 2013, 106, 181–185.
[7] Pakarinen JMH, Teräväinen MJ, Pirskanen A, Wickström K, Vainiotalo P. A positive-ion electrospray ionization fourier transform ion cyclotron resonance mass spectrometry study of Russian and North Sea crude oils and their six distillation fractions. Energy Fuels, 2007, 21, 3369–3374.
[8] Yerabolu R, Kotha RR, Niyonsaba E. et al., Molecular profiling of crude oil by using distillation precipitation fractionation mass spectrometry (DPF-MS). Fuel, 2018, 234, 492–501.
[9] Romanczyk M, Zhang Y, Easton M, Li W, Viidanoja J, Kenttämaa H. Distinguishing isomeric aromatic radical cations by using energy-resolved ion trap and medium energy collision-activated dissociation mass spectrometry. J Am Soc Mass Spectrom, 2020, 31, 58–65.
[10] Tang W, Sheng H, Jin C, Riedeman JS, Kenttämaa HI. Characterization of aromatic organosulfur model compounds relevant to fossil fuels by using atmospheric pressure

chemical ionization with CS_2 and high-resolution tandem mass spectrometry. Rapid Commun Mass Spectrom, 2016, 30, 953–962.
[11] Duan P, Fu M, Pinkston DS, Habicht SC, Kenttämaa HI. Gas-phase reactions of $ClMn(H_2O)^+$ with polar and nonpolar hydrocarbons in a mass spectrometer. J Am Chem Soc, 2007, 129, 9266–9267.
[12] Woods JR, Kung J, Kingston D, Kotlyar L, Sparks B, McCracken T. Canadian crudes: A comparative study of SARA fractions from a modified HPLC separation technique. Oil Gas Sci Technol, 2008, 63, 151–163.
[13] Jewell DM, Weber JH, Bunger JW, Henry P, Latham DR. Ion-exchange, coordination, and adsorption chromatographic separation of heavy-end petroleum distillates. Anal Chem, 1972, 44, 1391–1395.
[14] Bissada KK (Adry), Tan J, Szymczyk E, Darnell M, Mei M. Group-type characterization of crude oil and bitumen. Part I: Enhanced separation and quantification of saturates, aromatics, resins and asphaltenes (SARA). Org Geochem, 2016, 95, 21–28.
[15] Niyonsaba E, Manheim JM, Yerabolu R, Kenttämaa HI. Recent advances in petroleum analysis by mass spectrometry. Anal Chem, 2019, 91, 156–177.
[16] Bissada KK (Adry), Tan J, Szymezyk E, Darnell M, Mei M. Group-type characterization of crude oil and bitumen. Part II: Efficient separation and quantification of normal-paraffins iso-paraffins and naphthenes (PIN). Fuel, 2016, 173, 217–221.
[17] Buenrostro-Gonzalez E, Lira-Galeana C, Gil-Villegas A, Wu J. Asphaltene precipitation in crude oils: Theory and experiments. AIChE J, 2004, 50, 2552–2570.
[18] Miadonye A, Evans L. The solubility of asphaltenes in different hydrocarbon liquids. Pet Sci Technol, 2010, 28, 1407–1414.
[19] Alzaga R, Montuori P, Ortiz L, Bayona J, Albaigés J. Fast solid-phase extraction-gas chromatography-mass spectrometry procedure for oil fingerprinting-application to the prestige oil spill. J Chromatogr A, 2004, 1025, 133–138.
[20] Guan X, Zhao Z, Cai S, Wang S, Lu H. Analysis of volatile organic compounds using cryogen-free thermal modulation based comprehensive two-dimensional gas chromatography coupled with quadrupole mass spectrometry. J Chromatogr A, 2019, 1587, 227–238.
[21] Niyonsaba E, Wehde KE, Yerabolu R, Kilaz G, Kenttämaa HI. Determination of the chemical compositions of heavy, medium, and light crude oils by using the distillation, precipitation, fractionation mass spectrometry (DPF MS) method. Fuel, 2019, 255, 115852–115858.
[22] Luning Prak DJ, Romanczyk M, Wehde KE, Ye S, McLaughlin M, Luning Prak PJ. et al., Analysis of catalytic hydrothermal conversion jet fuel and surrogate mixture formulation: Components, properties, and combustion. Energy Fuels, 2017, 31, 13802–13814.
[23] Manheim JM, Milton JR, Zhang Y, Kenttämaa HI. Fragmentation of saturated hydrocarbons upon atmospheric pressure chemical ionization is caused by proton-transfer reactions. Anal Chem, 2020, 92, 8883–8892.
[24] Tissot BP, Welte DH. Composition of crude oils. In: Petroleum formation and occurrence: A new approach to oil and gas exploration. ed, Bernard, 2nd ed, Springer-Verlag, Springer Berlin, Heidelberg, 1978, 333–368.
[25] Hinkle A, Shin E-J, Liberatore MW, Herring AM, Batzle M. Correlating the chemical and physical properties of a set of heavy oils from around the world. Fuel, 2008, 87, 3065–3070.
[26] Schneider DF. Select the right hydrocarbon molecular weight correlation. Chem Eng Prog, 1998, 94, 40–45.
[27] Overton E, Wade T, Radović J, Meyer B, Miles S, Larter SR. Chemical composition of Macondo and other crude oils and compositional alterations during oil spills. Oceanography, 2016, 29, 50–63.

[28] Oguamah I, Oseh J, Yekeen N. Effects of freezing point depression on molecular weight determination of hydrocarbon mixtures. Pac J Sci Technol, 2014, 15, 240–244.
[29] Acevedo S, Gutierrez LB, Negrin G. et al., Molecular weight of petroleum asphaltenes: A comparison between mass spectrometry and vapor pressure osmometry. Energy Fuels, 2005, 19, 1548–1560.

Roman S. Borisov, Vladimir G. Zaikin

14 Hyphenated gas chromatography and mass spectrometry techniques for the analysis of crude oil and petroleum products

Abstract: Gas chromatography is one of the most power separation technique for analysis of nonpolar and semipolar components of complex mixtures of hydrocarbons and heteroatomic compounds. Combinations of various types of gas chromatography and mass spectrometry allow studying the main components of oil at molecular level and find the greatest practical application for fuel and oil refining industry. The chapter describes fundamentals of hyphenated gas chromatography and mass spectrometry techniques and recent developments in their applications for researches in the field of crude oil and petroleum products analysis.

14.1 Introduction

Petroleum is the most important and versatile natural resource for fuels and various chemicals. It contains millions of components which are being separated by fraction distillation and extraction into various fractions: gases, naphtha, gasoline, kerosene, jet fuel, diesel fuel, lubricant oil, fuel (or heating) oil, and asphalt. From a chemical point of view, the components present in oil are distinguished by a variety of structures: aliphatic (linear and branched alkanes or paraffins), alicyclic (naphthenes), and aromatic hydrocarbons; N- and S-containing hetero-organic compounds; naphthenic acids; asphaltenes; resins; and even organo-element compounds). Over the years, various refining processes have been developed to improve process efficiency and product quality (isomerization/reforming to improve octane number of gasoline, desulfurization by hydrotreating to eliminate undesired sulfur components, cracking and hydrocracking to convert heavy fractions (such as gas oils and residua) into higher-value lighter fractions (such as fuels and lubricant oil).

Each stage of these manipulations, in both scientific and industry laboratories, requires the use of high-precision and speedy techniques for qualitative and quantitative analysis of complex mixtures. At the same time, the tasks for the analysis of crude oils are constantly being challenged to address geochemical studies related

Roman S. Borisov, Vladimir G. Zaikin, A.V. Topchiev Institute of Petrochemical Synthesis RAS, Moscow

https://doi.org/10.1515/9783110694529-014

to the problems associated with oil origin, its migration, diagenesis, and catagenesis in deposits. Another important issue is related to the need to provide suitable examination of oil spills on soil and water surfaces that is crucial for a rapid and complete biodegradation of oils and oil products and useful for arbitration purposes.

Among other physical–chemical methods, mass spectrometry (MS) as a method for molecular analysis appeared to be the most important and popular in the comprehensive study of oil, products of its transformation and processing. It should be noted that the emergence of MS as a structural analytical method in the 1930s is associated with the study of hydrocarbons, which are the main components of crude oils [1]. To monitor the oil refining processes and to evaluate the quality of products, MS turned out to be virtually irreplaceable tool during the Second World War, when there was an urgent need of military aviation for high-octane aviation fuels.

At first, mass spectrometric analysis of oil and petroleum products was limited by the structural group analysis to provide an average qualitative and quantitative data on the presence of selected structural groups of compounds (structural group analysis). However, the situation started changing in the late 1950s when MS was combined with a powerful separation technique as gas chromatography (GC) [2]. This hyphenated method (GC-MS) has become the most important tool in the study of complex mixtures of organic compounds, among which crude oils and various products of their transformations occupy a significant place. Subsequent improvements to GC-MS combines were accompanied by both the involvement of various ionization and ion separation techniques and the creation of a combination of multidimensional (MDGC-MS), mainly, comprehensive two-dimensional GC (GC×GC-MS) systems. The most important advantage of the latter method is the ability to separate, detect, and identify components that coelute in a one-dimensional GC-MS. It should be noted, however, that despite the high analytical potential, the GC-MS method can only be used for the analysis of sufficiently volatile compounds. Fortunately, many components of petroleum and petroleum products are quite volatile and can be analyzed using GC-MS methods with great efficiency.

Work in the development and practical application of MS for the analysis and comprehensive study of crude oils is continuously progressing. Several review articles published during past decade are focused on application of MS to petroleum analysis [3], on special separation methods [4], on new ionization techniques [5] and, particularly, on soft ionization methods [6]. The recent review [7] is of particular importance, as it is entirely devoted to research in the field of petroleomics, a new scientific field, the analytical basis of which is mainly MS [8].

In this chapter, we will restrict ourselves to considering the possibilities and practical applications of only MS, conjugated with such a separation technique as gas chromatography. It is quite obvious that this powerful technique (GC-MS and MDGC-MS) is used in the study of the actual main components of oil at molecular level, namely, volatile fractions, which still find the greatest practical application for fuel and oil refining industry.

14.2 Gas chromatography technique for online combination with mass spectrometry

Being extremely effective tool for the separation of complex mixtures of organic compounds, GC has become a most popular and routine technique in the analysis of petroleum fractions and oil products at a qualitative and quantitative level [9]. When applied to oil analysis, this method has one fundamental limitation, consisting in the need to transfer samples into the gas phase in the chromatograph injector port and their further separation on the sorbent of a particular chromatographic column by sequential sorption/desorption processes. In most cases, the temperatures of the injector port and the gas chromatograph oven are determined by the thermal stability of the sorbents and do not exceed 300–330 °C. This is why detailed information about the individual components of a petroleum is possible only for light fractions and generally limited to 40 carbon atom hydrocarbons. The occurrence of a great number of isomeric compounds in heavier fractions does not allow complete separation and analysis. Naturally, this affects mostly barely volatile and nonvolatile petroleum components (such as medium- and high-molecular weight hetero-organic and organo-element compounds, resins and asphaltenes). The problem is partially addressed by the use of a high temperature GC (HTGC), operating in some cases with temperatures above 400 °C and allowing the study of heavy oil distillates (i.e., gas oils, light residua), including high molecular hydrocarbons with the number of carbon atoms over 60.

When applying the GC-MS to petroleum analysis, more suitable chromatographic columns should be chosen. For example, one can be guided by the value of the phase ratio (β):

$$\beta = 250 \times \mathrm{ID}/d_\mathrm{f} \text{ (where ID = internal diameter of a column in μm,}$$
$$d_f = \text{film thickness in μm).}$$

For example, if analytes have low retention (volatile), a column with a low β can be used to increase retention. On the other hand, columns with higher β value are suitable for heavier analytes.

Early GC-MS systems included packed chromatographic columns, the combination of which with mass spectrometers required the use of special molecular separators that remove a significant portion of the carrier gas before entering the mass spectrometer. Later, capillary columns began to be introduced, providing a high resolution of mixtures and connected to a mass spectrometer without special interfaces. Among them, fused silica capillary columns (wall coated open tabular) are particularly efficient and popular in petroleum analysis.

A number of stationary phases can be used in petroleum analysis by GC-MS and MDGC-MS. However, fused silica capillary columns coated with slightly polar 5%-phenyl–95%-methylpolysiloxane are the most suitable for GC-MS, because they can operate up to 300 °C and separate many nonpolar and slightly polar compounds.

With an increase in the content of phenyl groups, the polarity of such phases increases. This is why, in MDGC-MS, for example, the second more polar column can be 50%-phenyl–50%-methylpolysiloxane.

Within the framework of this review, we will not consider the various instrumental approaches used to detect separated components in GC. Note only that the exceptional complexity of the composition of petroleum feedstock containing tens of thousands of compounds [8] actually predetermines the choice of a detector for each particular study. In this respect, it is mass spectrometric detectors alone that should be considered as the most universal, since they make it possible to detect compounds of the most diverse elemental composition and structural features. They provide high accuracy and reproducibility of detection over a wide range of concentrations of components in analyzed mixture.

14.3 Mass spectrometry technique used in gas chromatography-mass spectrometry (GC-MS)

14.3.1 Ionization methods

Mass spectrometers based on different ionization principles can be used for the determination by GC-MS of qualitative and quantitative composition of crude oils, oil fractions and of products manufactured on their basis.

14.3.1.1 Electron ionization (EI)

EI is the earliest and till now popular ionization technique widely used in practical MS (EI-MS). It usually operates on vapors (such as effluents from GC) and is based on the interaction of analyte molecules in the gas phase with an electron beam. Since the electron energy (usually 70 eV) is significantly higher than the ionization energy of organic analyte molecules, molecular radical ions are mainly formed, which then undergo decay to form fragment ions. An important advantage of the method is that it is capable of ionizing molecules of any elemental composition and provides high inter-instrument reproducibility of recorded the mass spectra. As a result, it all makes possible to use the method for general-purpose identification of compounds using databases of standard EI mass spectra. In addition, the formation of a predictable set of fragment ions predetermines the use of this method in a mass chromatography mode by constructing a gas chromatogram for a specific ion, which is characteristic of a particular class of compounds (selected ion monitoring, SIM). As a rule, the method allows lowering the detection limits of target substances and detecting them even in unresolved chromatographic zones. It is to be noted,

however, that EI mode can be accompanied by a low scanning rate and a low speed of switching between ions in the SIM mode. All these can reduce the sensitivity, do not allow the mass spectra of the coeluting components to be fully processed, and distort the mass spectra due to a change in the amount of analyte in the ion source during the scanning process. Another disadvantage of EI is that it can produce too many fragment ions and extremely unstable $M^{+\cdot}$ ions which make the structural identification difficult.

The use of electron ionization with vibrationally cold molecules (supersonic molecular beam mass spectrometry, SMB-MS) eliminates some problems and demonstrates particular efficiency in the detection and identification of compounds with low stability of molecular ions (for example, nonaromatic compounds and aromatics with long side alkyl chains). The method was developed by A. Amirav et al., suggesting insertion of an analyte and carrier gas through a small nozzle into the evacuated ion source in the form of a supersonic molecular beam [10]. At supersonic flow velocity, the vibrational and rotational energies of analyte molecules sharply decrease whereas the molecular radical ions produced have a much lower degradation rate. As a result, more intense $M^{+\bullet}$ ion peaks are recorded along with a set of fragment ion peaks which are typical of conventional EI. This makes it possible to reliably determine the molecular weight of analytes and identify them using standard libraries of IE mass spectra [11]. The approach was efficiently applied to qualitative and quantitative determination of n-alkanes in jet fuels [12] and to the analysis of diesel fuel and a mixture of petroleum hydrocarbons in order to simulate the formation of organic aerosols in the atmosphere [13].

It is worth noting that combinations of EI ion sources with such compact mass analyzers as toroidal and cylindrical ion trap allow manufacturing miniaturized GC-MS instruments capable of analysis of hydrocarbons mixtures. Unfortunately, there are still no published examples of the application of such instruments in the analysis of crude oil or main petroleum products.

14.3.1.2 Chemical ionization (CI)

Chemical ionization (CI) is usually referred to as “soft” or low-energy ionization and is based on a gas-phase chemistry. The arrangement of most CI ion sources is very close to EI. The ion source in this case operates at an elevated pressure of a reactant gas (most frequently, methane, isobutane, ammonia) introduced into the source at ~1 torr. Molecules of reactant gas undergo EI to yield primary ions that interact with neutral reactant molecules to give rise to plasma consisting of a variety of secondary ions. Subsequent interaction of such ions with the molecules of a simultaneously introduced analyte is accompanied by protonation, deprotonation, cationization and/or charged cluster formation. The analyte ions thus formed practically do not decompose, with the exception of the elimination of easily leaving

groups. The method allows increasing the intensity of ions in molecular region and makes it possible to determine the molecular weights of analytes. Modern mass spectrometer can operate with fast switching EI/CI to record mass spectra with both abundant molecular peaks and fragment ion peaks. Since the ionization efficiency of CI depends on the ability of the analyte to participate in certain secondary ion–molecule reactions, the technique allows the development of procedures for the selective analysis of compounds by selecting specific reagent gases.

14.3.1.3 Atmospheric-pressure chemical ionization (APCI)

Like CI, atmospheric-pressure chemical ionization (APCI) belongs to "soft" ionization methods. It is also based on to the interaction of analyte molecules with ionized reagent gas molecules and secondary ionization products (such as water clusters) in the ion source at atmospheric pressure. A corona discharge is frequently used to generate reagent gas ions. It should be noted that the mechanism of ion generation by APCI largely depends on the nature of reagent gas used and, along with the protonation and deprotonation products, molecular radical ions are also formed. This ionization technique is mostly used in combination with HPLC, but its coupling with GC has been shown.

14.3.1.4 Field ionization (FI)

Field ionization (FI) is based on the detachment of an electron from a molecule via the quantum-mechanical tunneling effect in strong electric field. Unlike the case of EI, the resulting molecular radical ions have a relatively low internal energy and do not decompose further. The peak of popularity of the method occurs in the late 1970s to early 1980s. However, there is currently a resurgence of interest in its use because it demonstrates greater versatility compared to other "soft" techniques: under FI conditions, saturated and aromatic hydrocarbons have similar ionization efficiencies.

14.3.1.5 Photoionization (PI), atmospheric pressure photoionization (APPI) and atmospheric pressure photochemical ionization (APPCI)

Photoionization (PI) MS has been known for quite some time. The principle of PI is based on the interaction of analyte molecules in the gas phase with photons resulting in the generation of molecular radical cations. The ionization efficiency of PI depends on the photon energy value: the higher the energy, the more efficient is the ionization. At the same time, the amount of fragment ions increases simultaneously with raising the energy. PI using high-energy photons from UV laser and

excimer lamp light sources is designated as single-photon ionization (SPI) or vacuum PI (VPI).

Atmospheric pressure PI (APPI) and photochemical ionization (APPCI) techniques were developed by Russian scientist I.A. Revelsky [14, 15]. Both methods are also based on the interaction of organic molecules with photons at atmospheric pressure. In both cases, analyte $M^{+\bullet}$ ions along with products of secondary ion–molecule reactions are formed. APPCI version is based on the introduction of dopants into the ionization region which gives rise to increasing the probability of secondary ion formation.

14.3.2 Ion separation methods and mass resolution

The choice of a mass analyzer, which provides separation and detection of charged particles formed in the ion source, is of no less importance for studying complex mixtures by hyphenated GC-MS.

14.3.2.1 Sector analyzers

Generally, sector analyzers include electrostatic and magnetic fields in a different sequence. They can provide both low and high resolution of mass spectrometers. These analyzers belong to scanning systems, which provide a relatively low rate of registration of mass spectra and this is their disadvantage. This drawback is especially acute in GC-MS, when it is necessary to record mass spectra for sharp, as well as poorly separated elution chromatographic zones. Nonetheless, sector analyzers were used in GC/MS instruments for quite some time, until they were replaced by mass spectrometers with quadrupole and later time-of-flight (TOF) analyzers.

14.3.2.2 Quadrupole analyzers

Quadrupole analyzers include a combination of radio frequency (rf) and direct current (dc) voltages and belong to a technique providing a relatively low resolution. Like sector mass analyzers, quadrupole analyzers have a scanning type of mass spectra recording. However, owing to fast scanning, they are ideally suited to interfacing to GC, HPLC, and other separation techniques. Main disadvantage of such systems is the loss of ions, which do not get into the particular interval of m/z values, passed by the mass analyzer, at each time moment. As a result, such a drawback leads to a decrease in sensitivity and the “visible” chromatographic resolution particularly for components with narrow elution zones. Modern quadrupole analyzers are capable of providing quit high scanning speeds as compared to sector

analyzers and most often are the most suitable systems for GC-MS. Although such analyzers do not provide a sufficiently low detection limits for the identification of minor amounts of components, there is a possibility to lower this parameter by one to two orders of magnitude when using the selected monitoring of ions (SIM) that are characteristic of certain classes of organic compounds [6]. In addition, such an approach allows the extraction of the target analyte zone from the complete chromatogram and from unresolved chromatographic zones. Using the tandem MS (MS–MS) and the selected reaction monitoring (SRM) provides an even better solution to this problem. Mass spectrometers, including the triple quadrupole analyzers, are very convenient for such experiments. In the corresponding systems, the first quadrupole analyzer selects target characteristic ions (precursor ions), which are decomposed in the second quadrupole collision cell owing to interacting with inert gas atoms [collision activated (or induced) dissociation (CAD or CID)]. Finally, the generated product ions are separated in accordance with their m/z values to obtain mass spectral parameters.

14.3.2.3 Time-of-flight (TOF) analyzers

TOF analyzers are based on measuring the time it takes for an ion, accelerated by a high potential, to travel a certain distance to the detector. Accordingly, ions with different masses fly this path at different speeds and, as they reach the detector, they are sequentially recorded forming a mass spectrum. Being nonscanning, it is characterized by an exceptionally high speed of registration of mass spectra and is especially suitable for combinations of GC-MS, MDGC-MS, LC-MS and others.

The first prototypes of such devices for ion separation had an extremely low resolution, but this characteristic was significantly increased by introducing a reflectron (reflector) designed by Russian physicist B.A. Mamyrin [1]. TOF analyzers have recently been developed to provide even higher resolution up to 100,000 full-width at half maximum (FWHM). These are multi-path TOF systems are based on folded flight path technology and are already equipped with some commercially available mass spectrometers. The resolving power of such TOF-MS instruments can be up to 50,000 for the case of GC-MS and this is sufficient to mass resolve many isobaric molecules of hydrocarbons and heterorganic compounds.

14.3.2.4 Orbital ion trap (FT-Orbitrap-MS)

Fourier-transform Orbitrap MS (FT-Orbitrap-MS) is based on the use of electrostatic axially harmonic orbital trapping invented by Alexander Makarov [16]. Corresponding mass analyzer (Orbitrap) consists of inner and outer electrodes. Ions, injected into the device from an inner ion source, orbit around the inner electrode and oscillate along the z axis under action of a static electric field. The m/z values of ions are

determined by measuring the frequency of their axial oscillation. Orbitrap mass spectrometers deliver a total possible maximum resolution (FWHM) of 10^6 at m/z 200 and ~0.0001 mass accuracy. It can distinguish specific atoms comparable to those of an FT-ICR analyzer that will be considered next, at a significantly lower cost. Initially, only LC was used in conjunction with the Orbitrap-MS. However, later it was possible to overcome the existing problems and GC was also merged with the Orbitrap [17].

14.3.2.5 Fourier-transform ion cyclotron resonance mass spectrometry (FT-ICR-MS)

Undoubtedly of considerable interest is the use of an ultrahigh-resolution mass analyzers in GC-MS, which are implemented on the basis of Fourier-transform ion cyclotron resonance (FT-ICR). The FT-ICR analyzers determine the m/z ratio according to the cyclotron frequency of an ion in a fixed magnetic field. Corresponding instruments belong to a type of ion trap but unlike a conventional ion trap, they are capable to provide very high mass resolution of more than 10^7. It should be noted, however, the resolution of such instruments directly depends on the ion circulation time and the speed of recording mass spectra is usually low, discouraging their interfacing with GC or LC. Nevertheless, although the resolution decreases with increasing the speed of recording mass spectra, it can reach 10^5, which is sufficient to determine the exact mass and to distinguish between isobaric ions for relatively low-molecular-weight components which are usually available for GC separation. It should be noted, however, that there are still few studies focusing on the application of this method in the GC-MS systems.

14.4 Examples of applying the GC-MS method to the analysis of oil and petroleum products

In conclusion of the consideration of the main components of GC-MS systems, we present the most general scheme of their arrangement in practically used instruments (Figure 14.1).

Generally, application of GC-MS to petrochemical and geochemical analysis involves the study of gaseous and liquid fractions. The main goal of such explorations is targeted or nontargeted detection and identification of various alkanes (branched alkanes, isoprenes), mono- and polycyclic cycloalkanes, aromatic and heteroorganic compounds. For many years, special attention has been paid to the discovering and identification of so-called biomarkers (steranes and their aromatized analogues, tri-

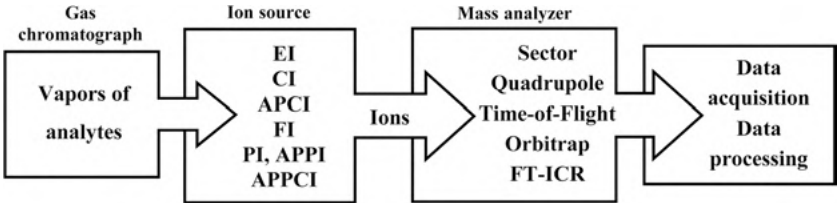

Figure 14.1: Schematic of experimental system in GC-MS.

and tetracyclic terpanes, pentacyclic triterpenes of hopane and oleanane series), which are originated during diagenesis of squalene (Figure 14.2). These compounds are widely used in establishing the origin of oil, typing oil, its transformation during spills, etc. [18].

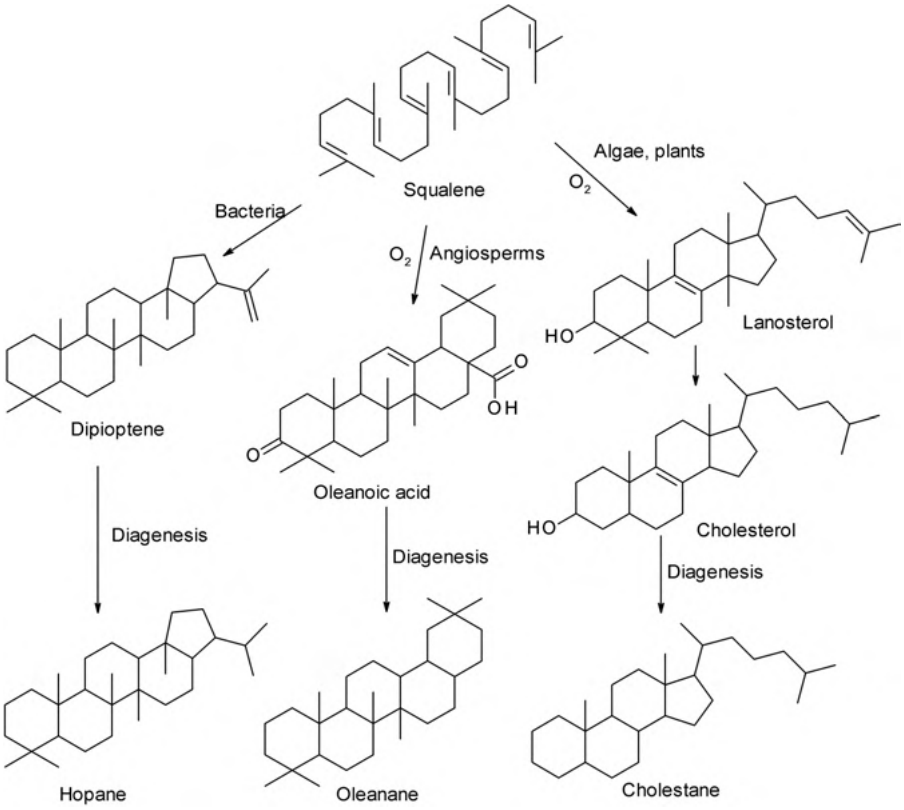

Figure 14.2: Biosynthesis of polycyclic compounds from squalene and further formation of biomarkers in the course of diagenesis.

In the majority of such GC-MS analyses, MS is used in electron ionization mode (GC-EIMS) since the latter method allows obtaining a large amount of information from the spectra. Moreover, the formation of characteristic ions allows using SIM and MRM to detect biomarkers, the quantities of which usually are lower than hundreds and even tens of ppm (Figures 14.3 and 14.4). More abundant biomarkers can be automatically identified using EI mass spectra databases.

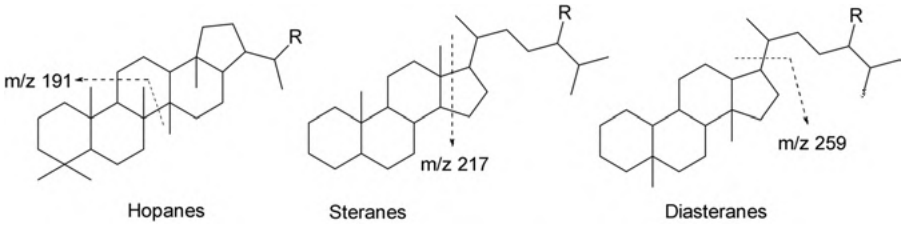

Figure 14.3: Formation of characteristic fragment ions of *m*/*z* 191 for hopanes and *m*/*z* 217 for steranes.

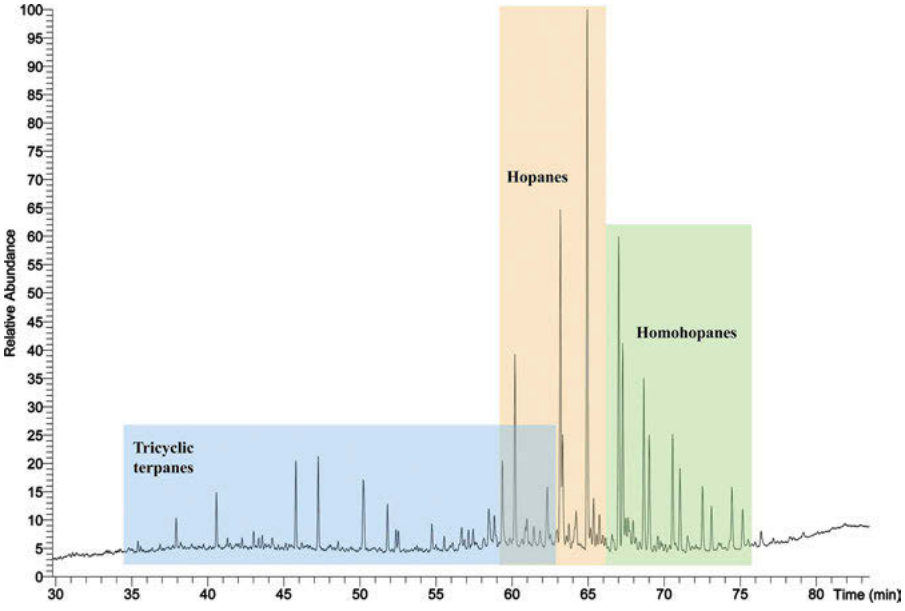

Figure 14.4: Reconstructed *m*/*z* 191 ion chromatograms showing the distribution of saturated biomarkers in an oil from Usinskoye oil field.

As was noted, quadrupole mass analyzers provide a high scanning speed when compared with sector analyzers with rather sufficient resolution and have gained great popularity for the study of petroleum hydrocarbons and, despite the creation of new ion

separation methods, are still widely used in routine petrochemical and geochemical studies. It should be noted that one can meet a huge array of publications concerning the use of GC/EI-MS with quadrupole analyzers in petroleum chemistry. Here we will try to present the most interesting results obtained by this method only in recent years.

One example concerns the use of GC-MS for the analysis of a unique object, the oil from the hydrothermal field of the Uzon volcano in Kamchatka Peninsula, which allowed proving its low maturity [19]. The results of comparative study of oils from traditional reservoirs of various geneses in the South China Sea were given in the article [20]. The GC-MS (quadrupole) analysis of the mineral from unconventional source, the Eagle Ford rock formation (USA), proved that organic matter accumulation occurred under photic-zone anoxia in the depositional environment [21]. The same method was used for the detection and identification of saturated and aromatic compounds produced during a simulated biodegradation conversion of heavy components (resins) in heavy oil in the presence of biosurfactants [22]. Comparatively low-molecular weight S-containing compounds belonging to reactive (mercaptanes, thiacyclanes, aliphatic sulfides and disulfides) and nonreactive (polycyclic thiophenes) series can be effectively analyzed by GC-MS. However, special preliminary separation of such fractions is suitable for the determination of such sulfur classes in complex petroleum mixtures which is important to understand their role in oil processing [23].

As noted in the Introduction, before the creation of the GC-MS method, MS was used to analyze only unresolved mixtures of petroleum compounds. In this case, the approach allowed the structural group analysis of the main hydrocarbon classes of compounds on the basis of mathematical processing of the total mass spectrum was most widespread. Currently, the structural group analysis was implemented using GC-MS which allowed the contents of the main hydrocarbon classes in super-complex oil mixtures to be determined [24, 25].

Works are continuing on the detection of known and discovery of new biomarker compounds as well as new characteristic compound types in oil with the aid of GC-MS. These works on the identification of standard and discovery of new saturated hydrocarbon biomarkers is very important because they provide valuable geochemical parameters which are used to establish the origin, thermal maturity, metamorphism, biodegradation of oils. Note the study of oils from unconventional source rock unit, the Bakken Formation (North Dakota, the United States; and Canada), where the characteristic ratios of typical biomarker triterpanes was discovered that are helpful in solving environmental problems [26]. As a result of a study of a representative set of crude oils and coal from various deposits, a new set of hexacyclic benzohopanes C33–C35 that can belong to biomarker compounds was identified with the aid GC-MS [27]. It is interesting to pay attention to the discovery of biomarker-like compounds obtained during the simulation of oil generation processes. For example, they were found in the soluble parts and the thermolysis products of the insoluble prokaryote biomass of various origin [28, 29].

Another example of GC-MS application relates to the detection and identification of trace amounts of diamond-like compounds, such as di-, tri-, and tetramantanes [30]. Specific new set of anoxia markers, namely branched di(alkylaryl)alkanes, were discovered during GC-MS analysis of dispersed organic matter and crude oils from the Volga–Urals and West Siberian basins [31].

Chemical ionization (CI) in GC-MS is also helpful in the determination of molecular weights of hydrocarbons possessing unstable molecular ions under EI conditions. Often, it is applied to obtain data to complement the GC/EI-MS results, the most suitable configuration of GC-MS system containing the combined ion source with fast switching between EI/CI modes. This was demonstrated by the identification of a group of hydrocarbons of unknown genesis with relatively large elution times that were discovered in a study of Dama Formation oils (China) [32]. The EI mass spectra permitted the suggestion to be made that these hydrocarbons are either branched alkanes or alkylated cycloalkanes, but the class of these compounds could not be accurately determined because of the absence of the $M^{+\cdot}$ ion peaks. However, they were unambiguously assigned to branched alkanes on the basis of the GC-CIMS data.

As was noted in the Section 3.1.2, combination of GC with CIMS may be useful for the selective detection of particular compounds in petroleum. In fact, the determination of sulfur- and nitrogen-containing heterocyclic compounds in crude oils and their refining products can be accomplished by using ammonia gas reagent because such analytes can interact with the NH_4^+ cations in CI plasma [33].

Another variety of CI, namely atmospheric-pressure chemical ionization (APCI), has been successfully used in GC-MS combines. The efficiency of the GC-APCIMS method has been demonstrated by the detection of biomarker compounds in oils. In contrast to EI mass spectra revealing the $M^{+\cdot}$ peaks of rather low abundance, the APCI spectra display quite intense peaks of molecular radical ions [34] or cations [35] facilitating the identification of biomarker components. Additional use of MRM mode reduces the limits of detection of the corresponding components [36] (Figure 14.5), which is particularly important for their determination in oil spills containing lower concentration of biomarker compounds, as compared to initial oils, owing to multifold dilution and biodegradation [37].

An interesting example of using the GC-APCIMS and tandem MS was described in the paper [38]. The combination of low (4 eV) and high energy (15–30 eV) ion activation in sequential scans allowed recording not only mass spectra with intense peaks of molecular ions, but also spectra with a large set of structure-informative fragment ions (Figure 14.6). Generally, this approach provided much greater sensitivity and selectivity for the analysis of biomarker compounds than GC-EIMS.

The use of the field ionization (FI) in GC-MS technique has also considerable prospects. This is clearly demonstrated by its application in the analysis of various diesel hydrocarbons [39, 40]. The technique was also used in the qualitative and quantitative determination of alkanes and olefins in coal tar [41]. The results confirmed the advantages of this technique in the rapid analysis of such objects and showed that the results are consistent with those obtained by the conventional methods. Of interest is the use

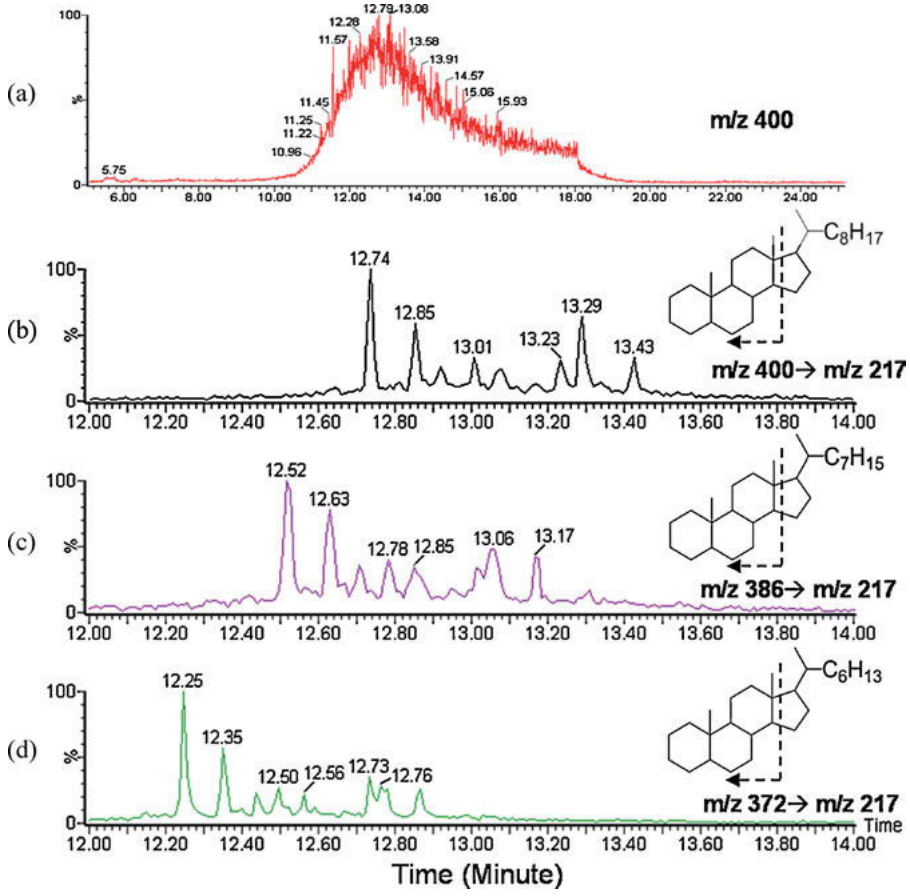

Figure 14.5: Selected ion chromatogram of *m*/*z* 400 (a) and transitions *m*/*z* 400→ *m*/*z* 217 (b), *m*/*z* 386→ *m*/*z* 217 (c), *m*/*z* 372→ *m*/*z* 217 registered using APGC tandem instrument. Reprinted from [36] with permission. Copyright (2015) Elsevier B.V.

of combined sources EI/FI in GC-MS. However, their applications are limited owing to a small number of commercially available systems of this kind. Interesting results in comparing APCI and FI are given in the paper [34]. The results of determining the distribution of various classes of hydrocarbons in lubricating oils turned out to be close, but better reproducibility was shown in the case of APCI.

PI is also fairly popular technique for studying hydrocarbon mixtures by GC-MS. The main advantage of PI and its SPI and VPI versions is that it predominantly allows recording the $M^{+\cdot}$ ion peaks. This method was shown to be effective in the observation of hydrocarbons of various structures with low limits of detection [42]. Since the ionization efficiency of various classes of compounds under PI conditions depends on the photon energy, the SPI technique can be applied to their selective

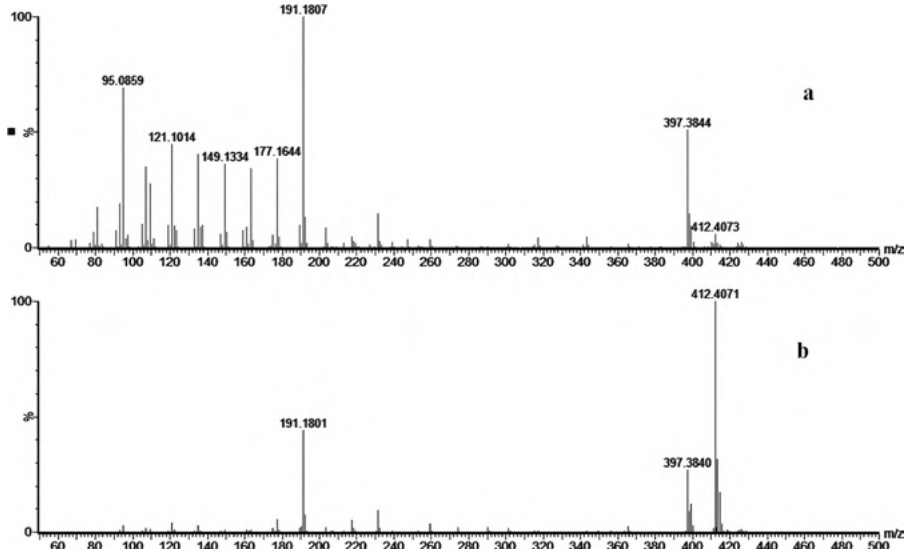

Figure 14.6: Tandem mass spectra of $C_{30}H_{52}$ hopane molecular ions, produced in APCI conditions, registered using high-energy MSECID ramp from 15 to 30 eV (a) and low-energy MSE4 eV CID (b). Reprinted from [38] with permission. Copyright (2012) American Chemical Society.

detection by varying this parameter. For example, it was shown that almost all tested compounds are ionized at a photon energy of 10.5 eV whereas compounds with multiple bonds are selectively ionized at an energy of 10 eV [43]. In the latter work, the authors also managed to separate and identify isomeric hydrocarbons. Similar approach was applied to the study of crude oil and a wide range of compounds was identified and quantified [44]. In the other case, GC-SPIMS in combination with thermogravimetry was used for the identification of products formed during heating of crude oils of various geographical origins [45].

Although other mass spectrometric PI techniques, namely, APPI and APPCI are more popular in combination with HPLC, they are also promising for the application in GC-MS for the analysis of to a wide range of compounds, including hydrocarbons [46].

Along with quadrupole analyzers, TOF systems have become increasingly popular in GC- MS combinations. For example, such instruments were used for detecting multifunctional hopanoids in biomass [47] and identifying hydrocarbons and metalloporphyrins using high-temperature GC [48].

Perhaps because GC is able to separate relatively low-molecular-weight substances whose conventional mass spectra are sufficient for identification, this separation technique is less commonly used in combination with ultrahigh resolution MS, such as Orbitrap and FT-ICR-based MS. However, in the literature one can find examples of the development and application of such methods to specific studies of

small molecules, mostly in metabolomics. At the same time, there are works focused on the analysis of oil and oil products.

Relatively recently has a technique been developed that combines GC and Orbitrap. Such a system, namely, GC/Quadrupole-Orbitrap, not only "enables high mass accuracy and high-resolution analysis, but does so at scan rates amenable to the timescale of GC separations" [17]. To expand the analytical potential of GC/Orbitrap-MS, interfaces on the basis of APCI [49] and APPI [50] were developed. For example, the use of a combined EI/APPI ion source in such system permitted a wider range of hydrocarbons in gas condensate to be identified [51].

The role of the mass analyzer resolution dramatically increases with a growth of number of heteroatomic compounds. This was clearly seen, for example, when analyzing the water samples used in the extraction of organic matter from the Alberta oil sands (Canada) by a combination of GC with FT-ICR-MS [52]. The authors demonstrated that high accuracy determination of m/z ratio allows distinguishing different classes of compounds with close elution times (Figure 14.7). As a result, the method allowed identifying a large set of hetero-organic compounds that act as the "fingerprint" of the production site. In the other case, polyaromatic hydrocarbons in various fossil oil and petroleum crude oil were characterized by combination of GC with atmospheric-pressure laser ionization FT-ICR-MS [53].

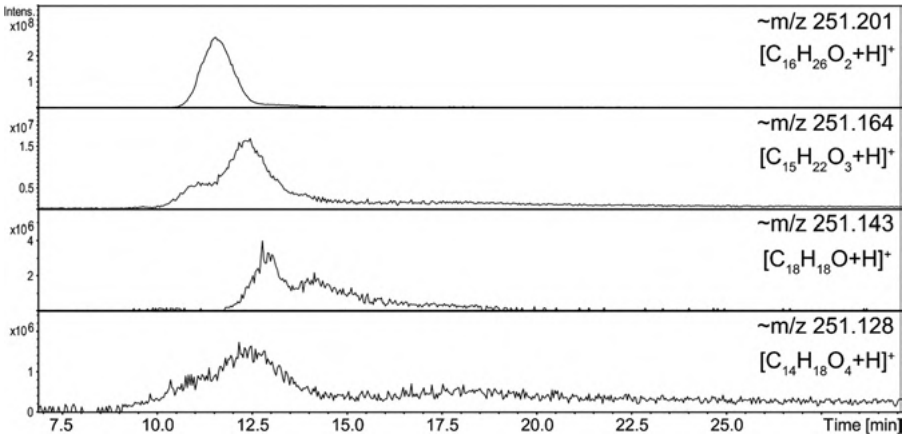

Figure 14.7: Example extracted ion chromatograms, showing ions of the same nominal m/z 251: the application of uHRMS allowed detecting compounds belonging to the O1, O2, O3, and O4 classes. Reprinted from [52] with permission. Copyright (2014) American Chemical Society.

14.5 Comprehensive two-dimensional gas chromatography-mass spectrometry (GCxGC–MS)

GC×GC hyphenated with MS has great prospects in the investigation of complex mixtures of hydrocarbons. The first instruments having heart-cutting two-dimensional chromatographic systems clearly showed advantages of such technique. But further development of comprehensive GC×GC allowed one to engineer the instruments combining superior chromatographic resolution and the power of MS. Separation module in such systems includes a combination of GC columns with two chromatographic phases of orthogonal polarity. Fractions eluted from the first column consistently enter into the second column via a special intermediate device (thermal modulator) and those that have not been resolved in the first column are further separated. Commonly, modulators use fast cryogenic cooling (cryogen-free approaches are also described) to capture the eluates separated in the first column and further heat-release into the second column in short duration [54] (Figure 14.8). This ensures fast continuous collection of a single fraction or a certain set of fractions after separation in the first column followed by fast introducing them into the second chromatographic column, whereas shorter second dimension is polar. The first column is typically of conventional length about 15–30 m and wide, whereas the second column is shorter (about 0.5–2 m), narrower and thinner. Generally, the first long GC column contains nonpolar stationary phase (e.g., 100% polydimethylpolysiloxane) and the second one contains polar phase (e.g., partially phenyl-substituted polydimethylpolysiloxane). Rather frequently, the set off GC column consists of slightly polar 5%-phenyl–95%-methylpolysiloxane as the first-dimension column and more polar 50%-phenyl–50%-methylpolysiloxane as the second column is used in practical GC × GC-MS analysis. Such arrangement of two columns (the first column is longer and wider and the second column is shorter and narrower) ensures that the total second dimension separation is completed before the next eluent from the first column enters the second column. However, there are a lot of works showing that the reverse

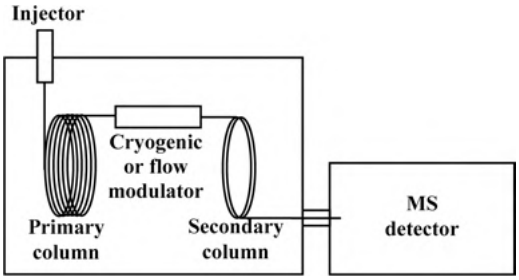

Figure 14.8: Principal scheme of MDGC-MS instrument.

column arrangement, when a polar column (also long) precedes a nonpolar column (short), allows achieving better results in case of petroleum analysis.

Since the separation in the second short column proceeds very quickly and there is the need in its readiness to take the next fraction from the first column, this places high requirements on the speed of recording mass spectra. This requirement is partially met by the use of quadrupole mass spectrometers. For example, such a combination, including Dean pneumatic switches as intermediate device was used for the determination of polyaromatic compounds in crude oils [55]. However, it should be emphasized that the application of systems with quadrupole [56] and triple quadrupole analyzers [57] is rather limited. They cannot provide a complete analysis of the sample and are commonly used only to detect target compounds.

Optimal solution of the problem is the insertion of TOF mass analyzers in such devices (GC×GC – TOFMS). Being nonscanning, TOF analyzers ensure extremely high speed of recording mass spectra and are characterized by smaller ion losses and, hence, by providing the greater sensitivity. An essential feature of the method is that corresponding instruments produce a huge array of data, which often requires the use of multivariate statistical analysis [58]. Attention should be paid to the possibility of realizing a high-temperature variant of the method which allowed the separation and identification of hydrocarbons with the carbon numbers up to 60. On the basis of data obtained, a new approach to two-dimensional simulated distillation of crude oils was suggested [59]. Using high chromatographic resolution of GC × GC-TOFMS, many classes of compounds were identified in Brazilian oils: linear and branched alkanes, alkylmono-, bi- and polycyclanes, alkylated benzenes, naphthalenes, phenanthrenes, chrysene and indanes, as well as alkyl-tetrahydro-naphthalenes, pyrenes, fluorenes and sulfur compounds [60]. Considerable attention is paid to the use of the method for the detection and identification of biomarker compounds in oil. High chromatographic resolution makes it possible, for example, to separate and identify various conventional and unconventional biomarker compounds, such as substituted tetracyclic [61–63], pentacyclic and other triterpenoid hydrocarbons [64–67], as well as diamondoids [68, 69], which are present in oil in minor amounts and are often coeluted when using one dimensional chromatography. Very interesting compounds representing heteroatomic adamantanes were found in Sichuan Basin oils [70] (Figure 14.9). Analysis of biodegraded oils allowed the separation and identification of various tricyclic terpanes, hopanes, 25-nor-hopanes, secohopanes as well as complete series of 25-nor-hopanes, nor-gammacerane, C29 28-nor-spergulanes and oleanane [64]. In addition, three new parameters to characterize biodegraded oils were suggested.

Analysis of literature data indicates an increasing involvement of GC×GC- TOFMS in the study of various aspects of petroleum chemistry and oil refining [71]. Already early work indicated the superiority of GC×GC-TOFMS for separation and identification of isomeric compounds in crude oils, that were co-eluted in one-dimensional GC-MS [72]. This technique is actively applied to the analysis of products of primary oil

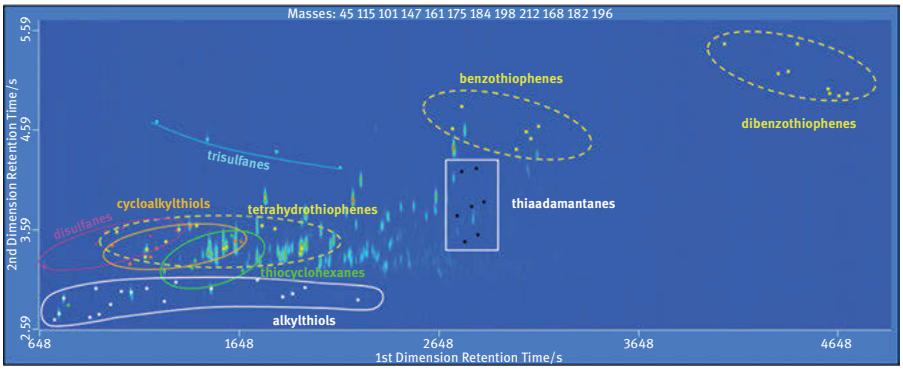

Figure 14.9: 2D selected ion chromatogram of sulfur compounds identified in a gas condensate sample by GC×GC-TOF MS. Reprinted from [70] with permission. Copyright (2020) American Chemical Society.

refining, especially heavy distillates [73] and atmospheric residues [74] in order to separate and detect various classes of aromatic compounds.

In further studies, approaches were developed to a detailed description of individual classes of compounds belonging to the series of sulfur [75, 76] and nitrogen heterocycles [77]. In addition to conventional oils, GC×GC-MS is also used in the analysis of other potential sources of energy and processing feedstock: the biomass pyrolysis products bio-oils [78] and heavy hydrocarbon shale [79].

GC×GC-MS is also useful for structural group analysis allowing individual components to be assigned to their respective compound classes on the basis of the presence of characteristic fragment ions in the mass spectrum [80]. For a more reliable identification and differentiation of compounds, revealing an identical set of fragment ions, algorithms are used that take into account the chromatographic properties [81]. Dependable quantification of hydrocarbon classes in oil mixtures may be accomplished with the use internal standards. In ideal cases, the standards should be structurally related to the detected groups of compounds, should be well resolved chromatographically but should not be present in oils. This approach was practically employed for structural group analysis of fuels [82, 83] and, in particular, for the determination of classes of hydrocarbons and sulfur compounds in demercaptanized jet fuel [84].

As was noted above, inverse sequential arrangement of GC columns (i.e., a short polar column precedes the long nonpolar one) may have its advantage in the analysis of oils. In fact, such a combination of columns allows for better separation of low- and medium-molecular-weight hydrocarbons owing to the higher resolving power of the first polar column (Figure 14.10) [85, 86]. In addition, the same approach made it possible not only to separate different classes of compounds, but also to make the semiquantitative assessment of their amounts [87]. In this regard,

it is interesting to pay attention to the use of ionic liquids as a polar phase in one of GC column [88]. Regular arrangement of a conventional weakly polar column (polydimethylsiloxane with 5% phenyl groups) and a column coated with the special ionic liquid appeared to be effective for separation of organic sulfur compounds, whereas their reverse arrangement was successful for separation of nitrogen compounds.

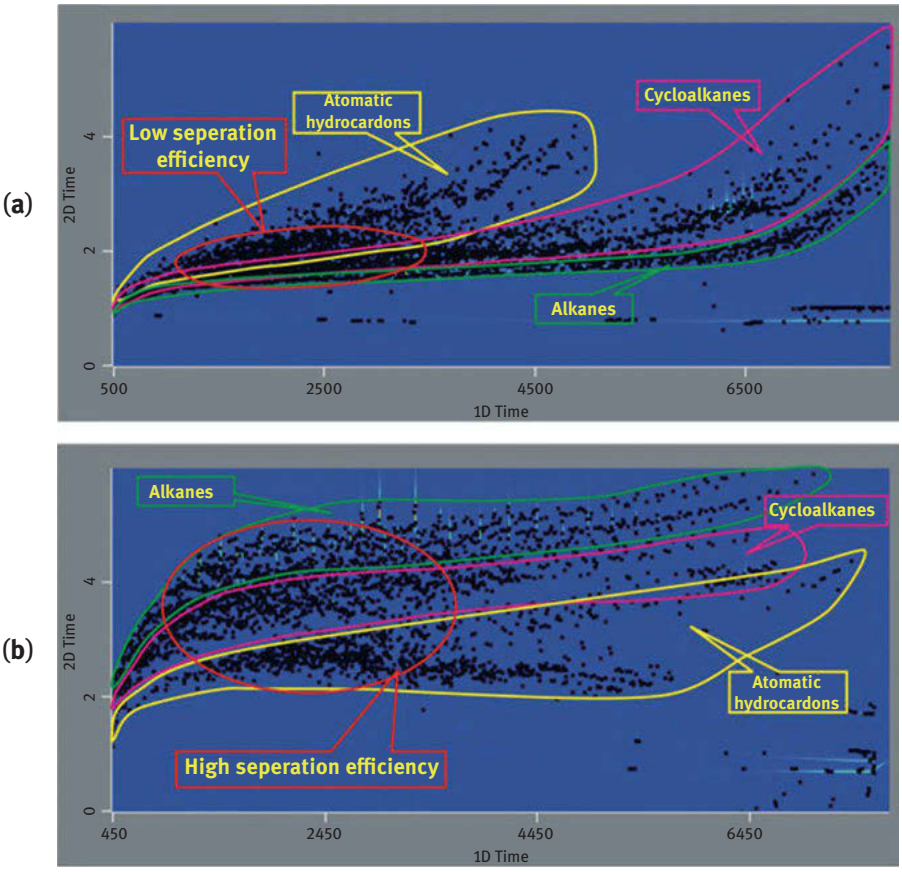

Figure 14.10: Total ion current GC×GC-TOFMS chromatograms showing separation of hydrocarbon compounds by normal (a) and reversed (b) column systems. Reprinted from [86]. Copyright (2014) Taylor & Francis Group, LLC.

Application of selective and sensitive GC×GC-TOFMS method makes a significant contribution to understanding of oil degradation processes when complex mixtures of native petroleum hydrocarbons convert into even more complex mixtures of products. For example, the method was used to study the composition of highly degraded Trinidad oil [89], to characterize a wide range of hydrocarbon metabolites resulted from bacterial degradation of hydrocarbons under anoxia conditions [90]

and the products of metabolic transformations of hydrocarbons in groundwater [91], to find a correlation between biodegradation and contact with water of North Sea oils [92], to identify alkylnaphthalenes as a new series of oil biodegradation products [93].

GC×GC-TOFMS method is widely applied to the analysis of the products of petrochemical synthesis. An interesting way to study the composition of the products of the high temperature Fischer–Tropsch process was proposed by Potgieter et al. [94], who used online catalytic hydrogenation in a reactor placed between a gas chromatograph and a mass spectrometer, by analogy with earlier works [95, 96]. Comparison of mass spectra of separated initial and hydrogenated products allowed distinguishing between dienes and cyclic olefins, which have identical empirical formulas and frequently similar EI mass spectra.

Rather important results were obtained by using GC×GC-MS for the analysis of rocket fuels [97]. It was found that their complete chemical compositions are correlated with the physical parameters of the samples (density, kinematic viscosity, calorific value, etc.). Note that such data could not be obtained with the aid of a conventional GC-MS.

As in the case of crude oils, GC×GC-MS can be used with success to study the degradation of refinery products under various conditions. For example, the degradation of jet fuels obtained from crude oil, by the Fischer–Tropsch process, or by biomass processing was investigated using this approach [98]. As a result, a wide range of hydrocarbons oxidation products were identified.

Note, that in the case of GC×GC-MS, EI mode is most frequently used for recording the spectra. This is especially important, since available databases of EI mass spectra can be used for automatic identification of substances. However, one can find some helpful modification or combination of the EI method, which makes it possible to obtain the missing structural information by using GC×GC-TOFMS. One of the varieties is the so-called tandem electron ionization. In this case, in addition to recording EI mass spectra at a standard ionization energy (70 eV), spectra are simultaneously recorded at a reduced electron energy (12–15 eV). At low energy, mass spectra reveal practically only the resulting $M^{+\cdot}$ ion peaks allowing the determination of molecular weight. For example, such an approach was used for structure determination and quantification of isomeric hydrocarbons [99, 100], as well as for the detection of components artificially introduced into diesel fuel [101].

In order to increase the abundance of molecular ions, the application of FI mass spectrometers in such combines is also of interest. In particular, the hydrocarbon composition of the middle distillate fraction of crude oil was studied in detail with the use of GC×GC-FIMS [102]. In this case, the presence of intense peaks of $M^{+\bullet}$ ions made it possible to unambiguously differentiate hydrocarbons of various structures even within overlapping elution zones.

Single-photon ionization (SPI) is also actively used in combination with 2D-GC. For example, an ionization source with a deuterium lamp (photon energy 10.8 eV) was applied to analyze mixtures of various petroleum compounds, including branched

hydrocarbons [103]. The mass spectra of the latter hydrocarbons revealed the sets of peaks for characteristic fragments in addition to the intense $M^{+\cdot}$ peaks. Detailed characterization of oils of different geographical origins was made by using mass spectral data obtained in two parallel and selective ionization of aromatic compounds by 9 and 10.5 eV photon energy [104].

Although the GC×GC-EIMS method allows obtaining sufficiently reproducible and reliable results, the most routine and popular ionization technique, IE, has a significant drawback which is due to the dependence of the effective ionization cross section on the structure of the compound. In most cases, this fact does not allow a survey quantitative analysis of mixtures containing various classes of organic compounds. To overcome this disadvantage, parallel use of mass spectrometric and flame ionization detection (FID) looks particularly convenient because it provides identification and FID quantification of components [105,106]. Otherwise, parallel combination of EIMS and with an atomic emission detector ensured selective detection of GC separated nitrogen- and oxygen-containing compounds, thereby complementing the results gained with the use of MS [107].

Along with significant improvements in mass spectral technology, GC×GC-MS methods utilizing a combination of different ionization techniques have recently become used. This is due to the fact that ionization methods often have their own specific disadvantages, while their combined use by means of ultrafast switching between methods makes it possible to obtain complementary structural and qualitative information in virtually simultaneous mode.

An example of the application of such instruments was given in the works devoted to the development of a universal biomarker analysis method based on GC×GC combined with FID and EI/FI-MS detection [108, 109]. By superimposing the EI and FI data, a certain mass spectrum containing an intense peak of a molecular ion and a set of peaks of characteristic fragments is simulated (Figure 14.11). Unlike tandem MS/MS EI spectrometry, the described approach gives rise to reproducible EI mass spectra that can be used for database searching to identify compounds. At the same time, the response of FID does not depend on the analyte structure, affording the possibility of quantitative analysis. The authors [108, 109] noted that the proposed approach actually provides four-dimensional separation of the sample (two measurements due to GC and two ones due to EI and FI) in combination with quantitative analysis.

Further example of the same concept was given in the article [110], where the data for petroleum products obtained using GC×GC coupled to EI/CI/FI/SPI MS were compared. It was pointed out that the most exhaustive information can be obtained using EI and FI combination. Unfortunately, this approach involves two separate analyses of the sample using EI and FI, which significantly increases the required analysis time. At the same time, the technique based on the combination of EI and SPI looks more attractive. In this case, the ion source allowed switching between the ionization modes with a frequency of up to 80 Hz, actually emulating simultaneous data acquisition using both ionization techniques [111]. This advantage was clearly

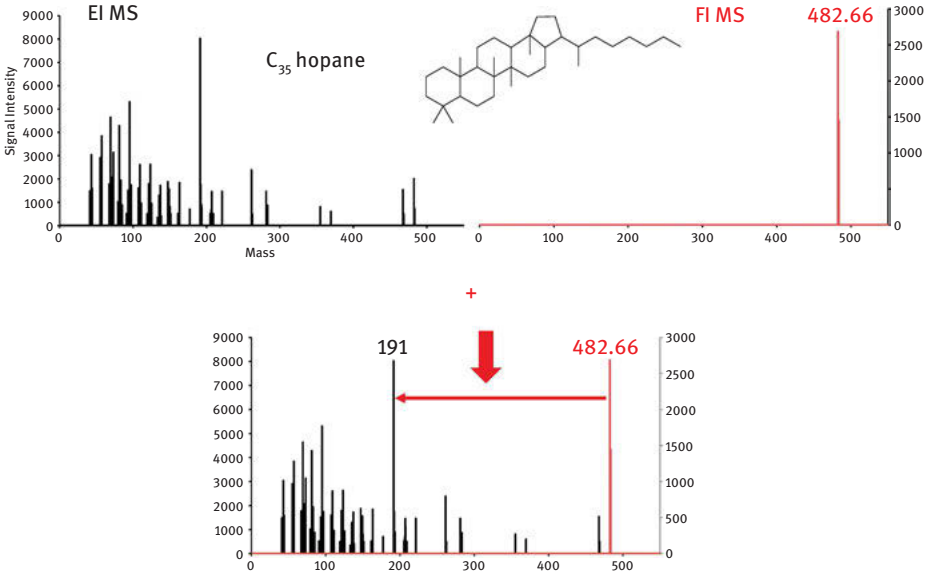

Figure 14.11: An example of combining using electron and field ionization data to yield pseudo-MS/MS parent-daughter spectrum. Reprinted from [108]. Copyright (2018) Elsevier.

demonstrated by the study of diesel fuel by both GC×GC-MS and GC-MS, which resulted in identification of various aromatic compounds.

There are also examples of combining GC×GC technique with ultrahigh resolution mass analyzers. Thus GC×GC-MS-EI and CI instrument on the basis of Orbitrap was used for characterization of biofuels (Figure 14.12) [112].

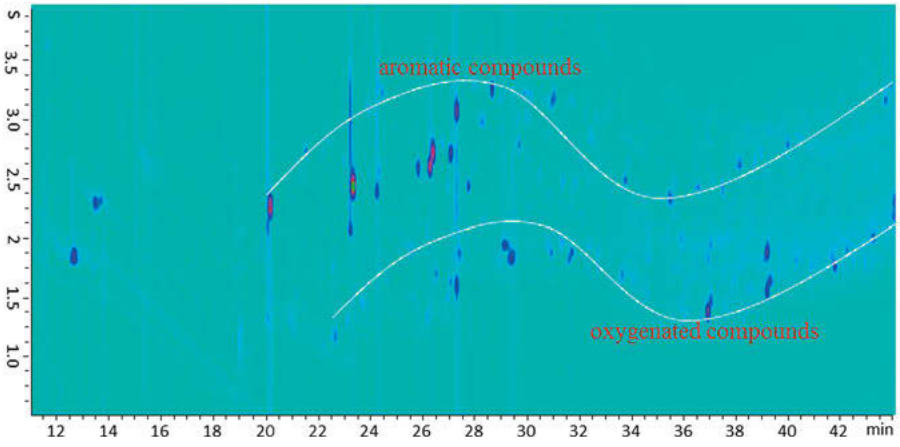

Figure 14.12: Total ion current GC×GC-MS-EI chromatogram of cellulose bio-oil. Reprinted from [112]. Copyright (2020) John Wiley & Sons, Inc.

Table 14.1: Characteristics and practical applications of hyphenated gas chromatography-mass spectrometry methods for oil exploration.

Gas chromatography option	Ionization method	Method capabilities	Advantages and disadvantages	Examples of solved applied problems [Ref.]
			Nonpolar and semipolar compounds of oil	
GC	EI	Target and nontarget analysis of mixtures with the possibility of using SIM.	The cheapest and most convenient method of analysis using a well-developed methodological base. It does not allow analyzing mixtures of relatively high-boiling oil compounds. The absence of molecular ion peaks in the spectra of compounds with a large number of carbon atoms or branching complicates the interpretation of the data	Detection of geochemical biomarkers in oils [19–21,26]
				Search for new biomarker compounds in oils [27,30, 31]
				Simulation of oil formation processes [28, 29]
		Targeted analysis of specific of compound classes using SRM	Provides greater sensitivity and selectivity than conventional GC-MS with recording the complete spectra. Does not allow nontargeted analysis; detector response may differ from that observed during full spectra recording, which distorts the results of using classical approaches	Detection of geochemical biomarkers in oils [113–115]
		Structural group analysis	It is used to calculate the relative content of hydrocarbons in oils (in some cases, it requires individual calibration of responses). Not intended for targeting compounds	Determination of the content of the main hydrocarbon classes [24, 25]
	EI with vibrationally cold molecules (SMB-MS)	Targeted and nontargeted analysis of complex mixtures	Compared to IE, it provides a higher intensity of molecular ion peaks while maintaining a set of characteristic ions. The method is still not widely used; the methodological base for its application in the analysis of oils is not yet sufficiently developed	Study of the qualitative composition of hydrocarbon mixtures [11–13, 116]

	CI	Targeted analysis of complex mixtures	In most cases, it provides the formation of protonated molecules or cluster ions of analytes. The formation of a set of diagnostic ions does not occur; for hydrocarbons, the method is structurally not informative. At the same time, its use in tandem mass spectrometry allows increasing the information content of mass spectra.	Supplements IE data to identify compounds [32] Targeted detection of compounds by generating intense protonated molecules or cluster ions [33]
	APCI	Targeted analysis of compound mixtures	Like CI, the method allows determination of the molecular weights of compounds, but does not provide reliable information about the structure. The use of tandem MS and ultra-high-resolution MS drastically expands the boundaries of its applicability.	Detection of geochemical biomarkers and other marker compounds in oils [37, 39, 52]
	FI	Targeted analysis of compound mixtures	Provides the formation of stable molecular radical ions, which makes it possible to determine the molecular weights of analytes. Compared with CI and APCI, it provides a higher ionization efficiency of aliphatic compounds. In this case, however, there is a blurring of the zones of high-molecular-weight components due to their sorption on the emitter	Detection of hydrocarbons of various structures [41]
	PI	Targeted and nontargeted analysis of compound mixtures	Despite the fact that the method is relatively “soft,” the higher energy of ionizing photons can lead to the formation of sets of characteristic ions.	Selective detection of various hydrocarbon classes by using changes in the energy of ionizing photons [43,44]
GC-GC	EI	Targeted analysis of compound mixtures	The possibility of additional separation of the selected elution zone can significantly reduce the detection limits of target compounds.	Determination of polyaromatic compounds in oils [55]

(continued)

Table 14.1 (continued)

Gas chromatography option	Ionization method	Method capabilities	Advantages and disadvantages	Examples of solved applied problems [Ref.]
GC×GC	EI	Targeted and nontargeted analysis of compound mixtures	A sharp increase in chromatographic resolution in comparison with 1D-GC can significantly increase the information content of the results obtained and the probability of component identification. In this case, however, as in GC-EI, molecular ion peaks may be absent.	Detection of geochemical biomarkers in oils [58, 61–63, 65, 67–69, 117]
				Detection of organ-element compounds in oils and refined products [75, 77, 84, 88]
				Study of the degradation processes of oils and refined products [89, 90–93, 98]
		Structural group analysis of mixtures of compounds	The ability to take into account the position of chromatographic peaks on a two-dimensional plane of the chromatogram increases the analysis accuracy compared to GC-EIMS.	Determination of the content of the main hydrocarbon classes [59, 81–83, 87, 180]
	FI	Targeted analysis of compound mixtures	As in the previous case, the disadvantages and advantages of using these ionization methods in combination with GC as a whole remain. However, an increase in chromatographic resolution allows an increase in the probability of correct identification and a decrease in detection limits.	Detection of hydrocarbons of various structures [102]
	PI	Targeted and nontargeted analysis of compound mixtures		Nontargeted analysis of hydrocarbon mixtures [103]
				Selective detection of aromatic compounds [104]

Combination of EI and FI	Targeted and nontargeted analysis of compound mixtures	The combination of “hard” and “soft” ionization methods can dramatically increase the possibilities of identifying compounds in mixtures.	Detection of geochemical biomarkers in oils [108,109]
Combination of EI and APCI	Targeted and nontargeted analysis of compound mixtures		Detection of aromatic compounds in oil refined products [111]

14.6 Conclusion

Summarizing the foregoing, it should be noted that despite the comparatively developed and routine nature of GC-MS, the emergence of new approaches to the chromatographic separation of sample components and the elaboration of ion separation technologies still has significant prospects to the analysis of crude oils and their transformation products. Further development of the methods is aimed at reducing the limits of detection of various compounds and increasing the structural and analytical information content of the obtained data. In this regard, significant prospects are opening up with the further experimental developments of combinations of two-dimensional and multidimensional GC with various versions of MS. The summarized information concerning GC- and MDGC-MS application to the analysis of crude oils and refinery products is presented in Table 14.1

References

[1] Zaikin VG, Tret'yakov KV. History of mass spectrometry in dates. Moscow, Russia, VMSO, 2018. (in Russian).
[2] Gohlke RS, McLafferty FW. Early gas chromatography/mass spectrometry. J Am Soc Mass Spectrom, 1993, 4, 367–371.
[3] Rodgers RP, McKenna AM. Petroleum analysis. Anal Chem, 2011, 83, 4665–4687.
[4] Alama MS, Harrison RM. Recent advances in the application of 2-dimensional gas chromatography with soft and hard ionisation time-of-flight mass spectrometry in environmental analysis. Chem Sci, 2016, 7, 3968–3977.
[5] Li D-X, Gan L, Bronja A, Schmitz OJ. Gas chromatography coupled to atmospheric pressure ionization mass spectrometry (GC-API-MS): Review. Anal Chim Acta, 2015, 891, 43–61.
[6] Niyonsaba E, Manheim JM, Yerabolu R, Kenttamaa HI. Recent advances in petroleum analysis by mass spectrometry. Anal Chem, 2019, 91, 156–177.
[7] Borisov RS, Kulikova LN, Zaikin VG. Mass Spectrometry in petroleum chemistry (petroleomics) (review). Pet Chem, 2019, 59, 1055–1076.
[8] Marshall AG, Rodgers RP. Acc. Chem. Res. Petroleomics: The next grand challenge for chemical analysis. Acc Chem Res, 2004, 37, 53–59.
[9] Vigdergauz MS. Gas chromatography as an oil investigation technique, Moscow, Russia, Nauka-Publisher, 1973. (In Russian).
[10] Amirav A, Gordin A, Poliak M, Fialkov AB. Gas chromatography-mass spectrometry with supersonic molecular beams. J Mass Spectrom, 2008, 43, 141–163.
[11] Fialkov AB, Gordin A, Amirav A. Hydrocarbons and fuels analyses with the supersonic gas chromatography mass spectrometry–the novel concept of isomer abundance analysis. J Chromatogr, 2008, 1195, 127–135.
[12] Islam F, Granot O, McIndoe JS. Determination of n-alkanes in jet fuel by cold-electron ionization gas chromatography–mass spectrometry. Anal Lett, 2017, 50, 1593–1601.
[13] Goodman-Rendall KAS, Zhuang YR, Amirav A, Chan AWH. Resolving detailed molecular structures in complex organic mixtures and modeling their secondary organic aerosol formation. Atmos Environ, 2016, 128, 276–285.

[14] Revelskii IA, Yashin YS, Voznesenskii VN, Kurochkin VK, Kostyanovskii RG. Atmospheric pressure photoionization mass spectrometry of n-alkanes, alcohols, ketones, esters and amines. Bull Acad Sci USSR Div Chem Sci, 1986, 35, 1806–1810.
[15] Revelsky IA, Yashin YS. New approach to complex organic compounds mixtures analysis based on gas chromatography-atmospheric pressure photoionization-mass-spectrometry. Talanta, 2012, 102, 110–113.
[16] Makarov A. Electrostatic axially harmonic orbital trapping: A high-performance technique of mass analysis. Anal Chem, 2000, 72, 1156–1162.
[17] Peterson AC, Hauschild J-P, Quarmby ST, Krumwiede D, Lange O, Lemke RAS, Grosse-Coosmann F, Horning S, Donohue TJ, Westphall MS. et al, Development of a GC/quadrupole-orbitrap mass spectrometer, part I: Design and characterization. Anal Chem, 2014, 86, 10036–10043.
[18] Peters KE, Walters CC, Moldowan JM. The biomarker guide, vol. 2: Biomarkers and isotopes in petroleum exploration and earth history. Cambridge, England, Cambridge Univ. Press, 2005.
[19] Pekov SI, Kononikhin AS, Popov IA, Kukuev EN, Varfolomeev SD, Nikolaev EN. Determination of hydrocarbon composition of volcano oil by GC-MS method. Izv Akad Nauk, Ser Energ, 2014, N 2, 170–173, (in Russian).
[20] Zhu Y, Sun L, Hao F, Tuo L. Geochemical composition and origin of Tertiary oils in the Yinggehai and Qiongdongnan Basins, offshore South China Sea. Mar Pet Geol, 2018, 96, 139–153.
[21] Sun X, Zhang T, Sun Y, Milliken KL, Sun D. Geochemical evidence of organic matter source input and depositional environments in the lower and upper Eagle Ford Formation, south Texas. Org Geochem, 2016, 98, 66–81.
[22] Wang X, Cai T, Wen W, Zhang Z. Effect of biosurfactant on biodegradation of heteroatom compounds in heavy oil. Fuel, 2018, 230, 418–429.
[23] Lobodin VV, Robbins WK, Lu J, Rodgers RP. Separation and characterization of reactive and non-reactive sulfur in petroleum and its fractions. Energy Fuels, 2015, 29, 6177–6186.
[24] Brodskii ES, Shelepchikov AA. Three-dimensional ionic mass chromatograms of hydrocarbon groups and oil heteroatomic compounds. Mass-Spektrometriya, 2012, 9, 197–201, in Russian.
[25] Brodskii ES, Shelepchikov AA, Kalinkevich GA, Mir-Kadyrova EY, Zhil'nikov VG. Type analysis of petroleum heavy distillates and residua by gas chromatography/mass spectrometry. Pet Chem, 2014, 54, 28–36.
[26] Yang C, Lambert P, Zhang G, Yang Z, Landriault M, Hollebone B, Fieldhouse B, Mirnaghi F, Brown CE. Characterization of chemical fingerprints of unconventional Bakken crude oil. Environ Pollut, 2017, 230, 609–620.
[27] Nytoft HP, Vukovic NS, Kildahl-Andersen G, Rise F, Zivotic DR, Stojanovic KA. Identification of a novel series of benzohopanes and their geochemical significance. Energy Fuels, 2016, 30, 5563–5575.
[28] Gordadze GN, Poshibaeva AR, Giruts MV, Perevalova AA, Koshelev VN. Formation of petroleum hydrocarbons from prokaryote biomass: 1. Formation of petroleum biomarker hydrocarbons from Thermoplasma sp. Archaea biomass. Pet Chem, 2018, 58, 186–189.
[29] Gordadze GN, Poshibaeva AR, Giruts MV, Gayanova AA, Semenova EM, Koshelev VN. Formation of petroleum hydrocarbons from prokaryote biomass: 2. formation of petroleum hydrocarbon biomarkers from biomass of Geobacillus jurassicus Bacteria isolated from crude oil. Pet Chem, 2018, 58, 1005–1012.
[30] Gordadze GN, Kerimov VY, Gaiduk AV, Giruts MV, Lobusev MA, Serov SG, Kuznetsov NB, Romanyuk TV. The first results of study of hydrocarbon biomarkers and hydrocarbons of a diamond-like structure in the Riphean, Vendian, and Lower Cambrian rocks of the Katanga Saddle. Dokl Earth Sci, 2018, 478, 253–257.

[31] Smirnov MB, Poludetkina EN. Assessment of bioproduction relevance in the photic layer anoxia conditions at the formation of dispersed organic matter of source rocks and oils by mass spectrometry data. Mass-Spektrometriya, 2018, 15, 93–101, in Russian.
[32] Huang H, Lartera SR, Love GD. Analysis of wax hydrocarbons in petroleum source rocks from the Damintun depression, eastern China, using high temperature gas chromatography. Org Geochem, 2003, 34, 1673–1687.
[33] Creaser CS, Krokos F, Óneill KE, Smith MJC, McDowell PG. Selective chemical ionization of nitrogen and sulfur heterocycles in petroleum fractions by ion trap mass spectrometry. J Am Soc Mass Spectrom, 1993, 4, 322–326.
[34] Hsu CS, Shi Q. Prospects for petroleum mass spectrometry and chromatography. Sci China Chem, 2013, 56, 833–839.
[35] Jin C, Viidanoja J, Li M, Zhang Y, Ikonen E, Root A, Romanczyk M, Manheim J, Dziekonski E, Kenttämaa HI. Comparison of atmospheric pressure chemical ionization and field ionization mass spectrometry for the analysis of large saturated hydrocarbons. Anal Chem, 2016, 88, 10592–10598.
[36] Wu C, Qian K, Walters CC, Mennito A. Application of atmospheric pressure ionization techniques and tandem mass spectrometry for the characterization of petroleum components. Int J Mass Spectrom, 2015, 377, 728–735.
[37] Lobodin VV, Maksimova EV, Rodgers RP. Gas chromatography/atmospheric pressure chemical ionization tandem mass spectrometry for fingerprinting the Macondo oil spill. Anal Chem, 2016, 88, 6914–6922.
[38] Stevens D, Shi Q, Hsu CS. Novel analytical technique for petroleum biomarker analysis. Energy Fuels, 2012, 27, 167–171.
[39] Briker Y, Ring Z, Iacchelli A, McLean N, Fairbridge C, Malhotra R, Coggiola MA, Young SE. Diesel fuel analysis by GC-FIMS: Normal paraffins, isoparaffins, and cycloparaffins. Energy Fuels, 2001, 15, 996–1002.
[40] Briker Y, Ring Z, Iacchelli A, McLean N, Rahimi PM, Fairbridge C, Malhotra R, Coggiola MA, Young SE. Diesel fuel analysis by GC–FIMS: Aromatics, n-paraffins, and isoparaffins. Energy Fuels, 2001, 15, 23–37.
[41] Ni H, Hsu CS, Ma C, Shi Q, Xu C. Separation and characterization of olefin/paraffin in coal tar and petroleum coker oil. Energy Fuels, 2013, 27, 50–75.
[42] Mühlberger F, Streibel T, Wieser J, Ulrich A, Zimmermann R. Single photon ionization time-of-flight mass spectrometry with a pulsed electron beam pumped excimer VUV lamp for on-line gas analysis: Setup and first results on cigarette smoke and human breath. Anal Chem, 2005, 77, 7408–7414.
[43] Isaacman G, Wilson KR, Chan AWH, Worton DR, Kimmel JR, Nah T, Hohaus T, Gonin M, Kroll JH, Worsnop DR, Goldstein AH. Improved resolution of hydrocarbon structures and constitutional isomers in complex mixtures using gas chromatography-vacuum ultraviolet-mass spectrometry. Anal Chem, 2012, 84, 2335–2342.
[44] Worton DR, Zhang H, Isaacman-vanwertz G, Chan AWH, Wilson KR, Goldstein AH. Comprehensive chemical characterization of hydrocarbons in NIST standard reference material 2779 Gulf of Mexico crude oil. Environ Sci Technol, 2015, 49, 13130–13138.
[45] Wohlfahrt S, Fischer M, Saraji-Bozorgzad M, Matuschek G, Streibel T, Post E, Denner T, Zimmermann R. Rapid comprehensive characterization of crude oils by thermogravimetry coupled to fast modulated gas chromatography–single photon ionization time-of-flight mass spectrometry. Anal Bioanal Chem, 2013, 405, 7107–7116.
[46] Revelsky IA, Tikhonova IN, Yashin YS. Fast detection of polycyclic aromatic hydrocarbons in complex mixtures of organic compounds based on gas chromatography–mass spectrometry with atmospheric pressure photoionization. Eur J Mass Spectrom (Chichester), 2015, 21, 753–757.

[47] Sessions AL, Zhang L, Welander PV, Doughty D, Summons RE, Newman DK. Identification and quantification of polyfunctionalized hopanoids by high temperature gas chromatography–mass spectrometry. Org Geochem, 2013, 56, 120–130.
[48] Sutton PA, Rowland SJ. High temperature gas chromatography–time-of-flight-mass spectrometry (HTGC–ToF-MS) for high-boiling compounds. J Chromatogr A, 2012, 1243, 69–80.
[49] Kersten H, Kroll K, Haberer K, Brockmann KJ, Benter T, Peterson A, Makarov A. Design study of an atmospheric pressure photoionization interface for GC-MS. J Am Soc Mass Spectrom, 2016, 27, 607–614.
[50] Powers JB, Campagna SR. Design and evaluation of a gas chromatograph-atmospheric pressure chemical ionization interface for an exactive orbitrap mass spectrometer. J Amer Soc Mass Spectrom, 2019, 30, 2369–2379.
[51] Kondyli A, Schrader W. High-resolution GC/MS studies of a light crude oil fraction. J Mass Spectrom, 2019, 54, 47–54.
[52] Barrow MP, Peru KM, Headley JV. An added dimension: GC atmospheric pressure chemical ionization FTICR MS and the Athabasca oil sands. Anal Chem, 2014, 86, 8281–8288.
[53] Benigni P, DeBord JD, Thompson CJ, Gardinali P, Fernandez-Lima F. Increasing polyaromatic hydrocarbon (PAH) molecular coverage during fossil oil analysis by combining gas chromatography and atmospheric-pressure laser ionization Fourier transform ion cyclotron resonance mass spectrometry (FT-ICR MS). Energy Fuels, 2016, 30, 196–203.
[54] Boswell H, Carrillo KT, Górecki T. Evaluation of the performance of cryogen-free thermal modulation-based comprehensive two-dimensional gas chromatography-time-of-flight mass spectrometry (GC×GC-TOFMS) for the qualitative analysis of a complex bitumen sample. Separations, 2020, 7, 13. doi:10.3390/separations7010013.
[55] Wei O, Xu X, Zhang Y, Yang B, Ye Q, Yang Z. Multidimensional gas chromatography–mass spectrometry method for fingerprinting polycyclic aromatic hydrocarbons and their alkyl-homologs in crude oil. Anal Lett, 2018, 51, 483–495.
[56] Prata PS, Alexandrino GL, Mogollón NGS, Augusto F. Discriminating Brazilian crude oils using comprehensive two-dimensional gas chromatography–mass spectrometry and multiway principal component analysis. J Chromatogr A, 2016, 1472, 99–106.
[57] Alexandrino GL, Augusto F. Comprehensive two-dimensional gas chromatography–mass spectrometry/selected ion monitoring (GC×GC–MS/SIM) and chemometrics to enhance inter-reservoir geochemical features of crude oils. Energy Fuels, 2018, 32, 8017–8023.
[58] Zhang W, Zhu S, He S, Wang Y. Screening of oil sources by using comprehensive two-dimensional gas chromatography/time-of-flight mass spectrometry and multivariate statistical analysis. J Chromatogr A, 2015, 1380, 162–170.
[59] Jennerwein MK, Eschner MS, Wilharm T, Zimmermann R, Gröger TM. Proof of concept of high-temperature comprehensive two-dimensional gas chromatography time-of-flight mass apectrometry for two-dimensional simulated distillation of crude oils. Energy Fuels, 2017, 31, 11651–11659.
[60] Vanini G, Pereira VB, Romão W, Gomes AO, Oliveira LMSL, Dias JCM, Azevedo DA. Analytical advanced techniques in the molecular-level characterization of Brazilian crude oils. Microchem J, 2018, 137, 111–118.
[61] Quirino AB, Azevedo DA. Uncommon steranes in Brazilian marginal crude oils: Dinoflagellate molecular fossils in the Sergipe-Alagoas Basin. Brazil Org Geochem, 2016, 99, 38–52.
[62] Araújo BQ, Neto FRA, Azevedo DA. Occurrence of extended tetracyclic polyprenoid series in crude oils. Org Geochem, 2018, 118, 27–35.
[63] Laakia J, Casilli A, Araújo BQ, Gonçalves FTT, Marotta E, Oliveira CJF, Carbonezi CA, Loureiro MRB, Azevedo DA, Neto FRA. Characterization of unusual tetracyclic compounds and possible

novel maturity parameters for Brazilian crude oils using comprehensive two-dimensional gas chromatography-time of flight mass spectrometry. Org Geochem, 2017, 106, 93–104.
[64] Soares RF, Pereira R, Silva RSF, Mogollon L, Azevedo DA. Comprehensive two-dimensional gas chromatography coupled to time of flight mass spectrometry: New biomarker parameter proposition for the Characterization of biodegraded oil. J Braz Chem Soc, 2013, 24, 1570–1581.
[65] Kiepper AP, Casilli A, Azevedo DA. Depositional paleoenvironment of Brazilian crude oils from unusual biomarkers revealed using comprehensive two dimensional gas chromatography coupled to time of flight mass spectrometry. Org Geochem, 2014, 70, 62–75.
[66] Silva RSF, Aguiar HGM, Rangel MD, Azevedo DA, Neto FRA. Comprehensive two-dimensional gas chromatography with time of flight mass spectrometry applied to biomarker analysis of oils from Colombia. Fuel, 2011, 90, 2694–2699.
[67] Santos LC, Da Cruz GF, Ávila BMF, Pereira VB, Azevedo DA. Exploratory analysis of campos basin crude oils via geochemical parameters by comprehensive two-dimensional gas chromatography/time-of-flight mass spectrometry. Energy Fuels, 2018, 32, 10321–10332.
[68] Silva RC, Silva RSF, de Castro EVR, Peters KE, Azevedo DA. Extended diamondoid assessment in crude oil using comprehensive two-dimensional gas chromatography coupled to time-of-flight mass spectrometry. Fuel, 2013, 112, 125–133.
[69] Wang Y, Ma W, Zhou N, Ren J, Cao J. Analyzing crude oils from the Junggar Basin (NW China) using comprehensive two-dimensional gas chromatography coupled with time-of-flight mass spectrometry (GC×GC-TOFMS). Acta Geochim, 2017, 36, 66–73.
[70] Zhu G, Wang M, Chi L, Li J, Wu Z, Zhang Z. Discovery and molecular characterization of organic caged compounds and polysulfanes in Zhongba81 crude oil, Sichuan Basin. China Energy Fuels, 2020. doi:10.1021/acs.energyfuels.0c00392.
[71] Pollo BJ, Alexandrino GL, Augusto F, Hantao LW. The impact of comprehensive two-dimensional gas chromatography on oil and gas analysis: Recent advances and applications in petroleum industry. TrAC Trends Anal Chem, 2018, 105, 202–207.
[72] Frysinger GS, Gaines RB. Comprehensive two-dimensional gas chromatography with mass spectrometric detection (GC x GC/MS) applied to the analysis of petroleum. J High Res Chromatogr, 1999, 22, 215–255.
[73] Ávila BMF, Pereira R, Gomes AO, Azevedo DA. Chemical characterization of aromatic compounds in extra heavy gas oil by comprehensive two-dimensional gas chromatography coupled to time-of-flight mass spectrometry. J Chromatogr A, 2011, 1218, 3208–3216.
[74] Parastar H, Radović JR, Jalali-Heravi M, Diez S, Bayona JM, Tauler R. Resolution and quantification of complex mixtures of polycyclic aromatic hydrocarbons in heavy fuel oil sample by means of GC× GC-TOFMS combined to multivariate curve resolution. Anal Chem, 2011, 83, 9289–9297.
[75] Ávila BMF, Pereira VB, Gomes AO, Azevedo DA. Speciation of organic sulfur compounds using comprehensive two-dimensional gas chromatography coupled to time-of-flight mass spectrometry: A powerful tool for petroleum refining. Fuel, 2014, 126, 188–193.
[76] Han Y, Zhang Y, Xu C, Hsu CS. Molecular characterization of sulfur-containing compounds in petroleum. Fuel, 2018, 221, 144–158.
[77] Von Mühlen C, de Oliveira EC, Zini CA, Caramão EB, Marriott PJ. Characterization of nitrogen-containing compounds in heavy gas oil petroleum fractions using comprehensive two-dimensional gas chromatography coupled to time-of-flight mass spectrometry. Energy Fuels, 2010, 24, 3572–3580.

[78] Tessarolo NS, Dos Santos LRM, Silva RSF, Azevedo DA. Chemical characterization of bio-oils using comprehensive two-dimensional gas chromatography with time-of-flight mass spectrometry. J Chromatogr A, 2014, 1279, 68–75.
[79] Li S, Cao J, Hu S, Luo G. Characterization of compounds in unresolved complex mixtures (UCM) of a Mesoproterzoic shale by using GC×GC-TOFMS. Mar Pet Geol, 2015, 99, 791–800.
[80] Lissitsyna K, Huertas S, Quintero LC, Polo LM. PIONA analysis of kerosene by comprehensive two-dimensional gas chromatography coupled to time of flight mass spectrometry. Fuel, 2014, 116, 716–722.
[81] Jennerwein MK, Eschner M, Gröger T, Wilharm T, Zimmermann R. Complete group-type quantification of petroleum middle distillates based on comprehensive two-dimensional gas chromatography time-of-flight mass spectrometry (GC×GC-TOFMS) and visual basic scripting. Energy Fuels, 2014, 28, 5670–5681.
[82] Jennerwein MK, Sutherland AC, Eschner M, Gröger T, Wilharm T, Zimmermann R. Quantitative analysis of modern fuels derived from middle distillates – The impact of diverse compositions on standard methods evaluated by an offline hyphenation of HPLC-refractive index detection with GC×GC-TOFMS. Fuel, 2017, 187, 16–25.
[83] Jennerwein M, Eschner M, Wilharm T, Gröger T, Zimmermann R. Evaluation of reversed phase versus normal phase column combination for the quantitative analysis of common commercial available middle distillates using GC × GC-TOFMS and Visual Basic Script. Fuel, 2019, 235, 336–338.
[84] Kulsing C, Rawson P, Webster RL, Evans DJ, Marriott PJ. Group-type analysis of hydrocarbons and sulfur compounds in thermally stressed Merox jet fuel samples. Energy Fuels, 2017, 31, 8978–8984.
[85] Li S, Cao J, Hu S. Analyzing hydrocarbon fractions in crude oils by two-dimensional gas chromatography/time-of-flight mass spectrometry under reversed-phase column system. Fuel, 2015, 158, 191–199.
[86] Hu SZ, Li SF, Cao J, Zhang DM, Ma J, He S, Wang XL, Wu M. A comparison of normal and reversed phase columns in oil analysis by comprehensive two-dimensional gas chromatography with time-of-flight mass spectrometry. Pet Sci Technol, 2014, 32, 565–574.
[87] Coutinho DM, Franca D, Vanini G, Mendes LAN, Gomes AO, Pereira VB, Avila BMF, Azevedo DA. Rapid hydrocarbon group-type semi-quantification in crude oils by comprehensive two-dimensional gas chromatography. Fuel, 2018, 220, 379–388.
[88] Fontanive FC, Souza-Silva EA, Da Silva JM, Caramão EB, Zini CA. Characterization of sulfur and nitrogen compounds in Brazilian petroleum derivatives using ionic liquid capillary columns in comprehensive two-dimensional gas chromatography with time-of-flight mass spectrometric detection. J Chromatogr A, 2016, 1461, 131–143.
[89] Scarlett AG, Despaigne-Diaz AI, Wilde SA, Grice K. An examination by GC×GC-TOFMS of organic molecules present in highly degraded oils emerging from Caribbean terrestrial seeps of Cretaceous age. Geosci Front, 2019, 10, 5–15.
[90] Aitken CM, Head IM, Jones DM, Rowland SJ, Scarlett AG, West CE. Comprehensive two-dimensional gas chromatography-mass spectrometry of complex mixtures of anaerobic bacterial metabolites of petroleum hydrocarbons. J Chromatogr A, 2018, 1536, 96–109.
[91] O'Reilly KT, Mohler RE, Zemo DA, Ahn S, Tiwary AK, Magaw RI, Devine CE, Synowiec KA. Identification of ester metabolites from petroleum hydrocarbon biodegradation in groundwater using GC×GC-TOFMS. Environ Toxicol Chem, 2015, 34, 1959–1961.
[92] Forsythe JC, Kenyon-Roberts S, O'Donnell M, Betancourt SS, Masurek N, Gisolf A, Bennett B, Nelson RK, Canas JA, Reddy CM, Peters KE, Zuo JY, Mullins OC. Biodegradation and water washing in a spill-fill sequence of oilfields. Fuel, 2019, 237, 707–719.

[93] Wang H, Zhang S, Weng N, Zhang B, Zhu G, Liu L. Discovery and identification of a series of alkyl decalin isomers in petroleum geological samples. Analyst, 2015, 140, 4694–4701.
[94] Potgieter H, Bekker R, Govender A, Rohwer E. Two-dimensional gas chromatography-online hydrogenation for improved characterization of petrochemical samples. J Chromatogr A, 2016, 1445, 118–125.
[95] Halket JM, Zaikin VG. Derivatization in mass spectrometry—7. On-line derivatization/degradation. Eur J Mass Spectrom, 2006, 12, 1–13.
[96] Zaikin V, Halket JM. A Handbook of derivatives for mass spectrometry. Chichester, England, IM Publications, 2009.
[97] Kehimkar B, Hoggard JC, Marney LC, Billingsley MC, Fraga CG, Bruno TJ, Synovec RE. Correlation of rocket propulsion fuel properties with chemical composition using comprehensive two-dimensional gas chromatography with time-of-flight mass spectrometry followed by partial least squares regression analysis. J Chromatogr A, 2014, 1327, 132–140.
[98] Webster RL, Rawson PM, Kulsing C, Evans DJ, Marriott PJ. Investigation of the thermal oxidation of conventional and alternate aviation fuels with comprehensive two-dimensional gas chromatography accurate mass quadrupole time-of-flight mass spectrometry. Energy Fuels, 2017, 31, 4886–4894.
[99] Alam MS, Stark C, Harrison RM. Using variable ionization energy time-of-flight mass spectrometry with comprehensive GC×GC to identify isomeric species. Anal Chem, 2016, 88, 4211–4220.
[100] Alam MS, Zeraati-Rezaei S, Stark C, Xu H, MacKenzie AR, Harrison RM, Liang Z. Mapping and quantifying isomer sets of hydrocarbons (≥C12) in diesel exhaust, lubricating oil and diesel fuel samples using GC×GC-ToF-MS. Atmos Meas Tech, 2018, 11, 3047–3058.
[101] Freye CE, Moore NR, Synovec RE. Enhancing the chemical selectivity in discovery-based analysis with tandem ionization time-of-flight mass spectrometry detection for comprehensive two-dimensional gas chromatography. J Chromatogr A, 2018, 1537, 99–108.
[102] Genuit W, Chaabani H. Comprehensive two-dimensional gas chromatography-field ionization time-of-flight mass spectrometry (GCxGC-FI-TOFMS) for detailed hydrocarbon middle distillate analysis. Int J Mass Spectrom, 2017, 413, 27–32.
[103] Giri A, Coutriade M, Racaud A, Okuda K, Dane J, Cody RB, Focant J-F. Molecular characterization of volatiles and petrochemical base oils by photo-ionization GC×GC-TOF-MS. Anal Chem, 2017, 89, 5395–5403.
[104] Nowak JA, Weber RJ, Goldstein AH. Quantification of isomerically summed hydrocarbon contributions to crude oil by carbon number, double bond equivalent, and aromaticity using gas chromatography with tunable vacuum ultraviolet ionization. Analyst, 2018, 143, 1396–1405, [correction: Analyst 2019, 144, 3898].
[105] França D, Pereira VB, Coutinho DM, Ainstein LM, Azevedo DA. Speciation and quantification of high molecular weight paraffins in Brazilian whole crude oils using high-temperature comprehensive two-dimensional gas chromatography. Fuel, 2018, 234, 1154–1164.
[106] Ristic ND, Djokic MR, Konist A, Van Geem KM, Marin GB. Quantitative compositional analysis of Estonian shale oil using comprehensive two dimensional gas chromatography. Fuel Process Technol, 2017, 167, 241–249.
[107] van Stee LLP, Beens J, Vreuls RJJ, Brinkman UAT. Comprehensive two-dimensional gas chromatography with atomic emission detection and correlation with mass spectrometric detection: Principles and application in petrochemical analysis. J Chromatogr A, 2003, 1019, 89–99.
[108] Walters CC, Wang FC, Higgins MB, Madincea ME. Universal biomarker analysis using GC×GC with dual FID and ToF-MS (EI/FI) detection. Org Geochem, 2018, 115, 57–66.

[109] Walters CC, Wang FC, Higgins MB, Madincea ME. Universal biomarker analysis: Aromatic hydrocarbons. Org Geochem, 2018, 124, 205–214.
[110] Giri A, Coutriade M, Racaud A, Stefanuto P-H, Okuda K, Dane J, Cody RB, Focant J-F. Compositional elucidation of heavy petroleum base oil by GC × GC-EI/PI/CI/FI-TOFMS. J Mass Spectrom, 2019, 54, 148–157.
[111] Eschner MS, Gröger TM, Horvath T, Gonin M, Zimmermann R. Quasi-simultaneous acquisition of hard electron ionization and soft single-photon ionization mass spectra during GC/MS analysis by rapid switching between both ionization methods: Analytical concept, setup, and application on diesel fuel. Anal Chem, 2011, 83, 3865–3872.
[112] Hung NV, Mohabeer C, Vaccaro M, Marcotte S, Agasse-Peulon V, Abdelouahed L, Taouk B, Cardinael P. Development of two-dimensional gas chromatography (GC×GC) coupled with orbitrap-technology-based mass spectrometry: Interest in the identification of biofuel composition. J Mass Spectrom, 2020, 55, e4495. doi:10.1002/jms.4495.
[113] Qian Y, Wang Z, Tuo J, Zhang M, Wu C, Zhang T. Multiple reaction monitoring of GC/MS/MS analysis of terpanes and its application to petroleum exploration. Pet Sci Technol, 2017, 35, 134–140.
[114] Stojadinović S, Kostić A, Nytoft HP, Stoianović K. Applicability of calculated vitrinite reflectance for assessment of source rock's organic matter maturity in hyperthermal basins (Banat Depression, Serbia). Pet Chem, 2015, 55, 444–454.
[115] Faraj MAM, Knudsen TS, Stojanović K, Pavlović SI, Nyroft HP, Jovančićević B. GC–MS vs. GC–MS-MS analysis of pentacyclic terpanes in crude oils from Libya and Serbia – A comparison of two methods. J Serb Chem Soc, 2017, 82, 1315–1331.
[116] Keshet U, Fialkov AB, Alon T, Amirav A. A new pulsed flow modulation GC× GC–MS with cold EI system and its application for jet fuel analysis. Chromatografia, 2016, 79, 741–754.
[117] Zhang W, Jiang X, Pang L, Gao X, Zhu S. 2α-Methylhopane: Indicator for oil–source correlation in the pearl river mouth basin, China. Aquat Geochem, 2017, 23, 185–198.

List of contributing authors

Ch 1, Ch 2
Merv Fingas
Spill Science
Edmonton, Alberta, Canada

Ch 2
Chun Yang
Emergencies Science and Technology Section (ESTS),
Environment and Climate Change Canada
Ottawa, ON, Canada
E-mail: chun.yang@ec.gc.ca

Zhendi Wang
Emergencies Science and Technology Section (ESTS),
Environment and Climate Change Canada
Ottawa, ON, Canada

Zeyu Yang
Emergencies Science and Technology Section (ESTS),
Environment and Climate Change Canada
Ottawa, ON, Canada

Bruce Hollebone
Emergencies Science and Technology Section (ESTS),
Environment and Climate Change Canada
Ottawa, ON, Canada

Ben Fieldhouse
Emergencies Science and Technology Section (ESTS),
Environment and Climate Change Canada
Ottawa, ON, Canada

Patrick Lambert
Emergencies Science and Technology Section (ESTS),
Environment and Climate Change Canada
Ottawa, ON, Canada

Ch 3
Ian J. Vander Meulen
Department of Civil, Geological and Environmental Engineering
University of Saskatchewan
57 Campus Drive
Saskatoon
Saskatchewan
Canada S7N 5A9
and
Watershed Hydrology and Ecology Research Division
Water Science and Technology Directorate
Environment and Climate Change Canada
11 Innovation Boulevard
Saskatoon
Saskatchewan
Canada S7N 3H5

Rory P. Downham
Department of Chemistry
University of Warwick
Coventry
CV4 7AL
United Kingdom

Latifa Alostad
Department of Chemistry
University of Warwick
Coventry
CV4 7AL
United Kingdom

Kerry M. Peru
Watershed Hydrology and Ecology Research Division
Water Science and Technology Directorate
Environment and Climate Change Canada
11 Innovation Boulevard
Saskatoon
Saskatchewan
Canada S7N 3H5

https://doi.org/10.1515/9783110694529-015

Dena W. McMartin
Department of Civil, Geological and Environmental Engineering
University of Saskatchewan
57 Campus Drive
Saskatoon
Saskatchewan
Canada S7N 5A9
And
Office of the Vice President (Research)
University of Lethbridge
4401 University Drive West
Lethbridge
Alberta
Canada T1K 3M4

Mark P. Barrow
Department of Chemistry
University of Warwick
Coventry
CV4 7AL
United Kingdom

John V. Headley
Watershed Hydrology and Ecology Research Division
Water Science and Technology Directorate
Environment and Climate Change Canada
11 Innovation Boulevard
Saskatoon
Saskatchewan
Canada S7N 3H5
John.headley@canada.ca

Ch 4
M. R. Yakubov
Arbuzov Institute of Organic and Physical Chemistry
FRC Kazan Scientific Center
Russian Academy of Sciences
Kazan
Russia

G. R. Abilova
Arbuzov Institute of Organic and Physical Chemistry
FRC Kazan Scientific Center
Russian Academy of Sciences
Kazan
Russia

S. G. Yakubova
Arbuzov Institute of Organic and Physical Chemistry
FRC Kazan Scientific Center
Russian Academy of Sciences
Kazan
Russia

D. V. Milordov
Arbuzov Institute of Organic and Physical Chemistry
FRC Kazan Scientific Center
Russian Academy of Sciences
Kazan
Russia

N. A. Mironov
Arbuzov Institute of Organic and Physical Chemistry
FRC Kazan Scientific Center
Russian Academy of Sciences
Kazan
Russia

Ch 5
Yunlong Zhang
ExxonMobil Research and Engineering Company
Annandale
NJ 08801
USA

Bruno Schuler
IBM Research – Zurich
8803 Rueschlikon
Switzerland
And
Empa
Swiss Federal Laboratories for Materials Science and Technology
8600 Dübendorf
Switzerland

Fang Liu
Energy Institute and Department of Chemical Engineering
City College of New York
New York
NY 10031
USA

Yosadara Ruiz-Morales
Instituto Mexicano del Petróleo
Eje Central Lázaro Cárdenas Norte 152
México
D.F. 07730
México

Leo Gross
IBM Research – Zurich
8803 Rueschlikon
Switzerland
Andrew E. Pomerantz
Schlumberger-Doll Research
Cambridge
MA 02139
USA

Vincent Pauchard
Energy Institute and Department of Chemical Engineering
City College of New York
New York
NY 10031
USA

Sanjoy Banejee
Energy Institute and Department of Chemical Engineering
City College of New York
New York
NY 10031
USA

Oliver C. Mullins
Schlumberger-Doll Research
Cambridge
MA 02139
USA

Ch 6
Oliver C. Mullins
Schlumberger-Doll Research
Cambridge
MA 02139
USA

Jesus A. Cañas
Schlumberger-Doll Research
Cambridge
MA 02139
USA

Soraya S. Betancourt
Schlumberger-Doll Research
Cambridge
MA 02139
USA

Andrew E. Pomerantz
Schlumberger-Doll Research
Cambridge
MA 02139
USA

Ch 7
Chuanyuan Wanga
Key Laboratory of Coastal Environmental Processes and Ecological Remediation
Yantai Institute of Coastal Zone Research
Chinese Academy of Sciences
Yantai 264003
P.R. China

Shijie He
School of Resource and Environmental Engineering
Ludong University
Yantai 264025
China

Zixuan Zhanga
Key Laboratory of Coastal Environmental Processes and Ecological Remediation
Yantai Institute of Coastal Zone Research
Chinese Academy of Sciences
Yantai 264003
P.R. China

Chs 8, 14
Roman. S. Borisov
A.V. Topchiev Institute of Petrochemical Synthesis RAS
Moscow

Vladimir G. Zaikin
A.V. Topchiev Institute of Petrochemical Synthesis RAS
Moscow

Ch 9
J. R. Radović
Department of Geoscience
University of Calgary
Calgary
Canada T2N1N4
Jagos.Radovic@ucalgary.ca

R. C. Silva
Department of Geoscience
University of Calgary
Calgary
Canada T2N1N4

Ch 10
R. Paul Philp
School of Geosciences
University of Oklahoma
Norman
OK 73019
USA
pphilp@ou.edu

Gregory T. Connock
School of Geosciences
University of Oklahoma
Norman
OK 73019
USA

Ch 11
Christoph Aeppli
Bigelow Laboratory for Ocean Sciences
East Boothbay
ME 04544
USA
caeppli@bigelow.org

Ch 12
Thamina Acter
Department of Mathematical and Physical Sciences
East West University
A/2
Jahurul Islam Avenue
Aftabnagar
Dhaka 1212
Bangladesh

Nizam Uddin
Department of Nutrition and Food Engineering
Faculty of Allied Health Science
Daffodil International University
102, Shukrabad
Dhanmondi
Dhaka 1207
Bangladesh

Sunghwan Kim
Kyungpook National University
Department of Chemistry
Daegu 702-701
Republic of Korea
And
Green-Nano Materials Research Center
Daegu 41566
Republic of Korea

Index

https://doi.org/10.1515/9783110694529-016